B. Rushi Kumar
R. Sivaraj
J. Prakash *Editors*

Advances in Fluid Dynamics

Selected Proceedings of ICAFD 2018

Springer

Lecture Notes in Mechanical Engineering

B. Rushi Kumar · R. Sivaraj · J. Prakash
Editors

Advances in Fluid Dynamics

Selected Proceedings of ICAFD 2018

Springer

Editors
B. Rushi Kumar
Vellore Institute of Technology
Vellore, Tamil Nadu, India

R. Sivaraj
Vellore Institute of Technology
Vellore, Tamil Nadu, India

J. Prakash
University of Botswana
Gaborone, Botswana

Preface

The Department of Mathematics, School of Advanced Sciences, Vellore Institute of Technology (Deemed to be University), Vellore, Tamil Nadu, India had organized the International Conference on Applications of Fluid Dynamics—2018 (ICAFD 2018) during December 13–15, 2018 in association with University of Botswana, Botswana and Society for Industrial and Applied Mathematics (SIAM), USA. The major objective of ICAFD 2018 was to promote scientific and educational activities towards the advancement of common man's life by improving the theory and practice of various disciplines of applied mathematics and mechanics. This prestigious conference was partially financially supported by the Council of Scientific and Industrial Research (CSIR), India. The Department of Mathematics has 110 qualified faculty members and 90 research scholars, and all were delicately involved in organizing ICAFD 2018 grandly. In addition, 30 leading researchers worldwide served as an advisory committee member for this conference. Overall more than 450 participants (Professors/Scholars/Students) enrich their knowledge in the wings of applied mathematics and mechanics.

There were 11 eminent speakers from overseas and 10 experts from various states of India had delivered the keynote address and invited talks in this conference. Many leading scientists and researchers worldwide submitted their quality research articles to ICAFD. Moreover, 171 original research articles were shortlisted for ICAFD 2018 oral presentations authored by dynamic researchers from various states of India and several countries around the world. We hope that ICAFD will further stimulate research in applied mathematics and mechanics; share research interest and information, and create a forum of collaboration and build a trust relationship. We feel honored and privileged to serve the best recent developments in the field of applied mathematics and mechanics to the readers.

A basic premise of this book is that the quality assurance is effectively achieved through the selection of quality research articles by the scientific committee that consists of more than 100 reviewers from all over the world. This book comprises the contribution of several dynamic researchers in 90 chapters. Each chapter identifies the existing challenges in the areas of differential equations, fluid dynamics and Numerical methods and emphasizes the importance of establishing

new methods and algorithms to addresses the challenges. Each chapter presents a selection of research problem, the technique suitable for solving the problem with sufficient mathematical background, and discussions on the obtained results with physical interruptions to understand the domain of applicability. This book also provides a comprehensive literature survey which reveals the challenges, outcomes and developments of higher level mathematics and mechanics in this decade. The theoretical coverage of this book is relatively at a higher level to meet the global orientation of mathematics and its applications in mechanical engineering.

The target audience of this book is postgraduate students, researchers and industrialists. This book promotes a vision of applied mathematics as integral to mechanical engineering. Each chapter contains important information emphasizing core mathematics, intended for the professional who already possesses a basic understanding. In this book, theoretically oriented readers will find an overview of mathematics and its applications. Industrialists will find a variety of techniques with sufficient discussion in terms of physical point of view to adapt for solving the particular application based mathematical models. The readers can make use of the literature survey of this book to identify the current trends in mathematics and mechanics. It is our hope and expectation that this book will provide an effective learning experience and referenced resource for all young mathematicians and mechanical engineers.

As Editors, we would like to express our sincere thanks to all the administrative authorities of Vellore Institute of Technology, Vellore; for their motivation and support. We also extend our profound thanks to all faculty members and research scholars of the Department of Mathematics; and all staff members of our institute. We especially thank all the members of the organizing committee of ICAFD 2018 who worked as a team by investing their time to make the conference as a great success one. We thank the national funding agency, Council of Scientific and Industrial Research (CSIR), Government of India for the financial support that contributed towards the successful completion of this international conference. We express our sincere gratitude to all the referees for spending their valuable time to review the manuscripts which led to substantial improvements and sort out the research papers for publication. We are thankful to the project coordinator and team members from Springer Nature for their commitment and dedication towards the publication of this book. The organizing committee is grateful to Dr. Akash Chakraborty, associate editor applied sciences, engineering and physics, Springer for his continuous encouragement and support towards the publication of this book.

Editors

Contents

Contents

About the Editors

Dr. B. Rushi Kumar is an eminent Professor of Mathematics. He is presently the Head of the Department of Mathematics, School of Advanced Sciences of VIT. His research interests include convection in porous media, magnetohydrodynamics, fluid dynamics, CFD, finite-difference methods. His research is funded by DST under a bilateral exchange programme and CSC follow-on grants by Royal Society, London. Dr. Kumar's teaching covers subjects such as Advanced Mathematical Methods, Applied Numerical Methods, Applications of Differential and Difference Equations and Calculus for Engineers. Dr. Rushi's consulting activities primarily focus on the development of optimization-based analytic solutions in various industries, including defence, financial, electronic marketplace and information technology. Dr. Kumar is an eminent scholar in Applied Mathematics research and the recipient of many research and teaching awards. He is a Life Member of the Indian Society of Theoretical and Applied Mechanics (ISTAM) and Andhra Pradesh Society for Mathematical Sciences (APSMS). He presented papers at various national and international conferences and reviewed various research articles and thesis. He delivered several invited talks at national and international conferences/seminars/workshops and Faculty Development Programmes. He was also instrumental in organizing several workshops / FDP's / seminars and national and international conferences in VIT. He guided eight Ph.D. students. He is acclaimed in the academic circles for his erudition in the field of Mathematics.

Dr. R. Sivaraj is working as a Senior Assistant Professor in the Department of Mathematics, School of Advanced Sciences, Vellore Institute of Technology, Vellore, India. His area of research is in fluid dynamics, and he works on non-Newtonian fluids, MHD, heat transfer and porous media. He has published 32 research papers in highly reputed international journals. Under his guidance, two scholars received the Ph.D. degree and presently four scholars are working. He received the VIT Research Award continuously for the years 2012-2018 and travel grant from the Royal Society of London and CSIR, India. He worked at Guangdong

University of Technology, Guangzhou, China, under Faculty Exchange Programme. He visited the National Defence University of Malaysia, Kuala Lumpur, Malaysia, as a Visiting Scientist. He delivered a set of lectures on applications of fluid dynamics at the University of the West Indies, St. Augustine, Trinidad, West Indies. He delivered an invited lecture in international conferences and seminars organized by the University of Botswana, National University of Singapore and Universiti Putra Malaysia. He attended over 20 national and international conferences in India and abroad. He was invited to deliver lectures in several conferences, workshops, seminars and guest lectures, and he has organized several international conferences, seminars, workshops, etc., to promote the research activities. He served as a reviewer for 39 scientific journals. He served as one of the editors for the book Applied Mathematics and Scientific Computing published by Springer book series Trends in Mathematics and the proceedings Recent Trends in Pure and Applied Mathematics published by AIP Conference Proceedings. He is the Joint Secretary of Academia for Advanced Research in Mathematics Society.

Dr. J. Prakash is a Visiting Professor in the Faculty of Engineering and the Built Environment, University of Johannesburg, South Africa. Prof. Prakash obtained his M.Sc. (Mathematics) from Agra University, India, in 1965 and M.Sc. (Statistics) from Meerut University, India, in 1971 both in the first division and his D.Phil. (Doctor of Philosophy) degree in Applied Mathematics (Fluid Mechanics) in June 1984 from Garhwal University, India. He has worked in several prestigious universities in India, Iraq, Zambia, New Zealand and Botswana. He has teaching and research experience of over 45 years and risen to the current position in 2020. He has taught several courses in Mathematics, Statistics and Engineering Mathematics at undergraduate and graduate levels in the universities he has served. He was awarded the professional honours as Fellow (FIMA) in 1989, status as a Chartered Mathematician (C. Math.) in 1993 and Chartered Scientist (C. Sci.) in 2005 by the Institute of Mathematics and Its Applications (UK). He is a recipient of a Prestigious Award of the C. V. Raman International Fellowship for African Researchers under Visiting Fellowship Programme from FICCI Science and Technology, International Cooperation Division, Government of India, New Delhi, India, in 2012 and also a prestigious Global Visionary Award in 2014 by Vision Foundation, Ahmedabad, India. Prof. Prakash has visited the Institute of Fundamental Sciences, Massey University, New Zealand as a Visiting Researcher in the past several times for short durations in the past years. His research interests are in the areas of bio-fluid dynamics, fluid mechanics, computational fluid dynamics (CFD), mathematical modelling and mathematical methods. As a published researcher, he has authored over 150 publications in peer-reviewed journals and at international conferences. He has presented research papers in over 60 international conferences in India and abroad, and he has organized several international conferences. Prof. Prakash's unique contribution to the Department of Mathematics, University of Botswana, is that the European Mathematical Society labelled the Department of Mathematics as

an Emerging Centre of Excellence for 4 years (2016–2020) during his time; he was Head of Mathematics Department. He also compiled a custom edition book on Introductory Mathematics for First Year Courses MAT111 and MAT122 published by CENGAGE publishers in 2014. He received Long Service Award (29 years) on 14th June 2019 from the Vice Chancellor in an event organized by the University of Botswana.

Deriving Shape Functions for a 20-Nodal Tri-quadratic Serendipity Element and Verified

P. Reddaiah

Abstract In this paper, I derived shape functions for a 20-nodal tri-quadratic serendipity element which consists of eight corner nodes and twelve mid-side nodes using natural coordinate system. I derived two shape function verification conditions, first verification condition sum of all the shape functions is equal to one, and second verification condition each shape function has a value of one at its own node and zero at all other nodes. For mathematical computations, I used Mathematica 9 Software.

Keywords 20-nodal tri-quadratic serendipity element · Natural coordinate system · Shape functions

1 Introduction

Usage of Lagrange type of elements is very limited because it consist interior nodes. Due to this limitation. serendipity type of elements has got more importance, because in this type of elements interior nodes are not needed. Serendipity element means nodes are located on the boundary only. Shape functions usage has many applications in solid mechanics problems, fluid mechanics problems, electrical engineering problems, and heat flow problems. If node s is located in the boundary of the element such type of elements are called serendipity elements.

2 Geometrical Description

The 20-nodal tri-quadratic element is shown in Fig. 1. This element consists of eight corner nodes and twelve mid-side nodes. The eight corner nodes are 1, 2, 3, 4, 5, 6, 7 and 8, and twelve mid-side nodes are 9, 10, 11, 12, 13, 14, 15, 16, 17, 18, 19 and 20 as shown in Fig. 1.

P. Reddaiah (✉)
Global College of Engineering and Technology, Kadapa, Andhra Pradesh, India
e-mail: reddaiah007@gmail.com

1
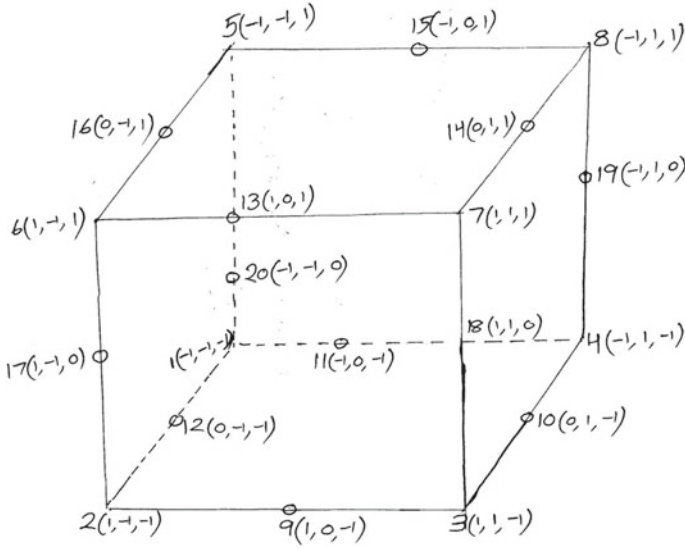
Fig. 1 Schematic diagram of a 20 nodal tri-quadratic serendipity element

3 Deriving Shape Functions for a 20-Nodal Tri-quadratic Serendipity Element

In Fig. 1, for displacement function u, v and w, there are 20 nodal values. In displacement function, there should be only 20 constants.

$$
\begin{aligned}
u = {} & \alpha_1 + \alpha_2 \xi + \alpha_3 \eta + \alpha_4 \zeta + \alpha_5 (\xi * \eta) + \alpha_6 (\eta * \zeta) + \alpha_7 (\xi * \zeta) \\
& + \alpha_8 \xi^2 + \alpha_9 \eta^2 + \alpha_{10} \zeta^2 + \alpha_{11} (\xi * \eta * \zeta) + \alpha_{12} (\xi * \eta^2) + \alpha_{13} (\xi * \zeta^2) \\
& + \alpha_{14} (\eta * \xi^2) + \alpha_{15} (\eta * \zeta^2) + \alpha_{16} (\zeta * \xi^2) + \alpha_{17} (\zeta * \eta^2) \\
& + \alpha_{18} (\xi^2 * \eta * \zeta) + \alpha_{19} (\eta^2 * \xi * \zeta) + \alpha_{20} (\xi * \eta * \zeta^2)
\end{aligned}
$$

Substituting nodal coordinates $1(-1, -1, -1), 2(1, -1, -1) \ldots 20(-1, -1, 0)$ in u we get nodal velocities $u_1, u_2 \ldots, u_{20}$ and writing in matrix form.

$$
\{u\}_e =
\begin{Bmatrix}
u_1 \\ u_2 \\ u_3 \\ u_4 \\ u_5 \\ u_6 \\ u_7 \\ u_8 \\ u_9 \\ u_{10} \\ u_{11} \\ u_{12} \\ u_{13} \\ u_{14} \\ u_{15} \\ u_{16} \\ u_{17} \\ u_{18} \\ u_{19} \\ u_{20}
\end{Bmatrix}
\begin{bmatrix}
1 & -1 & -1 & -1 & 1 & 1 & 1 & 1 & 1 & 1 & -1 & -1 & -1 & -1 & -1 & -1 & -1 & 1 & 1 & 1 \\
1 & 1 & -1 & -1 & -1 & 1 & -1 & 1 & 1 & 1 & 1 & 1 & 1 & -1 & -1 & -1 & -1 & 1 & -1 & -1 \\
1 & 1 & 1 & -1 & 1 & -1 & -1 & 1 & 1 & 1 & -1 & 1 & 1 & 1 & 1 & -1 & -1 & -1 & -1 & 1 \\
1 & -1 & 1 & -1 & -1 & 0 & 1 & 1 & 1 & 1 & 1 & -1 & -1 & 1 & 1 & -1 & -1 & -1 & 1 & -1 \\
1 & -1 & -1 & 1 & 1 & -1 & -1 & 1 & 1 & 1 & 1 & -1 & -1 & -1 & -1 & 1 & 1 & -1 & -1 & 1 \\
1 & 1 & -1 & 1 & -1 & -1 & 1 & 1 & 1 & 1 & -1 & 1 & 1 & -1 & -1 & 1 & 1 & -1 & 1 & -1 \\
1 & 1 & 1 & 1 & 0 & 1 & 1 & 1 & 1 & 1 & 1 & 1 & 1 & 1 & 1 & 1 & 1 & 1 & 1 & 1 \\
1 & -1 & 1 & 1 & 0 & 1 & -1 & 1 & 1 & 1 & -1 & -1 & -1 & 1 & 1 & 1 & 1 & 1 & -1 & -1 \\
1 & 1 & 0 & -1 & 0 & 0 & -1 & 1 & 0 & 1 & 0 & 0 & 1 & 0 & 0 & -1 & 0 & 0 & 0 & 0 \\
1 & 0 & 1 & -1 & 0 & -1 & 0 & 0 & 0 & 1 & 0 & 0 & 0 & 0 & 1 & 0 & -1 & 0 & 0 & 0 \\
1 & -1 & 0 & -1 & 0 & 0 & 1 & 1 & 0 & 1 & 0 & 0 & -1 & 0 & 0 & -1 & 0 & 0 & 0 & 0 \\
1 & 0 & -1 & -1 & 0 & 1 & 0 & 0 & 1 & 1 & 0 & 0 & 0 & 0 & -1 & 0 & -1 & 0 & 0 & 0 \\
1 & 1 & 0 & 1 & 0 & 0 & 1 & 1 & 0 & 1 & 0 & 0 & 1 & 0 & 0 & 1 & 0 & 0 & 0 & 0 \\
1 & 0 & 1 & 1 & 0 & 1 & 0 & 0 & 1 & 1 & 0 & 0 & 0 & 0 & 1 & 0 & 1 & 0 & 0 & 0 \\
1 & -1 & 0 & 1 & 0 & 0 & -1 & 1 & 0 & 1 & 0 & 0 & -1 & 0 & 0 & 1 & 0 & 0 & 0 & 0 \\
1 & 0 & -1 & 1 & 0 & -1 & 0 & 0 & 1 & 1 & 0 & 0 & 0 & 0 & -1 & 0 & 1 & 0 & 0 & 0 \\
1 & 1 & -1 & 0 & -1 & 0 & 0 & 1 & 1 & 0 & 0 & 1 & 0 & -1 & 0 & 0 & 0 & 0 & 0 & 0 \\
1 & 1 & 1 & 0 & 1 & 0 & 0 & 1 & 1 & 0 & 0 & 1 & 0 & 1 & 0 & 0 & 0 & 0 & 0 & 0 \\
1 & -1 & 1 & 0 & -1 & 0 & 0 & 1 & 1 & 0 & 0 & -1 & 0 & 1 & 0 & 0 & 0 & 0 & 0 & 0 \\
1 & -1 & -1 & 0 & 1 & 0 & 0 & 1 & 1 & 0 & 0 & -1 & 0 & -1 & 0 & 0 & 0 & 0 & 0 & 0
\end{bmatrix}
\begin{bmatrix}
\alpha_1 \\ \alpha_2 \\ \alpha_3 \\ \alpha_4 \\ \alpha_5 \\ \alpha_6 \\ \alpha_7 \\ \alpha_8 \\ \alpha_9 \\ \alpha_{10} \\ \alpha_{11} \\ \alpha_{12} \\ \alpha_{13} \\ \alpha_{14} \\ \alpha_{15} \\ \alpha_{16} \\ \alpha_{17} \\ \alpha_{18} \\ \alpha_{19} \\ \alpha_{20}
\end{bmatrix}
$$

$$
\{\alpha\} = [A]^{-1}\{u\}_e
$$

where $\{u\}_e$ is the vector of nodal displacements in ξ directions, $[A]$ is the 20×20 matrix.

$\{\alpha\}$ is the vector of generalized coordinates (constants in polynomials).

Calculating inverse of A using Wolfram Mathematica 9

$$
A :=
\begin{Bmatrix}
1 & -1 & -1 & -1 & 1 & 1 & 1 & 1 & 1 & 1 & -1 & -1 & -1 & -1 & -1 & -1 & -1 & 1 & 1 & 1 \\
1 & 1 & -1 & -1 & -1 & 1 & -1 & 1 & 1 & 1 & 1 & 1 & 1 & -1 & -1 & -1 & -1 & 1 & -1 & -1 \\
1 & 1 & 1 & -1 & 1 & -1 & -1 & 1 & 1 & 1 & -1 & 1 & 1 & 1 & 1 & -1 & -1 & -1 & -1 & 1 \\
1 & -1 & 1 & -1 & -1 & 0 & 1 & 1 & 1 & 1 & 1 & -1 & -1 & 1 & 1 & -1 & -1 & -1 & 1 & -1 \\
1 & -1 & -1 & 1 & 1 & -1 & -1 & 1 & 1 & 1 & 1 & -1 & -1 & -1 & -1 & 1 & 1 & -1 & -1 & 1 \\
1 & 1 & -1 & 1 & -1 & -1 & 1 & 1 & 1 & 1 & -1 & 1 & 1 & -1 & -1 & 1 & 1 & -1 & 1 & -1 \\
1 & 1 & 1 & 1 & 0 & 1 & 1 & 1 & 1 & 1 & 1 & 1 & 1 & 1 & 1 & 1 & 1 & 1 & 1 & 1 \\
1 & -1 & 1 & 1 & 0 & 1 & -1 & 1 & 1 & 1 & -1 & -1 & -1 & 1 & 1 & 1 & 1 & 1 & -1 & -1 \\
1 & 1 & 0 & -1 & 0 & 0 & -1 & 1 & 0 & 1 & 0 & 0 & 1 & 0 & 0 & -1 & 0 & 0 & 0 & 0 \\
1 & 0 & 1 & -1 & 0 & -1 & 0 & 0 & 0 & 1 & 0 & 0 & 0 & 0 & 1 & 0 & -1 & 0 & 0 & 0 \\
1 & -1 & 0 & -1 & 0 & 0 & 1 & 1 & 0 & 1 & 0 & 0 & -1 & 0 & 0 & -1 & 0 & 0 & 0 & 0 \\
1 & 0 & -1 & -1 & 0 & 1 & 0 & 0 & 1 & 1 & 0 & 0 & 0 & 0 & -1 & 0 & -1 & 0 & 0 & 0 \\
1 & 1 & 0 & 1 & 0 & 0 & 1 & 1 & 0 & 1 & 0 & 0 & 1 & 0 & 0 & 1 & 0 & 0 & 0 & 0 \\
1 & 0 & 1 & 1 & 0 & 1 & 0 & 0 & 1 & 1 & 0 & 0 & 0 & 0 & 1 & 0 & 1 & 0 & 0 & 0 \\
1 & -1 & 0 & 1 & 0 & 0 & -1 & 1 & 0 & 1 & 0 & 0 & -1 & 0 & 0 & 1 & 0 & 0 & 0 & 0 \\
1 & 0 & -1 & 1 & 0 & -1 & 0 & 0 & 1 & 1 & 0 & 0 & 0 & 0 & -1 & 0 & 1 & 0 & 0 & 0 \\
1 & 1 & -1 & 0 & -1 & 0 & 0 & 1 & 1 & 0 & 0 & 1 & 0 & -1 & 0 & 0 & 0 & 0 & 0 & 0 \\
1 & 1 & 1 & 0 & 1 & 0 & 0 & 1 & 1 & 0 & 0 & 1 & 0 & 1 & 0 & 0 & 0 & 0 & 0 & 0 \\
1 & -1 & 1 & 0 & -1 & 0 & 0 & 1 & 1 & 0 & 0 & -1 & 0 & 1 & 0 & 0 & 0 & 0 & 0 & 0 \\
1 & -1 & -1 & 0 & 1 & 0 & 0 & 1 & 1 & 0 & 0 & -1 & 0 & -1 & 0 & 0 & 0 & 0 & 0 & 0
\end{Bmatrix}
$$

Inverse[A]//MatrixForm

$$
A-1=
$$

$$
\begin{bmatrix}
-\tfrac14 & -\tfrac14 & -\tfrac14 & -\tfrac14 & -\tfrac14 & -\tfrac14 & \tfrac14 & \tfrac{3}{16} & \tfrac{5}{16} & \tfrac14 & \tfrac{5}{16} & \tfrac{3}{16} & \tfrac14 & \tfrac{5}{16} & \tfrac14 & \tfrac{3}{16} & \tfrac14 & \tfrac14 & \tfrac14 \\[4pt]
\tfrac18 & -\tfrac18 & -\tfrac18 & -\tfrac18 & 0 & 0 & -\tfrac14 & \tfrac{1}{32} & -\tfrac{1}{32} & \tfrac14 & -\tfrac{1}{32} & \tfrac{1}{32} & -\tfrac14 & -\tfrac{1}{32} & \tfrac14 & \tfrac{1}{32} & \tfrac14 & -\tfrac14 & \tfrac14 \\[4pt]
\tfrac18 & \tfrac18 & -\tfrac18 & -\tfrac18 & 0 & 0 & 0 & -\tfrac{7}{32} & -\tfrac{7}{32} & 0 & \tfrac{9}{32} & -\tfrac{9}{32} & 0 & \tfrac{9}{32} & 0 & -\tfrac{9}{32} & \tfrac14 & -\tfrac14 & -\tfrac14 \\[4pt]
\tfrac18 & \tfrac18 & \tfrac18 & -\tfrac18 & 0 & 0 & -\tfrac14 & \tfrac{7}{32} & -\tfrac{9}{32} & \tfrac14 & \tfrac{7}{32} & \tfrac{9}{32} & -\tfrac14 & \tfrac{7}{32} & \tfrac14 & \tfrac{9}{32} & \tfrac14 & \tfrac14 & -\tfrac14 \\[4pt]
0 & 0 & 0 & 0 & 0 & -\tfrac14 & 0 & 0 & 0 & 0 & 0 & 0 & 0 & 0 & 0 & 0 & 0 & 0 & 0 \\[4pt]
0 & 0 & 0 & 0 & 0 & -\tfrac14 & 0 & -\tfrac14 & \tfrac14 & 0 & \tfrac14 & -\tfrac14 & 0 & \tfrac14 & \tfrac14 & -\tfrac14 & \tfrac14 & \tfrac14 & 0 \\[4pt]
0 & 0 & 0 & -\tfrac18 & -\tfrac14 & 0 & \tfrac14 & 0 & 0 & \tfrac14 & 0 & 0 & \tfrac14 & 0 & 0 & 0 & \tfrac14 & 0 & -\tfrac14 \\[4pt]
\tfrac18 & \tfrac18 & \tfrac18 & \tfrac18 & 0 & \tfrac18 & 0 & -\tfrac{7}{32} & -\tfrac{9}{32} & 0 & -\tfrac{9}{32} & -\tfrac{7}{32} & 0 & -\tfrac{9}{32} & 0 & -\tfrac{7}{32} & \tfrac14 & -\tfrac14 & 0 \\[4pt]
\tfrac18 & \tfrac18 & \tfrac18 & \tfrac18 & 0 & \tfrac18 & -\tfrac14 & \tfrac{1}{32} & -\tfrac{1}{32} & -\tfrac14 & -\tfrac{1}{32} & \tfrac{1}{32} & -\tfrac14 & -\tfrac{1}{32} & -\tfrac14 & \tfrac{1}{32} & 0 & 0 & 0 \\[4pt]
\tfrac18 & \tfrac18 & \tfrac18 & \tfrac18 & 0 & \tfrac18 & 0 & \tfrac{1}{32} & -\tfrac{1}{32} & 0 & -\tfrac{1}{32} & \tfrac{1}{32} & 0 & -\tfrac{1}{32} & 0 & \tfrac{1}{32} & 0 & 0 & 0 \\[4pt]
-\tfrac18 & -\tfrac18 & -\tfrac18 & -\tfrac18 & 0 & -\tfrac18 & \tfrac14 & -\tfrac{1}{32} & \tfrac{1}{32} & \tfrac14 & \tfrac{1}{32} & -\tfrac{1}{32} & \tfrac14 & \tfrac{1}{32} & \tfrac14 & -\tfrac{1}{32} & \tfrac14 & \tfrac14 & \tfrac14 \\[4pt]
-\tfrac18 & \tfrac18 & \tfrac18 & -\tfrac18 & 0 & \tfrac18 & 0 & -\tfrac{7}{32} & \tfrac{1}{32} & 0 & \tfrac{1}{32} & -\tfrac{7}{32} & 0 & \tfrac{1}{32} & 0 & -\tfrac{7}{32} & 0 & 0 & 0 \\[4pt]
-\tfrac18 & \tfrac18 & \tfrac18 & -\tfrac18 & 0 & \tfrac18 & 0 & \tfrac{7}{32} & \tfrac{1}{32} & 0 & \tfrac{1}{32} & \tfrac{7}{32} & 0 & \tfrac{1}{32} & 0 & \tfrac{7}{32} & 0 & 0 & 0 \\[4pt]
-\tfrac18 & -\tfrac18 & -\tfrac18 & \tfrac18 & \tfrac14 & \tfrac18 & -\tfrac14 & \tfrac{1}{32} & -\tfrac{1}{32} & -\tfrac14 & -\tfrac{1}{32} & \tfrac{1}{32} & -\tfrac14 & -\tfrac{1}{32} & -\tfrac14 & \tfrac{1}{32} & 0 & 0 & 0 \\[4pt]
-\tfrac18 & -\tfrac18 & -\tfrac18 & \tfrac18 & 0 & \tfrac18 & 0 & \tfrac{7}{32} & -\tfrac{7}{32} & 0 & -\tfrac{7}{32} & \tfrac{7}{32} & 0 & -\tfrac{7}{32} & 0 & \tfrac{7}{32} & 0 & 0 & 0 \\[4pt]
\tfrac18 & \tfrac18 & \tfrac18 & \tfrac18 & \tfrac14 & \tfrac18 & -\tfrac14 & \tfrac{1}{32} & -\tfrac{1}{32} & -\tfrac14 & -\tfrac{1}{32} & \tfrac{1}{32} & -\tfrac14 & -\tfrac{1}{32} & -\tfrac14 & \tfrac{1}{32} & 0 & 0 & 0 \\[4pt]
\tfrac18 & -\tfrac18 & \tfrac18 & \tfrac18 & \tfrac14 & -\tfrac18 & \tfrac14 & \tfrac{1}{32} & \tfrac{1}{32} & \tfrac14 & \tfrac{1}{32} & \tfrac{1}{32} & \tfrac14 & \tfrac{1}{32} & \tfrac14 & \tfrac{1}{32} & \tfrac14 & \tfrac14 & \tfrac14 \\[4pt]
\tfrac18 & -\tfrac18 & \tfrac18 & \tfrac18 & \tfrac14 & -\tfrac18 & -\tfrac14 & -\tfrac{1}{32} & -\tfrac{1}{32} & -\tfrac14 & -\tfrac{1}{32} & -\tfrac{1}{32} & -\tfrac14 & -\tfrac{1}{32} & -\tfrac14 & -\tfrac{1}{32} & \tfrac14 & \tfrac14 & -\tfrac14 \\[4pt]
\tfrac18 & -\tfrac18 & \tfrac18 & \tfrac18 & 0 & -\tfrac18 & 0 & -\tfrac{1}{32} & \tfrac{1}{32} & 0 & \tfrac{1}{32} & -\tfrac{1}{32} & 0 & \tfrac{1}{32} & 0 & -\tfrac{1}{32} & \tfrac14 & -\tfrac14 & -\tfrac14
\end{bmatrix}
$$

$$u = [(1\ \xi\ \eta\ \zeta\ (\xi * \eta)\ (\eta * \zeta)\ (\xi * \zeta)\ \xi^2\ \eta^2\ \zeta^2\ (\xi * \eta * \zeta)\ (\xi * \eta^2)$$
$$(\xi * \zeta^2)\ (\eta * \xi^2)\ (\eta * \zeta^2)\ (\zeta * \xi^2)\ (\zeta * \eta^2)\ (\zeta^2 * \eta * \zeta)\ (\eta^2 * \xi * \zeta)\ (\xi * \eta * \zeta^2))]\{\alpha\}$$

$$u = [(1\ \xi\ \eta\ \zeta\ (\xi * \eta)\ (\eta * \zeta)\ (\xi * \zeta)\ \xi^2\ \eta^2\ \zeta^2\ (\xi * \eta * \zeta)\ (\xi * \eta^2)$$
$$(\xi * \zeta^2)\ (\eta * \xi^2)\ (\eta * \zeta^2)\ (\zeta * \xi^2)\ (\zeta * \eta^2)\ (\zeta^2 * \eta * \zeta)\ (\eta^2 * \xi * \zeta)\ (\xi * \eta * \zeta^2))][A]^{-1}\{u\}_e$$

$$u = \left\{\left\{ -\frac{1}{4} + \frac{\zeta}{8} + \frac{\zeta^2}{8} + \frac{\eta}{8} - \frac{\zeta^2\eta}{8} + \frac{\eta^2}{8} - \frac{\zeta\eta^2}{8} + \frac{\xi}{8} - \frac{\zeta^2\xi}{8} - \frac{\zeta\eta\xi}{8} + \frac{1}{8}\zeta^2\eta\xi - \frac{\eta^2\xi}{8} \right.\right.$$
$$\left. + \frac{1}{8}\zeta\eta^2\xi + \frac{\xi^2}{8} - \frac{\zeta\xi^2}{8} - \frac{\eta\xi^2}{8} + \frac{1}{8}\zeta\eta\xi^2, \right.$$

$$-\frac{1}{4} + \frac{\zeta}{8} + \frac{\zeta^2}{8} + \frac{\eta}{8} - \frac{\zeta^2\eta}{8} + \frac{\eta^2}{8} - \frac{\zeta\eta^2}{8} - \frac{\xi}{8} + \frac{\zeta^2\xi}{8} + \frac{\zeta\eta\xi}{8} - \frac{1}{8}\zeta^2\eta\xi + \frac{\eta^2\xi}{8}$$
$$- \frac{1}{8}\zeta\eta^2\xi + \frac{\xi^2}{8} - \frac{\zeta\xi^2}{8} - \frac{\eta\xi^2}{8} + \frac{1}{8}\zeta\eta\xi^2,$$

$$-\frac{1}{4} + \frac{\zeta}{8} + \frac{\zeta^2}{8} - \frac{\eta}{8} + \frac{\zeta^2\eta}{8} + \frac{\eta^2}{8} - \frac{\zeta\eta^2}{8} - \frac{\xi}{8} + \frac{\zeta^2\xi}{8} - \frac{\zeta\eta\xi}{8} + \frac{1}{8}\zeta^2\eta\xi + \frac{\eta^2\xi}{8}$$
$$- \frac{1}{8}\zeta\eta^2\xi + \frac{\xi^2}{8} - \frac{\zeta\xi^2}{8} + \frac{\eta\xi^2}{8} - \frac{1}{8}\zeta\eta\xi^2,$$

$$-\frac{1}{4} + \frac{\zeta}{8} + \frac{\zeta^2}{8} - \frac{\eta}{8} + \frac{\zeta^2\eta}{8} + \frac{\eta^2}{8} - \frac{\zeta\eta^2}{8} + \frac{\xi}{8} - \frac{\zeta^2\xi}{8} + \frac{\zeta\eta\xi}{8} - \frac{1}{8}\zeta^2\eta\xi - \frac{\eta^2\xi}{8}$$
$$+ \frac{1}{8}\zeta\eta^2\xi + \frac{\xi^2}{8} - \frac{\zeta\xi^2}{8} + \frac{\eta\xi^2}{8} - \frac{1}{8}\zeta\eta\xi^2,$$

$$-\frac{1}{4} - \frac{\zeta}{8} + \frac{\zeta^2}{8} + \frac{\eta}{8} - \frac{\zeta^2\eta}{8} + \frac{\eta^2}{8} + \frac{\zeta\eta^2}{8} + \frac{\xi}{8} - \frac{\zeta^2\xi}{8} + \frac{\zeta\eta\xi}{8} + \frac{1}{8}\zeta^2\eta\xi - \frac{\eta^2\xi}{8}$$
$$- \frac{1}{8}\zeta\eta^2\xi + \frac{\xi^2}{8} + \frac{\zeta\xi^2}{8} - \frac{\eta\xi^2}{8} - \frac{1}{8}\zeta\eta\xi^2,$$

$$-\frac{1}{4} - \frac{\zeta}{8} + \frac{\zeta^2}{8} + \frac{\eta}{8} - \frac{\zeta^2\eta}{8} + \frac{\eta^2}{8} + \frac{\zeta\eta^2}{8} - \frac{\xi}{8} + \frac{\zeta^2\xi}{8} - \frac{\zeta\eta\xi}{8} - \frac{1}{8}\zeta^2\eta\xi + \frac{\eta^2\xi}{8}$$
$$+ \frac{1}{8}\zeta\eta^2\xi + \frac{\xi^2}{8} + \frac{\zeta\xi^2}{8} - \frac{\eta\xi^2}{8} - \frac{1}{8}\zeta\eta\xi^2,$$

$$-\frac{1}{4} - \frac{\zeta}{8} + \frac{\zeta^2}{8} - \frac{\eta}{8} + \frac{\zeta^2\eta}{8} + \frac{\eta^2}{8} + \frac{\zeta\eta^2}{8} - \frac{\xi}{8} + \frac{\zeta^2\xi}{8} + \frac{\zeta\eta\xi}{8} + \frac{1}{8}\zeta^2\eta\xi + \frac{\eta^2\xi}{8}$$
$$+ \frac{1}{8}\zeta\eta^2\xi + \frac{\xi^2}{8} + \frac{\zeta\xi^2}{8} + \frac{\eta\xi^2}{8} + \frac{1}{8}\zeta\eta\xi^2,$$

$$-\frac{1}{4} - \frac{\zeta}{8} + \frac{\zeta^2}{8} - \frac{\eta}{8} + \frac{\zeta^2\eta}{8} + \frac{\eta^2}{8} + \frac{\zeta\eta^2}{8} + \frac{\xi}{8} - \frac{\zeta^2\xi}{8} - \frac{\zeta\eta\xi}{8} - \frac{1}{8}\zeta^2\eta\xi - \frac{\eta^2\xi}{8}$$
$$- \frac{1}{8}\zeta\eta^2\xi + \frac{\xi^2}{8} + \frac{\zeta\xi^2}{8} + \frac{\eta\xi^2}{8} + \frac{1}{8}\zeta\eta\xi^2,$$

$$\frac{1}{4} - \frac{\zeta}{4} - \frac{\eta^2}{4} + \frac{\zeta\eta^2}{4} + \frac{\xi}{4} - \frac{\zeta\xi}{4} - \frac{\eta^2\xi}{4} + \frac{1}{4}\zeta\eta^2\xi,$$

$$\frac{3}{16} - \frac{7\zeta}{32} + \frac{\zeta^2}{32} + \frac{7\eta}{32} - \frac{\zeta\eta}{4} + \frac{\zeta^2\eta}{32} + \frac{\eta^2}{32} - \frac{\zeta\eta^2}{32} + \frac{\xi}{32} - \frac{\zeta^2\xi}{32} + \frac{\zeta\eta\xi}{32} - \frac{1}{32}\zeta^2\eta\xi - \frac{\eta^2\xi}{32}$$
$$+ \frac{1}{32}\zeta\eta^2\xi - \frac{7\xi^2}{32} + \frac{7\zeta\xi^2}{32} - \frac{7\eta\xi^2}{32} + \frac{7}{32}\zeta\eta\xi^2,$$

$$\frac{1}{4} - \frac{\zeta}{4} - \frac{\eta^2}{4} + \frac{\zeta\eta^2}{4} - \frac{\xi}{4} + \frac{\zeta\xi}{4} + \frac{\eta^2\xi}{4} - \frac{1}{4}\zeta\eta^2\xi,$$

$$\frac{5}{16} - \frac{9\zeta}{32} - \frac{\zeta^2}{32} - \frac{7\eta}{32} + \frac{\zeta\eta}{4} - \frac{\zeta^2\eta}{32} - \frac{\eta^2}{32} + \frac{\zeta\eta^2}{32} - \frac{\xi}{32} + \frac{\zeta^2\xi}{32} - \frac{\zeta\eta\xi}{32} + \frac{1}{32}\zeta^2\eta\xi + \frac{\eta^2\xi}{32}$$

$$-\frac{1}{32}\zeta\eta^2\xi - \frac{9\xi^2}{32} + \frac{9\zeta\xi^2}{32} + \frac{7\eta\xi^2}{32} - \frac{7}{32}\zeta\eta\xi,$$

$$\frac{1}{4} + \frac{\zeta}{4} - \frac{\eta^2}{4} - \frac{\zeta\eta^2}{4} + \frac{\xi}{4} + \frac{\zeta\xi}{4} - \frac{\eta^2\xi}{4} - \frac{1}{4}\zeta\eta^2\xi,$$

$$\frac{5}{16} + \frac{7\zeta}{32} - \frac{\zeta^2}{32} + \frac{9\eta}{32} + \frac{\zeta\eta}{4} - \frac{\zeta^2\eta}{32} - \frac{\eta^2}{32} + \frac{\zeta\eta^2}{32} - \frac{\xi}{32} + \frac{\zeta^2\xi}{32} - \frac{\zeta\eta\xi}{32} + \frac{1}{32}\zeta^2\eta\xi + \frac{\eta^2\xi}{32}$$

$$-\frac{1}{32}\zeta\eta^2\xi - \frac{9\xi^2}{32} - \frac{7\zeta\xi^2}{32} - \frac{9\eta\xi^2}{32} - \frac{7}{32}\zeta\eta\xi^2,$$

$$\frac{1}{4} + \frac{\zeta}{4} - \frac{\eta^2}{4} - \frac{\zeta\eta^2}{4} - \frac{\xi}{4} - \frac{\zeta\xi}{4} + \frac{\eta^2\xi}{4} + \frac{1}{4}\zeta\eta^2\xi,$$

$$\frac{3}{16} + \frac{9\zeta}{32} + \frac{\zeta^2}{32} - \frac{9\eta}{32} - \frac{\zeta\eta}{4} + \frac{\zeta^2\eta}{32} + \frac{\eta^2}{32} - \frac{\zeta\eta^2}{32} + \frac{\xi}{32} - \frac{\zeta^2\xi}{32} + \frac{\zeta\eta\xi}{32} - \frac{1}{32}\zeta^2\eta\xi - \frac{\eta^2\xi}{32}$$

$$+\frac{1}{32}\zeta\eta^2\xi - \frac{7\xi^2}{32} - \frac{9\zeta\xi^2}{32} + \frac{9\eta\xi^2}{32} + \frac{7}{32}\zeta\eta\xi^2,$$

$$\frac{1}{4} - \frac{\zeta^2}{4} - \frac{\eta}{4} + \frac{\zeta^2\eta}{4} + \frac{\xi}{4} - \frac{\zeta^2\xi}{4} - \frac{\eta\xi}{4} + \frac{1}{4}\zeta^2\eta\xi,$$

$$\frac{1}{4} - \frac{\zeta^2}{4} + \frac{\eta}{4} - \frac{\zeta^2\eta}{4} + \frac{\xi}{4} - \frac{\zeta^2\xi}{4} + \frac{\eta\xi}{4} - \frac{1}{4}\zeta^2\eta\xi,$$

$$\frac{1}{4} - \frac{\zeta^2}{4} + \frac{\eta}{4} - \frac{\zeta^2\eta}{4} - \frac{\xi}{4} + \frac{\zeta^2\xi}{4} - \frac{\eta\xi}{4} + \frac{1}{4}\zeta^2\eta\xi,$$

$$\frac{1}{4} - \frac{\zeta^2}{4} - \frac{\eta}{4} + \frac{\zeta^2\eta}{4} - \frac{\xi}{4} + \frac{\zeta^2\xi}{4} + \frac{\eta\xi}{4} - \frac{1}{4}\zeta^2\eta\xi\}\}\{u\}_e$$

$$u = [N_1\ N_2\ N_3\ N_4\ N_5\ N_6\ N_7\ N_8\ N_9\ N_{10}\ N_{11}\ N_{12}\ N_{13}\ N_{14}\ N_{15}\ N_{16}\ N_{17}\ N_{18}\ N_{19}\ N_{20}]\{u\}_e\ \text{Where}$$

$$N_1 := -\frac{1}{4} + \frac{\zeta}{8} + \frac{\zeta^2}{8} + \frac{\eta}{8} - \frac{\zeta^2\eta}{8} + \frac{\eta^2}{8} - \frac{\zeta\eta^2}{8} + \frac{\xi}{8} - \frac{\zeta^2\xi}{8} - \frac{\zeta\eta\xi}{8}$$
$$+ \frac{1}{8}\zeta^2\eta\xi - \frac{\eta^2\xi}{8} + \frac{1}{8}\zeta\eta^2\xi + \frac{\xi^2}{8} - \frac{\zeta\xi^2}{8} - \frac{\eta\xi^2}{8} + \frac{1}{8}\zeta\eta\xi^2 \tag{1}$$

$$N_2 := -\frac{1}{4} + \frac{\zeta}{8} + \frac{\zeta^2}{8} + \frac{\eta}{8} - \frac{\zeta^2\eta}{8} + \frac{\eta^2}{8} - \frac{\zeta\eta^2}{8} - \frac{\xi}{8} + \frac{\zeta^2\xi}{8} + \frac{\zeta\eta\xi}{8} - \frac{1}{8}\zeta^2\eta\xi$$
$$+ \frac{\eta^2\xi}{8} - \frac{1}{8}\zeta\eta^2\xi + \frac{\xi^2}{8} - \frac{\zeta\xi^2}{8} - \frac{\eta\xi^2}{8} + \frac{1}{8}\zeta\eta\xi^2 \tag{2}$$

$$N_3 := -\frac{1}{4} + \frac{\zeta}{8} + \frac{\zeta^2}{8} - \frac{\eta}{8} + \frac{\zeta^2\eta}{8} + \frac{\eta^2}{8} - \frac{\zeta\eta^2}{8} - \frac{\xi}{8} + \frac{\zeta^2\xi}{8} - \frac{\zeta\eta\xi}{8}$$
$$+ \frac{1}{8}\zeta^2\eta\xi + \frac{\eta^2\xi}{8} - \frac{1}{8}\zeta\eta^2\xi + \frac{\xi^2}{8} - \frac{\zeta\xi^2}{8} + \frac{\eta\xi^2}{8} - \frac{1}{8}\zeta\eta\xi^2 \tag{3}$$

$$N_4 := -\frac{1}{4} + \frac{\zeta}{8} + \frac{\zeta^2}{8} - \frac{\eta}{8} + \frac{\zeta^2\eta}{8} + \frac{\eta^2}{8} - \frac{\zeta\eta^2}{8} + \frac{\xi}{8} - \frac{\zeta^2\xi}{8} + \frac{\zeta\eta\xi}{8}$$
$$- \frac{1}{8}\zeta^2\eta\xi - \frac{\eta^2\xi}{8} + \frac{1}{8}\zeta\eta^2\xi + \frac{\xi^2}{8} - \frac{\zeta\xi^2}{8} + \frac{\eta\xi^2}{8} - \frac{1}{8}\zeta\eta\xi^2 \tag{4}$$

$$N_5 := -\frac{1}{4} - \frac{\zeta}{8} + \frac{\zeta^2}{8} + \frac{\eta}{8} - \frac{\zeta^2\eta}{8} + \frac{\eta^2}{8} + \frac{\zeta\eta^2}{8} + \frac{\xi}{8} - \frac{\zeta^2\xi}{8} + \frac{\zeta\eta\xi}{8}$$
$$+ \frac{1}{8}\zeta^2\eta\xi - \frac{\eta^2\xi}{8} - \frac{1}{8}\zeta\eta^2\xi + \frac{\xi^2}{8} + \frac{\zeta\xi^2}{8} - \frac{\eta\xi^2}{8} - \frac{1}{8}\zeta\eta\xi^2 \tag{5}$$

$$N_6 := -\frac{1}{4} - \frac{\zeta}{8} + \frac{\zeta^2}{8} + \frac{\eta}{8} - \frac{\zeta^2\eta}{8} + \frac{\eta^2}{8} + \frac{\zeta\eta^2}{8} - \frac{\xi}{8} + \frac{\zeta^2\xi}{8}$$
$$- \frac{\zeta\eta\xi}{8} - \frac{1}{8}\zeta^2\eta\xi + \frac{\eta^2\xi}{8} + \frac{1}{8}\zeta\eta^2\xi + \frac{\xi^2}{8} + \frac{\zeta\xi^2}{8} - \frac{\eta\xi^2}{8} - \frac{1}{8}\zeta\eta\xi^2 \qquad (6)$$

$$N_7 := -\frac{1}{4} - \frac{\zeta}{8} + \frac{\zeta^2}{8} - \frac{\eta}{8} + \frac{\zeta^2\eta}{8} + \frac{\eta^2}{8} + \frac{\zeta\eta^2}{8} - \frac{\xi}{8} + \frac{\zeta^2\xi}{8} + \frac{\zeta\eta\xi}{8}$$
$$+ \frac{1}{8}\zeta^2\eta\xi + \frac{\eta^2\xi}{8} + \frac{1}{8}\zeta\eta^2\xi + \frac{\xi^2}{8} + \frac{\zeta\xi^2}{8} + \frac{\eta\xi^2}{8} + \frac{1}{8}\zeta\eta\xi^2 \qquad (7)$$

$$N_8 := -\frac{1}{4} - \frac{\zeta}{8} + \frac{\zeta^2}{8} - \frac{\eta}{8} + \frac{\zeta^2\eta}{8} + \frac{\eta^2}{8} + \frac{\zeta\eta^2}{8} + \frac{\xi}{8} - \frac{\zeta^2\xi}{8} - \frac{\zeta\eta\xi}{8}$$
$$- \frac{1}{8}\zeta^2\eta\xi - \frac{\eta^2\xi}{8} - \frac{1}{8}\zeta\eta^2\xi + \frac{\xi^2}{8} + \frac{\zeta\xi^2}{8} + \frac{\eta\xi^2}{8} + \frac{1}{8}\zeta\eta\xi^2 \qquad (8)$$

$$N_9 := \frac{1}{4} - \frac{\zeta}{4} - \frac{\eta^2}{4} + \frac{\zeta\eta^2}{4} + \frac{\xi}{4} - \frac{\zeta\xi}{4} - \frac{\eta^2\xi}{4} + \frac{1}{4}\zeta\eta^2\xi \qquad (9)$$

$$N_{10} := \frac{3}{16} - \frac{7\zeta}{32} + \frac{\zeta^2}{32} + \frac{7\eta}{32} - \frac{\zeta\eta}{4} + \frac{\zeta^2\eta}{32} + \frac{\eta^2}{32} - \frac{\zeta\eta^2}{32} + \frac{\xi}{32} - \frac{\zeta^2\xi}{32} + \frac{\zeta\eta\xi}{32} - \frac{1}{32}\zeta^2\eta\xi$$
$$- \frac{\eta^2\xi}{32} + \frac{1}{32}\zeta\eta^2\xi - \frac{7\xi^2}{32} + \frac{7\zeta\xi^2}{32} - \frac{7\eta\xi^2}{32} + \frac{7}{32}\zeta\eta\xi^2 \qquad (10)$$

$$N_{11} := \frac{1}{4} - \frac{\zeta}{4} - \frac{\eta^2}{4} + \frac{\zeta\eta^2}{4} - \frac{\xi}{4} + \frac{\zeta\xi}{4} + \frac{\eta^2\xi}{4} - \frac{1}{4}\zeta\eta^2\xi \qquad (11)$$

$$N_{12} := \frac{5}{16} - \frac{9\zeta}{32} - \frac{\zeta^2}{32} - \frac{7\eta}{32} + \frac{\zeta\eta}{4} - \frac{\zeta^2\eta}{32} - \frac{\eta^2}{32} + \frac{\zeta\eta^2}{32} - \frac{\xi}{32} + \frac{\zeta^2\xi}{32} - \frac{\zeta\eta\xi}{32} + \frac{1}{32}\zeta^2\eta\xi$$
$$+ \frac{\eta^2\xi}{32} - \frac{1}{32}\zeta\eta^2\xi - \frac{9\xi^2}{32} + \frac{9\zeta\xi^2}{32} + \frac{7\eta\xi^2}{32} - \frac{7}{32}\zeta\eta\xi^2 \qquad (12)$$

$$N_{13} := \frac{1}{4} + \frac{\zeta}{4} - \frac{\eta^2}{4} - \frac{\zeta\eta^2}{4} + \frac{\xi}{4} + \frac{\zeta\xi}{4} - \frac{\eta^2\xi}{4} - \frac{1}{4}\zeta\eta^2\xi \qquad (13)$$

$$N_{14} := \frac{5}{16} + \frac{7\zeta}{32} - \frac{\zeta^2}{32} + \frac{9\eta}{32} + \frac{\zeta\eta}{4} - \frac{\zeta^2\eta}{32} - \frac{\eta^2}{32} + \frac{\zeta\eta^2}{32} - \frac{\xi}{32} + \frac{\zeta^2\xi}{32} - \frac{\zeta\eta\xi}{32} + \frac{1}{32}\zeta^2\eta\xi$$
$$+ \frac{\eta^2\xi}{32} - \frac{1}{32}\zeta\eta^2\xi - \frac{9\xi^2}{32} - \frac{7\zeta\xi^2}{32} - \frac{9\eta\xi^2}{32} - \frac{7}{32}\zeta\eta\xi^2 \qquad (14)$$

$$N_{15} := \frac{1}{4} + \frac{\zeta}{4} - \frac{\eta^2}{4} - \frac{\zeta\eta^2}{4} - \frac{\xi}{4} - \frac{\zeta\xi}{4} + \frac{\eta^2\xi}{4} + \frac{1}{4}\zeta\eta^2\xi \qquad (15)$$

$$N_{16} := \frac{3}{16} + \frac{9\zeta}{32} + \frac{\zeta^2}{32} - \frac{9\eta}{32} - \frac{\zeta\eta}{4} + \frac{\zeta^2\eta}{32} + \frac{\eta^2}{32} - \frac{\zeta\eta^2}{32} + \frac{\xi}{32} - \frac{\zeta^2\xi}{32} + \frac{\zeta\eta\xi}{32} - \frac{1}{32}\zeta^2\eta\xi$$
$$- \frac{\eta^2\xi}{32} + \frac{1}{32}\zeta\eta^2\xi - \frac{7\xi^2}{32} - \frac{9\zeta\xi^2}{32} + \frac{9\eta\xi^2}{32} + \frac{7}{32}\zeta\eta\xi^2 \qquad (16)$$

$$N_{17} := \frac{1}{4} - \frac{\zeta^2}{4} - \frac{\eta}{4} + \frac{\zeta^2\eta}{4} + \frac{\xi}{4} - \frac{\zeta^2\xi}{4} - \frac{\eta\xi}{4} + \frac{1}{4}\zeta^2\eta\xi \qquad (17)$$

$$N_{18} := \frac{1}{4} - \frac{\zeta^2}{4} + \frac{\eta}{4} - \frac{\zeta^2\eta}{4} + \frac{\xi}{4} - \frac{\zeta^2\xi}{4} + \frac{\eta\xi}{4} - \frac{1}{4}\zeta^2\eta\xi \qquad (18)$$

$$N_{19} := \frac{1}{4} - \frac{\zeta^2}{4} + \frac{\eta}{4} - \frac{\zeta^2\eta}{4} - \frac{\xi}{4} + \frac{\zeta^2\xi}{4} - \frac{\eta\xi}{4} + \frac{1}{4}\zeta^2\eta\xi \qquad (19)$$

$$N_{20} := \frac{1}{4} - \frac{\zeta^2}{4} - \frac{\eta}{4} + \frac{\zeta^2\eta}{4} - \frac{\xi}{4} + \frac{\zeta^2\xi}{4} + \frac{\eta\xi}{4} - \frac{1}{4}\zeta^2\eta\xi \qquad (20)$$

4   Verification

First Verification Condition
Sum of all the shape functions is equal to one

$$N_1 + N_2 + N_3 + N_4 + N_5 + N_6 + N_7 + N_8 + N_9 + N_{10}$$
$$+ N_{11} + N_{12} + N_{13} + N_{14} + N_{15} + N_{16} + N_{17} + N_{18} + N_{19} + N_{20}$$

Output
1

IInd Verification Condtion
Each shape function has a value of one at its own node and zero at other nodes.
   Node 1
   Substituting

$$\xi := -1$$
$$\eta := -1$$
$$\zeta := -1 \text{ Values in Equations } 1-20 \text{ we get } N_1 \text{ to } N_{20} \text{ values}$$

N_1 N_2 N_3 N_4 N_5 N_6 N_7 N_8 N_9 N_{10} N_{11} N_{12} N_{13} N_{14} N_{15} N_{16} N_{17} N_{18} N_{19} N_{20}
Output
1 0 0 0 0 0 0 0 0 0 0 0 0 0 0 0 0 0 0 0
   Node 2
   Substituting

$$\xi := 1$$
$$\eta := -1$$
$$\zeta := -1 \text{ Values in Equations } 1-20 \text{ we get } N_1 \text{ to } N_{20} \text{ values}$$

N_1 N_2 N_3 N_4 N_5 N_6 N_7 N_8 N_9 N_{10} N_{11} N_{12} N_{13} N_{14} N_{15} N_{16} N_{17} N_{18} N_{19} N_{20}
Output

0 1 0 0 0 0 0 0 0 0 0 0 0 0 0 0 0 0 0 0
Node 3
Substituting

$$\xi := 1$$
$$\eta := 1$$
$$\zeta := -1 \text{ Values in Equations } 1-20 \text{ we get } N_1 \text{ to } N_{20} \text{ values}$$

N_1 N_2 N_3 N_4 N_5 N_6 N_7 N_8 N_9 N_{10} N_{11} N_{12} N_{13} N_{14} N_{15} N_{16} N_{17} N_{18} N_{19} N_{20}
Output
0 0 1 0 0 0 0 0 0 0 0 0 0 0 0 0 0 0 0 0
Node 4
Substituting

$$\xi := -1$$
$$\eta := 1$$
$$\zeta := -1 \text{ Values in Equations } 1-20 \text{ we get } N_1 \text{ to } N_{20} \text{ values}$$

N_1 N_2 N_3 N_4 N_5 N_6 N_7 N_8 N_9 N_{10} N_{11} N_{12} N_{13} N_{14} N_{15} N_{16} N_{17} N_{18} N_{19} N_{20}
Output
0 0 0 1 0 0 0 0 0 0 0 0 0 0 0 0 0 0 0 0
Node 5
Substituting

$$\xi := -1$$
$$\eta := -1$$
$$\zeta := 1 \text{ Values in Equations } 1-20 \text{ we get } N_1 \text{ to } N_{20} \text{ values}$$

N_1 N_2 N_3 N_4 N_5 N_6 N_7 N_8 N_9 N_{10} N_{11} N_{12} N_{13} N_{14} N_{15} N_{16} N_{17} N_{18} N_{19} N_{20}
Output
0 0 0 0 1 0 0 0 0 0 0 0 0 0 0 0 0 0 0 0
Node 6
Substituting

$$\xi := 1$$
$$\eta := -1$$
$$\zeta := 1 \text{ Values in Equations } 1-20 \text{ we get } N_1 \text{ to } N_{20} \text{ values}$$

N_1 N_2 N_3 N_4 N_5 N_6 N_7 N_8 N_9 N_{10} N_{11} N_{12} N_{13} N_{14} N_{15} N_{16} N_{17} N_{18} N_{19} N_{20}
Output
0 0 0 0 0 1 0 0 0 0 0 0 0 0 0 0 0 0 0 0
Node 7
Substituting

$\xi := 1$
$\eta := 1$
$\zeta := 1$ Values in Equations $1-20$ we get N_1 to N_{20} values

N_1 N_2 N_3 N_4 N_5 N_6 N_7 N_8 N_9 N_{10} N_{11} N_{12} N_{13} N_{14} N_{15} N_{16} N_{17} N_{18} N_{19} N_{20}
Output
0 0 0 0 0 0 1 0 0 0 0 0 0 0 0 0 0 0 0 0
Node 8
Substituting

$\xi := -1$
$\eta := 1$
$\zeta := 1$ Values in Equations $1-20$ we get N_1 to N_{20} values

N_1 N_2 N_3 N_4 N_5 N_6 N_7 N_8 N_9 N_{10} N_{11} N_{12} N_{13} N_{14} N_{15} N_{16} N_{17} N_{18} N_{19} N_{20}
Output
0 0 0 0 0 0 0 1 0 0 0 0 0 0 0 0 0 0 0 0
Node 9
Substituting

$\xi := 1$
$\eta := 0$
$\zeta := -1$ Values in Equations $1-20$ we get N_1 to N_{20} values

N_1 N_2 N_3 N_4 N_5 N_6 N_7 N_8 N_9 N_{10} N_{11} N_{12} N_{13} N_{14} N_{15} N_{16} N_{17} N_{18} N_{19} N_{20}
Output
0 0 0 0 0 0 0 0 1 0 0 0 0 0 0 0 0 0 0 0
Node 10
Substituting

$\xi := 0$
$\eta := 1$
$\zeta := -1$ Values in Equations $1-20$ we get N_1 to N_{20} values

N_1 N_2 N_3 N_4 N_5 N_6 N_7 N_8 N_9 N_{10} N_{11} N_{12} N_{13} N_{14} N_{15} N_{16} N_{17} N_{18} N_{19} N_{20}
Output
0 0 0 0 0 0 0 0 0 1 0 0 0 0 0 0 0 0 0 0
Node 11
Substituting

$\xi := -1$
$\eta := 0$
$\zeta := -1$ Values in Equations $1-20$ we get N_1 to N_{20} values

N_1 N_2 N_3 N_4 N_5 N_6 N_7 N_8 N_9 N_{10} N_{11} N_{12} N_{13} N_{14} N_{15} N_{16} N_{17} N_{18} N_{19} N_{20}
Output
0 0 0 0 0 0 0 0 0 0 0 1 0 0 0 0 0 0 0 0
Node 12
Substituting

$$\xi := 0$$
$$\eta := -1$$
$$\zeta := -1 \text{ Values in Equations } 1-20 \text{ we get } N_1 \text{ to } N_{20} \text{ values}$$

N_1 N_2 N_3 N_4 N_5 N_6 N_7 N_8 N_9 N_{10} N_{11} N_{12} N_{13} N_{14} N_{15} N_{16} N_{17} N_{18} N_{19} N_{20}
Output
0 0 0 0 0 0 0 0 0 0 0 0 1 0 0 0 0 0 0 0
Node 13
Substituting

$$\xi := 1$$
$$\eta := 0$$
$$\zeta := 1 \text{ Values in Equations } 1-20 \text{ we get } N_1 \text{ to } N_{20} \text{ values}$$

N_1 N_2 N_3 N_4 N_5 N_6 N_7 N_8 N_9 N_{10} N_{11} N_{12} N_{13} N_{14} N_{15} N_{16} N_{17} N_{18} N_{19} N_{20}
Output
0 0 0 0 0 0 0 0 0 0 0 0 0 1 0 0 0 0 0 0
Node 14
Substituting

$$\xi := 0$$
$$\eta := 1$$
$$\zeta := 1 \text{ Values in Equations } 1-20 \text{ we get } N_1 \text{ to } N_{20} \text{ values}$$

N_1 N_2 N_3 N_4 N_5 N_6 N_7 N_8 N_9 N_{10} N_{11} N_{12} N_{13} N_{14} N_{15} N_{16} N_{17} N_{18} N_{19} N_{20}
Output
0 0 0 0 0 0 0 0 0 0 0 0 0 0 1 0 0 0 0 0
Node 15
Substituting

$$\xi := -1$$
$$\eta := 0$$
$$\zeta := 1 \text{ Values in Equations } 1-20 \text{ we get } N_1 \text{ to } N_{20} \text{ values}$$

N_1 N_2 N_3 N_4 N_5 N_6 N_7 N_8 N_9 N_{10} N_{11} N_{12} N_{13} N_{14} N_{15} N_{16} N_{17} N_{18} N_{19} N_{20}
Output
0 0 0 0 0 0 0 0 0 0 0 0 0 0 0 1 0 0 0 0

Node 16
Substituting

$\xi := 0$
$\eta := -1$
$\zeta := 1$ Values in Equations $1-20$ we get N_1 to N_{20} values

N_1 N_2 N_3 N_4 N_5 N_6 N_7 N_8 N_9 N_{10} N_{11} N_{12} N_{13} N_{14} N_{15} N_{16} N_{17} N_{18} N_{19} N_{20}
Output
0 0 0 0 0 0 0 0 0 0 0 0 0 0 0 1 0 0 0 0
Node 17
Substituting

$\xi := 1$
$\eta := -1$
$\zeta := 0$ Values in Equations $1-20$ we get N_1 to N_{20} values

N_1 N_2 N_3 N_4 N_5 N_6 N_7 N_8 N_9 N_{10} N_{11} N_{12} N_{13} N_{14} N_{15} N_{16} N_{17} N_{18} N_{19} N_{20}
Output
0 0 0 0 0 0 0 0 0 0 0 0 0 0 0 0 1 0 0 0
Node 18
Substituting

$\xi := 1$
$\eta := 1$
$\zeta := 0$ Values in Equations $1-20$ we get N_1 to N_{20} values

N_1 N_2 N_3 N_4 N_5 N_6 N_7 N_8 N_9 N_{10} N_{11} N_{12} N_{13} N_{14} N_{15} N_{16} N_{17} N_{18} N_{19} N_{20}
Output
0 0 0 0 0 0 0 0 0 0 0 0 0 0 0 0 0 1 0 0
Node 19
Substituting

$\xi := -1$
$\eta := 1$
$\zeta := 0$ Values in Equations $1-20$ we get N_1 to N_{20} values

N_1 N_2 N_3 N_4 N_5 N_6 N_7 N_8 N_9 N_{10} N_{11} N_{12} N_{13} N_{14} N_{15} N_{16} N_{17} N_{18} N_{19} N_{20}
Output
0 0 0 0 0 0 0 0 0 0 0 0 0 0 0 0 0 0 1 0
Node 20
Substituting

$$\xi := -1$$
$$\eta := -1$$
$$\zeta := 0 \text{ Values in Equations } 1{-}20 \text{ we get } N_1 \text{ to } N_{20} \text{ values}$$

N_1 N_2 N_3 N_4 N_5 N_6 N_7 N_8 N_9 N_{10} N_{11} N_{12} N_{13} N_{14} N_{15} N_{16} N_{17} N_{18} N_{19} N_{20}
Output
0 0 0 0 0 0 0 0 0 0 0 0 0 0 0 0 0 0 0 1

5 Conclusions

1. Derived shape functions for 20 nodal tri-quadratic serendipity element.
2. Verified first verification condition sum of all the shape functions is equal to one.
3. Verfied second verification condition at each shape function of node value is equal to one and zero at remaining nodes.

References

1. Liu GR, Quek SS (2003) The finite element method: a practical course. Elsevier Science Ltd., Amsterdam
2. Wolfram Mathematica® 9 Software, Version number 9.0.0.0

Cosinusoidally Fluctuating Temperature and Chemical Reacting Effects on MHD-Free Convective Fluid Flow Past a Vertical Porous Plate with Hall, Ion-Slip Current, and Soret

K. S. Balamurugan, K. V. B. Rajakumar, and J. L. Rama Prasad

Abstract In this paper, an exact solution and cosinusoidally fluctuating temperature of unsteady MHD-free convective flow through an infinite moving vertical permeable plate with hall, ion-slip current, and chemical reaction as well as soret effects has been analyzed. The exact solution of the governing equations was attained using perturbation method. The influence of dissimilar parameters on velocity, temperature as well as concentration fields is stated graphically. In this investigation, it was conclude that as rise in hall and ion-slip current parameter leads to rise in velocity, but contrast effect was occurred in case of heat source and Prandtl number. In addition, concentration and velocity are declined with rise in Reynolds number and soret parameter.

Keywords Hall and Ion-slip parameter · MHD · Perturbation · Chemical reaction · Radiation

1 Introduction

The noticeable fact heat and mass transfer on MHD have been gaining attention of huge number of researchers owing to its practical relevance's in manufacturing as well as science and technology, fabric reprocessing mechanized operations, geophysical as and planetary science, etc. Now the following literature has been presented a lot of researchers related to soret, chemical reaction, Radiation along with heat and mass transform but hall and ion-slip current was not worth mentioning.

K. S. Balamurugan (✉)
Department of Mathematics, R.V.R & J.C. College of Engineering, Guntur,
Andhra Pradesh 522109, India
e-mail: muruganbalaks@gmail.com

K. V. B. Rajakumar
Department of Mathematics, Kallam Haranadhareddy Institute of Technology, Guntur,
Andhra Pardesh, India

J. L. Rama Prasad
Department of Mathematics, PB Siddhartha College of Arts and Science, Vijayawada,
Andhra Pradesh, India

Mathew et al. [1] have presented the consequence of spanwise fluctuation and heat and mass transform on MHD flow passes during porous medium in a perpendicular channel using thermal radiation along with chemical reaction. In this investigation, it has been found that the velocity turns down by means of the accelerated values of Prandtl number in addition to radiation parameter. Das [2] have examined spanwise cosinusoidally fluctuating as well as non-Newtonian fluid model on MHD convective double diffusion flow through a hot non-parallel absorbent plate through heat absorption. In this paper, it was found that the governing equations are solved analytically. Ram et al. [3] have discussed the importance of cosinusoidally fluctuation heated permeable plate on MHD-free convective flow by means of radiating as well as reacting fluid. In this analization, it was observed that the outcomes indicate diminished velocity with the acceleration of magnetic field. Garg et al. [4] have reported spanwise cosinusoidal temperature and heat radiation effects on hydromagnetic forced as well as natural convective flow past a hot non-parallel channel by means of a porous medium. Ram et al. [5] have presented consinusoidally fluctuating temperature on MHD-free convective fluid flow. In this research paper, it was concluded that fluctuating the skin friction as well as Nusselt number by means of the variation in physical parameters. In addition, it was found that velocity as well temperature diminished by means of the accelerated of Prandtl number along with thermal radiation. Anuradha [6] has discussed the impact of cosinusoidally fluctuating temperature on MHD oscillatory natural convective fluid flow during the boundless non-parallel permeable plate. In the above, all investigations hall and ion-slip current were not taken into consideration in the equation of momentum. Singh et al. [7] obtained exact solution of MHD-free convective flow with spanwise fluctuation on second grade fluid past porous medium non-parallel absorbent channel by means of slip condition as well as radiation. Singh et al. [8] have illustrated that sway of hall current on MHD spanwise fluctuating free convective flow during porous medium in a non-parallel porous channel by means of radiation. In this examination, the results indicate that more rapid flows show the way to additional skin friction and for sluggish flows skin friction is fewer. Garg et al. [9], Chand et al. [10], and Krishna et al. [11] studied analytically, the influence of spanwise sinusoidal fluctuation on MHD forced and natural convection flow past in a non-parallel porous channel in presence of injection/suction by means of thermal radiation. Hamza et al. [12] concluded that the fluid velocity declined by means of a rise in magnetic field, porous parameters as well as Grashof number (Gr) but the reverse effect was shown in the case of slip parameter. In this investigation, analytical model (perturbation method) was utilized for solving the governing equations.

The effort has been made in this examination is to scrutinize the influence of cosinusoidally fluctuating temperature on unsteady MHD-free convective flow through an infinite moving vertical permeable plate with hall, ion-slip current, and chemical reaction as well as soret effects In this investigation, the governing equations are solved by using perturbation method. In this investigation, hall and ion-slip current is very important in fundamental inflows of lab plasma when a solid magnetic field of uniform quality is connected and drawn the consideration of the analysts because of their differed hugeness in fluid metals electrolytes arrive ionized gasses.

2 Formulation and Solution of the Problem

Unsteady 3D MHD-free convective flow of incompressible, viscous, electrically conducting fluid passes through an infinite non-parallel sizzling permeable plate on $x*y*z*$ plane. By considering all physical fluid quantities are independent of $x*$ along the direction of $x*$ with the assumption of the plate is to be considered in infinite length and it has strength B_0 under uniform normally magnetic field. Let $(u*, v*, w*)$ be the components of the velocity in the direction of (x^*, y^*, z^*) correspondingly. Here w^* tends to zero as independent of $z*$. With the effect of suction by means of fixed velocity $v* = -V$ at the surface of the plate. Now it was supposed that there be present hall and ion-slip current in the equation of momentum, moreover, chemical reaction between the fluid as well as species concentration.

The flow field is governed by the following set of equations.

Continuity equation:

$$\frac{\partial v*}{\partial y*} = 0 \tag{1}$$

Equation of Momentum:

$$\left[\frac{\partial u*}{\partial t*}\right] + v*\left[\frac{\partial u*}{\partial y*}\right] = g\beta[T* - T_\infty] + g\beta*[C* - C_\infty] + \upsilon\left[\frac{\partial^2 u*}{\partial y*^2} + \frac{\partial^2 u*}{\partial z*^2}\right] \\ - \frac{\sigma_e B_0^2[\alpha_e u* + \beta_e w*]}{\rho[\alpha_e^2 + \beta_e^2]} - \left[\frac{\upsilon}{k*}\right]u* \tag{2}$$

$$\left[\frac{\partial w*}{\partial t*}\right] + v*\left[\frac{\partial w*}{\partial y*}\right] = \upsilon\left[\left[\frac{\partial^2 w*}{\partial y*^2}\right] + \left[\frac{\partial^2 w*}{\partial z*^2}\right]\right] + \frac{\sigma_e B_0^2[\beta_e u* - \alpha_e w*]}{\rho[\alpha_e^2 + \beta_e^2]} - \left[\frac{\upsilon}{k*}\right]w* \tag{3}$$

Equation of energy

$$\rho C_P\left[\frac{\partial T*}{\partial t*}\right] + v*\left[\frac{\partial T*}{\partial y*}\right] = \kappa\left[\frac{\partial^2 T*}{\partial y*^2}\right] + \left[\frac{\partial^2 T*}{\partial z*^2}\right] + Q_0[T* - T_\infty] - \left[\frac{\partial q_r}{\partial y*}\right] \tag{4}$$

Equation of Concentration:

$$\rho C_P\left[\frac{\partial C*}{\partial t*}\right] + v*\left[\frac{\partial C*}{\partial y*}\right] = D\left[\frac{\partial^2 C*}{\partial y*^2}\right] + \left[\frac{\partial^2 C*}{\partial z*^2}\right] \\ - \Gamma[C* - C_\infty] + D_1\left[\frac{\partial^2 T*}{\partial y*^2}\right] + \left[\frac{\partial^2 T*}{\partial z*^2}\right] \tag{5}$$

The plate temperature is to vary spanwise cosinusoidally fluctuating with time 't' has been considered and is of the form

$$T_w(z^*, t^*) = T_0 + \varepsilon[T_0 - T_\infty]\cos\left[\frac{\pi z^*}{l} - w^* t^*\right] \tag{6}$$

The initial boundary conditions are as follows:

$$\left.\begin{array}{l} u^* = 0,\, T^* = T_0 + \varepsilon[T_0 - T_\infty]\cos\left[\frac{\pi z^*}{l} - w^* t^*\right],\, C^* = C_w \text{ at } y^* = 0 \\ u^* = 0,\, T^* = T_0,\, C^* = C_0 \hspace{4.5cm} \text{as } y \to \infty \end{array}\right\} \tag{7}$$

For the case of an optimality thin gray gas, local radiative heat flux in the energy equation

$$\frac{\partial q_r}{\partial y^*} = 4\sigma_s k_e\left[T^{*4} - T_\infty^4\right] \tag{8}$$

$$T^{*4} \cong 4T_\infty^3 T^* - 3T_\infty^4 \tag{9}$$

Form the Eq. (8), (9), and (4), the modified energy equation is

$$\left.\begin{array}{l} \rho C_P\left[\left[\frac{\partial u^*}{\partial t^*}\right] + v^*\left[\frac{\partial u^*}{\partial y^*}\right]\right] = \kappa\left[\left[\frac{\partial^2 T^*}{\partial y^{*2}}\right] + \left[\frac{\partial^2 T^*}{\partial z^{*2}}\right]\right] + Q_0[T^* - T_\infty] \\ +16 k_e \sigma T_\infty^3[T^* - T_\infty] \end{array}\right\} \tag{10}$$

The non-dimensional parameters as follows:

$$\left.\begin{array}{l} y = \frac{y^*}{l},\, uv = u^*,\, zl = z^*,\, kl = k^*,\, t = w^* t^*,\, v\omega = \omega^* l^*,\, z = \frac{z^*}{l} \\ \gamma = \frac{l^2 k_1}{v},\, \phi = \frac{C^* - C_\infty}{C_w - C_\infty},\, \theta = \frac{T^* - T_\infty}{T_w - T_\infty} \end{array}\right\} \tag{11}$$

Using the transformation (11) and Eq. (6), the momentum Eq. (2), (3), Eq. (10), and concentration Eq. (5) reduce to the following dimensionless form:

$$\left.\begin{array}{l} \omega\left[\frac{\partial u}{\partial t}\right] - \text{Re}\left[\frac{\partial u}{\partial y}\right] = \text{Re}^2\,\text{Gr}[\theta] + \text{Re}^2\,\text{Gm}[C] + \left[\frac{\partial^2 u}{\partial y^2}\right] + \left[\frac{\partial^2 u}{\partial z^2}\right] - \left[\frac{u}{k}\right] \\ -M^2\frac{[\alpha_e u + \beta_e w]}{[\alpha_e^2 + \beta_e^2]} \end{array}\right\} \tag{12}$$

$$\omega\left[\frac{\partial w}{\partial t}\right] - \text{Re}\left[\frac{\partial w}{\partial y}\right] = \left[\frac{\partial^2 w}{\partial y^2}\right] + \left[\frac{\partial^2 w}{\partial z^2}\right] - \left[\frac{w}{k}\right] - M^2\frac{[\beta_e u - \alpha_e w]}{[\alpha_e^2 + \beta_e^2]} \tag{13}$$

$$\omega\left[\frac{\partial\theta}{\partial t}\right] - \text{Re}\left[\frac{\partial\theta}{\partial y}\right] = \frac{1}{\text{Pr}}\left[\left[\frac{\partial^2\theta}{\partial y^2}\right] + \left[\frac{\partial^2\theta}{\partial z^2}\right]\right] - \left(\frac{R\,\text{Re}}{\text{Pr}}\right)\theta + \chi\,[\theta] \tag{14}$$

$$\omega\left[\frac{\partial\phi}{\partial t}\right] - \text{Re}\left[\frac{\partial\phi}{\partial y}\right] = \frac{1}{Sc}\left(\left[\frac{\partial^2\phi}{\partial y^2}\right] + \left[\frac{\partial^2\phi}{\partial z^2}\right]\right) - K_c\phi + So\left(\left[\frac{\partial^2\theta}{\partial y^2}\right] + \left[\frac{\partial^2\theta}{\partial z^2}\right]\right) \tag{15}$$

The corresponding boundary conditions are

$$u = 0, \theta = 1 + \varepsilon \cos(\pi z - t), \phi = 1 \quad \text{at } y = 0 \atop u = 0, \theta = 0, \phi = 0 \qquad \text{as } y \to \infty \Big\}$$

(16)

where

$$\begin{cases} \text{Re} = \frac{Vl}{v}, \text{Gr} = vg\beta(T_0 - T_\infty)(V^3)^{-1}, \text{Gm} = vg\beta(C_0 - C_\infty)(V^3)^{-1} \\ M^2 = l\sigma_e B_0^2(v)^{-1} R = 16k_e v^2 T_\infty^3 (kV^2)^{-1} \text{Pr} = \mu C_p k^{-1}, \text{Sc} = vD^{-1} \\ \chi = l^2 Q_0(vpC_p)^{-1}, \text{So} = \frac{D}{v}\left(\frac{T_0 - T_\infty}{C_0 - C_\infty}\right) N = \left[\frac{1}{k} + \frac{M^2[-\alpha_e + i\beta_e]}{[\alpha_e^2 + \beta_e^2]}\right] \end{cases}$$

(17)

Equations (12) and (13) are displayed, in a reduced form, as

$$\omega\left[\frac{\partial F}{\partial t}\right] - \text{Re}\left[\frac{\partial F}{\partial y}\right] = \text{Re}^2 \text{ Gr}[\theta] + \text{Re}^2 \text{ Gm}[C] + \left[\frac{\partial^2 F}{\partial y^2}\right] + \left[\frac{\partial^2 F}{\partial z^2}\right] - N[F]$$

(18)

The related boundary conditions are

$$F = 0, \theta = 1 + \varepsilon \cos[\pi z - t], \phi = 1 \text{ at } y = 0 \atop F = 0, \theta = 0, \phi = 0 \qquad \text{as } y \to \infty \Big\}$$

(19)

The solution of partial differential equations [(14), (15), and (17)] in conjunction with boundary condition (19) is attained utilizing regular perturbation method similar to one used in Ramakrishna Reddy et al. [11] as well as Singh et al. [8] through which is assumed the components of velocity, temperature, and concentration, respectively, as follows:

$$\begin{aligned} F &= F_0 + \varepsilon \ F_1 \exp[i\pi z - li] + \varepsilon^2 F_2 \exp[2i\pi z - 2li] \dots \\ \theta &= \theta_0 + \varepsilon \ \theta_1 \exp[i\pi z - li] + \varepsilon^2\theta_2 \exp[2i\pi z - 2li] \dots \\ \phi &= \phi_0 + \varepsilon \ \phi_1 \exp[i\pi z - li] + \varepsilon^2\phi_2 \exp[2i\pi z - 2li] \dots \end{aligned} \Bigg\}$$

(20)

Substituting Eq. (20) into set of Eqs. (14), (15), and (18) and equating the like powers, then we obtain

$$F = \left[(-k_3 - k_4)e^{-m_{13}y} + k_3 e^{-m_1 y} + k_4 e^{-m_7 y}\right] \\ + \varepsilon\left[\left((-k_5 - k_6)e^{-m_{15}y} + k_5 e^{-m_3 y} + k_6 e^{-m_9 y}\right)e^{i(\pi z - t)}\right]$$

(21)

$$\theta = \left[e^{-m_1 y}\right] + \varepsilon\left[\theta_1 e^{-m_3 y}\right]$$

(22)

$$\phi = \left[(1 - k_1)e^{-m_7 y} + k_1 e^{-m_1 y}\right] + \varepsilon\left[-k_2 e^{-m_9 y} + k_2 e^{-m_2 y}\right]$$

(23)

3 Results and Discussions

Figure 1 represents for dissimilar values of Hall parameter on the velocity. In this figure, it reflects that velocity rises with the enhancement of (β_e) near the plate and ultimately converges to its limiting value. Due to the production of an extra prospective dissimilarity transverse to the direction of accumulate free charge and applied magnetic field among the opposite surfaces induces an electric current perpendicular to both magnetic and electric. Figure 2 illustrated that variation of velocity for diverse values of ion-slip (β_i). From this figure, the outcomes reflects that the incremental values of β_i leads to rise in velocity and it is very close to the plate and reached converging point it is depend on the hall. The variation of velocity distribution under the sway of magnetic field (M) is reported in the Fig. 3. Therefore, Fig. 3 of outcomes indicates that the velocity reduced by means of augmentation of M. Owing to magnetic field employs a retarding force on free convection flow. Figures 4 and 5 exhibits the influence of chemical reaction (Kc) on velocity as well as concentration. Here, the incremental values of Kc leads to diminished in velocity and concentration. Chemical reaction ($Kc > 0$) distinguished as destructive reaction declines the flow velocity. Figures 6 and 7 reflects that for diverse values of soret (So) on velocity as well as concentration. From this figure, it was found that velocity and concentration rises with the enhancement of soret. Figure 8 reported that the sway of Schmidt number (Sc) on concentration. Here, this figure reflects that concentration declined with the rise in Sc. Physically, it is obviously, because rise of Sc means decline of

Fig. 1 Influence of β_e on velocity
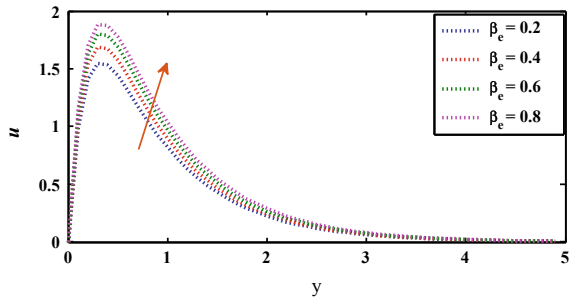
Fig. 2 Influence of β_i on velocity
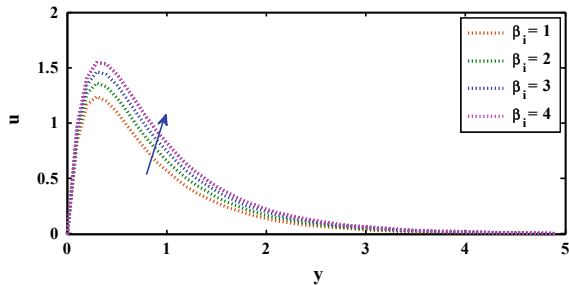
Fig. 3 Influence of *M* on velocity
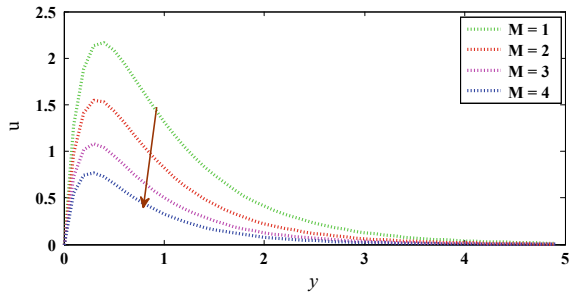
Fig. 4 Influence of *Kc* on velocity
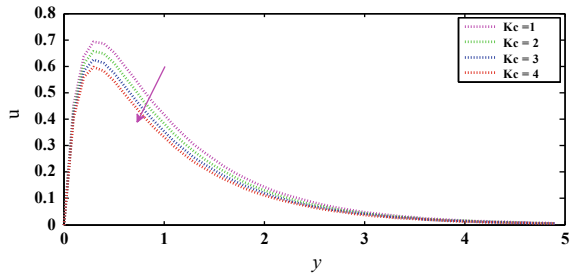
Fig. 5 Influence of *Kc* on concentration
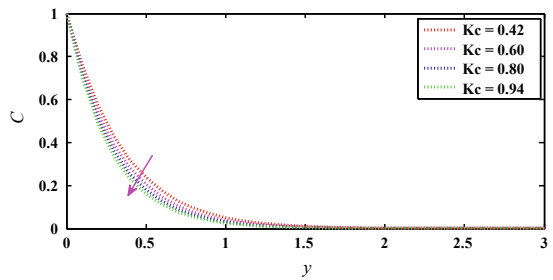
Fig. 6 Influence of So on velocity
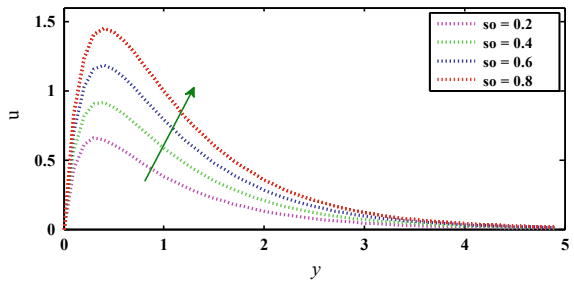
Fig. 7 Influence of So on concentration
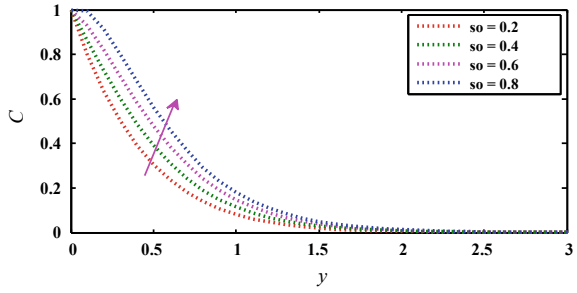
Fig. 8 Influence of Sc on concentration
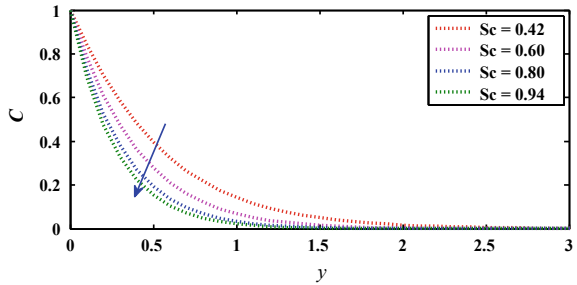
molecular diffusivity. Hence, the concentration of species is higher for small values of Sc and lower for large values of Sc.

Figures 9 and 10 demonstrated that velocity and temperature profile due to the variations in heat source parameter χ. From these figures, the results indicate that velocity declined with the rise in χ. Physically, in the presence of heat source has the propensity to decline the fluid velocity transversely the momentum boundary layer. Owing to the sway of thermal buoyancy to reduces which outcome in a net reduction in the velocity. This form of behavior is shown near to the plate. Also temperature declined with the rise in heat source parameter.

Fig. 9 Influence of χ on velocity
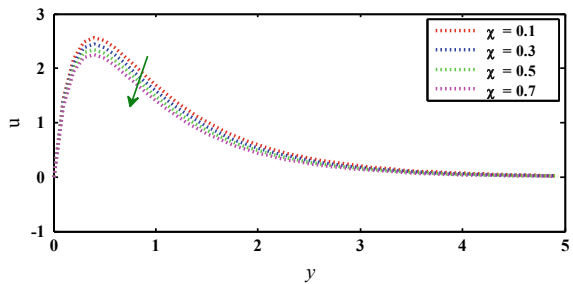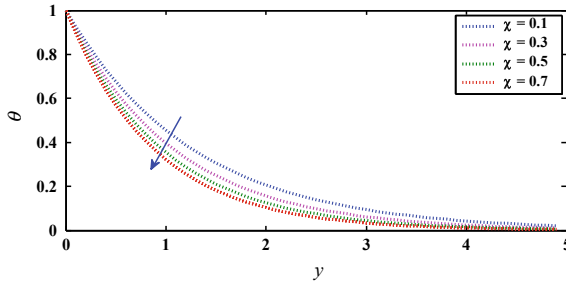
Fig. 10 Influence of χ on temperature
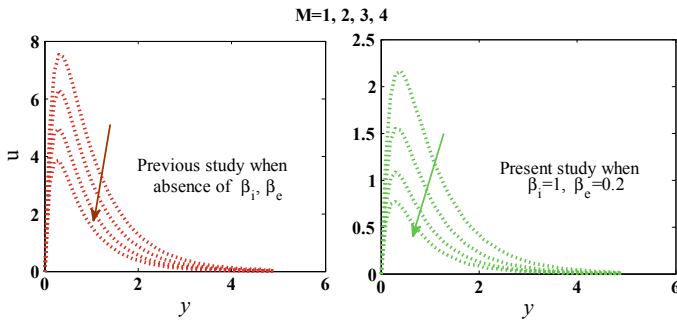
Fig. 11 Influence of M on velocity

4   Validity of the Results

In this examination, it is supposed to be revealed that the outcomes obtained herein are compared with the results of Ramakrishna and Raju [11] in the nonappearance of Hall and ion-slip parameter, i.e., β_e and β_i by taking dissimilar values for magnetic field parameter M keeping the other parameters unchanging and these outcomes are obtainable in Fig. 11. The consequences of this comparison are established to be in excellent agreement.

5   Conclusions

- The velocity as well as temperature diminished with the rise in Prandtl number (Pr) and heat source parameter (χ).
- As rise in Hall and ion-slip parameter, leads to rise in velocity.

- Velocity accelerated with the incremental values of Gr, Gm & So, but contrast effect was established in case of *M*.
- As concentration and velocity declined then it leads to a rise in a chemical reaction, Reynolds number Re, and soret parameter.

References

1. Mathew A, Singho KD (2015) Span-wise fluctuating MHD convective heat and mass transfer flow through porous medium in a vertical channel with thermal radiation and chemical reaction. Int J Heat Technol 33(2):135–142
2. Das UJ (2014) Viscoelastic effects on unsteady MHD free convection and mass transfer for viscoelastic fluid flow past a hot vertical porous plate with heat generation/absorption through porous medium. Int J Eng 2(12):165–172
3. Ram P, Singh H, Kumar R, Kumar V, Joshi VK (2017) Free convective boundary layer flow of radiating and reacting MHD fluid past a cosinusoidally fluctuating heated plate. Int J Appl Comput Math 3(1):261–294
4. Garg BP, Singh KD, Bansal N (2014) Hydro magnetic mixed convection flow through porous medium in a hot vertical channel with span wise co sinusoidal temperature and heat radiation. Int J Eng Innov Technol 3(12):249–255
5. Ram P, Singh H, Joshi VK (2014) Cosinusoidally fluctuating temperature and mass diffusivity in radiating and reacting MHD free convective fluid flow past a vertical porous plate. In: International conference on modelling and simulation of diffusive processes and applications, pp 67–73
6. Anuradha S (2013) heat and mass transfer of oscillatory free convective MHD flow past an infinite vertical porous plate with cosinusoidally fluctuating temperature. Int J Math Comput Appl Res 3(2):289–300
7. Singh KD (2015) Exact solution of span-wise fluctuating MHD convective flow of second grade fluid through porous medium in a vertical channel with heat radiation and slip condition. Kragujevac J Sci 37(2):65–78
8. Singh KD, Mathew A (2015) Hall current effect on radiating span wise fluctuating MHD convective flow through porous medium in a vertical porous channel. Kragujevac J Sci 37(2):49–63
9. Garg BP, Singh KD (2015) Neeraj Injection/suction effect on spanwise sinusoidal fluctuating MHD mixed convection flow through porous medium in a vertical porous channel with thermal radiation. J Rajasthan Acad Phys Sci 14(1):73–88
10. Chand K, Thakur N (2016) Span-wise fluctuating hydromantic free convective heat transfer flow past a hot vertical porous plate with thermal radiation and viscous dissipation in slip flow regime. J Rajasthan Acad Phys Sci 15(4):267–281
11. Ramakrishna P, Raju MC (2018) MHD free convective flow past a porous plate. Int J Pure Appl Math 118(5):507–529
12. Hamza MM, Isah BY, Usman H (2011) Unsteady heat transfer to MHD oscillatory flow through a porous medium under slip condition. Int J Comput Appl 33(4):12–17

Fluid Motion in Finite Length Tubes in Peristaltic Pumps

André Small and P. Nagarani

Abstract We considered the flow of an incompressible Newtonian fluid within a finite tube, which is driven by multiple train waves or a single peristaltic wave. The solutions of the governing equations were taken as a pertubation series with pertubation parameter being the wave number. These infinite series were truncated at the first corrective term. Expressions for the axial and transverse conponents of the velocity, the pressure, the shear stress at the walls as well as the volume flow rate were obtained. From this study, the effects of the wave number, the occlusion of the tube, the wave amplitude, as well as the wave type were analyzed. It was observed that the pressure distribution is affected by the wave type, the time-averaged volume flow is slightly affected non-integral number of waves and is independent of the axial position for the case of multiple train waves. However, in the case of single wave, the time-averaged volume flow depends on the axial position and we saw reflux at the entrance of the tube even for co-pumping conditions. Also, changes in the wave number resulted in tranformations of the plots of the results which became more obvious for highly occluded tubes.

Keywords Peristaltic transport · Lubrication theory · Finite tubes · Perturbation methods

1 Introduction

The mechanism of peristalsis is very well known to physiologists and engineers as one of the major mechanisms for fluid transport in many biological systems and industrial pumping. Peristalsis is a mechanism used to pump fluids within a tube

A. Small · P. Nagarani (✉)
Department of Mathematics, The University of the West Indies, Mona Campus,
Kingston, Jamaica
e-mail: nagarani_ponakala@yahoo.co.in

A. Small
Faculty of Engineering and Applied Technology, Caribbean Maritime University,
Palisadoes Park, Norman Manley Highway, Kingston, Jamaica

by means of moving contractile rings around the tube, which pushes the material onward. The peristaltic wave generated along the flexible walls of the tube provides an efficient means of transport of fluids in these biological and industrial pumping systems. Regarded as pumping without a piston, peristalsis is the prime method of transport in several biological processes. Whether chyme is being transported through the intestines, urine from the kidneys to the bladder, lymphatic fluids in the lymphatic ducts, the swallowing of a bolus of food in the esophagus, or the transportation of an embryo from the ovary to the womb via the fallopian tubes, the relevant fluids are thrust in the direction of waves of contractions. These waves are generated by either the muscles embedded in the walls of the vessels themselves or by exo-skeletal muscles which line the tubes.

The first mathematical attempt to understand the fluid mechanics of peristalsis is by Latham [6], although it has been a very well-observed pumping phenomenon in biological systems for many decades in advance. Fung and Yih [3] also made early contributions in mathematical models on peristaltic transport. They considered and included the non-linear convective accelerations and analyzed the model under small peristaltic wave amplitudes in a two-dimensional channel. In their study, it was observed that the mean flow induced by peristaltic motion of the wall is proportional to the square of the amplitude ratio. The velocity of the fluid was found to be dependent on the mean pressure gradient and for a particular positive pressure gradient (critical value), the velocity was zero. There was no reflux when pumping against a pressure head ($\nabla p = p_{\text{outlet}} - p_{\text{inlet}}$) less than this critical pressure gradient. However, if the pressure gradient was greater than this value, then a backward flow was induced. The infinite length tube model, later introduced by Shapiro et al. [15], capitalized on the steady nature of such flow in the wave frame of reference. Unlike the model postulated by Fung and Yih [3], the inertial effects were neglected and hence the flow was considered viscous driven. By considering the streamlines, two important phenomena were explored, viz. reflux and trapping. Reflux refers to the existence of particles that move on average in the retrograde direction and occurs at the periphery of the tube. Trapping, on the other hand, refers to circulating parcels of fluid located at the center of the tube moving at the speed of the wave as if trapped by the wave. These results were compared with experimental observations which confirmed a linear relationship in the time-averaged volume flow rate and the pressure head.

By obtaining an asymptotic series solution for low Reynolds number flow in a slowly varying axisymmetric tube, Manton [8] provided expressions for the pressure drop along the tube and the shear stress at the wall. Here, the stream function and the vorticity component were used to provide solutions to the governing equations up to the second order and the wall shape was formulated as a function of a perturbation parameter. The zeroth-order solution was identified in this work as Poiseuille flow, and the first- and second-order solutions provided the inertial correction. This analysis was deemed applicable to problems such as flow through blood vessels and capillary tubes. Manton [8] later studied long wavelength peristaltic pumping at low Reynolds number. Again, using the stream functions and vorticity component, he obtained asymptotic series solutions for the flow fields for varying wave shapes. Here, the

chosen perturbation parameter is the wave number, hence incorporating the analysis of the inertial effects of the flow. He examined the conditions necessary and sufficient for trapping and established also that reflux is only possible with an adverse mean pressure gradient.

On the other hand, the finite tube models consider inherently the non-steady nature of the flow. These models are suited for biological transport systems in which the flow is induced by peristaltic waves and in commercial pumps. Pressures are prescribed at the ends of the tubes and the resulting pressure head is either a function of time or a constant. The solutions of the conservation equations are found in this case in the stationary frame of reference. In the model proposed by Li and Brasseur [7], several wall shapes were considered to include a single wave in the tube, tear drop-shaped wave trains, and sinusoidal wave trains. For integral number of waves within the tubes, the finite length tube model coincides with the infinite length tube model proposed by Shapiro et al. [15]. Non-integral numbers of waves present within the tubes however had differences in the local flow parameters however minute differences in the global pumping performance. Also, single-wave pumping displayed significant differences in the pressure distribution and the pumping performance. Reflux at the inlet in single-wave pumping occurred even with favorable pressure heads $\nabla p < 0$ and could only be prevented when $\frac{\varepsilon}{a} = 0$ or $\frac{\varepsilon}{a} = 1$, that is full occlusion or no occlusion. Here, $\frac{\varepsilon}{a}$ is a measure of the tube occlusion which is normalized and $\frac{\varepsilon}{a} \in [0, 1]$. For train wave pumping, reflux is only possible for an adverse pressure head.

Later, several theoretical and experimental attempts have been made to understand peristaltic transport in different flow and geometric situations. For application to biological fluid transport and other physical transportation of fluid, peristaltic flow of several fluid types other than Newtonian fluid was also considered. Much of the theoretical papers that are available in the literature on peristaltic pumping may be classified in two categories: (i) The infinite tube/channel model and (ii) the finite tube/channel model. Generally, in both models mentioned, the lubrication theory is applied, that is the mean radius a is much smaller when compared with the wavelength λ and the effective Reynolds number ($R = \text{Re}(\frac{a}{\lambda})$) is low enough to classify the flow as laminar, where Re is the Reynolds number. Usha and Rao [20] examined the effects of a two-layered fluid being transported in a tube of elliptical cross section. They observed the effects of the peripheral layer viscosity on the flow rate and frictional force for a slightly elliptical tube. It was shown that the time-averaged flux is not significantly affected by the pressure drop when the eccentricity is large. However, the pumping seems to improve with the eccentricity. Rani and Sarojamma [12] investigated peristaltic transport of a Casson fluid in an asymmetric channel and considered the walls having different amplitudes and phase difference. Ravi Kumar et al. [13] investigated peristaltic transport of a power law fluid in asymmetric channels bounded by permeable walls. The lower wall expression was adjusted here to facilitate the asymmetry of the walls. With these conditions, they obtained expressions for the velocity, pressure rise, and frictional force as well as the behavior of these quantities for various parameters. Later Roy et al. [14] formulated a mathematical model for the flow of chyme during gastrointestinal endoscopy, by considering the effects on the flow of in inserted endoscope, for varying aspect ratios and wave amplitudes.

Further, Kavitha et al. [5] considered a Jeffrey fluid again with porous walls, with suction and injection.

Eytan et al. [2] developed a model where again the flow was induced by the walls within a finite two-dimensional channel, for application to embryo transport within the uterine cavity. They considered symmetric and asymmetric wall displacements and showed that the transport phenomena is strongly dependent on the phase shift of the wall displacement and the angle between the walls. It was also revealed that whenever the contraction is completely out of phase, the velocities, pressure, flow rate, and axial transport are reduced to zero. They provided the bases for reflux in tappered channels and showed that reflux is more likely when the wall is asymmetric while trapping is enhanced as the asymmetry decreases. Misra and Pandey [9] formulated a model considering the flow of a food bolus through the esophagus. A power law fluid is used to model the flow through an axisymmetric tube of finite length, with a single contractile peristaltic wave responsible for fluid propulsion. The dependency of the pressure within the tube over time and space were studied for a fixed time-averaged flow rate, in the stationary frame of reference. Comparisons between single and train wave transport, with an integral number of waves, were made. The effects of the wave nature and the power law index number on the pressure distribution along the tube were examined. To establish a model suitable to the physiological occurrence during peristalsis, Hariharan et al. [4] considered peristaltic transport of both power law and Bingham fluids within diverging tubes for a wide range of waveforms. They obtained expressions for some of the wall waveforms using Fourier series and identified the effects of not just the waveform on the flow but also the power law index, the wave amplitude, and the yield stress. In their report, it is established that the wave amplitude and the index number are critical parameters in peristaltic transport. Furthermore, the thickness of the reflux region depends strongly on these parameters and the wave shape. Later, Tripathi et al. [17] also added to the model introduced by Li and Brasseur [7] by considering the mechanical efficiency and reflux of peristaltic pumping of a Newtonian fluid.

Again to understand the dynamics of esophageal swallowing of a variety of foods such as honey, Pandey and Tripathi [11] studied peristaltic transport of Casson fluids. They provided information on the pressure distribution along the esophagus and investigated non-integral number of waves at different instances of time. They also offered information on the local shear stress, yield stress, and the mechanical efficiency of esophageal pumping during Casson fluid transport. Reflux and the limits of reflux are also discussed in this investigation. In an effort to provide a model which closely simulates esophageal swallowing, Toklu [16] formulated a revised mathematical model highly dependent on experimental data. Using monometric measurements of the luminal pressure in the esophagus and video-flouroscopy to show the motion of the esophageal wall, experimental data was gathered and later used to guide the formulation of the model. Here, single waves were considered along a tube of circular cross section. The conclusion reached was that the model is qualified to provide information on peristaltic transport of fluids in a finite tube with a single wave present within the tube, in particular esophageal swallowing and transport in the ureter. Misra and Maiti [10] explored finite length tube peristaltic pumping of a power law fluid (a

model for fluid transport in the esophagus) and reported that local pressure was highly sensitive to the fluid index n (where $n = 1$ implies a Newtonian fluid), a result which later confirmed the conclusions of Hariharan et al. [4]. Seeking a perturbation method of solution with the viscosity parameter chosen as the perturbation parameter, Adb Elmabouda et al. [1] observed peristaltic motion of an incompressible Newtonian fluid with variable viscosity. Here, the viscosity is a function of the radial coordinate r and is described by $\mu(r) = 1 - ar^n$ where $n \geq 2$ and viscosity parameter $\alpha \ll 1$. Tripathi et al. [20] also investigated non-steady peristaltic flow with variable viscosity, to simulate the transport in physiological vessels. Here, as many models mentioned before, the model is analyzed for large wavelengths in comparison with mean radius of the tube and low Reynolds number. In particular, the viscosity is taken to vary exponentially and it is revealed that increasing the viscosity results in a reduction in the mechanical efficiency. Later, Tripathi et al. [19] studied peristaltic transport of a bi-viscosity fluid through a curved tube: A mathematical model for intestinal flow. The fluid was modeled using the Nakamura–Sawada bi-viscosity non-Newtonian formulation. The effects of the curvature of the tube, the volume flow rate, and the apparent viscosity of the fluid on the flow were observed. Here, it was observed that increasing curvature increases the pressure rise in the pumping region. Also, the bolus size slightly increases with increase in the non-Newtonian effects.

With the aforementioned applications of peristaltic transport in a finite length tube, we intend to study the peristaltic transport of a Newtonian fluid in a finite length tube in the present paper. We extend the study of Li and Brasseur [7] by including the first-order terms using a perturbation series solution with perturbation parameter being the wave number ($k = \frac{a}{\lambda}$). The mathematical formulation of the present model is given in Sect. 2. Section 3 explains the method of solution of the problem. Analytic expressions for velocity and pressure gradient up to $O(k)$ terms are included. Results are discussed in Sect. 4 with pictorial representations. The effect of multiple non-integral number of train waves, when compared with integral number of wave trains within the tube, is explored. The local flow fields and global pumping performance for a single wave within the tube, when compared with multiple integral train waves, are investigated. Along with the pressure and shear stress at the wall, the other flow characteristics observed are the volume flow rate and the time-averaged volume flow rate. Concluding remarks are given in Sect. 5.

2   Mathematical Formulation

We consider the flow of an incompressible Newtonian fluid with viscosity μ and density ρ, in a tube of length L with mean radius a. The fluid is being driven by oscillations of the wall (i.e., dominantly viscous driven flow) due to the propagation of the peristaltic wave represented by

$$\hat{H}(\hat{x}, \hat{t}) = \varepsilon + 0.5\hat{A}\left(1 - \cos\left(\frac{2\pi}{\lambda}(\hat{x} - c\hat{t})\right)\right) \tag{1}$$
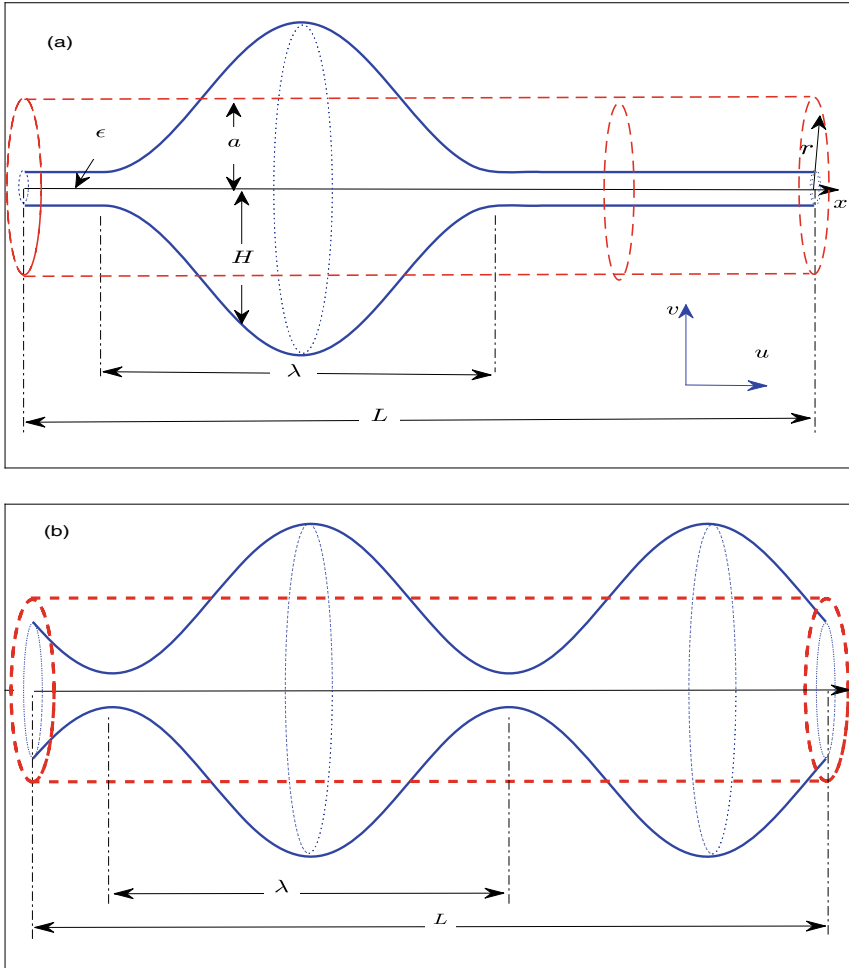
Fig. 1 (a) Single peristaltic wave within a tube of length L and (b) multiple peristaltic waves within the tube

Here, ε is the occlusion in the tube or the radius of the tube at the trough, $\hat{x}$ and $\hat{t}$ are the space and time coordinates, c is the wave speed, λ is the wavelength of the peristaltic wave, and $\hat{A}$ is the amplitude of the wave. The wave shapes being considered here are sinusoidal integral and non-integral train waves as well as a single wave within the tube, as shown in Fig. 1. The wall moves only in the radial direction however, with a speed $\frac{\partial \hat{H}}{\partial \hat{t}}$. Axisymmetric flow is assumed in a tube of circular cross section and the volume of the fluid in one wave is V_b. Pressures are prescribed at the tube inlet $\hat{p}(0, \hat{t})$ and outlet $\hat{p}(L, \hat{t})$ of the tube which are considered here as constants with respect to time.

The problem is fashioned in the stationary (laboratory) frame of reference. We desire to obtain expressions for the flow fields as well as expressions for the shear

stress on the wall of the tube and the instantaneous and time-averaged volume flow rate. Under the above assumptions, the equations that govern the flow are:

$$\rho\left(\frac{\partial}{\partial \hat{t}} + \hat{v}\frac{\partial}{\partial \hat{r}} + \hat{u}\frac{\partial}{\partial \hat{x}}\right)\hat{u} = -\frac{\partial \hat{p}}{\partial \hat{x}} + \mu\left(\frac{1}{r}\frac{\partial}{\partial \hat{r}}\left(\hat{r}\frac{\partial \hat{u}}{\partial \hat{r}}\right) + \frac{\partial^2 \hat{u}}{\partial \hat{x}^2}\right) \tag{2}$$

$$\rho\left(\frac{\partial}{\partial \hat{t}} + \hat{v}\frac{\partial}{\partial \hat{r}} + \hat{u}\frac{\partial}{\partial \hat{x}}\right)\hat{v} = -\frac{\partial \hat{p}}{\partial \hat{r}} + \mu\left(\frac{1}{r}\frac{\partial}{\partial \hat{r}}\left(\hat{r}\frac{\partial \hat{v}}{\partial \hat{r}}\right) + \frac{\partial^2 \hat{v}}{\partial \hat{x}^2} - \frac{\hat{v}}{\hat{r}^2}\right) \tag{3}$$

$$\frac{1}{\hat{r}}\frac{\partial}{\partial \hat{r}}(\hat{r}\hat{v}) + \frac{\partial \hat{u}}{\partial \hat{x}} = 0 \tag{4}$$

where $\hat{u}$ is the axial velocity component, $\hat{v}$ is the radial velocity component, and $\hat{p}$ is the pressure. The corresponding boundary conditions are given by:

$$\hat{u}|_{\hat{r}=\hat{H}} = 0,\ \hat{v}|_{\hat{r}=\hat{H}} = \frac{\partial \hat{H}}{\partial \hat{t}},\ \frac{\partial \hat{u}}{\partial \hat{r}}\bigg|_{\hat{x}r=0} = 0,\ \hat{v}|_{\hat{r}=0} = 0 \tag{5}$$

We now introduce the following non-dimensional quantities

$$x = \frac{\hat{x}}{\lambda},\ r = \frac{\hat{r}}{a},\ u = \frac{\hat{u}}{c},\ v = \frac{\hat{v}}{ck},\ t = \frac{c\hat{t}}{\lambda},\ A = \frac{\hat{A}}{a},\ p = \frac{ak\hat{p}}{\mu c} \tag{6}$$

Here, $k = \frac{a}{\lambda}$ is the wave number. By introducing the above non-dimensional quantities in (2)–(4), we obtain

$$\text{Re}\,k\left(\frac{\partial}{\partial t} + v\frac{\partial}{\partial r} + u\frac{\partial}{\partial x}\right)u = -\frac{\partial p}{\partial x} + \frac{1}{r}\frac{\partial}{\partial r}\left(r\frac{\partial u}{\partial r}\right) + k^2\frac{\partial^2 u}{\partial x^2} \tag{7}$$

$$\text{Re}\,k^3\left(\frac{\partial}{\partial t} + v\frac{\partial}{\partial r} + u\frac{\partial}{\partial x}\right)v = -\frac{\partial p}{\partial r} + k^2\frac{1}{r}\frac{\partial}{\partial r}\left(r\frac{\partial v}{\partial r}\right) + k^4\frac{\partial^2 v}{\partial x^2} - k^2\frac{v}{r^2} \tag{8}$$

$$\frac{1}{r}\frac{\partial}{\partial r}(rv) + \frac{\partial u}{\partial x} = 0 \tag{9}$$

where $\text{Re} = \frac{\rho a c}{\mu}$ is the Reynolds number. The corresponding expression for wall shape in the dimensionless form is

$$H(x,t) = \frac{\varepsilon}{a} + 0.5A\left(1 - \cos 2\pi(x-t)\right) \tag{10}$$

The boundary conditions in non-dimensional form are also expressed as

$$u|_{r=H} = 0,\ v|_{r=H} = \frac{\partial H}{\partial t},\ \frac{\partial u}{\partial r}\bigg|_{r=0} = 0,\ v|_{r=0} = 0 \tag{11}$$

3 Method of Solution

We assume the solution of (7)–(9) subjected to the conditions (11), as a series solution in terms of the chosen perturbation parameter k, that is

$$u = u_0 + k u_1 + O(k^2) \tag{12}$$

$$v = v_0 + k v_1 + O(k^2) \tag{13}$$

$$p = p_0 + k p_1 + O(k^2) \tag{14}$$

Substituting (12)–(14) into (7)–(9), collecting the zeroth-order terms and rearranging these terms we acquire the equations

$$\frac{\partial p_0}{\partial x} = \frac{1}{r} \frac{\partial}{\partial r} \left\{ r \frac{\partial u_0}{\partial r} \right\} \tag{15}$$

$$\frac{\partial p_0}{\partial r} = 0 \tag{16}$$

$$\frac{1}{r} \frac{\partial}{\partial r} (r v_0) + \frac{\partial u_0}{\partial x} = 0 \tag{17}$$

These equations are subjected to the corresponding boundary conditions

$$u_0|_{r=H} = 0, \; v_0|_{r=H} = \frac{\partial H}{\partial t}, \; \left. \frac{\partial u_0}{\partial r} \right|_{r=0} = 0, \; v_0|_{r=0} = 0 \tag{18}$$

Also, by collecting the first-order perturbation correction terms ($O(k)$) and again rearranging the terms we obtain the equations

$$\mathrm{Re}\left(\frac{\partial}{\partial t} + v_0 \frac{\partial}{\partial r} + u_0 \frac{\partial}{\partial x} \right) u_0 + \frac{\partial p_1}{\partial x} = \frac{1}{r} \frac{\partial}{\partial r} \left(r \frac{\partial u_1}{\partial r} \right) \tag{19}$$

$$\frac{\partial p_1}{\partial r} = 0 \tag{20}$$

$$\frac{1}{r} \frac{\partial}{\partial r} (r v_1) + \frac{\partial u_1}{\partial x} = 0 \tag{21}$$

with boundary conditions

$$u_1|_{r=H} = 0, \; v_1|_{r=H} = 0, \; \left. \frac{\partial u_1}{\partial r} \right|_{r=0} = 0, \; v_1|_{r=0} = 0 \tag{22}$$

First the system (15)–(17) is solved subjected to the boundary conditions listed in (18) to obtain (u_0, v_0, p_0). Next the system of (19)–(21) subjected to the boundary conditions registered in (22) is solved for (u_1, v_1, p_1). Later, the results are combined to give the solution $(u, v, p) = (u_0, v_0, p_0) + k(u_1, v_1, p_1) + O(k^2)$.

3.1 The Flow Field

Since $p = p_0 + kp_1$ is independent of r, the expression for u_0, the zeroth-order term of u the axial velocity, is obtained from (15) as

$$u_0 = \frac{1}{4} \frac{\partial p_0}{\partial x} (r^2 - H^2) \tag{23}$$

An expression for v_0, the zeroth-order term of the transverse velocity, is acquired by substituting (23) into (17). Again integrating with respect to r and using the boundary conditions listed in (18), we obtain v_0 as

$$v_0 = \frac{r}{4} \left\{ H \frac{\partial H}{\partial x} \frac{\partial p_0}{\partial x} - \frac{\partial^2 p_0}{\partial x^2} \left(\frac{r^2}{4} - \frac{H^2}{2} \right) \right\} \tag{24}$$

Substituting the second boundary condition given in (22) into (24), we obtain

$$\frac{\partial H}{\partial t} = \frac{H^2}{4} \frac{\partial H}{\partial x} \frac{\partial p_0}{\partial x} + \frac{H^3}{16} \frac{\partial^2 p_0}{\partial x^2}. \tag{25}$$

Solving (25), we have

$$\frac{\partial p_0}{\partial x}(x, t) = H^{-4}(x, t) \left\{ G_0(t) + 16 \int_0^x H(s, t) \frac{\partial H}{\partial t}(s, t) ds \right\}, \tag{26}$$

$$p_0(x, t) = p_0(0, t) + \int_0^x \frac{\partial p_0}{\partial x}(s, t) ds. \tag{27}$$

Here, $G_0(t)$ is a constant of integration and is at most a function of time. Keeping $p(0, t)$ and $p(L, t)$ invariant with respect to time, evaluating this constant of integration we have,

$$G_0(t) = \frac{\nabla p - 16 \int_0^L H^{-4}(\xi, t) \left(\int_0^\xi H(s, t) \frac{\partial H}{\partial t}(s, t) ds \right) d\xi}{\int_0^L H^{-4}(\eta, t) d\eta} \tag{28}$$

where $\nabla p = p(L) - p(0)$. Equations (23)–(28) give the complete solution to the system (15)–(17) subjected to the boundary condition listed in (18). Now, the solution

of the second system of equations, (19)–(21) subjected to the conditions provided in (22), is obtained as:

$$u_1 = F_2(x, r, t) + \frac{1}{4} \frac{\partial p_1}{\partial x} (r^2 - H^2) \tag{29}$$

where $F_2(x, r, t)$ is described by the equation

$$
\begin{aligned}
F_2(x, r, t) = \operatorname{Re} \Big\{ & \frac{1}{8} \frac{\partial p_0}{\partial x} \frac{\partial^2 p_0}{\partial x^2} \Big(\frac{r^6}{144} - \frac{r^4 H^2}{32} + \frac{r^2 H^4}{8} - \frac{29 H^6}{288} \Big) \\
& + \frac{1}{4} \frac{\partial^2 p_0}{\partial x \partial t} \Big(\frac{r^4}{16} - \frac{r^2 H^2}{4} + \frac{3 H^4}{16} \Big) \\
& + \frac{1}{32} \Big(\frac{\partial p_0}{\partial x} \Big)^2 \frac{\partial H}{\partial x} (r^2 H^3 - H^5) \\
& - \frac{1}{8} \frac{\partial p_0}{\partial x} \frac{\partial H}{\partial t} (r^2 H - H^3) \Big\}
\end{aligned}
\tag{30}
$$

$$v_1 = -F_3(x, r, t) - \frac{1}{4} \frac{\partial^2 p_1}{\partial x^2} \Big(\frac{r^3}{4} - \frac{r H^2}{2} \Big) + \frac{1}{4} \frac{\partial p_1}{\partial x} \frac{\partial H}{\partial x} r H \tag{31}$$

where the function $F_3(x, r, t)$ is obtained as

$$
\begin{aligned}
F_3(x, r, t) = \operatorname{Re} \Big\{ & \frac{1}{8} \frac{\partial p_0}{\partial x} \Big(\frac{\partial^3 p_0}{\partial x^3} \Big(\frac{r^7}{1152} - \frac{r^5 H^2}{192} + \frac{r^3 H^4}{32} - \frac{29 r H^6}{576} \Big) \\
& + \frac{\partial^2 p_0}{\partial x^2} \frac{\partial H}{\partial x} H \Big(-\frac{r^5}{96} + \frac{r^3 H^2}{8} - \frac{29 r H^4}{96} \Big) \Big) \\
& + \frac{1}{4} \frac{\partial^3 p_0}{\partial x^2 \partial t} \Big(\frac{r^5}{96} - \frac{r^3 H^2}{16} + \frac{3 r H^4}{32} \Big) \\
& + \frac{1}{8} \Big(\frac{\partial p_0}{\partial x} \Big)^2 \Big(\frac{r^7}{1152} - \frac{r^5 H^2}{192} + \frac{r^3 H^4}{32} - \frac{29 r H^6}{576} \Big) \\
& + \frac{1}{16} \frac{\partial p_0}{\partial x} \frac{\partial^2 p_0}{\partial x^2} \frac{\partial H}{\partial x} H^3 \Big(\frac{r^3}{4} - \frac{r H^2}{2} \Big) \\
& + \frac{1}{4} \frac{\partial^2 p_0}{\partial x \partial t} \frac{\partial H}{\partial x} H \Big(-\frac{r^3}{8} + \frac{3 r H^2}{8} \Big) \\
& - \frac{1}{8} \frac{\partial^2 p_0}{\partial x^2} \frac{\partial H}{\partial t} H \Big(\frac{r^3}{4} - \frac{r H^2}{2} \Big) \\
& + \frac{1}{32} \Big(\frac{\partial p_0}{\partial x} \Big)^2 \Big(\frac{\partial^2 H}{\partial x^2} H^3 \Big(\frac{r^3}{4} - \frac{r H^2}{2} \Big) \\
& + \Big(\frac{\partial H}{\partial x} \Big)^2 H^2 \Big(\frac{3 r^3}{4} - \frac{5 r H^2}{2} \Big) \Big) \\
& - \frac{1}{8} \frac{\partial p_0}{\partial x} \Big(\frac{\partial^2 H}{\partial x \partial t} H \Big(\frac{r^3}{4} - \frac{r H^2}{2} \Big) \\
& + \frac{\partial H}{\partial t} \frac{\partial H}{\partial x} \Big(\frac{r^3}{4} - \frac{3 r H^2}{2} \Big) \Big) \Big\}
\end{aligned}
\tag{32}
$$

$$\frac{\partial p_1}{\partial x}(x, t) = H^{-4}(x, t)\left\{G_1(t) + 16 \int\limits_0^x H(s, t)F_3(s, t)\mathrm{d}s\right\}, \tag{33}$$

where

$$G_1(t) = \frac{-16 \int_0^L H^{-4}(\xi, t)\left(\int_0^\xi H(s, t)F_3(s, t)\mathrm{d}s\right)\mathrm{d}\xi}{\int_0^L H^{-4}(\eta, t)\mathrm{d}\eta} \tag{34}$$

and

$$p_1(x, t) = \int\limits_0^x \frac{\partial p_1}{\partial x}(s, t)\mathrm{d}s. \tag{35}$$

Here, G_1 like G_0 is again at most a function of t. Using the results obtained in (23)–(35), we therefore construct the series solution for u, v and p as

$$u = \frac{1}{4}\left(\frac{\partial p_0}{\partial x} + k\frac{\partial p_1}{\partial x}\right)(r^2 - H^2) + kF_2(x, r, t) + O(k^2), \tag{36}$$

$$v = \frac{r}{4}\left\{\left(\frac{\partial p_0}{\partial x} + k\frac{\partial p_1}{\partial x}\right)\frac{\partial H}{\partial x}H - \left(\frac{\partial^2 p_0}{\partial x^2} + k\frac{\partial^2 p_1}{\partial x^2}\right)\left(\frac{r^2}{4} - \frac{H^2}{2}\right)\right\}$$
$$- kF_3(x, r, t) + O(k^2), \tag{37}$$

and

$$p(x, t) = p(0, t) + \int\limits_0^x \frac{\partial p_0}{\partial x}(s, t) + k\frac{\partial p_1}{\partial x}(s, t)\mathrm{d}s + O(k^2) \tag{38}$$

Equations (36)–(38) give the complete solution to the system of (15)–(22) and offer a series solution with perturbation parameter k, up to the first-order corrective term.

3.2 The Local Shear Stress at the Wall of the Tube

The local shear stress at the wall of the tube can be obtained by

$$\tau_{\mathrm{wall}} = \left.\frac{\partial u}{\partial r}\right|_{r=H} = \left.\frac{\partial u_0}{\partial r}\right|_{r=H} + \left.\frac{\partial u_1}{\partial r}\right|_{r=H} \tag{39}$$

Therefore, the shear stress at the wall is therefore obtained as

$$\tau_{\text{wall}} = \frac{1}{2}\left(\frac{\partial p_0}{\partial x} + k\frac{\partial p_1}{\partial x}\right)H + kF_5(x,t) \tag{40}$$

where

$$F_5(x,t) = \text{Re}\left\{\frac{1}{48}\frac{\partial p_0}{\partial x}\frac{\partial^2 p_0}{\partial x^2}H^5 + \frac{1}{16}\left(\frac{\partial^2 p_0}{\partial x^2}\right)^2\frac{\partial H}{\partial x}H^4 \right.$$
$$\left. - \frac{1}{16}\frac{\partial^2 p_0}{\partial x \partial t}H^3 - \frac{1}{4}\frac{\partial p_0}{\partial x}\frac{\partial H}{\partial t}H^2\right\} \tag{41}$$

3.3 The Volume Flow Rate

For multiple wave trains, with both integral and non-integral number of waves within the tube, we remove the dimensions of $\hat{Q} = 2\pi \int_0^{\hat{H}} \hat{u}\hat{r}\,d\hat{r}$ by using the volume of a completely occluded pump over one wave period, that is $\frac{\pi a^2 \lambda}{\hat{T}_\lambda}$, where $\hat{T}_\lambda = \frac{\lambda}{c}$. Using similar normalization parameters as [7], for single waves, we non-dimensionalize $\hat{Q}$ using the volume of a completely occluded pump over the time it takes the wave to travel the length of the tube, that is $\frac{\pi a^2 \lambda}{\hat{T}_L}$, where $\hat{T}_L = \frac{L}{c}$. There-fore, $Q = 2M \int_0^H ur\,dr$, that is $Q = 2M \int_0^H (u_0 r + ku_1 r)\,dr$, where $M = 1$ for train wave peristaltic pumping and $M = \frac{L}{\lambda}$ for single-wave transport. This integral gives $Q = Q_0 + kQ_1$ the instantaneous volume flow rate, which is obtained as

$$Q = -\frac{M}{8}\left(\frac{\partial p_0}{\partial x} + k\frac{\partial p_1}{\partial x}\right)H^4 - 2Mk\text{Re}\left\{\frac{3}{1024}\frac{\partial p_0}{\partial x}\frac{\partial^2 p_0}{\partial x^2}H^8 \right.$$
$$\left. + \frac{1}{128}\left(\frac{\partial p_0}{\partial x}\right)^2\frac{\partial H}{\partial x}H^7 - \frac{1}{96}\frac{\partial^2 p_0}{\partial x \partial t}H^6 - \frac{1}{32}\frac{\partial p_0}{\partial x}\frac{\partial H}{\partial t}H^5\right\} \tag{42}$$

Now, the volume of fluid displaced over the time for the wave to travel one wavelength λ that is the volume of fluid transported in one wave period is given by the equation $\bar{Q} = \frac{1}{T}\int_0^T Q\,dt$, where T is the period of the wave. Evaluating this integral produces $\bar{Q}$, known as the time-averaged volume flow rate, a quantity of significant interest found as

$$\bar{Q} = -\frac{M}{T}\int_0^T\left[\frac{1}{8}\left(\frac{\partial p_0}{\partial x} + k\frac{\partial p_1}{\partial x}\right)H^4 + 2k\text{Re}\left\{\frac{3}{1024}\frac{\partial p_0}{\partial x}\frac{\partial^2 p_0}{\partial x^2}H^8 \right.\right.$$
$$\left.\left. + \frac{1}{128}\left(\frac{\partial p_0}{\partial x}\right)^2\frac{\partial H}{\partial x}H^7 - \frac{1}{96}\frac{\partial^2 p_0}{\partial x \partial t}H^6 - \frac{1}{32}\frac{\partial p_0}{\partial x}\frac{\partial H}{\partial t}H^5\right\}\right] \tag{43}$$

3.4 The Limiting Case $k \to 0$

Note that for the limiting case $k \to 0$, the axial and radial velocities described in (12) and (13), respectively, reduces to $u = u_0$ and $v = v_0$. Likewise, the pressure described by the (14), reduces to $p = p_0$. The shear stress at the wall τ_{wall}, the instantaneous volume flow rate Q, and the time-averaged volume flow rate $\bar{Q}$ reduces to (44), (45), and (46), respectively [6], given below

$$\tau_{\text{wall}} = \frac{1}{2} \frac{\partial p_0}{\partial x} H, \tag{44}$$

$$Q = -\frac{M}{8} \frac{\partial p_0}{\partial x} H^4, \tag{45}$$

$$\bar{Q} = -\frac{M}{T} \int_0^T \frac{1}{8} \frac{\partial p_0}{\partial x} H^4 dt. \tag{46}$$

By evaluating the integral in (46), the time-averaged volume flow rate $\bar{Q}$ can, therefore, be explicitly shown to have a linear relation with the pressure head ∇p as described by

$$\bar{Q} = \bar{Q}_{\nabla p = 0} \left(1 - \frac{\nabla p}{\nabla p_{\bar{Q}=0}}\right) \tag{47}$$

Here, $\bar{Q}_{\nabla p = 0}$ and $\nabla p_{\bar{Q}=0}$ are constants and represent the time-averaged volume flow when $\nabla p = 0$ (i.e., there is no pressure head) and pressure head required for $\bar{Q} = 0$ (i.e., no volume being transported over time) which are obtained as

$$\bar{Q}_{\nabla p = 0} = \frac{2M}{T} \int_0^T \frac{\int_0^L H^{-4}(\xi, t) \left(\int_0^\xi H(s, t) \frac{\partial H}{\partial t}(s, t) ds\right) d\xi}{\int_0^L H^{-4}(\eta, t) d\eta} dt, \tag{48}$$

$$\nabla p_{\bar{Q}=0} = \frac{8\bar{Q}_{\nabla p = 0}}{M} \left\{\frac{1}{T} \int_0^T \frac{dt}{\int_0^L H^{-4} dx}\right\}^{-1} \tag{49}$$

These results are superimposed in the graphical discussion to analyze the effects of considering the wave number and hence the inertial terms initially considered trivial in aforementioned papers.

4 Results and Discussion

The volume of the fluid within one wave V_b is kept constant with changes made in the occlusion $\frac{\varepsilon}{a}$. This is achieved by simultaneously adjusting the wave amplitude A. Hence, the relation between A and $\frac{\varepsilon}{a}$ is obtained as

$$A = \frac{4}{3}\left(\sqrt{\frac{3}{2} - \frac{1}{2}\left(\frac{\varepsilon}{a}\right)^2} - \frac{\varepsilon}{a}\right) \tag{50}$$

This expression is obtained by finding the volume enclosed in a single wave and keeping this value constant. We can observe that as $\frac{\varepsilon}{a}(\in [0, 1])$ increases, the amplitude of peristatic wave decreases. Also, $\frac{\varepsilon}{a} = 0$ means, the peristaltic pump is completely occluded and $\frac{\varepsilon}{a} = 1$, and there is no occlusion.

In order to evaluate p_0 and p_1, the integrals acquired in (38) were evaluated numerically using the trapezoidal rule. Due to extreme variations of the functions associated, the integrals are extremely sensitive to the step size taken in space and time. Thus, the step sizes are chosen small enough to appropriately capture the nature of the function. By varying the length of the tube, the choice of having an integral versus a non-integral number of waves within the tube is obtained. In this section, the figures for the local pressures, the shear stress at the wall, and the volume flow rate are generated for $\frac{\varepsilon}{a} = [0.1, 0.3, 0.5, 0.9], A = [1.497, 1.208, 0.897, 0.195]$ and $k = [0, 0.1, 0.5, 0.9]$ at time instants $t = [0, 0.5, 0.9]$ using MATLAB. The Reynolds number Re is taken to be 1 throughout these calculations, isolating the effects of the wave number.

4.1 Biological Data

The wave number $k = \frac{a}{\lambda} \in (0, 1)$ is the ratio of the mean radius of the tube to the wavelength of the wave. For the ureter, this value ranges from 0.01 to 0.5 (in extreme cases), with the length of the ureter being 250–300 mm and wave speed 20 to 40 millimeters per second [3]. In the esophagus however, the wave number ranges from 0.05 to 0.2 with the length of the esophagus being 250–300 mm and wave speed 20–40 mm per second [18]. In all the examples of peristaltic transport listed in Sect. 1 above, we see that the wave number lies in the above prescribed domain. For these reasons, in the preceding calculations, the solutions of (7)–(9), subjected to the conditions in (11) are chosen as a series solution with the perturbation parameter being k. Hence, we have included in our analysis, the effects of this parameter on the flow for values of k within this range including an extreme case $k = 0.9$. We have also included, for validation, the case $k = 0$ which corresponds with neglecting the inertial components of the flow. Considering the effective Reynolds number $R = k$ Re, and taking Re $= \frac{\rho ac}{\mu} = 1$, then $R = k$ which is consistent with low Reynolds number flow conditions present in the esophagus and the ureter.

4.2   Multiple Integral Train Waves

In this section, we analyze the variation of pressure distribution, shear stress at the wall, and the time-averaged volume flow by choosing $\frac{L}{\lambda} = 2$ (that is $\frac{L}{\lambda} \in Z^{+}$). Describing the wall position by (1), manipulating the length of the tube L and keeping the wavelength constant, we are able to manipulate the number of sinusoidal waves $\frac{L}{\lambda}$ present within the tube.

4.2.1   The Pressure Distribution over the Tube

Figures 2a–c describe the pressure distribution along the tube, for different values of wave number k when $\frac{\varepsilon}{a} = 0.5$ at $t = 0.0, 0.5$ and 0.9. The wave number k is taken as $k = 0, 0.1, 0.5, 0.9$. We considered the case of $\nabla p = 0$ known as free pumping, to discuss the characteristics of peristaltic pumping in the finite tube for different time instants $t = 0, 0.5$ and 0.9. Wall shapes are scaled and superimposed on these plots at the corresponding instances of time. From Fig. 2a–c and for all the values of t, the peak pressure is identified at the region immediately after the occluded region (region of greatest constriction) and the least pressure directly before this region. The pressure then decreases gradually within the body of the wave. It is also identified that the pressure takes two peaks in each peristaltic wave one large positive peak and one large negative peak. A shift of the plot is observed due to the systematic movement of the fluid with the peristaltic wave with time. The same pattern as in Fig. 2 is observed for all values of $\frac{\varepsilon}{a}$ and k. However, we observed the quantitative changes. The magnitude of the pressure is observed to be decreasing as $\frac{\varepsilon}{a}$ increases, which could be due to decrease in wave amplitude. We noticed that the effect of k on the pressure is either an increase or decrease, depending on the values of p_1 for the corresponding times. For all values of $\frac{\varepsilon}{a}$, the greatest deviation from the case $k = 0$ is observed for $k = 0.9$ as expected, however there are critical positions within the tube where k and hence the contribution of p_1 has no effect. It is also noticed that as $\frac{\varepsilon}{a}$ increases (that is, pumping at lower occlusions), the relative significance of p_1 and hence the deviation of p from the limiting case p_0 is larger. It is observed over time and noted that these features of the pressure transition along with the wave.

4.2.2   The Shear Stress at the Wall of the Tube

The variation of shear stress at the wall over the tube at different times for variations of k is projected in Fig. 3 for $\frac{\varepsilon}{a} = 0.3$. Again, we considered free pumping (that is $\nabla p = 0$) at time $t = 0$. It is seen that the maximum shearing force on the surface area of the wall of the tube is experienced at the region of greatest occlusion. Similar pattern is observed over a variation of time with a shift of the plot along the axial direction progressing with the wave. It is noticed that the effect of k on the shear stress at the wall is not as pronounced as its effect on the pressure distribution. We
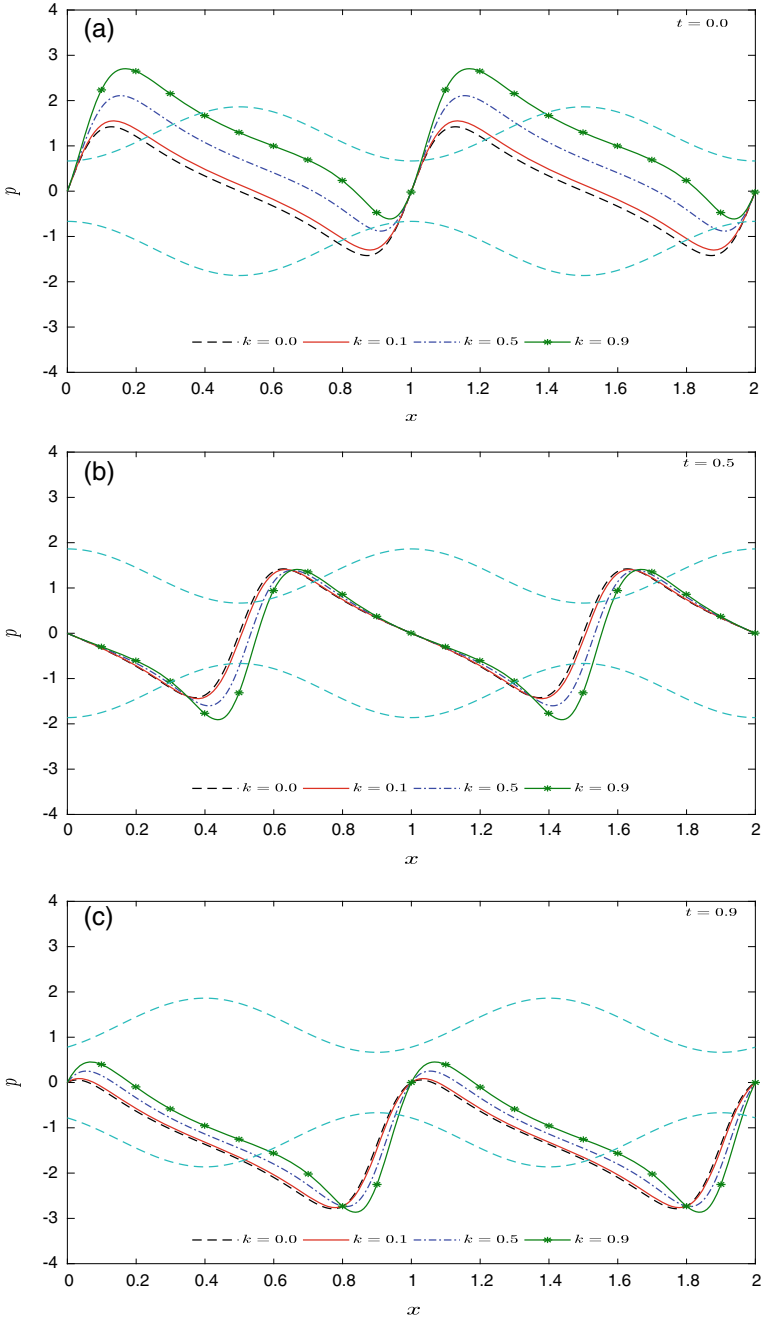
Fig. 2 The pressure distribution, for $\frac{\varepsilon}{a} = 0.5$, $A = 0.897$ with $\nabla p = 0$, $\frac{L}{\lambda} = 2.0$, for varing values of k
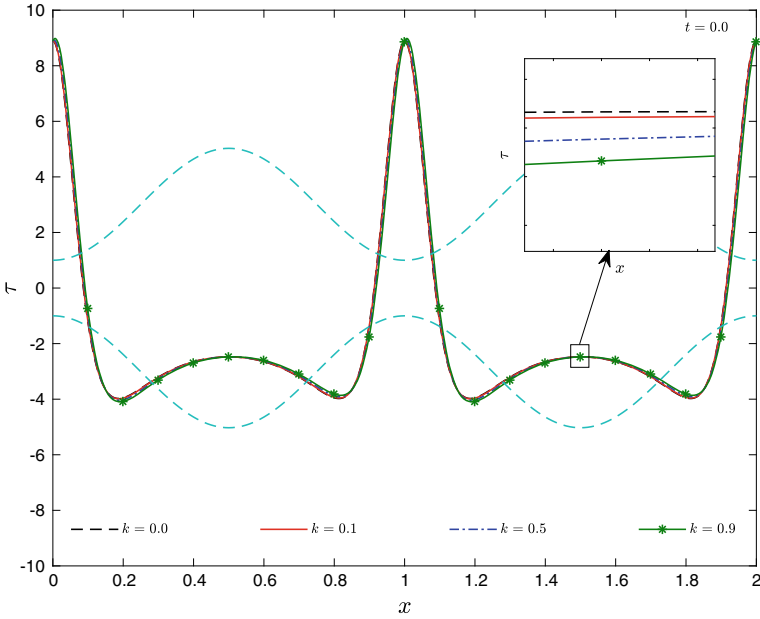
Fig. 3 Shear stress at the wall at time $t = 0$ for $\frac{\varepsilon}{a} = 0.3$, $A = 1.208, \nabla p = 0$, $\frac{L}{\lambda} = 2.0$

also noticed that as $\frac{\varepsilon}{a}$ increases, the effect of k become more noticeable as the relative significance of τ_1 increases. The general features (described for Fig. 3) of the plot are conserved, however there is a reduction in the magnitude of τ with increase in $\frac{\varepsilon}{a}$, due to a reduction in the wave amplitude.

4.2.3   The Time-Averaged Volume Flow

Figure 4 shows the variation of the time-averaged volume flow $(\bar{Q})$, against the pressure head (∇p), for different values of k for $\frac{L}{\lambda} = 2, \frac{\varepsilon}{a} = 0.313, 0.411$. For $\frac{\varepsilon}{a} = 0.313$ and 0.411, the corresponding values of the wave amplitude are $A = 1.189$ and 1.038. Here, it is recognized that $\bar{Q}$ has a linear relation with ∇p for all the values of $\frac{\varepsilon}{a}$ and k. Also, an increase in $\frac{\varepsilon}{a}$ results in a decrease in volume flow. Observing also the effect of the wave number k on $\bar{Q}$, we noticed that there is a transformation of this linear relation depending on $\bar{Q}_1$ (which also display a linear relation with ∇p). The effect of k on volume flow rate is not much significant. However, it can be seen that an increase in k increases the volume flow rate.
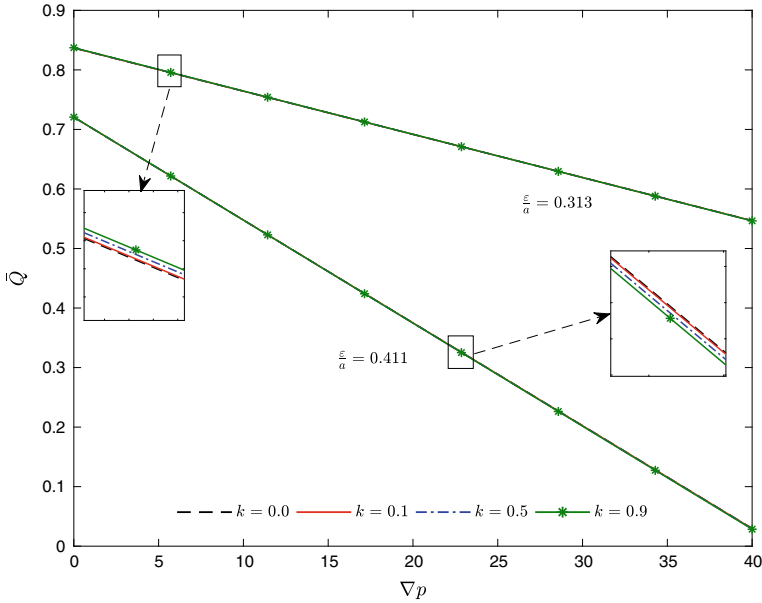
Fig. 4 Time-averaged volume flow $\bar{Q}$, distributed over the pressure head ∇p, for $\frac{\varepsilon}{a} = 0.313, 0.411$, with corresponding values of $A = 1.189, 1.038$ and $\frac{L}{\lambda} = 2.0$

4.3 Multiple Non-integral Train Waves

Choosing $\frac{L}{\lambda} = 1.82$ (that is $\frac{L}{\lambda} \notin Z^+$), we now have a non-integral number of waves within the tube. The pressure, shear stress at the wall, and the volume flow are therefore discussed later under this condition.

4.3.1 The Pressure Distribution over the Tube

Figure 5 shows the axial variation of pressure distribution for $\nabla p = 0, \frac{L}{\lambda} = 1.82, \frac{\varepsilon}{a} = 0.5$ at $t = 0.5$ for $k = 0, 0.1, 0.5, 0.9$, with the wall shape scaled and laid over the plot. From Fig. 5 (as in the case of $\frac{L}{\lambda}$ integral), it is observed that the peak pressures are identified just before and after the point of most contraction, with gradual decrease in the pressure within the wave from the maximum to the minimum. These peaks along with the entire plots shift with the wave over time. The effect of k is a slight deviation of the pressure from the case $k = 0$ at this value of $\frac{\varepsilon}{a}$. As $\frac{\varepsilon}{a}$ increases, we saw similar patterns established for the pressures, however noted that the magnitude of pressure decreases. Also, the deviation of the pressure due to k from p_0 (case $k = 0$), becomes more apparent with larger values of $\frac{\varepsilon}{a}$, that is the relative significance of p_1 is greater for pumps with lower wave amplitudes.
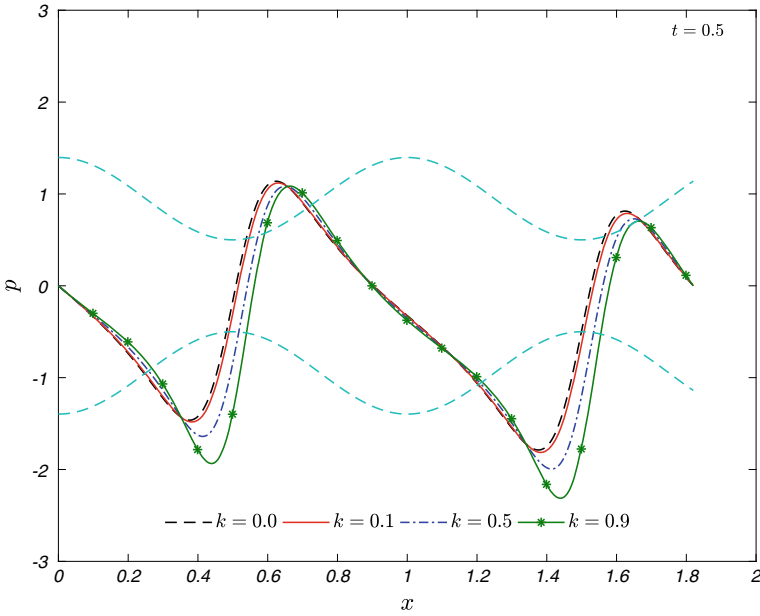
Fig. 5 Pressure distribution, for $\frac{\varepsilon}{a} = 0.5$, $A = 0.897$ with $\nabla p = 0, \frac{L}{\lambda} = 1.82$ at $t = 0.5$, for varing values of k

4.3.2 The Shear Stress at the Wall of the Tube

Figure 6 depicts the variation of the wall shear stress for $\frac{\varepsilon}{a} = 0.5, \nabla p = 0, \frac{L}{\lambda} = 1.82$, at times $t = 0.5$. Scaled and superimposed in each plot are the wall shapes at the corresponding instances of time. From this figure, the maximum stress is observed at the point of most occlusion within the tube. Also, within the wave τ decreases to a minimum, increase to a local maximum, and then decreases to a minimum. These general features of the shear stress were recurring with changes in time with shifts in the plot along the axial direction due to the passage of the wave. The effect of the wave number is not obvious for this value of $\frac{\varepsilon}{a}$. The response of the shear stress with changes in $\frac{\varepsilon}{a}$ noted. The general features of the plot (as described for Fig. 6) were preserved, with changes in $\frac{\varepsilon}{a}$. However, as $\frac{\varepsilon}{a}$ increases, the magnitude of τ decreases and the effect of k become more apparent. Also, we see the similar pattern with the variation of time.

4.3.3 The Time-Averaged Volume Flow

The time-averaged volume flow for non-integral number of waves, as in the case of integral wave forms within the tube, shows a linear relation with ∇p. The effect of having a non-integral number of waves within the tube is a slight reduction in
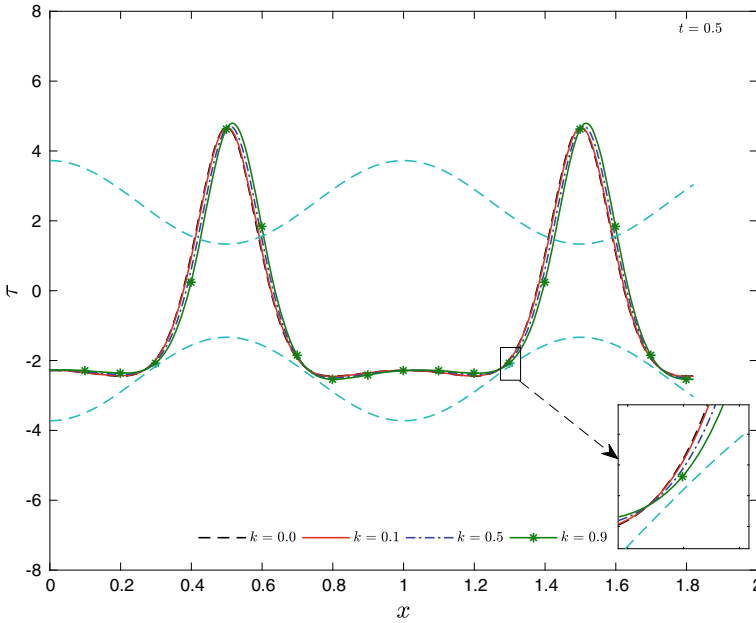
Fig. 6 Shear stress at the wall at time $t = 0.5$ for $\frac{\varepsilon}{a} = 0.5$, $A = 0.897$, $\nabla p = 0$, $\frac{L}{\lambda} = 1.82$

$\bar{Q}$ when compared with $\frac{L}{\lambda}$ integral. For this case also, the values of $\bar{Q}$ at any cross section of the tube measured are observed to be the same. The effect of k like the effect for $\frac{L}{\lambda}$ integral is a rotation about a point ∇p for which $\bar{Q}_1 = 0$. This was noticed by closely observing Fig. 7 which is a plot of $\bar{Q}$ against ∇p, for $\frac{L}{\lambda} = 1.82$ at $\frac{\varepsilon}{a} = 0.313, 0.411, 0.509$. Furthermore, $\bar{Q}$ decreases with increase in $\frac{\varepsilon}{a}$ and the effect of k of $\bar{Q}$ increases initially with increase in $\frac{\varepsilon}{a}$ and then decreases.

4.4 Single Wave

Describing the wall functions as a piecewise function on the domain, as shown below, we achieve the idea of a single wave within the tube as illustrated in Fig. 1a.

$$H(x, t) = \begin{cases} \frac{\varepsilon}{a} + 0.5A\left(1 - \cos 2\pi(x - t)\right) & t \le x \le t + 1 \\ \frac{\varepsilon}{a} & \text{elsewhere} \end{cases} \tag{51}$$

The local pressure within the tube, the shear stress at the wall, and the time-averaged volume flow are therefore discussed for a single wave within the tube in this section.
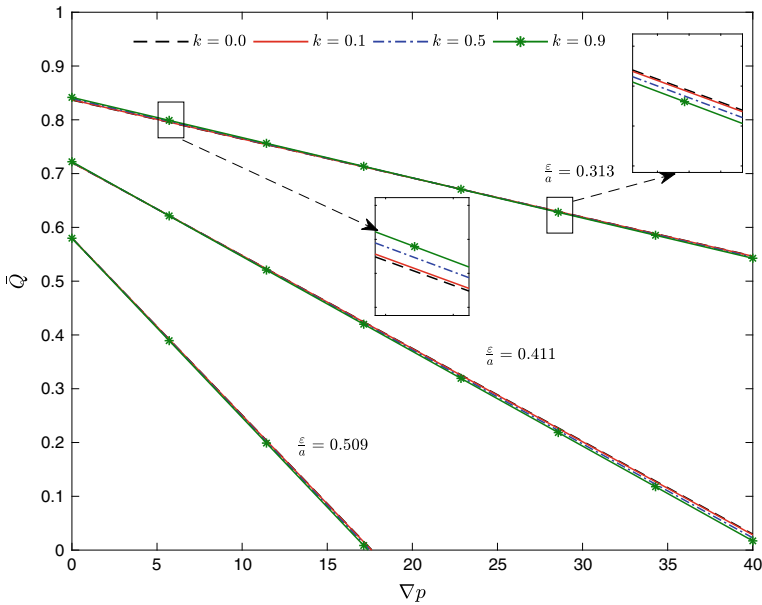
Fig. 7 Time-averaged volume flow $\bar{Q}$, distributed over the pressure head ∇p, for $\frac{\varepsilon}{a} = 0.313, 0.411, 0.509$ with corresponding values of $A = 1.189, 1.038, 0.882$ and $\frac{L}{\lambda} = 1.82$

4.4.1 The Pressure Distribution over the Tube

Figure 8 describes the pressure variation within the tube, for $\frac{\varepsilon}{a} = 0.5, \frac{L}{\lambda} = 1.82, \nabla p = 0$, with a single wave within the tube for $t = 0.9$. In this plot, the corresponding wall shapes are scaled and placed in the plots. We saw that the peak pressure is identified in the region just after the point of most constriction and the least pressure just before this point. Within the wave, there is a gradual decrease of the pressure from this peak, to a minimum value of p. On the other hand, considering the positions along the tube for which the wave is not present, we observed a linear relation with the pressure and the axial position. These observations were also made for other instances in time, with a shift of the graphs due to the propagation of the wave with time. As different values of $\frac{\varepsilon}{a}$ were observed, it was noted that as $\frac{\varepsilon}{a}$ increases, the magnitude of p decreases and the effect of k become more pronounced. Due to the presence of wave number, we saw a deviation of the pressure from the case $k = 0$ and this effect increases with increase in k. The general features of the pressure described above were however maintained, for all values of t and $\frac{\varepsilon}{a}$.
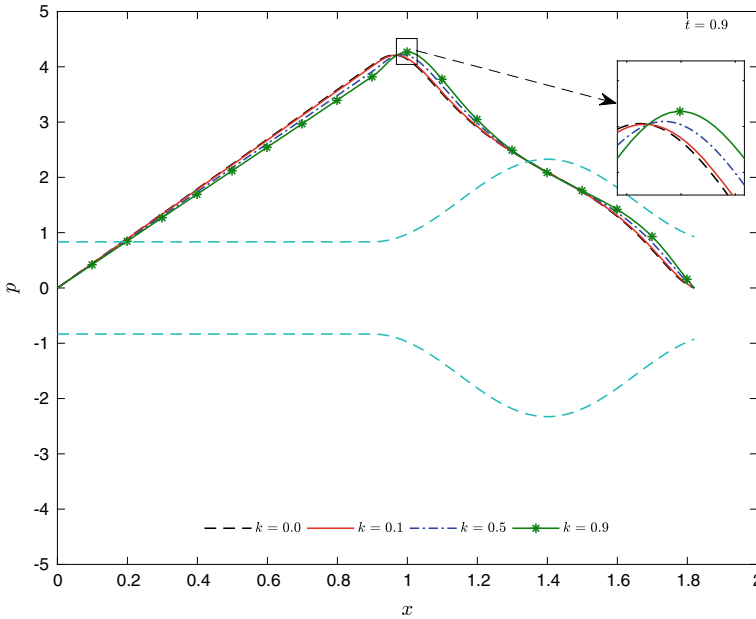
Fig. 8 Pressure distribution, for $\frac{\varepsilon}{a} = 0.5$, $A = 0.897$ with $\nabla p = 0$, $\frac{L}{\lambda} = 1.82$ (single wave) at $t = 0.9$, for varing values of k

4.4.2 The Shear Stress at the Wall of the Tube

Figure 9 gives the shear stress at the wall, distributed over the tube length, for $\frac{\varepsilon}{a} = 0.5$ and $t = 0.9$. The corresponding wall shape is scaled and superimposed in each plot. Here, it is noted that τ has a linear relation with the axial position along the tube, for sections of the tube without the wave present. Within the wave, however, it was observed that the shear stress has peak minimum values just after and before the points of most constriction bounding the wave. Then, τ increases to a local maximum then decreases to this minimum just before the constriction. As $\frac{\varepsilon}{a}$ increases, the range of τ decreases due to a reduction in the wave amplitude and the effect of k on τ now becomes more apparent. The general features discussed earlier were preserved for all changes in $\frac{\varepsilon}{a}$.

4.4.3 The Time-Averaged Volume Flow

Unlike the volume flow for multiple train waves, it is noticed that $\bar{Q}$ is dependent on the position along the tube. The time-averaged volume flow at the inlet ($\bar{Q}(0)$) and at the outlet ($\bar{Q}(L)$) is observed for $\frac{\varepsilon}{a} = 0.313$ and 0.411, with corresponding wave amplitudes $A = 1.189$ and 1.038. For each of value of $\frac{\varepsilon}{a}$, we observed the variation for $k = 0, 0.1, 0.5$, and 0.9. The time-averaged volume flow at the inlet
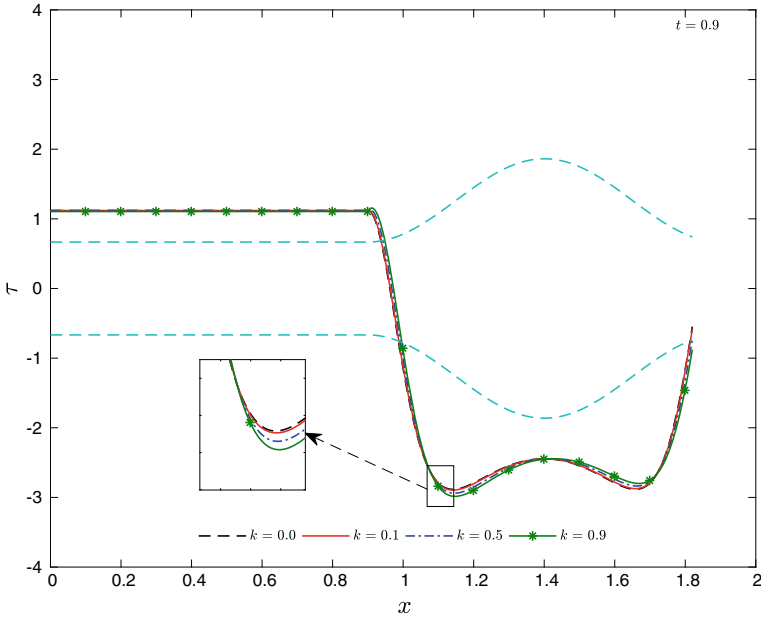
Fig. 9 Shear stress at the wall at time $t = 0.9$ for $\frac{\varepsilon}{a} = 0.5$, $A = 0.897$, $\nabla p = 0$, $\frac{L}{\lambda} = 1.82$ (single wave)

$\bar{Q}(0)$ is plotted in Fig. 10 against ∇p which was chosen to provide co-pumping (favorable pressure head) that is $\nabla p < 0$. We observed that $\bar{Q}(0)$ displays a linear relation with ∇p and that even with co-pumping, a reflux flow is present at the tube inlet. The amount of reflux at the inlet increases with ∇p, that is for changes in ∇p from favorable to adverse pressure heads. Reflux is the retrograde flow of fluid in the opposite direction to the direction of the wave. Like the other case here also the contribution of k is not much significant for smaller values of $\frac{\varepsilon}{a}$ and its significance increases with increase in $\frac{\varepsilon}{a}$. Figure 11 shows the distribution of $\bar{Q}(0)$ over $\frac{\varepsilon}{a}$ for $\nabla p = -2.0, -1.0, 0.0$, with $\frac{L}{\lambda} = 2.0$ for different k. We observed here that the amount of reflux at the inlet increases with $\frac{\varepsilon}{a}$ to a critical point of occlusion ε_c and then decreases. This critical point ε_c decreases as ∇p increases. It is also seen that reflux decreases with k and the effect of k is significant in the case of free pumping than the co-pumping. This significance decreases as negative ∇p increases. Therefore, this reflux can be prevented in single-wave pumps provided that either a suitable pressure head is chosen or complete occlusion ($\frac{\varepsilon}{a} = 0$) or no peristalsis ($\frac{\varepsilon}{a} = 1$) as indicated in the plots. This result is made obvious in Fig. 12 which is a plot of $\bar{Q}_1(0)$ over $\frac{\varepsilon}{a}$ for corresponding values stated in Fig. 10. This increase in the effect of k will result in an overall decrease in the reflux at the inlet. It is important to note however, that although there is a reflux flow at the inlet of the tube, at the outlet of the tube, we have a positive volume flow in the direction of the wave for the same
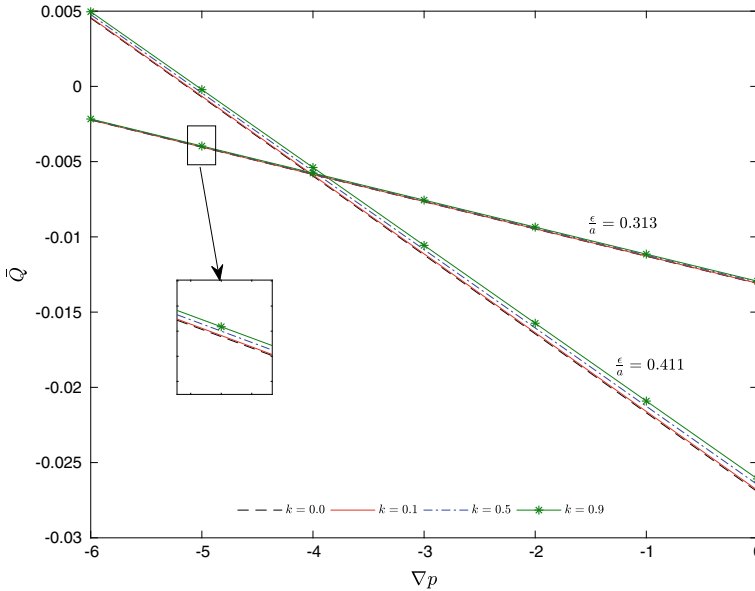
Fig. 10 Volume flow rate at the inlet $\bar{Q}(0)$, for a range of favorable pressure heads, with $\frac{L}{\lambda} = 2.0$ for $\frac{\varepsilon}{a} = 0.313, 0.411$ and $k = 0.0, 0.1, 0.5, 0.9$

values of pressure head. This is described in Fig. 13 which projects the variation of the time averaged volume flow rate at the outlet $(\bar{Q}(L))$, for $\frac{\varepsilon}{a} = 0.131, 0.411$ with $\frac{L}{\lambda} = 2$. Here also we observed a linear relation between $\bar{Q}(L)$ and ∇p but the slope of the lines are less in this case if we compare with $\bar{Q}(0)$. The effect of the wave number observed here is an increase in $\bar{Q}(L)$, and however, it can be shown that there is a value of ∇p for which $\bar{Q}(L)$ is unaffected by $\bar{Q}_1(L)$. Unlike $\bar{Q}(0)$, $\bar{Q}(L)$ decreases with $\frac{\varepsilon}{a}$.

4.5 Comparing Multiple Integral with Non-integral Train Waves

Although the pressure distribution for non-integral and integral train waves is similar in many of their features but there are significant differences for corresponding instances of time. The corrective term p_1 has greater contribution within a full wave and hence we noticed an aggregate that the correction to p due to p_1 is greater for integral train wave pumping. The shear stress at the wall shows minimal differences in its distribution over the tube length in these two cases. The time-averaged volume flow rate for non-integral waves shows a decrease in quantity when compared
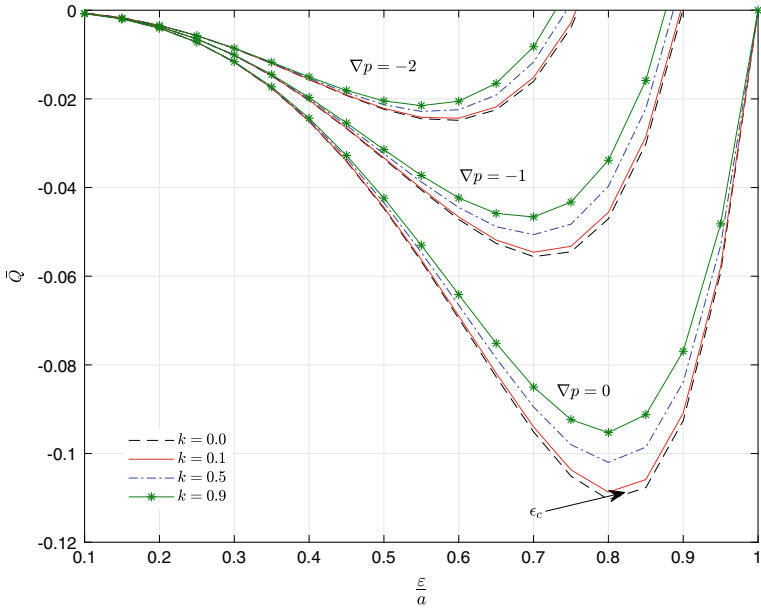
Fig. 11 Variation of $\bar{Q}$ at the inlet against the occlusion $\frac{\varepsilon}{a}$, $\nabla p = 0, -1.0, -2.0$ with $\frac{L}{\lambda} = 2.0$
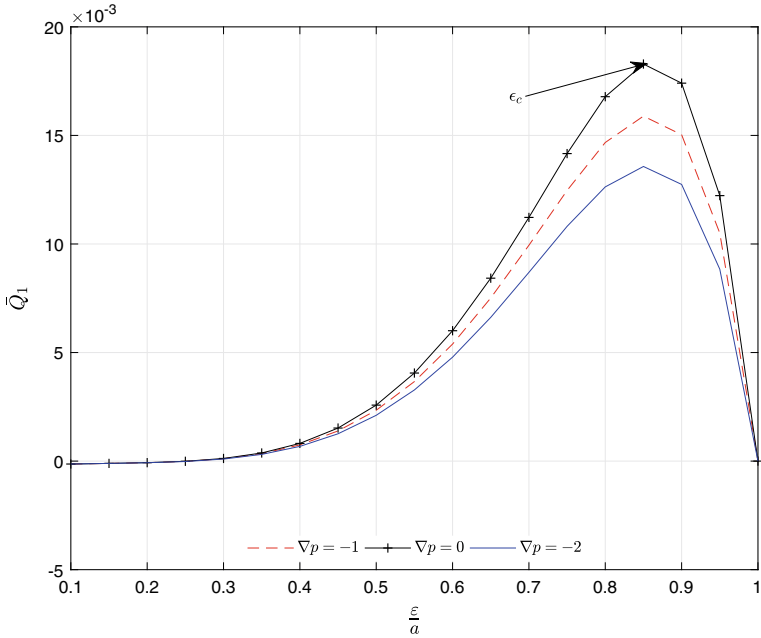
Fig. 12 Plot of $\bar{Q}_1$ at the inlet against $\frac{\varepsilon}{a}$ for $\nabla p = 0, -1.0, -2.0$, with $\frac{L}{\lambda} = 2.0$
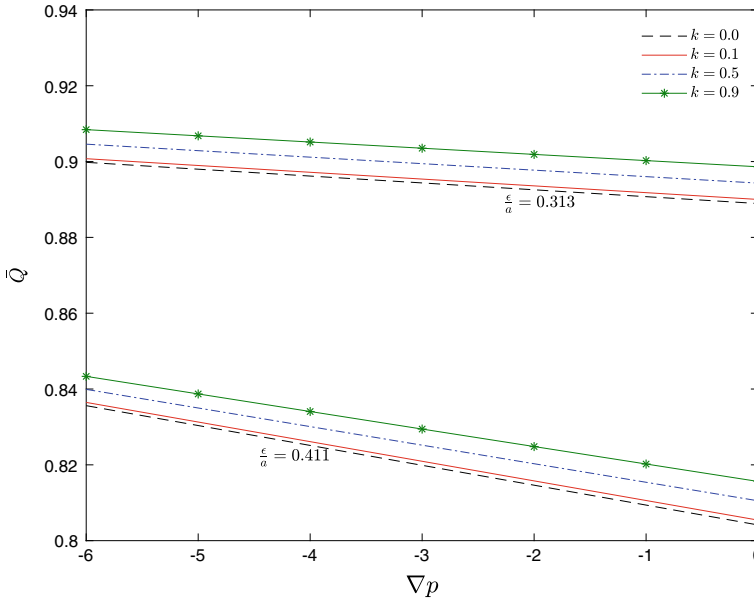
Fig. 13 Time-averaged flow rate at the outlet of the tube, for a range of favorable pressure heads, with $\frac{L}{\lambda} = 2.0$ for $\frac{\varepsilon}{a} = 0.313, 0.411$ and $k = 0.0, 0.1, 0.5, 0.9$

with integral waves in the tube for corresponding parameters. In both cases, we also observed that $\bar{Q}$ responses similarly with k and the response of $\bar{Q}$ with variations of $\frac{\varepsilon}{a}$ is also similar.

4.6　Comparing Multiple Train Waves with Single Wave

Although the pressure profile for single-wave pumping has similar features with multiple train waves, we found that the profiles have differences. These differences are primarily due to the region of the tube where there is no wave form. In these regions, the pressure is observed to vary linearly over the tube length for which there are no such regions present in the case of multiple train waves. Within the body of the wave, however, the pressure profiles have similar features in both the cases. Also, the corrective term p_1 and hence the effect of k have more contribution within the wave compared with the regions without a wave form. Hence, there is an overall reduction in the effect of k on p for single wave when compared with multiple waves present within the tube. The shear stress at the wall also has similarities in both the cases and again we noticed that τ is constant in the region without the wave present and varies with the axial position within the wave. Unlike $\bar{Q}$ for multiple train waves, for single-wave transport $\bar{Q}$ depends on the position along the tube.

As in the case of multiple train waves, there is a net positive flow at the outlet for single wave. Additionally, $\bar{Q}$ is distributed linearly over ∇p in both cases. At the tube inlet, reflux is present for single-wave transport and is possible in the presence of a favorable pressure head (co-pumping, i.e., $\nabla p < 0$). In contrast, reflux is possible when pumping with multiple train waves only if there is an adverse pressure head present ($\nabla p > 0$).

5 Conclusion

Peristaltic transport of a Newtonian fluid in a finite length tube is studied using perturbation analysis, with the perturbation parameter the wave number k. For multiple train waves, the non-integral waves within the tube have implications on the local pressure when compared with integral train waves. However, non-integral wave forms within the tube only slightly influenced the time-averaged volume flow rate. In addition, we noticed that the effect of the wave number and hence the inertial effects on the pressure distribution is a shift either increasing or decreasing the pressure, which varies with the locations within the tube. The shear stress at the wall of the tube is less disturbed by the first-order corrective term when compared with the pressure, with maximum contribution within the occluded region. The time-averaged volume flow, for both single and multiple train waves, has a linear relation with ∇p, for all values of the wave number and is slightly affected by the wave number in all cases.

We identified that reflux is present at the inlet for single-wave peristaltic transport even for favorable pressure heads and is only possible in multiple train waves whenever pumping against an adverse pressure head. This reflux can only be prevented by choosing a pressure head (co-pumping) high enough to prevent reflux, or total occlusion of the pump or no occlusion. The reflux increases with increase in $\frac{\varepsilon}{a}$ up to a critical point ε_c and then further decreases with $\frac{\varepsilon}{a}$. The first-order time-averaged volume flow at the inlet, on the other hand, increases to a maximum value for the same ε_c and then decreases, which serves to reduce the amount of reflux at the inlet. At the outlet of single-wave pumps, a positive time-averaged volume flow is possible even with reflux at the tube inlet. The volume flow for multiple train waves, on the other hand, is independent of the position along the tube.

References

1. Adb Elmabouda Y, Mekheimere KS, Adbelsalame SI (2014) A study of nonlinear variable viscousity in finite-length tube with peristalsis. Appl Bionics Biomech 11:197–206
2. Eytan O, Jaffa AJ, Elad D (2001) Peristaltic flow in a tappered channel: application to embryo transport within the uterine cavity. Med Eng Phys 23:475–484
3. Fung YC, Yih CS (1968) Peristaltic transport. J Appl Mech 35:669–675
4. Hariharan P, Seshadri V, Banerjee RK (2008) Peristaltic transport of non-Newtonian fluid in a diverging tube with different wave forms. Math Comput Model 48:998–1017

5. Kavitha A, Reddy R, Srinivas A, Sreenadh S, Saravana R (2012) Peristaltic pumping of a Jeffrey fluid between porous walls, with suction and injection. Int J Mech Mat Eng 7:152–157
6. Latham TW (1996) Fluid motions in a peristaltic pump. Cambridge, MA
7. Li M, Brasseur J (1993) Non-Steady peristaltic transport in finite-length tubes. Journal Fluid Mechanics 248:129–151
8. Manton MJ (1975) Long-wavelength perestaltic pumping at low Reynolds number. J Fluid Mech 68:467–476
9. Misra J, Pandey S (2001) A mathematical model for oesophageal swallowing of a food bouls. Math Comput Model 33:997–1009
10. Misra J, Maiti S (2011) Peristaltic transport of a rheological fliud: model for movement of food bolus through esophagus. Appl Math Mech 33:315–332
11. Pandey SK, Tripathi D (2010) Peristaltic transport of a Casson fluid in a finite channel: application to flow of concentrated fluids in oesophagus. Int J Biomath 3:453–472
12. Rani PN, Sarojamma G (2004) Peristaltic transport of a Casson fluid in an asymmetric channel. Austr Phys Eng Sci Med 27:49–59
13. Ravi Kumar YVK, Krishna Kumari PSVHN, Ramana Murthy MV, Sreenadh S (2011) Peristaltic transport of a power-law fluid in an asymmetric channel. Adv Appl Sci Res 2:396-406
14. Roy R, Rios F, Riahi DN (2011) Mathematical models for flow of chyme during gastrointestinal endoscopy. Appl Math 2:600–607
15. Shapiro AH, Jaffrin M, Weinberg S (1969) Peristaltic pumping with long wavelengths at low Reynolds number. J Fluid Mech 3:799–825
16. Toklu E (2011) A new mathematical model of peristaltic flow on oesophagial bolus transport. Sci Res Essays 6:6606–6614
17. Tripathi D, Pandey S, Chaube M (2010) Mechanical efficiency and reflux of peristatic pumping through a finite length vessel. Int J Appl Math Comput 2:63–72
18. Tripathi D, Pandey S, Siddiqui A, Beg OA (2014) Non-steady peristaltic propulsion with exponential variable velocity: a study of the transport through the digestive system. Comput Models Biomech Biomed Eng 17:571–603
19. Tripathi D, Akbar NS, Khan ZH, Bég OA (2016) Peristaltic transport of bi-viscosity fluids through a curved tube: a mathematical model for intestinal flow. J Eng Med 230:817–828
20. Usha S, Rao AR (1996) Peristaltic transport of two-layered Power-law fluid. J Biomech Eng 119:483–488

Hall Effects on MHD Rotating Nano Fluid Over a Moving Flat Plate with Radiation and Chemical Reaction

Pushpabai Pavar, L. Harikrishna, and M. Suryanarayana Reddy

Abstract In this manuscript, we have deliberated an unstable free convection stream of Nano fluid limited with a "moving vertical flat plate" through a porous medium in revolving framework with conditions of diffusion and convection and also bringing current of Hall into account. We acknowledged two kinds of Nano fluids: they are TiO_2–water and Ag–water. The governing equations would be illuminated analytically by utilizing the method of perturbation. Last, the impacts of different dimensionless factors on temperature, velocity, and concentration profiles along with Sherwood numbers, shear stress, and local Nusselt are deliberated with support of graphs.

Keywords Nano fluid · Rotation · Radiation · MHD · Chemical reaction

1 Introduction

The exchange of convective temperature in Nano fluids has various applications and participates in a critical part in engineering and sciences. They exist in almost each methodology that needs solar energy, exchange fluids of temperature (cooling or heating), and nuclear reactors and so on. Therefore, from previous years, the scientists of fluid dynamics have demonstrated an interest in the investigation of Nano liquids because of their requisitions in different fields. It may be the way that the usually utilizing liquids displays less "thermal conductivity" compared with the metals. Consequently, it will be needed to combine the metals and liquid expanding the heat exchange capacity of liquids. The "suspension of Nano-sized elements" in

P. Pavar (✉)
JNTU Anantapur, Anantapur, Andhra Pradesh, India
e-mail: Pushpapavar66@gmail.com

L. Harikrishna
Department of Mathematics, Annamacharya Institute of Technology and Sciences, Rajampet, Andhra Pradesh, India
e-mail: lhkmaths@gmail.com

M. Suryanarayana Reddy
Department of Mathematics, JNTUA College of Engineering, Pulivendula, Andhra Pradesh, India
e-mail: machireddysnr.maths@jntua.ac.in

base liquid will be known as the Nano fluid. The idea of Nano fluids might have been implemented by [1, 2] throughout an examination of cooling methodologies in Argonne national lab. The work [3] examined the thermal conductivity of Nano fluid. The work [4] analyzed through his research that there is a powerful thermal conductivity in "ethylene glycol-based copper Nano fluid". The contribution [5] has researched the improvement of heat exchange in natural flow of convection in porous media. The work [6] deliberated the impacts of injection or suction factors on "Marangoni boundary layer flow of a Nano fluid". The work [7] explored an unstable flow of Nano fluid over vertical plate in revolving framework. The authors in [8] concentrated on the viscosity impacts and thermal conductivity on Al_2O_3-water Nano fluid flow.

The authors in [9] considered the impacts of thermal radiations on "unstable natural convective flow of EG-Nimonic 80A Nano liquid". The work [10] examined the "volume fraction of Nano particles" impact by deliberating three kinds of Nano fluids known as TiO_2, Al_2O_3–water, and Cu–water, and finished that the kind of Nano fluid will be also the main component to enhance the transfer rate of temperature. The authors in [11] examined the outcomes of adjusted magnetic field, radiation, and revolution impacts of a Nano fluid in revolving framework.

Keeping the above-mentioned facts, in this manuscript, we have studied the "Hall current effects on a Nano fluid through porous medium" with the boundary conditions of diffusion and convection.

2 Mathematical Formulation and Solution of the Problem

We have considered Hall impacts on unstable free convective flow of "incompressible Nano fluid of an ambient temperature T_∞ past a semi-infinite vertical moving plate" embedded in a "uniform porous medium" in existence of thermal buoyancy impact with boundary conditions of diffusion–convection and constant heat source. The physical configuration of problem is as presented in Fig. 1. The flow has assumed in x-direction that will be taken along with the plate in z-axis and upward direction will be normal to it. Similarly, it will be assumed that complete framework will be revolving with constant velocity Ω about z-axis. A "uniform external magnetic field" B_0 will be taken to be acting with z-axis. A slight magnetic "Reynolds number for oscillating plate because of semi-infinite plate surface assumption", moreover, the flow variables are functions of t and z only. The governing equations are in non-dimensional form of flow are provided by

$$J_1\left(\frac{\partial u}{\partial t} - S\frac{\partial u}{\partial z} - Rv\right) = \frac{1}{(1-\varphi)^{2.5}}\frac{\partial^2 u}{\partial z^2} + J_2\theta + J_3 L\psi - \left(J_4\frac{M^2}{1+m^2} + \frac{1}{K}\right)u \tag{1}$$

$$J_1\left(\frac{\partial v}{\partial t} - S\frac{\partial v}{\partial z} - Ru\right) = \frac{1}{(1-\varphi)^{2.5}}\frac{\partial^2 v}{\partial z^2} - \left(J_4\frac{M^2}{1+m^2} + \frac{1}{K}\right)v. \tag{2}$$
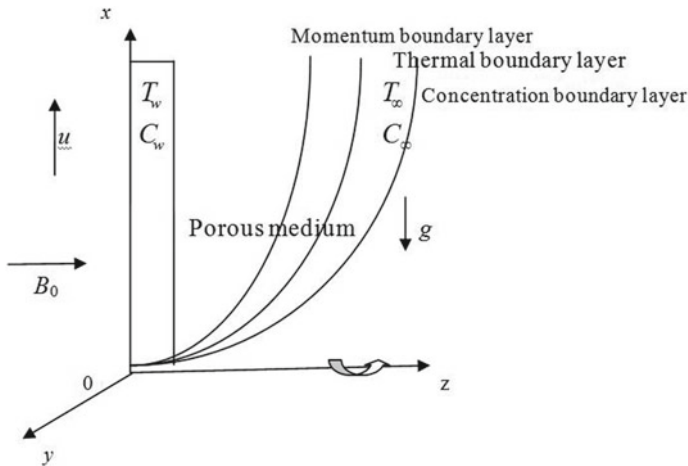
Fig. 1 Physical configuration of the problem

$$J_5\left(\frac{\partial\theta}{\partial t} - S\frac{\partial\theta}{\partial z}\right) = \frac{1}{\text{Pr}}\left(N\frac{\partial^2\theta}{\partial z^2}\right) + Q_{\text{H}}\theta. \tag{3}$$

$$\left(\frac{\partial\psi}{\partial t} - S\frac{\partial\psi}{\partial z}\right) = \frac{1}{\text{Sc}}\left(\frac{\partial^2\psi}{\partial z^2}\right) + \text{Kr}\psi. \tag{4}$$

Here, $S = \frac{w_0}{U_r}$ is the injection ($S < 0$) or suction ($S > 0$) factor, $R = \frac{2\Omega\,v_f}{U_r^2}$ is rotational parameter, $M = \frac{\sigma_f B_0^2}{\rho_f U_r^2}$ is the factor of magnetic field, $K = \frac{kU_r^2}{v_f^2}$ is permeability of porous medium, $\text{Pr} = \frac{v_f}{\alpha_f}$ be the Prandtl number, $Q_{\text{H}} = \frac{Qv_f^2}{U_r^2 k_f}$ is the factor of heat source, $\text{Kr} = \frac{k_1 v_f}{U_r^2}$ is the factor of chemical reaction, $\text{Sc} = \frac{v_f}{D_B}$ be Schmidt number, and $F = \frac{4\sigma^* T_\infty^3}{k_f k^*}$ be the factor of thermal radiation and $U_r = [g\beta_f(T_w - T_\infty)]^{\frac{1}{3}}$ be the characteristic of velocity.

Also conditions of boundary become

$$u = 0, \quad v = 0, \quad \theta = 0, \quad \psi = 0 \quad \text{for } t \le 0 \text{ and for any } z \tag{5}$$

$$\left.\begin{array}{ll} u = \left[1 + \frac{\epsilon}{2}\left(e^{\text{int}} + e^{-\text{int}}\right)\right], & v = 0 \\ \theta'(z) = -N_c(1 - \theta(z)), & \psi' = -N_d(1 - \psi(z)) \end{array}\right\} \quad \text{for } t > 0 \text{ and } z = 0. \tag{6}$$

$$u \to 0, \quad v \to 0, \quad \theta \to 0, \quad \psi \to 0 \quad \text{for } t > 0 \text{ and } z \to \infty \tag{7}$$

where $N_c = \frac{h_f v_f}{K_f U_r}$ is the connective parameter and $N_d = \frac{h_s v_f}{D_B U_r}$ be the factor of diffusion. We calculate the Eqs. (8) and (9) by putting the "fluid velocity" in composite form as $q = u + i\,v$ and we get

$$J_1\left(\frac{\partial q}{\partial t} - S\frac{\partial q}{\partial z} - i\,R\,q\right) = \frac{1}{(1-\varphi)^{2.5}}\frac{\partial^2 q}{\partial z^2} + J_2\theta + J_3 L\psi - \left(J_4\frac{M^2}{1+m^2} + \frac{1}{K}\right)q$$

(8)

The equivalent condition of boundary become

$$q = 0, \quad \theta = 0, \quad \psi = 0 \quad \text{for } t \le 0$$

(9)

$$\left.\begin{array}{l} V(z) = \left[1 + \frac{\in}{2}\left(e^{\text{int}} + e^{-\text{int}}\right)\right], \\ \theta'(z) = -N_c(1 - \theta(z)), \quad \psi' = -N_d(1 - \psi(z)) \end{array}\right\} \quad \text{a } z = 0 \text{ and } t > 0.$$

(10)

$$V \to 0, \quad \theta \to 0, \quad \psi \to 0 \quad \text{for } t > 0 \text{ and } z \to \infty$$

(11)

To attain the explanation of framework of fractional differential Eqs. (8), (3), and (4) under the condition of boundary signified in (9)–(11), we described V, θ and ψ as.

$$q(z,t) = q_0 + \frac{\varepsilon}{2}\left[e^{\text{int}}q_1(z) + e^{-\text{int}}q_2(z)\right]$$

(12)

$$\theta(z,t) = \theta_0 + \frac{\varepsilon}{2}\left[e^{\text{int}}\theta_1(z) + e^{-\text{int}}\theta_2(z)\right]$$

(13)

$$\psi(z,t) = \psi_0 + \frac{\varepsilon}{2}\left[e^{\text{int}}\psi_1(z) + e^{-\text{int}}\psi_2(z)\right]$$

(14)

Substituting the above Eqs. (12)–(14) in Eqs. (8), (3) and (4), and equating the terms of non-harmonic, harmonic, and ignoring the higher sequence terms of ε^2, we acquire the second-order differential equations. Solving these equations with relevant conditions of boundary, we get the solutions of temperature, velocity, and concentration distributions.

For engineering interest C_f be the "local skin friction coefficient", Sh_x be the "local Sherwood number", and Nu_x be the "local Nusselt number" are discussed by

$$C_f = \frac{\tau_w}{\rho_f U_w^2}, \quad \text{Nu} = \frac{xq_w}{k_f(T_w - T_\infty)} \quad \text{and} \quad \text{Sh}_x = \frac{xq_m}{D_B(C_w - C_\infty)}$$

(15)

3 Results and Discussion

Figures 2, 3, 4, 5, 6, 7, 8, 9, 10, 11, 12, 13, 14, 15, 16, 17, and 18 represent the concentration, temperature, and velocity distributions with respect to the governing parameters. Table 1 represented the physical properties of thermal about Ag, water, and TiO$_2$ are provided in Table 1.

Fig. 2 Concentration
profiles with S
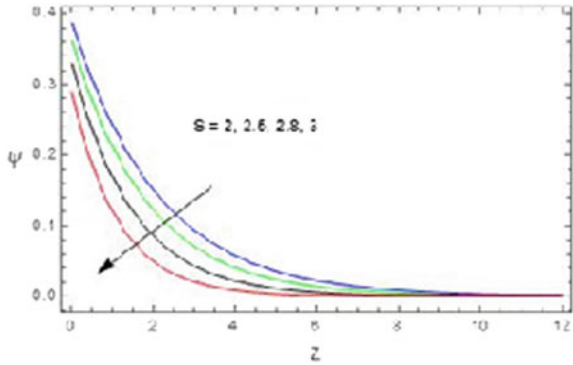
Fig. 3 Concentration
profiles with S
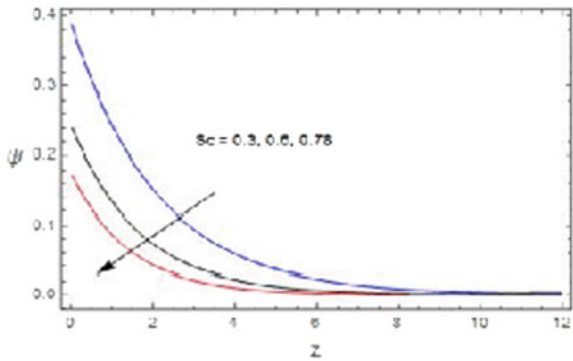
Fig. 4 Concentration
profiles with Kr
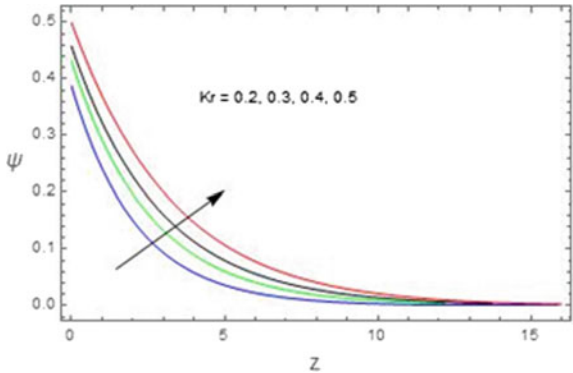
Figures 2, 3, 4, and 5 shows that growth in the parameter of suction or Schmidt number reduces the concentration profiles of flow, whereas chemical reaction factor and diffusion factor augments the concentration throughout the fluid region.

Fig. 5 Concentration profiles with S

$N_d = 0.3, 0.5, 0.7, 0.9$

Fig. 6 The temperature profiles with F

Thick line: Ag water
Dashed line: Tio$_2$ water

$F = 1, 1.5, 2$
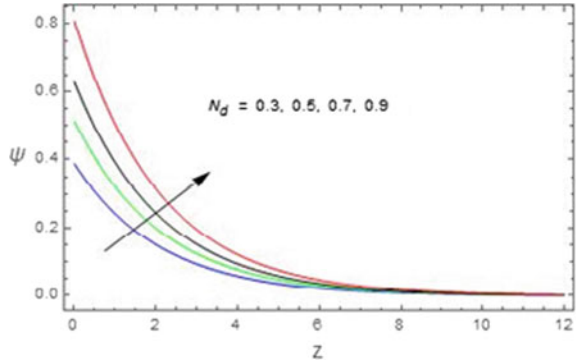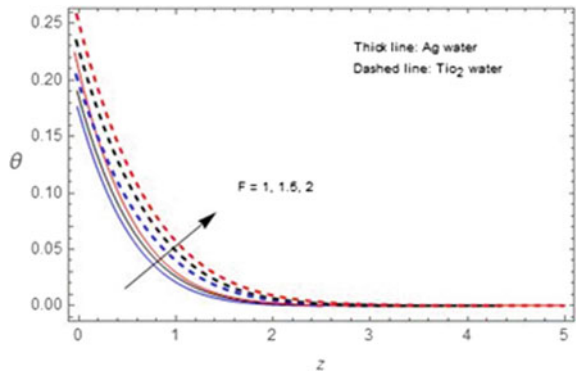
Fig. 7 The temperature profiles with N_c

Thick line: Ag water
Dashed line: Tio$_2$ water

$N_c = 0.2, 0.4, 0.6$
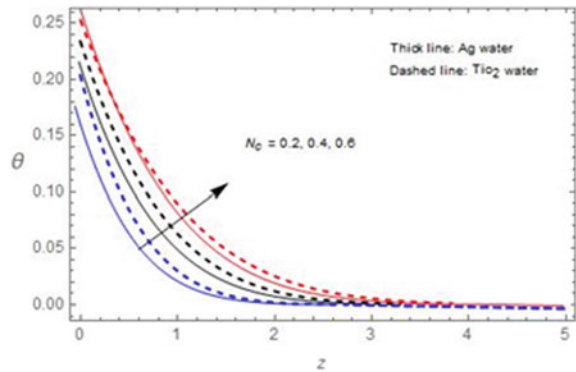
From Figs. 6, we detected that an escalation in the radiation factor increases the heat profiles of flow. It will be detected that an enhancement in convective factor escalations the heat profiles of flow (Fig. 7). It will be clear that from Fig. 8, with development in "volume fraction of nanoparticles" enhances the heat profiles of

Fig. 8 The temperature profiles with ϕ
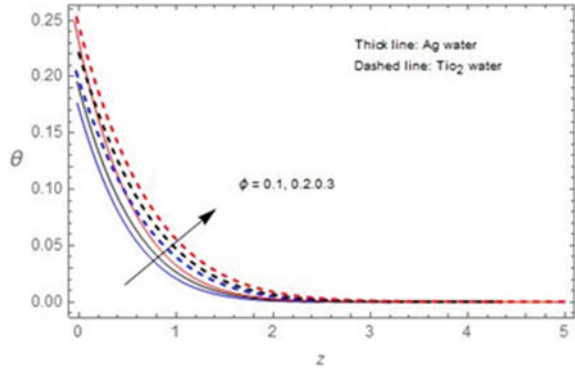
Fig. 9 The temperature profiles with Q_H
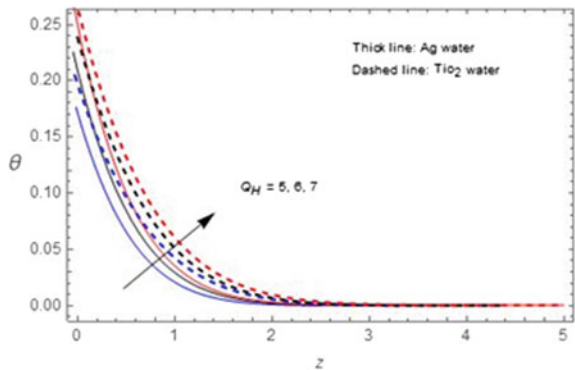
Fig. 10 The Temperature Profiles with S
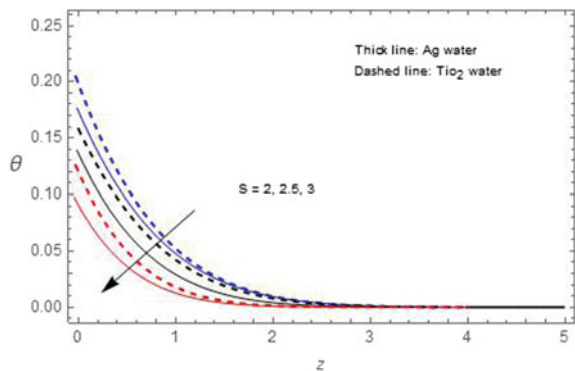
TiO$_2$–water and Ag–water. Figure 9 represents that the heat enhances with increasing heat source factor Q_H. It is noticed that expand in suction factor denigrate the boundary layer of thermal (Fig. 10).

Fig. 11 The velocity
profiles with M
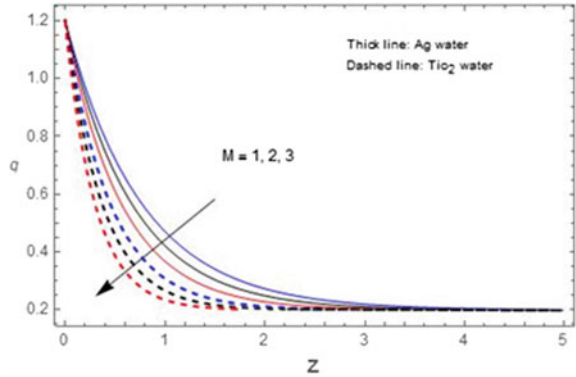
Fig. 12 The velocity
profiles with m
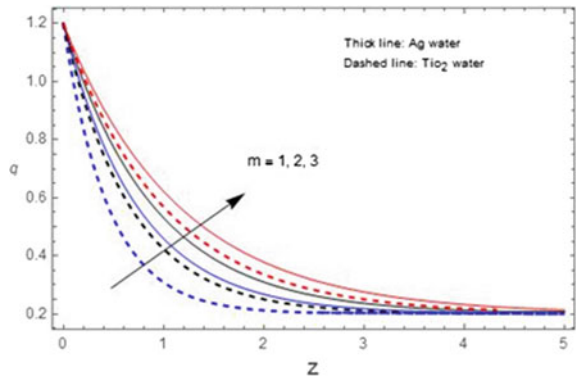
Fig. 13 The velocity
profiles with K
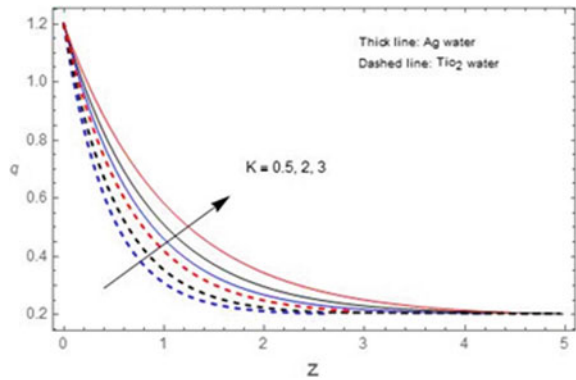
Figures 11 displays, an increase in M and R disparages the "velocity profiles of the flow (VPF)". This might be finished by the magnetic field strengthening reasons to improve the opposed force to flow. Figures 12 and 13 depicts the Hall current effects and porous medium permeability. The magnitude of the velocity improves

Fig. 14 The velocity profiles with ϕ
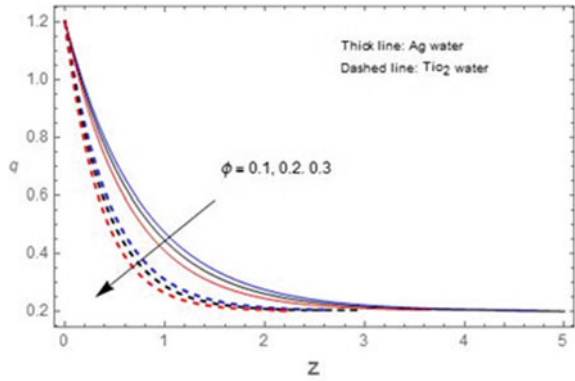
Fig. 15 The velocity profiles with Q_H
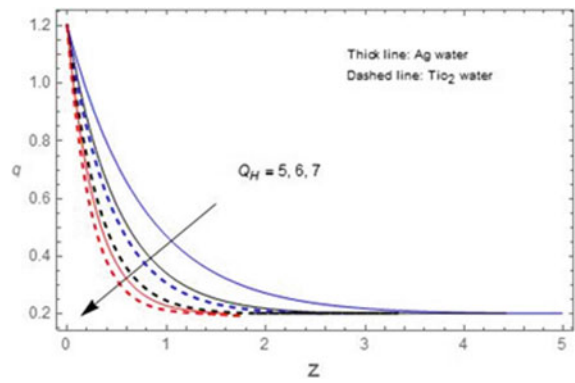
Fig. 16 The velocity profiles with Q_H
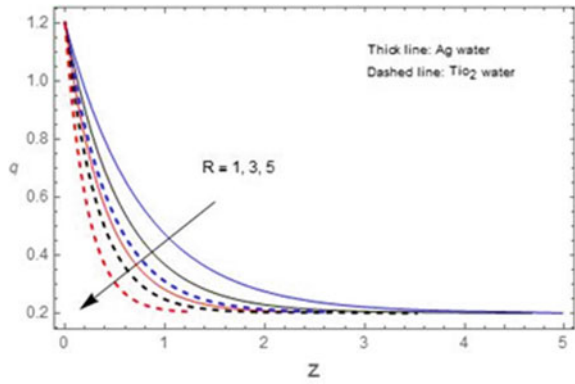
Fig. 17 The velocity profiles with F
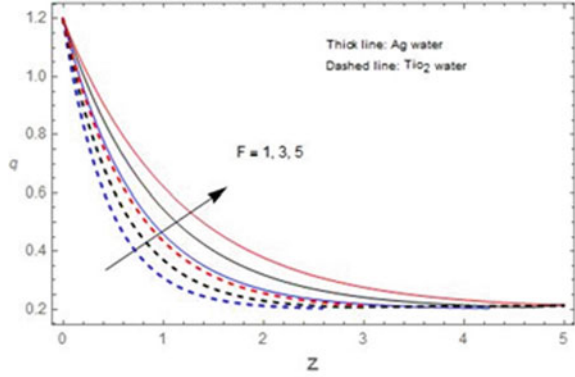
Fig. 18 The velocity profiles with S
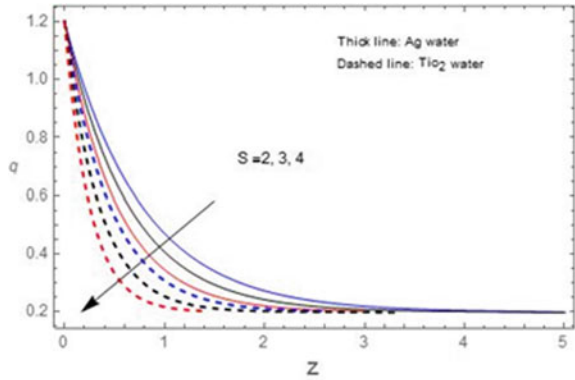
Table 1 Thermo physical properties of Ag, water, TiO$_2$

Thermo physical properties	Ag	Water	TiO$_2$
C_p (J/kg K)	235	4179	686.2
K (W/m K)	429	0.613	8.9538
ρ (kg/m^3)	10500	997.1	4250
$\beta \times 10^{-5}$ (1/K)	1.89	21	0.9
σ (S/m)	62.1×10^6	5.5×10^{-6}	2.6×10^6

with increasing Hall factor m and the permeability factor K. Figure 14 depicts the Nanoparticle volume fraction impact on VPF. We noticed that the velocity reduces with incrementing the source factor of heat Q_H and rotation factor R (Figs. 15 and 16). It is recognized that an increment in generation of heat or absorption factor expands the temperature profiles and declines the velocity profiles of flow. Figure 17 represents a radiation impact on the velocity profiles separately. It is noticed that an expansion in radiation factor increases the VPF. Figure 18 shows the impact of

Table 2 Sherwood number

N_d	Kr	Sc	S	Sh
0.3	**0.2**	**0.22**	**2**	0.146503
0.5				0.182068
0.7				0.203210
	0.5			0.159036
	0.8			0.182482
		0.3		0.183601
		0.6		0.235247
			2.5	0.180452
			3	0.198277

suction factor on velocity of flow. It will be noticed that development in suction factor decays the boundary layer of momentum.

Tables 2, 3 and 4 represent Sherwood number, Nusselt number and skin friction factor, with respect to the governing factors. From Table 2, we noticed that Sherwood number Sh enhance with increasing all parameters diffusion parameter N_d, Schmidt number Sc, chemical reaction factor Kr, and suction factor S. From Table 3, we noticed that Nusselt number raise with increasing convection parameter N_c, radiation parameter F, and factor of volume fraction ϕ, and it reduces with increasing heat source parameter Q_H and suction factor S. Finally, it is evident that with an increment in Hall factor m, permeability factor K, rotation factor R, and suction parameter S the "skin friction coefficient" reduces. Likewise, it enhances with increasing Hartmann number M, radiation factor F, volume fraction factor ϕ, and heat source parameter Q_H (Table 4). Table 5 shows the comparison of current outcomes with existed outcomes of Das [12]. We establish an outstanding agreement of current outcomes with existed outcomes.

Table 3 Nusselt number (Nu)

N_c	F	Q_H	ϕ	S	Ag–water	TiO$_2$–water
0.2	**1**	**5**	**0.1**	**2**	0.199978	0.204458
0.4					0.258855	0.288595
0.6					0.325568	0.366658
	1.5				0.266589	0.345889
	2				0.355622	0.452216
		6			0.144152	0.152245
		7			0.099589	0.114588
			0.2		0.255458	0.289960
			0.3		0.326656	0.399901
				3	0.114552	0.189663
				4	0.045585	0.144785

Table 4 Shear stress (C_f)

M	m	K	ϕ	R	F	Q_H	S	Ag–water	TiO$_2$–water
1	1	0.5	0.1	1	1	5	2	0.655258	0.788595
2								0.859960	0.966985
3								0.954478	1.244581
	2							0.488579	0.620145
	3							0.345878	0.470141
		1						0.520012	0.699589
		2						0.412558	0.588749
			0.2					0.744512	0.885922
			0.3					0.996636	0.998877
				3				0.322562	0.566258
				5				0.155524	0.336625
					3			0.708859	0.996658
					5			0.911245	1.188541
						6		0.822145	0.888474
						7		1.002522	1.114528
							3	0.522146	0.669980
							4	0.355896	0.541155

Table 5 Comparison of results ($F = \mathrm{Kr} = \mathrm{Sc} = m = 0$)

M	ϕ	R	C_f Das [12]	C_f Present results	$\mathrm{Nu}_x/\mathrm{Re}_x$ Das [12]	$\mathrm{Nu}_x/\mathrm{Re}_x$ Present results
1	0.1	1	2.145221	2.145855	0.521452	0.521455
2			1.855472	1.855485	0.485596	0.485599
3			1.655212	1.655522	0.445201	0.445204
	0.2		2.336650	2.336625	0.552468	0.552469
	0.3		2.666325	2.666745	0.589985	0.589988
		3	2.544481	2.544855	0.524252	0.524255
		5	2.880112	2.880411	0.528854	0.528856

4 Conclusions

Radiation and Hartmann numbers have the tendency to reduce the velocity. The velocity enhances with increasing Hall parameter m. The convective factor is support to increase the heat profiles of flow. Concentration reduces with increasing suction parameter. Nanoparticle volume fraction and radiation parameter increments the transfer rate of heat. The suction factor is support to increment the transfer rate of mass near the flow boundary.

References

1. Choi SUS, Eastman JA (1995) Enhancing thermal conductivity of fluids with nanoparticles. No. ANL/MSD/CP-84938; CONF-951135-29, Argonne National Labaratory, IL, USA
2. Choi SUS et al (2001) Anomalous thermal conductivity enhancement in nanotube suspensions. Appl Phys Lett 79(14):2252–2254
3. Singh AK (2008) Thermal conductivity of nano-fluids. Def Sci J 58:600–607
4. Eastman JA et al (2001) Anomalously increased effective thermal conductivities of ethylene glycol-based nanofluids containing copper nanoparticles. Appl Phys Lett 78(6):718–720
5. Uddin Z, Harmand S (2013) Natural convection heat transfer of nanofluids along a vertical plate embedded in porous medium. Nanoscale Res Lett 8(1):64
6. Remeli A et al (2012) Marangoni-driven boundary layer flow in a nanofluid with suction and injection. World Appl Sci J 17:21–26
7. Hamad MAA, Pop I (2011) Unsteady MHD free convection flow past a vertical permeable flat plate in a rotating frame of reference with constant heat source in a nanofluid. Heat Mass Transf 47(12):1517
8. Abu-Nada Eiyad (2009) Effects of variable viscosity and thermal conductivity of Al2O3–water nanofluid on heat transfer enhancement in natural convection. Int J Heat Fluid Flow 30(4):679–690
9. Sandeep N, Sugunamma V, Mohankrishna P (2013) Effects of radiation on an unsteady natural convective flow of a EG-Nimonic 80a nanofluid past an infinite vertical plate. Adv Phys Theor Appl 23:36–43
10. Yasin M, Hafizi M et al (2013) Mixed convection boundary layer flow embedded in a thermally stratified porous medium saturated by a nanofluid. Adv Mech Eng 5:121943

11. Naramgari S, Vangala S, Penem M (2014) Aligned magnetic field, radiation, and rotation effects on unsteady hydromagnetic free convection flow past an impulsively moving vertical plate in a porous medium. Int. J Eng Math
12. Das K (2014) Flow and heat transfer characteristics of nanofluids in a rotating frame. Alexandria Eng J 53(3):757–766

An Analytical Study of Aerosol Dispersion in the Atmosphere Bounded by Porous Layers

P. Meenapriya and K. Uma Maheswari

Abstract The mathematical model is developed using analytical method to examine the effects of aerosol dispersion in atmospheric fluid, both in the presence and absence of chemical reaction. Its applications are in many fields especially to human health, environmental pollution, and climate change. Taylor's dispersion model is applied to study aerosol dispersion in a channel bounded by porous layers with applied electric and magnetic field. It is perceived that the presence of chemical reaction intensifies the aerosol dispersion while in the absence of chemical reaction, the aerosol dispersion reduces.

Keywords Atmospheric fluid · Concentration of aerosol · Chemical reaction · Taylor's dispersion model

1 Introduction

More than two decades the atmospheric dispersion modeling has attracted many researchers since the dispersion study has an immense range of applications in environmental pollution, material science processing, and industries. Atmospheric dispersion modeling is the mathematical simulation of how air pollutants disperse in the atmosphere. These air pollutants are emitted from diverse sources and some of them react together to form new compounds in the air. The main constituent of the air pollutant is atmospheric aerosols.

An aerosol is defined as a disperse system of solid or liquid particles suspended in the atmosphere. They are efficient scatterers as it can be transported to some significant distance from their sources. It occurs in great amount proximate the Earth's

P. Meenapriya · K. Uma Maheswari (✉)
Department of Mathematics, Annamalai University, Annamalainagar, Chidambaram, Tamil Nadu 608002, India
e-mail: umamohansusd@gmail.com

P. Meenapriya
e-mail: meenapriyapal@gmail.com

67

surface and its concentration decreases rapidly with increasing altitude. The very high concentration of aerosols is the major cause of cardiovascular disease and is suspected to cause cancer. Aerosols limit visibility due to high concentration, which is the foremost problem prevailing in heavy industrialized areas and cities. To reduce the concentration of aerosols, the effects of dispersion coefficient of the aerosol are examined.

The dispersion of solute has attracted considerable interest among researchers since the classic paper on dispersion by Taylor [1]. The dispersion of solute matter in a circular pipe is explored by Taylor [2] and is valid asymptotically for large time. Gupta and Gupta [3] examined the dispersion of a solute using Taylor's model in the presence of first-order chemical reaction. Shivakumara et al. [4] developed a model to study dispersion in porous media, which is valid for all time. The effects of chemical reaction on the dispersion of a solute in the porous medium are considered by Pal [5]. Manjula [6] deals with the mathematical modeling of some complex fluids in composite layers.

Das et al. [7] studied hydromagnetic Couette flow of a viscous incompressible fluid in a rotating system. Due to the advanced measurement technologies, understanding of chemical composition, and physical properties of atmospheric aerosols, the literature on aerosols has increased enormously in recent years. The dispersion of aerosols in the presence of an electric field with and without chemical reaction was investigated by Meenapriya [8, 9]. Rudraiah et al. [10] developed a model of poorly conducting couple stress fluid in the presence of electric field bounded by porous layers.

The objective of this paper is to formulate a mathematical model to investigate the dispersion of aerosols in a horizontal channel bounded by porous beds in the atmospheric fluid (modeled as poorly conducting fluid) using Taylor's method. The electric and magnetic field is applied to the porous layers of rectangular channels externally. The dispersion coefficient of aerosols both with and without homogeneous first-order chemical reaction has been evaluated numerically. Results are discussed for various values of parameters including electric number, Hartmann number, porous parameter, and chemical reaction rate parameter through graphs.

2   Mathematical Formulation

A Cartesian coordinate system is taken so that the channel of width $2h$ is symmetric about the x-axis. An electroconducting impermeable rigid plates embedded with electrodes are placed on the porous layers, also uniform magnetic field B_0 is applied externally in the transverse direction as shown in Fig. 1. The electric potential $\phi = \frac{V}{h}(x)$ at y = -h and $\phi = \frac{V}{h}(x - x_0)$ at y = h are maintained at the boundary of the channel. Assume the flow to be laminar, incompressible flowing with a uniform axial pressure gradient.
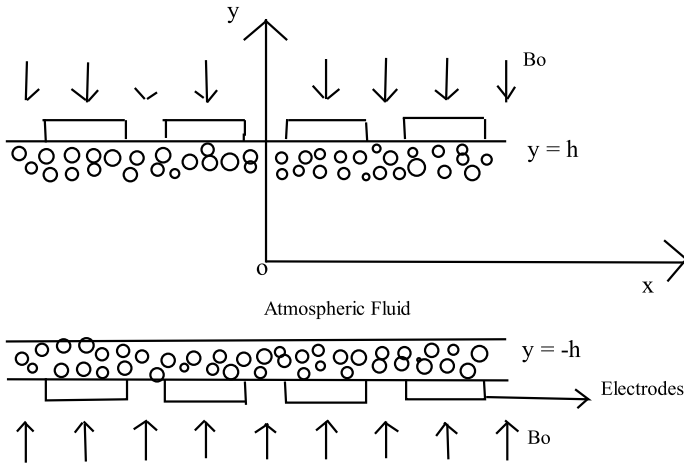
Fig. 1 Physical configuration

The basic governing equations are given below,

Conservation of mass

$$\nabla \cdot \mathbf{q} = 0 \tag{1}$$

where $\mathbf{q}$ is the velocity of the fluid.

Conservation of momentum

$$\rho[\frac{\partial \mathbf{q}}{\partial t} + (\mathbf{q} \cdot \nabla)\mathbf{q}] = -\nabla p + \mu\nabla^2\mathbf{q} + \rho e\mathbf{E} + (\mathbf{J} \times \mathbf{B}) \tag{2}$$

where ρ is the density of the fluid, p is the pressure, ρe is the density of the charge distribution, $\mathbf{E}$ is the electric field, μ is the coefficient of viscosity, $\mathbf{J}$ is the current density, and $\mathbf{B}$ is the magnetic induction.

Conservation of species

$$\frac{\partial C}{\partial t} + (\mathbf{q} \cdot \nabla)C = D\nabla^2 C - KC \tag{3}$$

where C is the concentration of aerosols, K is the chemical reaction that takes place in the channel, and D is the mass diffusivity.

Conservation of charges

$$\frac{\partial \rho e}{\partial t} + (\mathbf{q} \cdot \nabla)\rho e + (\nabla \cdot \mathbf{J}) = 0 \tag{4}$$

Maxwell's equations

$$\nabla \cdot \mathbf{E} = \frac{\rho e}{\epsilon_0} \text{ (Gauss law)} \tag{5}$$

$$\nabla \times \mathbf{E} = -\frac{\partial B_0}{\partial t} \text{ (Faraday's law)} \tag{6}$$

$$\mathbf{J} = \sigma_c(\mathbf{E} + \mathbf{u} \times B_0) \text{ (Ohm's law)} \tag{7}$$

where σ_c is the electrical conductivity and B_0 is the applied uniform magnetic field. With all the assumptions made above, Eqs. (2) (3) and(4) can be written in the cartesian form as

$$\mu \frac{\partial^2 u}{\partial y^2} - \sigma_c B_0^2 u = \frac{\partial p}{\partial x} - \rho e E_x \text{ (conservation of momentum)} \tag{8}$$

$$\frac{\partial C}{\partial t} + u \frac{\partial C}{\partial x} = D \left(\frac{\partial^2 C}{\partial y^2} + \frac{\partial^2 C}{\partial x^2} \right) - KC \text{ (conservation of species)} \tag{9}$$

$$\frac{\partial J}{\partial y} = 0 \text{ (conservation of charges)} \tag{10}$$

The boundary conditions on the velocity are,

$$\frac{\partial u}{\partial y} = -\frac{\alpha}{\sqrt{k}}(u - u_p), \quad \text{at } y = h \tag{11}$$

$$\frac{\partial u}{\partial y} = \frac{\alpha}{\sqrt{k}}(u - u_p), \quad \text{at } y = -h \tag{12}$$

$$u_p = \frac{-k}{\mu} \frac{\partial p}{\partial x} \tag{13}$$

$$u = U \quad \text{at } y = h \tag{14}$$

we are considering Beaver and Joseph [11] slip conditions for upper and lower permeable surfaces and α is called the slip parameter. The value of the porous parameter σ is given by (Darcy) $\sigma = \frac{h}{\sqrt{k}}$, where k is the permeability of the porous layer and u_p is the Darcy velocity of the porous layer.

2.1 Determination of Velocity

Using the following dimensionless quantities, Eqs. (8)–(14) are made dimensionless
$y^* = \frac{y}{h}$, $u^* = \frac{u}{(\frac{V}{h})}$, $u_p^* = \frac{u_p}{(\frac{V}{h})}$, $E_x{}^* = \frac{E_x}{(\frac{V}{h})}$, $p^* = \frac{p}{\rho(\frac{V}{h})^2}$, $x^* = \frac{x}{h}$, $\rho e^* = \frac{\rho e}{(\frac{\epsilon_0 V}{h^2})}$

The non-dimensional form of momentum equation is given by

$$\frac{\partial^2 u}{\partial y^2} - M^2 u = P - W_e \rho e E_x \tag{15}$$

let $P = \frac{\rho V}{\mu} \frac{\partial p}{\partial x}$, the electric number $W_e = \frac{\epsilon_0 V}{\mu}$, and the Hartmann number $M^2 = \frac{\sigma_c B_0^2 h^2}{\mu}$.
Maxwell's equations are used to calculate the electric force $\rho e E_x$ and hence

$$\rho e E_x = \frac{\alpha^2 x_0 e^{-\alpha y}}{2 \sinh \alpha} \tag{16}$$

So, the momentum equation (15) takes the form,

$$\frac{\partial^2 u}{\partial y^2} - M^2 u = P + W e a_0 e^{-\alpha y} \tag{17}$$

where $a_0 = \frac{-\alpha^2 x_0}{2 \sinh \alpha}$.

The solution for Eq. (17) is

$$u = A \cosh My + B \sinh My + a_1 e^{-\alpha y} - \frac{P}{M^2} \tag{18}$$

where $a_1 = \frac{W e a_0}{\alpha^2 - M^2}$. The constants A and B are calculated using the dimensionless boundary conditions on velocity given by

$$\frac{\partial u}{\partial y} = -\alpha \sigma (u - u_p) \quad \text{at } y = 1 \tag{19}$$

$$\frac{\partial u}{\partial y} = \alpha \sigma (u - u_p) \quad \text{at } y = -1 \tag{20}$$

$$u - u_p = u + \frac{Pk}{h^2} \tag{21}$$

$$u = U \quad \text{at } y = 1 \tag{22}$$

Using the above equations, the constant values are obtained as follows $A = \frac{\alpha \sigma}{\alpha \sigma \cosh M + M \sinh M} \left[\frac{a_1 e^{-\alpha}}{\sigma} - a_1 e^{-\alpha} - \frac{a_1 \cosh \alpha}{\sigma} - \frac{\alpha a_1 \cosh \alpha \tanh M}{M} + \frac{P}{M^2} - \frac{Pk}{h^2} \right]$

$$B = \frac{\alpha a_1 (\cosh \alpha)}{M \cosh M}.$$

The average velocity $\bar{u}$ is given by

$$\bar{u} = \frac{1}{2} \int_{-1}^{1} u \, dy \;\; = \frac{A \sinh M}{M} + \frac{a_1 \sinh \alpha}{\alpha} - \frac{P}{M^2} \tag{23}$$

Let $V = u - \bar{u} = A \cosh My + B \sinh My + a_1 e^{-\alpha y} + f \tag{24}$

where $f = [\frac{-A \sinh M}{M} - \frac{a_1 \sinh \alpha}{\alpha}]$.

2.2 Concentration of Aerosols

The concentration of aerosols C with chemical reaction K in the atmosphere which diffuse in a fully developed flow is given by Eq. (9). Following Taylor [1], we assume that the transverse diffusion is very much higher than the longitudinal diffusion, $\frac{\partial^2 C}{\partial x^2} \ll \frac{\partial^2 C}{\partial y^2}$ so Eq. (9) becomes,

$$\frac{\partial C}{\partial t} + u \frac{\partial C}{\partial x} = D \frac{\partial^2 C}{\partial y^2} - KC \tag{25}$$

We assume that homogeneous chemical reaction is taking place inside the channel and Eq. (25) is solved for concentration with the boundary conditions,

$$C = C_0 \quad \text{at } y = h \tag{26}$$

$$C = C_1 \quad \text{at } y = -h \tag{27}$$

We now make Eqs. (25)–(27) dimensionless by introducing the dimensionless variables, $y^* = \frac{y}{h}$, $C^* = \frac{C}{C_0}$, $t^* = \frac{t}{\bar{t}}$, $\xi = \frac{x - \bar{u}t}{L}$, and $\beta^2 = \frac{h^2 K}{D}$.
where β is the reaction rate parameter, L is the characteristic length along the flow direction. After non-dimensionalizing equation (25) becomes,

$$\frac{\partial^2 C}{\partial y^2} = VQ + \beta^2 C \tag{28}$$

where $Q = \frac{h^2}{DL} \frac{\partial C}{\partial \xi}$, $\beta^2 = \frac{Kh^2}{D}$ and Eqs. (26) and (27) becomes,

$$C = c_0 \quad \text{at } y = 1 \tag{29}$$

$$C = c_1 \quad \text{at } y = -1 \tag{30}$$

We now consider two cases based on the presence and absence of chemical reaction in the channel.

2.3 Case 1: Dispersion of Aerosols in the Presence of Chemical Reaction (when $\beta \neq 0$)

The solution for Eq. (28) using the boundary conditions (29) and (30) is,

$$C = f_1 \cosh \beta y + f_2 \sinh \beta y + Q \left[\frac{A}{M^2 - \beta^2} \cosh My + \frac{B}{M^2 - \beta^2} \sinh My + \frac{a_1 e^{-\alpha y}}{\alpha^2 - \beta^2} - \frac{f}{\beta^2} \right] \tag{31}$$

$$f_1 = \frac{1}{\cosh \beta} \left[\frac{(c_0 + c_1)}{2} - \frac{Q A \cosh M}{M^2 - \beta^2} + \frac{a_1 Q}{\alpha^2 - \beta^2} (\cosh \alpha) + \frac{Qf}{\beta^2} \right]$$

$$f_2 = \frac{1}{\sinh \beta} \left[\frac{(c_0 - c_1)}{2} - \frac{Q B \sinh M}{M^2 - \beta^2} + \frac{a_1 Q}{\alpha^2 - \beta^2} \left(e^{-\alpha} + \cosh \alpha \right) \right]$$

The atmospheric fluid is transported across a section of layer of unit breadth whose volumetric rate is given by the equation,

$$M = \frac{h}{2} \int_{-1}^{1} C V \, dy \tag{32}$$

using Eqs. (24) and (31) we have

$$M = \frac{h^2 G}{DL} \frac{\partial C}{\partial \xi} \tag{33}$$

Following Taylor [1], the assumption that the variation of C with ξ is small compared with those in the longitudinal direction is made and if C_m is the mean concentration, $\frac{\partial C}{\partial \xi}$ is indistinguishable from $\frac{\partial C_m}{\partial \xi}$. So, Eq. (33) becomes,

$$M = \frac{h^2 G}{DL} \frac{\partial C_m}{\partial \xi} \tag{34}$$

Using the aspect that no material is lost in the process is given by the continuity equation,

$$\frac{\partial M}{\partial \xi} = \frac{-2}{L} \frac{\partial C_m}{\partial t} \tag{35}$$

where $\frac{\partial}{\partial t}$ represents differentiation with respect to time at point where ξ is a constant. From equations (34) and (35), we get

$$\frac{\partial C_m}{\partial t} = D^* \frac{\partial^2 C_m}{\partial \xi^2} \tag{36}$$

$$D^* = \frac{-h^3 G}{2D} \tag{37}$$

D^* is the dispersion coefficient of aerosols in the presence of chemical reaction.

2.4 Case 2: Dispersion of Aerosols in the Absence of Chemical Reaction(when $\beta = 0$)

Suppose if chemical reaction does not takes place in the considered horizontal channel, then the reaction rate parameter becomes zero. Let the concentration of aerosols in the absence of chemical reaction be C_0, then Eq. (28) becomes,

$$\frac{\partial^2 C_0}{\partial y^2} = QV \tag{38}$$

using Eq. (24),

$$\frac{\partial^2 C_0}{\partial y^2} = Q \left[A\cosh My + B\sinh My + a_1 e^{-\alpha y} + f \right] \tag{39}$$

where $f = \left[\frac{-A\sinh M}{M} - \frac{a_1 \sinh \alpha}{\alpha} \right]$.

The value of C_0 is

$$C_0 = \left[\frac{QA}{M^2}\cosh My + \frac{QB}{M^2}\sinh My + \frac{a_1 Q e^{-\alpha y}}{\alpha^2} + \frac{Qfy^2}{2} + f_3 y + f_4 \right] \tag{40}$$

where f_3 and f_4 are integration constants and their values are obtained by using the boundary conditions given in Eqs. (29) and (30) hence,

$f_3 = \left[\frac{(C_0 - C_1)}{2} - \frac{QB}{M^2}\sinh M + \frac{a_1 Q}{\alpha^2}(\cosh \alpha - e^{-\alpha}) \right]$

$f_4 = \left[\frac{(C_0 + C_1)}{2} - \frac{QA}{M^2}\cosh M + \frac{a_1 Q}{\alpha^2}\cosh \alpha - \frac{Qf}{2} \right]$

As explained in case (1), the value of volumetric rate is calculated. Hence,

$$M_0 = \frac{h}{2} \int_{-1}^{1} C_0 V \, dy \tag{41}$$

and the dispersion coefficient of aerosols in the absence of chemical reaction D_1^* is given by,

$$D_1^* = \frac{-h^3 G_0}{2D} \tag{42}$$

C_m is the mean concentration over a section. From Eqs. (37) and (42), the expressions of dispersion coefficients D^* and D_1^* are computed and results obtained from the study are discussed in Sect. 3.

3 Results and Discussion

An analysis of aerosol dispersion in the atmospheric fluid in a channel bounded by porous beds with an external electric and magnetic field has been discussed analytically using Taylor's method. The obtained analytical results are evaluated numerically using MATHEMATICA, and the results are depicted graphically through figures. Figure 2 represents the velocity for various values of electric number. The dispersion coefficient in the presence and absence of chemical reaction has been discussed separately in Sects. 3.1 and 3.2, respectively.

3.1 Effects of Dispersion Coefficient D* (Dispersion in the Presence of Chemical Reaction)

Figure 3 represents the dispersion coefficient D^* is plotted against the Hartmann number M for some values of electric number W_e. It is evident that an increase in both the Hartmann number and electric number increases the dispersion coefficient. In Fig. 4, the dispersion coefficient D^* is plotted against the Hartmann number M for some values of porous parameter σ. It is seen that an increase in the Hartmann
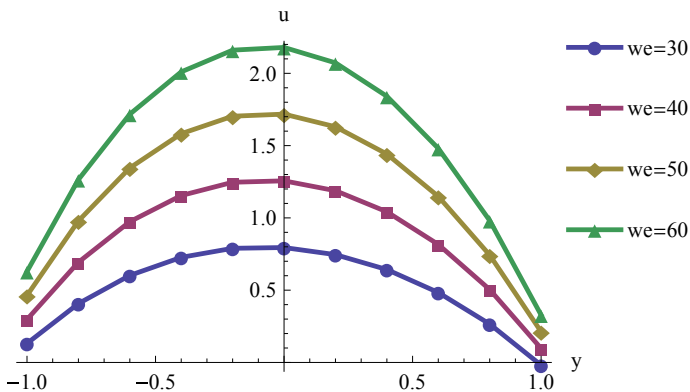
Fig. 2 Plots of velocity for different values of electric number
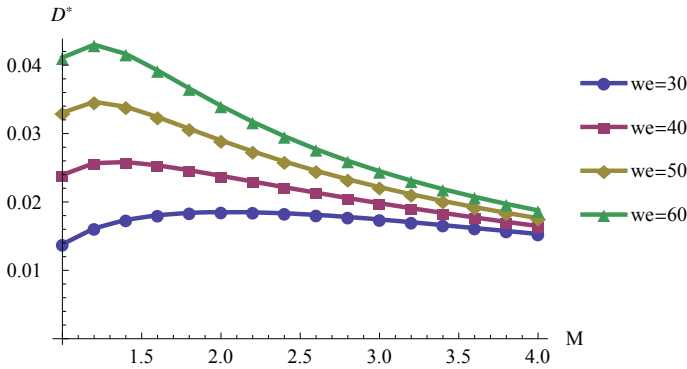
Fig. 3 Plot of dispersion coefficient D^* versus Hartmann number M for different values of electric number W_e
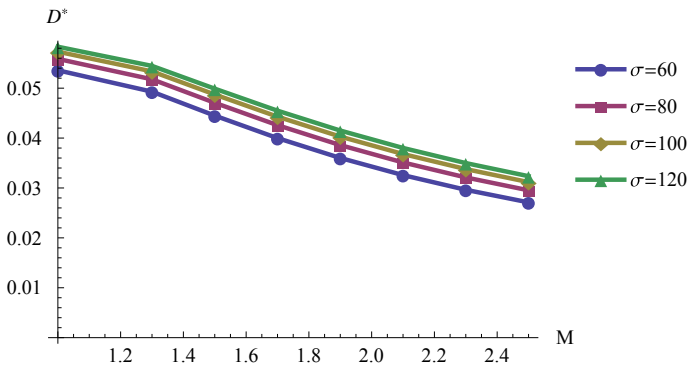
Fig. 4 Plot of dispersion coefficient D^* versus Hartmann number M for different values of porous parameter σ

number and porous parameter increases the dispersion coefficient. Figure 5 represents the plots of dispersion coefficient D^* versus electric number W_e for different values of porous parameter σ. It shows that an increase in both electric number and porous parameter increases the dispersion coefficient.

3.2 Effects of Dispersion Coefficient D_1^* (Dispersion in the Absence of Chemical Reaction)

In Fig. 6, the dispersion coefficient D_1^* is plotted against Hartmann number M for some values of electric number W_e. It is clear that an increase in both electric number and Hartmann number increases the dispersion coefficient. In Fig. 7, the dispersion coefficient D_1^* is plotted against Hartmann number M for some values of the porous
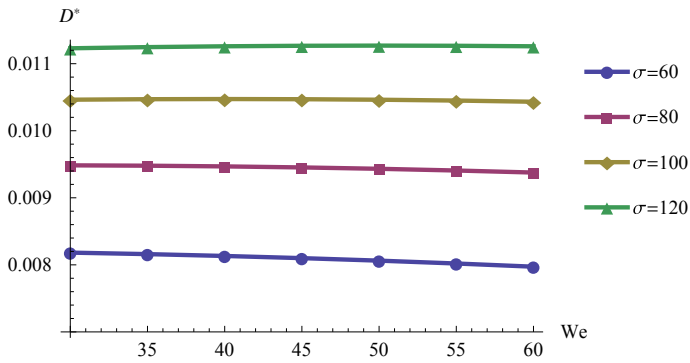
Fig. 5 Plot of dispersion coefficient D^* versus electric number W_e different values of porous parameter σ
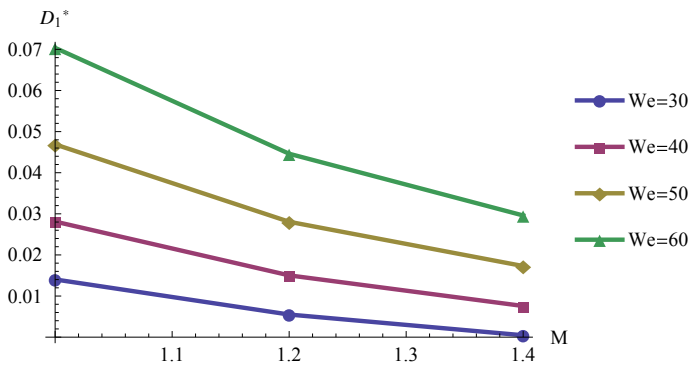
Fig. 6 Plot of dispersion coefficient D_1^* versus Hartmann number M for different values of electric number W_e

parameter. It is noted that an increase in both porous parameter and Hartmann number decreases the dispersion coefficient. Figure 8 represents the plots of dispersion coefficient D_1^* versus electric number W_e for some values of the porous parameter. It shows that an increase in both electric number and porous parameter decreases the dispersion coefficient.

Comparison Study Thus, dispersion coefficients both in the presence and absence of chemical reaction increase with an increase in electric number and Hartmann number. But results differ when comparing Figs. 4 and 7 and it is perceived that D^*, the dispersion coefficient in the presence of chemical reaction increases with an increase in Hartmann number and porous parameter, while D_1^* the dispersion coefficient in the absence of chemical reaction decreases with an increase in both Hartmann number and porous parameter. This comparative study is depicted in Fig. 9 where plots of D^* and D_1^* are drawn using the same values of Hartmann number and porous parameter.
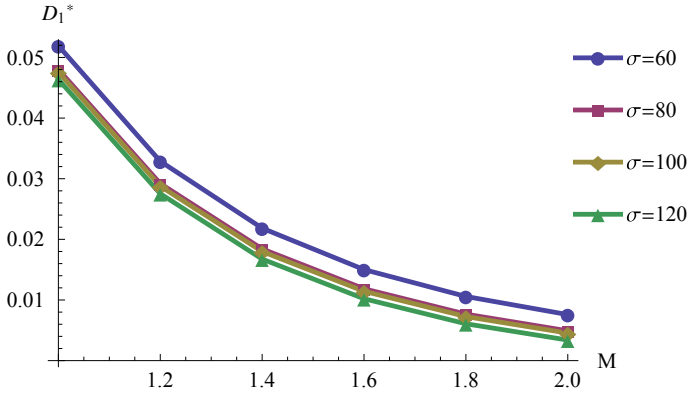
Fig. 7 Plot of dispersion coefficient D_1^* versus Hartmann number M for different values of porous parameter σ
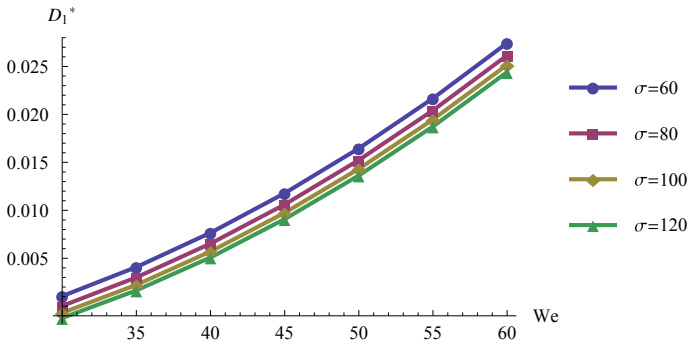
Fig. 8 Plot of dispersion coefficient D_1^* versus electric number W_e different values of porous parameter σ
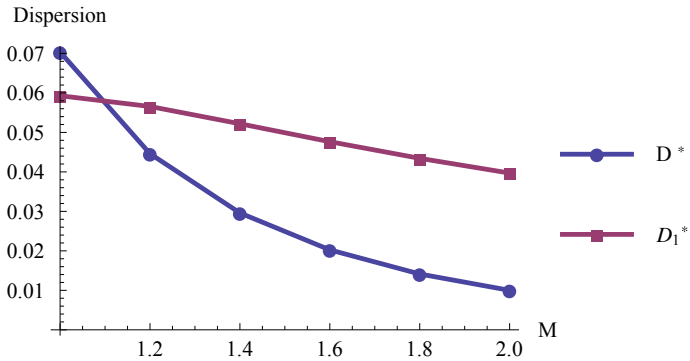
Fig. 9 Plot of dispersion coefficients D^* and D_1^*

4 Conclusion

Aerosol dispersion in the channel of atmospheric fluid bounded by porous beds with and without the effect of the chemical reaction is studied using Taylor's approach. It is noted that in the absence of chemical reaction the dispersion of aerosols reduces, so the concentration of aerosol is maximum. On the other hand, the presence of chemical reaction enhances the dispersion of aerosols and hence the concentration of aerosols is reduced. Thus, reducing the concentration of aerosols will lessen some serious health problems and visibility issues. It is concluded that the homogeneous first-order chemical reaction enhances the dispersion of aerosols, while in the absence of chemical reaction, the dispersion of aerosols reduces.

References

1. Taylor GI (1953) Dispersion of solute matter in solvent flowing through a tube. Proc R Soc Lond A 219:186–203
2. Taylor GI (1954) Dispersion of matter in turbulent flow through a pipe. Proc R Soc Lond A 223:446–468
3. Gupta PS, Gupta AS (1972) Effect of homogeneous and heterogeneous reactions on the dispersion of a solute in the laminar flow between two plates. Proc R Soc Lond A 330:59–63
4. Shivakumar PN, Rudraiah N, Pal D, Siddheshwar PG (1987) Closed form solution for unsteady diffusion in a fluid saturated sparsely packed porous medium. Int Commun Heat Mass Transfer 14:137–145
5. Pal D (1999) Effect of chemical reaction on the dispersion of a solute in a porous medium. Appl Math Model 23:557–566
6. Manjula GJ (2008) Mathematical modelling of some complex fluids in composite layers. Ph.D. thesis, Bangalore University, India, pp 90–112
7. Das S, Maji SL, Guria M, Jana RN (2009) Unsteady MHD couette flow in a rotating system. Math Comput Model 50(7–8):1211–1217
8. Meenapriya P (2019) Electrohydrodynamic convection of aerosols in a vertical channel. Int J Res Sci Tech Eng and Maths s:252–263
9. Meenapriya P (2019) Analysis of transport phenomena in air contaminants with chemical reaction in the presence of electric field. Int J Sci Res Mathe and Stat Sci 6(1):69–75
10. Rudraiah N, Mallika KS, Sujatha N (2016) Electro hydrodynamic Dispersion with interphase mass transfer in a poorly conducting couple stress fluid bounded by porous layers. J Appl Fluid Mech 9(1):71–81
11. Beavers GS, Joseph DD (1967) Boundary conditions at a naturally permeable wall. J Fluid Mech 30:197–207

Solution of Gas Dynamic and Wave Equations with VIM

Nahid Fatima

Abstract In the present research paper, we will solve homogeneous and non-homogeneous gas dynamics equation, KdV, K (2, 2) equations and wave equation with different boundary conditions. In the current research paper, to arbitrate solutions for KdV, the K (2, 2) and the wave equation reliable iteration approach is taken into consideration. We apply VIM to solve all the equations. The study highlights the efficiency of the approach and its confidence on the Lagrange multiplier. This work completes the coordination of KdV condition by the guide of any other strategy. This prompts the unpredictable answers for the condition of homogeneous and non-homogeneous gas dynamics equation, KdV and wave equations.

Keywords Gas dynamics equation · Wave equation · KdV equation

1 Introduction

Analytical methods are most commonly used to solve nonlinear equations by many authors [1–4] are very restricted and numerical techniques involving discretization of the variables, on the other hand, gives rise to rounding off errors. Recently introduced variational iteration method (VIM) by He [5–7], which gives rapidly convergent successive approximations of the exact solution if such a solution exists, has proved successful in deriving analytical solutions of linear and nonlinear differential equations. This method is preferred over other numerical methods as it is free from rounding off errors and it does not require large computer power/memory. He [6, 7] has applied this method for obtaining analytical solutions of autonomous ordinary differential equation and nonlinear partial differential equations with variable coefficients. The VIM was successfully applied to seventh-order Sawada equations [8]. Wazwaz [9] used the VIM to solve the linear and nonlinear wave equations, Burgers and Cubic Boussinesq equations. Nonlinear development assumes a significant job in applied mathematics and material science. Moreover, when a unique nonlinear condition is

N. Fatima (✉)
Amity University, Manesar, Gurgaon, India
e-mail: drnahidfatima@gmail.com

legitimately determined, the arrangement will protect the genuine physical charac-
ters of arrangements. In this paper, the variational iteration method (VIM) created
by He [10] will be utilized to lead an expository investigation on the KdV, the K (2,
2) and the wave equation. The strategy gives quickly joined progressive solutions of
the precise arrangement if such an answer exists; generally, approximations can be
utilized for numerical purposes.

Various nonlinear developments in numerous parts of sciences, for example, phys-
ical, convection, affordable and natural procedures are portrayed by the interchange
of response and dissemination or by the association among convection and dispersion.

To represent the fundamental idea of the strategy, we assume the accompanying
general nonlinear differential condition given in the structure

$$\mathrm{L}u(t) + \mathrm{N}u(t) = g(t)$$

where Lu is a straight administrator, Nu is a nonlinear administrator and $g(t)$ is a
known explanatory capacity. We can develop a rectification operation as per the
variational strategy as

$$u_{n+1} = u_n + \int_0^t \lambda(\mathrm{L}u_n(s) + \mathrm{N}\tilde{u}m_n(s) - g(s))\mathrm{d}s$$

We assume $\delta\tilde{u}_n = 0$.
We have,

$$\delta u_{n+1} = \delta u_n + \int_0^t \lambda(t, s)(\delta u_n)'\mathrm{d}s = 0$$

Its stationary conditions can be determined as follows:

$$\lambda'(s) = 0$$

$$1 + \lambda(s)|_{s=t} = 0.$$

From which the Lagrange multiplier can be distinguished as

$$\lambda = -1,$$

and the following iteration equation is acquired

$$u_{n+1} = u_n - \int_0^t \lambda(t, s)(\mathrm{L}u_n(s), \mathrm{N}\tilde{u}_n(s) - g(s))\mathrm{d}s.$$

Thus, the arrangement is given by

$$u = \lim_{n \to \infty} u_n.$$

The Korteweg-de Vries (KdV) equation is

$$u_t + uu_x + u_{xxx} = 0 \tag{1}$$

Composed here in authoritative structure.

In above condition, $u(x, t)$ is a proper field variable, t is time and x is a space orga-nize toward proliferation. The KdV condition is generally perceived as a worldview for the portrayal of feebly nonlinear long waves in numerous parts of physics and engineering. Without a doubt, on the off chance that it is assumed that x-subordinates scale as $\in$ where $\in$ is the small parameter portraying long waves (e.g., regularly the proportion of a pertinent foundation length scale to a wavelength scale), at that point, the plentifulness scales as $\in^2$ and the time advancement happens on a scale of $\in^3$.

Despite the fact that the KdV Eq. (1) is truly connected with water waves, it happens in numerous other physical settings, where it tends to be determined by an asymptotic multi-scale decrease from the applicable administering conditions.

Regularly, the result is

$$u_t + cu_x + \mu uu_x + \lambda u_{xxx} = 0 \tag{2}$$

Here, c is the important linear long wave speed for the mode whose adequacy is $u(x, t)$, while μ and λ, the coefficients of the quadratic nonlinear and straight dispersive terms separately, are resolved from the properties of this equivalent linear long wave mode and, similar to c rely upon the specific physical framework being considered.

2 Korteweg-de Vries Equation

After change and rescaling, the altered condition can be changed to the denoted KdV (or Gardner) equation $u_t + \alpha uu_x + \beta(u^2)_x + u_{xxx} = 0$.

Like the KdV condition, the Gardner condition is combined by the backward dissipating change. Here, the coefficient β can be either positive or negative, and the structure of the arrangements depends urgently on which sign is suitable.

Illustrative Example: To show efficacy of the method, we shall consider the below examples with initial condition.

3 Problems

In the beginning, we contemplate KdV equation

$$u_t - 5(u^2)_x + u_{xxx} = 0 \tag{3}$$

$$u(x, 0) = 6x$$

$$u_{n+1} = u_n + \int_0^t \lambda(\xi)\left(\frac{\partial u_n}{\partial \xi} - 5\frac{\partial (u_n)^2}{\partial x} + \frac{\partial^3 (u_n)}{\partial x^3}\right)d\xi \tag{4}$$

It gives

$$\lambda' = 0,$$
$$1 + \lambda = 0 \tag{5}$$

Hence,

$$\lambda = -1. \tag{6}$$

From Eq. (4)

$$u_{n+1}(x_2 t) = u_n(x, t) - \int_0^t \left(\frac{\partial u_n(x, \xi)}{\partial \xi} - 5\frac{\partial (u_n)^2(x, \xi)}{\partial x} + \frac{\partial^3 (u_n)(x, \xi)}{\partial x^3}\right)d\xi, n \geq 0$$

$$u_0(x, t) = 6x - \int_0^t (-5 * 72x)d\xi = 6x + 360xt = x(6 + 360t)$$

$$u_1(x, t) = 6x(1 + 3t) - \int_0^t \left(216x - 216x - 279936xt^2 - 15552xt\right)d\xi$$

$$= 6x(1 + 3t) + 6x\left(1296t^2 + 15552\right)t^3$$
$$= 6x\left(1 + 3t + 1296t^2 + 15552t^3\right) \tag{7}$$

Choosing value $u(x, 0) = 6x$ for $u_0(x, t)$,

$u_0 = 6x,$
$u_1 = 6x(1 + 60t),$
$u_2 = 6x\left(1 + 60t + 3600t^2 + 15552t^3\right),$
$u_3 = 6x\left(1 + 60t + 3600t^2 + 15552t^3 + 1119744t^4 + 20155392t^5\right) + \cdots$

$$u_4 = 6x\left(1 + 60t + 3600t^2 + 46656t^3 + 1679616t^4 + 60466176t^5 + \cdots\right)$$

$$u_n = 6x\left(1 + 60t + 3600t^2 + 46656t^3 + 1679616t^4 + 60466176t^5 + \cdots\right)$$

$$u = \lim_{n\to\infty} u_n,$$

$$u = \frac{6x}{1 - 60t^2}, \quad |60t| < 1 \tag{8}$$

K (2, 2) equation

We contemplate k (2, 2) equation

$$u_t + \left(u^2\right)_x + \left(u^2\right)_{xxx} = 0, \tag{9}$$

$$u(x, 0) = 5x$$

$$u_{n+1} = u_n + \int_0^t \lambda(\xi)\left(\frac{\partial u_n}{\partial \xi} + \frac{\partial (u_n)^2}{\partial x^2} + \frac{\partial^3 (u_n)^2}{\partial x^3}\right) d\xi \tag{10}$$

$$\lambda = -1 \tag{11}$$

Equation (10) becomes

$$u_{n+1} = u_n - \int_0^t \left(\frac{\partial u_n}{\partial \xi} + \frac{\partial (u_n)^2}{\partial x^2} + \frac{\partial^3 (u_n)^2}{\partial x^3}\right) d\xi, n \geq 0 \tag{12}$$

choosing $u(x, 0) = x$ for (x, t) and using (12),

$$u_1 = 5x(1 - 2t),$$
$$u_2 = 5x\left(1 - 2t + 4t^2 - (8/3)t^3\right),$$
$$u_3 = 5x\left(1 - 2t + 4t^2 - 8t^3 + (32/3)t^4 - (32/3)t^5\right) + \cdots$$
$$u_4 = 5x\left(1 - 2t + 4t^2 - 8t^3 + 16t^4 - 32t^5 + 64t^6\right) + \cdots$$
$$\vdots$$
$$u_n = 5x\left(1 - 2t + 4t^2 - 8t^3 + 16t^4 - 32t^5 + 64t^6 - \cdots\right) \tag{13}$$

Recalling that

$$u = \lim_{n\to\infty} u_n, \tag{14}$$

Therefore, we have

$$u = \frac{5x}{1 + 2t}.$$

Homogeneous Non Linear Gas Dynamic Equation

$$u_t + u(u)_x + u(1 - u) = 0 \tag{15}$$

With initial condition

$$u(x, 0) = e^{-x} \tag{16}$$

$$u_{n+1} = u_n + \int_0^t \lambda(\xi)\left(\frac{\partial u_n}{\partial \xi} + u_n(x, \xi)\frac{\partial u_n}{\partial x} + u(1 - u)\right)d\xi \tag{17}$$

This gives

$$\lambda' = 0$$
$$1 + \lambda = 0$$
$$\lambda = -1 \tag{18}$$

Put the value of λ into functional (17) obtain the Eq. (19)

$$u_{n+1} = u_n - \int_0^t \left(\frac{\partial u_n}{\partial \xi} + u_n\frac{\partial u_n}{\partial x} + u(1 - u)\right)d\xi \tag{19}$$

$$u_0 = \left(1 - e^{-x}\right)$$
$$u_1 = \left(1 - e^{-x}\right)$$
$$u_2 = \left(1 - e^{-x}\right)$$
$$u_n = \left(1 - e^{-x}\right) \tag{20}$$

Recalling that

$$u = \lim_{n \to \infty} u_n$$

Therefore,

$$u = n\left(1 - e^{-x}\right)$$

Homogeneous Differential Equation

$$u_t + \frac{1}{2}\left(u^2\right)_x + u(1 - u) = 0 \tag{21}$$

With condition

$$u(x, 0) = e^{-x} \tag{22}$$

The formula for Eq. (22)

$$u_{n+1} = u_n + \int_0^t \lambda(\xi) \left(\frac{\partial u_n}{\partial \xi} + \frac{1}{2} \frac{\partial u_n^2}{\partial x} + u(1 - u) \right) d\xi \tag{23}$$

This gives

$$\lambda' = 0,$$

$$1 + \lambda = 0. \tag{24}$$

$$\lambda = -1. \tag{25}$$

Put value of λ into Eq. (23) and we get,

$$u_{n+1} = u_n - \int_0^t \left(\frac{\partial u_n}{\partial \xi} + \frac{1}{2} \frac{\partial u_n^2}{\partial x} + u(1 - u) \right) d\xi \tag{26}$$

$$u_1 = u_0 - \int_0^t \left(\frac{du_0}{\partial \xi} + \frac{1}{2} \frac{\partial u_0^2}{\partial x} + u(1 - u) \right) d\xi$$

$$= e^{-x} - \int_0^t \left(u_t + \frac{1}{2} (u^2)_x + u(1 - u) \right) d\xi$$

$$= e^{-x} + \int_0^t \left(e^{-2x} + e^{-x} (1 - e^{-x}) \right) d\xi$$

$$= e^{-x} (1 + t)$$

$$u_2 = u_1 - \int_0^t \left(\frac{\partial u_1}{\partial \xi} + \frac{1}{2} \frac{\partial u_1^2}{\partial x} + u(1 - u) \right) d\xi$$

$$= e^{-x} (1 + t) - \int_0^t \left(e^{-x} - (1 + 2t + t^2) e^{-x} + e^{-x} (1 - e^{-x}) \right) d\xi$$

$$= e^{-x} (1 + t + t^2)$$

And so on…

$$u_n = e^{-x}\left(1 + t + t^2 + t^3 + \cdots\right) \tag{27}$$

Recalling that

$$u = \lim_{n\to\infty} u_n,$$

Therefore,

$$u = \frac{e^{-x}}{1 - t}.$$

VIM for solving Homogeneous and Non-Homogeneous Wave Equation

Example:

$$u_{tt} = \frac{x^2}{12}u_{xx} \tag{28}$$

Initial conditions are

$$u(x, 0) = 0, \quad u_t(x, 0) = x^4$$

Using VIM, we get,

$$u_{n+1}(x, t) = u_n - \int_0^t \left[\frac{\partial u_n}{\partial \tau} - x^4 - \frac{\partial}{\partial \tau}L^{-1}\left(\frac{1}{s^2}L\frac{x^2}{12}u_{nxx}\right)\right](d\tau).$$

Consequently, following approximations are obtained.

$$u_0 = x^4 t$$

$$u_1 = x^4 t + \frac{x^4 t^3}{3!}$$

$$u_2 = x^4 t + \frac{x^4 t^3}{3!} + \frac{x^4 t^5}{5!}$$

$$u_3 = x^4 t + \frac{x^4 t^3}{3!} + \frac{x^4 t^5}{5!} + \frac{x^4 t^7}{7!}$$

$$u_n = x^4\left[t + \frac{t^3}{3!} + \frac{t^5}{5!} + \frac{t^7}{7!} + \cdots\right]$$

Since

$$u = \lim_{n \to \infty} u_n$$

Hence, we have exact solution

$$u(x, t) = x^4 \sinh t$$

Example:

$$u_{tt} = \frac{x^2}{2} u_{xx} \tag{29}$$

$$u(x, 0) = x^2 \quad u_t(x, 0) = x^2$$

Using VIM, we have

$$u_{n+1}(x, t) = u_n - \int_0^t \left[\frac{du_n}{d\tau} - x^2 - x^2 - \frac{\partial}{\partial \tau} L^{-1} \left(\frac{1}{s^2} L \frac{x^2}{2} u_{nxx} \right) \right] (d\tau).$$

Consequently, following approximations are obtained successive

$$u_0 = x^2 + x^2 t$$

$$u_1 = x^2 + x^2 t + \frac{x^2 t^2}{2!} + \frac{x^2 t^3}{3!}$$

$$u_2 = x^2 + x^2 t + \frac{x^2 t^2}{2!} + \frac{x^2 t^3}{3!} + \frac{x^2 t^4}{4!} + \frac{x^2 t^5}{5!}$$

$$u_3 = x^2 + \frac{x^2 t^2}{2!} + \frac{x^2 t^3}{3!} + \frac{x^2 t^4}{4!} + \frac{x^2 t^5}{5!} + \frac{x^2 t^6}{6!} + \frac{x^2 t^7}{7!}$$

$$\vdots$$

$$u_n = x^2 \left(1 + \frac{t^2}{2!} + \frac{t^3}{3!} + \frac{t^4}{4!} + \frac{t^5}{5!} + \frac{t^6}{6!} + \frac{t^7}{7!} + \cdots \right)$$

And using the fact that

$$u = \lim_{n \to \infty} u_n$$

Hence, we have exact solution

$$u = x^2 e^t$$

Example:

$$u_{tt} = \frac{x^2}{6} u_{xx} \tag{30}$$

Initial condition

$$u(x, 0) = x^3 \quad u_t(x, 0) = x^3$$

Applying (VIM), we get

$$u_{n+1}(x, t) = u_n - \int_0^t \left[\frac{\partial u_n}{\partial \tau} - x^3 - x^3 - \frac{\partial}{\partial \tau} L^{-1} \left(\frac{1}{s^2} L \frac{x^2}{2} u_{nxx} \right) \right] (d\tau).$$

We have successive approximations as follows

$$u_0 = x^3 + x^3 t$$

$$u_1 = x^3 + x^3 t + \frac{x^3 t^2}{2!} + \frac{x^3 t^3}{3!}$$

$$u_2 = x^3 + x^3 t + \frac{x^3 t^2}{2!} + \frac{x^3 t^3}{3!} + \frac{x^3 t^4}{4!} + \frac{x^3 t^5}{5!}$$

$$u_3 = x^3 + x^3 t + \frac{x^3 t^2}{2!} + \frac{x^3 t^3}{3!} + \frac{x^3 t^4}{4!} + \frac{x^3 t^5}{5!} + \frac{x^3 t^6}{6!} + \frac{x^3 t^7}{7!}$$

$$\vdots$$

$$u_n = x^3 \left(1 + \frac{t^2}{2!} + \frac{t^3}{3!} + \frac{t^4}{4!} + \frac{t^5}{5!} + \frac{t^6}{6!} + \frac{t^7}{7!} + \cdots \right)$$

And using

$$u = \lim_{n \to \infty} u_n$$

Hence, we have exact solution

$$u = x^3 e^t$$

4 Conclusion

Homogeneous gas dynamics and wave equation and non-homogeneous have been solved by VIM. The amount of calculations are tremendously reduced by the VIM and it eliminates the computation of Adomian polynomials. He's variational iteration method facilitates the computational work and gives the solution rapidly when compared to Adomian method.

The shut structure arrangements of higher request non-straight beginning worth issues can be acquired utilizing VIM strategy in less calculations. The VIM strategy can likewise be connected to tackle such issues in the future.

References

1. Salih, Burger's equation. Indian Institute of Space Science and Technology, Thiruvananthapuram—18 Feb 2016
2. Grimshaw R (2008) Kortwege-de varies equation. Loughborough University, UK, 11 Jan 2008
3. Hamid P. Application of extended Tanh method to generalized burgers-type equations. Department of Mathematical Sciences, Safahan College, Isfahan 81747–43196, Iran
4. Singh V, Rani M, Bhatti HS (2017) Analytical solution of (1+n) dimensional nonlinear Burgers' equation using variational iteration method. In: Proceedings of the World Congress on Engineering 2017, vol I WCE 2017, 5–7 July 2017, London, U.K
5. He JH (1998) A variational iteration approach to nonlinear problems and its applications. Mech Appl 30–31
6. He JH (2004) Variational principles for some nonlinear PDE with variable coefficients. Chaos, Solitons Fractals 19:847–851
7. He JH (2000) Variational iteration method for autonomous ordinary differential systems. Appl Math Comput 114:115–123
8. Jawad AJM, Petkovic MD, Biswas A (2010) Soliton solutions of Burgers equations and perturbed Burgers equation. Appl Math Comput 216:3370–3377
9. Wazwaz M (2007) The variational iteration method for rational solutions for KdV, K(2,2), Burgers, and cubic Boussinesq equations. J Comput Appl Math 207(1):18–23
10. He JH (2006) Some asymptotic methods for strongly nonlinearly equations. Int J Modern Math 20(10):1141–1199

Comparison Analysis Through Condition Monitoring for Fault Detection of Bearing in Induction Motor

Y. Seetharama Rao and Devarabhotla Sai Chandra

Abstract In Industries, maintenance is an important activity to keep the equipment in a healthy condition. Condition-based maintenance (CBM) is a proactive maintenance technique that helps to fault diagnose of a machine system in running condition. This program is carried out in three steps: (i) detection; (ii) analysis; and (iii) correction. In CBM techniques, vibration analysis plays a vital role in identifying problems. The objective of this paper is to perform a comparison analysis of newly replaced bearings and corrected misaligned shaft for 630 kW induction motor with already existing healthy condition induction motor. This is done by vibration monitoring technique using fast Fourier transform (FFT) analyzer. The main attraction of this technique is that it can be performed even while the equipment is in normal working condition, thus saving precious downtime and avoiding production loss. This technique helps in diagnosing motor health by taking readings on drive end and non-drive end for both motors. By placing the accelerometer sensor in the tri-axial direction of motor vibration, data is obtained. These are in amplitude and time waveform signals and are collected at full load condition. This comparison analysis is a technique that helps to know the motor health condition. The obtained results are encouraging and identified the motor rolling bearing health status in running condition.

Keywords Vibration monitoring · Fault identification · Vibration spectrum analysis

1 Introduction

Condition-based maintenance involves regular inspection of equipment and sophisticated instruments to assess the health of the machine, most of the activities ought to be preferably done while equipment is running. While on the one hand, it improves the effectiveness of inspection; on the other side, it reduces the downtime which is a limiting factor in time-based preventive maintenance. Vibration monitoring is one of the

---
Y. Seetharama Rao (✉) · D. Sai Chandra
Gayatri Vidya Parishad College of Engineering (Autonomous), Kommadi, Visakhapatnam, Andhra Pradesh 530048, India
e-mail: yseetharamarao24@gvpce.ac.in

techniques in condition-based maintenance. Rolling element bearings are the most precisely made devices, do not fail prematurely, unless some other forces are responsible. Such forces are often the same as causing vibration. Vibration monitoring is a time reliable technique and aids to assess the machinery health condition. Kankar et al. [1] investigated the feature recognition system for the detection of bearing faults by classifying those using soft computing techniques like artificial neural networks (ANN) and support vector machine (SVM). The performance of SVM is found to be better due to its inherent generalization capability. Ma and Zhang [2] investigated the rolling element bearing using SVM classifier for initial classification. SVM classification results show basic probability assignment (BPA). The experimental results indicated that since SVM method has high recognition accuracy, stability, and broad applicability, it can effectively identify roller bearing health status. Rummaan et al. [3] conducted experiment on roller bearing using support vector method (SVM). Vibration signal is followed by feature extraction in time and frequency domain, and on this basis, fault classification is performed. Through the results and simulations produced, efficient fault detection can not only be done using classical SVM but even better results are obtained using one-class SVM. Saravanan et al. [4] have performed experiments on condition of an inaccessible gear in an operating machine using vibration signal of machine which deals with the effectiveness wavelet-based features for fault diagnosis using support vector machine and proximal support vector machines. These data are classified by an algorithm and predominant features were fed as input for training and testing SVM and PSVM and this helps in classifying faults in gearbox. Siddiqui et al. [5] diagnosed bearing fault on squirrel cage induction motor in transient condition further as steady-state condition by signal processing techniques, like FFT by time domain as well as wavelet transform for early fault detection. Nandi and Toliyat [6] gave a brief review of bearing, stator, rotor, and eccentricity-related faults by non-invasive motor current signature analysis (MCSA) and diagnose faults in machine. Yavanarani et al. [7] demonstrated experiment on engine test bed so as to verify that it meets the particular at various load accumulations. These are usually carried with troubleshooting so as to determine whether vibration levels are inside acceptable limits at a given speed.

The above-discussed literature gives an idea of how to conduct experiment using FFT analyzer on rotating machines. From vibration data, it gives an idea how to analyze a problem on a rotating system. Different methods to analyze vibration signals other than FFT analyzer are used. The data obtained helps in optimizing the machine life and diagnosis the cause to root level but it takes a long period to diagnose. This paper performs a simple and time reliable technique to diagnose motor health in running condition.

2 Comparison Analysis of Induction Motor Using Fast Fourier Transform Analyzer

Fast Fourier transform analyzer is useful to take readings, record them, and track the trend of the machine over a period of time. An accelerometer is held on motor drive and non-drive end bearing housing for diagnosing. The overall readings are taken in amplitude vs frequency in the tri-axial direction on both ends of the bearing housing. These are analyzed by collected data depending on its vibration characteristics; the nature of the defect is identified. The recorded readings are dumped into a computer where all data is stored by using CSI Master Trend software that will be helpful for comparing the present data with past data trends, and it can diagnose the mechanical condition of the motor (Fig. 1).

2.1 General Defects in Anti-friction Bearings

Rolling element bearings are the most precisely made devices, do not fail prematurely, unless some other forces are responsible. Such forces are often the same as causing vibration. So, even when a vibration analysis indicates symptoms of bearing problems, that should not eliminate the possibility of something else, is the primary cause of trouble. Always make a careful check for other difficulties, such as unbalance and misalignment, after replacing the bearing, especially where premature bearing failures have been frequent. Rolling element bearing having flaws in raceways, rolling elements, or cage will usually cause a high frequency of vibration. Actually, the defective bearing will not generally cause a single discrete frequency of vibration, but, instead may generate several frequencies simultaneously the spectrum taken out from fault bearing machine.

It is observed that there are several high frequencies which are generated by the faulty bearing. The vibration signature further suggests that vibration is somewhat random and unsteady (Table 1).

Fig. 1 Measuring points to collect vibration data from induction motor

Table 1 Equipment details for mill fan

Equipment type	Single suction overhung rotor fan
Impeller diameter	2600 MM
Motor type	3-Phase induction motor
Rating	630 kW
Operating voltage	6600 V
Full load current	69 Amp
Motor speed	1000 RPM
Handling medium	Nitrogen
Coupling type	Pin bush
Foundation type	Concrete
Motor bearing	Double row spherical roller (22,230)

As per ISO 2372, this equipment belongs to class-3 and the maximum vibration limit for this equipment is 4.5 mm/s and the collected vibration readings should not exceed this value.

3 Experimental Setup

After disassembly of motor bearings from induction motor, the motor drive end bearing defect is observed on outer race like knurling pattern due to rubbing of rolling elements. On non-drive end, it is also noted that normal wear appeared on outer race of bearing (Figs. 2 and 3).

3.1 Physical Observations

- Abnormal and rhythmic knocking sounds appeared because the motor intensity is high at bearing points as compared to motor body.
- Motor temperature readings are also reached to 62 °C at motor DE bearing on the housing, and shaft temperatures are at the level of 58 °C.
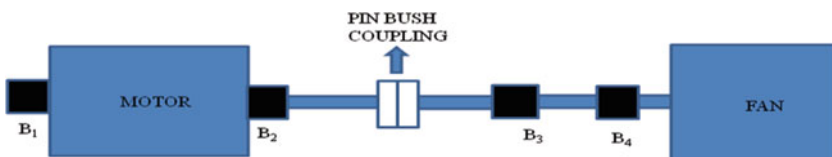
Fig. 2 Measuring point layout for mill fan motor where B1—motor non-drive end (MNDE), B2—motor drive end (MDE), B3—fan drive end (FDE), and B4—fan non-drive end (FNDE)

Fig. 3 **a** Knurling pattern defect identified on motor drive end side bearing and **b** normal wears on outer race due to deterioration on non-drive end

- Fan side readings are more or less at the moderate level.
- Lubrication condition also has appeared to be dry.
- Motor base plate vibrations readings are also high in vertical direction at drive end and non-drive end base plate bolts.

4   Detection of Defective Bearing on Induction Motor

The overall vibrations are taken mm/s in the tri-axial direction for induction motor helpful in analyzing the motor health condition. It is helpful in knowing at what direction the maximum amplitude is appeared. Depending upon the nature of vibration amplitude and direction at which amplitudes appear, the type of defect can be detected in advance (Table 2).

The spectrum from Fig. 4 shows the velocity amplitude of 3.05 mm/s at 960 cpm in vertical direction, and Fig. 5 shows the velocity amplitude 5.49 mm/s at 3960 cpm in axial direction on motor drive end before replacement of motor bearing (Figs. 6, 7, and 8).

Table 2   Overall vibration data of induction motor before replacement of bearing on motor drive and non-drive end

Axis	MNDE	MDE
Vertical	2.81	3.05
Horizontal	1.71	2.72
Axial	3.63	5.49
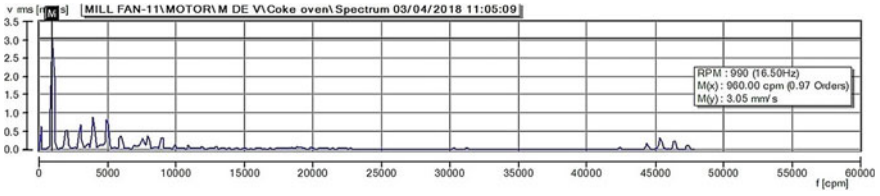
Fig. 4 Motor drive end vertical spectrum before replacement of bearing
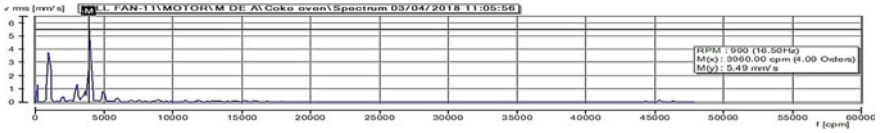
Fig. 5 Motor drive end axial spectrum before replacement of bearing
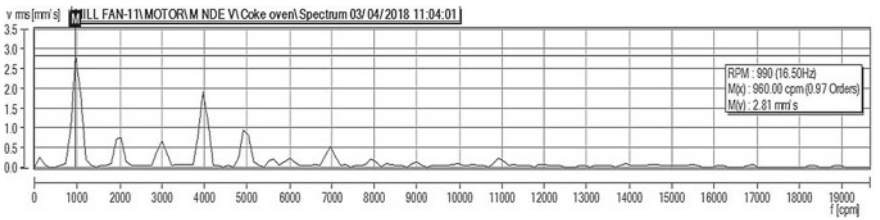
Fig. 6 Motor non-drive end vertical spectrum before replacement of bearing
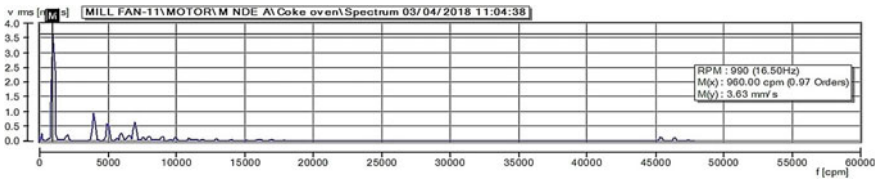
Fig. 7 Motor non-drive end axial spectrum before replacement of bearing
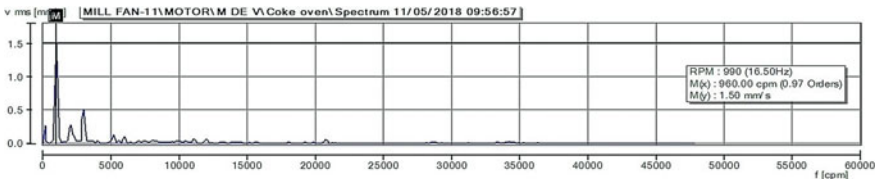
Fig. 8 Motor drive end vertical spectrum after replacement of bearing

4.1 Observation

1. Dominating vibration amplitudes are observed at motor DE bearing in vertical and axial directions only, pattern directing us toward the localized problem, not influencing the other bearings in the equipment.
2. In the fast Fourier transform spectrums of motor bearing, dominating peaks appeared at 3974 cpm which is not matching with any harmonic frequencies of rotating RPM of the motor.
3. Sub-harmonic frequencies of rotating motor revolution per minute (RPM) are also not matching with 3974 CPM at any order.
4. Mapping of vibration amplitude on motor bearings shows an increasing trend with time and is an indication that the rate of increase is high and the condition of the bearing may deteriorate proportionally with the increase of vibration amplitude.
5. Vibration phase at motor DE bearing with respect to tacho signal has appeared very erratic in both radial and axial directions.
6. The time waveform has also appeared like amplitude modulation pattern in the axial direction readings of motor DE bearing.

5 Analysis of Spectrum After Replacement of Bearing for Induction Motor

From the spectrum in Fig. 9, it is seen that there is velocity amplitude of 1.5 mm/s at 960 cpm in the vertical direction. From the spectrum in Fig. 10, it is seen that there is a velocity amplitude of 1.15 mm/s at 960 cpm in horizontal direction, and from
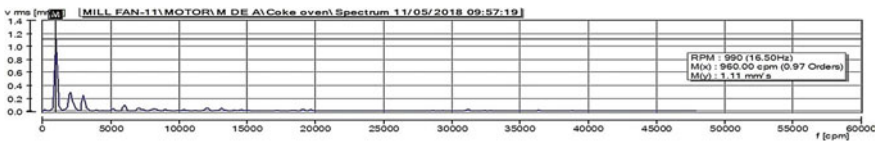
Fig. 9 Motor drive end axial spectrum after replacement of bearing
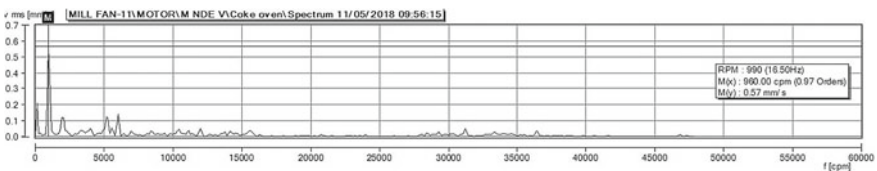
Fig. 10 Motor non-drive end vertical spectrum after replacement of bearing
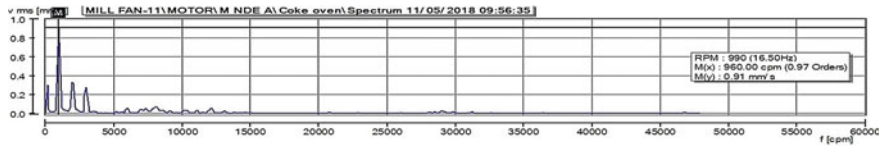
Fig. 11 Motor non-drive end axial spectrum after replacement of bearing

the spectrum Fig. 11, it is seen that the velocity amplitude is 1.11 mm/s at 960 cpm in axial direction after replacement of bearing on motor drive end.

From the spectrum in Fig. 8, it is seen that there is velocity amplitude of 1.5 mm/s at 960 cpm in the vertical direction and from the spectrum Fig. 9, it is seen that the velocity amplitude is 1.11 mm/s at 960 cpm in axial direction after replacement of bearing on motor drive end.

From the above spectrums in Fig. 10 it is observed that, the velocity amplitude 0.57 mm/s at 960 cpm in vertical direction in Motor Non-Drive End, and Fig. 11 the velocity amplitude 0.91 mm/s at 960 cpm in axial direction in Motor Non-Drive End before replacement of motor bearing. These peaks showing machine is running in a healthy condition. The maximum amplitudes are found in vertical and axial directions only, whereas in the horizontal direction, the amplitudes are within acceptable limits. This shows that the motor is in an unhealthy condition.

6 Comparison Analysis for the Existing and Newly Replaced Bearing for Induction Motor

From the spectrum in Fig. 12, it is seen that there is a velocity amplitude of 0.88 mm/s at 960 cpm on axial direction. And from the spectrum Fig. 13, it is seen that the velocity amplitude is 1.33 mm/s at 960 cpm in vertical direction after replacement of bearing on motor drive end of existing healthy condition induction motor.

From the above spectrums in Fig. 14, it is observed that, the velocity amplitude 0.52 mm/s at 960 cpm in vertical direction in motor non-drive end, and in Fig. 15, the velocity amplitude 0.51 mm/s at 960 cpm in axial direction in motor non-drive end for existing healthy condition induction motor. These peaks showing machine running in a healthy condition.
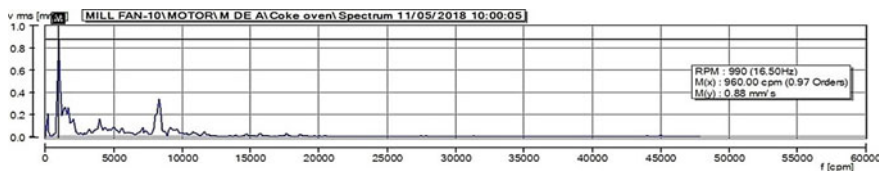
Fig. 12 Motor drive end axial spectrum velocity amplitude 0.88 mm/s at 960 cpm
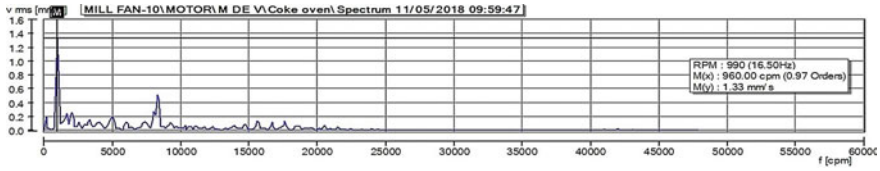
Fig. 13 Motor drive end vertical spectrum velocity amplitude 1.33 mm/s at 960 cpm
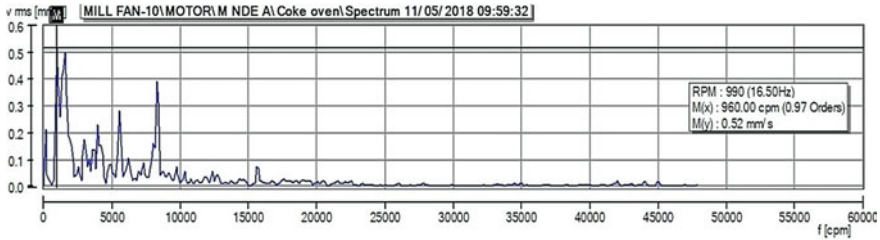
Fig. 14 Motor non-drive end axial spectrum velocity amplitude 0.52 mm/s at 960 cpm
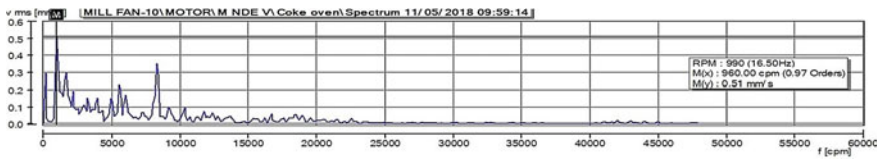
Fig. 15 Motor non-drive end vertical spectrum velocity amplitude 0.51 mm/s at 960 cpm

6.1 Trends Observed After Replacement of Bearing for Induction Motor on Motor Drive End

From Figs. 16 and 17, it is observed that there is a decrease in trend over a period of time after replacement of bearing on motor drive end and non-drive end of the induction motor and these values are within the permissible limit as per ISO 2372 which is less than 4.5 mm/s for class-3 equipment.
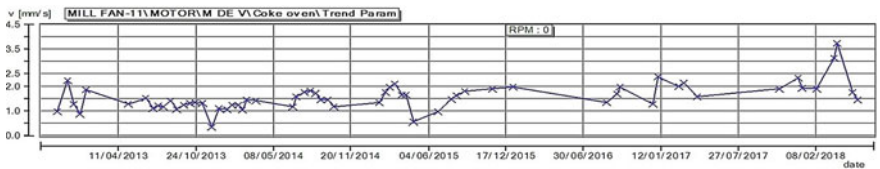
Fig. 16 Trends on motor drive end vertical direction
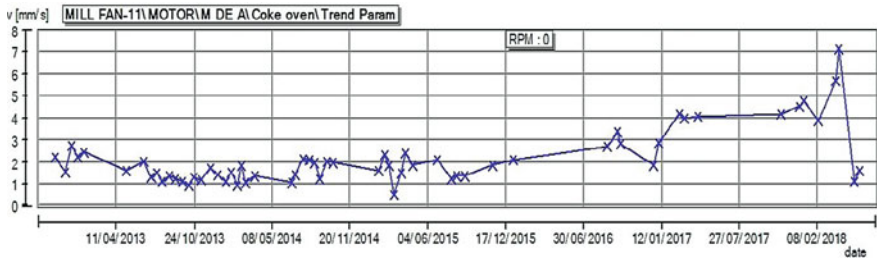
Fig. 17 Trends on motor drive end axial direction

Table 3 Overall vibrations reading after replacing with new bearing for motor on drive and non-drive ends in mm/s

Direction	MNDE	MDE
Vertical	0.57	1.5
Horizontal	0.51	1.15
Axial	0.91	1.11

Table 4 Vibration reading collected for existing healthy condition induction motor

Direction	MNDE	MDE
Vertical	0.51	1.33
Horizontal	1.16	1.59
Axial	0.52	0.88

From Tables 3 and 4, it can be clearly observed that there is a reduction in vibration amplitudes readings on both drive end and non-drive end of bearings for the induction motor. From the above data, it clearly shows the motor is running in a healthy condition (Tables 5 and 6).

Table 5 Comparison readings taken after newly replaced bearing induction motor with existing healthy condition induction on motor non-drive end (MNDE)

Direction	Newly replaced motor MNDE(mm/s)	Existing healthy motor MNDE(mm/s)
Vertical	0.57	0.51
Horizontal	0.51	1.16
Axial	0.91	0.52

Table 6 Comparison readings taken after newly replaced bearing for induction motor with existing healthy condition induction on motor drive end

Direction	Newly replaced motor MDE (mm/s)	Existing healthy motor MDE (mm/s)
Vertical	1.5	1.33
Horizontal	1.15	1.59
Axial	1.11	0.88

7 Conclusions

In this paper, an easy technique comparison analysis is adapted to compare induction motor health status with already existing healthy running condition induction motor to easily identify the defects. Early failure of bearing after taking into the operation is not the problem of bearing but some external forces are responsible for their failure. Early and efficient fault detection is very important in process industries, and failure of any machine leads to huge production loss. Vibration analysis is the versatile tool in the identification of bearing failures at an early stage and also helps in identification of root cause like misalignment in the system, misalignment of bearing with its shaft or in the housing, unbalance in the rotors, and resonant conditions in the surrounding supporting structures.

1. This technique helps in diagnosing a machine within less time which is important for processing industries machines, and failure of any machine leads to huge production loss.
2. It is found that the predominant frequency in the spectrum, i.e., 3960 cpm is very close to harmonic of ball pass frequency of the outer race (BPFO) of a double row spherical roller bearing.
3. From Tables 3 and 4, it is observed that the overall readings of two motors are running in healthy condition and these are within the limits as per ISO 2372.
4. The vibration amplitudes were greatly reduced from 5.49 mm/s to 1.11 mm/s in the axial direction of the motor drive end bearing after replacing with the new bearing.
5. The temperatures readings also came within the limits on shafts 50° and on bearing 53 °C on motor drive end bearing.

References

1. Kankar PK, Satish Sharma, Harsha SP (2013) Fault diagnosis of rolling element bearing using cyclic autocorrelation and wavelet transform. Neurocomputing 110:9–17
2. Ma L, Zhang T (2016) Health status identification of rolling bearing based on SVM and improved evidence theory. IEEE, pp 378–382
3. Rummaan BA, Sufi TG, Abdul QK (2016) A comparative analysis of classical and one class SVM classifiers for machine fault detection using vibration signals. IEEE
4. Saravanan N, Kumar Siddabattuni VNS, Ramachandran KI (2008) A comparative study on the classification of features by SVM and PSVM extracted using Morlet Wavelet for fault diagnosis. Expert Syst Appl 35:1351–1366
5. Siddiqui KM, Sahay K, Giri VK (2014) Modelling and detection of bearing fault in PWM inverter fed induction motor drives. Manager's J Electr Eng 8(1):11–24
6. Nandi S, Toliyat HA (1999) Fault diagnosis of electrical machines. In: Proceeding of IEEE IAS Annual Meeting, no 1, pp 219–221
7. Yavanarani K, Simon Sundar Raj GS (2010) Multi resolution analysis for bearing fault diagnosis. IEEE, vol 10, pp 322–327

Influence of Thin Baffle and Magnetic Field on Buoyant Convection in a Vertical Annulus

B. V. Pushpa, M. Sankar, B. M. R. Prasanna, and Zailan Siri

Abstract This paper numerically investigates buoyancy-driven convection in an annular cavity having differently heated cylindrical side walls and a thin baffle attached to the inner cylinder. The annular enclosure is packed with electrically conducting low Prandtl number fluid (Pr = 0.054). Along the radial or axial direction, a magnetic field of uniform intensity is applied. The finite difference method consisting of ADI and SLOR techniques is employed to solve the model equations governing the physical processes. The simulation results are presented through streamlines, isotherms, local, and average Nusselt numbers to illustrate the effects of various parameters. The simulation results explain that the Hartmann number and baffle length restrained the heat transfer rate, while the Rayleigh number and baffle location enhance the rate of heat transfer.

Keywords Magnetic field · Annulus · Baffle · Finite difference method

1 Introduction

Buoyancy-driven convection in finite geometries, such as rectangular and annular enclosures with an applied magnetic field, has been widely examined because of its occurrence in important applications, such as electrical power generation, astrophysical flows, and crystal growth techniques. During the casting process, natural convection takes place while melting the liquid metal in the mold; this causes the movement of impurities, resulting reduction of the product quality. To improve the

B. V. Pushpa
Department of Mathematics, BMS Institute of Technology and Management, Bangalore, India

M. Sankar (✉)
Department of Mathematics, School of Engineering, Presidency University, Bangalore, India
e-mail: manisankariyer@gmail.com

B. M. R. Prasanna
Department of Mathematics, Siddaganga Institute of Technology, Tumakuru, India

Z. Siri
Institute of Mathematical Sciences, University of Malaya, 50603 Kuala Lumpur, Malaysia

quality of the product, it is necessary to control the unwanted convection. Several techniques have been used to reduce the unwanted convection. One of the best ways to control this undesirable movement is the application of magnetic field in one or more directions. Realizing this important aspect of the applied magnetic field, several investigations have been carried out on heat transport in various finite-sized cavities with an applied magnetic field. Among the finite shaped enclosures, an annular geometry designed from two vertical coaxial cylinders is an important enclosure in many scientific and industrial applications and hence investigated by many researchers [1–3].

In a cylindrical annulus, Sankar et al. [4] numerically examined convection heat transport by applying a constant magnetic field. It is observed that the direction of magnetic field has profound influence on the type of enclosures. Wrobel et al. [5] experimentally investigated convection in an annular geometry with magnetic field. In an annular geometry, Venkatachalappa et al. [6] analyzed thermosolutal convection to understand the magnetic field effects applied in either axial or radial directions. They found that the suppression of double-diffusive convection by the magnetic field greatly depends on the buoyancy ratio. Later, Sankar et al. [7] numerically investigated the collective impact of magnetic field and thermocapillary force on buoyancy-driven convection. Kakarantazas et al. [8] performed 3D magnetoconvection in a vertical annular enclosure. The vertical surfaces are heated differently, and horizontal surfaces are considered as insulated. The results reported that the turbulent flow is developed for the non-magnetic case, and an increase of magnetic force makes the flow to be laminar. Afrand et al. [9] studied magnetoconvection in an annular space filled with liquid potassium by applying a horizontal constant magnetic field. They observed that the flow is axisymmetric for non-magnetic field case, but for horizontal magnetic force, the flow is asymmetric and causes decrease in thermal transport in the cavity. Later, in an inclined annular geometry, Afrand et al. [10] examined three-dimensional magnetoconvection for wider parametric ranges. Malvandi [11] examined the anisotropic behavior of nanoparticles in nanofluids in the vertical cylinder filled with film boiling magnetic nanofluids and magnetic field.

The impact of magnetic force on buoyancy-driven flow in a rectangular cavity is studied by Oreper and Szekely [12]. They found that the reduction of heat transport rates by the magnetic field strongly depends on the size of the enclosure. Magnetoconvection in a rectangular geometry has been numerically examined by Venkatachalappa and Subbaraya [13]. They observed that the convection is suppressed for sufficiently large magnetic strength, and thermal transport rate is increasing with an increase in Rayleigh number. Later, Rudraiah et al. [14] extended the similar work on magnetoconvection in a rectangular enclosure with uniform heat flux and found sharp decline in thermal transport rate with an increase in Ha. Seller and Walker [15] studied flow of liquid metal in tall cavity with magnetic field and electrically insulated boundaries. Parvin and Nasrin [16] reported the results on magnetoconvection in square geometry containing a solid body of circular shape. The results

demonstrated that flow and temperature patterns are strongly disturbed by the Hartmann and Rayleigh numbers. In a square enclosure, Sathiyamoorthy and Chamkha [17] presented the results on the impact of an applied magnetic field on natural convection. The results report that there is a substantial impact on the local and global Nusselt numbers when the magnetic field strength is very high. Magnetoconvection in a trapezoidal enclosure has been numerically investigated by Hasanuzzaman et al. [18] and observed that convection is decreasing with an increasing in the magnetic field strength.

Using finite element method, Turk and Tezer-Sezgin [19] numerically investigated the combined influence of enclosure inclination and oblique magnetic field on magnetoconvection in a tilted geometry. The recent theoretical studies on magnetoconvection in finite enclosures are due to Ganji and Malvandi [20] and Basant et al. [21]. Mahmoudi et al. [22] analyzed convective heat transport of nanofluids in a square geometry with magnetic field and heat sinks. It has been demonstrated that the convective flow and thermal transport in a differentially heated geometry can be efficiently organized by attaching baffles to the heated or cooled wall, which are essential in many industrial applications, and have been widely investigated by many researchers [23–25]. Few important studies on magnetoconvection in finite enclosures can be found in the works of Sivasankaran and co-workers [26–29]. Based on the detailed literature survey, the influence of magnetic field and baffle on convective transport is not available for a vertical annulus. Hence, a numerical investigation is performed to analyze the influences of magnetic force and a thin baffle on buoyancy-driven convection in a vertical annulus. The proposed configuration is an interesting work for many industrial applications, particularly to the situations where control of heat transfer is essential.

2 Mathematical Formulation

In the present study, we considered the vertical annulus of width D and height H with r_i and r_o as radii of inner and outer cylinders as shown in Fig. 1. The inner cylinder is maintained at higher (θ_h) temperature, and outer cylinder is at lower (θ_c) temperature, upper and lower boundaries are considered as adiabatic. The inner hot wall is attached with a thin circular baffle whose temperature is same as that of inner cylindrical wall. It is assumed that the annular gap is filled with an electrically conducting fluid having low Prandtl number ($Pr = 0.054$), and a magnetic field of uniform strength B_0 is applied along horizontal (radial) or vertical (axial) direction. Further, the motion of electrically conducting fluid produces an induced magnetic field. As corroborated by several investigations in the literature, the induced magnetic field is ignored in comparison with applied magnetic field B_0. By applying Boussinesq approximations, the non-dimensional governing equations are:
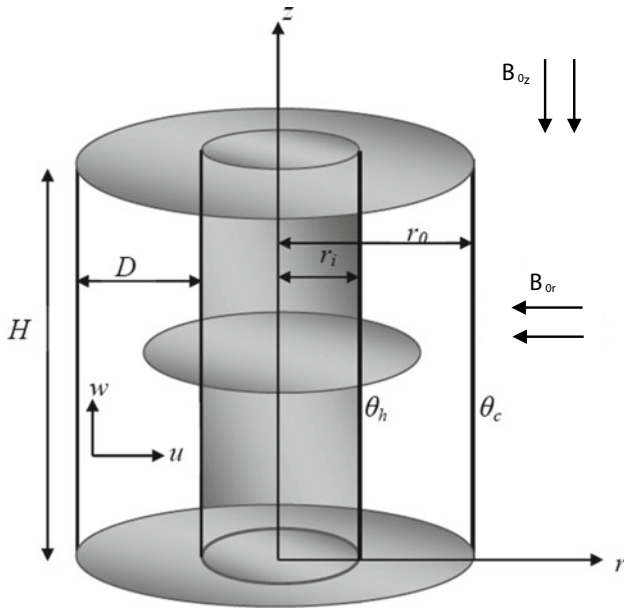
Fig. 1 Schematic diagram of the annular enclosure

$$\frac{\partial T}{\partial t} + U \frac{\partial T}{\partial R} + W \frac{\partial T}{\partial Z} = \nabla^2 T, \tag{1}$$

$$\frac{\partial \zeta}{\partial t} + \left[U \frac{\partial \zeta}{\partial R} + W \frac{\partial \zeta}{\partial Z} - \frac{U \zeta}{R} \right] = \Pr \left[\nabla^2 \zeta - \frac{\zeta}{R^2} \right] - \Pr \operatorname{Ra} \frac{\partial T}{\partial R}$$

$$- \Pr \operatorname{Ha}_z^2 \frac{\partial U}{\partial Z} + \Pr \operatorname{Ha}_r^2 \frac{\partial W}{\partial R} \tag{2}$$

$$\zeta = \frac{1}{R} \left[\frac{\partial^2 \psi}{\partial R^2} - \frac{1}{R} \frac{\partial \psi}{\partial R} + \frac{\partial^2 \psi}{\partial Z^2} \right] \text{ and } U = \frac{1}{R} \frac{\partial \psi}{\partial Z}, \quad W = -\frac{1}{R} \frac{\partial \psi}{\partial R} \tag{3}$$

where $\nabla^2 = \frac{\partial^2}{\partial R^2} + \frac{1}{R} \frac{\partial}{\partial R} + \frac{\partial^2}{\partial Z^2}$.

The above dimensionless equations are obtained from the following transformations:

$$(R, Z) = (r, z)/D, \ (U, W) = (u, w) \cdot D/\alpha, \ t = t^* \alpha/D^2, \ T = (\theta - \theta_c)/(\theta_h - \theta_c),$$
$$P = p/(\rho_0 \alpha^2/D^2), \ \zeta = \zeta^*/(\alpha/D^2), \ \psi = \psi^*/(D\alpha), \ \text{where } D = r_0 - r_i.$$

The present problem has seven non-dimensional parameters. They are:

Ra $= \frac{g\beta \Delta \theta D^3}{\nu \alpha}$, the Rayleigh number, Pr $= \frac{\nu}{\alpha}$, the Prandtl number, Har $=$
$B_{0r} D \sqrt{\frac{\sigma}{\rho \nu}}$, Haz $= B_{0z} D \sqrt{\frac{\sigma}{\rho \nu}}$ Hartmann numbers in radial and axial directions,

$A = \frac{H}{D}$, the aspect ratio, $\lambda = \frac{r_o}{r_i}$, the radius ratio, $\varepsilon = \frac{l}{D}$, length of the baffle and $L = \frac{h}{D}$, location of the baffle.

The dimensionless boundary conditions are:

on all rigid walls: $\psi = \frac{\partial \psi}{\partial R} = \frac{\partial \psi}{\partial Z} = 0$;　on the inner wall and baffle: $T = 1$;

on the outer wall: $T = 0$;　on the bottom and top walls: $\frac{\partial T}{\partial Z} = 0$.

The local and global thermal transport rates are respectively, given by $\mathrm{Nu} = -\frac{\partial T}{\partial R}$ and $\overline{\mathrm{Nu}} = \frac{1}{A} \int\limits_{0}^{A} \mathrm{Nu}\, dZ$.

3　Numerical Method

The model Eqs. (1)–(3) are numerically solved using the stable, implicit finite difference methods. The energy and vorticity equations are discretized by time splitting technique, and line over-relaxation method is applied to elliptic type of equation. The system of equations from these finite difference techniques is solved using TDMA algorithm, and Simpson's integration is applied for the evaluation of global Nusselt number. A more information on the methods can be found in our recent papers [24, 25, 30], and for brevity, the same is not provided here.

4　Results and Discussion

This segment illustrates the simulation effects to analyze the combined effects of magnetic field and baffle on flow and temperature patterns, heat transfer in the vertical annulus. Since the main focus is to analyze the impacts of external magnetic field and baffle, the important governing parameters are varied. This investigation involves seven dimensionless parameters, of which only four parameters, namely Rayleigh number (Ra), Hartmann number (Ha), baffle location (L), and baffle length (ε), are varied and remaining three parameters, namely Prandtl number (Pr), aspect ratio (A), and radius ratio (λ) are fixed, respectively, at Pr = 0.054, A = 1, and λ = 2. The range of parameter considered in this analysis is $10^3 \leq \mathrm{Ra} \leq 10^6$, $0 \leq \mathrm{Ha} \leq 100$, 0.25 $\leq$ L $\leq$ 0.75, and 0.125 $\leq \varepsilon \leq$ 0.875. The flow and thermal formation are illustrated in terms of streamlines and isotherms, and the thermal transport is measured through local and average Nusselt numbers.

Figures 2 and 3 illustrate the impact of horizontal and vertical magnetic field on flow fields and thermal distribution for fixed values of Ra = 10^6, ε = 0.25, and L = 0.5. For the case of non-magnetic force, it is noticed that the streamlines move
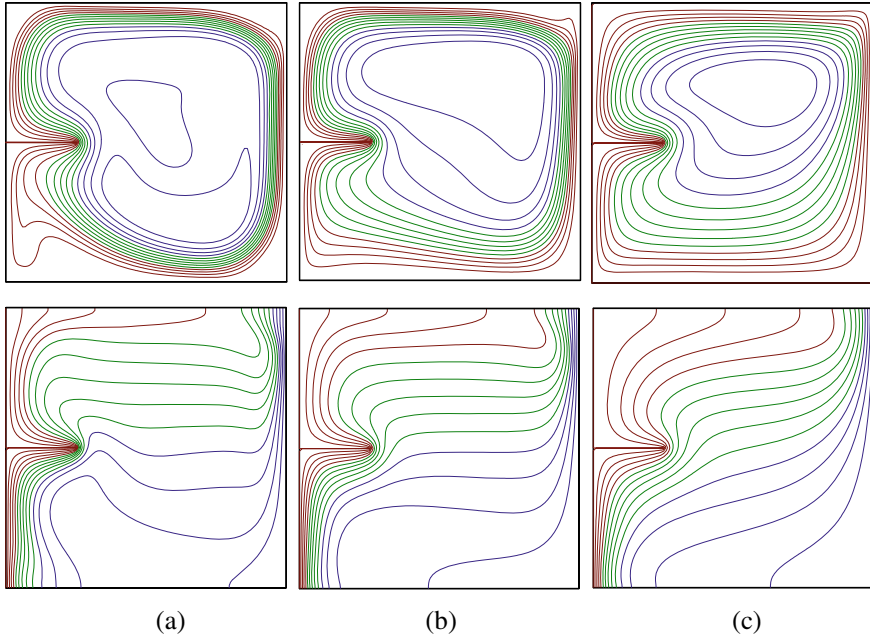
Fig. 2 Flow and thermal distributions for different Har at Ra $= 10^6$, Hax $= 0$, $\varepsilon = 0.25$, L $= 0.5$, **a** Har $= 0$, $|\psi_{\max}| = 16.9$ **b** Har $= 50$, $|\psi_{\max}| = 13.2$ and **c** Har $= 100$, $|\psi_{\max}| = 9.4$

faster due to enhanced convection strength and are packed near the vertical walls. However, as magnetic field is introduced in the lateral direction (Har $= 50$ & 100), the flow movement is drastically declined due to the drag from the magnetic force. The impact of magnetic strength can also be seen from the variation of isotherms. For zero magnetic field strength, the core of the annulus is thermally stratified and this structure is significantly altered by the strong applied magnetic force. As the magnetic force is changed to the axial direction, a drastic change in the flow field is observed with the primary vertex that is elongated vertically as the intensity of magnetic force is increased. The isotherm contours reveal the diagonal variation with magnetic field strength.

Figure 4 depicts the combined effects of baffle length and magnetic force strength on flow and thermal patterns by fixing the values of Rayleigh number (Ra $= 10^6$), baffle position ($L = 0.5$), and the radial Hartmann number (Har $= 100$). It is observed that the baffle length has severe influence on the flow and thermal pattern. An increase in the baffle length leads to bi-cellular flow pattern in the annulus with one vortex below and above the baffle. As regards to the effect of baffle length on the isotherms, the increase of baffle length creates the existence of thermally inactive zones above the baffle. The inclusion of magnetic force causes the slow movement of fluid flow and less distorted isotherms.
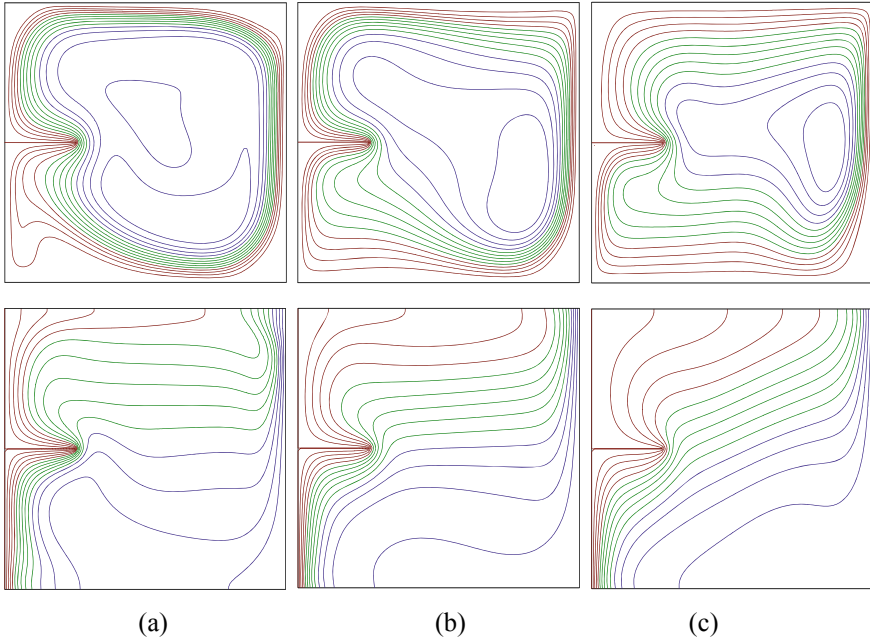
Fig. 3 Flow and thermal distributions for different Hax at Ra $= 10^6$, Har $= 0$, $\varepsilon = 0.25$, L $= 0.5$, **a** Hax $= 0$, $|\psi_{max}| = 16.9$ **b** Hax $= 50$, $|\psi_{max}| = 13.2$ and **c** Hax $= 100$, $|\psi_{max}| = 9.9$

The impact of vertical magnetic force on the flow and thermal fields in the presence of three baffle lengths is exhibited in Fig. 5. On comparing with Fig. 4, the influence of axial magnetic field can be vividly witnessed through streamlines and isotherms. As the axial magnetic field is increased, the streamlines are extended along the axial direction and the isotherms are diagonally elongated. For the maximum baffle length, the portion over the baffle is sparsely filled by the isotherms. From Figs. 4 and 5, it is noted that in the presence of magnetic force in either radial or vertical direction, the maximum stream function increases with the baffle length.

Figures 6 and 7 report the effect of baffle location on contours of streamline and isotherm for the constant values of Ra $= 10^6$, $\varepsilon = 0.25$ with different magnetic forces. In general, the existence of magnetic force reduces the flow intensity as well as temperature stratification in the annulus. Although the flow structure is not disturbed significantly with the baffle location, the flow intensity is reduced as the baffle is shifted near to top adiabatic wall. In a similar way, a small thermally inactive region is observed near the top wall as the baffle is placed near the upper boundary. For the case of vertical magnetic field, the flow direction is changed and the main vortex is elongated vertically as the value of Hax is enhanced.

The combined effects of baffle size and external magnetic field, in radial or axial direction, on local heat transport rate are measured through the local *Nu* along the inner as well as outer cylinders. The variation of local *Nu* alongside the inner and

(a)   (b)   (c)
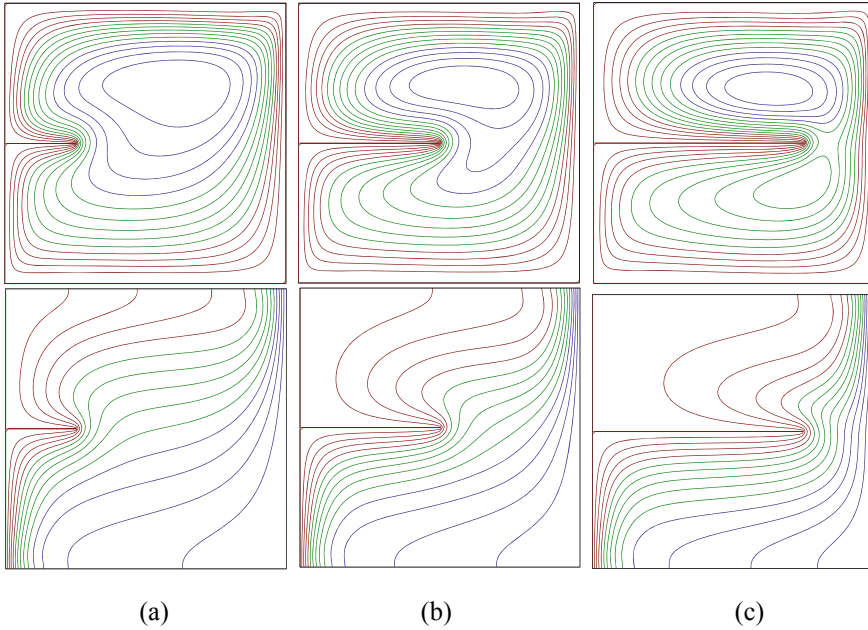
Fig. 4 Flow and thermal distributions for various baffle lengths at Ra $= 10^6$, L $= 0.5$, Har $= 100$, Hax $= 0$, **a** $\varepsilon = 0.25$, $|\psi_{\max}| = 9.0$ **b** $\varepsilon = 0.5$, $|\psi_{\max}| = 10.9$ and **c** $\varepsilon = 0.75$, $|\psi_{\max}| = 11.1$

outer cylinders (Nu$_L$ and Nu$_R$) with and without the magnetic force, for different baffle lengths and baffle positions is shown in Fig. 8. The numerical simulations that are carried out for the baffle lengths varied from $\varepsilon = 0.125$–0.75, and magnetic force Ha $= 100$ is applied in radial and axial directions. It is witnessed that the local heat transport declines below the baffle but increases above the baffle depending on the baffle length. The increase in local heat transfer above the baffle can be anticipated to the additional heat produced from the baffle. A cautious scrutiny of results exposes that the local heat transport rate is greater over and below the baffle for Ha $= 0$ and $\varepsilon = 0.125$. However, as baffle length increases or the magnetic force is introduced, the local heat transport rate decreases.

In any heat transfer analysis, the quantitative interest is the overall thermal transport rate and is estimated by the overall Nusselt number. Figure 9 displays the combined influences of baffle length, Rayleigh, and Hartmann numbers on the global heat transport performance for a fixed baffle position $L = 0.5$. A close scrutiny of results reveals that the overall heat transport rate can be significantly controlled through the Rayleigh number and baffle length. However, the heat transport amount reduces as the Hartmann number increases in either directions. In common, the heat transport is higher for smaller baffle length ($\varepsilon = 0.25$) and lower heat transfer is predicted with larger baffle length ($\varepsilon = 0.75$). Also, the applied magnetic force significantly reduces the heat transport for all baffle lengths.
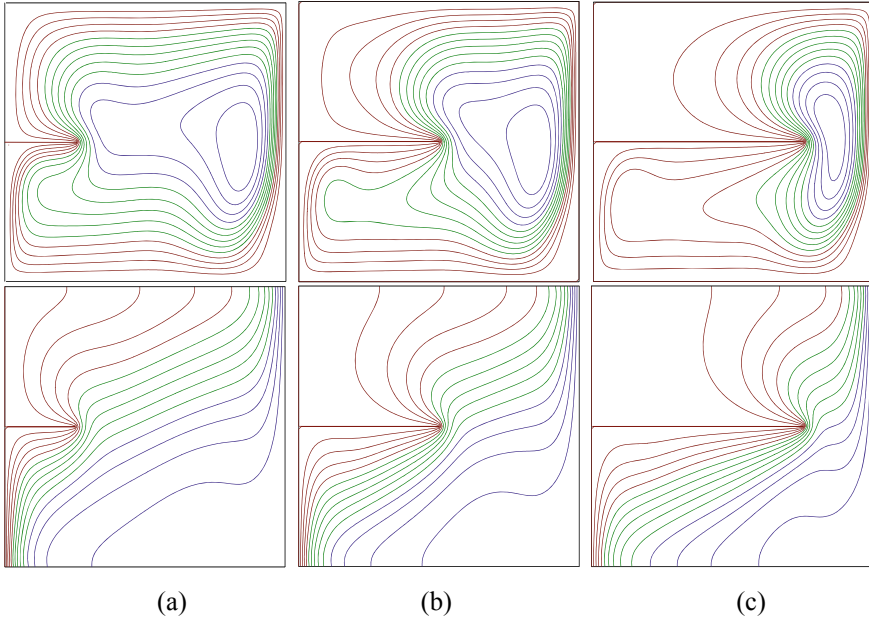
Fig. 5 Flow and thermal distributions for various baffle lengths at Ra $= 10^6$, L $= 0.5$, Har $= 0$, Hax $= 100$, **a** $\varepsilon = 0.25$, $|\psi_{\max}| = 9.4$ **b** $\varepsilon = 0.5$, $|\psi_{\max}| = 10.5$ and **c** $\varepsilon = 0.75$, $|\psi_{\max}| = 12.3$

The location of baffle on the heat transport rate is very interesting and is presented in Fig. 10 for different Rayleigh number and magnetic field strengths by fixing the baffle length at $\varepsilon = 0.25$. It is found that the heat transport rate enhances with the Rayleigh number and baffle location, but heat transfer declines as Ha value is increased.

5 Conclusions

The objective of the present analysis is to investigate the convective heat transport in an annular geometry with magnetic field and baffle. From the extensive numerical simulations, it has been observed that the addition of baffle and magnetic force plays a major role in declination of heat transfer rate. It is observed that the baffle length increases flow circulation rate, while decreases the heat transfer rate. Based on these observations, we conclude that it is possible to increase or decrease the flow intensity with the help of a baffle fixed to the annular wall.
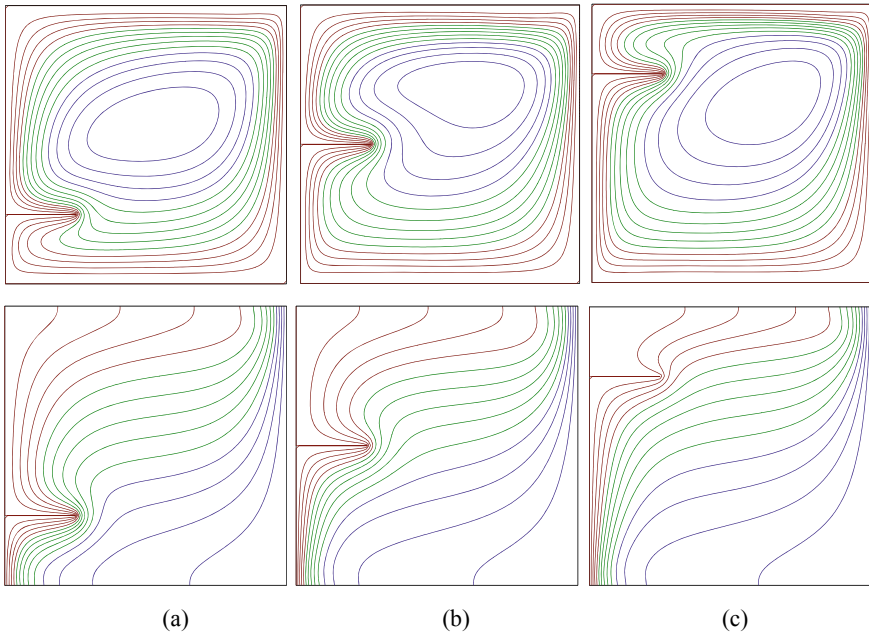
Fig. 6 Effect of baffle position on streamlines and isotherms for $Ra = 10^6$, $\varepsilon = 0.25$, $Har = 100$, $Hax = 0$, **a** $L = 0.25$, $|\psi_{max}| = 10.0$ **b** $L = 0.5$, $|\psi_{max}| = 9.4$ and **c** $L = 0.75$, $|\psi_{max}| = 8.5$
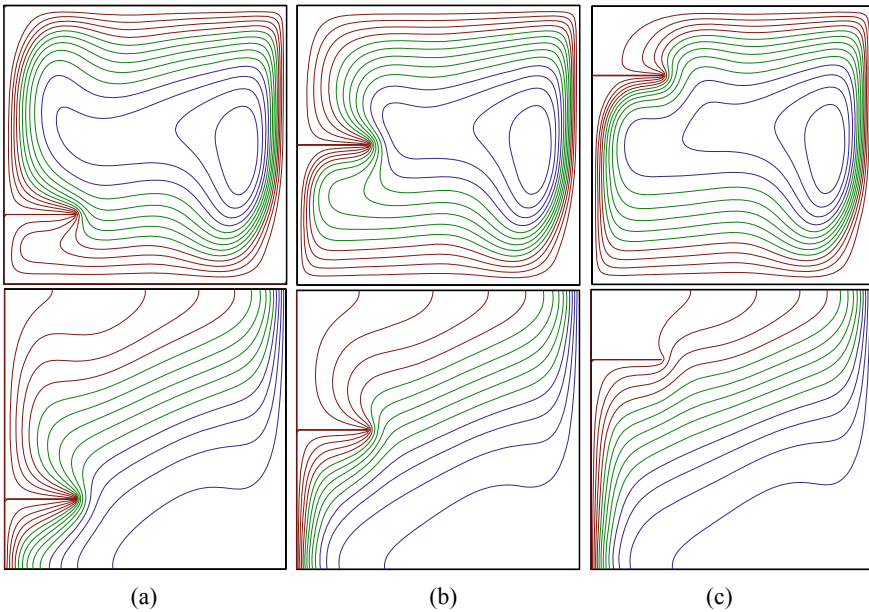
Fig. 7 Flow and thermal distributions for various baffle positions at $Ra = 10^6$, $\varepsilon = 0.25$, $Har = 0$, $Hax = 100$, **a** $L = 0.25$, $|\psi_{max}| = 10.0$ **b** $L = 0.5$, $|\psi_{max}| = 9.9$ and **c** $L = 0.75$, $|\psi_{max}| = 9.8$
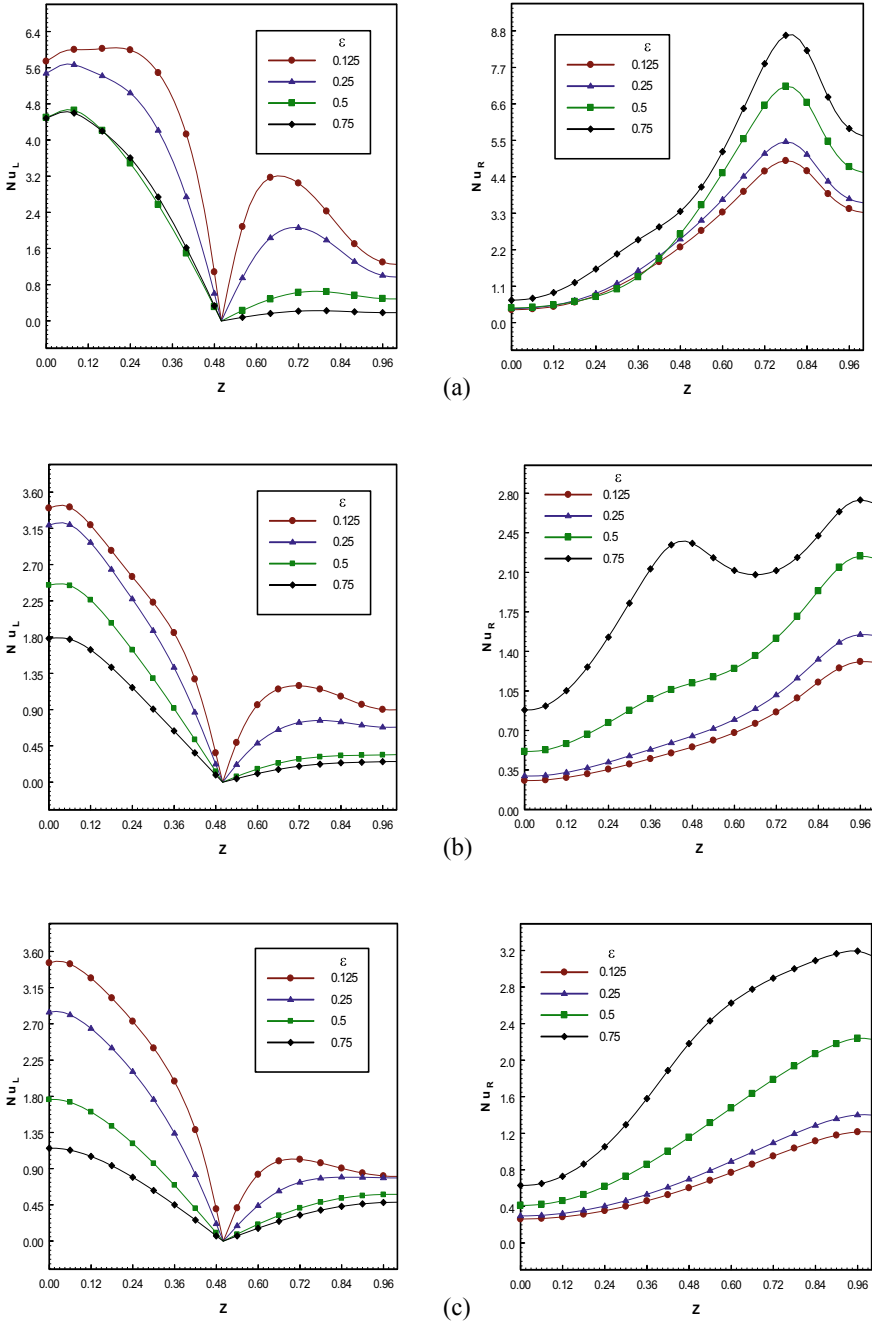
Fig. 8 Distribution of Nu alongside inner and outer cylinders for various baffle lengths at Ra = 10^5, L = 0.5, **a** Har = 0 = Hax, **b** Har = 100, Hax = 0 and **c** Har = 0, Hax = 100

(a) Har = 0, Hax = 0

(b) Har = 100, Hax = 0.

(c) Har = 0, Hax = 100
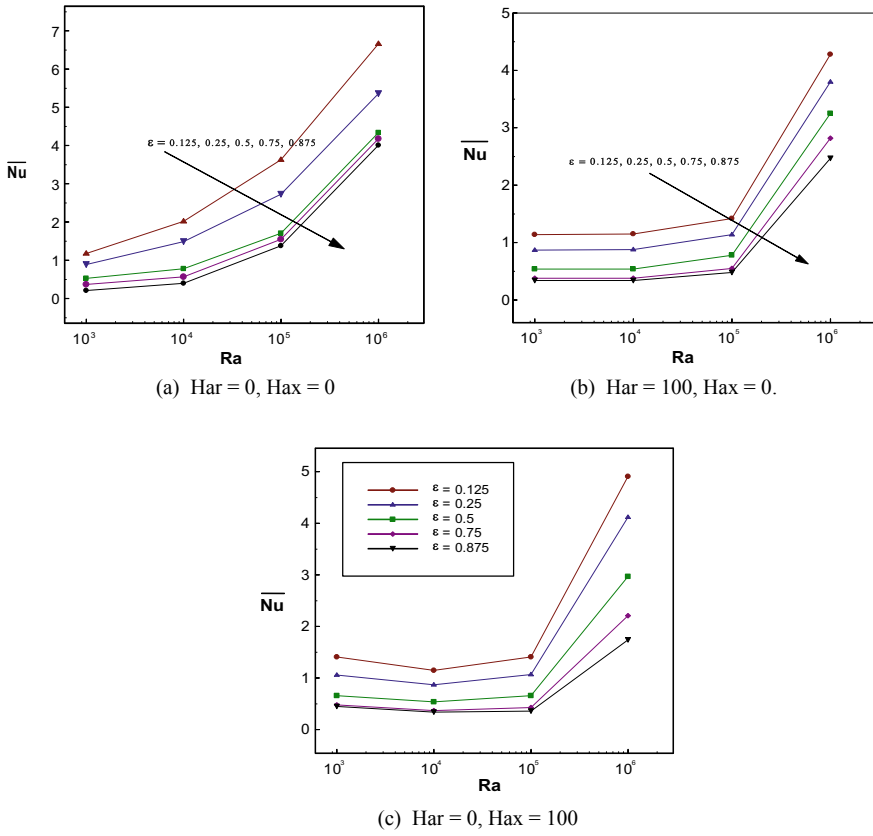
Fig. 9 Effect of baffle length on overall thermal transport rates for various Rayleigh numbers and Hartmann numbers at L = 0.5

(a) Har = 0, Hax = 0

(b) Har = 100, Hax = 0.

(c) Har = 0, Hax = 100.
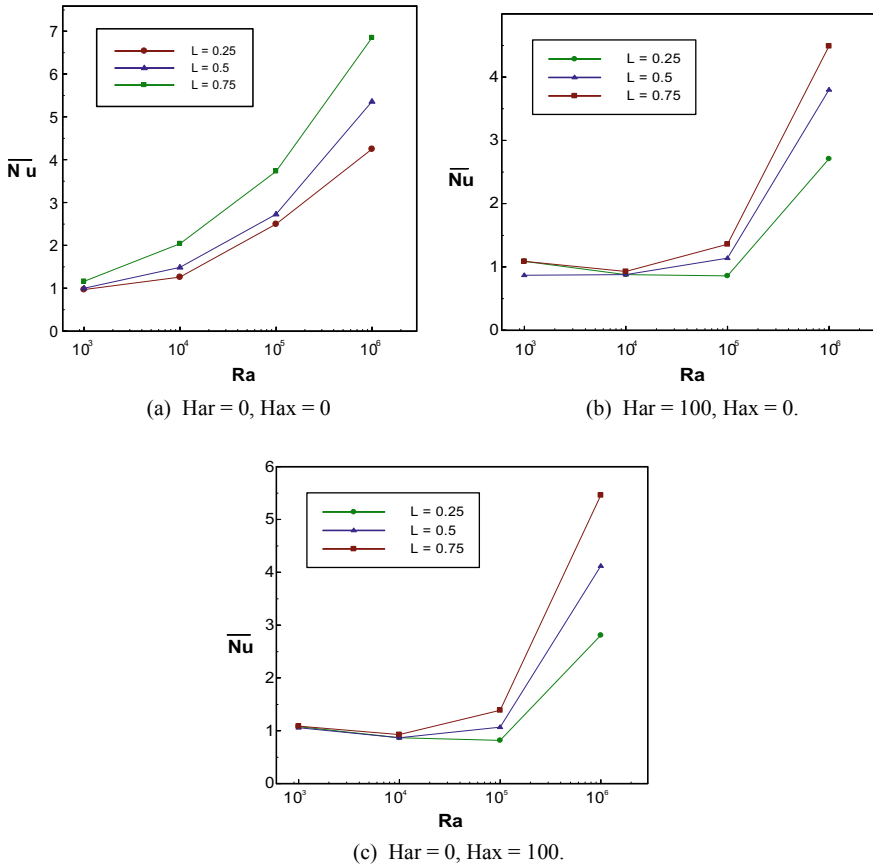
Fig. 10 Baffle location versus global Nusselt number for different Ra and Ha at $\varepsilon = 0.25$

References

1. Sankar M, Do Y, Ryu S, Bongsoo J (2015) Cooling of heat sources by natural convection heat transfer in a vertical annulus: numerical heat transfer. Part A: Appl 68(8):847–869. https://doi.org/10.1080/10407782.2015.1023097
2. Sankar M, Kemparaju S, Prasanna BMR, Eswaramoorthi S (2018) Buoyant convection in porous annulus with discrete sources-sink pairs and internal heat generation. IOP Conf Ser J Phys Conf Ser 1139. https://doi.org/10.1088/1742-6596/1139/1/012026
3. Girish N, Makinde OD, Sankar M (2018) Numerical investigation of developing natural convection in vertical double-passage porous annuli. Defect Diffus Forum 387:442–460

4. Sankar M, Venkatachalappa M, Shivakumara IS (2006) Effect of magnetic field on natural convection in a vertical cylindrical annulus. Int J Eng Sci 44:1556–1570
5. Wrobel W, Fornalik-wajs E, Szmyd JS (2010) Experimental and numerical analysis of thermo-magnetic convection in a vertical annular enclosure. Int J Heat Fluid Flow 31:1019–1031
6. Venkatachalappa M, Do Y, Sankar M (2011) Effect of magnetic field on the heat and mass transfer in a vertical annulus. Int J Eng Sci 49:262–278
7. Sankar M, Venkatachalappa M, Do Y (2011) Effect of magnetic field on the buoyancy and thermocapillary driven convection of an electrically conducting fluid in an annular enclosure. Int J Heat Fluid Flow 32:402–412
8. Kakarantzas C, Sarris IE, Vlachos NS (2011) Natural convection of liquid metal in a vertical annulus with lateral and volumetric heating in the presence of horizontal magnetic field. Int J Heat Mass Transf 54:3347–3356
9. Afrand M, Rostami S, Akbari M, Wongwishes S, Esfe MH, Karimipour A (2015) Effect of magnetic field on magneto-convection in a vertical cylindrical annulus filled with liquid potassium. Int J Heat Mass Transf 90:418–426
10. Afrand M, Farahat S, Nezhad AH, Sheikhzadeh GA, Sarhaddi F, Wongwises S (2015) Multi-objective optimization of natural convection in a cylindrical annulus mold under magnetic field using particle swarm algorithm. Int Commun Heat Mass Transf 60:13–20
11. Malvandi A (2016) Anisotropic behaviour of magnetic nanofluids at film boiling over a vertical cylinder in the presence of a uniform variable—directional magnetic field. Powder Technol 294:307–314
12. Oreper GM, Szekely J (1983) The effect of an externally imposed magnetic field on buoyancy driven flow in a rectangular cavity. J Cryst Growth 64:505–515
13. Venkatachalappa M, Subbaraya CK (1993) Natural convection in a rectangular enclosure in the presence of magnetic field with uniform heat flux from the side walls. Acta Mech 96:13–26
14. Rudraiah N, Barron RM, Venkatachalappa M, Subbaraya CK (1995) Effect of magnetic field on free convection in a rectangular enclosure. Int J Eng Sci 33:1075–1084
15. Sellers CC, Walker JS (1999) Liquid-metal flow in an electrically insulated rectangular duct with a nonuniform magnetic field. Int J Eng Sci 37:541–552
16. Parvin S, Nasrin R (2011) Analysis of the flow and heat transfer characteristics for MHD free convection in an enclosure with a heated obstacle. Nonlinear Anal Model Control 16:89–99
17. Sathiyamoorthy M, Chamkha AJ (2012) Natural convection flow under magnetic field in a square cavity for uniform or linearly heated adjacent walls. Int J Numer Methods Heat Fluid Flow 22:677–698
18. Hasanuzzaman M, Oztop HF, Rahman MM, Rahim NA, Saidur R, Varol Y (2012) Magnetohydrodynamic natural convection in trapezoidal cavities. Int Commun Heat Mass Transf 39:1384–1394
19. Turk O, Tezer-Sezgin M (2013) FEM solution of natural convection in square enclosure under magnetic field. Int J Numer Meth Heat Fluid Flow 23:844–866
20. Ganji DD, Malvandi A (2014) Natural convection of nanofluids inside a vertical enclosure in the presence of a uniform magnetic field. Powder Technol 263:50–57
21. Basant KJ, Aina B, Isa S (2016) MHD natural convection flow in a vertical micro-concentric-annuli in the presence of radial magnetic field: an exact solution. Ain Shams Eng J 7:1061–1068
22. Mahmoudi A, Mejri I, Omri A (2016) study of natural convection in a square cavity filled with nanofluids and subjected to a magnetic field. Int J Heat Technol 34:73–79
23. Shi X, Khodadadi JM (2003) Laminar natural convection heat transfer in differentially heated square cavity due to a thin fin on the hot wall. J Heat Transf 125:624–634
24. Sankar M, Pushpa BV, Prasanna BMR, Do Y (2016) Influence of size and location of a thin baffle on natural convection in a vertical annular enclosure. J Appl Fluid Mechan 9:2671–2684
25. Pushpa BV, Prasanna BMR, Do Y, Sankar M (2017) Numerical study of double-diffusive convection in a vertical annular enclosure with a baffle. IOP Conf Ser J Phys Conf Ser 908:012081 https://doi.org/10.1088/1742-6596/908/1/012081
26. Sivasankaran S, Lee J, Bhuvaneswari M (2011) Effect of a partition on hydro-magnetic convection in an enclosure. Arab J Sci Eng 36(7):1393–1406

27. Bhuvaneswari M, Sivasankaran S, Kim YJ (2011) Magnetoconvection in a square enclosure with sinusoidal temperature distributions on both side walls. Numer Heat Transf Part A: Appl 59(3):167–184
28. Sivasankaran S, Malleswaran A, Lee J, Sundar P (2011) Hydro-magnetic combined convection in a lid-driven cavity with sinusoidal boundary conditions on both sidewalls. Int J Heat Mass Transf 54(1–3):512–525
29. Rashad AM, Sivasankaran S, Mansour MA, Bhuvaneswari M (2017) Magneto-convection of nanofluids in a lid-driven trapezoidal cavity with internal heat generation and discrete heating. Numer Heat Transf Part A: Appl 71(12):1223–1234
30. Sankar M, Kiran S, Do Y (2018) Effect of nonuniform heating on natural convection in a vertical porous annulus. In: Narayanan N, Mohanadhas B, Mangottiri V (eds) Flow and transport in subsurface environment, springer transactions in civil and environmental engineering. Springer, Singapore

Study of Rayleigh-Bénard Convection of a Newtonian Nanoliquid in a Porous Medium Using General Boundary Conditions

P. G. Siddheshwar and T. N. Sakshath

Abstract In the paper we make a linear stability analysis of Rayleigh-Bénard convection (RBC) in a Newtonian, nanoliquid-saturated porous medium. Single-phase model is used for nanoliquid description and values of thermophysical quantities concerning ethylene glycol-copper and the saturated porous medium it occupies are calculated using mixture theory or phenomenological relations. The study is carried out using general boundary conditions on the velocity and temperature. The Galerkin method is used to obtain the critical eigen value. The results of free-free, rigid-free and rigid-rigid isothermal/adiabatic boundaries are obtained from the present study by considering appropriate limits. The results of the limiting cases of the present study are in excellent agreement with those observed in earlier investigations. This problem is an integrated approach to studying Rayleigh-Bénard convection covering 34 different boundary combinations.

Keywords Nanoliquid · Rayleigh-Bénard convection · Porous medium · Linear stability · Single-phase

Nomenclature

α	Thermal diffusivity of the nanoliquid in saturated porous medium
α_1	Thermal diffusivity of the base liquid in saturated porous medium
α_s	Slip coefficient
β	Thermal expansion coefficient of the nanoliquid in saturated porous medium

P. G. Siddheshwar (✉) · T. N. Sakshath
Department of Mathematics, Jnana Bharathi Campus, Bangalore University,
Bengaluru 560056, India
e-mail: mathdrpgs@gmail.com

T. N. Sakshath
e-mail: sakshath.tn@gmail.com

β_1	Thermal expansion coefficient of the base liquid in saturated porous medium
χ	Nanoparticle volume fraction
ΔT	Temperature difference
Λ	Brinkman number or ratio of viscosities
μ	Viscosity of the nanoliquid
μ'	Viscosity of the nanoliquid in saturated porous medium
ν	Wave number
ω	Angular frequency
ϕ	Porosity
Ψ	Non-dimensional stream function
ψ	Dimensional stream function
ρ	Density of the nanoliquid in saturated porous medium
σ^2	Porous parameter
Θ	Non-dimensional temperature
A, B	Amplitudes of convection
Bi_l	Biot number at the lower plate
Bi_u	Biot number at the upper plate
C_p	Specific heat capacity of the nanoliquid in saturated porous medium at constant pressure
d	Channel depth
Da_{sl}	Slip Darcy number at the lower plate
Da_{su}	Slip Darcy number at the upper plate
F	Free boundary
$g = (0, 0, -g)$	Acceleration due to gravity
H_c	Heat transfer coefficient
I	Isothermal boundary
K	Permeability of the porous medium
k	Thermal conductivity of the nanoliquid in saturated porous medium
k_1	Thermal conductivity of the base liquid in saturated porous medium
k_l	Thermal conductivity of the base liquid
k_{nl}	Thermal conductivity of the nanoliquid
k_{np}	Thermal conductivity of the nanoparticle
M	Ratio of specific heats
p	Pressure
Pr	Prandtl number
$q = (u, 0, w)$	Velocity vector
R	Rigid boundary
Ra	Rayleigh number of the nanoliquid in saturated porous medium
T	Dimensional temperature
T_0	Reference temperature
u, w	Horizontal and vertical velocity components
x, X	Dimensional and non-dimensional horizontal coordinates

z, Z	Dimensional and non-dimensional vertical coordinates
h	Distance between the plates
0	At reference value
1	Liquid property in saturated porous medium
b	Basic state
c	Critical
l	Base liquid
nl	Nanoliquid
np	Nanoparticle
s	Solid
′	Perturbed quantity

1 Introduction

The study of convection in a porous medium has received significant attention and has many practical applications. This is due to the fact that numerous engineering and biological applications [1] concern heat energy containment or removal. Since the combination of both nanoparticles and porous medium can be used to regulate the residence time of heat in the system the convection of nanoliquids in a porous medium is of utmost importance.

In literature, we come across many works that consider only a single boundary combination (see Table 1). However, with the availability of many sophisticated mathematical tools it is now possible to unify all existing boundary combinations into a single problem and the paper emphasizes on this fact. Such a very general study encompasses the results of all the boundary combinations on velocity and temperature. In the present problem the convection of nanoliquids in a porous medium has been studied using general boundary conditions with respect to velocity and

Table 1 Works considering single boundary condition

Boundary considered	Author (year, Journal)
FIFI	Vadasz (1998, J. Fluid Mech.)
	N. Rudraiah, P. G. Siddheshwar (1998, Heat Mass Trans.)
	M. S. Malashetty and D. Basavaraja (2002, Heat Mass Trans.)
	R. K. Vanishree and P. G .Siddheshwar (2010, Transp. Porous Med.)
	B. S. Bhadauria and S. Agarwal (2011, Transp. Porous Med.)
	R. Chand and G. C. Rana (2012, Int. J. Heat Mass Trans.)
RIRI	J. K. Bhattacharjeee (1988, Phys. Fluids)
	A. R. Lopez et al. (1990, Phys. Fluids)
	T. Desaive et al. (2002, Eur. Phys. J. B.)

$$\boxed{h \ll L}$$

$$z = \frac{h}{2} + L$$

$$z = \frac{h}{2}$$

$$z = -\frac{h}{2}$$

z

y

g

T_0

x

$T_0 + \Delta T$

$$z = -\left(\frac{h}{2} + L\right)$$
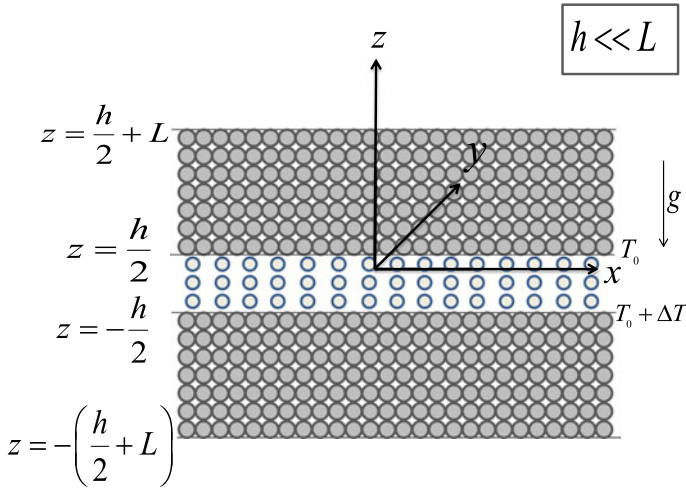
Fig. 1 Schematic representation of the flow configuration

temperature where the boundary conditions on velocity are derived from the Beavers and Joseph slip condition [2]. A summarized, clear cut view of historical background of Beavers-Joseph (BJ) boundary condition is reported by Nield [3]. The convective instability of a ferromagnetic fluid in a Rayleigh-Bénard situation using the general boundary condition on velocity was first studied by Siddheshwar [4].

Studies on Brinkman-Bénard convection can serve as a bridge between the clear fluid case and low-porosity medium. This is apart from its yielding results on a high-porosity medium. Each of these above 3 problems involve many different boundary combinations, namely,

  (i) Brinkman-Bénard convection with 16 boundary combinations (see Fig. 1),
 (ii) Darcy-Bénard convection with 2 boundary combinations (see Fig. 2) and
(iii) Rayleigh-Bénard convection with 16 boundary combinations.

Most reported studies on convection in porous media do not consider thermo-physical values and are thus not very general in their conclusion. With abundant data now being available on the values of thermophysical quantities, the predictions on convection can be made more specific. The objective of the paper is to investigate the following aspects in the current problem:

  (i) Studying onset of RBC in nanoliquid-saturated porous medium using general boundary conditions,
 (ii) Obtaining the results on RBC of Newtonian base liquids as a limiting case,
(iii) Arriving at the results pertaining to 34 different boundary combinations as limiting cases,
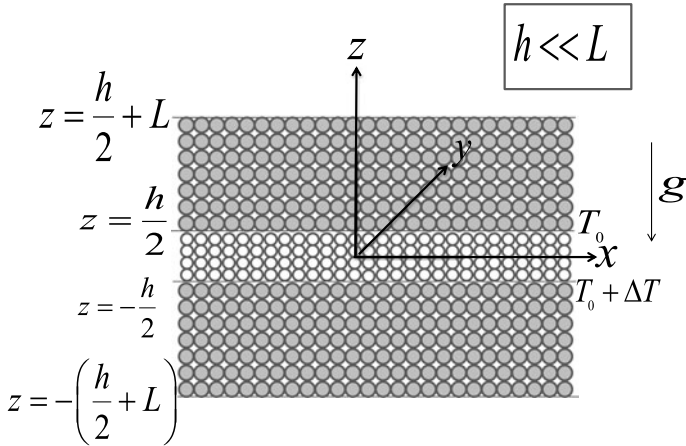
Fig. 2 Schematic representation of the Darcy-Bénard configuration

(iv) Regulating the residence time of heat in the system using nanoparticles and porous matrix and

(v) Make predictions on onset of convection for specific fluids and specific porous medium.

2 Mathematical Formulation

The schematic of the flow configuration is as shown in Fig. 1.

The dimensionless form of the governing equations for the problem are:

$$\frac{1}{\Pr}\frac{\partial}{\partial \tau}(\nabla^2 \Psi) = a_1 \Lambda \nabla^4 \Psi - a_1 \sigma^2 (\nabla^2 \Psi) - a_1^2 Ra \frac{\partial \Theta}{\partial X}, \tag{1}$$

$$M\frac{\partial \Theta}{\partial \tau} = -\frac{\partial \Psi}{\partial X} + a_1 M \nabla^2 \Theta + \frac{\partial(\Psi, \Theta)}{\partial(X, Z)}, \tag{2}$$

where

$$\Pr = \frac{\mu}{\rho \alpha}, \ a_1 = \frac{\alpha}{\alpha_1}, \ \alpha = \frac{\phi k_{nl} + (1 - \phi)k_s}{(\rho C_p)}, \ \Lambda = \frac{\mu'}{\mu}, \ \sigma^2 = \frac{h^2}{K} \text{ and } Ra = \frac{(\rho \beta)h^3 g \Delta T}{\mu \alpha}.$$

We now carry out the linear stability analysis and study the onset of convection.

3 Linear Theory

In order to make a linear stability analysis, we consider the linear and steady-state version of Eqs. (1) and (2). The general boundary conditions suitable for the study are:

$$\left. \begin{aligned}
\Psi = D^2\Psi - Da_{sl}D\Psi = D\Theta - Bi_l\Theta = 0 \ \text{ at } Z = -\frac{1}{2}, \\
\Psi = D^2\Psi + Da_{su}D\Psi = D\Theta + Bi_u\Theta = 0 \ \text{ at } Z = \frac{1}{2}.
\end{aligned} \right\}. \tag{3}$$

where $Da_s = \dfrac{\alpha_s d}{\sqrt{K}}$ (slip Darcy number), $Bi = \dfrac{H_c d}{\sqrt{K}}$ (Biot number).

The eigen solutions of the Eqs. (1) and (2) are:

$$(\Psi(X, Z, \tau), \Theta(X, Z, \tau)) = (A \sin(\nu X) F(Z), B \cos(\nu X) G(Z)) \, e^{i\omega\tau} \tag{4}$$

where A and B are amplitudes of the stream function and temperature respectively and ν is the wave number. Substituting (4) in the linearised version of Eqs. (1) and (2) and following the orthogonalisation procedure, we get

$$\left[\frac{i\omega}{Pr}(I_2 - \nu^2 I_1) + a_1 G\Lambda + a_1\sigma^2(I_2 - \nu^2 I_1)\right] A - a_1^2\nu \, Ra I_4 B = 0, \tag{5}$$

$$\nu I_4 A + \left[Mi\omega I_5 - a_1 M(I_6 - \nu^2 I_5)\right] B = 0, \tag{6}$$

where

$$\left. \begin{aligned}
I_1 = \langle F(Z)^2 \rangle, \ I_2 = \langle F(Z) \, D^2 F(Z) \rangle, \ I_3 = \langle F(Z) \, D^4 F(Z) \rangle, \\
I_4 = \langle F(Z) \, G(Z) \rangle, \ I_5 = \langle G(Z)^2 \rangle, \ I_6 = \langle G(Z) \, D^2 G(Z) \rangle.
\end{aligned} \right\}. \tag{7}$$

All the quantities within angular brackets in Eq. (7) are definite integrals with respect to Z in $\left[-\frac{1}{2}, \frac{1}{2}\right]$. For a non-trivial solution to A and B, we require

$$\begin{vmatrix}
\dfrac{i\omega}{Pr}(I_2 - \nu^2 I_1) + a_1 U\Lambda + a_1\sigma^2(I_2 - \nu^2 I_1) & -a_1^2\nu \, Ra I_4 \\
\nu I_4 & \begin{aligned} Mi\omega I_5 - a_1 \\ M(I_6 - \nu^2 I_5) \end{aligned}
\end{vmatrix} = 0.$$

This gives us the expression of the critical value of nanoliquid Rayleigh number as:

$$Ra = \frac{M\left[a_1^2 Pr\left(I_6 - I_5\nu^2\right)\left(U\Lambda + \sigma^2\left(I_2 - I_1\nu^2\right)\right) - I_5\omega^2\left(I_1\nu^2 - I_2\right)\right]}{a_1^2 I_4^2 \nu^2 \, Pr} \tag{8}$$

$$+ i\omega N,$$

where $U = \left(-I_1 v^4 + 2I_2 v^2 - I_3\right)$,

$$N = \frac{M}{a_1 I_4^2 v^2 \, \mathrm{Pr}} \left[I_1 v^2 \left(I_5 \left(v^2 \Lambda \mathrm{Pr} + \mathrm{Pr}\sigma^2 + v^2\right) - I_6\right) \right. \\ \left. + I_2 \left(I_6 - I_5 \left(2v^2 \Lambda \mathrm{Pr} + \mathrm{Pr}\sigma^2 + v^2\right)\right) + I_3 I_5 \Lambda \mathrm{Pr} \right]. \tag{9}$$

Following Galerkin procedure, we choose $F(Z)$ and $G(Z)$ (See Appendix) in the form

$$F(Z) = Z^4 + \frac{4(\mathrm{Da}_{su} - 2\mathrm{Da}_{sl})Z^3 - (\mathrm{Da}_{sl} + 6)(\mathrm{Da}_{su} + 6)Z^2}{2\mathrm{Da}_{sl}(\mathrm{Da}_{su} + 4) + 8(\mathrm{Da}_{su} + 3)} \\ + \frac{8(\mathrm{Da}_{sl} - \mathrm{Da}_{su})Z + [\mathrm{Da}_{sl}(\mathrm{Da}_{su} + 8) + 8\mathrm{Da}_{su} + 60]}{16\mathrm{Da}_{sl}(\mathrm{Da}_{su} + 4) + 64(\mathrm{Da}_{su} + 3)}, \tag{10}$$

$$G(Z) = Z^4 - Z^2 \\ \left(\frac{16d_2 \mathrm{Bi}_l \mathrm{Bi}_u + 16d_2 \mathrm{Bi}_l + 16d_2 \mathrm{Bi}_u + \mathrm{Bi}_l \mathrm{Bi}_u + 5\mathrm{Bi}_l + 5\mathrm{Bi}_u + 16}{4 \left(\mathrm{Bi}_l \mathrm{Bi}_u + 3\mathrm{Bi}_l + 3\mathrm{Bi}_u + 8\right)} \right) \\ - Z \left(\frac{\mathrm{Bi}_l - \mathrm{Bi}_u - 16d_2 \mathrm{Bi}_l + 16d_2 \mathrm{Bi}_u}{4 \left(\mathrm{Bi}_l \mathrm{Bi}_u + 3\mathrm{Bi}_l + 3\mathrm{Bi}_u + 8\right)} \right) + d_2 \tag{11}$$

Since Ra is a physical quantity, imaginary part of Eq. (8) needs to be zero. Using Eqs. (10) and (11) in Eq. (9), we found on computation that for all parameters' combination $N \neq 0$ and so ω must be zero. Hence we conclude that oscillatory convection is not possible.

4 Results and Discussion

The study of Brinkman-Bénard convection is carried out by considering general boundary conditions on velocity and Robin boundary condition with respect to temperature. Figure 3 demonstrates the fact that the boundary effect on onset of convection is classical.

Fig. 3 Plot of Ra_c, versus Da_{sl} for different values of Da_{su}, for $\Lambda = 1.2$ and $\sigma^2 = 5$, $\mathrm{Bi}_l = 0$ and $\mathrm{Bi}_u = 0$
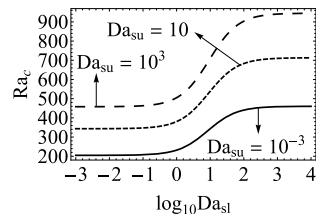
Fig. 4 Plot of Ra_c, versus Da_{sl} for different values of Λ, for $\sigma^2 = 5$, $Da_{su} = 10^{-3}$, $Bi_l = 0$ and $Bi_u = 0$
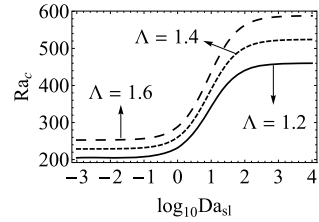
Fig. 5 Plot of Ra_c, versus Da_{sl} for different values of σ^2, for $\Lambda = 1.2$, $Da_{su} = 10^{-3}$, $Bi_l = 0$ and $Bi_u = 0$
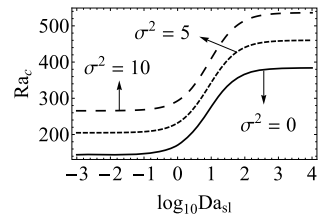
Fig. 6 Plot of Ra_c versus Bi_l for different values of Bi_u, for $\Lambda = 1.2$, $\sigma^2 = 5$, $Da_{sl} = 0$ and $Da_{su} = 0$
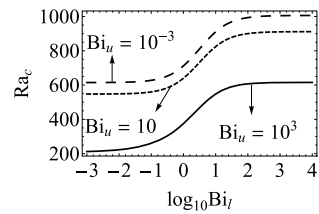
The results pertaining to permeable boundaries can be obtained by considering the limits in between those of free-free and rigid-rigid boundaries. Thus from the linear theory we obtain the following result for Ra_c: $Ra_c^{RIRI} > Ra_c^{RARI} = Ra_c^{RIRA} > Ra_c^{RIFI} = Ra_c^{FIRI} > Ra_c^{RAFI} = Ra_c^{FIRA} > Ra_c^{RARA} > Ra_c^{RIFA} = Ra_c^{FARI} > Ra_c^{FIFI} > Ra_c^{FAFI} = Ra_c^{FIFA} > Ra_c^{RAFA} = Ra_c^{FARA} > Ra_c^{FAFA}$.

From Figs. 4 and 5 it is apparent that the critical value of effective Rayleigh number increases with increase in both Λ and σ^2. Increase in the value of both Λ and σ^2 leads to decrease in value of permeability (or porosity) and hence less space is available for the nanoliquid to flow. Hence this results in delayed onset.

The results pertaining to isothermal and adiabatic boundaries are well observed in Fig. 6 by considering larger values of Bi_l, Bi_u and smaller values of Bi_l, Bi_u respectively. We can also conclude that onset of convection is delayed in isothermal boundaries than in adiabatic boundaries.

Figures 7 and 8 show similar results as in the cases explained for plots considering Ra_c versus Da_{sl}.

Table 2 reveals that different boundary combinations can be obtained from the present problem by considering appropriate limits. In the current problem, the values

Fig. 7 Plot of Ra_c versus Bi_l for different values of Λ, for $\sigma^2 = 5$, $Bi_u = 10^{-3}$, $Da_{sl} = 0$ and $Da_{su} = 0$
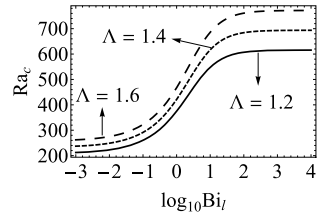
Fig. 8 Plot of Ra_c versus Bi_l for different values of σ^2, for $\Lambda = 1.2$, $Bi_u = 10^{-3}$, $Da_{sl} = 0$ and $Da_{su} = 0$
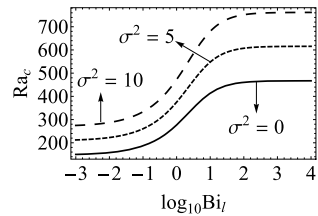
of Da_{sl}, Da_{su}, Bi_l and Bi_u are considered as 10^3 for ∞ and 10^{-3} for 0. We also observe that 16 different problems are obtained in the case of sandwiched porous medium. Likewise, we can also obtain 16 different problems in case of clear fluid layer by considering $\Lambda = 1$, $\sigma^2 = 0$, $M = 1$ and $a_1 = 1$.

Table 3 demonstrates the fact that our results with general boundary conditions compare well with those of earlier works. The comparison of critical value of Rayleigh number and wave number has been made for the limiting case $M = 1$; $\Lambda = 1$ and $\sigma^2 = 0$. We observe that the values obtained are well within the expected range when compared with Platten and Legros [5] and Siddheshwar et al. [6]. The methodology used by Platten and Legros [5] is local potential theory and that used by Siddheshwar et al. [6] is a higher-order Galerkin procedure. Even though lower order Galerkin method is used for the present study, the results obtained are accurate enough when compared with those obtained by earlier works. Although there is a maximum percentage error of 5.74, it can be further decreased by considering more terms in the Galerkin approximation (Table 4).

Table 5 compares the values of Ra_c and ν_c obtained from the present study by the Galerkin technique with that obtained by the shooting method. Good agreement is found between the two.

The thermophysical properties of ethylene-glycol [7] as the base liquid, copper [7] as the nanoparticle and 30% glass fiber reinforced polycarbonate porous material [8] are considered. The thermophysical properties of ethylene-glycol copper saturated porous medium is calculated and the same is tabulated in Table 4.

Table 2 Limits of Da_{sl}, Da_{su}, Bi_l and Bi_u for different boundary combinations

Boundary combinations	FIFI	RIRI	RIFI (FIRI)	FAFA	RARA
Limits of $(Da_{sl}, Da_{su}, Bi_l, Bi_u)$	$(0,0, \infty, \infty)$	$(\infty, \infty, \infty, \infty)$	$(\infty, 0, \infty, \infty)$	$(0, 0, 0, 0)$	$(\infty, \infty, 0, 0)$
Boundary combinations	RAFA	FAFI	RARI	RAFI	RIFA
	(FARA)	(FIFA)	(RIRA)	(FIRA)	(FARI)
Limits of $(Da_{sl}, Da_{su}, Bi_l, Bi_u)$	$(\infty, 0, 0, 0)$	$(0, 0, 0, \infty)$	$(\infty, \infty, 0, \infty)$	$(\infty, 0, 0, \infty)$	$(\infty, 0, \infty, 0)$

5 Conclusion

(a) The numerical study is carried out for general boundary conditions using the single-term Galerkin technique. Maximum error in the eigen value is a little over 5%.

(b) Results in the case of 34 different boundary combinations are obtained as limiting cases of the present problem:

   (i) 16 problems in the case of sandwiched porous media.
   (ii) 16 problems in the case of sandwiched clear fluid layer.
   (ii) 2 problems in the case of Darcy-Bénard configuration.

(c) The effect of increasing Λ and/or σ^2 on the onset of convection is to stabilize the system.

(d) Rather than solving an individual problem one can think of considering an integrated problem involving all limiting cases.

(e) $Ra_c^{EG+Cu+GF} < Ra_c^{EG+GF}$, $Ra_c^{EG+Cu} < Ra_c^{EG}$, $Ra_c^{EG} < Ra_c^{EG+GF}$, (EG: Ethylene glycol, Cu: Copper, GF: 30% glass fiber reinforced polycarbonate).

6 Appendix

The eigen functions F(Z) and G(Z) of the boundary value problem

$$\left[a_1 \Lambda \left(\frac{d^2}{dZ^2} - v^2 \right)^2 - a_1 \sigma^2 \left(\frac{d^2}{dZ^2} - v^2 \right) \right] F(Z) + a_1^2 v \, Ra \, G(Z) = 0 \quad (12)$$

$$- v F(Z) + a_1 M \left(\frac{d^2}{dZ^2} - v^2 \right) G(Z) = 0 \quad (13)$$

Table 3 Comparison of Ra_c and v_c obtained from the present study with those obtained by earlier works and shooting method for the limiting case $M = 1$, $\Lambda = 1$ and $\sigma^2 = 0$

BCs	Platten and Legros [5]		Siddheshwar et al. [6]		Shooting method		d_2 chosen	Present study		% error in	
	Ra_c	v_c	Ra_c	v_c	Ra_c	v_c		Ra_c	v_c	Ra_c	v_c
1. FIFI	657.511	2.22	657.592	2.22157	657.53354	2.21	0.28684	657.983	2.22212	0.07179	0.0955
2. RIRI	1707.762	3.12	1706.760	3.11632	1707.7569	3.12	0.16862	1708.87	3.1131	0.06488	0.22115
3. RIFI (FIRI)	1100.657	2.68	1112.020	2.68348	1100.64685	2.68	0.2353	1123.65	2.66405	2.08902	0.59515
4. FAFA	120	0	120	0	120.00945	0.02	18461.614	120.002	0	0.0075	0
5. RARA	720	0	720	0	720.00265	0.01	13333.396	720.003	0	0.00042	0
6. RAFA (FARA)	320	0	320	0	320.00263	0.01	16363.706	320.003	0	0.00094	0
7. FAFI (FIFA)	384.693	1.76	387.558	1.75757	384.69340	1.76	0.31763	389.152	1.7499	1.15911	0.57386
8. RARI (RIRA)	1295.781	2.55	1303.530	2.56007	1295.81612	2.55	0.17407	1313.22	2.54276	1.34583	0.28392
9. RAFI (FIRA)	816.748	2.21	816.777	2.21468	816.7465	2.21	0.18538	858.237	2.16235	5.07978	2.15611
10. RIFA (FARI)	669.001	2.05	669.249	2.0852	669.21604	2.05	0.32422	670.454	2.09116	0.21719	2.00780

Table 4 Thermo-physical properties of ethylene glycol-copper saturated porous medium at 300 K for volume fraction, $\chi = 0.06$. and $\phi = 0.88$.

ρ (kg/m^3)	C_p (J/kg K)	k (W/m K)	β (K^{-1} $\times$ 10^5)	μ' (kg/m s)	α (m^2 s^{-1} $\times$ 10^7)	(ρC_p) (J/m^3 K $\times$ 10^{-6})	$(\rho\beta)$ (kg/m^{3}K)
1565.09	1662.34	0.29294	39.17174	0.02522673	1.12545	2.60172	0.613073

subject to the boundary conditions

$$\frac{d^2 F}{dZ^2} - Da_{sl} F = \frac{dG}{dZ} - Bi_l G = 0 \text{ at } Z = \frac{-1}{2}, \tag{14}$$

$$\frac{d^2 F}{dZ^2} + Da_{su} F = \frac{dG}{dZ} + Bi_u G = 0 \text{ at } Z = \frac{1}{2} \tag{15}$$

are chosen in the form

$$F(Z) = Z^4 + aZ^3 + b_1 Z^2 + c_1 Z + d_1, \tag{16}$$

$$G(Z) = Z^4 + b_2 Z^2 + c_2 Z + d_2. \tag{17}$$

Fourth degree polynomials are chosen for $F(Z)$ and $G(Z)$ keeping in mind the order of the differential equations in Eqs. (12) and (13). The constants a, b_i, c_i and $d_i, i = 1, 2$ are determined such that the eigen functions $F(Z)$ and $G(Z)$ are mutually orthogonal in the domain R={$(X, Z)/X \in [0, 1]$ and $Z \in \left[-\frac{1}{2}, \frac{1}{2}\right]$} , i.e., $\int_{-\frac{1}{2}}^{\frac{1}{2}} F(Z) G(Z) dZ = 0$ and these functions satisfy the boundary conditions (14)–(15). The quantities Da_{sl} and Da_{su} are slip Darcy numbers at lower and upper plates respectively, Bi_l and Bi_u are Biot numbers at lower and upper plates respectively. From the above considerations the constants are found as follows:

$$a = \frac{2Da_{su} - 2Da_{sl}}{Da_{sl}(Da_{su} + 4) + 4(Da_{su} + 3)}, \quad b_1 = -\frac{(Da_{sl} + 6)(Da_{su} + 6)}{2Da_{sl}(Da_{su} + 4) + 8(Da_{su} + 3)},$$

$$c_1 = \frac{Da_{sl} - Da_{su}}{2Da_{sl}(Da_{su} + 4) + 8(Da_{su} + 3)}, \quad d_1 = \frac{Da_{sl}(Da_{su} + 8) + 8Da_{su} + 60}{16Da_{sl}(Da_{su} + 4) + 64(Da_{su} + 3)},$$

$$b_2 = -\frac{16d_2(Bi_l Bi_u + Bi_l + Bi_u) + Bi_l Bi_u + 5Bi_l + 5Bi_u + 16}{4(Bi_l Bi_u + 3Bi_l + 3Bi_u + 8)},$$

$$c_2 = -\frac{Bi_l - Bi_u - 16d_2 Bi_l + 16d_2 Bi_u}{4(Bi_l Bi_u + 3Bi_l + 3Bi_u + 8)}.$$

The constant d_2 varies according to the boundary combination.

Table 5 Comparison of Ra_c and v_c obtained from the present study with those obtained by shooting method for M=1, $\Lambda = 1.2$ and $\sigma^2 = 5$

Boundary Combinations	Shooting method		Value of d_2 chosen in Galerkin	Present study		% error in Ra_c	% error in v_c
	Ra_c	v_c		Ra_c	v_c		
1. FIFI	1006.89085	2.35	0.28697	1007.45	2.35065	0.05553	0.02766
2. RIRI	2271.245	3.13	0.16840	2273.75	3.12604	0.11029	0.12651
3. RIFI (same as FIRI)	1542.14446	2.7	0.23471	1577.73	2.72051	2.30754	0.75963
4. FAFA	204.68949	0.01	18461.6	204.718	0.01	0.01393	0
5. RARA	949.30513	0.01	13333.4	949.718	0.01	0.04349	0
6. RAFA (same as FARA)	459.75508	0.01	16363.7	460.194	0.01	0.09547	0
7. FAFI (same as FIFA)	607.20347	1.85	0.30179	615.507	1.84166	1.36750	0.45081
8. RARI (same as RIRA)	1723.34676	2.551	0.17423	1748.83	2.54036	1.47871	0.41748
9. RAFI (same as FIRA)	1150.98220	2.2	0.18235	1217.15	2.19979	5.74881	0.95454
10. RIFA (same as FARI)	950.36552	2.12	0.31873	951.995	2.12364	0.17145	0.17189

References

1. Nield DA, Bejan A (2006) Convection in porous media, vol 3. Springer, New York
2. Beavers GS, Joseph DD (1967) Boundary conditions at a naturally permeable wall. J Fluid Mech 30:197–207
3. Nield DA (2009) The Beavers-Joseph boundary condition and related matters: a historical and critical note. Transp Porous Media 78(3):537–540
4. Siddheshwar PG (1995) Convective instability of ferromagnetic fluids bounded by fluid-permeable, magnetic boundaries. J Magn Magn Mater 149:148–150
5. Platten JK, Legros JC (2012) Convection in liquids. Springer Science and Business Media, New York
6. Siddheshwar PG, Ramachandramurthy V, Uma D (2011) Rayleigh-Bénard and Marangoni magnetoconvection in Newtonian liquid with thermorheological effects. Int J Eng Sci 49(10):1078–1094
7. Siddheshwar PG, Meenakshi N (2017) Amplitude equation and heat transport for Rayleigh-Bénard convection in Newtonian liquids with nanoparticles. Int J Appl Comput Math 3(1):271–292
8. Siddheshwar PG, Veena BN (2018) A theoretical study of natural convection of water-based nanoliquids in low-porosity enclosures using single phase model. J Nanofluids 7(1):163–174

Rotary Oscillations of a Permeable Sphere in an Incompressible Couple Stress Fluid

P. Aparna , **N. Pothanna, and J. V. R. Murthy**

Abstract In this paper, an attempt is made to study the flow generated by rotary oscillations of a permeable sphere in an infinite expanse of an incompressible couple stress fluid. The flow generated is solved under Stokesian assumption for velocity field in the form of modified Bessel functions. The couple acting on the sphere due to external flow as well as internal flow is calculated. The couple has contributions to both couple stress tensor and stress tensor. Contour for the flow at different couple stress parameters is drawn to analyze the flow. It is noted that, due to couple stresses, the particles near the surface of the sphere are thrown away with velocity more than the velocity of the surface of the sphere. Comparative study of type B and type A conditions is presented through pictorial representations.

Keywords Couple stress fluid · Rotary oscillations · Permeable sphere

1 Introduction

Due to the heavy technical demand of industries, many researchers are using non-Newtonian fluids extensively in the problems of the extraction of petrol from porous wells, sedimentation, dilute polymers, suspensions, and lubrication journal bearings. Rotational effects of the fluid particles are shown by some non-Newtonian fluids like colloidal and suspension, animal blood and liquid rocks. Such behavior of the fluids is explained by couple stress fluid theory. The constitutive equations and basic theory for couple stress fluids were first established by Stokes [1]. Stokes has proposed a couple stress fluid theory in the year 1966. This theory was developed based on the pure kinematic behavior of fluid. Micropolar fluid theory of Eringen [2] was based on microstructural effects present within a fluid element.

Ramakisson [3] derived a mathematical formula for drag experienced by sphere for couple stress fluids. The formula for couple, acting on a solid axisymmetric body

P. Aparna (✉) · N. Pothanna
VNRVJIET, Hyderabad 500090, India
e-mail: aparnapodila@gmail.com

J. V. R. Murthy
NIT Warangal, Warangal 506002, India

in a rotary flow of viscous fluids, was derived by Jeffery [4]. Lakshmana Rao and Iyengar [5] analyzed the flow past a spheroid. The flow of a couple stress fluid past an approximate sphere was considered by Iyengar and Srinivasacharya [6]. Resonance-type flow due to rotary oscillations of a sphere as well as composite sphere in a micropolar fluid was investigated and couple experienced by the fluid on the porous surface is obtained analytically [7, 8].

Study of flow past sphere for viscous fluid was reported [9–11]. Srivatava [12] examined the flow due to rotation of axisymmetric body. The author discussed the oscillatary and uniform flow of an incompressible couple stress fluid past permeable sphere previously and reported [13, 14]. Aparna et al. [15] analyzed the couple acting on a rotating permeable sphere in a couple stress fluid.

Nagaraju and Murthy Ramana [16] examined and reported an unsteady flow of a micropolar fluid generated by a circular cylinder. Pothanna and Aparna [17] studied the effects of various material parameters on velocity and temperature fields.

In the present paper, the flow produced due to rotary oscillations of a permeable sphere in a couple stress fluid is analyzed.

2 Basic Equations and Formulation of the Problem

The basic equations of motion of couple stress fluid which were introduced by Stokes [1] are:

$$\rho \frac{\mathrm{d}\overline{V}}{\mathrm{d}t} = -\nabla p + (\lambda + \mu)\nabla(\nabla \cdot \overline{V}) + \eta \nabla^2 \left\{ \nabla(\nabla \cdot \overline{V}) \right\}$$
$$+ \mu \nabla^2 \overline{V} - \eta \nabla^4 \overline{V} + \rho \overline{f} + (1/2)\nabla \times (\rho I). \tag{1}$$

together with the continuity condition

$$\frac{\mathrm{d}\rho}{\mathrm{d}t} + \nabla \cdot \left(\rho \overline{V} \right) = 0. \tag{2}$$

Since the fluid is incompressible, Eq. (2) reduces to

$$\nabla . \overline{V} = 0. \tag{3}$$

Avoiding the body moment and the body forces, Eq. (1) becomes

$$\rho \frac{\mathrm{d}\overline{V}}{\mathrm{d}t} = -\nabla p - \mu \nabla \times \nabla \times \overline{V} - \eta \nabla \times \nabla \times \nabla \times \nabla \times \overline{V}. \tag{4}$$

We analyze the rotary oscillations of a permeable sphere an incompressible couple stress fluid having radius 'a' and angular velocity $\Omega e^{i\omega t}$. The amplitude Ω of the angular velocity is assumed to be small so that Stokes approximation can be adopted

Fig. 1 Rotating permeable
sphere
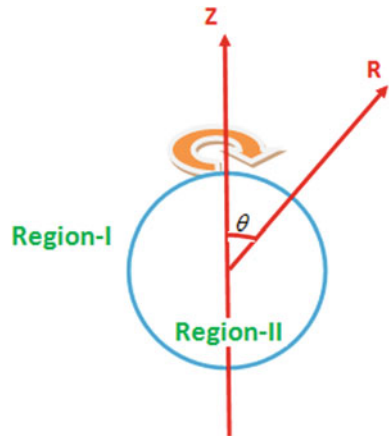
and the nonlinear terms in Eq. (4) can be neglected. With this, we have (Fig. 1)

$$\rho \frac{\partial \overline{V}}{\partial t} = -\nabla p - \mu \nabla \times \nabla \times \overline{V} - \eta \nabla \times \nabla \times \nabla \times \nabla \times \overline{V}. \tag{5}$$

To satisfy the oscillatory nature of the sphere and incompressibility condition (3), we assume that

$$\overline{V} = \overline{Q} e^{i\omega t} = \left(\frac{W}{h_3} e^{i\omega t} \right) \overline{e}_\varphi, \, p = P e^{i\omega t} \tag{6}$$

Substituting (6) in (5) we get,

$$i\rho \omega q \overline{Q} = -\nabla P - \mu \nabla \times \nabla \times \overline{Q} - \nabla \times \nabla \times \nabla \times \nabla \times \overline{Q} \tag{7}$$

Taking the components of toroidal direction e_ϕ, the equation for swirl W is obtained as below:

$$\left(E_0^2 - \frac{\lambda_1^2}{a^2} \right) \left(E_0^2 - \frac{\lambda_2^2}{a^2} \right) W = 0. \tag{8.1}$$

$$E_0^2 = \frac{\partial^2}{\partial R^2} + \frac{1}{R^2} \left(\frac{\partial^2}{\partial \theta^2} - \cot \theta \frac{\partial}{\partial \theta} \right) \tag{8.2}$$

$$\lambda_1^2 + \lambda_2^2 = \frac{\mu a^2}{\eta} = S \text{ and } \lambda_1^2 \lambda_2^2 = \frac{i\rho \omega a^4}{\eta} = i\sigma \tag{8.3}$$

Non-dimensional scheme:

$$R = ra, \quad W = \Omega a^2 w, \quad p_1 = \mu \Omega p, \quad S = \frac{\mu a^2}{\eta},$$

$$\text{Re} = \frac{\rho \Omega a^2}{\mu}, \quad \sigma = \frac{\rho \Omega a^4}{\eta} = \text{Re}.S, \quad E_0^2 = \frac{1}{a^2} E^2. \tag{9}$$

Using (9) in (8) we have,

$$\left(E^2 - \lambda_1^2\right)\left(E^2 - \lambda_2^2\right) w = 0. \tag{10}$$

We solve Eq. (10) for 'w' under the following conditions.

3   Boundary Conditions

Region 1   Region 2
(i) $\underset{r\to\infty}{\text{Lt}} \ w_e = 0$ $\underset{r\to 0}{\text{Lt}} \ w_i$ is finite
(ii) $w_e = \sin^2\theta$ on $r = 1$ $w_i = \sin^2\theta$ on $r = 1$
(iii) $M = 0$ on $r = 1$ for type A condition
$\overline{\omega} = \frac{1}{2}\nabla \times \overline{q}_\Gamma$ on $r = 1$ for type B condition.

Type A: This condition gives the couple stress tensor as zero on $r = 1$.

$$M = mI + 2\eta\nabla(\nabla \times \overline{V}) + 2\eta'\nabla(\nabla \times \overline{V})^T. \tag{11}$$

The components that contribute to couple are M_{rr} and $M_{r\theta}$. $M_{r\theta} = 0$ gives the condition that

$$E^2 w + \frac{(1-e)}{r}\left(\frac{\partial w}{\partial r} - \frac{2w}{r}\right) = 0 \text{ on } r = 1 \tag{12}$$

for external flow and internal flow.

$M_{rr} = 0$ gives the condition that

$$\overline{m} + \frac{(1+e)}{r^2}\left(\frac{d\overline{w}}{dr} - \frac{2\overline{w}}{r}\right) = 0 \tag{13}$$

Type B: Hyper-stick condition along the tangential direction on the sphere.

$$\frac{\partial w}{\partial r} = 2 \sin^2\theta \text{ on } r = 1 \tag{14}$$

4 Solution of the Problem

The solution of Eq. (10) can be written in the following form

$$w = w_1 + w_2 \tag{15}$$

where

$$\left(E^2 - \lambda_1^2\right)w_1 = 0, \left(E^2 - \lambda_2^2\right)w_2 = 0. \tag{16, 17}$$

The solution of Eq. (10) by separation of variables method which satisfies condition (i) is given by

$$w_e = \sqrt{r}\left(a_1 K_{3/2}(\lambda_1 r) + b_1 K_{3/2}(\lambda_2 r)\right)G_2(x). \tag{18.1}$$

$$w_i = \sqrt{r}\left(a_2 I_{3/2}(\lambda_1 r) + b_2 I_{3/2}(\lambda_2 r)\right)G_2(x). \tag{18.2}$$

Where $G_2(x) = \frac{1}{2}(1 - x^2)$, $x = \cos\theta$, $I_{3/2}(\lambda_1 r)$, $I_{3/2}(\lambda_2 r)$ and $K_{3/2}(\lambda_1 r)$, $K_{3/2}(\lambda_2 r)$ are modified Bessel functions. The constants a_1, b_1, a_2, b_2 are to be found by using above boundary conditions (ii) and (iii).

$$a_1' = a_1 K_{3/2}(\lambda_1), b_1' = a_1 K_{3/2}(\lambda_2), a_2' = a_2 I_{3/2}(\lambda_1), b_2' = b_2 I_{3/2}(\lambda_2). \tag{19}$$

$$\Delta_1(\lambda_1) = 1 + \frac{\lambda_1 K_{1/2}(\lambda_1)}{K_{3/2}(\lambda_1)}; \Delta_2(\lambda_1) = 1 - \frac{\lambda_1 K_{1/2}(\lambda_1)}{K_{3/2}(\lambda_1)} \tag{20}$$

Hence we have,

$$a_1' + b_1' = 2, \ a_2' + b_2' = 2. \tag{21.1, 21.2}$$

For *type A condition*: $M_{r\theta} = 0$ gives

$$\left[\lambda_1^2 a_1' + \lambda_2^2 b_1'\right] = (1 + e)\left[(2 + \Delta_1(\lambda_1))a_1' + (2 + \Delta_1(\lambda_2))b_1'\right] \tag{22.1}$$

$$\left[\lambda_1^2 a_2' + \lambda_2^2 b_2'\right] = (1 + e)\left[(2 + \Delta_2(\lambda_1))a_2' + (2 + \Delta_2(\lambda_2))b_2'\right] \tag{22.2}$$

For *type B condition*, Eq. (14) gives

$$a_1' \Delta_1(\lambda_1) + b_1' \Delta_1(\lambda_2) = -4. \tag{23.1}$$

$$a_2' \Delta_2(\lambda_1) + b_2' \Delta_2(\lambda_2) = -4. \tag{23.2}$$

Solving equations from 21.1–22.2 for type A condition we get,

$$b_1' = \frac{4\lambda_1^2 - 2(1-e)[\Delta_1(\lambda_1) + 2]}{2(\lambda_1^2 - \lambda_2^2) + (1-e)[\Delta_1(\lambda_2) - \Delta_1(\lambda_1)]}, \; a_1' = 2 - b_1', a_2' = 2 - b_2'$$

$$b_2' = \frac{4\lambda_1^2 - 2(1-e)[\Delta_2(\lambda_1) + 2]}{2(\lambda_1^2 - \lambda_2^2) + (1-e)[\Delta_2(\lambda_2) - \Delta_2(\lambda_1)]}. \tag{24}$$

Substituting (21.1, 21.2), (21.1, 21.2) in (22.1), (22.2) we can find the normal couple stress $\overline{m}$ as:

$$\overline{m}_e = (1+e)\{a_1'\Delta_1(\lambda_1) + b_1'\Delta_1(\lambda_2) + 4\} \text{ and}$$
$$\overline{m}_i = (1+e)\{a_2'\Delta_2(\lambda_1) + b_2'\Delta_2(\lambda_2) + 4\} \tag{25}$$

Solving (21.1, 21.2) and (23.1) for the type B condition we get

$$b_1' = \frac{2\Delta_1(\lambda_1) + 4}{\Delta_1(\lambda_1) - \Delta_1(\lambda_2)}, a_1' = 2 - b_1', b_2' = \frac{2\Delta_2(\lambda_1) + 4}{\Delta_2(\lambda_1) - \Delta_2(\lambda_2)}, a_2' = 2 - b_2'. \tag{26}$$

From Eqs. (23.1) and (25), we see that the permeability of the surface does not affect the flow. This flow is not similar to micropolar fluid where the flow is affected by the permeability of the boundary. This shows that, under Stokesian approximation, in spite of the fact that the boundary is permeable, the flow in the exterior region and the flow in the interior region do not interfere with one another under the two types of boundary conditions considered.

From type A condition, we can find the normal couple stress 'm' on the boundary. The function 'm' at all points cannot be determined, but only the form of 'm' can be known. From type B condition, this 'm' is undeterministic.

5 Couple on the Sphere

The couple acting on sphere is given by

$$C = 2\pi a^3 \int_0^\pi T_{r\varphi} \sin^2\theta \, d\theta. \tag{27}$$

The constitutive equation for stress tensor T for couple stress fluids is given by

$$T = -pI + \lambda(\nabla \cdot \overline{V})I + \mu\{\nabla\overline{V} + (\nabla\overline{V})^T\} + \frac{1}{2}I \times (DivM + \rho\overline{c}). \tag{28}$$

From which

$$T_{r\varphi} = \mu\left\{\frac{1}{R\sin\theta}\left(\frac{dW}{dR} - \frac{2W}{R}\right) - \frac{1}{R\sin\theta} \cdot \frac{d}{dR}E^2W - \frac{1}{2R} \cdot \frac{\partial m}{\partial\theta}\right\}e^{i\omega t}.$$

For type A condition, the couple for external flow C_{tx} and couples due to internal flow C_{tn} are given by

$$C_{tx} = \frac{4\pi a^3 \mu \Omega}{3S} \left[(\lambda_1^2 + S)\Delta_1(\lambda_1)a_1' + (\lambda_2^2 + S)\Delta_1(\lambda_2)b_1' + 4S\right]e^{i\omega t}. \quad (29.1)$$

$$C_{tn} = \frac{4\pi a^3 \mu \Omega}{3S} \left[\begin{array}{l}(\lambda_1^2 + S)\Delta_2(\lambda_1)a_2' \\ + (\lambda_2^2 + S)\Delta_2(\lambda_2)b_2' + 4S\end{array}\right]e^{i\omega t}. \quad (29.2)$$

For type B, the couple for external flow C_{tx} and couples due to internal flow C_{tn} are given by

$$C_{tx} = \frac{4\pi a^3 \mu \Omega}{3S} \left[\lambda_1^2 \Delta_1(\lambda_1)a_1' + \lambda_2^2 \Delta_1(\lambda_2)b_1'\right]e^{i\omega t}. \quad (29.3)$$

$$C_{tn} = \frac{4\pi a^3 \mu \Omega}{3S} \left[\lambda_1^2 \Delta_2(\lambda_1)a_2' + \lambda_2^2 \Delta_2(\lambda_2)b_2'\right]e^{i\omega t}. \quad (29.4)$$

6   Couple Due to Couple Stress Tensor

The couple due to couple stress tensor for type A condition is zero, since couple stress vanishes on the boundary. The couple C_m due to couple stress is

$$C_m = 2\pi a^2 \int_0^\pi (M_{rr} \cos\theta - M_{r\theta} \sin\theta) \sin\theta \, d\theta. \quad (30)$$

After simplifying for external and internal couples we get, for type B condition;

$$C_{mx} = \frac{8}{3} \frac{\pi \mu \Omega a^3}{S} \left(\lambda_1^2 a_1' + \lambda_2^2 b_1'\right)e^{i\omega t} \text{ for external flow} \quad (31.1)$$

$$C_{mn} = \frac{8}{3} \frac{\pi \mu \Omega a^3}{S} \left(\lambda_1^2 a_2' + \lambda_2^2 b_2'\right)e^{i\omega t} \text{ for internal flow} \quad (31.2)$$

The steady flow for the internal region is similar to viscous fluid case. But the unsteady flow differs from viscous fluid case. The total couple on the sphere is $C_{ex} = C_{tx} + C_{mx}$ and $C_{in} = C_{tn} + C_{mn}$ for external and internal flows. We can observe that this total couple is independent of m.

$$C_{ex} = \frac{4\pi a^3 \mu \Omega}{3S} \left[\begin{array}{l}(\lambda_1^2 + S)\Delta_1(\lambda_1)a_1' + (\lambda_2^2 + S)\Delta_1(\lambda_2)b_1' \\ + 4S\end{array}\right]e^{i\omega t}. \quad (32.1)$$

$$C_{\text{in}} = \frac{4\pi a^3 \mu \Omega}{3S} \left[(\lambda_1^2 + S)\Delta_2(\lambda_1)a_2' + (\lambda_2^2 + S)\Delta_2(\lambda_2)b_2' + 4S \right] e^{i\omega t}. \quad (32.2)$$

$$C_{\text{ex}} = \frac{4\pi a^3 \mu \Omega}{3S} \left[(\lambda_1^2(2 + \Delta_1(\lambda_1))a_1' + (\lambda_2^2(2 + \Delta_1(\lambda_2))b_1' \right] e^{i\omega t} \quad (32.3)$$

$$C_{\text{in}} = \frac{4\pi a^3 \mu \Omega}{3S} \left[(\lambda_1^2(2 + \Delta_2(\lambda_1))a_2' + (\lambda_2^2(2 + \Delta_2(\lambda_2))b_2' \right] e^{i\omega t}. \quad (32.4)$$

7   Discussions and Conclusions

In this analysis of finding flow field and couple, the values of length parameters λ_1 and λ_2 are found by taking suitable values to S and σ and solving the quadratic equation, $x^2 - Sx + i\sigma = 0$ where $x = \lambda_1^2$ or λ_2^2.

Then, the velocity field in the form of swirl 'w' is found from Eq. (18.1). Equation (32.1) is helpful for calculating couple. The effects of different parameters on couple and swirl are presented in the form of diagrams.

In Fig. 2, velocity at different values of couple stress parameter S is shown. As S increases, for type B and type A conditions, swirl decreases, showing that swirl is maximum for viscous fluids. (Since $s \to \infty$, implies that $\eta \to 0$, i.e., no couple stresses and we get the case of viscous fluids.) But we can observe that for type A condition, swirl at any distance 'r' is less than the swirl on the surface ($r = 1$) of the sphere. For type B condition, the swirl near to the sphere is more than the swirl on the surface of the sphere. Again, since the curves are not grouping, the effect of
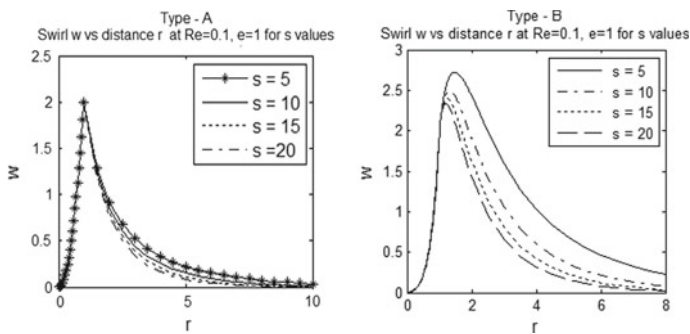
Fig. 2   Variation of swirl for different values of couple stress parameter S
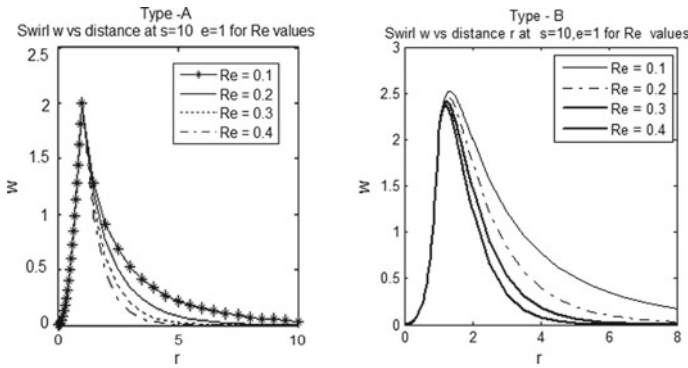
Fig. 3 Swirl for various values of Reynold's number Re

couple stresses on the flow is clear in type B condition, whereas in type A conditions, all curves are grouped without much variations.

In Fig. 3, variation of swirl for different values of Reynold's number Re for type A and B conditions is shown. As Re increases, swirl decreases and goes to zero drastically as 'r,' increases. This implies that (as Re is proportional to Ω,) as amplitude of oscillations of sphere increases, the particles of fluid confines to the region near to the sphere.

In Fig. 4, it is shown that as θ increases, swirl decreases. In Fig. 5, the variation of couple for external and internal flows at different values of relative couple stress parameter e is shown for type A condition. For type B condition, the couple is independent of the parameter. As 'e' increases, the value of couple decreases and as
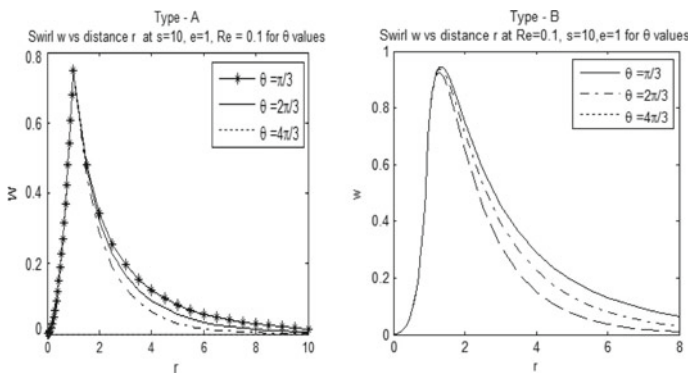
Fig. 4 Swirl w at different values of angles of θ
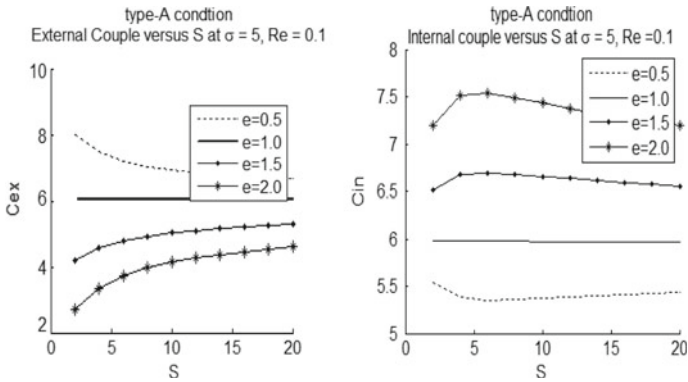
Fig. 5 Variation of couple for external and internal flows at different e values

S increases, couple tends to reach a constant value near to 6. This implies that, this is the value of couple due to a viscous fluid.

From Fig. 6, we can observe that as Re increases, couple due to internal flow decreases for type A condition. But the values are near to 6 and less than 6 for small values of frequency parameter σ. Type B condition does not show variations to the variations of Re but couple increases drastically from -12 to 2 as S increases.

In Fig. 7, the contours of swirl are shown. For type A condition, we can notice that the internal flow follows almost a straight line path. Flow circulation from outside to inside is more for type B condition. As the values of Re and S increase, the flow develops a secondary circulation region confined concentric spheres of radius 2 and 3.
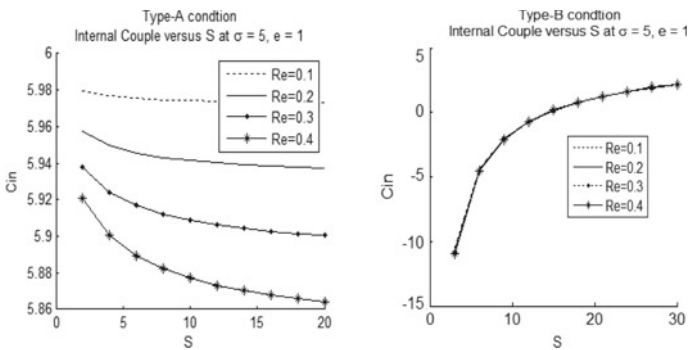
Fig. 6 Variation of couple due to internal flow at different values of Reynold's numbers Re
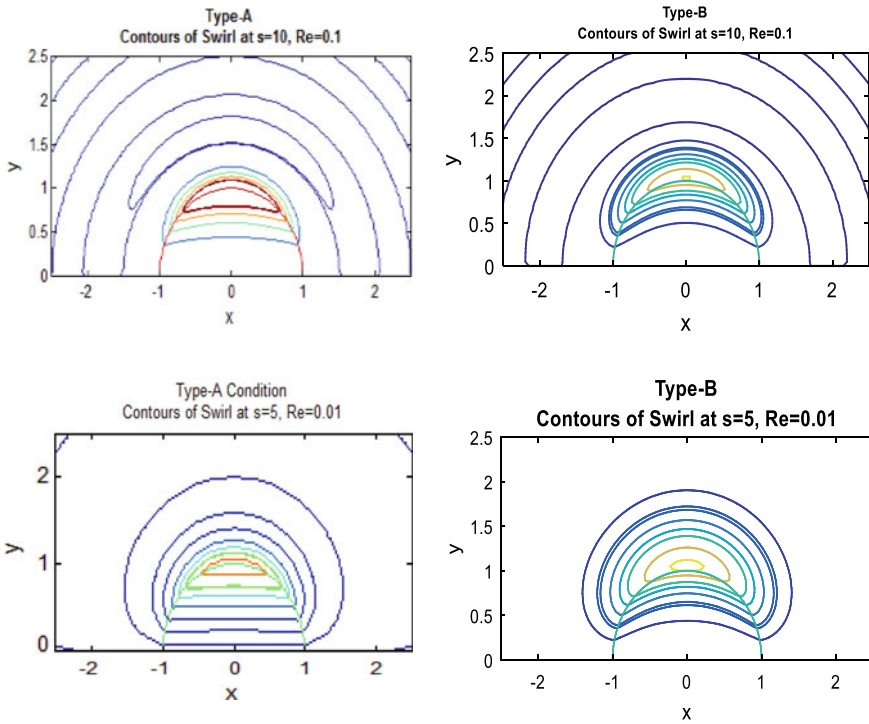
Fig. 7 Contours of swirl *w* at various values of Reynold's number Re and couple stress parameter S

References

1. Stokes VK (1966) Couple stresses in fluids. Phy Fluids 9:1710–1715. https://doi.org/10.1063/1.1761925
2. Eringen AC (1966) Theory of micropolar fluids. J Math Mech 16:1–18
3. Ramkissoon H (1978) Drag in couple stress fluids. ZAMP 29:341–346. https://doi.org/10.1007/bf01601529
4. Jeffery GB (1915) Steady rotation of a solid of revolution in a viscous fluid. Proc Lond Math Soc 14:327–338. https://doi.org/10.1112/plms/s2_14.1.327
5. Lakshmana Rao SK, Iyengar TKV (1981) The slow stationary flow of incompressible micropolar fluid past a spheroid. Int J Eng Sci 19:189–220. https://doi.org/10.1016/0020-7225(81)90021-5
6. Iyengar TKV, Srinivasacharya D (1993) Stokes flow of an incompressible micropolar fluid past an approximate sphere. Int J Eng Sci 31:115–123. https://doi.org/10.1016/0020-7225(93)90069-7

7. Ramana Murthy JV, Bhaskara Rao GS, Govind Rao T (2015) Resonance type flow due to rotary oscillations of a sphere in a micro-polar fluid. Proced Eng 127:1323–1329. https://doi.org/10.1016/j.proeng.2015.11.490

8. Ashmawy EA (2015) Rotary oscillation of a composite sphere in a concentric spherical cavity using slip and stress jump conditions. Eur Phys J Plus 14:130–163. https://doi.org/10.1140/epjp/i2015-15163-8

9. Leonov AI (1962) The slow stationary flow of a viscous fluid about a porous sphere. J Appl Mech 26:564–566. https://doi.org/10.1016/0021-8928(62)90050-3

10. Padmavathi BS, Amarnath T, Palaniappan P (1994) Stokes flow past a permeable sphere—non-axisymmetric case. ZAMM 74:290–292. https://doi.org/10.1007/bf00914360

11. Wolfersdorf LV (1989) Stokes flow past a sphere with permeable surface. ZAMM 69:111–112. https://doi.org/10.1002/zamm.19890690220

12. Srivastava DK (2013) Stokes flow around rotating axially symmetric pervious body. J Appl Fluid Mech 6(3):435–442

13. Ramana Murthy JV, Srinivasacharyulu N, Aparna P (2007) Uniform flow of an incompressible couple stress fluid past a permeable sphere. Bull Cal Math Soc 99

14. Aparna P, Ramana Murthy JV (2008) Oscillatory flow of an incompressible couple stress fluid past a permeable sphere. Proceedings of 53rd congress ISTAM, pp 164–173

15. Aparna P, Ramana Murthy JV, Nagaraju G (2018) Couple on a rotating permeable sphere in a couple stress fluid. Ain Shams Eng J 9(4):665–673

16. Nagaraju G, Ramana Murthy JV (2014) Unsteady flow of a micropolar fluid generated by a circular cylinder subject to longitudinal and torsional oscillations. Theoret Appl Mech 41:71–91

17. Pothanna N, Aparna P (2019) Unsteady thermoviscous flow in a porous slab over an oscillating flat plate. J Porous Media 22(5):531–543

Simulation of Natural Convective Heat Transfer in a Triangular Enclosure Filled with Nanofluid: Buongiorno's Mathematical Model

K. Venkatadri , **V. Ramachandra Prasad** , **B. Md. Hidayathulla Khan** ,
M. Suryanarayan Reddy, and R. Bhuvanavijaya

Abstract Natural convection of triangular enclosure filled with water-based nanofluid under the influence of Brownian diffusion and thermophoresis is studied numerically in two cases by depending on wall boundary conditions. The high (hot) temperature vertical wall and the insulated bottom wall are considered in case (i) and the other case the bottom wall is uniformly heated while the vertical wall is thermally insulated. In both cases, the inclined wall is maintained low temperature (i.e., cold inclined wall). The coupled governing vorticity–stream function formulation equations are employed by the help of finite difference method (FDM). The influence of the Rayleigh number, Lewis number on fluid flow, heat have been examined through graphically and discussed. It has been found that in the case of uniform heating is high sensitive to rising of the Ra, while the uniform heating of the left wall of the cavity is not so sensitive to changes of Ra.

Keywords Natural convection · Triangular enclosure · Nanofluid · Heat transfer

K. Venkatadri (✉)
Department of Mathematics, Vemu Institute of Technology, P. Kothakota, Chitoor,
Andhra Pradesh, India
e-mail: venkatadri.venki@gmail.com

V. R. Prasad
Department of Mathematics, School of Advanced Sciences,
Vellore Institute of Technology [VIT University], Vellore, India

B. Md. Hidayathulla Khan
Department of Mathematics, Sri Vishveshwaraiah Institute of Science and Technology,
Madanapalle, Andhra Pradesh, India

M. Suryanarayan Reddy
Department of Mathematics, JNTUA College of Engineering, Pulivendula, Andhra Pradesh, India

R. Bhuvanavijaya
Department of Mathematics, Jawaharlal Nehru Technological University, Anantapur,
Andhra Pradesh, India

1 Introduction

Buoyancy convective flow within an enclosure with various shapes has been examined last several decades due to its prevalence in the area of science and engineering applications such as geothermal systems, nuclear reactors cooling, food processing, glass production, drying technologies, solar power collectors, chemical processing equipment, etc. The researches focused on much attention on triangular enclosures because of its has several applications in various fields which include building and thermal insulation systems, geophysical fluid mechanics, and so on.

LBM method based simulation is carried by [1]. They studied power-law nanofluid flow characteristics within a square enclosure under the uniform moving top lid using two-phase model. Sheremet [2] have examined natural convection porous enclosure filled with nanofluid for the wavy left wall under the effect of thermal dispersion. Sheikholeslami [3] demonstrated heat transfer in nanofluid due to Lorentz forces in a lid-driven enclosure with hot square obstacle. Sheikholeslami [4] reported on Buongiorno Model-based nanofluid is studied fluid flow over a stretching plate with the influence of the magnetic field. Several mathematical models are employed theoretically by several researchers to illustrate heat transfer utilizing no fluids. Khanafer et al. [5] studied the enhancement of heat transfer in an enclosure with utilizing nanofluids. Oztop et al. [6] reported numerical investigation of natural convection under effect partially active left wall of enclosure filled with nanofluid. The account of Brownian motion and thermophoresis effects, Buongiorno [7] proposed a two-component nonhomogeneous equilibrium model to examine heat transfer utilizing nanofluid. The influence of the Brownian motion and thermophoresis on convective flow of nanofluids has been examined with various numerical techniques by several authors [8–13]. Sheremet and Pop applied Buongiorno's model [7] to study the natural convection within enclosure filled with nanofluid [14], triangular enclosure with one angle is right angle [15], square enclosure [16], entrapped triangular enclosure [17].

In this paper, the impacts of thermal boundary conditions on the nanofluid flow in an enclosure are examined. The fine grid based method is chosen to examine the pertinent results by using finite difference. The influence of the Ra and Lewies number on thermal characteristics is examined in presence of the Nb (Brownian motion) and Nt (thermophoresis parameter) effects.

2 Basic Equations

Let us consider two-dimensional regime with triangular shape filled with conducting water-based nanofluid and nanoparticles. Figure 1, reveals the physical diagram of the present computational model. The assumptions of the current study are as follows:

1. Incompressible nanofluid
2. All fluid properties are considered to be constant except density

Case (i)   Case (ii)
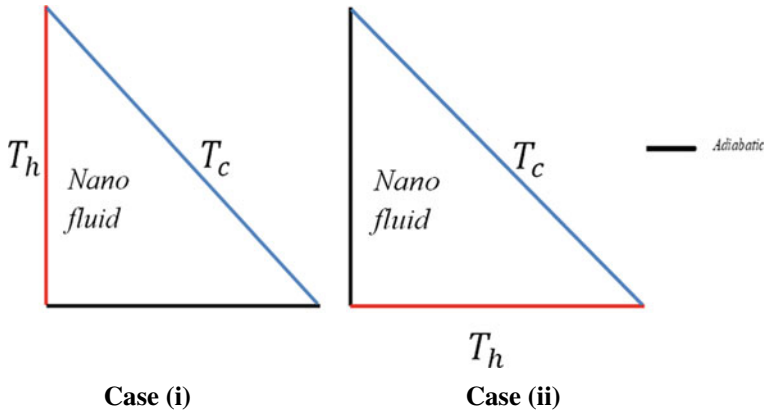
Fig. 1 Schematic physical model

3. Invoked Boussinesq approximation
4. Radiation, dissipation effects, electric field, heat generation are neglected.

Based on the above-mentioned assumptions, the conservative equations are written as follows (see Buongiorno [7]).

$$\frac{\partial U}{\partial X} + \frac{\partial V}{\partial Y} = 0 \tag{1}$$

$$\frac{\partial U}{\partial \tau} + U\frac{\partial U}{\partial X} + V\frac{\partial U}{\partial Y} = -\frac{\partial P}{\partial X} + \Pr\left(\frac{\partial^2 U}{\partial X^2} + \frac{\partial^2 U}{\partial Y^2}\right) \tag{2}$$

$$\frac{\partial V}{\partial \tau} + U\frac{\partial V}{\partial X} + V\frac{\partial V}{\partial Y} = -\frac{\partial P}{\partial Y} + \Pr\left(\frac{\partial^2 V}{\partial X^2} + \frac{\partial^2 V}{\partial Y^2}\right) + \text{Ra}.\Pr(\theta - \text{Nr}\phi) \tag{3}$$

$$\frac{\partial \theta}{\partial \tau} + U\frac{\partial \theta}{\partial X} + V\frac{\partial \theta}{\partial Y} = \left(\frac{\partial^2 \theta}{\partial X^2} + \frac{\partial^2 \theta}{\partial Y^2}\right) + \text{Nb}\left(\frac{\partial \phi}{\partial X}.\frac{\partial \theta}{\partial X} + \frac{\partial \phi}{\partial Y}.\frac{\partial \theta}{\partial Y}\right)$$

$$+ \text{Nt}\left[\left(\frac{\partial \theta}{\partial X}\right)^2 + \left(\frac{\partial \theta}{\partial Y}\right)^2\right] \tag{4}$$

$$\frac{\partial \phi}{\partial \tau} + U\frac{\partial \phi}{\partial X} + V\frac{\partial \phi}{\partial Y} = \frac{1}{Le}\left(\frac{\partial^2 \phi}{\partial X^2} + \frac{\partial^2 \phi}{\partial Y^2}\right) + \frac{\text{Nt}}{Nb.Le}\left(\frac{\partial^2 \theta}{\partial X^2} + \frac{\partial^2 \theta}{\partial Y^2}\right) \tag{5}$$

the dimensionless parameters

$$\tau = \frac{tu_0}{L}, \quad X = \frac{x}{L}, \quad Y = \frac{y}{L}, \quad U = \frac{u}{u_0}, \quad V = \frac{v}{u_0}$$

$$\theta = \frac{T - T_c}{T_h - T_c}, \quad \phi = \frac{C - C_c}{C_h - C_c}, \quad P = \frac{p}{u_0^2 \rho_f} \tag{6}$$

where $u_0 = \frac{\alpha}{L}$, dimensionless stream function and vorticity and their corresponding boundary conditions

$$U = \frac{\partial \psi}{\partial Y}, \quad V = -\frac{\partial \psi}{\partial X} \tag{7}$$

$$\omega = \frac{\partial V}{\partial X} - \frac{\partial U}{\partial Y} = -\frac{\partial^2 \psi}{\partial X^2} - \frac{\partial^2 \psi}{\partial X^2} \tag{8}$$

$$\text{Nr} = \frac{(C_h - C_c)(\rho_p - \rho_{f_0})}{\beta(1 - C_c)\rho_{f_0}(T_h - T_c)}, \quad \text{Nb} = D_B \frac{(\rho c)_p}{(\rho c)_f} \frac{(C_h - C_c)}{\alpha_f}, \quad \text{Pr} = \frac{\nu_f}{\alpha_f},$$

$$\text{Nt} = \frac{D_T}{T_c} \frac{(\rho c)_p}{(\rho c)_f} \frac{(T_h - T_c)}{\alpha_f}, \quad \text{Ra} = \frac{g\beta(T_h - T_c)(1 - C_c)L^3}{\nu_f^2}, \quad \text{Le} = \frac{\alpha_f}{D_B}$$

The boundary conditions are in vorticity–stream function as follows:

$$\left.\begin{array}{l} \psi = 0, \ \theta = 1 \text{ or } \dfrac{\partial \theta}{\partial X} = 0, \ \text{Nb}\dfrac{\partial \phi}{\partial Y} + \text{Nt}\dfrac{\partial \theta}{\partial Y} = 0 \text{ on } Y = 0 \\[2mm] \psi = 0, \ \theta = 1 \text{ or } \dfrac{\partial \theta}{\partial X} = 0, \ \text{Nb}\dfrac{\partial \phi}{\partial Y} + \text{Nt}\dfrac{\partial \theta}{\partial Y} = 0 \text{ on } X = 0 \\[2mm] \psi = 0, \ \theta = 0, \ \text{Nb}\dfrac{\partial \phi}{\partial n} + \text{Nt}\dfrac{\partial \theta}{\partial n} = 0 \text{ on } Y = 1 - X \end{array}\right\} \tag{9}$$

The interesting physical quantities are local Nusselt number Nu and the average Nusselt avg_Nu. These parameters are defined as $\text{Nu} = -\frac{\partial \theta}{\partial n}$, $\text{avg\_Nu} = \int_0^L \text{Nu} \, ds$.

3 Solution Procedure

The finite difference based discretization of nonlinear differential equations in the form of vorticity—stream function and with boundary conditions were solved numerically. In this numerical computation, we considered uniform-based grid system. The convective terms were approximated with second-order accuracy and diffusion terms were approximated by the central difference scheme. The transient partial equations are computed by the explicit iterative scheme while the most emerging parameter stream function is evaluated by the iterative method of Gauss–seidel iterative method. The explicit time iterative loop was exit when the time loop reaches converges condition for each parameter (i.e., vorticity, stream function, temperature). The house computational MATLAB code is developed and validated by [18] for natural convection of triangular enclosure and also compared with the results of Basak et al. [18].

4   Results and Discussion

The numerical investigation of natural convection within a triangular enclosure filled with water-based nanofluid for two cases is conducted. The flow characteristics and heat transfer of triangular enclosure have been studied for a wide range of Rayleigh number (Ra = $10^3 - 2 \times 10^5$) with Pr = 6.2, Nb = 0.1, Nt = 0.1, the buoyancy ratio parameter (Nr = 0.1–5) and Lewis number (Le = 1–100).

Figure 2 illustrates streamlines and isotherms of the first case, the effect of Rayleigh number (Ra = $10^3 - 2 \times 10^4$), Lewis number (Le = 2), Nr = 0.1 and fixed Pr = 6.2 when the vertical wall is heated uniformly and the bottom wall is thermally insulated while the inclined wall kept at cold temperature. When expected the fluid rises up along the left wall and flow down to slant wall (cold wall) which produces the clockwise circulation within enclosure. The enlarged clockwise circulation is developed with enclosure shape due to the effect of wall resistance of the fluid flow at Ra = 10^3. The corresponding isotherms are smooth and monotonic, distributed the whole cavity. When the Rayleigh number is increasing, the flow patterns and isotherms are considerable changes registered. Further increasing of Ra leads to the formation of thermal plume over the inclined (cold) wall with an increase in the nanofluid clockwise circulation. We found the high-density thermal flume over the cold wall at Rayleigh number Ra = 2×10^4. The smooth patterns of the isotherms are distracted at the Rayleigh number Ra = 10^4.

Figure 3 presents the second case of flow patterns and temperature contours for various values of Rayleigh number, Le = 2 and Nr = 0.1. First of all, it is to be notified that the right-angled triangular enclosure presents the instability convective flow of natural convection with uniformly heated bottom wall with inclined cold wall whereas the adiabatic wall of the other one. Irrespective values of Rayleigh number, the mono clockwise cell is developed within the enclosure. The nanofluid particles descend along the inclined cold walls while developing a clockwise circulation. For Ra = 10^3, the nanofluid flow forms the enlarged mono cell within a cavity and the corresponding isotherm contours are spread throughout the cavity which are smooth curves and increases monotonically. The domination of heat conduction in an enclosure is noticed at Ra = 10^4, where the temperature contours are shifted from smooth curves to straight patterns. When enhancing the Rayleigh number illustrates the shape of the circular cell changes within the triangular enclosure. The mono circulation within the cavity gradually moves towards to right corner (i.e., hot and cold area corner) of the bottom wall with increasing of the Rayleigh number. The distribution of isotherms is parallel to uniformly heated wall is noticed at the Rayleigh number Ra = 2×10^5. The effect of buoyancy ratio parameter on flow patterns and temperature contours are depicted Figs. 4 and 6 for both cases. We are noticed that with rising of Nr leads to no changes registered in streamlines and isotherms. The influence of Lewis number on streamlines and isotherms are presented in Fig. 5. For two cases of uniform heated wall. We found that increasing Le leads to non-considerable modifications are observed on the characteristics of flow field and temperature contours.
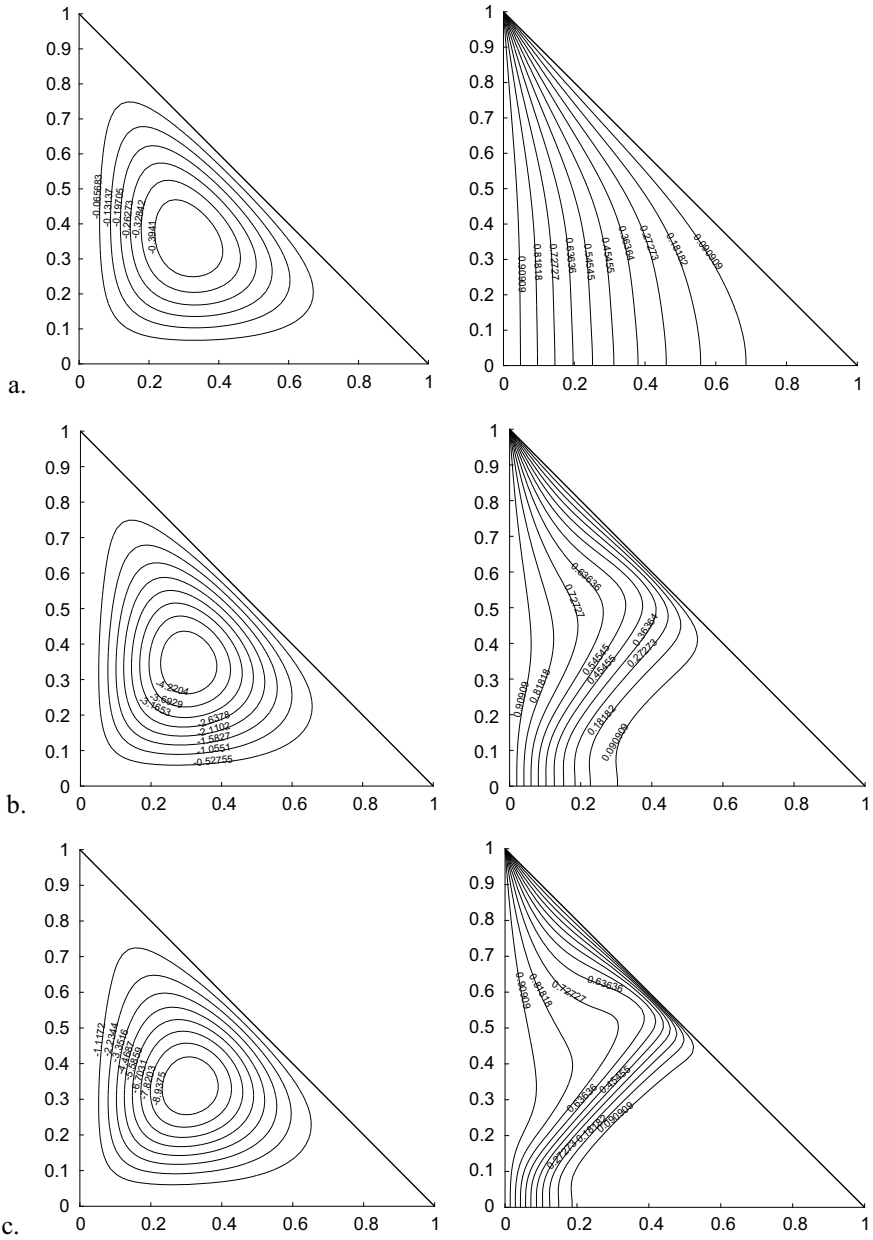
Fig. 2 Streamlines ψ and isotherms θ contours for uniformly heated left vertical wall, $\theta(0, Y) = 1$, Le $= 2$, Nr $= 0.1$: Ra $= 10^3$ (**a**), Ra $= 10^4$ (**b**), Ra $= 2 \times 10^4$ (**c**)
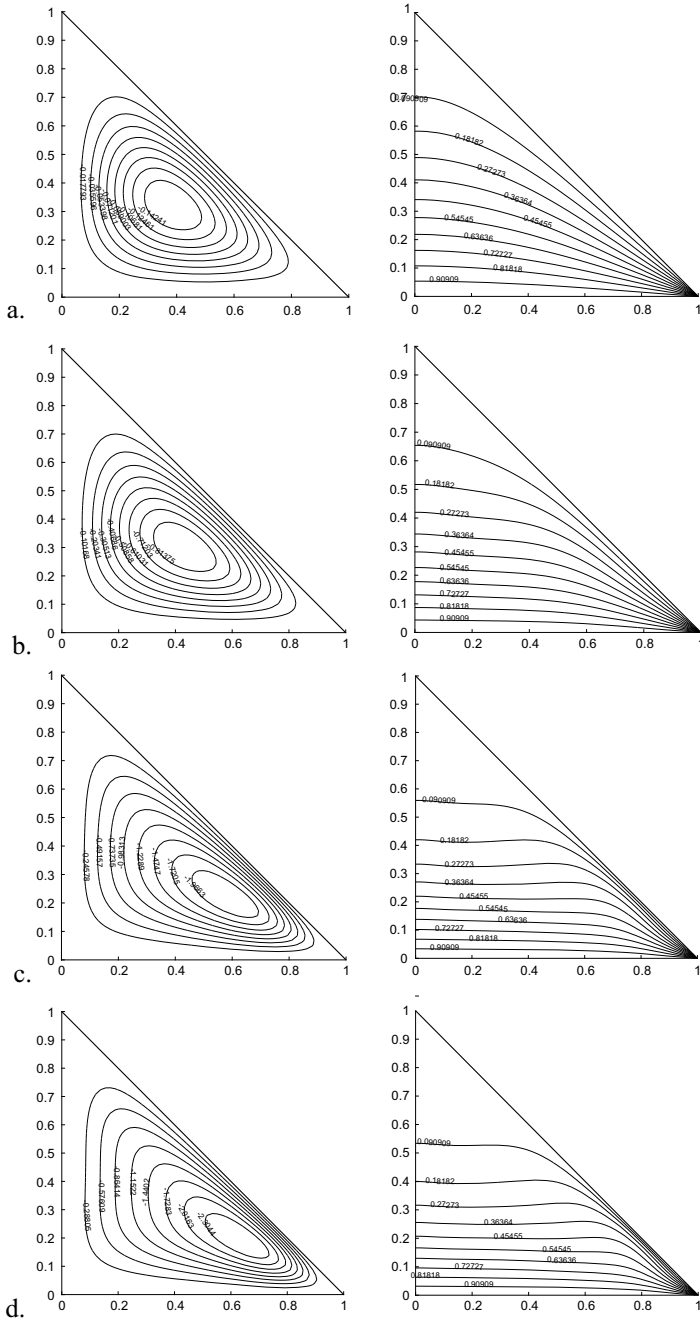
Fig. 3 Streamlines ψ and isotherms θ contours for uniformly heated bottom wall, $\theta(X, 0) = 1$, Le $= 2$, Nr $= 0.1$ Ra $= 10^3$ (**a**), Ra $= 10^4$ (**b**), Ra $= 10^5$ (**c**), Ra $= 2 \times 10^5$ (**d**)
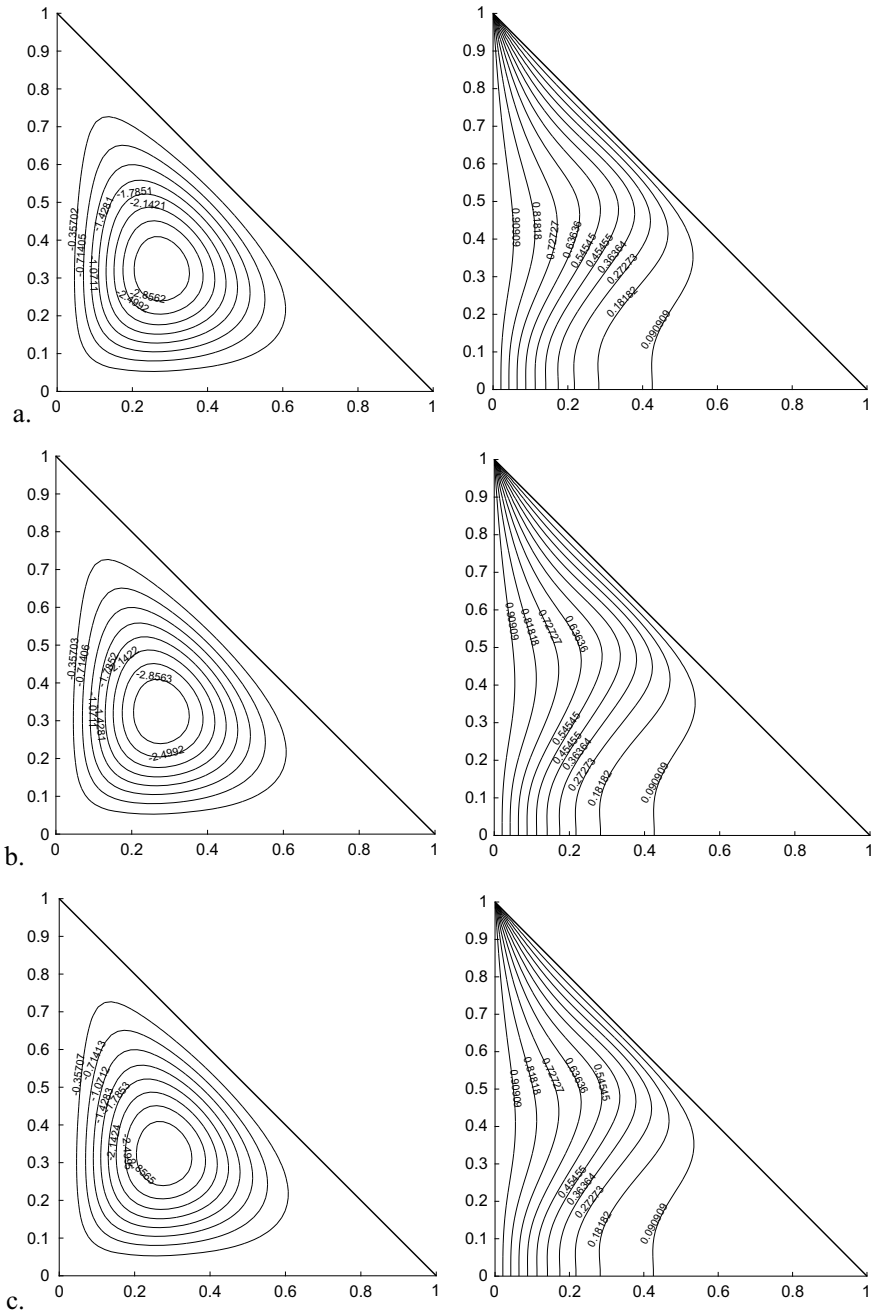
Fig. 4 Streamlines ψ and isotherms θ contours for uniformly heated left vertical wall, $\theta(0, Y) = 1$, Ra = 10^4, Le = 10: Nr = 0.1 (**a**), Nr = 1.0 (**b**), Nr = 5.0 (**c**)
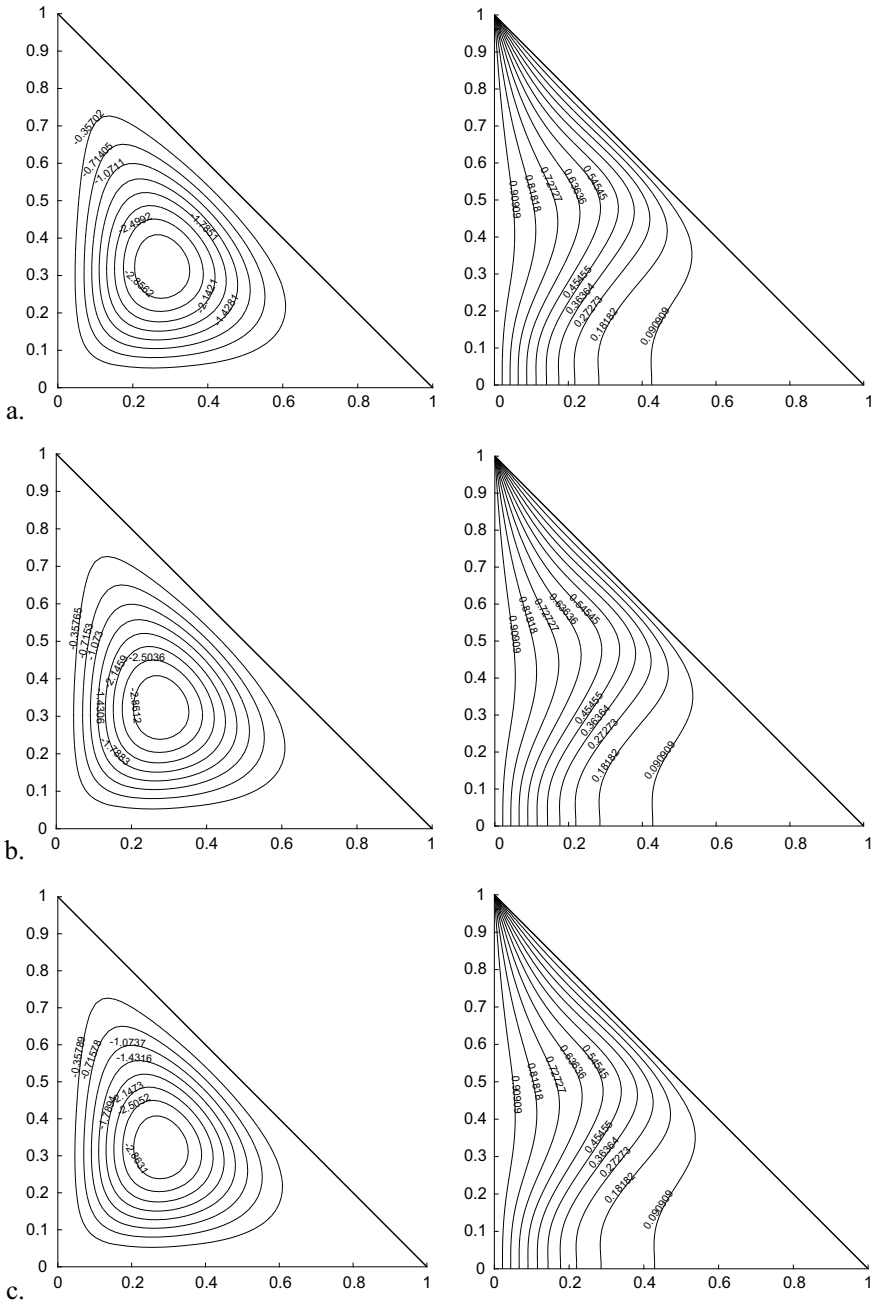
Fig. 5 Streamlines ψ and isotherms θ contours for uniformly heated left vertical wall, $\theta(0, Y) = 1$, Ra $= 10^4$, Nr $= 0.1$: Le $-$ 10 (**a**), Le $-$ 50 (**b**), Le $-$ 100 (**c**)
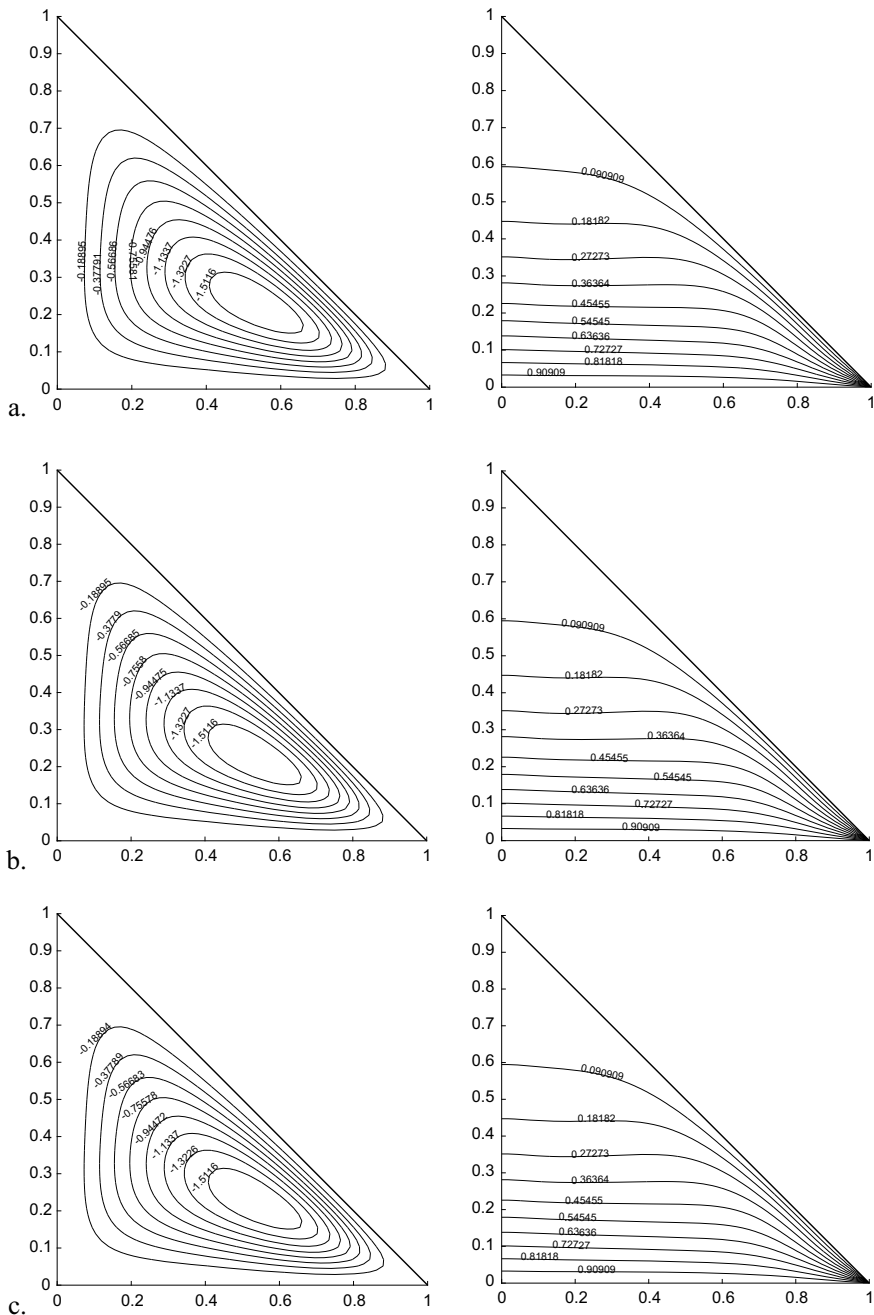
Fig. 6 Streamlines ψ and isotherms θ contours for uniformly heated bottom wall, $\theta(X, 0) = 1$, Ra = 105, Le = 10: Nr = 0.1 (**a**), Nr = 1.0 (**b**), Nr = 5.0 (**c**)

5 Conclusions

We studied in this investigation, the natural convective nanofluid in a triangular enclosure applying the effect of Nb and Nt in two cases. The interest of domain has left heated walls and cooled wall is the first case and heated bottom walls and cold wall is the second case. The governing partial differential equations converted into vorticity–stream function formulation and then solved by second-order accuracy scheme with fine grid FDM. The fluid flow, heat transfer phenomenon such as flow patterns and temperature contours, in addition, the most important scaling of heat transfer rate of average Nusselt numbers along hot surfaces of triangular enclosure were depicted in a graphical form for various values of the non-dimensional parameters. More intensive flow regime and convective heat distribution occur within the enclosure in case (ii) are noticed. We found that regardless of the thermal Rayleigh number value, mono circular convective eddy is developed within the cavity for both cases. The average Nusselt number increasing functions of the Rayleigh number and decreasing functions of the Lewis number. In case (ii), the convective eddy is moved towards the right side corner of bottom wall with increasing of Rayleigh number. The Lewis number plays a major role on average Nusselt number of the hot wall in both cases.

References

1. Kefayati GHR (2017) Mixed convection of non-Newtonian nanofluid in an enclosure using Buongiorno's mathematical model. Int J Heat Mass Transf 108:1481–1500 (2017). https://doi.org/10.1016/j.ijheatmasstransfer.2016.12.103
2. Sheremet MA, Revnic C, Pop I (2017) Free convection in a porous wavy cavity filled with a nanofluid using Buongiorno's mathematical model with thermal dispersion effect. Appl Math Comput 299:1–15. https://doi.org/10.1016/j.amc.2016.11.032
3. Sheikholeslami M, Shehzad SA, Abbasi FM, Li Z (2018) Nanofluid flow and forced convection heat transfer due to Lorentz forces in a porous lid driven cubic enclosure with hot obstacle. Comput Methods Appl Mech Eng 338:491–505. https://doi.org/10.1016/j.cma.2018.04.020
4. Sheikholeslami M, Rokni HB (2017) Effect of melting heat transfer on nanofluid flow in existence of magnetic field considering Buongiorno model. Chin J Phys 55(4):1115–1126. https://doi.org/10.1016/j.cjph.2017.04.019
5. Khanafer K, Vafai K, Lightstone M (2003) Buoyancy-driven heat transfer enhancement in a two-dimensional enclosure utilizing nanofluids. Int J Heat Mass Transf 46(19):3639–3653. https://doi.org/10.1016/S0017-9310(03)00156-X
6. Oztop HF, Abu-Nada E (2008) Numerical study of natural convection in partially heated rectangular enclosures filled with nanofluids. Int J Heat Fluid Flow 29(5):1326–1336. https://doi.org/10.1016/j.ijheatfluidflow.2008.04.009
7. Buongiorno J (2006) Convective transport in nanofluids. J Heat Transfer 128(3):240–250. https://doi.org/10.1115/1.2150834
8. Haddad Z, Abu-Nada E, Oztop HF, Mataoui A (2012) Natural convection in nanofluids: are the thermophoresis and brownian motion effects significant in nanofluid heat transfer enhancement? Int J Therm Sci 57:152–162. https://doi.org/10.1016/j.ijthermalsci.2012.01.016
9. Sheikhzadeh GA, Dastmalchi M, Khorasanizadeh H (2013) Effects of nanoparticles transport mechanisms on Al_2O_3—water nanofluid natural convection in a square enclosure. Int J Therm Sci 66:51–62. https://doi.org/10.1016/j.ijthermalsci.2012.12.001

10. Celli M (2013) Non-homogeneous model for a side heated square cavity filled with a nanofluid. Int J Heat Fluid Flow 44:327–335. https://doi.org/10.1016/j.ijheatfluidflow.2013.07.002
11. Choi SK, Kim SO, Lee TH (2014) Computation of the natural convection of nanofluid in a square cavity with homogeneous and nonhomogeneous models. Numer Heat Transf Part A Appl 65(4):287–301. https://doi.org/10.1080/10407782.2013.831695
12. Pakravan HA, Yaghoubi M (2013) Analysis of nanoparticles migration on natural convective heat transfer of nanofluids. Int J Therm Sci 68:79–93. https://doi.org/10.1016/j.ijthermalsci.2012.12.012
13. Quintino A, Ricci E, Corcione M (2017) Thermophoresis-induced oscillatory natural convection flows of water-based nanofluids in tilted cavities. Numer Heat Transf Part A Appl 71(3):270–289. https://doi.org/10.1080/10407782.2016.1264775
14. Sheremet MA, Pop I (2015) Natural convection in a wavy porous cavity with sinusoidal temperature distributions on both side walls filled with a nanofluid: Buongiorno's mathematical model. J Heat Transf 137(7). https://doi.org/10.1115/1.4029816
15. Sheremet MA, Pop I (2015) Free convection in a triangular cavity filled with a porous medium saturated by a nanofluid: Buongiorno's mathematical model. Int J Numer Methods Heat Fluid Flow 25:1138–1161
16. Sheremet MA, Pop I (2014) Natural convection in a square porous cavity with sinusoidal temperature distributions on both side walls filled with a nanofluid: Buongiorno's mathematical model. Transp Porous Media 105(4):11–29
17. Sheremet MA, Revnic C, Pop I (2017) Natural convective heat transfer through two entrapped triangular cavities filled with a nanofluid: Buongiorno's mathematical model. Int J Mech Sci 133:484–494
18. Basak T, Roy S, Thirumalesha Ch (2007) Finite element analysis of natural convection in a triangular enclosure: effects of various thermal boundary conditions. Chem Eng Sci 62:2623–2640

Influence of Ohmic Heating and Viscous Dissipation on Steady MHD Non-Newtonian Mixed Convective Fluid Flow Over an Infinite Vertical Porous Plate with Hall and Ion-Slip Current

K. V. B. Rajakumar, M. Umasankara Reddy, and K. S. Balamurugan

Abstract   Impact of Hall and ion-slip on steady MHD (non-Newtonian fluid) Casson fluid model based on mixed convective dissipative Casson fluid model flow over an infinite vertical permeable plate with Ohmic heating in aspect of soret as well as chemical reaction has been presented. The modelling equations are transformed into dimensionless equations and then solved analytically through multiple regular perturbation law. Computations were carried out graphically to examine the behaviour of fluid velocity, temperature, and concentration on the vertical plate with the difference of emerging physical parameters. This study reflects that the incremental values of Casson fluid parameter and Schmidt number lead to reduction in velocity. However, fluid velocity rises due to enhancement of ion-slip parameter, but reverser effect has been shown in case of Hall parameter.

Keywords MHD · Casson fluid · Multiple regular perturbation law · Ohmic heating · Hall and ion-slip current

1   Introduction

The Newtonian theory has worked extremely well in explaining numerous physical phenomena in diverse fields of fluid dynamics; this entices us to comment that for the most part of fluids at least in ordinary situations perform similar to Newtonian fluids. But in the modern years, in particular with the materialization of polymers, it has been established that there are fluids which illustrate a different deviation from Newtonian theory. Such fluids are known as non-Newtonian fluids. The non-Newtonian fluids are generally categorized into the following classifications which are Maxwell fluids,

K. V. B. Rajakumar (✉) · M. Umasankara Reddy
Department of Mathematics, Kallam Haranadhareddy Institute of Technology, Guntur, Andhra Pradesh 522109, India
e-mail: kvbrajakumar@gmail.com

K. S. Balamurugan
Department of Mathematics, R.V.R & J.C. College of Engineering, Guntur, Andhra Pradesh 522109, India
e-mail: muruganbalaks@gmail.com

dilatants fluids, Reiner-Rivlin fluids, purely viscous fluids, visco-plastic fluids as well as perfectly plastic materials, couple stress fluid, power law fluids, visco-elastic fluids, pseudo-plastic fluids, Casson fluid, and micro-plar fluid; currently, in this paper, it was studied on Casson fluid model.

Etwire et al. [1] have addressed numerically Casson fluid model based on MHD flow over a normal plate immersed in porous media by means of joule heating as well as convective boundary condition. Vinod Kumar et al. [2] and Prasad et al. [3] have assayed steady MHD stagnation Casson fluid flow over a stretching sheet subjected to slip boundary conditions in the existence of viscous dissipation and chemical reaction along with Joule heating. Ullah et al. [4] have described MHD mixed convective viscous dissipative Casson fluid model flow owing to affecting wedge bounded in a porous medium in the alive of chemical reaction. In this report, it was noticed that Joule heating owing to a magnetic field and porous medium heating have been discussed. Abd El-Aziz et al. [5] and Biswas et al. [6] have explored Casson fluid on unsteady MHD natural convective flow past a non-parallel porous plate along with doubled diffusion, radiation, and chemical reaction. Lakshmanna et al. [7], Seth et al. [8] and Srinivas et al. [9] have investigated numerically impact of joule heating as well as Casson fluid model on unsteady MHD flow imminent an oscillating vertical plate during a non-Darcy porous medium in aspect viscous dissipation as well as thermodiffusion. Implicit Crank–Nicolson finite difference technique was employed for solving coupled governing equations. Sobamowo et al. [10] have considered the influence of nanoparticles as well as thermal radiation on MHD free convection flow along with heat transfer of Casson nanofluids over a non-parallel plate. Vijaya et al. [11] have discussed chemical reaction as well as thermophysical properties on MHD Casson fluid through an oscillating non-parallel wall enclosed through permeable and effect of crosswise magnetic field and radiation in the aspect of heat source.

Joule heating is also renowned as ohmic heating, and resistive heating is the process by which the channel of an electric current during a conductor generated heat; i.e., the power of heating produced by an electrical conductor is relative to the product of its resistance as well as the square of the current. Recently, Chen et al. [12], Abo-Eldahab et al. [13], Babu et al. [14], Mohammed Ibrahim et al. [15, 16], and Barletta et al. [17] have presented the Joules as well viscous dissipation as at the same time heat generation has been taken into consideration in the equation of energy.

The objective of the current scrutinize is to investigate the impact of Hall as well as ion-slip current on steady MHD mixed convective Casson fluid flow over an infinite vertical porous plate with Ohmic heating as well as viscous dissipation in the aspect of soret and chemical reaction. The modelling equations are revolutionized into dimensionless equations and after that solved analytically utilizing perturbation law. Computations were performed graphically to explain the behaviour of fluid velocity, temperature as well as concentration with the dissimilarity of emerging physical parameters. Such examination has noteworthy applications in paper manufacturing industries, polymer processing industries and biomechanics, chemical engineering fields as well as industrialized processes for instance metal spinning, nuclear squander repositories, polymer extrusion, transpiration cooling, strengthening oil recovery

products, crammed bed catalytic reactors, continuous casting of metals, glass as well as fibre manufacture, and wire drawing.

2 Mathematical Formulation and Method of Solution

Contemplate the 2D MHD mixed convective dissipative Casson fluid model flow over an infinite perpendicular porous plate among a saturated porous medium through double diffusion in a homogeneous of a pressure grading. In this exploration, an account of that x^*-axis is purloined along the plate in upward way & y^*-axis is in the way of orthogonal to the flow. The physical model of the problem is shown in Fig. 1: Presumptively that transverse magnetic field of the uniform strength B_0 is to be employed in the way of y^*-axis. In view that the motion is two dimensional nevertheless, the length of the plate is large enough; therefore, all the physical variables are independent of x^*. u^* and v^* are the dimensional velocities components along x^* and y^* directions. Joules, viscous dissipation, and heat generation are contemplated in the equation of energy; in the same manner, Hall and ion-slip current is contemplated in equation of momentum. From the above hypothesis, the unsteady flow is governed by the following partial differential equations.

Equation of continuity:

$$\frac{\partial v^*}{\partial y^*} = 0 \tag{1}$$

i.e. $v^* = \text{constant} = -v_0$.
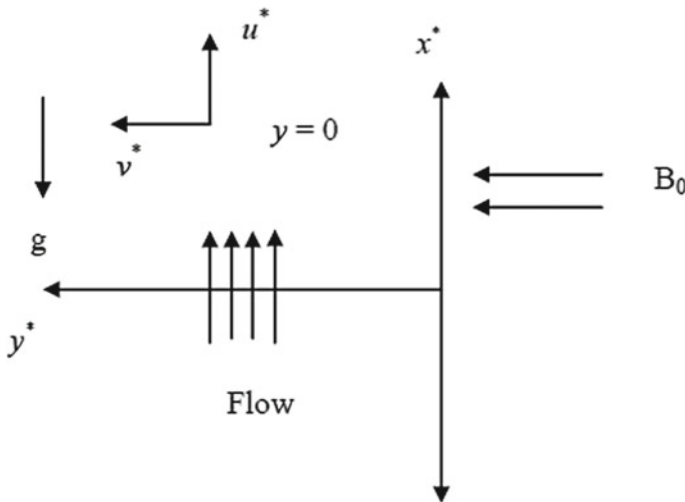
Fig. 1 Physical model of the problem

Equation of momentum:

$$
v^* \frac{\partial u^*}{\partial y^*} = \vartheta \left(1 + \beta^{-1}\right) \frac{\partial^2 u^*}{\partial y^{*2}} + g\beta\left(T^* - T^*_\infty\right) + g\beta^*\left(C^* - C^*_\infty\right) \left.\begin{array}{r}\\[1em]- \frac{\vartheta}{K^*}\left(1 + \beta^{-1}\right)u^* - \frac{B_0^2 \sigma_e (\alpha_e u^* + \beta_e w^*)}{\rho\left(\alpha_e^2 + \beta_e^2\right)}\end{array}\right\} \qquad (2)
$$

$$
v^* \frac{\partial w^*}{\partial y^*} = \vartheta \left(1 + \beta^{-1}\right) \frac{\partial^2 w^*}{\partial y^{*2}} - \frac{\vartheta}{k^*}\left(1 + \beta^{-1}\right)w^* + \frac{B_0^2 \sigma_e (\beta_e u^* - \alpha_e w^*)}{\rho\left(\alpha_e^2 + \beta_e^2\right)} \qquad (3)
$$

Equation of energy:

$$
v^* \frac{\partial T^*}{\partial y^*} = \frac{k}{\rho C_p} \frac{\partial^2 T^*}{\partial y^{*2}} + \frac{Q_0}{\rho C_p}\left(T^* - T^*_\infty\right) + \frac{\vartheta}{C_p}\left(1 + \frac{1}{\beta}\right)\left[\left(\frac{\partial u^*}{\partial y^*}\right)^2 + \left(\frac{\partial w^*}{\partial y^*}\right)^2\right] \left.\begin{array}{r}\\[1em]+ \frac{B_0^2 \sigma_e}{(\alpha_e^2 + \beta_e^2)\rho C_p}\left(\left[u^{*2}\right] + \left[w^{*2}\right]\right)\end{array}\right\} \qquad (4)
$$

Concentration species diffusion equation:

$$
v^* \frac{\partial C^*}{\partial y^*} = D \frac{\partial^2 C^*}{\partial y^{*2}} + D_1 \frac{\partial^2 T^*}{\partial y^{*2}} - k_1\left(C^* - C^*_\infty\right) \qquad (5)
$$

The corresponding boundary conditions of the problem:

$$
\left.\begin{array}{l} u = 0,\, T^* = T_w,\, C^* = C_w \quad \text{at } y = 0 \\[0.5em] u \to 0,\, T^* \to T_\infty,\, C^* = C_\infty \text{ as } y \to \infty \end{array}\right\} \qquad (6)
$$

$$
\chi(\eta) = \frac{u^*}{v_0},\, \Gamma(\eta) = \frac{w^*}{v_0},\, \eta = \frac{v_0 y^*}{\vartheta},\, k^* = \frac{\vartheta}{v_0^2 K_0}, \qquad (7)
$$

$$
\left.\begin{array}{l} \theta = \frac{(T^* - T_\infty)}{(T_w - T_\infty)},\, \phi = \frac{(C^* - C_\infty)}{(C_w - C_\infty)},\, Gr = \frac{\vartheta g\beta(T_w - T_\infty)}{v_0^3},\, k_r = \frac{\vartheta k_1}{v_0^2},\, \vartheta = \frac{\mu}{\rho} \\[0.8em] So = \frac{D_1(T_w - T_\infty)}{\vartheta(C_w - C_\infty)},\, M^2 = \frac{\sigma B_0^2 \vartheta}{\rho v_0^2},\, Gm = \frac{\vartheta g\beta^*(C_w - C_\infty)}{v_0^3},\, Sc = \frac{\vartheta}{D}, \\[0.8em] Pr = \frac{\vartheta \rho C_p}{k}\, Ec = \frac{v_0^2}{C_p(T_w - T_\infty)},\, Q = \frac{Q_0}{C_p \rho v_0^2}, \\[0.8em] N = \left[\left[1 + \frac{1}{\beta}\right]K_0 + \frac{M^2[-\alpha_e + i\beta_e]}{[\alpha_e^2 + \beta_e^2]}\right] \end{array}\right\} \qquad (8)
$$

Dropping asterisk in Eqs. (1)–(5) using Eq. (7), then we get

$$
\left(1 + \beta^{-1}\right)\chi'' + \chi' - K_0\left(1 + \beta^{-1}\right)[\chi] - \frac{M[\alpha_e \chi + \beta_e \Gamma]}{[\alpha_e^2 + \beta_e^2]} = -Gr\,\theta - Gm\,\phi \qquad (9)
$$

$$
\left(1 + \beta^{-1}\right)\Gamma'' + \Gamma' - Ka\left(1 + \beta^{-1}\right)[\Gamma] + \frac{M[\beta_e \chi - \alpha_e \Gamma]}{[\alpha_e^2 + \beta_e^2]} = 0 \qquad (10)
$$

$$
\theta'' + Pr\,\theta' = -Ec\,Pr\left[1 + \frac{1}{\beta}\right]\left(\left(\chi'\right)^2 + \left(\Gamma'\right)^2\right) - Q\,Pr\,\theta
$$

$$- \Pr Ec \frac{M^2}{\left[\alpha_e^2 + \beta_e^2\right]} \left(\chi^2 + \Gamma^2\right) \tag{11}$$

$$\phi'' + Sc\,\phi' - Kr\,Sc\,\phi = -So\,Sc\,\theta'' \tag{12}$$

The relevant boundary conditions are:

$$\left.\begin{array}{l} \eta = 0: \ \chi = 0, \Gamma = 0, \theta = 1, \phi = 1 \\ \eta \to 0: \ \chi \to 0, \Gamma \to 0, \theta \to 0, \phi \to 0 \end{array}\right\} \tag{13}$$

$$\left[1 + \frac{1}{\beta}\right] F'' + F' - N\left[F\overline{F}\right] = -Gr\,\theta - Gm\,\phi \tag{14}$$

The relevant boundary conditions are:

$$\left.\begin{array}{l} \eta = 0: \ F = 0, \theta = 1, \phi = 1 \\ \eta \to 0: \ F \to 0, \theta \to 0, \phi \to 0 \end{array}\right\} \tag{15}$$

where

$$F = \chi + i\Gamma \Rightarrow \frac{d}{dy}F = \frac{d}{dy}\chi + i\frac{d}{dy}\Gamma \ \& \ \overline{F}$$

$$= \chi - i\Gamma \Rightarrow \frac{d}{dy}\overline{F} = \frac{d}{dy}\chi - i\frac{d}{dy}\Gamma \tag{16}$$

To solve Eqs. (11), (12), and (14) let as assume

$$\left.\begin{array}{l} F(\eta) = F_0(\eta) + Ec\,F_1(\eta) + O(Ec)^2 \\ \theta(\eta) = \theta_0(\eta) + Ec\,\theta_1(\eta) + O(Ec)^2 \\ \phi(\eta) = \phi_0(\eta) + Ec\,\phi_1(\eta) + O(Ec)^2 \end{array}\right\} \tag{17}$$

Subject to the boundary conditions:

$$\left.\begin{array}{ll} \text{at} \ \eta = 0: & F_0 = 0, F_1 = 0, \theta_0 = 1, \theta_1 = 0, \phi_0 = 1, \phi_1 = 0 \\ \text{as} \ \eta \to \infty: & F_0 \to 0, F_1 \to 0, \theta_0 \to 0, \theta_1 \to 0, \phi_0 \to 0, \phi_1 \to 0 \end{array}\right\} \tag{18}$$

Using Eqs. (17) and (18), we get velocity, temperature, and concentration.

$$\left.\begin{array}{l} F(\eta) = \psi_2\,e^{-R_2 y} + \psi_3\,e^{-R_1 y} + A_2\,e^{-R_3 y} + Ec\,\psi_{17}\,e^{-2R_2 y} + Ec\psi_{18}\,e^{-2R_1 y} \\ \qquad + Ec\,\psi_{19}\,e^{-2R_3 y} + Ec\,\psi_{20}\,e^{-(R_1+R_2)y} + Ec\,\psi_{21}\,e^{-(R_1+R_3)y} \\ \qquad + Ec\psi_{22}\,e^{-(R_2+R_3)y} + Ec\psi_{23}\,e^{-R_1 y} + Ec\psi_{24}\,e^{-R_2 y} + Ec A_5\,e^{-R_3 y} \end{array}\right\} \tag{19}$$

$$\theta(\eta) = \mathrm{e}^{-R_1 y} + Ec\ \psi_4 \mathrm{e}^{-2R_2 y} + Ec\psi_5 \mathrm{e}^{-2R_1 y} + Ec\psi_6 \mathrm{e}^{-2R_3 y} + Ec\psi_7 \mathrm{e}^{-(R_1+R_2)y} \left.\right\}$$
$$+ Ec\ \psi_8 \mathrm{e}^{-(R_1+R_3)y} + Ec\psi_9 \mathrm{e}^{-(R_2+R_3)y} + EcA_3 \mathrm{e}^{-R_1 y} \left.\right\}$$

$$(20)$$

$$\phi(\eta) = \psi_1 \mathrm{e}^{-R_1 y} + A_1 \mathrm{e}^{-R_2 y} + Ec\psi_{10} \mathrm{e}^{-2R_2 y} + Ec\psi_{11} \mathrm{e}^{-2R_1 y} + Ec\psi_{12} \mathrm{e}^{-2R_3 y} \left.\right\}$$
$$+ Ec\psi_{13} \mathrm{e}^{-(R_1+R_2)y} + Ec\psi_{14} \mathrm{e}^{-(R_1+R_3)y} + Ec\psi_{15} \mathrm{e}^{-(R_2+R_3)y} \left.\right\}$$
$$+ Ec\psi_{16} \mathrm{e}^{-R_1 y} + EcA_4 \mathrm{e}^{-R_2 y} \left.\right\}$$

$$(21)$$

3 Results and Discussion

Figure 2 represents the behaviour of velocity for dissimilar estimators of Hall parameter β_e. From this figure, it was found that the enhancement of various values of Hall parameter leads to reduction in velocity and it is very near to the plate. Figure 3 reflects
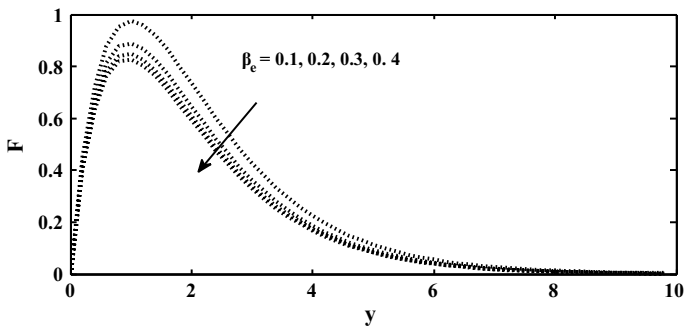
Fig. 2 Plot of velocity for varying β_e
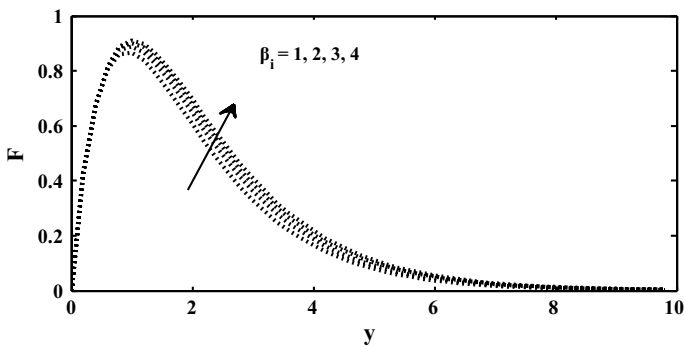
Fig. 3 Plot of velocity for varying β_i
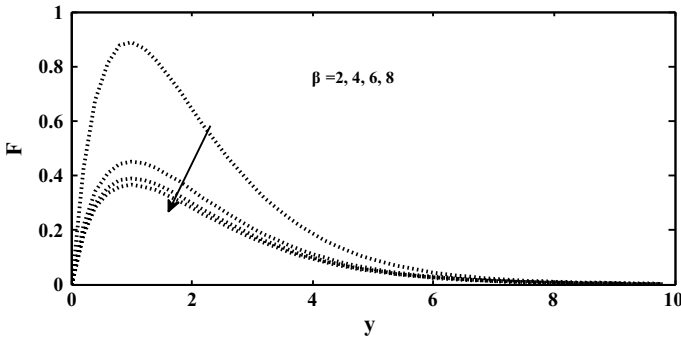
Fig. 4 Plot of velocity for varying β

the rise in velocity owing to enhancement of diverse values of ion-slip parameter β_i. Figure 4 depicts the distinction of velocity for diverse values of Casson fluid parameter in both cases. At this juncture from the figure, it was examined that the velocity is diminished owing to the incremental estimators of β. Figure 5 indicates that the outcomes of Eckert number Ec on velocity; here, in this figure, it was investigated that for dissimilar incremental values of Ec show the way to rise in velocity. Figure 6 establishes that for dissimilar values of Prandtl number (Pr) rises, then it leads to reduction in temperature. Figure 7 displays distinction of temperature for diverse values of soret parameter so. In this figure, it was observed that the enhancement of dissimilar estimator's of soret parameter leads to ascend in temperature. Figure 8 confirms that the influence of Eckert number on the temperature. As of the figure, it was determined that as the values of Ec rises, it leads to rise in temperature. For dissimilar values of the Schmidt number on the fluid concentration is illustrated in Fig. 9: From this figure, the outcomes indicate that the enhancement of Sc leads to decrease in concentration. Representative dissimilarity of the concentration along the spanwise coordinate y is exhibited in Fig. 10: As of this figure, it was recognized that for diverse values of soret, So rises; then, it leads to concentration rises significantly.
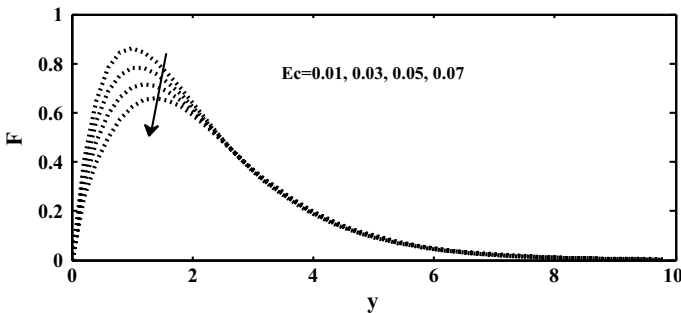
Fig. 5 Plot of velocity for varying Ec
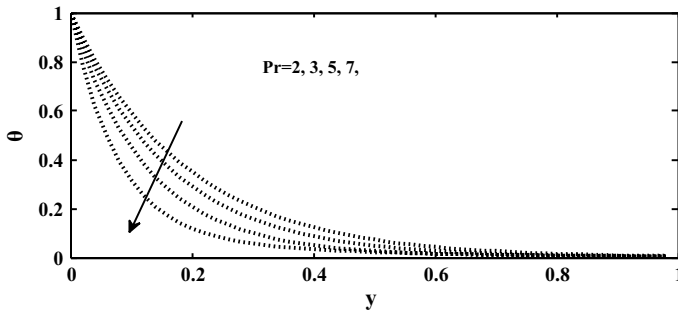
Fig. 6 Plot of temperature for varying Pr
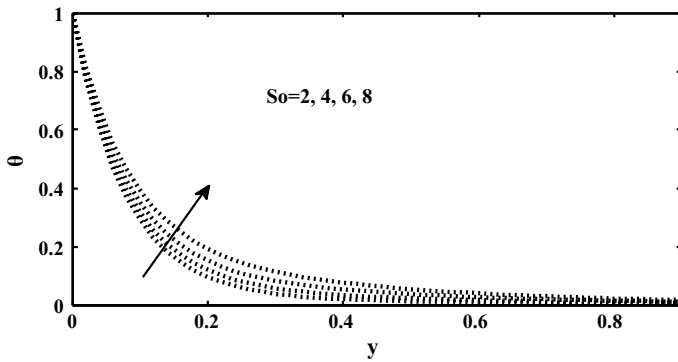
Fig. 7 Plot of temperature for varying *So*
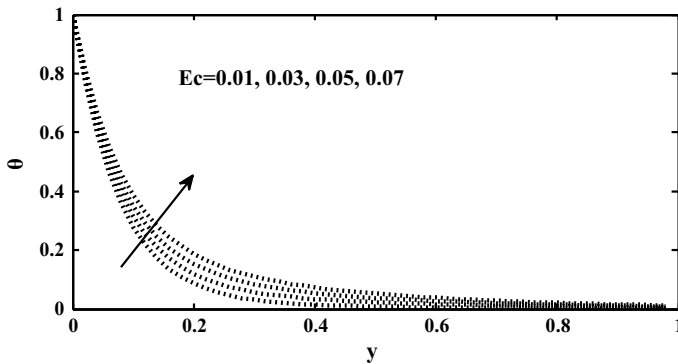
Fig. 8 Plot of temperature for varying *Ec*
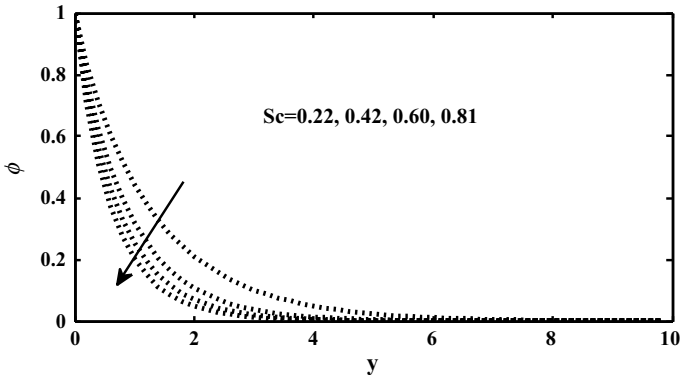
Fig. 9 Plot of concentration for varying *Sc*
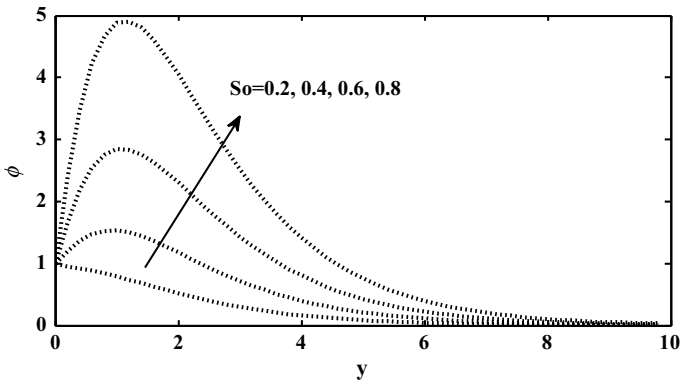
Fig. 10 Plot of concentration for varying *So*

Figure 11 demonstrates the performance of concentration for disparate estimators of chemical reaction (*Kr*). The results obtained from this figure were perceived that the concentration reduced due to rise in chemical reaction parameter.

4   Conclusions

- Velocity rises due to enhancement of diverse values of ion-slip parameter β_i. But reverser effect has been shown in case of Hall parameter β_e.
- As velocity profile is diminished due to the incremental values of β.
- As the fluid velocity rises with the dissimilar incremental values of *Ec* in velocity.
- As the concentration diminished with the enhancement values of Schmidt number *Sc* and chemical reaction *Kr*. But inverse effect was occurred in case of Soret.
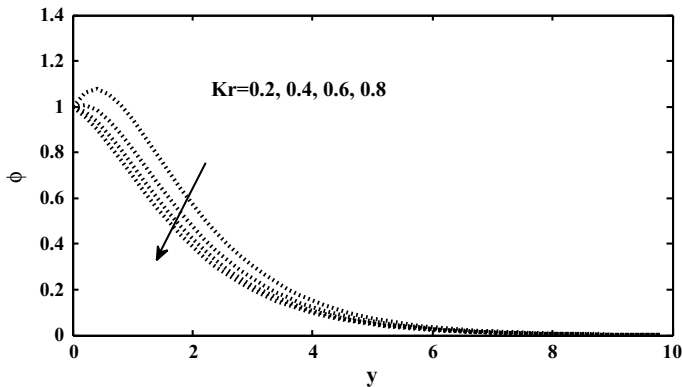
Fig. 11 Plot of concentration for varying *Kr*

References

1. Etwire CJ, Seini YI, Abe-I-Kpeng G (2017) MHD flow of Casson fluid over a vertical plate embedded in porous media with joule heating and convective boundary condition. Asian J Math Comput Res 19(2):50–64
2. Vinod Kumar G, Kiran Kumar R, Varma SVK (2018) Multiple slips and chemical reaction effects on MHD stagnation point flow of Casson fluid over a stretching sheet with viscous and joules heating. Front Heat Mass Transf 10(23):105–115
3. Prasad KV, Vajravelu K, Vaidya H, Rashidi M, Basha NZ (2018) Flow and heat transfer of a Casson liquid over a vertical stretching surface: optimal solution. Columbia Int Publ Am J Heat Mass Transf 5(1), 1–22
4. Ullah I, Khan I, Shafie S (2017) Heat and mass transfer in unsteady MHD slip flow of Casson fluid over a moving wedge embedded in a porous medium in the presence of chemical reaction. Numerical methods for partial differential Equations. Wiley Publ Online 35(5):1867–1891
5. Abd El-Aziz M, Afify AA (2018) Influences of slip velocity and induced magnetic field on MHD stagnation-point flow and heat transfer of Casson fluid over a stretching sheet. Hindawi Math Probl Eng 1(1):1–11
6. Biswas R, Mondal M, Sarkar DR, Ahmmed SF (2017) Effects of radiation and chemical reaction on MHD unsteady heat and mass transfer of Casson fluid flow past a vertical plate. J Adv Math Comput Sci 23(2):1–16
7. Lakshmanna B, Venkateswarlu S (2018) Unsteady MHD convective flow of an incompressible viscous fluid through porous medium over a vertical plate. Ann Pure Appl Math 16(2):451–460
8. Seth GS, Kumar R, Tripathi R, Bhattacharyya A (2018) Double diffusive MHD Casson fluid flow in a non-Darcy porous medium with Newtonian heating and thermo-diffusion effects. Int J Heat Technology 36(4):1571–1527
9. Srinivas S, Kumar CK, Reddy AS (2018) Pulsating flow of Casson fluid in a porous channel with thermal radiation, chemical reaction and applied magnetic field. Nonlinear Anal Model Control 23(2):213–233
10. Sobamowo MG (2018) Combined effects of thermal radiation and nano particles on free convection flow and heat transfer of Casson fluid over a vertical plate. Int J Chem Eng 18(1):1–25
11. Vijaya N, Hari Krishna Y, Kalyani K (2018) Soret and radiation effects on unsteady flow of a Casson fluid through porous vertical channel with expansion and contraction. Front in Heat Mass Transf 11(19):1–20

12. Chen C-H (2004) Combined heat and mass transfer in MHD free convection from a vertical surface with ohmic heating and viscous dissipation. Int J Eng Sci 42(7):699–13
13. Abo-Eldahab EM, El Aziz MA (2015) Viscous dissipation and Joule heating effects on MHD-free convection from a vertical plate with power-law variation in surface temperature in the presence of Hall and ios-slips currents. Appl Math Model 29(2):579–95
14. Babu VS, Reddy GVR (2011) Mass transfer effects on MHD mixed convective flow from a vertical surface with ohmic heating and viscous dissipation. Adv Appl Sci Res 2(4):138–46
15. Mohammed Ibrahim S, Effects of mass transfer, radiation, joule heating and viscous dissipation on steady MHD marangoni convection flow over a flat surface with suction and injection. Int J Eng Math 2013:9 (903818) (On press)
16. Mohammed Ibrahim S, Suneetha K (2016) Heat source and chemical effects on MHD convection flow embedded in a porous medium with Soret, viscous and Joules dissipation. 7(1):811–818
17. Barletta A, Celliv M (2018) Mixed convection MHD flow in a vertical channel. Int J Heat Mass Transf 5(4):6110–6117

Effect of Rotation and Fluid on Radial Vibrations in a Micropolar Elastic Solid Having a Fluid-Loaded Spherical Cavity

K. Somaiah

Abstract The main objective of this study is to investigate the angular rotation effect of the solid and density of the fluid on the radial vibrations in an unbounded micropolar elastic solid with a fluid-loaded spherical cavity. The micropolar elastic solid is homogeneous and isotropic, but the loaded fluid is homogenous, isotropic, and in viscid. Dispersion relation for radial vibrations of macro-displacements is derived and which is influenced by the loaded fluid and angular rotation of the solid, while the micro-rotational vibrations are not influenced by the loaded fluid and angular rotation. All these results are not obtained in any classical theory of elasticity. Under the MATLAB program, the numerical computations for a particular solid have been performed and have also been shown graphically to understand the effect of angular rotation of the solid and density of the loaded fluid on the behavior of phase velocity and dispersion relation.

Keywords Rotation · Fluid · Radial vibrations · Micropolar elastic solid · Spherical cavity

1 Introduction

The radial vibration study in a rotating elastic media is an important consideration of theoretical and practical applications in geophysics, seismology, and synthetic porous materials. It is also greatly applicable for verity engineering fields such as civil, mechanical, chemical, aerospace, and nuclear engineering. Chand et al. [1] presented his investigations on uniformly rotating homogeneous isotropic solids. The rotation effect on classical waves is discussed by many authors like Schenberg and Censor [2], Clarke and Burdess [3], and Destrade [4]. Rotation effect in magneto-thermo elastic solids is investigated by Sharma Thakur [5] and Othman and Song [6]. Mahmoud [7] discussed the angular rotation effect on Rayleigh waves. Recently, the effect of rotation on plane waves is studied by Somaiah [8].

K. Somaiah (✉)

Department of Mathematics, Kakatiya University, Warangal, Telangana 506009, India
e-mail: somaiahkamidi@gmail.com

In this chapter, we computed the frequency equation for radial vibrations in an unbounded rotating micropolar elastic media having a fluid filled spherical cavity. It is observed that these types of frequency equations are not obtained in any classical theory of elasticity.

2 Governing Equations

The governing equations of motion for an angular rotating homogenous generalized isotropic micropolar elastic solid are given by Eringen and Suhibi [9].

The equation of motion for rotating elastic solid is

$$(\lambda + \mu)u_{i,il} + (\mu + K)u_{l,ii} + K\varepsilon_{\lim}\phi_{m,i} + \rho\left[f_l - \ddot{u}_l + \vec{\Omega} \times \left(\vec{\Omega} \times \vec{u}_l\right)\right] = 0 \tag{1}$$

The balance of the stress moment equation is

$$(\alpha + \beta)\phi_{i,ll} + \gamma\phi_{l,ii} + K\varepsilon_{\lim}u_{m,i} - 2K\phi_l + \rho\left(L_l - J\ddot{\phi}_{lk}\right) = 0 \tag{2}$$

The stress tensor t_{kl} and couple stress tensor m_{kl} are given by

$$t_{ij} = \lambda u_{l,l}\delta_{ij} + \mu\left(u_{i,j} + u_{j,i}\right) + K\left(u_{i,j} - \varepsilon_{\lim}\phi_m\right) \tag{3}$$

$$m_{li} = \alpha\phi_{m,m}\delta_{li} + \beta\phi_{m,i} + \gamma\phi_{i,m} \tag{4}$$

where the vectors $\bar{u}$, $\bar{f}$, $\bar{L}$, $\bar{\phi}$, $\vec{\Omega}$ indicate the macro-displacements, body forces, body couples, micro-rotations, and angular rotations, respectively, and the scalars; namely, J is the micro-inertia, ρ is the density of the body, λ, μ, K, α, β, γ indicate elastic constants, and δ_{ij} is the Kronecker delta, while $\varepsilon_{\lim}$ is the permutation symbol; a suffix index l following a comma indicates partial differentiation with respect to the coordinate (x_l); dot superposed on a symbol denotes partial differentiation with respect to the time t.

3 Problem Formulation and Its Solution

Consider the uniform micropolar elastic medium of infinite extent with radius $r = a$. The medium is assumed to be rotating at a constant rate with constant angular velocity $\vec{\Omega} = (0, 0, \Omega)$ abut z-axis. Under the dynamical deformation of the medium, the additional terms are namely the time dependent part of centripetal acceleration

$\vec{\Omega} \times \left(\vec{\Omega} \times \vec{u} \right)$ and the Coriolis acceleration $2\,(\vec{\Omega} \times \dot{\vec{u}})$. We are interested in the derivation of frequency equations for the radial vibrations of macro-displacements and micro-rotations, so we consider those vectors in the following manner:

$\vec{u} = (u, 0, 0), \varphi^{\rightarrow} = (\varphi, 0, 0),$

with

$$\vec{u} = u(r, t)\hat{e}_r \tag{5}$$

$$\vec{\phi} = \phi(r, t)\hat{e}_r \tag{6}$$

where $\hat{e}_r$ is the unit vector at the position vector in the direction of tangent to the r-curve. On neglecting the body forces and body couples in the governing Eqs. (1)–(4), we obtain the following partial differential equations

$$\frac{\partial^2 u}{\partial r^2} + \frac{2}{r}\frac{\partial u}{\partial r} - \frac{2}{r^2}u = \frac{\rho}{(\lambda + 2\mu + K)}\left[\frac{\partial^2 u}{\partial t^2} - \Omega^2 u\right] \tag{7}$$

$$\frac{\partial^2 \phi}{\partial r^2} + \frac{2}{r}\frac{\partial \phi}{\partial r} - \frac{2}{r^2}\phi - \frac{2K}{(\alpha + \beta + \gamma)}\phi = \frac{\rho J}{(\alpha + \beta + \gamma)}\frac{\partial^2 \phi}{\partial t^2} \tag{8}$$

$$t_{rr} = (\lambda + 2\mu + K)\frac{\partial u}{\partial r} + \frac{2\lambda}{r}u \tag{9}$$

$$m_{rr} = (\alpha + \beta + \gamma)\frac{\partial \phi}{\partial r} + \frac{2\alpha}{r}\phi \tag{10}$$

For deriving the dispersion relation of the radial vibrations in an unbounded micropolar elastic solid having a spherical cavity filled with homogeneous in viscid fluid with density $\rho^{(f)}$, the governing equations for homogeneous in viscid fluid are taken from [10] as follows:

$$\nabla\left(\nabla \cdot u^{(f)}\right) = \frac{\rho^{(f)}}{\xi^{(f)}}\frac{\partial^2 u^{(f)}}{\partial t^2} \tag{11}$$

and

$$t_{rr}^{(f)} = \xi^{(f)}\left(\nabla \cdot u^{(f)}\right)\delta_{rr} \tag{12}$$

where $u^{(f)}$ represents the displacement vector of the solid in the presence of fluid, $\xi^{(f)}$ and $\rho^{(f)}$ are, respectively, the bulk modulus and density of the fluid.

For deriving the vibration relations in the radial direction, we assume that

$u^{(f)} = \left(u^{(f)}, 0, 0\right)$

with

$$u^{(f)} = \frac{\partial \psi^{(f)}}{\partial r} \tag{13}$$

where $\psi^{(f)}$ is the fluid potential.

Inserting Eq. (13) in Eqs. (11) and (12), we obtain the differential equation for the displacement potential $\psi^{(f)}$ in the liquid medium as,

$$\nabla^2 \psi^{(f)} = \frac{\rho^{(f)}}{\xi^{(f)}} \frac{\partial^2 \psi^{(f)}}{\partial t^2} \tag{14}$$

and

$$t_{rr}^{(f)} = \xi^{(f)} \nabla^2 \psi^{(f)} \tag{15}$$

where $\nabla^2 = \frac{\partial^2}{\partial r^2} + \frac{2}{r} \frac{\partial}{\partial r}$.

Equation (14) can be solved as [12], and it is given by

$$\psi^{(f)}(r, \ t) = F \sqrt{\frac{\pi}{2l}} \, \mathrm{e}^{-lr} \frac{1}{r} \mathrm{e}^{i\omega t} \tag{16}$$

The radial displacements in the presence of liquid $P^{(f)}$ are given by

$$P^{(f)} = -t_{rr}^{(f)} = F \sqrt{\frac{\pi}{2l}} \, \rho^{(f)} \frac{\omega 2}{r} \mathrm{e}^{i\omega t - lr} \tag{17}$$

$$u^{(f)} = \frac{\partial \psi^{(f)}}{\partial r} = -F \sqrt{\frac{\pi}{2l}} \frac{\rho^{(f)}}{r^2} \mathrm{e}^{i\omega t - lr} \tag{18}$$

The appropriate boundary condition is

$$t_{rr} = -P^{(f)} \text{ at } r = a \tag{19}$$

One can solve Eq. (7) in the form

$$u(r, \ t) = R(r) \, \mathrm{e}^{i\omega t} \tag{20}$$

On using Eq. (20) in Eq. (7), we obtain

$$\left[\nabla^2 - \frac{2}{r^2} + \frac{\rho(\omega^2 + \Omega^2)}{(\lambda + 2\mu + K)} \right] R = 0 \tag{21}$$

Suppose

$$x = gr \tag{22}$$

where

$$g^2 = \frac{\rho(\omega^2 + \Omega^2)}{(\lambda + 2\mu + K)} \tag{23}$$

Using Eqs. (22) and (23), Eq. (21) can be converted into the following second-order ordinary differential equation

$$\left[D^2 + \frac{2}{x}\left(D - \frac{1}{x} \right) + 1 \right] R = 0, \, D \equiv \frac{d}{dx} \tag{24}$$

The general solution of Eq. (24) is

$$R(x) = M \frac{d}{dx}\left(\frac{e^{ix}}{x} \right)$$

Hence,

$$u(r, \, t) = M\left[\frac{i}{gr} - \frac{1}{(gr)^2} \right] e^{i(\omega t + gr)} \tag{25}$$

where x is defined in Eq. (22); M is an arbitrary constant.

On using Eqs. (25) and (17) in Eq. (19), one can obtain the following frequency equation for radial macro-displacements

$$M(\lambda + 2\mu + K)\left[2i\left(\frac{\lambda - 1}{ga^2} \right) + 2\left(\frac{1 - \lambda}{g^2 a^3} \right) - \frac{1}{a} \right] = -F\left(\frac{\pi}{2a} \right)^{\frac{1}{2}} \xi^{(f)} \omega^{3/2} e^{(l+ig)a} \tag{26}$$

From Eq. (26), we observed that dispersion relation of radial macro-displacements is effected by loaded fluid in the cavity of the solid and this relation coincides with the results of Srinivas and Somaiah [11] in non-rotating and un loaded fluid solids. The additional dispersion relations are same as the results of Srinivas and Somaiah [11]. Also we observed that the classical dispersion results are obtained as K approaches to zero in Eq. (26).

4   Numerical Illustration

To understand the relation derived in Eq. (26), and square phase velocity $\upsilon^2 = \frac{\omega^2 a^2}{\pi^2}$ of radial displacement for $g = \sqrt{\frac{\rho(\omega_0^2 + \Omega^2)}{\lambda + 2\mu + K}}$ in great detail, we consider the natural frequency ω_0 of the solid as, $\omega_0 = 0.8$ (non-dimensional) and the material values of aluminum epoxy from [12] and the liquid parameters from [13] taken as follows: $\lambda = 7.59 \times 10^9$ N/m^2, $\mu = 1.89 \times 10^9$ N/m^2, $K = 0.015 \times 10^9$ N/m^2, $\rho = 2.192 \times 10^3$ kg/m^3, $J = 0.196 \times 10^{-6}$ m^2, $\xi^{(f)} = 2.14 \times 10^9$ N/m^2 and $\rho^{(f)} = 1.0 \times 10^3$ kg/m^3.

The frequency, square phase velocity curves against non-dimensional amplitude ratios $\frac{M}{F}$ for the speed of angular velocity $= 0, 1, 5, 100$ are shown in Figs. 1 and 2. It is observed that dispersions and phase velocities are inverse proportional to the speed of angular velocity in the given range of amplitude ratios, and also it is observed that zero dispersions and phase velocities appeared at angular rotation 100.

The frequency and square phase velocity against non-dimensional density ratios $\frac{\rho^{(f)}}{\xi^{(f)}}$ for angular velocity $= 0, 5, 20, 100$ are shown in Figs. 3 and 4. It is observed that dispersions and phase velocities are not effected by the fluid density in the rotating solids. Constant phase velocities and dispersions appeared in rotating fluid-loaded solids. Dispersions and phase velocities are inversely proportional to the density of the fluid in non-rotating solids.
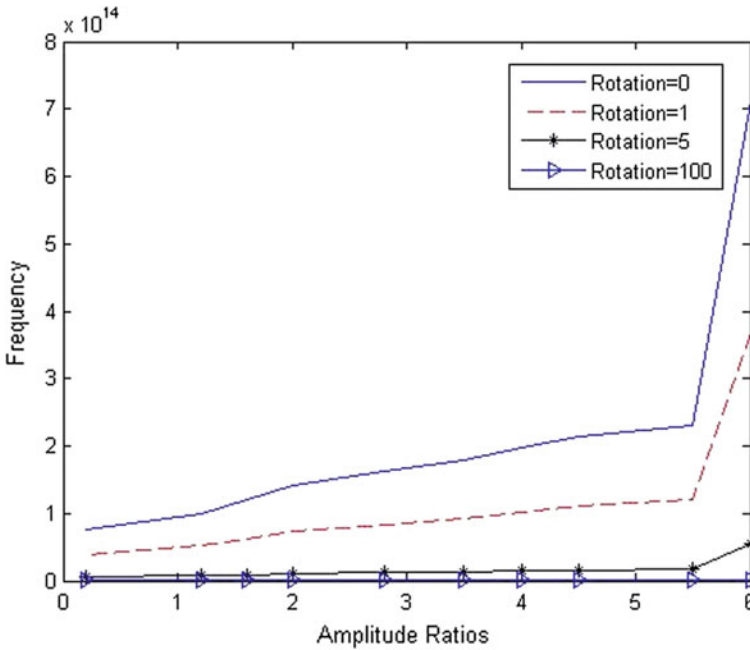
Fig. 1   Variation of frequency versus non-dimensional amplitude ratios
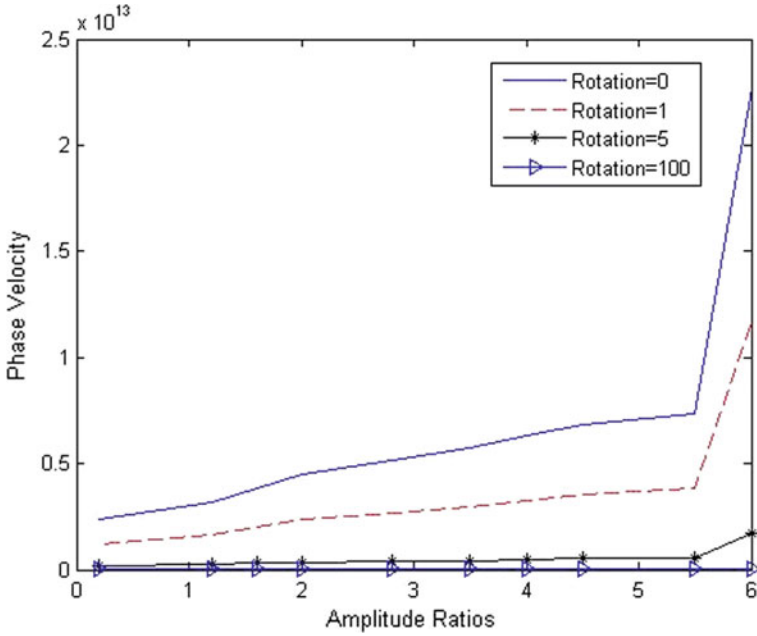
Fig. 2 Phase velocity against non-dimensional amplitude ratios
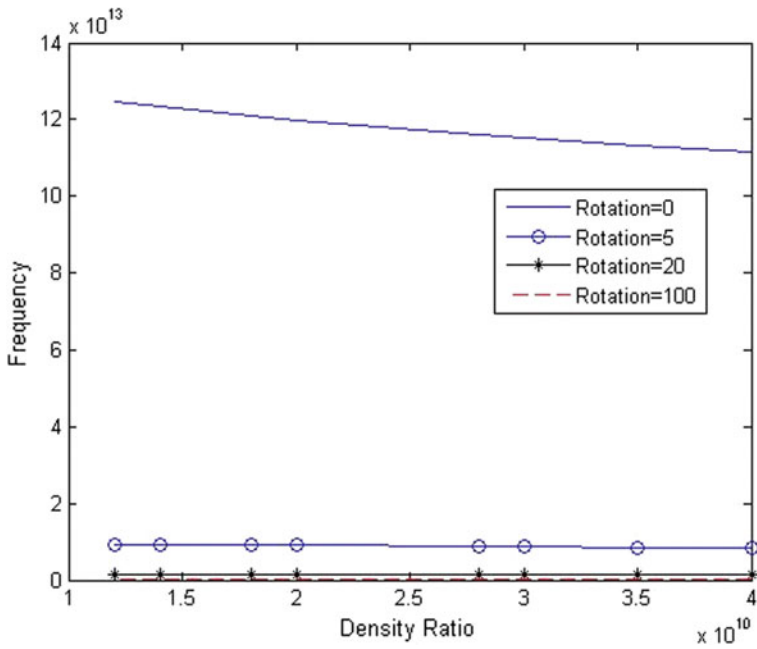
Fig. 3 Variation of frequency versus non-dimensional density ratios
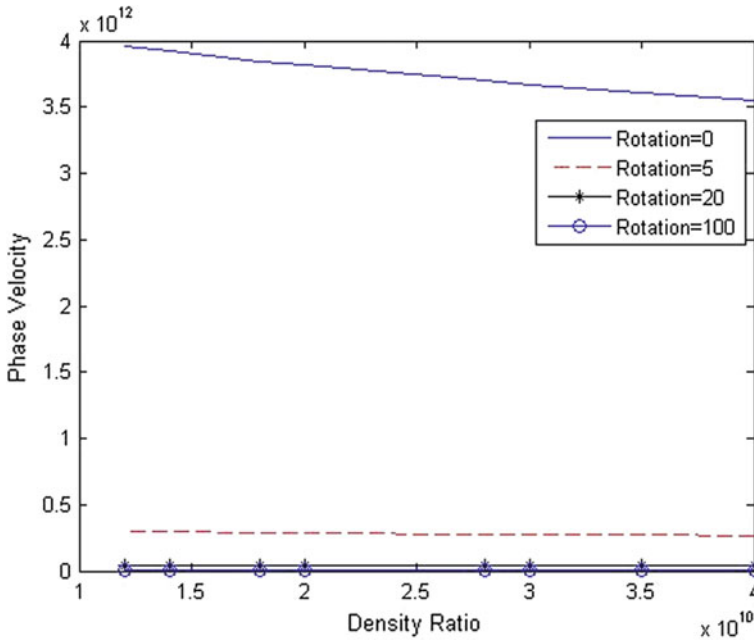
Fig. 4 Phase velocity against non-dimensional density ratios

The dispersion and phase velocity curves for non-dimensional rotations for different amplitude ratios are shown in Figs. 5 and 6. It is observed that dispersions approach to zero at rotation speeds 4×10^{12} and 6.5×10^{12} and dispersion, phase velocity curves are suddenly falling down at rotation speed 5×10^{12} for all amplitude ratios.

5   Concluding Remarks

For investigating the rotation effect and loaded fluid on radial vibrations, we consider a micropolar elastic media with a spherical cavity. Throughout this theoretical computations and numerical calculations, we conclude the following:

1. Frequencies pertaining to displacements are depending on loaded fluid and angular velocity.
2. The dispersion relations of micro-rotations coincide with the results of [12].
3. Frequencies and phase velocities are inversely proportional to the speed of angular velocity.
4. Frequencies and phase velocities are not effected by the fluid density in the rotating solids.
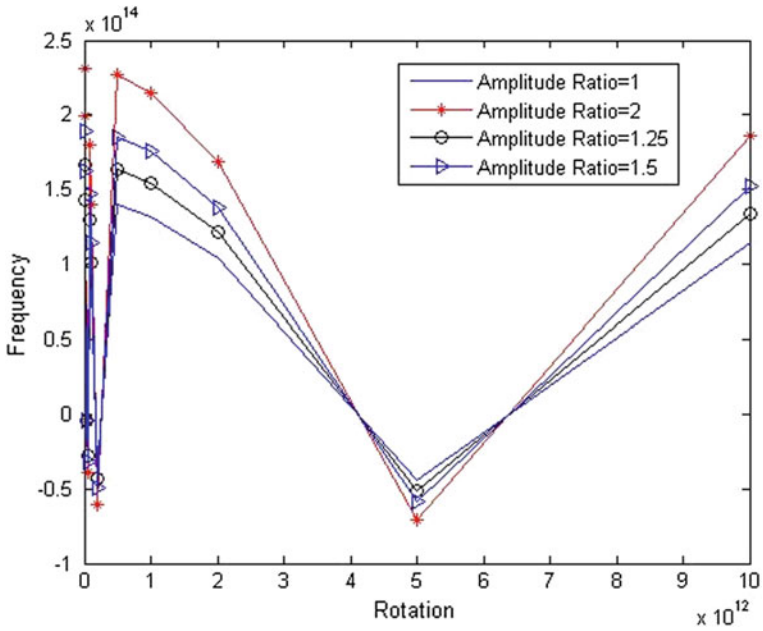
Fig. 5 Variation of frequency versus rotation
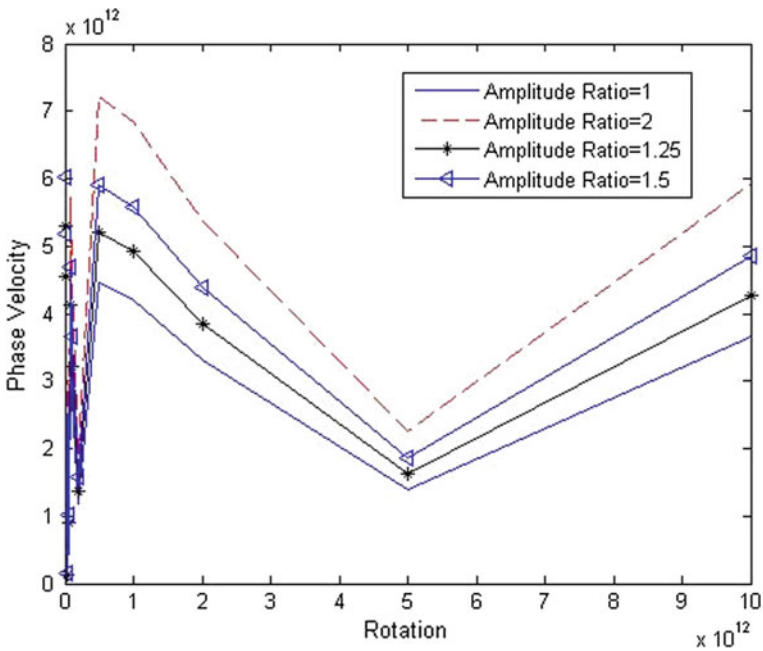
Fig. 6 Phase velocity against rotation

5. Constant phase velocities and frequencies appeared in rotating fluid-loaded solids.
6. Frequencies and phase velocities are inversely proportional to the density of the fluids in non-rotating solids.

References

1. Chand D, Sharma JN, Sud SP (1990) Transient generalized magneto-thermo-elastic waves in a rotating half-space. Int J Eng Sci 28(6):547–556
2. Schoenberg M, Censor D (1973) Elastic waves in rotating media. Quart Appl Math 31(1):115–125
3. Clarke NS, Burdess JS (1994) Rayleigh waves on a rotating surface. J Appl Mech Trans ASME 61(3):724–726
4. Destrade M (2004) Surface a acoustic waves in rotating orthorhombic crystals. Proc Royal Soc A Math Phys Eng Sci 460(2042):653–665
5. Sharma JN, Thakur MD (2006) Effect of rotation on Rayleigh Lamb waves in magneto-thermo elastic media. J Sound Vibr 296(4–5):871–887
6. Othman MIA, Song Y (2004) Effect of magneto-thermo elastic waves from rotation on plane waves in generalized thermo elasticity with two relaxation times. Int J Solids Struct 41(11–12):2939–2956
7. Mahmoud SR (2011) Effect of rotation, gravity field and initial stress on generalized magneto-thermo elastic Rayleigh waves in a granualar medium. Appl Math Sci 5(41–44):2013–2032
8. Somaiah K (2018) Plane wave propagation in a rotating micro-stretch elastic solid in special case. Springer Lecture Notes in Mechanical Engineering, pp 661–672
9. Eringen AC, Suhubi ES (1964) Non-linear theory of simple micro-elastic solids-I. Int J Eng Sci 2:189–203
10. Kumar R, Divya, Kumar K (2013) Propagation of wave through cylindrical bore in a swelling porous elastic media. Mater Phys Mech 16:135–143
11. Srinivas R, Somaiah K (2018) Radial vibrations in unbounded micropolar elastic solid with fluid-loaded spherical cavity. Springer Lecture Notes in Mechanical Engineering, pp 431–438
12. Deswal S, Kumar R (2010) Wave motion in a viscous fluid filled bore in a micropolar elastic medium with voids. Proc Natl Acad Sci India, Section-A 80:223–234
13. Ewing WM, Jardetzky WS, Press F (1957) Elastic waves in layered media. The Mac-Graw. Hill Company, New York

Convex Cylindrical Surface-Modified Rayleigh Waves

A. Chandulal

Abstract In this paper, we consider the effect of curvature on the surface wave propagation in a micromorphic medium. It is interesting to observe that the additional waves found in the study of surface waves with curved boundary are dispersive without any cutoff frequency.

1 Introduction

Wave propagation theory is usually discussed in terms of two general phenomena, namely the propagation of longitudinal and transverse waves by omitting the body forces f_x, f_y, f_z, i.e., by neglecting the effect of gravity. Moreover, we consider wave propagation only in those cases where all boundaries and interfaces are parallel planes, but in some cases of importance, the interfaces are curved usually being cylinders and spheres. The media are assumed to be perfectly elastic in these problems. It is well known; however, the dissipation accompanies vibrations in solid media, because of conversion of elastic energy to heat. Several mechanisms have been proposed for energy dissipation in vibrating solids, and these may be grouped collectively under internal friction. For a discussion of internal friction, one may refer the work of Kolsky [5]. In general, the effect of internal friction is to produce attenuation and dispersion of elastic waves. In practice, however, the attenuation is slight and dispersion is negligible for earthquake waves.

Gravity is the principal force which concerns in the problem of wave propagation in such cases $f_x = f_y$ and $f_z = g$. Jefferys [4] showed that the gravity terms are significant for compressional waves in the earth. The effect of gravity on Rayleigh wave propagation in a solid half-space is studied by Bromwich [1]. The effect of gravity on surface wave propagation in a compressible solid half-space was discussed

A. Chandulal (✉)
Department of Mathematics, R. S. Vidyapeetha, Tirupati, Andhra Pradesh 517507, India
e-mail: chandulal2009@gmail.com

by Love [6], and he shows that the velocity of Rayleigh wave on the whole is likely to be increased by the gravity.

The surface waves in an elastic solids also effected by the curvature and gravity. The effect of curvature on surface waves are initially disucussed by Sezawa [8], and Viktorv [9] investigated the effect of curvature on surface waves for both convex and slightly.

Concave cylindrical surface. Surface waves on a cured surface are dispersive. The effect of curvature on Stoneley waves is considered in detail by Epstein [2]. Sambaiah et al. [7] have discussed the Rayleigh wave propagation in micromorphic elastic half-space and have shown that the additional waves found are dispersive with certain cutoff frequencies.

2 Basic Equations

Using the principles of vector calculus related to curvilinear coordinates, it can be shown that

$$\Delta = \frac{1}{r}\frac{\partial}{\partial r}(r\,u_r) + \frac{1}{r}\frac{\partial u_\theta}{\partial \theta} + \frac{\partial u_z}{\partial z} \tag{1}$$

$$\Delta^1 = \frac{1}{r}\frac{\partial}{\partial r}(r\,\phi_r) + \frac{1}{r}\frac{\partial \phi_\theta}{\partial \theta} + \frac{\partial \phi_z}{\partial z} \tag{2}$$

$$\text{Curl}\,\vec{u} = \left[\left(\frac{1}{r}\frac{\partial u_z}{\partial \theta} - \frac{\partial u_\theta}{\partial z}\right), \left(\frac{\partial u_r}{\partial z} - \frac{\partial u_z}{\partial r}\right), \frac{1}{r}\frac{\partial}{\partial r}(ru_\theta) - \frac{1}{r}\frac{\partial u_r}{\partial \theta}\right] \tag{3}$$

$$\text{curl}\,\vec{\phi} = \left[\left(\frac{1}{r}\frac{\partial \phi_z}{\partial \theta} - \frac{\partial \phi_\theta}{\partial z}\right), \left(\frac{\partial \phi_r}{\partial z} - \frac{\partial \phi_z}{\partial r}\right), \left(\frac{1}{r}\frac{\partial}{\partial r}(r\phi_\theta) - \frac{1}{r}\frac{\partial \phi_r}{r\theta}\right)\right] \tag{4}$$

The equations of motion involving macro-displacement and micro-rotation in vectorial form are given by

$$(A_1 + 2A_2)\text{grad}\,\Delta - (A_2 + A_3)\text{curl}(\text{curl}\,\vec{u}) + 2A_3\,\text{curl}\,\vec{\phi} + \rho\vec{f} = \rho\ddot{\vec{u}} \tag{5}$$

$$2(B_3 + B_4 + B_5)\text{grad}\,\Delta^1 - 2B_3\,\text{curl}\left(\text{curl}\,\vec{\phi}\right)$$
$$- 2A_3\,\text{curl}\,\vec{u} - 4A_3\vec{\varphi} + \rho\vec{\ell} = \rho j\ddot{\vec{\phi}} \tag{6}$$

The equations of motion involving micro-strains are given by

$$(A_1 + 2A_2)\frac{\partial}{\partial r}\Delta - 2(A_2 + A_3)\left(\frac{1}{r}\frac{\partial \widetilde{w_z}}{\partial \theta} - \frac{\partial \widetilde{w_\theta}}{\partial z}\right) + 4A_3\widetilde{w_r}^1 + \rho f_r = \rho\frac{\partial^2 u_r}{\partial t^2} \tag{7}$$

$$(A_1 + 2A_2)\frac{1}{r}\frac{\partial \Delta}{\partial \theta} - 2(A_2 + A_3)\left(\frac{\partial w_r^{\sim}}{\partial z} - \frac{\partial w_z^{\sim}}{\partial r}\right) + 4A_3 w_\theta^{\sim^1} + \rho f_\theta = \rho \frac{\partial^2 u_\theta}{\partial t^2} \quad (8)$$

$$(A_1 + 2A_2)\frac{\partial}{\partial z}\Delta - 2(A_2 + A_3)\left(\frac{1}{r}\frac{\partial}{\partial r}(rw^{\sim}\theta)\frac{-1}{r}\frac{\partial w_r^{\sim}}{\partial \theta}\right) + 4A_3 w_z^{\sim^1}$$

$$+ \rho f_z = \rho \frac{\partial^2 u}{\partial t^2} \quad (9)$$

$$2(B_3 + B_4 + B_5)\frac{\partial}{\partial r}\Delta^1 - 4B_3\left[\frac{1}{r}\frac{\partial w_z^{\sim^1}}{\partial \theta} - \frac{\partial w_\theta^{\sim^1}}{\partial z}\right] + 4A_3 w_r^{\sim}$$

$$- 4A_3\phi_r + \rho \ell_r = \rho j \frac{\partial^2 \phi_r}{\partial t^2} \quad (10)$$

$$2(B_3 + B_4 + B_5) - \frac{1}{r}\frac{\partial}{\partial r}\Delta^1 - 4B_3\left[\frac{\partial w_r^{\sim^1}}{\partial z} - \frac{\partial w_z^{\sim^1}}{\partial r}\right] + 4A_3 w_\theta^{\sim}$$

$$- 4A_3\phi_\theta + \rho \ell_\theta = \rho j \frac{\partial^2 \phi_\theta}{\partial t^2} \quad (11)$$

$$2(B_3 + B_4 + B_5)\frac{1}{r}\frac{\partial}{\partial z}\Delta^1 - 4B_3\left[\frac{1}{r}\frac{\partial}{\partial r}\left(rw_\theta^{\sim^1}\right) - \frac{1}{r}\frac{\partial w_r^{\sim^1}}{\partial \theta}\right]$$

$$+ 4A_3 w_z^{\sim} - 4A_3\phi_z + \rho \ell_z = \rho j \frac{\partial^2 \phi_z}{\partial t^2} \quad (12)$$

The equations of motion given by (5) and (6) or (7)–(12) can also be written in other form. We know that from vector calculus

$$\nabla^2 \vec{F} = \nabla\left(\nabla.\vec{F}\right) - \nabla \times \left(\nabla \times \vec{F}\right) \quad (13)$$

Using (13), Eqs. (5) and (6) can be expressed as

$$(A_1 + A_2 - A_3)\text{grad}\,\Delta + (A_2 + A_3)\nabla^2\,\tilde{u} + 4A_3\,\vec{w} + \rho\vec{f} = \rho\ddot{\vec{u}} \quad (14)$$

$$2(B_4 + B_5)\,\text{grad}\,\Delta^1 + 2B_2\nabla^2\,\vec{\phi} + 4A_3\tilde{w} - 4A_3\vec{\phi} + \rho\vec{\ell} = \rho\ddot{\vec{\phi}} \quad (15)$$

Equations (14) and (15) in terms of components are

$$(A_1 + A_2 - A_3)\frac{\partial}{\partial r}\Delta + (A_2 + A_3)\nabla^2 u_r + 4A_3 w_r^{\sim^1} + \rho f_r = \rho \frac{\partial^2 u_r}{\partial t^2} \quad (16)$$

$$(A_1 + A_2 - A_3)\frac{1}{r}\frac{\partial}{\partial \theta}\Delta + (A_2 + A_3)\nabla^2 u_\theta + 4A_3 w_\theta^{\sim^1} + \rho f_\theta = \rho \frac{\partial^2 u_\theta}{\partial t^2} \quad (17)$$

$$(A_1 + A_2 - A_3)\frac{\partial}{\partial z}\Delta + (A_2 + A_3)\nabla^2 u_z + 4A_3 w_{\widetilde{z}} + \rho f_z = \rho \frac{\partial^2 u_z}{\partial t^2} \qquad (18)$$

$$2(B_4 + B_5)\frac{\partial}{\partial r}\Delta^1 + 2B_3 \nabla^2 \phi_r + 4A_3 w_{\widetilde{r}} - 4A_3 \phi_r + \rho \ell_r = \rho j \frac{\partial^2 \phi_r}{\partial t^2} \qquad (19)$$

$$2(B_4 + B_5)\frac{1}{r}\frac{\partial}{\partial \theta}\Delta^1 + 2B_3 \nabla^2 \phi_\theta + 4A_3 w_{\widetilde{\theta}} - 4A_3 \phi_\theta + \rho \ell_\theta = \rho j \frac{\partial^2 \phi_\theta}{\partial t^2} \qquad (20)$$

$$2(B_4 + B_5)\frac{\partial}{\partial z}\Delta^1 + 2B_3 \nabla^2 \phi_z + 4A_3 w_{\widetilde{z}} - 4A_3 \phi_z + \rho \ell_z = \rho j \frac{\partial^2 \phi_z}{\partial t^2} \qquad (21)$$

where

$$\nabla^2 = \frac{\partial^2}{\partial r^2} + \frac{1}{r}\frac{\partial}{\partial r} + \frac{1}{r^2}\frac{\partial^2}{\partial \theta^2} + \frac{\partial^2}{\partial z^2} \qquad (22)$$

3   Solution of the Problem

Consider a convex cylindrical surface and let the axial components of displacement be set equal to zero, i.e.,

$$u_z = 0 \quad \text{And} \quad \phi_r = \theta_\theta = 0 \qquad (23)$$

Then, for the plane strain problem under discussion, the macro-displacement and micro-rotation vector are

$$\vec{u} = (u_r, u_\theta, 0) \qquad (24)$$

and

$$\vec{\phi} = (0, 0, \phi_z) \qquad (25)$$

And we suppose that these are independent of z and are function of r, θ and time t only. In view of (24) and (25), Eqs. (1)–(4) and (22) give

$$\Delta^1 = 0 \ w_{\widetilde{r}} = 0$$
$$w_{\widetilde{\theta}} = 0 \ w_{\widetilde{z}}^{1} = 0 \qquad (26)$$

$$\Delta = \frac{1}{r}\frac{\partial}{\partial r}(ru_r) + \frac{1}{r}\frac{\partial u_\theta}{\partial \theta} \quad \text{And} \quad \nabla^2 = \frac{\partial^2}{\partial r^2} + \frac{1}{r}\frac{\partial}{\partial r} + \frac{1}{r^2}\frac{\partial^2}{\partial \theta^2} \qquad (27)$$

Introducing

$$\phi_z = \phi \tag{28}$$

For convenience, the equations of motion (16)–(21) for plane strain problem in the absence of body forces and surface loads are reduced to

$$(A_1 + A_2 - A_3)\frac{\partial}{\partial r}\Delta + (A_2 + A_3)\nabla^2 u_r + 4A_3\frac{1}{r}\frac{\partial \phi}{\partial \theta} = \rho\frac{\partial^2 u_r}{\partial t^2} \tag{29}$$

$$(A_1 + A_2 - A_3)\frac{1}{r}\cdot\frac{\partial \Delta}{\partial \theta} + (A_2 + A_3)\nabla^2 u_\theta + 4A_3\frac{\partial \phi}{\partial r} = \rho\frac{\partial^2 u_\theta}{\partial t^2} \tag{30}$$

and

$$2B_3\nabla^2\varphi + 4A_3\left(\frac{\partial u_\theta}{\partial r} + \frac{u_\theta}{r} - \frac{1}{r}\frac{\partial u_\theta}{\partial \theta}\right) - 4A_3\phi = \rho j\frac{\partial^2 \phi}{\partial t^2} \tag{31}$$

Equations (29)–(31) are the coupled equations which are the field equations for the problem under study. Similarly, the equations from (7)–(12) reduce to

$$(A_1 + 2A_2)\frac{\partial}{\partial r}\Delta - 2(A_2 + A_3)\frac{1}{r}\frac{\partial}{\partial \theta}\widetilde{w_z} + 4A_3\frac{r}{r}\frac{\partial \phi}{\partial \theta} = \rho\frac{\partial^2 u_r}{\partial t^2} \tag{32}$$

$$(A_1 + 2A_2)\frac{1}{r}\frac{\partial \Delta}{\partial \theta} + 2(A_2 + A_3)\frac{\partial \widetilde{w_z}}{\partial r} - 4A_3\frac{\partial \phi}{\partial r} = \rho\frac{\partial^2 u\theta}{\partial t^2} \tag{33}$$

and

$$2B_3\nabla^2 + 4A_3\widetilde{w_z} - 4A_3\phi = \rho j\frac{\partial^2 \phi}{\partial t^2} \tag{34}$$

Suppose

$$
\begin{array}{ll}
C_1^2 = \frac{A_1+2A_2-2A_3}{\rho}; & C_2^2 = \frac{A_2-A_3}{\rho}; \\
C_3^2 = \frac{2A_3}{\rho}; & C_4^2 = \frac{2B_3}{\rho j}; \\
C_5^2 = \frac{2(B_4+B_5)}{\rho j}; & \omega_0^2 = \frac{2A_3}{\rho j}
\end{array} \tag{35}
$$

Now, Eqs. (32)–(34) can also be written as

$$\left(C_1^2 + C_3^2\right)\nabla^2\Delta = \frac{\partial^2}{\partial t^2}\Delta \tag{36}$$

$$\left(C_2^2 + C_3^2\right)\nabla^2\widetilde{w_z} - C_3^2\nabla^2\phi = \frac{\partial^2 \widetilde{w_z}}{\partial t^2} \tag{37}$$

$$C_4^2 \nabla^2 \phi = \frac{\partial^2 \phi}{\partial t^2} + 2w_0^2 \phi - 2w_0^2 \widetilde{w_z} \tag{38}$$

Now, the solution of the above three equations in the form of time-harmonic wave can be taken as

$$u_r = \left[-\frac{A}{k_\alpha^2} \frac{d}{dr} J_n(k_\alpha r) + \frac{2ni}{k_\beta^2} \frac{B}{r} \frac{1}{r} J_n(k_\beta r) \right] + \frac{2niC}{rk_\alpha^2} . J_n(k_\gamma r) \exp[i(\omega t + n\theta)] \tag{39}$$

$$u_\theta = \left[-\frac{A}{k_\alpha^2} \frac{in}{r} J_n(k_\alpha r) - \frac{2b}{k_\beta^2} \frac{d}{dr} J_n(k_\beta r) - \frac{2C}{k_r^2} \frac{d}{dr} J_n(k_r r) \right] \exp[i(wt + n\theta)] \tag{40}$$

$$\phi = \left[\frac{2B}{k_\beta^2} b_1 J_n(k_\beta r) + \frac{b_0 C}{k_\gamma^2} J_n(k_\gamma r) \right] \exp[i(\omega t - n\theta)] \tag{41}$$

where

$$\begin{aligned}
& k_\alpha^2 = \frac{\omega^2}{C_1^2 + C_3^2}, \; k_\beta = \frac{\omega^2}{C_2^2 + C_3^2}, \; k_\gamma^2 = \frac{\omega^2 - 2\omega_0^2}{C_4^2}, \; \omega = kc \\
& b_0 = \frac{2\omega_0^2 - \omega}{\omega_0^2} \quad k = \frac{2\pi}{\Lambda}, \qquad b_1 = \frac{C_4^2(k_\beta^2 - k_\gamma^2)}{2\omega_0^2}, \\
& k = \frac{2\pi}{\Lambda} \qquad \text{and} \qquad n = ka = \frac{n\pi a}{\Lambda}
\end{aligned} \tag{42}$$

k is the wave number, c is the phase velocity, n is the number of complete circum perennial wave, as is the radius of the convex cylindrical surface, $J_n(x)$ is Bessel function of first kind of order n and A, B, C are constants. The conditions of a traction-free surface at $r = a$ and bounded stresses at $r = 0$ are imposed and they are

$$t_{rr} = A_1 \left[\frac{\partial u_r}{\partial r} + \frac{u_r}{r} + \frac{1}{r} \frac{\partial u_\theta}{\partial \theta} \right] + 2A_2 \frac{\partial u_r}{\partial r} = 0 \quad \text{at } r = a \tag{43}$$

$$t_{r\theta} = 2A_2 \left[\frac{1}{r} \frac{\partial u_r}{\partial \theta} + \frac{\partial u_\theta}{\partial r} - \frac{u_\theta}{r} \right] + 2A_3 \left[\frac{\partial u_\theta}{\partial r} + \frac{u\theta}{r} - \frac{1}{r} \frac{\partial u_r}{\partial \theta} \right]$$
$$+ 2A_3 \varphi = 0 \quad \text{at } r = a \tag{44}$$

$$m_{13} = -2B_3 \frac{\partial \phi}{\partial r} = 0 \quad \text{at } r = a \tag{45}$$

and these stresses must remain bounded as r approaching to zero.

Now, substituting the macro-displacement and micro-rotation components given by (39)–(41) into the boundary conditions (43)–(45) yields a set of homogenous equations in A, B and C.

$$\left[-(A_1 + 2A_2) J_n^{11}(k_\alpha a) - \frac{A_1}{a} \left[J_n^1(k_\alpha a) - \frac{n^2}{a} J_n(k_\alpha a) \right] A \right.$$

$$+ \frac{2A_2 ni}{a} \left\{ J_n^1(k_\beta a) - \frac{1}{a} J_n(k_\beta a) \right\} B$$

$$+ \frac{2A_2 ni}{a} \left\{ J_n^1(k_\gamma a) - \frac{1}{a} J_n \right\} C = 0 \tag{46}$$
$$\left. (k_\gamma a) \right]$$

$$\left[\frac{-in(A_2 + 2A_3)}{a} \left\{ J_n^1(k_\alpha a) - \frac{1}{a}(k_\gamma a) \right\} A \right.$$

$$+ \left[(-A_2) \left\{ J_n^{11}(k_\beta a) - \frac{1}{a} J_n^1(k_\gamma a) + \frac{n^2}{a^2} J_n(k_\beta a) \right\} \right]$$

$$+ \left[(-A_3) \left\{ J_n^{11}(k_\alpha a) - a J_n(k_\beta a) \right\} B \right.$$

$$+ \left[-2A_2 \left\{ J_n(k_\gamma a) - \frac{1}{a} J_n^1(k_\alpha a) + \frac{n^2}{a^2} J_n(k_r a) \right\} C = 0 \tag{47}$$

$$b_1 J_4(k_\beta a) B + b_0 J_n^1(k_r a) c = 0 \tag{48}$$

For this existence of non-trivial solution of the Eqs. (46)–(48), the determinant of the coefficients must vanish, i.e., (49)

$$\left| a_{ij} \right| = 0 \tag{49}$$

where

$$a_{11} = -(A_1 + 2A_2) J_n^{11}(k_\alpha a) - \frac{A_1}{a} \left\{ J_n^1(k_\alpha a) - \frac{n^2}{a} J_n(k_\alpha a) \right\}$$

$$a_{12} = \frac{2A_2 ni}{a} \left\{ J_n^1(k_\beta a) - \frac{1}{a} J_n(k_\beta a) \right\}$$

$$a_{13} = \frac{2A_2 ni}{a} \left\{ J_n^1(k_\gamma a) - \frac{1}{a} J_n(k_\gamma a) \right\}$$

$$a_{21} = \frac{-in(A_2 + 2A_3)}{a} \left\{ J_n^1(k_\alpha a) - \frac{1}{a} J_n(k_\alpha a) \right\}$$

$$a_{22} = -A_2 \left[J_n^{11}(k_\beta a) - \frac{1}{a} J_n^1(k_\gamma a) + \frac{n^2}{a^2} J_n(k_\beta a) \right] - 2A_3 \left[J_n^{11}(k_\gamma a) + a J_n(k_\beta a) \right]$$

$$a_{23} = -2A_2 \left[J_n(k_\gamma a) - \frac{1}{a} J_n^1(k_\gamma a) + \frac{n^2}{c^2} J_n(k_\gamma a) \right]$$

$$a_{31} = 0, \ a_{32} = b_1 J_n^1(k_\beta a), \ a_{33} = b_0 J_n^1(k_\gamma a) \tag{50}$$

Now, expanding the determinant and incorporating the amendments made by Ewing et al. [3], the required frequency equation can be written as

$$\left|a_{ij}\right| = \overline{R_\in}(c) = 0 \tag{51}$$

i.e.,

$$\overline{R_\in(c)} = \left[\overline{R_1}(c) + \Delta_0(c)\,\overline{R_2}(c)\right] + \in \left[\Delta_1(c) + \Delta_0(c)\Delta_2(c)\right] = 0 \tag{52}$$

where $\overline{R_1(c)} = \left[\left(k_\beta^2 - 2k_\alpha^2\right)J_n(k_\alpha a) - 2J^{11}(k_\alpha(c))\right].$

$$\left[\left(k_\beta^2 - 2k^2\right)J_n\left(k_\beta a\right) + \frac{2}{a}J_n^1\left(k_\beta c\right)\right]$$
$$-4k^2\left[J_n^1(k_\alpha a) - \frac{1}{a}J_n(k_\alpha a)\right]\left[J_n^1\left(k_\beta a\right) - \frac{1}{a}J_n\left(k_\beta a\right)\right] \tag{53}$$

$$\overline{R_2(c)} = \left[(k_\beta^2 - 2k_\alpha^2)J_n(k_\alpha a) - 2J_n^{11}(k_\alpha a)\right]\left[\left(k_\gamma^2 - 2k^2\right)J_n\left(k_\gamma a\right) + \frac{2}{a}J_n^1\left(k_\gamma a\right)\right]$$
$$- 4k^2\left[J_n^1(k_\alpha a) - \frac{1}{a}J_n(k_\alpha a)\right]\left[J_n^1\left(k_\gamma a\right) - \frac{1}{a}J_n\left(k_\gamma c\right)\right] \tag{54}$$

$$\Delta_1(c) = \left[\left\{\left(k_\beta^2 - 2k_\alpha^2\right)J_n(k_\alpha a) - 2J_n(k_\alpha a)\right\}\left\{\left(k_\beta^2 - 2k^2\right)J_n\left(k_\beta a\right) + \frac{1}{a}J_n^1\left(k_\beta a\right)\right\}\right]$$
$$+ \left[\left(k_\beta^2 - 8A_3^2\right)J_n\left(k_\beta a\right) + \frac{2}{a}J_n^1\left(k_\beta a\right)\right][(1 + 2A_3)J_n(k_\alpha a)]$$
$$- 4k^2\left[J_n^1(k_\alpha a) - \frac{1}{a}J_n(k_\alpha a)\right]\left[J_n^1\left(k_\beta a\right) - \frac{1}{a}J_n\left(k_\beta a\right)\right] \tag{55}$$

$$\Delta_0(c) = \frac{-b_1 J_n^1\left(k_\beta a\right)}{b_0 J_n^1(k_\alpha a)} \tag{56}$$

$$\Delta_2(c) = [(1 + 2A_3)J_n(k_\alpha a)]\left[\left(k_\alpha^2 - 2k^2\right)J_n\left(k_\gamma^a\right) + \frac{2}{a}J_n^1\left(k_\gamma a\right)\right]$$
$$+ \left[(k_\beta^2 - 2k_\alpha^2)J_n(k_\alpha a) - 2J_n^{11}(k_\alpha a)\right]\left[\left(k_\alpha^2 - k^2\right)J_n\left(k_\gamma a\right) + \frac{1}{a}J_n^1\left(k_\gamma a\right)\right]$$
$$- 4k^2\left[J_n^1(k_\alpha a) - \frac{1}{a}J_n(k_\alpha a)\right]\left[J_n^1(k_r a) - \frac{1}{a}J_n\left(k_\gamma c\right)\right] \tag{57}$$

In Eq. (52), the terms other than $R_1(c)$ contribute the effect of curvature in the surface wave propagation. When the micro-effects are neglected, i.e., $\sigma_1 = 0, \sigma_2 = 0$, $\in = 0$, Eq. (52) reduces to

$$\overline{R_1(c)} = \left[\left(k_\beta^2 - 2k_\alpha\right)^2 J_n(k_\alpha c) - 2J_n^{11}(k_\alpha a)\right]\left[\left(k_\beta^2 - 2k^2\right)J_n\left(k_\beta^a\right) + \frac{2}{a}J_n^1\left(k_\beta a\right)\right]$$
$$- 4k^2\left[J_n^1\left(k_\alpha^a\right) - \frac{1}{a}J_n(k_\alpha a)\right]\left[J_n^1\left(k_\beta a\right) - \frac{1}{a}J_n\left(k_\beta a\right)\right] = 0$$

which agrees with the equation given by Ewing et al. [3]. The equation (52) is suitable for discussion in such a complicated form.

Now consider the equation of motion for micro-strains. For the problem under discussion, we have

$$\phi_{rr} = \phi_{rr}(r, \theta, t)\phi_{\theta\theta} = \phi_{\theta\theta}(r, \theta, t) \tag{58}$$

$$\phi_{(r\theta)} = \phi_{r\theta}(r, \theta, t) \text{ and } \phi_{(zz)} = \phi_{(rz)} = \phi_{(\theta z)} = 0$$

The filed equations involving these micro-strains are

$$2B_2 \nabla^2 \phi_{rr} - 2A_5 \phi_{rr} = \frac{1}{2}\rho j \frac{\partial^2 \phi_{rr}}{\partial t^2} \tag{59}$$

$$2B_2 \nabla^2 \phi_{\theta\theta} - 2A_5 \phi_{\theta\theta} = \frac{1}{2}\rho j \frac{\partial^2 \phi_{\theta\theta}}{\partial t^2} \tag{60}$$

$$2B_2 \nabla^2 \phi_{(r\theta)} - 2A_5 \phi_{r\theta} = \frac{1}{2}\rho j \frac{\partial^2 \phi_{(r\theta)}}{\partial t^2} \tag{61}$$

We suppose that solution of (59) in the form

$$\phi_{rr} = a^1 \psi(r) \exp[i(\omega t + n\theta)] \tag{62}$$

where a^1 is consistent and $\psi(r)$ is function of r only.

Substituting (62) in (59), we get

$$\psi^{11} + \frac{1}{r}\psi^1 + \left(p^2 - \frac{n^2}{r^2}\psi = 0\right) \tag{63}$$

where

$$p^2 = \frac{\omega^2 \rho j - 4A_5}{4B_2} \tag{64}$$

The solution of equation (63) is of the form

$$\psi(r) = J_n(pr) \tag{65}$$

Thus, the solution of (59) is

$$\phi_{rr} = a^1 J_n(pr) \exp[i(\omega t - n\theta)] \tag{66}$$

As Eqs. (60) and (61) are similar to (59), we have

$$\phi_{\theta\theta} = b^1 \, J_n(pr) \exp[i(\omega t + n\theta)] \tag{67}$$

$$\phi_{(r\theta)} = c^1 \, J_n(pr) \exp[i(\omega t + n\theta)] \tag{68}$$

where b^1, c^1 are constants.

The boundary conditions to be satisfied are

$$t_{r(rr)} = t_{r(\theta\theta)} = t_{r(rz)} = 0 \tag{69}$$

Substituting (66)–(68) in (69), we get three frequency equations and each is of the form

$$\omega^2 = \frac{4A_5}{\rho j} \ \ \text{or} \ \ c^2 = \frac{4A_5}{\rho j k^2}$$

where c is the phase velocity. We can observe that it is a dispersive wave.

4 Conclusions

In case of surface waves in planes, these waves are found to the dispersive and have the same cutoff frequency [7]. In the present case, there is no such cutoff frequency; this can be attributed to the effect of curvature on surface wave propagation. The additional wave found in the curved surface is dispersive without cutoff frequency, whereas this wave in planes is dispersive with some cutoff frequency.

References

1. Bromwich TJ, On the influence of gravity on elastic waves and in particular on the vibration of an elastic globe proc. London Math Soc 30:98–120
2. Epstein HI (1976) J Sound Vibr 46(1):60–66
3. Ewing WM, Jardetzky WS, Press F (1957) Elastic waves in layered media. Mc Graw-Hill Book Comp., New York
4. Jeffrfeys H (1931) On the cause of oscillatory moment in seismograms monthly notices Roy Astor. Soc Geophys Suppl. 2:407–416
5. Kolsky H (1963) Stress waves in solids. Dova Publications INC., New York
6. Love AEH (1911) Problems of geodynamics. Cambridge University Press, London (1926)

7. Sambaiah K, Parameswara Rao M, Kesava Rao B (1985) The Rayleigh wave propagation in micromorphic elastic half-space. Proc Natl Acad Sci India 55(A), III:216–222
8. Sezawa K (1927) Dispersion of elastic waves propagated on a surface of stratified bodies and on curved surfaces. Bull Earthq Res Inst (Tokyo) 3:1–18
9. Viktorov IV (1958) Soviet physics acoustics. American Institute of Phys Translation 4:131–136

Modelling Third-Grade Liquid Past Vertical Isothermal Cone with Variable Temperature and BIOT Number Effects

S. Abdul Gaffar , **V. Ramachandra Prasad** ,
B. Md. Hidayathulla Khan , **and K. Venkatadri**

Abstract The non-similar natural convection flows of an incompressible viscoelastic fluid past an isothermal cone with BIOT number effects and variable temperature are investigated. The Keller-Box technique is utilized to solve the transformed conservation equations subject to physically appropriate boundary conditions. The variations of different emerging dimensionless parameters on *velocity*, *temperature, skin friction coefficient and heat transfer rate* profiles are presented.

Keywords Third-grade fluid · Material fluid parameter · BIOT number · Heat transfer rate · Skin friction

1 Introduction

The enthusiasm for non-Newtonian liquid elements keeps on developing because of expanding applications in different parts of cutting-edge mechanical advances that incorporate warm oil recuperation, slurry movement, polymer amalgamation and nourishment handling. In non-Newtonian liquid elements, scientific issues muddled because of solid nonlinearity and higher request differential transport conditions. Researchers and architects are engaged with non-Newtonian liquid elements in the light of the fact that the examination and execution of these liquids are basic to numerous differing frameworks, for example restorative and substance designing,

S. Abdul Gaffar
Department of Information Technology, Mathematics Section, Salalah College of Technology, Salalah, Oman

V. Ramachandra Prasad
Department of Mathematics, School of Advanced Science, Vellore Institute of Technology [VIT University], Vellore, India

B. Md. Hidayathulla Khan (✉)
Department of Mathematics, Aditya College of Engineering, Madanapalle, India
e-mail: bmdhkh@gmail.com

K. Venkatadri
Department of Mathematics, Sreenivasa Institute of Technology and Management Studies, P. Kothakota, India

plastic production and biotechnology. Numerous examinations of rheological hydro-dynamics have been conveyed [1, 2]. A few liquid models have risen in effectively impersonating genuine non-Newtonian qualities. The third-grade liquid is an easi-est subclass of viscoelastic models which can foresee ordinary pressure and shear diminishing or thickening attributes. Numerous analysts analysed the streams of third-grade liquid for different situations, typically for a scientific accentuation and next to know if any physical comprehension or understanding of the arrangements. Sahoo [3] researched the stream and warmth exchange of third-grade liquid from an exponentially extending sheet with fractional slip limit conditions. In the present examination, a scientific model is created to look at the regular convective limit layer streams of third-grade viscoelastic liquid past a vertical isothermal cone with BIOT number and variable temperature. Suitable non-comparative changes are connected to change over the preservation conditions into dimensionless structure. An under-stood limited distinction "Keller-Box" system is executed to acquire the surmised computational arrangements [4]. Approval with prior Newtonian arrangements is additionally recorded. The impact of chosen parameters on speed, temperature, skin rubbing number and warmth exchange rate qualities is contemplated.

1.1   Third-Grade Fluid Model

In this article, a simple class of non-Newtonian liquids called the third-grade liquid is examined. The Cauchy stress tensor [5] of third-grade non-Newtonian liquid takes the structure:

$$\tau = -pI + \mu A_1 + \alpha_1 A_2 + \alpha_2 A_1^2 + \beta_1 A_3 + \beta_2(A_1 A_2 + A_2 A_1) + \beta_3\left(tr A_1^2\right)A_1 \tag{1}$$

where τ, p and I are additional tensor, hydrostatic pressure and character tensor, respectively. $\alpha_i (i = 1, 2)$, $\beta_i (i = 1, 2, 3)$ are material constants. $A_k (k = 1, 2, 3)$ is first Rivlin–Ericksen tensors [6] characterized as:

$$A_1 = (\nabla V) + (\nabla V)^T \tag{2}$$

$$A_n = \frac{\mathrm{d}A_{n-1}}{\mathrm{d}t} + A_{n-1}(\nabla V) + A_{n-1}(\nabla V)^T; \quad n > 1 \tag{3}$$

1.2   Mathematical Model

A steady, natural convective flows of *viscoelastic fluid* from a cone with vertex angle 2A illustrated in Fig. 1 are considered. The cone vertex is placed at $(0, 0)$, the x and y
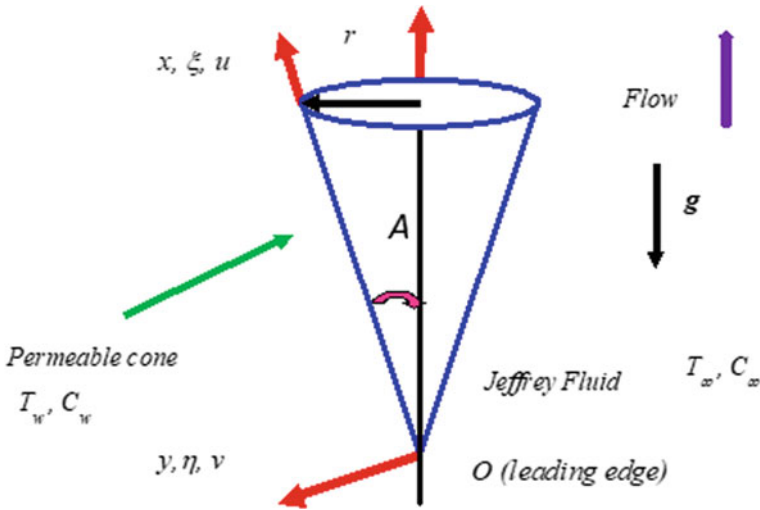
Fig. 1 Physical model and coordinate system

axes are considered along and normal to cone surface. The surface is set to a variable temperature, $T_w(x) = T_\infty + Bd_1 x^n$, where B and d_1 are constants. Also, we suppose that the Boussinesq approximation holds. In approach with Sahoo [3] and Hayat [7], the eqns. for *continuity, momentum and energy are* as:

$$\frac{\partial(ru)}{\partial x} + \frac{\partial(rv)}{\partial y} = 0 \tag{4}$$

$$u\frac{\partial u}{\partial x} + v\frac{\partial u}{\partial y} = \upsilon\frac{\partial^2 u}{\partial y^2} + \frac{\alpha_1}{\rho}\left[u\frac{\partial^3 u}{\partial x\partial y^2} + v\frac{\partial^3 u}{\partial y^3} + \frac{\partial u}{\partial x}\frac{\partial^2 u}{\partial y^2} + 3\frac{\partial u}{\partial y}\frac{\partial^2 u}{\partial x\partial y}\right]$$

$$+ \frac{2\alpha_2}{\rho}\frac{\partial u}{\partial y}\frac{\partial^2 u}{\partial x\partial y} + \frac{6\beta_3}{\rho}\left(\frac{\partial u}{\partial y}\right)^2\frac{\partial^2 u}{\partial y^2} + g\beta(T - T_\infty)\cos A \tag{5}$$

$$u\frac{\partial T}{\partial x} + v\frac{\partial T}{\partial y} = \alpha\frac{\partial^2 T}{\partial y^2} \tag{6}$$

Subject to:

$$u = 0, \quad v = 0, \quad -k\frac{\partial T}{\partial y} = h_w(T_w(x) - T) \quad \text{at} \quad y = 0,$$

$$u \to 0, \quad T \to T_\infty, \quad \text{as} \quad y \to \infty, \tag{7}$$

Define $ru = \frac{\partial(r\psi)}{\partial y}$, $rv = -\frac{\partial(r\psi)}{\partial x}$, $r(x) = x\sin A$

$$\xi = \frac{V_w x}{\upsilon} Gr_x^{-1/4}, \quad \eta = \frac{y}{x} Gr_x^{1/4},$$

$$\psi = r\upsilon^4 \sqrt{Gr_x}\left(f + \frac{1}{2}\xi\right), \theta(\xi, \eta) = \frac{T - T_\infty}{T_w - T_\infty}, \quad \Pr = \frac{\upsilon}{\alpha}$$

$$Gr_x = \frac{g\beta(T_w - T_\infty)x^3 \cos A}{4\upsilon^2}, \quad \phi = \frac{\beta_3 \upsilon}{\rho x^4} Gr_x^{3/2},$$

$$\varepsilon_1 = \frac{\alpha_1}{\rho x^2} Gr_x^{1/2}, \varepsilon_2 = \frac{\alpha_2}{\rho x^2} Gr_x^{1/2} \tag{8}$$

The reduced non-dimensional equations for velocity and temperature are:

$$f' + \left(\frac{7+n}{4}\right)f' - \left(\frac{1+n}{2}\right)(f')^2 + \xi f' + 6\phi(f')^2 f' + \theta$$

$$+ \varepsilon_1 \left[\frac{1+3n}{2} f' f' - \frac{7+n}{4} ff' - \xi f'\right]$$

$$+ (3\varepsilon_1 + 2\varepsilon_2)\frac{1+3n}{4}(f')^2 - (4\varepsilon_1 + 2\varepsilon_2)n\frac{1-n}{4} f' f'$$

$$= \xi \frac{1-n}{4}\left[f'\frac{\partial f'}{\partial \xi} - f'\frac{\partial f}{\partial \xi} - (3\varepsilon_1 + 2\varepsilon_2)f''\frac{\partial f''}{\partial \xi}\right.$$

$$\left. -\varepsilon_1\left(f'\frac{\partial f''}{\partial \zeta} + f''\frac{\partial f'}{\partial \xi} - f''\frac{\partial f}{\partial \xi}\right)\right] \tag{9}$$

$$\frac{\theta''}{\Pr} + \frac{7+n}{4}f\theta' + \xi\theta' - nf'\theta = \xi\frac{1-n}{4}\left(f'\frac{\partial \theta}{\partial \xi} - \theta'\frac{\partial f}{\partial \xi}\right) \tag{10}$$

Subject to:

$$f = 0, \quad f' = 0, \quad \theta = 1 + \frac{\theta'}{\gamma}, \quad \text{at} \quad \eta = 0$$

$$f' = 0, \quad \theta \to 0 \quad \text{as} \quad \eta \to \infty \tag{11}$$

Here $\gamma = \frac{xh_w}{k} Gr^{-1/4}$. The shear stress coefficient and heat transfer rate are:

$$Gr^{-1/4}C_f = f'(\xi, 0) + \varepsilon_1\left(\frac{5+7n}{4} f' f''(\xi, 0) - \frac{7+n}{4} ff''(\xi, 0)\right)$$

$$+ 2\phi(f''(\xi, 0))^3 \tag{12}$$

$$Gr^{-1/4} \text{Nu} = -\theta'(\xi, 0) \tag{13}$$

2 Results and Discussion

Complete arrangements of numerical outcomes have been obtained and are shown in Tables 1 and 2 and Figs. 2, 3, 4, 5 and 6. To approve the Keller-Box numerical code utilized, examination with prior Newtonian arrangements displayed by Hossain and Paul [8] is directed and appears in Table 1. Table 2 provides the influence of the *third-grade fluid parameter (ϕ), material fluid parameters (ε_1, ε_2), BIOT number (γ) and surface temperature exponent (n)* on skin friction (C_f) and heat transfer rate (Nu). We see that with expanding ϕ, C_f is enhanced, while *Nu* is decreased. However, Nu is reduced. Also, increasing ε_1 is observed to decrease C_f and Nu. Further, increasing ε_2 is seen to increase both C_f and Nu. Increasing γ values is seen to enhance both C_f and Nu. Increasing n reduces C_f but enhances Nu. Figure 2a, b presents the velocity (f') and temperature (θ) profiles for different ϕ values. Velocity is seen to elevate strongly with increasing ϕ values. A slight increase in temperature is observed in Fig. 2b, and thus, the thermal boundary layer thickness is also enhanced. Figure 3a, b presents profiles for velocity (f') and temperature (θ) for different values of ε_1. The parameter ε_1 straightforwardly corresponds to the first material viscoelastic modulus, α_1. An increase in α_1 reduces viscosity and enhances fluid elasticity which leads to deceleration in the boundary layer flow and hence reduces velocity. In Fig. 3b, we see that the temperature is increased slightly with increasing ε_1 values and hence increases thermal boundary layer thickness. Figure 4a, b presents velocity (f') and temperature (θ) profiles for greater ε_2 values. An increase in ε_2 increases the fluid velocity (Fig. 4a) significantly, whereas a very slight decrease in temperature is observed with an increase in ε_2. Figure 5a, b presents velocity (f') and temperature (θ) profiles for increasing γ values. Both velocity and temperature profiles (Fig. 5a, b) are enhanced with increasing γ values. Figure 6a, b illustrates the velocity (f') and temperature (θ) profiles for increasing n values. Both velocity and temperature are shown to decrease with increasing n values.

Table 1 Comparison values of $-\theta(\xi, 0)$ for various values of ξ *with* Pr = 0.71, $\phi = \varepsilon_1 = \varepsilon_2 = 0$

ξ	$-\theta(\xi, 0)$	
	Hossain and Paul [8]	Present
0.0	0.24 584	0.24 587
0.1	0.25 089	0.25 091
0.2	0.25601	0.25603
0.4	0.26630	0.26633
0.6	0.27662	0.27665
0.8	0.28694	0.28698
1.0	0.29731	0.29735
2.0	0.35131	0.35136

Table 2 C_f and Nu values for different ϕ, ε_1, ε_2, γ, n and ξ with Pr = 0.71

ϕ	ε_1	ε_2	γ	n	$\xi = 1.0$		$\xi = 2.0$		$\xi = 3.0$	
					C_f	Nu	C_f	Nu	C_f	Nu
0	0.3	0.3	0.5	0.5	0.1271	0.1614	0.0479	0.2909	0.0196	0.4307
5					0.1388	0.1613	0.0488	0.2908	0.0197	0.4304
10					0.1478	0.1612	0.05	0.2907	0.0201	0.4304
15					0.1546	0.1611	0.0511	0.2907	0.0203	0.4303
20					0.1599	0.1611	0.0521	0.2906	0.0205	0.4302
0.1	0.1				0.163	0.1634	0.0772	0.2925	0.0365	0.4358
	0.4				0.1157	0.1607	0.0401	0.2915	0.0164	0.4328
	0.7				0.093	0.1593	0.0301	0.2912	0.0122	0.4315
	1				0.8	0.1586	0.0256	0.2908	0.0113	0.4308
	1.5				0.0689	0.158	0.0238	0.2907	0.013	0.4305
0.1	0.3	0			0.1268	0.1613	0.0478	0.2909	0.0195	0.4299
		0.5			0.1277	0.1614	0.0482	0.291	0.0196	0.4308
		2			0.13343	0.1614	0.0511	0.2919	0.0199	0.4308
		3			0.1397	0.1615	0.0578	0.2945	0.0234	0.4352
		5			0.1561	0.1615	0.0766	0.3042	0.0302	0.4432
		0.3	0.3		0.115	0.1326	0.0402	0.2421	0.0159	0.3589
			0.4		0.2309	0.3148	0.0917	0.5498	0.0384	0.8111
			0.6		0.3333	0.5077	0.1418	0.8609	0.0612	1.2642
			0.8		0.3816	0.6071	0.1663	1.0176	0.0725	1.491
			1		0.4099	0.6675	0.1809	1.112	0.0793	1.6272

(continued)

Table 2 (continued)

ϕ	ε_1	ε_2	γ	n	$\xi = 1.0$		$\xi = 2.0$		$\xi = 3.0$	
					C_f	Nu	C_f	Nu	C_f	Nu
			0.5	0	0.3132	0.4138	0.1239	0.731	0.0522	1.0812
				0.12	0.3078	0.4181	0.1234	0.7702	0.0518	1.0816
				0.24	0.3029	0.422	0.1229	0.7714	0.0516	1.0821
				0.35	0.2987	0.4254	0.1225	0.7726	0.0515	1.0826
				0.62	0.2895	0.4325	0.1214	0.7763	0.0513	1.0827
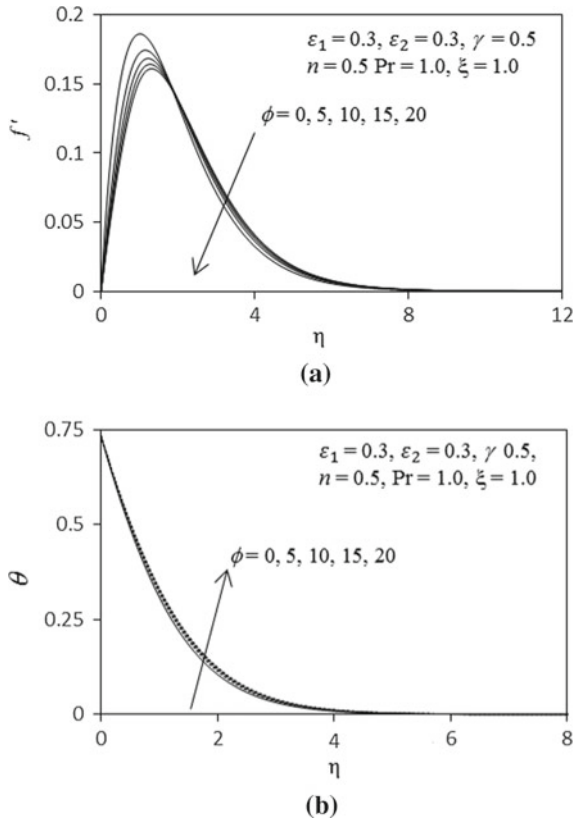
Fig. 2 **a** Influence of ϕ on the velocity profiles. **b** Influence of ϕ on the temperature profiles

2.1   Tables

See Tables 1 and 2.

2.2   Figures

See Figs. 1, 2, 3, 4, 5 and 6.
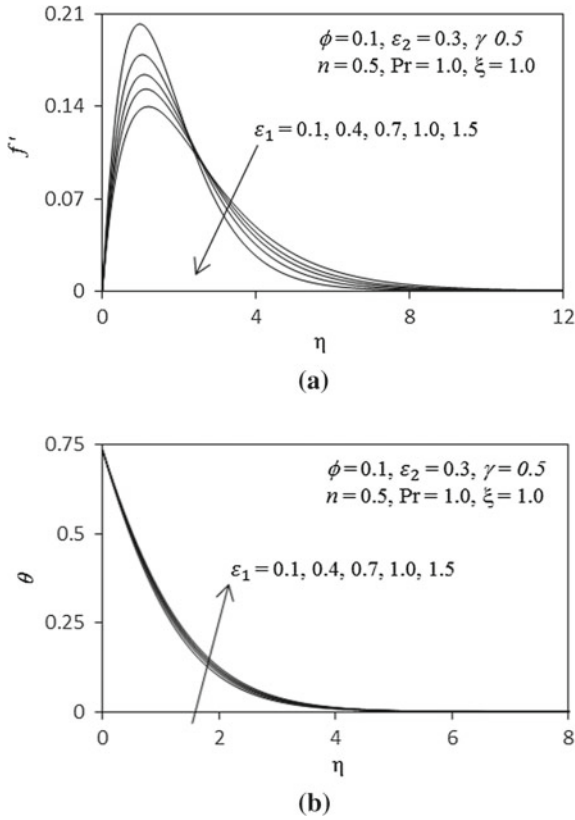
Fig. 3 **a** Influence of ε_1 on the velocity profiles. **b** Influence of ε_1 on the temperature profiles

3 Conclusions

The buoyancy-driven, non-similar convective flow and heat transfer of third-grade viscoelastic fluid external to a vertical isothermal cone are presented numerically. The implicit second-order accurate finite-difference Keller-Box numerical technique is implanted to solve the transformed, non-dimensional boundary layer equations, with prescribed boundary conditions. A comprehensive assessment of the effects of the third-grade parameter (ϕ) viscoelastic material fluid parameters. (ε_1, ε_2), BIOT number (γ) and surface temperature exponent (n) has been conducted. Very stable and accurate solutions are obtained with the present finite-difference code. Validation of the implicit Keller-Box method solutions has been achieved with earlier Newtonian solutions. In this regard, this method is explored with other non-Newtonian fluids.
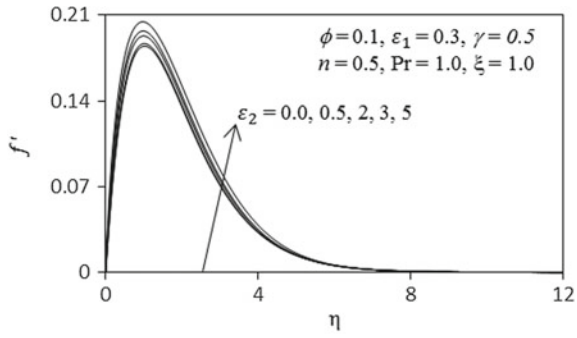
$$\phi=0.1,\ \varepsilon_1=0.3,\ \gamma=0.5$$
$$n=0.5,\ \mathrm{Pr}=1.0,\ \xi=1.0$$

$$\varepsilon_2=0.0,\ 0.5,\ 2,\ 3,\ 5$$

(a)

$$\phi=0.1,\ \varepsilon_1=0.3,\ \gamma=0.5$$
$$n=0.5,\ \mathrm{Pr}=1.0,\ \xi=1.0$$

$$\varepsilon_2=0.0,\ 0.5,\ 2,\ 3,\ 5$$

(b)

Fig. 4 **a** Influence of ε_2 on the velocity profiles. **b** Influence of ε_2 on the temperature profiles

$\phi=0.1, \varepsilon_1=\varepsilon_2=0.3$
$n=0.5, Pr=1.0, \xi=1.0$

$\gamma= 0.3, 0.4, 0.6, 0.8, 1.0$

(a)

$\phi=0.1, \varepsilon_1=\varepsilon_2=0.3$
$n=0.5, Pr=1.0, \xi=1.0$

$\gamma= 0.3, 0.4, 0.6, 0.8, 1.0$

(b)
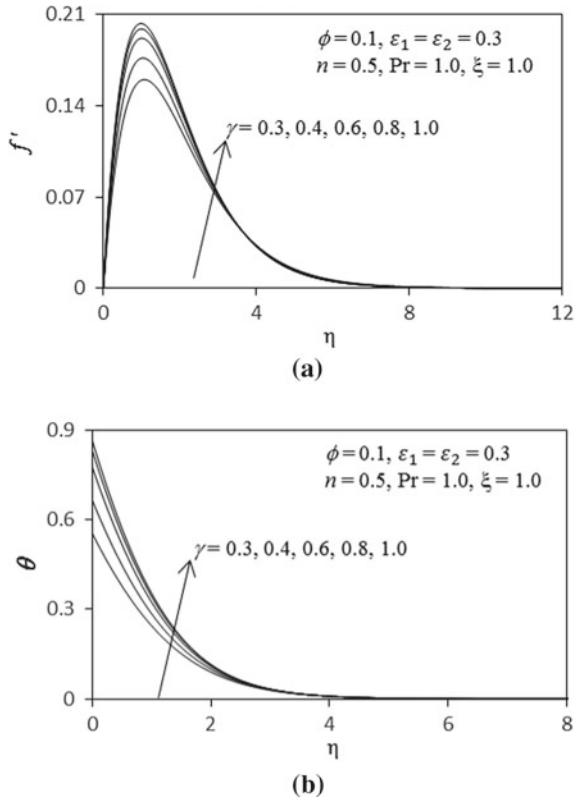
Fig. 5 **a** Influence of γ on the velocity profiles. **b** Influence of γ on the temperature profiles
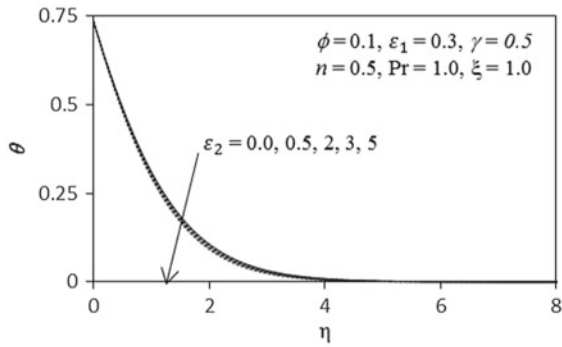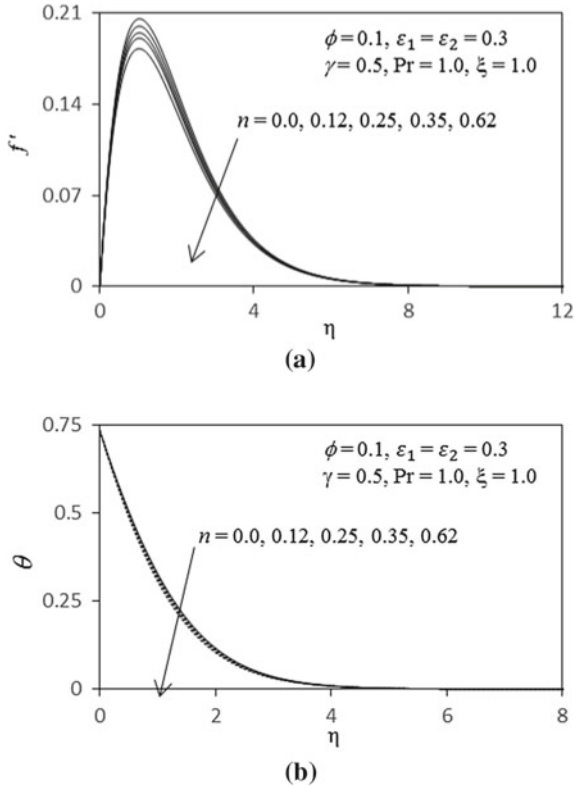
Fig. 6 **a** Influence of n on the velocity profiles. **b** Influence of n on the temperature profiles

References

1. Nadeem S, Ahmad S, Muhammad N (2017) Cattaneo-Christov flux in the flow of a viscoelastic fluid in the presence of Newtonian heating. J Mol Liq 237:180–184
2. Nawaz M, Naz R, Awais M (2017) Magnetohydrodynamic axisymmetric flow of Casson fluid with variable thermal conductivity and free stream. Alexandria Eng J 57(3):2043–2050
3. Sahoo B, Poncet S (2011) Flow and heat transfer of third grade fluid past an exponentially stretching sheet with partial slip boundary conditions. Int J Heat Mass Trans 54(23–24):5010–5019
4. Keller HB (1978) Numerical methods in boundary-layer theory. Ann Rev Fluid Mech 10:417–433
5. Bird RB, Armstrong RC, Hassager O (1987) Dynamics of polymeric liquids. In: Volume 1: fluid mechanics, vol. 1, 2nd edn, Wiley Inter science, New York, USA. ISBN: 978-0-471-80245-7
6. Rivlin RS, Ericksen JL (1955) Stress-deformation relations for isotropic materials. J Rational Mech Anal 4:323–425
7. Hayat T, Shafiq A, Alsaedi A, Awais M (2013) MHD axisymmetric flow of third grade fluid between stretching sheets with heat transfer. Comput Fluids 86(5):103–108
8. Hossain MA, Paul SC (2001) Free convection from a vertical permeable circular cone with non-uniform surface temperature. Acta Mech 151:103–114

Nonlinear Kelvin–Helmholtz Instability of Viscous Fluids with Heat and Mass Transfer

Rishi Asthana and Mukesh Kumar Awasthi

Abstract A nonlinear stability analysis of novel Kelvin–Helmholtz instability of two superposed viscous fluids is performed. We are allowing transferring of heat/mass at the juncture of two fluids. The multiple timescale expansion method is utilized to study various modes of instability. The stability of arrangement is finally governed by a partial differential equation which is nonlinear in nature. The stable/unstable zones are represented graphically showing the impacts of physical variables. The nonlinear analysis shows that transferring of heat at the juncture of two fluids induces instability, while nonlinearity induces stability.

Keywords Interfacial stability · Nonlinear investigation · Viscous potential flow · Timescale perturbation · Plane geometry

1 Introduction

If the heat transfer includes mass at the juncture of two viscous fluids, the instability investigation becomes complicated. Various applications in chemical engineering and geophysics contain the phenomenon of mass transferring including heat. The analytical revision of interfacial stability of Kelvin–Helmholtz and Rayleigh–Taylor type in Cartesian plane was made by Hsieh [1]. Ho [2] considered the heat transfer effect at the juncture of two viscous liquids of identical viscosity. The heat transfer effect on interfacial instability in Cartesian plane assuming liquid as viscous while vapor as inviscid was examined by Khodaparast et al. [3].

The analysis of Kelvin–Helmholtz instability with the use of viscous potential flow theory does not permit for no-slip conditions, but contrasting from inviscid theory, the normal viscous stresses are included at the interface. Joseph and Liao

R. Asthana (✉)
Department of Applied Sciences, SoET, BML Munjal University, Sidhrawali, Gurgaon, Haryana 122413, India
e-mail: rasthana4@gmail.com

M. K. Awasthi
Department of Mathematics, Babasaheb Bhimrao Ambedkar University, Lucknow, India
e-mail: mukeshiitr.kumar@gmail.com

[4] invented the basic idea of viscous flow theory. The mass transfer effect at the juncture of two viscous fluids of unequal viscosities was checked by Awasthi and Agrawal [5]. Joseph and Funada [6] included the viscous effects at the juncture of two fluids in case of Kelvin–Helmholtz instability. Asthana and Agrawal [7] studied the mass transfer effect at the juncture of two viscous fluids when they are streaming with unequal velocities.

The nonlinear stability examination is quite tough as the number of equations increases, but from linear theory, we cannot find the complete stability mechanism. The weakly nonlinear theory for unbounded inviscid fluids was developed by several authors in the literature [8, 9]. The nonlinear interfacial instability of Kelvin–Helmholtz type between two semi-infinite fluids was analyzed by Weissman [10]. He established amplitude equations which are first- and second-order time-dependent equations, and these equations are also depending on the different dispersion relation which was used for linear theory. The impact of transferring of mass on the juncture of two ideal fluids was investigated by Hsieh [11] using nonlinear analysis. The nonlinear instability of Kevin-Helmholtz type of two non-viscous fluids in plane geometry was analyzed by Lee [12] taking heat transfer through the interface. The mass transfer effect on the juncture of two viscous fluids including nonlinear contributions was examined by various authors [13, 14].

In this paper, we made an attempt to study the nonlinear impact of disturbance waves on the interfacial instability of Kelvin–Helmholtz type for two incompressible as well as viscous fluids. The irrotational viscous flow theory is utilized to include viscous effects. Heat is transferring including mass at the juncture of two fluids. The compound timescale perturbation method is considered to investigate, and a partial differential equation which is nonlinear in nature is derived to describe the nonlinear waves. The comparison between obtained results and linear theory [7] has been made.

2   Mathematical Formulation of the Problem

The schematic of the problem is presented in Fig. 1. A planar patch $y = 0$ at temperature T_i is considered between phases of water and vapor of velocities V_w, V_v, temperatures T_w, T_v, viscosities μ_w, μ_v, width d_w, d_v, and densities ρ_w, ρ_v, respectively. A sudden disruption makes the patch elevated by $\zeta(x, t)$, and hence, the patch takes shape as $y = \zeta(x, t)$. The normalized vector in outward direction is [13]

$$\hat{n} = \left\{ 1 + \left(\frac{\partial \zeta}{\partial x} \right)^2 \right\}^{-1/2} \left(-\frac{\partial \zeta}{\partial x} \hat{i} + \hat{j} \right) \qquad (2.1)$$

The perturbed flow above and below is supposed to be irrotational, and their potentials are harmonic.

$$\nabla^2 \varphi_w = 0, \nabla^2 \varphi_v = 0\} \qquad (2.2)$$
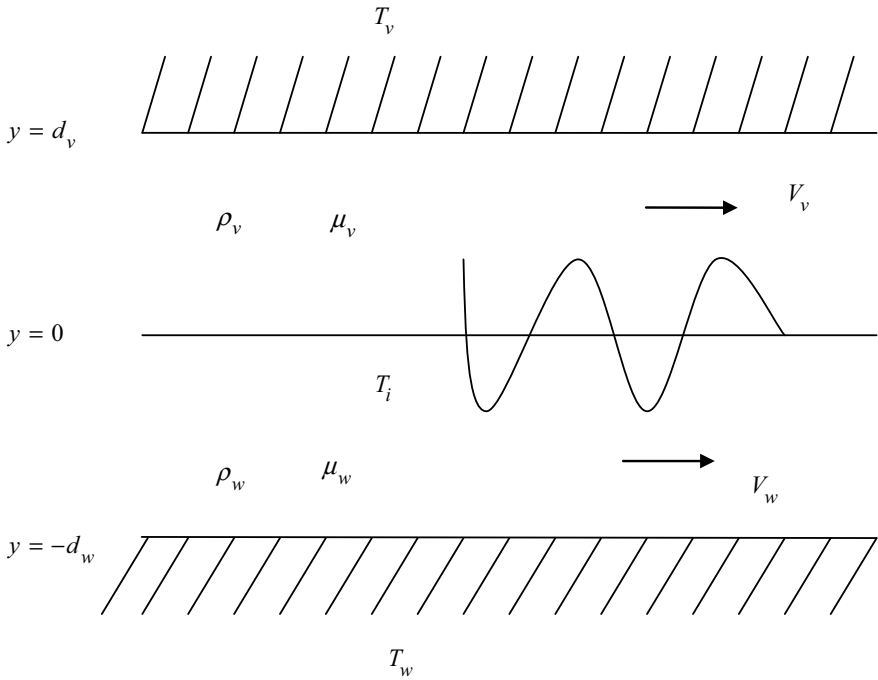
Fig. 1 Schematic of the arrangement

The boundary conditions can be summarized as:
There is no normal velocity at $y = -d_w$ and $y = d_v$ i.e.

$$\left.\begin{array}{l} \partial\varphi_w/\partial y = 0 \text{ at } y = -dw \\ \partial\varphi_v/\partial y = 0 \text{ at } y = dv \end{array}\right\}, \tag{2.3}$$

At the patch $y = \zeta(x, t)$, we should have

(i) The mass transfer equations as;

$$\rho_w\left(-\frac{\partial\zeta}{\partial t} + \frac{\partial\varphi_w}{\partial y} - \frac{\partial\zeta}{\partial x}\frac{\partial\varphi_w}{\partial x}\right) = \rho_v\left(-\frac{\partial\zeta}{\partial t} + \frac{\partial\varphi_v}{\partial y} - \frac{\partial\zeta}{\partial x}\frac{\partial\varphi_v}{\partial x}\right) \tag{2.4}$$

(ii) The transfer of heat is governed by;

$$\rho_w\left(-\frac{\partial\zeta}{\partial t} + \frac{\partial\varphi_w}{\partial y} - \frac{\partial\zeta}{\partial x}\frac{\partial\varphi_w}{\partial x}\right) = H(\zeta)\big/ L \tag{2.5}$$

The details for $H(\zeta)/L$ were expressed by Awasthi et al. [13].
The nonlinear equation of energy transfer can be written as

$$\rho_w\left(-\frac{\partial\zeta}{\partial t} + \frac{\partial\varphi_w}{\partial y} - \frac{\partial\zeta}{\partial x}\frac{\partial\varphi_w}{\partial x}\right) = \alpha\left(\zeta + \alpha_2\zeta^2 + \alpha_3\zeta^3\right) \tag{2.6}$$

where $\alpha = \frac{Q}{L}\left(\frac{1}{d_w} + \frac{1}{d_v}\right)$, $\alpha_2 = -\frac{1}{d_w} + \frac{1}{d_v}$, $\alpha_3 = \frac{d_w^3 + d_v^3}{(d_w + d_v)d_w^2 d_v^2}$.

(iii)   The dynamical condition

$$\rho_w\left(\frac{\partial\varphi_w}{\partial y} - \frac{\partial\zeta}{\partial x}\frac{\partial\varphi_w}{\partial x}\right)\left(-\frac{\partial\zeta}{\partial t} + \frac{\partial\varphi_w}{\partial y} - \frac{\partial\zeta}{\partial x}\frac{\partial\varphi_w}{\partial x}\right) - \rho_v\left(\frac{\partial\varphi_v}{\partial y} - \frac{\partial\zeta}{\partial x}\frac{\partial\varphi_v}{\partial x}\right)$$

$$\left(-\frac{\partial\zeta}{\partial t} + \frac{\partial\varphi_v}{\partial y} - \frac{\partial\zeta}{\partial x}\frac{\partial\varphi_v}{\partial x}\right) = \left(p_v - p_w - 2\mu_v\hat{n}\cdot\nabla\otimes\nabla\varphi_v\cdot\hat{n}\right.$$

$$\left. + 2\mu_w\hat{n}\cdot\nabla\otimes\nabla\varphi_w\cdot\hat{n} + \sigma\nabla\cdot\hat{n}\right)\left\{1 + \left(\frac{\partial\zeta}{\partial x}\right)^2\right\} \tag{2.7}$$

Using Bernoulli's equation, we may get;

$$\rho_w\left(\frac{\partial\varphi_w}{\partial y} - \frac{\partial\zeta}{\partial x}\frac{\partial\varphi_w}{\partial x}\right)\left(-\frac{\partial\zeta}{\partial t} + \frac{\partial\varphi_w}{\partial y} - \frac{\partial\zeta}{\partial x}\frac{\partial\varphi_w}{\partial x}\right)$$

$$- \rho_v\left(\frac{\partial\varphi_v}{\partial y} - \frac{\partial\zeta}{\partial x}\frac{\partial\varphi_v}{\partial x}\right)\left(-\frac{\partial\zeta}{\partial t} + \frac{\partial\varphi_v}{\partial y} - \frac{\partial\zeta}{\partial x}\frac{\partial\varphi_v}{\partial x}\right)$$

$$= \rho_w\left(\frac{\partial\varphi_w}{\partial t} + \frac{1}{2}\left(\frac{\partial\varphi_w}{\partial y}\right)^2 + \frac{1}{2}\left(\frac{\partial\varphi_w}{\partial x}\right)^2\right)\left\{1 + \left(\frac{\partial\zeta}{\partial x}\right)^2\right\}$$

$$- \rho_v\left(\frac{\partial\varphi_v}{\partial t} + \frac{1}{2}\left(\frac{\partial\varphi_v}{\partial y}\right)^2 + \frac{1}{2}\left(\frac{\partial\varphi_v}{\partial x}\right)^2\right)\left\{1 + \left(\frac{\partial\zeta}{\partial x}\right)^2\right\}$$

$$- 2\mu_w\left\{1 + \left(\frac{\partial\zeta}{\partial x}\right)^2\right\}^{-1}\left(\frac{\partial^2\varphi_w}{\partial y^2} - 2\frac{\partial\zeta}{\partial x}\frac{\partial^2\varphi_w}{\partial y\partial x} + \frac{\partial^2\varphi_w}{\partial x^2}\left(\frac{\partial\zeta}{\partial x}\right)^2\right)$$

$$- 2\mu_v\left\{1 + \left(\frac{\partial\zeta}{\partial x}\right)^2\right\}^{-1}\times\left(\frac{\partial^2\varphi_v}{\partial y^2} - 2\frac{\partial\zeta}{\partial x}\frac{\partial^2\varphi_v}{\partial y\partial x} + \frac{\partial^2\varphi_v}{\partial x^2}\left(\frac{\partial\zeta}{\partial x}\right)^2\right)$$

$$+ \sigma\frac{\partial^2\zeta}{\partial x^2}\left\{1 + \left(\frac{\partial\zeta}{\partial x}\right)^2\right\}^{-3/2} \tag{2.8}$$

We study the nonlinear temporal growth on the interfacial stability of Kelvin–Helmholtz type taking the approach adopted by Awasthi et al. [13]. The expansion of variables is taken as follows;

$$
\begin{aligned}
\zeta = {} & \iota\zeta_1(t_0, t_1, t_2, x) + \iota^2\zeta_2(t_0, t_1, t_2, x) \\
& + \iota^3\zeta_3(t_0, t_1, t_2, x)
\end{aligned}
\tag{2.9}
$$

$$
\begin{aligned}
\varphi_w = {} & \varphi_{0,w}(x) + \iota\varphi_{1,w}(t_0, t_1, t_2, y, x) + \iota^2\varphi_{2,w}(t_0, t_1, t_2, y, x) \\
& + \iota^3\varphi_{3,w}(t_0, t_1, t_2, y, x)
\end{aligned}
\tag{2.10}
$$

$$
\varphi_v = \varphi_{0,v}(x) + \iota\varphi_{1,v}(t_0, t_1, t_2, y, x) + \iota^2\varphi_{2,v}(t_0, t_1, t_2, y, x) + \iota^3\varphi_{3,v}(t_0, t_1, t_2, y, x)
\tag{2.11}
$$

Here, ι reveal the order of disruption and $t_0 = t, t_1 = \iota t, t_2 = \iota^2 t$. The other variables φ_w, φ_v and ζ coming in the above equations are expanded according to Maclaurin's series about the patch $y = 0$. Now, we use the above expression for φ_w, φ_v and ζ. The coefficients of ι, ι^2, ι^3 are separated which gives us the equations of distinct perturbation orders.

3 Linear Theory

As we suppose, the flows below and above the patch have velocities V_w, V_v, i.e.,

$$
\varphi_{0,w} = V_w x, \; \varphi_{0,v} = V_v x \}
\tag{3.1}
$$

Technique of normal mode is utilized to analyze the linear stability, and patch disruption is considered as;

$$
\zeta_1 = D(t_1, t_2) \cdot e^{ikx} e^{-i\omega t} + \text{complex conjugate},
\tag{3.2}
$$

Linear form solution for Eq. (2.2) is

$$
\varphi_{1,w} = \frac{1}{k}\left(\frac{\alpha}{\rho_w} - i\omega + ikV_w\right)D(t_1, t_2)\frac{\cosh(k(y + d_w))}{\sinh(kd_w)} \cdot e^{ikx}e^{-i\omega t} + \text{c.c.}
\tag{3.3}
$$

$$
\varphi_{1,v} = -\frac{1}{k}\left(\frac{\alpha}{\rho_v} - i\omega + ikV_v\right)D(t_1, t_2)\frac{\cosh(k(y - d_v))}{\sinh(kd_v)} \cdot e^{ikx}e^{-i\omega t} + \text{c.c.}
\tag{3.4}
$$

Based on Eqs. (3.2)–(3.4) and linear normal stress balance equation, the characteristic equation achieved by Asthana and Agrawal [7] was obtained.

$$c_0\omega^2 + (c_1 + id_1)\omega + c_2 + id_2 = C(\omega, k) = 0 \tag{3.5}$$

$$c_0 = \rho_w \coth(kd_w) + \rho_v \coth(kd_v)$$

$$c_1 = -2k(\rho_w V_w \coth(kd_w) + \rho_v V_v \coth(kd_v))$$

$$d_1 = \alpha(\coth(kd_w) + \coth(kd_v)) + 2k^2(\mu_w \coth(kd_w) + \mu_v \coth(kd_v))$$
$$c_2 = k^2\left(\rho_w V_w^2 \coth(kd_w) + \rho_v V_v^2 \coth(kd_v)\right) + (\rho_v - \rho_w)gk - \sigma k^3$$
$$\qquad - 2k^2\alpha\left(\frac{\mu_w}{\rho_w}\coth(kd_w) + \frac{\mu_v}{\rho_v}\coth(kd_v)\right)$$
$$d_2 = -\alpha k(V_w \coth(kd_w) + V_v \coth(kd_v))$$
$$\qquad - 2k^3(\mu_w V_w \coth(kd_w) + \mu_v V_v \coth(kd_v))$$

The adequate condition for roots with negative real parts is:

$$c_0 d_2^2 - c_1 d_1 d_2 + c_2 d_1^2 < 0 \tag{3.6}$$

which gives us

$$
\begin{aligned}
&- \coth(kd_w)\coth(kd_v)\left[\alpha^2 k^2(\rho_v \coth(kd_w) + \rho_w \coth(kd_v))\right.\\
&\quad + 4k^6\left(\rho_v \mu_w^2 \coth(kd_w) + \rho_w \mu_v^2 \coth(kd_v)\right)\\
&\quad + 4\alpha k^4(\rho_v \mu_w \coth(kd_w) + \rho_w \mu_v \coth(kd_v))\left]U^2 + \left[(\rho_w - \rho_v)gk + \sigma k^3\right]\right.\\
&\quad \times \left[\alpha(\coth(kd_w) + \coth(kd_v)) + 2k^2(\mu_w \coth(kd_w) + \mu_v \coth(kd_v))\right]^2\\
&\quad + 2\alpha k^2\left(\frac{\mu_w}{\rho_w}\coth(kd_w) + \frac{\mu_v}{\rho_v}\coth(kd_v)\right)\\
&\left[\alpha(\coth(kd_w) + \coth(kd_v)) + 2k^2(\mu_w \coth(kd_w) + \mu_v \coth(kd_v))\right]^2 < 0 \quad (3.7)
\end{aligned}
$$

Here, $U = V_v - V_w$.

4   Second-Order Solution

The governing equations of potential function for second-order perturbations are given as

$$\nabla^2\varphi_{2,v} = 0; \ \nabla^2\varphi_{2,w} = 0 \tag{4.1}$$

If we substitute the expression of ξ_1, $\varphi_{1,w}$ and $\varphi_{1,v}$ in 2nd order equation, we have

$$\xi_2 = -2\alpha_2 D\overline{D} + D_2 D^2 e^{2ikx} e^{-2i\omega t} + \overline{D}_2 \overline{D}^2 e^{2ikx} e^{2i\omega t} \tag{4.2}$$

$$\varphi_{2,w} = M_2^1 D^2 \frac{\cosh(2k(y+d_w))}{\sinh(2kd_w)} e^{2ikx} e^{-2i\omega t} + \text{complex conjugate} + d^1(t_0, t_1, t_2) \tag{4.3}$$

$$\varphi_{2,v} = -M_2^2 D^2 \frac{\cosh(2k(y-d_v))}{\sinh(2kd_v)} e^{2ikx} e^{-2i\omega t} + \text{complex conjugate} + d^2(t_0, t_1, t_2) \tag{4.4}$$

where

$$
\begin{aligned}
D_2 = {} & \frac{2k}{C(2\omega, 2k)} \Bigg\{ \Bigg[\Bigg[\frac{\rho i(\omega - kV)}{k} \gamma \, \coth(2kd) \\
& + \frac{\rho}{2}(\coth^2(kd+1))\left(\frac{\alpha}{\rho} - i\omega + ikV\right)^2 \\
& + 2\rho(\omega - kV)^2 - i3\alpha kV - 6k^2\mu\left(\frac{\alpha}{\rho} - i\omega + ikV\right) - k\mu\gamma \, \coth(2kd) \Bigg] \Bigg] \\
& - \frac{i\alpha\alpha_2}{k}[(\omega - kV_w)\coth(kd_w) + (\omega - kV_v)\coth(kd_v)] \\
& + 4k\alpha\alpha_2\left[\frac{\mu_w}{\rho_w}\coth(2kd_w) + \frac{\mu_v}{\rho_v}\coth(2kd_v) \right] \Bigg\}
\end{aligned}
$$

$$M_2^i = \frac{1}{2k}\left[\gamma_i + \left\{ \frac{\alpha}{\rho_i} - 2i(\omega - kV_i) \right\} D_2 + \frac{\alpha\alpha_2}{\rho_i} \right] \quad (i = w, v)$$

$$\gamma_j = -2k\left\{ \frac{\alpha}{\rho_j} - i(\omega - kV_j) \right\} \coth(kd_j) \quad (j = w, v)$$

$$\rho_v \frac{\partial d^2}{\partial t_0} - \rho_w \frac{\partial d^1}{\partial t_0} = \left[\left[\rho\left\{ \frac{\alpha^2}{\rho^2} + (\omega - kV)^2 \right\}(1 - \coth^2(kd)) + 2\rho g\alpha_2 \right] \right] |D|^2$$

5 Third-Order Solutions

The velocity potentials in third approximation are

$$\nabla^2 \varphi_{3,w} = 0; \ \nabla^2 \varphi_{3,v} = 0 \tag{5.1}$$

If we substitute the expression for ζ_1, ζ_2, $\varphi_{1,w}$, $\varphi_{1,v}$, $\varphi_{2,w}$ and $\varphi_{2,v}$ in equation interfacial stress balance equation, the solution for third-order problem can be computed as

$$\varphi_{3,w} = \left\{ N_3^1 D^2 \overline{D} + \frac{1}{k}\frac{\partial D}{\partial t_2} \right\} \frac{\cosh(k(y + d_w))}{\sinh(kd_w)} e^{ikx} e^{-i\omega t} + \text{complex conjugate} \quad (5.2)$$

$$\varphi_{3,v} = \left\{ N_3^2 D^2 \overline{D} - \frac{1}{k}\frac{\partial D}{\partial t_2} \right\} \frac{\cosh(k(y - d_v))}{\sinh(kd_v)} e^{ikx} e^{-i\omega t} + \text{complex conjugate} \quad (5.3)$$

where N_3^1 and N_3^2 are as follows;

$$N_3^1 = -k\left[2M_2^1 \coth(2kd_w) - 2\coth(kd_w)\left(\frac{\alpha}{\rho_w} - i\omega + ikV_w \right)\frac{\alpha_2}{k}\right.$$
$$+ \frac{1}{2}\left\{ \frac{\alpha}{\rho_w} - 3i\left(\omega - kV_w\right) \right\} + \frac{\alpha}{\rho_w k^2}\left(4\alpha_2^2 - 3\alpha_3\right)$$
$$\left. - \left\{ \left(\frac{\alpha}{\rho_w} + i\omega - ikV_w \right)\coth(kd_w) + \frac{2\alpha\alpha_2}{\rho_w k} \right\}\frac{D_2}{k} \right]$$

$$N_3^2 = -k\left[2M_2^2 \coth(2kd_v) - 2\coth(kd_v)\left(\frac{\alpha}{\rho_v} - i\omega + ikV_v \right)\frac{\alpha_2}{k}\right.$$
$$- \frac{1}{2}\left\{ \frac{\alpha}{\rho_v} - 3i\left(\omega - kV_v\right) \right\} - \frac{\alpha}{\rho_v k^2}\left(4\alpha_2^2 - 3\alpha_3\right)$$
$$\left. + \left\{ -\left(\frac{\alpha}{\rho_v} + i\omega - ikV_v \right)\coth(kd_v) + \frac{2\alpha\alpha_2}{\rho_v k} \right\}\frac{D_2}{k} \right]$$

Here, we have assumed that the secular terms are zero because the expansion is uniformly valid. If we put first- and second-order solution in the stress balance equation, a nonlinear equation is achieved as follows:

$$\frac{i}{k}\frac{\partial C}{\partial \omega}\frac{\partial D}{\partial t_2} + \delta D^2 \overline{D} = 0 \quad (5.4)$$

If we put viscosity $\mu_w = \mu_v = 0$ in Eq. (5.4), the relation given by Lee [12] can be achieved.

Equation (5.4) can also be written as

$$\frac{\partial D}{\partial t_2} + \Gamma D^2 \overline{D} = 0 \quad (5.5)$$

From above equation,

$$|D|^2 = \frac{1}{|D_0|^{-2} + 2(\mathrm{Re}\Gamma)t_2} \quad (5.6)$$

It can be concluded from the above expression that if denominator gets zero, D goes to infinity and therefore the stability condition one can obtain as

$$\text{Re}\Gamma > 0 \tag{5.7}$$

6 Numerical Results and Discussion

The phenomenon of transferring of heat along with transfer of mass exists quite frequently in multiphase flow. The case of film boiling contains two rigid plates containing liquid in between where the lower plate has more temperature than the upper one. The liquid at the lower plate vaporizes, and due to gravity effect, it comes above the liquid where it condenses. The process repeats periodically and affects the stability of the flow.

The critical stability condition (5.7) predicted by the nonlinear theory will be presented in this part for a fluid–fluid interface where fluid below the interface is water and fluid above is water vapor.

$$\rho_w = 1.0 \text{ gm/cm}^3, \ \mu_w = 0.01 \text{ poise}, \ \sigma = 72.3 \text{ dyne/cm},$$
$$g = 980 \text{ cm/s}^2, \ \rho_v = 0.001 \text{ gm/cm}^3, \ \mu_v = 0.00001 \text{ poise}$$

The total length of the channel is taken as 1 inch, i.e., $d_v + d_w = 2.54$ cm, and the fluid below the patch is considered immovable, i.e., $V_w = 0$ throughout the numerical computations. The unstable zone is denoted by U and stable zone by S.

Linear analysis of considered problem was analyzed by Asthana and Agrawal [7]. In this study, irrotational viscous theory was applied to get the growth of disturbance waves. The stability range achieved in the present study and that represented by Asthana and Agrawal [7] are plotted in Fig. 2. Flow is unstable above this curve, and it is stable below this curve. The lower curve represents linear theory. The zone above this curve is unstable, while below the curve is a stable zone. The mid region was unstable in the linear study and now becomes stable. The stability range of two viscous fluids with transferring of heat has been enlarged due to nonlinearity.

To examine the effect of fluid viscosities, a comparison between irrotational viscous flow theory and irrotational inviscid flow theory is made in Fig. 3. The zone below the dotted line now becomes stable in irrotational viscous flow theory which was in the beginning unstable in the inviscid potential flow theory. VPF analysis contains the effect of viscous normal stresses, and IPF solution does not contain its effect. It can be concluded that the stable region is enlarged because there is resistance of the flow due to viscosity in the nonlinear investigation. The combined effect of nonlinearity and viscosity is shown in Fig. 4. The coupled viscosity and nonlinearity resists the perturbations to grow.
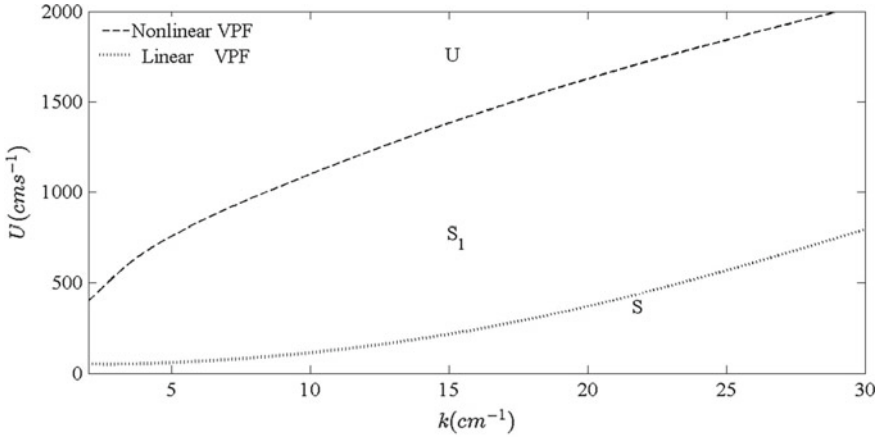
Fig. 2 Stability range for nonlinear and linear analysis; VPF—viscous potential flow
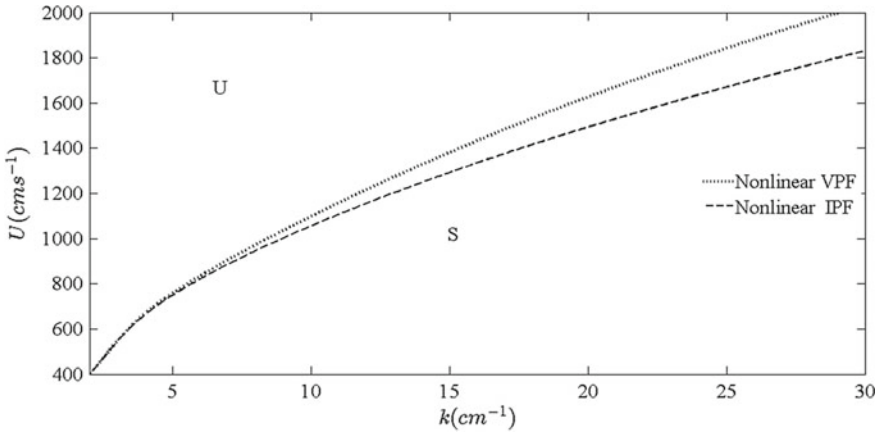
Fig. 3 Stability range for nonlinear analysis; VPF—viscous potential flow; IPF—inviscid potential flow

Figure 5 plots the relative velocity curves for vapor width $d_v = 0.3$, 0.5 and 0.7. At crest, the pressure exerted by vapor will be lower than symmetrical vapor pressure. On increasing vapor fraction, evaporation will take place. Amplitude of disturbance wave will lower down due to this, and system will be stabilized. The influence of transfer of heat in the nonlinear analysis is analyzed in Fig. 6. The increase in transfer of heat at the patch of water and vapor increases evaporation, and disturbance grows faster when transfer of heat at the juncture increases and interface will be unstable. The nature of transfer of heat at the juncture of two fluids is same irrespective of viscosity, but the inclusion of viscosity enhances the stability range.
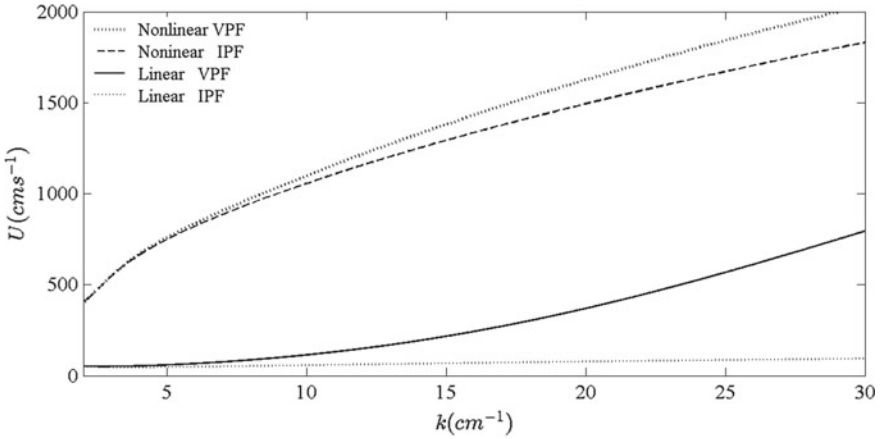
Fig. 4 Stability range for linear as well as nonlinear analysis
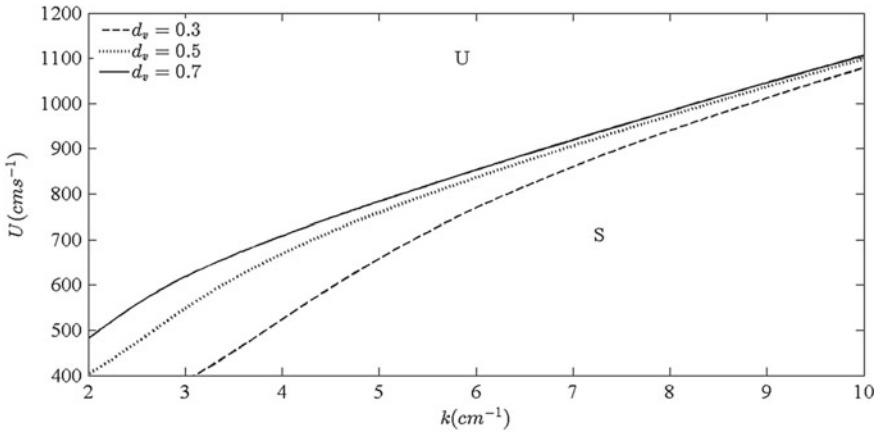
Fig. 5 Stability range for various values of d_v with $\mu_w = 0.001$, $\mu_v = 0.00001$ poise

7 Conclusions

We have examined the nonlinear Kelvin–Helmholtz instability of two superposed viscous fluids. The transferring of heat and mass at the juncture of two viscous fluids is allowed. The irrotational viscous flow theory is used to include viscosity. Timescale multiple expansion method is employed, and a partial differential equation which is nonlinear in nature is achieved.
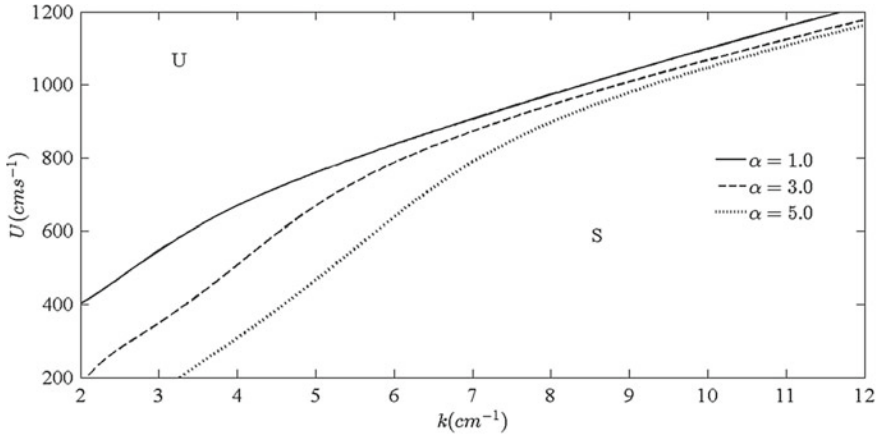
Fig. 6 Stability range for various values of α with $\mu_w = 0.001$, $\mu_v = 0.00001$ poise

The main observations are as follows:

1. The nonlinear effects resist the growth of disturbance waves.
2. Vapor width induces stability.
3. Viscosity of both fluids is also playing stabilizing role.
4. Heat/mass transfer destabilizes the interface.

References

1. Hsieh DY (1972) Effects of heat and mass transfer on Rayleigh-Taylor stability. Trans ASME 94 D:156
2. Ho SP (1980) Linear Rayleigh-Taylor stability of viscous fluids with mass and heat transfer. J Fluid Mech 101:111
3. Khodaparast KA, Kawaji M, Antar BN (1995) The Rayleigh-Taylor and Kelvin-Helmholtz stability of a viscous liquid-vapor interface with heat and mass transfer. Phys Fluids 7:359
4. Joseph DD, Liao T (1994) Potential flows of viscous and viscoelastic fluids. J Fluid Mech 265:1–23
5. Awasthi MK, Agrawal GS (2011) Viscous potential flow analysis of Rayleigh-Taylor instability with heat and mass transfer. Int J App Math Mech 7(12):73–84
6. Funada T, Joseph DD (2001) Viscous potential flow analysis of Kelvin-Helmholtz instability in a channel. J Fluid Mech 445:263
7. Asthana R, Agrawal GS (2007) Viscous Potential flow analysis of Kelvin-Helmholtz instability with mass transfer and vaporization. Phys A 382:389–404
8. Drazin PG (1970) Kelvin-Helmholtz instability of a finite amplitude. J Fluid Mech 42:321–336
9. Maslowe SA, Kelly RE (1970) Finite-amplitude oscillations in a Kelvin-Helmholtz flow. Int J Nonlinear Mech 5:427–435
10. Weissman MA (1979) Nonlinear wave packets in the Kelvin-Helmholtz instability. Phil Trans R Soc London 290 A:639–681
11. Hsieh DY (1979) Nonlinear Rayleigh-Taylor stability with mass and heat transfer. Phys Fluids 22:1435–1439

12. Lee DS (2005) Nonlinear Kelvin-Helmholtz instability of fluid layers with mass and heat transfer. J Phys A Math Gen 38:2803
13. Awasthi MK, Asthana R, Agrawal GS (2012) Viscous potential flow analysis of nonlinear Rayleigh-Taylor instability with heat and mass transfer. Microgravity Sci Technol 24:351–363
14. Awasthi MK, Asthana R, Uddin Z (2016) Nonlinear study of Kelvin-Helmholtz instability of cylindrical flow with mass and heat transfer. Int Comm Heat Mass Transf 71:216–224

Influence of Ion-Slip and Hall Current on Magneto Hydrodynamic Free Convective Flow Past an Accelerated Plate with Dufour Effect and Ramped Temperature

G. Dharmaiah, K. S. Balamurugan, and K. V. B. Raja Kumar

Abstract An analytical solution is proclaimed the significance of ion-slip and Hall current on magnetohydrodynamic convective free flow of radiation absorbing as well as a chemical reacting fluid past an accelerated affecting vertical porous plate with ramped temperature and Dufour effect. The modelling equations are reformed into dimensionless equations, further illuminated systematically by multiple standard perturbation law. Appraisals were operationalized graphically to scrutinize the performance of fluid velocity, temperature as well as concentration on the vertical plate by means of the disparity of emerging physical parameters.

Keywords Hall current · Ion-slip · Chemical reaction · Dufour · MHD

1 Introduction

Due to multifaceted industrial as well as manufacturing applications, it is a great understanding to examine the MHD flow. The noteworthy purpose of MHD principles is to interrupt the flow field in a requisite way by fluctuating the formation of the point of the confinement layer. Thus, with the intention to modify the flow kinematics, the idea to execute MHD seems to be more flexible and consistent. In pharmaceutical as well as ecological science, MHD has been playing a critical role in the application of fluid dynamics and therapeutic sciences, owing to its implications in chemical fluids

G. Dharmaiah (✉)
Department of Mathematics, Narasaraopeta Engineering College, Narasaraopet,
Andhra Pradesh 522601, India
e-mail: dharma.g2007@gmail.com

K. S. Balamurugan
Department of Mathematics, R.V.R & J.C. College of Engineering, Guntur,
Andhra Pradesh 522109, India
e-mail: muruganbalaks@gmail.com

K. V. B. Raja Kumar
Department of Mathematics, Kallam Haranadhareddy Institution of Technology,
Guntur, Andhra Pradesh 522109, India
e-mail: kvbrajakumar@gmail.com

as well as metallurgical fields. The production of an extra prospective dissimilarity transverse to the direction of accumulating free charge and applied magnetic field among the opposite surfaces induces an electric current vertical to both the fields, magnetic as well as electric. This current is renowned as Hall current. Numerous explorers have been reviewed on Ion-slip as well as Hall current. Vijayaragavan and Karthikeyan [1] examined the significance of Hall current effect on MHD Casson fluid in presence Dufour as well as thermal radiation effects by means of chemically reaction. The noteworthiness of double diffusion, Ion-slip and Hall current on MHD free convection flow of couple stretch fluid during porous channels through chemical reaction and Dufour along with soret effects scrutinized [2, 3].

The impact of Hall and ion-slip current on unsteady 2D fluid flow in presence of Dufour as well as heat source described by [4]. In this study, the modelling equations are reformed into dimensionless equations, further illuminated systematically by multiple standard perturbation law and a consistent magnetic field is employed perpendicularly to the way of the flow. Abuga et al. [5] have discussed prominence of Hall current along with rotating system on magnetohydrodynamic fluid flow through an infinite plate affecting which is perpendicular, with externally heating as well as cooling of the plate in the occurrence of ramped wall temperature and isothermal in the aspect of thermal diffusion as well as diffusion thermo. The implication of hall current on convective double diffusion flow past stretching sheet along with dissipation as well as radiation contemplated by [6, 7]. Based on this scrutiny it was confirmed that Galerkin finite element was employed for solving nonlinear coupled equations. Makinde [8] has explored numerically, ion-slip and hall current importance on transient MHD flow by means of convective external boundary conditions in the presence of an infinite porous plate. Based on the outcomes it was perceived that the explicit finite difference method was employed for solving unsteady coupled nonlinear PDE's. Seth et al. [9] have dissected, affect of a rotational system on unsteady hydromagnetic flow which is natural convective flow over impulsively affecting erect plate thereby ramped temperature implanted in a permeable medium by taking thermal diffusion as well as heat absorption. Deka and Das [10], Seth [11] and Rajesh and Chamkha [12] have analyzed the significance of ramped wall temperature on transient 2D, passes through a vertical surface with radiation as well as a chemical reaction.

Objective of present study mainly discussed effect of Hall as well as ion-slip current on MHD natural convective with double diffusion of a chemical reacting and radiation absorbing past fluid an accelerated moving vertical porous plate with ramped temperature in presence of Dufour effect. Natural convection emerging from such a plate temperature profile is probable to be of importance in numerous manufacturing applications particularly where the underlying temperature is of noteworthiness in the design of electromagnetic gadgets as well as a number of natural phenomena occurring owing to convection as well as heat generation/absorption.

2 Formulation and Solution of the Problem

Contemplate transient 2D MHD natural convection stream with the help of double diffusion, synthetically responding with temperature-dependent heat retaining fluid past an accelerated boundless orthogonal affecting porous plate in a homogeneous of a stress grading in the aspect of thermal as well as mass diffusions. Contemplate x^*-axis is along the permeable in the upward surface way and z^*-axis in the way of non-parallel to the plane of the plate also y^* is normal to the x^*z^*—plane. The fluid is saturated by uniform crosswise appealing field B_0 employing parallel to z^*-axis. Initially, i.e. at the time $t^* \leq 0$; the fluid as well as plate are at rest and retained at uniform temperature T_∞^* uniform surface concentration C_∞^*. At time $t^* > 0$, plate starts affecting in x^*- direction opposite the gravitational field with time-dependent velocity $U_0^* \cos \omega^* t^*$. Temperature of the surface is accelerated or else declined to $T^* = T_\infty^* - t^*(T_\infty^* - T_w^*)/t_0$ and the scale of concentration at the surface of the plate is accelerated or declined to $C^* = C_\infty^* - t^*(C_\infty^* - C_w^*)/t_0$ when $(0, t_0]$ thereafter i.e. at (t_0, ∞). The schematic outline assumed flow setup is shown in Fig. 1: The Hall current and Ion-slip was contemplated in the equation of momentum. Furthermore, Dufour as well as radiation absorption was reflected in the equation of energy.

On the basis of the exceeding hypothesis, the transient fluid is represented by the consequent partial differential equations.

Equation of Momentum:

$$\left.\begin{aligned}\left[\frac{\partial u^*}{\partial t^*}\right] &= \vartheta\left[\frac{\partial^2 u^*}{\partial z^{*2}}\right] + v_{\mathrm{r}}\left[\frac{\partial^2 u^*}{\partial z^{*2}}\right] - \beta\left[T_\infty^* - T^*\right]g - \beta^*\left[C_\infty^* - C^*\right]g \\ &\quad - u^*\vartheta\left[K^*\right]^{-1} - \frac{v_{\mathrm{r}}}{K^*}\left[u^*\right] - \frac{\left[\beta_e w^* + \alpha_e u^*\right]B_0^2 \sigma_e}{\rho\left[\beta_e^2 + \alpha_e^2\right]}\end{aligned}\right\} \tag{1}$$
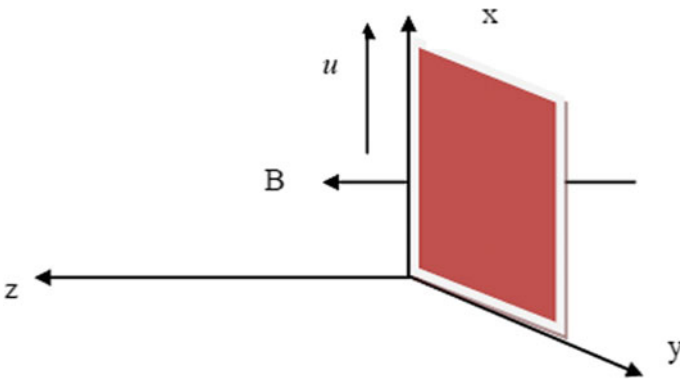

Fig. 1 Schematic outline assumed flow setup

$$\left[\frac{\partial w^*}{\partial t^*}\right] = \vartheta\left[\frac{\partial^2 w^*}{\partial z^{*2}}\right] + v_r\left[\frac{\partial^2 w^*}{\partial z^{*2}}\right] - \frac{\vartheta}{k^*}[w^*]$$
$$- \frac{v_r}{K^*}[w^*] + \frac{B_0^2\sigma_e[\beta_e u^* - \alpha_e w^*]}{\rho[\alpha_e^2 + \beta_e^2]} \tag{2}$$

Equation of Energy:

$$\frac{\partial T^*}{\partial t^*} = \frac{k}{\rho C_p}\left(\frac{\partial^2 T^*}{\partial z^{*2}}\right) + \frac{Q_0}{\rho C_p}(T^* - T_\infty^*)$$
$$+ \frac{16\sigma_s^* T_\infty^{*3}}{3\rho C_p k_e^*}\frac{\partial^2 T^*}{\partial z^{*2}} + \frac{D_m K_T}{C_s C_P}\frac{\partial^2 C^*}{\partial z^{*2}} + R^*(C^* - C_\infty^*) \tag{3}$$

Equation of Concentration:

$$\frac{\partial C^*}{\partial t^*} = \tilde{D}\frac{\partial^2 C^*}{\partial y^{*2}} + K_r(C_\infty^* - C^*) \tag{4}$$

The relevant confinement conditions are

$$\left\{\begin{array}{c} u^* = 0, T^* = T_\infty^*, C^* = C_\infty^* \text{ if } t^* \le 0 \text{ for } z \ge 0 \\ u^* = [U_0^* \cos\omega^* t^*], \dfrac{[T^* - T_\infty^*]}{[T_w^* - T_\infty^*]} = t^*[t_0]^{-1} \\ \dfrac{[C_\infty^* - C^*]}{[C_\infty - C_w^*]} = \left[\dfrac{t^*}{t_0}\right] \\ u^* \to 0, T^* \to T_\infty^*, C^* \to C_\infty^* \text{ as } z^* \to \infty \end{array} \quad \begin{array}{c} \\ \\ \text{if } (0, t_0] \text{ at } z^* = 0 \\ \\ \end{array}\right\} \tag{5}$$

Presently, non-dimensional amounts are characterized as

$$\left.\begin{array}{c} f = \dfrac{u^*}{U_0}, g = \dfrac{w^*}{U_0}, U_\infty = \dfrac{U_\infty^*}{U_0}, z = \dfrac{V_0 y^*}{\vartheta}, t = \dfrac{V_0^2 t^*}{\vartheta}, t_0 = \dfrac{\upsilon}{U_0^2} \\ K^* = \dfrac{K\vartheta^2}{V_0^2}, n^* = \dfrac{V_0^2 n}{\vartheta}, \dfrac{(T_\infty^* - T^*)}{(T_\infty^* - T_w^*)} = \theta, \dfrac{(C_\infty^* - C^*)}{(C_\infty^* - C_w^*)} = C \end{array}\right\} \tag{6}$$

After substituting the confinement conditions and non-dimensional variables in the governing Eqs. (1)–(4) then we obtain:

$$\frac{\partial f}{\partial t} = (1+\beta)\frac{\partial^2 f}{\partial z^2} + G_r\theta + G_m C - (1+\beta)[f] - \frac{B_0^2\sigma_e[\alpha_e f + \beta_e g]}{\rho[\alpha_e^2 + \beta_e^2]} \tag{7}$$

$$\left[\frac{\partial g}{\partial t}\right] = (1+\beta)\left[\frac{\partial^2 g}{\partial z^2}\right] + v_r\left[\frac{\partial^2 g}{\partial z^2}\right] - (1+\beta)[g] + \frac{B_0^2\sigma_e[\beta_e f - \alpha_e g]}{\rho[\alpha_e^2 + \beta_e^2]} \tag{8}$$

$$\frac{\partial \theta}{\partial t} = (\text{Pr})^{-1}\left(1 + \frac{4R}{3}\right)\frac{\partial^2 \theta}{\partial z^2} + \eta\theta + Du\frac{\partial^2 C}{\partial z^2} + R_{\text{a}}C \tag{9}$$

$$\frac{\partial C}{\partial t} = (Sc)^{-1}\frac{\partial^2 C}{\partial z^2} - K_{\text{r}}C \tag{10}$$

The corresponding confinement conditions are

$$\left.\begin{array}{c} f = g = \theta = C = 0 \quad \forall z, t \leq 0 \\ u = \cos\omega t, \quad g = 0, \quad \theta = C = t \text{ at } z = 0 \\ u, \theta, C \to 0 \text{ as } z \to \infty \end{array}\right\} : t > 0 \right\} \tag{11}$$

$$\left.\begin{array}{c} M = \dfrac{\sigma B_0^2 \vartheta}{\rho V_0^2}, G_{\text{m}} = \dfrac{\vartheta\beta^* g\left(C_w^* - C_\infty^*\right)}{V_0^2 U_0}, G_{\text{r}} = \dfrac{\vartheta\beta g\left(T_w^* - T_\infty^*\right)}{V_0^2 U_0}, R = \dfrac{4\sigma T_\infty^{*3}}{k_e k} \\ Sc = \dfrac{\vartheta}{\bar{D}}, \text{Dr} = \dfrac{D_{\text{m}}K_{\text{T}}\left[C_w^* - C_\infty^*\right]}{\vartheta C_S C_{\text{P}}\left[T_w^* - T_\infty^*\right]}, R_{\text{a}} = \dfrac{R^* \vartheta\left(C_w^* - C_\infty^*\right)}{V_0^2\left(T_w^* - T_\infty^*\right)}, \text{Pr} = \dfrac{\rho\vartheta C_{\text{P}}}{k} \\ \xi = \left[\dfrac{M[-\alpha_e + i\beta_e]}{\left[\alpha_e^2 + \beta_e^2\right]} + \dfrac{1+\beta}{K}\right], K_{\text{r}} = \dfrac{k_1\vartheta}{V_0^2}\beta = \dfrac{v_{\text{r}}}{\vartheta}\eta = \dfrac{\vartheta Q_0}{\rho V_0^2 C_{\text{P}}}, \Gamma = \left(\dfrac{3+4R}{3\,\text{Pr}}\right) \end{array}\right\} \tag{12}$$

$$\frac{\partial \chi}{\partial t} = (1 + \beta)\frac{\partial^2 \chi}{\partial z^2} + G_{\text{r}}\theta + G_{\text{m}}C - \chi\xi \tag{13}$$

Here $\chi = f + ig$

The relevant confinement conditions are

$$t > 0 : \left\{\begin{array}{c} \chi = \theta = C = 0 \quad \forall z, t \leq 0 \\ \chi = \cos\omega t, \theta = C = t \text{ at } z = 0 \\ \chi, \theta, C \to 0, \text{ as } z \to \infty \end{array}\right\} \tag{14}$$

Equations (9), (10) and (13) are illuminated systematically with the help of single perturbation method subject to initial and confinement conditions (14).

$$\chi = \chi_0(z)\exp(i\omega t)\ldots, \quad \theta = \theta_0(z)\exp(i\omega t)\ldots, \quad C = C_0(z)\exp(i\omega t)\ldots\} \tag{15}$$

Substituting Eq. (15) in Eqs. (9), (10) and (13) then we obtain:

$$(1 + \beta)\chi_0'' - (\xi - i\omega) \quad \chi_0 = -G_{\text{r}}\theta_0 - G_{\text{m}}C_0 \tag{16}$$

$$\Gamma\theta_0'' - (i\omega - \eta)\theta_0 = -DuC_0'' - R_{\text{a}}C_0 \tag{17}$$

$$C_0'' - Sc(K_r + i\omega)C_0 = 0 \tag{18}$$

The appropriate confinement conditions are

$$\left\{ \begin{array}{r} \chi_0 = e^{-i\omega t}\cos(\omega t),\, \theta_0 = C_0 = te^{-i\omega t} \text{ at } z = 0 \\ \chi_0, \theta_0, C_0 \quad \to 0 \text{ as } z \to \infty \end{array} \right\} \tag{19}$$

Solve Eqs. (16)–(18) by using (19) then we get,

$$\chi = \left(\begin{array}{c} \left((\cos\omega t)e^{-i\omega t} - \psi_2 - \psi_3\right)\exp\left(-\left(\sqrt{\dfrac{(S-i\omega)}{1+\beta}}\right)z\right) \\ +\psi_2\exp\left(-\left(\sqrt{\dfrac{(i\omega-\eta)}{\Gamma}}\right)z\right) + \psi_3\exp\left(-\left(\sqrt{Sc(K_r+i\omega)}\right)z\right) \end{array} \right)e^{i\omega t} \tag{20}$$

$$\theta = \left(\left(te^{-i\omega t} - \psi_1\right)e^{-\left(\sqrt{\frac{(i\omega-\eta)}{\Gamma}}\right)z} + \psi_1 e^{-\left(\sqrt{Sc(K_r+i\omega)}\right)z} \right)e^{i\omega t} \tag{21}$$

$$C = \left(te^{-i\omega t}e^{-\left(\sqrt{Sc(K_r+i\omega)}\right)z}\right)e^{i\omega t}. \tag{22}$$

3 Discussion of Ideal Convergence

Figures 2, 3 and 4 Reaffirmed that the sway of time (t) on the velocity and temperature as well as concentration. From this figure, it was identified that as the values of "t" rises then it leads to rise in temperature and concentration as well as velocity. Figures 5, 6, 7 and 8 Illustrated that the performance of velocity and temperature for disparate estimators of Dufour (Dr) and radiation absorption (R_a). The results obtained from this figure it was perceived that enhance in temperature as well as velocity. Representative dissimilarity of the velocity along the spanwise coordinate
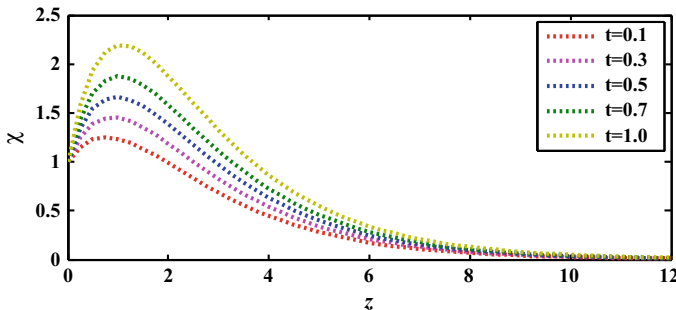
Fig. 2 Performance of **t** on $\chi(z)$
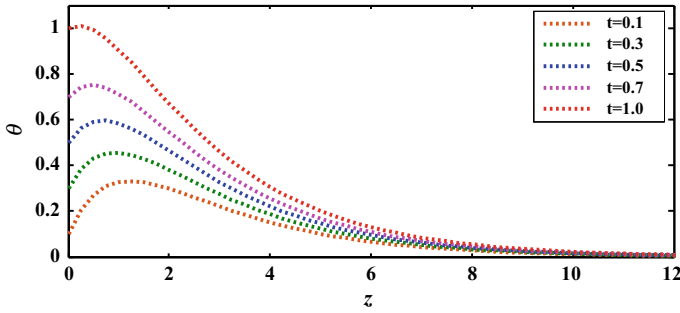
Fig. 3 Performance of **t** on $\theta(z)$
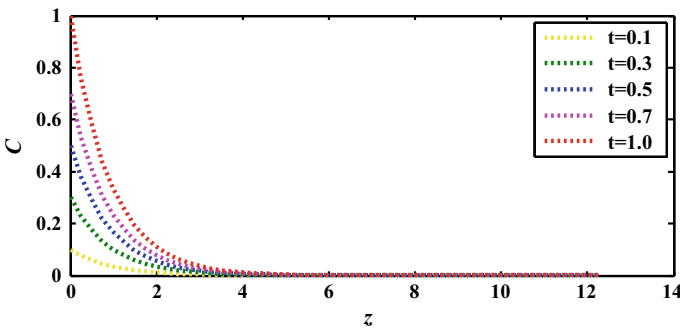
Fig. 4 Performance of **t** on $C(z)$
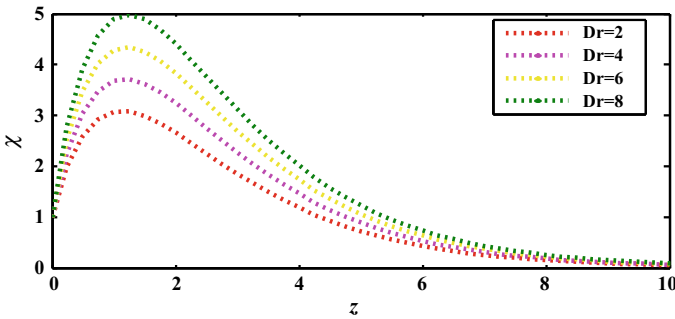
Fig. 5 Performance of Dr on $\chi(z)$

yare exhibit in Figs. 9 and 10: From these figures, it was recognized that for diverse values of Ion-slip estimator (β_i) rises then it leads to enhance in velocity, but reverse effect occurred in case of Hall current (β_e). Figures 11 and 12: demonstrated that the impact of C.R. (K_r) as well as S.nu. (Sc) on concentration. On the basis of figures, it was perceived that velocity and concentration reduced with the raise of K_r and Sc.
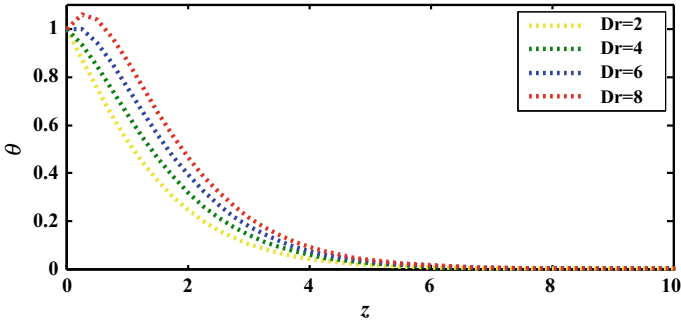
Fig. 6 Performance of Dr on $\theta(z)$
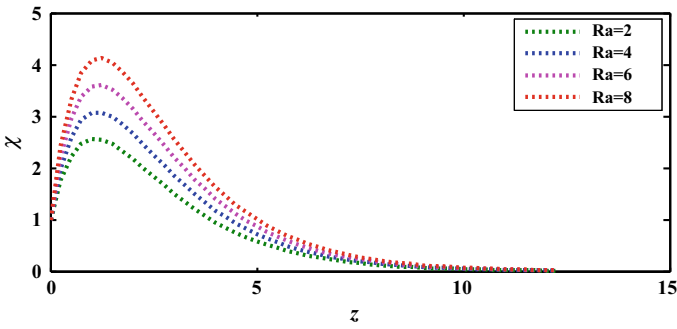
Fig. 7 Performance of R_a on $\chi(z)$
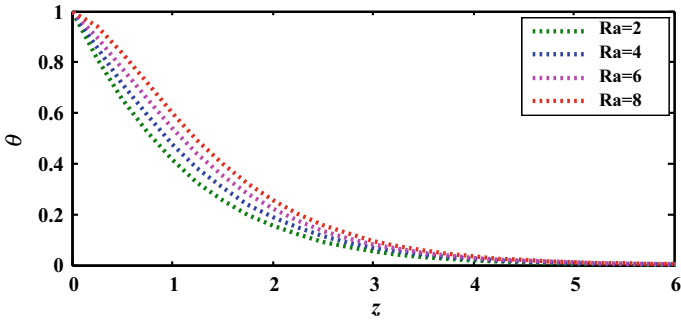
Fig. 8 Performance of R_a on $\theta(z)$
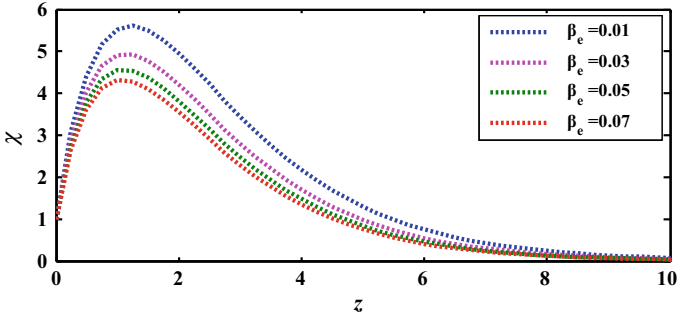
Fig. 9 Performance of β_e on $\chi(z)$
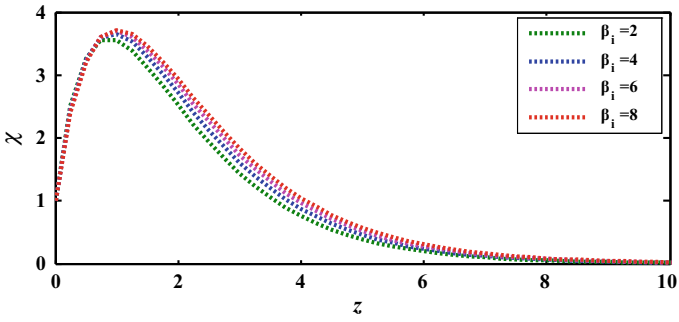
Fig. 10 Performance β_i on $\chi(z)$
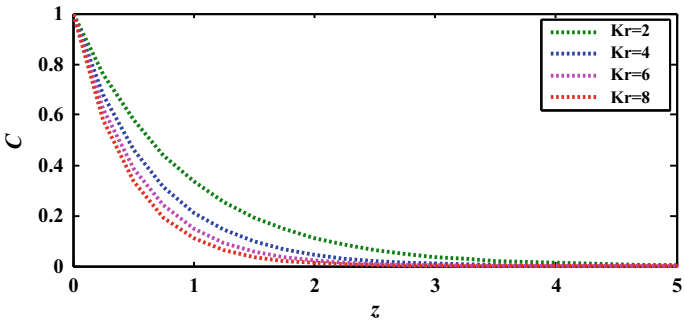
Fig. 11 Performance of Kr on $C(z)$
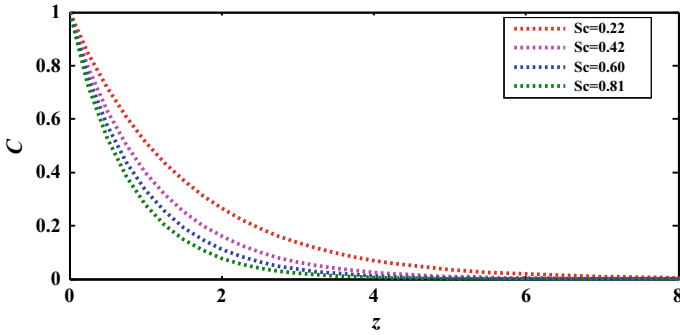
Fig. 12 Performance of *Sc* on *C(z)*

4   Conclusions

- As velocity, temperature as well as concentration rises with rise in time *t*.
- Temperature and velocity rises owing to the enhancement of Dufour Dr as well as radiation absorption R_a
- As rise in chemical reaction K_r leads to decline in velocity as well as concentration.
- As Velocity rises with the enhancement of Hall parameter (β_e), but inverse effect was occurred in case of Ion-slip current (β_i).

References

1. Vijayaragavan R, Karthikeyan S (2018) Hall current effect on chemically reacting MHD Casson fluid flow with dufour effect and thermal radiation. Asian J Appl Sci Technol 2:228–245
2. Anika N, Hoque M, Hossain I (2015) Thermal diffusion effect on unsteady viscous MHD microplar fluid flow through an infinite vertical plate with hall and ion-slip current. Procedia Eng 105:160–166
3. Srinivasacharya D, Shafeeurrahaman Md (2017) Mixed convection flow of Nanofluid in a vertical channel with hall and ion-slip effects. Front Heat Mass Transfer 8:1–10
4. Pannerselvi R, Kowsalya J (2015) Ion slip and Dufour effect on unsteady free convection flow past an infinite vertical plate with oscillatory suction velocity and variable permeability. Int J Sci Res 4:2079–2090
5. Abuga JG, Kinyanju M, Sigey JK (2011) An investigation of the effect of Hall currents and rotational parameter on dissipative fluid flow past a vertical semi-infinite plate. J Eng Tech Res 3:314–320
6. Ojjela O, Naresh Kumar K (2014) Hall and Ion slip effects on free convection heat and mass transfer of chemically reacting couple stress fluid in a porous expanding or contracting walls with soret and Dufour effects. Front Heat Mass Transfer 5:1–12
7. Alivene G, Sreevani M (2017) Effect of hall current, thermal radiation, dissipation and chemical reaction on hydromagnetic non-darcy mixed convective heat and mass transfer flow past a stretching sheet in the presence of heat sources. Adv Phys Theor Appl 61:14–25

8. Makinde OD (2012) Heat and mass transfer by MHD mixed convection stagnation point flow toward a vertical plate embedded in a highly porous medium with radiation and internal heat generation. Meccanica 47:1173–1184
9. Seth GS, Nandkeolyar R, Ansari MS (2011) Effect of rotation on unsteady hydromagnetic natural convection flow past an impulsively moving vertical plate with ramped temperature in a porous medium with thermal diffusion and heat absorption. Int J Appl Math Mech 7:52–69
10. Deka RK, Das SK (2011) Radiation effects on free convection flow near a vertical plate with ramped wall temperature. Engineering 3:1197–1206
11. Seth GS, Nandkeolyar R, Ansari MS (2013) Effects of thermal radiation and rotation on unsteady hydromagnetic free convection flow past an impulsively moving vertical plate with ramped temperature in a porous medium. J Appl Fluid Mech 6:27–38
12. Rajesh V, Chamkha AJ (2014) Effects of ramped wall temperature on unsteady two-dimensional flow past a vertical plate with thermal radiation and chemical reaction. Commun Num Anal 2014:1–17

Effect of Permeable Boundaries on the Flow of a Jeffrey Fluid in a Channel of Varying Cross-Section

P. Devaki [ORCID]**, C. H. Badari Narayana, A. Kavitha, and S. Sreenadh**

Abstract In this paper, the flow of a simplest Non-Newtonian fluid in a channel of varying cross-section with permeable boundaries is investigated. The paper finds its significance in understanding the flow of Bio-fluids in the ducts of varying cross section. Perturbation technique is used to solve the governing equations of the flow phenomenon. The expressions for velocity, flow rate, wall shear stress, and the pressure drop are derived. The flux is a function of external pressure, Jeffrey parameter, and the permeability parameter. Further, if $\lambda_1 \to 0$ our results agree with Krishna Prasad and Chandra (Proc Nat Acad Sci 60(A) III: 317–326, 1990 [1]). Mathematica software is used find the pressure, which place a vital role in varying cross sections. Shear stress increases with increasing effects of permeability and Jeffrey parameters which is observed graphically. It is noticed that shear thinning reduces the wall shear stress and this point is stresses in the paper as well. This work helps the young researcher to develop interest in the field of Bio-fluids with varying cross-section.

Keywords Shear stress · External pressure · Flow rate · Pressure drop

1 Introduction

Nowadays flow in a tube or channel with varying cross-section through permeable boundaries, has become an interesting topic among researchers. There are several bio-fluids present in human ducts that are considered as Non-Newtonian fluids. Among

P. Devaki (✉)
Department of Mathematics, School of Engineering and Technology, CMR University, Bangalore, India
e-mail: palluru.d@cmr.edu.in

C. H. Badari Narayana
Department of Mathematics, The Hindu College, Machlipatnam, India

A. Kavitha
Department of Mathematics, School of Advanced Sciences, VIT, Vellore 632014, India

S. Sreenadh
Department of Mathematics, Sri Venkateswara University, Tirupati, Andhra Pradesh, India

several Non-Newtonian fluids, Jeffrey fluid is the simplest model of Non-Newtonian fluids. Permeable boundaries play a vital role in the field of medicine and engineering.

Varying cross-section of a tube or channel also includes the elastic nature in the tube wall. Vajravelu et al. [2, 3] concentrated on a circular tube that includes elastic behavior of the tube for the flow of Hershel-Bulkley and Casson fluid. Badari et al. [4] investigated on the inclination effect in an elastic tube for a Jeffrey fluid. Berhane [5] analyzed the effect of slop, slip and reabsorption parameters on the flow of an incompressible fluid in a rigid tube with varying cross-section. Recently Devaki et al. [6] studied on a channel with flexible walls of a Casson fluid with heat transfer and slip effects.

Permeable walls find its significance in the filtering of physiological fluids in field of engineering and medicine. Some of the physical parameters used as permeable materials are limestone and sand. In human body, the skin act as a permeable material to send out toxins in our body in the form of sweat. Fakour et al. [7] studied on the MHD flow of a Nanofluid in a permeable channel and found that the Reynolds and Hartman number reduces the Nanofluid flow in a channel. Rasoulzadeh and Panfilov [8] found the effects of inertial and visco-inertial effects on the flow of a fluid in channel with wavy walls. Many researchers concentrated on the flow of wavy channels, diverging channel with the flow of Newtonian/ no-Newtonian fluids [9–13].

Based on these facts, it is noticed that very few researchers are concentrating on the flow of simplest Non-Newtonian fluid in a permeable channel with different cross-sections. The influence of many physical parameters like permeability parameter, Jeffrey parameter, Reynolds number, and others on the wall shear stress, flow rate, and pressure drop are discussed graphically.

2 Formulation of the Physical Situation

Consider the steady flow of a Jeffrey fluid in a permeable channel with varying cross-section. We considered the fluid flow is two dimensional and incompressible. The governing equations are framed in Cartesian coordinate system (X, Y), where X is the axial distance and Y is the distance across the channel Fig. 1. The cross-section varies with the boundary of the wall as

$$Y = \pm H(X) = \pm H_0 h\left(\frac{X}{L}\right) \text{ and } h(0) = 1, \tag{1}$$

where $2H_0$ is the initial channel width, L is the characteristic length of the channel and $h\left(\frac{X}{L}\right)$ is an arbitrary function of axial distance and represents the cross-section variation.
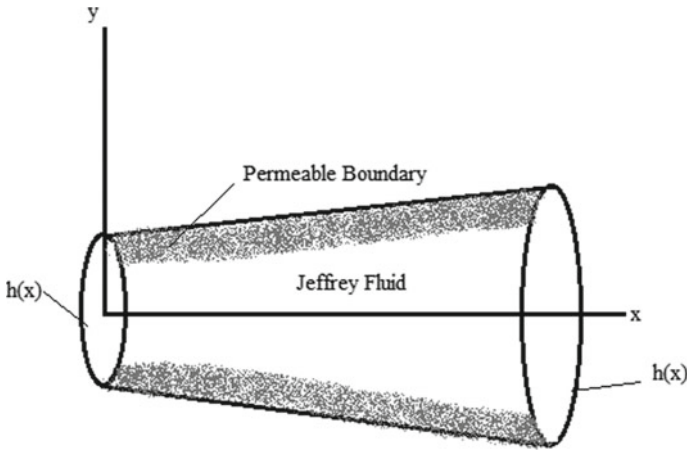
Fig. 1 Physical geometry

The non-dimensional quantities are defined as.

$$x = \frac{X}{L}, y = \frac{Y}{H_0}, u = \frac{2H_0 U}{Q_0}, v = \frac{2LV}{Q_0}, (p, p_{ext}) = \frac{2H_0^3(P, P_{ext})}{\mu L Q_0},$$

$$k = \frac{\mu L^2 K}{H_0^3}, q = \frac{Q}{Q_0}, h = \frac{H}{H_0}, T_W = \frac{2H_0^3 \tau_w}{\mu L Q_0} \tag{2}$$

By applying these non-dimensional quantities, the non-dimensional governing equations are

$$\text{Re}\,\varepsilon\left(u u_x + v u_y\right) = -p_x + \frac{1}{1 + \lambda_1}\left[\varepsilon^2 u_{xx} + u_{yy}\right], \tag{3}$$

$$\text{Re}\,\varepsilon^3\left(u v_x + v v_y\right) = -p_y + \frac{1}{1 + \lambda_1}\varepsilon^2\left[\varepsilon^2 v_{xx} + v_{yy}\right], \tag{4}$$

$$u_x + v_y = 0, \tag{5}$$

and the corresponding boundary conditions are:

$$\varepsilon^2 u + \varepsilon^2 v h_x = 0 \text{ and } v - u h_x = K(p - p_{ext}) \text{ at } y = \pm h(x), \tag{6a, b}$$

$$v = 0 \text{ and } u_y = 0 \text{ at } y = 0, \tag{6c, d}$$

$$q = 1 \text{ and } \overline{P} = P^* \text{ at } x = 0, \tag{6e, f}$$

Here, we considered the analysis for $\varepsilon \ll 1$ and Re is chosen in such a way that $\text{Re} = O(\varepsilon)$ where $\varepsilon = \frac{H_0}{L}$ and $\text{Re} = \frac{Q_0}{2\nu}$ is the flow Reynolds number.

3 Solution of the Problem

To solve the Eqs. (3–6e, f), we use an asymptotic power series in terms of ε as follows:

$$(u, v, p) = (u_0, v_0, p_0) + \varepsilon(u_1, v_1, p_1) + O(\varepsilon^2), \qquad (7)$$

Substituting the above expansion in Eqs. (3–6e, f) and collecting the like powers of ε, we get the following sets of equations:

Zeroth Order

$$\frac{1}{1 + \lambda_1} u_{0yy} = p_{0x}, \; p_{0y} = 0, \; u_{0x} + v_{0y} = 0, \qquad (8a, b, c)$$

$$u_0 = 0 \text{ and } v_0 - u_0 h_x = K(p_0 - p_{\text{ext}}) \text{ at } y = \pm h(x), \qquad (8d, e)$$

$$v_0 = 0 \text{ and } u_{0y} = 0 \text{ at } y = 0, \qquad (8f, g)$$

$$p_{0x} = \frac{-3}{1 + \lambda_1} \text{ and } \overline{P}_0 = P^* \text{ at } x = 0, \qquad (8h, i)$$

First Order

$$(1 + \lambda_1)\big[p_{1x} + \text{Re}\big(u_0 u_{0x} + v_0 u_{0y}\big)\big] = u_{1yy}, \; p_{1y} = 0, \; u_{1x} + v_{1y} = 0 \quad (9a, b, c)$$

$$u_1 = 0 \text{ and } v_1 - u_1 h_x = K p_1 \quad \text{at } y = \pm h(x), \qquad (9d, e)$$

$$v_1 = 0 \text{ and } u_{1y} = 0 \text{ at } y = 0, \qquad (9f, g)$$

$$p_{1x} = \frac{27\text{Re}(1 + \lambda_1)}{35}\big[3p^* k + 2h_x\big] \text{ and } \overline{P}_1 = 0 \text{ at } x = 0, \qquad (9h, i)$$

Solving the zeroth-order and first-order equations and using the boundary conditions for velocity components, the expressions for u_0, v_0, u_1 and v_1 are obtained as

$$u_0 = (1 + \lambda_1)\frac{p_{0x}}{2}(y^2 - h^2), \tag{10}$$

$$v_0 = \frac{(1 + \lambda_1)}{6}\left(p_{0x}6hh_x y + 3h^2 y p_{0xx} - p_{0xx}y^3\right), \tag{11}$$

$$u_1 = (1 + \lambda_1)\left[\frac{p_{0x}}{2}(y^2 - h^2) + \frac{(1 + \lambda_1)^2}{360}\text{Re}\left\{\begin{array}{c}(y^6 + 45h^4 y^2 - 46h^6)p_{0x}p_{0xx}+ \\ 15hh_x p_{0x}^2(y^4 + 6h^2 y^2 - 7h^4)\end{array}\right\}\right], \tag{12}$$

$$v_1 = -(1 + \lambda_1)y\left[\begin{array}{c}\frac{1}{6}\left\{p_{1xx}(y^2 - 3h^2) - 6p_{1x}hh_x\right\} \\ +\frac{(1+\lambda_1)^2}{2520}\text{Re}\left\{\begin{array}{c}(p_{0xx}^2 + p_{0xxx}p_{0x})(y^6 + 105h^4 y^2 - 322h^6) \\ +42hh_x p_{0xx}p_{0x}(y^4 + 20h^2 y^2 - 81h^4) + 21hh_{xx}p_{0x}^2 \\ (y^4 + 10h^2 y^2 - 35h^4) + h_x^2(y^4 + 30h^2 y^2 - 175h^4)\end{array}\right\}\end{array}\right], \tag{13}$$

The differential equations governing the zeroth- and first-order pressure p_0 and p_1, respectively are given by

$$p_{0xx} + \frac{3h_x}{h}p_{0x} - \frac{3k}{h^3(1 + \lambda_1)}(p_0 - p_{\text{ext}}) = 0, \tag{14}$$

$$p_{1xx} + \frac{3h_x}{h}p_{1x} - \frac{3k}{h^3(1 + \lambda_1)}p_1 = -3\text{Re}(1 + \lambda_1)^2\left[\begin{array}{c}(p_{0xx}^2 + p_{0x}p_{0xx})\frac{3h^4}{35} \\ + h_x p_{0x}p_{0xx}h^3 + \frac{h^2}{5}(hh_x + 6h_x^2)\end{array}\right], \tag{15}$$

The differential Eqs. (14) and (15) with the initial conditions (8h, i) and (9h, i), respectively form a two-point initial value problem and for a given $h(x)$. So we can find p_0 and p_1.

Shear Stress and Flow Rate
The non-dimensional shear stress T_w is given by $T_w = \frac{\partial u}{\partial y}\left(1 + \varepsilon^2 h_x^2\right)$, at $y = \pm h(x)$ and the volumetric flow rate is given by $q = \int_0^{h(x)} u dy$.
In view of (7), T_w and q can be expressed as

$$T_w = T_{0w} + \varepsilon T_{1w} + O(\varepsilon^2), \tag{16}$$

$$q = q_0 + \varepsilon q_1 + O(\varepsilon^2), \tag{17}$$

where
$T_{0w} = h(1 + \lambda_1)p_{0x},, \quad T_{1w} = h(1 + \lambda_1)p_{1x} + \frac{2(1+\lambda_1)^2}{15}\text{Re}p_{0x}h^2\left[6k(p_0 - p_{\text{ext}}) - (1 + \lambda_1)h^2 h_x p_{0x}\right], \quad q_0 = -\frac{(1+\lambda_1)}{3}h^3 p_{0x},$
$q_1 = -(1 + \lambda_1)h^3\left[\frac{p_{1x}}{3} + \frac{(1+\lambda_1)^2}{35}\text{Re}hp_{0x}(9k(p_0 - p_{\text{ext}}) - 2h^2 h_x p_{0x})\right]$, and we define $q^* = q|_{x=1}$

3.1 Particular Case

It is to be noted that even though numerical solutions of (14) and (15) can be given for any arbitrary $h(x)$, it is not possible to find out an analytical solution always. So, here we consider a particular case when $h(x) = e^{\alpha x}$ for which we give an analytical solution for the differential equation governing the zeroth-order pressure p_0. Equation (14) reduces to

$$p_{0xx} + 3\alpha p_{0x} - 3ke^{-3\alpha x}(p_0 - p_{\text{ext}}) = 0 \tag{18}$$

and the initial conditions are

$$\overline{p} = p^* \text{ and } p_{0x} = \frac{-3}{(1 + \lambda_1)} \text{ at } x = 0 \tag{19}$$

Now using the transformation $p_0(x) - p_{\text{ext}} = w(z); z = e^{-3\alpha x}$, Eq. (18) becomes

$$zw_{zz} - w_z - \beta^2 zw = 0 \tag{20}$$

where $\beta = \sqrt{4k/3\alpha^2(1 + \lambda_1)}$. Again using $w = zW(s)$, where $s = z\beta$, we get

$$s^2 W_{ss} + sW_s - (s^2 + 1)W = 0 \tag{21}$$

Equation (21) is modified Bessel's equation and the solution is given by

$$W = AI_1(s) + BK_1(s)$$

where $I_1(s)$ and $K_1(s)$ are modified Bessel functions of first and second kind, respectively.

$$p_0(x) - p_{ext} = z[AI_1(s) + BK_1(s)] \tag{22}$$

By using initial conditions (19), we get

$$A = (p^* - p_{\text{ext}})\beta K_0(\beta) + 2K_1(\beta)/\alpha \text{ and } B = (p^* - p_{\text{ext}})\beta I_0(\beta) + 2I_1(\beta)/\alpha$$

Now using the expressions of p_0 from (22), we numerically solve the differential Eq. (15) along with the initial conditions (9h, i) for the first order pressure p_1.

The pressure drop Δp is given by

$$\begin{aligned} \Delta p = p|_{x=0} - p|_{x=1} &= p_0(0) - p_0(1) + \varepsilon(p_1(0) - p_1(1)) \\ &= p^* - e^{-3\alpha/2}\big[AI_1(e^{-3\alpha/2}\beta) + BK_1(e^{-3\alpha/2}\beta)\big] - \varepsilon p_1(1). \end{aligned} \tag{23}$$

4 Results and Discussions

Flow of a Jeffrey fluid with variable cross-section with permeable walls is investigated. The numerical values of velocity, flow rate at $x = 1$, wall shear stress, and the pressure drop are determined by using the expressions (16), (18), (22), and (23) respectively.

The behavior of velocity with y is shown in Figs. (2, 3 and 4). Figure 2 shows the variation of velocity with ε, we observe that as the ε increases the velocity is increasing. The variation of velocity with y for different values of permeability parameters are shown in Fig. 3. From the figure it is noticed that as the permeability parameter increases the velocity is increasing. From Fig. 4 we observe that as the Jeffrey parameter increases the velocity is increasing.
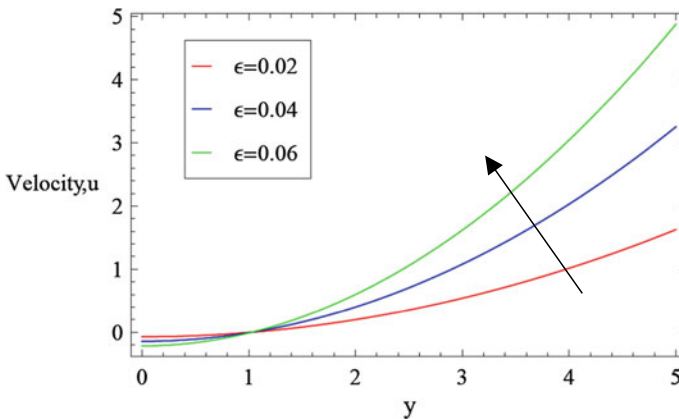
Fig. 2 Variation of velocity with y for different ε values
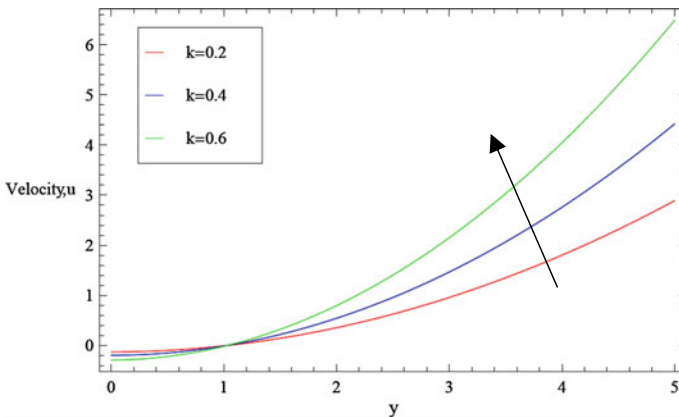
Fig. 3 Variation of velocity with y for different values of permeability parameter
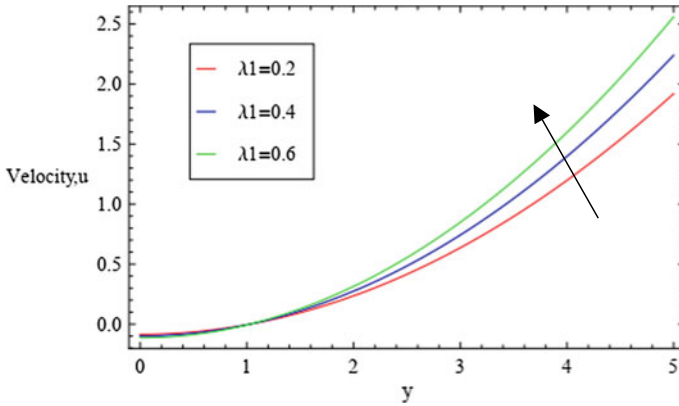
Fig. 4 Variation of velocity with *y* for different values Jeffrey parameter

The behavior of flow rate with *x* is shown in Figs. 5 and 6. From Fig. 5 we notice that as the permeability parameter increases the flux is increasing. As the Jeffrey parameter increases the flux of the tube increases, which is shown in Fig. 6.

The behavior of Shear Stress with *x* is shown in Figs. 7, 8 and 9. We notice from Fig. 7 that as α value increases the Shear Stress decreases. From Figs. 8 and 9 we conclude that as the Jeffrey parameter and the permeability parameter increases the Shear Stress is increasing.

The behavior of pressure with the change in permeability parameter is shown in Figs. 10, 11 and 12. Figure 10 shows the variation of pressure with permeability for different values of α. Here we observe that as the value of α increase, the pressure is increasing. From Fig. 11 we notice that as the value ε increases the pressure
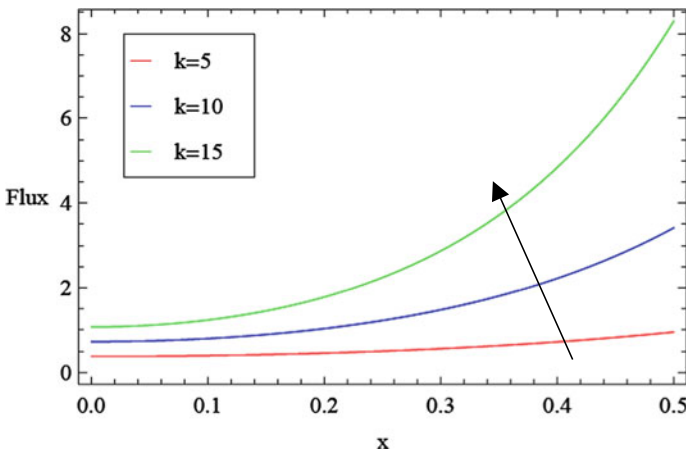
Fig. 5 Variation of flux with *x* for different values permeability parameter
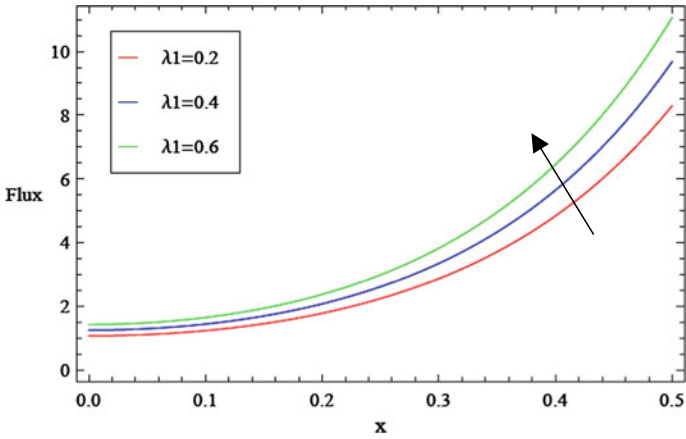
Fig. 6 Variation of flux with x for different values Jeffrey parameter
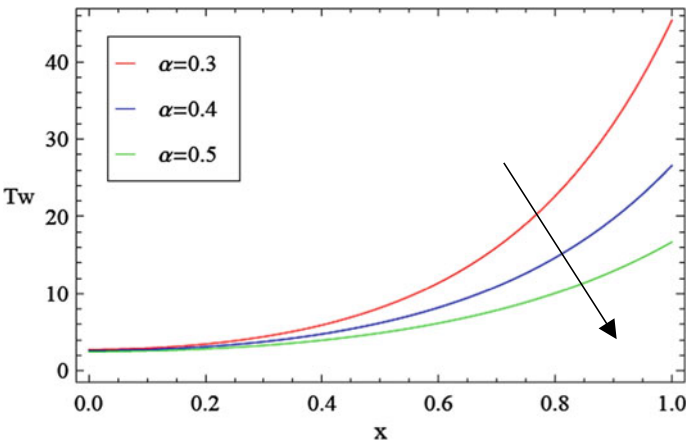
Fig. 7 Variation of shear tress with x for different α values

decreases. As the external pressure increases the pressure drop decreases, which is shown in Fig. 12.

5 Conclusion

Non-Newtonian Jeffrey fluid in a channel with varying cross-section which includes permeable boundaries is considered in the paper. The following conclusions were made by investigating this paper:
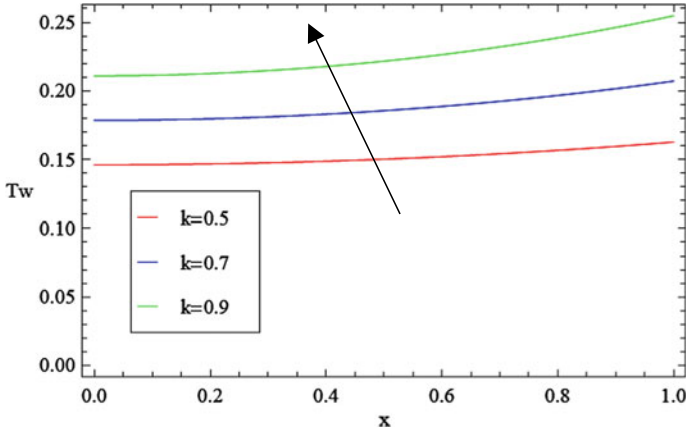
Fig. 8 Variation of shear tress with x for different values of permeability parameter
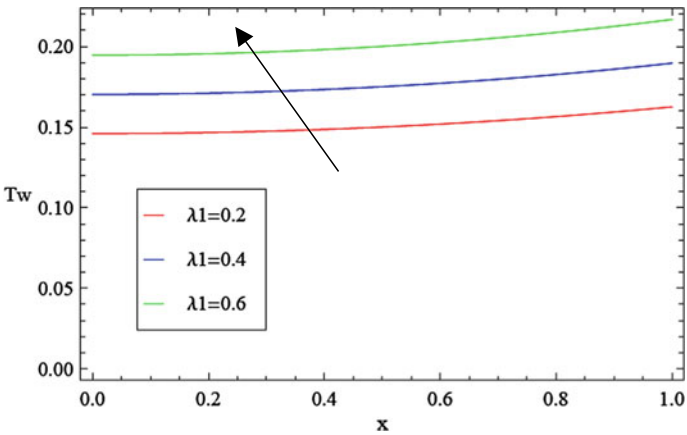
Fig. 9 Variation of shear tress with x for different values of Jeffrey parameter

1. Increment in ε results out in increment of velocity, shear stress and decrement in pressure.
2. As the permeability parameter increases, velocity, flux and shear stress increase, where it has reverse impact on pressure.
3. Velocity and shear stress increases with increase of Jeffrey parameter.
4. Pressure decreases with the increase of external pressure.
5. Pressure increases with the increase of α.
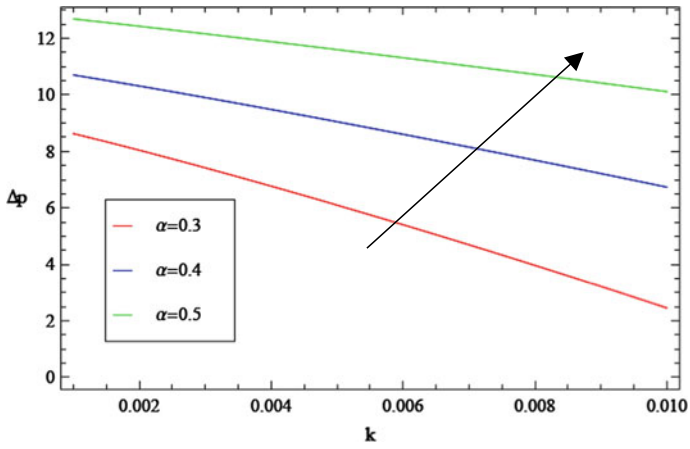
Fig. 10 Variation of pressure with k for different α values
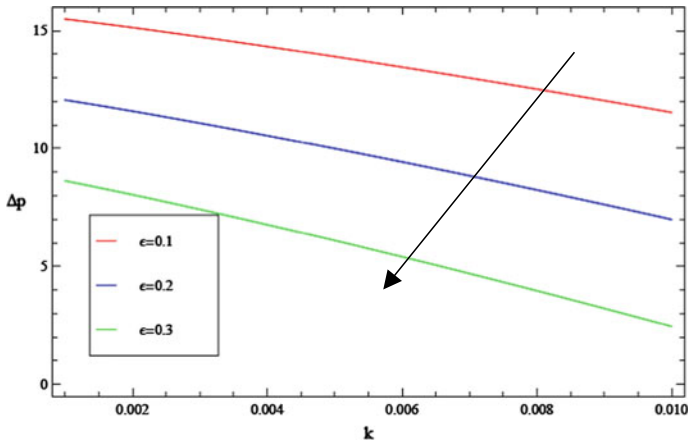
Fig. 11 Variation of pressure with k for different ε values
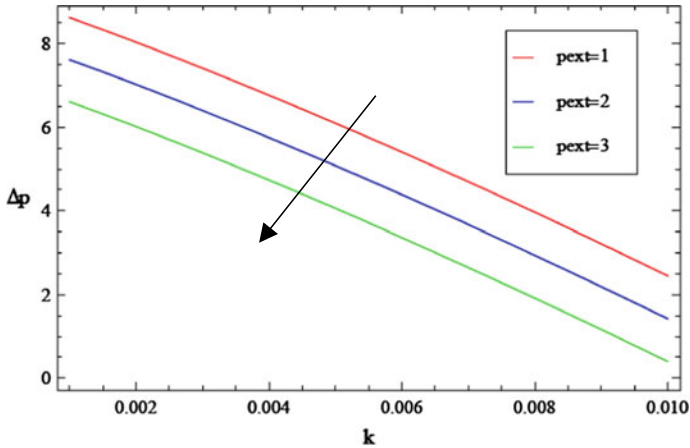
Fig. 12 Variation of pressure with *k* for different external pressure values

References

1. Krishna Prasad JSVR, Chandra P (1990) Flow in channels of varying cross-section with permeable boundaries. Proc Nat Acad Sci 60(A) III: 317–326
2. Vajravelu K, Sreenadh S, Devaki P, Prasad KV (2015) Peristaltic transport of Herschel Bulkley fluid in an elastic tube. Heat Transf Asian Res 44(7):585–598. https://doi.org/10.1002/htj.21137
3. Vajravelu K, Sreenadh S, Devaki P, Prasad KV (2016) Peristaltic transport of Casson fluid in an elastic tube. J Appl Fluid Mech 9(4):1897–1905. https://doi.org/10.18869/acadpub.jafm.68.235.24695
4. Badari Narayana CH, Devaki P, Sreenadh S (2017) Effect of elasticity and inclination on Hershel- Bulkley fluid flow in a tube. Int J Adv Inf Sci Technol 6(2):6–12. https://doi.org/10.15693/ijaist/2017.v6i2.6-12
5. Berhane Tesfahun (2017) Flow of a Newtonian fluid in a non-uniform wavy and permeable tube. New Trends Math Sci 5(4):12–23. https://doi.org/10.20852/ntmsci.2017.210
6. Devaki P, Sreenadh S, Vajravelu K, Prasad KV, Vaidya H (2018) Wall properties and slip consequences on peristaltic transport of a casson liquid in a flexible channel with heat transfer. Appl Math Nonlinear Sci 3(1):277–290. https://doi.org/10.21042/AMNS.2018.1.00021
7. Fakour M, Ganji DD, Khalili A, Bakhshi A (2017) Study of heat transfer in nanofluid mhd flow in a channel with permeable walls. Heat Transf Res 48(3):221–238. https://doi.org/10.1615/HeatTransRes.2016011839
8. Rasoulzadeh M, Panfilov M (2018) Asymptotic solution to the viscous/inertial flow in wavy channels with permeable walls. Phys Fluids 30:106604. https://doi.org/10.1063/1.5041748
9. Makinde OD (1995) Laminar flow in a channel of varying width with permeable boundaries. Rom J Phys 40(4–5):403–417
10. Makinde OD, Alagoa KD (1999) Effect of magnetic field on steady flow through an indented channel. AMSE Modell Measure Control B 68(1):25–32
11. Makinde OD (1999) Steady flow and heat transfer in a diverging tube. AMSE Modell Measure Control B 67(1):51–63
12. Makinde OD, Sibanda P (2000) Steady flow in a diverging symmetrical channel: numerical study of Bifurcation by analytic continuation. Quaestiones Math 23:45–57. https://doi.org/10.2989/16073600009485956
13. Mhone PY, Makinde OD (2006) Unsteady MHD flow with heat transfer in a diverging channel. Rom J Phys 51(9–10):967–979

Marangoni Convection of Titanium Dioxide/Ethylene Glycol Dusty Nanoliquid MHD Flow Past a Flat Plate

N. Indumathi, A. K. Abdul Hakeem, B. Ganga, and R. Jayaprakash

Abstract The effects of magneto hydro dynamic Marangoni convection flow of titanium dioxide/ethylene glycol dusty nanofluid past a flat plate is investigated for the first time. The surface tension is required to change directly with temperature. Titanium dioxide/ethylene glycol dusty nanofluid has been enlisted for the improvement of heat transfer rate. By using appropriate similarity transformation for dusty nanoliquid, dimensionless non-linear ordinary differential equations are reformed from the governing equations. The physical parameters for temperature and velocity fields are inspected graphically and elaborately conversed numerically. The heat transfer rate values for the physical parameters are illustrated and tabulated. The average Nusselt number has been enhanced by the Marangoni flow.

Keywords Marangoni convection · MHD · Dusty nanoliquid · Flat plate · Heat transfer

1 Introduction

The Marangoni effect is primarily recognized by the deviation of liquid-liquid or liquid-gas surface tension with the temperature. In past two decades the studies on Marangoni convection have drawn extensive scrutiny as a result of the vast utilization in crystal growth melts, welding, semiconductor processing, drying silicon wafers. Plenty of authors [1–7] have investigated the different physical phenomena problem with water based nanofluid past a flat plate together with Marangoni convection.

N. Indumathi · A. K. Abdul Hakeem (✉)
Department of Mathematics, Sri Ramakrishna Mission Vidyalaya College of Arts and Science, Coimbatore 641020, India
e-mail: abdulhakeem6@gmail.com

B. Ganga
Department of Mathematics, Providence College for Women, Coonoor 643104, India

R. Jayaprakash
Department of Physics, Sri Ramakrishna Mission Vidyalaya College of Arts and Science, Coimbatore 641020, India

Mahanthesh et al. [8] studied solar radiative Marangoni flow of dusty nanofluid over a flat plate. They resulted that Marangoni flow enhanced the rate of energy transfer.

Meanwhile modeling, preparation and characterization of nanofluids have been deliberated by plenty of researchers. All the while, lots of works away at the heat exchange impacts of nanofluids have been finished by the specialists [9–14]. Additionally by the trial and numerical examination it is inferred that the heat exchange rate has been expanded by a sensible rate due to the nanofluid.

The mixture of millimeter or micrometer sized conducting dust particles into the nanofluid is known as dusty nanofluid. At first the laminar dusty gas was investigated by Saffman [15]. Many papers were worked on two/multi-phase nanofluid by the wide range of engineering applications. Sandeep et al. [16] studied on exponentially stretching surface with MHD radiative unsteady flow of two-phase fluid. Cabaleiro et al. [17] tentatively found a non-Newtonian shear diminishing conduct for a nanofluid with base fluid as ethylene glycol and nanoparticles as titanium dioxide.

By considering the above results, in the present work by taking ethylene glycol non-Newtonian fluid as the base fluid and titanium dioxide as nanoparticles together with the dust particles is investigated numerically with MHD Marangoni convection past a flat plate.

2   Problem Formulation

Consider a steady, two-dimensional, laminar, incompressible, MHD, Marangoni convection, two-phase boundary layer flow in an ethylene glycol (EG) predicated dusty nanoliquid consisting TiO_2 as the nanoparticles. TiO_2/EG is a non-Newtonian shear thinning nanoliquid, hence ethylene glycol based titanium dioxide nanofluid is Casson fluid. No slip occurs between titanium dioxide nanoparticles and ethylene glycol base fluid, further they are in thermal equilibrium. Additionally assume that the surface tension is to vary linearly with temperature

$$\xi = \xi_0(1 - \gamma_0(t - t_0)) \tag{1}$$

where ξ_0 is the surface tension at the interface, t_0 is temperature of the ambient fluid and we considered that $t_0 = t_\infty$. For most liquids the surface tension ξ declines along with temperature. That is $\gamma_0 > 0$ fluid property. Table 1 provides the thermo physical properties of nanoparticles and base fluid. The boundary temperature of each, fluid and particles are expected to be quadratic functions of the extent x. The equations that govern for this investigation are given as follows

Table 1 Thermophysical properties of nanoparticles and base fluid

Property	TiO$_2$	Ethylene Glycol
C_p (J/kgK)	686.2	2430
ρ (kg/m^3)	4250	1115
k (W/mK)	8.9538	0253
$\sigma(\Omega/\text{m})^{-1}$	1×10^{-12}	1.07×10^{-6}

$$\frac{\partial \bar{u}}{\partial \bar{x}} + \frac{\partial \bar{v}}{\partial \bar{y}} = 0 \tag{2}$$

$$\frac{\partial \bar{U}}{\partial \bar{x}} + \frac{\partial \bar{V}}{\partial \bar{y}} = 0 \tag{3}$$

$$\bar{u}\frac{\partial \bar{u}}{\partial \bar{x}} + \bar{v}\frac{\partial \bar{u}}{\partial \bar{y}} = \left(1 + \frac{1}{\beta_0}\right)\frac{\mu_{nf}}{\rho_{nf}}\frac{\partial^2 \bar{u}}{\partial \bar{y}^2} + \frac{\rho_P}{\rho_{nf}\bar{\tau}_m}(\bar{U} - \bar{u}) - \frac{\sigma_{nf} B_0^2 \bar{u}}{\rho_{nf}} \tag{4}$$

$$\bar{U}\frac{\partial \bar{U}}{\partial \bar{x}} + \bar{V}\frac{\partial \bar{U}}{\partial \bar{y}} = \frac{1}{\bar{\tau}_m}(\bar{u} - \bar{U}) \tag{5}$$

$$(\rho C)_{nf}\left(\frac{\bar{u}\partial \bar{t}}{\partial \bar{x}} + \bar{v}\frac{\partial \bar{t}}{\partial \bar{y}}\right) = k_{nf}\frac{\partial^2 \bar{t}}{\partial \bar{y}^2} + \frac{\rho_P C_P}{\bar{\tau}_t}(\bar{T} - \bar{t}) \tag{6}$$

$$\bar{U}\frac{\partial \bar{T}}{\partial \bar{x}} + \bar{V}\frac{\partial \bar{T}}{\partial \bar{y}} = \frac{1}{\bar{\tau}_t}(\bar{t} - \bar{T}) \tag{7}$$

under the limit conditions

$$\mu_{nf}\left(1 + \frac{1}{\beta_0}\right)\frac{\partial \bar{u}}{\partial \bar{y}} = \frac{\partial \sigma}{\partial \bar{T}}\frac{\partial \bar{T}}{\partial \bar{x}}, \quad \bar{v} = 0, \quad \bar{t} = \bar{t}_0 + A\bar{x}^2 \quad \text{at} \quad \bar{y} = 0 \tag{8}$$

$$\bar{u} \to 0, \quad \bar{U} \to 0, \quad \bar{V} \to \bar{v}, \quad \bar{t} \to \bar{t}_\infty, \quad \bar{T} \to \bar{T}_\infty \quad \text{as} \quad \bar{y} \to \infty \tag{9}$$

here $(\bar{u}, \bar{v})$ and $(\bar{U}, \bar{V})$ are velocity fields of fluid and particle phase respectively, $\bar{t}$—fluid temperature, $\bar{T}$—particle temperature, ρ_P—particle density, ν—kinematic viscosity, β_0 is that the Casson parameter, B_0—magnetic field strength. $\bar{\tau}_m = m_0/6\pi\mu r_P^*$ is momentum relaxation time, $\bar{\tau}_T = m_0 C_P/6\pi\mu r_P^*$ thermal relaxation time, m_0 and r_P^* are the mass and radius of dust particles. C_P specific heat of the dust particles. $\bar{t}_0$, $\bar{T}_0$—constants, $\bar{t}_\infty$ and $\bar{T}_\infty$—fluid and particle ambient temperature and $A = \frac{\Delta \bar{T}}{L}$ where $\Delta \bar{T}$ is the constant characteristic temperature and L is the length of the surface. For the nanofluid ρ_{nf}—fluid density, μ_{nf}—dynamic viscosity, k_{nf}—thermal conductivity, C_{nf}—specific heat and σ_{nf}—electrical conductivity which are given by

$$\rho_{nf} = (1 - \phi)\rho_f + \phi\rho_s, \ \mu_{nf} = \frac{\mu_f}{(1-\phi)^{2.5}}, \left.\begin{array}{l} \\ \\ \end{array}\right\}$$

$$\frac{k_{nf}}{k_f} = \frac{(2k_f + k_s) - 2\phi(k_f - k_s)}{(2k_f + k_s) + \phi(k_f - k_s)}, \ (\rho C)_{nf} = (1 - \phi)(\rho C)_f + \phi(\rho C)_s,$$

$$\sigma_{nf} = \left[1 + \left(\frac{3\left(\frac{\sigma_s}{\sigma_f} - 1\right)\phi}{\left(\frac{\sigma_s}{\sigma_f} + 2\right) - \left(\frac{\sigma_s}{\sigma_f} - 1\right)\phi}\right)\right]\sigma_f \tag{10}$$

Implementing the next transformation of similarity

$$\left.\begin{array}{l} \psi^*(\eta) = \zeta_2 \overline{x} f(\eta), \ \theta = \frac{\overline{t} - \overline{t}_\infty}{A\overline{x}^2}, \ \eta = \zeta_1 \overline{y}, \\ \\ \Psi^*(\eta) = \zeta_2 \overline{x} F(\eta), \ \Theta = \frac{\overline{T} - \overline{t}_\infty}{A\overline{x}^2} \end{array}\right\} \tag{11}$$

where ψ^* and Ψ^* are the stream functions such that $\overline{u} = \frac{\partial \psi^*}{\partial \overline{y}}, \overline{U} = \frac{\partial \Psi^*}{\partial \overline{y}}$ and $\overline{v} = -\frac{\partial \psi^*}{\partial \overline{x}}$, $\overline{V} = -\frac{\partial \Psi^*}{\partial \overline{x}}$. Further $\zeta_1 = \left(\frac{\sigma_* \gamma A \rho_f}{\mu_f^2}\right)^{\frac{1}{3}}, \zeta_2 = \left(\frac{\sigma_* \gamma A \mu_f}{\rho_f^2}\right)^{\frac{1}{3}}$ are constants.

Substituting Eqs. (10) and (11) into Eqs. (4–9) we have

$$\left(1 + \frac{1}{\beta_0}\right)\frac{g'''}{(1 - \phi)^{2.5}} + (1 - \phi + \phi\frac{\rho_s}{\rho_g})(gg'' - g'^2) + l\beta_V[G' - g']$$

$$-\left\{1 + \frac{(3\frac{\sigma_s}{\sigma_f} - 1)\phi}{(\frac{\sigma_s}{\sigma_f} + 2) + (\frac{\sigma_s}{\sigma_f} - 1)\phi}\right\}Mg' = 0 \tag{12}$$

$$GG'' + \beta_V(g' - G'') - G'^2 = 0 \tag{13}$$

$$\frac{1}{Pr}\frac{k_{nf}}{k_f}\theta'' - (1 - \phi + \phi\frac{\rho C_s}{\rho C_f})(2g'\theta - g\theta') + l\gamma\beta_T(\Theta - \theta) = 0 \tag{14}$$

$$G\theta' + \beta_T(\theta - \Theta) - 2G'\Theta = 0 \tag{15}$$

Under the limit conditions

$$g(0) = 0, \ g''(0) = -2(1 - \phi)^{2.5}\left(1 + \frac{1}{\beta_0}\right)^{-1}, \ \theta(0) = 1$$

$$g'(\infty) \to 0, \ G(\infty) \to g(\infty), \ G'(\infty) \to 0, \ \theta(\infty) \to 0, \ \Theta(\infty) \to 0 \tag{16}$$

here $l = \rho_P/\rho_f$ is the dust particle mass concentration, $\beta_V = 1/\tau_m\zeta_1\zeta_2$ is the momentum dust parameter, $M = \sigma_f B_0^2/\rho_f\zeta_1\zeta_2$ is the magnetic parameter, $Pr = \mu C/k$ is the Prandtl number, $\gamma = C_P/C_f$ is the specific heat ratio, $\beta_T = 1/\tau_t\zeta_1\zeta_2$ is the thermal dust parameter.

The local Nusselt number, is denoted as

$$\text{Nu}_{\overline{x}} = \frac{-k_{nf}}{k_f} \zeta_1 \overline{x} \theta'(0) \tag{17}$$

The average Nusselt number depends on the common temperature distinction between the temperature of the surface and also the temperature **far away** from the surface is obtained by

$$\text{Nu}_L = \frac{k_{nf}}{k_f} \text{Ma}^{1/3} Pr^{1/3} \theta'(0) \tag{18}$$

where Marangoni number based on L is defined as

$$\text{Ma} = \frac{\sigma_* A L^2}{\mu_f \alpha_f} \tag{19}$$

3 Numerical Solution

Runge-Kutta-Felhberg method in sync with shooting technique has been used to calculate the non-linear boundary value problem (BVP) given in Eqs. (12)–(16) numerically. The suitable initial assumptions for the unknowns $g'(0)$, $G(0)$, $G'(0)$, $\theta'(0)$ and $\Theta(0)$ are created so as to satisfy the asymptotic boundary conditions. The focused results are attained among a tolerance limit of 10^{-5} level by the above shooting iteration process. Numerical solutions are found and drawn through graphs and tables.

4 Results and Discussion

The numerical calculations are performed to generate the results by handling the aforesaid numerical process for different values of suitable parameters for dusty TiO$_2$/ethylene glycol nanofluid. For this motive, **we** have got Figs. 1, 2, 3, 4, 5, 6, 7 and 8 framed, in which the velocity and temperature distribution phase of fluid and dust are investigated. Next we figure out that $g'(\eta)$, $G'(\eta)$, $\theta(\eta)$ and $\Theta(\eta)$ fields are abating as η steps up. All of these distributions have come closer asymptotically and fulfill the condition of the far-field boundary. This led to greater certainty about the revealed solution's accuracy. Furthermore Fig. 9 and Table 2 show the effect of heat transfer rate.

Impact of solid volume fraction ϕ of titanium dioxide nanoparticles (TiO$_2$) on $g'(\eta)$ and $G'(\eta)$ is illustrated in Fig. 1. We see that the dusty phase is lower that
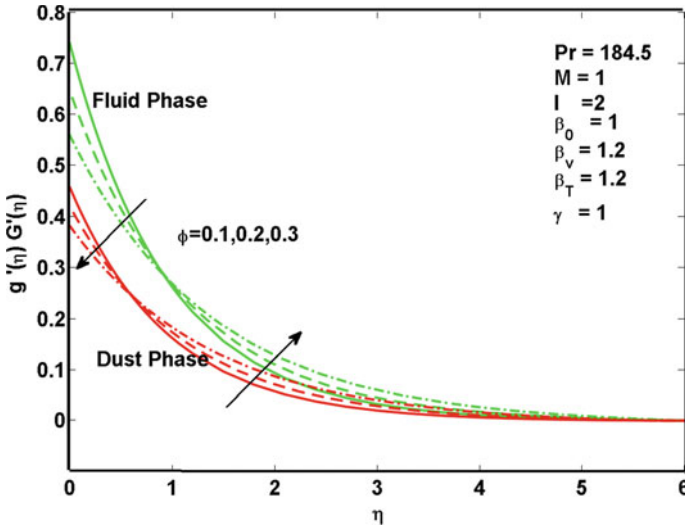
Fig. 1 Impact of ϕ, $g'(\eta)$ and $G'(\eta)$
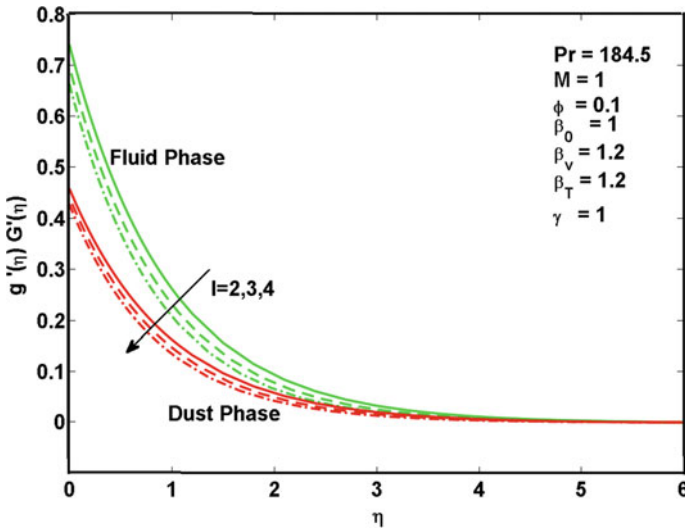
Fig. 2 Impact of l, $g'(\eta)$ and $G'(\eta)$

of the fluid phase for momentum layer. It is visible in Fig. 1 that both $g'(\eta)$ and $G'(\eta)$ decayed near the plate, as higher ϕ increases the frictional force in the liquid movement. Whereas for away from the plate for both $g'(\eta)$ and $G'(\eta)$, an opposite behavior is noted. Figure 2 illustrates the $g'(\eta)$ and $G'(\eta)$ curves for increasing l. Here both $g'(\eta)$ and $G'(\eta)$ decreases as l is enhanced. Physically speaking, the drag force within the liquid is boosted while there is enhancement in dust particle volume
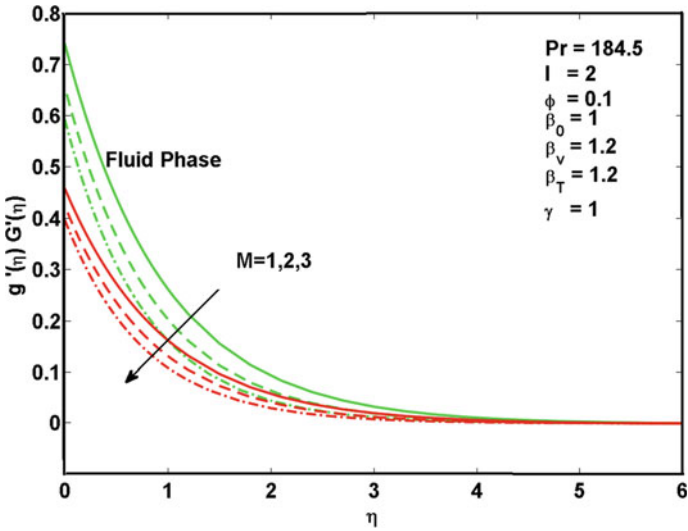
Fig. 3 Impact of M, $g'(\eta)$ and $G'(\eta)$
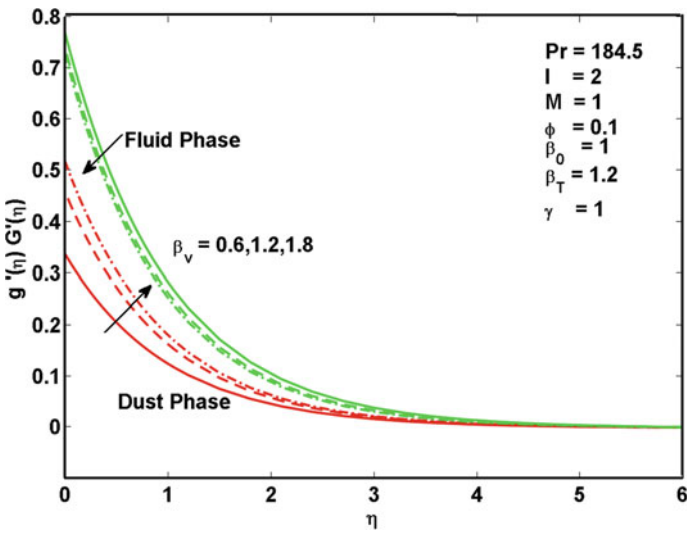
Fig. 4 Impact of β_V, $g'(\eta)$ and $G'(\eta)$

concentration. Figure 3 sketches the influence of M on $g'(\eta)$ and $G'(\eta)$. In both cases, an increase in M decreases the flow. This behavior is evident since the Lorentz drag force has the propensity to lessen the flow of the fluid phase and dust phase due to the magnetic field. Figure 4 shows the $g'(\eta)$ and $G'(\eta)$ curves for momentum dust parameter β_v. The velocity profile enhances for dust phase and decays for fluid phase.
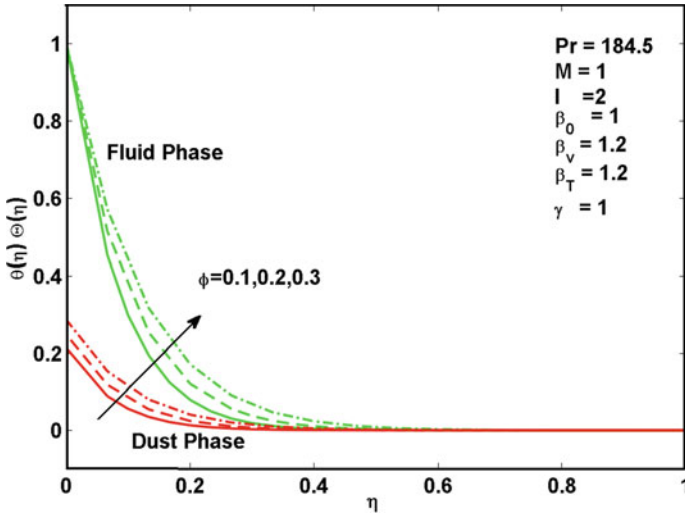
Fig. 5 Impact of ϕ, $\theta(\eta)$ and $\Theta(\eta)$
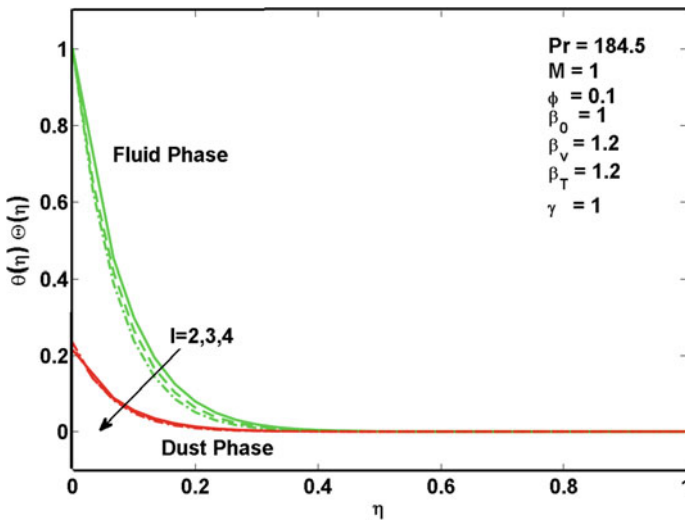
Fig. 6 Impact of l, $\theta(\eta)$ and $\Theta(\eta)$

Since the base fluid loses the kinematic energy by increasing the interaction with the dust particles. Figure 5 exhibits the influence of ϕ on $\theta(\eta)$ and $\Theta(\eta)$. As the volume concentration of nanoparticles increases, the thermal conductivity thus increases the distribution of temperatures for the phase of fluid and dust. Figure 6 depicts the effect of parameter l on the temperature distribution for the phase of fluid and dust. In general, the heat exchanges between the dust particles and the nanofluid declines the
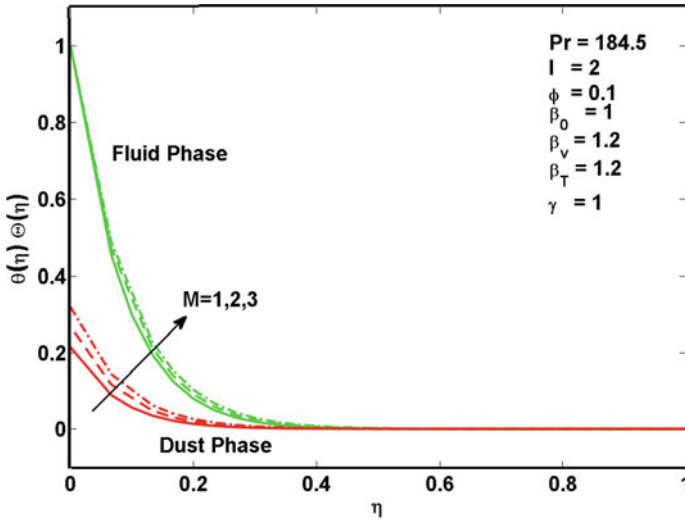
Fig. 7 Impact of M, $\theta(\eta)$ and $\Theta(\eta)$
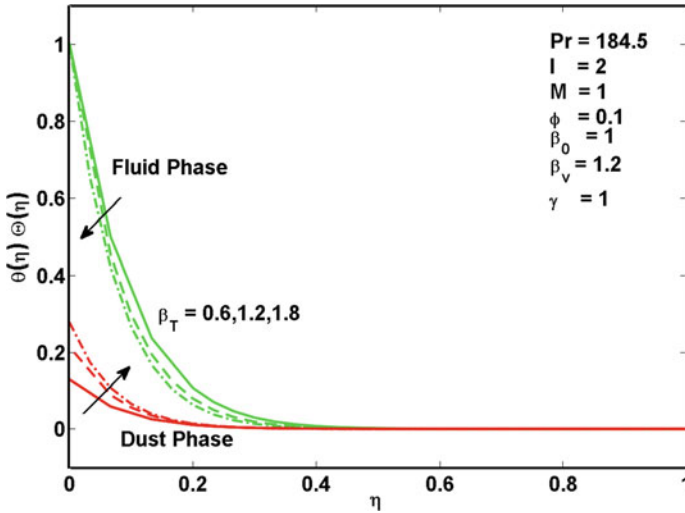
Fig. 8 Impact of β_T, $\theta(\eta)$ and $\Theta(\eta)$

temperature distribution. Temperature actions with M fluctuation is shown in Fig. 7. A rise in M tends to increase the thickness of the energy boundary layer and thus increases the distribution of temperature for the phase of fluid and dust. In Fig. 8, we noticed an interesting result, that the dust phase increases and the fluid phase temperature profile decreases while the thermal dust parameter β_T increases. This also happens subjectively for velocity of β_v (Fig. 4). From the Fig. 9, the heat transfer
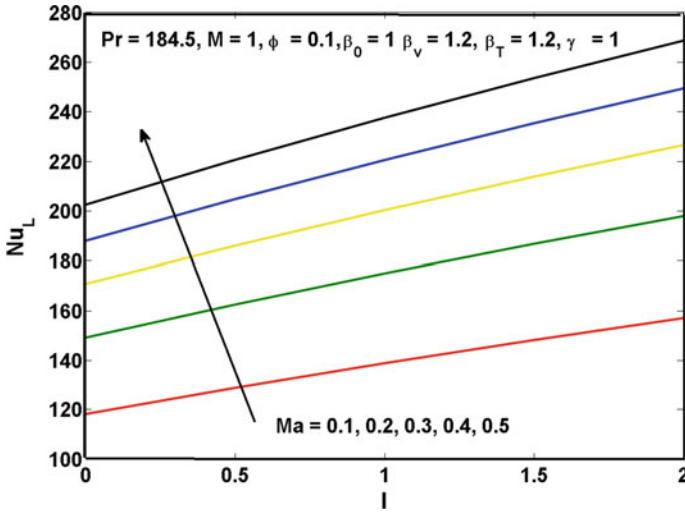
Fig. 9 Impact of Ma, l and Nu_L

Table 2 Variation in rate of heat transfer for the flow with $\beta_v = 1.2$, $\gamma = 1$

M	l	β_T	$-\theta'(0)$
0.5	2	1.2	11.83923
1			11.53229
1.5			11.24987
2			10.98902
2.5			10.74754
3			10.52318
1	3		12.73685
	4		13.83612
	5		14.85015
	6		15.79341
	2	1.8	12.62768
		2.4	13.51292
		3.0	14.25415
		3.6	14.88973

rate can be observed to improve for the increment of l and Ma. At long last, Table 2 introduced to examine the effect of M, l, β_T on heat transfer rate $(-\theta'(0))$. While expanding M the heat transfer rate diminishes though for the expanding estimations of l and β_T it increments.

5 Conclusion

The problem of steady, laminar, two-phase, two-dimensional and incompressible dusty nanoliquid with base fluid as ethylene glycol and nanoparticles as TiO_2 has been investigated mathematically. The notable results that follow are perceived.

The momentum and thermal behaviors were found to be strongly dependent on the value of the fraction of solid volume of nanoparticle, concentration of dust particle mass, magnetic parameter and Marangoni parameter. The velocities of two phase fluids for the increment of nanoparticle volume fraction decreases close to the wall and have a different trend for away from the wall, however, fluid phase dusty nanoliquid is of higher velocity than dust phase dusty nanoliquid. The velocity and temperature layer retards by dust particle mass concentration parameter. The parameter of concentration of dust particles therefore has a very significant and remarkable effect on the flow of the two–phase dusty nanofluid. The momentum layer decreased and thermal layer increased by magnetic field parameter for both phases. Momentum/thermal dust parameters accelerate the dust phase dusty nanoliquid velocity/temperature profile. But the opposite phenomenon for the liquid phase field is observed. The average heat transfer rate increased by dust particle mass concentration and Marangoni parameter.

References

1. Christopher DM, Buxuan W (2002) Tsinghua Sci Technol 7:171–176 (2002)
2. Al-Mudhaf A, Chamka AJ (2005) Heat Mass Transf 42:112–121 (2005)
3. Arifin NM, Nazar R, Pop I (2013) J Appl Math 8p
4. Abu Bakar NA, Hamid RA, Wan Mohd Khairy Adly Wan Zaimi (2015) AIP Conf Proc 1522:55–60
5. Lin Y, Zheng L (2015) AIP Adv 5:107–225
6. Abdullah AA, Althobaiti SA, Lindsay KA (2018) Euro J Mech/B Fluids 67:259–268
7. Hayat T, Shaheen U, Shafiq A, Alsaedi A, Asghar S (2015) AIP Adv 5:077–140
8. PrasannaKumara BC, Shashikumar NS, Mahanthesh B, Gireesha BJ (2017) Nucl Eng Technol 49:1660–1668
9. Sheikholeslami M, Ganji DD, Rashidi MM (2016) J Magn Magn Mater 416:164–173
10. Abdul Hakeem AK, Vishnu Ganesh N, Ganga B (2015) J Magn Magn Mater 381:243–257
11. Kalaivanan R, Renuka P, VishnuGanesh N, AbdulHakeem AK, Ganga B, Saranya S (2015) Proc Eng 127:531–538
12. Rashidi MM, Vishnu Ganesh N, Abdul Hakeem AK, Ganga B (2014) J Mol Liq 198:234–238
13. Ganga B, Mohamed Yusuff Ansari S, Vishnu Ganesh N, Abdul Hakeem AK (2015) J Nigerian Math Soc 34(2):181–194
14. Aly EH, Vajravelu K (2014) Appl Math Comput 232:191–204
15. Saffman PG (1962) J Fluid Mech 13:120–128
16. Sandeep N, Sulochana C, Rushi Kumar B (2015) Int J Eng Sci Technol. https://doi.org/10.1016/j.jestch.2015.06.004
17. Cabaleiro D, Pastoriza-Gallego MJ, Gracia-Fernndez C, Pineiro MM, Lugo L (2013) Nanoscale Res Lett. https://doi.org/10.1186/1556-276X-8-286

Aligned Magnetic Field Effect on Unsteady MHD Double Diffusive Free Convection Flow of Kuvshinski Fluid Past an Inclined Moving Porous Plate

J. L. Rama Prasad, K. S. Balamurugan, and S. V. K. Varma

Abstract The current paper scrutinizes the sway of the aligned magnetic field and Kuvshinski fluid model on unsteady MHD free convective flow past a moving inclined plate in the occurrence of thermal radiation as well as radiation absorption with chemical effect and mass blowing or suction. It is implicit that the plate is entrenched in a uniform porous medium moving with a steady velocity in the flow direction and in the existence of a transverse magnetic field. Perturbation technique was employed for solving non-dimensional governing equations. Significant consequences with regard to embedded parameters are illustrated graphically for the temperature, velocity, and concentration profiles. The expression for the Skin friction coefficient is also obtained.

Keywords Unsteady · MHD · Kuvshinski fluid · Aligned magnetic · Inclined plate

1 Introduction

There are numerous fluids in the industry as well as technology whose performance fails to be described by the classical linearly viscous Newtonian fluid model. The divergence from the Newtonian comportment demonstrates itself in an assortment of manners: non-Newtonian viscosity, stress relaxation, non-linear creeping, development of normal stress differences, and yield stress. The Navier–Stokes equations are insufficient to prognosticate the activities of such a category of fluids, consequently

J. L. Rama Prasad (✉)
Department of Mathematics, PB Siddhartha College of Arts and Science, Vijayawada, Andhra Pradesh, India
e-mail: jlrprasad@gmail.com

K. S. Balamurugan
Research Scholar, Dr. Department of Mathematics, R.V.R. & J.C. College of Engineering, Guntur, Andhra Pradesh, India
e-mail: muruganbalaks@gmail.com

S. V. K. Varma
Department of Mathematics, S. V. University, Tirupati, Andhra Pradesh 522109, India
e-mail: profsvkvarma@gmail.com

multitudinous significant associations of non-Newtonian fluids. These substantial relations yields ascend to the differential equations, which, in comprehensive are higher perplexed and higher order compared with Navier–Stokes equations. For that reason, it is complicated to attain exact analytical solutions for Kuvshinski fluids.

Reddy et al. [1] have scrutinized radiation assimilation and Kuvshinski fluid model on unsteady MHD free convective flow all the way through an infinite non-parallel porous plate in the existence of chemical effect and heat source. Sakthikala et al. [2] investigated the influence of Kuvshinski fluid model on unsteady free convective fluid flow through an infinite moving porous plate by means of dependable as well as variable temperatures. Reddy et al. [3] examined the influence of Soret and Kuvshinski type fluid on MHD natural convective flow inside a porous medium through a semi-infinite non-parallel moving plate with heat source. In this examination, perturbation technique was employed for solving the governing equations. Buggaramulu et al. [4] have reported visco-elastic fluid model on unsteady MHD-free convective fluid stream through a porous medium in the existence of chemical effect and radiation.

Devasena et al. [5], Reddy et al. [6] and VidyaSagar et al. [7] have analyzed analytically the influence of Kuvshinski fluid on unsteady MHD natural convective flow with radiation absorption. Sharma et al. [8] have examined influence of stratified Kuvshinski fluid on MHD free convective stream through a non-parallel porous plate by means of heat and mass transfer. Chamkha [9] and Hady et al. [10] have analyzed unsteady natural convective flow through a semi-infinite porous moving plate by means of heat absorption. Hossian et al. [11] have discussed the problem of natural convection flow along a non-parallel wavy surface by means of uniform surface temperature in the existence of heat generation/absorption. Chamkha et al. [12], Muthucumaraswamy et al. [13] and Ibrahim et al. [14] investigated the influence of heat generation and chemical reaction on MHD unsteady free convection flow over perpendicular moving porous plate.

All these studies paid attention towards MHD unsteady free convection flow of Kuvshinski fluid past an inclined surface, where thermal radiation, radiation absorption, chemical reaction, heat generation, and aligned magnetic impacts are contemplated. The predominant purpose is to scrutinize the unsteady MHD free convection flow of Kuvshinski fluid past a moving inclined plate with heat production in the demeanor of mass blowing or suction and with the special effects of aligned magnetic, chemical reaction, thermal radiation, and radiation absorption.

2 Mathematical Formulation

Let us contemplate the 2D unsteady MHD free convection Kuvshinski fluid flow through a semi-infinite inclined moving porous plate in a uniform porous medium under the sway of a uniform magnetic field, radiation absorption, chemical effect, heat generation and thermal radiation. Here x^*-axis is taken along the porous plate in the upward direction and y^*-axis perpendicular to it. The fluid is to be gray, absorbing—emitting however non-scattering medium. In the x^*-way, the radiative heat flux is

significantly small against to that in the y^*-direction. Each and every flow variable excluding pressure are functions of y^* and t^* only. The plate in x^*-direction is of infinite length. The induced magnetic field is insignificant. The size of the porous plate is large compared to typical microscopic length scale of the porous medium. Chemical reactions occur in the flow.
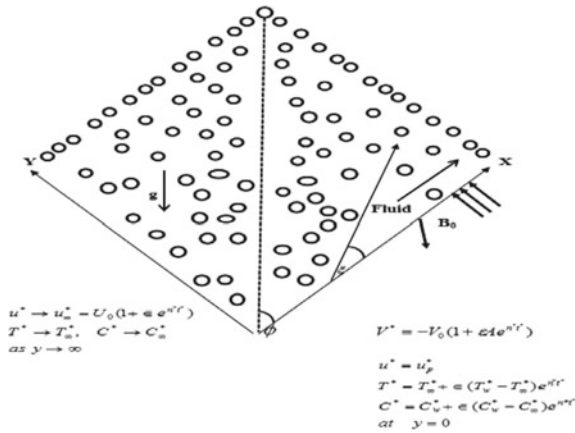
Under these suppositions, the governing equations are

$$\frac{\partial v^*}{\partial y^*} = 0 \tag{1}$$

$$\left(1 + \lambda_1^* \frac{\partial}{\partial t^*}\right)\frac{\partial u^*}{\partial t^*} + V^*\frac{\partial u^*}{\partial y^*} = \left(1 + \lambda_1^* \frac{\partial}{\partial t^*}\right)\frac{\partial U_\infty^*}{\partial t^*} + v\frac{\partial^2 U^*}{\partial y^{*2}}$$
$$+ g\beta \cos\phi\left(T^* - T_\infty^*\right) + g\beta^* \cos\phi\left(C^* - C_\infty^*\right)$$
$$+ \left(\frac{\sigma B_0^2 \sin^2 \xi}{\rho} + \frac{v}{K^*}\right)\left(1 + \lambda_1^*\frac{\partial}{\partial t^*}\right)\left(U_\infty^* - u^*\right) \tag{2}$$

$$\frac{\partial T^*}{\partial t^*} + V^*\frac{\partial T^*}{\partial y^*} = \frac{k}{\rho C_p}\frac{\partial^2 T^*}{\partial y^{*2}} + \frac{Q_0}{\rho C_p}(T^* - T_\infty^*)$$
$$- \frac{16\sigma^* T_\infty^{*3}}{3\rho C_p K_1^*}\frac{\partial^2 T^*}{\partial y^{*2}} - \frac{R_1^*}{\rho C_p}(C^* - C_\infty^*) \tag{3}$$

$$\frac{\partial C^*}{\partial t^*} + V^*\frac{\partial C^*}{\partial y^*} = D_m\frac{\partial^2 C^*}{\partial y^{*2}} - R^*(C - C_\infty^*) \tag{4}$$

The conditions at the boundary are

$$u^* = u_p^*, \quad T^* = T_\infty^* + \in (T_w^* - T_\infty^*)\,e^{n^* t^*},$$
$$C^* = C_w^* + \in (C_w^* - C_\infty^*)\,e^{n*t^*} \text{ at } y = 0 \tag{5}$$

$$u^* \to u^*_\infty = U_0(1 + \in e^{n^*t^*}), \quad T^* \to T^*_\infty, \quad C^* \to C^*_\infty \text{ at } y \to \infty \qquad (6)$$

Let us suppose that in the direction of the fluid flow, the porous plate moves by a stable velocity u^*_p and the free stream velocity U^*_∞ abide by exponentially increasing small perturbation law. In addition, the temperature, concentration and the suction velocity are exponentially varying with time. It is clear from Eq. (1) that the suction velocity at the plate surface is a function of time only and it takes the following form

$$V^* = -V_0\left(1 + \in Ae^{n^*t^*}\right) \qquad (7)$$

where A is a real positive constant $\in$ and $\in A$ are small and less than unity and V_0 is a scale of suction velocity which is a non-zero positive constant.

Let us set the dimensionless variables as follows:

$$u = \frac{u^*}{U_0}, v = \frac{v^*}{V_0}, y = \frac{y^*V_0}{v}, U^*_\infty = U_\infty U_0,$$

$$u^*_p = U_p U_0, t = \frac{t^*V_0^2}{v}, n = \frac{n^*v}{V_0^2},$$

$$\theta = \frac{T^* - T^*_\infty}{T^*_w - T^*_\infty}, C = \frac{C^* - C^*_\infty}{C^*_w - C^*_\infty},$$

$$\text{Gr} = \frac{vg\beta(T^*_w - T^*_\infty)}{V_0^2 U_0}, \text{Gm} = \frac{vg\beta^*(C^*_w - C^*_\infty)}{V_0^2 U_0},$$

$$K = \frac{K^*V_0^2}{v^2}, S = \frac{\phi_0 v^2}{\kappa V_0^2}, \text{Pr} = \frac{\mu Cp}{\kappa}\text{Ra} = R^*_1\left(\frac{C^*_\omega - C^*_\infty}{T^*_\omega - T^*_\infty}\right)\frac{v^2}{V_0^2}$$

$$\lambda_1 = \frac{\lambda_1^*V_0^2}{v}, R = \frac{4\sigma^*T^{*3}_\infty v^2}{K_1\kappa V_0^2}, K_r = \frac{R^*v}{v_0^2}, S_e = \frac{v}{D_m} \qquad (8)$$

Substituting the Eq. (8) into Eqs. (2), (3) and (4), we obtain

$$\left(1 + \lambda_1\frac{\partial}{\partial t}\right)\frac{\partial u}{\partial t} - \left(1 + \in Ae^{nt}\right)\frac{\partial u}{\partial y} = \left(1 + \lambda_1\frac{\partial}{\partial t}\right)\frac{dU_\infty}{dt} + \frac{\partial^2 u}{\partial y^2} + \text{Gr}_1\theta + \text{Gm}_1 C$$

$$+ N\left(1 + \lambda_1\frac{\partial}{\partial t}\right)(U_\infty - u) \qquad (9)$$

$$\frac{\partial\theta}{\partial t} - (1 + \in Ae^{nt})\frac{\partial\theta}{\partial y} = \frac{1}{\text{Pr}}\left(1 + \frac{4R}{3}\right)\frac{\partial^2\theta}{\partial y^2} + \frac{S}{\text{Pr}}\theta - \frac{\text{Ra}}{\text{Pr}}C \qquad (10)$$

$$\frac{\partial C}{\partial t} - (1 + \in Ae^{nt})\frac{\partial C}{\partial y} = \frac{1}{Sc}\frac{\partial^2 C}{\partial y^2} - \text{Kr}C \qquad (11)$$

The corresponding boundary conditions are

$$u = U_P, \theta = 1 + \in e^{nt}, C = 1 + \in e^{nt} \text{ , at } y = 0 \qquad (12)$$

$$u \rightarrow U_\infty = 1 + \epsilon\, e^{nt}, \theta \rightarrow 0, C \rightarrow 0 \text{ as } y \rightarrow \infty \tag{13}$$

where, $N = M\,\sin^2 \xi + \frac{1}{K}$. $\text{Gr}_1 = \text{Gr}\cos\phi$, $\text{Gm}_1 = \text{Gm}\cos\phi$.

3 Solution of the Problem

To solve the Eqs. (9)–(11) subject to the boundary conditions (12) and (13), we apply the perturbation technique. Let the velocity, temperature and concentration fields as

$$u = u_0(y) + \epsilon\, e^{nt} u_1(y) + O(\epsilon^2)$$
$$\theta = \theta_0(y) + \epsilon\, e^{nt} \theta_1(y) + O(\epsilon^2)$$
$$C = C_0(y) + \epsilon\, e^{nt} C_1(y) + O(\epsilon^2) \tag{14}$$

Using (14) in Eqs. (9)–(11) and comparing the coefficients of the same degree terms and neglecting terms of $0(\epsilon^2)$, a set of ODE are obtained and on solving, the following solutions are obtained.

$$u(y,t) = \left(1 + L_1 e^{-l_1 y} + P_7 e^{-R_1 y} + P_8 e^{-R_3 y}\right) + \epsilon\, e^{nt}$$
$$\left(1 + L_2 e^{-l_2 y} + P_9 e^{-l_1 y} + P_{10} e^{-R_1 y} + P_{11} e^{-R_2 y} + P_{12} e^{-R_3 y} + P_{13} e^{-R_4 y}\right) \tag{15}$$

$$\theta(y,t) = \left(P_2 e^{-R_1 y} + (1 - P_2) e^{-R_3 y}\right)$$
$$+ \epsilon\, e^{nt} \left(P_3 e^{-R_1 y} + P_4 e^{-R_2 y} + P_5 e^{-R_3 y} + P_6 e^{-R_4 y}\right) \tag{16}$$

$$C(y,t) = e^{-R_1 y} + \epsilon\, e^{nt} \left((1 - P_1) e^{-R_2 y} + P_1 e^{-R_1 y}\right) \tag{17}$$

Shear Stress: The skin friction at the plate $y = 0$ in terms of shear stress is given by

$$\tau = \left.\frac{-\partial u}{\partial y}\right|_{y=0} = (l_1 L_1 + R_1 P_7 + R_3 P_8)$$
$$+ \epsilon\, e^{nt} (l_1 L_2 + l_1 P_9 + R_1 P_{10} + R_2 P_{11} + R_3 P_{12} + R_4 P_{13}) \tag{18}$$

4 Results and Discussion

From analytical solutions, the numerical values for velocity, temperature, concentration, skin friction, Nusselt number as well as Sherwood number are computed by fixing diverse values of the non-dimensional parameters in the problem, i.e., $n = 0.2$, $A = 1$, $\varepsilon = 0.002$, $t = 1$, $S = 0.01$, $Ra = 1$, $R = 1$, $Pr = 0.71$, $M = 1$, $Sc = 0.60$, Gr $= 5$, Gm $= 3$, $K_r = 1$, $U_p = 1$, K $= 5$, $\lambda_1 = 1$, $\phi = \frac{\pi}{6}$ and $\xi = \frac{\pi}{6}$.

Figure 1 illustrated the effects on velocity of magnetic field M as well as Prandtl number Pr for cooling of the plate (Gr > 0). The velocity declined for both water (Pr = 7) as well as air (Pr = 0.71). The reason is that the magnetic field generates Lorentz force which resists the fluid flow and hence velocity falls. From Fig. 2: it is lucid that the velocity diminishes with the rise of aligned angle ξ for the reason that the influence of the applied magnetic field is higher while aligned angle accentuates. From Fig. 3, it is observed that fluid velocity decreases with the increase of angle ϕ. If the plate is inclined, as a result of gravity components, the buoyancy effect decrements and consequently the fluid has higher velocity for vertical surface ($\phi =$ 0) as against that of inclined surface. The influence of radiation, heat absorption as well as absorption radiation parameters on the temperature field is revealed in Fig. 4.

Fig. 1 Velocity profiles for different values of M and Pr
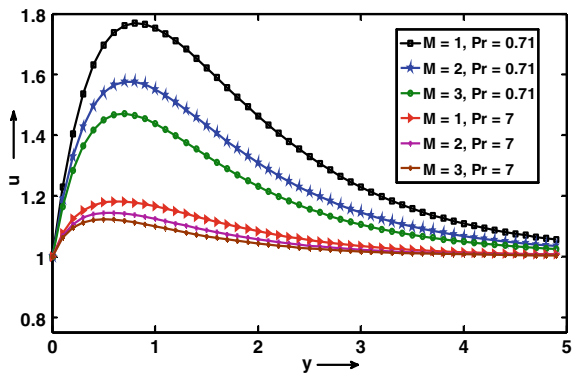
Fig. 2 Velocity profiles for different values of ξ
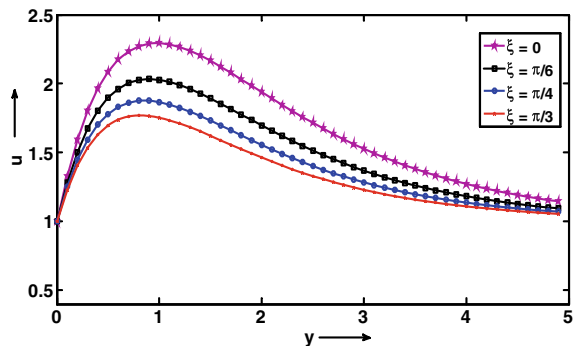
Fig. 3 Velocity profiles for different values of ϕ
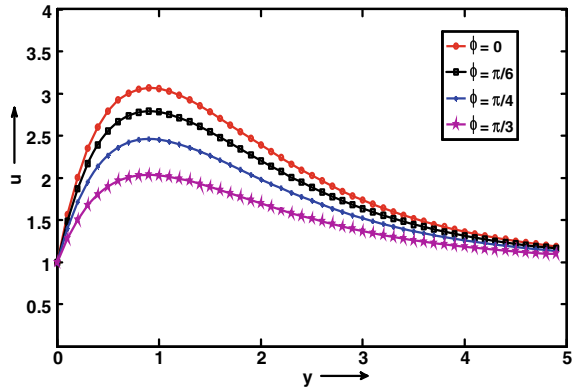
Fig. 4 Temperature profiles for different values of R, S, and Ra
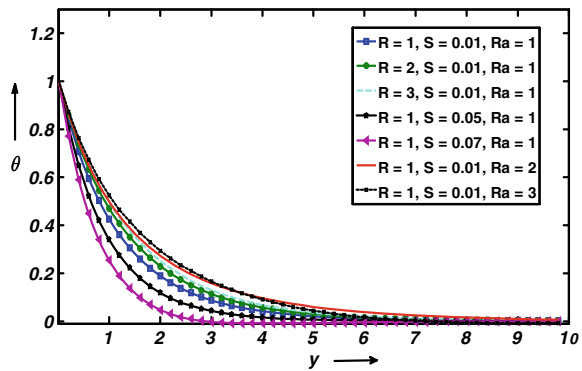
It is perceived that the temperature rises with the rise in radiation and radiation absorption parameters.

Conclusions

- The velocity declines, with the incremental values of magnetic field.
- The temperature rises with the rise in thermal radiation and radiation absorption and the skin friction rise with the rise in solutal Grashof number.
- The rise of aligned angle or angle of inclination leads to a decrease in fluid velocity (Table 1).

Validation of the results: In this examination, the outcomes obtained herein are compared with the results of Chamkha [9] in the absence of Kr, R and Ra on skin friction τ for different values of Gm. The consequences of this comparison are in good agreement with Chamka [9].

Table 1 Skin friction coefficient when $Kr = R = Ra = \phi = \xi = \lambda_1 = 0$

Gm	Skin friction coefficient τ	
	Present study	Chamka [9]
0	2.7203	2.7200
1	3.2786	3.2772
2	3.8387	3.8343
3	4.3960	4.3915
4	4.9493	4.9487

References

1. Reddy SH, Raju MC, Reddy EK (2015) Unsteady MHD free convection flow of a Kuvshinski fluid past a vertical porous plate in the presence of chemical reaction and heat source/sink. Int J Eng Res Afr 14(1):13–27
2. Sakthikala R, Prahala S (2018) Heat and mass transfer of unsteady MHD flow of Kuvshinski fluid with heat source/sink and soret effects. Int J Mech Eng Technol 9:1064–1077
3. Reddy VKRGV, Varma SVK (2016) MHD convection flow of Kuvshinski fluid past an infinite vertical porous plate with thermal diffusion and radiation effects. Chem Mater Res 8(2):18–31
4. Buggaramulu J, Venkata Krishna M (2017) MHD convection flow of Kuvshinski fluid past an infinite vertical porous plate with radiation and chemical reaction effects. Int J Recent Innov Trends Computing Commun 5(9):64–74
5. Devasena Y, LeelaRatnam A (2014) Combined influence of chemical reaction, thermo diffusion and thermal radiation on the convective heat and mass transfer flow of a Kuvshinski fluid past a vertical plate. Int J Adv Sci Tech Res 1(4):774–787
6. Reddy SH, Raju MC, Reddy EK (2015) Unsteady MHD free convection flow of a Kuvshinski fluid past a vertical porous plate in the presence of chemical reaction and heat source/sink. Int J Eng Res Afr 14(3):13–27
7. VidyaSagar B, Raju MC, Varma SVK, Venkataramana S (2014) Unsteady MHD free convection boundary layer flow of radiation absorbing Kuvshinski fluid through porous medium. Rev Adv Phys Theor Appl 1(3):48–62
8. Sharma G, Varshney NK (2013) Stratified Kuvshinski fluid effect on MHD free convection flow with heat and mass transfer past a vertical porous plate. Int J Math Arch 4(9):29–34
9. Chamkha AJ (2004) Unsteady MHD convective heat and mass transfer past a semi-infinite vertical permeable moving plate with heat absorption. Int J Eng Sci 42(1):217–230
10. Hady FM, Mohamed RA, Mahdy A (2006) MHD free convection flow along a vertical wavy surface with heat generation or absorption effect. Int Commun Heat Mass Transfer 33:1253–1263
11. Hossain MA, Molla MM, Yao LS (2004) Natural convection flow along a vertical wavy surface with uniform surface temperature in presence of heat generation/absorption. Int J Therm Sci 43(2):157–163
12. Chamkha AJ (2003) MHD flow of a numerical of uniformly stretched vertical permeable surface in the presence of heat generation/absorption and a chemical reaction. Int Commun Heat Mass Transf 30:413–422
13. Muthucumaraswamy R, Ganesan P (2001) Effect of the chemical reaction and injection on flow characteristics in an unsteady upward motion of an isothermal plate. J Appl Mech Techn Phys 42(4):665–671
14. Ibrahim FS, Elaiw AM, Bakr AA (2008) Effect of the chemical reaction and radiation absorption on the unsteady MHD free convection flow past a semi-infinite vertical permeable moving plate with heat source and suction. Commun Non-linear Sci Numer Simul 13:1056–1066

Nonlinear Radiative Williamson Fluid Against a Wedge with Aligned Magnetic Field

K. Subbarayudu, L. Wahidunnisa, S. Suneetha, and P. Bala Anki Reddy

Abstract The foremost importance of this presentation is to explore the nonlinear thermal radiation on a Williamson liquid model on a wedge in the company of a heat generation/absorption which is not uniform. An aligned magnetic field, Brownian diffusion and thermophoresis aspects are also investigated. The flow and temperature equations are derived and solved by Runge–Kutta based *MATLAB bvp4c solver*. Results for different flow characteristics are plotted through graphs and discussed in detail. The wall temperature raises as temperature ratio parameter increases and results in a deep penetration for temperature. The concentration of the species seems to be increased with Brownian diffusion and radiation.

Keywords Williamson fluid model · Wedge shape geometry · Aligned magnetic field · Nonlinear thermal radiation

1 Introduction

The contemporary era, researchers are doing many experimental and theoretical studies on the fluid flow and transformation of energy in the non-Newtonian fluid models that have significant applications in engineering, for instance, emulsions, lubricants, polymers, and nuclear fuel slurries. Some alive rheological models are Power law, Carreau, Jeffery, Williamson fluid, and so forth. Out of these, Williamson fluid model is a simple model to suggest the viscoelastic nature and shear thin out features which were introduced by Williamson [1] in 1929. The fluid flow and transfer of heat across wedge-shaped geometries are important in several engineering applications and also in fluid dynamics. Particularly such flows occur in aerodynamics, heat exchangers, geothermal industries, and so on. A number of surveys have been found considering Williamson wedge flow in Ref. [2–4]. The study of fluid past a wedge with MHD has vital applications in nuclear reactor cooling, MHD power generators and

K. Subbarayudu · L. Wahidunnisa · S. Suneetha (✉)
Department of Applied Mathematics, Yogi Vemana University, Kadapa 516005, India
e-mail: suneethayvu@gmail.com

P. Bala Anki Reddy
Department of Mathematics, School of Advanced Sciences, VIT, Vellore 632014, India

263

so forth. Several authors [5–8] examined the MHD effects over a wedge in various types of fluids in different situations. Electromagnetic radiation is the major reason for radiation heat transfer. While framing a system in the industry with a negligible temperature variation inside a fluid, a troublesome is observed. To avoid this complexity, researchers included an extra parameter nonlinear thermal radiation in place of linear thermal radiation. Brief information on this area is quoted in Refs. [9–12]. At present, we consider heat source/sink which is not uniform, i.e., dependent on space and temperature. Some related studies were carried out by some investigators [13–16].

It is noted by the literature survey that a little information is existing on the MHD Williamson fluid model flow via a wedge with heat source/sink which is not uniform and radiation which is nonlinear. Inspired by these uses, the present study examines the influence of the thermophoresis effect and Brownian motion of Williamson fluid model for a radiating flow over a wedge.

2   Description of Physical Model

A two-dimensional, viscous, non-Newtonian liquid with Williamson model over a wedge with time-dependent aligned magnetic field is considered. A non-uniform heat generation/absorption and thermal radiation which is not linear is added. $u_w(x, t')$ represents wedge stretching velocity and is referred by $u_w(x, t') = bx^m(1 - ct')^{-1}$ where b-stretching rate and c-stable value. The flow velocity at free stream, $u_e(x, t') = ax^m(1 - ct')^{-1}$, while a and c are stable values more than zero with $0 \leq m \leq 1$, along the wedge axis. $\Omega = \beta\pi$ supposed to be the angle of the wedge and the pressure gradient β is given as $\beta = \frac{2m}{m+1}$. The x-axis is incident in the elongating direction and y-axis makes 90° angle outside from it. A geometrical configuration and schematic model of the present objective model is put on viewed in Fig. 1. To study the heat flow on the surface of wedge, the temperature, $T_w(x, t') =$
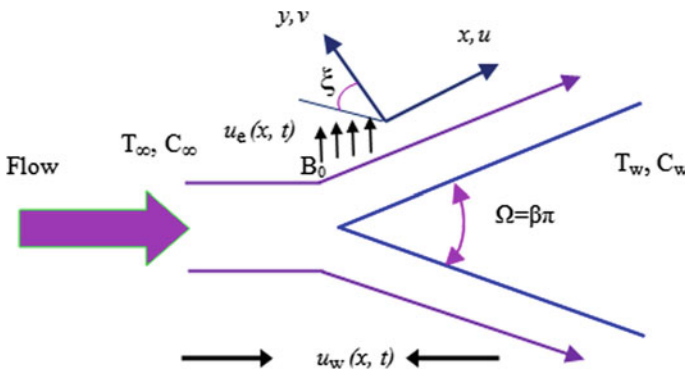
Fig. 1 Flow geometry

$\frac{T_0 u_w x}{v} \left(1 - ct'\right)^{-\frac{1}{2}} + T_\infty$, concentration $C_w(x, t') = \frac{C_0 u_w x}{v} \left(1 - ct'\right)^{-\frac{1}{2}} + C_\infty$, magnetic field $B(t') = B_0 \left(1 - ct'\right)^{-\frac{1}{2}}, T_0, C_0$ be the initial temperature and concentration are considered and also, as y tends to ∞, the free stream gain the constants values T_∞, C_∞. With the above assumption, the equations are

$$\frac{\partial u}{\partial x} + \frac{\partial v}{\partial y} = 0 \tag{1}$$

$$\frac{\partial u}{\partial t'} + \frac{\partial u}{\partial x} u + \frac{\partial u}{\partial y} v = \frac{\partial u_e}{\partial t'} + u_e \frac{\partial u_e}{\partial x} + v \frac{\partial^2 u}{\partial y^2} \left[\beta^* + \left(1 - \beta^*\right)\left(1 - \Gamma \frac{\partial u}{\partial y}\right)^{-1} \right]$$

$$+ v\Gamma\left(\frac{\partial u}{\partial y}\right) \frac{\partial^2 u}{\partial y^2} \left[\left(1 - \beta^*\right)\left(1 - \Gamma \frac{\partial u}{\partial y}\right)^{-2} \right]$$

$$- \frac{\sigma B_0^2(t')}{\rho} \sin^2 \xi (u - u_e) \tag{2}$$

$$\frac{\partial T}{\partial t'} + \frac{\partial T}{\partial x} u + \frac{\partial T}{\partial y} v = \alpha \frac{\partial^2 T}{\partial y^2} - \frac{\partial q_r}{\partial y} \frac{1}{\left(\rho c_p\right)}$$

$$+ \tau \left[\frac{\partial T}{\partial y} \frac{\partial C}{\partial y} D_B + \frac{D_T}{T_\infty} \left(\frac{\partial T}{\partial y}\right)^2 \right] + \frac{q'''}{\rho c_p} \tag{3}$$

$$\frac{\partial C}{\partial t'} + \frac{\partial C}{\partial x} u + \frac{\partial C}{\partial y} v = \frac{\partial^2 C}{\partial y^2} D_B + \frac{\partial^2 T}{\partial y^2} \frac{D_T}{T_\infty} \tag{4}$$

From Eq. (2) the fluid flow drive to viscous fluid case when $\beta^* = 0 = \Gamma$. The heat generation or absorption which is not uniform, is denoted as $q''' = \left[f'(T_w - T_\infty) A^* + (T - T_\infty) B^* \right] \frac{k u_w}{x v}$ where A^*—dependent relative to space and B^*—dependent relative to temperature of heat generation/absorption. The internal heat generation and absorption is noticed when $A^* > 0$, $B^* > 0$ and $A^* < 0$, $B^* < 0$.

For optically thick fluid, we use Rosseland approximation in which q_r denote radiative heat flux, is specified as

$$q_r = -(1.333) \frac{\sigma^*}{k^*} \frac{\partial T^4}{\partial y}, \tag{5}$$

We can set the term T^4 stirring in Eq. (5) and availing Taylor series by supposing an undersized deviation in temperature of the fluid and ambient fluid and within the boundary layer, preserving to first-order terms only. Hence T^4 referred to as

$$\frac{1}{4} T^4 \cong T_\infty^3 T - \frac{3}{4} T_\infty^4 \tag{6}$$

Equation (3) appears as Eq. (7) by utilizing Eqs. (5) and (6).

$$\frac{\partial T}{\partial t'} + \frac{\partial T}{\partial x}u + \frac{\partial T}{\partial y}v = \frac{\partial^2 T}{\partial y^2}\alpha + \frac{16\sigma^* T^3}{3(\rho c_p)k_1^*}\frac{\partial T}{\partial y}$$

$$+ \tau\left[\frac{\partial C}{\partial y}\frac{\partial T}{\partial y}D_B + \left(\frac{\partial T}{\partial y}\right)^2\frac{D_T}{T_\infty}\right] + \frac{q'''}{\rho c_p} \qquad (7)$$

related to the boundary conditions.

The wedge is assumed to be as there is no-slip condition on its surface and it follows:

On the shell of the wedge i.e., at $y = 0$

$$u = u_w, T = T_w, v = 0, C = C_w \qquad (8)$$

At open water course i.e., as $y \to \infty$

$$u \to u_e,\ T \to T_\infty, C \to C_\infty \qquad (9)$$

Using the quantities of non-dimensional [17]:

$$\eta = y\left(\frac{(m+1)u_e}{2\upsilon x}\right)^{\frac{1}{2}}, \psi = f(\eta)\left(\frac{2\upsilon x u_e}{m+1}\right)^{\frac{1}{2}},$$

$$\phi(\eta) = \frac{C - C_\infty}{C_w - C_\infty}, \theta(\eta) = \frac{T - T_\infty}{T_w - T_\infty} \qquad (10)$$

at this juncture, the stream function $\psi\ (x,\ y,\ t)$ satisfies Eq. (1). The velocities are $u = \frac{\partial\psi}{\partial y}$ and $v = -\frac{\partial\psi}{\partial x}$. By using Eq. (10) in Eqs. (2), (7) and (4) we get the corresponding OD equations:

$$f'''\left[\beta^* + \left(1 - wef''\right)^{-2}\left(1 - \beta^*\right)\right] + ff'' + \left(\beta - \beta(f')^2\right)$$
$$- \left(f' + \eta(0.5)f'' - 1\right)(2 - \beta)A - \mathrm{Ha}^2\{f' - 1\}(2 - \beta)\sin^2\xi = 0, \qquad (11)$$

$$\frac{1}{\mathrm{Pr}}\left[(1.333)\mathrm{Rd}[1 + (\theta_w\theta - \theta)]^3 + 1\right]\theta''$$
$$+ (1.333)\frac{\mathrm{Rd}}{\mathrm{Pr}}(\theta_w - 1)[(\theta_w\theta - \theta) + 1]^2\theta'^2 + \left(f\theta' - 2f'\theta\right)$$
$$- \frac{A}{2}(2 - \beta)\left(\eta\theta' + 3\theta\right) + \mathrm{Nt}\theta'^2 + \mathrm{Nb}\phi'\theta' + (A^*f' + B^*\theta) = 0 \qquad (12)$$

$$\frac{1}{\mathrm{Le}}\left[\phi'' + \frac{\mathrm{Nt}}{\mathrm{Nb}}\theta''\right] - \frac{A}{2}(2 - \beta)\left(\eta\phi' + 3\phi\right) - 2\phi f' + f\phi' = 0, \qquad (13)$$

with reduced conditions at boundary:

$$f = 0,\ f' = \lambda, \theta = 1, \phi = 1 \text{ at } \eta = 0 \qquad (14)$$

$$f' \to 1 \; \theta \to 0, \; \phi \to 0 \text{ as } \eta \to \infty \tag{15}$$

Here, the wedge moving parameter, $\lambda = \frac{b}{a}$ and $\lambda > 0$: a stretching wedge, $\lambda < 0$: a shrinking wedge and $\lambda = 0$: a steady wedge.

The other engaged physical non-dimensional factors are:

$\beta^* = \frac{\mu_0}{\mu_\infty}$ is the ratio of viscosities, $\alpha = \frac{\kappa}{\rho c_p}$ the effective thermal diffusivity, $\text{We} = \sqrt{\frac{\Gamma^2 (m+1) u_e^3}{2 \upsilon x}}$ the Weissenberg number, $\text{Pr} = \frac{\mu c_p}{k}$ the Prandtl number, $\text{Rd} = \frac{4 \sigma^* T_\infty^3}{k k_1^*}$ the Radiation parameter, $A = \frac{c}{a x^{m-1}}$ the unsteadiness parameter, $\beta = \frac{2m}{m+1}$ the wedge angle parameter, $\theta_w = \frac{T_w}{T_\infty}$ (>1) the temperature ratio parameter, $\text{Ha}^2 = \frac{\rho B_0^2}{\rho a x^{m-1}}$ the Hartmann number, $\text{Le} = \frac{\upsilon}{D_B}$ the Lewis number, $Nt = \frac{\tau D_T (T_w - T_\infty)}{T_\infty \upsilon}$ the thermophoresis parameter, $Nb = \frac{\tau D_B (C_w - C_\infty)}{\upsilon}$ the Brownian motion parameter.

The parameters which are useful in engineering are the local non-dimensional friction factor C_{f_x}, Nusselt number Nu_x and Sherwood number Sh_x. They are:

$$C_{f_x} = \frac{\tau_w}{\rho U_w^2}, \text{Nu}_x = \frac{x q_w}{k(T_w - T_\infty)} \text{ and } \text{Sh}_x = \frac{x q_m}{D_B(C_w - C_\infty)}$$

where τ_w, q_w and q_m are given as

$$\text{At } y = 0, \tau_w = \mu_0 \left(\frac{\partial u}{\partial y} \right) \left[\beta^* + (1 - \beta^*) \left(1 - \Gamma \frac{\partial u}{\partial y} \right)^{-1} \right],$$

$$q_w = [q_r] - \left[\frac{\partial T}{\partial y} \left(k + \frac{16 \sigma T^3}{3 k^*} \right) \right] \text{ and}$$

$$q_m = -D_B \left(\frac{\partial C}{\partial y} \right) \tag{16}$$

Using (10) and (16), the dimensionless Engineering quantities are given by

$$C_{f_x} \text{Re}_x^{\frac{1}{2}} = \frac{1}{\sqrt{2 - \beta}} \left[\beta^* + \{1 - \text{we } f''(0)\}^{-1} (1 - \beta^*) \right] f''(0),$$

$$\text{Nu}_x \text{Re}_x^{\frac{1}{2}} = -\frac{1}{\sqrt{2 - \beta}} \left(1 + \frac{4}{3} \text{Rd}[(\theta_w - 1)\theta(0) + 1]^3 \right) \theta'(0) \text{ and}$$

$$\text{Sh}_x \text{Re}_x^{\frac{1}{2}} = -\frac{1}{\sqrt{2 - \beta}} \phi'(0), \tag{17}$$

where Reynolds number $\text{Re}_x = \frac{u_e x}{\upsilon}$.

3   Results and Discussions

The set of Eqs. (11)–(13) with (14) and (15) have been solved using the MATLAB bvp4c solver. This section analyzes the effects of parameters $A = 1.0$, We $= 0.5$, $\beta = 0.1$, $\beta^* = 0.2$, $Nt = 0.5$, $\theta_w = 1.1$, $Nb = 0.5$, Le $= 0.5$, $\lambda = 0.1$, $Rd = 0.5$, Ha $= 0.5$, $A^* = -0.05$, $B^* = -0.05$, $\xi = 45°$, Pr $= 7.2$ associated with the flow problem. All the above values are kept steady unless mentioned in the figure. The mathematical results are plotted in diagrams and tables.

To attest to the genuineness of the attained results, an assessment is made with Hamid et al. [3] (Table 1). A wonderful agreement with the results is noticed. The skin friction values for diverse factors are submitted in Table 2. The development in the enormity of the skin friction is noticed as A, β, Ha and ξ increases. A reverse trend is noticed for λ. Table 3 provides the impact of numerous physical factors on Nusselt number. A rise in Nusselt number is observed as Pr, A rises. A fall in Nusselt number is noticed for a rise in Nb, Nt and We. Table 4 put on view the inspiration

Table 1 Comparison of wall friction coefficient for assorted β whilst $A =$ Ha $= \beta^* =$ We $= \lambda = 0$

β	Hamid et al. [3]	Present study
0.0	0.469600	0.4696
0.1	0.587035	0.5869
0.3	0.774755	0.7747
0.5	0.927680	0.8543
0.9	1.232588	0.9392

Table 2 Variations in the skin friction coefficient for variant values of A, β, λ, Ha and ξ when We $= 0.5$, $\beta^* = 0.2$, $\theta_w = 1.1$, Rd $= 0.5$, $Nt = 0.5$, $Nb = 0.5$, Le $= 0.5$, $A^* = -0.05$, $B^* = -0.05$, Pr $= 7.2$

A	β	λ	Ha	ξ	$-f''(0)$
1.0	0.1	0.1	0.5	$\pi/4$	0.3730
2.0	0.1	0.1	0.5	$\pi/4$	0.5370
3.0	0.1	0.1	0.5	$\pi/4$	0.6461
1.0	0.2	0.1	0.5	$\pi/4$	0.3804
1.0	0.3	0.1	0.5	$\pi/4$	0.3877
1.0	0.1	0.2	0.5	$\pi/4$	0.3114
1.0	0.1	0.3	0.5	$\pi/4$	0.2434
1.0	0.1	0.1	1.0	$\pi/4$	0.4638
1.0	0.1	0.1	1.5	$\pi/4$	0.5758
1.0	0.1	0.1	0.5	$\pi/4$	0.3899
1.0	0.1	0.1	0.5	$\pi/4$	0.4060

Table 3 Variations in the Nusselt number for variant values of Pr, Rd, θ_w, A^*, B^*, A, Nb, Nt, and We when $\beta = 0.1$, $\beta^* = 0.2$, Le $= 0.5$, $\lambda = 0.1$, Ha $= 0.5$, $\xi = 45°$

Pr	Rd	θ_w	A	Nb	Nt	We	$\theta'(0)$
7.2	0.5	1.1	1.0	0.5	0.5	0.5	2.6121
10.0	0.5	1.1	1.0	0.5	0.5	0.5	2.8462
15.0	0.5	1.1	1.0	0.5	0.5	0.5	3.0025
7.2	1.0	1.1	1.0	0.5	0.5	0.5	4.0137
7.2	1.5	1.1	1.0	0.5	0.5	0.5	5.5615
7.2	0.5	1.2	1.0	0.5	0.5	0.5	3.1535
7.2	0.5	1.3	1.0	0.5	0.5	0.5	3.8511
7.2	0.5	1.1	2.0	0.5	0.5	0.5	3.7261
7.2	0.5	1.1	3.0	0.5	0.5	0.5	4.6236
7.2	0.5	1.1	1.0	1.0	0.5	0.5	2.2656
7.2	0.5	1.1	1.0	2.0	0.5	0.5	1.9774
7.2	0.5	1.1	1.0	0.5	1.0	0.5	2.2710
7.2	0.5	1.1	1.0	0.5	2.0	0.5	1.9390
7.2	0.5	1.1	1.0	0.5	0.5	1.0	2.6036
7.2	0.5	1.1	1.0	0.5	0.5	2.0	2.6003

Table 4 Variations in the Sherwood number for variant values of β, Le, A, Nb, Nt and We when $\beta^* = 0.2$, $\theta_w = 1.1$, Rd $= 0.5$, Le $= 0.5$, $\lambda = 0.1$, Ha $= 0.5$, $A^* = -0.05$, $B^* = -0.05$, $\xi = 45°$, Pr $= 7.2$

β	Le	A	Nb	Nt	We	$\phi'(0)$
0.1	0.5	1.0	0.5	0.5	0.5	0.7887
0.2	0.5	1.0	0.5	0.5	0.5	0.8450
0.3	0.5	1.0	0.5	0.5	0.5	0.9038
0.1	0.6	1.0	0.5	0.5	0.5	0.8372
0.1	0.7	1.0	0.5	0.5	0.5	0.8815
0.1	0.5	2.0	0.5	0.5	0.5	0.2527
0.1	0.5	3.0	0.5	0.5	0.5	0.0412
0.1	0.5	1.0	1.0	0.5	0.5	1.2178
0.1	0.5	1.0	1.5	0.5	0.5	1.3409
0.1	0.5	1.0	0.5	1.0	0.5	1.0334
0.1	0.5	1.0	0.5	1.5	0.5	2.0021
0.1	0.5	1.0	0.5	0.5	1.0	0.6514
0.1	0.5	1.0	0.5	0.5	1.5	0.5401

of different physical factors on Sherwood number. A hike in Sherwood number is observed as β, Le, Nt, and Nb rise and an opposite trend is noticed for A and We.

The inspiration of Ha on velocity is shown in Fig. 2. In point of physics, hydro-magnetic flow for positive values of Ha and neutral for hydrodynamic flow. As of Fig. 2, it is noted an enhancement in Ha enhances the velocity. Influence of A on velocity is plotted in Fig. 3. With higher unsteadiness parameter, the fluid velocity
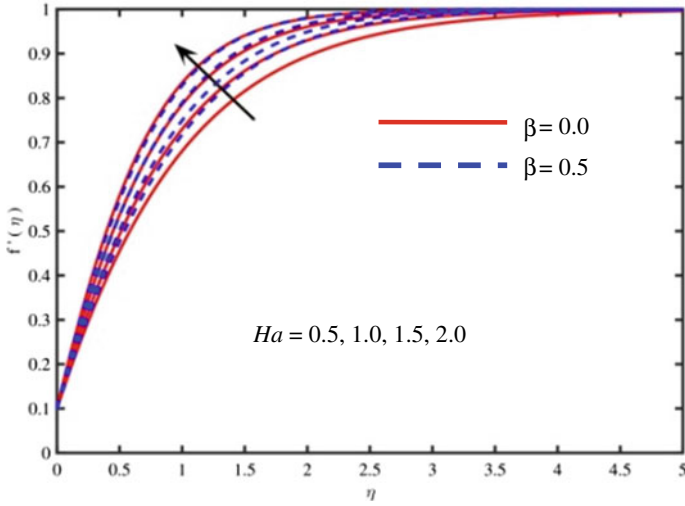
Fig. 2 $f'(\eta)$ via Ha
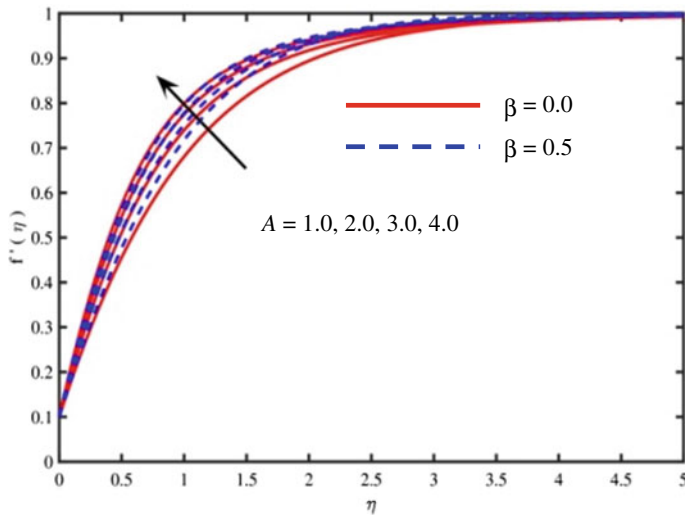
Fig. 3 $f'(\eta)$ via A

demonstrates an escalate behaviour near the boundary whereas a reverse trend is noticed for temperature. Figure 4 displays the upshot of Pr on temperature distribution over a wedge. Fluid temperature simply reduces for elevated Pr. As Pr promoted the rate of thermal diffusion is demoted. That is, accelerating Pr leads a loss in the boundary layer width of temperature. It is also noted that the thermal energy is high for $\beta = 0.5$ case compared with the other case. The outcome of thermophoresis on temperature is captured in 5. From Fig. 5, it is revealed that the temperature in the
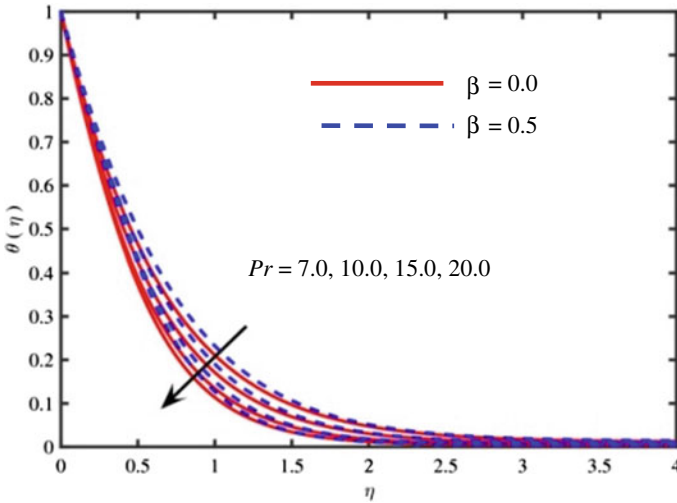
Fig. 4 $\theta(\eta)$ via Pr
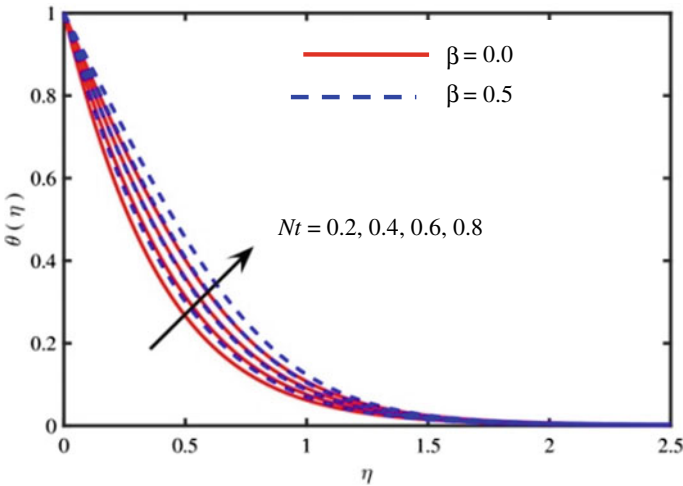
Fig. 5 $\theta(\eta)$ via Nt
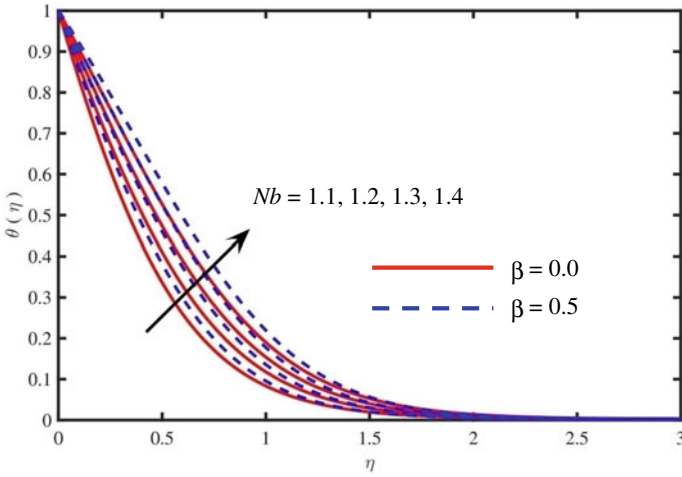
Fig. 6 $\theta(\eta)$ via Nb

boundary layer has increasing behaviour with an enhancement of Nt. In physics, it is a force generated by a tiny particle applying a force physically on another particle so that it moves from hot phase to a cold phase which fruitage a thicker boundary layer for thermal and species. Therefore, far above Nt match up to elevated thermophoretic force because of temperature gradient, which promotes a speedy flow far from the wedge. Figure 6 divulge temperature distribution for various values of Nb. It can be viewed from Fig. 6 that the temperature is the proportion with Nb. The reason is that the Nb exhibits heat conduction. In addition, an enhancement in the Brownian motion heightens the random movement of the particles thus the width of the border layer grows for temperature. Figure 7 shows the impact of θ_w on temperature. The wall temperature raises as θ_w increases and results in a deep penetration for temperature. At high temperatures, the border layer for a temperature becomes bulky in the vicinity of the wall and skeletal far away from the sheet for low temperatures results in a modulation point at the surface of the wall for larger θ_w. Figure 8a, b depicts Nusselt number and Sherwood number for θ_w. Enhancement of θ_w enhances both the numbers for $\beta = 0.0$, and $\beta = 0.5$. Rising of the rate of heat transfer is observed from Figs. 9 and 10 which results in a growth in A^* and B^* for $\beta = 0.0$, and $\beta = 0.5$.
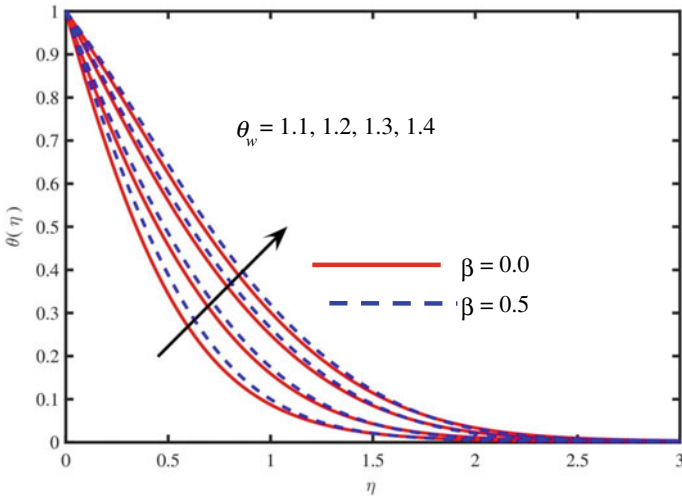
Fig. 7 $\theta(\eta)$ via θ_w.
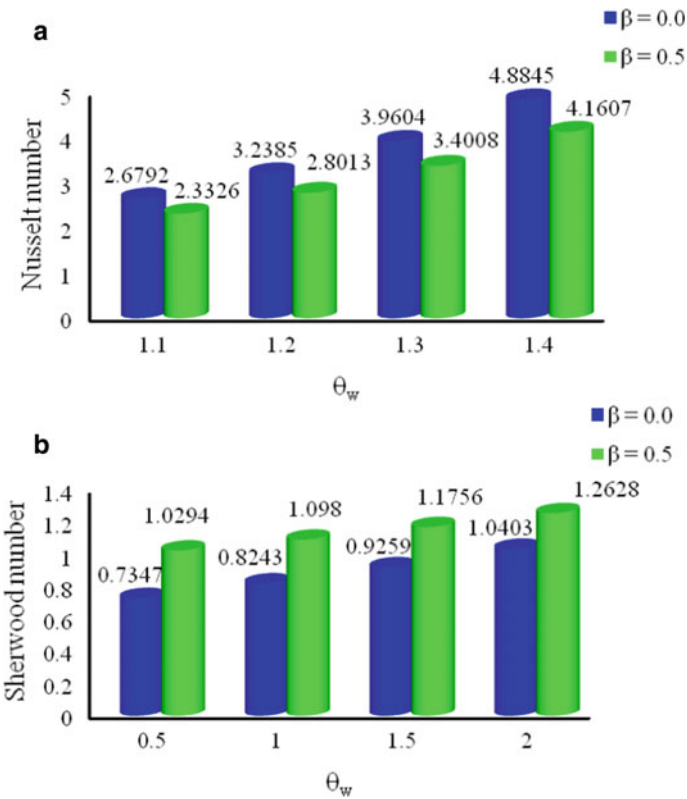
Fig. 8 **a** Nusselt number via θ_w, **b** Sherwood number via θ_w
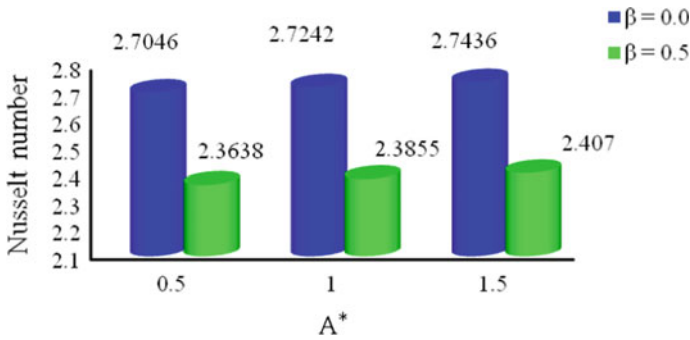
Fig. 9 Nusselt number via A^*
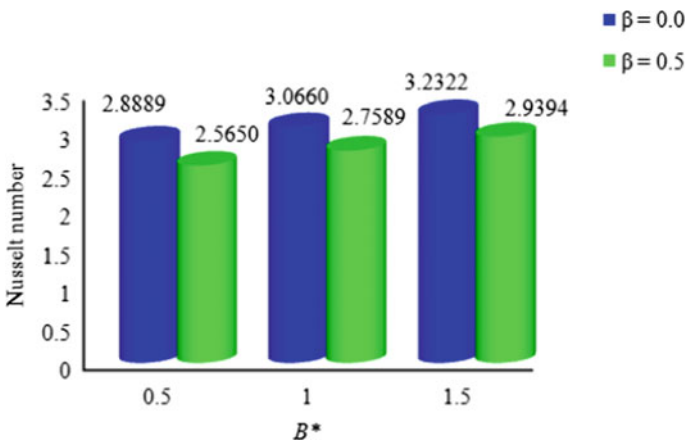
Fig. 10 Nusselt number via B^*

References

1. Williamson RV (1929) The flow of pseudoplastic materials. Ind Eng Chem 21(11):1108–1111. https://doi.org/10.1021/ie50239a035
2. Hamid A, Khan M (2018) Numerical investigation on heat transfer performance in time-dependent flow of Williamson fluid past a wedge-shaped geometry. Res Phys 9:479–485. https://doi.org/10.1016/j.rinp.2018.01.025
3. Khan M, Hamid A (2018) Numerical investigation on time-dependent flow of Williamson nanofluid along with heat and mass transfer characteristics past a wedge geometry. Int J Heat Mass Transf 118:480–491. https://doi.org/10.1016/j.ijheatmasstransfer.2017.10.126
4. Subbarayudu K, Suneetha S, Wahidunnisa L, Bala Anki Reddy P (2018) Impact of chemical reaction on radiating Falkner-Skan flow over a wedge moving in a Carreau nanofluid with convective condition. Int J Tech Innov Modern Eng Sci IJTIMES 4(6):1353–1362
5. Bala Anki Reddy P, Suneetha S, Bhaskar Reddy N (2017) Numerical study of magnetohydrodynamics (MHD) boundary layer slip flow of a Maxwell nanofluid over an exponentially stretching surface with convective boundary condition. Propul Power Res 6(4):259–268. https://doi.org/10.1016/j.jppr.2017.11.002

6. Hayat T, Qayyum S, Alsaedi A, Shafiq A (2016) Inclined magnetic field and heat source/sink aspects in flow of nanofluid with nonlinear thermal radiation. Int J Heat Mass Transf. 103:99–107. https://doi.org/10.1016/j.ijheatmasstransfer.2016.06.055

7. Ahmad R, Khan WA (2014) Numerical study of heat and mass transfer MHD viscous flow over a moving wedge in the presence of viscous dissipation and heat source/sink with convective boundary condition. Heat Transf Asian Res 43(1):17–38. https://doi.org/10.1002/htj.21063

8. Khan M, Hamid A (2017) Influence of non-linear thermal radiation on 2D unsteady flow of a Williamson fluid with heat source/sink. Res Phys 7:3968–3975. https://doi.org/10.1016/j.rinp.2017.10.014

9. Kandasamy R, Muhaimin I, Mohammad R (2016) Single-walled carbon nanotubes on MHD unsteady flow over a porous wedge with thermal radiation with variable stream conditions. Alexandria Eng J 55:75–285. https://doi.org/10.1016/j.aej.2015.10.006

10. Hayat T, Awais M, Asghar S (2013) Radiative effects in a three-dimensional flow of MHD Eyring-Powell fluid. J Egypt Math Soc 21:379–384. https://doi.org/10.1016/j.joems.2013.02.009

11. Pandey AK, Kumar M (2017) Chemical reaction and thermal radiation effects on boundary layer flow of nanofluid over a wedge with viscous and Ohmic dissipation. St. Petersburg Polytech Univ J Phys Math. 3(4):322–332. https://doi.org/10.1016/j.spjpm.2017.10.008

12. Khan M, Azam M, Alshomrani AS (2017) Unsteady slip flow of Carreau nanofluid over a wedge with nonlinear radiation and new mass flux condition. Res Phys 7:2261–2270. https://doi.org/10.1016/j.rinp.2017.06.038

13. Kasmani RM, Sivasankaran S, Bhuvaneswari M, Siri Z (2015) Effect of thermal radiation and suction on convective heat transfer of nanofluid along a wedge in the presence of heat generation/absorption. AIP Conf Proc 1682:020008. https://doi.org/10.1063/1.4932417

14. Khan M, Azam M, Alshomrani AS (2017) Effects of melting and heat generation/ absorption on unsteady Falkner-Skan flow of Carreau nanofluid over a wedge. Int J Heat Mass Transfer. 110:437–446. https://doi.org/10.1016/j.ijheatmasstransfer.2017.03.037

15. Patil PM, Kumbarwadi N, Shashikant A (2018) Effects of MHD mixed convection with non-uniform heat source/sink and cross-diffusion over exponentially stretching sheet. Int J Numer Methods Heat Fluid Flow 28(6):1238–1255. https://doi.org/10.1108/hff-04-2017-0149

16. Jain S, Choudhary R (2018) Dufour-Soret and thermophoretic effects on magnetohydrodynamic mixed convection casson fluid flow over a moving wedge and non-uniform heat source/sink. Int J Fluid Mech Res 45(1):51–74. https://doi.org/10.1615/interjfluidmechres.2018020450

17. Alam MS, Islam T, Rahman MM (2015) Unsteady hydromagnetic forced convective heat transfer flow of a micropolar fluid along a porous wedge with convective surface boundary condition. Int J Heat Tech 33(2):115–125. https://doi.org/10.18280/ijht.330219

Studies on the Load Carrying Capacity of a Multi-Pad Adjustable Bearing Under Misaligned Conditions

Girish Hariharan, D. Srikanth Rao, and Raghuvir Pai

Abstract This paper deals with the effect of journal misalignment on the load capacity of a multi-pad externally adjustable bearing. Pad adjustments can be provided in radial and tilt directions. A modified film thickness equation is applied to determine the variation in film thickness under different pad adjustment conditions. Governing Reynolds equation is discretized using finite difference approximation technique. In the present study, misalignment is considered in only one plane. Variation in load capacity is analyzed for different degrees of misalignment and pad adjustment positions. An improvement in the bearing load capacity is observed by applying a combination of negative radial and negative tilt adjustment to the four bearing pads.

Keywords Adjustable bearing · Misalignment · Fluid film thickness · Load capacity

Nomenclature

C	Radial clearance (m)
DM	Degree of misalignment
R	Journal radius (m)
R_{adj}	Radial pad adjustment
e	Eccentricity (m), $\varepsilon = (e|C)$
F	Friction force (N), $\overline{F} = (F|LCp_{\text{s}})$
h	Lubricant film thickness (m), $\bar{h} = (h|C)$
L	Bearing length (m)
N'	Journal speed (rps)
p	Constant supply pressure (N/m^2)
p_{s}	Static film pressure (N/m^2), $\bar{p} = p|p_{\text{s}}$
t	Time (s)

G. Hariharan · D. Srikanth Rao · R. Pai (✉)
Department of Mechanical and Manufacturing Engineering, Manipal Institute of Technology, Manipal Academy of Higher Education, Manipal 576104, India
e-mail: raghuvir.pai@manipal.edu

W Load capacity (N), $\overline{W} = (W|LDp_s)$

W_r Radial load component (N), $\overline{W}_r = (W_r|LDp_s)$

W_t Transverse load component (N), $\overline{W}_t = (W_t|LDp_s)$

U Peripheral journal velocity (m/s), $U = \omega R$

x Circumferential coordinate axis (m), $x = R\theta$

z Axial coordinate (m), $z = \bar{z}L$

α Pad angle (rad)

α' Angle between central eccentricity vector and projected journal axis (rad)

δ Tilt angle (rad)

ε' Dimensionless projected distance of the journal, $\varepsilon = (e'/C)$

η Fluid viscosity (Ns/m^2)

θ', θ Angular coordinates of the bearing (rad), $\theta' = (\theta - (\alpha/2))$

Λ Bearing number, $\Lambda = 6\eta\omega/[p_s(C/R)^2]$

μ Friction coefficient

$\overline{\mu}$ Friction variable, $\overline{\mu} = \mu(R/C)$

ϕ Attitude angle (rad)

ψ Assumed attitude angle (rad)

ω Angular velocity of journal (rad/s)

1 Introduction

Journal bearings under misaligned conditions can significantly alter the bearing performance characteristics. Misalignment is an important factor to be considered in bearing design. Journal bearing misalignment often results from various factors such as offset loads, shaft distortion due to thermal effects, housing supports and manufacturing issues. In heavy rotating machineries, misalignment often occurs due to shaft deflection under its own weight. Over the last few decades, the misalignment phenomenon has been increasingly studied by various researchers. Initial studies were focused on evaluating the role of misalignment on the pressure distribution in journal bearings [1, 2]. Dubois et al. [3] extended the work to determine the journal eccentricities at bearing ends and flow rates in axial direction. Smalley and McCallion [4] theoretically evaluated the effect of misaligned journal conditions on the steady-state characteristics of a plain bearing configuration. Both the axial and twisting misalignment was considered in the analysis and design information relating to the effect of misaligning couple was presented. Similar studies were carried out by Guha [5] on misaligned journal bearings having isotropic roughness effects for different degrees of misalignment and eccentricity ratios. Later, Bouyer and Fillon [6] conducted experimental studies on misaligned journal bearings considering the temperature distribution in axial and circumferential direction.

Different forms of bearing geometries are developed over the years with focus on improving the performance of turbomachinery applications. However, the circular and non-circular profiled bearings exhibited a significant drawback on controlling the hydrodynamic lubrication in the clearance space between journal and bearing surfaces. Adjustable bearing geometry has the ability to control the hydrodynamic operation and provide a stable spindle support system for rotating machinery. A journal bearing system with a hydraulic damper and deformable flexible sleeve was mathematically modelled by Krodkiewski et al. [7]. The relative positions of the flexible sleeve can be altered during operation, to enhance the vibration characteristics of rotor-bearing system. Studies were later extended to multi-rotor bearing systems and linear and non-linear techniques were used for dynamic analysis [8]. Experimental studies were carried out by Sun and Krodkiewski [9], on an active fluid film bearing and observed a good agreement between experimental results and numerical calculations. Chasalevris and Dohnal [10] designed a variable bearing geometry to control the system vibrations generated under resonance conditions. A prototype of the proposed bearing geometry was developed, and various experimental tests were conducted for measuring the system dynamic responses [11].

Martin and Parkins [12] designed different types of adjustable bearing geometries, having unique ability in controlling the bearing operation. A mathematical modelling technique was formulated by Martin [13], to consider the non-uniform variation of fluid film thickness. An extended Reynolds equation and film thickness equation considering the segment adjustments were derived in the study. Martin and Parkins [14] conducted experimental studies on different types of bearing geometries and analyzed their ability in suppressing the journal orbits and repositioning of journal center position. A dynamic test rig was manufactured, which included a specialized electromagnet loading method [15]. Later, the steady-state and dynamic behaviour of a single pad adjustable bearing was evaluated by Shenoy [16]. Static performance of the proposed adjustable bearing was evaluated for various pad adjustment positions by considering the effect of turbulent flow and journal misalignment [17]. Using linearized perturbation technique, dynamic characteristics of the adjustable pad were studied for different pad adjustments. A significant improvement in dynamic properties was obtained for negative radial and tilt configurations [18].

This paper presents the theoretical study carried out to analyze the load capacity of a four-pad adjustable bearing under misaligned conditions. Figure 1 illustrates the adjustable bearing geometry considered in the present analysis. The four adjustable pads can be displaced in radial and tilt directions. A modified film thickness equation from [19], is employed in this study to take account of the pad adjustment parameters. Results obtained for different degrees of misalignment and pad adjustments are presented. Under misaligned conditions, superior load capacity is attained for pads under negative R_{adj} and negative tilt conditions.
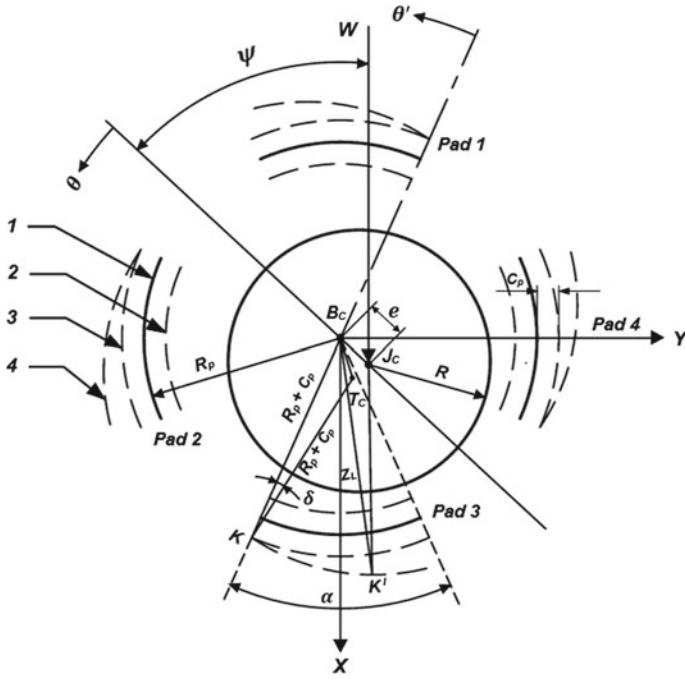
Fig. 1 Mathematical formulation technique to derive the film thickness relation. 1 pad profile, 2 negative R_{adj}, 3 positive R_{adj}, 4 positive tilt angle

2 Analysis

The governing Reynolds equation is expressed as

$$\frac{\partial}{\partial x}\left(\frac{h^3}{12}\frac{\partial p}{\partial x}\right) + \frac{\partial}{\partial z}\left(\frac{h^3}{12}\frac{\partial p}{\partial z}\right) = \frac{1}{2}\eta U\frac{\partial h}{\partial x} + \eta\frac{\partial h}{\partial t} \tag{1}$$

Time dependant term is neglected for static conditions and the above Reynolds equation can be expressed in non-dimensional form as follows:

$$\frac{\partial}{\partial \theta}\left((\bar{h})^3\frac{\partial \bar{p}}{\partial \theta}\right) + \frac{1}{4}\left(\frac{D}{L}\right)^2\frac{\partial}{\partial \bar{z}}\left((\bar{h})^3\frac{\partial \bar{p}}{\partial \bar{z}}\right) = \Lambda\frac{\partial \bar{h}}{\partial \theta} \tag{2}$$

where $\Lambda = \dfrac{6\eta\omega}{\left(p_s\left[\frac{C}{R}\right]^2\right)}$.

3 Film Thickness Formulation

The formulation technique adopted for deriving the modified film thickness relation is shown in Fig. 1. All four adjustable bearing pads are applied with similar adjustments in radial and tilt directions. A detailed mathematical procedure for the film thickness formulation is described in Hariharan and Pai [19].

Mathematical relations are used to derive the film thickness equation and is clearly depicted in Fig. 1. The modified film thickness expression from [19] is given in Eq. 3.

$$\bar{h} = \frac{(Z_L - R)}{C} + \varepsilon \cos(\theta' - \psi) \tag{3}$$

where, $\theta' = \left(\theta - \frac{\alpha}{2}\right)$.

This study considers the journal under misaligned conditions as shown in Fig. 2. The film thickness equation is modified and is given in Eq. 4, with reference to the studies described in Guha [5].

$$\bar{h} = \frac{(Z_L - R)}{C} + \varepsilon \cos\theta' + \varepsilon'(\bar{z} - 0.5)\cos(\theta' - \alpha') \tag{4}$$

where

$$\varepsilon' = 2DM\left\{\left[1 - (\varepsilon \sin\alpha')^2\right]^{1/2} - \varepsilon|\cos\alpha'|\right\}. \tag{5}$$

Similar to the studies presented by Hargreaves [20], misalignment is assumed in only one plane, i.e., $\alpha = 0$ and Eq. 5 can be simplified to
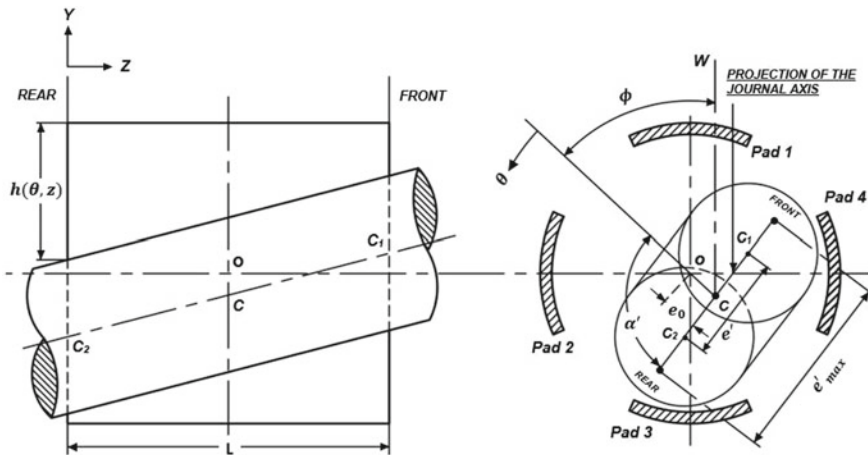
Fig. 2 Schematic representation of misaligned bearing

$$\varepsilon' = 2\mathrm{DM}(1 - \varepsilon). \tag{6}$$

4 Boundary Conditions

Pressure variation on the bearing edges is considered as zero and is expressed as

$$\bar{p} = \bar{p}_a = 0; \ \text{at} \ \bar{z} = 0 \ \text{and} \ \bar{z} = 1 \ \text{and}$$
$$\bar{p} = \bar{p}_a = 0; \ \text{at} \ \theta = 0 \ \text{and} \ \theta = 2\pi \tag{7}$$

At ambient pressures, cavitation takes place and is defined by setting the negative pressures to zero, i.e.,

$$\bar{p} = \frac{\partial \bar{p}}{\partial \theta} = 0. \tag{8}$$

5 Load Capacity

The bearing load capacity is determined using the generated radial and transverse force components.

$$\overline{W}_r = \left[\frac{W_r}{LDp_s}\right] = -\int_0^1 \int_0^{2\pi} \bar{p} \cos\theta' d\theta \, d\bar{z} \tag{9}$$

$$\overline{W}_t = \left[\frac{W_t}{LDp_s}\right] = \int_0^1 \int_0^{2\pi} \bar{p} \sin\theta' d\theta \, d\bar{z} \tag{10}$$

Resultant force generated

$$\overline{W} = \left[\frac{W}{LDp_s}\right] = \sqrt{\overline{W}_r^2 + \overline{W}_t^2} \tag{11}$$

Attitude angle

$$\phi = \tan^{-1}\left(\frac{\overline{W}_t}{\overline{W}_r}\right). \tag{12}$$

6 Friction Variable

The non-dimensionalized form of friction force is written as

$$\overline{F} = \left(\frac{F}{LCp_s}\right) = \int\limits_0^1 \int\limits_0^{2\pi} \left(\frac{\bar{h}}{2}\frac{\partial \bar{p}}{\partial \theta} + \frac{\Lambda}{6}\frac{1}{\bar{h}}\right) d\theta \, d\bar{z} \tag{13}$$

Friction variable is given by

$$\overline{\mu} = \mu\left(\frac{R}{C}\right) = \frac{\overline{F}}{\overline{W}}. \tag{14}$$

7 Computational Technique

A computer program is developed to analyze the effect of misalignment on the load capacity of a multi-pad adjustable bearing. To solve the Reynolds equation given in Eq. 2, finite difference method is applied along with Gauss–Siedel method and successive over relaxation approach. Boundary conditions are applied by setting negative pressure gradients equal to zero. Attitude angle (ψ) is initially assumed for the iteration process. Film thickness equation given in Eq. 4 is applied, to predict the film profile for different values of DM and pad adjustments. The iteration procedure for pressure convergence is repeated until a convergence criterion of less than 0.0001 is attained. Once pressure convergence takes place, attitude angle ϕ determined from Eq. 11 is compared with the assumed attitude angle ψ. The value of ψ is modified iteratively using a convergence criterion, until ψ becomes nearly equal to ϕ. The load capacity of the adjustable bearing is calculated using Eq. 10.

8 Validation

The computational technique employed in the present study is validated with the results given in Shenoy [16] for a single pad adjustable bearing having shaft misalignment. By setting zero radial and tilt adjustments, single pad adjustable bearing acts as a conventional partial arc bearing. A pad angle of 120° is considered with *L/D* ratio as 1. Figure 3a, b compares the friction variable obtained from present analysis and Shenoy [16] for DM of 0.50 under negative and positive pad adjustment conditions. A considerable agreement in results are observed, which validates the correctness of the present computational approach. The percentage deviation
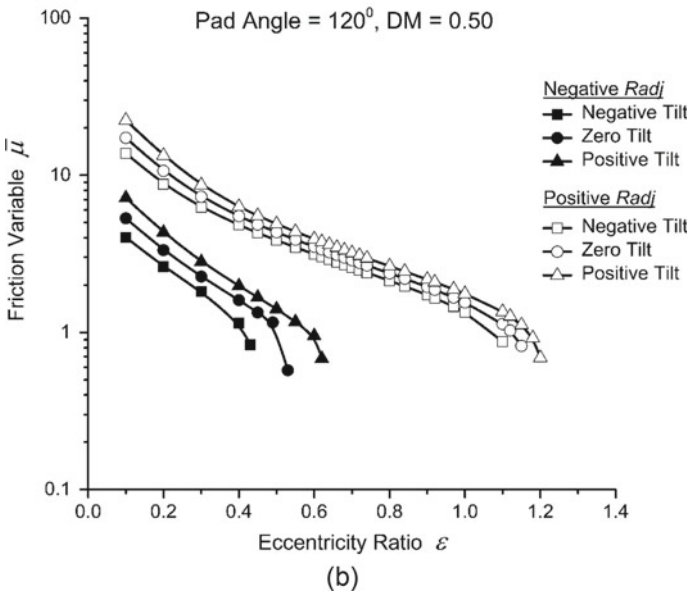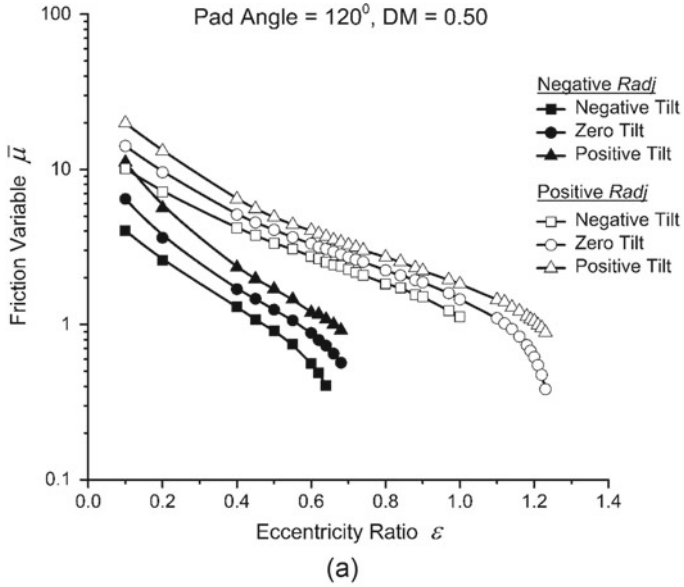
Fig. 3 Comparison of friction variable for a single pad adjustable bearing with DM = 0.50 under different adjustments conditions. **a** Shenoy [16], **b** present analysis

between the results of Shenoy [16] and the present analysis is found to 9.92% for different pad adjustment conditions.

9 Results and Discussion

Figures 4, 5 and 6 demonstrate the variation in load capacity observed for a four-pad adjustable bearing under the influence of different values of DM and pad adjustments. A radial adjustment of $\pm 30\%$ of clearance was considered. Tilt angle of $\pm 0.0064°$ is applied to the leading ends of four pads. Under negative pad adjustment conditions, reduction in clearance spaces occurs due to the inward movement of adjustable pads. However, a significant increase in pad clearances is obtained with outward movement of bearing pads (i.e., with positive R_{adj} and positive tilt angles).

Under journal misaligned conditions, minimum film thickness will be attained at the ends of the bearing. This influences the development of higher hydrodynamic pressures at the bearing ends. From Fig. 4, incremental rise in load capacity is noted for increasing eccentricity ratios. For a certain degree of misalignment (either DM $= 0.25$ or DM $= 0.50$), higher load capacity is obtained for pads applied with negative tilt angles than zero or positive tilt angles. This is due to the presence of higher hydrodynamic forces generated at smaller clearance spaces, which is normally developed at larger journal eccentricities and negative tilt adjustments. For negative radial adjustment conditions, the degree of misalignment is found to have a significant effect on the load capacity. An increase in load capacity is noted for DM $= 0.50$ in
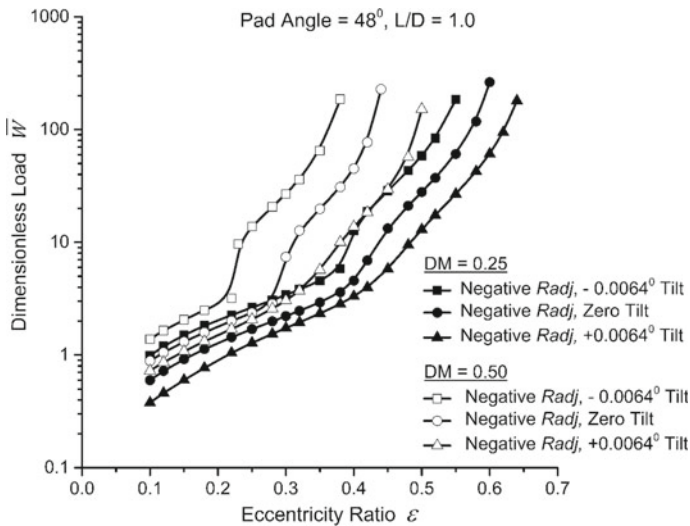
Fig. 4 Dimensionless load of 4-pad adjustable bearing under negative R_{adj} and various degrees of misalignment
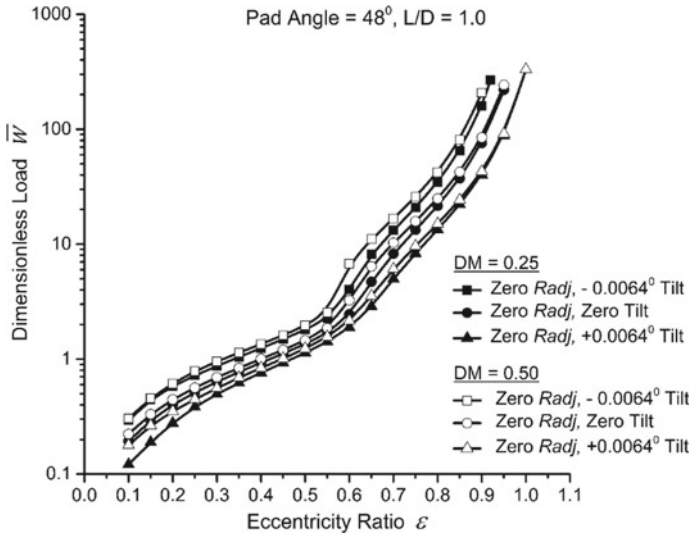
Fig. 5 Dimensionless load of 4-pad adjustable bearing under zero R_{adj} and various degrees of misalignment

Fig. 6 Dimensionless load of 4-pad adjustable bearing under positive R_{adj} and various degrees of misalignment

comparison with DM = 0.25. At larger degrees of misalignment, the possibility of shaft contact is found to be higher for negative radial and tilt adjustments.

Figures 5 and 6 indicate that for zero and positive radial adjustments, a marginal variation in load capacity is observed for different degrees of misalignment. This is because of the presence of larger clearance spaces under zero or positive pad adjustments than negative adjustment conditions. For differe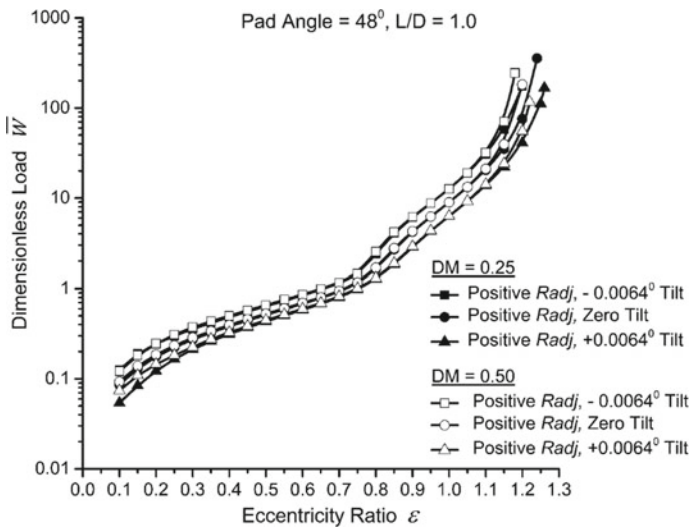nt eccentricity ratios, a similar increase in load capacity is observed for zero and positive radial adjustments in combination with different tilt angles. By comparing Figs. 4, 5, and 6, it is noted that higher magnitudes of load capacity are obtained for negative R_{adj} in comparison with zero and positive R_{adj}. Further increase in load capacity is obtained by tilting the bearing pads in a negative direction.

10 Conclusion

The load capacity of a multi-pad adjustable bearing under misaligned conditions is analyzed in the present study. Due to journal misalignment, minimum fluid film thickness is developed at the ends of the bearing. Maximum pressures are developed at the bearing edges, which significantly influences the bearing load capacity. The degree of misalignment is found to have a pronounced influence over load capacity under negative radial and tilt adjustment conditions. For positive radial adjustments, a marginal variation in load capacity is observed for different values of DM, due to the presence of larger clearance spaces. In comparison with other pad adjustments, higher load carrying capacity is recorded for pads displaced to negative radial and tilt positions.

References

1. Buske A, Rolli W (1949) Measurements of oil-film pressure in bearings under constant and variable loads. NACA Tech Note 1200:43
2. Dubois GB, Ocvirk FW, Mabie HH (1951) Experimental investigation of oil film pressure distribution for misaligned plain bearings. NACA Tech Note 2507
3. Dubois GB, Mabie HH, Ocvirk FW (1955) Experimental investigation of misaligning couples and eccentricity at ends of misaligned plain bearings. NACA Tech Note 3352
4. Smalley AJ, McCallion H (1966) The effect of journal misalignment on the performance of a journal bearing under steady running conditions. Proc Inst Mech Eng Conf Proc 181:45–54
5. Guha SK (2000) Analysis of steady-state characteristics of misaligned hydrodynamic journal bearings with isotropic roughness effect. Tribol Int 33:1–12
6. Bouyer J, Fillon M (2001) An experimental analysis of misalignment effects on hydrodynamic plain journal bearing performances. J Tribol 124:313–319
7. Krodkiewski JM, Cen Y, Sun L (1997) Improvement of stability of rotor system by introducing a hydraulic damper into an active journal bearing. Int J Rotating Mach 3:45–52
8. Krodkiewski JM, Sun L (1997) Modelling of multi-bearing rotor systems incorporating an active journal bearing. J Sound Vib 210:215–229

9. Sun L, Krodkiewski JM (2000) Experimental investigation of dynamic properties of an active journal bearing. J Sound Vib 230:1103–1117

10. Chasalevris A, Dohnal F (2012) A journal bearing with variable geometry for the reduction of the maximum amplitude during passage through resonance. J Vib Acoust 134:061005

11. Chasalevris A, Dohnal F (2015) A journal bearing with variable geometry for the suppression of vibrations in rotating shafts: Simulation, design, construction and experiment. Mech Syst Signal Process 52:506–528

12. Martin JK, Parkins DW (1998) Fluid film bearings. US Patent 5,772,334

13. Martin JK (1999) A mathematical model and numerical solution technique for a novel adjustable hydrodynamic bearing. Int J Numer Methods Fluids 30:845–864

14. Martin JK, Parkins DW (2001) Testing of a large adjustable hydrodynamic journal bearing. Tribol Trans 44:559–566

15. Martin JK (2004) Measuring the performance of a novel fluid film bearing supporting a rotor on a stationary shaft, by non-contacting means. Proc Inst Mech Eng Part K J Multi-Body Dyn 218:143–151

16. Shenoy BS (2008) Performance evaluation of single pad externally adjustable fluid film bearing. In: PhD thesis. Manipal University, Manipal

17. Shenoy BS, Pai R (2009) Theoretical investigations on the performance of an externally adjustable fluid-film bearing including misalignment and turbulence effects. Tribol Int 42:1088–1100

18. Shenoy BS, Pai R (2011) Dynamic characteristics of a single pad externally adjustable fluid film bearing. Ind Lubr Tribol 63:146–151

19. Hariharan G, Pai R (2018) Mathematical formulation of a modified film thickness equation for multipad externally adjustable fluid film bearing. Cogent Eng 5:1–15

20. Hargreaves DJ (1995) Predicted performance of a tri-taper journal bearing including turbulence and misalignment effects. Proc Inst Mech Eng Part J J Eng Tribol 209:85–97

Influence of Aerodynamic Parameters on Dragonfly Inspired Corrugated Aerofoil

Md. Akhtar Khan and **Chinmaya Padhy**

Abstract This work is focused on the variation of corrugation angle and peak height of 2-D corrugated aerofoil inspired from the forewing of 'Pantala Flavescens' or yellow dragonfly basal wing section. A computational analysis is done on a newly designed dragonfly corrugated aerofoil wing-A and wing-B at Re = 15.603×10^3 and the flow is considered as steady and density of the flow is constant. In this study, the aerodynamic performance of 2-D dragonfly corrugated aerofoil is performed at different angle of attack (AoA) with variation in corrugation angle and peak height. With the varying peak height and corrugation angle, there is low wake formation, reduced drag, and increase in flight performance compared to streamlined aerofoil and flat plate. The computational fluid dynamic (CFD) analysis is performed using a high fidelity fluent solver. The CFD result shows that the aerodynamic performance, i.e., the gliding ratio $\left(\frac{C_L}{C_D}\right)$ of wing-A is higher than wing-B and streamlined aerofoil. The vortex formed is trapped inside the valleys which re-energizes the flow and delays separation leads to an increment in lift coefficient (C_L). This finding enhances the knowledge of insect-inspired corrugated wing structure and facilitate the application for improved design of artificial wings for MAVs and UAVs.

Keywords Dragonfly · 2-D corrugated aerofoil · Flight · Computational fluid dynamics · FLUENT · Peak height · MAVs

Md. A. Khan (✉)
Aerospace Engineering Department, GITAM School of Technology, Hyderabad, India
e-mail: Khan.akhtar24@gmail.com

C. Padhy
Mechanical Engineering Department, GITAM School of Technology, Hyderabad, India
e-mail: dr.padhy.iitkgp@gmail.com

1 Introduction

The dragonfly species in particular 'Pantala flavescens' widely known as globe skimmer or wandering glider because of its long-range flight capability are found throughout the tropics and many temperature areas. Insects such as a dragonfly and damselfly employ corrugated wings and these corrugations vary along the longitudinal axis flattening out towards the wingtip [1]. Bio-inspired designs offer a viable solution for MAVs.

The flight speed of dragonfly varies from 2 m/s to 10 m/s. The Reynolds numbers in a typical MAV flight are in the range of 10^3–10^4 [2, 6]. Surprisingly, the corrugated wing in gliding flight has higher aerodynamic performance in comparison to conventional aerofoil [2]. The thermoregulatory nature of the insect wings makes them more feasible as an aerofoil for which the aerodynamic characteristics of the corrugated wing can be calculated using simple steady-state conditions [3]. The corrugated wing has 'smart properties' adapted to deform automatically in response to the forces they receive. Most of the lift generation in flapping insects takes place due to delayed stall; circulation and wake capture [4].

'Pantala flavescens' forewing reveals a highly corrugated structure where the corrugation varies along the longitudinal axis rendering aerodynamic characteristics as shown in Fig. 1. Dragonfly wings are the complex biological corrugated structure of different pattern where vortices are trapped in the valleys and become stagnate or rotate slowly [3]. Due to varying corrugation angle and peak height, there is no stall observed for the corrugated dragonfly airfoil till 8° angle of attack [5, 7]. Dragonfly wings have a high aspect ratio compared to other small insects which allows them to have better gliding and powerless effort [8]. The typical arrangement of the dragonfly wing cross-section is very different from the low and thin cambered aerofoil due to which there is no spontaneous collapse of lift or massive flow separation [9]. With the increase of angle of attack, the vortex shedding generated in the v-grooves has greater magnitude which reattaches sooner at the progressive corrugation peak resulting in higher aerodynamic performance [10, 11].

(a)   (b)

Fig. 1 **a** Pantala flavescens dragonfly, **b** sketch of dragonfly

2 Geometric Modeling

The different wing models used in this research are: Two corrugated wing models of different corrugation angle and peak height, flat plate and streamlined symmetrical aerofoil of NACA series having maximum thickness 0.15 of chord. The wing-A and wing-B airfoil consist of varying triangular wave at different corrugation angles with varying pitch length and peak height as depicted in Fig. 2 [10].
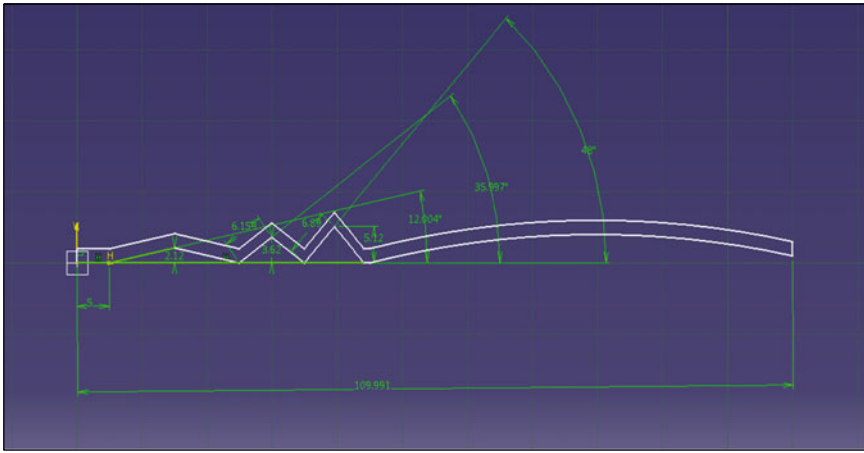
(a)
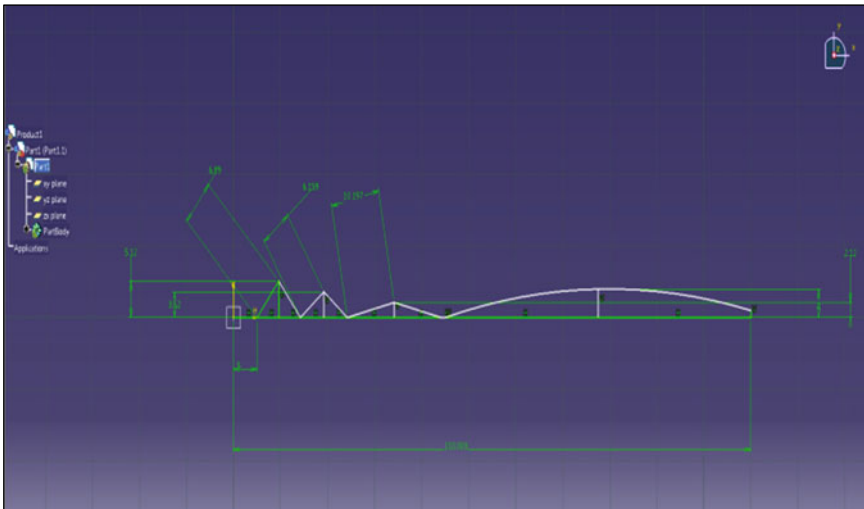
(b)

Fig. 2 **a** Wing–A, **b** Wing-B, **c** streamlined symmetrical aerofoil NACA 0015, **d** flat plate
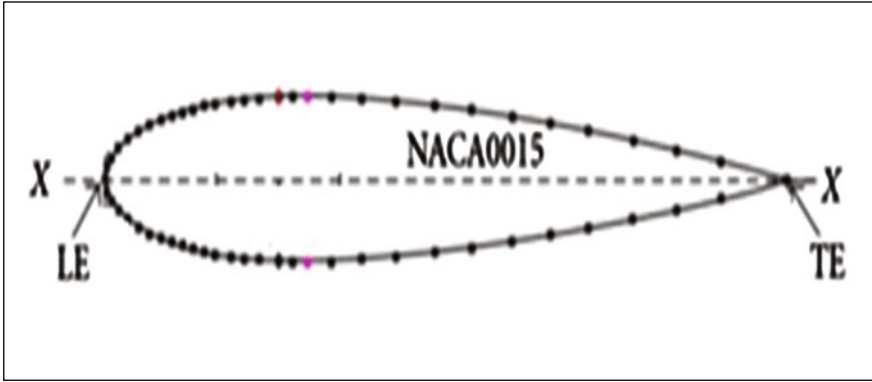
(c)
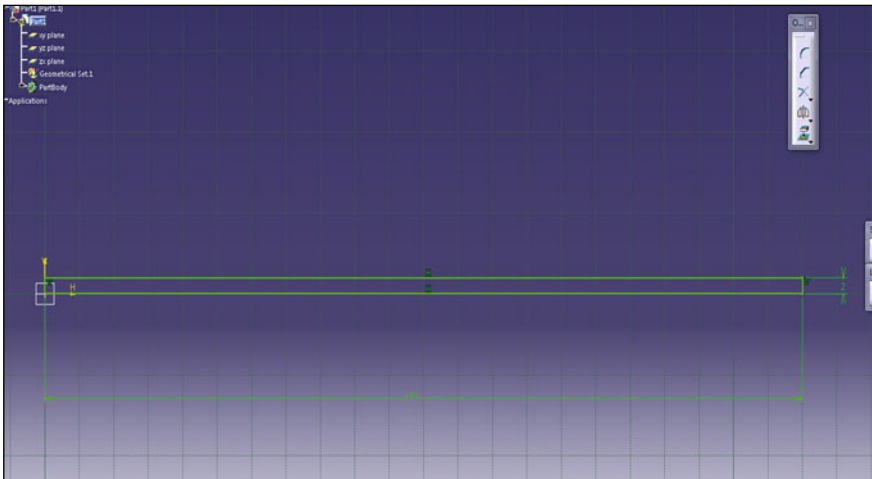
(d)

Fig. 2 (continued)

3 CFD Methodology

The CFD analysis of the four aerofoil models is done in FLUENT-15. The governing equations are:

$$\left(\nabla.\overrightarrow{u_i}\right) = 0 \tag{1}$$

$$\frac{\partial}{\partial x_j}\left(u_i u_j\right) = -\frac{\partial p}{\partial x_i} + \frac{1}{\text{Re}}\frac{\partial^2 u_i}{\partial x_i \partial x_j} \tag{2}$$

The lift and drag coefficient and the ratio is given as

$$C_L = \frac{L}{0.5\rho u_\infty^2 C} \tag{4}$$

$$C_D = \frac{D}{0.5\rho u_\infty^2 C} \tag{5}$$

$$\text{Gliding ratio} = C_L/C_D \tag{6}$$

3.1 Computational Domain and Boundary Conditions

In this study, Ansys Workbench 15.0 is used to create the wing models, meshing and solving the continuity and momentum equations of an incompressible fluid. The domain size is 910 mm × 600 mm and geometric models were meshed using tetrahedral elements of 4.65 million volume cells around the corrugated structure. The inlet velocity in X-direction is set to 2.067 m/s. The Reynolds number is considered as 15,000 and the dynamic viscosity of air is taken as 1.7895×10^{-5} Ns/m^2 (Fig. 3).

3.2 Analysis of Wing-A at Different Angles of Attack (AoA)

As seen in Fig. 4a, the stagnation point lies at the leading edge and maximum at the peak of the corrugated wing. As the flow past over the structure and velocities increase the vortex trapped within the grooves as shown in Fig. 4b, due to adverse pressure gradient the flow reversal takes place and separated flow reattaches sooner towards the trailing edge and leaves smoothly over the surface. There is no apparent stall till 8° angle of attack and lift coefficient goes on increasing. A higher lift-to-drag ratio results in superior climb performance. The turbulence contour as shown in Fig. 4c shows that the vorticity is much higher towards the trailing edge valleys. In this particular configuration as the angle of attack increase the value of the lift coefficient also goes on increasing till stalling angle and flow is getting reattached with the surface due to low-pressure zone created in the valley.

3.3 Analysis of Wing-B at Different Angles of Attack (AoA)

As the corrugation angle is kept in reverse order, i.e., 48°, 36°, and 12° in comparison with Fig. 4 due to which the flow is getting separated at the first peak itself. The velocity is zero at the stagnation point and pressure is maximum at that particular
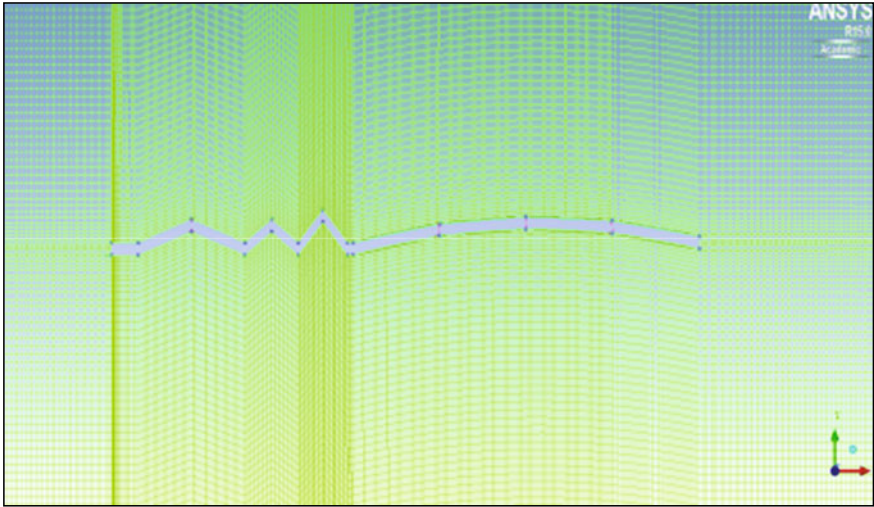
(a)
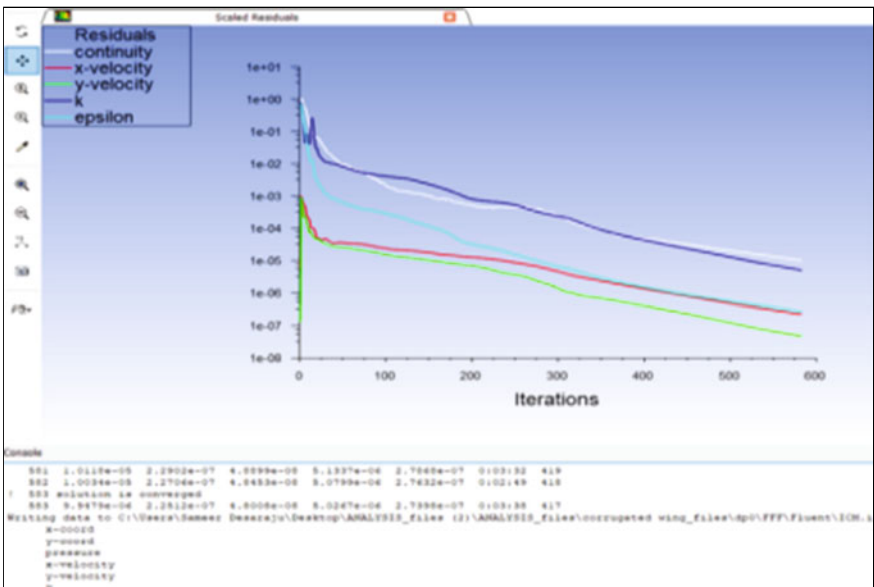
(b)

Fig. 3 **a** Computational mesh of wing-A, **b** mesh convergence model
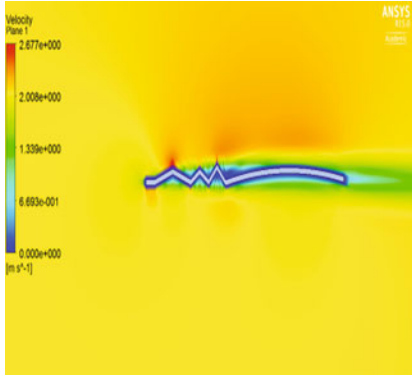
(a)
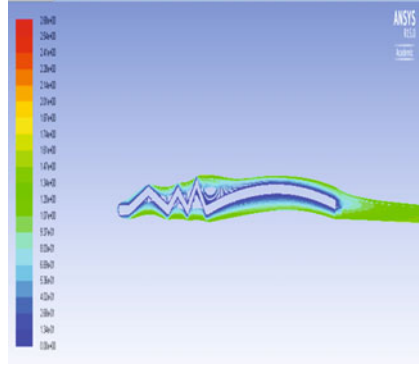
(b)
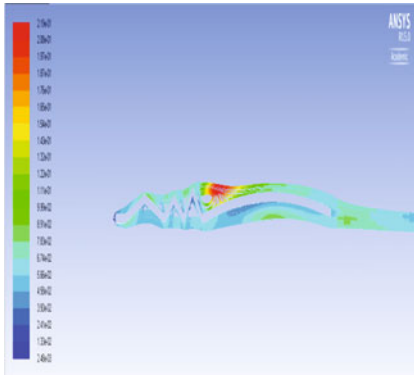
(c)
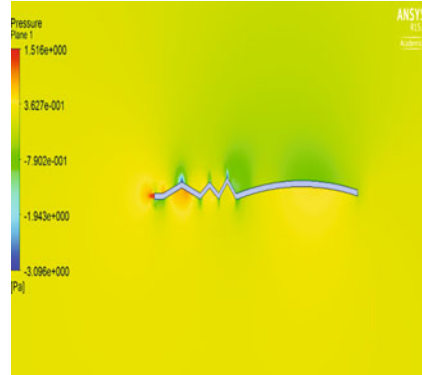
(d)
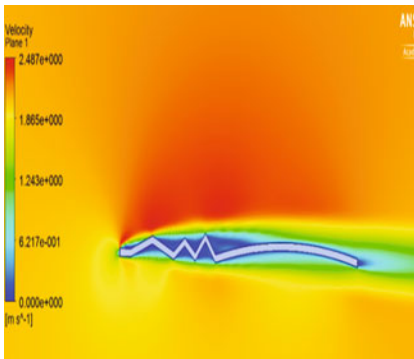
(e)
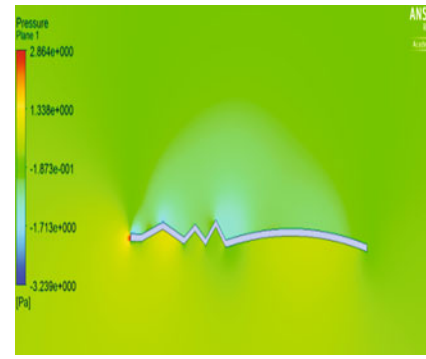
(f)

Fig. 4 Computational results for Wing-A, **a** velocity profile at $\alpha = 0°$, **b** pathline velocity at $\alpha = 0°$, **c** turbulence contour at $\alpha = 0°$, **d** pressure distribution at $\alpha = 0°$, **e** velocity distribution $\alpha = 2°$, **f** pressure distribution at $\alpha = 2°$, **g** velocity distribution at $\alpha = 4°$, **h** pressure distribution at $\alpha = 4°$, **i** velocity distribution at $\alpha = 8°$, **j** pressure distribution at $\alpha = 8°$

(g)

(h)

(i)

(j)
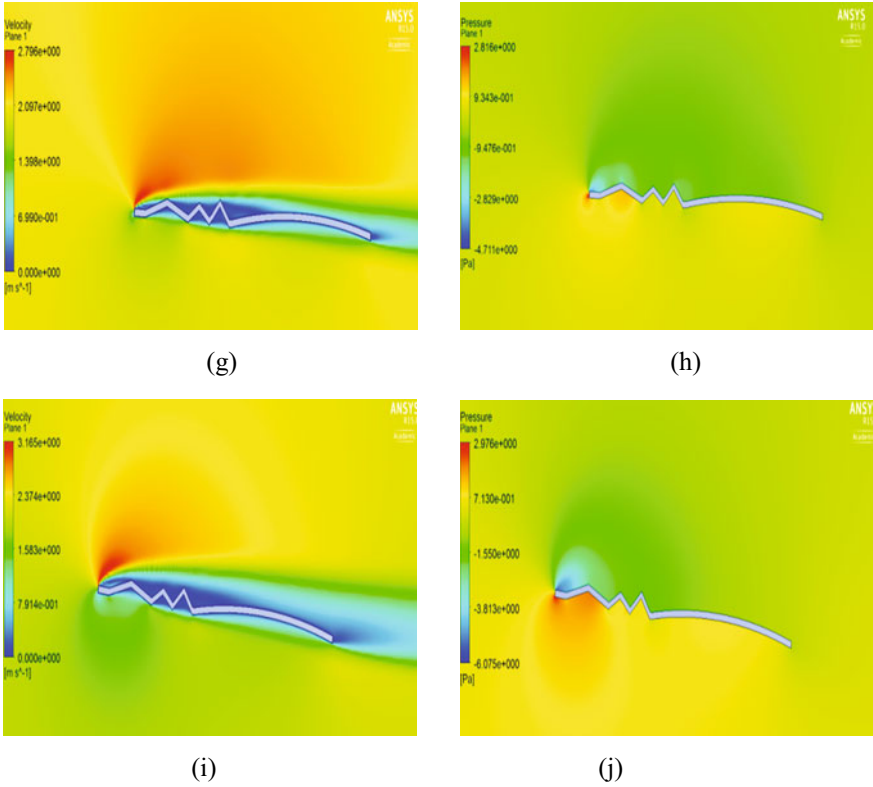
Fig. 4 (continued)

point. As seen in Fig. 4c the corrugation angle is higher at the starting and then its decreasing due to which the flow got separated at the first peak itself creating eddies and vortices lead to an increase in pressure drag. As the angle of attack increases pressure goes on increasing as shown in Fig. 5i.

3.4 Analysis of Flat Plate at Different Angles of Attack

The thickness of the flat plate is considered as 2 mm. The result showed less favorable aerodynamic performance of the plate with an increase in the angle of attack (Fig. 6).

(a)

(b)

(c)

(d)
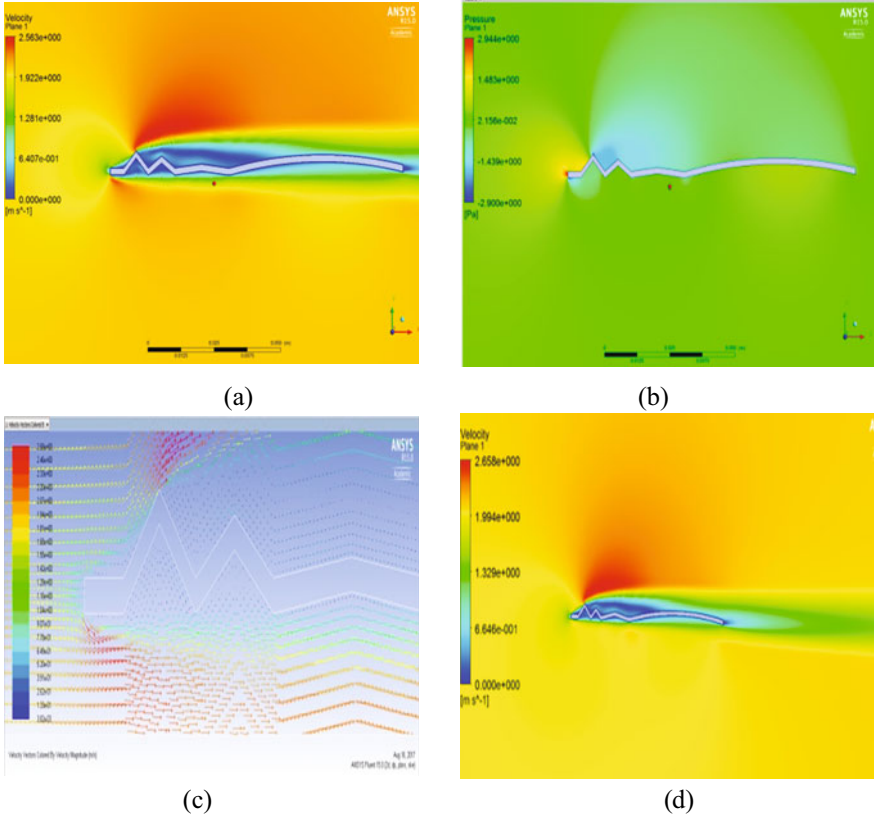
Fig. 5 Computational results for Wing-B, **a** velocity profile at $\alpha = 0°$, **b** pressure profile at $\alpha = 0°$, **c** velocity vector at $\alpha = 0°$, **d** velocity distribution at $\alpha = 2°$, **e** pressure distribution at $\alpha = 2°$, **f** velocity distribution at $\alpha = 4°$, **g** pressure distribution at $\alpha = 4°$, **h** velocity distribution at $\alpha = 8°$, **i** pressure distribution at $\alpha = 8°$

3.5 Analysis of Airfoil NACA 0015 at Different Angle of Attack

The NACA 0015 aerofoil is a streamlined symmetrical aerofoil with maximum thickness of 15% of chord. The NACA 0015 is extensively used for low Reynolds number MAVs and UAVs (Fig. 7).

4 Computational Results Data

The computational results of all the four wings are compared at different angle of attack, i.e., (0°, 2°, 4°, 8°). The value of C_L, C_D and C_L/C_D is calculated for Wing-A,
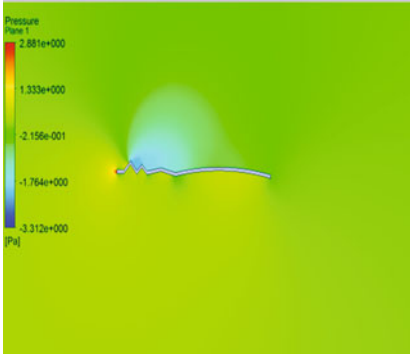
(e)
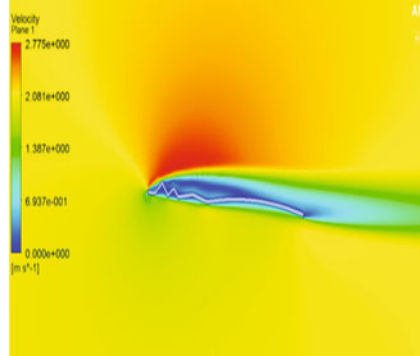
(f)
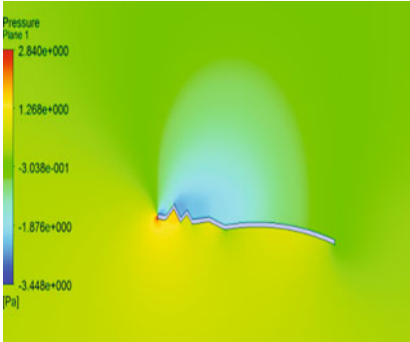
(g)
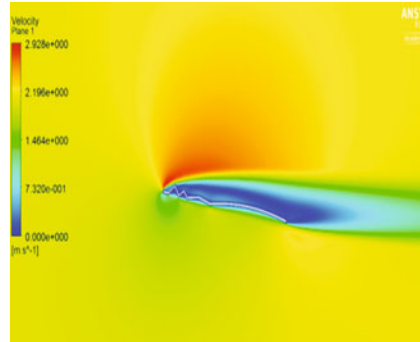
(h)
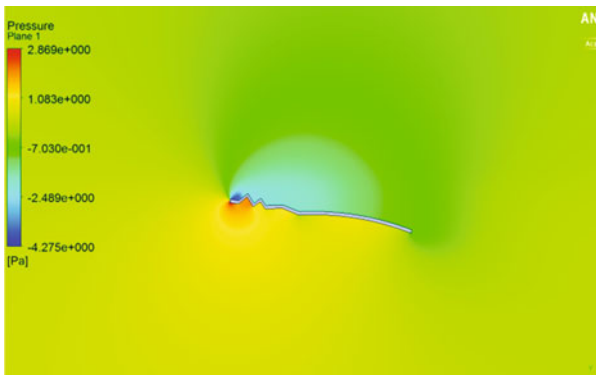
(i)

Fig. 5 (continued)
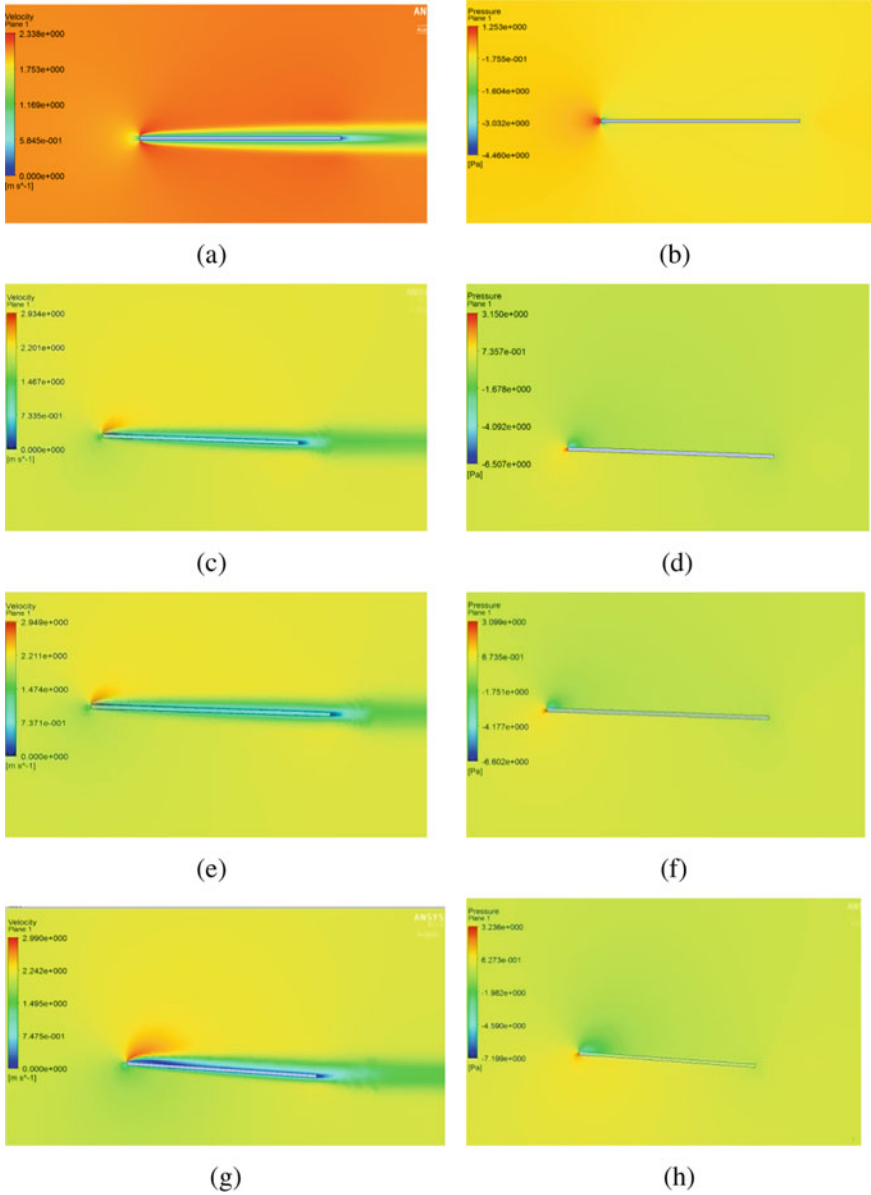
Fig. 6 Computational results for flat plate, **a** velocity profile at $\alpha = 0°$, **b** pressure profile at $\alpha = 0°$, **c** velocity distribution at $\alpha = 2°$, **d** pressure distribution at $\alpha = 2°$, **e** velocity distribution at $\alpha = 4°$, **f** pressure distribution at $\alpha = 4°$, **g** velocity distribution at $\alpha = 8°$, **h** pressure distribution at $\alpha = 8°$
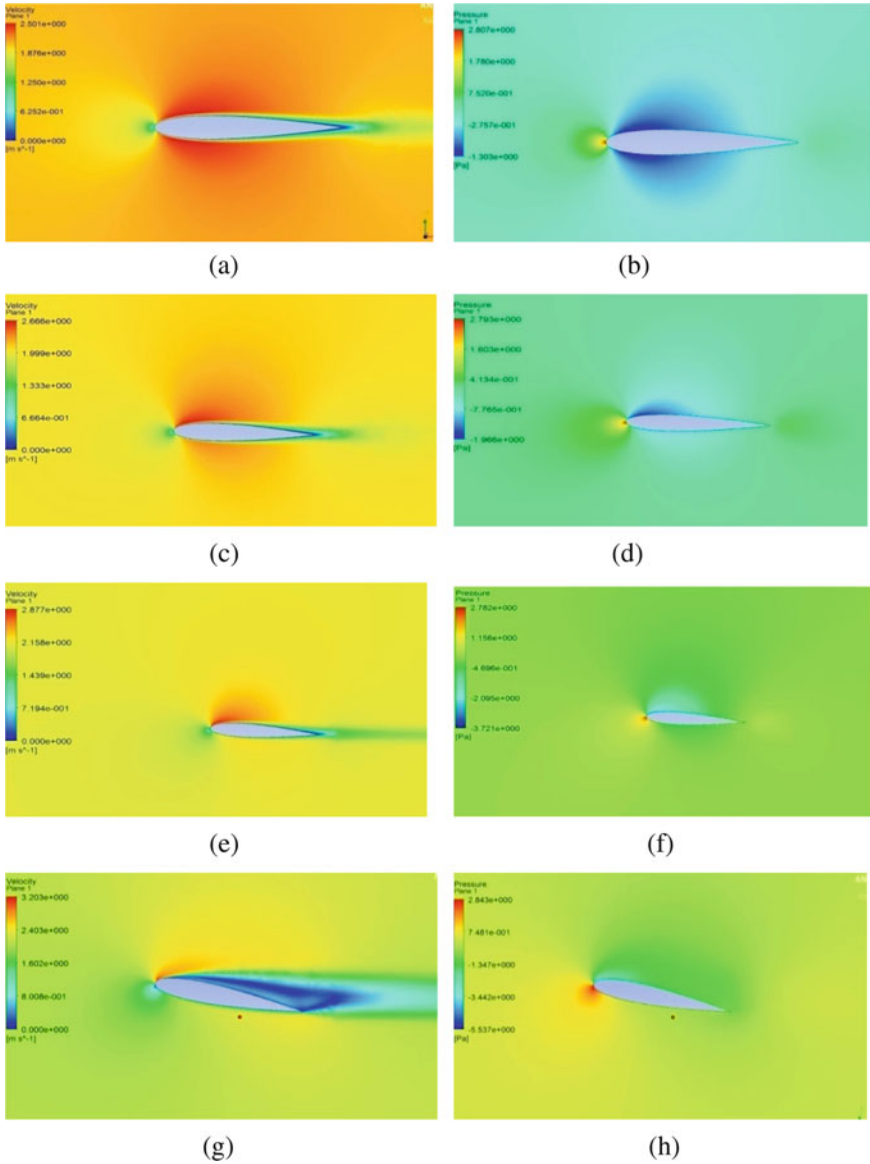
Fig. 7 Computational results for NACA 0015, **a** velocity profile at $\alpha = 0°$, **b** pressure profile at $\alpha = 0°$, **c** velocity distribution at $\alpha = 2°$, **d** pressure distribution at $\alpha = 2°$, **e** velocity distribution at $\alpha = 4°$, **f** pressure distribution at $\alpha = 4°$, **g** velocity distribution at $\alpha = 8°$, **h** pressure distribution at $\alpha = 8°$

Wing-B, Flat plate, and NACA 0015. The results are compared as shown in Table 1 and plotted in terms of graphs.

As seen in Fig. 8a lift coefficient of wing-A is higher compared to wing-B and traditional aerofoil. Even though the drag coefficient of wing-A is increasing with an increase in the angle of attack as seen in Fig. 8b. A higher lift to drag ratio results in superior climb performance but a decline of gliding performance occurs beyond 8° as shown in Fig. 8c. The lift-to-drag ratio of wing-A is better than the profiled counterpart. In contrast to this, the advantages of corrugation are that the flow separates at the tip of the downstream valley and again reattaches at the tip of the upstream of next corrugation.

5 Validation of Computational Results

We have validated the computational results of wing-A, wing-B, flat plate, and symmetrical aerofoil by comparing it with the available result of Kesel [3] (Table 2).

We observe that the results are comparable and even marginally better. The maximum lift coefficient of the Wing-A and Wing-B is 24% more than that of Kesel, model at Re = 10,000.

6 Conclusion

This paper concludes the effect of aerodynamic characteristics on the bio-mimetic dragonfly corrugated wing. Both the corrugated wing performs better at Re = 15.603 $\times 10^3$ compared to a flat plate and conventional aerofoil. The lift-to-drag ratio of wing-A is best at 4° angle of attack and has maximum gliding ratio which is higher compared to all the wing models studied here. The aerodynamic performance of the corrugated pleated aerofoil i.e. Wing-A which is bio-mimicked from 'Pantala flavescens' is giving surprisingly better and consistent results compared to Kesel model (2000) near the radius or subcosta part of the forewing. In due course of this work, it is observed that CFD analysis helped us to give more insight into the flow physics of the dragonfly corrugated wing structure. The formation of separation bubbles due to adverse pressure gradient leads to recirculation zone inside the cavities and the flow reattaches at the upstream of the next corrugation. Finally, we come to the conclusion that corrugation provides better aerodynamic performance, i.e., high lift-to-drag ratio and helps in the reduction of shear drag which is mostly suitable for very lightweight and structurally stable micro-air vehicles and unmanned air vehicles.

Table 1 Comparison of all the four wings

	Wing type	C_L At ($\alpha = 0°, 2°, 4°, 8°$)	C_D At ($\alpha = 0°, 2°, 4°, 8°$)	$\frac{C_L}{C_D}$ At ($\alpha = 0°, 2°, 4°, 8°$)
a	Wing-A	0°—0.2177	0°—0.0670	0°—3.25
		2°—0.4340	2°—0.0696	2°—6.229
		4°—0.6327	4°—0.0797	4°—7.933
		8°—0.9465	8°—0.1232	8°—7.677
b	Wing-B	0°—0.25096	0°—0.0807	0°—3.108
		2°—0.4706	2°—0.0872	2°—5.39
		4°—0.81953	4°—0.1170	4°—6.002
		8°—0.9699	8°—0.1688	8°—4.74
c	Flat plate	0°—0	0°—0.0347	0°—0
		2°—0.2209	2°—0.0522	2°—4.12
		4°—0.2539	4°—0.05565	4°—4.56
		8°—0.4412	8°—0.0683	8°—5.45
d	NACA 0015	0°—0.0011	0°—0.0392	0°—0.028
		2°—0.1674	2°—0.04057	2°—4.12
		4°—0.3310	4°—0.04125	4°—6.025
		8°—0.5347	8°—0.1459	8°—3.029
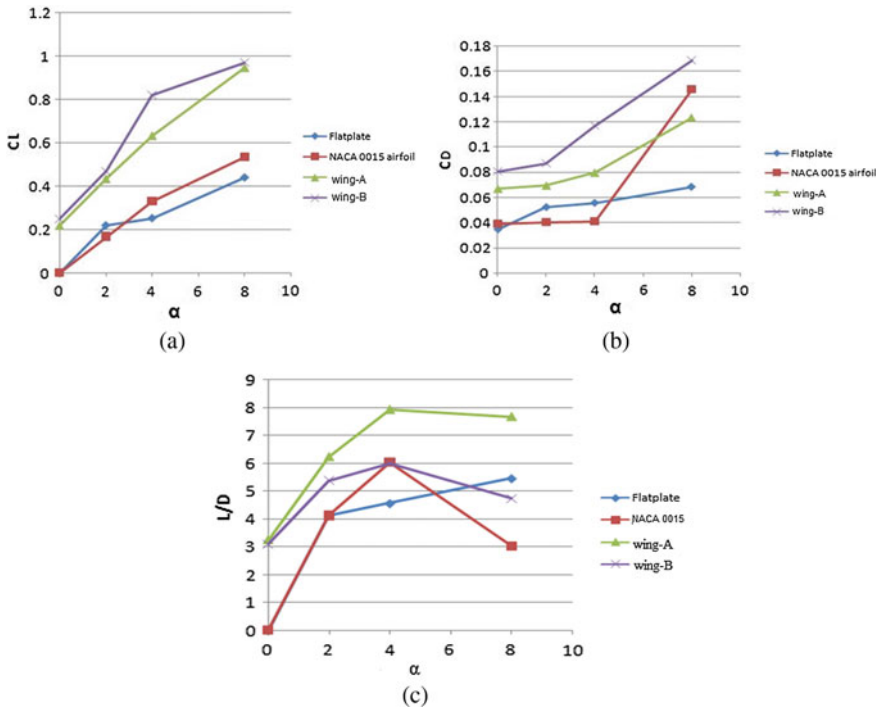
Fig. 8 **a** C_L versus α, **b** C_D versus α, **c** L/D versus α

Table 2 Comparison of results with Kesel [4] model

Performance parameter	Flat plate	NACA 0015	Kesel model (at Re = 10000)	Wing-A	Wing-B
C_{Lmax}	0.441	0.5347	0.698	0.9464	0.9699
C_{Dmax}	0.068	0.1459	0.124	0.1232	0.1688

References

1. Chen YH, Skotes M (2016) Gliding performance of 3-D corrugated dragonfly wing with spanwise variation. J Fluids Struct
2. Tamai M, Wang Z, Rajagopalan G, Hu H (2007) Aerodynamic performance of a corrugated dragonfly airfoil compared with smooth airfoils at low Reynolds number. In: 45th AIAA aerospace science meeting and exhibit
3. Kesel AB (2000) Aerodynamic characteristics of dragonfly wing sections compared with technical aerofoil. J Exp Biol 203:3125–3135
4. Levy DE, Seifert A (2009) Simplified dragonfly airfoil aerodynamics at Reynolds numbers below 8000. Phys Fluids: 071901. https://doi.org/10.1063/1.3166867
5. Okamoto M, Yasuda K, Azuma A (1996) Aerodynamic Characteristics of the wings and the body of a dragonfly. J Exp Biol 199:281–294

6. Kyle H, Lian Y (2010) Numerical Investigation of the aerodynamic and structural characteristics of a corrugated airfoil. 40th Fluid Dyn Conf Exhib. https://doi.org/10.18297/etd/634

7. Rees CJC (1975) Aerodynamic properties of an insect wing section and a smooth aerofoil compared. Nature 258:141–142

8. Vargas A, Mittal R, Dong H (2008) A computational study of the aerodynamic performance of a dragonfly wing section in gliding flight. Bioinspiration Bio-mimetics 3. https://doi.org/10.1088/1748-3182/3/2/026004

9. Levy DE, Seifert A (2009) Simplified dragonfly airfoil aerodynamics at Reynolds number below 8000. Phys Fluids. https://doi.org/10.1063/1.3166867

10. Khan MA, Padhy C, Nandish M, Rita K (2018) Computational analysis of a bio-inspired corrugated aerofoil with varying corrugation angle. J Aeronaut Aerosp Eng 7:1–4. https://doi.org/10.4172/2168-9792.100208

11. Wakeling JM, Ellington CP (1997) Dragonfly flight I. Gliding flight and steady-state aerodynamic forces. J Exp Biol 200:543–556

Computational Analysis of Unsteady MHD Flow of Third Grade Fluid Between Two Infinitely Long Porous Plates

Sukanya Padhi and Itishree Nayak

Abstract In current work the unsteady MHD flow behaviour of a fluid of grade three between two infinitely long flat porous plates is scrutinized where the top lamina is fixed and the lower lamina moves with a velocity which vary with respect to time. Then the non linear p.d.e governing the flow behaviour are reduced to a system of algebraic equations using fully implicit finite difference scheme and numerical solution is obtained using damped-Newton method, which is then coded using MATLAB programming. Influence on velocity with variations in m, α, γ, Re is interpreted through different graphical representation.

Keywords Fluid of grade three · Finite difference methodology · Magneto hydrodynamics · Damped-Newton method

1 Introduction

Due to substantial use of non-Newtonian fluids in the field of industry and engineering, the modern research has captivated the attention of number of researchers in this field. A sole paradigm exhibiting every aspect of non-Newtonian fluids is unobtainable, because of which different non-Newtonian models and constitutive equations have been recommended. Second grade fluid model is one of the simplest model which is capable of predicting normal stress differences, but lacks the shear thinning and thickening property of the non-Newtonian fluids described by Joseph and Fosdick [1] which became a motivation for many researchers like Fosdick and Rajagopal [2], Erdogan [3], Ariel [4, 5], Sahoo and Poncet [6], Nayak et al. [7, 8], Awais [9], Samuel and Falade [10], Hayat et al. [11], Okoya [12].

Recently Carapau and Corria [13] have analysed the numerical solution of a third grade fluid in a tube through a contraction. Using numerical simulation they analysed

S. Padhi (✉) · I. Nayak
Veer Surendra Sai University of Technology, Burla 768018, Odisha, India
e-mail: sukanya.padhi23@gmail.com

I. Nayak
e-mail: itii.nayak@gmail.com

the unsteady flow over a finite set or a tube with performed contraction. Saadatmandi et al. [14] used notion of Chebyshev polynomials and rational Legendre functions for numerical solution. He used the specific features of RLC, ChFD techniques to lessen the computation to a few algebraic equations and made a comparison between the result obtained by this method to results obtained by other techniques which manifested its competent accuracy and rate of convergence. Akinshilo [15] examined the stationary flow and analysed the conduction of heat transfer of fluid of grade three in the porous medium and solution was obtained to the arising non linear differential equation using a domain method. He studied the influence of thermal fluidic parameter on the flow and heat transfer, and discovered the inverse variation of porosity term and velocity distribution, and direct variation of heat and temperature distribution towards the upper plate and revealed its diverse application.

Here, we make an attempt to analyse the unsteady magnetohydrodynamics fluid flow of grade three passing through two infinitely long porous plates. The bottom plate moves instantaneously with a velocity that varies with time in its own plane in the presence of a uniform magnetic field applied transversely. After attaining a numerical solution for the problem, the influence of various physical parameters on momentum boundary layers is audited through several graphs.

The technique used here is a powerful tool to solve strong non-linear complex problem numerically for small as well as large values of elastic parameters and also handle large system of equations with insignificant cost of time which might be difficult to solve analytically. Also derivation of entire problem need not be required for every change of boundary conditions. Due to the benefits of its mathematical features and advantages of its application, the present study is worthwhile and has not been analysed by any above cited researcher to the best of my knowledge.

A brief synopsis of our work is illustrated consecutively. Section 2 is concerned with framing of the problem. Section 3 focuses on the solution strategy. Section 4 reviews influence of several parameters on the velocity field, with magnetic field being present, with the aid of graphical representations followed by the epilogue.

2 Devising the Problem

We choose $x^{'}$ along the lower wall and $y^{'}$ axis perpendicular to it. It is presumed that the walls are unbounded either side of the $x^{'}$ axis, where the top lamina is stationary and the lower plate moves suddenly with a velocity which vary with time.

Since both the plates are porous we represent the velocity of suction/injection by a constant V.

We denote $u^{'}$, $v^{'}$, the constituents of velocity in the domain of flow at any point $(x^{'}, y^{'})$ by

$$u^{'} = u^{'}(y^{'}, t^{'}) , \ v^{'} = V. \tag{1}$$

The cauchy stress P for an incompressible homogeneous and thermodynamically accordant with fluid of grade three by Fosdick and Rajagopal [2] is given as

$$P = -pI + \mu A_1 + \alpha_1 A_2 + \alpha_2 A_1^2 + \beta_3 (tr A_1^2) A_1. \tag{2}$$

where A_1, A_2 are first two tensors by Rivlin and Ericson [16].

μ = Viscosity.

α_1, α_2, β_3 are the elastic parameters of second order and third order respectively.

p = Pressure.

I = Identity Tensor.

Under these physical assumptions and the stress components given in equation(2), the equation of momentum for the fluid of grade three becomes

$$\rho\left(\frac{\partial u'}{\partial t'} + V\frac{\partial u'}{\partial y'}\right) = \mu\frac{\partial^2 u'}{\partial y'^2} + \alpha_1\frac{\partial^3 u'}{\partial y'^2 \partial t'} + 6\beta_3\frac{\partial^2 u'}{\partial y'^2}\frac{\partial u'}{\partial y'}^2 + \alpha_1 V\frac{\partial^3 u'}{\partial y'^3} - \sigma\beta_0^2 u'. \tag{3}$$

Equation (3) is subjected to the subsequent conditions

$$t' = 0 : u' = 0, \quad \forall y',$$
$$t' > 0 : \quad u' = At^n \quad \text{for } y' = 0, \tag{4}$$
$$u' = 0, \quad \text{for } y' = 1.$$

The dimensionless variables and parameters are introduced as:

$u = \frac{u'}{A}$, $y = \frac{y'}{\sqrt{v_1 T}}$, $t = \frac{t'}{T}$

$Re = \frac{V\sqrt{T}}{\sqrt{v_1}}$, $\alpha = \frac{\alpha_1}{\rho v_1 T}$, $\gamma = \frac{6\beta_3 A^2}{\rho v_1^2 T}$, $m^2 = \frac{\sigma\beta_0^2 T}{\rho}$

$v_1 = \frac{\mu}{\rho}$, is the kinematic viscosity, m is Hartmann number,

Re = Reynolds number, α = visco-elastic parameter, γ = third grade elastic parameter, T = Time, σ = conductivity of the medium, β_0 = Magnetic Strength, A = constant, ρ = Density of fluid, μ = dynamic viscosity.

The above notations are employed in the equation of motion (3) to obtain the following dimensionless form

$$\frac{\partial u}{\partial t} + Re\frac{\partial u}{\partial y} = \frac{\partial^2 u}{\partial y^2} + \alpha\frac{\partial^3 u}{\partial y^2 \partial t} + Re\,\alpha\frac{\partial^3 u}{\partial y^3} + \gamma\left(\frac{\partial u}{\partial y}\right)^2\frac{\partial^2 u}{\partial y^2} - m^2 u. \tag{5}$$

along with the subsequent conditions

$$t = 0 : u = 0, \quad \forall\, y,$$
$$t > 0 : u = t^n, \quad \text{for } y = 0, \tag{6}$$
$$u = 0 \quad \text{when } y = 1.$$

3   Solution Strategy

The solution strategy is discussed as follows.

3.1   Finite Difference Method

Equation (5) is solved by implementing the crank-Nickolson type implicit finite difference scheme for space discretization and time discretization with a uniform mesh of space step h and time step k. The obtained difference scheme is represented as

$$d_{1i}^j = u_{i+1}^j - u_{i-1}^j.$$
$$d_{2i}^j = u_{i+1}^j - 2u_i^j + u_{i-1}^j.$$
$$d_{3i}^j = -u_{i-2}^j + 2u_{i-1}^j - 2u_{i+1}^j + u_{i+2}^j.$$
$$d_{3i}^{'j} = -3u_{i-1}^j + 10u_i^j - 12u_{i+1}^j + 6u_{i+2}^j - u_{i+3}^j.$$
$$d_{3i}^{''j} = u_{i-3}^j - 6u_{i-2}^j + 12u_{i-1}^j - 10u_i^j + 3u_{i+1}^j.$$

We use the following notations for difference approximations for the derivatives $(ih, j\triangle t), i = 0(1)N + 1$ and $j = 0(1)M - 1$ as

$$\frac{\partial u}{\partial t} \approx \frac{u_i^{j+1} - u_i^j}{\triangle t}.$$

$$\frac{\partial u}{\partial y} \approx \frac{1}{4h}(d_{1i}^{j+1} + d_{1i}^j).$$

$$\frac{\partial^2 u}{\partial y^2} \approx \frac{1}{2h^2}(d_{2i}^{j+1} + d_{2i}^j).$$

$$\frac{\partial^3 u}{\partial y^3} \approx \frac{1}{2h^3}(d_{3i}^{j+1} + d_{3i}^j) \ , \ i \neq 1, N.$$

$$\frac{\partial^3 u}{\partial y^2 \partial t} \approx \frac{(d_{2i}^{j+1} - d_{2i}^j)}{h^2 \triangle t}. \tag{7}$$

The third order derivative $\frac{\partial^3 u}{\partial y^3}$ is substituted by $\frac{1}{2h^3}(d_{3i}^{'j+1} + d_{3i}^{'j})$ and $\frac{1}{2h^3}(d_{3i}^{''j+1} + d_{3i}^{''j})$ at nodes $(1, j\triangle t), (N, j\triangle t)$ respectively. The fully implicit finite difference scheme used here is unconditionally stable and satisfy second order convergence in time as well as in space.

Using the above differences for the partial derivatives, the governing velocity equation is written as

$$\frac{u_i^{j+1} - u_i^j}{\triangle t} + \frac{\text{Re}}{4h}(d_{1i}^{j+1} + d_{1i}^j) = \frac{1}{2h^2}(d_{2i}^{j+1} + d_{2i}^j) + \frac{\alpha}{h^2 \triangle t}(d_{2i}^{j+1} - d_{2i}^j)$$

$$+\frac{\text{Re}\,\alpha}{2h^3}(d_{3i}^{j+1} + d_{3i}^j) + \frac{\gamma}{32h^4}(d_{1i}^{j+1} + d_{1i}^j)^2(d_{2i}^{j+1} + d_{2i}^j) - m^2\frac{u_i^{j+1} + u_i^j}{2}. \tag{8}$$

along with the subsequent conditions in discretized form are

$$u_i^0 = 0, \quad i = 0(1)N + 1,$$
$$u_0^j = (j\triangle t)^n \quad \text{and,} \tag{9}$$
$$u_{N+1}^j = 0, \quad j = 1(1)M.$$

The approximate choice of M is made according to the algorithm given in Jain [17], where the choice of N is made in such a way, to impose the boundary conditions at infinity so that the modulus value of the difference between the two solutions obtained by presuming the boundary conditions at infinity to hold at $((N + 1)h, j\triangle t)$ and $((N + 2)h, j\triangle t)$ successively, and their difference becomes less than a prescribed error ϵ.

The system of non-linear equations for velocity (8) is solved using above mentioned numerical scheme, where the said method gives the quadratic convergent result for sufficiently good choice of initial solution. For better choice of initial velocity, equation of motion is arranged in tridiagonal form after making the parameter values α, γ, and m to zero in Eq. (8) and solution is obtained using special form of Gaussian elimination method. For applying the damped-Newton method we evaluate the residuals (R_i, where i ranges from 1 to N and the elements in Jacobian matrix $\left(\frac{\partial R_i}{\partial u_j}\right)$, $i = 1(1)N$ and $j = 1(1)M$ that are not equal to zero. A new approximated solution is accepted as $x^{k+1} = \left(x^k + \frac{h}{2^i}\right)$ for that i, where $i = \min\left(j : 0 \leq j \leq j_{\max} \mid \parallel \text{residue}\,(x^k + \frac{h}{2^j})\parallel_2 < \parallel \text{residue}(x^k)\parallel_2\right).$

This ensures that the residual error decreases in each iteration, which guarantees about the convergence of the scheme. The MATLAB coding is verified with the existing result in Conte De Boor [18] and found exact upto fifth decimal place.

4 Results and Discussion

The flow characteristics for the concerned problem is investigated through several graphs depicted in Fig. 1, 2, 3, 4, 5, 6, 7, 8, 9 and 10.

It is observed from Figs. 1 and 2 that the increase in the parametric values of the Hartmann number (m) leads to increase in Lorentz force of the fluid, which causes increase of resistance to the flow velocity and as a result velocity decelerates through

Fig. 1 Influence on velocity
with variations in m when
$\alpha = 3$, $\gamma = 4$, Re = 7
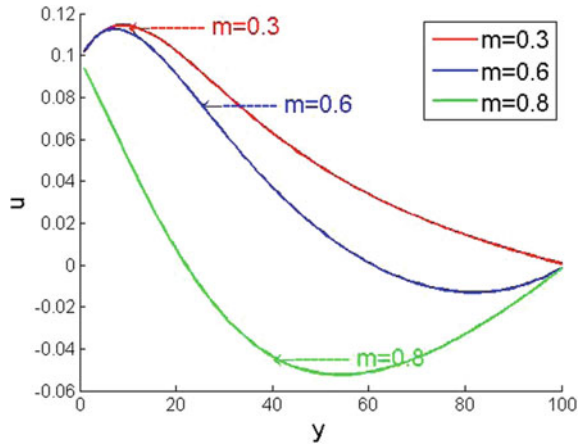
Fig. 2 Influence on velocity
with variations in m when
$\alpha = 3$, $\gamma = 4$, Re = 8
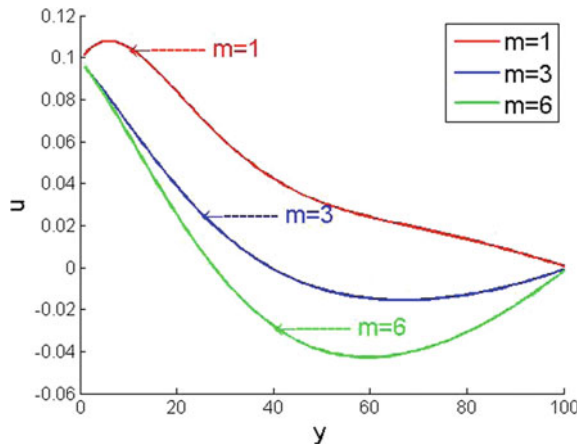
Fig. 3 Influence on velocity
with variations in m when
$\alpha = 0$, $\gamma = 0$, Re = 8
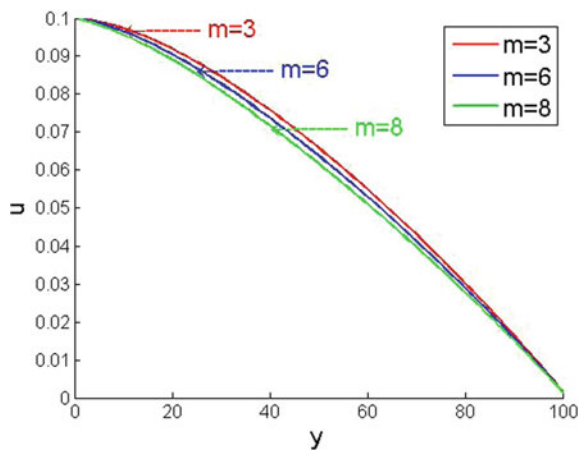
Fig. 4 Influence on velocity with variations in α when $\gamma = 4$, Re = 8, $m = 9$
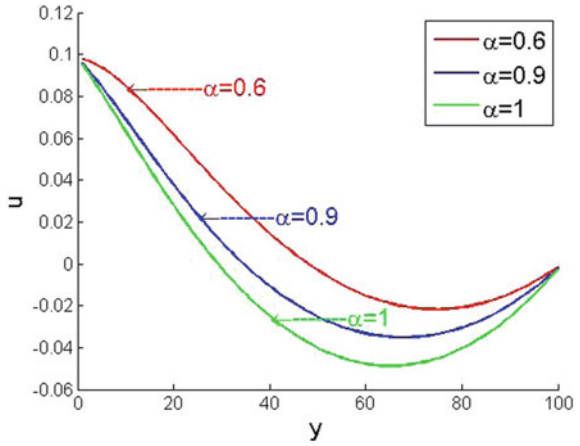
Fig. 5 Influence on velocity with variations in α when, $\gamma = 4$, Re = 8, $m = 8$
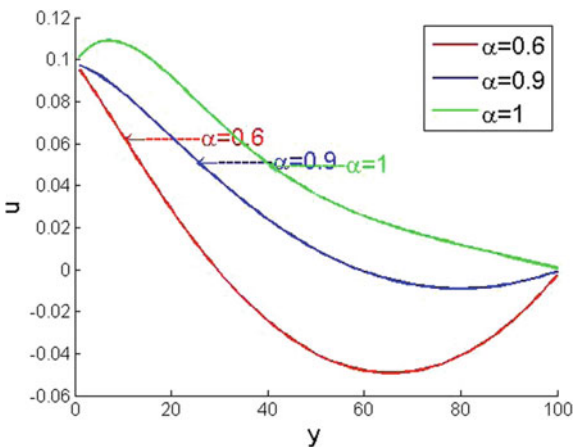
Fig. 6 Influence on velocity with variations in α when $\gamma = 2$, Re = 9, $m = 8$
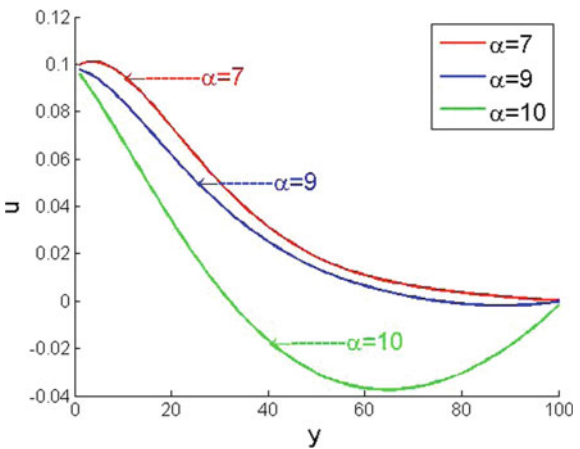
Fig. 7 Influence on velocity with variations in γ when, $\alpha = 3$, Re $= 8$, $m = 8$
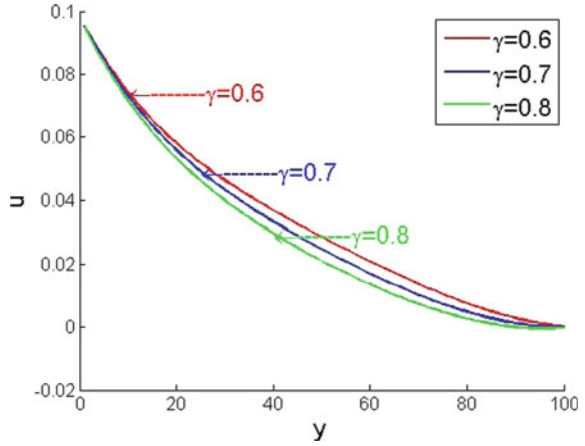
Fig. 8 Influence on velocity with variations in γ when $\alpha = 3$, Re $= 8$, $m = 8$
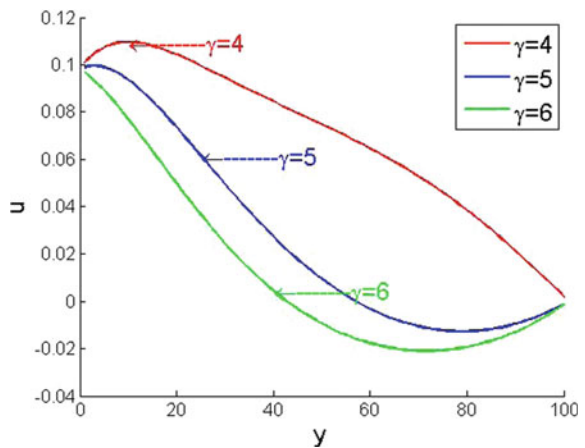
Fig. 9 Influence on velocity with variations in Re when $\alpha = 3$, $\gamma = 3$, $m = 8$
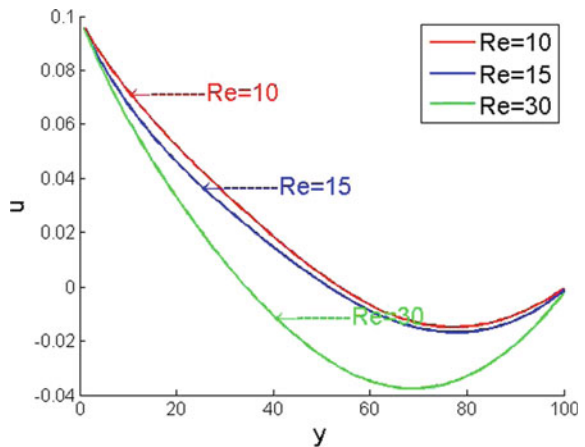
Fig. 10 Effect on velocity
with variations in Re when,
$\alpha = 0.01$, $\gamma = 1$, $m = 7$
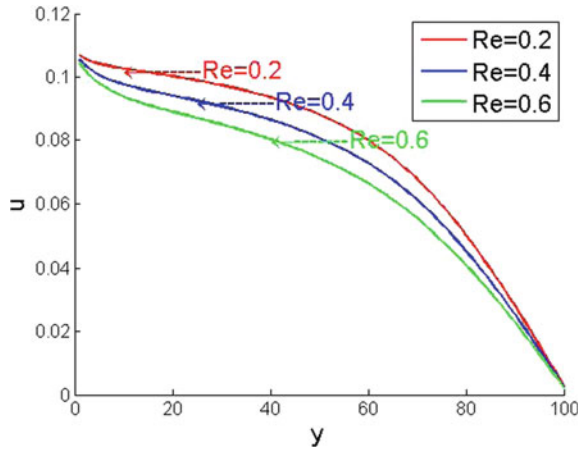
out the flow field. A similar effect from Fig. 3 is also obtained for Newtonian fluid
i.e, when α and γ are considered as zero.

Visco-elasticity of the fluid rises, with increase of the visco-elastic parameter (α)
values, that gives rise to reduction of velocity in the entire flow field, for both less
and bigger values of α. When the values of elastic parameter α is small, the influence
of it on velocity is quite opposite, when damping magnetic strength value is 8 or less.

The effect of non-newtonian parameter γ on the velocity field is seen from Figs. 7
and 8. For large values of γ ($\gamma > 1$), a sudden rise in the velocity field is observed
near the plate, but there is a decrease in velocity through out the domain field, with an
increase in the parametric value γ. For $\gamma < 1$, with other parameters kept fixed, the
decreasing effect on velocity seems to be insignificant near the plates and gradually
becomes noticeable at a considerably far distance from the plate and again appears
to diminish.

Figure 9 shows that velocity profile gradually slows down with increase in the
suction parameter Re. A similar behaviour is observed for smaller values of Re,
shown in Fig. 10, which is obtained by reducing values of elastic parameters as well
as magnetic factor.

5   Conclusion

The present study is concerned with the numerical study of a time- dependent flow of
a third grade fluid passing through two infinite parallelly placed plates is investigated
with the magnetic field being present. Using above mentioned scheme the governing
constitutive equation of motion is converted into system of non-linear algebraic
equations and is solved numerically using highly convergent aforesaid method and
presented graphically.

The principal and noteworthy finding of this investigation is that the increase in Hartmann number m substantially decrease velocity profile, however the fluid shows newtonian or non-Newtonian behaviour. With increase of Re, α, and γ slow down the fluid motion both for large and small values of the parameters. For very small values of visco-elastic parameter α, when we decrease the value of magnetic strength, a reduction in the fluid viscosity is noticed which minimises the resistance to flow velocity, resulting in remarkable gradual enhancement in velocity of the fluid. Hence it is apparent that velocity profile is controlled with proper variations of parameters α and m.

References

1. Joseph DD, Fosdick RL (1973) The free surface on a liquid between cylinders rotating at different speeds. Arch Rat Mech Anal 49:321–401
2. Fosdick RL, Rajagopal KR (1980) Thermodynamics and stability of fluids of third grade. Proc R Soc Lond-A 369:351–377
3. Erdogan ME (1995) Plane surface suddenly set in motion in a non-Newtonian fluid. Acta Mech 108:179–187
4. Ariel PD (2002) On exact solution to flow problems of a second grade fluid through two parallel porous walls. Int J Eng Sci 40:913–941
5. Ariel PD (2003) Flow of third grade fluid through a porous flat channel. Int J Eng Sci 41:1267–1285
6. Sahoo B, Poncet S (2011) Flow and heat transfer of a third grade fluid past an exponentially stretching sheet with partial slip boundary condition. Int J Heat Mass Transf 54:5010–5019
7. Nayak I, Nayak AK, Padhy S (2012) Numerical solution for the flow and heat transfer of a third grade fluid past a porous vertical plate. Adv Stud Theor Phys 6:615–624
8. Nayak I, Padhy S (2012) Unsteady MHD flow analysis of a third grade fluid between two porous plates. J Orissa Math Soc 31:83–96
9. Awais M (2015) Application of numerical inversion of the Laplace transform to unsteady problems of third grade fluid. Appl Math Comput 250:228–234
10. Adesanya SO, Falade JA (2015) Thermodynamics analysis of hydromagnetic third grade fluid through a channel filled with porous medium. Alexandria Eng J 54:615–622
11. Hayat T, Shafiq A, Alsaedi A (2015) MHD antisymmetric flow of a third grade fluid by stretching cylinder. Alexandria Eng J 54:205–212
12. Okoya SS (2016) Flow, Thermal criticality and transition of a reactive third grade fluid in a pipe with Reynolds' model viscosity. J Hydrodyn 28:84–94
13. Carapau F, Corria P (2017) Numerical simulations of third grade fluid flow on a tube through a contraction. Euro J Mech B/ fluids 65:45–53
14. Saadatmandi A, Sanatkar Z, Toufighi SP (2017) Computational methods for solving the steady flow of a third grade fluid in a porous half space. Appl Math Comput 298:133–140
15. Akinshilo AT (2017) Steady flow and heat transfer analysis of third grade fluid with porous medium and heat generation. Int J Eng Sci Technol 20:1602–1609
16. Rivlin RS, Erickson JL (1955) Stress deformation relation for isotropic materials. J Ration Mech Anal 4:323–425
17. Jain MK (1984) Numerical solution of differential equations, 2nd edn. Wiley Eastern Ltd., New Delhi, pp 193–194
18. Conte SD, De Boor C (1980) Elementary numerical analysis an algorithmic approach. McGraw-Hill Inc., New York, pp 219–221

Interaction of Oblique Waves by Base Distortion on a Permeable Bed in an Ice-Covered Sea

S. Khuntia and S. Mohapatra

Abstract The problem involving diffraction of oblique water waves by a little base distortion over permeable sea-bed is investigated in this paper. The top surface of the sea is covered by a lean uniform ice-sheet, where the base of the sea is of permeable type with a little base distortion. The problem is solved by utilizing the Fourier transform method and the 1st-order correction of the reflection and transmission coefficients are calculated. Here, two special kinds of base distortion are taken to calculate the aforesaid coefficients. The values of both reflection and transmission coefficients acquired in this paper are obtained to fulfill the energy identity almost precisely.

Keywords Permeable bed · Ice-sheet · Base distortion · Fourier transform technique · Reflection and transmission coefficients · Energy identity

1 Introduction

The interaction of surface waves with a submerged or floating geometrical obstacle in an ice-covered sea raises exciting mathematical challenges pulling consideration of different types for achieving their valuable solutions [1–4]. Studies of such type of problems have achieved reasonable importance because of several motivations. One of these is to frame the productive reflector of the incident wave energy for saving the coastal zones from the rough sea in the arctic regions. Utilizing the Fourier transform method, Davies [5] investigated the hydrodynamic coefficients in the case of normal incident waves proliferate over the patch of sinusoidal base distortion of a sea. Linton and Chung [6] studied the diffraction of surface water waves by a floating semi-infinite adaptable plate in a sea of finite depth. Gu and Wang [7] considered the scattering problem of water waves involving a permeable sea-bed. Jeng [8] constructed the dispersion relation for the problem of wave-seabed interaction by introducing the complex wave number in the pro-versatile frame.

S. Khuntia (✉) · S. Mohapatra
Veer Surendra Sai University of Technology, Burla 768018, India
e-mail: sagarikakhuntia113@gmail.com

Mohapatra [9, 10] analyzed the problem of water wave scattering by a base distortion on a permeable sea-bed. Utilizing the Green's function method and Fourier transform method, Mohapatra and Sarangi [11] studied the surface water wave scattering by a permeable channel-bed with base distortion. Mohapatra [10] has studied the problem of water wave scattering by a base distortion on a permeable sea bed by using Green's function technique. However, in this paper we have studied the same problem by utilizing the Fourier transform technique.

In this article, we consider the diffraction of oblique waves by a small base distortion over a permeable surface of the sea, where the top of the sea is covered by a lean regular ice-sheet. We solve the problem by utilizing the Fourier transform method and then the 1st-order correction of reflection as well as transmission coefficients are calculated. Here, two special kinds of base distortion are taken to calculate the aforesaid coefficients.

2 Formulation of the Physical Problem

Let us assume an inviscid and incompressible fluid, where the top of the sea is cover up by a lean regular ice-plate and the base surface is of permeable type with a little distortion. The sea bed is represented by $y = d + \kappa\tau(x)$, where κ measures the smallness of the base distortion and $\tau(x)$ represents the shape of the distortion and $\tau(x) \to 0$ as $|x| \to \infty$. The fluid motion is of irrotational type and time harmonic with angular frequency ω. Considering the linear water wave hypothesis, the potential function can be represented as:

$$\Psi(x, y, z, t) = \mathcal{R}e[\mathrm{e}^{-i\omega t} \, \varphi(x, y)\mathrm{e}^{i\nu z}], \quad -\infty < x, z < \infty, \quad y \in [0, d + \kappa\tau(x)], \quad (1)$$

where ν denotes the z-component of the occurring field wave number and φ follows the Helmholtz equation:

$$(\nabla^2 - \nu^2)\varphi = 0, \quad -\infty < x < \infty, \quad 0 \in (0, d + \kappa\tau(x)), \quad (2)$$

where $\nabla^2 = \frac{\partial^2}{\partial x^2} + \frac{\partial^2}{\partial y^2}$. The linear conditions near the ice-plate andon the permeable bottom surface are, respectively, as

$$K\varphi + \left[D\left(\frac{\partial^2}{\partial x^2} - \nu^2\right)^2 + 1 - \epsilon K\right]\varphi_y = 0, \quad |x| < \infty, \quad y = 0, \quad (3)$$

and

$$\varphi_n - P\varphi = 0, \quad |x| < \infty, \quad y = d + \kappa\tau(x). \quad (4)$$

where D is the flexural rigidity parameter of the ice-plate, $K = \omega^2/\widetilde{g}$; $\widetilde{g}$ is the gravitational acceleration, $\partial/\partial n$ denotes the normal derivative to the base surface, P is the permeability parameter.

The asymptotic behavior of φ is

$$\varphi = \begin{cases} (e^{iu_0x\cos\theta} + Re^{-iu_0x\cos\theta})g(u_0, y), & x \to -\infty, \\ Te^{iu_0x\cos\theta}g(u_0, y), & x \to \infty, \end{cases} \tag{5}$$

where R is the reflection coefficient, T is the transmission coefficients and

$$g(u_0, y) = \frac{\cosh u_0(d-y) - (P/u_0)\sinh u_0(d-y)}{\cosh u_0 d - (P/u_0)\sinh u_0 d}, \quad |x| < \infty, \ 0 < y < d, \tag{6}$$

where, $\cosh u_0 d - (P/u_0)\sinh u_0 d \neq 0$ and u_0 follows the dispersion equation:

$$\mathbf{F}(u) \equiv [(Du^4 + 1 - \epsilon K)u + (P/u)K]\tanh ud - [(Du^4 + 1 - \epsilon K)P + K] = 0. \tag{7}$$

For any non-zero values of K, there exists two non-zero roots (say, u_0 and $-u_0$) of Eq. (7), which represent the wave numbers of propagating waves; and a set of imaginary roots $\pm iu_n$, $n = 1(1)n$ represents the wave numbers of evanescent waves, where u_n's are satisfying the following condition:

$$[(Du_n^4 + 1 - \epsilon K)u_n - (P/u_n)K]\tan u_n d + [(Du_n^4 + 1 - \epsilon K)P + K] = 0. \tag{8}$$

The positive root of Eq. (7) is the wave number of the waves traveling in the positive horizontal direction, where the negative root being the wave number traveling in the negative of x-direction.

Assume that an oblique incident wave train proliferates from the negative horizontal direction is of the form:

$$\varphi_0(x, y) = e^{iu_0x\cos\theta}\, g(u_0, y), \tag{9}$$

Considering κ as a small parameter of base distortion of the permeable sea-bed and omitting $O(\kappa^2)$ term, then Eq. (4) can be illustrated in the following form:

$$\varphi_y - \kappa\left\{\frac{d}{dx}[\tau(x)\varphi_x(x, d)] - \tau(x)\nu^2\varphi(x, d)\right\} \tag{10}$$

$$- P\left[\varphi + \kappa\tau(x)\varphi_y\right] + O(\kappa^2) = 0 \quad \text{on } y = d.$$

Here, the perturbation analysis is used to reduce the entire fluid domain $0 \leq y \leq d + \kappa\tau(x)$, $|x| < \infty$ to $0 \leq y \leq d$, $|x| < \infty$.

3   Solution of the Problem

Suppose an oblique proliferating wave train proliferates over the base distortion of the permeable sea-bed. If the base of the fluid has no distortion, then only the transmitted waves propagate in the fluid region. This, along with Eq. (10), indicate that φ, R and T can be represented in terms κ as:

$$\left.\begin{array}{l} \varphi = \varphi_0 + \kappa\,\varphi_1 + O(\kappa^2), \\ R = \kappa\,R_1 + O(\kappa^2), \\ T = 1 + \kappa\,T_1 + O(\kappa^2), \end{array}\right\} \tag{11}$$

where φ_0 is mentioned in Eq. (9). Employing Eq. (11) in Eqs. (2), (3), (5) and (10), andthen comparing the 1st-order terms of κ on both sides of these equations, we get

$$(\nabla^2_{x,y} - \nu^2)\varphi_1 = 0, \quad |x| < \infty, \ y \in (0,d), \tag{12}$$

$$\left[D\left(\frac{\partial^2}{\partial x^2} - \nu^2\right)^2 + 1 - \epsilon K\right]\varphi_{1y} + K\varphi_1 = 0 \quad \text{on} \ |x| < \infty, \ y = 0, \tag{13}$$

$$\varphi_{1y} - P\varphi_1 = \frac{iu_0 \cos\theta \frac{d}{dx}[\tau(x)e^{iu_0 x \cos\theta}] + (P^2 - u_0^2 \sin^2\theta)\tau(x)\,e^{iu_0 x \cos\theta}}{\cosh u_0 d - (P/u_0)\sinh u_0 d}$$

$$\equiv V(x, u_0) \qquad\qquad \text{on} \ -\infty < x < \infty, \ y = d, \tag{14}$$

$$\varphi_1(x,y) = \begin{cases} R_1 e^{-iu_0 x \cos\theta} g(u_0, y), \ x \to -\infty, \\ T_1 e^{iu_0 x \cos\theta} g(u_0, y), \quad x \to \infty. \end{cases} \tag{15}$$

4   Introduction of Fourier's Transform Technique

Assume the Fourier transform of $\varphi(x, y)$ with respect to x is defined as

$$\overline{\varphi_1}(\zeta, y) = \int\limits_{-\infty}^{\infty} \varphi_1(x, y)e^{-i\zeta x}dx. \tag{16}$$

Taking the Fourier transform to Eqs. (12)–(14), we acquire

$$\overline{\varphi_1}_{yy} - \widehat{\zeta}^2\overline{\varphi_1} = 0 \quad \text{on} \ 0 < y < d, \tag{17}$$

$$(D\widehat{\zeta}^4 + 1 - \epsilon K)\overline{\varphi_1}_y + K\overline{\varphi_1} = 0 \quad \text{on} \ y = 0, \tag{18}$$

$$\overline{\varphi_1}_y - P\overline{\varphi_1} = \overline{V}(\zeta, u_0) \quad \text{on} \ y = d, \tag{19}$$

where $\overline{\varphi_{1yy}}$, $\overline{\varphi_{1y}}$, $\overline{\varphi_1}$ and $\overline{V}(\zeta, u_0)$ are the Fourier transforms of φ_{1yy}, φ_{1y}, φ_1 and $V(x, u_0)$, respectively and $\widehat{\zeta}^2 = \zeta^2 + \nu^2$. The solution of $\overline{\varphi_1}(\zeta, y)$ is

$$\overline{\varphi_1}(\zeta, y) = \frac{(D\widehat{\zeta}^4 + 1 - \epsilon K)\overline{V}(\zeta, u_0)Z(\widehat{\zeta}) + \mathbf{F}(\widehat{\zeta})\overline{V}(\zeta, u_0) \sinh \widehat{\zeta} y}{\mathbf{F}(\widehat{\zeta})(\widehat{\zeta} \cosh \widehat{\zeta} d - P \sinh \widehat{\zeta} d)}, \qquad (20)$$

where

$$Z(\widehat{\zeta}) = \widehat{\zeta} \cosh \widehat{\zeta}(d - y) - P \sinh \widehat{\zeta}(d - y),$$

$$\overline{V}(\zeta, u_0) = \frac{(P^2 - u_0^2 \sin^2 \theta - u_0 \zeta \cos^2 \theta)}{\cos u_0 d - (P/u_0) \sinh u_0 d} \int\limits_{-\infty}^{\infty} \tau(x)e^{i(u_0 - \zeta)x \cos \theta} dx, \qquad (21)$$

The inverse Fourier transform of $\overline{\varphi_1}(\zeta, y)$ is defined by

$$\varphi_1(x, y) = \frac{1}{2\pi} \int\limits_{-\infty}^{\infty} \overline{\varphi_1}(\zeta, y)e^{i\zeta x} d\zeta. \qquad (22)$$

Taking the inverse Fourier transform of the Eq. (20), the solution $\varphi_1(x, y)$ is obtained as:

$$\varphi_1(x, y) = \frac{1}{2\pi} \int\limits_{-\infty}^{\infty} \frac{(D\widehat{\zeta}^4 + 1 - \epsilon K)[\widehat{\zeta} \cosh \widehat{\zeta}(d-y) - P \sinh \widehat{\zeta}(d-y)]}{\mathbf{F}(\widehat{\zeta})[\widehat{\zeta} \cosh \widehat{\zeta} d + P \sinh \widehat{\zeta} d][\cosh u_0 d - (P/u_0) \sinh u_0 d]}$$

$$\times \left[\overline{V}(\zeta, u_0)e^{i\zeta x} + \overline{V}(-\zeta, u_0)e^{-i\zeta x} \right] d\zeta, \qquad (23)$$

Here, $\mathbf{F}(\widehat{\zeta})$ has one positive root at $\widehat{\zeta} = u_0$. Therefore, the integrand given in Eq. (23) is having a pole at $\zeta = u_0 \cos \theta$. Hence, the path of the integral is drawn under the pole at $\zeta = u_0 \cos \theta$.

To obtain the transmission coefficient T_1, we take x tends to ∞ in Eq. (23) and then comparing with Eq. (15), we obtain

$$T_1 = \frac{i(Du_0^4 + 1 - \epsilon K)(P^2 - u_0^2) \sec \theta}{\mathbf{F}'(u_0)[\cosh u_0 d - (P/u_0) \sinh u_0 d]} \int\limits_{-\infty}^{\infty} \tau(x) dx, \qquad (24)$$

Similarly, to obtain the value of R_1, we take x tends to $-\infty$, in Eq. (23) and then comparing with Eq. (15), we acquire

$$R_1 = \frac{i(Du_0^4 + 1 - \epsilon K)(P^2 + u_0^2 \cos 2\theta) \sec \theta}{\mathbf{F}'(u_0)[\cosh u_0 d - (P/u_0) \sinh u_0 d]} \int\limits_{-\infty}^{\infty} \tau(x) e^{2iu_0 x \cos \theta}. \qquad (25)$$

5 Special Kinds of Base Profile

In this section, we consider two special kinds of base distortion (exponentially damped base and sinusoidal base) to demonstrate the analytical results [12]. These forms of the base distortion have the capability to reverse occurring wave energy which has significant connections in respect of seacoast conservation as well as feasible swell development, when the sea-base is erodible.

5.1 Example-I

Assuming the base distortion of the sea-bed which is of the forms

$$\tau(x) = c_0 e^{-b|x|}, \quad (b > 0), \qquad -\infty < x < \infty. \qquad (26)$$

The crest of the altitude locates at $(0, c_0)$ and it reduces exponentially on each side. Substituting $\tau(x)$ from the above equation into Eq. (24), we acquire T_1 as:

$$T_1 = \frac{2ic_0(Du_0^4 + 1 - \epsilon K)(P^2 - u_0^2) \sec \theta}{\mathbf{F}'(u_0)b[\cosh u_0 d - (P/u_0) \sinh u_0 d]}. \qquad (27)$$

Similarly, substituting $\tau(x)$ from Eq. (26) into Eq. (25), we obtain R_1 as follows:

$$R_1 = \frac{2ic_0 b(Du_0^4 + 1 - \epsilon K)(P^2 + u_0^2 \cos 2\theta) \sec \theta}{(b^2 + 4u_0^2 \cos^2 \theta)\mathbf{F}'(u_0)[\cosh u_0 d - (P/u_0) \sinh u_0 d]}. \qquad (28)$$

5.2 Example-II

Suppose a frame of sinusoidal ripples on a permeable sea-bed with amplitude a on an otherwise flat permeable bed is of the form:

$$\tau(x) = \begin{cases} a \sin \gamma x, & -n\pi/\gamma \le x \le m\pi/\gamma, \\ 0 & \text{otherwise,} \end{cases} \qquad (29)$$

where $m, n \in \mathrm{N}$ and γ denotes the wave-number of the ripples in $[-n\pi/\gamma, m\pi/\gamma]$. Using $\tau(x)$ from Eq. (29) into Eq. (25) and (24), we acquire R_1 and T_1, are as follows:

$$R_1 = \frac{ia\gamma(Du_0^4 + 1 - \epsilon K)(P^2 - u_0^2 \cos 2\theta) \sec \theta}{\mathbf{F}'(u_0)[\cosh u_0 d - (P/u_0) \sinh u_0 d]}$$

$$\times \left[\frac{(-1)^n e^{2iu_0 \cos \theta(-n\pi/\gamma)} - (-1)^m e^{2iu_0 \cos \theta(m\pi/\gamma)}}{\gamma^2 - 4u_0^2 \cos^2 \theta} \right], \tag{30}$$

$$T_1 = \frac{ia(Du_0^4 + 1 - \epsilon K)(P^2 - u_0^2) \sec \theta}{\mathbf{F}'(u_0)[\cosh u_0 d - (P/u_0) \sinh u_0 d]} \times \left[\frac{(-1)^n - (-1)^m}{\gamma} \right]. \tag{31}$$

From Eq. (30), we have seen when $\gamma = u_0 \cos \theta$, the theory indicates that the resonant interaction of surface water waves and the permeable base surface. Therefore, near resonance, $(u_0 \approx (\gamma \sec \theta)/2)$, the limiting value of R_1 takes the value

$$R_1 \approx -\frac{\gamma ia(m+n)(Du_0^4 + 1 - \epsilon K)(P^2 + u_0^2 \cos 2\theta)}{4u_0 \mathbf{F}'(u_0) \cos^2 \theta[\cosh u_0 d - (P/u_0) \sinh u_0 d]}. \tag{32}$$

Note that, R_1 is a constant times of sum of ripples of the sinusoidal bed $(m+n)/2$ and R_1 raises with increase in ripple numbers m and n. Thus, R_1 becomes unbounded for a large value of $(m+n)/2$ which is a contradiction that R_1 is a small quantity.

In water wave scattering problem, energy identity has an important aspect for checking the solution of such mixed BVP. When oblique incident wave train proliferates over a permeable bed with the presence of floating ice-plate, the energy identity which involving R and T, satisfies the following relation:

$$|R|^2 + |T|^2 = 1. \tag{33}$$

6 Numerical Results

In the previous section, the numerical estimations are demonstrated for R_1 and T_1, related to two special kinds of base profile: the exponentially damped distortion and the sinusoidal ripple bed. First, we consider the case of exponentially damped distortion. The value of R_1 given in Eq. (28) is computed numerically. In Fig. 1, $|R_1|$ depicted against $K c_0$ for different angle of incidence whereas the various parameters are fixed as $d/c_0 = 5$, $D/c_0^4 = 1$, $\epsilon/c_0 = 0.01$, $c_0 b = 1$ and $P c_0 = 0.01$. From this figure, it has been noticed that the absolute value of R_1 is decreasing with raise in the angle of incidence. This shows that, for the normal case (i.e., $\theta = 0$), the absolute value of R_1 is maximum. The reflection coefficient $|R_1|$ is plotted in Fig. 2 for various permeability parameters $P c_0$. Here, we assume $D/c_0 = 1$, $\epsilon/c_0 = 0.01$ and $\theta = \pi/6$. It is seen from this figure that the absolute value of R_1 increases as $P c_0$ increases. That means, the reflected energy is quite conscious to the changes of permeability parameter of the permeable sea-bed. In Fig. 3, $|R_1|$ is plotted against $K c_0$ for various sets of ice parameters, whereas we fixed $\theta = \pi/6$ and $P c_0 = 0.01$. It has been shown from this figure that the absolute value of R_1 raises with the raise of ice parameters.
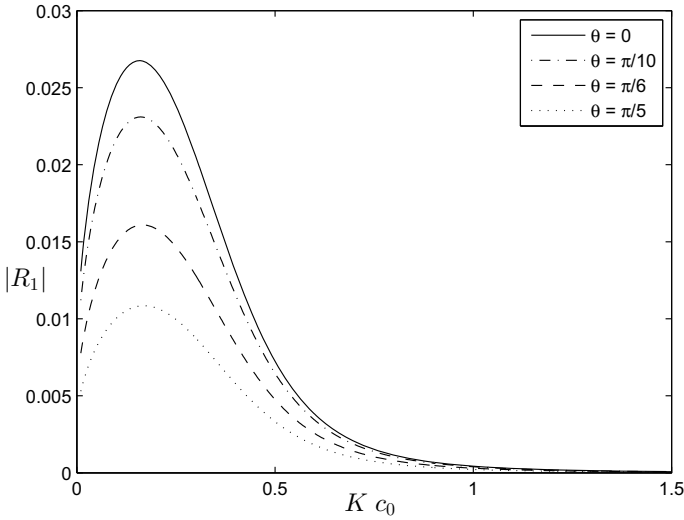
Fig. 1 R_1 plotted against Kc_0 (for exponentially damped bed)
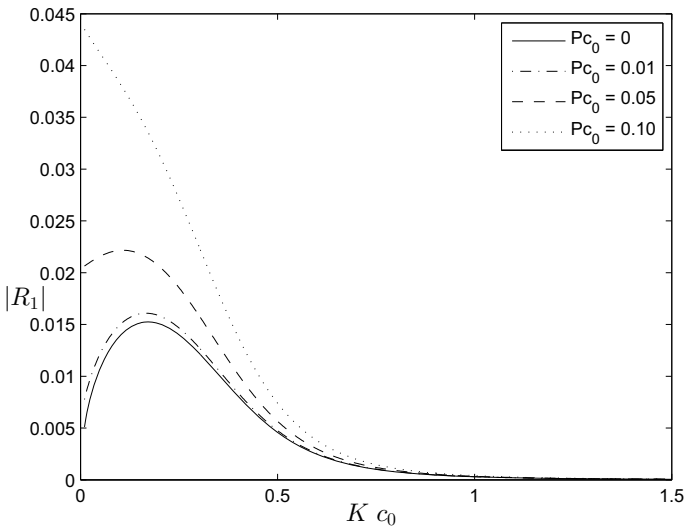
Fig. 2 R_1 plotted against Kc_0 (for exponentially damped bed)

Moreover, $|R_1|$ is quite insensitive and the surface wave is not much disturbed to the changes in the ice parameter.

Next, we consider the case of sinusoidal ripple bed. The reflection coefficient $|R_1|$ as given in Eq. (30) is computed numerically and is depicted against Kd. In Fig. 4, $|R_1|$ is depicted for different angle of incidence with other parameters are taken as $a/d = 0.1, \gamma d = 1, m = 2, n = 3, Pd = 0.1, D/d^4 = 1$ and $\epsilon/d = 0.01$. It is most
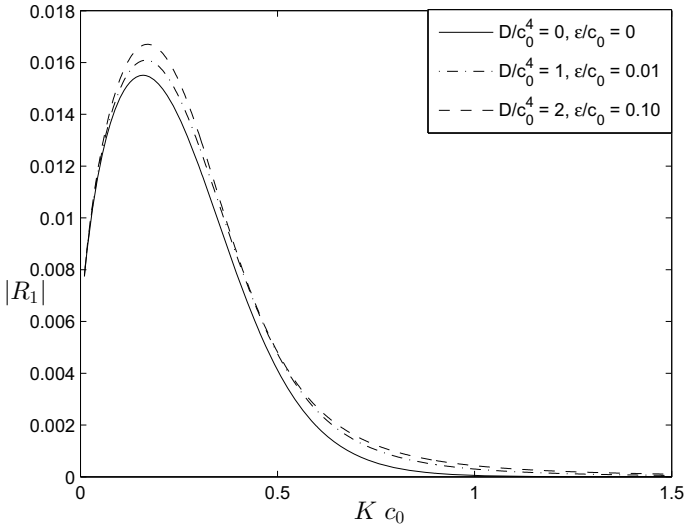
Fig. 3 R_1 plotted against $K c_0$ (for exponentially damped bed)
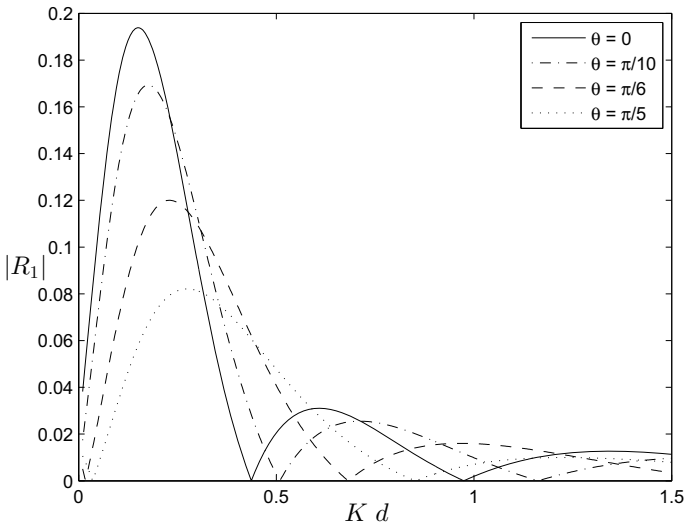
Fig. 4 R_1 plotted against $K d$ (for sinusoidal bed)

evident that the absolute value of R_1 raises, whenever the incidence angle reduces. When $\theta = \pi/4$, the value of $|R_1|$ is much less as compared to the other angles of oblique incidence. The utmost value of $|R_1|$ is maximum for the normal incidence case.
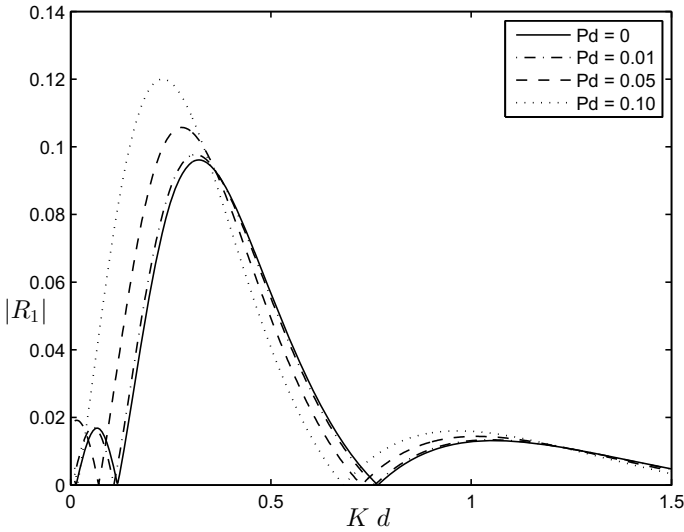
Fig. 5 R_1 plotted against Kd (for sinusoidal bed)
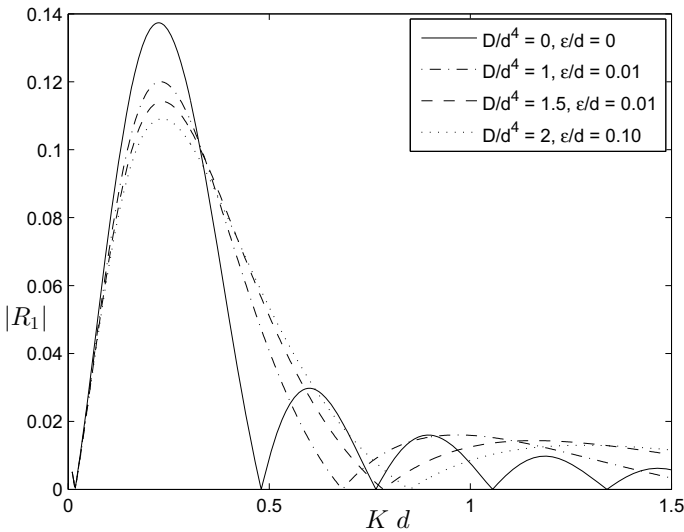
Fig. 6 R_1 plotted against Kd (for sinusoidal bed)

In Fig. 5, $|R_1|$ is depicted for different permeability parameters. Here, we fixed $\theta = \pi/6, \gamma d = 1, m = 2$ and $n = 3$. From this figure, it is cleared that the absolute value of R_1 increases when the permeability parameter increases. That means, the reflected energy is sensitive to the change of the permeability parameter of the permeable seabed. In Fig. 6, the peak value of $|R_1|$ is plotted for different sets of ice parameters.

Table 1 Variation of $|R|$, $|T|$ and $|R|^2 + |T|^2$ for different estimations of Kc_0 (Example-I)

Kc_0	k_0c_0	$|R|$	$|T|$	$|R|^2 + |T|^2$
0.02	0.1650	0.000428985	1.000329622	1.000659536
0.22	0.2848	0.000293904	1.000477813	1.000955941
0.42	0.4390	0.000111629	1.000261740	1.000523560
0.62	0.5899	0.000026655	1.000082428	1.000164863
0.82	0.7053	0.000007332	1.000028344	1.000056689
1.02	0.7913	0.000002640	1.000012269	1.000024539

Table 2 Variation of $|R|$, $|T|$ and $|R|^2 + |T|^2$ for different estimations of Kd (Example-II)

Kd	k_0d	$|R|$	$|T|$	$|R|^2 + |T|^2$
0.02	0.3505	0.000022000	1.000394805	1.000789766
0.22	0.5750	0.001350041	1.000627549	1.001257314
0.42	0.7481	0.000417109	1.000734760	1.001470233
0.62	0.8953	0.000260443	1.000761307	1.001523262
0.82	1.0227	0.000039361	1.000734957	1.001470456
1.02	1.1330	0.000117171	1.000682211	1.001364902

In this case, we fixed $\theta = \pi/6$, $Pd = 0.1$, $m = 2$ and $n = 3$. From this figure, it is observed that $|R_1|$ decreases as the ice parameter increases. Moreover, it is noticed that the highest values of $|R_1|$ are reached when the wave number of the base distortion on the permeable sea-bed turns into just about twice the component of the occurring wave number along the surface beneath the drifting ice-plate. When D/d^4 and ϵ/d are assumed to be 0 (that is, the absence of ice-plate), the result for the problem with free-surface can be achieved as a special case.

The numerical estimations of $|R_1|$, $|T|$ and $|R|^2 + |T|^2$ are displayed in the following tables to verify the energy identity. For the example of exponentially damped distortion, we have demonstrated the estimations of $|R_1|$, $|T|$ and $|R|^2 + |T|^2$ for different estimations of k_0c_0 with $D/c_0^4 = 1$, $\epsilon/c_0 = 0.1$, $\theta = \pi/6$, $Pc_0 = 0.1$, $d/c_0 = 5$ and $c_0b = 1$ in Table 1. From this table, it is clear that the energy identity is satisfied almost precisely. Similarly, for the example of sinusoidal ripple bed, we have demonstrated the deviation of $|R_1|$, $|T|$ and $|R|^2 + |T|^2$ for different estimations of k_0d with $D/d^4 = 1$, $\epsilon/d = 0.01$, $\theta = \pi/6$, $Pd = 0.1$, $m = 2$, $n = 3$ and $\kappa = 0.01$ in Table 2. Also, from this table it is clear that the energy identity is satisfied almost precisely.

7   Conclusion

Consider a single-layer fluid in a sea, where the top surface is cover up by a thin uniform ice-plate and the base is of permeable type with a little distortion. Based on the linear water wave hypothesis, the governing boundary value problem is solved by utilizing the perturbation method in conjunction with the Fourier transform method. It is observed that the reflection and transmission coefficients rely on the frame of the base distortion. Here, two special kinds of base distortion: the exponentially damped distortion and the sinusoidal bed, are taken to calculate the aforesaid coefficients. The reflected energy decreases with the increase of ice parameter of the ice-plate and the angle of incident waves (except at $\theta = \pi/4$). Moreover, the reflected energy increases when the permeability parameter increases. The main advantage of this paper is that the scientific estimations of R and T are developed in this paper to be satisfied the "*energy balance relation*" most precisely. The outcomes acquired in this problem are supposed to be quantitatively useful in handling the water wave diffraction issues with base distortions on a permeable bed in arctic regions.

References

1. Balmforth NJ, Craster RV (1999) Ocean waves and ice-sheets. J Fluid Mech 395:89–124
2. Chakrabarti A (2000) On the solution of the problem of scattering of surface-water waves by the edge of an ice-cover. Proc R Soc Lond A 456:1087–1099
3. Chakrabarti A, Mohapatra S (2013) Scattering of surface water waves involving semiinfinite floating elastic plates on water of finite depth. J Mar Sci Appl 12:325–333
4. Porter D, Porter R (2004) Approximations to wave scattering by an ice sheet of variable thickness over undulating topography. J Fluid Mech 509:145–179
5. Davies AG (1982) The reflection of wave energy by undulations of the sea bed. Dyn Atmosp Oceans 6:207–232
6. Linton CM, Chung H (2003) Reflection and transmission at the ocean/sea-ice boundary. Wave Motion 38:43–52
7. Gu Z, Wang H (1991) Gravity waves over porous bottoms. Coastal Eng 15:497–524
8. Jeng DS (2001) Wave dispersion equation in a porous seabed. Coastal Eng 28:1585–1599
9. Mohapatra S (2014) Scattering of surface waves by the edge of a small undulation on a porous bed in an ocean with ice-cover. J Marine Sci Appl 13:167–172
10. Mohapatra S (2016) The interaction of oblique flexural gravity waves with a small bottom deformation on a porous ocean-bed: green's function approach. J Marine Sci Appl 15:112–122
11. Mohapatra S, Sarangi MR (2017) A note on the solution of water wave scattering problem involving small deformation on a porous channel-bed. J Marine Sci Appl 16:10–19
12. Mohapatra S (2017) The effect of free-surface tension on scattering of water waves by small bottom undulation. ANZIAM J 58:39–80

Nonlinear Unsteady Marangoni Convection with Variable Properties

M. Sathish Kumar, C. S. K. Raju, S. U. Mamatha, B. Rushi Kumar, and G. Kumaran

Abstract The analysis of thin film flow of non-Newtonian fluid with MHD heat transfer in an unsteady stretching sheet in the suspension of variable thickness and thermal conductivity. The governing PDEs are reduced to nonlinear coupled ODEs by applying the appropriate similarity transformations. These coupled nonlinear ODEs subject to the suitable margin conditions and then solved numerically via RK with shooting method. The influences of various parameters on the stream and heat transfer behaviour of the problem are studied through tables and graphs. The friction factor and reduced Nusselt number are obtainable in tables.

Keywords Marangoni convection · Unsteadiness parameter · Thermal conductivity · And variable viscosity

M. Sathish Kumar
Department of Mathematics, VSB Engineering College, Karudayampalayam,
Karur, India
e-mail: msathismani@gmail.com

C. S. K. Raju (✉)
Department of Mathematics, GITAM University, Bangaluru, India
e-mail: sivaphd90@gmail.com

S. U. Mamatha
Department of Mathematics, Kristu Jayanti College, Autonomous, K. Narayanapura, Kothanur,
Bangalore, Karnataka 560077, India
e-mail: mamathasupadhya@gmail.com

B. Rushi Kumar · G. Kumaran
Department of Mathematics, School of Advanced Sciences, VIT, Vellore, Tamil Nadu 632014,
India

1 Introduction

The investigation of thin liquid film surface has got major affection owed to its huge usages and application in the discipline of technology and manufacturing in modern days. The research problems of thin liquid film flow were used in various fields like extraction of the blood flow, lubrication models of human body control, in mechanical and various engineering aspects. Some of the well-known applications are extrusion of metal and polymer, continuous casting, foodstuff processing, fluidization reactor, chemical equipment, plastic drawing sheets, etc. By reviewing the these important applications, many researchers are extended the influence of thin film liquid over a stretching sheet. The stream of thin film liquid was initially examined for thick stream, and in addition, it is extensive to Casson fluid.

The analytical studies of viscid fluid flow past a straight stretching sheet were examined by Crane [1]. Lakshmisha et al. [2] discussed 3D unsteady MHD flow with mass and heat transfer past a stretching sheet. Wang [3] discussed the influence of heat transfer flow of unsteady thin film liquid on MHD stretched surface. The influence of thermocapillarity on the MHD heat transfer flow in a thin film liquid past a stretching sheet was investigated by Dandapat et al. [4]. The characteristic of MHD heat transfer Casson fluid flow past a stretching sheet with thermal energy was depicted by Pramanik [5] and found that raising value of Casson fluid parameter decreases the velocity profile. Kameswarini et al. [6] investigated the study of incompressible Casson fluid flow scheduled stagnation point towards a stretching sheet and summarized that the shrinking case decreases the velocity filed.

The effect of thermophoresis on mass transfer Casson fluid flows past a porous vertical plate was reported by Animasaun [7]. Makinde [8] depicted the analytical solution of steady variable viscosity thin liquid film past a vertical plate. The 2D unsteady flow of Casson fluid past a stretching surface is presented by Mukhopadhyay et al. [9] and concluded that the temperature field is increased with enhancing Casson parameter. The analysis of heat transfer on Jeffery nanofluid past a stretched plate with thermophoresis effect was presented by Mehmood et al. [10]. Khan et al. [11] reported the comparative study of non-Newtonian fluid with heterogeneous–homogeneous reaction.

The viscous dissipation on magnetohydrodynamic convective non-Newtonian flow towards a stretching surface was considered for heat and mass transfer applictions by Sathish Kumar et al. [12] and result that thermal and momentum boundary layer of Ag-kerosene and Cu-kerosene nanofluids are not consistent. The effect of erratic viscosity on MHD unsteady heat transfer in a thin film liquid past a stretching sheet was discussed by Pal and Saha [13]. Ali et al. [14] presented the influence of thermophoretic and Brownian moment of Williamson fluid on liquid thin film towards a stretching surface and analytically solved by HAM method. The unsteady 3D Maxwell, Oldroyed-B and Jeffrey fluids flow considering thin film liquid towards a stretching sheet through thermophoretic effect was depicted by Khan et al. [15]. Hsiao [16] examined the efficiency of heat transfer flow of a nanofluid with thermal radiation effect towards various geometries.

The result of viscous dissipation lying on MHD convective mass transfer boundary layer flow of a thin film liquid towards a stretching sheet was deliberated by Palwasha et al. [17]. Raju et al. [18] examined the study of erratic viscosity on unsteady non-Newtonian fluid past a cone crammed by titanium nanoparticles. The major intend behind the current study is analysing the effect of thermal convection and thermal conductivity on thin film liquid past an uneven stretching sheet. No one of the author conceded this kind of investigation. So, by making use of mentioned in the above all references, we create an effort to present the behaviour of uneven flow on thin film past an unsteady stretching surface by taking into account buoyancy effects.

2 Mathematical Formulation

In the present theoretical model, a liquid thin film of consistent width $h(t)$ which deceits on the flat sheet is considered. The fluid action inside the liquid film is initially caused due to the stretching elastic thin sheet (see Fig. 1). The stretching surface at $y = 0$ passes through the flow rate $\hat{U} = bx/(1 - \alpha)$ where ($\alpha - b$—positive constants) in its own plane. $\hat{T}_s = T_o - (1/2)\hat{T}_{ref} \cdot (Re_x)(1/1 - \alpha t)$—temperature surface of the sheet changes among the distance x as of the slit. Here, $Re_x = bx^2/v_o(1 - \alpha t) = \hat{U}x/v_o$—reduced Reynolds number associated with the stretching sheet velocity $\hat{U}$. $\hat{T}_o$—represents temperature at the slit, $\hat{T}_{ref}\left(0 \leq \hat{T}_{ref} \leq T_o\right)$ represents constant reference temperature. In the present model variation of the viscosity (μ_o), thermal conductivity (k_o) and surface tension (σ_o) with temperature are considered to be in the shape;

$$\sigma = \sigma_o\left(1 - \gamma\left(\hat{T} - \hat{T}_o\right)\right), \mu = \mu_o\left(e^{-\xi\left(\hat{T}-\hat{T}_o\right)}\right), k = k_o\left(1 + c\left(\hat{T} - \hat{T}_o\right)\right) \quad (1)$$
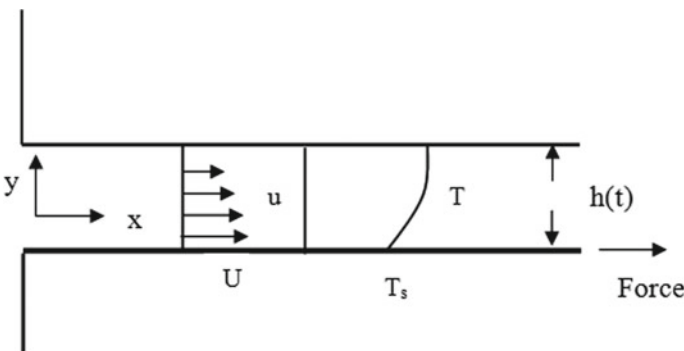
Fig. 1 Schematic diagram of the flow model

In the thin liquid layer, temperature and velocity fields governed via the 2D margin layer equations designed for momentum and thermal energy take the shape:

$$\frac{\partial \hat{u}}{\partial x} + \frac{\partial \hat{v}}{\partial y} = 0 \tag{2}$$

$$\frac{\partial \hat{u}}{\partial t} + \hat{u}\frac{\partial \hat{u}}{\partial x} + \hat{v}\frac{\partial \hat{u}}{\partial y} = \frac{1}{\rho_o}\frac{\partial}{\partial y}\left(\mu\left(1 + \frac{1}{\beta}\right)\frac{\partial \hat{u}}{\partial y}\right)$$
$$+ g\left(\beta_T(T - T_o) + \beta_{T_1}(T - T_o)^2\right) - \frac{\sigma B_0^2}{\rho_0}u \tag{3}$$

$$\frac{\partial \hat{T}}{\partial t} + \hat{u}\frac{\partial \hat{T}}{\partial x} + \hat{v}\frac{\partial \hat{T}}{\partial y} = \frac{1}{\rho_o c_p}\frac{\partial}{\partial y}\left(k\frac{\partial \hat{T}}{\partial y}\right) \tag{4}$$

The limit conditions linked through the flow are

$$\text{at } y = 0, \quad \hat{v} = 0, \quad \hat{u} = \hat{U}, \quad \hat{T} = \hat{T}_s \tag{5}$$

$$\text{at } y = h, \quad \mu\frac{\partial \hat{u}}{\partial y} = \frac{\partial \sigma}{\partial x}, \quad \frac{\partial \hat{T}}{\partial y} = 0, \quad \hat{v} = \frac{dh}{dt}. \tag{6}$$

Here, g represents gravitational acceleration, β and β_1 represent linear and nonlinear thermal expansions coefficients.

f and θ—dimensionless variables, ζ—similarity variable are taken as

$$\Psi = \left(\hat{v}_o b(1 - \alpha t)^{-1}\right)^{1/2} x f(\zeta), \hat{T} = \hat{T}_0 - \hat{T}_{\text{ref}}\left(\frac{bx^2}{2\hat{v}_o}\right)(1 - \alpha t)^{(-3/2)}\theta(\zeta), \tag{7}$$

$$\zeta = \left(\frac{b}{\hat{v}_o}\right)^{(1/2)}(1 - \alpha t)^{(-1/2)}y \tag{8}$$

Here, $\Psi(x, y, t)$-stream function and the velocity mechanism are obtained as

$$\hat{v} = -\frac{\partial \Psi}{\partial x} = -\left(v_o b(1 - \alpha t)^{-1}\right)^{(1/2)} f(\zeta), \hat{u} = \frac{\partial \Psi}{\partial y} = f'(\zeta)bx(1 - \alpha t)^{-1}, \tag{9}$$

With the similarity transformations, the flow Eqs. (1)–(8) are transformed as follows:

$$S\left(f'(\zeta) + \frac{\zeta}{2}f''(\zeta)\right) - f(\zeta)f10(\zeta) + \left(f'(\zeta)\right)^2$$
$$= \left(e^{(A\theta(\zeta))}\left(f'''(\zeta)\left(1 + \frac{1}{\beta}\right) - Mf(\zeta)\right)\right)$$
$$+ \lambda(1 + \lambda_1\theta(\zeta))\theta(\zeta) + Af10(\zeta)\theta'(\zeta)) \tag{10}$$

$$\frac{S}{2}\big(3\theta(\zeta) + \zeta\theta'(\zeta)\big) + 2\theta(\zeta)f'(\zeta) - \theta'(\zeta)f(\zeta)$$

$$= \left(\left(\frac{1}{\mathrm{Pr}}\right)(1 - \delta\theta(\zeta))\theta''(\zeta) - \delta\big(\theta'(\zeta)\big)^2\right) \tag{11}$$

$$f(0) = 0, \quad f'(0) = 1, \quad \theta(0) = 1, \tag{12}$$

$$f''(\beta) = \mathrm{Mc}\,\theta(\beta)\mathrm{e}^{-A\theta(\beta)}, \quad f(\beta) = S\left(\frac{\beta}{2}\right)\theta'(\beta) = 0 \tag{13}$$

In this problem, the resultant dimensionless boundary conditions at $\zeta = 0$ and $\zeta = \beta$. Here, $\hat{T} = \hat{T}_o + \theta(\zeta)\big(\hat{T}_s - \hat{T}_o\big)$, $\delta = c\big(\hat{T}_o - \hat{T}_s\big)$ is the thermal conductivity parameter, $A = (-\xi)\big(\hat{T}_s - \hat{T}_o\big)$ (A is positive, as $T_o > T_s$) is the variable viscosity parameter, $S = \alpha/b$ is unsteadiness parameter, $\lambda = \mathrm{Gr}/\mathrm{Re}_x^2$ is mixed convection parameter, $\mathrm{Gr} = g\beta\big(\hat{T}_s - T_o\big)/v_o^2$—Grashof number associated with temperature, $\mathrm{Pr} = v_o\rho_o c_p/k_o$—Prandtl number, $\lambda_1 = \beta_1\big(\hat{T}_s - \hat{T}_o\big)/\beta$ nonlinear convection parameter due to temperature, and $M = \gamma\sigma_o T_{\mathrm{ref}}/\mu_o(bv_o)^{\frac{1}{2}}$ is the thermocapillary parameter which is closely associated with Marangoni number. In this study, width of the thin liquid sheet is arranged in $\sqrt{v_o/b}$, and hence, based on this level, Marangoni number is given by $\mathrm{Ma} = \gamma\sigma_o T_{\mathrm{ref}}\big(\sqrt{v_o/b}\big)\rho_o c_p/\mu_o k_o = \mathrm{Pr}\cdot M$

(C_f)—friction factor and (Nu_x)—reduced Nusselt number can be expressed as

$$C_f = \frac{2(\tau_s)}{\big(\rho\hat{U}^2\big)} = -2\mathrm{e}^{(A)}f''(0)\cdot\left(\mathrm{Re}_x^{-\frac{1}{2}}\right) \tag{14}$$

$$N\hat{u}_x = -\frac{x}{\hat{T}_{\mathrm{ref}}}\left(\frac{\partial\hat{T}}{\partial y}\right)_{y=0} = \frac{1}{2\sqrt{(1 - \alpha t)}}\theta'(0)\big(\mathrm{Re}_x^{3/2}\big). \tag{15}$$

3   Results and Discussion

The present model investigates the impact of pertinent parameters such as Marangoni convection, unsteadiness parameter, thermal conductivity parameter, variable viscosity parameter, thermocapillary parameter, buoyancy ratio and nonlinear thermal convection on the flow quantities are thermal, flow and concentration fields beside with skin friction and reduced Nusselt number. For numerical analysis of pertinent parameter, values are considered as S, Mc, $A = 1$, $\mathrm{Pr} = 2$, λ, $\zeta = 0.5$, $\delta = 0.2$, $\beta = 6$, $Mg = 0.5$. The mentioned values are kept stable in the whole study exclusive of when varied in relevant tables and figures. The set of partially coupled nonlinear
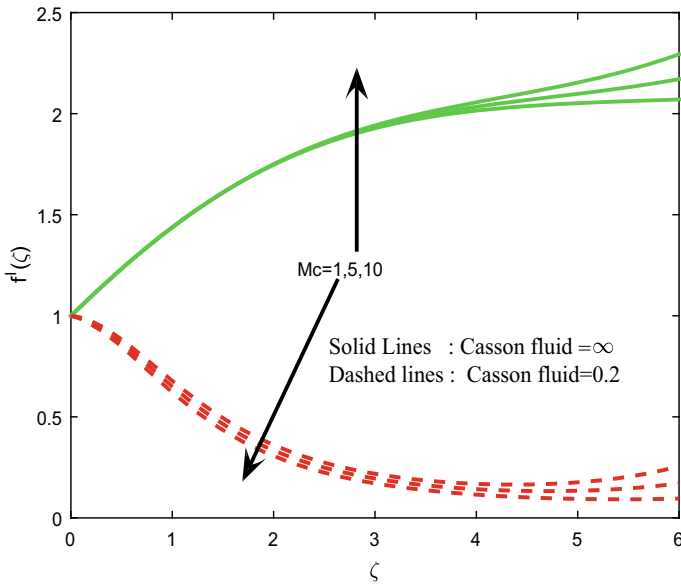
Fig. 2 Effect of Mc on $f'(\zeta)$

ODEs (11) and (12) with related limit condition (13) are numerically solved by RK through shooting technique.

Figures 2 and 3 show to study the impact of Mc on $f'(\zeta)$ and $\theta(\zeta)$. From these figures, we observed that rising values of Mc depreciate the velocity profiles and opposite behaviour is shown in temperature profiles. Generally, Marangoni convection was constantly found from the region high to low temperature at the surface, due to this reason reduces the $f'(\zeta)$. Figures 4 and 5 represent the deviation of $f'(\zeta)$ and $\theta(\zeta)$ in response to a change in the values of S. It is concluded that the temperature profile reduces by uplifting the S, but the mixed behaviour has been examined for the velocity profile. This is due to that unsteadiness parameter increase, the liquid film loses more heat energy due to that temperature profile reduces.

The non-dimensional velocity and temperature profile increase with increasing value of thermocapillary parameter as illustrated in Figs. 6 and 7. Physically, thermocapillary parameters are determined by the inequity of the tangential stress on the boundary layer caused by temperature dependence of surface tension. Figures 8 and 9 show the non-dimensional $f'(\zeta)$, and $\theta(\zeta)$ enhances with the rising of λ_1. This may happen due to the fluid through lesser Pr is more subjected to the effect of buoyancy force. Figs. 10 and 11 depict that the $f'(\zeta)$ increases and $\theta(\zeta)$ decreases significantly by an improvement in the standards of λ. Generally, for the large value, thermal convection parameter transforms more heat energy to the sheet.

Figures 12 and 13 exhibit variable A versus non-dimensional $f'(\zeta)$ and $\theta(\zeta)$. It is concluded that enhancement in both $f'(\zeta)$ and $\theta(\zeta)$ takes place with rising values of A. The influence of δ is seen in Figs. 14 and 15 which depicts that $f'(\zeta)$ and $\theta(\zeta)$
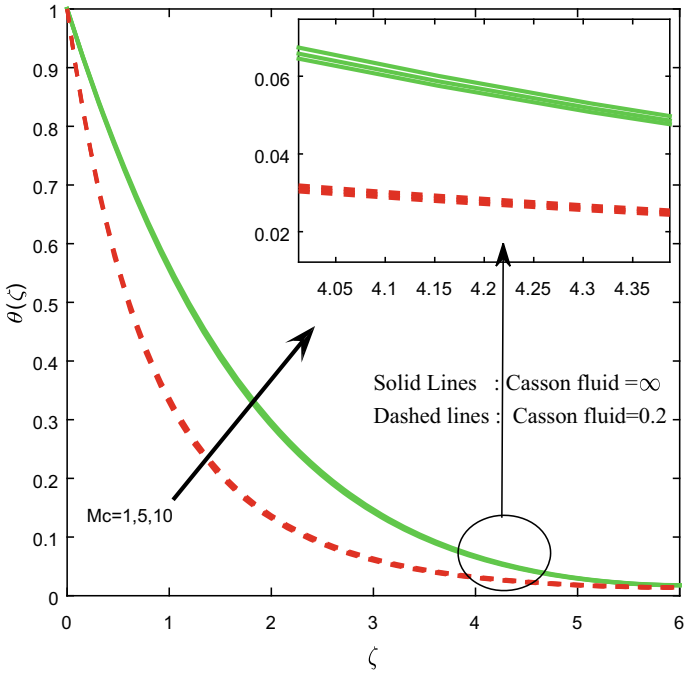
Fig. 3 Effect of Mc on $\theta(\zeta)$
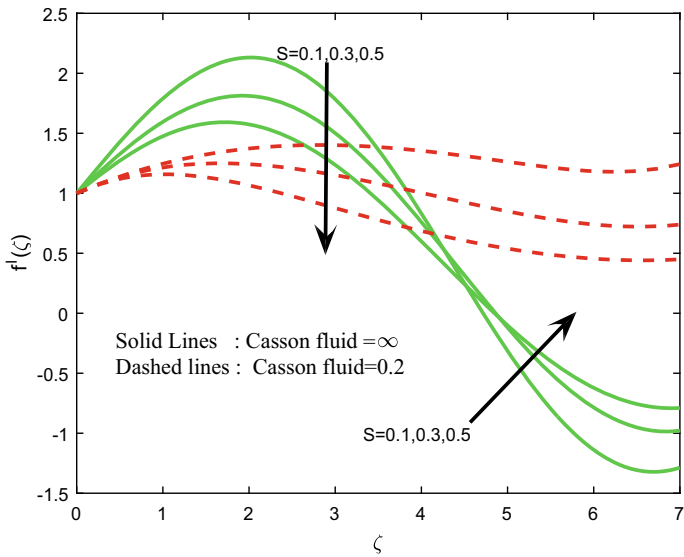
Fig. 4 Effect of S on $f'(\zeta)$
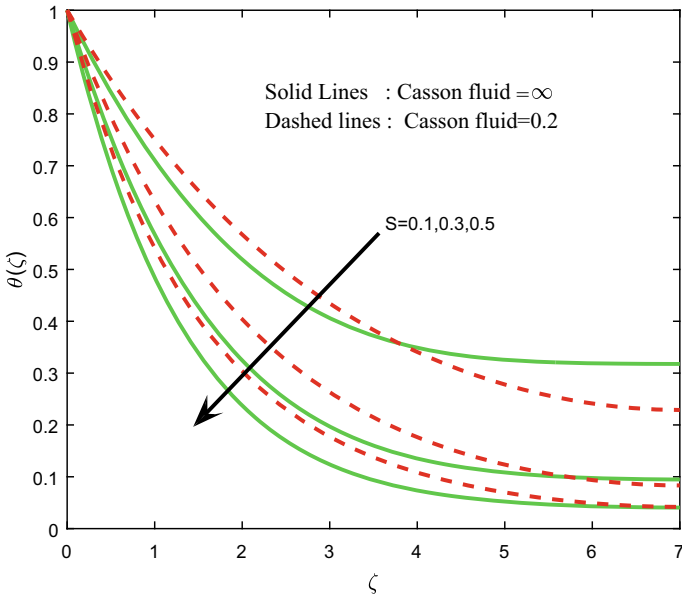
Fig. 5 Effect of S on $\theta(\zeta)$
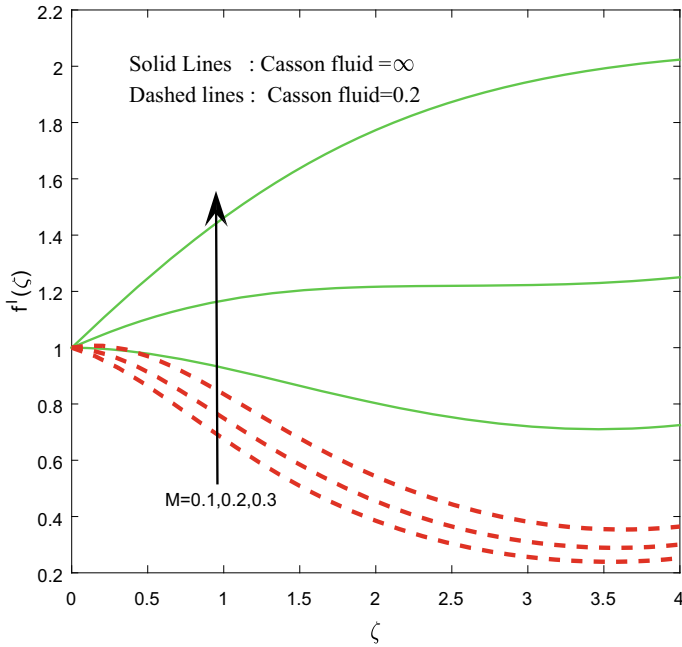
Fig. 6 Effect of M on $f'(\zeta)$
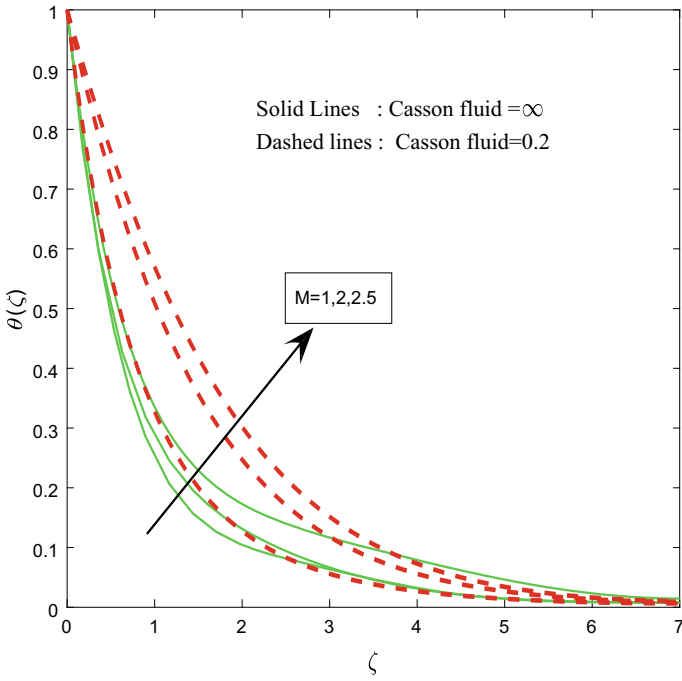
Fig. 7 Effect of M on $\theta(\zeta)$
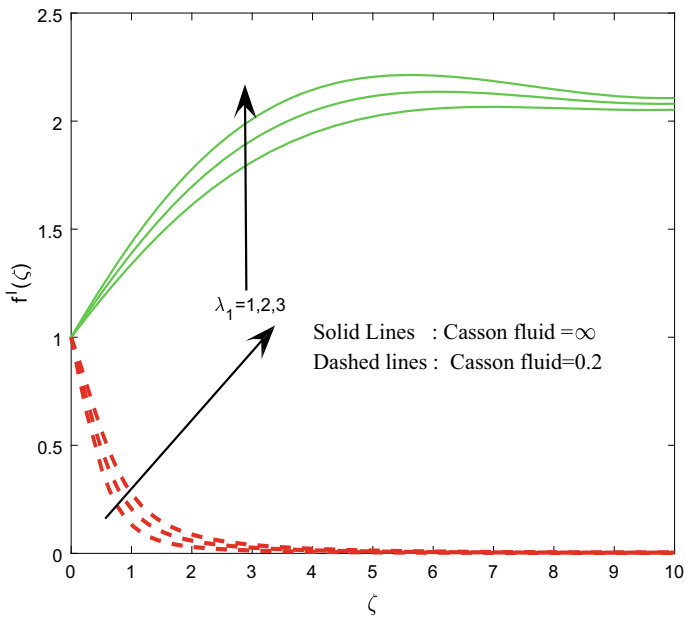
Fig. 8 Effect of λ_1 on $f'(\zeta)$
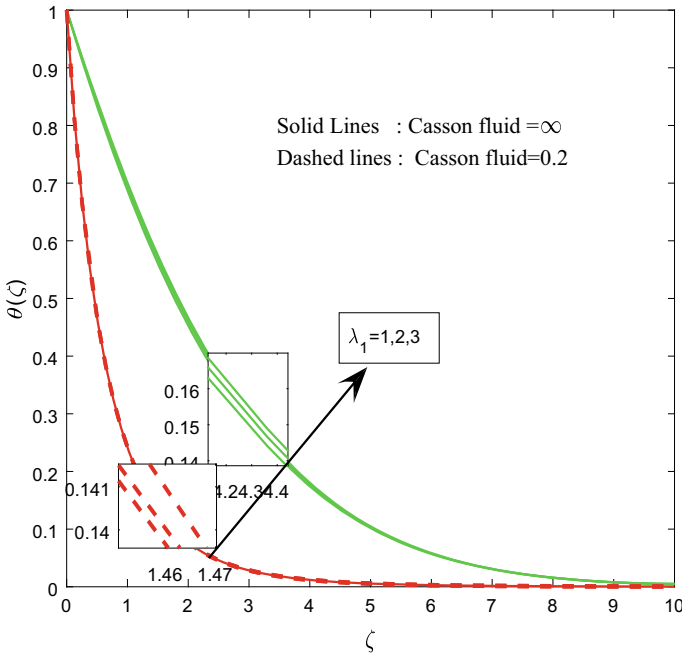
Fig. 9 Effect of λ_1 on $\theta(\zeta)$

depreciate. This may occur due to the survival of heat generation cause is higher than for survival of heat inclusion source. Table 1 is portrayed to indicate the effect of S, Mc, A, Pr, λ, η, δ, β, Mg on $-f'(0)$ and $-\theta'(0)$ when Casson fluid $(\infty, 0.2)$. It is revealed the friction factor is declined by rising values of Marangoni λ and M. And also, rising values of S encourage the Nusselt number.

4 Conclusions

From the numerical results, we observe some of the exciting conclusions are as follows: Increase in Marangoni convection parameter decrease both friction factor and reduced Nusselt number. The impact of thermocapillary factor is to decrease the friction factor coefficient. With the result of S, λ, λ_1 and A, the coefficient of skin friction is decreased.
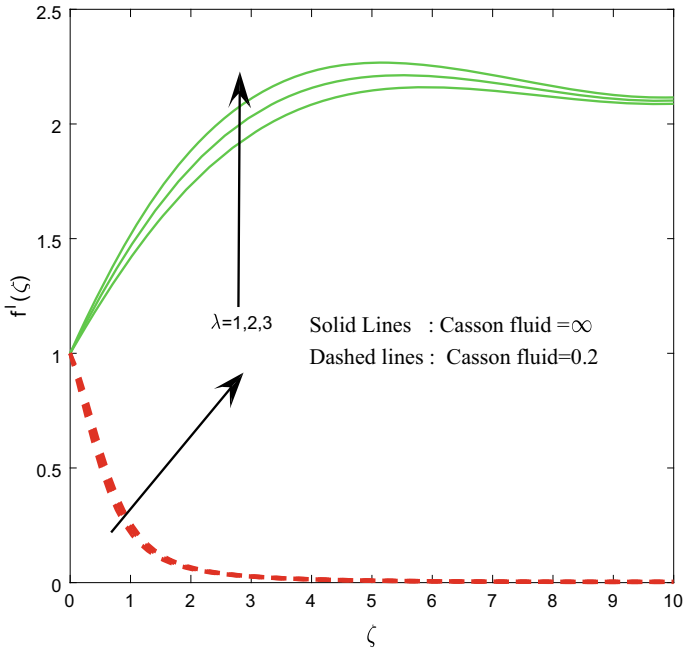
Fig. 10 Effect of λ on $f'(\zeta)$
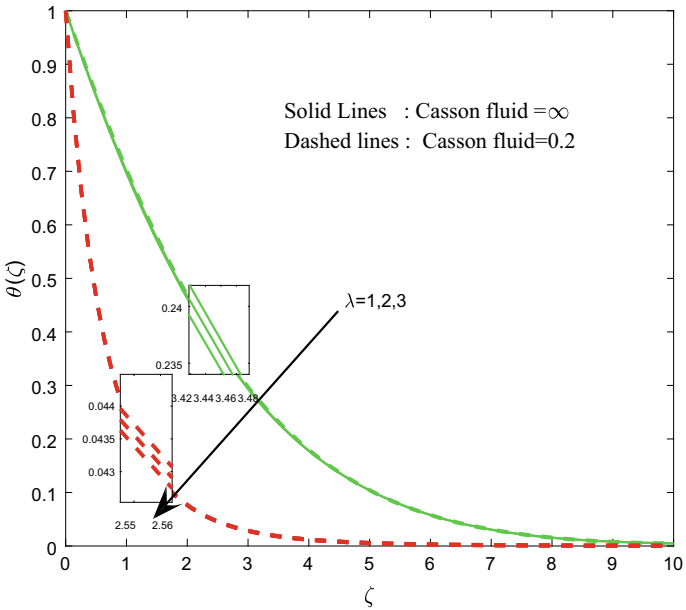
Fig. 11 Effect of λ on $\theta(\zeta)$
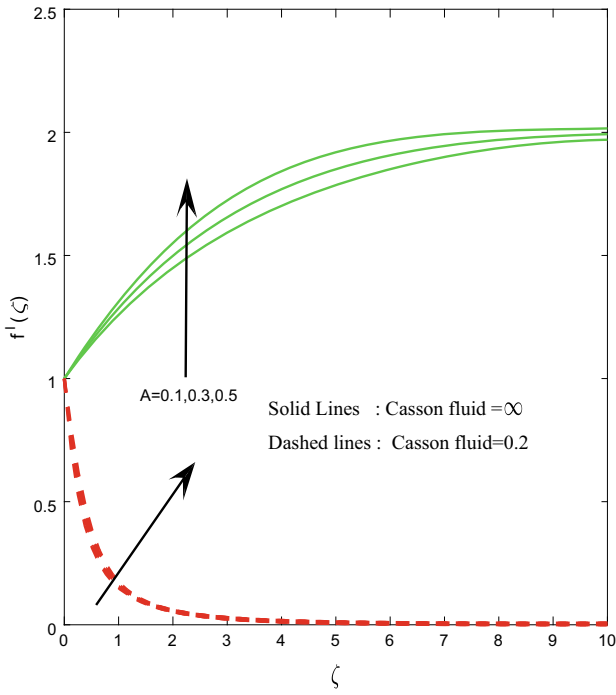
Fig. 12 Effect of A on $f'(\zeta)$
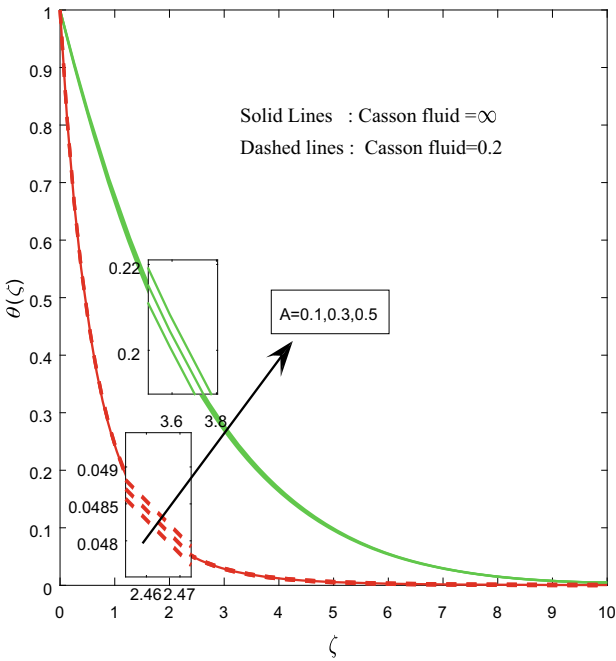
Fig. 13 Effect of A on $\theta(\zeta)$
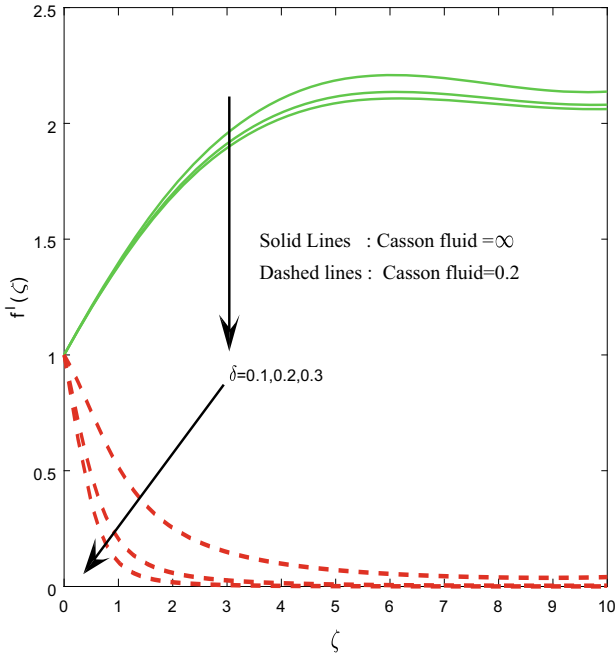
Fig. 14 Effect of δ on $f'(\zeta)$
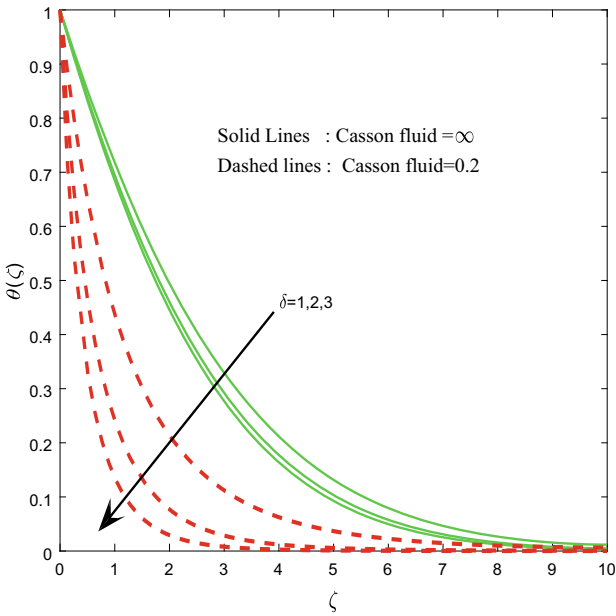
Fig. 15 Effect of δ on $\theta(\zeta)$

Table 1 Impact of various parameter on $f''(0)$ and $-\theta'(0)$ when Casson fluid $= \infty$, 0.2

Mg	S	M	λ_1	λ	δ	A	$\beta = \infty$		$\beta = 0.2$	
							C_{fx} coefficient friction	Nu_x	C_{fx}	Nu_x
1							−2.22278	−1.27944	2.47300	−0.97541
5							−2.22327	−1.28511	1.94647	−1.26876
10							−2.22349	−1.29180	1.76285	−1.27750
	0.1						−4.72416	−1.88006	−1.3087	−1.71336
	0.3						−3.26058	−1.47678	−0.3455	−1.12495
	0.5						−2.59959	−1.35507	0.28958	−0.92882
		1					0.28013	−1.48192	1.90244	−1.22381
		2					−1.06790	−1.52861	1.37490	−1.29465
		2.5					−2.65215	−1.58721	0.70196	−1.37160
			1				−1.16096	−0.79022	0.72565	−0.34362
			2				−1.26717	−0.80371	1.31203	−0.40017
			3				−2.04792	−1.32068	1.62361	−0.39987
				1			−1.08624	−0.67700	1.40052	−0.39951
				2			−0.94997	−0.60409	1.57579	−0.39821
				3			−1.75424	−1.02199	1.74886	−0.39693
					0.1		−1.36805	−0.87637	1.70832	−0.70862
					0.2		−1.26717	−0.80371	1.31203	−0.40017
					0.3		−1.22589	−0.77351	0.61490	−0.17086
						0.1	−0.46576	−1.24654	0.26289	−0.34756
						0.3	−0.44867	−0.75794	0.43458	−0.40414
						0.5	−0.55317	−0.68457	0.59214	−0.40308

References

1. Crane CJ (1970) Flow past a stretching plate. Angrew Math Phys 21:645–647. https://doi.org/10.1007/BF01587695
2. Lakshmisha KN, Venkateswaran S, Nath G (1988) Three dimensional unsteady flow with heat and mass transfer over a continuous stretching surface. ASME J Heat Transf 110:590–595. https://doi.org/10.1115/1.3250533
3. Wang CY (1990) Liquid film over a stretching surface. Q. Appl. Maths 48:601–61. www.jstor.org/stable/43637666
4. Dandapat BS, Santra B, Andersson HI, Dandpat BS (2000) Heat transfer in a liquid film on unsteady stretching surface. Int J Heat Mass Transf 43:69–74. https://doi.org/10.1016/S0017-9310(99)00123-4
5. Pramanik S (2014) Casson fluid flow and heat transfer past an exponentially porous stretching sheet in presence of thermal radiation. Aim Shams Eng J 5:205–212. https://doi.org/10.1016/j.asej.2013.05.003
6. Kameswarani PK, Shaw S, Sibanda P (2014) Dual solution of Casson fluid flow over a stretching and shrinking sheet. Sadhana 39(6):1573–1583. https://doi.org/10.1007/s1204
7. Animasaun IL (2015) Effects of thermophoresis, variable viscosity and thermal conductivity on free convective heat and mass transfer of non-darcian MHD dissipative Casson fluid flow with suction and nth order chemical reaction. J Nigerian Math Soc 34:11–31. https://doi.org/10.1016/j.jnnms.2014.10.008
8. Makinde OD (2006) Laminar falling liquid film with variable viscosity along an inclined heated plate. Appl Math Comput 175:80–88. https://doi.org/10.1016/j.amc.2005.07.021
9. Mukhopadhyay S, De PR, Bhattacharyya K, Layek GC (2013) Casson fluid flows over an unsteady stretching surface. Aim Shams Eng J 4(4):933–938. https://doi.org/10.1016/j.asej.2013.04.004
10. Mehmood R, Nadeem S, Saleem S, Akbar NS (2017) Flow and heat transfer analysis of Jeffery nano fluid impinging obliquely over a stretched plate. J Taiwan Inst Chem Eng 74:49–58. https://doi.org/10.1016/j.jtice.2017.02.001
11. Khan M, Waqas M, Hyat T (2017) A comparative study of Casson fluid with homogeneous-heterogeneous reaction. J Colloid Interf Sci 498:85–90. https://doi.org/10.1016/j.jcis.2017.03.024
12. Sathish Kumar, M., Sandeep, N., Rushi Kumar, B.: Free convective heat transfer of MHD dissipative Carreau nano fluid flow over a stretching sheet. Front. Heat Mass Transf. 8 (2017). https://doi.org/10.5098/hmt.8.13
13. Pal D, Saha P (2016) Influence of nonlinear thermal radiation and variable viscosity on hydromagnetic heat and mass transfer in a thin liquid film over an unsteady stretching surface. Int J Mech Sci 119:208–216. https://doi.org/10.1016/j.ijmecsci.2016.09.026
14. Ali L, Islam S, Gul T, Khan I, Dennis LCC, Khan W, Khan A (2017) The Brownian and Thermophoretic analysis of the non-Newtonian Williamson fluid flow of thin film in a porous space over an unstable stretching surface. Appl Sci 7(4):404. https://doi.org/10.3390/app7040404
15. Khan W, Idress M, Gul T, Khan MA, Bonyah E (2018) Three dimensional fluids flow considering thin film over an unsteady stretching surface with variable fluid properties. Adv Mech Eng. https://doi.org/10.1177/1687814018807361
16. Hsiao K (2017) To promote radiation electrical MHD activation energy thermal extrusion manufacturing system efficiency by using Carreau-nanofluid with parameter control. Energy 130:486–499. https://doi.org/10.1016/j.energy.2017.05.004
17. Palwasha, Z., Khan, N.S., Shah, Z., Islam, S., Bonyah, E.: Study of two-dimensional boundary layer thin film fluid flow with variable thermo-physical properties in three dimensional spaces. AIP Advances 8, (2018). https://doi.org/10.1063/1.5053808
18. Raju CSK, Sekhar KR, Ibrahim SM, Lorenzini G, Reddy GV, Lorenzini E (2017) Variable viscosity on unsteady dissipative Carreau fluid over a truncated cone filled with titanium alloy nanoparticles. Continuum Mech Thermodyn 29(3):699–713. https://doi.org/10.1007/s00161-016-0552-8

Thermo-Diffusion and Diffusion-Thermo Effects for a Forchheimer Model with MHD Over a Vertical Heated Plate

N. Nalinakshi and P. A. Dinesh

Abstract Heat and mass transfer for a Forchheimer model of electrically conducting fluid with Soret and Dufour effects over a vertical heated plate is studied. The governing equations for the physical problem in consideration are highly coupled and nonlinear in nature. A shooting technique is applied to the first-order ODEs' which are obtained by using similarity transformations to PDEs' and then to higher-order ordinary differential equations. The effects of various non-dimensional significant parameters such as Richardson number, Prandtl number, magnetic parameter, Soret and Dufour parameters and so on are interpreted. Attenuation with the velocity of fluid flow occurs due to the cause of magnetic force. The diffusion effects which are crossed in the energy and solutal equation enhance the thermal effects. Skin friction, rate of heat, and mass transfer are also computed. Results obtained are compared with the existing work and found to be in good agreement.

Keywords Heat and mass transfer · Soret and Dufour effects · Boundary layer · Porous medium · MHD

Nomenclature

U_o	Free stream velocity
G	Gravitational field
T_w	Uniform constant temperature
C_w	Uniform constant concentration
T_∞	Ambient temperature
C_∞	Ambient concentration

N. Nalinakshi (✉)
Department of Mathematics, Atria Institute of Technology, Bengaluru, Karnataka, India
e-mail: nalinakshi.n@atria.edu

P. A. Dinesh
Department of Mathematics, M.S. Ramaiah Institute of Technology, Bengaluru, Karnataka 560054, India
e-mail: dineshdpa@msrit.edu

u	Velocity component along x-direction
v	Velocity component along y-direction
ε	Porosity
$\vec{g}$	Acceleration due to gravity
p	Pressure
T	Temperature of the fluid
C	Concentration of the fluid
$\overline{\mu}$	Effective viscosity of the fluid
μ	Fluid viscosity
$k(y)$	Variable permeability of the porous medium
$\varepsilon(y)$	Variable porosity of the saturated porous medium
$\alpha(y)$	Variable effective thermal diffusivity of the medium
$\gamma(y)$	Variable effective solutal diffusivity
σ^*	Ratio of the thermal conductivity of solid to the conductivity of the fluid
γ^*	Ratio of the thermal diffusivity of solid to the diffusivity of the fluid
D_f	Dufour number
Pr	Prandtl number
σ	Local permeability parameter
β^*	Local inertial parameter
Gr_C	Solutal Grashof number
τ	Skin friction
Nu	Nusselt number
$\vec{q} = (u, v),$	u and v are the velocity components along the x and y planes
C	Specific heat at constant pressure
C_b	Empirical constant of the second-order resistance term due to inertia effect
κ	Variable thermal conductivity
κ_c	Variable solutal diffusivity,
β_T	Coefficient of volume expansion volumetric
β_C	Coefficient of expansion with species concentration
ϕ	Viscous dissipation term
D_{12}	Concentration gradient (i.e. Dufour coefficient)
D_{21}	Temperature gradient (i.e. Soret coefficient)
ρ	Density of the fluid
$\psi(x, y)$	Stream function
N	Buoyancy ratio
α^*	Ratio of viscosities
Ec	Eckert number
η	Similarity variable
k_o	Permeability at the edge
ε_o	Porosity at the edge
α_o	Thermal conductivity at the edge
γ_o	Solutal diffusivity at the edge of the boundary layer

d and d^*	3.0 and 1.5 resp. for variable permeability and $d = d^* = 0$ for uniform permeability
Sr	Soret number
Sc	Schmidt number
Re	Reynolds number
Gr_T	Thermal Grashof number
Ri	Richardson number
Sh	Sherwood number

1 Introduction

Soret and Dufour effects are taken to be physical and second-order phenomena find applications in many engineering fields, hydrology, geosciences, etc. When heat and mass transport process occurs simultaneously in the moving fluid, the relation between driving potentials and the fluxes is more complex. The energy flux generated not only by temperature gradients but also by composition gradients, thereby causing the heat transfer is called the diffusion-thermo or Dufour effect. Also, mass transfer caused by temperature gradients is called thermal diffusion or Soret effect. Eckert and Drake [1] initiated for the analysis of heat and mass transfer. The Forchheimer's extension in the momentum equation of Darcy's law with the velocity squared term is important at higher flow rate due to its inertia effect. Nield and Bejan [2] has given a very good insight into the heat transfer process with and without Darcy porous medium. Magneto-hydrodynamics (MHD) has many notable applications in generators, flowmeters, pumps used for pumping liquid metals in metallurgy, physiological process with magnetic therapy, couplers and bearings, etc., where bearing performance can be improved due to the presence of additives.

The Dufour and Soret effects over a vertical surface were investigated by Anghel et al. [3] for natural convection Postelnicu [4], later analysed numerically for heat and mass transport process by natural convection from vertical surfaces in porous media with the influence of magnetic and Soret and Dufour effects. Gnaneswara et al. [5] studied Soret and Dufour effects on steady MHD natural convection flow past a moving vertical plate in a porous medium with viscous dissipation and found that skin friction coefficient rises, whereas a rise in Sherwood number and fall in Nusselt number and vice versa, respectively. Hence, Soret and Dufour effects cannot be neglected.

Alam and Rahman [6] made numerical analysis using Brinkman model and found that wall suction reduces the boundary layer velocity with Dufour and Soret effects. Balasubrahmanyam et al. [7] examined the Soret effect confined in a cylindrical annulus for heat and mass transport with radial magnetic field and constant heat source/sink. Motsa [8] investigated the double-diffusive convection by introducing Dufour and Soret effects with Darcy model in a horizontal layer, and Awad et al. [9] extended by adding inertial effects using the modified Darcy–Brinkman model in a

Maxwell fluid. Cylinder filled with moist porous grains and exposed to a constant wall heat flux was studied for double-diffusive natural convection by Zili-Ghedira et al. [10]. Most of the literature has been found where the authors treat the fluid properties as constants for the analysis of double-diffusive convection over a vertical heated plate.

The importance of varying the fluid properties particularly the porosity and permeability was systematically studied by Mohammadein and El-shaer [11] over a vertical heated plate. Later Nalinakshi et al. [12] made an attempt to vary the fluid properties for heat and mass transfer with Soret and Dufour effects. Girinath et al. [13] attempted to analyse the effect of variable porosity and viscosity with Soret and Dufour over an accelerating surface. Later, Veera Krishna et al. [14] investigated Soret, Joule and Hall effects on MHD rotating mixed convective flow past an infinite vertical porous plate.

In view of the above understandings of different authors, the main aim here in this investigation is to analyse systematically and numerically the Soret and Dufour effects on mixed convection for a Forchheimer model with MHD over a vertical heated plate by varying the fluid properties. To arrive at this aim, highly coupled nonlinear PDE's arising for the physical system is reduced to ODE's and further to first-order differential equation with unknowns. A numerical technique is applied to obtain the results for heat and mass transport process for different values of pertinent non-dimensional parameters. The results obtained are verified for the accuracy under the limiting conditions.

2 Mathematical Formulation

The heated porous plate embedded with porous medium in two-dimensional, laminar, steady-state, for double-diffusive convection varying the fluid properties are considered vertically along x-coordinate and normally along y-coordinate. The surface of the plate is maintained so that $T_w > T_\infty$, $C_w > C_\infty$ of the fluid with gravitational force in the downward direction.

Applying the boundary layer theory for the physical system arising, the general equations in vector form for continuity, momentum, energy and species concentration, respectively, can be written as:

$$\nabla . \vec{q} = 0 \tag{1}$$

$$\rho_o\left(\vec{q}.\nabla\right)\vec{q} = -\nabla p + \rho\,\vec{g} + \overline{\mu}\nabla^2\,\vec{q} - \frac{\mu\varepsilon}{k}\,\vec{q} - \varepsilon^2\frac{\rho_o C_b}{\sqrt{k}}\left|\vec{q}\right|\vec{q} + \varepsilon\,\vec{J}\times\vec{B} \tag{2}$$

$$\left(\rho_o C_p\right)\left(\vec{q}.\nabla\right)T = \nabla.(\kappa\nabla T) + \Phi + D_{12}\nabla^2 C \tag{3}$$

$$\left(\vec{q}.\nabla\right)C = \nabla.(\kappa_c\nabla C) + D_{21}\nabla^2 T \tag{4}$$

Equation (2) is the well-known Darcy–Lapwood–Brinkman–Forchheimer equation which was first proposed by Brinkman [15] to include the boundary layer effect in the momentum equation. With Boussinesq approximation being valid, the varying fluid properties' functions of the vertical coordinate y and using the expression for free stream velocity, eliminating the pressure gradient, Eqs. (1)–(4) can be expressed in the form:

$$\frac{\partial u}{\partial x} + \frac{\partial u}{\partial y} = 0, \tag{5}$$

$$u\frac{\partial u}{\partial x} + v\frac{\partial u}{\partial y} = g\beta_T(T - T_\infty) - g\beta_c(c - c_\infty) + \frac{\bar{\mu}}{\rho}\frac{\partial^2 u}{\partial y^2}$$
$$- \frac{\mu\varepsilon(y)}{\rho k(y)}(U_o - u) + C_b\frac{\varepsilon^2(y)}{\sqrt{k(y)}}\left(U_o^2 - u^2\right) - \frac{\sigma_m B_0^2}{\rho}\varepsilon(y)u, \tag{6}$$

$$u\frac{\partial T}{\partial x} + v\frac{\partial T}{\partial y} = \frac{\partial}{\partial y}\left(\alpha(y)\frac{\partial T}{\partial y}\right) + \frac{\bar{\mu}}{\rho_o C_p}\left(\frac{\partial u}{\partial y}\right)^2 + \frac{D_m K_T}{C_s C_p}\frac{\partial^2 C}{\partial y^2}, \tag{7}$$

$$u\frac{\partial C}{\partial x} + v\frac{\partial C}{\partial y} = \frac{\partial}{\partial y}\left(\gamma(y)\frac{\partial C}{\partial y}\right) + \frac{D_m K_T}{T_m}\frac{\partial^2 T}{\partial y^2}, \tag{8}$$

where $\Phi = \frac{\bar{\mu}}{\rho_o C_p}\left(\frac{\partial u}{\partial y}\right)^2$, $D_{12} = \frac{D_m K_T}{C_s C_p}$, $D_{21} = \frac{D_m K_T}{T_m}$,

The flow fields are determined by solving the above general equations under the rigid surfaces boundary conditions near and far away from the plate. The boundary conditions are:

$$u = 0, v = 0, T = T_W, C = C_W \text{ at } y = 0, \tag{9}$$

$$u = U_o, v = 0, T = T_\infty, C = C_\infty \text{ as } y \to \infty. \tag{10}$$

Equations (6), (7) and (8) are coupled and nonlinear in nature. To solve the above complex partial differential equations, dimensionless variables η, f, θ and ϕ are introduced:

$$\eta = \left(\frac{y}{x}\right)\left(\frac{U_o x}{v}\right)^{1/2}, \psi = \sqrt{vU_o x}\, f(\eta), \theta = \frac{T - T_\infty}{T_W - T_\infty}, \phi = \frac{C - C_\infty}{C_W - C_\infty}, \tag{11}$$

$u = \frac{\partial \psi}{\partial y}, v = -\frac{\partial \psi}{\partial x}$, so that Eq. (5) is satisfied. The velocity components are given by (see Hady et al. [16], Mohammadein and El-shaer [11])

$$u = U_o f'(\eta), v = -\frac{1}{2}\sqrt{\frac{vU_o}{x}}\left(f(\eta) - \eta f'(\eta)\right), \tag{12}$$

The varying fluid properties are defined as:

$$k(\eta) = k_o\big(1 + de^{-\eta}\big), \alpha(\eta) = \alpha_o\big[\varepsilon_o\big(1 + d^*e^{-\eta}\big) + \sigma^*\big\{1 - \varepsilon_o\big(1 + d^*e^{-\eta}\big)\big\}\big],$$
(13)

$$\varepsilon(\eta) = \varepsilon_o\big(1 + d^*e^{-\eta}\big), \gamma(\eta) = \gamma_o\big[\varepsilon_o\big(1 + d^*e^{-\eta}\big) + \gamma^*\big\{1 - \varepsilon_o\big(1 + d^*e^{-\eta}\big)\big\}\big],$$

Substituting (11) and (12) in Eqs. (6), (7) and (8) and using Eq. (13), we get the following transformed equations

$$f''' + \frac{1}{2}ff'' + \frac{Gr}{Re^2}(\theta - N\phi) + \frac{\alpha^*(1 + d^*e^{-\eta})}{\sigma Re(1 + de^{-\eta})}(1 - f')$$
$$+ \beta^*\frac{(1 + d^*e^{-\eta})^2}{(1 + de^{-\eta})^{1/2}}(1 - f'^2) + M^2\varepsilon_o(1 + d^*e^{-\eta})(1 - f') = 0,$$
(14)

$$\theta'' = -\frac{(1/2)\,Pr\,\theta' f + Pr\,Ef''^2 + \varepsilon_o d^*e^{-\eta}(\sigma^* - 1)\theta' + Pr\,D_f\phi''}{\varepsilon_o + \sigma^*(1 - \varepsilon_o) + \varepsilon_o d^*e^{-\eta}(1 - \sigma^*)},$$
(15)

$$\phi'' = -\frac{(1/2)Sc\,f\phi' + \varepsilon_0 d^*e^{-\eta}(\gamma^* - 1)\phi' + ScSr\theta''}{\varepsilon_o + \gamma^*(1 - \varepsilon_o) + \varepsilon_o d^*e^{-\eta}(1 - \gamma^*)}$$
(16)

where $Sc = \overline{\mu}\big/\rho\gamma_o$, $Pr = \overline{\mu}\big/\rho\alpha_o$, $\alpha^* = \mu\big/\overline{\mu}$, $N = \frac{\beta_C(C_W - C_\infty)}{\beta_T(T_W - T_\infty)}$, $Ec = U_o^2\big/C_p(T_W - T_\infty)$, $\sigma = k_o\big/x^2\varepsilon_o$ $Re = U_o x\big/v$, $\beta^* = C_b\frac{\varepsilon_o^2 x}{k_o^{1/2}}$, $Gr_T = g\beta_T(T_W - T_\infty)x^3\big/v^2$, $Gr_C = g\beta_C(C_W - C_\infty)x^3\big/v^2$, $D_f = \frac{D_m k_T(C_W - C_\infty)}{c_s c_p(T_W - T_\infty)}$, $S_r = \frac{D_m k_T(T_W - T_\infty)}{vT_m(C_W - C_\infty)}$, and $Ri = Gr/Re^2$. Here $Gr_T = Gr_C$.. $M^2 = \frac{\sigma_m B_0^2 x}{(\rho U_0)}$.

The transformed boundary conditions are:

$$f = 0, f' = 0, \theta = 1, \phi = 1 \text{ at } \eta = 0 \quad f' = 1, \theta = 0, \phi = 0 \text{ as } \eta \to \infty \quad (17)$$

For any convective heat and mass transport process, the skin friction and the rate of heat and mass transfer expressions are important. Hence, they can be calculated, respectively, by using,

$$\tau = -f''(0)/\sqrt{Re} \quad Nu = -\sqrt{Re}\,\theta'(0) \text{ and } Sh = -\sqrt{Re}\,\phi'(0), \quad (18)$$

3 Method of Solution

For the physical system under consideration, the arising boundary value problem is difficult to solve as the equations involved are complicated. Hence, a numerical technique called as shooting technique is employed where initially the coupled ODE's are

transformed to first-order differential equations which are simultaneous. In the procedure, a suitable guess value is shooting at the initial point. Runge–Kutta–Fehlberg integration method is employed where we have third-order and second-order of $f(\eta)$, $\theta(\eta)$ and $\emptyset(\eta)$ respectively, reduced to a system of simultaneous equations as follows:

$$\frac{df_3}{d\eta} = -\frac{1}{2}f_1f_3 - \frac{Gr}{Re^2}(f_4 - Nf_7) - \frac{\alpha^*(1 + d^*e^{-\eta})}{\sigma Re(1 + de^{-\eta})}(1 - f_2)$$

$$-\frac{\beta^*(1 + d^*e^{-\eta})}{(1 + de^{-\eta})^{1/2}}(1 - f_2^2) + M^2\varepsilon_o(1 + d^*e^{-\eta})(1 - f_2)$$

$$\frac{df_5}{d\eta} = -\frac{(1/2)\,Pr\,f_1f_5 + Pr\,Ef_3^2 + \varepsilon_o d^*e^{-\eta}(\sigma^* - 1)f_5 + Pr\,D_f f_9}{\varepsilon_o + \sigma^*(1 - \varepsilon_o) + \varepsilon_o d^*e^{-\eta}(1 - \sigma^*)}$$

$$\frac{df_8}{d\eta} = -\frac{(1/2)Sc f_1f_5 + \varepsilon_o d^*e^{-\eta}(\gamma^* - 1)f_8 + ScSr f_6}{\varepsilon_o + \gamma^*(1 - \varepsilon_o) + \varepsilon_o d^*e^{-\eta}(1 - \gamma^*)} \tag{19}$$

where $f_1 = f$, $f_2 = f'$, $f_3 = f''$, $f_4 = \theta$, $f_5 = \theta'$, $f_7 = \phi$, $f_8 = \phi'$ and a prime denotes differentiation with respect to η.

The boundary conditions (17) now take the form

$$f_1(0) = 0,\ f_2(0) = 0,\ f_4(0) = 1,\ f_7(0) = 1$$

$$f_2(\infty) = 1,\ f_4(\infty) = 0,\ f_7(\infty) = 0. \tag{20}$$

While guessing the values at initial state for suitable η_∞ due to which convergence depends, the accuracy is verified by comparing the values at the terminal point. If the accuracy is not reached, the iterative process is repeated for the improved values and the same is terminated and is said to have converged results when the two successive values reach a difference of up to 10^{-6}. The slight deviation here is due to fifth-order accuracy when compared to Mohammadein and El-Shaer [11].

4 Results and Discussion

In the analysis, for the physical system arising and the method used the accuracy to be measured, the transformed system of Eq. (19) is solved applying Runge–Kutta–Fehlberg method numerically and computed the values of $f''(0)$, $\theta'(0)$ and $\phi'(0)$ by varying the values of various pertinent non-dimensional parameters with certain fixed values for uniform permeability (UP) ($d = 0.0$, $d^* = 0.0$) and variable permeability (VP) ($d = 3.0$, $d^* = 1.5$) cases. Values are given in Table 1. Representation of the results is depicted graphically in Figures 1, 2, 3, 4, 5, 6, 7, 8, 9, 10, 11, 12, 13, 14, 15, 16, 17 and 18.

Table 1 Results for UP and VP cases with fixed $\varepsilon_o = 0.4$, $Pr = 0.71$, $Ec = 0.1$, $Sc = 0.22$

D_f, Sr	N	M	Gr/Re^2	$\alpha^*/\sigma Re^2$	β^*	UP $f''(0)$	UP $-\theta'(0)$	UP $-\phi'(0)$	VP $f''(0)$	VP $-\theta'(0)$	VP $-\phi'(0)$
2.00, 0.03	1	0	0.2	0.1	0.0	0.449345	0.378450	0.377500	0.452345	0.381450	0.378500
					0.1	0.464565	0.394567	0.390004	0.474565	0.404567	0.393564
					0.5	0.554567	0.438780	0.429500	0.564567	0.441780	0.436500
					1.5	0.647800	0.507030	0.499900	0.657800	0.510030	0.509900
				0.0	0.1	0.423450	0.351340	0.348020	0.433450	0.361340	0.350020
				0.1		0.464565	0.394567	0.390004	0.474565	0.404567	0.393564
				0.5		0.534560	0.458250	0.457210	0.554560	0.463450	0.461110
		1	0.0	0.1	0.1	0.397800	0.279800	0.273700	0.367800	0.291340	0.281780
			0.2			0.464565	0.394567	0.390004	0.474565	0.404567	0.393564
			1.0			0.715650	0.518900	0.500050	0.720050	0.502903	0.491050
			2.0			0.843560	0.541250	0.538500	0.851260	0.540250	0.531200
			0.2	0.1	0.1	0.464565	0.394567	0.390004	0.474565	0.404567	0.393564
						0.495678	0.411780	0.408010	0.501548	0.423280	0.410010
						0.552453	0.431789	0.425897	0.569870	0.443219	0.433164
	0.0	5	0.2	0.1	0.1	0.399450	0.312450	0.310010	0.401250	0.323900	0.320010
	1.0					0.464565	0.394567	0.390004	0.474565	0.404567	0.393564
	5.0					0.745640	0.441890	0.440010	0.731240	0.450018	0.448410
	10.0					0.889070	0.491050	0.491550	0.895070	0.509070	0.498550
2.00, 0.03	1.0	10	0.2	0.1	0.1	0.464565	0.394567	0.390004	0.474565	0.404567	0.393564
1.00, 0.06						0.481120	0.400250	0.399500	0.483120	0.413453	0.400134

(continued)

Table 1 (continued)

D_f, Sr	N	M	Gr/Re²	$\alpha^*/\sigma Re^2$	β^*	Uniform permeability (UP)			Variable permeability (VP)		
						$f''(0)$	$-\theta'(0)$	$-\phi'(0)$	$f''(0)$	$-\theta'(0)$	$-\phi'(0)$
0.40, 0.15						0.494500	0.416700	0.412020	0.498500	0.420054	0.418945
0.15, 0.40						0.528900	0.421890	0.420040	0.531670	0.429918	0.427896
0.06, 1.00						0.548965	0.434560	0.430010	0.557891	0.438763	0.433981
0.03, 2.00						0.565678	0.451780	0.449010	0.569821	0.463789	0.457654
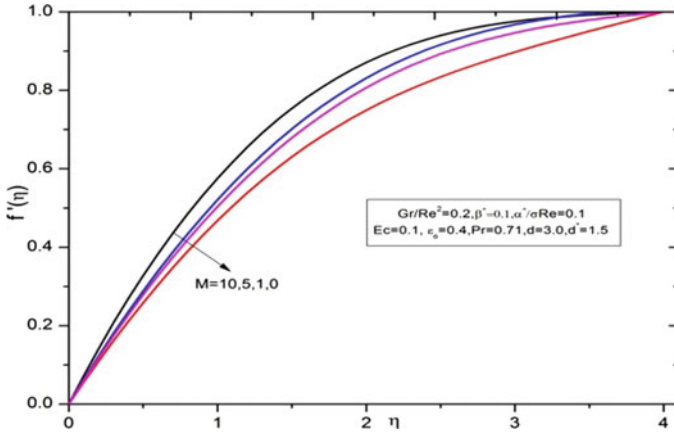
Fig. 1 Variations of M for VP case with fixed Soret and Dufour number observed in velocity plots
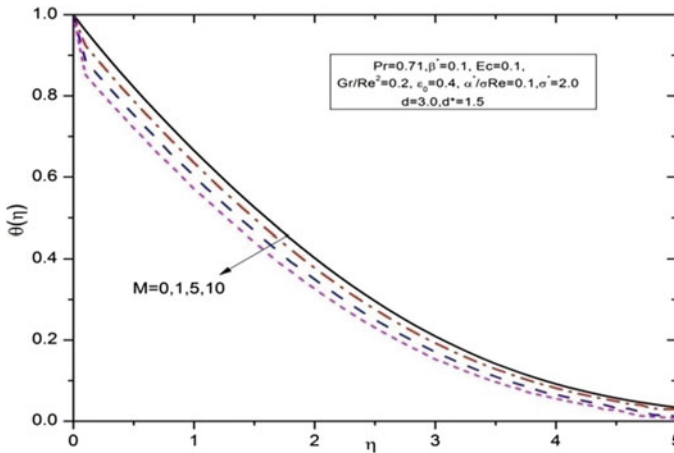
Fig. 2 Variations of M for VP case with fixed Soret and Dufour number in temperature plots

The force arising acts as an accelerating force due to magnetic field, which reduces the frictional resistance leading to increase in velocity profile and decreases the temperature profile as the value of M increases as shown in Figs. 1 and 2 for the variable permeability case fixing the Dufour and Soret parameters. Depending on the gradient of the magnitude of magnetic field, the magnetic force reinforces or weakens the buoyancy effects responsible for the interaction between temperature and velocity distributions.

Variations of N which is ratio of concentration to thermal buoyancy force parameters for variable permeability case, fixing the Soret and Dufour number and M the magnetic field parameter, velocity and concentration graphs are shown in Figs. 3 and 4. The pressure gradient influenced by buoyancy force accelerates the fluid for
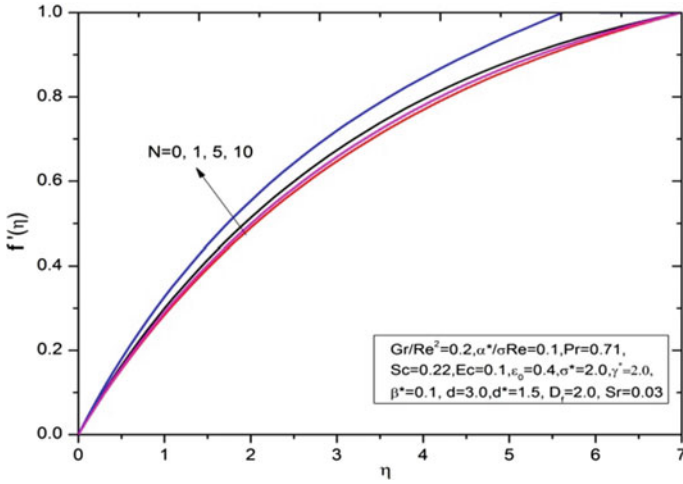
Fig. 3 Variation of buoyancy ratio N for VP case observed in velocity profiles
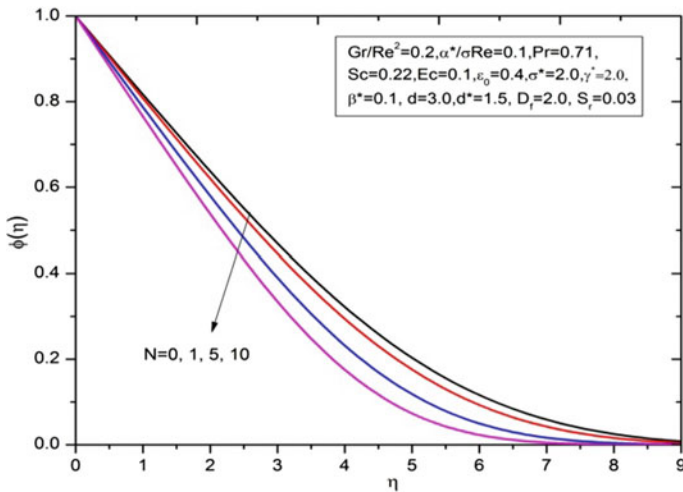
Fig. 4 Variations of buoyancy ratio N for VP case in concentration profiles

lower Pr, for fixed D_f and Sr parameters, the velocity profile is observed for positive values of N ranging from 0 to 10, as N increases velocity increases. But the impact of N is very small for solutal effects as it appears only in momentum equation.

The contribution and effect of species and energy gradients to the flux energy in the flow and inducing significant mass diffusion effects are observed in the profiles for different values of D_f and Sr, respectively, in Figs. 5, 6, 7. An increase in D_f and decrease in Sr observe the rise in the velocity and asymptotes towards the free stream as shown in Fig. 5. The rise in Dufour number and drop in Soret number rise
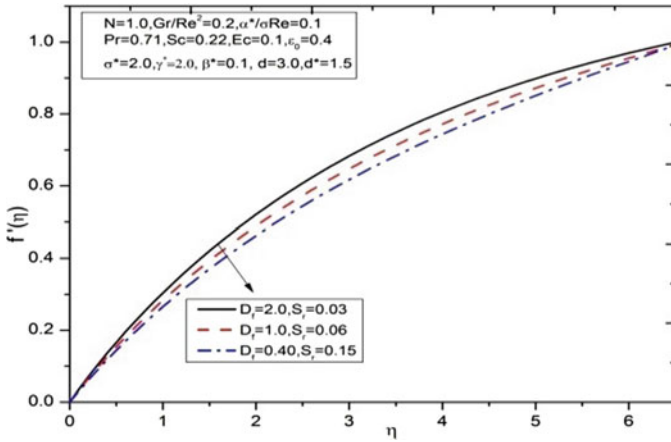
Fig. 5 Variations of values of Sr and D_f numbers for VP case in velocity profiles
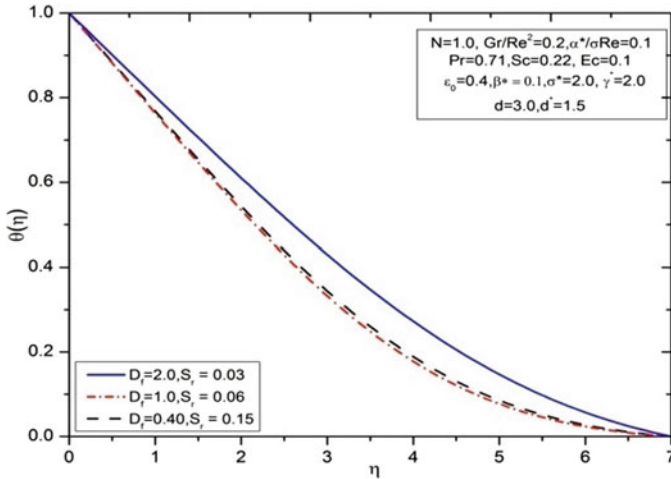
Fig. 6 Variations of Sr and D_f numbers for VP case in temperature profiles

the temperature and steeps downward. For $D_f < 1$, the energy and species marked profiles decay smoothly from the plate and steeps downward to the free stream. However for $D_f > 1$, the profiles fall to zero at the edge of the free stream layer very rapidly as observed in Figs. 6 and 7.

The expression with the Forchheimer term and the ratio of porosity to the permeability which is second-order resistance β^* are varied, and its effects are observed from Figs. 8, 9, 10. Due to the ratio of porosity to the permeability, increase its values leads to increase in velocity profile and decrease in energy and species profiles decreases proportionally.
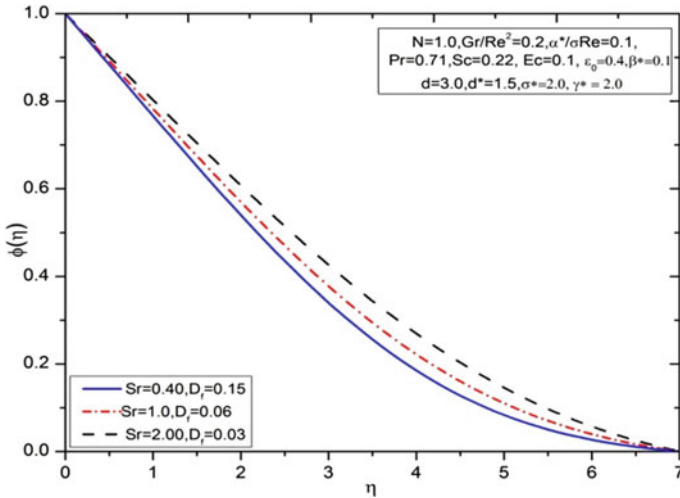
Fig. 7 Variations of Soret and Dufour numbers variable case observed in the graph of concentration
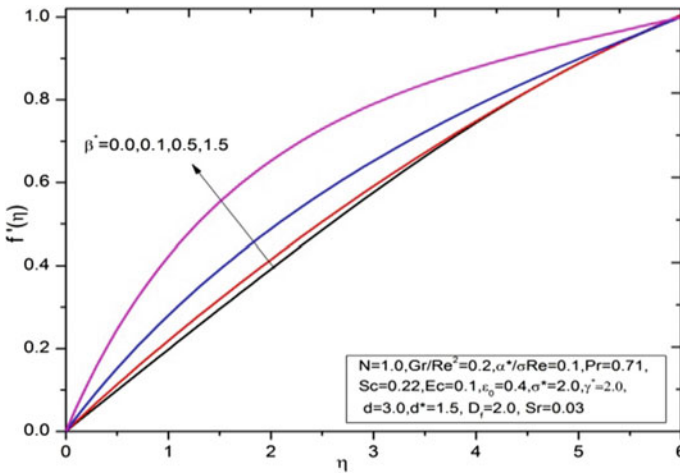
Fig. 8 Variations of second-order resistance β^* for VP case observed in velocity plots

The Richardson number Ri which characterizes the mixed convection, profiles for velocity, energy and species concentration are observed in Figs. 11, 12, 13. For higher buoyancy force, the number rises leading to free convection currents to be carried away from the plate to the free stream with a downward acceleration acting leading the velocity to increase as shown in Fig. 11. Drop in the number enhances the boundary layer for both uniform and variable permeability cases as shown in Figs. 12 and 13. Variable permeability is little more dominant when compared to uniform permeability. The effects of parameter $\alpha^*/\sigma \mathrm{Re}$ for velocity variations are
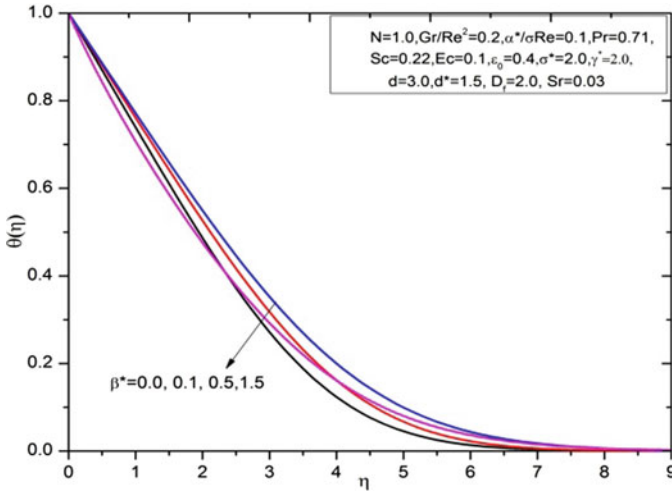
Fig. 9 Variations for β^* for VP case in temperature profiles
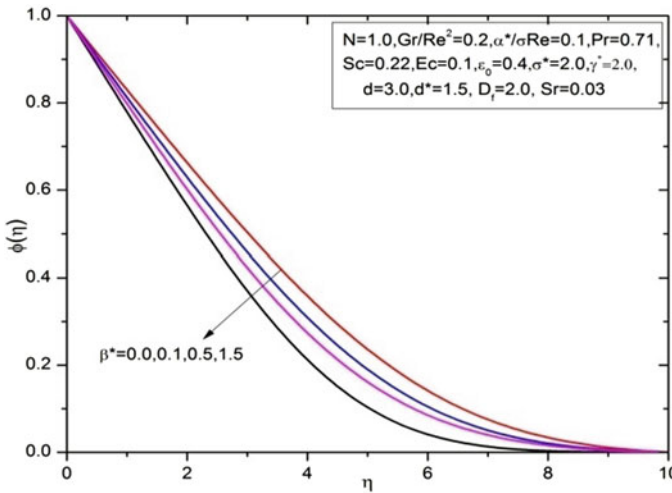
Fig. 10 Variations of β^* for variable case observed in concentration profiles

shown in Fig. 14. Due to the presence of low Reynolds number multiplied with the ratio of viscosities resulting in the range of 0.0–0.5 in the momentum equation causes the velocity to increase with its increasing value.

The significances of Pr on velocity plots are seen in Fig. 15. Near the wall there is a significant overshoot for fluid with low Pr, but for high Pr the overshoot is weak due to the low viscosity of fluid. Importance of Pr in the concentration profiles is very less; hence, variation of Sc is observed in Fig. 16. Increase in its value decreases the
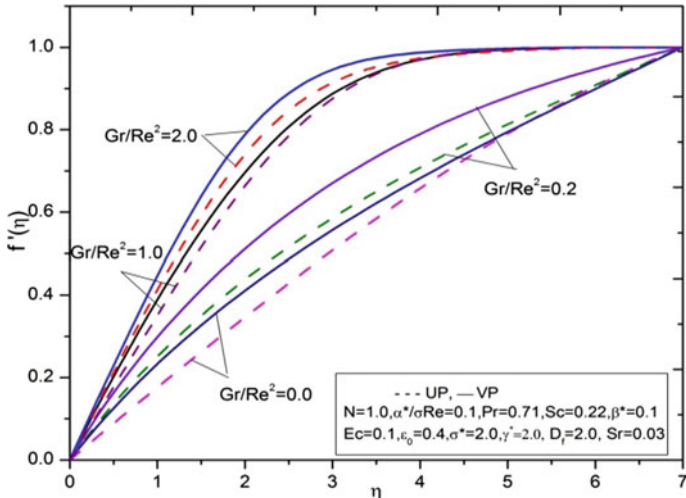
Fig. 11 Velocity distributions for values of Gr/Re^2 for uniform and variable permeability cases
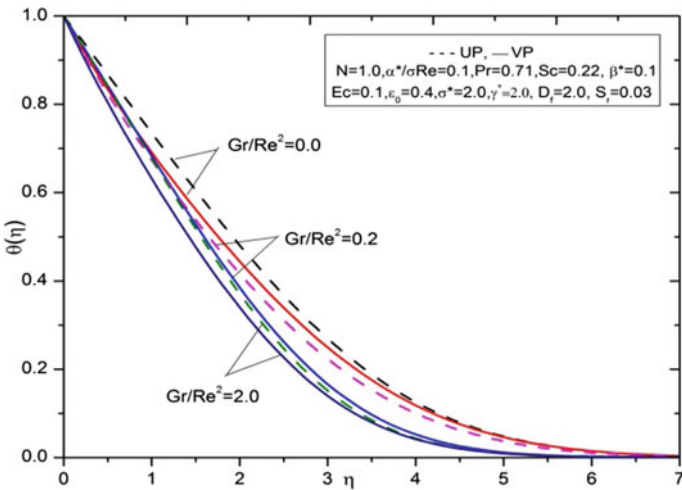
Fig. 12 Temperature distributions observed of Gr/Re^2 values

profiles towards the free stream. The rate of heat and mass transfer with variations of the Nu and Sh as a function of D_f for various values of Sr is observed in Figs. 17 and 18. Since the fluid properties are varied, the heat and mass transport is much prominent comparatively.
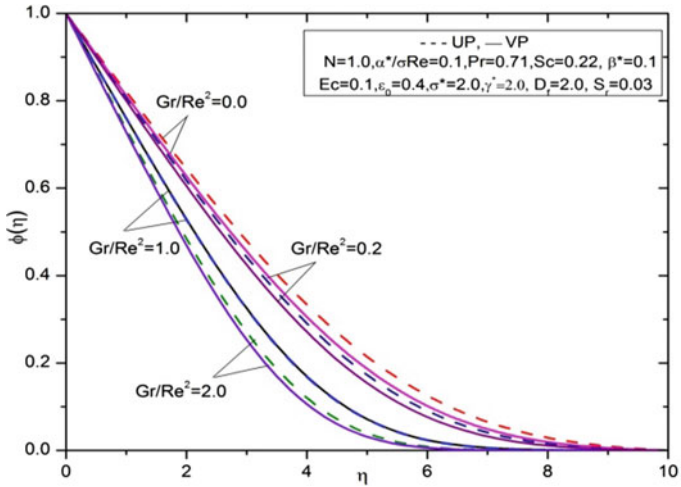
Fig. 13 Concentration distributions for different values of Gr/Re^2 for uniform and variable permeability cases
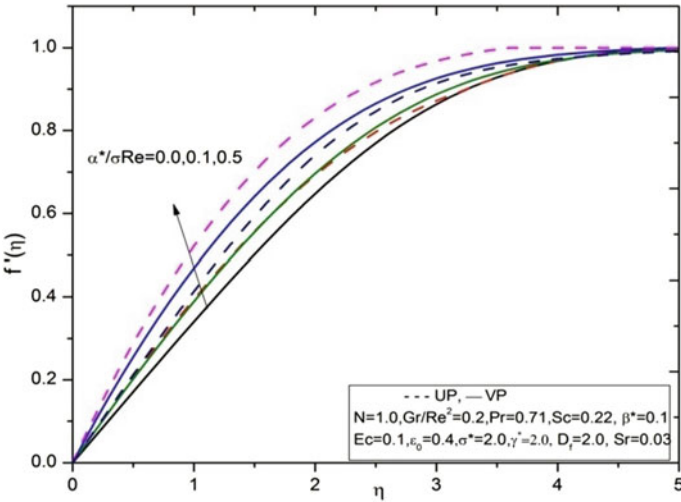
Fig. 14 Velocity distributions observed for $\alpha^*/\sigma Re$ values
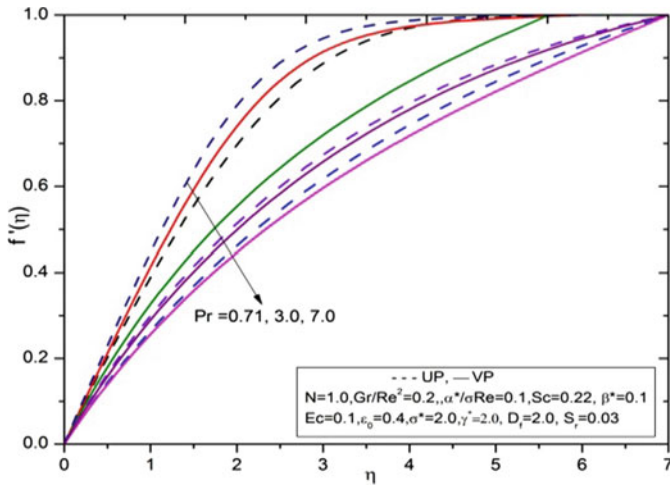
Fig. 15 Variations of Pr observed in velocity profiles
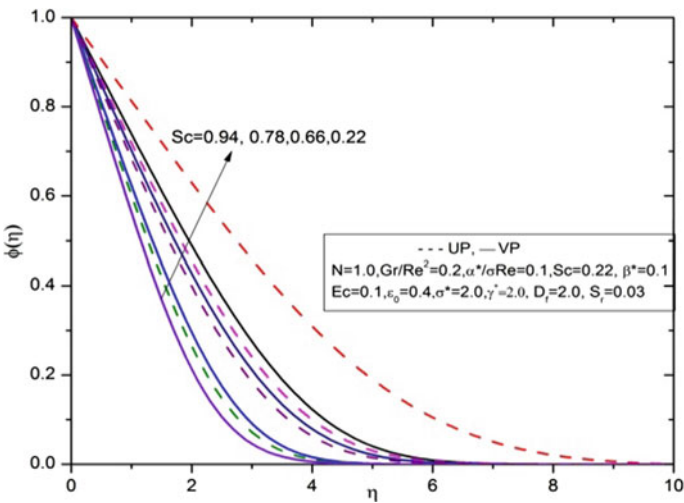
Fig. 16 Variations of Sc observed in concentration profiles
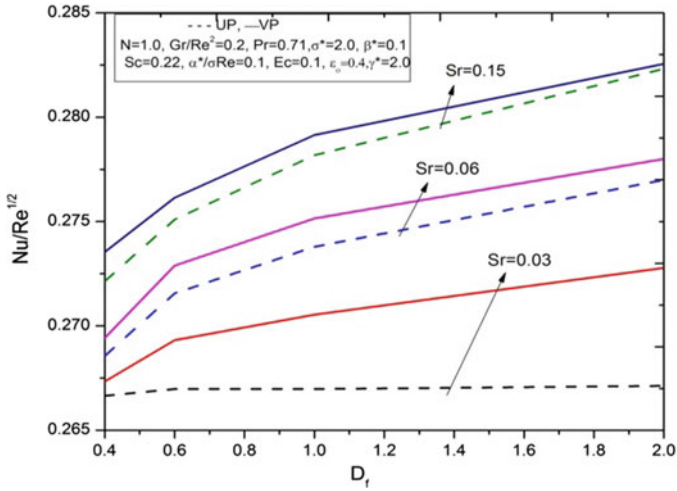
Fig. 17 Variations of Sr with D_f and Nusselt number
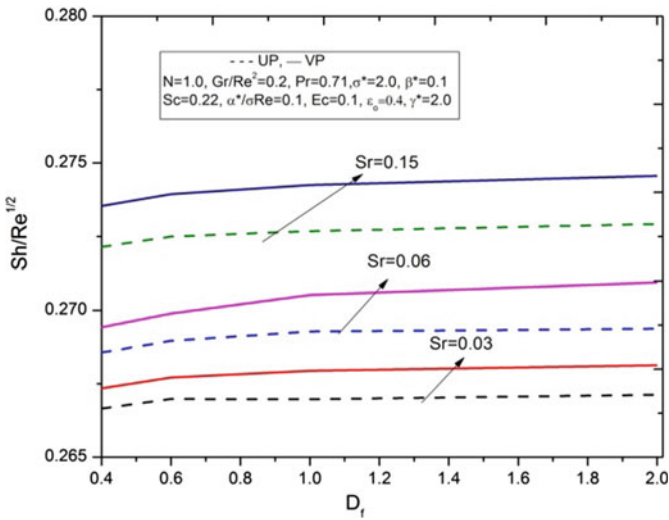
Fig. 18 Variations of Sr with D_f and Sherwood number

References

1. Eckert ERG, Drake RM (1972) Analysis of heat and mass transfer. McGraw-Hill Book, New York
2. Nield DA, Bejan A (1991) Convection in porous media. Springer-Verlag, Berlin
3. Anghel M, Takhar HS, Pop I (2000) Dufour and Soret effects on free convection boundary layer over a vertical surface embedded in a porous medium. J Heat Mass Transfer 43:1265–1274
4. Postelnicu A (2004) Influence of a magnetic field on heat and mass transfer by natural convection from vertical surfaces in porous media considering Soret and Dufour effects. Int J Heat Mass Transfer 47:1467–1472
5. Reddy G, Reddy B (2011) Finite element analysis of Soret and Dufour effects on unsteady MHD free convection flow past an impulsively started vertical porous plate with viscous dissipation. J Naval Archit Mar Eng 8:1–12
6. Alam MS, Rahmam MM (2006) Dufour and Soret effects on mixed convection flow past a vertical porous flat plate with variable suction. Nonlinear Anal Modell Control 11(1):3–12
7. Balasubrahmanyam M, Sudarshan Reddy P, Siva Prasad R (2011) Soret effect on mixed convective heat and mass transfer through a porous medium confined in a cylindrical annulus under a radial magnetic field in the presence of a constant heat source/sink. Int J Appl Math Mech 7(8):1–17
8. Motsa S (2008) On the onset of convection in a porous layer in the presence of Dufour and Soret effects. SJPAM 3:58–65
9. Awad FG, Sibanda P, Motsa S (2010) On the linear stability analysis of a Maxwell fluid with double-diffusive convection. Appl Math Modell 34:3509–3517
10. Zili-Ghedira L, Slimi K, Ben Nasrallah S (2003) Double diffusive natural convection in a cylinder filled with moist porous grains and exposed to a constant wall heat flux. J Porous Media 6(2):123–136
11. Mohammadein AA, El-Shaer NA (2004) Influence of variable permeability on combined free and forced convection flow past a semi-infinite vertical plate in a saturated porous medium. Heat Mass Transfer 40:341–346
12. Nalinakshi N, Dinesh PA, Chandrashekhar DV (2013) Soret and Dufour effects on mixed convection heat and mass transfer with variable fluid properties. Int J Math Arch 4(11):203–215
13. Reddy G, Dinesh PA, Sandeep N (2017) Effects of variable viscosity and porosity of fluid, Soret and Dufour mixed double diffusive convective flow over an accelerating surface. IOP Conf Ser Mater Sci Eng 263: 062012, 1–13
14. Veera Krishna M, Swarnalathamma BV, Chamkha AJ Investigations of Soret, Joule and hall effects on MHD rotating mixed convective ßow past an inÞnite vertical porous plate. J Ocean Eng Sci 4: 263–275. https://doi.org/10.1016/j.joes.2019.05.002
15. Brinkman HC (1947) A calculation of the viscous force exerted by a flowing fluid on a dense swarm of particles. Appl Sci Res A1:27–34
16. Hady FM, Bakier AK, Gorla RSR (1996) Mixed convection boundary layer flow on a continuous flat plate with variable viscosity. Heat Mass Transfer 31:169–172

Chemical Reaction-Driven Ferroconvection in a Porous Medium

Nisha Mary Thomas and S. Maruthamanikandan

Abstract The effect of chemical reaction on the outset of convection of a ferromagnetic fluid in a horizontal porous layer which is heated from below is studied using small perturbation method. Assuming an exothermic zero-order chemical reaction, the eigenvalues are found by employing the Galerkin method. The effect of magnetic parameters and Frank-Kamenetskii number is discussed. It is established that both magnetic forces and chemical reaction accelerate the threshold of ferroconvection. Further, the fluid layer is destabilized marginally when the nonlinearity of magnetization is strong enough.

Keywords Chemical reaction · Ferrofluid · Porous media · Galerkin method

1 Introduction

The fact that an external magnetic field could be used to discipline ferrofluids justifies the employment of ferromagnetic fluids in engineering applications. A number of intriguing and expedient applications of magnetic fluids have emerged due to the enrichment of heat transfer by virtue of ferroconvection [1]. Several researchers got interested in the ferroconvective instability problem since the magnetic force substantially modifies the critical values [2–17].

On the other hand, curiosity in the topic of reaction-driven porous medium convection was stirred by its applications to reactors and oxidation and synthesis of materials [18, 19]. Assuming an exothermic chemical reaction of order zero, Malashetty et al. [20] successfully attacked this problem for a horizontal inert porous layer. They found that nonlinear temperature distribution of the basic state resulting from

N. M. Thomas (✉)
Department of Sciences and Humanities, School of Engineering and Technology,
CHRIST (Deemed to be University), Bengaluru 560074, India
e-mail: nisha.mary@christuniversity.in

S. Maruthamanikandan
Department of Mathematics, School of Engineering, Presidency University,
Itgalpur, Yelahanka, Bengaluru 560064, India
e-mail: maruthamanikandan@presidencyuniversity.in
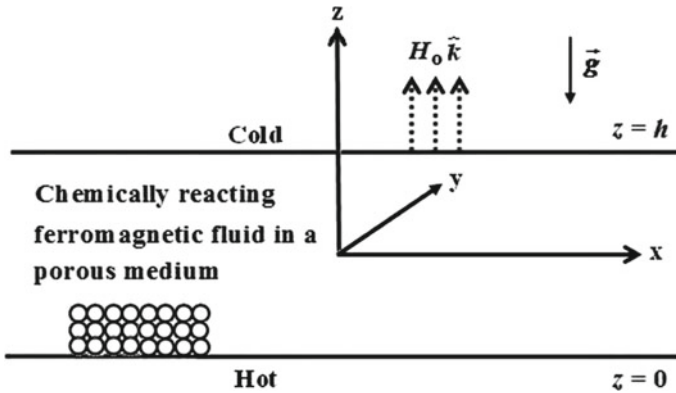
Fig. 1 Schematic of the problem

chemical reaction is responsible, to a great extent, for the instability due to chemical reaction. Using the same formulation, Taj et al. [21] and Khudeja et al. [22, 23] extended the problem with couple-stress and Maxwell viscoelastic fluids, respectively. Zhang et al. [24] examined radiation heat transfer of nanofluids with chemical reaction. Recently, Majeed et al. [25] investigated how the chemical reaction influences the Maxwell ferrofluid along with Soret and suction effects. In this article, we would like to deal with the problem of ferromagnetic instability in a horizontal porous layer of Darcy type in the presence of chemical reaction (Fig. 1).

2 Mathematical Formulation

We consider a chemically reactive ferromagnetic fluid located between two surfaces of infinite length horizontally with finite thickness h. The inert porous layer is cooled at a temperature of T_c from the top. A zero-order reaction can be invoked when the temperature varies slightly in the whole domain from T_c. The governing equations that describe the problem are

$$\nabla \cdot \vec{v} = 0, \tag{1}$$

$$\rho_R \left[\frac{1}{\varepsilon} \frac{\partial \vec{v}}{\partial t} + \frac{1}{\varepsilon^2} (\vec{v} \cdot \nabla) \vec{v} \right] = -\nabla p + \rho \vec{g} - \frac{\mu_f}{k} \vec{v} + \nabla \cdot \left(\vec{H} \vec{B} \right), \tag{2}$$

$$\varepsilon C_f \left[\frac{\partial T}{\partial t} + (\vec{v} \cdot \nabla) T \right] + (1 - \varepsilon)(\rho_R C_o)_s \frac{\partial T}{\partial t}$$

$$+ \mu_o T \left(\frac{\partial \vec{M}}{\partial t} \right)_{V,H} \cdot \left[\frac{\partial \vec{H}}{\partial t} + (\vec{v} \cdot \nabla) \vec{H} \right]$$

$$= K \nabla^2 T + \varepsilon C_f Q \exp\left(-\frac{E}{R_{un} T} \right), \tag{3}$$

$$\rho = \rho_o [1 - \alpha(T - T_c)], \tag{4}$$

$$\vec{M} = \frac{\vec{H}}{H} M(H, T), \tag{5}$$

$$M = M_o + \chi(H - H_o) - K_m(T - T_c). \tag{6}$$

Various physical quantities appearing in Eqs. (1) through (6) have their usual meaning [12, 22, 23].

Maxwell's equations applicable to the problem at hand are

$$\nabla \cdot \vec{B} = 0, \ \nabla \times \vec{H} = \vec{0} \ \text{ and } \ \vec{B} = \mu_o \left(\vec{M} + \vec{H} \right). \tag{7}$$

The boundary conditions of temperature are taken to be

$$T = T_c \ \text{ at } \ z = h \text{ and } T = T_h \ \text{ at } \ z = 0, \tag{8}$$

where $T_h > T_c$. Following the procedure of Malashetty et al. [20], the expression for the basic state temperature reads

$$\theta_b = \log\left(\frac{C_1}{2\text{FK}} \right) + \log\left[1 - \left(\frac{1 - C_2 \exp(-\sqrt{C_1} z)}{1 + C_2 \exp(-\sqrt{C_1} z)} \right)^2 \right], \tag{9}$$

where $C = \frac{Q \exp\left(-\frac{E}{R_{un} T_c}\right)}{T_r}$, $\theta = \frac{T - T_c}{T_r}$, $T_r = \frac{R_{un} T_c^2}{E}$ and FK $= \frac{C h^2}{\kappa}$ is the Frank-Kamenetskii number with $\kappa = \frac{K}{\varepsilon C_f}$. The constants C_1 and C_2 appearing in Eq. (9) are to be determined implicitly from the following equations

$$\exp\left(\sqrt{C_1}\right) \left[\frac{1 - \sqrt{1 - \frac{2\text{FK}}{C_1}}}{1 + \sqrt{1 - \frac{2\text{FK}}{C_1}}} \right] = \left[\frac{1 - \sqrt{1 - \frac{2\text{FK} \exp(\theta_h)}{C_1}}}{1 + \sqrt{1 - \frac{2\text{FK} \exp(\theta_h)}{C_1}}} \right] \tag{10}$$

and

$$C_2 = \exp\left(\sqrt{C_1}\right)\left[\frac{1 - \sqrt{1 - \frac{2\mathrm{FK}}{C_1}}}{1 + \sqrt{1 - \frac{2\mathrm{FK}}{C_1}}}\right], \tag{11}$$

where $\theta_h = \frac{T_h - T_c}{T_r}$.

3 Stability Analysis

Following the standard stability analysis comprising normal modes [2, 17, 20, 26], one obtains the following dimensionless equations

$$\frac{\xi}{V}(D^2 - a^2)U = -R_d a^2 \Upsilon - (D^2 - a^2)U$$
$$- N_d a^2 \left(\frac{d\theta_b}{dz}\right)D\Psi + N_d a^2 \left(\frac{d\theta_b}{dz}\right)\Upsilon, \tag{12}$$

$$\xi\Upsilon + \frac{d\theta_b}{dz}U = (D^2 - a^2)\Psi + F\exp(\theta_b)\Upsilon, \tag{13}$$

$$(D^2 - M_3 a^2)\Psi - D\Upsilon = 0, \tag{14}$$

where Ψ is the magnetic scalar potential and ξ is the growth rate. The parameters of the study at hand are $V = \frac{\varepsilon \mu_f h^2}{\rho_R k \kappa}$, the Vadasz number, $R_d = \frac{\alpha \rho_R g R_u T_c^2 h k}{\mu_f \kappa E}$, the Darcy-Rayleigh number, $N_d = \frac{\mu_o K_m^2 T_r^2 k}{\mu_f \kappa (1+\chi)}$, the Darcy-magnetic number and $M_3 = \frac{H_o + M_o}{H_o(1+\chi)}$, the non-buoyancy magnetization parameter.

3.1 Stationary Instability

Since oscillatory instability can be substantiated to be non-existent, the system of equations concerning stationary instability is given as

$$(D^2 - a^2)U + R_d a^2 \Upsilon - N_d a^2 \left(\frac{d\theta_b}{dz}\right)\Upsilon + N_d a^2 \left(\frac{d\theta_b}{dz}\right)D\Psi = 0, \tag{15}$$

$$(D^2 - a^2)\Upsilon + F\exp(\theta_b)\Upsilon - \left(\frac{d\theta_b}{dz}\right)U = 0, \tag{16}$$

$$(D^2 - M_3 a^2)\Psi - D\Upsilon = 0. \tag{17}$$

The appropriate boundary conditions are

$$U = \Upsilon = D\Psi = 0 \ \text{ at } \ z = 0 \ \text{ and } \ z = 1. \tag{18}$$

4 Method of Solution

Since the presence of variable coefficients in the boundary value problem of the Eqs. (15) through (18) makes it difficult to solve the system analytically, an approximate solution is sought by resorting to the Galerkin method [27]. We therefore assume

$$U = \sum A_j U_j, \quad \Upsilon = \sum B_j \Upsilon_j, \quad \Psi = \sum C_j \Psi_j,$$

where A_j, B_j and C_j are constants. On successfully implementing the Galerkin method, one obtains the following system of homogenous algebraic equations

$$\left.\begin{aligned} D_{ij} A_j + E_{ij} B_j + F_{ij} C_j &= 0, \\ G_{ij} A_j + H_{ij} B_j &= 0, \\ K_{ij} B_j + L_{ij} C_j &= 0, \end{aligned}\right\} \tag{19}$$

where

$$D_{ij} = \langle U_i D^2 U_j \rangle - a^2 \langle U_i U_j \rangle, \ E_{ij} = R_d a^2 \langle U_i \Upsilon_j \rangle - N_d a^2 \left\langle U_i \frac{d\theta_b}{dz} \Upsilon_j \right\rangle,$$

$$F_{ij} = N_d a^2 \left\langle U_i \left(\frac{d\theta_b}{dz}\right) D\Psi_j \right\rangle, \ G_{ij} = \left\langle \Upsilon_i \left(\frac{d\theta_b}{dz}\right) U_j \right\rangle,$$

$$H_{ij} = a^2 \langle \Upsilon_i \Upsilon_j \rangle - \langle \Upsilon_i D^2 \Upsilon_j \rangle - F \langle \Upsilon_i \exp(\theta_b) \Upsilon_j \rangle,$$

$$K_{ij} = \langle \Psi_i D\Upsilon_j \rangle, \ L_{ij} = M_3 \, a^2 \langle \Psi_i \Psi_j \rangle - \langle \Psi_i D^2 \Psi_j \rangle.$$

The trial functions $U_j = \Upsilon_j = \sin[j\pi z]$ and $\Psi_j = \cos[j\pi z]$ are taken so that the boundary and orthogonality conditions are warranted.

5 Results and Discussion

The investigation is concerned with chemical reaction-driven ferromagnetic instability of Darcy type. Galerkin method is adopted to determine the numerical solution of stationary instability. Figure 2 represents the profiles of θ_b with variations in FK. It is noticed that there is a considerable shift from linearity in the temperature profiles
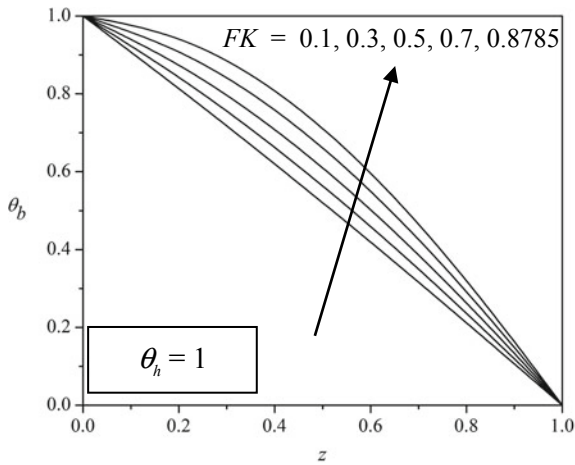
Fig. 2 Basic state temperature profiles

as FK increases. Further, the magnitude of the asymmetry of the curves is on the increase as FK increases. Physically, the escalation in the rate of heat generation due to chemical reaction is accountable for the observed nonlinearity and asymmetry.

Figure 3 puts into perspective the influence of both chemical reaction and forces due to magnetic mechanism. FK is the proportion of the characteristic flow time to reaction time, and N_d signifies the ratio of energy released by magnetic force and the dissipated energy due to viscosity plus temperature fluctuations. It is tacit that both chemical reaction and magnetic forces tremendously contribute to the instability. Indeed, the tight coupling between them is quite obvious from Fig. 3. On the other
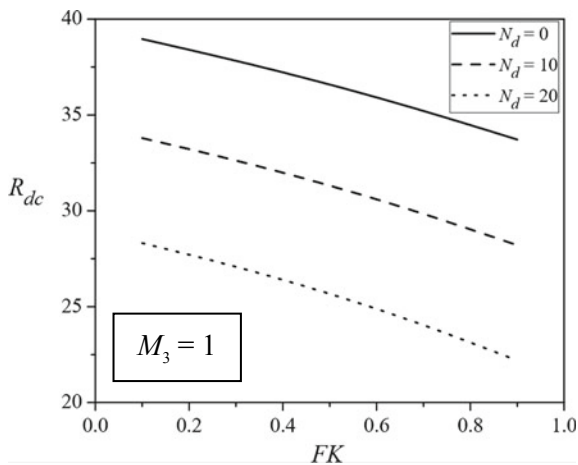
Fig. 3 Plot of R_{dc} versus FK with variations in N_d
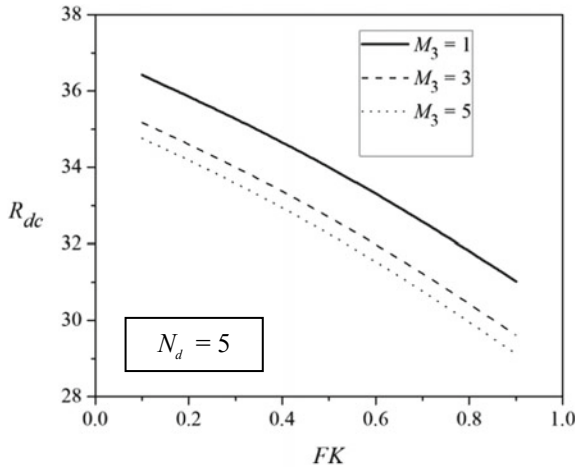
Fig. 4 Plot of R_{dc} versus FK with variations in M_3

hand, Fig. 4 delineates the role of M_3 on the stability of ferromagnetic fluid layer. The magnetization parameter M_3 is representative of the shift towards nonlinearity in the equation of state of the magnetic forces. It is evident from Fig. 4 that the destabilizing nature of M_3 slackens off as it takes on larger values. Further, when FK $= N_d = 0$, the celebrated values $a_c = \pi$ and $R_{dc} = 4\pi^2$ [28] could be acquired.

6 Conclusions

Darcy instability of a chemically reacting ferrofluid is studied by the technique of small perturbations. The analysis has prompted the below-mentioned conclusions:

- The nonlinearity and the asymmetry of the basic state thermal profiles are highly accountable for chemical reaction to have the destabilizing effect.
- Magnetic forces and chemical reaction have destabilizing impact, and they compete with each other in augmenting the threshold of instability.
- Nonlinearity of magnetization escalates convection threshold, and it becomes less strong when M_3 is significantly large.

The implications of the study may have a considerable bearing on engineering applications of heat transfer, wherein microfluidic devices are employed.

References

1. Bashtovoy VG, Berkovsky BM, Vislovich AN (1987) Introduction to thermomechanics of magnetic fluids. Hemisphere, Washington DC
2. Finlayson BA (1970) Convective instability of ferromagnetic fluids. J Fluid Mech 40:753–767
3. Gupta MD, Gupta AS (1979) Convective instability of layer of a ferromagnetic fluid rotating about a vertical axis. Int J Eng Sci 17:271–277
4. Gotoh K, Yamada M (1982) Thermal convection in a horizontal layer of magnetic fluids. J Phys Soc Jpn 51:3042–3048
5. Stiles PJ, Kagan M (1990) Thermoconvective instability of a horizontal layer of ferrofluid in a strong vertical magnetic field. JMMM 85:196–198
6. Aniss S, Belhaq M, Souhar M (2001) Effects of magnetic modulation on the stability of a magnetic liquid layer heated from above. ASME J Heat Transf 123:428–433
7. Abraham A (2002) Rayleigh-Bénard convection in a micropolar ferromagnetic fluid. Int J Eng Sci 40:449–460
8. Maruthamanikandan S (2003) Effect of radiation on Rayleigh-Bénard convection in ferromagnetic fluids. Int J Appl Mech Eng 8:449–459
9. Saravanan S (2009) Centrifugal acceleration induced convection in a magnetic fluid saturated anisotropic rotating porous medium. Transp Porous Med 77:79–86
10. Singh J, Bajaj R (2009) Temperature modulation in ferrofluid convection. Phys Fluids 21:064105
11. Bhuvaneswari M, Sivasankaran S, Kim YJ (2011) Magneto-convection in an enclosure with sinusoidal temperature distributions on both side walls. Numer Heat Transf A 59:167–184
12. Thomas NM, Maruthamanikandan S (2013) Effect of gravity modulation on the onset of ferroconvection in a densely packed porous layer. IOSR J Appl Phys 3:30–40
13. Sivasankaran S, Ananthan SS, Abdul Hakeem AK (2016) Mixed convection in a lid-driven cavity with sinusoidal boundary temperature at the bottom wall in the presence of magnetic field. Scientia Iranica: Trans B Mech Eng 23:1027–1036
14. Vatani A, Woodfield PL, Nam-Trung N, Dao DV (2018) Onset of thermomagnetic convection around a vertically oriented hot-wire in ferrofluid. JMMM 456:300–306
15. Thomas NM, Maruthamanikandan S (2018) Gravity modulation effect on ferromagnetic convection in a Darcy-Brinkman layer of porous medium. J Phys: Conf Ser 1139:012022
16. Mathew S, Maruthamanikandan S (2018) Darcy-Brinkman ferroconvection with temperature dependent viscosity. J Phys: Conf Ser 1139:012023
17. Maruthamanikandan S, Thomas NM, Mathew S (2018) Thermorheological and magnetorheological effects on Marangoni-ferroconvection with internal heat generation. J Phys: Conf Ser 1139:012024
18. Kordylewski W, Krajewski Z (1984) Convection effects on thermal ignition in porous media. Chem. Engg. Sci. 39:610–612
19. Farr WW, Gabitto JF, Luss D, Balakotaiah V (1991) Reaction-driven convection in a porous medium. AIChE J 37:963–985
20. Malashetty MS, Cheng P, Chao BH (1994) Convective instability in a horizontal porous layer with a chemically reacting fluid. Int J Heat Mass Transf 37:2901–2908
21. Taj M, Maruthamanikandan S, Khudeja S (2013) Effect of chemical reaction on convective instability in a horizontal porous layer saturated with a couple-stress fluid. Int J Eng Res Appl 3:1742–1748
22. Akbar SK, Nargund AL, Maruthamanikandan S (2013) Convective instability in a horizontal porous layer saturated with a chemically reacting Maxwell fluid. AIP Conf Proc 1557:130
23. Akbar SK, Nargund AL, Maruthamanikandan S (2015) Thermal instability of chemically reacting Maxwell fluid in a horizontal porous layer with constant heat flux lower boundary. Int J Eng Res Appl 5:168–177
24. Zhang Chaoli, Zheng Liancun, Zhang Xinxin, Chen Goong (2015) MHD flow and radiation heat transfer of nanofluids in porous media with variable surface heat flux and chemical reaction. Appl Math Model 39:65–181

25. Majeed A, Zeeshan A, Ellahi R (2017) Chemical reaction and heat transfer on boundary layer Maxwell Ferro-fluid flow under magnetic dipole with Soret and suction effects. Eng Sci Tech 20:1122–1128
26. Chandrasekhar S (1961) Hydrodynamic and hydromagnetic stability. Oxford University Press, Oxford
27. Finlayson BA (1972) The method of weighted residuals and variational principles. Academic Press, New York
28. Nield DA, Bejan A (2013) Convection in porous media. Springer, New York

Nevanlinna Theory for Existence of Meromorphic Solution to Stuart-Landau Equation

A. Tanuja and P. G. Siddheshwar

Abstract We employ the Nevanlinna theory to investigate the existence of meromorphic solution of the Stuart-Landau equation that is widely used to model supercritical bifurcations occurring in flow systems. We consider the corresponding complex differential equation with sharing value one counting multiplicity or ignoring multiplicity.

Keywords Meromorphic function · Nonlinear differential equation · Nevanlinna theory · Stuart-Landau equation · Sharing value

1 Introduction

Recently, many papers are focusing on complex differential equations [3, 8, 11, 13] and also entire or meromorphic functions with sharing one value [4, 5, 9, 15]. In this article, we find meromorphic solution to Stuart-Landau equation using Nevanlinna theory which is a leading tool for finding the entire or meromorphic solution of complex differential equations.

The main aim of this article is to find meromorphic solution, $\psi(z)$, of differential equation which is as follows

$$\psi' = c_1 \psi - \tilde{c}_3 \psi^3, \tag{1}$$

where c_1 and $\tilde{c}_3$ denotes small functions of ψ. Let $\psi' - 1$ and $\psi' - \psi$ share 0 CM (Counting Multiplicity) with $\overline{N}_{=3}(r, \psi) \neq S(r, \psi)$. In this case ψ and ψ' will share 1 CM. This type of sharing value play a prominent role in obtaining the solution of

A. Tanuja (✉)
Department of Mathematics, Siddaganga Institute of Technology, Tumkur 572103, India
e-mail: a.tanuja1@gmail.com

P. G. Siddheshwar
Department of Mathematics, Bangalore University, Jnana bharathi Campus, Bengaluru 560056, India
e-mail: mathdrpgs@gmail.com

complex differential equations. Throughout this article we make use of basic results and standard notations of Nevanlinna theory [2, 6, 7, 14].

We consider an equation of the form

$$\psi' = c_1 \psi + c_3 \psi^3, \tag{2}$$

where $c_3 = -\tilde{c}_3 < 0$ and while counting multiplicity we consider only odd multiplicity.

The following lemmas shall be put to use in the proof of two theorems.

Lemma 1 *Consider meromorphic function ψ so that ψ' is not a constant then we have either*

$$\left(\psi''\right)^3 = a \left(\psi' - \mu\right)^4, \tag{3}$$

for some non-constant a, or

$$N_{2)}(r, \psi) \leq \overline{N}_{(3}(r, \psi) + N_{2)}\left(r, \frac{1}{\psi' - \mu}\right) + \overline{N}\left(r, \frac{1}{\psi''}\right) + S(r, \psi), \tag{4}$$

where μ is a constant.

Proof Consider

$$\Phi = 2\frac{\psi'''}{\psi''} - 3\frac{\psi''}{\psi' - \mu}. \tag{5}$$

Suppose ψ has a pole z_∞ of order 2 and from Eq. (5) we obtain that

$$\Phi(z) = O((z - z_\infty)^3).$$

Clearly from this we can see that Φ has zero z_∞ with multiplicity 3. Therefore Eq. (3) does not holds from which we infer that $\Phi \not\equiv 0$, then

$$\begin{aligned} N_{2)}(r, H) &\leq N(r, \frac{1}{\Phi}), \\ &\leq T(r, \Phi) + O(1). \end{aligned} \tag{6}$$

Since Φ has poles of order 2 at zeros of ψ'' or $\psi' - \mu$ or multiple poles of ψ. Thus from Eq. (5) we obtain

$$N(r, \Phi) \leq \overline{N}_{(3}(r, \psi) + N_{2)}\left(r, \frac{1}{\psi' - \mu}\right) + \overline{N}\left(r, \frac{1}{\psi''}\right). \tag{7}$$

Again from Eq. (5), we have

$$m(r, \Phi) = S(r, \psi). \tag{8}$$

Adding Eqs. (7) and (8) and the resulting equation is substituted in Eq. (6), we can get Eq. (4).

Lemma 2 *Consider meromorphic function ψ which is a non-constant in nature then we have either Eq.* (4) *holds or*

$$\psi(z) = \frac{27}{2a[z + 3B_1]^2} + \mu z + B_2, \tag{9}$$

where $a \neq 0$, B_1, B_2 and μ are constants.

Proof If ψ be a non-constant and ψ' be a constant then ψ is a polynomial of degree at most 1 such that $N_{2)}(r, \psi) = S(r, \psi)$ due to this Eq. (4) is true. Let us consider ψ' is not a constant now by Lemma 1 if Eq. (4) does not holds then Eq. (3) must hold. Equation (3) can be also be written as

$$\left(\frac{\psi''}{\psi' - \mu} \right)^3 = a(\psi' - \mu). \tag{10}$$

Differentiating Eq. (10), we obtain

$$3 \left(\frac{\psi''}{\psi' - \mu} \right)^2 \left(\frac{\psi''}{\psi' - \mu} \right)' = a\psi''. \tag{11}$$

Combining Eqs. (10) and (11) yields

$$\left(\frac{\psi''}{\psi' - \mu} \right)^{-2} \left(\frac{\psi''}{\psi' - \mu} \right)' = \frac{1}{3}. \tag{12}$$

Integrating Eq. (12) once and then using Eq. (10), we get

$$\psi' - \mu = \frac{1}{a} \left[\frac{-3}{z + 3B_1} \right]^3. \tag{13}$$

By integrating Eq. (13) once and on rearranging, we can get Eq. (9).

We now prove two main results in this section one each on functions involving counting multiplicity(CM) and ignoring multiplicity(IM).

Theorem 1 *Consider meromorphic function ψ which is non-constant in nature satisfying the Eq.* (2). *If $\psi' - 1$ and $\psi' - \psi$ share 0 CM, then we have ψ and ψ' share 1 CM and also ψ will satisfy the equation*

$$\psi(z) = \frac{z + B_1}{1 - ae^{-z}}, \tag{14}$$

where B_1 and $a \neq 0$ are constants.

Proof Clearly from Eq. (2), we have $N_{(3}(r, \psi) + m(r, \psi) = S(r, \psi)$ which implies that $T(r, \psi) = N_{2)}(r, \psi) + S(r, \psi)$. Hence $N_{2)}(r, \psi) \neq S(r, \psi)$, i.e., $N_{=2}(r, \psi) \neq S(r, \psi)$. Following ([1]) we can obtain Eq. (14). Now substituting Eq. (14) in Eq. (2), we get

$$\left[\frac{z + B_1}{1 - ae^{-z}} \right]' = c_1 \left(\frac{z + B_1}{1 - ae^{-z}} \right) + c_3 \left(\frac{z + B_1}{1 - ae^{-z}} \right)^3. \tag{15}$$

Using Eq. (15) we can obtain $c_1(z) = \dfrac{z + B_1 + 2}{2(z + B_1)}$ and $c_3(z) = \dfrac{-1}{(z + B_1)^2}$.

Theorem 2 *Consider meromorphic function ψ which is non-constant in nature satisfying Eq. (2). Let ψ and ψ' sharing 1 IM, now we have either*

$$\psi' - 1 = c_3(\psi - 1)[\psi^2 + \psi - 1], \tag{16}$$

or

$$\psi' - 1 = c_3(\psi - 1)[\psi^2 + \psi + B_1], \tag{17}$$

where B_1 is a constant.

Proof Let z_3 be a zero of $\psi' - 1$ and $c_j(z_3) \not\equiv 0, \infty (j = 1, 3)$ with ψ and ψ' sharing 1 IM with $\psi - 1$ having zero z_3 of order 1. Now from Eq. (2), we get

$$(c_1 + c_3)(z_3) \equiv 1. \tag{18}$$

If $c_1 + c_3 \not\equiv 1$, we have

$$\begin{aligned}
\overline{N}\left(r, \frac{1}{\psi' - 1}\right) = N\left(r, \frac{1}{\psi - 1}\right) &\leq N\left(r, \frac{1}{c_1 + c_3 - 1}\right) + S(r, \psi), \\
&\leq T(r, c_1 + c_3) + S(r, \psi), \\
&\leq T(r, c_1) + T(r, c_3) + S(r, \psi), \\
&= S(r, \psi).
\end{aligned} \tag{19}$$

From Eq. (2), we write

$$N_{(3}(r, \psi) + m(r, \psi) = S(r, \psi). \tag{20}$$

Using Eqs. (19), (20) and one of the result in Yang and Yi [14], we arrive at the following expression

$$\begin{aligned}
T(r, \psi) &\leq N\left(r, \frac{1}{\psi - 1}\right) + \overline{N}\left(r, \frac{1}{\psi' - 1}\right) + \overline{N}(r, \psi) - N_0\left(r, \frac{1}{\psi''}\right) + S(r, \psi), \\
&= \overline{N}_{(3}(r, \psi) + N_{2)}(r, \psi) - N_0\left(r, \frac{1}{\psi''}\right) + S(r, \psi).
\end{aligned}$$

Also we can obtain that

$$N_0\left(r, \frac{1}{\psi''}\right) = S(r, \psi). \tag{21}$$

Using Eqs. (4) and (9), with $\mu = 1$, we get either

$$N_{2)}(r, \psi) \leq \overline{N}_{(3}(r, \psi) + N_{2)}\left(r, \frac{1}{\psi' - 1}\right) + \overline{N}\left(r, \frac{1}{\psi''}\right) + S(r, \psi), \tag{22}$$

or

$$\psi(z) = \frac{27}{2a[z + 3B_1]^2} + z + B_2, \tag{23}$$

where B_1, B_2 and $c \neq 0$ are constants. Using Eqs. (19), (20) and (22), we get

$$T(r, \psi) \leq \overline{N}\left(r, \frac{1}{\psi''}\right) + S(r, \psi). \tag{24}$$

From Eqs. (21) and (24) we write

$$T(r, \psi) \leq \overline{N}_{(3}\left(r, \frac{1}{\psi' - 1}\right) + S(r, \psi). \tag{25}$$

From Eqs. (25) and (19) we arrive at $T(r, \psi) = S(r, \psi)$, which is not possible. Thus Eq. (22) is not true. Now from Eq. (23), we have

$$\psi - 1 = \frac{2a[z + 3B_1]^2[z + B_2 - 1] + 27}{2a[z + 3B_1]^2}, \tag{26}$$

and

$$\psi' - 1 = \frac{-27}{a[z + 3B_1]^3}. \tag{27}$$

Now ψ and ψ' cannot share 1 IM this is not possible. Therefore

$$c_1 + c_3 \equiv 1. \tag{28}$$

Substituting Eq. (28) into the differential Eq. (2), we get

$$\psi' - 1 = c_3(\psi - 1)\left[\frac{1}{c_3} + \psi + \psi^2\right]. \tag{29}$$

If $\frac{1}{c_3} = -1$ or $\left(\frac{1}{c_3}\right)' = 0$, then we respectively arrive at the conclusion (16) or (17). Otherwise, we conclude that

$$N\left(r, \frac{1}{\frac{1}{c_3} + \psi + \psi^2}\right) = S(r, \psi).$$

Suppose $\frac{1}{c_3} + \psi + \psi^2$ has a zero at z_0, say, with multiplicity l so that $\frac{1}{-c_3} \frac{\psi' - 1}{\psi - 1}$ will also has a zero at z_0 with multiplicity l. We now consider the following cases:

(i) $\psi(z_0) = \infty$ or

(ii) $\psi(z_0) = \psi^2(z_0) = \psi'(z_0) = 1$ or

(iii) $c_3(z_0) = \infty$.

If $\psi(z_0) = \infty$, then c_3 will have pole at z_0 with multiplicity $l + 1$, while if $\psi'(z_0) = \psi^3(z_0) = \psi^2(z_0) = \psi(z_0) = 3$, then $\frac{c_1}{-c_3} + 2\frac{c_2}{-c_3} + 3$ has a zero at z_0 with multiplicity 3 and $1 + \left(\frac{c_1}{-c_3}\right)' + \left(\frac{c_2}{-c_3}\right)'$ has a zero of multiplicity min$\{l - 1, l + 1 - t\}$ at z_0, where t represents the possible multiplicity of the pole of c_3 at z_0. From case (iii), c_3 has a pole at z_0 with multiplicity l. Thus we get,

$$N\left(r, \frac{1}{\frac{1}{c_3} + \psi + \psi^2}\right) \leq N(r, c_3) + N\left(r, \frac{1}{\frac{1}{c_3} + 3}\right) + N\left(r, \frac{1}{\left(\frac{1}{c_3}\right)'}\right), \tag{30}$$

$$= S(r, \psi).$$

Equation (29) may now be written as

$$\frac{\left[\frac{1}{c_3} + \psi - z\right]' - \left(\frac{1}{c_3}\right)'}{\left[\frac{1}{c_3} + \psi + \psi^2\right]} = c_3(\psi - 1). \tag{31}$$

From Eqs. (20) and (31) it follows that, if $\left(\frac{1}{c_3}\right)' \not\equiv 0$, then

$$m\left(r, \frac{1}{\frac{1}{c_3} + \psi + \psi^2}\right) = S(r, \psi). \tag{32}$$

From Eqs. (30) and (32) we get $T(r, \psi) = S(r, \psi)$ which is not possible. Therefore, we conclude that

$$\left(\frac{1}{c_3}\right)' \equiv 0. \tag{33}$$

By integrating Eq. (33) w.r.t. 'z', we get

$$\frac{1}{c_3} = B_1. \tag{34}$$

From Eqs. (29) and (34), we arrive at Eq. (17).

2 Conclusion

Nevanlinna theory can be used to find the meromorphic solution of the complex counter part of the Stuart-Landau equation from which we may obtain the solution of the real one. Complex Stuart-Landau equation also appears naturally in Rayleigh-Benard convection problems (see Siddheshwar and Titus [10], and Siddheshwar et al. [12]).

References

1. Al-Khaladi AHH (2013) Meromorphic functions that share one value and the solution of Riccati differential equation. Arab J Math 2:129–137. https://doi.org/10.1007/s40065-012-0057-7
2. Cherry W, Ye Z (2001) Theory of value distribution. Springer Monographs in Mathematics. Springer, Berlin. https://www.springer.com/in/book/9783540664161
3. Cao TB, Xu JF, Chen ZX (2010) On the meromorphic solutions of linear differential equations on the complex plane. J Math Anal Appl 364:130–142. https://doi.org/10.1016/j.jmaa.2009.11.018
4. Fang ML (2002) Uniqueness and value-sharing of entire functions. Comput Math Appl 44:828–831
5. Gundersen GG (1983) Meromorphic functions that share two finite values with their derivative. Pac J Math 105:299–309
6. Hayman WK (1964) Meromorphic functions. Clarendon Press, Oxford
7. Laine I (1993) Nevanlinna theory and complex differential equations. Walter de Gruyter, Berlin. https://www.degruyter.com/viewbooktoc/product/173583
8. Li P (2008) Entire solutions of certain type of differential equations. J Math Anal Appl 344:253–259. https://doi.org/10.1016/j.jmaa.2010.09.026
9. Lin XQ, Lin WC (2011) Uniqueness of entire functions sharing one value. J Math Anal Appl 31B(3):1062–1076
10. Siddheshwar PG, Titus ST (2013) Nonlinear Rayleigh-Benard convection with variable heat source. J Heat Transfer 135(12):1–12. https://doi.org/10.1115/1.4024943
11. Siddheshwar PG, Tanuja A (2019) Existence of meromorphic solution of Riccati-Abel differential equation. Appl Math Sci Comput. 21–28. https://doi.org/10.1007/978-3-030-01123-93
12. Siddheshwar PG, Vanishree RK, Kanchana C (2017) Study of Rayleigh-Benard-Brinkman convection using LTNE model and coupled, real Ginzburg Landau equations. Int J Mech Aero Ind Mech Manuf Eng 6:1197–1204
13. Tang JF, Liao LW (2007) The transcendental meromorphic solutions of a certain type of nonlinear differential equations. J Math Anal Appl 334:517–527
14. Yang CC, Yi HX (2004) Uniqueness theory of meromorphic functions. Kluwer, Dordrecht
15. Zhang XY, Chen JF, Lin WC (2008) Entire or meromorphic functions sharing one value. Comput Math Appl 56:1876–1883. https://doi.org/10.1016/j.camwa.2008.04.008

Influence of Heat Generation/Absorption on 3D Magnetohydrodynamic Casson Fluid Flow Over a Porous Stretching Surface

Nainaru Tarakaramu and P. V. Satya Narayana

Abstract The objective of this numerical analysis is to describe the motion of a magnetohydrodynamic non-Newtonian fluid flow generated by a linear stretching surface with porous medium. The shear stresses defined for Casson fluid model are reduced into the form of nonlinear ODEs with the help of similarity transformations. The translated equations are solved numerically by applying shooting technique along with RKF algorithm. The results are examined for distinct values of physical parameters and are displayed through graphs. It is found that the magnetic field and heat generations are responsible for high heat transfer rate in the fluid flow.

Keywords Heat generation · Casson fluid · Stretching surface · 3D · Porous medium · Magnetohydrodynamic

1 Introduction

Recently, many researchers [1, 2] have focused their interest on the study of non-Newtonian Casson fluid flow over a stretching surface due to their solicitations in engineering and industry branches like, medicine (blood pumping machines), manufacturing (thermal insulators, polymer sheet) and chemical engineering (chemical and material processing, nuclear waste disposal, food preserving). The Casson fluid (Examples: polymer solutions, paints, human being blood, ketchup, drilling mud, mixed fruit juices and shampoos) is one of the non-Newtonian (The constitutive equation shows the nonlinear association between rate of shear strain and shear stress) models which was first introduced by Casson in 1959. Recently, Vijayaragavan and Karthikeyan [1] describe thermal radiation, Dufour and Hall current effects on Casson fluid motion. The mass transfer flow of Casson fluid caused by a stretching porous sheet was numerically examined by Hymavathi and Sridhar [2]. Some of the investigators [3, 4] considered three-dimensional Casson fluid flow generated due to

N. Tarakaramu · P. V. Satya Narayana (✉)
Department of Mathematics, SAS, Vellore Institute of Technology, Vellore, Tamil Nadu 632014, India
e-mail: pvsatya8@yahoo.co.in

the surface stretching. The Casson fluid motion over an exponential stretching surface at heated wall was described by Rehman et al. [5]. They solved the governing equations by Runge–Kutta–Fehlberg (RKF) algorithm and verified the numerical results with help of optimal Homotopy analytical method. Butt et al. [2] discussed the 3D Casson fluid flow induced by an unsteady stretching sheet. Ajayi et al. [6] investigated the 2D Casson fluid flow generated by the horizontal melting surface.

The influence of heat source/sink (transforms the heat energy in three types, one is electrical energy, nuclear reaction and chemical energy) on non-Newtonian fluid flow induced by a porous stretching surface has numerous practical applications in food processing and manufacturing industries [7–10]. Prasad et al. [11] discussed the influence of internal heat generation/absorption on Maxwell fluid over a stretching sheet by applying finite difference shame (Keller-Box method). The effect of heat source/sink on Jeffrey fluid motion through porous medium was studied by Jena et al. [12]. Hakeem et al. [13] explored non-uniform heat generation effect on an incompressible nanofluid past a vertical plate by utilizing Runge–Kutta 4th (RK 4th)-order method along with shooting technique. They found that, the non-uniform heat generation amplifies the heat and velocity profiles and diminishes the solid volume fraction of nanofluid profiles. Some of the researchers [14–17] established the fluid motion over a stretching sheet. Sharada and Shankar [18] presented the heat transfer phenomena on stagnation point flow of a nanofluid towards a stretching surface by applying homotopic procedure.

The aim of current article is to discuss the 3D magnetohydrodynamic Casson fluid flow caused by a sheet stretching with porous medium and heat source. The self-similar functions are used to translate governing PDEs into ODEs. The resulting equations are solved computationally by using MATLAB software. The impact of physical parameters on flow variables is presented and conferred in detail by plotting graphs.

2 Mathematical Analysis

The incompressible electrically conducting three-dimensional MHD Casson fluid flow caused by a stretching surface is considered. The surface can be taken as $z = 0$ and fluid flow occupies the region $z > 0$ as it displayed in Fig. 1. The stretching velocities along x and y-components are defined as: $A = A_w(x) = ax$, $B = B_w(y) = by$. The effect of constant magnetic field H_0 applied in the direction of z which is perpendicular to the surface (i.e. xy-plane). The rheological equation of state for an isotropic and steady Casson fluid flow is taken by (see Refs. [19–22]),

$$
\tau_{ij} = \begin{cases} 2\left(\mu_0 + \dfrac{p_y}{\sqrt{2\pi}}\right)e_{ij}, & \pi > \pi_c \\ 2\left(\mu_0 + \dfrac{p_y}{\sqrt{2\pi}}\right)e_{ij}, & \pi < \pi_c \end{cases}.
$$
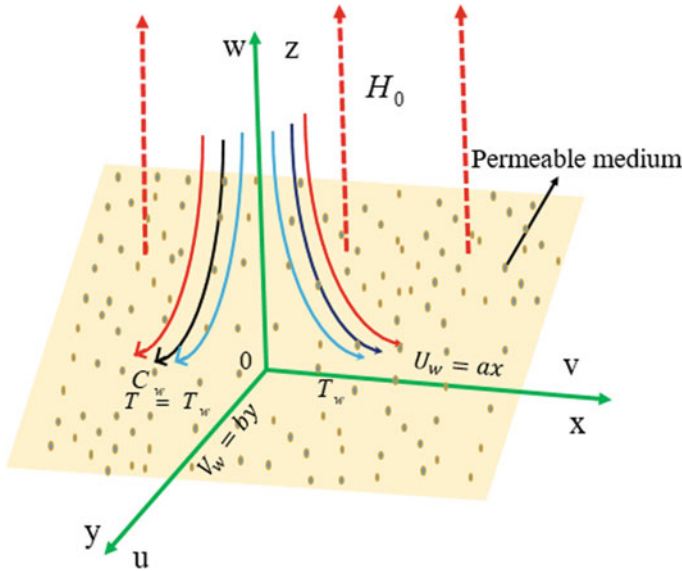
Fig. 1 Physical model of the problem

where $\pi = e_{ij}e_{ij}$ and $p_y = \mu_0\sqrt{2\pi}/\beta$ with the consideration, the basic governing equations for current flow representing continuity, energy and concentration are depicted as follows:

$$\frac{\partial A}{\partial x} + \frac{\partial B}{\partial y} + \frac{\partial C}{\partial z} = 0 \tag{1}$$

$$A\frac{\partial A}{\partial x} + B\frac{\partial A}{\partial y} + C\frac{\partial A}{\partial z} = \upsilon\left(1 + \frac{1}{\beta}\right)\frac{\partial^2 A}{\partial z^2} - \frac{\sigma H_0^2 A}{\rho_f} - \frac{\upsilon A}{K} \tag{2}$$

$$A\frac{\partial B}{\partial x} + B\frac{\partial B}{\partial y} + C\frac{\partial B}{\partial z} = \upsilon\left(1 + \frac{1}{\beta}\right)\frac{\partial^2 B}{\partial z^2} - \frac{\sigma H_0^2 B}{\rho_f} - \frac{\upsilon B}{K} \tag{3}$$

$$A\frac{\partial \Theta}{\partial x} + B\frac{\partial \Theta}{\partial y} + C\frac{\partial \Theta}{\partial z} = \alpha_m\frac{\partial^2 \Theta}{\partial z^2} + \frac{Q_0(\Theta - \Theta_\infty)}{\rho_f C_p} \tag{4}$$

The relevant boundary conditions of the present model as

$$\left.\begin{array}{l} A = A_w = ax \quad B = B_w = by \quad C = 0 \quad \Theta = \Theta_w(x) \ \ at \ \ z = 0 \\ A \to 0 \quad B \to 0 \quad \Theta \to \Theta_\infty \ \ as \ \ z \to \infty \end{array}\right\} \tag{5}$$

The similarity transformations as below

$$A = axf'(\eta), \quad B = ayg'(\eta), \quad \eta = \sqrt{\frac{a}{\upsilon_f}} z \left.\right\}$$

$$C = -\sqrt{a\upsilon}(f+g), \quad \theta(\eta) = \frac{\Theta - \Theta_\infty}{\Theta_w - \Theta_\infty} \qquad (6)$$

In view of Eq. (6), the Eqs. (2)–(5) are transformed to

$$f''(f+g) - f'(M+K_p) - (f')^2 + f'''\left(1 + \frac{1}{\beta}\right) = 0 \qquad (7)$$

$$g''(f+g) - g'(M+K_p) - (g')^2 + g'''\left(1 + \frac{1}{\beta}\right) = 0 \qquad (8)$$

$$\theta'' + \Pr((f'+g')\theta' + H\theta) = 0 \qquad (9)$$

Corresponding boundary conditions are as below

$$\left.\begin{array}{l} f = 0 \quad f' = 1 \quad g = 0 \quad g' = \lambda \quad \theta = 1 \quad \text{at} \ \eta = 0 \\ f' \to 0 \quad g' \to 0 \quad \theta \to 0 \ \text{as} \ \eta \to \infty \end{array}\right\} \qquad (10)$$

Moreover, the skin-friction coefficient and Nusselt number are as below

$$\left.\begin{array}{l} (\text{Re}_x)^{1/2} C_{fx} = -\left(1 + \frac{1}{\beta}\right) f''(0), \quad (\text{Re}_y)^{1/2} C_{fx} = -\left(1 + \frac{1}{\beta}\right) g''(0) \\ (\text{Re}_x)^{-1/2} \text{Nu}_x = -\theta'(0) \end{array}\right\} \qquad (11)$$

3   Results and Discussion

The transformed Eqs. (7), (8) and (9) with boundary conditions (10) have been solved computationally by Runge–Kutta–Fehlberg (RKF) scheme along with shooting technique. The graphical results are shown in Figs. 2, 3, 4, 5, 6, 7, 8, and 9 for different parameters on the flow variables.

The variation of M (Magnetic field parameter) on $f'(\eta)$, $g'(\eta)$ and $\theta(\eta)$ is depicted, respectively, in Figs. 2 and 3. It is demonstrated that, the velocity components along axial and transverse directions diminishes while reverse behaviour follows in the temperature for both three-dimensional ($\lambda = 0.2$) and two-dimensional ($\lambda = 0.0$) cases. It is seen that, the heat convergence monotonically to the boundary first in case of stretching than to that of non-stretching case. The drag coefficient reduces along axial and transverse directions of the fluid flow as presented in Figs. 4 and 5. In addition, the drag coefficient is more in the presence of porous medium than to

Fig. 2 Variation of M on $f'(\eta)$, $g'(\eta)$

$\lambda=0.8$, $\beta=0.5$, H=0.2, $k_P=0.2$, Pr=6.2

$f'(\eta)$

$g'(\eta)$

M=0.2, 0.4, 0.6, 0.8

Fig. 3 Variation of M on $\theta(\eta)$

$\beta=0.5$, H=0.1, $K_P=0.2$, Pr=6.2

$\lambda=0.0$

$\lambda=0.2$

M=0.5, 1.0, 1.5, 2.0
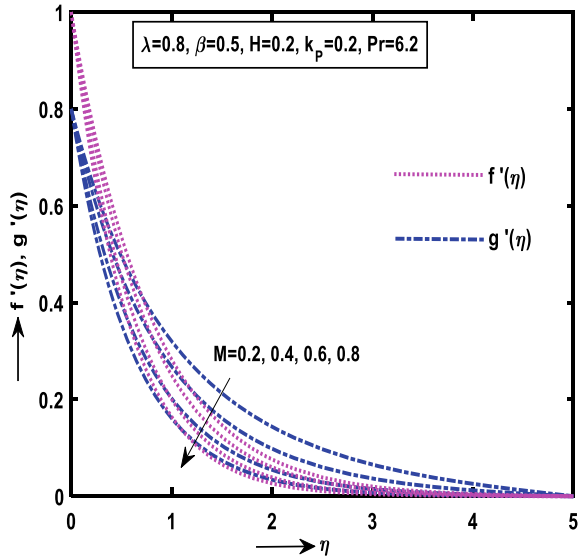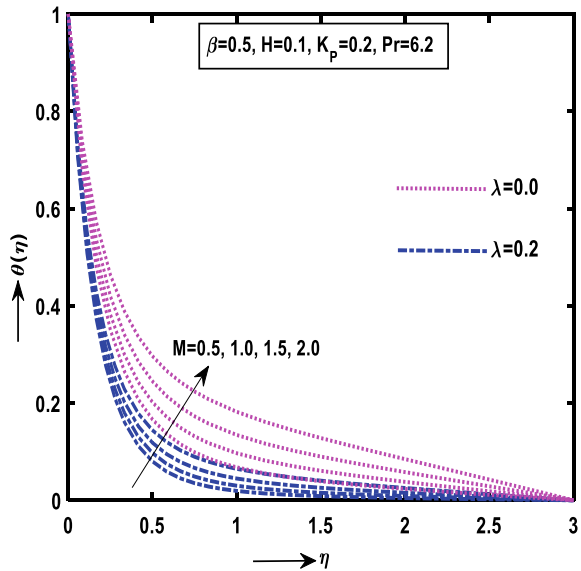
that of non-porous medium. Physically, Lorentz force amplifies the heat in thermal boundary layer and reduces the fluid motion.

The impact of β, K_p on $f'(\eta)$, $g'(\eta)$ is plotted, respectively, in Figs. 6 and 7. As the yield stress is inversely proportional to the Casson fluid, ascending values of β produce high viscosity and weaker yield stress. Such viscosity causes to reduce the velocities along x, y-directions as depict in Fig. 6. Figure 7 characterized the

Fig. 4 Variation of M on $\mathrm{Re}_x^{1/2} C_{fx}$
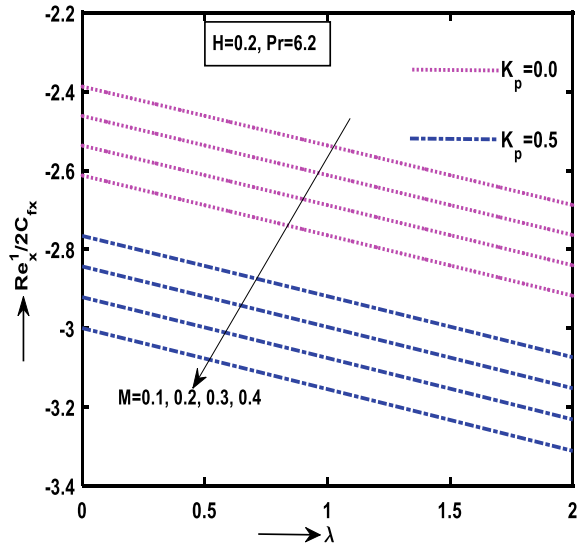
Fig. 5 Variation of M on $\mathrm{Re}_x^{1/2} C_{fy}$
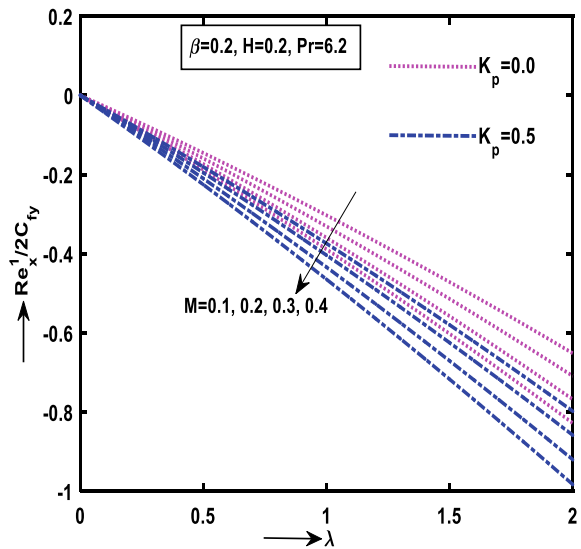
influence of porous parameter along axial and transverse velocities. Physically, the porosity parameter is interrelated between kinematic viscosity υ and permeability of porous medium K. The fluid velocity diminishes in both directions due to high porosity.

The significant variation of Pr (Prandtl number) on temperature is illustrated in Fig. 8. The temperature $\theta(\eta)$ diminishes with amplify values of Pr and reduces the

Fig. 6 Variation of β on $f'(\eta), g'(\eta)$

$\lambda=0.8, H=0.1, K_p=0.2, M=8, Pr=6.2$

$f'(\eta)$

$g'(\eta)$

$\beta=0.1, 0.2, 0.3, 0.4$
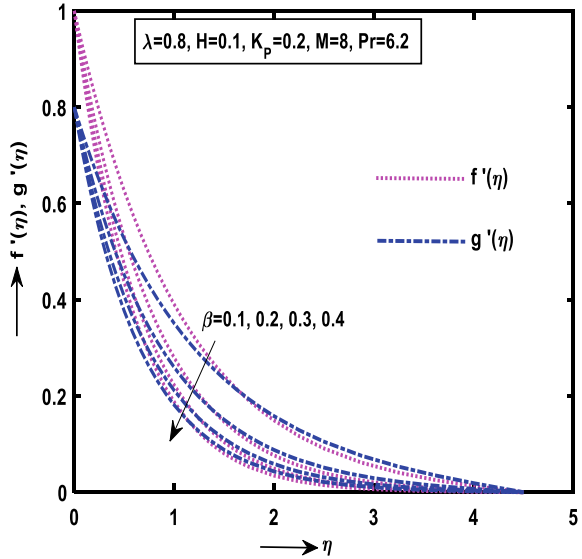
Fig. 7 Variation of K_p on $f'(\eta), g'(\eta)$

$\lambda=0.8, \beta=0.5, H=0.1, M=0.2, Pr=6.2$

$f'(\eta)$

$g'(\eta)$

$K_p=0.2, 0.4, 0.6, 0.8$
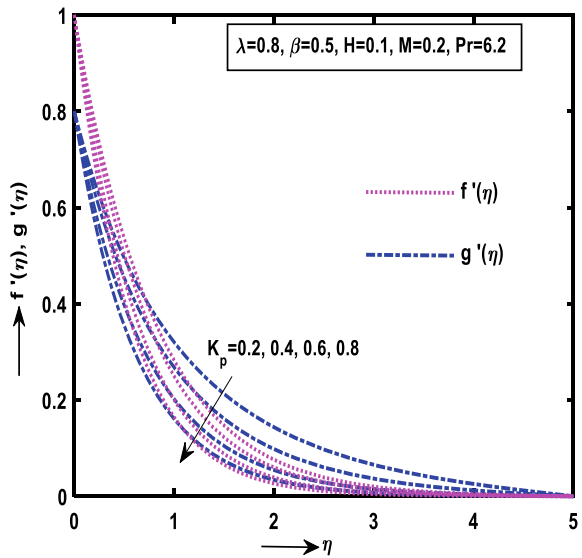
thermal boundary layer thickness. Physically, the Prandtl number is proportional to kinematic viscosity, as ascending values of Pr produce weaker thermal conductivity.

The characterization of heat generation and stretching ratio parameter on rate of heat transfer for various cases of magnetic field parameter is discussed in Fig. 9. It is noticed that, the rate of heat transfer amplifies for all the cases. Moreover, it is

Fig. 8 Variation of Pr on $\theta(\eta)$
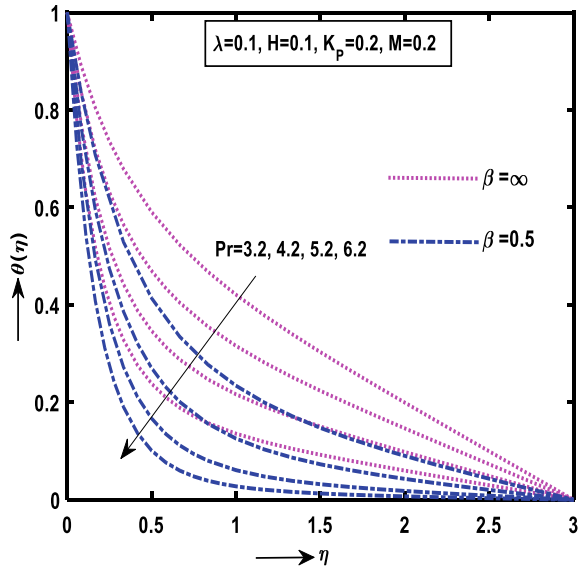
Fig. 9 Variation of H on $\mathrm{Re}_x^{-1/2}\mathrm{Nu}_x$
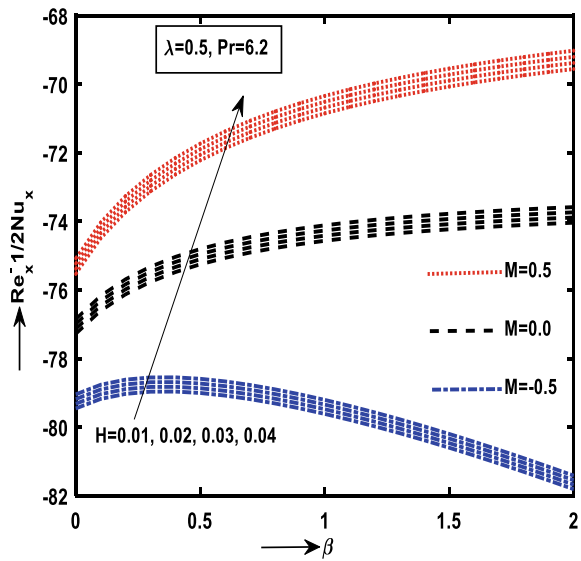
observed that the rate of heat transfer is very low for the presence of magnetic field than to that of non-magnetic field case.

Tables 1 and 2 depict the comparison values skin-friction coefficient for various values of M, β with those of Sarah et al. [23], Nadeem et al. [24] Gupta and Sharma [25] and Ahmad and Nazar [26]. In the absence of $H = 0$, $K = 0$, Pr $= 0$, and

Table 1 Comparison of $-\left(1+\frac{1}{\beta}\right)f''(0)$ (skin-friction coefficient) in the absence of $H=0$, $Pr=0$, $K_p=0$ for various values of M

M	β	Present study	Sarah et al. [23]	Nadeem et al. [24]	Gupta and Sharma [25]	Ahmad and Nazar [26]
0.0	∞	1.00000	1.00000	1.0004	1.0003181	1.0042
	1.0	1.41421	1.41421	1.4142	1.4142136	–
	2.5	1.18321	–	–	–	–
	3.5	1.13389	–	–	–	–
	5.0	1.09544	1.09544	1.0954	1.0954675	–
10	∞	3.31662	3.31662	3.3165	3.3165824	3.3165
	1.0	4.69041	4.69042	4.6904	4.6904349	–
	2.5	3.92428	–	–	–	–
	3.5	3.76069	–	–	–	–
	5.0	3.63318	3.63318	3.6331	3.6331824	–
100	∞	10.04987	10.04987	10.049	10.049864	10.049
	1.0	14.21670	14.21267	14.2127	14.212668	–
	2.5	11.89117	–	–	–	–
	3.5	11.39548	–	–	–	–
	5.0	11.00908	11.00909	11.0091	11.009112	–

Table 2 Comparison of $-\left(1+\frac{1}{\beta}\right)f''(0)$ (skin-friction coefficient) in the absence of $H=0$, $Pr=0$, $K_p=0$ for $\lambda=1$

M	β	Present study $-\left(1+\frac{1}{\beta}\right)f''(0)$	Nadeem et al. [24]
0.0	∞	1.1737	–
	1.0	1.6598	1.6599
	2.5	1.3887	–
	3.5	1.3308	–
	5.0	1.2857	1.2857
10	∞	3.3672	3.3667
	1.0	4.7619	4.7620
	2.5	3.9841	–
	3.5	3.8180	–
	5.0	3.6886	3.6886
100	∞	10.0664	10.066
	1.0	14.2361	14.2361
	2.5	11.9107	–
	3.5	11.4142	–
	5.0	11.5585	11.0272

$\Gamma = 0$. It is perceived that the outcomes are in very good agreement up to four decimal places for matching earlier articles.

4   Conclusion

This Mathematical model is related to study the impact of heat source on three-dimensional magnetohydrodynamic Casson fluid flow over a porous stretching surface. It is analysed by applying shooting technique with 4th order Runge-Kutta-Fehlberg algorithm. The main points of the current study are listed below:

- The temperature of the fluid in case of threedimensional ($\lambda = 0.2$) is more than that of twodimensional ($\lambda = 0.0$).
- The temperature of the non-Newtonian fluid ($\beta = 0.5$) is more than that of viscous fluid ($\beta = \infty$).
- The drag coefficients along axial and normal directions are more in case of non-porous medium than to that of porous medium.
- The rate of heat transfer is more in the presence of magnetic field.

Appendix

Heat absorption parameter $= H = \frac{Q_0}{a(\rho c)_f}$, Porous medium $= K_p = \frac{\upsilon}{K_a}$, Magnetic field parameter $= M = \frac{\sigma H_0^2}{\rho_f a}$, Prandtl number $= \text{Pr} = (\upsilon/\alpha_m)$, Casson fluid parameter $= \chi = \mu_0 \sqrt{2\pi c}/p_y$, Kinematic viscosity $= \upsilon = \mu/\rho_f$, Stretching ratio parameter $= \lambda = b/a$, μ_0 Plastic dynamic viscosity of non-Newtonian fluid.

References

1. Thammanna GT, Ganesh Kumar K, Ramesh GK, Prasannakumara BC (2017) Three dimensional MHD flow of couple stress Casson fluid past an unsteady stretching surface with chemical reaction. Results Phys 7:4104–4110
2. Gireesha BJ, Archana M, Prasannakumara BC, Reddy Gorla RS, Makinde OD (2017) MHD three dimensional double diffusive flow of Casson nanofluid with Buoyancy forces and non-linear thermal radiation over a stretching surface. Int J Num Methods Heat Fluid Flow 27(12):2858–2878. https://doi.org/10.1108/HFF-01-2017-0022
3. Vijayaragavan R, Karthikeyan S (2018) Hall current effect on chemically reacting MHD Casson fluid flow with Dufour effect and thermal radiation. Asian J App Sci Tech 2(2):228–245
4. Hymavathi T, Sridhar W (2018) Numerical solution to boundary layer flow and mass transfer of Casson fluid over a porous stretching sheet with chemical reaction and suction. J Comput Math Sci 9(6):599–608

5. Pramanik S (2014) Casson fluid flow and heat transfer past an exponentially porous stretching surface in presence of thermal radiation. Ain Shams Eng J 5:205–212

6. Rehman SU, Haq RU, Lee C, Nadeem S (2017) Numerical study of non-Newtonian fluid flow over an exponentially stretching surface: an optimal HAM validation. J Braz Soc Mech Sci Eng 39(5):1589–1596. https://doi.org/10.1007/s40430-016-0687-3

7. Butt AS, Tufail MN, Ali A (2016) Three-dimensional flow of a magnetohydrodynamic Casson fluid over an unsteady stretching sheet embedded into a porous medium. J Appl Mech Tech Phys 57(2):283–292

8. Ajayi TM, Omowaye AJ, Animasaun IL (2017) Viscous dissipation effects on the motion of Casson fluid over an upper horizontal thermally stratified melting surface of a paraboloid of revolution: boundary layer analysis. *Hindawi J App Math* 1–13. https://doi.org/10.1155/2017/1697135

9. Soomro FA, Haq RU, Mdallal QMA, Zhang Q (2018) Heat generation/absorption and nonlinear radiation effects on stagnation point flow of nanofluid along a moving surface. Results Phys 8:404–414

10. Aziz A, Alsaedi A, Muhammad T, Hayat T (2018) Numerical study for heat generation/absorption in flow of nanofluid by a rotating disk. Results Phys 8:785–792

11. Jha BK, Yusuf TS (2017) Transient-free convective flow with heat generation/absorption in an annular porous medium: a semi-analytical approach. J Process Mech Eng 232(18):599–612

12. Hayat T, Muhammad T, Shehzad SA, Alsaedi A (2017) An analytical solution for magnetohydrodynamic Oldroyd-B nanofluid flow induced by a stretching sheet with heat generation/absorption. Int J Therm Sci 111:274–288

13. Prasad KV, Vajravelu K, Sujatha A (2013) Influence of internal heat generation/absorption, thermal radiation, magnetic field, variable fluid property and viscous dissipation on heat transfer characteristics of a Maxwell fluid over a stretching sheet. J Appl Fluid Mech 6(2):249–256

14. Jena S, Mishra SR, Dash GC (2017) Chemical reaction effect on MHD Jeffery fluid flow over a stretching sheet through porous media with heat generation/absorption. Int J Appl Comput Math 3(2):1225–1238. https://doi.org/10.1007/s40819-016-0173-8

15. Hakeem AKA, Ganga B, Ansari SMY, Ganesh NV, Rahman MM (2016) Nonlinear studies on the effect of non-uniform heat generation/absorption on hydromagnetic flow of nanofluid over a vertical plate. Nonlinear Anal Model Contr 22(1):1–16. https://doi.org/10.15388/NA.2017.1.1

16. Venkateswarlu B, Satya Narayana PV, Tarakaramu N (2018) Melting and viscous dissipation effects on MHD flow over a moving surface with constant heat source. Trans A Razmadze Math Inst 172(3):619–630. https://doi.org/10.1016/j.trmi.2018.03.007

17. Satya Narayan PV, Tarakaramu N, Makinde OD, Venkateswarlu B (2018) Sarojamma G (2018) MHD stagnation point flow of viscoelastic nanofluid past a convectively heated stretching surface. Defect Diff Forum Subm 387:106–120. https://doi.org/10.4028/www.scientific.net/DDF.387.106

18. Tarakaramu N, Ramesh Babu K, Satyanarayana PV (2018) Effect of nonlinear thermal radiation, heat source on MHD 3D Darcy-Forchheimer flow of nanofluid over a porous medium with chemical reaction. Int J Eng Tech 7(4.10):605–609

19. Satya Narayana PV, Tarakaramu N, Akshit SM, Ghori JP (2017) MHD flow and heat transfer of an Eyring-Powell fluid over a linear stretching sheet with viscous dissipation -A numerical study. Front Heat Mass Transf 9(9):1–5

20. Hayat T, Qayyum S, Alsaedi A, Shafiq A (2016) Inclined magnetic field and heat source/sink aspects in flow of nanofluid with nonlinear thermal radiation. Int J Heat Mass Transf 103:99–107

21. Nadeem S, Ul HR, Lee C (2012) MHD flow of Casson fluid over an exponentially shrinking sheet. Sci Iran 19(6):1550–1553

22. Nakamura M, Sawada T (1988) Numerical study on the flow of a non-Newtonian fluid through an axisymmetric stenosis. J Biomech Eng 110:137–143

23. Sarah I, Mondal S, Sibanda P (2015) Unsteady Casson nanofluid flow over a stretching sheet with thermal radiation, convective and slip boundary conditions. Alexandria Eng J 55:1025–1035

24. Nadeem S, Haq RU, Akbar NS (2014) MHD three-dimensional boundary layer flow of Casson nanofluid past a linearly stretching sheet with convective boundary condition. IEEE Trans Nanotech 13:109. https://doi.org/10.1109/tnano.2013.2293735
25. Gupta S, Sharma K (2017) Numerical simulation for magnetohydrodynamic three dimensional flow of Casson nanofluid with convective boundary conditions and thermal radiation. Eng Comp 1–13:378. https://doi.org/10.1108/EC-02-2017-0064
26. Ahmad K, Nazar R (2011) Magnetohydrodynamic three-dimensional flow and heat transfer over a stretching surface in a viscoelastic fluid is discussed. J Sci Technol 3(1):1–14

Radiation and Chemical Reaction Effects on Unsteady Eyring–Powell Nanofluid Flow Over a Moving Surface

Nainaru Tarakaramu and P. V. Satya Narayana

Abstract The influence of heat source and radiation on magnetohydrodynamic, chemically reacting non-Newtonian nanofluid flow generated by a moving surface is analysed in this study. This nanofluid mathematical model is defined based on Brownian motion and thermophoresis effects. The similarity variables are adopted to convert the governing flow equations into coupled ODE's and hence solved by the RKF method with shooting technique. The distribution of different flow parameters on the flow, energy and species concentration is discussed and displayed graphically. The results revile that the drag coefficient and rate of heat transfer of the liquid along x-axis decrease for higher values of stretching parameter. In addition, the suction parameter shows an opposite behaviour on the above-said flow variables. The outcomes appear to be same with those of outstanding publicised results as a special limiting case.

Keywords Thermal radiation · Heat generation · Eyring–Powell · Nanofluid

1 Introduction

Nowadays, the study of rheology over various geometrical models has received the attention of many researchers in view of their extensive industrial and scientific applications such as: applied science (polymeric fluids, food processing) and mechanical engineering (thinning of copper wires and annealing). Eyring–Powell liquid was first developed by Powell and Eyring [1] which is one of the rheological fluids. Recently, Agbaje et al. [2] explored the non-Newtonian nanofluid characteristics on unsteady boundary-layer flow generated by a shrinking surface. The impact of radial magnetic field and Darcy–Forchheimer relation on Eyring–Powell fluid through a curved channel was observed by Hayat et al. [3]. They found that the Brownian and thermophoresis parameters show opposite effect on temperature and concentration distributions. The non-Newtonian nanoliquid motion through a nonlinear stretching

N. Tarakaramu · P. V. Satya Narayana (✉)
Department of Mathematics, SAS, Vellore Institute of Technology, Vellore, Tamil Nadu 632014, India
e-mail: pvsatya8@yahoo.com

surface with different physical situations was explored [4–7]. Mahanthesh et al. [8] analysed the unsteady electrically conducting Eyring–Powell nanofluid flow caused by a sheet stretching. They concluded that in heating process the thermal radiation plays a vital role. The non-Newtonian characteristics of different fluid flows along with diverse heat transfer conditions are presented by [9–14]. Jalil and Imran [15] presented the heat transfer characteristics of Powell fluid motion generated by a sheet stretching. Afridi and Qasim [16] discussed the nonlinear radiation influence over a moving parallel stream and conclude that the Bejan number decreases by enhancing the thermal radiation parameter. Alharbi et al. [17] explored the influence of MHD non-Newtonian fluid flow due to an oscillating porous stretching sheet in the presence of entropy generation. The influence of multiple slip effects on non-Newtonian fluid motion generated by a nonlinear stretching sheet was presented Majeed et al. [18]. It is concluded that the increase of slip parameter diminished the drag force and increased the rate of heat transfer. Khan et al. [19] analysed analytically the steady 2D magnetohydrodynamic non-Newtonian fluid flow caused by an inclined surface.

The nanofluid motion of gyrotactic microorganism through an upper layer parabola of revolution with various thermal effects was developed Makinde et al. [20]. Satyanarayana et al. [21] presented the numerical results on non-Newtonian fluid flow generated by a sheet stretching in the presence of chemical reaction. Tarakaramu and Satya Narayana [22] presented the effects of MHD on unsteady thermally radiative fluid flow towards a stretching sheet. The influence of chemical reaction on 3D flow of Darcy–Forchheimer flow over a sheet stretching was explored by Tarakaramu et al. [23]. Some of nanofluid flows along with non-Newtonian liquid due to sheet stretching over different flow geometries were presented [24–31]

This work explores the influence the thermal radiation and chemical reaction on unsteady Eyring–Powell nanofluid flow generated due to stretching. The transformed basic flow equations are solved computationally by RKF algorithm with shooting procedure. The effects of different physical parameters on flow field are discussed through graphs and associated with previously published results. The outcomes established good agreement with the available results.

2 Mathematical Formulation

Two dimensional an unsteady, thermally radiating and chemically reacting Eyring–Powell nanofluid flow caused due to the surface moving with a velocity $A_w(x, t)$ and free stream velocity $A_e(x, t)$ is considered. The moving surface should coincide at $y = 0$. The fluid flow region is $y > 0$. The free stream and fluid motion on moving surface are in the direction as displayed in Fig. 1. The mass flux velocity is v_0 injection or with drawl of the fluid for $A_0 > 0$, and the constant velocity A_0 is suction for $A_0 < 0$. The suction/injection velocity towards the surface and surface temperature is $\Theta_w(x)$.

The equations of continuity, boundary momentum, energy and nanoparticle concentrations for Eyring–Powell fluid (see Refs. [1, 32]) are:

$$\frac{\partial \tilde{A}}{\partial x} + \frac{\partial \tilde{B}}{\partial y} = 0, \tag{1}$$

$$\frac{\partial \tilde{A}}{\partial t} + \tilde{A}\frac{\partial \tilde{A}}{\partial x} + \tilde{B}\frac{\partial \tilde{B}}{\partial y} = A_e \frac{\partial A_e}{\partial x} + (1+\varepsilon)\frac{\partial^2 A}{\partial y^2} - \varepsilon\delta\left(\frac{\partial \tilde{A}}{\partial y}\right)^2\left(\frac{\partial^2 \tilde{A}}{\partial y^2}\right), \tag{2}$$

$$\frac{\partial \tilde{\Theta}}{\partial t} + \tilde{A}\frac{\partial \tilde{\Theta}}{\partial x} + \tilde{B}\frac{\partial \tilde{\Theta}}{\partial y} = \frac{\alpha_m}{\rho c_f}\left(\frac{\partial^2 \tilde{\Theta}}{\partial y^2}\right) + \frac{Q_0(\tilde{\Theta} - \tilde{\Theta}_\infty)}{\rho c_f} - \frac{1}{\rho c_f}\frac{\partial q_r}{\partial y} + \varsigma\left[D_0 \frac{\partial \tilde{\Phi}}{\partial y}\frac{\partial \tilde{\Theta}}{\partial y} + \frac{D_\Theta}{\Theta_\infty}\left(\frac{\partial \tilde{\Theta}}{\partial y}\right)^2\right]\}, \tag{3}$$

$$\frac{\partial \tilde{\Phi}}{\partial t} + \tilde{A}\frac{\partial \tilde{\Phi}}{\partial x} + \tilde{B}\frac{\partial \tilde{\Phi}}{\partial y} = \frac{D_0}{\upsilon}\frac{\partial^2 \tilde{\Phi}}{\partial y^2} + \frac{D_\Theta}{\Theta_\infty}\left(\frac{\partial^2 \tilde{\Theta}}{\partial y^2}\right) - k_1\left(\tilde{\Phi} - \tilde{\Phi}_\infty\right), \tag{4}$$

The boundary conditions are:

$$
\begin{aligned}
&t < 0 : \tilde{A} = \tilde{B} = 0, \quad \tilde{\Theta} = \Theta_w(x,t), \quad \tilde{\Phi} = \Phi_w(x,t), && \text{for any } x, y \\
&t \geq 0 : \tilde{A} = A_0 A_w\left(\frac{\tilde{x}}{L}, t\right), \quad A = A_0 A_w\left(\frac{\tilde{x}}{L}, t\right), \tilde{\Theta} - \Theta_\infty = \Theta_0 \Theta_w\left(\frac{\tilde{x}}{L}, t\right), && \\
&D_0 \frac{\partial \tilde{\Phi}}{\partial y} + \frac{D_\Theta}{\Theta_\infty}\frac{\partial \tilde{\Theta}}{\partial y} = 0 && \text{at } \tilde{y} = 0, \\
&\tilde{A} \to A_\infty A_e\left(\frac{\tilde{x}}{L}, t\right), \tilde{\Theta} \to \Theta_\infty, \tilde{\Phi} \to \Phi_\infty && \text{as } \tilde{y} \to \infty
\end{aligned} \tag{5}
$$

where A_0, B_0 and A_∞ are the reference characteristics, Θ_0 is the reference temperature and L is the characteristics length that introduces the following non-dimensional parameters:

$$x = \frac{\tilde{x}}{L}, \quad y = \frac{\tilde{y}}{L}\left(\frac{A_\infty L}{B}\right)^{1/2}, \quad A = \frac{\tilde{A}}{A_\infty}, \quad B = \frac{\tilde{B}}{B_\infty}\left(\frac{A_\infty L}{B}\right)^{1/2} \tag{6}$$

Equations (1)–(4) and (5) take the converted as below form:

$$\frac{\partial A}{\partial x} + \frac{\partial B}{\partial y} = 0, \tag{7}$$

$$\frac{\partial \tilde{A}}{\partial t} + \tilde{A}\frac{\partial \tilde{A}}{\partial x} + \tilde{B}\frac{\partial \tilde{B}}{\partial y} = A_e \frac{\partial A_e}{\partial x} + (1+\varepsilon)\frac{\partial^2 A}{\partial y^2} - \varepsilon\delta\left(\frac{\partial \tilde{A}}{\partial y}\right)^2\left(\frac{\partial^2 \tilde{A}}{\partial y^2}\right), \tag{8}$$

$$\frac{\partial \Theta}{\partial t} + A\frac{\partial \Theta}{\partial x} + B\frac{\partial \Theta}{\partial y} = \frac{\alpha_m}{\rho c_f}\left(\frac{\partial^2 \Theta}{\partial y^2}\right) + \frac{Q_0(\Theta - \Theta_\infty)}{\rho c_f}$$
$$- \frac{1}{\rho c_f}\frac{\partial q_r}{\partial y} + \varsigma\left[D_0 \frac{\partial \Phi}{\partial y}\frac{\partial \Theta}{\partial y} + \frac{D_\Theta}{\Theta_\infty}\left(\frac{\partial \Theta}{\partial y}\right)^2\right]\}, \tag{9}$$

$$\frac{\partial \Phi}{\partial t} + A\frac{\partial \Phi}{\partial x} + B\frac{\partial \Phi}{\partial y} = \frac{D_0}{\upsilon}\frac{\partial^2 \Phi}{\partial y^2} + \frac{D_\Theta}{\Theta_\infty}\left(\frac{\partial^2 \Theta}{\partial y^2}\right) - k_1(\Phi - \Phi_\infty), \tag{10}$$

The initial and boundary conditions are:

$$
\left.
\begin{aligned}
&t < 0 : A = B = 0, \quad \Theta = \Theta_w(x,t), \quad \Phi = \Phi_w(x,t), \quad for \ any \ x, y \\
&t \geq 0 : A = s B_w(x,t), \quad A = \lambda A_w(x,t), \quad \Theta = \Theta_w(x,t), \\
&\qquad\qquad D_0 \frac{\partial \Phi}{\partial y} + \frac{D_\Theta}{\Theta_\infty}\frac{\partial \Theta}{\partial y} = 0 \ \ at \ y = 0, \\
&A = A_e(x,t), \Theta \to \Theta_\infty, \Phi \to \Phi_\infty \ \ as \ y \to \infty
\end{aligned}
\right\} \tag{11}
$$

where the dimensionless velocity ratio parameter is λ, and s is a non-dimensionless constant. ε and δ are Powell–Eyring fluid parameters.

$$\varepsilon = \frac{1}{\rho \upsilon \beta C_1}, \quad \delta = \frac{A_\infty^3}{2\upsilon L C_1}, \quad \lambda = \frac{A_0}{A_\infty}, \quad s = \frac{B_0}{A_0}\left(\frac{A_0 L}{\upsilon}\right)^{1/2}, \quad Pr = \frac{\upsilon}{\alpha}$$

The stretching velocities defined as follows;

$$A_w(x,t) = x^{1/3}, \quad A_e(x,t) = x^{1/3}, \quad B_w(x,t) = x^{-1/3}. \tag{12}$$

Similarity variables are

$$\Psi = x^{2/3} f(\eta, \xi), \quad \xi = x^{-2/3}t, \quad \eta = x^{-1/3}y, \quad \theta(\xi, \eta)$$
$$= \frac{\Theta - \Theta_\infty}{\Theta_w - \Theta_\infty}, \quad \phi(\xi, \eta) = \frac{\Phi - \Phi_\infty}{\Phi_w - \Phi_\infty}, \tag{13}$$

where ψ is a stream function, and it is defined by

$$A = \frac{\partial \Psi}{\partial y}, \quad B = -\frac{\partial \Psi}{\partial x}.$$

Substituting Eq. (14) into Eqs. (8)–(11), we get

$$(1 + \varepsilon) f''' + \frac{2}{3} f f'' + \frac{1}{3}\left(1 - \left(f'\right)^2\right) - \varepsilon \delta f'''\left(f''\right)^2 - f'' = 0 \tag{14}$$

$$\frac{1}{Pr}(1 + R_d)\theta'' + \frac{2}{3} f\theta' + \mathrm{He}\theta + N_b\theta'\phi' + N_t\left(\theta'\right)^2 - \theta' = 0 \tag{15}$$

$$\phi'' + \frac{2}{3} Scf\phi' + \frac{N_t}{N_b}\theta'' - Sc\phi' + K\phi = 0 \tag{16}$$

The converted boundary conditions are:

$$f = f_w, \quad f' = \lambda, \quad \theta = 1, \quad N_b\phi' + N_t\theta' = 0 \text{ at } \eta = 0$$
$$f' = 1, \quad \theta = 0, \quad \phi = 0 \text{ as } \eta \to \infty \tag{17}$$

where $f_w = -3s/2$ is constant with $f_w > 0$ suction and $f_w < 0$ injection.
The drag force C_f and rate of heat transfer Nu_x are defined by:

$$C_f = \frac{\tau_w}{\rho U_\infty^2}, \quad \mathrm{Nu}_x = \frac{\tilde{x}q_w}{\alpha(T_w\tilde{x}/L) - T_\infty)}, \tag{18}$$

where

$$\tau_w = \mu\left(\frac{\partial \tilde{u}}{\partial \tilde{y}}\right)_{y=0}, \quad q_w = -\alpha\left(\frac{\partial \tilde{u}}{\partial \tilde{y}}\right)_{y=0}. \tag{19}$$

Using Eq. (14) by converting Eq. (13) as we get below expression

Fig. 1 .
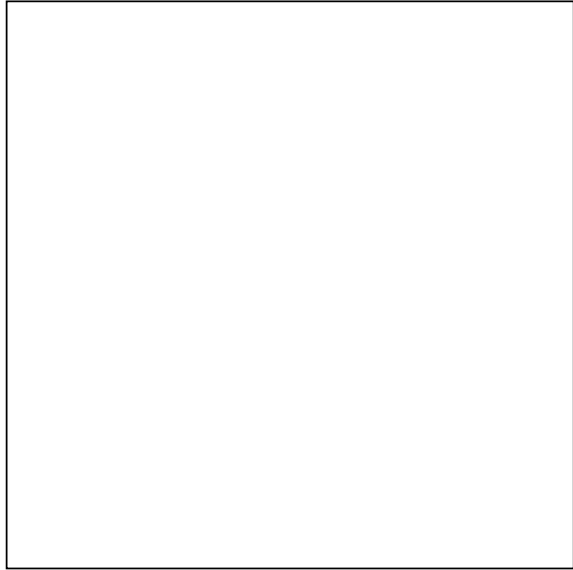
$$\left.\begin{array}{r}\mathrm{Re}_x^{1/2} C_f = (1 + \varepsilon) f''(0) - \dfrac{\varepsilon}{3}\delta\big(f''(0)\big)^3, \\[2mm] \mathrm{Re}_x^{-1/2} Nu_x = -\theta'(0),\end{array}\right\}$$ (20)

where local Reynolds number is $\mathrm{Re}_x = \frac{\tilde{x} u_w(\tilde{x}/L)}{v}$.

3 Results Analysis

The system of Eqs. (9)–(11) together with the BC's (12) has been computed computationally by RKF scheme with shooting procedure. The results are displayed pictorially in Figs. (2)–(14) for various parameters on the flow, energy and concentration as well as the $\mathrm{Re}_x^{1/2} C_{fx}$ and rate of heat transfer profiles.

Figure 2a, b present the significant influence of stretching velocity ($\lambda > 1$) and free stream velocity ($\lambda < 1$) on velocity profiles for suction parameter ($f_w > 0$) and injection parameter ($f_w < 0$). It is noticed that the velocity of the fluid decreases with ascending values of f_w for $\lambda > 1$, whereas reverse nature is noticed in case of $\lambda < 1$. Physically, the presence of suction on the surface decreases the boundary-layer thickness. It is also perceived that the stretching velocity of the fluid is more than that of free stream velocity. In addition, these results coincide with the results [see Refs. 1, 32] available in the literature.

The effect of f_w on $\theta(\eta)$ is displayed in Fig. 3. It is clear that $\theta(\eta)$ and thermal boundary-layer thickness decline with enhanced values of f_w. Physically, the hot
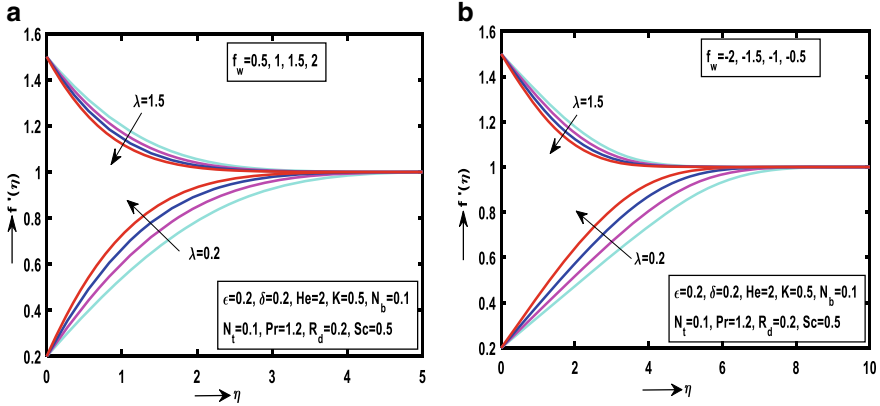
Fig. 2 **a** Effect of suction on $f'(\eta)$ and **b** behaviour of injection on $f'(\eta)$

Fig. 3 Behaviour of f_w on $\theta(\eta)$
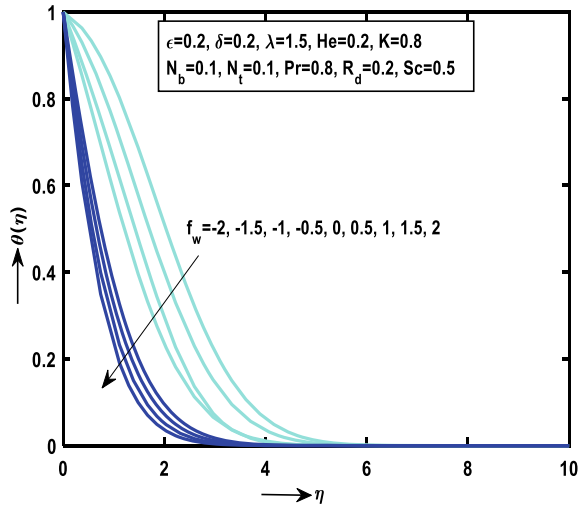
fluid moves towards the surface due to the presence of suction and hence the thermal boundary-layer thickness reduces.

Figure 4 illustrates the influence of Pr on $\theta(\eta)$. It is perceived that the energy boundary layer and temperature diminish with ascending values of Pr. Physically, the Pr is interaction between the kinematic energy and thermal diffusivity. Hence, the energy boundary layer becomes thicker due to the lower Pr values as a result heat transfer rate decreases.
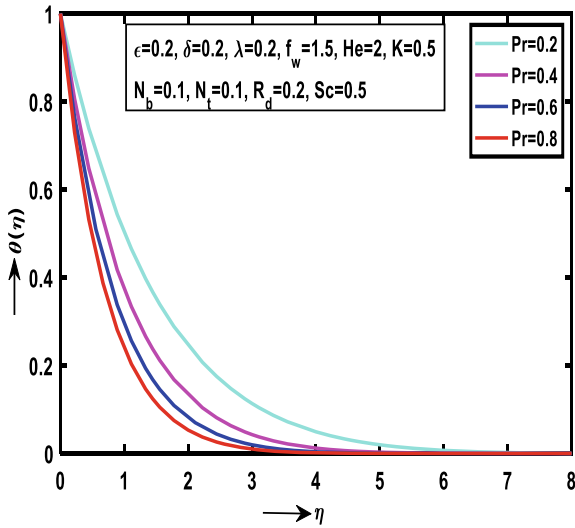
Fig. 4 Behaviour of Pr on $\theta(\eta)$

The effect of N_t on energy and $\phi(\eta)$ is presented, respectively, in Fig. 5a, b. It is clear that the $\theta(\eta)$ reduces and $\phi(\eta)$ of the fluid enhances for ascending values of N_t. Figure 6 presents the effect of N_b on $\phi(\eta)$. It is perceived that the $\phi(\eta)$ increase with ascending values of N_b. This is due to the fact that the high Brownian diffusion produces maximum concentration with large values of N_b. Figure 7 displays the impact of R_d on the $\theta(\eta)$ profile. The thermal boundary layer is enhanced with ascending values of thermal heat parameter. Physically, the radiation is inversely proportional to the thermal diffusivity and heat capacity of the fluid. Hence, high thermal diffusivity is responsible for enhanced values of radiation. Figure 8 illustrates
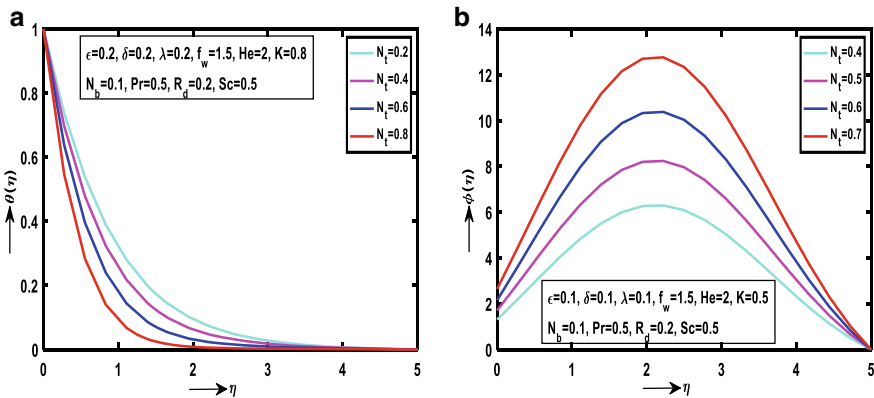
Fig. 5 **a** Behaviour of N_t on $\theta(\eta)$ and **b** behaviour of N_t on $\phi(\eta)$

Fig. 6 Behaviour of N_b on
$\phi(\eta)$
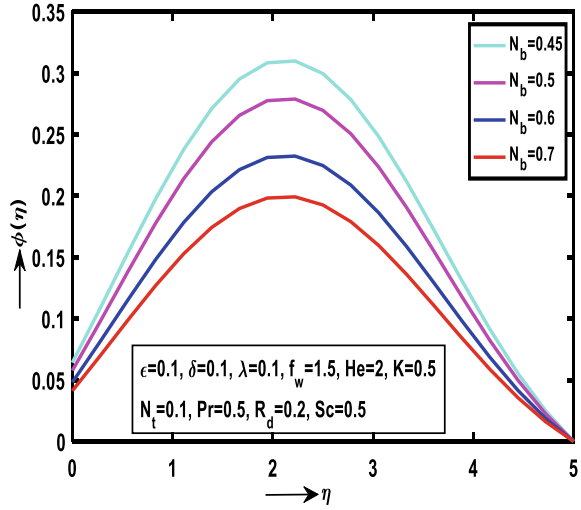
Fig. 7 Behaviour of R_d on
$\theta(\eta)$
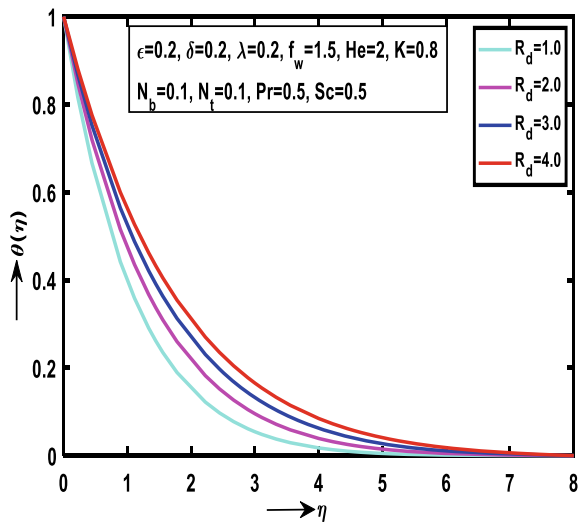
the influence of He (heat generation parameter) on $\theta(\eta)$. The temperature of the fluid
and the thermal boundary-layer thickness increases with rising values of He. Figure 9
represents the effect of chemical reaction parameter K on $\phi(\eta)$. The concentration
of the fluid is decreased with the increase of K.

Fig. 8 Behaviour of He on $\theta(\eta)$
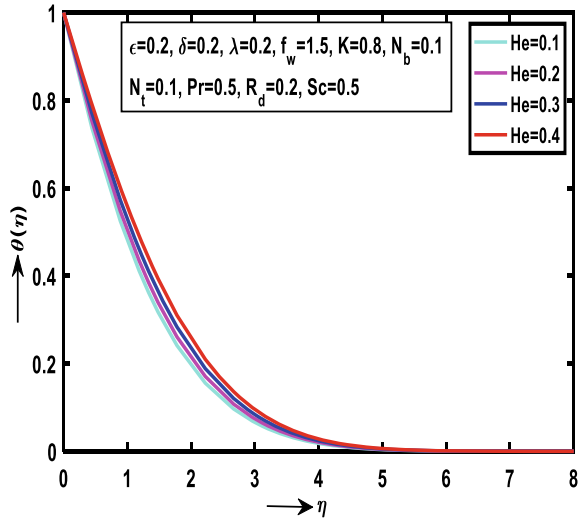
Fig. 9 Behaviour of K on $\phi(\eta)$
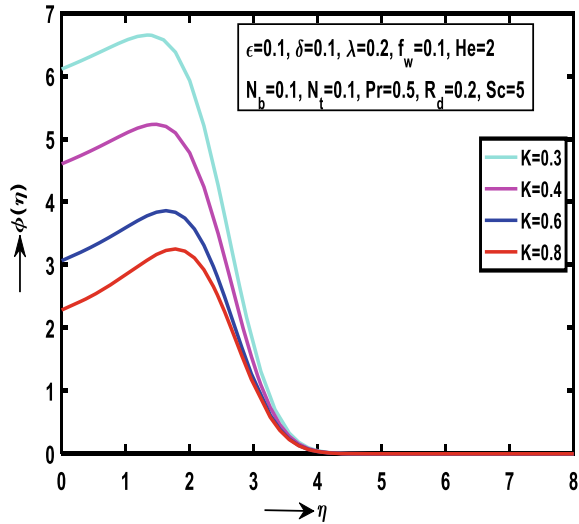
Figure 10a, b illustrates the variations of $Re_x^{1/2}C_{fx}$ and $Re_x^{-1/2}Nu_x$ with suction f_w for different values of velocity ratio parameter (λ). The $Re_x^{1/2}C_{fx}$ and $Re_x^{-1/2}Nu_x$ reduce with ascending values of λ in the case of free stream velocity $\lambda < 1$. On the other hand, $Re_x^{1/2}C_{fx}$ increases and $Re_x^{-1/2}Nu_x$ decreases with growing the suction parameter. These results coincide with the results of the Ref. [15].
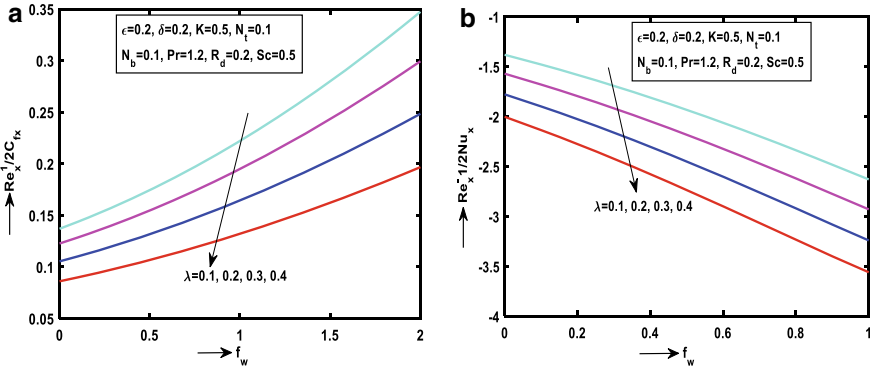
Fig. 10 a Behaviour of λ on $\mathrm{Re}_x^{1/2} C_{fx}$ and **b** behaviour of λ on $\mathrm{Re}_x^{-1/2} Nu_x$

The most significant parameter Eyring–Powell fluid parameters (ε, δ) with respect to f_w on $\mathrm{Re}_x^{1/2} C_{fx}$ is discussed, respectively, in Figs. 11 and 12. It is perceived that the $\mathrm{Re}_x^{1/2} C_{fx}$ grows for growing values of Eyring–Powell fluid parameter. The high $\mathrm{Re}_x^{1/2} C_{fx}$ in non-Newtonian fluid motion is due to the presence of high kinematic viscosity.

Fig. 11 Behaviour of ε on $\mathrm{Re}_x^{1/2} C_{fx}$
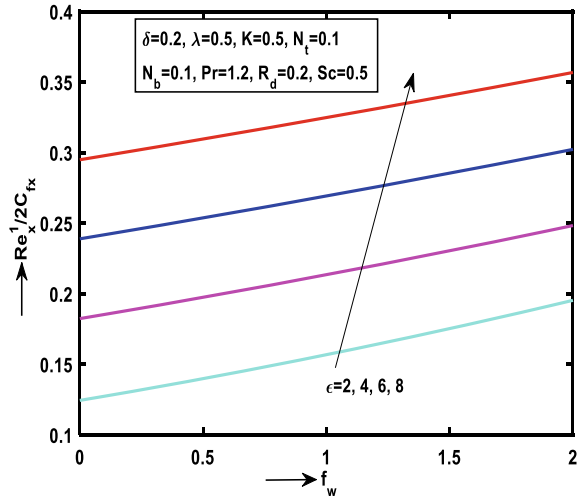
Fig. 12 Behaviour of δ on $Re_x^{1/2}C_{fx}$
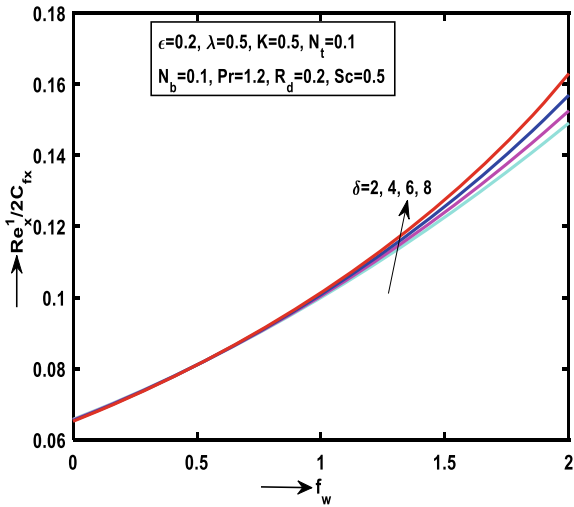
4 Conclusion

The effects of chemical reaction and suction on unsteady non-Newtonian nanofluid flow generated by a moving surface are discussed in this mathematical model. The main outcomes of this work are pointed out as below:

- The fluid velocity enhances with rising values of stretching and free stream velocity parameters.
- The free stream velocity of the fluid is less than that of stretching velocity.
- The concentration of the fluid decreases with increasing chemical reaction parameter.
- The temperature of the fluid increases with increasing heat source parameter.

References

1. Powell RE, Eyring RE (1944) Mechanisms for the relaxation theory of viscosity. Nature 154:427–428
2. Agbaje TM, Mondal S, Motsa SS, Sibanda P (2017) A numerical study of unsteady non-Newtonian Powell-Eyring nanofluid flow over a shrinking sheet with heat generation and thermal radiation. Alexandria Eng J 56:81–91
3. Hayat T, Farooq S, Ahmad B, Alsaedi A (2017) Peristalsis of Eyring-Powell magneto nanomaterial considering Darcy-Forchheimer relation. Int J Heat Transf 115:694–702
4. Hayat T, Ullah I, Alsaedi A, Farooq M (2017) MHD flow of Powell-Eyring nanofluid over a non-linear stretching sheet with variable thickness. Results Phys 7:189–196
5. Harish Babu D, Sudheer Babu M, Satya Narayana PV (2017) MHD mass transfer flow of an Eyring-Powell fluid over a stretching sheet. IOP Conf Ser Mater Sci Eng 263:1–8

6. Hayat T, Hussain S, Muhammad T, Alsaedi A, Ayub M (2017) Radiative flow of Eyring-Powell nanofluid with convective boundary conditions. Chin J Phys 55:1523–1538

7. Satya Narayana PV, Tarakaramu N, Moliya Akshit S, Ghori JP (2017) MHD flow and heat transfer of an Eyring-Powell fluid over a linear stretching sheet with viscous dissipation—a numerical study. Front Heat Mass Transf 9:1–5

8. Mahanthesh B, Gireesha BJ, Rama Subba Reddy G (2017) Unsteady three-dimensional MHD flow of a nano Eyring-Powell fluid past a convectively heated stretching sheet in the presence of thermal radiation, viscous dissipation and Joule heating. J Assoc Arab Univ Basic Appl Sci. 23:75–84

9. Madhu M, Kishan N, Chamkha A (2017) Unsteady flow of a Maxwell nanofluid over a stretching surface in the presence of magnetohydrodynamic and thermal radiation effects. Propul Power Res 6:31–40

10. Maqbool K, Mann AB, Tiwana MH (2017) Unsteady MHD convective flow of a Jeffery fluid embedded in a porous medium with ramped wall velocity and temperature. Alexandria Eng J 57:1–8. https://doi.org/10.1016/j.aej.2017.02.012

11. Pushpalatha K, Ramana Reddy JV, Sugunamma V, Sandeep N (2017) Numerical study of chemically reacting unsteady Casson fluid flow past a stretching surface with cross diffusion and thermal radiation. Open Eng 7:69–76

12. Makinde OD, Khan WA, Khan ZH (2017) Stagnation point flow of MHD chemically reacting nanofluid over a stretching convective surface with slip and radiative heat. Proc. Inst. Mech. Eng. Part E. J. Process Mech. Eng. 231:695–703

13. Gangadhar K, Venkata KR, Makinde OD, Kumar BR (2018) MHD flow of a Carreau fluid past a stretching cylinder with Cattaneo-Christov heat flux using spectral relaxation method. Defect Diff Forum 387:91–105

14. Nayak MK, Hakeem AKA, Makinde OD (2018) Influence of Cattaneo-Christov heat flux model on mixed convection flow of third grade nanofluid over an inclined stretched riga plate. Defect Diff Forum 387:121–134

15. Jalil M, Asghar S, Imran SM (2013) Self-similar solutions for the flow and heat transfer of Powell-Eyring fluid over a moving surface in a parallel free stream. Int J Heat Mass Transf 65:73–79

16. Afridi MI, Qasim M (2018) Entropy generation and heat transfer in boundary layer flow over a thin needle moving in a parallel stream in the presence of nonlinear Rosseland radiation. Int J Therm Sci 123:117–128

17. Alharbi SO, Dawar A, Shah Z, Khan W, Idrees M, Islam S, Khan I (2018) Entropy generation in MHD Eyring-Powell fluid flow over an unsteady oscillatory porous stretching surface under the impact of thermal radiation and heat source/sink. Appl Sci 8:1–18. https://doi.org/10.3390/app8122588

18. Majeed A, Zeeshan A, Xu H, Kashif M, Masud U (2019) Heat transfer analysis of magneto-Eyring–Powell fluid over a non-linear stretching surface with multiple slip effects: application of Roseland's heat flux. Canad J Phys. https://doi.org/10.1139/cjp-2018-0732

19. Khan I, Fatima S, Malik MY, Salahuddin T (2018) Exponentially varying viscosity of magnetohydrodynamic mixed convection Eyring-Powell nanofluid flow over an inclined surface. Results Phys 8:1194–1203

20. Makinde OD, Animasaun IL (2016) Bioconvection in MHD nanofluid flow with nonlinear thermal radiation and quartic autocatalysis chemical reaction past an upper surface of a paraboloid of revolution. Int J Therm Sci 109:159–171

21. Satyanarayana PV, Harish Babu D (2016) Numerical study of MHD heat and mass transfer of a Jeffrey fluid over a stretching sheet with chemical reaction and thermal radiation. J Taiwan Inst Chem Eng 59:18–25

22. Tarakaramu N, Satya Narayan PV (2017) Unsteady MHD nanofluid flow over a stretching sheet with chemical reaction. IOP Conf Ser Mat Sci Eng 263:1–8

23. Tarakaramu N, Ramesh Babu K, Satya Narayana PV (2018) Effect of nonlinear thermal radiation, heat source on MHD 3D Darcy-Forchheimer flow of nanofluid over a porous medium with chemical reaction. Int J Eng Tech 7(4.10):605–609

24. Makinde OD, Nagendramma V, Raju CSK, Leelarathnam A (2017) Effects of Cattaneo-Christov heat flux on Casson nanofluid flow past a stretching cylinder. Defect Diff Forum 378:28–38
25. Tarakaramu N, Satya Narayana PV (2019) MHD three dimensional Darcy-Forchheimer flow of a nanofluid with nonlinear thermal radiation. Appl Math Sci Comput Trends Math 2:87–97
26. Ibrahim SM, Kumar PV, Makinde OD (2018) Chemical reaction and radiation effects on non-Newtonian fluid flow over a stretching sheet with non-uniform thickness and heat source. Defect Diff Forum 387:319–331
27. Nayak MK, Shaw S, Makinde OD, Chamkha AJ (2018) Effects of homogenous–heterogeneous reactions on radiative NaCl-CNP nanofluid flow past a convectively heated vertical Riga plate. J Nanofluids 7(4):657–667
28. Satya Narayan PV, Tarakaramu N, Makinde OD, Venkateswarlu B, Sarojamma G (2018) MHD stagnation point flow of viscoelastic nanofluid past a convectively heated stretching surface. Defect Diff Forum 387:106–120
29. Kumar SG, Varma SVK, Prasad PD, Raju CSK, Makinde OD, Sharma R (2018) MHD reacting and radiating 3D flow of Maxwell fluid past a stretching sheet with heat source/sink and Soret effects in a porous medium. Defect Diff Forum 387:145–156
30. Tarakaramu N, Satya Narayana PV (2019) Nonlinear thermal radiation and joule heating effects on MHD stagnation point flow of nanofluid over a convectively heated stretching surface. J Nanofluids 5:1066–1075
31. Nadeem S, Saleem S (2015) Series solution of unsteady Eyring-Powell nanofluid flow on a rotating cone. Am J Comput Math 52:725–737
32. Rosca AV, Pop I (2014) Flow and heat transfer of Eyring-Powell fluid over shrinking surface in a parallel free stream. Int J Heat Mass Transf 71:321–327

Parametric Investigation of Beta Type Stirling Engine

H. Raghavendra [iD]**, P. Suryanarayana Raju** [iD]**, and K. Hema Chandra Reddy** [iD]

Abstract Stirling engines are one of the ideal candidates for the conversion of solar power to work since they can efficiently convert low-grade heat into mechanical work. However, there are a few challenges regarding the operation and control of the Stirling engines which need to be resolved before they can be deployed widely. Numerical modeling can be employed to supplement the experimental investigations in obtaining a deeper understanding of the intricacies in the operation of a Stirling engine. In this paper, a mathematical model is developed to accurately simulate a Stirling Engine of beta configuration with a rhombic drive mechanism. The model is formulated by combining the kinematic analysis of the engine mechanism and thermodynamic analysis of working fluid in the engine along with analysis of other transport phenomena occurring inside the engine viz. heat and mass transfer. The model is verified by comparing the predictions against the results published in the literature. The model is then used to conduct a parametric analysis to assess the influence of various operating parameters on the efficiency and power output of the Stirling engine.

Keywords Renewable energy · Stirling engine · Rhombic drive mechanism · Numerical model

1 Introduction

Stirling Engine is one potential technology that could produce mechanical work from renewable energy sources like solar and biomass. It is a sort of external combustion engine and works on alternating expansion and compression of working fluid inside a piston-cylinder arrangement. Stirling Engine is also an efficient heat engine that

H. Raghavendra (✉) · P. Suryanarayana Raju
Department of Mechanical Engineering, Madanapalle Institute of Technology & Science, Madanapalle, Andhra Pradesh, India
e-mail: h.raghavendra.rymec@gmail.com

H. Raghavendra · K. Hema Chandra Reddy
Department of Mechanical Engineering, JNTUA College of Engineering, Anantapuramu, Andhra Pradesh, India

could convert heat available at relatively low temperatures into mechanical work. The working principle of a Stirling Engine is that a gaseous working fluid is enclosed in two connected cylinders, with pistons, which are maintained at two different temperatures; one hot and one cold. The temperature difference between the hot and cold cylinders is maintained by adding heat to the hot side and removing heat from the cold side. A gaseous working fluid which is filled inside the two connected cylinders causes the two pistons to oscillate as it expands in the hot cylinder and contracts in the cold cylinder. The connection between the hot and cold cylinders allows for the working fluid to transfer between the hot and cold cylinders. Thus, the working fluid is cyclically heated and cooled wherein it expands and contracts causing the pistons to move continuously and thus the net heat supplied to the engine is converted to mechanical work. In general, there are three basic configurations of Stirling engine [1]: alpha type, beta type, and gamma type. The configuration with two separate cylinders fitted with two power pistons is known as alpha type Stirling Engine. Beta type engine has only one cylinder and two pistons, one known as displacer and other as power piston fitted into it. As is a Beta type engine, Gamma Stirling engine also has two pistons, a displacer, and a power piston, but the difference is that they are fitted in different cylinders. In all these configurations both pistons are connected to the same shaft through a suitable mechanism like cranks. A flywheel is provided to smooth the energy fluctuations over each cycle of operation of the engine.

Stirling engines of beta configuration have attracted considerable interest from researchers in recent years as potential candidates for energy conversion using renewable sources as well as for waste heat recovery. One common problem with the Stirling engines is the low power output. In an experimental investigation on a 192 cm^3 total swept volume Stirling engine by Cinar et al. [2], it was reported that power output was maximum (5.98 W) at an engine speed of 208 rpm and source temperature of 1000 °C.

The most investigated aspect of Stirling engines is developing strategies for improving the power output and efficiency of these engines though geometric optimization as well as the optimization of the operating conditions. Researchers have usually employed numerical modeling to supplement the experimental investigations to better understand the working of Stirling engines. Shendage et al. [3] have developed a numerical model and demonstrated its use in the design process of a Stirling engine. Beta configuration engine was studied in this work and the model is used for the optimization of the phase angle between the oscillations of two pistons, considering the influence of the volume overlap between the compression space and expansion space within the engine cylinder. The numerical model included the analysis of the engine mechanics and also the thermodynamic analysis. Cheng and Yu [4] also presented a dynamic simulation of a beta configuration Stirling engine with a cam-drive mechanism which was developed by combining the analysis of forces and torques with the thermodynamic model An extensive parametric study was carried out by the authors to characterize the effect of different geometrical dimensions of the engine as well as the operating conditions on its performance.

Shazly et al. [5] presented simulations through thermal analysis of a prototype Stirling engine using a mathematical model. The engine is of low temperature difference type and is powered by solar. The study concluded increasing the temperature of the heat source enhanced the shaft power output. The study also reported that increasing the engine's source temperature increases its Beale number. Toghyani et al. [6] presented an adiabatic analysis that was used to determine the power loss and efficiency of a Stirling engine.

Some studies in the literature resorted to detailed three-dimensional modeling of the components of Stirling engine to reveal in-depth information on the transport phenomena inside these devices. Chen et al. [7] presented a simulation study of gamma configuration Stirling Engine using CFD (Computational Fluid Dynamics) wherein the heat transfer inside the engine was investigated. In another CFD based study, Salazar and Chen [8] analyzed the fluid flow and heat transfer phenomena inside a Stirling engine of beta-type working on rhombic drive mechanism.

There are also investigations reported in the literature on integrating the Stirling Engines with collectors of solar energy using both experimental and computational techniques. Abdollahpour et al. [9] designed and analyzed a 3.5 kW capacity parabolic trough collector of solar radiation to assess its utility for integration with Stirling engine. Ahmadi et al. [10] developed a computational model, derived using thermodynamic principles, for a solar dish Stirling Engine, to predict its output power and thermal efficiency. Uzuneanu et al. [11] pointed out that a Stirling cycle engine can run on biomass, solar energy, geothermal energy and other types of renewable sources of heat. The main focus of the report was on conversion techniques which are at a high level of development, and the authors specifically highlighted the case of micro-CCHP units (Combine Cooling, Heating and Power) with the Stirling engine. This study reported a 10% saving on energy costs as a result of the installation of a CCHP based on a Stirling engine in residential applications.

As evident from the brief survey of the literature presented here, there are several studies in the open literature, both experimental and numerical, on improving the performance of different types and designs of Stirling engines operating under a range of different conditions. However, there is still a need for a more refined analysis of these devices to realize their full potential. The objective of the present study is to develop a numerical model to simulate the operation of a beta type Stirling engine with a rhombic drive mechanism. The mathematical model is based on that presented by Cheng and Yu [12]. A parametric study is performed via computational simulations using the model to assess the working of the engine is performed under various operating conditions and geometric proportions.

1.1 Description of the Engine

A schematic diagram of the beta type Stirling engine with a rhombic drive mechanism is shown in Fig. 1. The piston which is reaching farthest into the cylinder is called displacer and the piston below the displacer is called power piston. The power piston
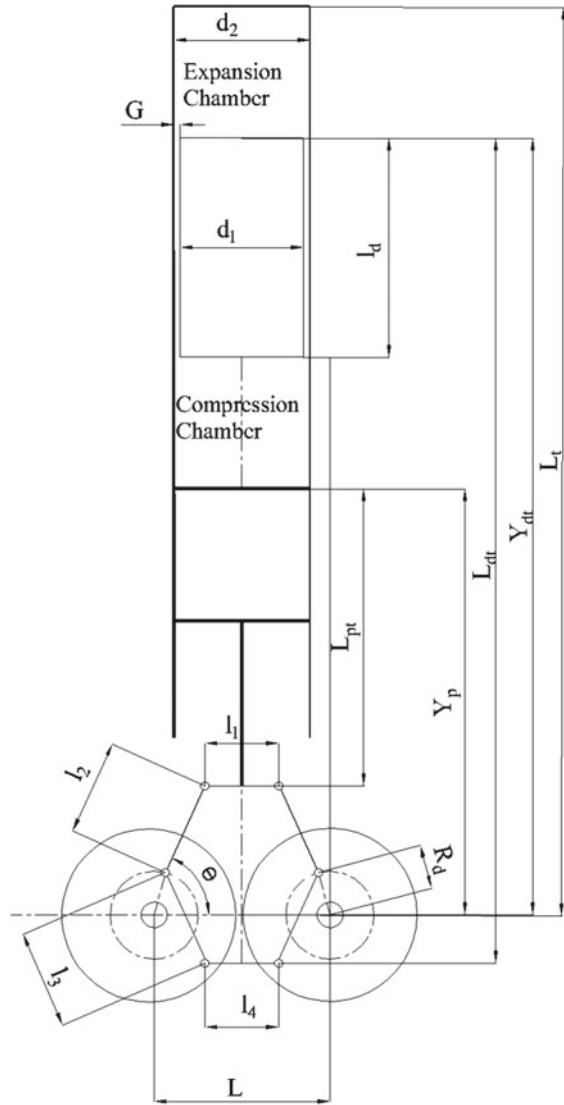
is connected to the top yoke of the rhombic drive and the displacer is connected to the
bottom yoke of the rhombic drive by a slender piston rod that passes through a hole
drilled in the power piston, its connecting rod, and the top yoke of the rhombic drive.
The top portion of the engine cylinder is the expansion chamber which is bound by
the top section of the cylinder and the displacer. The section of the cylinder between
the displacer and the power pistons is called the compression chamber.

There is good clearance between the cylinder and the top piston such that the
working fluid can transfer between the expansion and compression chambers without

much resistance as the piston oscillates and thus this piston is called a displacer. The power piston, on the other hand, has very little clearance and it compresses the working fluid and also gets pushed out by the working fluid as it moves in and out of the cylinder. The expansion chamber is heated by an external source and the compression chamber is maintained at a cooler temperature by removing heat. Once the engine is set in motion, the working fluid is cyclically heated and cooled as it moves between the expansion and compression chambers, producing net positive work over each cycle.

As the working fluid moves through the annular space between the cylinder and the displacer, it exchanges heat with the thermal mass in the system. This serves as a regenerator wherein the hot gases give their heat to the regenerator when they go from the expansion chamber to the compression chamber and enter the compression chamber at lower temperatures thus reducing the amount of heat rejected to the cold source. Later when the working fluid goes back to the expansion chamber it recovers the heat from the regenerator and enters the expansion chamber at a higher temperature so that the heat input required from the hot source is reduced. The design of the regenerator is thus crucial in achieving an improved performance of the engine.

2 Mathematical Model

The mathematical model presented here uses the kinematic equations of motion for the displacer and power pistons which are driven in sync with each other by the rhombic drive mechanism. Once the positions of the displacer and power piston are known, the volume inside the expansion and compression chambers can be calculated. Assuming fixed temperatures for the hot and cold sources, the temperatures in the expansion and compression chambers can be estimated. The pressure in the chambers will depend on the amount of working fluid in them which changes continuously as the pistons are moving. Major assumptions made in the model include:

1. Lumped modeling is employed where properties are assumed to be uniform inside each chamber.
2. Heat transfer is estimated using a simple model based on total thermal resistance which is constant.
3. Ideal gas model with constant specific heats assumption is used for working gas properties.
4. Regenerator working is modeled using a single parameter, "regenerator effectiveness".

As was mentioned already the engine mechanism is well constrained such that there is only one degree of freedom. Here we choose the crank angle, θ, as the free variable which is changing continuously at a steady rate, the angular velocity of the crank. The positions of the displacer and the power piston can be determined as a function of the crank angle and the geometrical parameters of the engine as:

$$Y_{\mathrm{d}}(t) = L_{\mathrm{dt}} + R_{\mathrm{d}}\sin\theta - \left[l_3^2 - \left(\frac{L}{2} - \frac{l_4}{2} - R_{\mathrm{d}}\cos\theta\right)^2\right]^{\frac{1}{2}} \tag{1}$$

and

$$Y_{\mathrm{p}}(t) = L_{\mathrm{pt}} + R_{\mathrm{d}}\sin\theta + \left[l_2^2 - \left(\frac{L}{2} - \frac{l_1}{2} - R_{\mathrm{d}}\cos\theta\right)^2\right]^{\frac{1}{2}} \tag{2}$$

The definitions of the geometric parameters in the above equations are clearly depicted in the schematic line diagram of the engine in Fig. 1 and the terms used to refer to them are given in Table 1. Using the instantaneous positions of the two pistons, the volumes inside the expansion and compression chambers can be calculated as:

$$V_{\mathrm{e}}(t) = \pi r_2^2(l_{\mathrm{t}} - Y_{\mathrm{d}}(t)) \tag{3}$$

$$V_{\mathrm{c}}(t) = \pi r_2^2\big(Y_{\mathrm{d}}(t) - l_{\mathrm{d}} - Y_{\mathrm{p}}(t)\big) \tag{4}$$

The rate at which working fluid is moving between the two chambers will depend upon the pressure difference between the chambers and the flow behavior in the annular chamber. Shendage et al. [3] derived the following equation for the flow rate

Table 1 Geometrical parameters of the Stirling engine considered in the study

Components label	Nomenclature	Dimensions (mm)
Diameter of displacer	d_1	38
Diameter of core cylinder	d_2	36
Regenerative channel gap	G	2
Height of displacer	L_{d}	130
Length of the linkage	l_1	26
Length of the linkage	l_2	44
Length of the linkage	l_3	44
Length of the linkage	l_4	26
Distance between the gears	L	80
Offset distance from the crank to the center	R_{d}	12
Height of the engine	l_{t}	294
Length from top yoke to piston	L_{pt}	93.5
Length from bottom yoke to displacer	L_{dt}	309.5

of working fluid movement.

$$\frac{\mathrm{d}m}{\mathrm{d}t} = \frac{\rho\pi}{8\mu}\left(\frac{(-P_e - P_c)}{l_d}\right)\left[r_2^4 - r_1^4 - \frac{(r_2^2 - r_1^2)^2}{\ln\left(\frac{r_2}{r_1}\right)}\right]$$
$$- \frac{2\pi v_d(t)\rho}{\ln\left(\frac{r_2}{r_1}\right)}\left[\frac{1}{2}(r_2^2 \ln r_2 - r_1^2 \ln r_1) - \frac{1}{4}(r_2^2 - r_1^2)\right]$$
$$+ \frac{2\pi v_d(t)\rho}{\ln\left(\frac{r_2}{r_1}\right)}\ln r_2\left[\frac{r_2^2}{2} - \frac{r_1^2}{2}\right] \tag{5}$$

Here P_e and P_c stand for pressure inside the cylinder on the expansion side and compression side, respectively. In addition to the geometric parameters, the above expression also involves the velocity of the displacer v_d, which can be determined by differentiating the expression for the position of the displacer with respect to time. We get:

$$v_d(t) = R_d\omega\left\{\cos\theta - \sin\theta\left[l_3^2 - \left(\frac{L}{2} - \frac{l_4}{2} - R_d\cos\theta\right)^2\right]^{-\frac{1}{2}}\left(\frac{L}{2} - \frac{l_4}{2} - R_d\cos\theta\right)\right\} \tag{6}$$

The mass of working fluid in the expansion chamber and compression chamber at any time step can be calculated by integrating the mass conservation equation over a small time step as:

$$m_e^{n+1} = m_e^n - \frac{\mathrm{d}m}{\mathrm{d}t}^n \Delta t \tag{7}$$

$$m_c^{n+1} = m_c^n + \frac{\mathrm{d}m}{\mathrm{d}t}^n \Delta t \tag{8}$$

Similarly, the temperatures inside the expansion and compression chambers can be found by integrating the energy equation for a small time step as:

$$T_e^{n+1} = \left(1 - \frac{\Delta t}{m_e C_v R_{t1}}\right)T_e^n + \frac{\Delta t}{m_e C_v}\left[\frac{T_H}{R_{t1}} - \frac{\overline{P}_e(V_e^{n+1} - V_e^n)}{\Delta t} - \frac{\mathrm{d}m}{\mathrm{d}t}\left(h_j + \frac{v_j^2}{2}\right)\right] \tag{9}$$

$$T_c^{n+1} = \left(1 - \frac{\Delta t}{m_c C_v R_{t2}}\right)T_c^n + \frac{\Delta t}{m_c C_v}\left[\frac{T_L}{R_{t2}} - \frac{\overline{P}_c(V_c^{n+1} - V_c^n)}{\Delta t} + \frac{\mathrm{d}m}{\mathrm{d}t}\left(h_i + \frac{v_i^2}{2}\right)\right] \tag{10}$$

In the above equations, R_{t1} and R_{t2} are the thermal resistances between the hot and cold heat sources and the respective engine chambers. The enthalpies in the convection terms, h_i and h_j are given the appropriate values depending on whether the mass is entering or leaving the corresponding chamber.

The regeneration in the engine is modeled using a parameter called "regenerator effectiveness", ϵ, which is a fraction. Once a value is given to ϵ, the temperature of the working fluid when entering the compression chamber or expansion chamber can be calculated using the equations:

$$T_i = T_e + \epsilon(T_c - T_e) \tag{11}$$

$$T_j = T_c + \epsilon(T_e - T_c) \tag{12}$$

Finally, the total heat transfer and work done during one cycle of operation can be calculated by integrating the instantaneous heat transfer and work transfer rates, over one time-period.

$$W_{out} = \int_{t_0}^{t_0+t_p} P_e dV_e + \int_{t_0}^{t_0+t_p} P_c dV_c \tag{13}$$

$$Q_{in} = \int_{t_0}^{t_0+t_p} \dot{Q}_{in,e} dt + \int_{t_0}^{t_0+t_p} \dot{Q}_{in,c} dt + \int_{t_0}^{t_0+t_p} \dot{Q}_{in,r} dt \tag{14}$$

$$\eta = \frac{W_{out}}{Q_{in}} \tag{15}$$

3   Results and Discussion

The model equations presented in the previous sections are a set of coupled equations that, together with the ideal gas model, yield a closed system which could be solved to find how the properties of the working fluid change with time starting from an initial condition. A MATLAB script is developed to solve the model equations. In order to verify the model, simulation is made of a particular engine which was also simulated by Cheng and Yu and it was ensured that the same results were obtained using the code developed in this study as in their report. A separate engine with different dimensions is then chosen as a base case for the parametric study presented here. The values of the geometric dimensions of the engine which are used in this study are given in Table 1. The values of the operating conditions for one case which is taken as the base case during the parametric study given in Table 2. The program predicts variation, with time, of the temperature, pressure, mass of working fluid, heat transfer rate and work transfer rate inside the expansion and compression chambers.

Table 2 Operating conditions used as the base cases

Variable	Value	Units
Hot source temperature	800	K
Cold source temperature	300	K
Charging pressure	101.3	K Pa
Regenerator effectiveness	0.45	No unit
Engine speed	2000	rpm

Also, the network and heat transfer per cycle are also estimated using Eqs. (13) and (14) and those values are used to assess the power and efficiency of the engine.

The results for the base case are presented first to demonstrate the type of results obtained from the model. Figures 2, 3, 4, and 5 show the variation of volume, mass, pressure, and temperature inside the expansion and compression chambers over a period of three cycles of engine revolutions. It can be seen from Fig. 2 that the total compression ratio for the engine is about 2.5. Figure 3 shows the mass of working fluid in the expansion and compression chambers as a function of time. As can be seen the total mass in the engine is constant since the complete system is assumed to be closed.

The pressure variation presented in Fig. 4 shows the pressure in the expansion and compression chambers to be similar since the pressure scale of the graph is far too large to show the small differences in pressure between the two. A separate plot of the variation of the pressure difference between the expansion and compression chambers
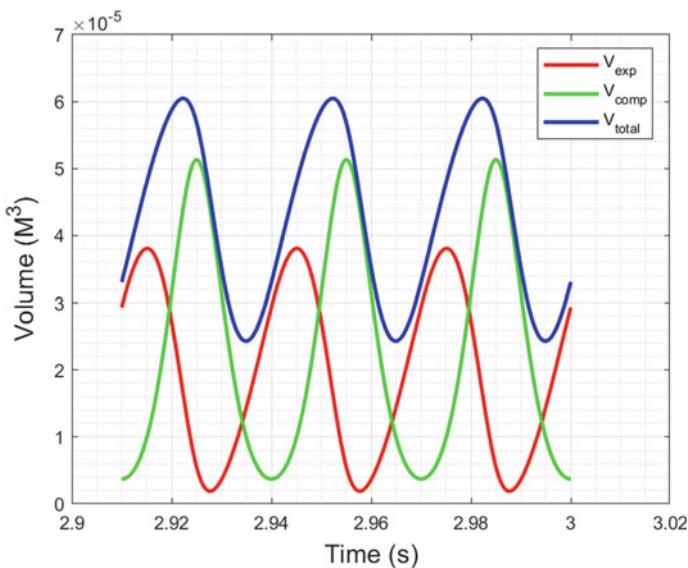
Fig. 2 Volume of gas in expansion and compression chambers and total volume—variation with time in the base case
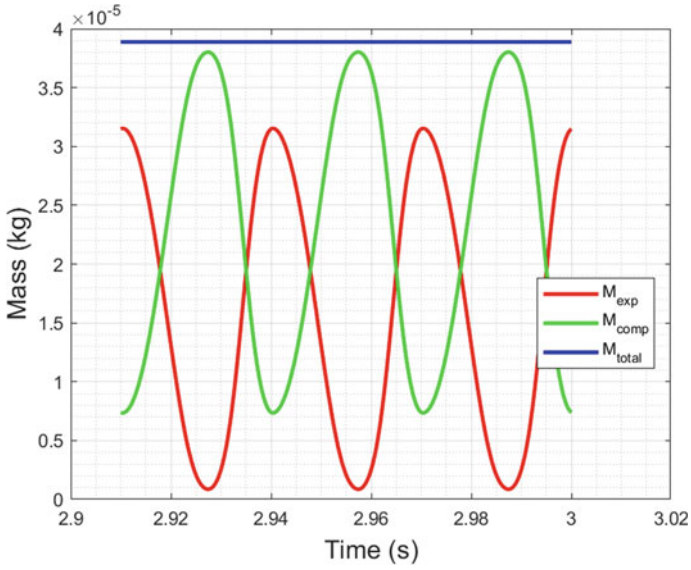
Fig. 3 Mass of gas in expansion and compression chambers and total mass—variation with time in the base case
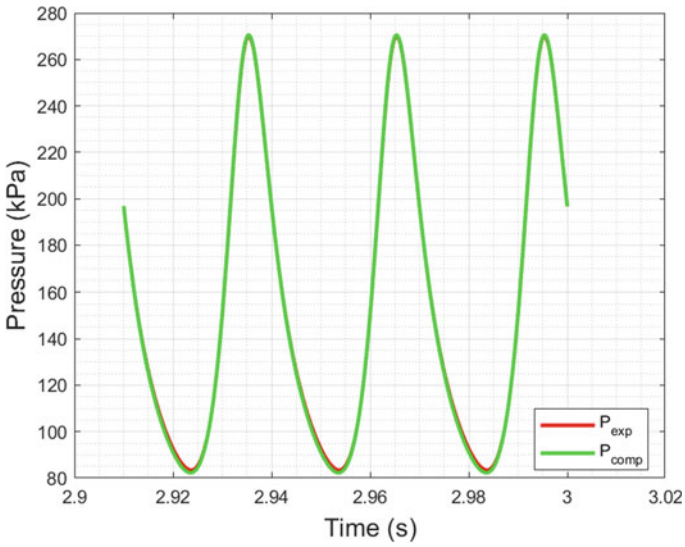
Fig. 4 Pressure of gas in expansion and compression chambers—variation with time in the base case
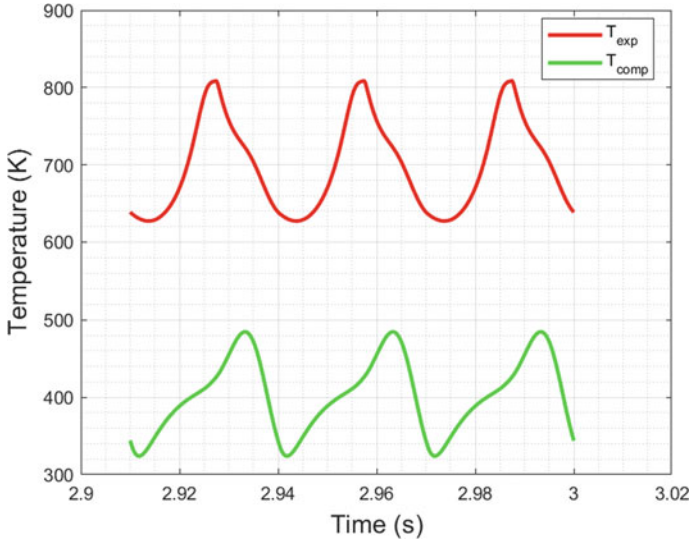
Fig. 5 Variation with time of gas temperatures inside expansion and compression spaces: base case

is thus given in Fig. 6. It can be seen from Fig. 6 that the pressure difference between the two chambers varies between -0.5 and 1.5 kPa. Also, the pressure difference variation plot is in sync with the mass variation plot in Fig. 3 with pressure difference
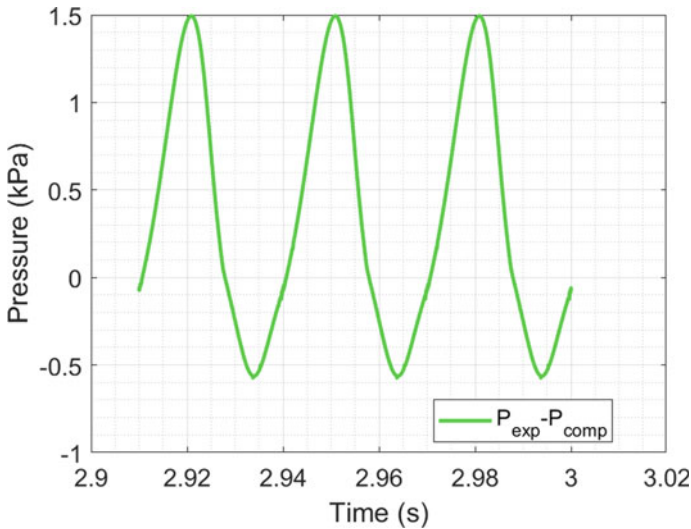
Fig. 6 Variation with time of difference between expansion chamber pressure and compression chamber pressure for base case

being zero at the same instances as mass in the expansion and compression chambers is at their extremums, which serves as a consistency check for the model.

The temperature evolution with time which is shown in Fig. 5 shows that with the 0.45 regeneration effectiveness used in the current simulations, there is a significant difference between the lowest temperature in the expansion chamber and the maximum temperature in the compression chamber. Due to the regenerator preheating the gas before entering the expansion chamber the temperature inside the expansion chamber is not falling below 620 K while for the same reason that the regenerator is cooling the gas before it enters the compression chamber, the temperature in the compression is not exceeding 480 K.

The instantaneous rates of heat and work transfer in the engine, as predicted by the model, are shown in Figs. 7 and 8. While the heat transfer is mostly positive in the expansion chamber and negative in the compression chamber as would be expected, the work transfer rate is either positive or negative at different times in both the chambers. Further, the network transfer is also alternating between positive and negative values showing the need for a properly designed flywheel. The information from this prediction could be used for flywheel design. Overall this base case engine is estimated to produce about 27 W power at an efficiency of about 11%. The P–V variations inside the compression and expansion chambers for one cycle of operation of the engine are shown in Figs. 9 and 10, respectively.

The model is used to assess the influence of some of the operating variables on the performance of the engine. The first variable considered for the parametric evaluation is the charging pressure. Charging pressure is the pressure inside the engine when it
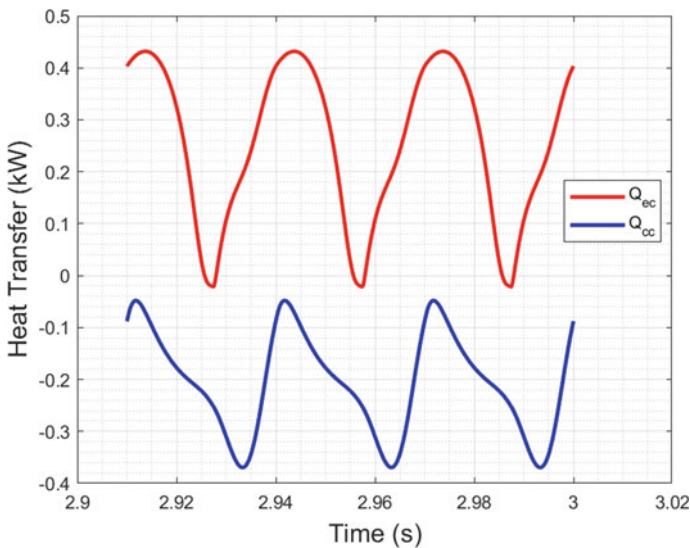
Fig. 7 Variation with time of the rate of heat transfer from hot source to expansion space and heat transfer from compression space to cold source for the base case
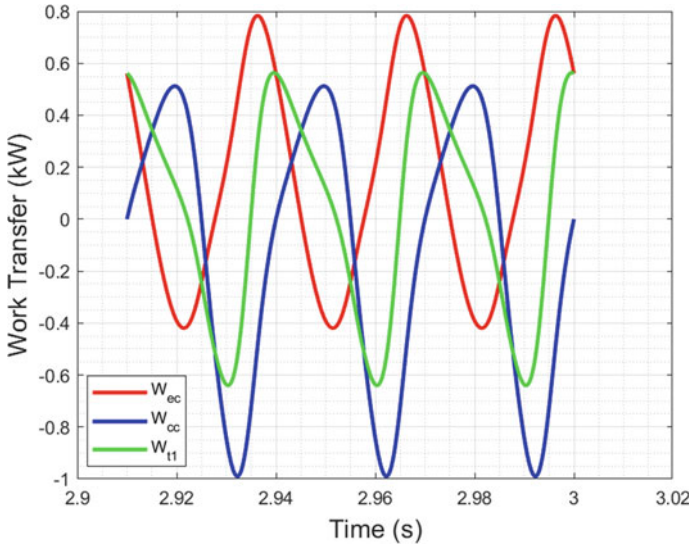
Fig. 8 Variation with time of work transfer rate to/from the expansion space, compression space and network transfer for the base case
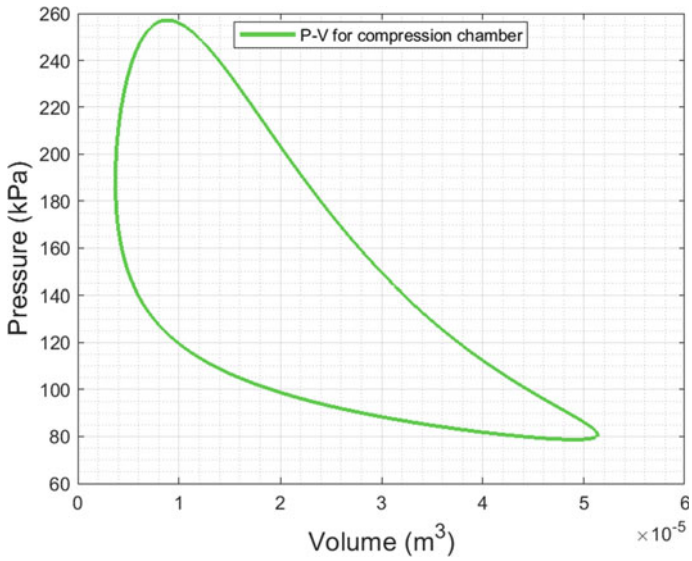
Fig. 9 PV diagram of the compression chamber for one cycle of operation of the base case engine
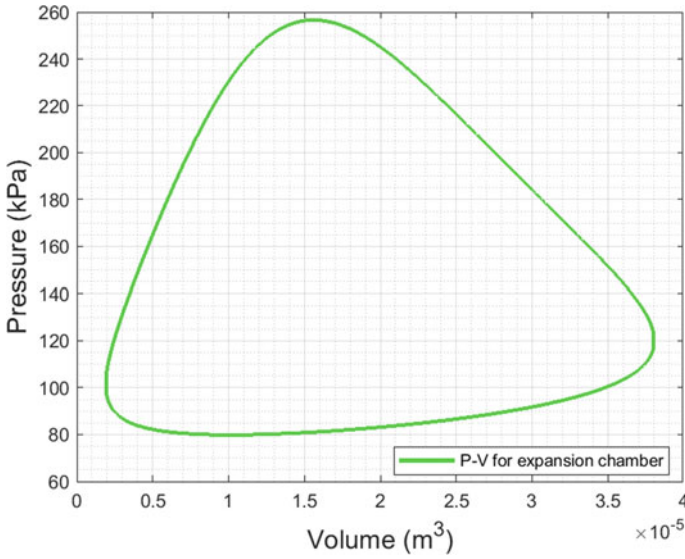
Fig. 10 PV diagram of the expansion chamber for one cycle of operation of the base case engine

is started. Simulations were conducted for different values of the charging pressure ranging between 1 bar and 5 bar and predictions were made on how the power output and efficiency of the engine is influence by the pressure in the engine. The effect of pressure on the power output of the engine and its efficiency are shown in Figs. 11 and
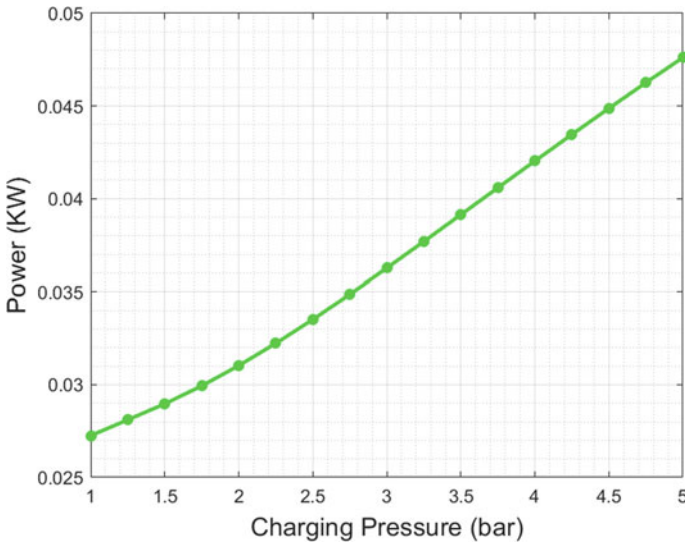
Fig. 11 Effect of charging pressure on the power generated by the engine
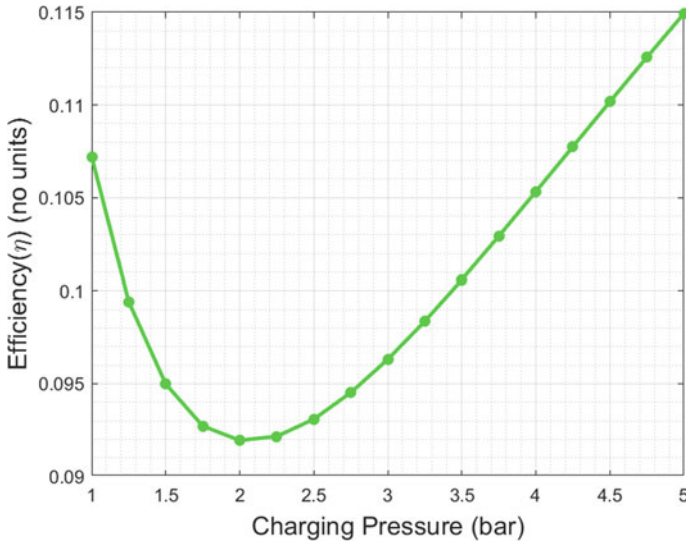
Fig. 12 Effect of charging pressure on the efficiency of the engine

12. It can be seen from Fig. 11 that the power output of the engine increases almost linearly with the charging pressure. The efficiency, on the other hand, has a more complicated response to the charging pressure. The efficiency decreased slightly as the charging pressure is increased from 1 bar to 2 bar and then it steadily increased with the pressure. It should be noted here that the efficiency varied within a narrow range between 9.3 and 11.5% as the pressure is varied across a rather wide range between 1 bar and 5 bar. It thus can be concluded that it is better to pressurize the engine to get more power output for given engine size. However, it is necessary to ensure that the pressure is sufficiently high to avoid the low-efficiency scenario which appears to occur at moderate pressures. Even though maintaining high pressure inside the engine yields higher performance in terms of power and efficiency, the set up required for the pressurization and retaining the pressure significantly increases the complexity of the engine. The improvement in performance may not fully justify the increased capital and maintenance costs involved in operating a pressurized Stirling engine. Thus, it is important to investigate other possible strategies for improving the performance which does not require adding more complexity to the system.

Temperature of heat source is an important thermodynamic parameter that has a strong influence on any heat engine. The predicted trends of how the performance of the Stirling engine under study varies with the source temperature are presented in Figs. 13 and 14. It can be seen from Fig. 13 that the power generated by the engine increased almost linearly with the source temperature as it is varied between 500 and 1000 K. As expected the efficiency also increased, rapidly at the beginning and then a bit more gradually, with the increasing temperature. This behavior is in-line with the variation of ideal efficiency of the heat engine as a function of the source
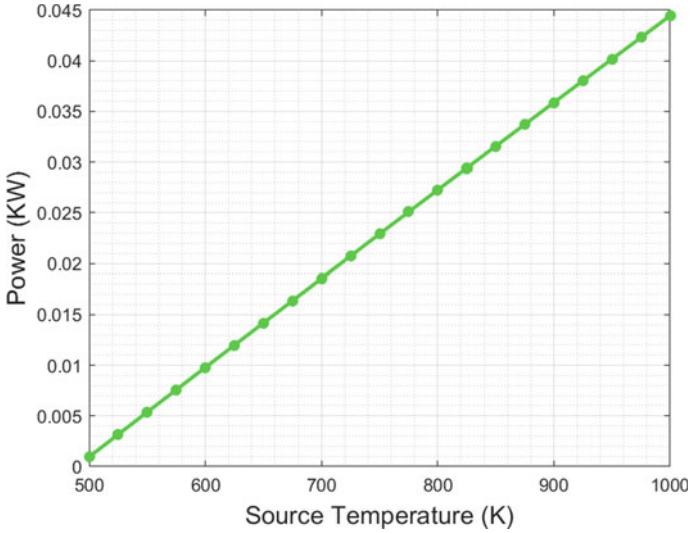
Fig. 13 Effect of source temperature on the power generated by the engine
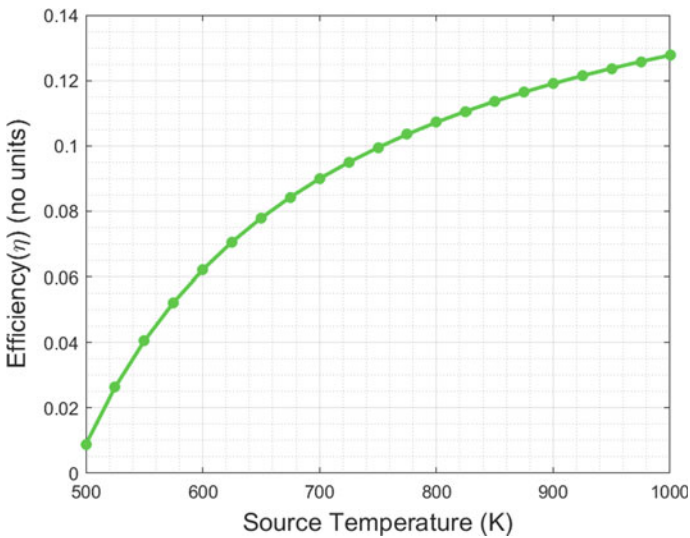
Fig. 14 Effect of source temperature on the efficiency of the engine

temperature. While source temperature has a favorable effect on the performance, material limitations usually limit the highest permissible temperature and further, Stirling engines are mainly being investigated for renewable energy where it may not be possible to achieve high temperatures.

As was mentioned in an earlier section, regeneration is a key aspect in achieving better performance from the Stirling engine. In this study, regenerator performance is modeled using a single parameter called "regenerator effectiveness" which is defined by Eqs. (11) and (12). As can be understood from these equations the higher values of the parameter "regenerator effectiveness", should mean that the regenerator is recuperating more heat between the air streams moving between the expansion chamber and compression chamber. In the simulations of the effect of charging pressure and source temperature on the performance of the engine, the results of which are presented in Figs. 11, 13, and 14, the regenerator effectiveness is taken as 0.45. It can be seen from Figs. 12 and 14 that the efficiencies obtained are rather low, especially at low pressures and temperatures.

To further study the influence of the regenerator effectiveness of the performance of the engine, simulations were performed for different values of the regenerator effectiveness to assess its influence on engine performance. Figure 15 shows how the power output from the engine varies as a function of regenerator effectiveness. It is clear from Fig. 15 that a high level of regeneration will give better power output from the engine. Further, efficiency is also significantly enhanced where there is a greater degree of regeneration in the engine (see Fig. 16). Achieving better regeneration in the engine requires providing more thermal mass and strategies for enhancing the heat transfer inside the regenerator gap. In reality, these additions may affect the operation of the engine in ways other than simply enhancing the effectiveness. The results presented in Figs. 15 and 16, should thus be considered with caution as the numerical values in those plots may not be accounting for all the factors that could influence the operation of the engine. Nevertheless, given the
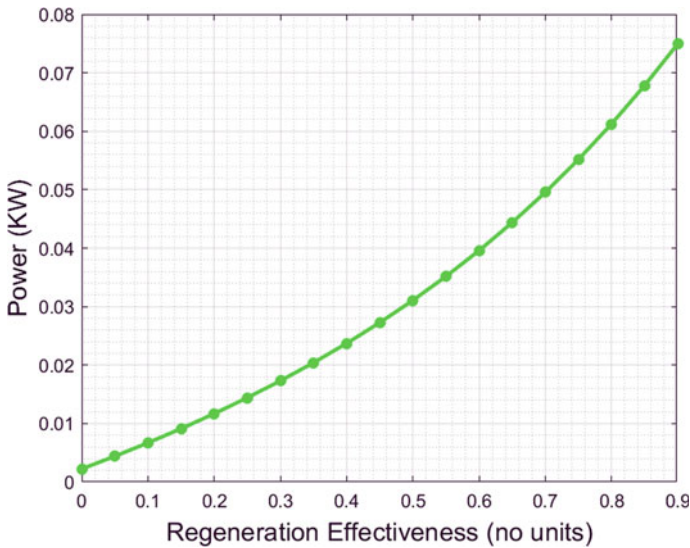
Fig. 15 Effect of regeneration effectiveness on the power produced by the engine
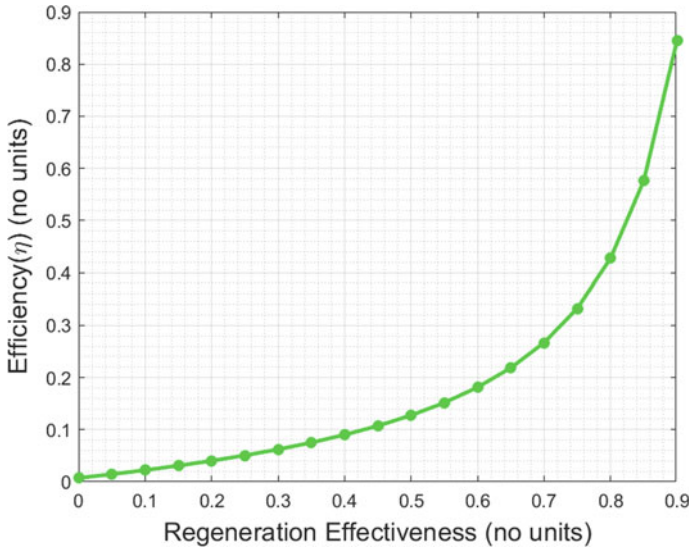
Fig. 16 Effect of regeneration effectiveness on the efficiency of the engine

strong improvement that power and efficiency seem to derive from an increase in the regenerator effectiveness, it may be safe to assume that effective regeneration will produce better performance in the engine. It was seen from the plots (not shown here) of the temperature histories inside the expansion and compression chambers that as the effectiveness is increased the gap between the minimum temperature in the expansion chamber and the maximum temperature in the compression chamber was also increasing. This also means that the range of temperature variation in the two chambers diminished with increasing effectiveness making the processes in the chambers relatively more isothermal.

4 Conclusion

In this paper, a mathematical model is presented for simulating the operation of a beta type Stirling engine with rhombic drive. The model is obtained by combined the kinematic analysis of the links of the mechanism with thermodynamic analysis, flow analysis, and heat transfer analysis. The model is used to predict the performance of a Stirling with unique dimensions. The base case simulations are presented in detail which show how the thermodynamic variables inside the engine vary inside the engine during steady operation. These results reveal the intricate details of the interplay between the different physical processes inside the engine.

A parametric study is presented on the influence of operating conditions on the performance of the engine. It is observed that the power output of the engine increases,

nearly linearly, with an increase in the charging pressure. The efficiency, however, initially decreased with a moderate increase in the pressure but beyond 2 bar pressure, the efficiency steadily increased with pressure. The source temperature showed a strong influence on the performance with both power output and the efficiency increasing with increasing temperature as would be expected from thermodynamic standpoint. The higher value of regenerator effectiveness is also shown to significantly improve the power output and efficiency of the engine. However, since the model does not account for all possible implications of increasing the regenerator effectiveness to the engine operation, these results should only be considered for their qualitative trends.

References

1. Ross A (1993) Making sterling engine
2. Cinar C, Yucesu S, Topgul T, Okur M (2005) Beta-type Stirling engine operating at atmospheric pressure. Appl Energy 81(4):351–357
3. Shendage DJ, Kedare SB, Bapat SL (2011) An analysis of beta type Stirling engine with rhombic drive mechanism. Renew Energy 36(1):289–297
4. Cheng CH, Yu YJ (2011) Dynamic simulation of a beta-type Stirling engine with cam-drive mechanism via the combination of the thermodynamic and dynamic models. Renew Energy 36(2):714–725
5. Shazly JH, Hafez AZ, El Shenawy ET, Eteiba MB (2014) Simulation, design and thermal analysis of a solar Stirling engine using MATLAB. Energy Convers Manage 79:626–639
6. Toghyani S, Kasaeian A, Ahmadi MH (2014) Multi-objective optimization of Stirling engine using non-ideal adiabatic method. Energy Convers Manage 80:54–62
7. Chen W-L, Wong K-L, Chang Y-F (2014) A computational fluid dynamics study on the heat transfer characteristics of the working cycle of a low-temperature-differential γ-type Stirling engine. Int J Heat Mass Transf 75:145–155
8. Salazar JL, Chen W-L (2014) A computational fluid dynamics study on the heat transfer characteristics of the working cycle of a β-type Stirling engine. Energy Convers Manage 88:177–188
9. Abdollahpour A, Ahmadi MH, Mohammadi AH (2014) Thermodynamic model to study a solar collector for its application to Stirling engines. Energy Convers Manage 79:666–673
10. Ahmadi MH, Sayyaadi H, Dehghani S, Hosseinzade H (2013) Designing a solar powered Stirling heat engine based on multiple criteria: maximized thermal efficiency and power. Energy Convers Manage 75:282–291
11. Uzuneanu K, Popescu G, Panait T, Gan MĂ (2011) Thermodynamic analysis of a Stirling engine used as prime mover in a CCHP biomass system, pp 81–86
12. Cheng CH, Yu YJ (2010) Numerical model for predicting thermodynamic cycle and thermal efficiency of a beta-type Stirling engine with rhombic-drive mechanism. Renew Energy 35(11):2590–2601

Experimental Approach and CFD Analysis on Flow Devices

S. Gowtham Sanjai, Vishal Suresh, Raman Bedi, and A. Sumanthran

Abstract This paper deals with the study of experimental approach and investigation by using computational fluid dynamics (CFD) on various flow devices. An orifice meter, venturimeter and a nozzle meter are the most common type of measuring devices used for rate of flow by creating the differences in velocity and pressure. Pressure drop is an important parameter occurring in these flow devices, which is due to restricted passage of flow, properties, diameter ratio, etc. The focus here is to calculate the coefficient of discharge and other flow parameters to analyze theoretically with the application of Bernoulli's equation. The main objective of this paper is to analyze the variations across the sections of orifice meter, venturimeter and nozzle meter. Comparison of results by both experimental and computational methods was clearly understood, and also, the flow level was calibrated by calculating the coefficient of discharge in both the methods.

Keywords CFD · Measuring device · Bernoulli's equation · Coefficient of discharge

1 Introduction

Differential pressure flow meters find their application in many of the industries owing to less cost and simple design and work on Bernoulli's principle. These include orifice plates, venturi tubes, flow nozzles and variable area—rotameters. The orifice plates have a turn down ratio of 5:1, and thus, the venturi tubes are preferred when higher turn down ratios are required. The differential pressure flow meters as follows:

In venturi tubes, the rate of flow is measured by determining the pressure difference across the reduced cross section of the tube, whereas in orifice plates, it is measured by measuring pressure difference across the obstruction placed in the pipe which narrow downs the flow path of the fluid. When a flow nozzle is placed in a pipe carrying whose rate of flow is to be measured, the flow nozzle causes a pressure drop which varies

S. Gowtham Sanjai (✉) · V. Suresh · R. Bedi · A. Sumanthran
Department of Mechanical and Automobile Engineering, Faculty of Engineering,
CHRIST (Deemed to be University), Bangalore, India
e-mail: gowthamsanjai.s@christuniversity.in

with the flow rate. This pressure drop is measured using a differential pressure sensor and when calibrated this pressure becomes a measure of flow rate. Tamhankar et al. [1] carried out an experiment to determine the coefficient of discharge and obtained accuracy within 5% of results of flow parameters measured experimentally and with computational fluid dynamics (CFD) analysis by using Ansys Fluent 13.0 (Figs. 1, 2 and 3).

Sudhakar and Visvesvaraya [2] and Hari Vijay and Subrahmanyam [3] conducted CFD analysis on different profiles of venturimeter and measured different parameters like pressure, velocity, turbulence and discharge. Perumal and Krishnan [4] attempted to optimize the design parameters (diameter, diameter ratio, convergent angle) and study their effects on performance of venturimeter. With increase in diameter, the effect of beta on discharge coefficient was found to decrease. Sanghani et al. [5] compared the results of various flow parameters measured through an orifice meter theoretically, experimentally and with CFD simulation. Sanghani and Jayani [6] observed that the beta ratio has the maximum influence on the pressure drop in a venturimeter when compared with other parameters like throat length, convergent

Fig. 1 Venturimeter
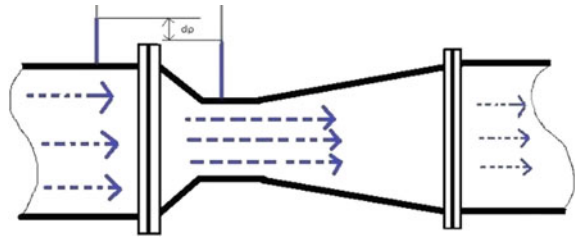
Fig. 2 Orifice plate
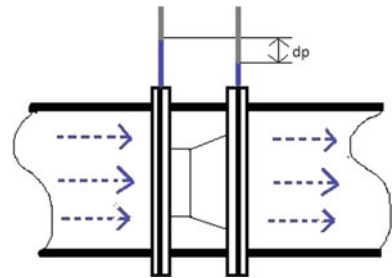
Fig. 3 Nozzle meter
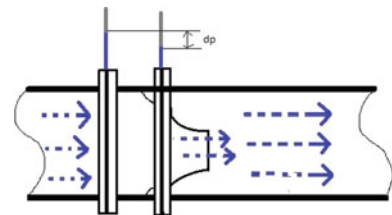
and divergent angles. The optimization of venturimeter geometry was also carried out using CFD analysis. Reddy [7] found out the variation of coefficient of discharge with respect to the Reynolds number. There were several other factors such as diameter ratio, convergence angle of nozzle and momentum transport coefficient which also affected the coefficient of discharge. Marginal coefficient of discharge was obtained when the Reynolds number was higher. Ouazzane and Barigou [8] did a comparative study on two flow conditioners and observed that in an orifice meter the pipe fitting causes distortion in the flow which affects the meter's calibration resulting in the error in flow metering. Reynolds number also plays an important role in reducing the error in discharge coefficient. It was found that the performance of orifice meter can be increased by vaned-plate flow conditioner. Verma [9] calculated the steam flow rate in a geothermal system by ActiveX component orifice meter. It was written in Visual Basic 6.0. It was also found that a calculation for a pipe line network is made easy by using orifice meter in MS-Excel. Jana et al. [10] have found the difference in the flow design. The factor which influences the flow design in upstream is found out to be the proximity to converging section. The presences of venturimeter, bubbles, inverted dispersed flow influencing the flow were found out.

2 Experimental Procedure

The experiments were conducted in our lab based on the requirements of this paper. Select the required orifice meter/venturimeter/nozzle meter and note down the dimension at inlet and outlet. Open the flow contact valve and allow a certain discharge. Take away the air bubbles from the manometer limbs. Note down the measuring levels on the two limbs of a manometer. Note down the diameter of the collecting tank and collect the water in it by closing the drain valve and time taken for a known rise of water in tank say 10 cm. Repeat the steps for different trials.

Specimen Calculations

a. **Theoretical Discharge**

$$Q_{\text{the}} = \frac{a_1 a_2 \sqrt{2gH}}{\sqrt{\left(a_1^2 - a_2^2\right)}} \text{ m}^3 \text{ s}$$

where

$a_1 = \frac{\pi D^2}{4}$ area of inlet section,

$a_2 = \frac{\pi d^2}{4}$ area of outlet section, m^2

$$H = 12.6 \times \frac{h}{1000} \ \text{m}$$

b. **Actual Discharge**

$$Q_{\text{act}} = \frac{A \times R}{t \times 1000} \ \text{m}^3 \ \text{s}$$

where

A Area of measuring tank in m^2
R Rise of water level in meters
t Time taken in seconds.

c. **Coefficient of Discharge C_d**

$$C_d = \frac{Q_{\text{act}}}{Q_{\text{the}}} = \frac{\text{Actual Discharge}}{\text{Theoretical Discharge}}$$

Orifice meter/venturimeter/nozzle meter have four valve opening positions, but here, we consider full opening and half opening. It has been observed the flow device as orifice meter, Venturimeter and nozzle meter will be considered and dealt based on the design. Here, the rise in water level in the collection tank is taken as constant as 100 mm, based on that time taken in sec, and differential head can be calculated as shown in Table 1. Based on the readings on the table, the calculations were carried out with the formulae.

Table 1 Observation readings

Flow device	Valve opening	Rise in water level in collection tank, R, mm	Time taken, t in s	Differential head, mm of Hg
Orifice meter	1/2 opening	100	25.6	133
	Full opening	100	17.6	270
Venturimeter	1/2 opening	100	22.4	80
	Full opening	100	16.7	166
Nozzle meter	1/2 opening	100	24.84	65
	Full opening	100	15.16	130

3   Results and Calculations

Based on the readings on Table 1, the velocity, discharge can be calculated.

Table 2 gives the readings calculated based on the formulae as experimental method for the various flow devices. The valve position was different where the theoretical discharge, actual discharge, coefficient of discharge and velocity can be calculated.

The results of CFD analysis are shown below:

3.1   For Full Opening of Inlet for Venturimeter

Figure 4 shows the analysis of full opening position for venturimeter where velocity varies from initial level to final level. Similarly, the flow level positions like 1/4, 1/2, 3/4 and full openings may be indicated for the flow devices.

Table 2 Calculations

Flow device	Valve opening	Velocity m/s	Theoretical discharge, Q_{th}, m^3/s	Actual discharge, Q_{act}, m^3/s	Coefficient of discharge, C_d
Orifice meter	1/2 opening	5.19×10^{-3}	7.28×10^{-6}	4.68×10^{-6}	0.64
	Full opening	0.015	1.03×10^{-5}	6.88×10^{-6}	0.66
Venturimeter	1/2 opening	3.57×10^{-3}	5.64×10^{-6}	5.35×10^{-6}	0.94
	Full opening	9.94×10^{-3}	8.13×10^{-6}	7.407×10^{-6}	0.91
Nozzle meter	1/2 opening	2.61×10^{-3}	5.09×10^{-6}	4.83×10^{-6}	0.94
	Full opening	8.57×10^{-3}	7.18×10^{-6}	6.95×10^{-6}	0.98
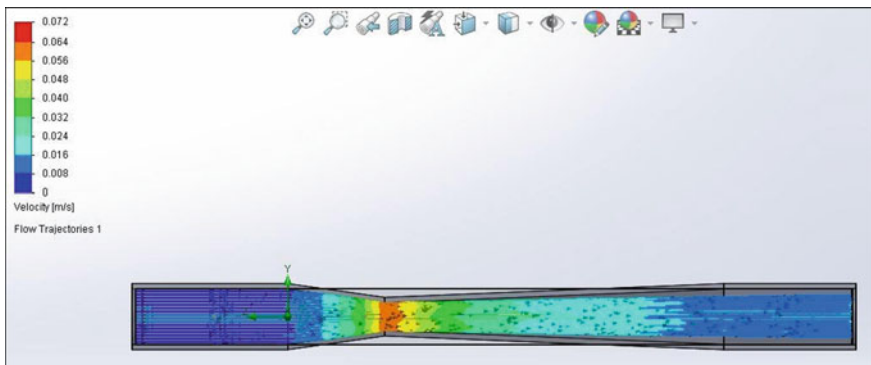
Fig. 4 CFD analysis for full opening of venturimeter
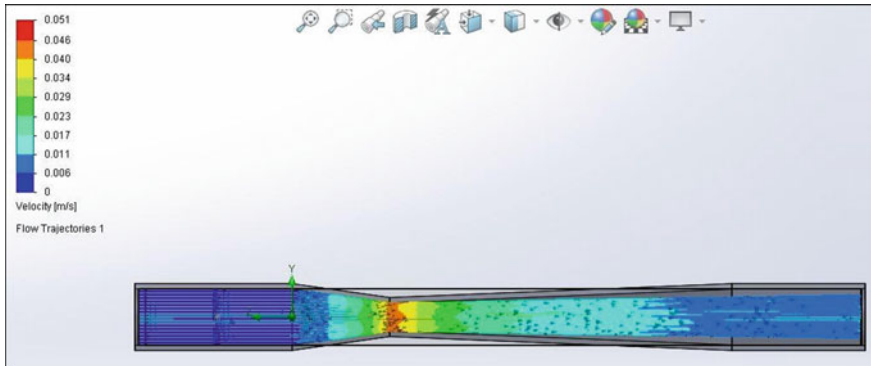
Fig. 5 CFD analysis for half opening of venturimeter

Here, we are analyzing the values for full and half opening so that flow level of inlet and outlet velocity, flow rate can be dealt as per the specifications which will be more precise. The coefficient of discharge is calculated by actual discharge and theoretical discharge which will be based on the parameters like area, velocity, time and the water level. The CFD analysis clearly shows the flow level from the initial position.

3.2 For Half Opening of Inlet for Venturimeter

Figure 5 shows the analysis of full opening position for venturimeter where velocity varies from initial level to final level. Similarly, the flow level positions like 1/4, 1/2, 3/4 and full openings may be indicated for the flow devices. The coefficient of discharge is calculated by actual discharge and theoretical discharge which will be based on the parameters like area, velocity, time and the water level. Based on the full valve opening position value, the position of half opening was fixed to analyze and also variations over it. This process of variations is possible while doing the experiments in the lab.

Figure 5 shows the analysis of half opening position for venturimeter where velocity varies from initial level to final level. Based on the values, discharge can be calculated.

3.3 For Full Opening of Inlet for Orifice Meter

Figure 6 shows the analysis of full opening position for orifice meter where velocity varies from initial level to final level.
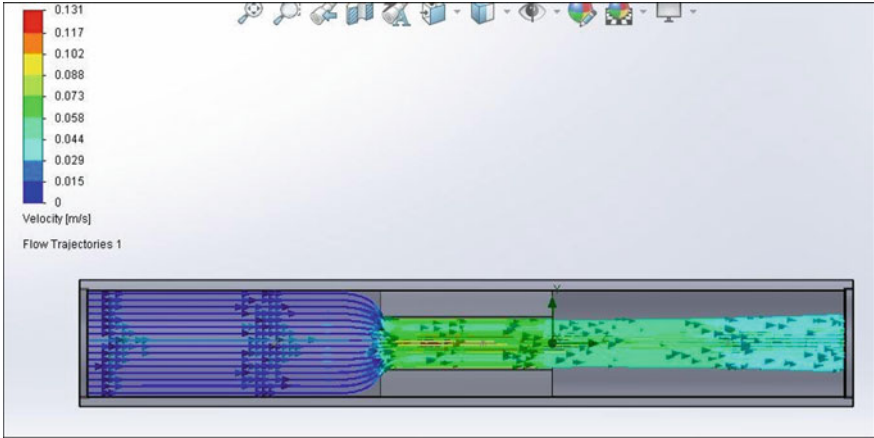
Fig. 6 CFD analysis for full opening of orifice meter

3.4 For Half Opening of Inlet for Orifice Meter

Figure 7 shows the analysis of half opening position for orifice meter where velocity varies from initial level to final level.
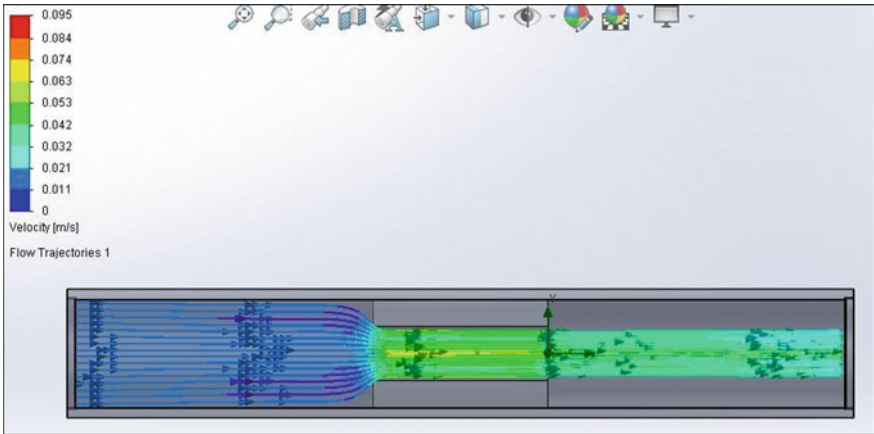
Fig. 7 CFD analysis for half opening of orifice meter

3.5 For Full Opening of Inlet for Nozzle Meter

Figure 8 shows the analysis of full opening position for nozzle meter where velocity varies from initial level to final level.
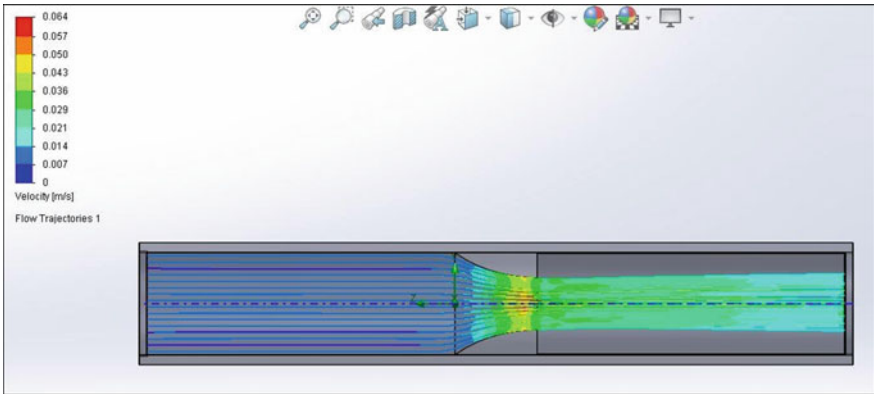
Fig. 8 CFD analysis for full opening of nozzle meter
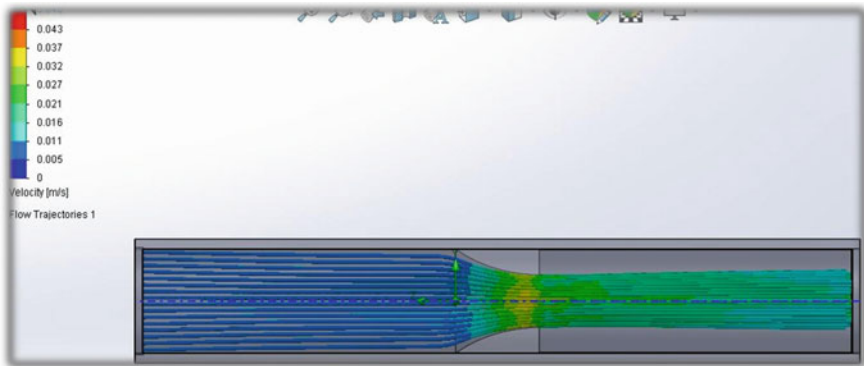
Fig. 9 CFD analysis for half opening of nozzle meter

Table 3 Comparison

Flow device	Valve opening	Coefficient of discharge—experimental	Coefficient of discharge—CFD
Orifice meter	1/2 opening	0.64	0.66
	Full opening	0.66	0.71
Venturimeter	1/2 opening	0.94	0.92
	Full opening	0.91	0.90
Nozzle meter	1/2 opening	0.94	0.92
	Full opening	0.98	0.97

3.6 For Half Opening of Inlet for Nozzle Meter

Figure 9 shows the analysis of half opening position for nozzle meter where velocity varies from initial level to final level.

Comparison—Experimental Approach and CFD Analysis
The experimental approach and CFD analysis of various flow devices like orifice meter, venturimeter and nozzle meter are shown in Table 3.

The table gives the comparison over the experimental approach with computational fluid dynamics (CFD) values.

From Table 3, it has been observed that there is very small variation in the discharge values conducted experimentally in our lab compared to the CFD analysis.

4 Conclusion

The experimental approach was carried in our lab as per the specifications, and CFD analysis also carried out successfully for the flow of discharge. Based on the Bernoulli s equation, the pressure drop and flow rate were carried out as per the parameters. The values of coefficient of discharge were found out in the lab, and CFD analysis is likely to be closer. The accuracy of results obtained to be within 4%. Calibration of the flow devices—venturimeter, orifice meter and nozzle meter—was successfully carried out. As per the approaches, the CFD analysis is the best approach based on the accuracy and time constraint.

References

1. Tamhankar N (2014) Experimental and CFD analysis of flow through venturimeter to determine the coefficient of discharge. Int J Latest Trends Eng Technol 3(4):194–200
2. Sudhakar K, Visvesvaraya S (2017) Original research paper. Indian J Res 6(7):8–10
3. Hari Vijay P, Subrahmanyam V (2014) CFD simulation on different geometries of venturimeter. Int J Res Eng Technol 3(7):456–463
4. Perumal K, Krishnan J (2013) A CFD study of the effect of venturi geometry on high pressure wet gas metering. Int J Oil Gas and Coal Technol 6(5):549–566
5. Sanghani CR, Jayani DC, Hingu AH, Jadav MY, Jiyavia DV (2016) Comparison of experimental, theoretical and simulation result for pressure drop in sharp edged orifice meter. Int J Sci Eng Technol Res 5(3):775–778
6. Sanghani C, Jayani D (2016) Optimization of venturimeter geometry for minimum pressure drop using CFD analysis. Recent Trends Fluid Mech 3(2):31–35
7. Reddy YR (1973) Herschel-type venturimeter discharge coefficients at low Reynolds number. Int J Mech Sci 15(9):757–763
8. Ouazzane AK, Barigou M (1999) A comparative study of two flow conditioners and their efficacy to reduce asymmetric swirling flow effects on orifice meter performance. Chem Eng Res Design 77(8):747–753
9. Verma MP (2010) OrificeMeter: an ActiveX component to determine fluid flow in a pipeline. Comput Geosci 36(8):1091–1096
10. Jana AK, Das G, Kumar P (2008) The hydrodynamics of liquid–liquid upflow through a venturimeter. Int J Multiph Flow 34(12):1119–1129

Power Law Lubricant Consistency Variation with Pressure and Mean Temperature Effects in Roller Bearing

N. Jalatheeswari and Dhaneshwar Prasad

Abstract The present paper squarely aims to scrutinize the normal velocity of a hydrodynamic lubrication of roller bearings. The changes that happen in lubrication consistency due to pressure and temperature are shown in figures and tables. Further, hydrodynamic lubricant pressure, film temperature, mean film temperature, load and traction for different consistency index n and squeezing velocity q are calculated and compared with the previous results. Those results are positively agreed with the previous findings.

Keywords Roller bearing · Power law · Hydrodynamic lubrication · Normal velocity · Pressure · Mean temperature · Load · Traction · Lubricant consistency

1 Introduction

Roller bearing contribution to the field of hydrodynamic lubrication is copious. Conveyance of load at low friction is its sole purpose. During transportation of lubricant, the temperature effect in lubrication has a serious impact. The attitude of temperature and pressure is not the same at normal and high speed and also at heavy load. The lubricant stops to behave Newtonian at high pressures and high shear rate [1]. Here comes the application of hydrodynamic lubrication to the friction of bearings. Newtonian characteristics of lubricant were presumed to be at the early stages of the development of the lubricants. Later, the lubricant's non-Newtonian features have also been invariably served in many lubrication problems. Hence, the non-Newtonian fluid models with solid particle flavors have become the center of focus on the cause that favors in improving and strengthening the life of bearings.

N. Jalatheeswari (✉) · D. Prasad
Kanchi Mamunivar Centre for Post Graduate Studies, Lawspet, Puducherry, India
e-mail: njalatheeswari@gmail.com

D. Prasad
e-mail: rpdhaneshwar@gmail.com

Earlier, Reynolds equation in one-dimensional case was used to determine the film thickness at different positions of discrete piston stroke by Elison and Saundars [2]. The formation of a fully developed thick fluid film throughout the engine cycle was clearly visible. Furuhama [3] augmented it by introducing squeeze film lubrication. It was believed that this would provide a thin and finite fluid lubricant film at piston reversal at place of no lubricant entertainment.

Elasto hydrodynamic lubrication may be considered as a lubrication regime wherever a thin lubricating film is created between two contacting moving surfaces in relative motion at heavy load. The pressure force here is assumed to be sufficient enough to produce extensive elastic deformation of the contacting surfaces. EHL typically happens in non-conformal contacts of moving surfaces, and lots of machine parts such as roller bearings and gears depend on it (EHL) in their operations. It was not discovered until 1949 that a skinny fluid film can even separate contact surfaces in high-pressure region. A straightforward image of EHL film was finally presented by Gohar and Cameron [4] in 1963. In this case of classical solutions of EHD, Reynolds equation was employed to explain the behavior of high-pressure region, whereas elastic deformation was typically evaluated by the method of Hertz theory of elastic contacts. Cameron and Wood [5] and Sassenfeld and Walther [6] were the first to derive the Reynolds equation for hydrodynamic lubrication in 1959 with full numerical solutions; however, it was limited to the rigid contact surfaces, whereas Dowson and Higginson [7] were the first to derive the full numerical solutions for EHL of rolling surfaces. Later, Dowson and co-workers and others studied these cases extensively and produced various important results related to EHL contacts.

Later, Punit and Khonsari [8] discovered the effects of temperature change and shear thinning on the EHL of rolling/sliding line contact, using Carreau viscosity model. Further, Lin et al. [9] studied parabolic-film slider bearings with a micropolar fluid and concluded that a non-Newtonian lubricant film provides higher values of the damping coefficients and steady load capacity and the dynamic stiffness in comparison with Newtonian fluids.

Rolling bearings usually offer support to the load in rolling elements. The centrifugal forces on balls become vital, and therefore, the inner and outer race contact angles are not any longer the same at high speed. In this regard, Harris [10] introduced a closed form solution method in order to predict sliding in thrust loaded, angular contact ball bearings. Liao and Lin [11] presented a simple elastic deformation formula using three-dimensional geometry of the contact surfaces at the inner and outer races. Han et al. [12] investigated high-speed bearings considering both the axial and radial loads and concluded that a better way to avoid bearings from sliding at high angular speeds is to enhance the deformation applied in the axial direction.

Takabi and Khonsari [13] carried out an investigation on the dynamic behavior of radially loaded rollers running at heavy loads but low speeds including surface roughness. The analysis took consideration of various lubrication regimes like rigid solid isoviscous, elastic solid isoviscous, rigid solid piezoviscous and elastic solid piezoviscous under the varied loaded and unloaded sections of the bearings. The results provide a good knowledge of the lubricant film thickness variation, heat production and wear-rate between the rollers and therefore the raceways because the rollers travel within the orbital direction. Accordingly, it might be thought that a rise in the wear-rate will associate substantial rise of the heat though it does not have an effect on the film thickness perceptibly.

Zhang et al. [14] investigated the resistance characteristics of nanometer-thick lubricant films at high slippery speeds employing a pin-on-disk kind tribotester wherever unidirectional sliding at constant speeds starting from 10 to 100.0 rpm is targeted, employing a extremely precise air-bearing spindle servomotor and a high resolution built-on progressive encoder. Further, they added that the development of a sliding-pin-and-suspension has successfully brought down the vibrations from the loaded one and therefore the friction force sensing mechanisms, thereby achieving steady contact slippery at speeds up to 0.2 m/s [15, 16].

Wang and Lu [17] presented theoretical as well as experimental investigations of the impact of viscosity on film cavitations of high-speed sleeve bearings. The study further included the cavitations shape and the location of a spiral oil wedge hydrodynamic bearing. The analysis considered was based on transparent bearing fitted with high-speed camera. The corresponding Reynolds equation was derived with cavitations using the new Elrod theoretical approach with the cavitations of varying viscosity sleeve bearings. Those results were also compared, and cavitations were observed in strip-shaped forms for both the cases of high and low viscosity lubricants. Also, the oil vapors/bubbles were generated in the rupture region of the oil film at higher speeds. Further, with the increase of the rotating speed and the decrease of the availability pressure also causes the raising of the cavitations space of the oil film clearly. Further, it was concluded that the low viscosity lubricant would be preferable to that of the high viscosity lubricant.

Fusi [18] in his paper on thermo hydrodynamic lubrication showed the way to acquire the constitutive equation using the maximization of entropy production methods. Also, he bestowed the model for the flow in a channel. Further, he discussed the initial and boundary conditions for the problem at length. In addition, the problem was restructured using a different dimensionless scheme considering the lubrication scaling and the leading order approximations. Then, he proved the existence of the analytical solution to be determined under acceptable hypotheses based on the available data. Then, the numerical scheme was categorically presented for the simulation for various types of initial and boundary data. Finally, a particular solution was obtained based on a small perturbation given to the analytical solution, and then, it was solved numerically.

In continuation to the above discussion, the present paper intends to analyze the effects of the hydrodynamic pressure and the lubricant temperature on power law lubricants under the rigid cylindrical rolling line contact with squeezing motions and cavitations. The effects of pressure along with mean lubricant temperature (isothermal boundaries) are considered for the lubricant consistency variation. The load and the traction are also calculated for the different values of the consistency index with normal squeezing parameter.

2 Mathematical Analysis

The governing equations for the one dimensional fluid flow are [19]

$$\frac{\mathrm{d}p}{\mathrm{d}x} = \frac{\partial \tau}{\partial y}. \tag{1}$$

$$\frac{\partial u}{\partial x} + \frac{\partial v}{\partial y} = 0. \tag{2}$$

where the shear stress relation for this case is

$$\tau = m \left| \frac{\partial u}{\partial y} \right|^{n-1} \frac{\partial u}{\partial y}. \tag{3}$$

The consistency m of the above power law is taken as

$$m = m_0 \mathrm{e}^{\alpha p + \left(\frac{T_0}{T_m}\right)}. \tag{4}$$

where the mean temperature T_m is defined as

$$T_m = \frac{2}{h} \int\limits_0^{h/2} T \mathrm{d}y. \tag{5}$$

u and v being, respectively, the velocity components in x- and y-directions and p and T are the hydrodynamics pressure and the temperature, respectively.

The boundary conditions for the Eqs. (1) and (2) are [20]

$$\text{When } y = 0, \ \frac{\partial u}{\partial y} = 0 \text{ at } y = \frac{h}{2}, \ u = U \ v_{h/2} = \frac{U}{2}\frac{\mathrm{d}h}{\mathrm{d}x} + \frac{V}{2} \text{ and } v_0 = 0 \tag{6}$$

Integrating Eq. (1) using the boundary conditions mentioned in (6), one may get

$$u_1 = U + \left[(1/m) \left(\frac{\mathrm{d}p_1}{\mathrm{d}x} \right) \right]^{1/n} \left(\frac{n}{n+1} \right) \left(y^{1+\frac{1}{n}} - \left(\frac{h}{2} \right)^{1+\frac{1}{n}} \right) \quad -\infty < x \le -x_1.$$

(7)

$$u_2 = U - \left[(1/m) \left(-\frac{\mathrm{d}p_2}{\mathrm{d}x} \right) \right]^{\frac{1}{n}} \left(\frac{n}{n+1} \right) \left(y^{1+\frac{1}{n}} - \left(\frac{h}{2} \right)^{1+\frac{1}{n}} \right) \quad -x_1 \le x \le x_2.$$

(8)

Integrating the above continuity Eq. (2) using the conditions (6) and $\frac{\mathrm{d}p_1}{\mathrm{d}x} = 0$ at $x = -x_1$ and $h = h_1$, one can get

$$\frac{\mathrm{d}p_1}{\mathrm{d}x} = \frac{2^{n+1} m}{h^{2n+1}} \left(\frac{2n+1}{n} \right)^n (U(h-h_1) + V(x+x_1))^n \quad -\infty < x \le -x_1. \quad (9)$$

$$\frac{\mathrm{d}p_2}{\mathrm{d}x} = -\frac{2^{n+1} m}{h^{2n+1}} \left(\frac{2n+1}{2n} \right)^n (-U(h-h_2) - V(x+x_2))^n \quad -x_1 \le x \le x_2. \quad (10)$$

Using dimensionless scheme given below, the above Eqs. (9) and (10) are reduced to

$$\frac{\mathrm{d}\overline{p}_1}{\mathrm{d}\overline{x}} = \frac{\overline{m}_0 \overline{E}}{\overline{h}^{2n+1}} \overline{f}^n \quad -\infty < \overline{x} \le -\overline{x}_1. \quad (11)$$

$$\frac{\mathrm{d}\overline{p}_2}{\mathrm{d}\overline{x}} = -\frac{\overline{m}_0 \overline{E}}{\overline{h}^{2n+1}} \overline{g}^n \quad -\overline{x}_1 \le \overline{x} \le \overline{x}_2. \quad (12)$$

$$\overline{x} = x/\sqrt{2Rh_0}; \quad \overline{y} = y/h_0; \quad \overline{h} = h/h_0; \quad \overline{p} = \alpha p; \quad \overline{g} = -\overline{f};$$

$$\overline{E} = e^{\overline{p} + (\overline{T}_0/\overline{T}_m)}; \quad \overline{m} = 2mc_n\alpha. \quad \overline{f} = \overline{x}^2 - \overline{x}_1^2 + 2q(\overline{x} + \overline{x}_1);$$

$$c_n = \left(\frac{2(2n+1)}{n} \right)^n \sqrt{\frac{2R}{h_0}} \left(\frac{U}{h_0} \right)^n; \quad \overline{T} = \beta T; \text{ etc.}$$

After dimensionlising (7) and (8), one can get a single equation

$$\overline{u} = 1 + \frac{\overline{f}}{\overline{h}^{(2n+1)/n}} \overline{s} \quad -\infty < x \le x_2. \quad (13)$$

where $\overline{s} = 2^{2+\frac{1}{n}} \left(\frac{2n+1}{n+1} \right) \left((\overline{y})^{1+\frac{1}{n}} - \left(\frac{\overline{h}}{2} \right)^{1+\frac{1}{n}} \right).$

The energy equation for the one-dimensional flow case may be assumed to be

$$k\frac{\partial^2 T}{\partial y^2} + \tau\frac{\partial u}{\partial y} = \rho c u\frac{dT_m}{dx}. \tag{14}$$

where k is the heat conduction of the fluid and is assumed to be constant.

$$\text{Assuming, at } y = 0, \frac{\partial T}{\partial y} = 0; \text{ and at } y = \frac{h}{2}, T = T_h. \tag{15}$$

This above Eq. (14) is solved under boundary conditions mentioned in (15) and is obtained as

$$T_1 = T_h + \frac{\rho c}{k}\frac{dT_{m_1}}{dx}\left(\frac{U}{2}\left(y^2 - \frac{h^2}{4}\right) + \left[\frac{1}{m}\left(\frac{dp_1}{dx}\right)\right]^{\frac{1}{n}}\left(\frac{n^3}{(3n+1)(2n+1)(n+1)}\right.\right.$$

$$(y)^{3+\frac{1}{n}} - \frac{n}{n+1}\left(\frac{h}{2}\right)^{1+\frac{1}{n}}\frac{y^2}{2} + \frac{n(4n+1)}{2(3n+1)(2n+1)}\left(\frac{h}{2}\right)^{3+\frac{1}{n}}\right)$$

$$- \frac{m}{k}\left[\frac{1}{m}\left(\frac{dp_1}{dx}\right)\right]^{1+\frac{1}{n}}\left(\frac{n^2}{(3n+1)(2n+1)}\right)\left(y^{3+\frac{1}{n}} - \left(\frac{h}{2}\right)^{3+\frac{1}{n}}\right)$$

$$- \infty < x \le -x_1. \tag{16}$$

$$T_2 = T_h + \frac{\rho c}{k}\frac{dT_{m_2}}{dx}\left(\frac{U}{2}\left(y^2 - \frac{h^2}{4}\right) - \left[-\frac{1}{m}\left(\frac{dp_2}{dx}\right)\right]^{\frac{1}{n}}\left(\frac{n^3}{(3n+1)(2n+1)(n+1)}\right.\right.$$

$$(y)^{3+\frac{1}{n}} - \frac{n}{n+1}\left(\frac{h}{2}\right)^{1+\frac{1}{n}}\frac{y^2}{2} + \frac{n(4n+1)}{2(3n+1)(2n+1)}\left(\frac{h}{2}\right)^{3+\frac{1}{n}}\right)$$

$$- \frac{m}{k}\left[-\frac{1}{m}\left(\frac{dp_2}{dx}\right)\right]^{1+\frac{1}{n}}\left(\frac{n^2}{(3n+1)(2n+1)}\right)\left(y^{3+\frac{1}{n}} - \left(\frac{h}{2}\right)^{3+\frac{1}{n}}\right)$$

$$- x_1 \le x \le x_2. \tag{17}$$

Using the dimensionless scheme, the above temperature Eqs. (16) and (17) are reduced to,

$$\overline{T}_1 = \overline{T}_h + \frac{Uh_0^2\rho c}{2k\sqrt{2Rh_0}}\frac{d\overline{T}_{m_1}}{d\overline{x}}\left(\left(\overline{y}^2 - \frac{\overline{h}^2}{4}\right) + \frac{\overline{l}\,\overline{f}}{\overline{h}^{\frac{2n+1}{n}}}\right) - \frac{\overline{m}_0\overline{E}\,\overline{f}^{n+1}\overline{\gamma}}{\overline{h}^{\frac{2n^2+3n+1}{n}}}\overline{t}$$

$$- \infty < \overline{x} \le -\overline{x}_1. \tag{18}$$

$$\overline{T}_2 = \overline{T}_h + \frac{U h_0^2 \rho c}{2k\sqrt{2Rh_0}} \frac{d\overline{T}_{m_2}}{d\overline{x}} \left(\left(\overline{y}^2 - \frac{\overline{h}^2}{4} \right) + \frac{\overline{l}}{\overline{h}^{\frac{2n+1}{n}}} \overline{g} \right) - \frac{\overline{m}_0 \overline{E} \, \overline{g}^{n+1} \overline{\gamma}}{\overline{h}^{\frac{2n^2+3n+1}{n}}} \overline{t}$$

$$- \overline{x}_1 \leq \overline{x} \leq \overline{x}_2. \tag{19}$$

where

$$\overline{l} = 2^{2+\frac{1}{n}} \left(\frac{2n+1}{n} \right) \left(\left(\frac{n^3}{(3n+1)(2n+1)(n+1)} \right) (\overline{y})^{3+\frac{1}{n}} - \frac{n}{n+1} \left(\frac{\overline{h}}{2} \right)^{1+\frac{1}{n}} \frac{\overline{y}^2}{2} \right.$$

$$\left. + \frac{n(4n+1)}{2(3n+1)(2n+1)} \left(\frac{\overline{h}}{2} \right)^{3+\frac{1}{n}} \right); \quad \overline{t} = 2^{2+\frac{1}{n}} \left(\frac{n}{3n+1} \right) \left((\overline{y})^{3+\frac{1}{n}} - \left(\frac{\overline{h}}{2} \right)^{3+\frac{1}{n}} \right);$$

$$\overline{y} = \frac{y}{h_0}; \quad \overline{\gamma} = \frac{\beta U h_0}{k\alpha} \sqrt{\frac{h_0}{2R}};$$

The mean temperature T_{m_1}, as given in (5), can be calculated as

$$T_{m_1} = T_h + \frac{\rho c}{k} \frac{dT_{m_1}}{dx} \left(\begin{array}{c} -\frac{U}{3}\left(\frac{h^2}{4}\right) + \left[\frac{1}{m}\left(\frac{dp_1}{dx}\right)\right]^{\frac{1}{n}} \left(\frac{h}{2}\right)^{3+\frac{1}{n}} \left(\frac{15n^4+23n^3+9n^2+n}{3(4n+1)(3n+1)(2n+1)(n+1)} \right) + \\ \frac{m}{k}\left[\frac{1}{m}\left(\frac{dp_1}{dx}\right)\right]^{1+\frac{1}{n}} \left(\frac{n^2}{(3n+1)(2n+1)} \right)\left(\frac{h}{2}\right)^{3+\frac{1}{n}} \end{array} \right)$$

$$- \infty < x \leq -x_1. \tag{20}$$

Similarly, in the next region,

$$T_{m_2} = T_h + \frac{\rho c}{k} \frac{dT_{m_2}}{dx} \left(\begin{array}{c} -\frac{U}{3}\left(\frac{h^2}{4}\right) + \left[-\frac{1}{m}\left(\frac{dp_2}{dx}\right)\right]^{\frac{1}{n}} \left(\frac{h}{2}\right)^{3+\frac{1}{n}} \left(\frac{15n^4+23n^3+9n^2+n}{3(4n+1)(3n+1)(2n+1)(n+1)} \right) \\ + \frac{m}{k}\left[-\frac{1}{m}\left(\frac{dp_2}{dx}\right)\right]^{1+\frac{1}{n}} \left(\frac{n^2}{(3n+1)(2n+1)} \right)\left(\frac{h}{2}\right)^{3+\frac{1}{n}} \end{array} \right)$$

$$- x_1 \leq x \leq x_2. \tag{21}$$

Using the dimensionless scheme, the above mean temperature Eqs. (20) and (21) are reduced to,

$$\frac{d\overline{T}_{m_1}}{d\overline{x}} = \left(\overline{T}_{m_1} - \overline{T}_h - \frac{\overline{m}_0 \overline{E} \, \overline{f}^{n+1} \overline{\gamma}}{\overline{h}^{2n}} B_n \right) / \left(\zeta \left(A_n \overline{f} \overline{h} - \overline{h}^2 \right) \right) \quad - \infty < \overline{x} \leq -\overline{x}_1.$$

$$\tag{22}$$

$$\frac{\mathrm{d}\overline{T}_{m_2}}{\mathrm{d}\overline{x}} = \left(\overline{T}_{m_2} - \overline{T}_h - \frac{\overline{m}_0 \overline{E}\,\overline{g}^{n+1}\overline{\gamma}}{\overline{h}^{2n}}B_n\right)\bigg/\left(\varsigma\left(-A_n\overline{g}\overline{h} - \overline{h}^2\right)\right) \quad -\overline{x}_1 \le \overline{x} \le \overline{x}_2.$$

$$(23)$$

where $A_n = \left(\frac{15n^3+23n^2+9n+1}{(n+1)(3n+1)(4n+1)}\right)$; $B_n = \left(\frac{n}{4(4n+1)}\right)$; $\varsigma = \frac{\rho c}{k\sqrt{2Rh_0}}\frac{Uh_0^2}{12}$.

The load component in y-direction is given by

$$w_y = \int_{-\infty}^{-x_1} p\mathrm{d}x + \int_{-x_1}^{x_2} p\mathrm{d}x.$$

$$(24)$$

Then, the dimensionless load is

$$\overline{w}_y = \frac{w_y\alpha}{\sqrt{2Rh_0}} = -\int_{-\infty}^{\overline{x}_2} \overline{x}\frac{\mathrm{d}\overline{p}}{\mathrm{d}\overline{x}}\mathrm{d}\overline{x}.$$

$$(25)$$

The surface traction force T_{Fh} can be written as

$$T_{Fh} = \int_{-\infty}^{-x_1} \left(\frac{h}{2}\left(\frac{\mathrm{d}p_1}{\mathrm{d}x}\right)\right)\mathrm{d}x + \int_{-x_1}^{x_2} \left(\frac{h}{2}\left(\frac{\mathrm{d}p_2}{\mathrm{d}x}\right)\right)\mathrm{d}x.$$

$$(26)$$

Then, the dimensionless traction $\overline{T}_{Fh} = 2\alpha T_{Fh}/h_0$ comes out to be

$$\overline{T}_{Fh} = \int_{-\infty}^{-\overline{x}_1} \overline{h}\left(\frac{\mathrm{d}\overline{p}_1}{\mathrm{d}\overline{x}}\right)\mathrm{d}\overline{x} + \int_{-\overline{x}_1}^{-\overline{x}_2} \overline{h}\left(\frac{\mathrm{d}\overline{p}_2}{\mathrm{d}\overline{x}}\right)\mathrm{d}\overline{x}.$$

$$(27)$$

Finally, one can get the consistency expression in the form

$$\overline{m} = \overline{m}_0\overline{E}.$$

$$(28)$$

3   Results and Discussion

In this present paper, the rolling and squeezing motions of two infinite rigid cylinders lubricated with a power law fluid under the thermal condition are analyzed. The altered energy and Reynolds equations are numerically solved yielding pressure and temperature. Consider the following numerical values for the calculations:

$$-0.1 < q < 0.1; 0.4 \leq n \leq 1.15; 0 \leq \overline{T_h} - \overline{T_0} \leq 5; \overline{\gamma} = 4; h_0 = 6 \times 10^{-5} \text{ m};$$

$$\alpha = 6 \times 10^{-8} \text{ Pa}^{-1} \text{ m}^2 \text{ and } R = 0.03 \text{ m}.$$

3.1   Velocity Distribution

For fixed values of q and n, the velocity distribution at various values of $\overline{x}$ between $\overline{x} = -9$ and $\overline{x} = -0.6$ is displayed. In this region, the velocity increases with $\overline{y}$, as shown Fig. 2, and this is comparable work done by Fusi [18] as well as predicted in Fig. 1. Further, at pressure peak $\overline{x} = -0.6$, the velocity does remain constant, as shown Fig. 3. This velocity distribution also matches well with Fig. 1 at the point of maximum pressure.

3.2   Pressure Distribution

For fixed n and ζ, the calculation of pressure $\overline{p}$ against $\overline{x}$ for different values of q is mentioned in Fig. 4; and for fixed q, the calculated value of pressure against $\overline{x}$ for various n and ζ is given in Figs. 5 and 6, respectively. The graphs illustrate that the input region collects increased pressure, and the same decreases at the outlet region [21]. The pressure peak falls down making a steep slope in graph and reduces to zero at the point of cavitations $\overline{x} = \overline{x}_2$, and this trend follows the work done by Hajishafiee et al. [22] and Hultqvist et al. [23].

3.3   Temperature Distribution

Corresponding to the different values of q, n and ζ, the temperature distribution is presented in Figs. 7, 8 and 9, respectively. It is quite piquant to observe that temperature dominates at inlet region, and its dominancy is ceased off near the maximum pressure point, $\overline{x} = -\overline{x}_1$ and then remains almost constant though temperature decreases numerically. The increase in temperature in the inlet zone is because of trailing action of the faster layers makes more viscous heat dissipation in the low
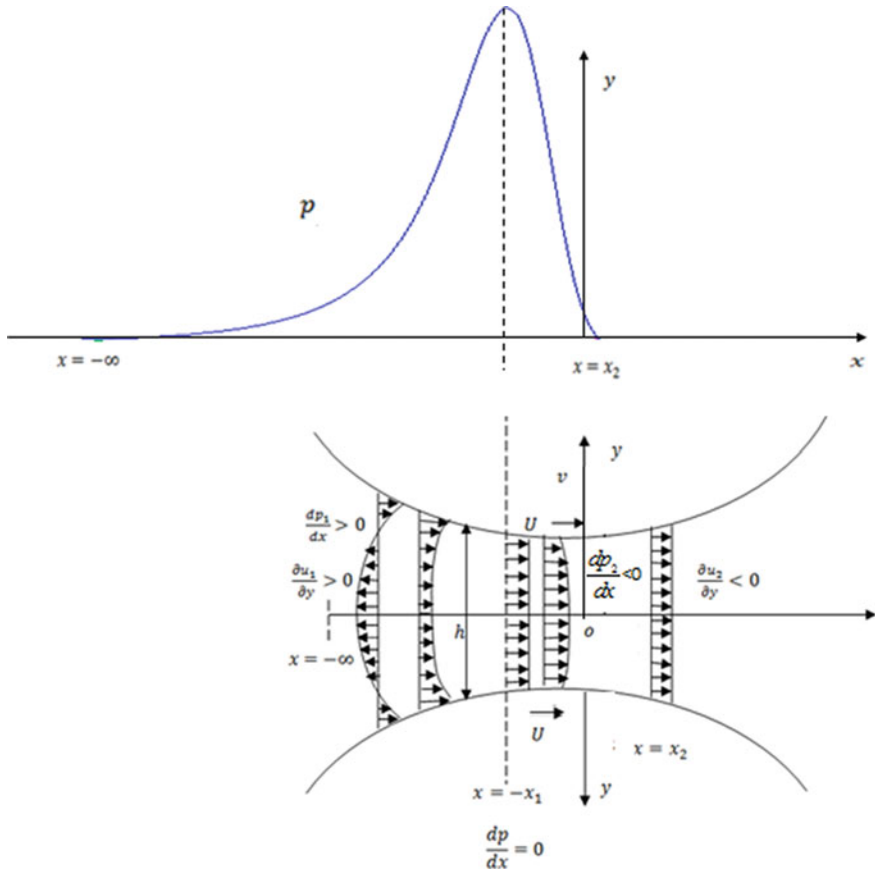
Fig. 1 Lubrication of cylindrical rollers

gap region and generates there more heat/temperature. From Figs. 7, 8 and 9, it is clear that temperature increases with n. Increasing n indicates an increase in effective viscosity [24]. The two-dimensional temperature is shown in Figs. 10 and 11 giving its distribution in the $\bar{x}$ and $\bar{y}$ plane. Figure 10 is drawn without convection because zeta is almost zero. Figure 11 shows the complete distribution of temperature with convection and conduction.
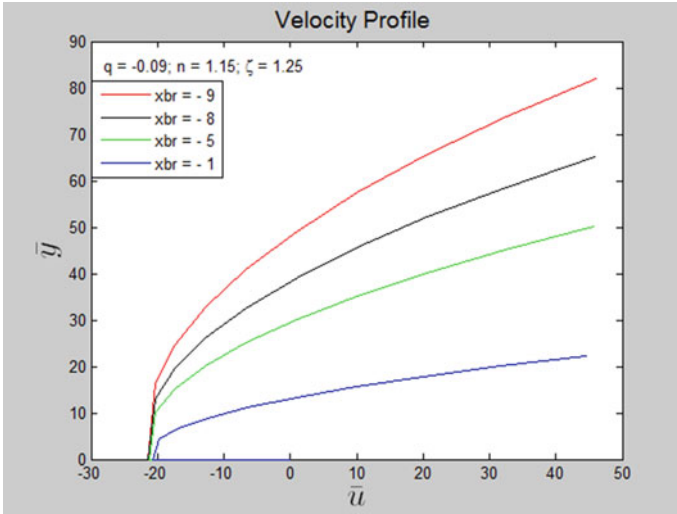
Fig. 2 $\bar{u}$ Vs $\bar{y}$
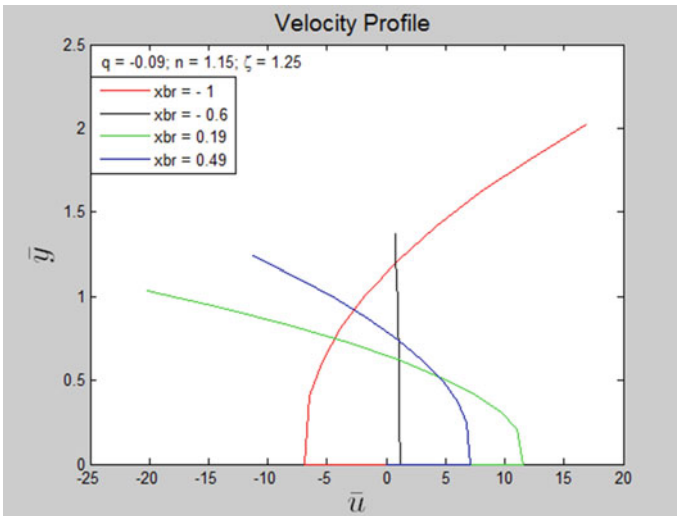
Fig. 3 $\bar{u}$ Vs $\bar{y}$

3.4 Load and Traction

The normal load $\overline{W}_y$ and the traction force $\overline{T}_F$ are the important features of bearings. It is presented in Table 1 with different n and q values and with different ζ. From
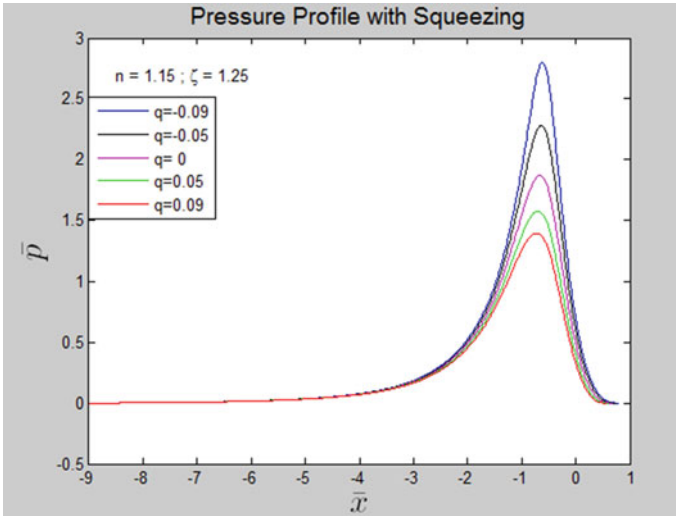
Fig. 4 $\bar{p}$ Vs $\bar{x}$
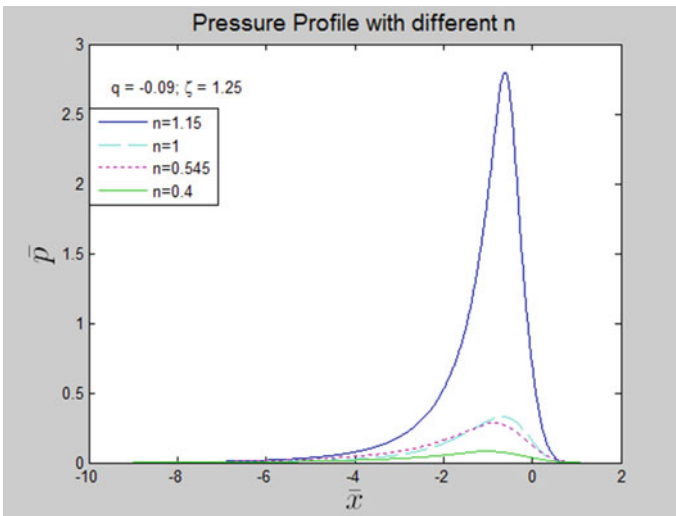
Fig. 5 $\bar{p}$ Vs $\bar{x}$

the table, it can be clearly stated that both quantities $\overline{W}_y$ and $\overline{T}_F$ increase with n that matches well with the previous findings [20].
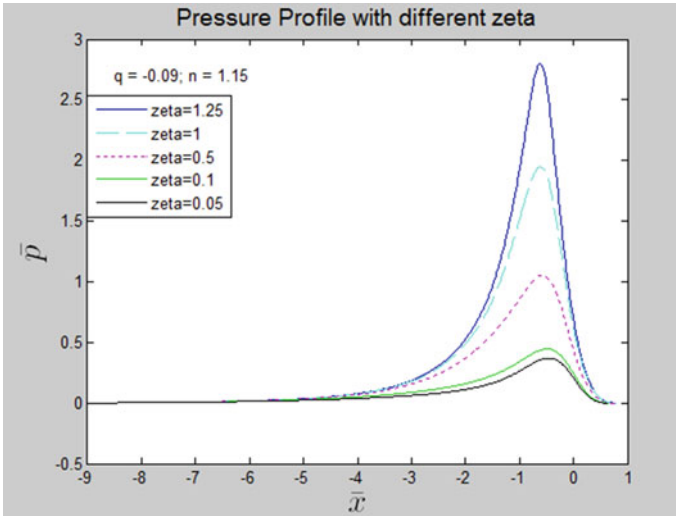
Fig. 6 $\bar{p}$ Vs $\bar{x}$
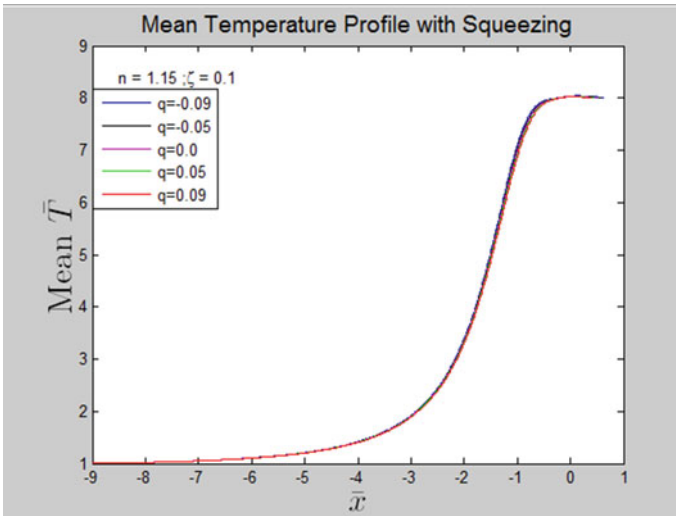
Fig. 7 $\bar{T}_m$ Vs $\bar{x}$

3.5 Consistency

The important feature of this article is to investigate the change in lubricant consistency $\bar{m}$ with $\bar{p}$ and $\bar{T}_m$, as shown in below figures. The overall consistency changes with $\bar{x}$ for different ζ, and different n and q are shown in Figs. 12, 13, 14, 15 and
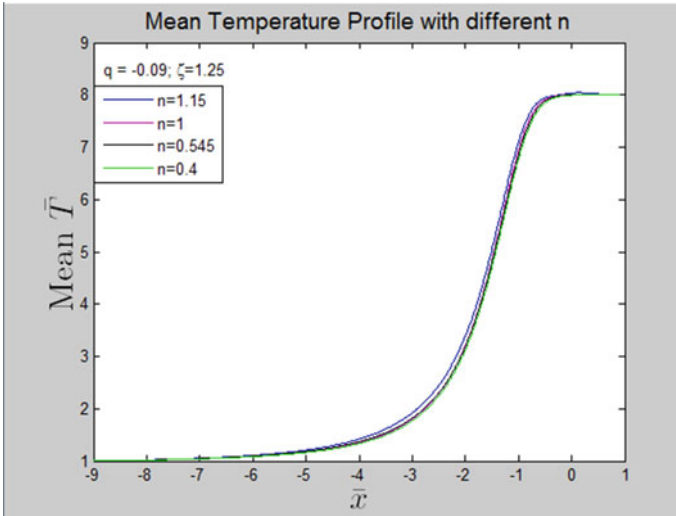
Fig. 8 $\overline{T}_m$ Vs $\overline{x}$
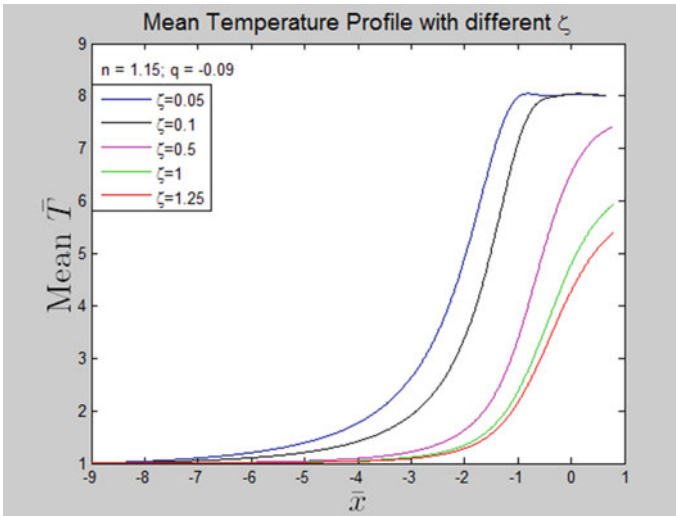
Fig. 9 $\overline{T}_m$ Vs $\overline{x}$

16. This indicates basically the dominance of temperature over the pressure for ζ value below 1 and vice versa for ζ value 1 and above. Hence, the consideration of the consistency variation with pressure and temperature is well justified [17, 25].
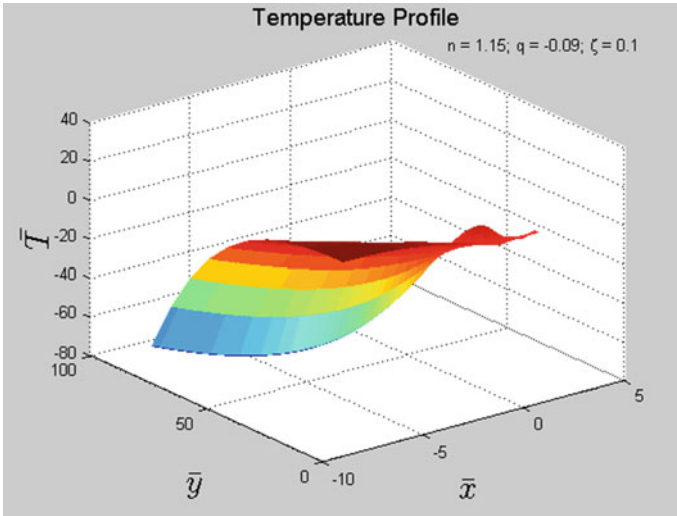
Fig. 10 $\overline{T}$ Vs ($\overline{x}$ & $\overline{y}$)
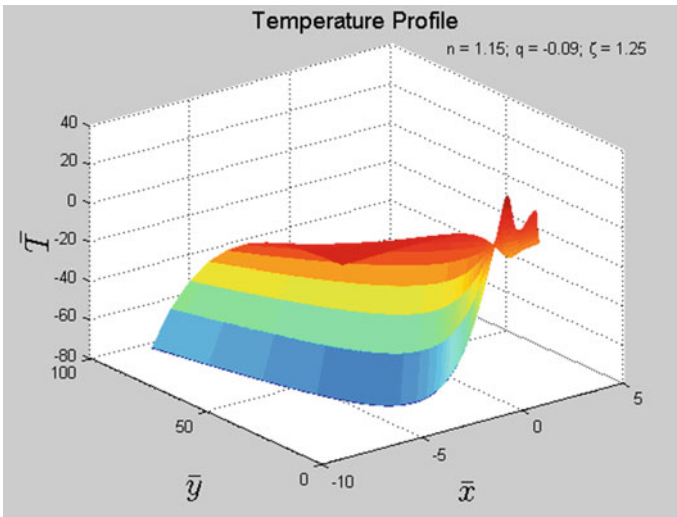
Fig. 11 $\overline{T}$ Vs ($\overline{x}$ & $\overline{y}$)

Table 1 Load and traction

$\zeta = 0.05$	Load	n/m_0	$q = -0.09$	$q = -0.05$	$q = 0.00$	$q = 0.05$	$q = 0.09$
		1.15/0.56	0.728034	0.682440	0.629819	0.581875	0.546628
		1.00/0.75	0.208763	0.198802	0.186989	0.180994	0.167527
		0.545/86.0	0.265015	0.258406	0.250933	0.242872	0.236964
		0.40/128.0	0.098246	0.096567	0.094229	0.091954	0.090209
	Traction	1.15/0.56	2.226022	2.167854	2.096716	2.026709	1.971799
		1.00/0.75	0.731992	0.717712	0.699773	0.691846	0.667472
		0.545/86.0	1.191339	1.182483	1.169261	1.157851	1.147185
		0.40/128.0	0.477440	0.474489	0.471510	0.468224	0.465292
$\zeta = 1.25$	Load	1.15/0.56	3.789767	3.373798	2.968427	2.637389	2.412915
		1.00/0.75	0.697567	0.665744	0.625182	0.585388	0.555494
		0.545/86.0	0.740060	0.721762	0.711351	0.676401	0.655152
		0.40/128.0	0.237968	0.233136	0.227288	0.218056	0.219732
	Traction	1.15/0.56	8.590294	8.013047	7.421760	6.935082	6.578432
		1.00/0.75	1.960195	1.909818	1.846486	1.781264	1.729900
		0.545/86.0	2.608419	2.577499	2.539537	2.494460	2.470183
		0.40/128.0	0.934524	0.928283	0.919203	0.904804	0.892762
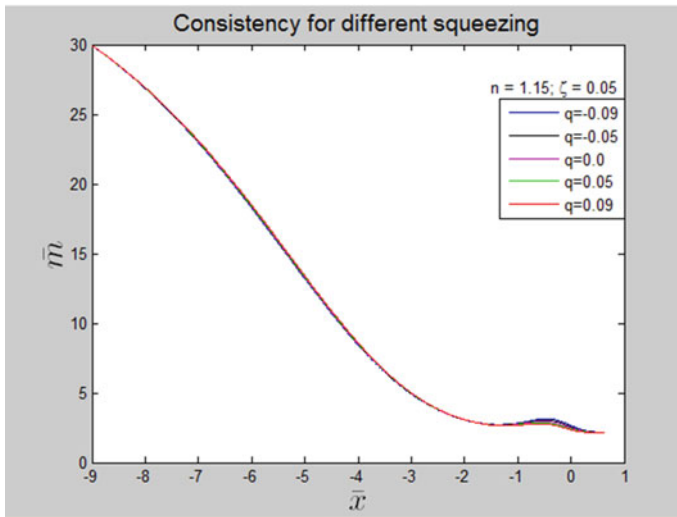
Fig. 12 $\overline{m}$ Vs $\overline{x}$
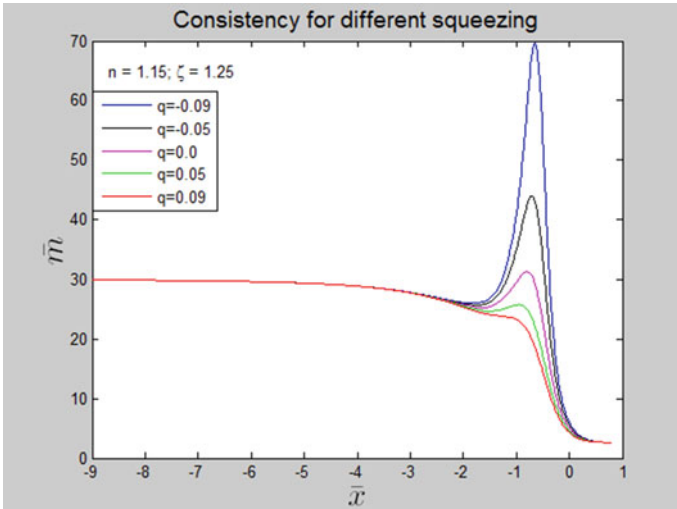
Fig. 13 $\overline{m}$ Vs $\overline{x}$
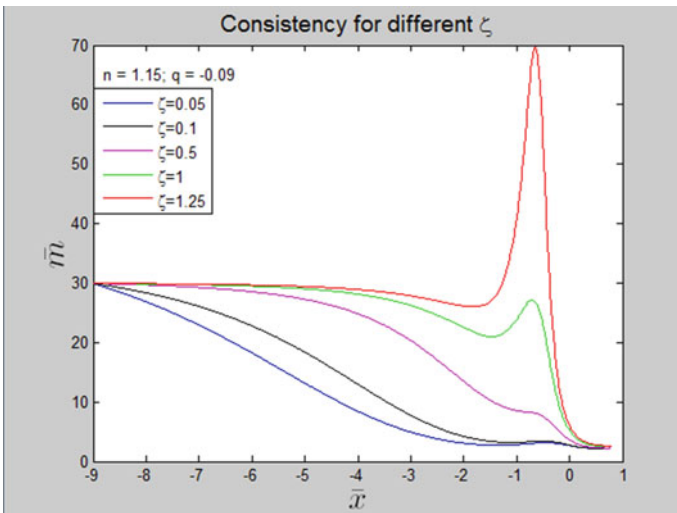
Fig. 14 $\overline{m}$ Vs $\overline{x}$
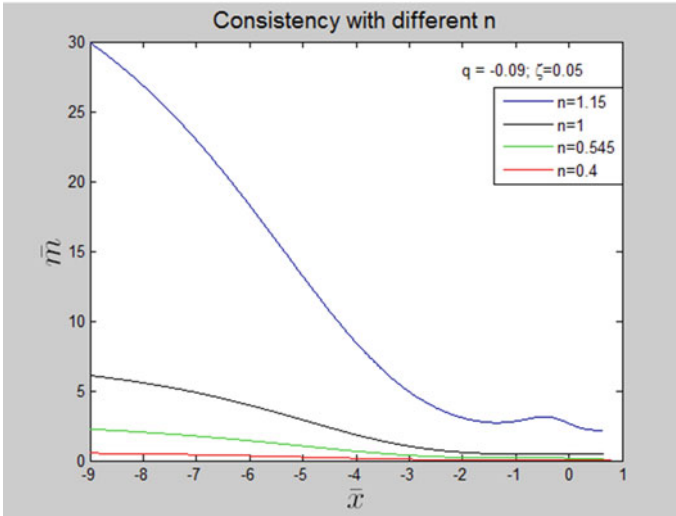
Fig. 15 $\overline{m}$ Vs $\overline{x}$
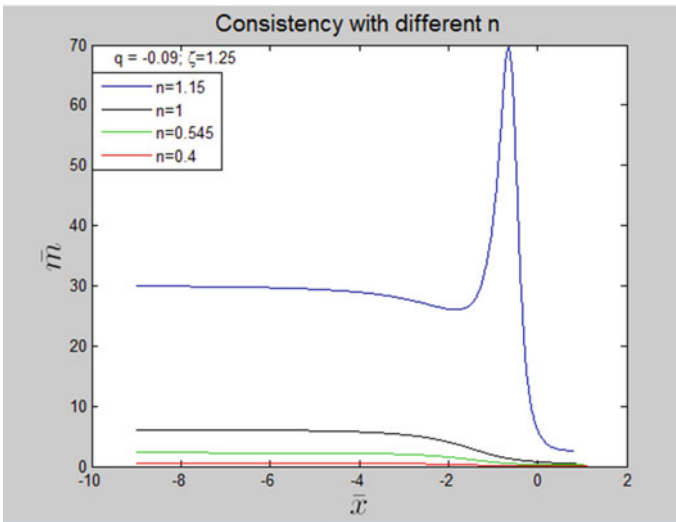
Fig. 16 $\overline{m}$ Vs $\overline{x}$

4 Conclusion

A thermo hydrodynamic fluid film lubrication of rollers by power law lubricants is completed along with squeezing velocity and cavitations. The main features of this investigation with and without convection are found to be:

(i) while q is fixed, the lubricant pressure and temperature, including load and traction increase as n increases, but for a fixed n, the above-said results decrease as q increases.

(ii) the point of maximum pressure advances away from the minimum gap between the rollers with decreasing value of q.

(iii) the consistency follows the temperature trend without convection (ζ is <1), and the pressure trend with convection (ζ is $\geq$1).

5 Future Scope

The future scope of this problem is to extend the consistency variation relation with pressure and temperature. Also, this can be extended with compressible, EHD, surface roughness and asymmetric case.

References

1. Hirst W, Moore AJ (1978) EHD lubrication of high pressure. Proc R Soc Lond Ser A 360(1702):403–425
2. Elison S, Saundars OA (1957) A study of piston-ring lubrication. Proc Inst Mech Eng 171(1):427–462
3. Furuhama S (1959) A dynamic theory of piston-ring lubrication, 1st report, calculation. JSME 2(7):423–428
4. Gohar R, Cameron A (1963) Optical measurement of oil film thickness under elasto-hydrodynamic lubrication. Nature 200(4905):458–459
5. Cameron A, Wood WI (1949) The full journal bearing. Proc Inst Mech Eng 161(1):59–72
6. Sassenfeld H, Walther A (1954) Gleitlagerberechnungen. VDI-Forschungsheft 441
7. Dowson D, Higginson GR (1959) A numerical solution to the elasto-hydrodynamic problem. J Mech Eng Sci 1(1):6–15
8. Punit K, Khonsari MM (2008) Combined effects of shear thinning and viscous heating on EHL characteristics of rolling/sliding line contacts. J Tribol 130(4):041505–041513
9. Lin J-R, Chou T-L, Liang L-J, Hung T (2012) Non-Newtonian dynamic characteristics of parabolic-film slider bearings: micro polar fluids. Tribol Int 48:226–231
10. Harris TA (1971) An analytical method to predict skidding in thrust-loaded, angular contact ball bearings. ASME J Lubr Technol 93:17–24
11. Liao NT, Lin JF (2001) A new method for the analysis of deformation and load in a ball bearing with variable contact angle. ASME J Mech Des 123:304–312
12. Han C-F, Chu H-Y, Kuo P-C, Liao N-T, Hwang Y-C, Chiu Y-L, Lin J-F (2017) Tribological behavior and thermoelastic instability demonstrated in ball-bearing-like specimens operating in dry contacts and with grease lubrication. Tribol Int 110:358–369

13. Takabi J, Khonsari MM (2015) On the dynamic performance of roller bearings operating under low rotational speeds with consideration of surface roughness. Tribol Int 86:62–71
14. Zhang H, Takeuchi Y, Chong WWF, Mitsuya Y, Fukuzawa K, Itoh S (2018) Simultaneous in situ measurements of contact behavior and friction to understand the mechanism of lubrication with nanometer-thick liquid lubricant films. Tribol Int 127:138–146
15. Mitsuya Y, Zhang H, Namba K, Fukuzawa K, Itoh S (2014) Development of a ball-suspension assembly for measuring speed-dependent friction characteristics of thin lubricant films coated on magnetic disks. IEEE Trans Magn 50:3302704
16. Zhang H, Yoshimi T, Fukuzawa K, Itoh S (2018) Is the trend of Stribeck curves followed by nano-lubrication with molecularly thin liquid lubricant films? Tribol Int 119:82–87
17. Wang L, Lu C (2015) The effect of viscosity on the cavitation characteristics of high speed sleeve bearing. J Hydrodyn 27(3):367–372
18. Fusi L (2018) Two-dimensional thin-film flow of an incompressible inhomogeneous fluid in a channel. J Non-Newton Fluid Mech 260:87–100
19. Prasad D, Sajja VS (2016) Non-Newtonian lubrication of asymmetric rollers with thermal and inertia effects. Tribol Trans 59(5):818–830
20. Prasad D, Singh P, Sinha P (1987) Thermal and squeezing effects in non-Newtonian fluid film lubrication of rollers. Wear 119:175–190
21. Sinha P, Prasad D (1995) Lubrication of rollers by power law fluids considering consistency variation with pressure and temperature. Acta Mech 111:223–239
22. Hajishafiee A, Kadiric A, Ioannides S, Dini D (2017) A coupled finite volume CFD solver for two dimensional EHL problems with particular application to rolling element bearings. Tribol Int 109:258–273
23. Hultqvista T, Shirzadegan M, Vrcek A, Baubet Y, Prakash B, Marklund P, Larsson R (2018) Elasto hydrodynamic lubrication for the finite line contact under transient loading conditions. Tribol Int 127:489–499
24. Prasad D, Sajja VS (2016) Thermal effect in non-Newtonian lubrication of asymmetric rollers under adiabatic and isothermal boundaries. Int J Chem Sci 14(3):1641–1656. ISSN 0972-768X
25. Morales-Espejel GE, Lugt PM, Pasaribu HR, Cen H (2014) Film thickness in grease lubricated slow rotating rolling bearings. Tribol Int 74:7–19

Second-Order Slip and Thermal Jump Effects on MHD Flow of Nano-second Grade Fluid Flow Over a Stretching Sheet

P. Ragupathi, S. Saranya, and A. K. Abdul Hakeem

Abstract The present examination is for the most part centered on the flow of a magnetohydrodynamic nano-second grade fluid over a stretching sheet implementing the second-order slip and thermal jump model. To analyze the problem elaborately, numerical simulations are carried out. For that, the partial differential equations that were employed to characterize the flow were transformed to ordinary differential equations with the aid of similarity transformations. Solving them with the much known Runge–Kutta strategy in association with shooting iteration technique, the outcomes for the nano-second grade fluid velocity, temperature, concentration, the local skin friction coefficient, the local Nusselt number and the local Sherwood number are discussed. Some of the notable results of second grade, thermophoresis and Brownian motion parameters along with Lewis number are brought out, which might be relevant for future research work.

Keywords MHD · Nano-second grade fluid · Second-order slip · Thermal jump · Stretching sheet

Nomenclature

B_0	Applied magnetic field
C_p	Specific heat capacity
f	Dimensionless velocity
Re_x	Reynold's number
U_w, V_w	Stretching velocities
u, v	Velocity components
x, y	Axial directions

P. Ragupathi · S. Saranya · A. K. Abdul Hakeem (✉)
Department of Mathematics, Sri Ramakrishna Mission Vidyalaya College of Arts and Science, Coimbatore 641020, India
e-mail: abdulhakeem6@gmail.com

Greek Symbols

ν Kinematic viscosity
α Second grade parameter
η Similarity variable
ρ Fluid density
σ Electrical conductivity
Λ_1, Λ_2 First-order and second-order velocity slip
Ω_1, Ω_2 First-order and second-order temperature jump
θ Dimensionless temperature
ϕ Dimensionless concentration

Superscript

$'$ Differentiation w.r.t η

1 Introduction

In the midst of the latest couple of years, the issues of heat and mass transfer in the boundary layers of continuous stretching surface have pulled in significant enthusiasm because of its various applications in modern assembling forms. The boundary layer flow concept was first brought into existence by Crane [1]. From that point, the spearheading work of Crane has been reached out by a few specialists [2–4] under various physical angles.

Far-reaching information on the theoretical or practical understanding of non-Newtonian liquid's flow attributes necessitate because of their mandatory function assumed as a part in the natural development of industrial and engineering practice. Distinctive sorts of non-Newtonian liquid models are produced in the past to portray the genuine conduct of these liquids [5, 6]. The liquid model utilized in the current scrutiny is a variant of a different type of non-Newtonian fluids and acknowledged as second grade liquid. Be that as it may, extremely less methodology has been accounted for within the sight of nanofluids [7, 8].

When all is said in done, the irregularity of the velocity at the solid–fluid interface might be viewed as obvious and evident slips. At this velocity irregularity, the molecular mean free path and the characteristic size of the geometry are related with each other and the Knudsen number (Kn) was labeled. Notwithstanding, in the scope of Kn between 0.01 and 0.1, the continuum theory is sustainable. However, the local thermodynamic equilibrium cannot be guaranteed. Consequently, the no-slip velocity will never again be dependable, and the slip velocity boundary condition must be put to practical use at the interface while effectively dealing with the Navier–Stokes

condition for the essentially considered fluid elements. In the ongoing past, modern test systems gave generous confirmations on the presence of fluid slippage along the solid–fluid interface for both Newtonian and non-Newtonian fluids [9, 10] and are completely surveyed somewhere else and henceforth are not rehashed here.

A close observation toward this path uncovers that so far no one has considered to build up a mathematical model for MHD flow of nano-second grade fluid over a stretching sheet with second-order velocity slip and thermal jump effects. Remembering this, an investigation has been done, the results are plotted and the numerical outcomes are displayed in tables. The chief observations of investigation are recorded in the conclusion.

2 Mathematical Formulations

We consider the hydromagnetic flow of an incompressible second grade nanofluid over a stretching sheet. The fluid is electrically conducting under the influence of a constant applied magnetic field B_0 as shown in Fig. 1. Physical properties of fluid are assumed constants. Effects of induced magnetic field and viscous dissipation are neglected. The governing boundary layer equations using the above-mentioned suppositions and Boussineq's approximation can be written as:

$$\frac{\partial u}{\partial x} + \frac{\partial v}{\partial y} = 0 \tag{1}$$

$$T(x,0) = T_w + L_1 \frac{\partial T}{\partial y} + L_2 \frac{\partial^2 T}{\partial y^2} \qquad u(x,0) = U_w + U_{slip}$$
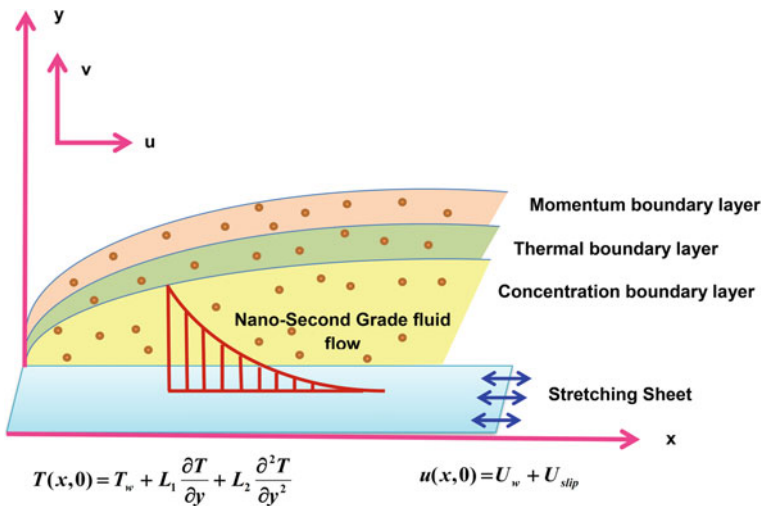
Fig. 1 Physical configuration

$$u\frac{\partial u}{\partial x} + v\frac{\partial u}{\partial y} = \nu\frac{\partial^2 u}{\partial y^2} + \frac{\alpha_1}{\rho}\left(u\frac{\partial^3 u}{\partial x \partial y^2} + \frac{\partial u}{\partial x}\frac{\partial^2 u}{\partial y^2} + \frac{\partial u}{\partial y}\frac{\partial^2 v}{\partial y^2} + v\frac{\partial^3 u}{\partial y^3}\right) - \frac{\sigma B_0^2(t)}{\rho}u$$

(2)

$$\left(u\frac{\partial T}{\partial x} + v\frac{\partial T}{\partial y}\right) = \frac{\alpha_1}{\rho C_p}\left(u\frac{\partial^2 u}{\partial x \partial y}\frac{\partial u}{\partial y} + v\frac{\partial^2 u}{\partial y^2}\frac{\partial u}{\partial y}\right) + \frac{k}{\rho C_p}\frac{\partial^2 T}{\partial y^2}$$

$$+ \tau\left(D_B\frac{\partial C}{\partial y}\frac{\partial T}{\partial t} + \frac{D_T}{T_\infty}\left(\frac{\partial T}{\partial y}\right)^2\right)$$

(3)

$$u\frac{\partial C}{\partial x} + v\frac{\partial C}{\partial y} = D_B\frac{\partial^2 C}{\partial y^2} + \frac{D_T}{T_\infty}\frac{\partial^2 T}{\partial y^2}$$

(4)

T is the fluid temperature, ν is the kinematic viscosity, σ is the electrical conductivity, ρ is the fluid density, D_B and D_T are the Brownian diffusion coefficient and thermophoretic diffusion coefficient, respectively, k is the thermal conductivity of the fluid, α_1 is the material parameter of second grade fluid, and C_p is the specific heat capacity.

The imposed boundary conditions are given below

$$u = U_w + U_{\text{Slip}}, \ v = V_w, \ T = T_w + L_1\frac{\partial T}{\partial y} + L_2\frac{\partial^2 T}{\partial y^2}, \ C = C_w \text{ at } y = 0$$

$$u \to U_w, \ T \to T_\infty, \ C \to C_\infty \text{ as } y \to \infty$$

(5)

Similarity transformation for the present case is given as follows:

$$\eta = \sqrt{\frac{a}{\nu}}y, \ \psi = \sqrt{a\nu}xf(\eta), \ \theta(\eta) = \frac{T - T_\infty}{T_w - T_\infty}, \ T_w = T_\infty + b\left(\frac{x}{l}\right)^2,$$

$$\phi(\eta) = \frac{C - C_\infty}{C_w - C_\infty}, \ C_w = C_\infty + C\left(\frac{x}{l}\right)^2$$

(6)

and the velocity components are $u = \frac{\partial \psi}{\partial y}, \ v = -\frac{\partial \psi}{\partial x}$ which identically satisfies Eq. (1) with stream function ψ while Eqs. (2)–(4) are converted into the following form:

$$f''' - f'^2 + ff'' + \alpha\left(2f'f''' - f''^2 - ff^{iv}\right) - Mf' = 0$$

(7)

$$\theta'' + \Pr(f\theta' - f'\theta) + \Pr \text{Ec} \alpha\left(f'f''^2 - ff''f'''\right) + \Pr\left(N_b\theta'\phi' + N_t\theta'^2\right) = 0$$ (8)

$$\phi'' + \left(\frac{N_t}{N_b}\right)\theta'' + \Pr \text{Le}\left(f\phi' - 2f'\phi\right) = 0$$

(9)

With the corresponding boundary condition

$$f'(0) = 1 + \Lambda_1 f'(0) + \Lambda_2 f'''(0), \ f'(0) = -s,$$

$$\theta(0) = 1 + \Omega_1 \theta'(0) + \Omega_2 \theta''(0), \quad \phi(0) = 1 \quad \text{at } \eta = 0$$
$$f'(\infty) \to 0, \quad \theta(\infty) \to 0, \quad \phi(\infty) \to 0 \quad \text{as } \eta \to \infty \tag{10}$$

$Re_x = U_w x / \nu$ is the local Reynold's number, $Pr = \frac{\mu C_p}{k}$ is the Prandtl number, $Ec = \frac{U_w^2}{C_p(T_w - T_\infty)}$ is the Eckert number, $\alpha = \alpha_1 a / \mu$ is the second grade parameter, $Nb = \frac{\tau D_B}{\nu}(C_w - C_\infty)$ is the Brownian motion parameter, $Nt = \frac{D_T}{T_\infty}\frac{\tau}{\nu}(T_w - T_\infty)$ is the thermophoresis parameter, and $Le = \frac{\alpha}{D_B}$ is the Lewis number.

The local skin friction coefficient, local Nusselt, and local Sherwood numbers are given by the expressions

$$C_f = \frac{\tau_w}{\rho U_w^2}, \quad Nu_x = \frac{x q_w}{k(T_w - T_\infty)}, \quad Sh_x = \frac{x j_w}{D_B(C_w - C_\infty)}, \tag{11}$$

where the skin friction τ_w, wall heat flux q_w, and the concentration flux j_w are defined as

$$\tau_w = \left(\mu \frac{\partial u}{\partial y} + \alpha_1 \left(2 \frac{\partial u}{\partial x}\frac{\partial u}{\partial y} + u \frac{\partial^2 u}{\partial x \partial y} + v \frac{\partial^2 u}{\partial y^2}\right)\right)_{y=0}, \quad q_w = -k\left(\frac{\partial T}{\partial y}\right)_{y=0},$$
$$j_w = -D_B\left(\frac{\partial C}{\partial y}\right)_{y=0},$$

Dimensionless forms of the local skin friction coefficient , the local Nusselt number and the local Sherwood number are

$$C_f Re_x^{1/2} = \left(f''(\eta) + \alpha\left(3 f'(\eta) f''(\eta) - f(\eta) f'''(\eta)\right)\right)_{\eta=0},$$
$$Nu_x Re_x^{-1/2} = -\theta'(0), \quad Sh_x Re_x^{-1/2} = -\phi'(0), \tag{12}$$

3   Results and Discussion

The magnetohydrodynamic flow of a nano-second grade fluid over a stretching sheet with second-order slip and thermal jump effects is analyzed numerically. Here, we assigned physically realistic numerical values to the embedded parameters as $M = 1.0$, $\alpha = 0.1$, $Ec = 1.0$, $Pr = 1.0$, $Nt = 0.7$, $Nb = 1.0$, $Le = 0.7$, $\Lambda_1 = 0.8$, $\Lambda_2 = 0.5$, $\Omega_1 = 0.5$, $\Omega_2 = 0.8$, $s = 0$ in the system in order to gain an insight into the flow structure with respect to velocity, temperature, and concentration profiles.

Figure 2 portrays the impact of the second-grade parameter α on the velocity, temperature, and concentration fields. It is obvious from the figure that by expanding the boundary layer extent this parameter will in general increase the velocity profile. In this progression, the impact of second-grade parameter α on the $\theta(\eta)$ and $\phi(\eta)$ is also shown in Fig. 2, respectively. This depicts that α has similar effect on both $\theta(\eta)$

Fig. 2 Effect of α on the velocity, temperature, and concentration profile
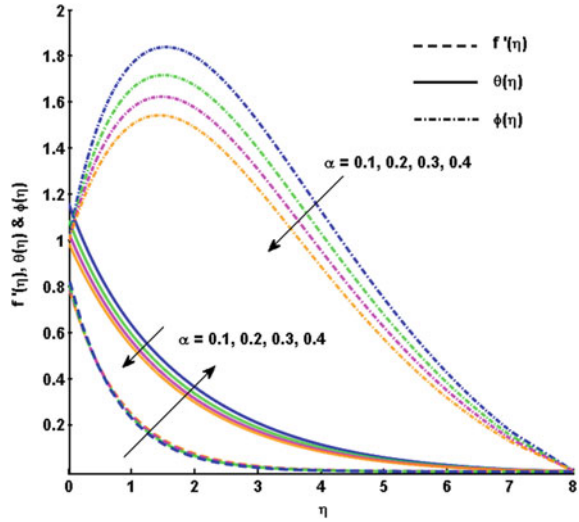
and $\phi(\eta)$. At the point, when α becomes greater than before, it starts declining both thermal and concentration boundary layer thickness.

Figure 3 builds up that the first-order slip parameter Λ_1 steps down the velocity of the fluid. Studying the temperature and concentration profiles of the fluid for the effect of Λ_1, it is watched that an expansion in Λ_1 increases $\theta(\eta)$ and $\phi(\eta)$, and their relative boundary layer thickness. Similarly, second-order slip parameter Λ_2 rises the fluid velocity by increasing the hydromagnetic boundary layer as shown in Fig. 4 and makes a negative effect on the thickness of the thermal and concentration

Fig. 3 Effect of Λ_1 on the velocity, temperature, and concentration profile
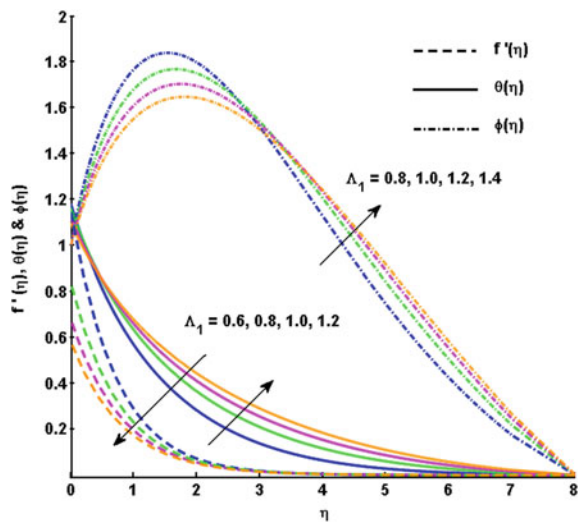
Fig. 4 Effect of Λ_2 on the velocity, temperature, and concentration profiles
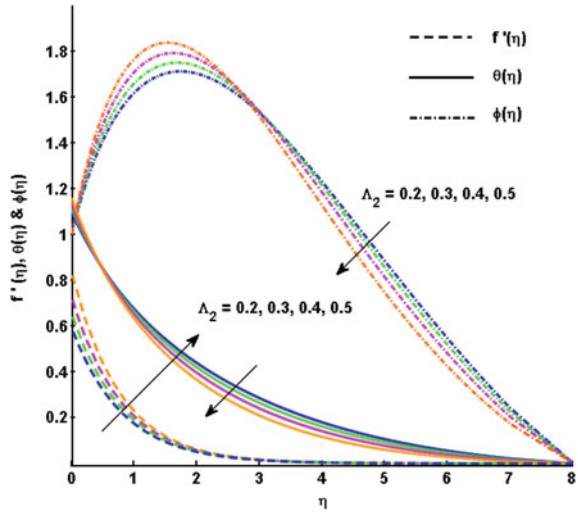
boundary layer which eventually decreases $\theta(\eta)$ and $\phi(\eta)$. Figure 5 delineates how the Eckert number **Ec** influences the temperature and concentration profiles. From the figure, we spot that both $\theta(\eta)$ and $\phi(\eta)$ are decreasing functions of **Ec**.

Moreover, Fig. 6 represents the Lewis number **Le** effect on $\theta(\eta)$ and $\phi(\eta)$. We find that the Lewis number effect on $\phi(\eta)$ is stronger than that on $\theta(\eta)$. It is noteworthy that both $\theta(\eta)$ and $\phi(\eta)$ decrease with increasing **Le**. The thermophoresis is a physical wonder that the nanoparticle relocates from hotter to the colder field in light

Fig. 5 Effect of Ec on the temperature and concentration profiles
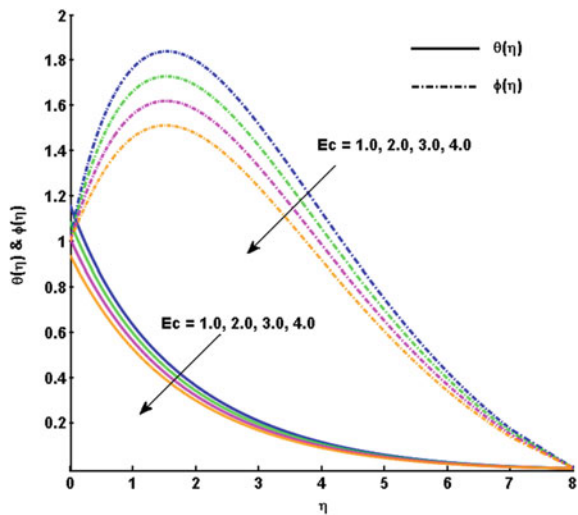
Fig. 6 Effect of Le on the temperature and concentration profiles
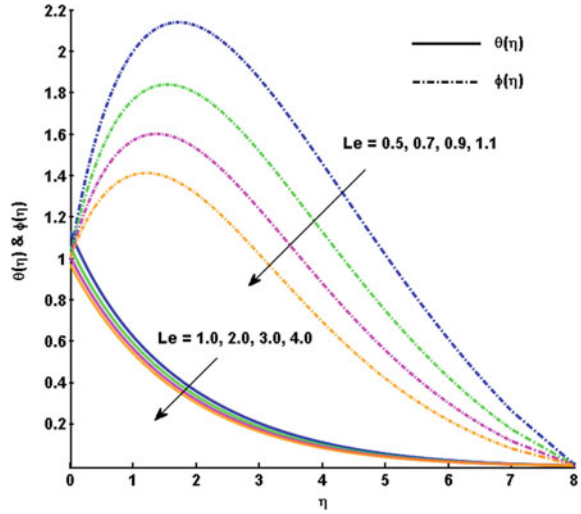
of the temperature dissimilarity. Figure 7 explains the effect of the thermophoresis parameter **Nt** on $\theta(\eta)$ and $\phi(\eta)$. It is detected that the rise in **Nt** promotes the development of the temperature and the concentration profiles of the fluid.

The Brownian movement alludes to the irregular floating suspended nanoparticles in the base fluid, which is caused from consistent crash among nanoparticles and fluid molecules. Figure 8 presents the outcome of Brownian motion parameter **Nb** on the $\theta(\eta)$ and $\phi(\eta)$. It is seen that the expansion in **Nb** advances the improvement of the thermal boundary layer, while restraining the concentration boundary layer.

Figure 9 shows the effect of first-order thermal jump parameter Ω_1 on $\theta(\eta)$ and $\phi(\eta)$. This figure indicates that increasing the first-order thermal jump parameter

Fig. 7 Effect of Nt on the temperature and concentration profiles
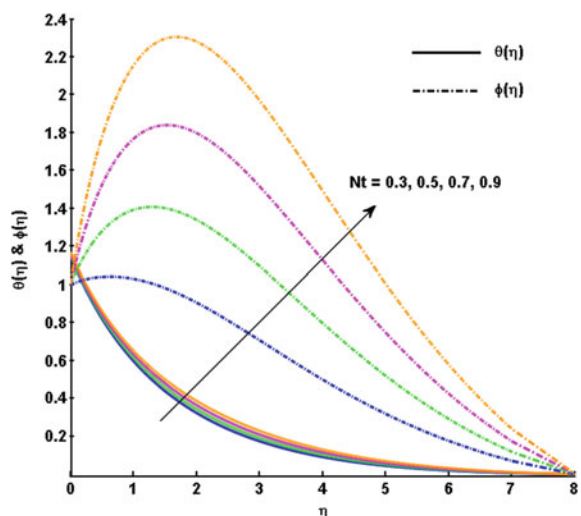
Fig. 8 Effect of Nb on the temperature and concentration profiles
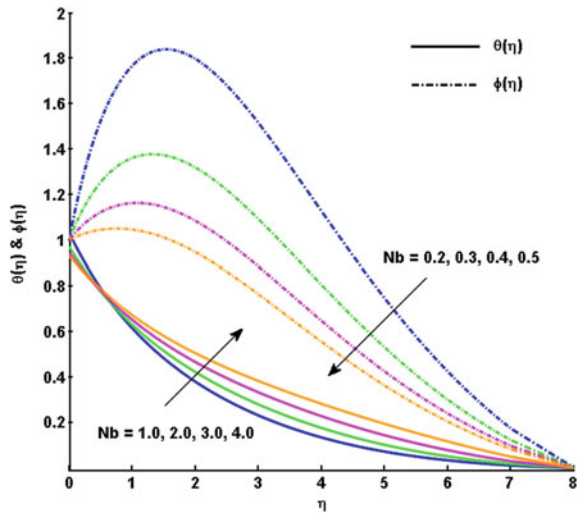
Fig. 9 Effect of Ω_1 on the temperature and concentration profiles
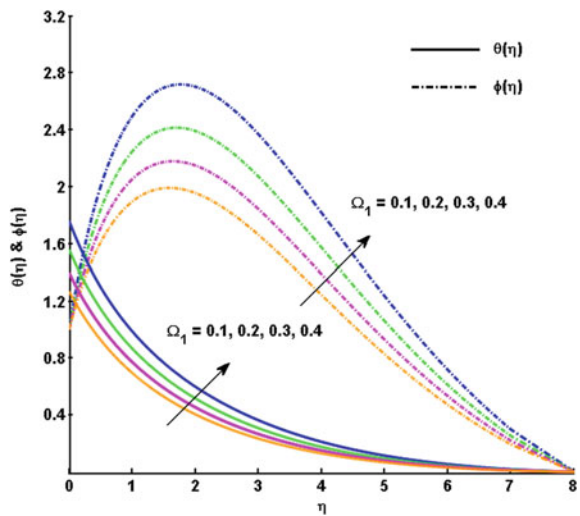
Ω_1, the temperature at the surface and the thickness of the thermal boundary layer decrease. The same is found from the curves of the concentration profile. Likewise, the second-order thermal jump parameter Ω_2 plays a role just opposite to that of Ω_1 by increasing $\theta(\eta)$ and $\phi(\eta)$ as shown in Fig. 10. Table 1 records the numerical values of the local skin friction coefficient, the local Nusselt number, and the local Sherwood number for different values of various physical parameters.

Fig. 10 Effect of Ω_2 on the temperature and concentration profiles
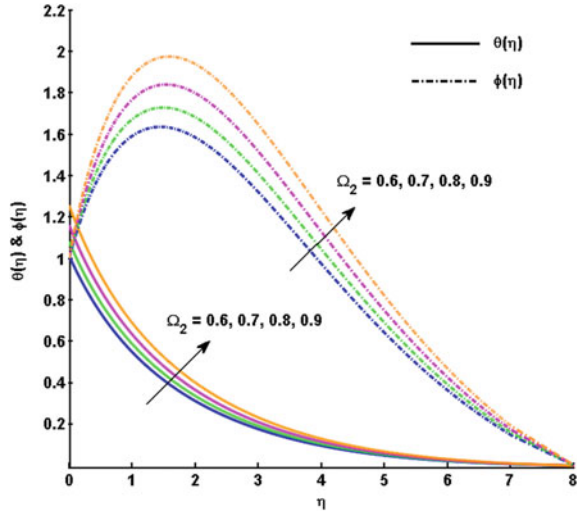
Table 1 The local skin friction coefficient $\left(\mathrm{Re}_x^{1/2} C_f\right)$, the local Nusselt number $\left(\mathrm{Re}_x^{-1/2} \mathrm{Nu}_x\right)$, and the local Sherwood number $\left(\mathrm{Re}_x^{-1/2} \mathrm{Sh}_x\right)$ values are given for different values of pertinent parameters

Parameters	Values	$\mathrm{Re}_x^{1/2} C_f$	$\mathrm{Re}_x^{-1/2} \mathrm{Nu}_x$	$\mathrm{Re}_x^{-1/2} \mathrm{Sh}_x$
α	0.1	−1.36467228	0.47039616	0.66735826
	0.2	−1.53174436	0.42757850	0.69463603
	0.3	−1.68393161	0.39409883	0.71781808
Λ_1	0.6	−2.15045023	0.47598449	0.87226885
	0.8	−1.36467228	0.47039616	0.66735826
	1.0	−1.02966769	0.43623227	0.56554089
Λ_2	0.2	−0.86047609	0.40967734	0.50743558
	0.3	−0.97307362	0.42813365	0.54673088
	0.4	−1.12873423	0.44868293	0.59718720
Ω_1	0.1	−1.36467228	0.58007622	0.61944352
	0.2	−1.36467228	0.54858508	0.63319957
	0.3	−1.36467228	0.52003747	0.64566995
Ω_2	0.6	−1.36467228	0.45046434	0.67606748
	0.7	−1.36467228	0.46016107	0.67183035
	0.8	−1.36467228	0.47039616	0.66735826

4 Conclusion

The magnetohydrodynamic flow of a nano-second grade fluid over a stretching sheet with second-order slip and thermal jump impacts are dissected numerically. The remarkable highlights of this investigation are attached underneath.

- The influence exerted by second grade parameter and second-order slip parameter elevates the velocity profile.
- Thermal boundary layer thickness and temperature $\theta(\eta)$ increments by increasing the second-order thermal jump parameter.
- The local skin friction coefficient increases with an increase in estimations of first-order slip parameter.
- For increasing values of magnetic, second-order slip and second-order thermal jump parameters, the local Nusselt number increases.
- The second grade, Brownian motion, second-order slip, and first-order thermal jump parameters increase the local Sherwood number.

References

1. Crane LJ (1970) Flow past a stretching plate. Z Angew Math Phys 21:645–647
2. Gireesha BJ, Mahanthesh B, Shivakumara IS, Eshwarappa KM (2016) Melting heat transfer in boundary layer stagnation-point flow of nanofluid toward a stretching sheet with induced magnetic field. Eng Sci Technol Int J 19(1):313–321
3. Sharma PR, Sinha S, Yadava RS, Filippov AN (2018) MHD mixed convective stagnation point flow along a vertical stretching sheet with heat source/sink. Int J Heat Mass Transf 117:780–786
4. Ganga B, Saranya S, Ganesh NV, Hakeem AKA (2015) Effects of space and temperature dependent internal heat generation/absorption on MHD flow of a nanofluid over a stretching sheet. J Hydrodyn Ser B 27(6):945–954
5. Eid MR, Mahny KL (2017) Unsteady MHD heat and mass transfer of a non-Newtonian nanofluid flow of a two-phase model over a permeable stretching wall with heat generation/absorption. Adv Powder Technol 28(11):3063–3073
6. Shivakumara IS, Dhananjaya M, Ng C-O (2015) Thermal convective instability in an Oldroyd-b nanofluid saturated porous layer. Int J Heat Mass Transf 84:167–177
7. Jamila M, Rauf A, Fetecau C, Khan NA (2011) Helical flows of second grade fluid due to constantly accelerated shear stresses. Commun Nonlinear Sci Numer Simul 16(4):1959–1969
8. Hayat T, Ahmad S, Ijaz Khan M, Alsaedi A (2017) Non-Darcy Forchheimer flow of ferromagnetic second grade fluid. Results Phys 7:3419–3424
9. Abdul Hakeem AK, Vishnu Ganesh N, Ganga B (2015) Magnetic field effect on second order slip flow of nanofluid over a stretching/shrinking sheet with thermal radiation effect. J Magn Magn Mater 381:243–257
10. Zhu J, Zheng L, Zheng L, Zheng X (2015) Second-order slip MHD flow and heat transfer of nanofluids with thermal radiation and chemical reaction. Appl Math Mech-Engl Ed. https://doi.org/10.1007/s10483-015-1977-6

Dampers to Suppress Vibrations in Hydro Turbine-Generator Shaft Due to Subsynchronous Resonance

Pounraj Manikandan(ID) **and Faheem Ahmed Khan**(ID)

Abstract There are numerous applications to evaluate the damage caused by sub-synchronous resonance (SSR) to a turbine-generator shaft. Despite multiple applications, there are relatively few studies on shaft misalignment in the literature. In this paper, stresses in the existing turbine-generator shaft due to subsynchronous resonance were studied using finite element analysis (FEA). The 3D finite element model reveals that the most stressed part of the shaft is near the generator terminal. A new nonlinear damping scheme is modeled to reflect the torsional interaction and to suppress the mechanical vibration caused by subsynchronous resonance (SSR). Stresses developed due to the addition of capacitors in the system at high rotational speeds and deformation of the shaft during various modes of oscillations were evaluated. Experimental investigations are carried out in reaction turbine connected to a 3 kVA generator. Simulation is carried out for the experimental setup using ANSYS. According to the simulation results, the damper installed near the generator terminal provides satisfactory damping performance and the subsynchronous oscillations are suppressed.

Keywords Damper · Modal analysis · Rotor dynamics · Subsynchronous resonance · Turbo-generator shaft

1 Introduction

Torsional vibration due to subsynchronous resonance is an angular motion which oscillates and causes twisting in the shaft of any rotating system. The oscillatory motion is overlaid on the steady-state rotational motion of the shaft. The vibration can be detected only using special measuring equipment, and its amplitude is more destructive. Motion by itself is an apprehension with torsional vibration; if not, it affects the normal operating function of the system [1–3]. It is the stresses developed

P. Manikandan (✉)
CHRIST (Deemed to be University), Bangalore, India
e-mail: manikandan.p@christuniversity.in

F. A. Khan
Ghousia College of Engineering, Ramanagaram, India

which upset the structure and life of the components; hence, it is necessary to fix the acceptable magnitude of the torsional vibration. Torsional vibratory motions may lead to stress reversals that source the metal fatigue. In addition, stress concentration features associated with machine components decrease the efficacy of its dynamic behavior.

When the frequency of any harmonic component of the exciting torque is equal to one of the natural torsional frequencies of the rotor, then a condition of resonance exists. The frequency of the rotor is affected by the series capacitors connected to the transmission line to improve reactive power compensation. The speed in which this concurrence of frequencies occur is called a critical speed. It is important that the dynamics of the system have to be studied and the forced response of system be appraised for these critical speeds in or near the operating range of speed [4–8]. Here, levels of response in the operating range of speed should be evaded if at all possible; otherwise, distinct damping devices are required to edge the resonant response.

2   Theory and Methodology

The fluctuations which arise in the generator rotor at subsynchronous frequency result in induced voltage on the armature. The voltage developed in the armature leads to currents in the armature. The magnitude and phase angle of the current rest on the net impedance. Supersynchronous currents lead to positive damping torque, while the subsynchronous frequency currents result in negative damping torque. The net torque can create negative damping when the magnitude of the subsynchronous frequency current is more when compared to supersynchronous frequency [9–12]

2.1   Rotor Dynamics of Turbine-Generator Shaft

The turbine-generator unit of any power generating station is a complex structure. The behavior of the shaft varies with respect to the sources which are driving the unit. For example, mechanism of energy exchange occurring in a hydro turbine generating unit is different from thermal turbine generating unit. The forces acting on the hydro turbine generating unit are determined from intensity of electric and magnetic field as well as water, wherein for the thermal turbine generating unit steam is the determination factor. The vibration created by the series capacitors leads to severe damage to the shaft. The nonlinear characteristics is determined by the interaction of machine components, electromagnetic field, and driving source (water, steam, etc.) and makes the model very hard to establish [13, 14].

The Riccati transfer matrix method is applied to solve rotor dynamic problem. Finite element method (FEM) has higher numerical stability than transfer matrix method, but it will take more memory space of the computer. Both the methods are widely used to solve the rotor dynamic problem. FEM was not used to analyze

rotor dynamic problem until 1970. The main theme of FEM is the transformation of infinite degrees of freedom problem into a finite and then solving it.

2.2 Finite Element Method

The finite element method is a mathematical practice to compute the natural frequency vibration, mode shapes, and forced response of an individually modeled rotor system. It includes forming objects that transform an intangible model such as the shaft into a set of matrix equations. Finite elements use Lagrange's equation of motion for rotor dynamics.

$$\frac{\mathrm{d}}{\mathrm{d}t}\left(\frac{\partial W}{\partial q}\right) - \frac{\partial W}{\partial q} + \frac{\partial U}{\partial q} = Q_i \qquad (1)$$

Kinetic energy is denoted as W, potential energy as U, and the generalized coordinates as q. The finite element equation of motion of rotating structures is valid for both rotating and fixed systems. Assessment of the rotating system is associated with uniform rotating speed which brings a set of equations. The system of equations is of constant coefficient matrices for non-uniform rotor with bearings. In uniform rotors, most of the nodes are positioned on the axis of rotation. For non-uniform rotors, bearing is connected to bring it to equilibrium. Euler's method can also be used instead of Lagrangian method for the axisymmetric rotors. If a rotor is symmetric, eigenvalue analysis is done separately for nodal diameters.

2.3 Modal Analysis Using ANSYS

Modal analysis is used to define the intrinsic dynamic characteristics of a structure. The structure may be static or dynamic. It gives important parameters like natural frequencies, damping factors, and mode shapes which are used in design of the structure and to evaluate the performance under dynamic loading. Conservatively, modal analysis is made with specific commercial tools. In contrast, modern FEA software has good options to perform modal analysis studies. The damped method is intended for problems where damping cannot be overlooked, such as rotor dynamics applications. It involves Lanczos algorithm and creates full matrices ($[K]$, $[M]$ and the damping matrix $[C]$). It calculates difficult eigenvalues and eigenvectors [15, 16].

3   Physical Test Arrangement

3.1   Francis Turbine

Francis turbines are the most commonly used type of hydro turbine because of its turbine efficiency and machine performance. It is used up to 800 MW, with a runner diameter of ten meters and weighing more than 400 tons. Francis turbines are able to withstand the mechanical stress subsequent from high heads. To investigate the stress developed in the shaft of the turbine, diameter and the mass of the shaft are calculated before installation of the entire setup. The torsional stiffness is calculated from rigidity modulus, form factor which defines the geometric property, and length of the shaft. The physical arrangement have solid shaft. The torsional stiffness k is well-defined as the torque per radian twist (Table 1).

In Fig. 1, physical test arrangement of Francis turbine is shown. The experimental setup is of reaction turbine type, and it is connected to the generator by a belt. To overcome the difficulty of modeling in ANSYS, it is assumed here the turbine shaft is connected to the generator directly and ball bearings are connected to avoid friction. In Fig. 2, turbine shaft end and in Fig. 3, generator shaft end is shown.

3.2   Drive System, Generator, and Capacitor Bank

Experimental setup has a drive system which pairs the turbine to the generator. At left end, it permits the turbine to whirl at its optimal RPM. At the right, it pushes the generator at a particular speed in such a way that it generates the required voltage and frequency. The most effective and dependable drive system is direct coupling between the turbine and generator. Considering the head of the turbine in the experimental setup, a belt is used to drive turbine and generator. Belt systems are used in most of the cases due to their lower cost. At the same time to overcome the design difficulties, it is assumed that the shaft connects the turbine-generator in 1:1 ratio. Series capacitors are connected to the system when the turbine and generator are fully loaded. The generator and capacitor technical specifications are shown in Table 2.

Table 1 Francis turbine specification

Component	Description	Dimensions
Venturimeter	Water flow measurement	Inlet dia. 100 mm
		Throat dia. 60 mm
Shaft length	Solid shaft	Length 380 mm
		Diameter 55 mm

Fig. 1 Experimental setup of hydro turbine-generator unit
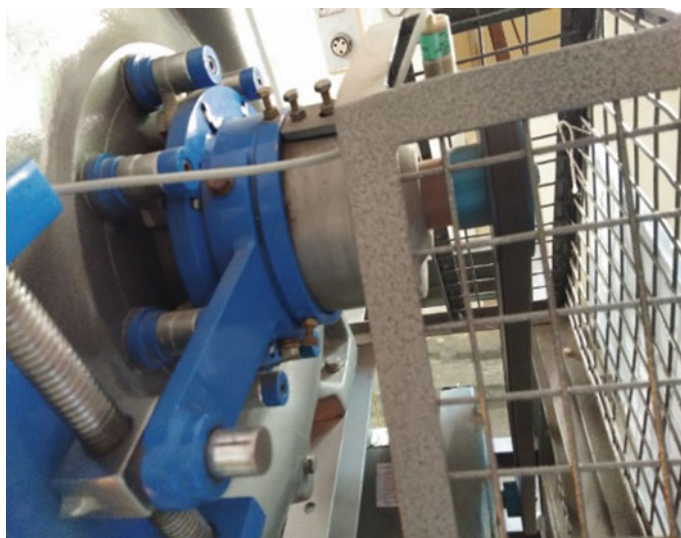
Fig. 2 Turbine shaft end

Fig. 3 Generator shaft end

Table 2 Generator and capacitor bank specifications

Component	Description	Magnitude
Generator	Output current	13 A
	Maximum rpm	1500 rpm
	Output power	3 kVA
Capacitor	Aluminum electrolytic capacitors	15 μF

4 Results and Discussion

4.1 Test Results

Keltron aluminum electrolytic capacitors are used for compensation. Three capacitors are connected in series for 10% compensation. Total of 15 capacitors are connected to the system which is considered as 50% compensation. The reason behind 50% compensation is based on the reactive power compensation during electric power transmission. The test results are shown in Table 3.

Table 3 Experiment results

Percentage of compensation, %	Speed of the shaft, rpm	Generator voltage, V	Generator current, I	Load, kW	Head on turbine
10	977	190	1.1	0.2	0.95
20	1273	200	2.4	0.6	0.85
30	1346	210	3.8	1.0	0.75
40	1493	230	4.4	1.2	0.65
50	1583	250	5.4	1.4	0.55

4.2 Modes of Oscillations

In modal characterization of any rotating machinery structures, the effects of gyroscopic and other forces are directly related to rotation [17]. The relation is associated with the asymmetry of the damping and stiffness matrices of rotating machinery. Total deformation of the shaft is found using MODAL analysis. The maximum stress point is determined. During the first iteration, Mode 1 is unstable due to the resonance created in the system. Figure 4 shows the Campbell diagram without a damper. It clearly indicates Mode 1 whirling is undermined and unstable. A longitudinal spring damper of 123 mm is modeled from the body to ground at the geometry
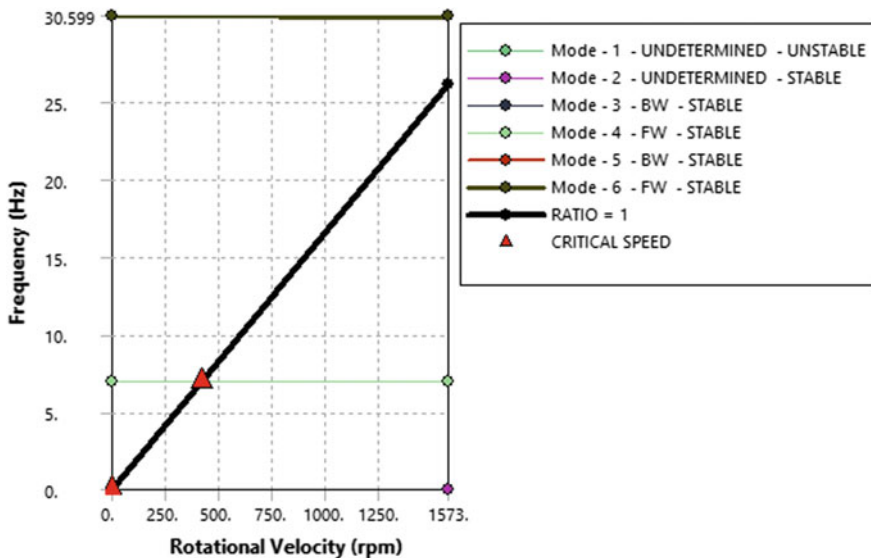
Fig. 4 Campbell diagram without damper
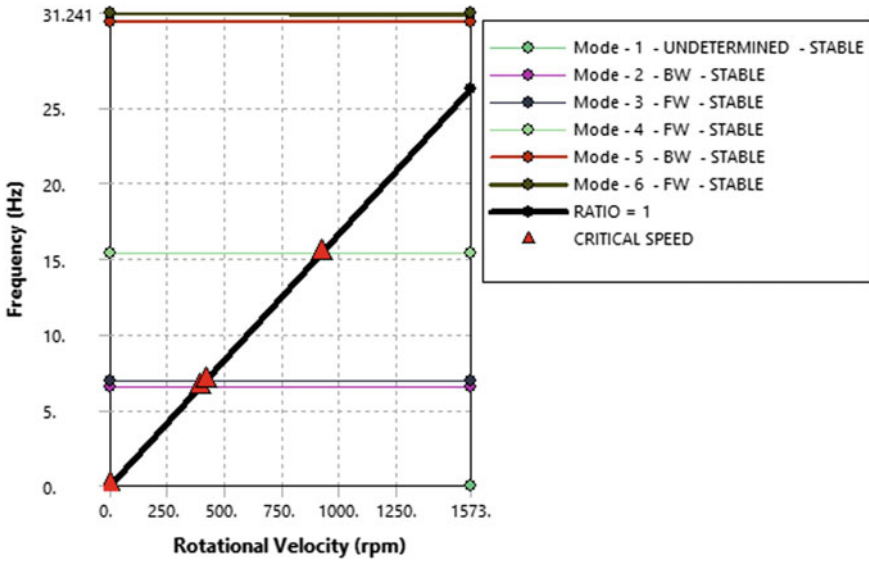
Fig. 5 Campbell diagram with damper

where the maximum stress occurs. The mathematical model is changed based on the spring damper attached to the rotating shaft. Figure 5 shows the Campbell diagram for the hydro turbine shaft with damper. Mode 1 becomes stable as the spring damper provides damping for the oscillations created by the resonance which is because of the addition of series capacitors.

Total deformation results are used to obtain displacements from stresses. Total deformation gives the summation of the square of *x*-direction, *y*-direction, and *z*-direction. In Fig. 6, total deformation of during mode 3, 4, 5, and 6 is shown. The maximum stress occurs in the intersection of turbine-generator shaft. A virtual damper is modeled in ANSYS at the point where the displacement is high due to stress. The Campbell diagram is derived for both conditions. The modes without damper is shown in Table 4 and modes with damper is shown in Table 5.
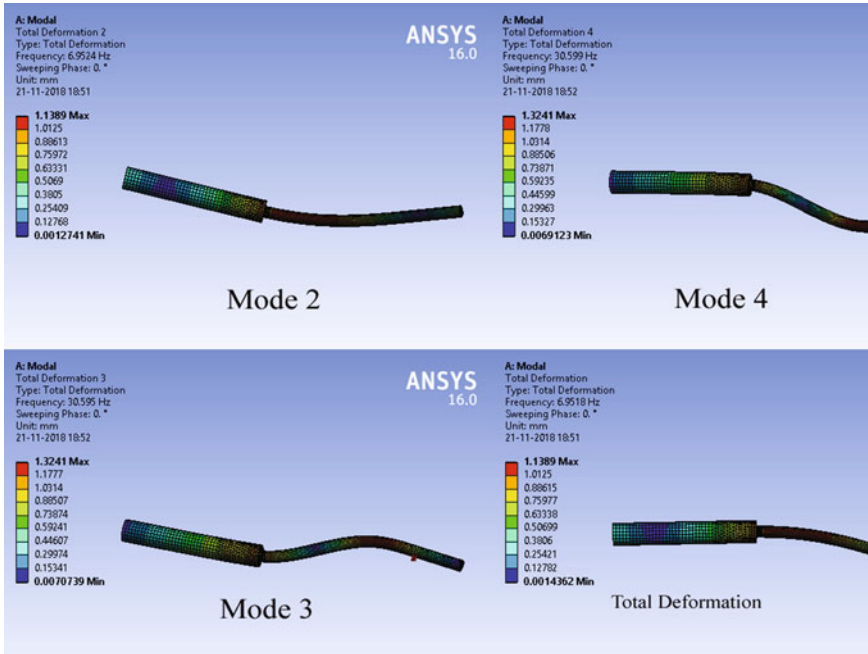
Fig. 6 Total stress deformation of the shaft in critical modes

Table 4 Simulation results without damper

Mode	Whirl direction	Mode stability	Critical speed	1573 rpm
1	Undetermined	Unstable	None	0 Hz
2	Undetermined	Stable	0.46001 rpm	7.6669e−003 Hz
3	BW	Stable	417.11 rpm	6.9515 Hz
4	FW	Stable	417.15 rpm	6.9527 Hz
5	BW	Stable	None	30.595 Hz
6	FW	Stable	None	30.599 Hz

Table 5 Simulation results with damper

Mode	Whirl direction	Mode stability	Critical speed	1573 rpm
1	Undetermined	Stable	0.38226 rpm	6.371e−003 Hz
2	BW	Stable	388.93 rpm	6.4822 Hz
3	FW	Stable	417.12 rpm	6.9521 Hz
4	FW	Stable	919.7 rpm	15.328 Hz
5	BW	Stable	None	30.597 Hz
6	FW	Stable	None	31.241 Hz

5 Conclusions

The damping performance of spring dampers to reduce rotational vibrations on the shaft of hydro turbine-generator subjected to turbulences caused by series capacitors in electric power generating unit has been justified. From the results obtained, the conclusions have been summarized.

1. The projected type of the dampers have benefits of less power loss under normal operation where there is no series compensation. For damping rotational vibrations, the projected spring damper using optimal stress outlook scheme, which is most cost-effective due to the energy which is stored.
2. Based on the deformation and the maximum stress from the excitation created by capacitors, the optimal point of mass–spring–damping turbine model can be determined. It is also concluded that dampers may be installed at the location with the heaviest vibrations.
3. From the excitations of the sub harmonic currents created by the capacitors, turbine-generator shaft may lead to long-term damage. As a result of the substantial sensitivity of exhaustion loss to the damping, a small part of damping for optimal damper could prevent the possibility of turbine and generator shaft.

References

1. Xie X, Zhang C, Liu H, Liu C, Jiang D, Zhou B (2016) Continuous mass model based mechanical and electrical co-simulation of SSR and its application to a practical shaft failure event. IEEE Trans Power Syst 31(6):5172–5180
2. Saxena A, Pareya A, Chouksey M (2016) Study of modal characteristics of a geared rotor system. Procedia Technol 23:225–231
3. Kirchg B (2016) Finite elements in rotor dynamics. Procedia Eng 144:736–750
4. Mankowski O, Wang Q (2013) Real-time monitoring of wind turbine generator shaft alignment using laser measurement. Procedia CIRP 11(1):291–295
5. Bai B, Zhang LX, Guo T, Liu CQ (2012) Analysis of dynamic characteristics of the main shaft system in a hydro-turbine based on ANSYS. Procedia Eng 31:654–658 (International conference on advances in computational modelling and simulation)
6. Elhefny A, Guozhu L (2012) Stress analysis of rotating disc with non-uniform thickness using finite element modeling. In: Proceeding of the international conference on engineering and technology (ICET), Cairo, pp 1–5
7. Karlberg M (2010) Approximated stiffness coefficients in rotor systems supported by bearings with clearance. Int J Rotating Mach
8. Hernandez M, Guardado JL, Venegas V, Melgoza E, Rodriguez L (2008) Analysis of the torsional modes of the turbine-synchronous generator group. In: IEEE/PES transmission and distribution conference and exposition: Latin America, Bogota, pp 1–7

9. Tsai J (2007) A new damper scheme to restrict torsional torques on the turbine generator shafts and blades near a HVDC link. Electr Eng 89:377–387
10. Tsai JI, Lin CH, Tsao TP (2003) Long-term fatigue life loss of turbine blades owing to non-characteristic harmonic currents in asynchronous HVDC links. J Electr Power Syst Res 65(2):135–147
11. IEEE Sub Synchronous Resonance Working Group (1985) Second benchmark model for computer simulation of sub synchronous resonance. IEEE Trans Power Apparatus Syst PAS-104(5):1057–1066
12. IEEE Sub Synchronous Resonance Working Group (1985) Terms, definitions and symbols for sub synchronous resonance oscillations. IEEE Trans Power Apparatus Syst PAS-104(6):1326–1334
13. Liang CC (1993) Torsional response of rotor system in steam turbine-generator. Taipower Eng J 538(6):35–52
14. IEEE Sub Synchronous Resonance Working Group (1992) Readers guide to sub synchronous resonance oscillations. IEEE Trans Power Apparatus Syst 7:150–157
15. Lambrecht D, Kulig T (1982) Torsional performance of turbine generator shafts especially under resonant excitation. IEEE Trans Power Apparatus Syst 101:3689–3697
16. Jackson MC (1979) Turbine generator shaft torques and fatigue: part I—simulation methods and fatigue analysis. IEEE Trans Power Apparatus Syst PAS-98(6)
17. Glienicke J (1967) Experimental investigation of the stiffness and damping coefficients of turbine bearings and their application to instability prediction. Proc Inst Mech Eng 181(3B):116–129

Distribution of Temperature and Thermal Stresses in Unidirectional Rod with Moving Point Heat Source

Yogita M. Ahire and Kirtiwant P. Ghadle

Abstract The present paper comprises the quasi-stationary, non-homogeneous thermoelastic problem with a second kind boundary condition in two-dimensional rod of isotropic material. The unidirectional rod is examined with the condition that ambient and initial temperature is zero. The rod has been observed under the activity of moving heat source located at x' moving with constant velocity along x-axis. Heat conduction equation is evaluated by using integral transform technique. The three materials, viz. aluminum, copper, and brass, have been studied, and the same are analyzed numerically and graphically for their respective thermal stresses. For aluminum, the change is observed from maximum to minimum stress. The response of copper to change in temperature is linear. The curve of copper shows constant value of stress because of its larger coefficient of thermal expansion. Tensile stress is reduced in copper. Minimum stress is observed in brass that indicates the hardness and tensile strength of brass.

Keywords Unidirectional rod · Second kind boundary conditions · Internal moving heat source · Thermal stresses · Heat generation

1 Introduction

Various changes in shape and sizes of solids have been found because of the variation in temperature. The elastic behavior of material in terms of stresses which are sensitive to temperatures is responsible for the same. Different materials show changes in heat when flows through it. Here is an attempt to study the thermal stresses in unidirectional rod. The temperature-dependent properties have been studied in the field of aerodynamics heating. The generation of intense thermal stresses decreases the strength of the structure of high-velocity aircraft [1]. The circular plate with upper

Y. M. Ahire (✉)
Department of Applied Science, PVG's College of Engineering, Nashik, Maharashtra, India
e-mail: yogitarajole7@gmail.com

K. P. Ghadle
Department of Mathematics, Dr. Babasaheb Ambedkar, Marathwada University, Aurangabad, Maharashtra 431004, India

surface at zero temperature w. r. t. lower surface has been studied by keeping circular edge thermally insulated by considering steady-state thermal stresses along with axisymmetric temperature distribution [2]. With reference to [3], it discussed the problem of thermal deflection of associated axisymmetry with fixed and simply supported edges, when heated circular plate. [4] has studied the circular plate with lower surface at zero temperature w. r. t. upper surface when momentary temperature provided through periphery of circle for quasi-static thermal stresses. Khobragade and Wankhede [5] analyzed thermoelastic problem of a thin rectangular plate by assuming an inverse unsteady state. Quasi-static thermoelastic problem of an infinitely long circular cylinder has been solved by Gaikwad and Ghadle [6]. Gaikwad and Ghadle [7] discussed non-homogeneous heat conduction problem and its thermal deflection which causes the generation of internal heat in a thin hollow circular disk. Patil et al. [8] solved semi-infinite rectangular slab with internal heat source using integral transform technique with the determination of the distribution of temperature, thermal parameters, and displacement at any point. Solanke and Durge [9] have determined distribution of temperature and thermal stresses with second kind boundary conditions in thin rectangular plate with moving line heat source by using integral transform technique and Green's theorem. Thakare et al. [10] have evaluated thermal stresses due to internal moving point heat source in thin rectangular plate by integral transform technique. Solanke and Durge [11] have solved problem of quasi-stationary thermo-elastic characteristic with moving heat source in unidirectional Robin's rod. Gaikwad [12] used Hankel transform technique to evaluate two-dimensional steady-state temperature distribution in thin circular plate due to the generation of uniform internal energy, and it has been presented graphically. Ahire and Ghadle [13] elaborate on three-dimensional unsteady-state temperature distribution in thin rectangular plate with moving point heat source.

A tool of integral transform technique has found the most suitable way to obtain the solution of various new general-purpose numerical methods. Due to its simple form, one can implement it to reveal parameters like variation of temperature. This technique has a lot of advantages as compared to other methods.

The analysis in the present paper constructs an effective solution and helps to study the thermal stresses in a unidirectional rod with internal moving line heat source.

The remainder of this paper elaborates the details of the determination of temperature and thermal stresses in unidirectional rod defined as $0 \leq x \leq a, 0 \leq y \leq b$. Heat conduction equation has been solved using integral transform technique. Result is composed of the terms in the form of infinite series. It has been determined by numerically and graphically.

2 Formulation of the Problem
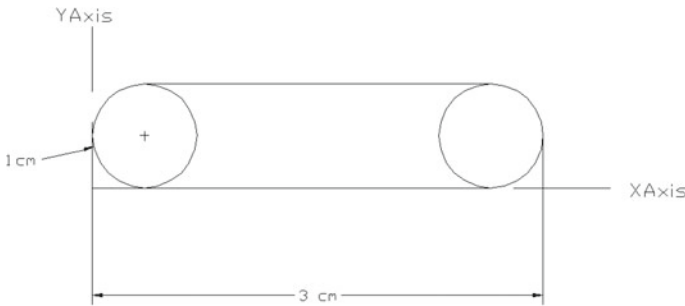
Consider a rod of length confined in the region $R: 0 \leq x \leq a, 0 \leq y \leq b$. The unidirectional rod is studied with an ambient temperature zero when initial temperature is also zero. The rod is kept under the instantaneous moving heat source located at the point x', which is moving with constant velocity u along x-axis. Atomic interaction due to moving heat source causes the generation of heat. The differential equation of heat conduction which contains heat generation term results in the distribution of temperature in two-dimensional rod.

The temperature distribution of the rod defined in [14] is given by

$$\frac{\partial^2 T}{\partial x^2} + \frac{\partial^2 T}{\partial y^2} + \frac{g}{k} = \frac{1}{\alpha} \frac{\partial T}{\partial t} \tag{1}$$

where k is thermal conductivity and α is thermal diffusivity of the material of the plate.

The volumetric moving heat source in rectangular coordinates (x', y) and produces the spontaneous heat at time t' which is given by

$$g(x, y, t) = g_P^i \delta(x - x') \delta(y) \delta(t - t') \tag{2}$$

where g_P^i is instantaneous heat source.

Hence, Eq. (1) becomes

$$\frac{\partial^2 T}{\partial x^2} + \frac{\partial^2 T}{\partial y^2} + \frac{1}{k} g_P^i \delta\left(x - x'\right) \delta(y) = \frac{1}{\alpha} \frac{\partial T}{\partial t} \tag{3}$$

The following are the initial and boundary conditions:

$$[T]_{t=0} = 0 \tag{4}$$

$$\left[\frac{\partial T}{\partial x}\right]_{x=0} = 0 \tag{5}$$

$$\left[\frac{\partial T}{\partial x}\right]_{x=a} = 0 \tag{6}$$

$$\left[\frac{\partial T}{\partial y}\right]_{y=0} = 0 \tag{7}$$

$$\left[\frac{\partial T}{\partial y}\right]_{y=b} = 0 \tag{8}$$

$$\chi = \chi_c + \chi_p \tag{9}$$

where χ in Eq. (9) is thermal stress function and χ_c is the C.F. and χ_p is P.I. χ_c and χ_p are governed by equations [15],

$$\left(\frac{\partial^2}{\partial x^2} + \frac{\partial^2}{\partial y^2}\right)^2 \chi_c = 0 \tag{10}$$

and

$$\left(\frac{\partial^2}{\partial x^2} + \frac{\partial^2}{\partial y^2}\right)^2 \chi_p = -\alpha E \Gamma \tag{11}$$

At $\Gamma = T - T_0$, where T_0 is initial temperature. Component of stress functions [15] for thin plate is given by

$$\sigma_{xx} = \frac{\partial^2 \chi}{\partial y^2} \tag{12}$$

$$\sigma_{yy} = \frac{\partial^2 \chi}{\partial x^2} \tag{13}$$

$$\sigma_{xy} = -\frac{\partial^2 \chi}{\partial x \partial y} \tag{14}$$

with boundary conditions $\sigma_{yy} = 0, \sigma_{xy} = 0$ at $y = b$ Eqs. (1)–(14) represent the statement of the problem.

3   Solution of the Problem

The solution of the moving heat source problem is obtained by conveniently assuming that the coordinate system move with the source. A new coordinate x' defined by Ozisik [14] is used to gain the same.

$$x' = x - ut$$

$$\frac{\partial^2 T}{\partial \xi^2} + \frac{\partial^2 T}{\partial y^2} + \frac{g_P^i \delta(x - x')\delta(y)}{k} = \frac{1}{\alpha}\left[\frac{\partial T}{\partial t} - u\frac{\partial T}{\partial \xi}\right] \tag{15}$$

$$\frac{\partial^2 T}{\partial \xi^2} + \frac{\partial^2 T}{\partial y^2} + \frac{g_P^i \delta(x - x')\delta(y)}{k} = \frac{-u}{\alpha}\left[\frac{\partial T}{\partial \xi}\right] \tag{16}$$

$$T(\xi, y) = \theta(\xi, y)e^{-\left(\frac{u}{2\alpha}\right)\xi}$$

$$\frac{\partial^2 \theta}{\partial \xi^2} + \frac{\partial^2 \theta}{\partial y^2} - \left(\frac{u}{2\alpha}\right)^2 \theta + \frac{g_P^i \delta(x - x')\delta(y)}{k} = 0 \tag{17}$$

Applying finite Fourier cosine transform twice defined in [16] Eq. (16) becomes,

$$\overline{\overline{T}} = \frac{g_P^i}{kQ}\left(1 - e^{\frac{\alpha}{u}Q\xi}\right) \tag{18}$$

where $Q = \left(\frac{m^2\pi^2}{a^2} + \frac{n^2\pi^2}{b^2}\right)$.

Taking inverse finite Fourier cosine transform twice,

$$T = \frac{4}{ab}\sum_{m,n=1}^{\infty}\frac{g_P^i}{kQ}\left(1 - e^{\frac{\alpha}{u}Q\xi}\right)\cos\frac{m\pi\xi}{a}\cos\frac{n\pi y}{b} \tag{19}$$

$$T = \frac{4}{ab}\sum_{m,n=1}^{\infty}\frac{g_P^i}{k\left(\frac{m^2\pi^2}{a^2} + \frac{n^2\pi^2}{b^2}\right)}\left(1 - e^{\frac{\alpha}{u}Q\xi}\right)\cos\frac{m\pi\xi}{a}\cos\frac{n\pi y}{b} \tag{20}$$

$$\Gamma = T - T_0$$

$$\Gamma = \frac{4}{ab}\sum_{m,n=1}^{\infty}\frac{g_P^i}{k\left(\frac{m^2 b^2 + n^2 a^2}{a^2 b^2}\right)\pi^2}\left(1 - e^{\frac{\alpha}{u}Q\xi}\right)\cos\frac{m\pi\xi}{a}\cos\frac{n\pi y}{b}$$

$$\Gamma = \sum_{m,n=1}^{\infty}\frac{4ab\,g_P^i}{k\left(m^2 b^2 + n^2 a^2\right)\pi^2}\left(1 - e^{\frac{\alpha}{u}Q\xi}\right)\cos\frac{m\pi\xi}{a}\cos\frac{n\pi y}{b} \tag{21}$$

$$\chi_c = \sum_{m=1}^{\infty}y\left[c_1 e^{\frac{m\pi y}{a}} + c_2 e^{-\frac{m\pi y}{a}}\right]\cos\left(\frac{m\pi x}{a}\right) + y\left[c_3 e^{\frac{m\pi y}{a}} + c_4 e^{-\frac{m\pi y}{a}}\right]\sin\left(\frac{m\pi x}{a}\right) \tag{22}$$

$$\chi_p = -\alpha E\Gamma$$

$$\chi_p = \sum_{m,n=1}^{\infty}\frac{-4a^3 b^3 \alpha E g_P^i}{\left(m^2 b^2 + n^2 a^2\right)^2 \pi^4}\left(1 - e^{\frac{\alpha}{u}Q\xi}\right)\cos\frac{m\pi\xi}{a}\cos\frac{n\pi y}{b} \tag{23}$$

$$\chi = \chi_c + \chi_p$$

$$\chi = \sum_{m=1}^{\infty} y\left[c_1 e^{\frac{m\pi y}{a}} + c_2 e^{-\frac{m\pi y}{a}}\right]\cos\left(\frac{m\pi x}{a}\right) + y\left[c_3 e^{\frac{m\pi y}{a}} + c_4 e^{-\frac{m\pi y}{a}}\right]\sin\left(\frac{m\pi x}{a}\right)$$

$$+ \sum_{m,n=1}^{\infty} \frac{-4a^3 b^3 \alpha E g_P^i}{\left(m^2 b^2 + n^2 a^2\right)^2 \pi^4}\left(1 - e^{\frac{\alpha}{u} Q\xi}\right)\cos\frac{m\pi\xi}{a}\cos\frac{n\pi y}{b} \tag{24}$$

4 Determination of Stress Function

Using Eq. (24) in Eqs. (12)–(14), we get,

$$\sigma_{xx} = \sum_{m,n=1}^{\infty} \left\{ \left[2\frac{m\pi}{a}\left(c_1 e^{\frac{m\pi y}{a}} - c_2 e^{-\frac{m\pi y}{a}}\right) + y\frac{m^2\pi^2}{a^2}\left(c_1 e^{\frac{m\pi y}{a}} + c_2 e^{-\frac{m\pi y}{a}}\right)\right]\cos\left(\frac{m\pi x}{a}\right) \right.$$

$$\left. + \left[2\frac{m\pi}{a}\left(c_3 e^{\frac{m\pi y}{a}} - c_4 e^{-\frac{m\pi y}{a}}\right) + y\frac{m^2\pi^2}{a^2}\left(c_3 e^{\frac{m\pi y}{a}} + c_4 e^{-\frac{m\pi y}{a}}\right)\right]\sin\left(\frac{m\pi x}{a}\right) \right\}$$

$$- \frac{4a^3 b\alpha E g_P^i}{\left(m^2 b^2 + n^2 a^2\right)^2 \pi^2} n^2\left(1 - e^{\frac{\alpha}{u} Qx}\right)\cos\left(\frac{m\pi x}{a}\right)\cos\left(\frac{n\pi y}{b}\right) \tag{25}$$

$$\sigma_{yy} = \frac{-m^2\pi^2 y}{a^2}\left\{\left[c_1 e^{\frac{m\pi y}{a}} + c_2 e^{-\frac{m\pi y}{a}}\right]\cos\left(\frac{m\pi x}{a}\right)\right.$$

$$\left. - \frac{ym^2\pi^2}{a^2}\left[c_3 e^{\frac{m\pi y}{a}} + c_4 e^{-\frac{m\pi y}{a}}\right]\sin\left(\frac{m\pi x}{a}\right)\right\}$$

$$+ \frac{4\alpha E a^3 b^3 g_P^i\left(1 - e^{\frac{\alpha}{u} Qx}\right)}{\pi^4 2^{\text{os}}\left(a^2 n^2 + b^2 m^2\right)^2}\cos\left(\frac{m\pi x}{a}\right)\cos\left(\frac{n\pi y}{b}\right)\left[\frac{\alpha^2 Q^2}{u^2} - \frac{m^2\pi^2}{a^2}\right] \tag{26}$$

$$\sigma_{xy} = \sum_{m,n=1}^{\infty} \left\{ \left[\left(\frac{m\pi}{a} + y\frac{m^2\pi^2}{a^2}\right)c_1 e^{\frac{m\pi y}{a}} + \left(\frac{m\pi}{a} - y\frac{m^2\pi^2}{a^2}\right)c_2 e^{-\frac{m\pi y}{a}}\right]\sin\left(\frac{m\pi x}{a}\right) \right.$$

$$\left. + \left[\left(-\frac{m\pi}{a} - y\frac{m^2\pi^2}{a^2}\right)c_3 e^{\frac{m\pi y}{a}} + \left(\frac{m\pi}{a} + y\frac{m^2\pi^2}{a^2}\right)c_4 e^{-\frac{m\pi y}{a}}\right]\cos\left(\frac{m\pi x}{a}\right)\right\}$$

$$- \frac{4a^2 b^2 \alpha E g_P^i mn}{\left(m^2 b^2 + n^2 a^2\right)^2 \pi^2}\left(1 - e^{\frac{\alpha}{u} Qx}\right)\sin\left(\frac{m\pi x}{a}\right)\sin\left(\frac{n\pi y}{b}\right) \tag{27}$$

Using the boundary condition $\sigma_{yy} = 0$ and $\sigma_{xy} = 0$ at $y = b$, we get

$$c_3 = 0, \ c_4 = 0, \ c_1 = \frac{2\alpha E\varphi a^2\left(u^2 + 2m^2\right)}{bm^2 u^2} e^{\frac{-m\pi b}{a}}, \ c_2 = \frac{2\alpha E\varphi a^4}{bm^2} e^{\frac{m\pi b}{a}}$$

where $\varphi = \frac{g_P^i\left(a^4\alpha^2 n^2 + a^2 b^2\alpha^2 m^2 - u^2 a^2 b^2 m^2\right)}{\pi^4 m^2\left(a^2 n^2 + b^2 m^2\right)^2}$

$$\varphi = \frac{2.3562}{15.5485} e^{-23.8\times 10^{-6}\times 12.4912t} \left\{ \int \left(e^{23.8\times 10^{-6}\times 12.4912t} + 23.8\times 10^{-6}(-0.9721 \right.\right.$$

$$\left.\left. -1.2639t)\right) - \int 23.8\times 10^{-6}((-0.9721 - 1.2639t))dt \right\}$$

$$\sigma_{xx} = \sum_{m,n=1}^{\infty} \left\{ \left[\left(\frac{2m\pi}{a} + y\frac{m^2\pi^2}{a^2} \right) \frac{2\alpha E\varphi a^2 \left(u^2 + 2m^2\right)}{bm^2 u^2} e^{\frac{-m\pi b}{a}} e^{\frac{m\pi y}{a}} \right.\right.$$

$$\left.\left. + \left(-\frac{2m\pi}{a} + y\frac{m^2\pi^2}{a^2} \right) \frac{2\alpha E\varphi a^4}{bm^2} e^{\frac{m\pi b}{a}} e^{-\frac{m\pi y}{a}} \right] \cos\left(\frac{m\pi x}{a}\right) \right\}$$

$$- \frac{4a^3 b\alpha E g_P^i}{\left(m^2 b^2 + n^2 a^2\right)^2 \pi^2} n^2 \left(1 - e^{\frac{\alpha}{u}Qx}\right) \cos\left(\frac{m\pi x}{a}\right) \cos\left(\frac{n\pi y}{b}\right)$$

$$\sigma_{yy} = \frac{-m^2\pi^2 y}{a^2} \left\{ \left[\frac{2\alpha E\varphi a^2 \left(u^2 + 2m^2\right)}{bm^2 u^2} e^{\frac{-m\pi b}{a}} e^{\frac{m\pi y}{a}} \right.\right.$$

$$\left.\left. + \frac{2\alpha E\varphi a^4}{bm^2} e^{\frac{m\pi b}{a}} e^{-\frac{m\pi y}{a}} \right] \cos\left(\frac{m\pi x}{a}\right) \right\}$$

$$+ \frac{4\alpha E a^3 b^3 g_P^i \left(1 - e^{\frac{\alpha}{u}Qx}\right)}{\pi^4 2 os \left(a^2 n^2 + b^2 m^2\right)^2} \cos\left(\frac{m\pi x}{a}\right) \cos\left(\frac{n\pi y}{b}\right) \left[\frac{\alpha^2 Q^2}{u^2} - \frac{m^2\pi^2}{a^2} \right]$$

$$\sigma_{xy} = \sum_{m,n=1}^{\infty} \left\{ \left[\left(\frac{m\pi}{a} + y\frac{m^2\pi^2}{a^2} \right) \frac{2\alpha E\varphi a^2 \left(u^2 + 2m^2\right)}{bm^2 u^2} e^{\frac{-m\pi b}{a}} e^{\frac{m\pi y}{a}} \right.\right.$$

$$\left.\left. + \left(\frac{m\pi}{a} - y\frac{m^2\pi^2}{a^2} \right) \frac{2\alpha E\varphi a^4}{bm^2} e^{\frac{m\pi b}{a}} e^{-\frac{m\pi y}{a}} \right] \sin\left(\frac{m\pi x}{a}\right) \right\}$$

$$- \frac{4a^2 b^2 \alpha E g_P^i mn}{\left(m^2 b^2 + n^2 a^2\right)^2 \pi^2} \left(1 - e^{\frac{\alpha}{u}Qx}\right) \sin\left(\frac{m\pi x}{a}\right) \sin\left(\frac{n\pi y}{b}\right)$$

5   Numerical Results

Physical Properties of Metals

Properties	Aluminum	Copper	Brass
Modulus of elasticity (E)	0.675×10^{11}	1.23×10^{11}	0.970×10^{11}
Coefficient of thermal expansion (lb/lb/°C) (α)	23.8×10^{-6}	16.2×10^{-6}	16.7×10^{-6}
Thermal diffusivity (cm^2/s) (k)	0.530	0.940	0.310

where $a = 3$, $b = 1$, $h = 0.5$, $m = 1$, $n = 1$, $g_P^i = 1$, $x' = 1.5$, $t = 1$, $t' = 1.5$,

$\lambda_l = 15.5485$, $p_l(0.2) = 2.3562$, $\varphi = 0.2056$, $Q = 12.4912$, $\emptyset = -4.5920$

5.1   *Aluminum Rod*

$$T = 0.5358\left\{\left[e^{-2.9729 \times 10^{-4}t}\right]\cos(\pi y)\right\}\sin\left(\frac{\pi x}{5}\right)$$

$$\sigma_{xx} = \sum_{m=1}^{\infty}\left\{\left[\left(\pi + \frac{\pi^2}{4}y\right)3.7057 \times 10^{12}e^{\frac{\pi y}{2}}\right.\right.$$
$$\left.+\left(-\pi + \frac{\pi^2}{4}y\right)3.8623 \times 10^{14}e^{\frac{-\pi y}{2}}\right]\cos\left(\frac{\pi x}{2}\right)\right\}$$
$$-\ 1.0205 \times 10^{11}\cos\left(\frac{\pi x}{2}\right)\cos(\pi y) \times \left(1 - e^{2.9362x}\right)$$

$$\sigma_{xy} = \sum_{m=1}^{\infty}\left\{\left[\left(\frac{\pi}{2} + \frac{\pi^2}{4}y\right)\sin\left(\frac{\pi x}{2}\right)2.3591 \times 10^{12}e^{\frac{\pi y}{2}}\right.\right.$$
$$\left.\left.-\left(\frac{\pi}{2} - \frac{\pi^2}{4}y\right)\sin\left(\frac{\pi x}{2}\right)3.8623 \times 10^{14}e^{\frac{-\pi y}{2}}\right]\right\}$$
$$+\ 5.0362 \times 10^{11}\sin\left(\frac{\pi x}{2}\right)\sin(\pi y) \times \left(1 - e^{2.9362x}\right)$$

$$\sigma_{yy} = \left(1 - e^{2.9362x}\right)\left\{\left[\left(1 - 2.9362 \times 10^{11}\right)ye^{\frac{\pi}{2}} + 9.5298 \times 10^{14}ye^{\frac{-\pi}{2}}\right]\cos\left(\frac{\pi x}{2}\right)\right\}$$
$$+\ 2.5181 \times 10^{11}\{\cos(\pi y)\}\cos\left(\frac{\pi x}{2}\right)$$

5.2 Copper Rod

$$T = 0.5356\left\{\left[e^{-2.0860\times10^{-4}t}\right]\cos(\pi y)\right\}\sin\left(\frac{\pi x}{5}\right)$$

$$\sigma_{xx} = \sum_{m=1}^{\infty}\left\{\cos\left(\frac{\pi x}{2}\right)\right\}(1 - e^{4.71x})(-1.4968\times10^8 - 1.1756\times10^8 y)e^{\pi y/2}$$
$$+ (1.2253\times10^9 - 1.56\times10^{10})\cos(\pi y)\times(-1.245\times10^{10})$$

$$\sigma_{xy} = \left\{\left[\left((1 - e^{4.71x})\sin\left(\frac{\pi x}{2}\right)(2.4674y + 1.5707)\times0.0298\times10^{11}e^{\frac{\pi}{2}}\right.\right.\right.$$
$$\left.\left.+\left(\frac{\pi}{2} - \pi^2 y\right)e^{-\frac{\pi}{2}}\right)0.04966\times10^{11}\right] + 0.06225\times10^{11}\times\sin(\pi y)\right\}$$

$$\sigma_{yy} = \left\{\left[\left((1 - e^{4.71x})\cos\left(\frac{\pi x}{2}\right)\left(1.1756\times10^8\times y\times e^{\frac{\pi y}{2}}\right) + 1.2253\times10^{10}e^{\frac{-\pi y}{2}}\right)\right]\right.$$
$$\left.-1.5563\times10^9\cos(\pi y)\right\}$$

5.3 Brass Rod

$$T = 0.5358\left\{\left[e^{-4.1603\times10^{-5}t}\right]\cos(\pi y)\right\}\sin\left(\frac{\pi x}{5}\right)$$

$$\sigma_{xx} = \sum_{m=1}^{\infty}\left\{\left[\left(\pi + \frac{\pi^2}{4}y\right)3.7645\times10^{12}e^{\frac{\pi y}{2}}\right.\right.$$
$$\left.\left.+\left(-\pi + \frac{\pi^2}{4}y\right)3.9235\times10^{14}e^{\frac{-\pi y}{2}}\right]\cos\left(\frac{\pi x}{2}\right)\right\}$$
$$- 1.0367\times10^{11}\cos\left(\frac{\pi x}{2}\right)\cos(\pi y)\times(1 - e^{2.9362x})$$

$$\sigma_{xy} = \left\{\left[\left((1 - e^{4.71x})\left(-\sin\left(\frac{\pi x}{2}\right)\right)(2.4674y + 1.5707)\times2.3966\times10^{12}\times e^{\frac{\pi y}{2}}\right.\right.\right.$$
$$\left.\left.+\left(\frac{\pi}{2} - \frac{\pi^2 y}{4}\right)e^{-\frac{\pi y}{2}}\sin\left(\frac{\pi x}{2}\right)\right)\times3.9235\times10^{14}\right]\sin(\pi y)\sin\left(\frac{\pi x}{2}\right)\right\}$$

$$\sigma_{yy} = \left\{(1 - e^{2.0603x})\left(-\frac{\pi^2}{4}y\right)\left(3.7645\times10^{12}\times e^{\frac{\pi y}{2}}\right)\right.$$
$$\left.+(3.9235\times10^{14}e^{\frac{-\pi y}{2}} - 2.5580\times10^{11}\cos(\pi y)\times\cos\left(\frac{\pi x}{2}\right)\right\}$$

6   Graphical Interpretation

Figure 1: Temperature gradually increases and becomes stable for small duration. Temperature decreases slightly after attaining the stable value. As length increases, temperature also increases with internal moving heat source.

Figure 2: Stress for aluminum is maximum, and for brass, it is minimum. But for copper, it remains constant. Aluminum is very sensitive to change in temperature as compared to copper and brass. Hence, stress shown along x-axis for aluminum is more than copper and brass.

Figure 3: Copper has a very small variation in stress while aluminum and brass have more moderate change in their stresses. Aluminum is the most affected material as compared to copper and brass. Maximum stress is produced in aluminum. As the stress is compared in brass and copper, it is observed that stress is minimum in copper.

Figure 4: As depicted in graph, thermal stress in aluminum varies from its maximum to minimum. For copper, it remains constant along the length while brass has its minimum to its maximum.

7   Discussion

The two-dimensional non-homogeneous heat conduction problems in a unidirectional rod have been discussed here. Numerical computations are performed for a unidirectional rod composed of brass, aluminum, copper. The source of heat
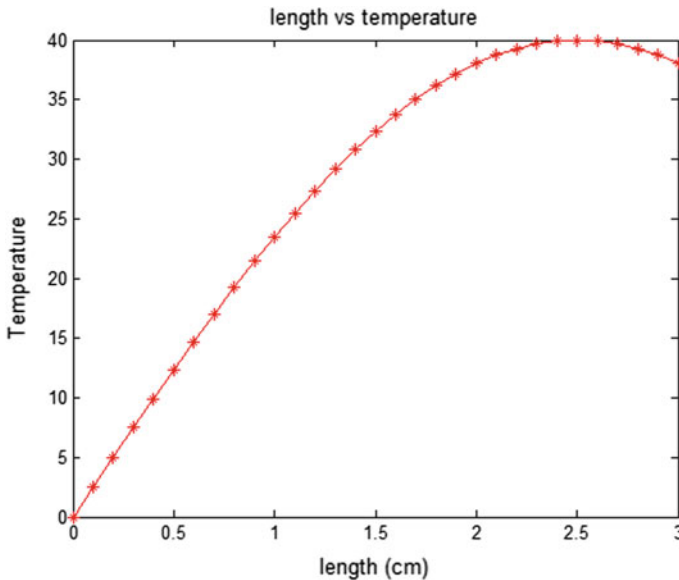
Fig. 1 Length versus temperature
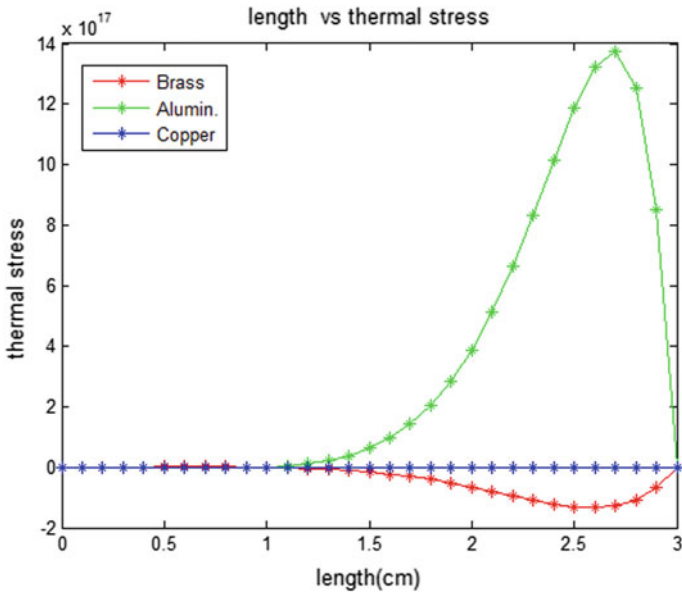
Fig. 2 *x* versus thermal stress (Sigma *xx*)
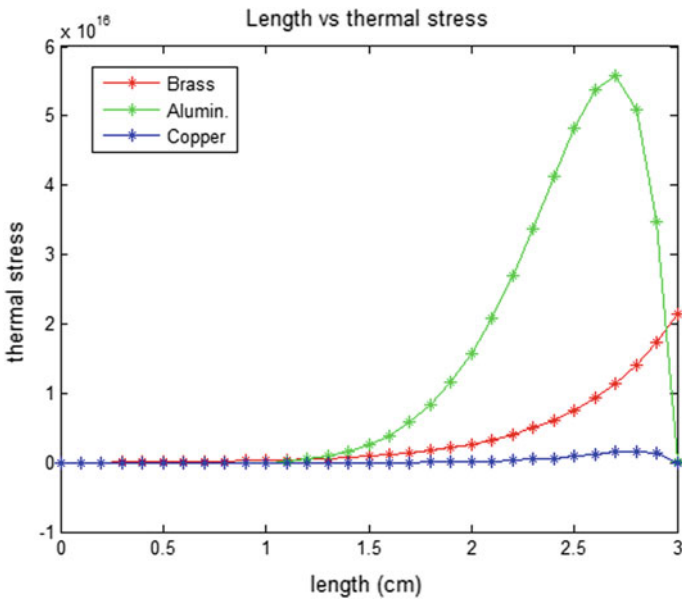
Fig. 3 *x* versus thermal stress (Sigma *yy*)
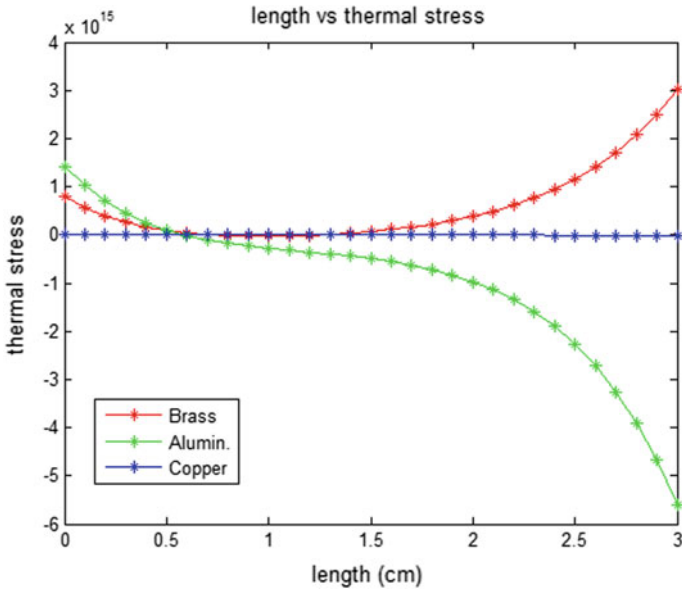
Fig. 4 x versus thermal stress (Sigma xy)

$g(x, y, z, t)$ is an instantaneous moving heat source and has strength g_P^i. The temperature-dependent elastic behavior is noted for various temperature and thermal stresses.

8 Conclusion

In this paper, we achieved the solution of non-homogeneous thermoelastic problem by using integral transform techniques numerically. The outcome of this analysis contains the terms in infinite series. Three materials brass, aluminum, copper were examined under unsteady-state temperature with initial value zero. In these three materials, thermal stresses observed for aluminum are maximum while brass and copper lie under the aluminum. These were carried out with initial zero temperature. When heat is provided to the rod, thermal stresses change along with *x-axis* as well as *y*-axis.

These results can be applied in engineering problems, such as industrial machines which come in the vicinity of the heating such as the central shaft of a machine, big turbines, the roll of rolling mill, and practical applications in aircraft structures.

Terminology

Notation	Meaning
$T(x, y, t)$	Temperature of the rod (°C)
$g(x, y, t)$	Volumetric energy of heat source (W cm^{-3})
k	Thermal diffusivity (cm^2 s^{-1})
E	Modulus of elasticity
λ	Thermal conductivity
α	Coefficient of thermal expansion
g_p^i	Point heat source

References

1. Nowinski JL (1978) Theory of thermoelasticity with application. Sijth of Noordhoff, Alphen Aan Den Rijn, The Netherlands, 407
2. Nowacki W (1957) The state of stresses in a thick circular plate due to temperature field. Bull Acad Polon Sci Scl Tech 5:227
3. Boley BA, Weiner JH (1960) Theory of thermal stresses. Wiley, New York
4. Roy Choudhary SK (1972) A note of quasi static stress in a thin circular plate due to transient temperature applied along the circumference of a circle over the upper face. Bull Acad Polon Sci Ser Sci Math, 20–21
5. Khobragade NW, Wankhede PC (2003) An inverse unsteady state thermoelastic problem of a thin rectangular plate. J. Indian Acad Math 25(2)
6. Gaikwad KR, Ghadle KP (2010) Quasi static thermoelastic problem of an infinitely long circular cylinder. J Korea Soc Indus Appl Math 14(3):141–149
7. Gaikwad KR, Ghadle KP (2012) Non-homogeneous heat conduction problem and its thermal deflection due to internal heat generation in a thin hollow circular disk. J Thermal Stress 35(6):485–498 (Taylor & Francis)
8. Patil VB, Ahirrao BR, Khobragade NW (2013) Thermal stresses of semi infinite rectangular slab with internal heat source. IOSR J Math 8(6):57–61
9. Solanke DT, Durge MH (2014) Quasi static thermal stresses in thin rectangular plate with internal moving line heat source. Sci Park Res J 1(44)
10. Thakare MS, Sutar CS, Khobragade NW (2015) Thermal stresses of a thin rectangular plate with internal moving heat source. IJEIT 4(9)
11. Solanke DT, Durge MH (2015) Quasi-stationary thermo elastic problem with moving heat source in unidirectional Robin's rod. Eng Sci Int J (ESIJ) 2(3)
12. Gaikwad KR (2016) Two dimensional steady state temperature distribution of a thin circular plate due to uniform internal energy generation. Cogent Math 3:1135720
13. Ahire YM, Ghadle KP (2016) Three-dimensional unsteady state temperature distribution of thin rectangular plate with moving point heat source. Indian J Mater Sci 2016:7, Article ID 7563215 (Hindawi Publishing Corporation)
14. Ozisik NM (1968) Boundary value problem of heat conduction, Dover Publication INC., Mineola, New York
15. Noda N, Hetnarski RB, Tanigawa Y (2002) Thermal stresses, 2nd edn
16. Sneddon IN (1972) The use of integral transform. McGraw Hill, New York, pp 235–238

Effect of Height of the Tornado Chamber on Vortex Touchdown

Sumit Verma and R. Panneer Selvam

Abstract Numerically modeled vortex chamber, both in 2D and 3D, have been employed to analyze the flow features of tornado-like vortex. In 2D analysis, flow structure was first investigated using a fixed overall height and varying swirl ratios (S) followed by the variation of overall chamber height to observe its effect on touchdown S. Increasing overall chamber height lowered the touchdown S. Ground pressure profile showed some contrast from experiment as the pressure was found to be increasing even after touchdown. A tentative projection of overall chamber height required to obtain touchdown similar to experiment was found to be at $H =$ 49.5. The proposition of increasing the chamber height alone to reach touchdown state would make the analysis computationally intensive and potentially infeasible. For further analysis, 3D model, brought in action, revealed touchdown to occur at similar parameters with similar trend of pressure plot as the 2D model.

Keywords Tornado · Numerical simulator · Swirl ratio · Touchdown · Ground pressure

1 Introduction

Tornado winds are rotating winds, and they produce much larger force coefficients compared to straight winds as reviewed by [13] and the reference there in. The interaction of rotating wind on structures has been reported in [11, 12] without any downdraft or updraft, but meteorological observations show that there is updraft and downdraft in the inner core. In the recent years, to consider the above effect, tornado chamber studies are utilized both by experiment as in [15] and computational fluid dynamics (CFD) point of view as in [2].

S. Verma (✉) · R. P. Selvam
Department of Civil Engineering, BELL 4190 University of Arkansas, Fayetteville, AR, USA
e-mail: sv015@uark.edu

R. P. Selvam
e-mail: rps@uark.edu
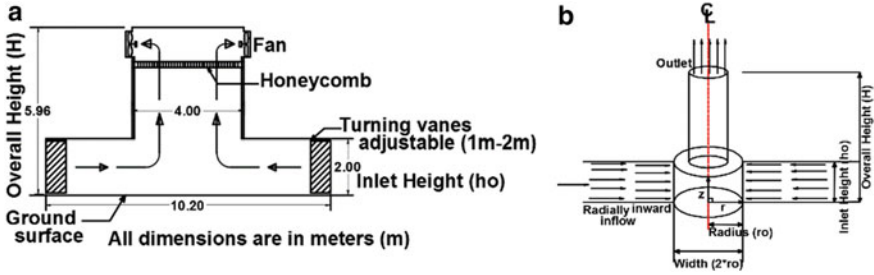
Fig. 1 Tornado chamber. **a** TTU tornado chamber, **b** simplified tornado chamber

The tornado chambers from different places are built with different configurations. The details of the structural configuration of Iowa State Univeristy (ISU), University of Western Ontario (UWO), and Texas Tech University (TTU) simulators are described in [4, 5, 15], respectively. As an illustration, only TTU chamber is shown in Fig. 1a. Since each configuration is so different, a simple model is suggested in [2] that can represent the flow features of any one of the testing facilities as shown in Fig. 1b.

The total height of the cylindrical chamber of the simplified model used in [2] is $16h_o$, where h_o is the height of the inlet chamber. It is said that maintaining a sufficiently large height as such would generate an appropriate pressure outlet boundary condition and doing so would make the flow structure independent of height of the cylindrical domain. Also, the touchdown condition in the TTU chamber occurs for a swirl ratio (S) of 0.22 with total height of the chamber $3h_o$ as reported in [15], whereas the simple model in [2] predicted touchdown at $S = 0.43$ for a total height of $16h_o$. Similarly, the influence of variation of convection region height on velocity flow field and pressure distribution of tornado-like vortex was carried out by [3], and a conclusion was drawn that the flow structure was likely to be a function of convection region height as well as S.

Hence, in this paper, the assumption of flow structure becoming independent of height by using a sufficiently high vortex chamber of height $16h_o$ as stated by [2] will be tested using 2D and 3D CFD models. The results of this study will be helpful to produce tornado at or beyond touchdown for Tornado Structure Interaction (TSI) study in numerical simulators based on ward-type configuration by just varying the height of the vortex chamber. Using a simple chamber will eliminate the complexity of modeling, grid generation and reduce the associated computational cost and time required for modeling of complicated chamber domain.

1.1 Nomenclature

In the following discussions, we will use the following terms to represent the tornado chamber flow:

A	Aspect ratio $= h_o/r_o$
h_o	Height of inlet chamber (see Fig. 1)
r_o	Radius of vortex chamber (see Fig. 1)
H	Overall height of vortex chamber (see Fig. 1)
Reynolds number (Re)	$V_r \, h_o/\nu$
Swirl ratio (S)	$V_\theta/(2AV_r) = \tan\theta/2A$; $\tan\theta = V_\theta/V_r$
V_θ	Tangential velocity
V_r	Radial velocity
Vz	Axial velocity
ν_e	Effective viscosity
ν	Average viscosity
$\nu_{turbulent}$	Turbulent viscosity
Pz	Pressure at elevation-z
Pn	Pressure normal to the surface

2 Numerical Setup

2.1 Governing Equation

Non-dimensionalized Navier–Stokes (NS) equation was used for the present study using large eddy simulation (LES) approach. In LES, Smagorinksy model is used for turbulent viscosity modeling. To reduce computational time, initial study was conducted using axisymmetric flow, and then, some results are presented for 3D flow. Here, h_o is considered to be the reference length, and the radial velocity at the reference height is considered to be reference velocity. In this case, they are considered to be $h_o = 2$ m and $Vr = 5.97$ m/s. The governing equations are obtained by filtering the time-dependent NS equations, and the details can be found in [1].

2.2 Continuity Equation

$$\frac{1}{r}\frac{\partial}{\partial r}(rVr) + \frac{\partial}{\partial z}(Vz) = 0 \tag{1}$$

2.3 Momentum Equations

r-component:

$$\frac{\partial Vr}{\partial t} + \frac{1}{r}\frac{\partial (rVr^2)}{\partial r} + \frac{\partial (VrVz)}{\partial z} = -\frac{\partial P}{\partial r} + \left[2ve\frac{\partial^2 (Vr)}{\partial r^2} + \frac{2}{r}ve\left(\frac{\partial Vr}{\partial r} - \frac{Vr}{r}\right)\right.$$
$$\left. + \frac{\partial}{\partial z}\left(ve * \left(\frac{\partial Vr}{\partial z} + \frac{\partial Vz}{\partial r}\right)\right)\right] + \frac{V\theta^2}{r} \qquad (2)$$

θ-component:

$$\frac{\partial V\theta}{\partial t} + \frac{1}{r}\frac{\partial (rVrV\theta)}{\partial r} + \frac{\partial (V\theta Vz)}{\partial z} = -\frac{VrV\theta}{r} + \left[2ve\left(\frac{\partial^2 V\theta}{\partial z^2}\right)\right.$$
$$+ \frac{\partial}{\partial r}\left(ve * \left(\frac{\partial V\theta}{\partial r} - \frac{V\theta}{r}\right)\right)$$
$$\left. + \frac{2}{r}ve\left(\frac{\partial V\theta}{\partial r} - \frac{V\theta}{r}\right)\right] \qquad (3)$$

Z-component:

$$\frac{\partial Vz}{\partial t} + \frac{1}{r}(rVrVz) + \frac{\partial Vz^2}{\partial z} = -\frac{\partial P}{\partial z} + \left[2ve\frac{\partial^2 Vz}{\partial z^2}\right.$$
$$\left. + \frac{1}{r}\frac{\partial}{\partial r}\left(ve\left(r\left(\frac{\partial Vr}{\partial Z} - \frac{\partial Vz}{\partial r}\right)\right)\right)\right] \qquad (4)$$

where $v_e = v + v_{turbulent}$.

2.4 Axisymmetric Model Detail

The above equations are solved in a semi-staggered grid system. This grid system helps to implement velocity boundary conditions easily compared to staggered grid system. The convection and diffusion are considered to be explicit. The convection equation is approximated using QUICK procedure. At the bottom wall, law of the wall condition is implemented, and at the inlet, a logarithmic velocity profile is provided to produce the boundary layer effect of atmospheric flow. The continuity is satisfied using SOLA-type solver reported in [6, 14]. The pressure iteration is done until the continuity error reduced to less than 1×10^{-3}. It is found that the number of iterations were very high for semi-staggered grid system compared to staggered grid system.

The boundary conditions applied to the axisymmetric computational domain are shown adjacent to their corresponding faces in Fig. 2. The boundary conditions (BCs) in this study are similar to that of BCs used in [7]. Even though all around, the pressure BC is normal derivative zero, and there is no need to fix one point of the pressure equation with Dirichlet BC because the velocity BC takes care of it in the SOLA-type solver.
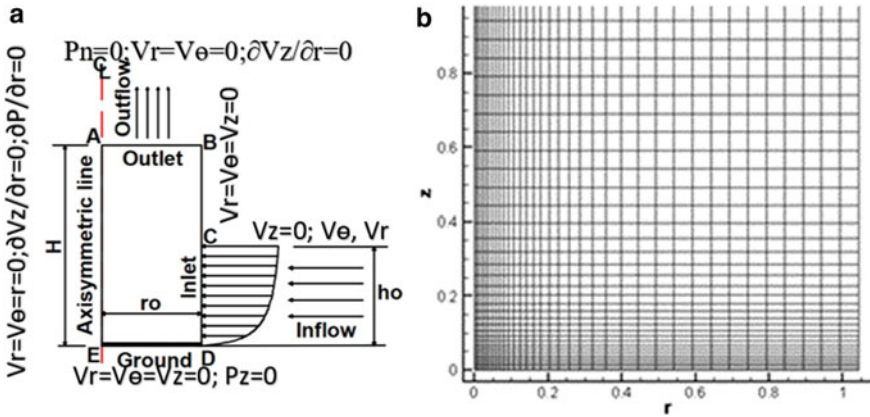
Fig. 2 **a** Axisymmetric domain with boundary conditions, **b** grid for computational domain

2.5 3D Model Detail

The 3D equations are solved in a nonstaggered grid system, and the equation and other details are reported in [10]. A square plan area is considered to create the grid, and only the circular region is considered for computation in the upper cylinder region. For pressure boundary condition, one point (the center point) on the top is considered to be zero, and at all other places, normal derivative is considered to be zero. This enables the preconditioned conjugate gradient solver to converge faster. At the same time, selection of one point for Dirichlet BC can be done if the flow is uniform from our experience. If the flow has much variation, this distorts the pressure and flow conditions, and hence, staggered grid system may be used. Here, Cartesian grid system is chosen instead of cylindrical system for the following reasons: (a) It is very difficult to control the aspect ratio of the grid system spacing at the center to outer flow region and (b) For cylindrical system, there is a singularity occurrence at the center or $r = 0$ and has to be taken care of with special approaches. These issues can be mitigated using Cartesian grid system.

2.6 Computational Domain

The computational domain used for the present study in non-dimensional form is ($r_o = 1$)*($H = 15$). Case studies for different values of heights such as with $H = 18$ and $H = 21$ were done in addition to $H = 15$, while the non-dimensional r_o was kept fixed at $r_o = 1$ in all the case studies. The inlet velocity profile is based on log law. The roughness parameters C_1 and z_o used in the current CFD model are $0.0924V_{ro}$ and $0.00004h_o$, respectively. For further detail of inlet velocities, one can refer to [7].

2.7 Mesh of the Computational Domain

The minimum grid spacing used was 0.005 units, and the aspect ratio maintained was ten meaning the maximum grid spacing used was $10*0.005 = 0.05$. In a separate study, it was found that having larger aspect ratio tends to disturb the continuity of the flow. The minimum grid spacing was then increased with a grid expansion factor of 1.1 in both the r- and z-direction until they reach a maximum grid spacing value. The program is run for a total non-dimensional time of 15 units. The mesh used for 2D analysis is of 37*317, 37*377 and 37*437 for 15.0, 18.0 and 21.0, respectively. Similarly, the mesh used in 3D study is of 55*55*160 for single height study of 15.0.

3 Results

3.1 Study Using Axisymmetric Flow

3.1.1 Touchdown Swirl Ratio (S) for a Total Chamber Height of $15h_o$

On increasing S from 0.29 to 0.35, the downdraft was seen to be progressively moving downwards, thus narrowing the gap from the ground than earlier case but still some upward rising velocity vector components were observed in the contour plot indicating that the touchdown condition had not been still reached at. On further increasing the S value from $S = 0.35$ to $S = 0.45$, finally the touchdown condition was observed to occur for $H = 15$. Some further simulations were run with higher S (0.50 and 0.60) beyond touchdown to observe the nature of flow structure beyond touchdown, and it was found that the width of the downdraft increased after increasing the swirl ratio beyond touchdown condition as shown in Fig. 3c.

(a) (b) (c)
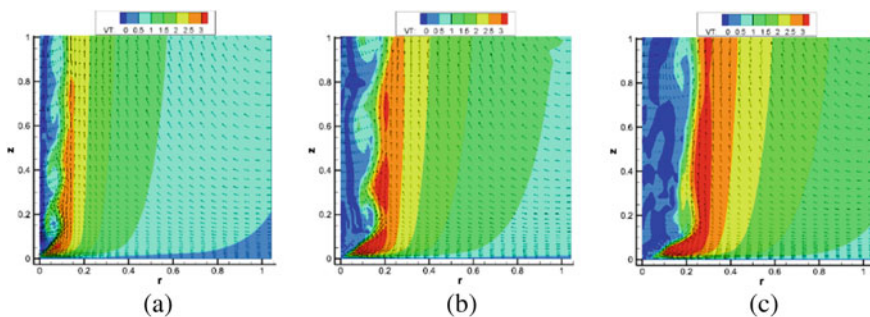
Fig. 3 Contour and velocity vector plot for V_θ at 15. **a** $S = 0.29$—before TD, **b** $S = 0.45$—TD, **c** $S = 0.60$—after TD (where TD is abbreviated for touchdown)

3.1.2 Influence of Chamber Height on Touchdown S

The corresponding S value for touchdown at $H = 15.0$, 18.0 and 21.0 was found to be 0.45, 0.43 and 0.41, respectively. From this, it can be observed that when H increases, the corresponding touchdown S value decreases. Overall, the amount of decrease in S is very low compared to the increase in H. This observation, in a way, can now be linked to [2] in which they used $16h_o$ as the overall height saying that at least up to $16h_o$, the flow structure was found to be independent of the chamber height for their study. In the present study also, the change has been found to be marginally low or negligible.

3.1.3 Comparison of Pressure Profile with Tang et al. Model

From Fig. 4, it can be seen that the magnitude of pressure increases throughout in the radial direction with increase in S values for $H = 15$. This pressure profile has some features similar to the pressure profile obtained by [15] and at the same time some contrasting features as well. It is observed, in pressure profile from [15], the magnitude of pressure first increases with increasing swirl ratio values, and after touchdown, it decreases to gain a relatively flat shape. But in the present study, it was observed that the pressure increased with increase in swirl ratio, but even after the touchdown, the pressure was found increasing. Furthermore, the curve gets somewhat flatter around the tornado core after touchdown, but the degree of flatness is very less as compared to the one reported in [15]. Another contrasting feature is the value of S reported for touchdown. In the present model, touchdown is reported at $S = 0.45$, whereas in [15], touchdown was reported for $S = 0.22$. To recapitulate, the pressure gradient around the tornado core seems to be relieved after touchdown in

Fig. 4 Radial ground pressure profile for different S
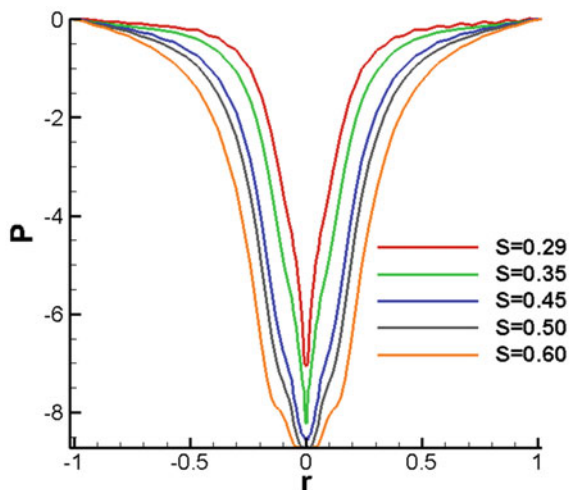
[15], whereas in the present model, the pressure gradient does not seem to be relieved that easy. It is suspected that the difference of domain feature may have attributed to this difference.

3.1.4 Extrapolation of Chamber Height for Experimental Touchdown at S = 0.22

TTU experimental model reported touchdown at $S = 0.22$ as per [15]. An attempt was then made to see, using a simplified numerical model, the value of total height required for touchdown. In that regard, an attempt was made to fit the available data into an equation. Considering the ordered pairs (H, S) with values (15.0, 0.45) and (18.0, 0.43), a linear equation was obtained from two-point form:

$$H = 150 * (0.55 - S) \tag{5}$$

Then, a check on the fitted equation was done by substituting the ordered pair (21.0, 0.41), and the ordered pair satisfied the equation. Thus, a first degree relationship between H and S was found to be valid at least for the available dataset. Hence, extrapolation of chamber height that may be required for the tornado touchdown at $S = 0.22$ was done using the type of domain used in this study, and using (5), the total height was obtained as $H = 49.5$. A rigorous statistical analysis (using regression and correlation) should have been done to ascertain the relationship between the parameters, but unavailability of adequate sample points for analysis and due to time constraints, it could not be done at this time. But, it is to be noted that when the height of computational domain is increased, the computational time increases by many folds and makes the process computationally very intensive. Thus, the idea of increasing the chamber height alone to reach the touchdown condition may not be a viable option.

3.2 Study Using 3D Flow

3.2.1 Necessity for 3D Analysis Followed by 3D Analysis

From an engineering standpoint, it a common practice to link these vortex flow field studies to their interaction with structures such as buildings. But a 2D analysis fails to fulfill the requirements to be considered to study the complex fluid-structure interaction of tornado vortex with structures/buildings. In addition to it, a close observation of the three-dimensional vortex flow field from [2] revealed that the complicated flow is carried up through a twisting three-dimensional motion (comprising of simultaneous rotation and translation acting upon the fluid mass). Similarly, the cumulative effect of all the three components of velocity vector field cannot be fully visualized in 2D analysis, and thus, it was felt necessary to study the complex twisting

motion through three-dimensional modeling/analysis using CFD. And some work has been done in that direction, and the observations and findings are delineated in the following sections.

The pressure iso-surface of the 3D tornado vortex flow field is shown in Fig. 5. For the 3D model, a cylindrical domain is considered with radius of 1.0 unit and a

Fig. 5 Pressure field iso-surface (3D)
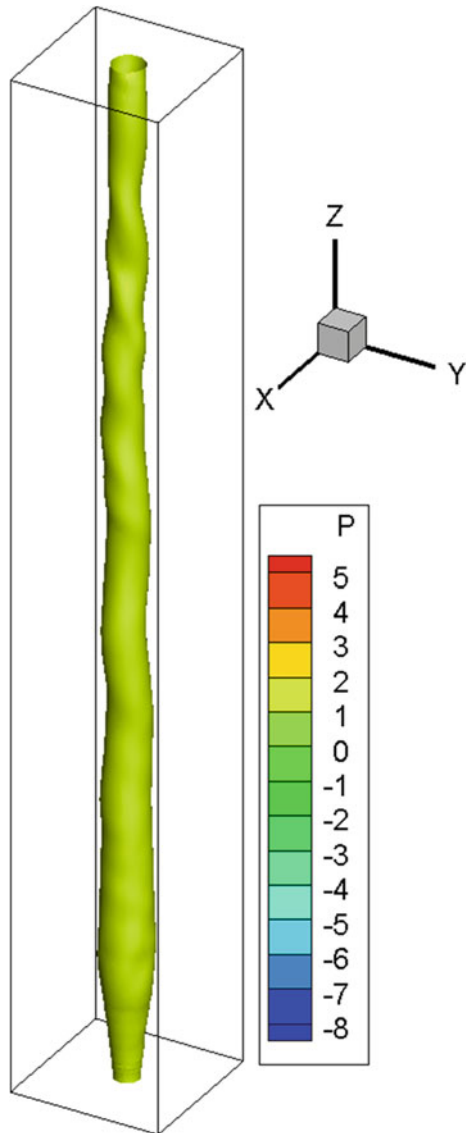
Fig. 6 Tornado vortex with stream-traces
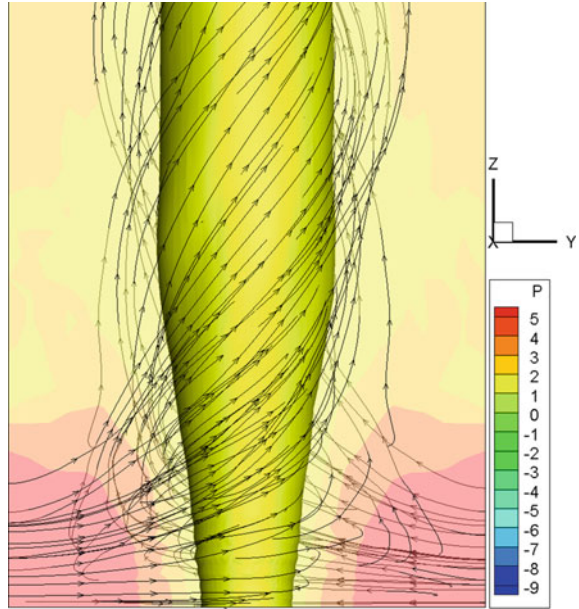
total chamber height of 15.0 (similar to 2D study). The helical winding of stream-traces around the pressure iso-surface in Fig. 6 clearly shows the three-dimensional simultaneous rotatory and translatory motion of tornado vortex.

3.2.2 Effect of Varying S on Touchdown with $H = 15.0$ in 3D

In the 3D study, swirl ratio values were varied from $S = 0.40$ to 0.45 and 0.50. The touchdown condition was again reported at $S = 0.45$ which is consistent with previous 2D study. In Fig. 7a, the downdraft component can be seen, but the small vectors
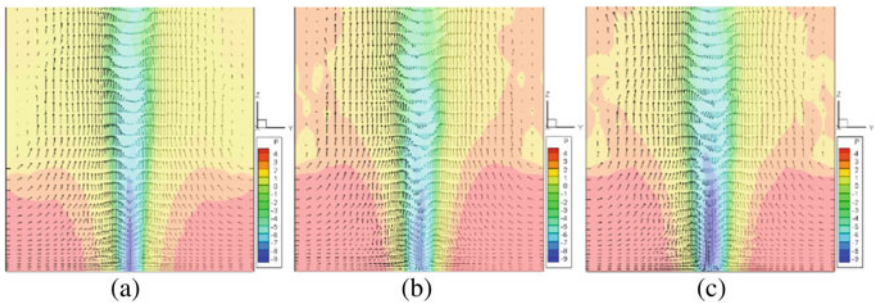
Fig. 7 Contour plots for pressure field at $H = 15.0$. **a** $S = 0.40$—before TD, **b** $S = 0.45$—at TD, **c** $S = 0.50$—after TD

indicate that the strength of velocity vector field (in downward direction) is very less, and due to the same reason, the velocity vectors could not produce a touchdown situation, but with the increase in S values, their strength has gone increasing from $S = 0.45$ to $S = 0.50$.

Based on this observation, it can be said that the 2D study using axisymmetric flow also provides a reasonable estimate for touchdown swirl ratio value. The downdraft core also can be seen widening with the increase in S values, and it is distinctly visible after touchdown in Fig. 7c. Besides, the downward pointing velocity vectors have become bulky after successive increase in S values from Fig. 7 indicating that the downdraft component of double-celled vortex system gets stronger with successive increase in S values. Based on the results obtained and observations made above, the next step would be to study the interaction of 3D tornado vortex field with a low-rise building, which would not have been possible with a 2D axisymmetric flow study.

3.2.3 Pressure Profile with Varying Swirl Ratio (S) at Fixed Height of H = 15.0

Figure 8a shows the section line AB passing through the center of tornado vortex core. This section line AB is also the line along which data have been extracted to obtain the radial pressure profile plot as shown in Fig. 8b. It was observed that the blue core (symbolic of tornado vortex core) observed in Fig. 8a shifted its position slightly with varying S values. So, the section line AB was shifted accordingly so that the geometric center of core would fall on the section line AB.

The shifting of tornado core has been described in the literature by a term called vortex wandering as reported in [2, 8, 9]. Due to this phenomenon, measuring pressure in experimental simulator with fixed probes or observing the data points at a fixed coordinate in numerical simulator could lead to misleading results as suggested in [9]. Care was taken to eliminate any such possible error by shifting the section line as necessary.
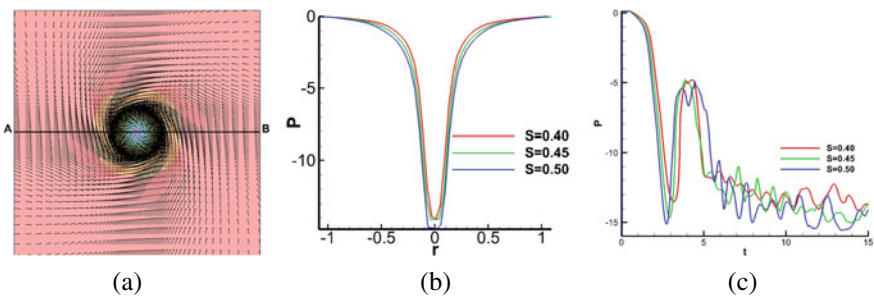
Fig. 8 **a** Section plane AB through diametric axis of vortex core, **b** pressure profile with variable S (3D study), **c** pressure versus time for different S

The pressure profile in Fig. 8b depicts the radial pressure distribution from 3D analysis which is in similitude with 2D study again as the pressure values are increasing with increasing S values and continuing even beyond touchdown condition.

Pressure Fluctuation Over Time

In Fig. 8c, the pressure values are recorded at the geometric center of tornado vortex chamber over time, which is run for a total time of 15 units. The time-variant nature of pressure is clearly visible in the plot. As the simulation time approaches final value of 15 units, the flow seems to be approaching near to a steady condition, and the continuous damping of pressure oscillation wave is being an indication for that. The amplitude of oscillation seems to be rising with increasing S indicating that the turbulence effect gets enhanced with introduction of larger flow helicity.

4   Conclusion

It can be concluded that the 2D axisymmetric analysis also provides reasonable results for preliminary investigation. Increasing swirl ratio values makes the downdraft component stronger before touchdown, and after touchdown, the vortex core width tends to get larger. Increasing the overall chamber height has a diminishing effect on touchdown S but at a slow rate. This observation contradicts the assumption of flow structure and critical touchdown swirl ratio being independent of height of tornado vortex chamber ($16h_{o}$). The extrapolated chamber height that may be required to obtain touchdown condition at $S = 0.22$ was obtained as $H = 49.5$. With such large heights, it was concluded that the computation would be immensely intensive and potentially infeasible. The time-variant nature of pressure fluctuation at the tornado chamber's geometric center indicates the time-dependent and unsteady nature of flow, but a progressive damping of pressure wave indicates that longer simulation time units could lead to steady state condition.

References

1. Barhaghi DG, Davidson L, Karlsson R (2006) Large-eddy simulation of natural convection boundary layer on a vertical cylinder. Int J Heat Fluid Flow 27:811–820
2. Gairola A, Bitsuamlak G (2019) Numerical tornado modeling for common interpretation of experimental simulators. J Wind Eng Ind Aerodyn 186:32–48

3. Gillmeier S, Sterling M, Hemida H (2017) A parametric study of the effect of a tornado generator's geometric design on the flow field. In: European African conference for wind engineering EACWE 2017, Liege, Belgium
4. Haan FL, Sarkar PP, Gallus WA (2008) Design, construction and performance of a large tornado simulator for wind engineering applications. Eng Struct 30:1146–1159
5. Hangan H (2014) The wind engineering energy and environment (WindEEE) dome at Western University, vol 39. Wind Engineers, JAWE, Canada
6. Hirt CW, Nichols BD, Romero NC (1975) SOLA—a numerical solution algorithm for transient fluid flows. Los Alamos Scientific Laboratory report LA-5852
7. Kashefizadeh MH, Verma S, Selvam RP (2019) Computer modelling of close-to-ground tornado wind-fields for different tornado widths. J Wind Eng Ind Aerodyn 191:32–40
8. Refan M, Hangan H (2016) Characterization of tornado-like flow fields in a new model scale wind testing chamber. J Wind Eng Ind Aerodyn 151:107–121
9. Refan M, Hangan H (2018) Near surface experimental exploration of tornado vortices. J Wind Eng Ind Aerodyn 175C
10. Selvam RP (1997) Computation of pressures on Texas tech building using large eddy simulation. J Wind Eng Ind Aerodyn 67, 68:647–657
11. Selvam RP, Millet P (2003) Computer modeling of tornado forces on buildings. Wind Struct 6:209–220
12. Selvam RP, Millet P (2005) Large eddy simulation of the tornado-structure interaction to determine structural loadings. Wind Struct 8:49–60
13. Selvam RP (2017) CFD as a tool for assessing wind loading. Bridge Struct Eng 47:1–8
14. Stein LR, Harlow FH (1974) Numerical solution of the flow structure in tornado-like vortices. Los Alamos Scientific Laboratory report LA 5713-MS
15. Tang Z, Feng C, Wu L et al (2018) Characteristics of tornado-like vortices simulated in a large scale ward type simulator. Bound-Layer Meteorol 166:327–350

Numerical Investigation of Blood Flow in Idealized Abdominal Aorta with Renal Bifurcation Using Fluid–Structure Interaction

S. M. Abdul Khader, B. Raghuvir Pai, D. Srikanth Rao, and K. Prakashini

Abstract Numerical simulations investigating the mechanics of blood flow through elastic arteries have demonstrated the significance of haemodynamics study in the cardiovascular flows. The present study investigates the flow behavior in an idealistic abdominal aorta with renal bifurcation obtained from the computed tomography (CT) image data. Geometric model is generated using ANSYS design modeler and numerical analysis is investigated using FSI technique in ANSYS-17. The fluid domain representing the blood flow is Newtonian, incompressible, and homogenous, while the solid domain representing the arterial wall is linearly elastic. The time varying two-way interacting sequentially coupled field simulation is carried out using FSI solver. The present study investigates the haemodynamic parameters to understand the influence of flow changes at the renal bifurcation region. The flow behavior is compared at rest and exercise conditions throughout pulsatile flow and the considerable changes are observed through the results obtained. This fundamental study shall be useful to understand the flow behavior in patient-specific cases.

Keywords Renal artery · Abdominal aorta · ANSYS FSI · Exercise and resting condition

S. M. Abdul Khader (✉) · B. Raghuvir Pai
Department of Mechanical and Manufacturing Engineering, Manipal Institute of Technology, Manipal Academy of Higher Education, Manipal 576104, India
e-mail: smak.quadri@manipal.edu

B. Raghuvir Pai
e-mail: raghuvir.pai@manipal.edu

D. Srikanth Rao · K. Prakashini
Department of Radiodiagnosis, Kasturba Hospital, Manipal Academy of Higher Education, Manipal 576104, Karnataka, India
e-mail: ds.rao@manipal.edu

K. Prakashini
e-mail: prakashini.k@manipal.edu

Nomenclature

ρ Density
T Stress tensor
v Velocity vector
v_{b} Grid velocity
P Pressure
b_{i} Body force at time, t
M Structural mass matrix
C Structural damping matrix
K Structural stiffness matrix
$\ddot{U}$ Acceleration
$\dot{U}$ Velocity
U Displacement vector
F^{a} Applied load vector

1 Introduction

Computational modelling and simulation have been extensively used to investigate the haemodynamics in cardiovascular diseases [1]. The critical anatomical regions such as arterial bifurcation/branching or curvature are more prone to growth of atherosclerosis due to flow recirculation [2]. Most of clinical imaging modalities such as ultrasound doppler imaging, magnetic resonance imaging, and computed tomography have been combined with the computational methods such as fluid–structure interaction (FSI) [3, 4]. These studies have enhanced the understanding of haemodynamics in diseased vessels to understand the mechanisms of stenosis, development, and progression in patients [5]. The behavior of blood flow through normal artery without any stenosis is significantly different when compared to the stenosed artery which demonstrates higher stress levels and high resistance to the blood flow. These investigations on physiological blood flow simulation through the stenosis have significantly influenced the diagnosis and treatment of the vascular diseases [6]. There are several previous investigations of pulsatile fluid flow focusing on the carotid artery bifurcation and end-to-side anastomosis; however, numerical studies of blood flow into abdominal aorta are limited [7]. Anatomically, blood flow in abdominal aorta is important as it is one of the largest vessels and further traversing through the abdomen and branching into two lower limbs. Hence, significant portion of the blood from the thoracic aorta flows into the renal arteries and about one-third of the blood flows into the legs under the resting condition [8]. However, stenosis in renal branch is also crucial as it is linked with secondary hypertension. Renal stenosis has also demonstrated that the pressure and velocity increase while the mass flow rate decreases with the severity of the stenosis [9, 10]. The angulation effects of stenosed renal artery based on the velocity of blood and renal mass flow

were also investigated [11], which related the cause of hypertension. Similar study based on the effect of renal artery stenosis on the arterial wall deformation and flow velocity and WSS based on patient-specific data was conducted in [3].

Regular exercise has numerous overall health benefits on human body such as improved cardiorespiratory fitness levels, increased cardiovascular functional capacity, and low cardiovascular mortality rates [12]. Even though, there are numerous studies which support the importance of exercise. However, the effect of exercise and mechanism involved in overall improvement of cardiovascular health and the amount and period of exercise required to maximize the advantage require further detailed studies [13]. Haemodynamic investigations are carried out during rest and exercise conditions especially in abdominal aorta model for different flow conditions. Regions with flow vortex formation and low intensity wall shear stress were observed along the posterior wall of the abdominal aorta bifurcating into renal artery in resting conditions and disappeared during exercise flow conditions [14]. Flow behavior in light and moderate exercise conditions was also compared with that of rest conditions to highlight the importance of exercise period on changes in the flow velocity field and wall shear stress. Flow behavior was also studied in the idealistic abdominal aorta with peripheral branches to compare the regions having low WSS and flow recirculation [15]. Hence, from previous available studies, it is hypothesized that, exercise shall help in retardation of cardiovascular disease progression by reducing WSS and flow recirculation. However, rest and exercise conditions with more emphasis on renal branches have been limited. In the present study, fundamental investigation is carried out to study the haemodynamics in idealistic abdominal aorta with renal artery branching under resting and exercise conditions.

2 Methodology

Blood flow in abdominal aorta with renal bifurcation as observed from several previous studies satisfies incompressible, Newtonian, and laminar behavior. Computationally these assumptions are governed by the Navier–Stokes equation adopted in incompressible flows [16]. During two-way coupled field FSI simulation, basic momentum and continuity equations have to be modified to satisfy the FSI behavior as shown in Eq. 1.

$$\frac{\partial}{\partial t} \int_{\Omega} \rho \partial \Omega + \int_{S} \rho (v - v_b) \cdot n \partial S = \int_{S} (\tau_{ij} - P i_i) \cdot n \cdot \partial S = \int_{\Omega} b_i \partial \Omega \quad (1)$$

In the present study, structural equations adopted during transient two-way FSI solution is described by Eq. 2. Abdominal aortic renal bifurcation artery wall is considered to behave isotropic, linearly elastic, and homogeneous [2, 16, 17].

$$[M]\{\ddot{U}\} + [C]\{\dot{U}\} + [K]\{U\} = \{F^{\mathrm{a}}\} \quad (2)$$

FSI simulation is carried out using FSI solver in ANSYS 17.0 implementing two-way sequentially coupled field technique as shown in Fig. 1. In this solver, fluid and solid domains are solved separately using ANSYS Fluent and ANSYS Mechanical, respectively. Initial fluid domain results in form of pressure load are transferred to the solid domain through the FSI interface at wall and followed by the solution of structural domain [17].

In the present study, geometry of idealistic abdominal aorta with the renal branches is constructed from a single mid-slice of CT image and the configuration of the model is shown in Fig. 2. Subject specific CT angio data is obtained from healthy individual from Kasturba Hospital, MAHE, Manipal, India. 3D modeling based on CT data is generated in ANSYS Design Modeler. Figure 3 shows the 3D model of normal idealistic abdominal model with renal branches after geometry cleanup and surface refining. Abdominal artery is highlighted by region 1 and 2, region-3 by left renal artery, and region-4 by right renal artery. Fluid region representing artery lumen

Fig. 1 FSI algorithm
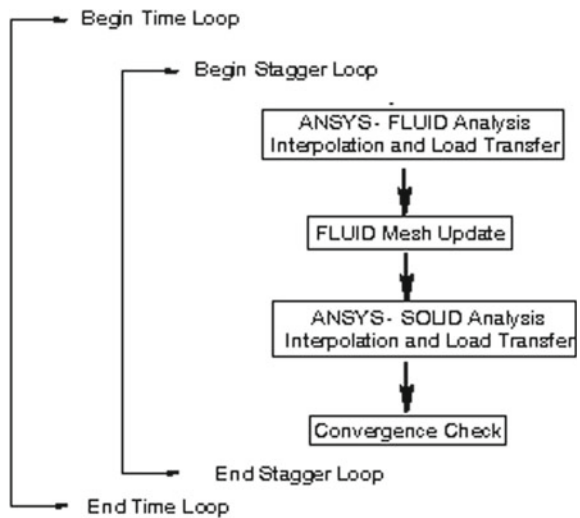
Fig. 2 CT slice geometry details
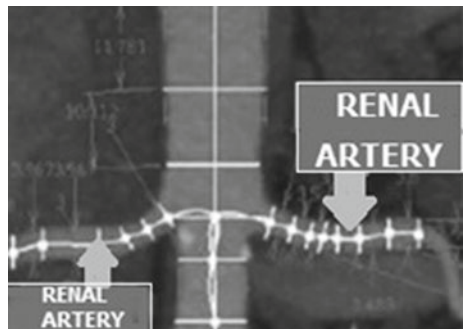
Fig. 3 3D FSI abdominal aorta model
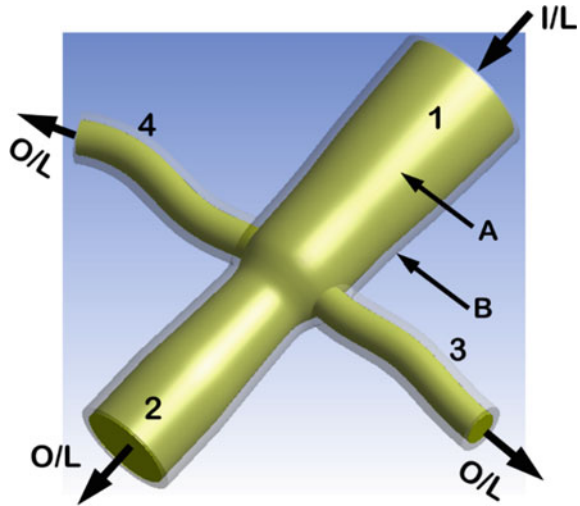
and solid region representing arterial wall is highlighted by A and B, respectively. I\L and O\L represent inlet and outlet, respectively. 3D fluid and solid models of abdominal aorta with renal branches are meshed with 85,000 and 55,000 hexahedral elements. Grid independency study is carried out under steady-state condition at the root of pulsatile flow velocity. Flow variables such as velocity, WSS, and pressure are monitored by maintaining the grid quality. Pulsatile velocity and pressure wave varying over a pulse cycle are applied as fluid flow boundary conditions at inlet and outlet of the fluid model, respectively.

Both inlet and outlet nodes of solid domain are fixed in all the directions, while remaining nodes are permitted for displacement in all the directions. Clinically observed pulse pressure in descending abdominal aorta is in the range of 110–120 mm Hg during systolic phase while 70–80 mm Hg in diastolic phase [18]. However, to establish the resistance due to peripheral arteries in the downstream end, time-varying pulsatile pressure is applied at the outlet as shown in Fig. 4 [10].

Pulsatile time varying velocity profile as shown in Fig. 5 is applied at the inlet. Two different inlet pulsatile velocities are carried out separately under rest and exercise conditions. Analysis under the rest condition is performed with pulse cycle of 0.9 s. In exercise condition, pulse cycle will be 0.5 s and the flow is observed with twofold increase as observed in Fig. 5 [8, 14]. Capturing of accurate flow behavior is achieved by discretizing the individual pulse waves, during rest and exercise conditions, and normal and high blood pressure into 180 time steps. The convergence criteria of fluid flow are set at 10^{-5} and across the fluid-surface interface is fixed at 10^{-4}, respectively. Blood flow and arterial wall properties are observed from [14, 18]. These numerical simulation results shall help in providing necessary data in quantifying the haemodynamic changes to understand the patient-specific cases.
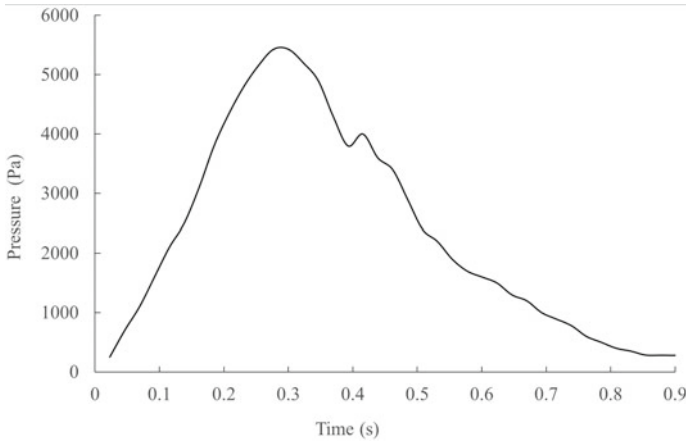
Fig. 4 Pulsatile pressure applied at outlet
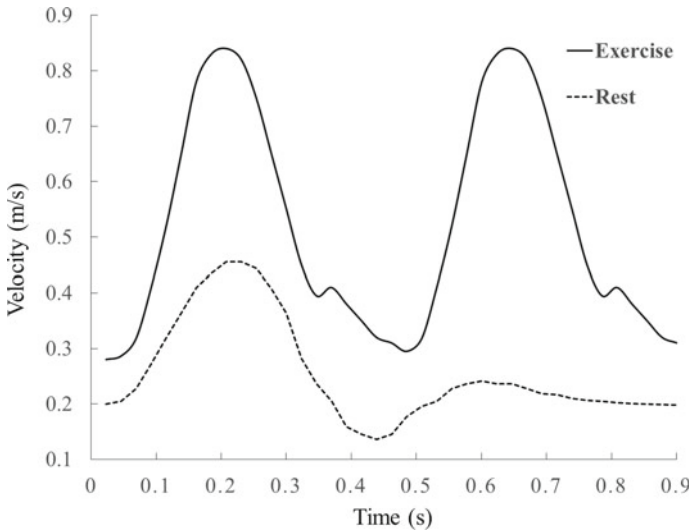
Fig. 5 Pulsatile velocity applied at inlet

3 Results and Discussion

The haemodynamics parameters like flow velocity, WSS, total pressure, elastic wall deformation of artery, and von-Mises stress from FSI simulation are studied from last pulse cycle at crucial time period of pulse cycle such as early systole, peak systole, early diastole, and late diastole.

Velocity: It is observed that velocity profiles are highly different throughout the cardiac cycle. Figure 6 demonstrates the flow velocity profile in abdominal aorta and renal branches. It describes the flow separation such that the flow divides into two streams with maximum velocity at the distal wall of the renal bifurcation and slower moving fluid on the proximal wall [6]. Flow separation is found to be more visible during peak systole and deceleration; however, later it drops at the diastole phase. These changes in blood flow patterns have been linked to the growth of atherosclerosis. Flow separation is found to be intense especially closer to the proximal wall in both the renal branches [11].

Flow during peak systole in renal branches is also characterized by the higher velocity closer to the distal walls and the low flow velocity adjacent to the proximal wall. However, the flow fluctuation is found to be more intense during exercise when compared with rest condition with high flow velocity close to distal walls in both the renal branches as clearly observed from Fig. 6 [13, 15]. However, velocity profiles during rest and exercise are similar without any significant changes in both the NBP and HBP cases.

Wall shear stress (WSS): Results shown in Fig. 7 depicts that WSS in the abdominal aorta wall tends to increase along its length in upstream side and especially at
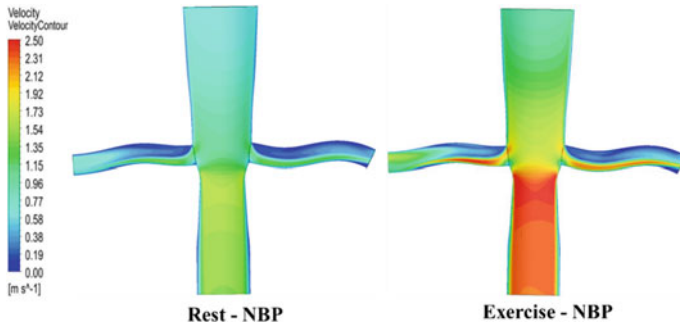
Fig. 6 Comparison of velocity contours in rest and exercise
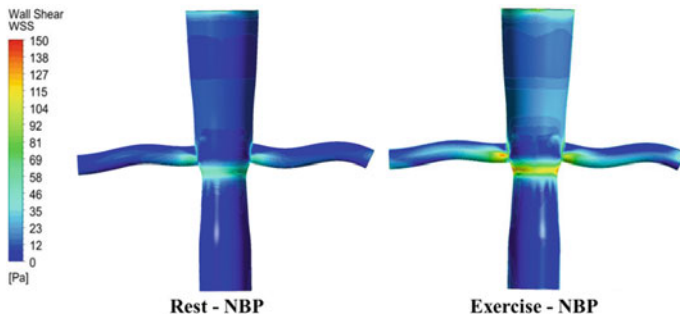
Fig. 7 Comparison of WSS contours in rest and exercise
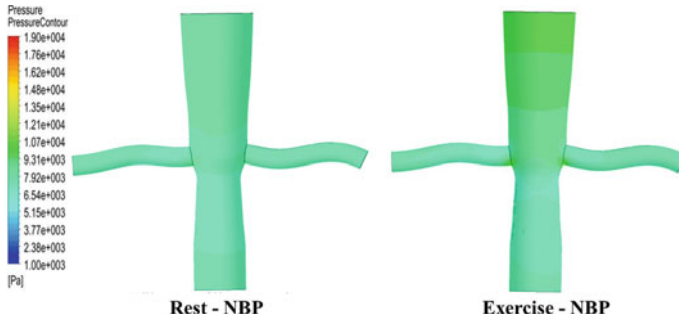
Fig. 8 Comparison of pressure contours in rest and exercise

the branching of renal artery [6]. At the renal walls, the WSS distribution is low towards the proximal wall and the high WSS along the distal renal wall [14]. The appearance of this low WSS in the proximal wall coincides with the presence of the recirculation. Along the distal wall, the WSS will be maximum in the entry of the bifurcation and tends to decrease along the distance. It is also observed that the distal wall in neighborhood of bifurcation experience high WSS. However, the proximal wall closer to the flow separation region is observed to have relatively low WSS as clearly in Fig. 7. Maximum WSS observed at renal bifurcation in distal side is relatively more intense during exercise in contrast to rest condition. WSS distribution in distal side extends to larger length in exercise conditions when compared to rest condition which is influenced by high flow velocity.

Pressure: Figure 8 demonstrates the pressure distribution during peak systole in rest and exercise conditions. Maximum pressure is found to be at the renal bifurcation tip in both branches on distal side during entire cardiac cycle. Upstream abdominal aorta also revealed higher pressure distribution in comparison with downstream side. Exercise condition had higher pressure build up in upstream side of abdominal aorta and at the renal bifurcation tip unlike rest condition as seen from Fig. 8.

Arterial wall deformation: Total arterial wall deformation behavior is compared in Fig. 9 during peak systole for rest and exercise conditions. The maximum deformation
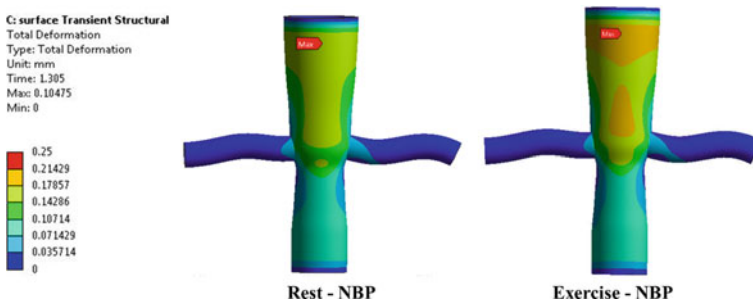
Fig. 9 Comparison of arterial wall deformation in rest and exercise
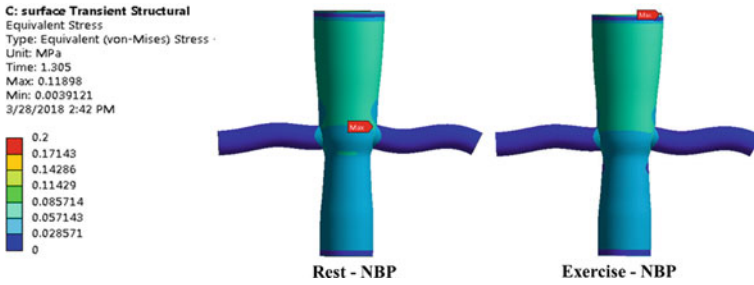
Fig. 10 Comparison of arterial von-Mises stress in rest and exercise

is found to be at the peak systole characterized by the accelerating flow in contrast to the diastole. It is also observed that upstream side of abdominal aorta deform significantly unlike downstream side. Low deformation is noticed at entry region of renal artery bifurcation on distal wall side and quite low at proximal wall side which decreases along the distance in rest condition. Similar wall deformation behavior slightly extends to larger length during exercise condition. However, the exercise condition has higher wall deformation especially in upstream side of abdominal aorta before branching into renal artery as compared to rest condition.

von-Mises stress: Figure 10 compares the von-Mises stress distribution during peak systole during rest and exercise conditions. In cardiac pulse cycle, stress distribution is found to be more visible during peak systole and flow deceleration; however, during late diastole, observed stress distribution reduces significantly. Upstream region of abdominal aorta is found have slightly larger stress distribution unlike downstream side. Stress distribution is found to be negligible at the renal artery bifurcation in both the branches during rest condition and similar observation during exercise condition.

4 Conclusion

Numerical simulation of abdominal aorta branching into renal artery using two-way FSI under rest and exercise conditions is carried out in the present study. Flow recirculation is observed in proximal side during rest which reduces significantly during exercise condition. Considerable changes in WSS at renal bifurcation are clearly observed during rest and exercise conditions. Arterial wall deformation and von-Mises stress distribution are found be relatively low at the renal artery bifurcation during rest condition and similar observation during exercise condition. The present study demonstrates the fundamental aspects of haemodynamics in idealized abdominal aorta with renal branches and can be further extended to patient-specific cases.

References

1. Charles AT, Thomas JRH, Christopher KZ (1998) Finite element modeling of three-dimensional pulsatile flow in the abdominal aorta: relevance to atherosclerosis. Ann Biomed Eng 26:975–987
2. Fung Y (1984) Biodynamics-circulation. Springer, New York Inc
3. George CK, Eugene DS, Dimitris K, George CN (2008) Computational representation and hemodynamic characterization of in vivo acquired severe stenotic renal artery geometries using turbulence modeling. Med Eng Phys 30:647–660
4. Marshall I, Zhao S, Peter H, Yun XX (2004) MRI and CFD studies of pulsatile flow in healthy and stenosed carotid bifurcation models. J Biomech 37:679–687
5. Young GS, Andrea S, Charles AT (2011) Hemodynamic changes quantified in abdominal aortic aneurysms with increasing exercise intensity using MR exercise imaging and image-based computational fluid dynamics. Ann Biomed Eng 39(8):2186–2202
6. Liang F, Yamaguchi R, Hao L (2006) Fluid dynamics in normal and stenosed human renal arteries: an experimental and computational study. J Biomech Sci Eng 1(1):171–182
7. Albert S, Robert SB, Jenn SR (2014) Influence of the renal artery ostium flow diverter on hemodynamics and atherogenesis. J Biomech 47(7):1594–1602
8. Tang TB, Cheng PC, Charles AT (2006) Abdominal aortic haemodynamic in young healthy adults at rest and during lower limb exercise: qualification using image-based computer modelling. Am J Heart Circ Physiol 291:H668–676
9. James EM, Chengpei X, Ku DN (1994) Fluid wall shear stress measurement in a model of human abdominal aorta: oscillatory behavior and relationship to atherosclerosis. Atherosclerosis 10:225–240
10. Zhang W, Yi Q, Mengsu Z (2014) Haemodynamic analysis of renal artery stenosis using computational fluid dynamics technology based on unenhanced steady-state free precession magnetic resonance angiography: preliminary results. Int J Cardiovasc Imaging 30:367–375
11. Mortazavinia Z, Arabi S, Mehdizadeh, AR (2014) Numerical investigation of angulation effects in stenosed renal arteries. J Biomed Phys Eng 4(1):1–8
12. Amirhossein A, Andrea SL, Shawn CS (2014) Effect of exercise on patient specific abdominal aortic aneurysm flow topology and mixing. Int J Numer Methods Biomed Eng 30(2):280–295
13. Andrea SL, Shawn CS, Alberto CF, Charles AT (2010) Quantification of hemodynamics in abdominal aortic aneurysms during rest and exercise using magnetic resonance imaging and computational fluid dynamics. Ann Biomed Eng 38(4):1288–1313
14. Charles AT, Thomas JRH, Christopher KZ (1999) Effect of exercise on hemodynamic conditions in the abdominal aorta. J Vasc Surg 29(6):1077–1089
15. Lee D, Chen JY (2002) Numerical simulation of steady flow fields in a model of abdominal aorta with its peripheral branches. J Biomech 35:1115–1122
16. Raghuvir P, Khader SMA, Anurag A, Ahmad KA, Zubair M, Rao VRK, Ganesh KS (2016) Fluid-structure interaction study of stenotic flow in subject specific carotid bifurcation—a case study. J Med Imaging Health Inf 6:1494–1499
17. ANSYS Release 17.0 Documentation (2016) ANSYS Company, Pittsburgh, PA
18. Khader SMA, Anurag A, Raghuvir P, Zubair M, Ahmed KA, Rao VRK (2013) Study of the influence of normal and high blood pressure on normal and stenosed carotid bifurcation using fluid-structure interaction. Appl Mech Mater 315:982–986

Simulation of MD Using OpenMP and OpenMP–SIMD

Naman Khurpia, Arunim Roy, Saransh Goyal, and J. Saira Banu

Abstract MD is used to understand the temperature and pressure dependencies of dynamical concept in liquids, solids, and liquid–solid interfaces. It is a computer simulation method to visualize the behavior of atoms and molecules. MD simulation techniques are also well defined for understanding surface phenomena, as they give a qualitative understanding of surface structure and dynamics of particles filled in a box. Our work uses MD methods to better comprehend surface pressure and calculation of time they take to interact with one another. We aim to use OpenMP and OpenMP + SIMD directives in our code to reduce time complexities. The OpenMP directive is applied to a loop to indicate such that multiple iterations of the loop can be executed at the same time by using SIMD instructs. Our studies have indicated that using SIMD directives in OpenMP tend to yield faster speedups. According to our data for the given algorithm for a maximum of 800 particles, a speedup of 1.27 was achieved for OpenMP + SIMD against OpenMP alone. We will implement SIMD parallelization to Verlet's algorithm used in MD calculations, such as updation and computation of position, velocity and acceleration. We also intend to bring out the percentage of error in total energy calculated in our work to convey the accuracy of the methods.

Keywords MD · Surface disorder · Premelting · Velocity · Position · Acceleration · Verlet's algorithm

1 Introduction

Molecular dynamics (MD) has been used for presently to visualize the temperature, velocities, acceleration, and weight conditions of dynamical idea in fluids, solids, and fluid strong interfaces. MD recreation procedures are additionally all around coordinated for understanding surface wonders, as they give a subjective comprehension of surface structure and dynamics. They help us to understand the surface

N. Khurpia (✉) · A. Roy · S. Goyal · J. Saira Banu
School of Information Technology & Engineering, VIT University, Vellore, Tamil Nadu, India
e-mail: naman.khurpia2016@vitstudent.ac.in

phenomenon of many surface metals to a higher degree and take clue of its temperature and pressure dependencies which may in future allow us to make newer and better discoveries. MD is of extreme value in medical sciences, and Today MD simulations are effectively used to study macromolecular structures of particles to function relationships [1]. MD simulation is used in medicinal biology for iterative drug design through prediction of protein ligand locking. MD is also used in sampling methods to find conformational changes in proteins on specific time scales [2].

In MD, the most commonly used time integration algorithm is Verlet algorithm. The essential thought is to compose two-third-arrange Taylor extensions for the positions, one forward and one in reverse in time. Calling the speeds, the increasing speeds, and the third subordinates of velocity with respect to time. Thus, Verlet algorithm can be used to calculate the time integration of particles in a box and the pressure exerted by them on walls, position with respect to time can be calculated.

OpenMP is an application programming interface; it let user parallise the work by distributing the jobs to different cores of a CPU, and OpenMP supports multi-platform shared memory multiprocessing programming in C, C++, and FORTRAN. OpenMP 4.0 has some more features that let us to use SIMD directives. The versions that do so are OpenMP 4.0/4.5. Using this approach, an OpenMP loop can vary by different executable instructions concurrently using SIMD instructions, and that those iterations will also be executed in parallel by threads probably in a different group, among many other things. Our work emphasizes the use of OpenMP along with SIMD for MD simulations as they yield higher speedups according to our results. We have introduced its usage in Verlet's algorithm; they used to calculate status of molecule's position, acceleration and speed on basis of classical mechanic principles, with some constraints.

The rest of the paper is organized as follows: Section 2 provides the related work, Sect. 3 gives the background of MD, Sect. 4 proposes the parallel verlets algorithm using SIMD, Sect. 5 provides the results and discussion, Sect. 6 provides the conclusion, and Sect. 7 mentions the future work.

2   Related Work

A new method to find the [3] ground state of Si3 molecule configuration using MD, a spectral density function of Si2 molecule at high and low excitation levels, is used to obtain the result.

Verlet algorithm is also used to find the angular velocity of water in a self-consistent way using an iterator in a quaternion-based algorithm, and this method is for liquid water and is also used to evaluate stress tensor for a system of hard block; the result of velocity is calculated by use of Verlet algorithm [4].

Old methods using the static external magnetic fields into MD computer simulations deals in simulation of time-step t to be a small value as compared to Larmor's oscillation time taken, i.e., 2pi/omega. This way is used to generate the strongly magnetized system of charged particles [5].

A new method called RATTLE for integrating lot of different equations of motion in MD for molecular models with internal constraints is presented and the algorithm is similar to SHAKE; on observation, we came to know that this method is used for getting results of such calculations. RATTLE uses the MD to calculate the positions and velocities at the nest time from positions and velocities at the present time-step. Similarly, SHAKE deals directly in velocities and constant temperature and constant pressure of the molecules and the non-equilibrium MD methods that make use of rescaling the atomic velocities [6].

Also, seeing protein frameworks of cells in a tube, we regularly need to utilize less-detail representations to demonstrate the general engineering of the molecular complex rather than the immaterial data connected with nuclear detail. The subsequent request of extent decrease in particles yields a critical driving force in execution, permitting intelligent representation of substantially bigger molecular edifices. For this, we utilize marching cubes calculation [7].

Quantum mechanics (QM) calculations revealed an angiotensin-converting enzyme inhibitor QSAR [8]; the solution limits energies of apomorphine analogues were found similar to their lifestyle activities.

3 Molecular Dynamics

3.1 Properties of MD

3.1.1 Atoms Continuously Move in a Closed Space Therefore Their Collisions Can Never Stop

In an MD simulation, atoms are always in consistent motion. They will not be at a particular excited state forever. After giving a suitable amount of time to the simulation, it examples the Boltzmann distribution which tells us the probability of detecting a unique layout of atoms as a function of the potential energy in a lattice. Now, we do not simulate long enough results to reach all energetically suitable arrangements. We have many ways to explore the energy patterns (i.e., sample the Boltzmann distribution); certainly, different methods give different outcomes with newer approach [9].

3.1.2 Energy Conservation

The law of conservation of energy states that the total potential energy and kinetic energy should be conserved. In atomic layouts with lower potential energy, atoms move faster. In practical approach, total energy inclines to grow substantially with respect to time due to numerical errors (passing errors).

3.1.3　Water Is Important

On observation of the solvent (the molecules next to the molecules of higher quantity) leads to main resulting examples that are Water, salt ions (e.g., sodium atoms, chloride atoms), lipids of the cell membrane.

Two reasons why water is taken as a solvent into account—Plainly denote solvent molecules and High computational cost but more precise.

Usually accepts periodic boundary settings (a water molecule that drives off the left side of the simulation box will come back in the right side, like in PacMan). Water is an implicit solvent, so it does not dissolve itself rather it dissolves other matter.

3.1.4　Explicit Solvent

Water acts as an explicit solvent, and it dissipates other matter and keeps it properties to itself.

In our project, we take Sects. 3.1.1 and 3.1.2 into consideration as our hypothesis takes molecules in a box and in our calculations, we take the law of energy conservation as our base to solve the equations.

3.2　Verlet Algorithm

The MD algorithm substantially consists of many steps that are computed by finding the integral, which is further used to prove the equations of motion. The Verlet integration scheme tells us that the entire method can be followed up with three mandatory steps; each step involving the revising of molecule position and velocity with respect to time and their derivatives with each time-step.

The energy function is considered though a potential function $V(X)$ which is a harmonic function (dependent on sin values) that will gain a maximum value at $\pi/2$: [10]

$$v(x) = (\sin(\min(x, \pi/2))) ** 2 \tag{1}$$

The derivative of the potential energy function is:

$$dv(x) = 2.0 * (\sin(\min(x, \pi/2))) * \cos(\min(x, \pi/2)) \tag{2}$$

$$dv(x) = \sin(2.0 * \min(x, \pi/2)) \tag{3}$$

Update velocity, position, and acceleration by using Verlet algorithm

$$x(t + dt) = x(t) + v(t) + 0.5 * a(t) * dt * dt \tag{4}$$

$$v(t + dt) = v(t) + 0.5 * (a(t) + a(t + dt)) * dt \tag{5}$$

$$a(t + dt) = f(t)/m \tag{6}$$

3.3 OpenMP + SIMD

The basic functionality of OpenMP SIMD directives is that the SIMD construct can be applied to any loop showing that the result can be converted into a vectorized loop, which allows multiple iterations for the same for loop; thereby, many iterations are executed simultaneously through the same SIMD instructions, and each SIMD instruction is passed to the SIMD register which parallizes the code. Only loops meeting the following criteria are vectorized through the SIMD construct. For loop, parellization with SIMD construct is done by distributing the iterations of the loop across the available threads in the CPU, and the iterations are further concluded using SIMD construct.

All used loops in the code should be nested (the instructions should not contain any code or any OpenMP directive among any loops), The loop body should be compact block (an executable description, possibly compound, that has a single entry and single exit point at the top of loop and the bottom of the loop). The number of iteration the loop must follow before executing the OpenMP and SIMD directives must be known to the compiler that is in serial execution, the code should be well optimized. Functions can be vectorised in SIMD with declare SIMD construct only if it is a structured block.

4 Proposed Methodology

In MD, the time integration algorithm is Verlet algorithm. The idea is to give two-third-order Taylor expansions regarding the positions and velocity of the molecules. The basic steps of Verlet algorithm using OpenMP + SIMD is illustrated as:

Task 1—First, we take the positions of particles in consideration and the interatomic forces are near to negligible as the atoms are in ground state; for computing forces on each atom, the effect of faraway atoms is ignored and the neighbors are considered.

Task 2—Then, at every time-step, we compute forces and energies associated with the particles and the potential functions and displacement functions are integrated with respect to time to get the required Taylor form.

Task 3—The time calculations take place in serial and then in parallel for getting the improved/lesser time. In OpenMP + SIMD, all the for loops are parallelized and
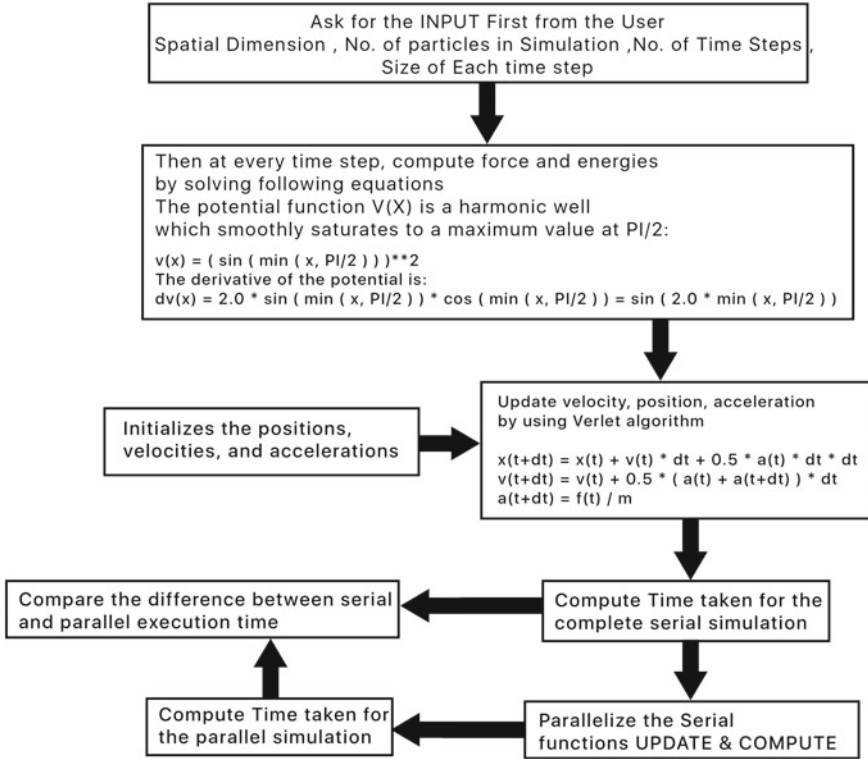
Fig. 1 Verlet algorithm with OpenMP + SIMD

given to different SIMD registers which divides the work into different threads and
hence improve the time taken (Fig. 1).

5 Results

We have executed our code using OpenMP and OpenMP along with SIMD directives.
The time for running the code was calculated for both and Table 1 was drawn. From
the table, we can see that the code for Verlet's algorithm [6] runs faster for OpenMP
used with SIMD directives rather than OpenMP alone. A graph has also been plotted
to show the variation of these two approaches (Figs. 2 and 3).

Table 1 Speedup data collected after comparison between Sequential OpenMP, OpenMP SIMD, and serial computation

Number of particles (Np)	Serial time (S)	OpenMP time	OpenMP + SIMD time	SpeedUp OpenMp serial	SpeedUp OpenMp + SIMD serial
400	415.5	285	196	1.45	2.11
500	496.3	315	272	1.575	1.82
600	743	579	409	1.283	1.81
700	832	698	549	1.191	1.51
800	1203	965	755	1.246	1.59
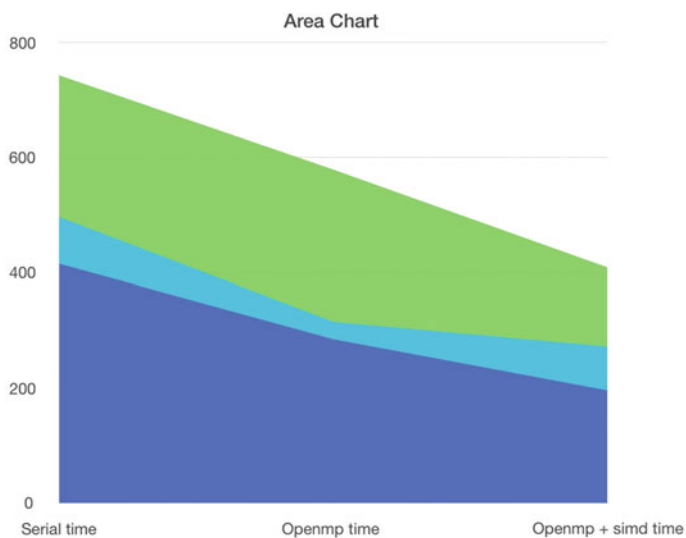
Fig. 2 Area chart for serial versus OpenMP versus OpenMP + SIMD

Fig. 3 Speedup of OpenMP and OpenMP + SIMD

6 Conclusion

MD is a noteworthy computational apparatus to reenact and fathom biochemical procedures at the nuclear level. In any case, exact reproduction of procedures, for example, protein collapsing needs countless iotas and time steps. This thus prompts gigantic runtime necessities. Consequently, searching for quick arrangements is of most astounding significance to explore. In this work, we present a parallel approach to deal with quicken MD recreations with economical item illustrations equipment. Our trial results demonstrate that the parallel calculation-based strategy permits speedups compared between OpenMP and OpenMP + SIMD. This acceleration can likewise be upgraded when we increment number of molecules and number of time steps. Experimental results show the parallelization with OpenMP + SIMD gives better speedup compared to OpenMP version of Verlets algorithm.

7 Future Work

We can incorporate graphics handling units (GPUs), initially created for translating constant impacts in PC recreations, now give unparalleled computational capacity to logical applications. We can build up a broadly useful MD code that runs totally on a solitary GPU. Molecular motion visualization would give us a better viewpoint of the dynamics involved and also help us to understand if OpenMP can be used in such visual applications along with SIMD directives.

References

1. Hospital A, Goñi JR, Orozco M, Gelpí JL (2015) Molecular dynamics simulations: advances and applications. Adv Appl Bioinf Chem AABC 8:37
2. Pierce LC, Salomon-Ferrer R, de Augusto F, Oliveira C, McCammon JA, Walker RC (2012) Routine access to millisecond time scale events with accelerated molecular dynamics. J Chem Theory Comput 8(9):2997–3002
3. Sankey OF, Niklewski DJ (1989) Ab initio multicenter tight-binding model for molecular-dynamics simulations and other applications in covalent systems. Phys Rev B 40(6):3979
4. Martys NS, Mountain RD (1999) Velocity Verlet algorithm for dissipative-particle-dynamics-based models of suspensions. Phys Rev E 59(3):3733
5. Spreiter Q, Walter M (1999) Classical molecular dynamics simulation with the velocity Verlet algorithm at strong external magnetic field. J Comput Phys 152:102–119
6. Andersen HC (1983) Rattle: a "velocity" version of the shake algorithm for molecular dynamics calculations. J Comput Phys 52(1):24–34
7. Krone M, Stone JE, Ertl T, Schulten K (2012) Fast visualization of Gaussian density surfaces for molecular dynamics and particle system trajectories. EuroVis-Short Papers 2012:67–71
8. Saunders MR, Tute MS, Webb GA (1987) A theoretical study of angiotensin-converting enzyme inhibitors. J Comput Aided Mol Des 1(2):133–142
9. www.web.stanford.edu
10. http://students.iitk.ac.in/projects/wiki/lib/exe/fetch.php?media=2014as:verlet.pdf

11. Walters JP, Balu V, Chaudhary V, Kofke D, Schultz A (2008) Accelerating molecular dynamics simulations with GPUs. In: ISCA PDCCS, pp 44–49
12. Brown WM, Wang P, Plimpton SJ, Tharrington AN (2011) Implementing molecular dynamics on hybrid high performance computers–short range forces. Comput Phys Commun 182(4):898–911
13. https://www.ibm.com/support/knowledgecenter/en/SSXVZZ_16.1.0/com.ibm.xlcpp161.lelinux.doc/compiler_ref/prag_omp_simd.html
14. Salomon-Ferrer R, Götz AW, Poole D, Le Grand S, Walker RC (2013) Routine microsecond molecular dynamics simulations with AMBER on GPUs. Explicit solvent particle mesh Ewald. J Chem Theory Comput 9(9):3878–3888
15. Rahman TS (2002) Molecular-dynamics simulation of surface phenomena. Charact Mater, 1–12
16. https://www.quora.com/Why-is-Molecular-Dynamics-Simulation-important-in-medicinal-biology
17. Vigonski S, Djurabekova F, Veske M, Aabloo A, Zadin V (2015) Molecular dynamics simulations of near-surface Fe precipitates in Cu under high electric fields. Modell Simul Mater Sci Eng 23(2):025009
18. www.eng.buffalo.edu/~kofke/ce530/Text/Basic_MD.doc
19. Haile JM (1992) Molecular dynamics simulation: elementary methods, vol 1. Wiley, New York

Design Fabrication and Testing of a Double-Pass Solar Air Heater

I. V. Kumar ⓘ **and M. Mohan Jagadeesh Kumar** ⓘ

Abstract In this paper, experimental investigations on a double-pass packed bed solar air heater are presented. Improvement in thermal performance of the air heater with mild steel chips as the packed bed material is found at different mass flow rates of air. Experiments are carried out at different mass flow rates of air in a range of 0.036–0.0625 kg/s. The maximum air temperature at SAH outlet with and without packed bed is 64 °C and 59 °C, respectively, at a mass flow rate of 0.047 kg/s. The thermal efficiency of double-pass SAH is found to be improved by 20.4% over conventional SAH without a packed bed.

Keywords Solar energy · Solar radiation · Solar collector · Heat transfer

1 Introduction

Solar air heater (SAH) basically consists of a heat-absorbing surface coated with a high absorptivity material which converts incident solar radiation into thermal energy. Hot air produced by sending air through SAH can be used for crop drying, space heating and in industrial heating/cooling applications. One such agricultural application is related to moisture removal from bagasse which is a raw material in convectional jaggery making units to produce heat by combustion. Combustion efficiency of jaggery units increases with decrease of moisture percentage in bagasse. Moisture from the bagasse can be removed conventionally in open sun drying up to a limit of 15%. SAH as an alternative to conventional method can remove moisture from bagasse up to a level of 2–3%. SAHs are having two major limitations: (i) lower heat transfer coefficients with air as a working fluid [1] and (ii) lower heat transfer rates with thin absorber plates [1]. Thermal performance of SAH is improved by adding sensible heat storage in the form of packed bed with materials like metal chips, pebbles, steel wool, gravel, etc. Ramadan et al. [1], EI-Sebaii et al. [2], Mishra and Sharma [3], Aldabbagh et al. [4], Sopian et al. [5], Dhiman et al. [6], Ramani

I. V. Kumar · M. Mohan Jagadeesh Kumar (✉)
Gayatri Vidya Parishad College of Engineering (Autonomous), Kommadi, Visakhapatnam, Andhra Pradesh 531048, India
e-mail: mohan_mandapati@gvpce.ac.in

et al. [7] with metal chips, gravel, pebbles, iron chips, steel wire mesh layers, steel wool, black painted wire mesh and mild steel machined chips as packed bed materials conducted experimental analysis on single- and double-pass SAHs. It was found that thermal efficiency of double-pass SAH increased with the use of gravel as packed bed by 22–27% [2], steel wool by 60–70% [5]. Aldabbagh et al. [4] and Ramani et al. [7] found that double-pass SAHs give better performance than a single-pass SAHs. Ramadan et al. [1] and Dhiman et al. [6] found from their experimental analysis that the thermal efficiency of SAHs running in double-pass arrangement increases with increase in mass flow rate of air.

From the literature, it is found that experimental investigations on double-pass SAH running in counterflow mode with mild steel chips are limited. In this paper, experiments were conducted on a double-pass SAH (with converging section at its inlet side and diverging section at its exit side), and results are analyzed to know the effect of packed bed on its thermal performance.

2 Methodology

2.1 Experimental Details

The physical model of a double-pass SAH with sensible heat storage in the form of packed bed is shown in Fig. 1. SAH is made with 1.8-cm-thick plywood in the form of a rectangular box having dimensions of 120 cm wide, 240 cm long and 20 cm deep. SAH is divided into two channels: upper and lower channel. SAH performance is
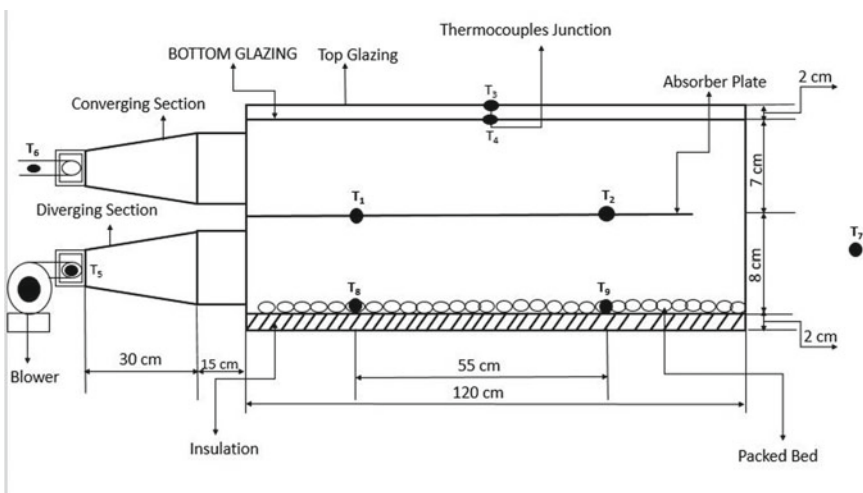
Fig. 1 Line diagram of experimental setup

found to be higher for depth ratio (ratio of depths of upper channel to lower channel) of one [5], and hence, the depth of each channel was fixed as 10 cm. The size of each channel is $120 \times 80 \times 10$ cm^3, and each has an aspect ratio equal to 8 (ASHRAE standards 93-97) [8]. SAH with double glazing (to reduce convection heat loss) and surface area of the single glass equal to 9600 cm^2 is used for experimentation. A normal window glass having a thickness of 0.5 cm is used for glazing, and the distance between two glasses is 2 cm. Air at different mass flow rates in the range of 0.036–0.625 kg/s is supplied with a variable speed blower of 0.74hp capacity. Lower channel of the SAH is filled with mild steel chips with an average thickness of 3 cm thickness to act as a packed bed material.

Air enters and flows through the lower channel of SAH; it takes a U turn at the end and leaves SAH after passing through its upper channel. G.I sheet (0.4 cm thickness) coated with blackboard paint is used as an absorbing surface. SAH is insulated with 2-cm-thick polystyrene sheet as insulating material on its bottom and sides. The total experimental setup is placed on a metal frame which is oriented toward south at an angle of 15°. The total solar radiation was recorded by placing the solar power meter (WACO TM-206 model) having maximum range of 2000 W/m^2. Temperatures at different locations of SAH are recorded manually using DIGIQUAL 12-P temperature indicator by connecting calibrated J (Fe–Cd)-type thermocouples with one end connected to the point of measurement and the other to the indicator.

Mass flow rate of air is varied in between 0.035 and 0.055 kg/s, and experiments are conducted to know the effect of mass flow rate on efficiency of SAH with and without packed bed. Regulator at the blower inlet is fixed at a fixed value to supply constant mass flow rate of air throughout a day. Blower is allowed to operate between 9 am and 5 pm at regular intervals of 30 min. Observations are noted as soon as the temperature values are attained steady state. Experiments are repeated for different air flow rates for six continuous days.

2.2 Performance Parameters

Performance of SAH is assessed in terms of heat absorbed by the air, air temperature at SAH exit and its thermal efficiency.

The energy absorbed by the air (W) is given by

$$Q_{\text{gain}} = \dot{m} C_p \Delta T \tag{1}$$

In Eq. (1), $\dot{m}$ is air mass flow rate in kg/s, C_p is the specific heat of air (kJ/kgK) and ΔT is temperature difference between air temperature at SAH exit and ambient temperature in °C.

Total energy supplied (W) to the SAH from solar radiation is given by,

$$Q_{\text{in}} = I_{\text{avg}} A_c \tag{2}$$

In Eq. (2), I_{avg} is average total incident radiation on the SAH in W/m^2, and A_C is the absorber plate area (8900 cm^2). Solar air heater efficiency is given by,

$$\eta_{\text{SAH}} = \left(Q_{\text{gain}}\big/ Q_{\text{in}}\right) = \dot{m}C_p\Delta T\big/\left(I_{\text{avg}}A_c\right) \tag{3}$$

3   Results and Discussion

Observations are noted by conducting experiments on SAH without using a packed bed at different air flow rates for six days. Thermocouples are attached to read the temperatures of absorber plate (T_p), upper glass (T_{gu}), lower glass (T_{gl}), air at SAH exit (T_{flo}), inlet air (T_{fli}) and atmosphere (T_{amb}). Solar meter is used to read incident solar radiation (I). Variation of all the observations with time on the last day of experimentation is shown in Fig. 2. All the temperatures measured in the experiment are in °C. It is found from Fig. 2 that solar radiation (I) incident on SAH is maximum and equal to 1024 W/m^2 at 12 noon. Upper and lower glass temperatures are maximum at 12 noon and equal to 50.66 °C and 62 °C, respectively. The maximum value of air temperature at SAH exit is 57 °C. The maximum value of T_p and ΔT is 77.3 °C and 20.2 °C at 1 pm and 12 noon. Efficiency of SAH without packed bed is found to be 65.89%. Similar observations are taken for SAH with packed bed for six different days for six different flow rates of air. The variation of T_p, T_{gl}, T_{gu}, T_{flo}, T_{fli}, T_{amb} and I with time on Day 6 is shown in Fig. 3. Incident solar radiation on SAH is maximum and equal to 1028 W/m^2 at 12 noon. Upper and lower glass temperature is maximum at 1 pm and equal to 54.66 °C and 69.25 °C, respectively.
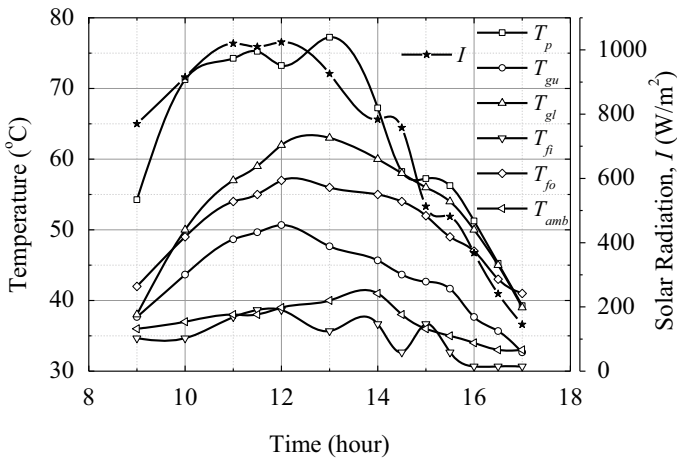
Fig. 2 *Temperatures* at various locations and *solar intensity* with *time*: SAH without packed bed at a mass flow rate of air = 0.0552 kg/s
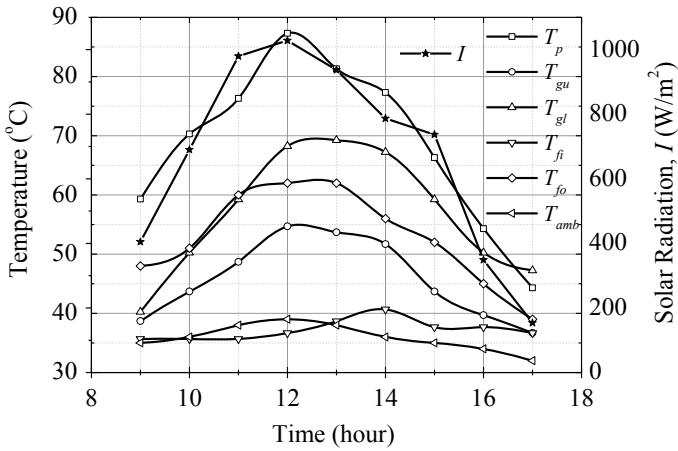
Fig. 3 *Temperatures* at various locations and *solar intensity* with *time*: SAH with packed bed and mass flow rate of air = 0.0552 kg/s

The maximum value of air temperature at SAH exit is 62 °C. The maximum value of T_p and ΔT is 87.25 °C and 26 °C at 12 noon. Efficiency of SAH with packed bed is found to be 78.2% at the mass flow rate of 0.0552 kg/s.

It is observed from the results that the absorber plate and air temperature at SAH exit are increasing from morning 8 am to 12 noon and thereafter decrease till 5 pm. ΔT is higher in the first half of the day till 2 pm compared to the second half of the day, i.e., after 2:00 pm. It is constant till 2 pm and then decreases. Higher heat transfer coefficients with hot air lead to higher temperatures at lower glazing compared to upper glazing. Convection heat losses from the SAH are minimized as the gap between the lower and upper glasses is filled with still air which is bad conductor of heat.

Variation of air temperature at SAH exit with time is shown in Fig. 4. Energy produced by absorbing solar radiation is also transferred to packed bed along with the absorber plate and stored in it as a sensible heat. Temperature of packed bed steadily increases and reaches to its maximum value when packed bed absorbs energy to its fullest sensible heat storage capacity. Hence it is observed that even though air exit temperature is lower at initial stage of experimentation, it steadily increases with the use of packed bed and reaches higher than that of its corresponding value without packed bed. The maximum fluid outlet temperature values of SAH without and with packed bed are 59 °C and 64 °C at a mass flow rate of 0.0552 kg/s. It is found that air temperature at exit of packed bed SAH is 6.75% higher than its corresponding value for SAH without packed bed.

Difference between air temperature at SAH exit and atmosphere, ΔT, is found, and its variation at different air mass flow rates is shown in Fig. 5. It is observed that for each air flow rate, ΔT for SAH with packed bed is higher than its corresponding value for SAH without packed bed. Value of ΔT is found to be equal to 16.84 °C and

Fig. 4 *Fluid temperature at SAH exit with time* at mass flow rate of 0.0552 kg/s
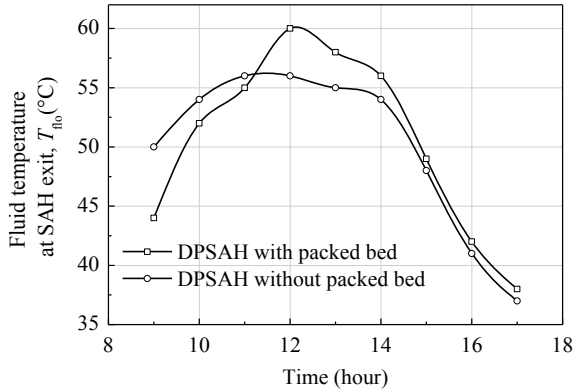
Fig. 5 *Temperature difference* with *mass flow rate*
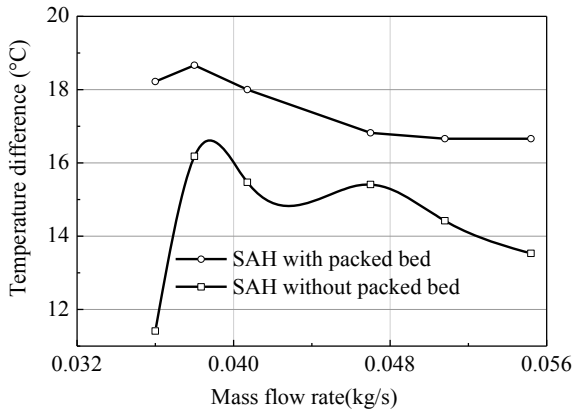
13.6 °C, respectively, for SAH with and without packed bed at air flow rate equal to 0.055 kg/s. Average ΔT is found to be 22.3% higher for SAH with packed bed when compared to corresponding value for SAH without packed bed.

Q_{in} and η_{SAH} are calculated, and their variations with mass flow rate of air are shown in Figs. 6 and 7, respectively. Q_{in} increased rapidly with mass flow rate of air up to a value of 0.0406 kg/s for SAH without packed bed. It is constant between 0.0406 and 0.0518 kg/s and steadily increased thereafter. Whereas in case of SAH with packed bed, Q_{in} increased steadily between 0.0406 and 0.0611 kg/s. Q_{in} reaches to an asymptotic value when mass flow rate of air reaches to 0.0611 kg/s. Mean temperature difference between absorber plate and air will increase linearly with mass flow rate of air for a constant heat flux boundary condition. Q_{in} and η_{SAH} increase up to mass flow rate of air reaches to its threshold value. η_{SAH} with mass flow rate of air in Fig. 7 shows similar trends as of Q_{in} in Fig. 6. η_{SAH} with packed bed is experimentally found to be 20.4% higher than its corresponding value for SAH without packed bed. It is due to the additional sensible energy stored by the packed bed. Heat transfer rate also increased with the increase in turbulence of air due to
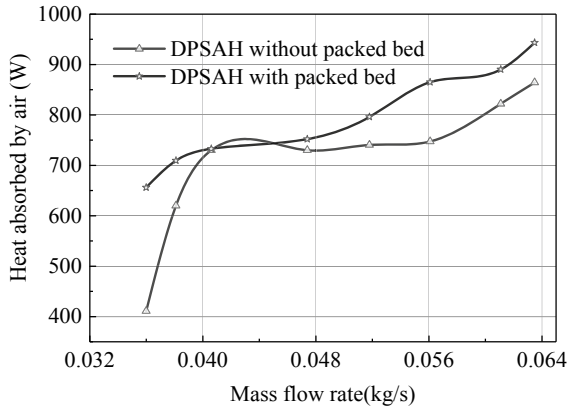
Fig. 6 Variation of *heat absorbed by air* with its *mass flow rate*
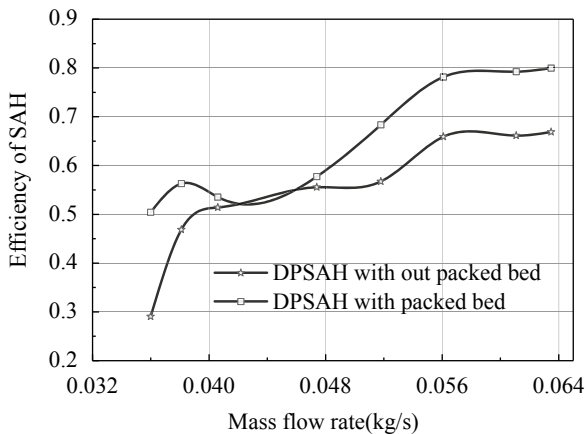
Fig. 7 *Efficiency of SAH* with *mass flow rate* of air

the presence of packed bed. Thermal efficiency is maximum and equal to 78.2% and 65.89%, respectively, for a double-pass SAH with and without packed bed at same mass flow rate of 0.055 kg/s.

4 Conclusions

Thermal efficiency of a double-pass SAH at different air flow rates is experimentally found with and without using a packed bed. It is found that SAH with packed bed produces 22.3% higher average temperature difference between air at SAH exit and atmosphere when compared to SAH without packed bed. Thermal efficiency of SAH

is maximum and equal to 78.2 and 65.89% for SAH with and without packed bed, respectively, at a mass flow rate of air equal to 0.0552 kg/s. It was found that thermal efficiency of SAH with packed bed is higher at an average of 20.4% compared to its corresponding value for SAH without packed bed at different mass flow rates of air.

References

1. Ramadan MRI, El-Sebaii AA, Aboul-Enein S, El-Bialy E (2007) Thermal performance of a packed bed double-pass solar air heater. Energy 32:1524–1535
2. El-Sebaii AA, Aboul-Enein S, Ramadan MRI, El-Bialy E (2007) Year round performance of double pass solar air heater with packed bed. Energy Convers Manage 48:990–1003. https://doi.org/10.1016/0038-092X(88)90065-5
3. Mishra CB, Sharma SP (1981) Performance study of air-heated packed bed solar-energy collectors. Energy 6:153–157
4. Aldabbagh LBY, Egelioglu F, Ilkan M (2010) Single and double pass solar air heaters with wire mesh as packing bed. Energy, 3783–3787
5. Sopian K, Alghoul MA, Alfegi EM, Sulaiman MY, Musa EA (2009) Evaluation of thermal efficiency of double pass solar collector with porous nonporous media. Renew Energy 34:640–645
6. Dhiman P, Thakur NS, Chauhan SR (2012) Thermal and thermohydraulic performance of counter and parallel flow packed bed solar air heaters. Renew Energy 46:259–268
7. Ramani BM, Gupta A, Kumar R (2010) Performance of a double pass solar air collector. Solar Energy 84:1929–1937
8. ASHRAE Standard 93-77 (ANSI B 1981-1977) (1977) Methods of testing to determine the thermal performance of solar collectors. ASHRAE, New York

Design Fabrication and Testing of a Heat Exchanger in a Solar Thermal Energy Conversion System

Vikash Gora and **M. Mohan Jagadeesh Kumar**

Abstract In this document, a shell and tube heat exchanger (STHE) is intended, produced, and experimentally tested for distinct mass flow rates of both warm and cold fluids in a solar thermal energy conversion system (STECS). STHE's performance is discovered by experiments conducted over 25 days at distinct combinations of heat and cold fluid mass flow rates. The studies are initially carried out to maintain the flow rate of warm fluid mass at a speed of 60 kg/h and the flow rate of cold fluid mass between 120 and 300 kg/h. Further studies with a set cold fluid flow rate of 60 kg/h are proceeded, and the warm fluid flow rate varies between 120 and 300 kg/h. The average maximum temperature of hot fluid by the use of evacuated tube solar collector (ETSC) is found to be 80 °C. Experimental results show that the STHE has a maximum effectiveness of 0.74 when the mass flow rate of warm and cold fluids is 60 and 300 kg/h, respectively. The effectiveness also averages up to 0.6508 with cold and hot fluids mass flow rates of 60 and 300 kg/h.

Keywords Solar energy · Heat exchanger · Solar collector · Heat transfer

1 Introduction

Due to rapid increase in population and economic growth of countries worldwide, it is becoming extremely important to use efficient techniques to reduce energy consumption. Modified processes utilizing solar energy are promising from the economic point of view in the long run. Analysis has been carried out across the globe to evaluate and enhance the performance of heat transfer units with solar collectors. The literature presents a comprehensive review of heat transfer analysis in solar collectors and STHEs. Solar thermal energy conversion system(s) STECS needs combination of a radiation collecting unit and a thermal heat transfer unit. Solar collectors convert

V. Gora
Malaviya National Institute of Technology, JLN Marg, Jaipur, Rajasthan, India

M. Mohan Jagadeesh Kumar (✉)
GVP College of Engineering (A), Kommadi, Visakhapatnam, Andhra Pradesh 531048, India
e-mail: mohan_mandapati@gvpce.ac.in

radiation to heat and store it in a primary working fluid. STHE can transfer heat stored in primary working fluid to a secondary fluid which is used for the end application.

Experimental analyses were conducted to know the performance of STECS with variation in their operating parameters by many researchers like Winter [1], Fanney and Klein [2], Hobbi and Siddiqui [3], Singh et al. [4], Al-Khaffajy et al. [5], Abubakar and Egbo [6], Budihardjo [7], Gao et al. [8], Mahendran et al. [9, 10], Mishra [11], Sabiha et al. [12], Ghaderian and Sidik [13]. Performance of STECs decreases with the use of integrated heat exchanger, and hence, a heat exchanger correction factor needs to be introduced to know the reduction in heat transfer [1]. Heat transfer in STECs can be increased by decreasing the thermal stratification in storage tank [2] and with the use of passive heat improvement equipment like twisted strips, coil spring cables, conical ridges, etc. [3]. STECS can even use parabolic through collectors in smaller size for domestic solar applications [4]. It was found that the thermal storage and thermal efficiency of glass in tube ETSC are lower than the U-pipe ETSC for same working conditions [8, 11]. In U-pipe ETSC, the heat loss during night time is more when compared to corresponding heat loss in glass in tube ETSC [8]. Heat transfer rates in STECS with ETSCs can be improved with the use nanofluids. The use of Al_2O_3, TiO_2, or CuO nanoparticles in water and single-walled carbon nanotubes in water will improve the heat transfer rates in ETSCs [9, 10, 12, 13]. Numerical analyses on performance of STECS equipped with flat plate solar collectors (FPSCs) were conducted to know the configuration for maximum heat transfer in solar collectors by Mossad et al. [14], Arslan et al. [15], Kumavat et al. [16], Naik et al. [17]. Thermal performance of STECS comprising FPSC with single row heat exchanger is better than FPSC with multi-row heat exchanger [14]. Thermal stratification and hence the performance of STECS are better with increase in fluid flow through the heat exchanger. Storage tank capability to deliver hot water decreases with increase in its discharge time [15]. Thermal performance of FPSC depends on collector length, tilt angle, mass flow rate of working fluids, solar intensity, wind velocity, etc. [16, 17]. Traditional design approach to rate large number of STHE geometrical and operating parameters was quite time-consuming and did not give surety of finding the optimum design. Algorithms using techniques like particle swarm optimization, genetic algorithms were developed, and programming codes were written by researchers across the globe to design STHEs with different configurations of tube arrangements Caputo et al. [18], Patel et al. [19]. Experiments were conducted to evaluate performance, study the impact of different geometric parameters, and validate experimental results with numerical simulations, mathematical modeling of STHEs Jayachandriah [20], Ambekar et al. [21]. STHEs with continuous helical baffle has maximum overall heat transfer coefficient when compared to STHEs with segmental baffles, and the pressure drop in STHEs is found to be decreasing with an increase in the helix angle [20]. Helical baffles showed nearly zero stagnation areas resulting in heat exchangers decreased fouling and long operating life [21].

It is found from literature that the heat transfer analysis on STECS with a combination of ETSC and STHE is limited. The literature does not address the effect of warm and cold fluid mass flow rates on STHE performance with segmental baffles.

Table 1 Input to the program: Heat exchanger design input data

Parameters	Value
Shell length to diameter ratio, L/D_s	7.5
Temperature of the tube side fluid inlet, T_{hi} (°C)	85
Temperature of the shell side fluid inlet, T_{ci} (°C)	20
Tube side mass flow rate of liquid, m_t (kg/hr)	150
Shell side mass flow rate of liquid, m_s (kg/hr)	200
Number of tube passes, n	1
Correction factor from data book, F	0.93

In this paper, the effect of cold and hot fluid mass flow rate on thermal performance of STECS is found experimentally to fill the gap in the literature.

2 Modeling and Fabrication of STHE

In the first step of STHE design, an algorithm is developed and based on the algorithm a program code is prepared using Microsoft Excel. Later, a heat exchanger is designed in SolidWorks and manufactured as per the design parameters obtained as an output from the program code. Detailed mathematical modeling of STHE is presented by the present authors in [22]. Input and final output of the program after number of iterations are given in Tables 1 and 2.

3 Experimental Setup

An experimental setup of heat recovery unit with ETSC and STHE is developed at the rooftop of the Mechanical Engineering Department, M.N.I.T., Jaipur, which is situated in eastern Rajasthan of western India. Total 35 T-type thermocouples (Copper/Constantan) are used in the experimental setup to measure temperatures at different locations. Specifications of ETSC are given in Table 3. STHE specifications are shown in Table 4.

Schematic diagram of the experimental configuration together with the places of all temperature sensors used in experiment is shown in Fig. 1. Experiments were conducted for 25 continuous days (from 28th April to 11th June 2017), and calculations were made to know the thermal performance of STECS. Initially, the ETSC was operated to produce hot water (primary fluid) and the heat stored in hot water is transferred to water (secondary fluid) using a STHE.

Table 2 Output from the program: Calculated parameters

Parameters	Type of tube grid	
	Staggered	Aligned
Shell inside diameter, D_s (cm)	10.47	10.47
Shell length, L (cm)	71.01	71.01
Tube inner diameter, d_i (mm)	11.00	11.00
Tube outer diameter, d_o (mm)	12.50	12.50
Baffle spacing, B (m)	0.25	0.25
Tube side Reynolds number, Re_t	307.40	388.3
Reynolds number for shell, Re_s	145.13	202
Overall heat transfer coefficient, U (W/m^2 K)	167.2	165.6
Heat Transfer rate, Q (kW)	4.51	3.88
Heat transfer area, A (m^2)	0.67	0.53
Temp difference at inlet, ΔT_{inlet} (°C)	65.00	65.00
Temp difference at outlet, ΔT_{outlet} (°C)	19.62	26.04
Temp lost by hot fluid, ΔT_h (°C)	25.93	22.26
Temp gain by cold fluid, ΔT_c (°C)	19.45	16.70
Calculated correction factor, F	0.29	0.24
Effectiveness, ε	0.40	0.34
Temperature of fluid at tube outlet, T_{ho} (°C)	59.07	62.74
Temperature of fluid at shell outlet, T_{to} (°C)	39.45	36.70
Logarithmic Mean Temperature Difference	42.23	45.46
Heat exchanger surface area, A (m^2)	0.69	0.55
No. of tubes, N_t	24	19

4   Results and Discussion

The overall efficiency of STECS was calculated as the ratio of heat absorbed by
secondary fluid in STHE to the heat collected by primary fluid in ETSC. Thermal
efficiency of ETSC is described as the proportion of the useful quantity of energy
transferred to the collector's complete solar radiation incident and is expressed as

$$\eta = \frac{Q_u}{A_c I} = \frac{\dot{m} C_P (T_{\text{out}} - T_{\text{in}})}{A_c I}. \tag{1}$$

In Eq. (1), $\dot{m}$ is mass flow of water through the storage tank in kg/s, C_p specific
heat of water in kJ/kg K, T_{out} and T_{in} are the temperature of the water at storage
tank exit and inlet, respectively, in °C, A_c collector surface area in m^2 and I total
solar radiation incident on the collector in kW/m^2. Solar intensity and temperatures
at various locations in the experimental setup with respect to time for different days

Table 3 Specifications of ETSC

Specifications	Details (explanation)
Gross area of collector (m^2)	1.45 (1.70 × 0.855)
Absorber area of collector (m^2)	0.986 (1.70 × 0.058 × 10)
Collector aperture area (m^2)	0.731 (1.70 × 0.043 × 10)
Total evacuated tube length (m)	1.80
Evacuated tube length exposed to solar radiation after installation (m)	1.70
Working temperature (°C)	10–100
Collector angle (°)	30
Absorber	Aluminum
Absorption (α)/emission (ε)	0.92/0.06
Collector housing	Aluminum
Collector glazing	Evacuated tubes (borosilicate glass)
Number of tubes	10 evacuated tubes
Glass tube outer diameter (cm)	5.8
Glass tube inner diameter (cm)	4.3
Material for sealing	Silicone
Material for frame	Stainless steel

Table 4 STHE specifications

Part	Specification	Detail	Material
Tube side	Tube pitch	Staggered grid	Copper (Cu)
	Tube passes, n	1	
	No. of tubes, N_t	24	
	Inner diameter of the tube, d_i (mm)	11.00	
	Outer diameter of the tube, d_o (mm)	12.50	
Shell side	Shell length, L (cm)	71.0	Mild steel (M.S.)
	Shell inside diameter, D_s (cm)	10.7	
	Shell outside diameter (cm)	11.2	
Baffle	Baffle spacing, B (cm)	22.3	Mild steel (M.S.)
Insulation	Thickness (cm)	1	Glass wool
Cover	Thickness (mm)	1	Aluminum sheet

are experimentally recorded. Thermal efficiency of ETSC is calculated using Eq. (1) and found to be changing from 55 to 68% depending on intensity of solar radiation.
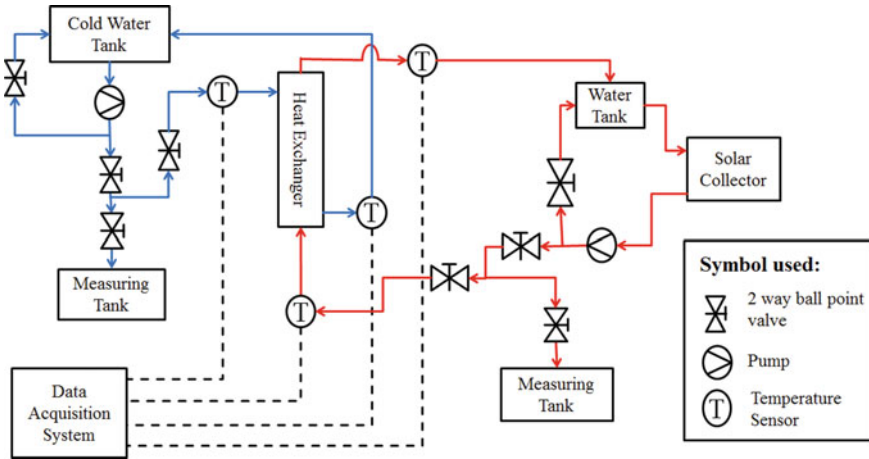
Fig. 1 Schematic diagram of the experimental setup of the heat exchanger

4.1 Experimental Results of STHE

The primary fluid (water) at higher temperature from exit of ETSC is allowed to flow through the tubes to transfer heat to the secondary fluid (water) flowing through shell of the STHE. Cold fluid is circulated again and again through STHE until and unless fluid temperature at tube inlet and fluid temperature at shell exit becomes more or less equal. Experiments are conducted with water and sugarcane juice as cold fluid at various mass flow rates. STHE effectiveness is described as the proportion of real heat transferred between the tube and shell fluids to the maximum heat transferable between the two. It is given by,

$$\varepsilon = \frac{\dot{Q}_{\text{avg}}}{\dot{Q}_{\text{max}}} = \frac{\dot{Q}_{\text{avg}}}{(\dot{m}c)_{\text{min}}(T_{\text{hi}} - T_{\text{ci}})}. \tag{2}$$

In Eq. (2), $\dot{Q}_{\text{avg}}$ is the average heat transferred (kW) between the two fluids and is equal to the average of heat lost by the warm fluid and heat gained by the cold fluid. T_{hi} and T_{ci} are the temperatures of warm and cold fluids at inlet sections, respectively. Observations for temperatures at various locations in the experimental setup are taken by putting warm and cold fluids mass flow rate at 60 kg/hr. Variations of temperatures of warm and cold fluids at inlet and exit sections with respect to the time are given in Fig. 2. Reynolds numbers for hot and cold fluids (Re_h and Re_c) are found to be 122.96 and 43.75, respectively, with the set fluid mass flow rates. The difference between warm fluid inlet temperatures and cold fluid outlet is found to drop steadily with time from a peak value of 32.7 °C at 17:57 pm to a minimum value of 1.5 °C at 18:30 pm. Cold fluid exit temperature is discovered near the temperature of the warm fluid inlet after 35 min of the working of STHE.

Fig. 2 Variation of hot and cold fluids inlet and exit *temperature* with *time* based on the experimental results on April 28, 2017
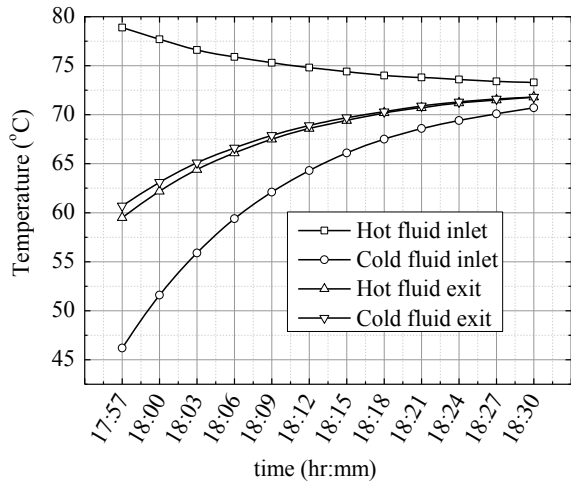
Logarithmic mean temperature difference (LMTD), effectiveness (ε), loss of heat from warm fluid ($\dot{Q}_h$), gain of heat by the cold fluid ($\dot{Q}_c$), and average heat transfer rate between hot and cold fluids ($\dot{Q}_{avg}$) are calculated using the observations. Variations of $\dot{Q}_h$, $\dot{Q}_c$, $\dot{Q}_{avg}$ and variations of LMTD ε wrt to time are shown in Figs. 3 and 4, respectively. The average heat transfer rate between the two fluids and LMTD decreases as the exit temperature of the cold fluid increases over time. Effectiveness of STHE is found to be constant throughout the experiment and equal to an average value of 0.514.

Fig. 3 Variation of *heat transfer rate* between hot and cold fluid with *time* based on the experimental results on April 28, 2017
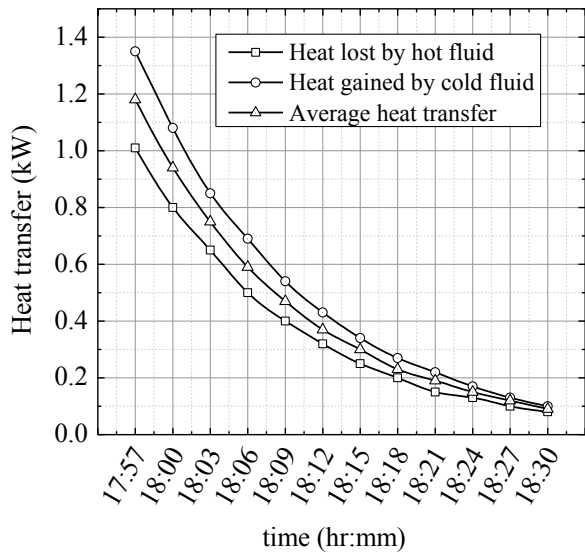
Fig. 4 Variation of *LMTD* and *effectiveness* with *time* based on the experimental results on April 28, 2017
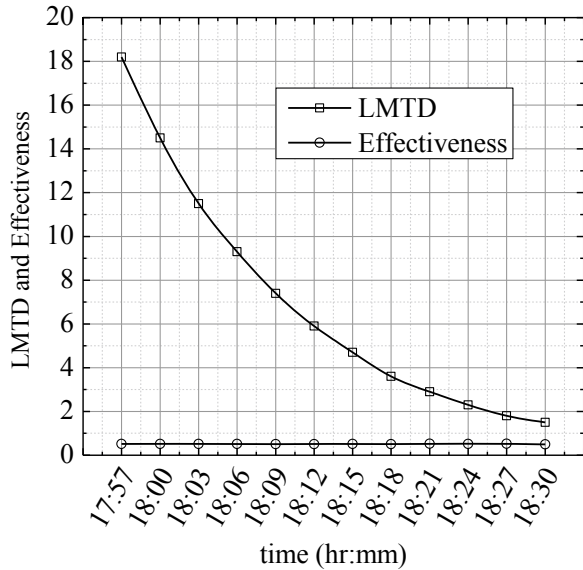
Variation of theoretically and experimentally determined values of effectiveness of STHE with tube and shell side fluids mass flow rate is presented in Table 5. The theoretical and experimental values of effectiveness of STHE are in good agreement. It is observed that at lower value of mass flow rate of tube side fluid, i.e., 60 kg/hr, the value of effectiveness of STHE grows with higher mass flow rates of shell side fluid from 120 to 300 kg/hr. At higher values of mass flow rate of tube side fluid, i.e., equal and above 120 kg/hr, ε of STHE is observed to decline with the rise in shell side fluid from 120 to 300 kg/hr. At higher values of mass flow rates, the thermal stratification effects are more on cold fluid which tends to decrease the heat transfer coefficients and hence the effectiveness is observed to decrease with increase in mass flow rate of the shell side fluid. Lower values of effectiveness are obtained when both hot and cold fluids are allowed to flow at a lower mass flow rate of 60 kg/hr. The effectiveness is observed to be higher when mass flow rate of shell side fluid is kept lower, i.e., 60 kg/hr and hot fluid mass flow rate is higher, i.e., 120–300 kg/hr.

5 Conclusions

A heat recovery unit comprising a heat exchanger and a solar collector is designed, fabricated, and experimentally tested. An algorithm is developed for designing STHE, and a user-defined program is developed and used in MS Excel to optimize the geometric parameters of STHE. Heat exchanger integrated with a solar collector is fabricated and tested to find its thermal performance. The experimental findings show that temperature of the liquid in the storage tank is steadily increasing

Table 5 Variation of effectiveness of STHE, tube and shell side Reynolds number with tube and shell side fluid mass flow rate

$\dot{m}_h$ (kg/hr)	$\dot{m}_c$ (kg/hr)	ε_{cal}	ε_{exp}	Re_t	Re_s
60	60	0.50	0.514	122.96	43.75
	120	0.62	0.629	122.96	87.1
	180	0.68	0.691	122.96	130.61
	240	0.71	0.719	122.96	174.15
	300	0.73	0.739	122.96	217.7
120	60	0.60	0.604	245.92	43.75
	120	0.40	0.408	245.92	87.1
	180	0.45	0.459	245.92	130.61
	240	0.48	0.489	245.92	174.15
	300	0.50	0.604	245.92	217.7
180	60	0.65	0.651	368.88	43.75
	120	0.45	0.449	368.88	87.1
	180	0.34	0.493	368.88	130.61
	240	0.37	0.372	368.88	174.15
	300	0.39	0.393	368.88	217.7
240	60	0.68	0.665	491.84	43.75
	120	0.48	0.477	491.84	87.1
	180	0.37	0.374	491.84	130.61
	240	0.30	0.270	491.84	174.15
	300	0.32	0.322	491.84	217.7
300	60	0.70	0.683	614.8	43.75
	120	0.50	0.500	614.8	87.1
	180	0.39	0.393	614.8	130.61
	240	0.32	0.325	614.8	174.15
	300	0.27	0.275	614.8	217.7

and reaching to maximum value by evening. ETSC during its one day operation is found to be achieving a maximum temperature of its working fluid (water) nearly equal to 85 °C. Hot fluid ETSC is then used to preheat a secondary liquid in STHE. Effectiveness of STHE reached a maximum value of 0.74 when hot fluid (flowing through the tube) mass flow rate is 60 kg/h and cold fluid (flowing through the shell) mass flow rate is 300 kg/h. Similarly, it reached an average maximum value of 0.65 when cold fluid mass flow rate is 60 kg/h and warm fluid mass flow rate changes from 120 to 300 kg/h. Hence, it is concluded that the heat transfer coefficients and hence the effectiveness of STHE would be maximum when either hot or cold fluid is set to be flowing at lower mass flow rate keeping other fluid mass flow rate at a higher value.

References

1. de Winter F (1975) Heat exchanger penalties in double-loop solar water heating systems. Sol Energy 17(6):335–337. https://doi.org/10.1016/0038-092X(75)90034-1
2. Fanney AH, Klein SA (1988) Thermal performance comparisons for solar hot water systems subjected to various collector and heat exchanger flow rates. Sol Energy 40(1):1–11. https://doi.org/10.1016/0038-092X(88)90065-5
3. Hobbi A, Siddiqui K (2009) Experimental study on the effect of heat transfer enhancement devices in flat-plate solar collectors. Int J Heat Mass Trans 52(19–20):4650–4658. https://doi.org/10.1016/j.ijheatmasstransfer.2009.03.018
4. Singh S, Saini P, Kumar M (2016) Performance evaluation of parabolic solar water heater. Imperial J Interdisc Res 2(6):1–5
5. Marwaan A K, Mossad R (2013) Optimization of the heat exchanger in a flat plate indirect heating integrated collector storage solar water heating system. Renew Energy. 57:413–421. https://doi.org/10.1016/j.renene.2012.11.033
6. Abubakar GB, Egbo G (2014) Performance evaluation of flat plate solar collector (Model Te39) In Bauchi. Americal J Eng Res 3(10):34–40
7. Budihardjo I, Morrison GL, Behnia M (2002) Performance of a water-in-glass evacuated tube solar water heater. In: Proceedings of Solar. pp 1–6
8. Gao Y, Zhang Q, Fan R, Lin X, Yu Y (2009) Effects of thermal mass and flow rate on forced-circulation solar hot-water system: Comparison of water-in-glass and U-pipe evacuated-tube solar collectors. Sol Energy 98:290–301. https://doi.org/10.1016/j.solener.2013.10.014
9. Mahendran M, Ali TS, Shahrani A, Bakar RA (2013) The efficiency enhancement on the direct flow evacuated tube solar collector using water-based titanium oxide nanofluids. Appl Mech Mater 465–466:308–315
10. Mahendran M, Lee GC, Sharma KV, Shahrani A, Bakar RA (2012) Performance of evacuated tube solar collector using water-based titanium oxide nanofluid. J Mech Eng Sci 3:301–310. https://doi.org/10.15282/jmes.3.2012.6.0028
11. Mishra D (2015) Experimental analysis of thermal performance of evacuated U-tube solar collector. Adv Phys Lett 2(3):1–7
12. Sabiha MA, Saidur R, Mekhilef S (2015) An experimental study on Evacuated tube solar collector using nanofluids. Trans Sci Technol 2(1):42–49
13. Ghaderian J, Sidik NC (2017) An experimental investigation on the effect of Al_2O_3/distilled water nanofluid on the energy efficiency of evacuated tube solar collector. Int J Heat Mass Trans 108:972–987. https://doi.org/10.1016/j.ijheatmasstransfer.2016.12.101
14. Mossad R, Khaffajy MA (2012) Investigating two configurations of a heat exchanger in an indirect heating integrated collector storage solar water heating system (IHICSSWHS). In: International conference on renewable energies and power quality—ICREPQ, Santiago de Compostela (Spain), 1, 1404–1409
15. Arslan M, Igci AA (2015) Thermal performance of a vertical solar hot water storage tank with a mantle heat exchanger depending on the discharging operation parameters. Sol Energy 116:184–204. https://doi.org/10.1016/j.solener.2015.03.045
16. Manilal KM (2016) Design, CFD analysis and fabrication of solar flat plate. Int Res J Eng Technol 3(1):1000–1004
17. Naik BK, Varshney A, Muthukumar P, Somayaji C (2016) Modelling and performance analysis of U type evacuated tube solar collector using different working fluids. In: 5th international conference on advances in energy research, ICAER, 90. pp 227–237
18. Caputo AC, Pelagagge PM, Salini P (2008) Heat exchanger design based on economic optimisation. Appl Thermal Eng 28(10):1151–1159. https://doi.org/10.1016/j.applthermaleng.2007.08.010
19. Patel VK, Rao RV (2010) Design optimisation of shell-and-tube heat exchanger using particle swarm optimisation technique. Appl Thermal Eng 30(11–12):1417–1425. https://doi.org/10.1016/j.applthermaleng.2010.03.001

20. Jayachandriah D, Kumar VV (2015) Design of helical baffle in shell and tube heat exchanger and comparing with segmental baffle using kern. Int J Emerg Technol Comput Sci Electron 13(2):157–162
21. Ambekar AS, Sivakumar R, Anantharaman N, Vivekenandan M (2016) CFD Simulation study of shell and tube heat exchangers with different baffle segment configurations. Appl Thermal Eng 108:999–1007. https://doi.org/10.1016/j.applthermaleng.2016.08.013
22. Vikash G (2017) Design fabrication and performance analysis of heat recovery unit in solar thermal energy conversion system used in jaggery making process. M. Tech Thesis, MNIT Jaipur, Rajasthan, India

Unsteady Casson MHD Flow Due to Shrinking Surface with Suction and Dissipation

P. Durga Prasad, R. Sivaraj, B. Madhusudhana Rao, C. S. K. Raju, K. Venkateswara Raju, and S. V. K. Varma

Abstract The present paper is on 2D Casson magnetohydrodynamic flow through exponentially shrinking surface. The set of nonlinear PDEs are established into ODEs by using R-K scheme connected by shooting methodology. Some of the physical quantities are implemented to demonstrate the effects of exponential, Eckert number, Casson and radiation parameters on temperature and velocity distributions. The constraint of Eckert numbers decelerates the rate of heat transfer in both $\Pr = 2$ and $\Pr = 9$ cases.

Nomenclature

U	Velocity constant
σ	Electric conductivity

P. Durga Prasad (✉) · K. Venkateswara Raju
Department of BS&H, Sree Vidyanikethan Engineering College, (A), Rangampet, Tirupati, India
e-mail: durga.prsd@gamil.com

K. Venkateswara Raju
e-mail: venky.sakku@gmail.com

R. Sivaraj
Department of Mathematics, SAS, VIT University, Vellore 632014 , India

B. Madhusudhana Rao
Higher College of Technology, Muscat, Oman

C. S. K. Raju
Department of Mathematics, GITAM University, Bangalore, India
e-mail: sivaphd90@gmail.com

S. V. K. Varma
Department of Mathematics, S.V. University, Tirupati, Andhra Pradesh, India
e-mail: profsvkvarma@gmail.com

T	Temperature of the fluid
B_0	Magnetic field
c	Positive constant
D_m	Coefficient of the mass diffusivity
q_r	Radiative heat flux
ρC_p	Heat capacitance of fluid
N	Exponential parameter
β	Casson fluid parameter
T_∞	Ambient fluid temperature
L	Characteristic length

1 Introduction

The renowned Navier–Stoke's equation is not enough so as to portray the conduct of non-Newtonian fluids. Hereafter, some physical models are most significant to bound up this gap; the models comprised Maxwell, Casson, Ellis and Cross models. It has several uses in various research areas are like illustration of plastic films, conveyor belt aerodynamics and paper manufacture. The physical conduct of non-Newtonian fluid flows is presently interesting subject in research with regard to explore and included researcher, mathematicians and engineers. Previously mentioned non-Newtonian fluid models are troublesome in nature, up to now there is no single constitutive model for appearing non-Newtonian fluid properties. So, inspired by this theory of an unsteady non-Newtonian Casson fluid over a stretching sheet [1, 2], Zaib et al. [3] elucidated that heat transfer effects on Casson flow with viscous dissipation by using shooting technique.

Boundary-layer flow through a shrinking surface is come over in various innovative procedures. Such circumstances occur in manufacturing of glass sheets, polymer processing, in material ventures and so on. Elbashbeshy [4] discussed numerically the heat transfer through an exponentially shrinking sheet. Hayat and Sajid [5] discussed the flow of a Jeffrey fluid through an exponential surface. A while later such a large number of researchers are examined on boundary-layer flow on contracting sheet can be understood in writing [6–14].

The determination of the current model is to investigate an unsteady MHD flow to shrinking surface with suction and dissipation. The governing PDEs have been converted to a couple of ODEs via similarity conditions which are then explained mathematically by utilizing bvp4c with MATLAB tool. The enhancements of various pertinent physical quantities on temperature and velocity distributions are studied, and graphically also some of numerical computations are shown in table.

2 Mathematical Formulation

We considered the unsteady 2D magnetohydrodynamic boundary-layer fluid flow of Casson fluid through an exponentially shrinking surface, which is presumed that the velocity and temperature of stretching sheet are $U = U_0 e^{Nx/L}/(1 - ct)$, $T = T_\infty + T_0 e^{Nx/2L}/(1 - ct)$. The fluid flow starts at $y = 0$ and for steady case when $y < 0$. Sheet is taken along x-axis, and y-axis is taken normal to it. A magnetic field of strength B_0 is applied in fluid flow direction, and N is exponential parameter.

According to the above assumptions, the physical governing system is expressed as

$$\frac{\partial u}{\partial y} + \frac{\partial u}{\partial x} = 0 \tag{1}$$

$$\frac{\partial u}{\partial t} + v\left(\frac{\partial u}{\partial y}\right) + u\left(\frac{\partial u}{\partial x}\right) = v_f\left(\frac{1+\beta}{\beta}\right)\frac{\partial^2 u}{\partial y^2} + [g(T - T_\infty)\beta_T] - u\left(\frac{\sigma B_0^2}{\rho}\right) \tag{2}$$

$$\frac{\partial T}{\partial t} + v\left(\frac{\partial T}{\partial y}\right) + u\left(\frac{\partial T}{\partial x}\right) = k\frac{1}{\rho C_p}\frac{\partial^2 T}{\partial y^2} - \frac{1}{\rho C_p}\frac{\partial q_r}{\partial y} + \frac{v}{C_p}\left(\frac{\beta+1}{\beta}\right)\left(\frac{\partial u}{\partial y}\right)^2 \tag{3}$$

The suitable boundary conditions are:

$$v = -V(x), u = -U, T = T_w \text{ at } y = 0$$
$$T \to T_\infty, u \to 0, \text{ as } y \to \infty \tag{4}$$

$$q_r = -\frac{16\sigma^* T_\infty^3}{3k^*}\frac{\partial T}{\partial y} \tag{5}$$

Using Eq. (5) in Eq. (3) is reduced as

$$\frac{\partial T}{\partial t} + v\left(\frac{\partial T}{\partial y}\right) + u\left(\frac{\partial T}{\partial x}\right) = \frac{k}{\rho C_p}\frac{\partial^2 T}{\partial y^2} + \frac{16\sigma^* T_\infty^3}{3\rho C_p k^*}\frac{\partial^2 T}{\partial y^2} + \frac{v}{C_p}\left(1 + \frac{1}{\beta}\right)\left(\frac{\partial u}{\partial y}\right)^2 \tag{6}$$

$$B = B_0 e^{Nx/2L} \Big/ (1-ct)^{1/2}, T = T_\infty + T_0 e^{Nx/2L} \Big/ (1-ct),$$

$$V(x) = -S\{U_0 \upsilon_f / 2L(1-ct)\}^{1/2} e^{Nx/2L}, u = \frac{U_0}{(1-ct)} e^{Nx/L} f'(\zeta),$$

$$v = -N[\upsilon_f U_0 / 2L(1-ct)]^{1/2} e^{Nx/2L} [f(\zeta) + \zeta f'(\zeta)]$$

$$\zeta = \{U_0 / 2L\upsilon_f (1-ct)\}^{1/2} e^{Nx/2L} y, (T - T_\infty) = T_0 e^{Nx/2L} \theta(\zeta) \Big/ (1-ct)$$

$$(7)$$

By an applying Eq. (7) into Eq. (1) which is satisfies an equation of continuity. Equations (2), (4) and (6) are transformed as

$$\left(\frac{1+\beta}{\beta}\right) f'' - N(f'^2 - ff') + 2Gr\theta - f'(2A+M) - Af' = 0 \qquad (8)$$

$$\left(1 + \frac{4}{3}R\right)\theta' - N(f\theta' - f'\theta) + Ec\,Pr\left(\frac{1+\beta}{\beta}\right) f'^2 + A(\theta' + \theta) = 0 \quad (9)$$

The converted boundary conditions are

$$f(\zeta) = S, \theta(\zeta) = 1, \ f'(\zeta) = -1, \text{ at } \zeta = 0$$
$$\theta(\zeta) \to 0, f'(\zeta) \to 0, \text{ as } \zeta \to \infty \qquad (10)$$

Non-dimensional friction factor coefficient and Nusselt numbers are

$$Re^{\frac{1}{2}} Cf = \left(1 + \frac{1}{\beta}\right) f''(0), \ Nu\,Re^{\frac{-1}{2}} = -(1+R)\theta'(0)$$

3   Results and Discussion

The dimensionless governing Eqs. (8) and (9) corresponding to the boundary condition (9) are elucidated numerical by using R-K scheme connected by shooting methodology. The effect of different flow physical factors on temperature and velocity distributions in addition to Nusselt numbers is studied through graphs and tables.

Figures 1 and 2 discussed the impact of β on temperature and velocity distributions. Here observed smaller values for Casson parameter increases the plastic dynamic viscosity, which produces a opposition to the fluid flow, can be observed in velocity distributions Fig. 1, the opposite behaviour can be detected in temperature distributions Fig. 2. Because in physically, which may can happen due to enhance in
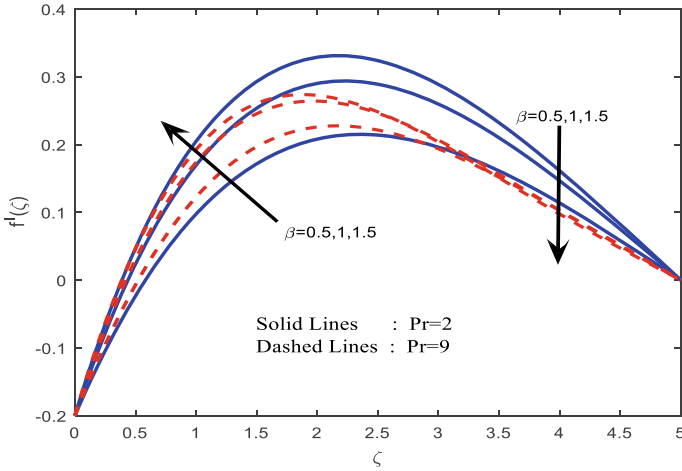
Fig. 1 Velocity distributions for β
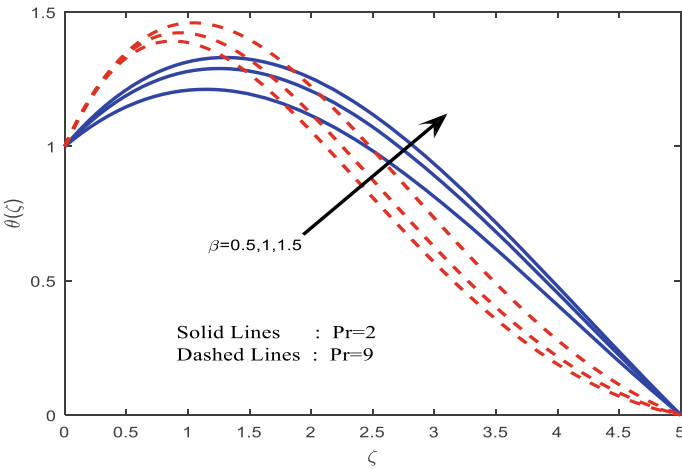
Fig. 2 Temperature distributions β

β increases the viscous forces, which have to decreases fluid temperature for both cases of $Pr = 2$ and 9.

The physical phenomena of magnetic field parameter M can be studied in temperature and velocity distributions for different cases of $Pr = 2$ and 9 can be seen in Figs. 3 and 4. From Fig. 3, the impact of M is observed that the strength of M decelerates the velocity fields. Practically, this lessening can be credited to point that the M (magnetic field) delivers a repelling kind of force which is called Lorentz's force. The similar way can be identified in temperature distributions which are displayed in Fig. 4.
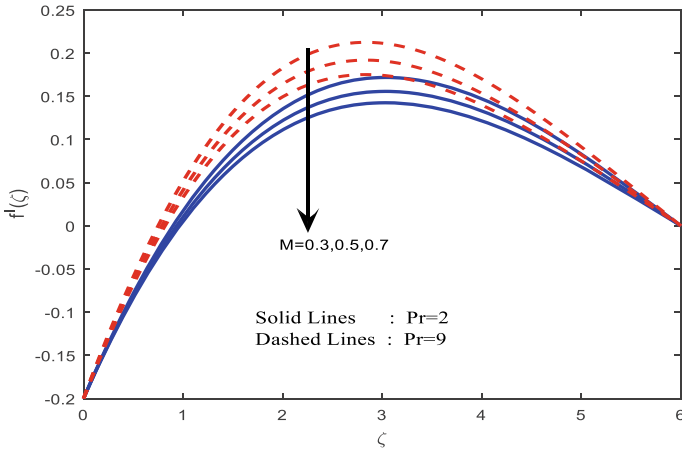
Fig. 3 Sketch of velocity distributions for M
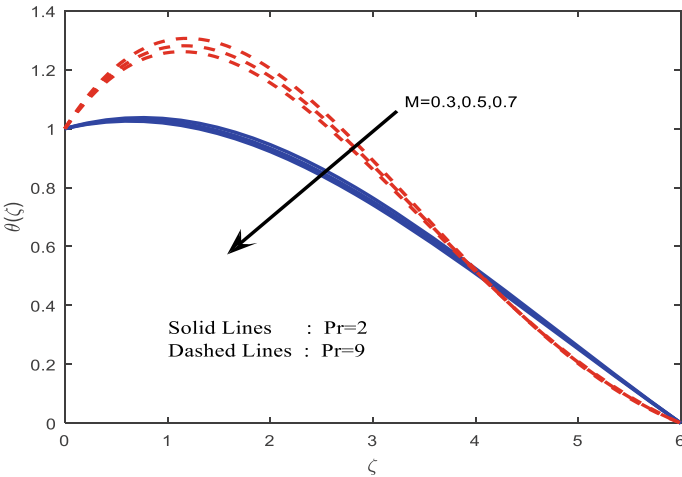
Fig. 4 Sketch of temperature distributions for M

Behaviour of temperature distributions is illustrated in Fig. 6 on R(radiation parameter). It is owing to fact that temperature of the fluid enhances the conduction effect of the fluid in the presence of radiation parameter. Generally, which imply higher surface heat flux, therefore increase the thickening of thermal boundary-layer. The reverse tendency can be experimental in velocity profiles (Fig. 5) for radiation parameter R. The effect of Ec on the velocity and temperature fields is revealed in Figs. 7 and 8.

We observed that the effect of Ec enriches the temperature flow region. Similar way can be found in velocity distributions (Fig. 7). Finally, we observed that the
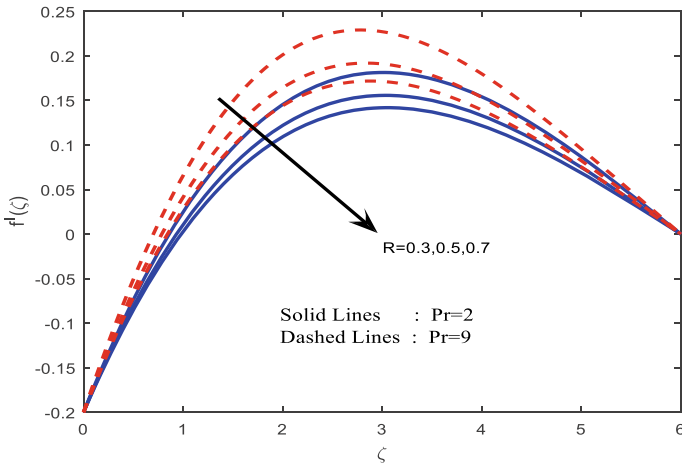
Fig. 5 Sketch of velocity distributions for R
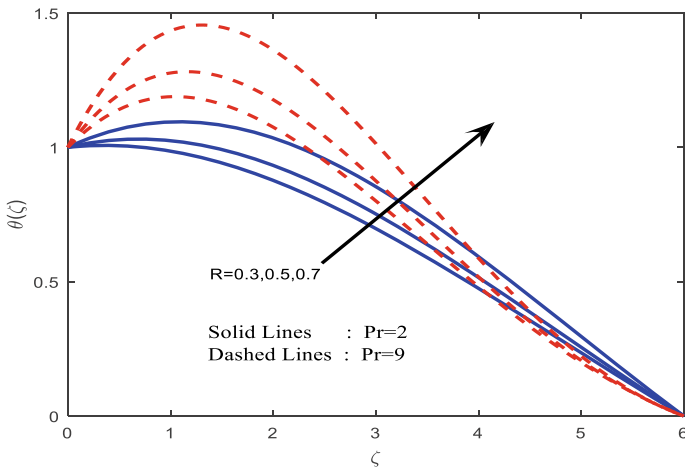
Fig. 6 Sketch of temperature distributions for R

exponential parameter N accelerates temperature and velocity distributions as shown in Figs. 9 and 10.

Finally, the numerical estimations of radiation parameter, exponential parameter and Eckert number on Nusselt number are displayed in Table 1. The radiation and Eckert number are enhancing the rate of heat transfer and then decelerate the exponential parameter for both $\text{Pr} = 2$ and $\text{Pr} = 9$ cases.
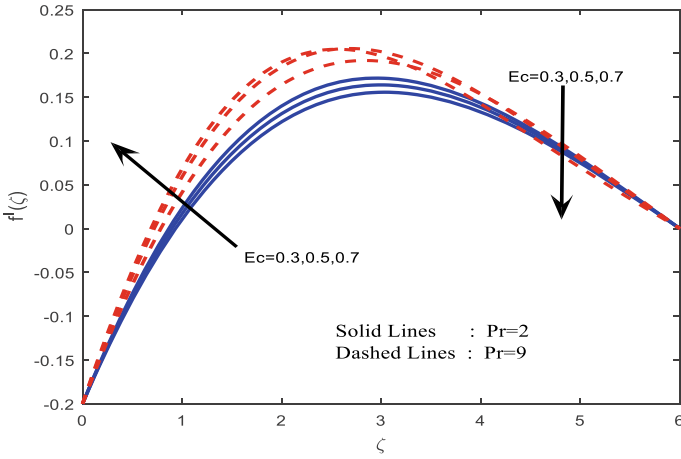
Fig. 7 Sketch of velocity distributions for Ec
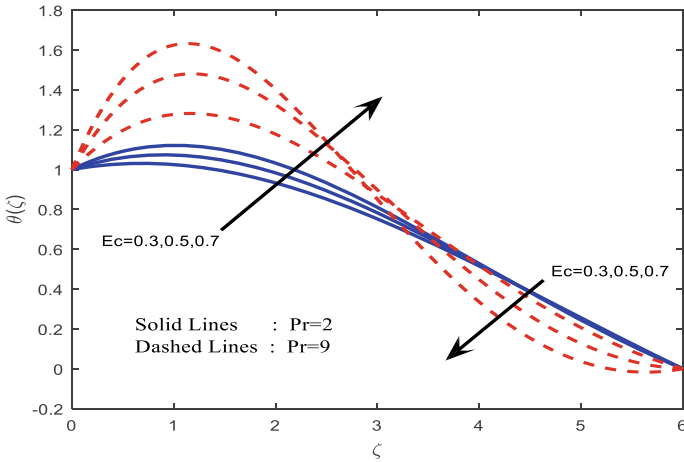
Fig. 8 Sketch of temperature distributions for Ec
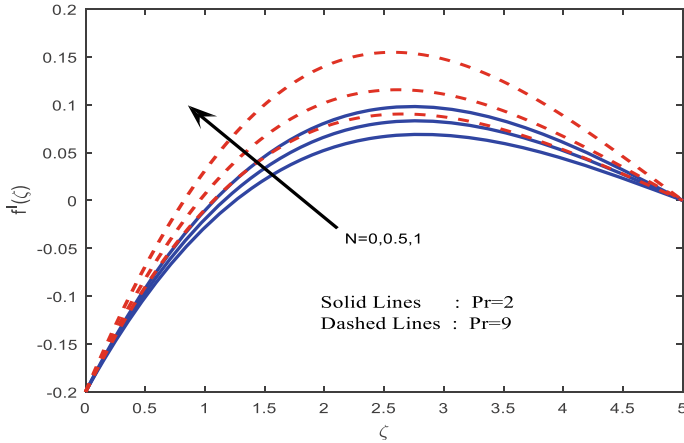
Fig. 9 Sketch of velocity distributions for N
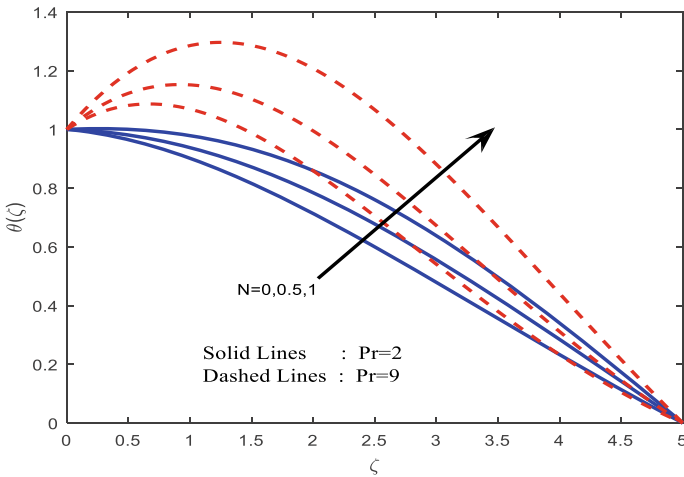
Fig. 10 Sketch of temperature distributions for N

4 Concluding Remarks

In this present study, an unsteady Casson magnetohydrodynamic is due to shrinking surface with suction and dissipation. The main conclusions are

- The magnetic field parameter decelerates the velocity for both cases of $Pr = 2$ and $Pr = 9$.
- The Casson parameter decreases in velocity and accelerates in temperature fields.
- The radiation parameter increases the heat transfer rate.
- Eckert number decelerates the Nusselt number for both $Pr = 2$ and $Pr = 9$ cases.

Table 1 Variation of heat transfer for various non-dimensional parameters for Pr = 2 and Pr = 9

R	N	Ec	$Nu\,Re^{\frac{-1}{2}}$	
			Pr = 2	Pr = 9
0.3			−0.249719	−1.062521
0.5			−0.150103	−0.871727
0.7			−0.076761	−0.750052
	0.3		−0.150103	−0.871727
	0.5		−0.282347	−1.489053
	0.7		−0.417959	−2.043019
		0	−0.062686	−0.457334
		0.5	−0.027855	−0.582397
		1	−0.025833	−0.818656

References

1. Mukhopadhyay S, De, PR, Bhattacharyya K, Layek GC (2013) Casson fluid flow over an unsteady stretching surface. Ain Shams Eng J 4(4): 933–938
2. Nadeem S, Haq RU, Lee C (2012) MHD flow of a Casson fluid over an exponentially shrinking sheet. Scientia Iranica 19(6):1550–1553
3. Zaib A, Bhattacharyya K, Uddin M, Shafie S (2016) Dual solutions of non-Newtonian Casson fluid flow and heat transfer over an exponentially permeable shrinking sheet with viscous dissipation.. 201:6968371. http://dx.doi.org/10.1155/2016/6968371
4. Elbashbeshy EMA (2001) Heat transfer over an exponentially stretching continuous surface with suction. Arch Mech 53:643–651
5. Sajid M, Hayat T (2005) Influence of thermal radiation on the boundary layer flow due to an exponentially stretching sheet. Int Commun Heat Mass Trans 35:347–356
6. Ishak A, Lok YY, Pop I (2010) Stagnation-point flow over a shrinking sheet in a micro polar fluid. Chem Eng Commun 197(11):1417–1427
7. Fang T, Zhang J (2009) Closed-form exact solutions of MHD viscous flow over a shrinking sheet. Commun Nonlinear Sci Numer Simul 14(7):2853–2857
8. Bhattacharyya K (2011) Effects of heat source/sink on MHD flow and heat transfer over a shrinking sheet with mass suction. Chem Eng Res Bull 15(1):12–17
9. Bhattacharyya K (2011) Effects of radiation and heat source/sink on unsteady MHD boundary layer flow and heat transfer over a shrinking sheet with suction/injection. Front Chem Eng China 5(3):376–384
10. Bhattacharyya K, Arif MG, Ali W (2012) Pramanik, MHD boundary layer stagnation-point flow and mass transfer over a permeable shrinking sheet with suction/blowing and chemical reaction. Acta Technica. 57(1):1–15
11. Rosali H, Ishak A, Pop I (2011) Stagnation point flow and heat transfer over a stretching/shrinking sheet in a porous medium. Int Commun Heat Mass Trans 38(8):1029–1032
12. Magyari E, Keller B (1999) Heat and mass transfer in the boundary layers on an exponentially stretching continuous surface. J Phys D Appl Phys 32:577–585
13. Partha MK, Murthy PV, Rajasekhar GP (2005) Effect of viscous dissipation on the mixed convection heat transfer from an exponentially stretching surface. Heat Mass Trans 41:360–366
14. Elbashbeshy EMA (2001) Heat transfer over an exponentially stretching continuous surface with suction. Arch Appl Mech 53:643–651

MHD Casson Fluid Flow Past a Stretching Sheet with Convective Boundary and Heat Source

K. Venkateswara Raju, P. Durga Prasad, M. C. Raju, and R. Sivaraj

Abstract In this manuscript, we investigate an electrically conducting, laminar and an incompressible 2D (two-dimensional) Casson fluid above a nonlinear permeable sheet in the occurrence of Newtonian heating and heat source. The nonlinear coupled arrangement of typical differential conditions are acquired through appropriate changes and after that figured by utilizing R-K method including shooting technique. The behaviour of dimensionless parameters is presented graphically and discussed velocity and temperature distributions along with friction aspect coefficient and rate of heat transfer concerning Nusselt number. It is discovered that the Casson and Newtonian warming parameters increase the grinding factor coefficient and heat transfer rates.

Keywords Newtonian heating · Casson fluid · MHD · Heat source parameter · Radiation parameter · Shooting technique

1 Introduction

The Navier–Stokes theory is limited, and no other constitutive condition is accessible in the literature which demonstrates the properties of non-Newtonian fluids. So, a number of non-Newtonian models have been recommended. Along these several constitutive models or equations are acquainted with concentrate their properties.

K. Venkateswara Raju (✉) · P. Durga Prasad
Department of BS&H (Mathematics), Sree Vidyanikethan Engineering College (Autonomous), Sree Sainathnagar, A.Rangampet, Tirupati, AP 517102, India
e-mail: venky.sakku@gmail.com

M. C. Raju
Department of Mathematics, J. N. T. U. A. College of Engineering Pulivendula, Pulivendula, Andhra Pradesh 516390, India

R. Sivaraj
Department of Mathematics, School of Advanced Sciences, Vellore Institute of Technology, Vellore 632014, India

The several non-Newtonian models are included and presented to study their characteristics, and also some of the diverse non-Newtonian models include visco-plastic [1], Bingham plastic [2], Oldroyd-B [3] and Walters-B [4], Brinkman type [5], power law [6], Jeffrey [7] and Maxwell [8]. There is some other model called Casson that is of past due to the maximum outstanding one. Casson within the year 1995 [9] first advanced this model for the estimation of the drift behaviour of colour oil suspensions of the printing ink type. Some fluids like slurries, food stuffs, human blood, molten plastics and artificial fibres exhibit the non-Newtonian fluid traits.

Generally, most of the non-Newtonian fluid models involve some type of adjustment to the impetus conservation equations. It has a broad range of applications in biomechanics and polymer-processing industries. Casson model at times affirmed to fit rheological data is better than the common visco-elastic model for many materials. The closed form of an exponential solution of 2D flow through a stretching sheet was examined by Crane [10]. An unsteady Casson liquid streams over extending sheet through permeable medium within the sight of sticky dissemination and heat generation by Madhusudhana Rao et al. [11]. Later on, Mustafa et al. [12] analysed an unsteady Casson fluid drift through a rough flat plate.

Most of the above studies deal with the 2D for the Casson fluid. There are rare studies available in the literature about Newtonian heating conduction that was neglected at the boundary. Merkin [13] in his creative work considers a free convection limit layer that moves through a vertical plate by considering the Newtonian heating. The convective heat transfer issues and attained solution of Newtonian heating condition are studied by Salleh et al. [15], Das et al. [16], Kasim et al. [17] and Salleh et al. [18] numerically. The magneto-hydrodynamic flow of a non-Newtonian fluid over solid sheet with heat transfer was studied by Abdul Hakeem et al. [21, 22].

The foremost principle of the present study is to scrutinize electrically conducting Casson fluid flow over a stretching sheet with the effect of heat source and Newtonian heating. The transformed ODEs are solved numerically. Also, we obtained the results with good agreement by previous papers [19, 20].

2 Mathematical Analyses

A stable 2D laminar-free convectional and incompressible progression of Casson fluid through a non-directly extending sheet is considered in an absorbed permeable medium. The consequence of uniform B_0 (magnetic field) is presumed. Due to the porous plate in which Darcy condition alone cannot be satisfied, Darcy–Brinkman slip velocity is imposed. The effects of Newtonian heating are additionally considered. A nonlinear stretching sheet alongside the $x-$ axis is assumed, the velocity $u_w(x) = cx^n$, and $y-$ direction is taken for fluid flow.

Here, c = steady parameter and n = nonlinear extending sheet factor. The impact of instigated attractive field is dismissed, in assessment with the applied magnetic field, in light of the fact that the magnetic Reynolds number is small.

The coefficient of electrically conductivity is constant. Viscous dissipation is neglected. The Joule's heating is also neglected.

Under the above assumptions, the rheological conditions are for Casson liquid (see Mukhopadhyay et al. [14]).

The limit layer conditions of 2D incompressible Casson fluid are expressed as:

$$\frac{\partial u}{\partial x} + \frac{\partial v}{\partial y} = 0 \tag{1}$$

$$\left(u\frac{\partial u}{\partial x} + v\frac{\partial u}{\partial y} \right) = v\left(1 + \frac{1}{\beta} \right)\frac{\partial^2 u}{\partial y^2} - \left(\frac{\sigma B^2(x)}{\rho} + \frac{v\phi}{K} \right)u + (g\beta_T(T - T_\infty)) \tag{2}$$

$$\left(u\frac{\partial T}{\partial x} + v\frac{\partial T}{\partial y} \right) = \alpha\left(\frac{\partial^2 T}{\partial y^2} \right) - \frac{1}{\rho c_p}\frac{\partial q_r}{\partial y} + \frac{Q_0}{\rho c_p}(T - T_\infty) \tag{3}$$

On top of mentioned equations, (u, v) = velocity component in $x-$ and $y-$ directions, respectively, v = kinematic viscosity, ρ = fluid density, σ = the electrical conductivity of the fluid, β = the Casson fluid parameter, $B(x) = B_0 x^{\frac{n-1}{2}}$ = constant magnetic strength B_0, ϕ = porosity, g = the acceleration because of gravity, β_T = the thermal buoyancy coefficient, α = the thermal diffusivity of the Casson fluid, K = the permeability of the porous medium and T = the fluid temperature.

The boundary conditions are

$$u = cx^n + N_1 v\left(1 + \frac{1}{\beta} \right)\frac{\partial u}{\partial y}, v = 0, \frac{\partial T}{\partial y} = -h_s T \text{ at } y = 0 \tag{4}$$

$$u \to 0, T \to T_\infty \text{ as } y \to \infty \tag{5}$$

Here, $N_1(x) = Nx^{-\frac{n-1}{2}}$ = velocity of slip factor that depends on x and $h_s = h_0 cx^{\frac{n-1}{2}}$ = heat transfer parameter for Newtonian fluid.

These are following similarity transformations:

$$\psi = \sqrt{\frac{2vcx^{n+1}}{n+1}}, \eta = \sqrt{\frac{(n+1)cx^{n-1}}{2v}}, \theta(\eta) = \frac{(T - T_\infty)}{T_\infty} \tag{6}$$

Here, the stream function ψ is defined with the following relationships

$$u = \frac{\partial \psi}{\partial y} \text{ and } v = -\frac{\partial \psi}{\partial x} \tag{7}$$

From these terms, continuity Eq. (1) is satisfied, also Eqs. (2)–(7) are non-dimensional system as follows:

$$\left(1 + \frac{1}{\beta}\right) f''(\eta) + f(\eta) f''(\eta) - \frac{2n}{n-1} f'(\eta)^2 - (M+K) f'(\eta) + \lambda \theta(\eta) = 0 \tag{8}$$

$$\left(1 + \frac{4}{3} R\right) \theta''(\eta) - \Gamma \theta(\eta) + \Pr f(\eta) \theta'(\eta) = 0 \tag{9}$$

The appropriate boundary conditions are as follows:

$$f'(\eta) = 1 + \delta\left(1 + \frac{1}{\beta}\right) f''(\eta), \ f(\eta) = 0, \ \theta'(\eta) = -\gamma[1 + \theta(\eta)], \ \text{at } \eta = 0$$

$$f'(\eta) = 0, \ \theta(\eta) = 0, \ \text{as } \eta \to \infty \tag{10}$$

Here, prime denotes the derivatives concerning η, and the parameters are defined as

$$M^2 = \frac{2\sigma B_0^2}{\rho(n+1)}, \ R = \frac{4\sigma^* T_\infty^3}{lk\kappa^*}, \ K = \frac{2\omega\phi x}{k(n+1)\alpha^n}, \ \mathrm{Re}_x = \frac{\alpha^{n+1}}{\nu},$$

$$G_x = \frac{2g\beta_T T_\infty x^3}{\nu^2(n+1)}, \ \mathrm{P} = \frac{\nu}{\alpha}, \ \Gamma = \frac{2Q_0 x \nu^2}{k(n+1)\alpha^n}$$

$$\gamma = h_0 \left(\frac{2\nu}{c(n+1)}\right)^{1/2}$$

$$Cf_x = \frac{\tau_w}{\rho u_w^2}, \ Nu_x = \frac{x q_w}{\alpha(T_w - T_\infty)} \tag{12}$$

where Cf_x and Nu_x are skin friction coefficient and Nusselt number which are defined as

$$\tau_w = \mu_B \left(1 + \frac{1}{\beta}\right) \frac{\partial u}{\partial x}\bigg|_{y=0}, \ q_w = -\alpha \frac{\partial T}{\partial x}\bigg|_{y=0} \tag{13}$$

Using Eq. (6) in Eq. (13), we get the skin friction coefficient and heat transfer in terms of Nusselt number

$$(\mathrm{Re})^{1/2} Cf_x \sqrt{\frac{2}{n+1}} = \left(1 + \frac{1}{\beta}\right) f''(0), \ (\mathrm{Re})^{-1/2} Nu_x \sqrt{\frac{2}{n+1}} = -\theta'(0) \tag{14}$$

3 Results and Discussion

Figures 1 and 2 elucidate the variation of temperature and velocity distributions because of increasing thermal boundary layer and momentum layer thickness for various values of radiation parameter R. Figure 7 is drawn to study the effect of magnetic field parameter (M) on the velocity profiles. It is observed that larger values of M decrease the momentum boundary layer thickness. Physically, increase in M results in boost of the Lorentz force which opposes the velocity of the fluid flow. The temperature of the fluid flow enhances with increase in magnetic field parameter M (Fig. 8).

Figure 3 exhibits the slip parameter δ on velocity distribution. It is noticed that increasing function of δ enhances momentum boundary layer thickness. Physically, the momentum boundary thickness enhances because the sheet is partly transferred to the fluid under the velocity slip δ on boundary condition. The same phenomena can be found in velocity and temperature profiles which are observed for the effect of Newtonian heating γ as presented in Figs. 4 and 5.

Figure 6 indicates the value of K on velocity distribution. From this, noticed that different values of permeability parameter K reduce the fluid velocity. Generally, the permeability expands opposition to permeable which tended to diminish in velocity of the fluid. Then again, the fluid velocity improves with enhanced K. Figure 11 depicts the thermal buoyancy parameter λ on velocity distributions. The thickness of momentum boundary layer was enhanced with increase in buoyancy parameter λ.
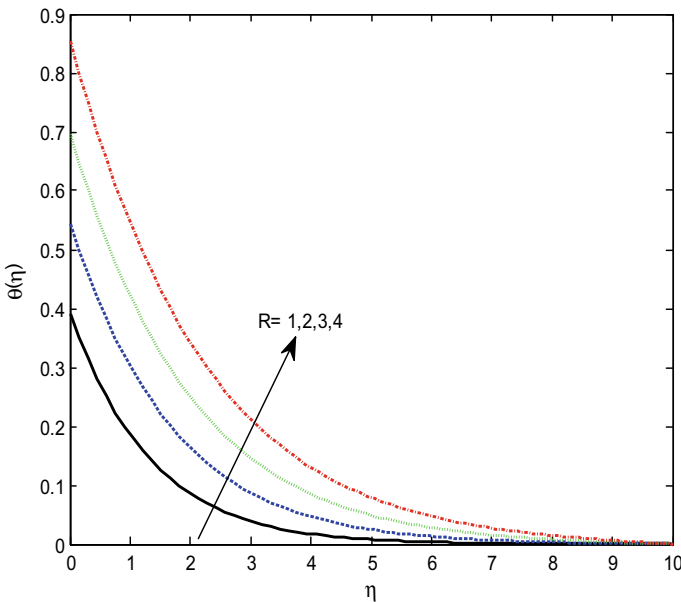
Fig. 1 Impact of R on temperature
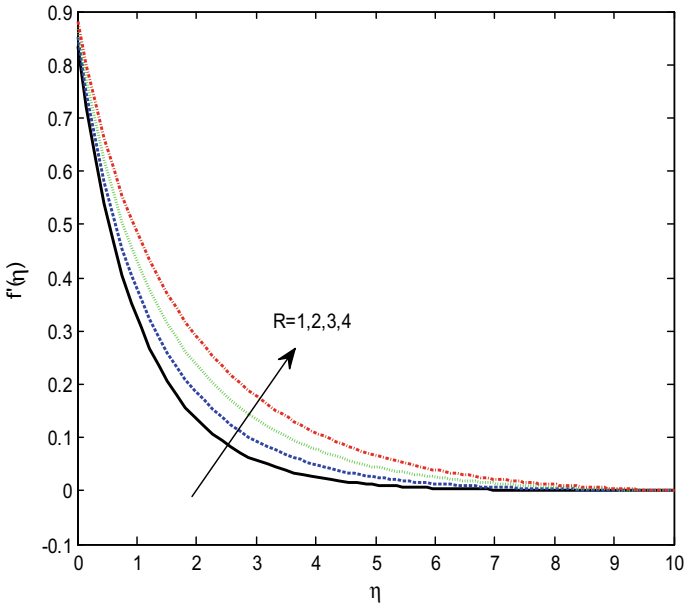
Fig. 2 Impact of R on velocity
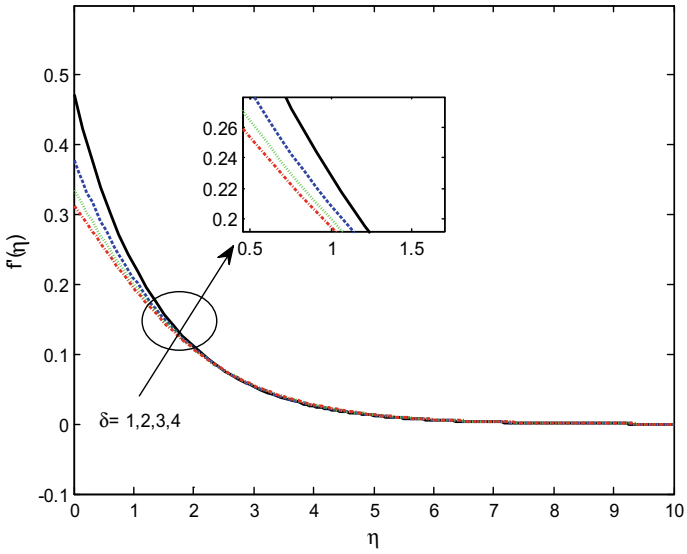
Fig. 3 Impact of δ on velocity

Fig. 4 Impact of γ on velocity

Fig. 5 Impact of γ on temperature
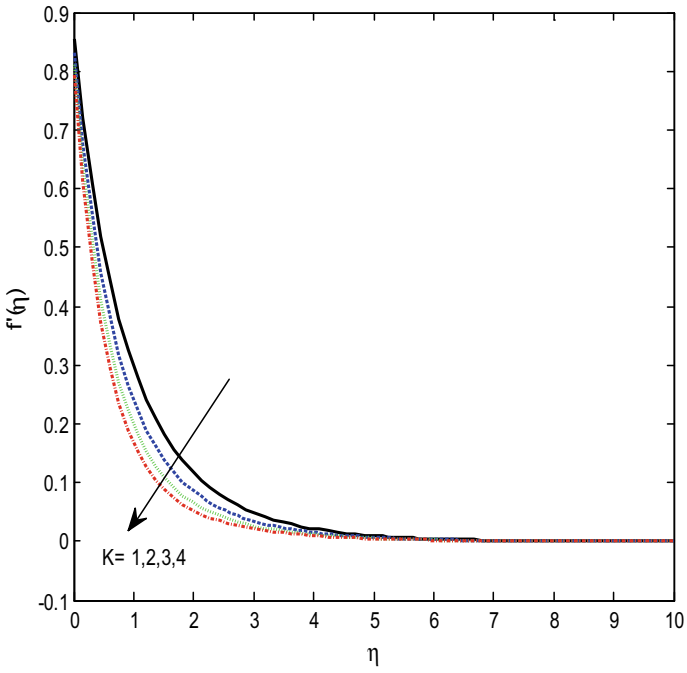
Fig. 6 Impact of K on velocity
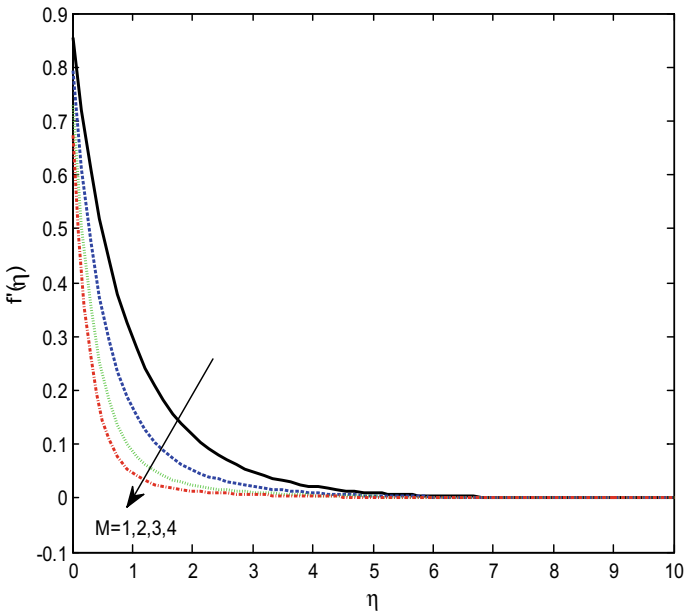
Fig. 7 Impact of M on velocity
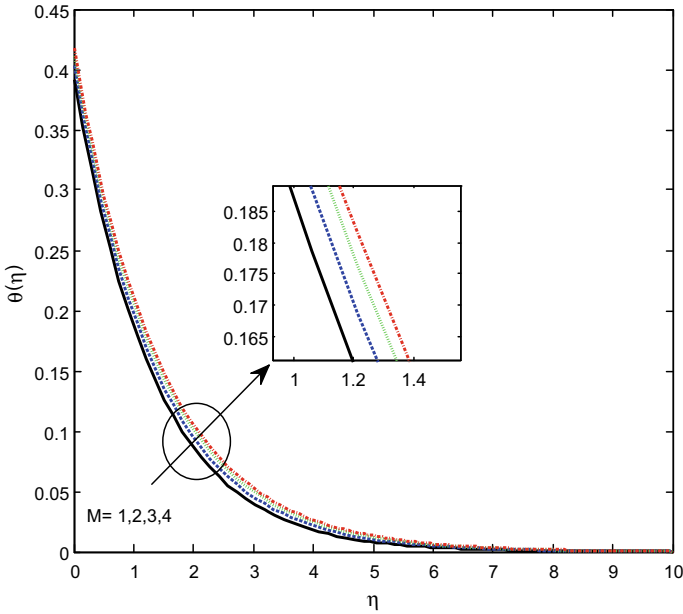
Fig. 8 Impact of M on temperature

The elucidation for this occurrence is that thermal buoyancy parameter λ is explained as the ratio of buoyancy to viscous forces in the boundary layer. For that reason, an increase in its values reduces the viscosity of the fluid and results in increasing the flow velocity and also the momentum boundary layer thickness (Fig. 11).

Figures 9 and 10 illustrate that temperature decreases with rise in heat source parameter Γ and also found that thermal boundary layer thickness decreases. The same phenomena are observed in velocity profiles (Fig. 10). Finally, Fig. 12 displays that the velocity of the fluid flow decreases with increase in β. Actually, with the increase in β, the fluid becomes more viscous and results in the reduction of fluid velocity. The momentum boundary layer thickness decreases as β increases.

Table 1 presents the values of skin friction coefficient sundry values of n. The present results are compared with the results published by Cortell [19] and Khan et al. [20].

From Table 2, we observe that Casson parameter, Newtonian heating parameter and slip parameter enhance the friction rate and heat transfer rate and decrease the Prandtl number and heat source parameter.

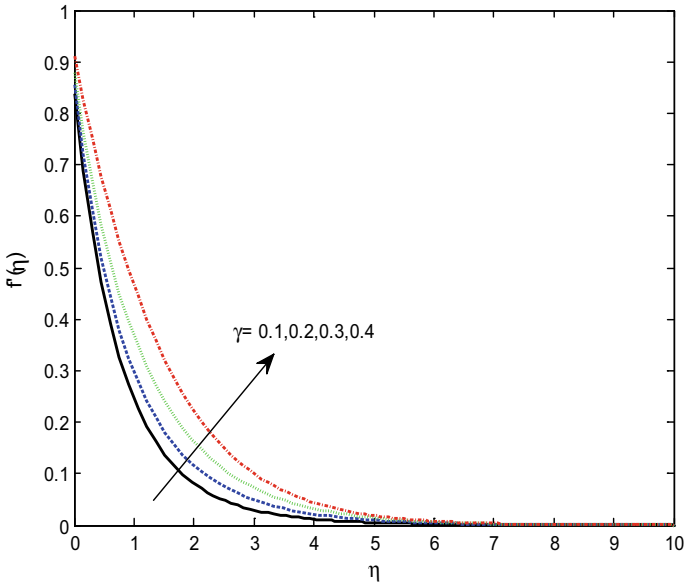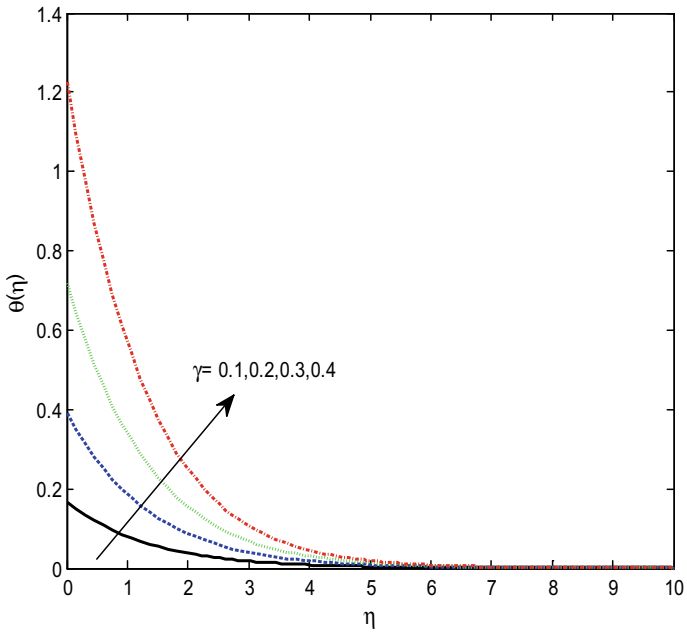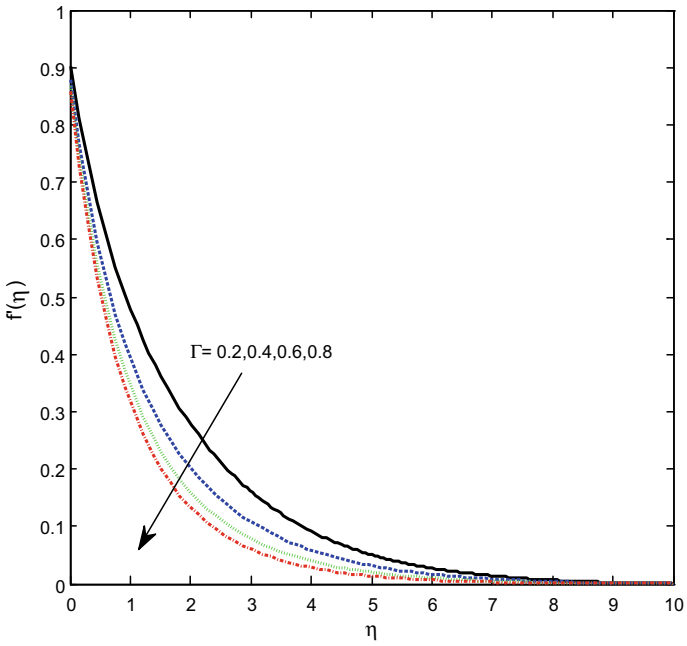**Fig. 9** Impact of Γ on velocity
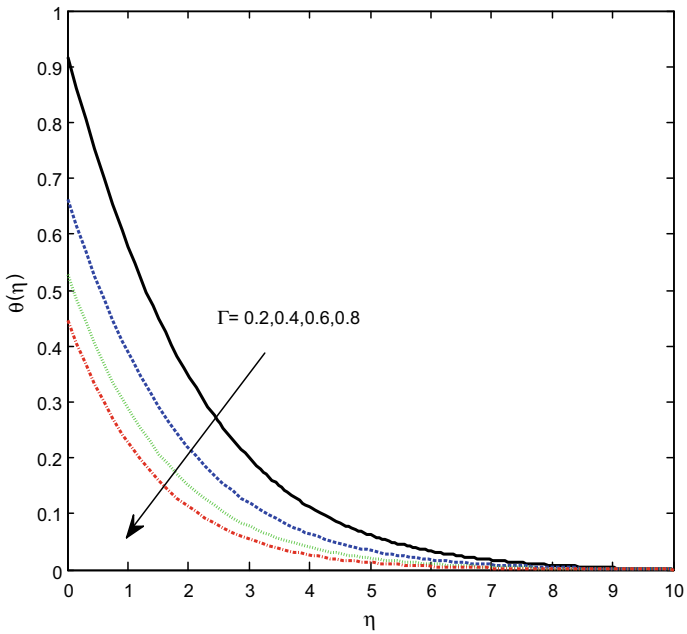
Fig. 10 Impact of Γ on temperature
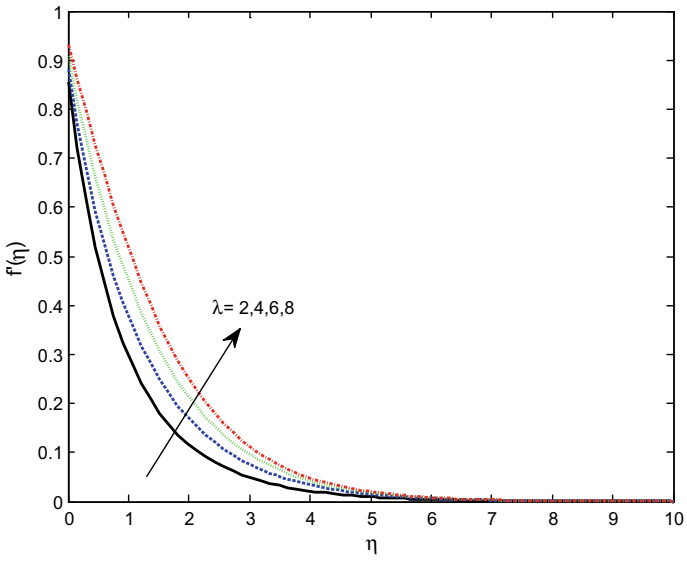
Fig. 11 Impact of λ on velocity
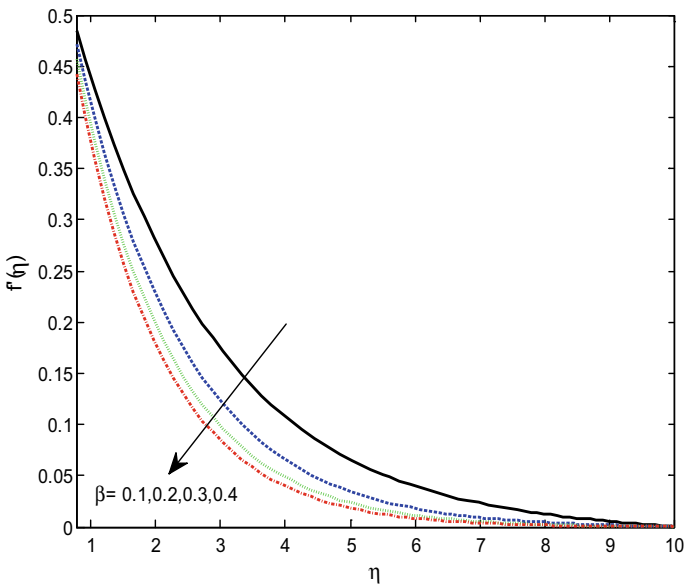
Fig. 12 Impact of β on velocity

Table 1 Validation of the results of $-f''(0)$ for different values of n with $\beta, n, \gamma, M, \delta, \Gamma, \lambda, R, \mathrm{Pr}, K$ $\quad \beta = 10^8, \mathrm{Pr} = 0.7$

$-f''(0)$			
n	Cortell [19]	Khan et al. [20]	Present
0	0.627547	0.6276	0.628316
0.2	0.766758	0.7688	0.767489
0.5	0.889477	0.8896	0.890104
1	1.0	1.0	1.000483
3	1.148588	1.1486	1.148986
10	1.234857	1.2349	1.235221
100	1.276768	1.2768	1.277099

Table 2 Variation of skin friction and Nusselt number for some physical parameters

β	n	γ	M	δ	Γ	λ	R	Pr	K	$\left(1+\frac{1}{\beta}\right)f''(0)$	$-\theta'(0)$
0.2	0.1	0.5	0.2	0.1	0.5	0.3	0.5	0.7	0.7	-1.029369	1.882582
0.4										-0.870118	1.890705
	0.3									-0.974931	1.919432
	0.6									-1.072269	1.946776
		0.1								-1.342030	0.117821
		0.2								-1.294194	0.286377
			0.5							-0.990239	1.931152
			1.0							-1.344439	2.059114
				0.2						-0.726936	1.940264
				0.4						-0.547104	2.007739
					0.1					-2.284116	-1.109584
					0.2					-2.684437	-1.796760
						0.5				-0.596552	1.815960
						1.0				-0.026888	1.689984
							0.1			-1.122247	1.280494
							0.2			-1.070871	1.405781

4 Conclusions

In the present investigation, the numerical solutions of magneto-hydrodynamic fluid flow of Casson fluid are over nonlinearly stretching sheet in the presence of Newtonian heating and velocity slip. The coupled nonlinear PDEs are transformed into ODE by using appropriate transformations and solved numerically by shooting technique. The following main conclusions are:

- The Casson fluid parameter enhances the friction factor coefficient and Nusselt number.
- Newtonian heating parameter and slip parameter motivate the skin friction and Nusselt number.
- The heat source parameter and Prandtl number decelerate heat transfer rate.
- The magnetic field parameter decreases the friction factor coefficient.

References

1. Hassan MA, Pathak M, Khan MK (2013) Natural convection of visco-plastic fluids ina square enclosure. J Heat Trans 135:122501–122512
2. Kleppe J, Marner WJ (1972) Transient free convection in a Bingham plastic on a vertical flat plate. J Heat Trans 94:371–376
3. Khan I, Fakhar K, Anwar MI (2012) Hydromagnetic rotating flows of an Oldroyd-B fluid in a porous medium. Spec Topics Rev Porous Media Int J 3(1):89–95
4. Khan I, Farhad A, Sharidan S, Qasim M (2014) Unsteady free convection flow in a Walters-B fluid and heat transfer analysis. Bull Malaysian Mathe Sci Soc 37:437–448
5. Zakaria MN, Hussanan A, Khan I, Shafie S (2013) The effects of radiation on free convection flow with ramped wall temperature in Brinkman type fluid. Jurnal Teknologi 62(3):33–39
6. Olajuwon BI (2009) Flow and natural convection heat transfer in a power law fluid past a vertical plate with heat generation. Int J Nonlinear Sci 7:50–56
7. Qasim M (2013) Heat and mass transfer in a Jeffrey fluid over a stretching sheet with heat source/sink. Alexandria Eng J 52:571–575
8. Khan I, Ali F, Shafie S (2013) Exact Solutions for Unsteady Magnetohydrodynamic oscillatory flow of a maxwell fluid in a porous medium. Zeitschrift für Naturforschung A 68(10–11):635–645
9. Casson N (1959) A flow equation for pigment oil suspensions of the printing ink type In: Mill CC (ed) Rheology of disperse systems. Pergamon Press Oxford, pp 84–102
10. Crane LJ (1970) Flow past a stretching plate. J Appl Mathe Phys 21:645–647
11. Madhusudhana Rao B, Durga Prasad P, Senthil Dhanasekar N, Varma SVK (2017) Unsteady Casson fluid flow over stretching sheet through porous medium with heat generation and viscous dissipation. J Ultra Sci Phys Sci B 29:325–336
12. Mustafa M, Hayat T, Pop I, Aziz A (2011) Unsteady boundary layer flow of a Casson fluid due to an impulsively started moving flat plate. Heat Trans-Asian Res 40:553–576
13. Merkin JH (1994) Natural convection boundary layer flow on a vertical surface with Newtonian Heating. Int J Heat Fluid Flow 15:392–398
14. Mukhopadhyay S, Bhattacharyya K, Hayat T (2013) Exact solutions for the flow of Casson fluid over a stretching surface with transpiration and heat transfer effects. Chinese Phys B 22(11):114701-6
15. Salleh MZ, Nazar R, Arifin NM, Pop I, Merkin JH (2011) Forced-convection heat transfer over a circular cylinder with Newtonian heating. J Eng Mathe 69(1):101–110
16. Das S, Mandal C, Jana RN (2012) Radiation effects on unsteady free convection flow past a vertical plate with Newtonian heating. Int J Comput Appl 41:36–41
17. Abdul Rahman Mohd Kasim, Mohammad NF, Sharidan S (2012) Natural convection boundary layer flow of a visco elastic fluid on solid sphere with Newtonian heating. World Acad Sci Eng Technol 64: 628-633
18. Salleh MZ, Nazar R, Pop I (2010) Boundary layer flow and heat transfer over a stretching sheet with Newtonian heating. J Taiwan Inst Chem Eng 41:651–655
19. Cortell R (2007) Viscous flow and heat transfer over a nonlinearly stretching sheet. Appl Mathe Comput 184:864–873

20. Ullah I, Shafie S, Khan I (2017) Effects of slip condition and Newtonian heating on MHD flow of Casson fluid over a nonlinearly stretching sheet saturated in a porous medium. J King Saud Univ Sci 29(2):250–259
21. AbdulHakeem AK, Renuka P, VishnuGanesh N, Kalaivanan R, Ganga B (2016) Influence of inclined Lorentz forces on boundary layer flow of Casson fluid over an impermeable stretching sheet with heat transfer. J Magn Magn Mater 401:354–361
22. Abdul Hakeem AK, Govindaraju M, Ganga B, Kayalvizhi M (2016) Second law analysis for radiative MHD slip flow of a nano fluid over a stretching sheet with non-uniform heat source effect Scientia Iranica F 23:1524–1538

Physical Significance of Rotation and Hall Current Effects on Hemodynamic Physiological Jeffery Fluid with Porous Medium Through a Tapered Channel

R. Sivaiah, S. Ravikumar, R. Hemadri Reddy, J. Suresh Goud, and R. Saravana

Abstract The aim of this research is to analyze the rotation and hall current effects on hemodynamic physiological Jeffery fluid through a tapered channel with porous medium. The pressure rise, velocity, pressure gradient, and frictional force are discussed analytically. An influence of varied governing parameters was illustrated diagrammatically with a set of figures. We identified that as we increase the rotation parameters, the velocity decreases. The velocity of the fluid enhances when we increase hall current parameter. We observed an increase in pumping rate in the retrograde pumping zone, the peristaltic pumping zone, the free pumping zone, and the co-pumping zone, pumping rate decreases when $\overline{Q} > 3$ by an increase in rotation parameter.

Keywords Rotation · Hall current · Porous medium · Tapered channel

1 Introduction

Peristalsis can be a radially symmetrical and relaxed muscle that spreads in an antegrade manner in the form of waves passing through a muscle tube. In humans, peristaltic movement occurs at intervals and smooth muscles contract to push the contents through the gastrointestinal tract. Similar mechanisms are used to promote the movement.

R. Sivaiah · R. Hemadri Reddy (✉)
Department of Mathematics, School of Advanced Sciences, VIT, Vellore 632014, India
e-mail: rhreddy@vit.ac.in

S. Ravikumar
NBKR Institute of Science & Technology (Autonomous), Vidyanagar, Nellore 524413, India

J. Suresh Goud
Institute of Aeronautical Engineering (Autonomous), Dundigal, Hyderabad 500043, India

R. Saravana
Madanapalle Institute of Technology & Science, Madanapalle 517325, India

To our knowledge, the physical effects of Hall current and rotation on the hemo-dynamic physiological Jeffery fluid in porous media through a channel have not been investigated earlier. Past few decades, a good diversity of researchers consummates blood flow through various channels. The literature of biomathematics has provided with an enormous variety of applications in drugs and biology. Peristalsis has monumental applications in medical anatomy. In that, it is concerned with the motion of food material, the propulsion of food bolus within the passage, conversion of food bolus into nutrient within the abdomen, and movement of nutrient within the bowel. Mahmud [1] experimented with the rotation and magnetic field through the porous media in the tube. Ajax Ahmed Dar and Elangovan [2] investigated a magnetic field influenced peristaltic flow of Micropolar fluid in the inclined channel. In another paper, AB-Ala and Abo Dahab [3] reviewed the rotation of the peristaltic transparency of the Jeffrey fluid in a gravitationally charged asymmetry. Abd-Alla et al. [4] studied the effect of rotation on the peristaltic flow of a micropolar fluid through a medium with an external magnetic field. A mathematical model on heat transfer on the MHD peristaltic rotary flow of a Jeffrey fluid in an asymmetric channel is discussed by Gnaneswara Reddy [5]. Hayat et al. [6] reported the influence of Hall current and Joule heating on creep of viscous fluid in a rotating channel with convective boundary conditions. The combined effects of the rotation and thermal radiation of transport in the peristaltic transport of Jeffrey fluid has been studied by Hayat et al. [7]. Few relevant studies may be seen in attempts [8–11]. Very recently, Saravana et al. [12] investigated the heat transfer effects on peristaltic flow of Rabinowitsch fluid in an inclined channel.

2 Formulation for the Problem

Considering the physiological Jeffrey fluid model in a non-uniform inclined two-dimensional vertical tapered channel with the influence of radiation and hall current. There is a tendency to assume that the fluid has transverse magnetic field B_0. Along the channel, fluid is tending to move as a sine wave with a constant velocity c.

The wall geometry is

$$y = H_1(x, t) = -b - m'x - d \sin\left[\frac{2\pi}{\lambda}(x - ct) + \phi\right] \tag{1}$$

$$y = H_2(x, t) = b + m'x + d \sin\left[\frac{2\pi}{\lambda}(x - ct)\right] \tag{2}$$

In the equations, d, c, b are the wave amplitude of the peristaltic wave, wave velocity, mean half-width of the channel, m' is dimensional non-uniform parameter, wavelength λ, time t, ϕ is the phase variance, and x is the direction of wave propagation (Fig. 1).

The governing equations are

Fig. 1 Physical model
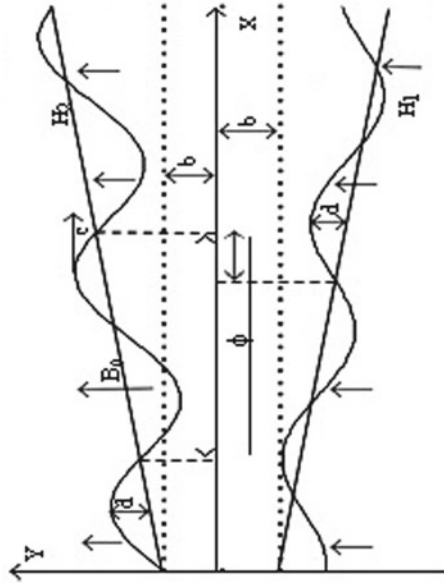
$$\left(\frac{\partial u}{\partial x} + \frac{\partial v}{\partial y}\right) = 0 \tag{3}$$

$$\rho\left(u\frac{\partial u}{\partial x} + v\frac{\partial u}{\partial y}\right) - \rho\left(\Omega^2 u + 2\Omega\frac{\partial v}{\partial t}\right) = -\frac{\partial p}{\partial x} + \frac{\partial}{\partial x}(S_{xx}) + \frac{\partial}{\partial y}(S_{xy})$$

$$+ \frac{\sigma B_0^2}{1 + m^2}(mv - (u + c))$$

$$- \frac{\mu}{k_1}(u + c) \tag{4}$$

$$\rho\left(u\frac{\partial v}{\partial x} + v\frac{\partial v}{\partial y}\right) + \rho\left(-\Omega^2 v + 2\Omega\frac{\partial u}{\partial t}\right) = -\frac{\partial p}{\partial x} + \frac{\partial}{\partial x}(S_{xy}) + \frac{\partial}{\partial y}(S_{yy})$$

$$- \frac{\sigma B_0^2}{1 + m^2}(m(u + c) + v) \tag{5}$$

where u and v are the velocity components in x and y directions, fluid pressure p, time t, the coefficient of the viscosity of the fluid μ, density of the fluid ρ, m the Hall current parameter, and Ω rotation parameter.

$$S_{xx} = \frac{2\mu}{1 + \lambda_1}\left(1 + \lambda_2\left(u\frac{\partial}{\partial x} + v\frac{\partial}{\partial y}\right)\right)\frac{\partial u}{\partial x}$$

$$S_{xy} = \frac{\mu}{1 + \lambda_1}\left(1 + \lambda_2\left(u\frac{\partial}{\partial x} + v\frac{\partial}{\partial y}\right)\right)\left(\frac{\partial u}{\partial y} + \frac{\partial v}{\partial x}\right)$$

$$S_{yy} = \frac{2\mu}{1 + \lambda_1}\left(1 + \lambda_2\left(u\frac{\partial}{\partial x} + v\frac{\partial}{\partial y}\right)\right)\frac{\partial v}{\partial y}$$

The non-dimensional quantities are

$$\left.\begin{array}{l}\bar{x} = \dfrac{x}{\lambda}, \bar{y} = \dfrac{y}{b}, \bar{t} = \dfrac{ct}{\lambda}, \bar{u} = \dfrac{u}{c}, \varepsilon = \dfrac{d}{b}, \bar{v} = \dfrac{v}{c\delta}, h_1 = \dfrac{H_1}{b}, \\[3mm] h_2 = \dfrac{H_2}{b}, \bar{p} = \dfrac{b^2\rho}{c\lambda\mu}, \delta = \dfrac{b}{\lambda}, \mathrm{Re} = \dfrac{\rho cb}{\mu}, M = B_0 d\sqrt{\dfrac{\sigma}{\mu}}, Da = \dfrac{k_1}{b^2}\end{array}\right\} \quad (6)$$

where the dimensionless amplitude of channel is $\epsilon = \frac{d}{b}$, Reynolds number Re, wave number $\delta = \frac{b}{\lambda}$, and Hartmann number M.

3   Solution of the Problem

Using the dimensionless values (6), after discarding the bars, Eqs. (3–5) are simplified to the following dimensionless form.

$$\delta\left(\frac{\partial u}{\partial x} + \frac{\partial v}{\partial y}\right) = 0 \tag{7}$$

$$\mathrm{Re}\delta\left(u\frac{\partial u}{\partial x} + v\frac{\partial v}{\partial y}\right) - \frac{\rho b^2 \Omega^2}{\mu}u - 2\mathrm{Re}\delta^2\Omega\frac{\partial v}{\partial t} = -\frac{\partial p}{\partial x} + \delta\frac{\partial}{\partial x}(S_{xx}) + \frac{\partial}{\partial y}(S_{xy})$$

$$+ \frac{M^2}{1 + m^2}(m\delta v - (u + 1)) - \frac{1}{Da}u - \frac{1}{Da} \tag{8}$$

$$Re\,\delta^3\left(u\frac{\partial v}{\partial x} + v\frac{\partial v}{\partial y}\right) - \frac{\rho\Omega^2 b^2\delta^2}{\mu}v + 2\mathrm{Re}\Omega\delta^2\frac{\partial u}{\partial t} = -\frac{\partial p}{\partial y} + \delta^2\frac{\partial S_{xy}}{\partial x} + \delta\frac{\partial S_{yy}}{\partial y}$$

$$- \frac{\delta M^2}{1 + m^2}(m(u + 1) + \delta v) \tag{9}$$

where

$$S_{xx} = \frac{2\delta}{1 + \lambda_1}\left(1 + \frac{\lambda_2\delta c}{d}\left(u\frac{\partial}{\partial x} + v\frac{\partial}{\partial y}\right)\right)\frac{\partial u}{\partial x}$$

$$S_{yy} = \frac{2\delta}{1 + \lambda_1}\left(1 + \frac{\lambda_2\delta c}{d}\left(u\frac{\partial}{\partial x} + v\frac{\partial}{\partial y}\right)\right)\frac{\partial v}{\partial y}$$

$$S_{xy} = \frac{1}{1 + \lambda_1}\left(1 + \frac{\lambda_2\delta c}{d}\left(u\frac{\partial}{\partial x} + v\frac{\partial}{\partial y}\right)\right)\left(\frac{\partial u}{\partial y} + \delta^2\frac{\partial v}{\partial x}\right)$$

Applying long-wavelength and low Reynolds number approximations. Equations (7–9) becomes

$$\frac{\partial^2 u}{\partial y^2} - A(1 + \lambda_1)u = \frac{dp}{dx} + B(1 + \lambda_1) \tag{10}$$

$$\frac{\partial p}{\partial y} = 0 \tag{11}$$

where

$$A = \left(\frac{M^2}{1 + m^2} + \frac{1}{Da} - \frac{\rho \, \Omega^2 b^2}{\mu} \right) \quad B = \left(\frac{M^2}{1 + m^2} + \frac{1}{Da} \right)$$

The dimensionless boundary conditions

$$u = -1 \text{ at } y = h_1 = -1 - k_2 x - \varepsilon \sin[2\pi(x - t) + \phi] \tag{12}$$

$$u = -1 \text{ at } y = h_2 = 1 + k_2 x + \varepsilon \sin[2\pi(x - t)] \tag{13}$$

Solving Eqs. (10 and 11) with boundary conditions (12 and 13)

$$u = H \, \sinh[\alpha y] + G \, \cosh[\alpha y] - pn_1 - n_2 \tag{14}$$

where

$$H = \left(\frac{G(\cosh[\alpha h_2] - \cosh[\alpha h_1])}{(\sinh[\alpha h_2] - \sinh[\alpha h_1])} \right) G = \left(\frac{(n_2 - 1) + pn_1}{F} \right)$$

$$n_1 = \left(\frac{1}{A(1 + \lambda_1)} \right) n_2 = \left(\frac{B}{A} \right)$$

$$F = \left(\frac{(\cosh[\alpha h_2] - \cosh[\alpha h_1])}{(\sinh[\alpha h_2] - \sinh[\alpha h_1])} \right) \sinh[\alpha h_1] + \cosh[\alpha h_1] \quad \alpha = \sqrt{A(1 + \lambda_1)}$$

The flow rate

$$q = \int_{h_2}^{h_1} u \, dy$$

$$= \int_{h_2}^{h_1} (H \, \sinh[\alpha y] + G \, \cosh[\alpha y] - pn_1 - n_2) dy = n_7 + pn_8 \tag{15}$$

where $n_3 = \left(\frac{\cosh[\alpha h_1] - \cosh[\alpha h_2]}{\alpha}\right)$ $n_4 = \left(\frac{\sinh[\alpha h_1] - \cosh[\alpha h_2]}{\alpha}\right)$ $n_5 = n_1(h_1 - h_2)$ $n_6 = n_2(h_1 - h_2)$ $n_7 = \left(\frac{(n_2-1)}{F}\left(\frac{\cosh[\alpha h_2] - \cosh[\alpha h_1]}{\sinh[\alpha h_1] - \cosh[\alpha h_2]}\right)n_3 + \left(\frac{(n_2-1)}{F}\right)n_4 - n_6\right)$ $n_8 = \left(\frac{(n_1 n_3)}{F}\left(\frac{\cosh[\alpha h_2] - \cosh[\alpha h_1]}{\sinh[\alpha h_1] - \cosh[\alpha h_2]}\right) + \left(\frac{(n_4 n_1)}{F}\right) - n_5\right)$

The pressure gradient that comes from Eq. (15)

$$\frac{dp}{dx} = \frac{q - n_7}{n_8} \tag{16}$$

The flux is

$$Q = \int_{h_2}^{h_1} (u + 1)dy = q + c(h_1 - h_2) \tag{17}$$

The average flow rate is

$$\bar{Q} = \frac{1}{T}\int_0^T Q\,dt = q + 1 + d \tag{18}$$

The pressure gradient by solving the Eqs. (16) and (18)

$$\frac{dp}{dx} = \left(\frac{(\bar{Q} - 1 - d) - n_7}{n_8}\right) \tag{19}$$

4 Discussion of the Problem

The motivation behind the study has been to analyze the rotation and Hall current effects on hemodynamic physiological Jeffery fluid with porous medium through a tapered channel. We used Mathematica software to find out numerical results. The following default parameter values are adopted for computations: $t = 0.4$, $x = 0.6$, $k_2 = 0.1$, $\varepsilon = 0.2$, $\phi = \frac{\pi}{6}$, $\Omega = 0.5$, $\rho = 1$, $\mu = 0.5$, $\lambda_1 = 1.5$, $Da = 0.1$, $M = 3$, $m = 1.5$, $b = 0.4$, $d = 2$.

4.1 Velocity Distribution

Figures 2, 3, 4, and 5 focus on changes in the velocity distribution for Hall current parameters (m), porosity parameters (Da), rotation parameters (Ω), and Jeffery fluid parameters (λ_1). Different values of hall current parameter (m) are plotted in Fig. (2), and it is stated that as increasing the Hall current parameter, the velocity of blood flow fluid increases. The purpose of Fig. (3) is to discuss the different values of

Fig. 2 Effect of *m* on *u*
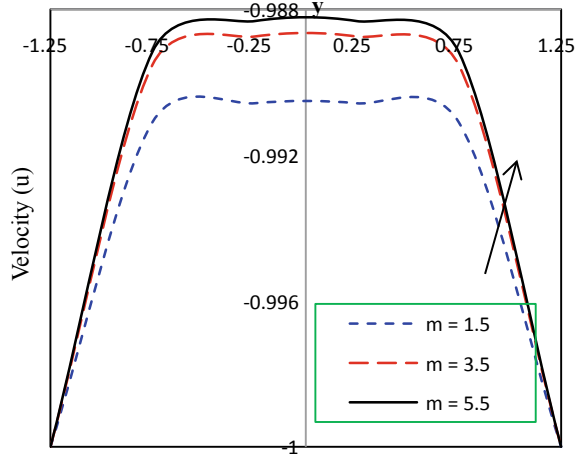
Fig. 3 Effect of *Da* on *u*
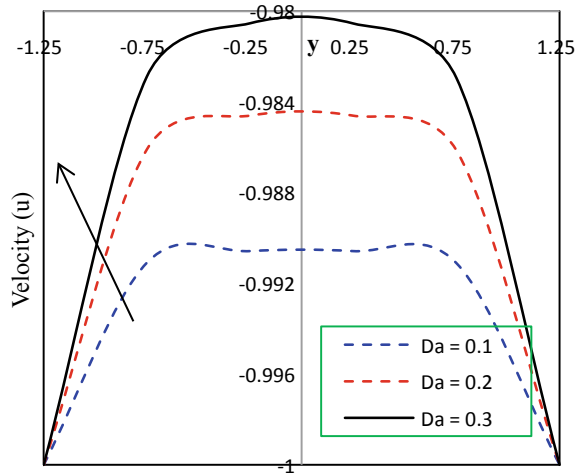
the porosity parameters in the velocity distribution. It shows that the velocity of the blood flow fluid increases as the porosity parameter increases. The impact of the rotation parameter (Ω) on the velocity distribution is exhibited in Fig. (4). Graphical results indicate that the velocity of the liquid decreases when the rotation parameter increases. The influence of the Jeffery fluid parameter (λ_1) on the velocity of the distribution is shown in Fig. (5). It is noticed that the velocity of the blood flow fluid deteriorates as the Jeffery fluid parameter is increased. Therefore, from these graphs, we finalized that the velocity of the blood fluid gains by an increase in the hall current parameter and the porosity parameter, while we observe that the opposite behavior when the parameter of rotation and the Jeffery fluid parameter increases.

Fig. 4 Impact of Ω on u
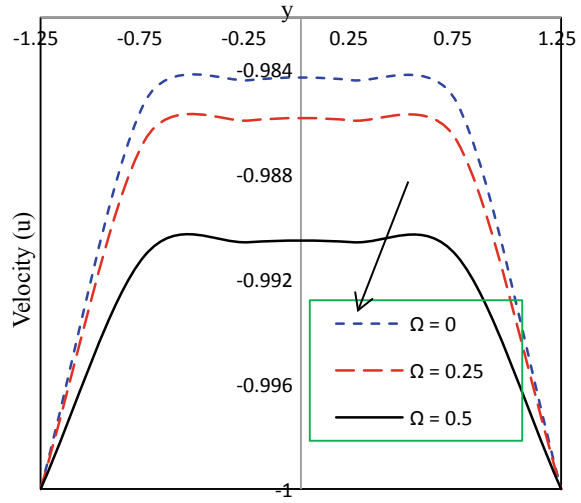
Fig. 5 Impact of λ_1 on u
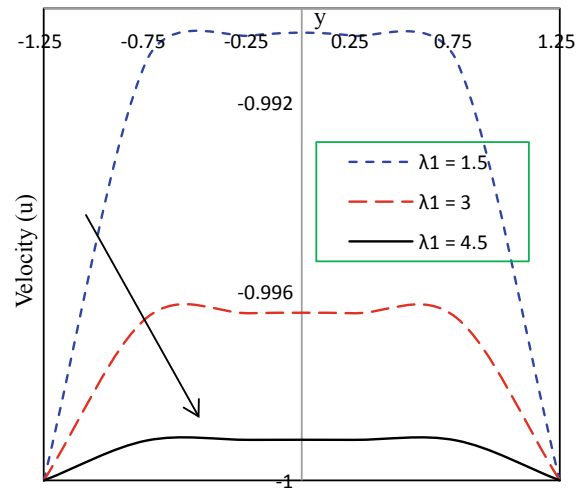
4.2 Pressure Rise

Impact of pressure rise with different parameters is presented in the Figs. 6, 7, 8, 9, and 10. Moreover, these figures are divided into three zones, which are defined as the pumping region $\Delta p > 0$, co-pumping region $\Delta p < 0$, and free pumping region $\Delta p = 0$. The aim of the Fig. (6) was to discuss the pressure rise for different values of porosity parameter. It is observed that the pumping rate reduces in retrograde pumping zone and in the peristaltic pumping region also while the pumping curves coincide at free pumping zone and enhance the pumping rate in the co-pumping

Fig. 6 Effect of *Da* on pressure rise (Δp)
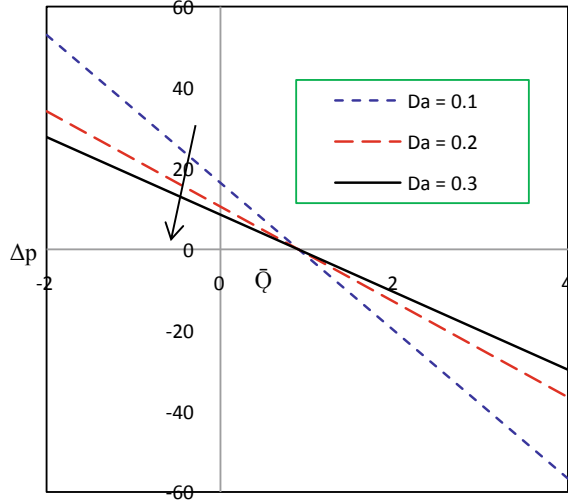
Fig. 7 Effect of λ_1 on pressure rise (Δp)
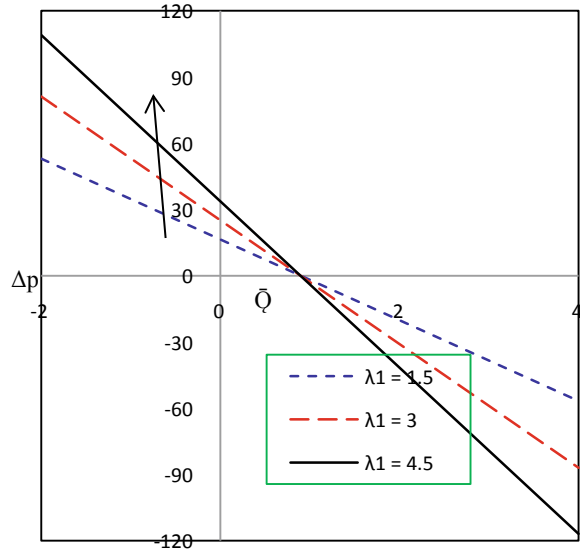
zone with the porosity parameter increases. The effect of Jeffery fluid parameters on pressure rise is shown in Fig. (7). We see from this graph that the pumping rate enhances in both peristaltic and retrograde pumping zone while the pumping rate gradually diminishes in the co-pumping region with increase in Jeffery fluid parameter ($\lambda_1 = 1.5, 3, 4.5$). Figure (8) exhibits the variation of hall current parameter on pressure rise. This graph shows that the pressure rate diminishes in both retrograde and peristaltic pumping region, while the pumping curves coincide at free pumping

Fig. 8 Impact of *m* on Δp
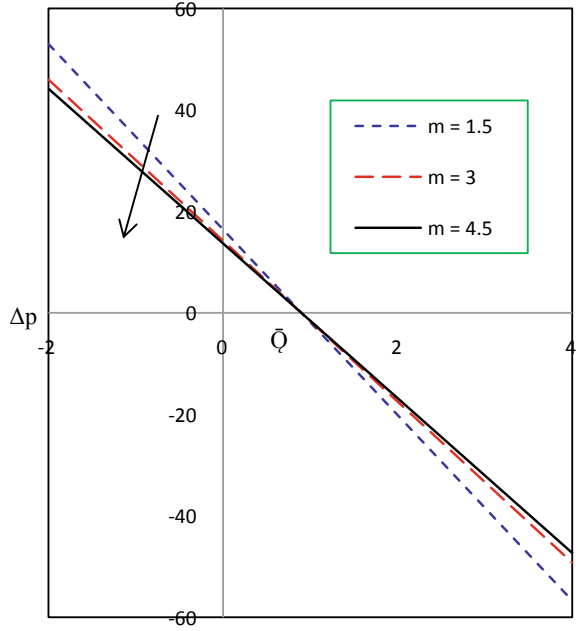
Fig. 9 Impact of *M* on Δp
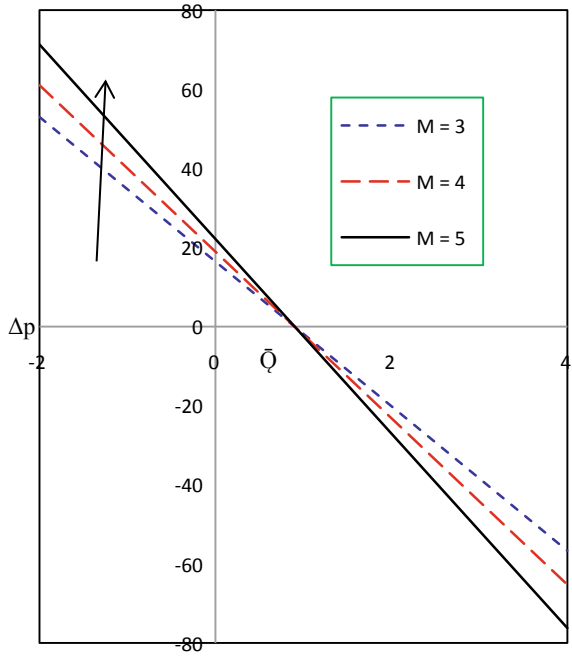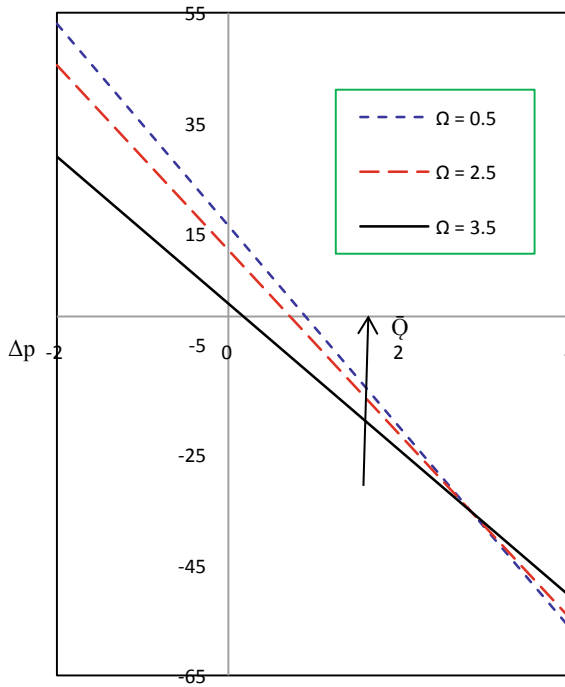
Fig. 10 Impact of Ω on Δp

zone and improves the pumping rate in the co-pumping zone by increase in hall current parameter ($m = 1.5, 3, 4.5$). From Fig. (8), we conclude that the pumping rate is not significant in the entire three regions; this is due to the impact of Hall current parameter. Figures (9) indicate that the pumping rate enhances in peristaltic pumping and retrograde region though the pumping rate gradually reduces in the co-pumping region with Hartmann number increases. Figure (10) is presented for various values of rotation parameter on pressure rise. It is identified that the pumping rate enhances in retrograde, peristaltic, and also in the free pumping zone and pumping rate decreases in the co-pumping zone when $\overline{Q} > 3$ by increase in rotation parameter.

4.3 Frictional Force

Figures (11, 12, 13, 14 and 15) describe the changes in the friction force F with flux for different parameters of interest. Friction forces behave opposite to the increase in pressure.

Fig. 11 Effect of *Da* on frictional force (*F*)
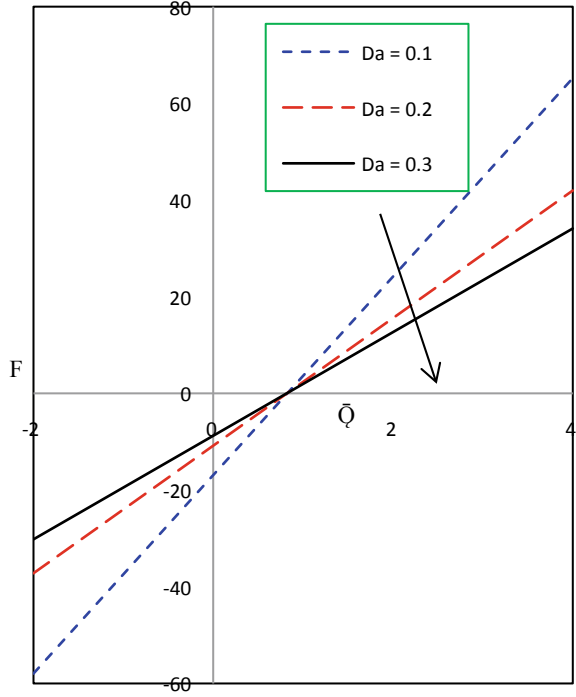
Fig. 12 Impact of λ_1 on frictional force (*F*)
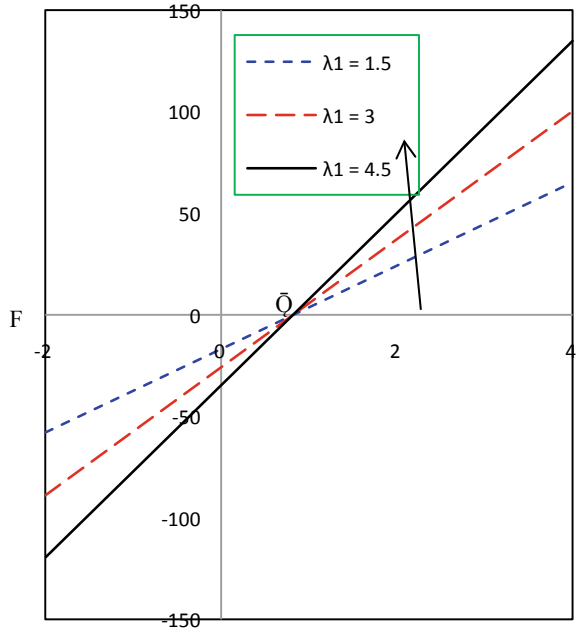
Fig. 13 Effect of *m* on frictional force (*F*)
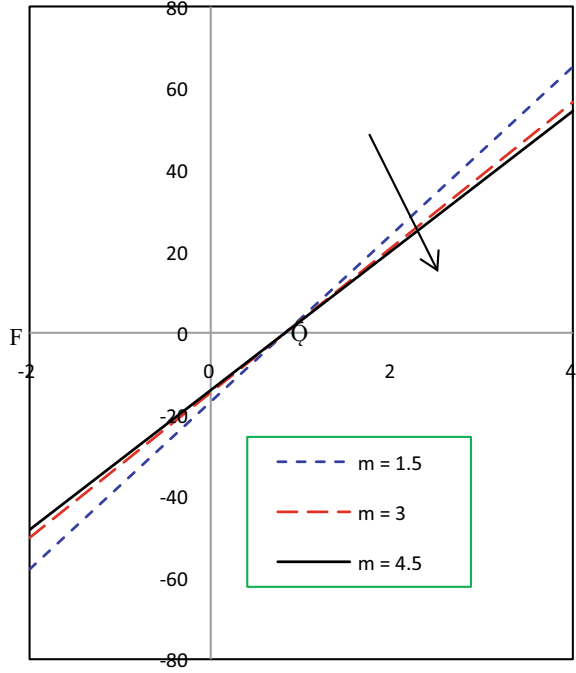
Fig. 14 Impact of *M* on frictional force (*F*)
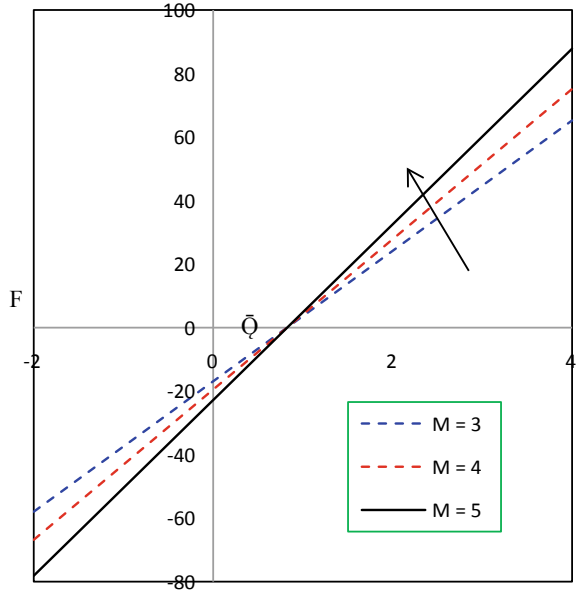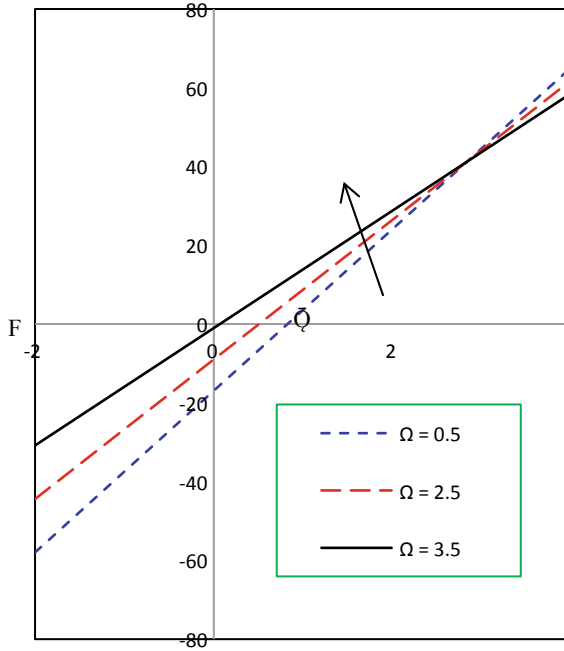
Fig. 15 Impact of Ω on frictional force (F)

5   Conclusions

Impact of rotation and hall current effects on the physiological Jeffery fluid were studied with a porous medium through a tapered channel. The main results are cited below.

1. Velocity decreases with increasing Jeffery fluid parameter and rotation parameter
2. Increasing of porosity parameter and Hall current parameter, the fluid velocity increases.
3. The pressure rate diminishes in the retrograde pumping zone and in the peristaltic pumping zone, while the pumping curve coincides in the free pumping zone, and the pumping rate increased in co-pumping zone with increasing the Hall current parameter.
4. The pumping rate improves in the retrograde pumping area, in the free pumping area, and also in the peristaltic pumping area, while the pumping rate in the co-pumping area is reduced as the rotational parameter increases.
5. Friction force have opposite behavior in terms of pressure rise.

References

1. Mahmoud SR (2011) Effect of rotation and magnetic field through porous medium on Peristaltic transport of a Jeffrey fluid in tube. Math Probl Eng 2011:971456
2. Ahmad Dar A, Elangovan K (2016) Influence of an inclined magnetic field and rotation on the peristaltic flow of a micropolar fluid in an inclined channel. New J Sci 2016:1–14
3. Abd-Alla AM, Abo-Dahab SM (2016) Rotation effect on peristaltic transport of a Jeffrey fluid in an asymmetric channel with gravity field. Alexandria Eng J 55:1725–1735
4. Abd-Alla AM, Abo-Dahab SM, Al-Simery RD (2013) Effect of rotation on peristaltic flow of a micropolar fluid through a porous medium with an external magnetic field. J Magn Magn Mater 348:33–43
5. Gnaneswara Reddy M, Venugopal Reddy K, Makinde OD (2017) Heat transfer on MHD Peristaltic rotating flow of a Jeffrey fluid in an asymmetric channel, Int J Appl Comput Math 3(4):3201–3227
6. Hayat T, Zahir H, Alsaedi A, Ahmad B (2017) Hall current and Joule heating effects on peristaltic flow of viscous fluid in a rotating channel with convective boundary. Results Phys 7:2831–2836
7. Hayat T, Rafiq M, Ahmad B (2015) Combined effects of rotation and thermal radiation on Peristaltic transport of Jeffrey fluid. Int J Biomathe 08(05):1550061
8. Chauhan DS, Rastogi P (2009) Hall current and heat transfer effects on MHD flow in a channel partially filled with a porous medium in a rotating system. Turkish J Eng Env Sci 33:167–184
9. Ravikumar S (2018) Study of hall current, radiation and velocity slip on hydromagnetic physiological hemodynamic fluid with porous medium through joule heating and mass transfer in presence of chemical reaction, Int J Heat Technol (IJHT) 36(2):422–432
10. Ravikumar S, Abzal SK (2017) Combined influence of hall currents and joule heating on hemodynamicperistaltic flow with porous medium through a vertical tapered asymmetric channel with radiation. Front Heat Mass Transfer (FHMT) 9–19:1–9
11. Mabood F, Khan WA, Makinde OD (2017) Hydromagnetic flow of a variable viscosity nanofluid in a rotating permeable channel with hall effects. J Eng Thermophys 26(4):553–566
12. Saravana R, Vajravelu K, Sreenadh S (2018) Influence of Compliant Walls and Heat Transfer on the Peristaltic Transport of a Rabinowitsch Fluid in an Inclined Channel. Zeitschrift für Naturforschung A 73(9): 833-843

Comparative Aerodynamics Analysis of Maruti Suzuki Alto Models

M. K. Pradhan (ORCID)**, Jai Kumar Verma, Suyash Kumar Jain, Kunal, Himal Pariyar, and Raja Das**

Abstract The automotive industry is now focusing on providing well-balanced commercial vehicle models based on performance and efficiency. The pressure from the environmental impacts and the increase in oil prices have led to the increased economy from both engines as well as outer car body over time. The aerodynamics of a vehicle was not substantial until the 1960s when the models were noisy and less efficient. However, with the arrival and advancement of fast-moving vehicles, it was highly essential to protect the vehicle from the effects of air drag and lift forces, which may cause loss of control at high speeds. This paper shows a comparative CFD analysis on Maruti Suzuki Alto models by highlighting the improvements done on aerodynamics in 2005 and 2012 models, respectively. The Alto is chosen as the subject of study in order to demonstrate the extent to which the fluid dynamic forces affect a commercial vehicle. The paper provides both 2D and 3D analysis on cruising conditions simulated on ANSYS® software and a qualitative study on the importance and significance of streamlining a vehicle in the present time.

Keywords CFD · Aerodynamic model · Automobile · Road vehicle aerodynamics · Turbulence modeling

1 Introduction

The automobile industry never fails to attract and amaze its customers by its high performance and luxury vehicles. Due to increase in today's competition among different brands, attention is drawn toward making a vehicle more comfortable, fast, and fuel efficient. But, the efficiency of a vehicle is determined by both external (wind and air effects) and internal factors (the engine and internal parts). The external factors tend to offer resistance in vehicle motion and generate undesirable lift effects. These factors can be controlled by having a streamlined or proper aerodynamic

M. K. Pradhan · J. K. Verma · S. K. Jain · Kunal · H. Pariyar
Maulana Azad National Institute of Technology, Bhopal 462003, India

R. Das (✉)
VIT, Vellore, Tamil Nadu 632014, India
e-mail: rajadasrkl@gmail.com

589

model of the vehicle. The technique for aero modeling a commercial vehicle relies upon certain factors [1, 2]. Some of these include making the vehicle as compact as possible, employing the use of low-cost material alternatives, seating capacity of the vehicle, and the body type (such as sedan, hatchback, SUVs.). It must be taken into account that any computerized analysis is not entirely accurate due to the distortion of the processed geometry. The design that is considered "fit" for production must pass through both the analytical and experimental tests and studies. It is also seen that no single type of analysis can provide the desired results. For this reason, the paper has coupled the results from 2D with 3D analysis for better understanding and demonstration [3, 4].

2   Alto Evolution

Suzuki initiated the production in 1979 in the European markets. Till date, Alto has undergone many changes, and many generations of this brand have hit the markets worldwide

- **First-Generation Alto (1979–1984)**: Variants consist of 539, 543, and 796 cc engines. These models had the seating capacity of two persons and generally followed the three-door cargo version trend.
- **Second-Generation Alto (1984–1988)**: The four-wheel drive (4WD) mechanism was installed with increased engine power. In 1985, the five-door body became commercially available.
- **Third-Generation Alto (1988–1994)**: The last generation to have an allied "Fronte" model. There is a more angular style in the body. There was a compromise in power produced due to emission controls. However, 660 cc variants began to be produced from this period.
- **Fourth-Generation Alto (1994–1998)**: The design was simplified, resorting back to the basic car definition. The slim slide configuration was stopped. The FWD and 4WD models were in production and were almost twice as efficient as the first-generation cars. "Alto Works" model has a sportier design, new grille and bumper, and a more prominent front opening.
- **Fifth-Generation Alto (1998–2004)**: Styling of the vehicles became more rounded. "Alto C" model had a deep chrome grille and a curious design of headlights through which the main globular lamp was connected with lights and ovoid sidelights indicators. By 2000, the facelift model was launched. Maruti Alto was launched in 2000, which was built in India.
- **Sixth-Generation Alto (2004–2009)**: The hood and headlights of the model were curved in the front. The car became more cost-effective to compete with other brands.
- **Seventh-Generation Alto (2009–2014)**: Vehicles offered an impressive fuel economy, even for 660 cc variants. Maruti Suzuki Alto-Star (A-Star) was launched that had a bigger body, engine, and larger capacity.

- **Eighth-Generation Alto (2014–present)**: Produced in Japan, the models resemble the retro model. The Turbo RS model was 60 kg lighter and offered more economy (mileage) and power than previous models. In India, the Alto K10 and Alto 800 model has been launched, more compact in design and greater performance following Bharat-Stage IV (BS IV) norms.

3 Methodology

3.1 Production of Simplified CAD Models

2D Model: The 2D model was generated in SolidWorks® 2016 software. The blueprints were imported, and the side view of the vehicle was traced using splines. A surface was then generated having the central cavity as the shape of the vehicle's side view. This cross section has been considered as the hypothetical cross section that would account for every variable cross section cut in the vertical plane. The file was converted to IGES format (Figs. 1 and 2).

3D Model: The 3D model was also generated in SolidWorks® 2016 software. The orthogonal views from the blueprints were imported, and the side view was traced by splines. The sketch was extruded, and it was trimmed by front traced view of the vehicle. Appropriate shaping was done using the top view to get the simplified 3D geometry of the car. The file was converted to the parasolid format for lesser import problems (Figs. 3 and 4).

Fig. 1 Alto 2005 model

Fig. 2 A-Star 2012 model

Fig. 3 3D Alto 2005 model
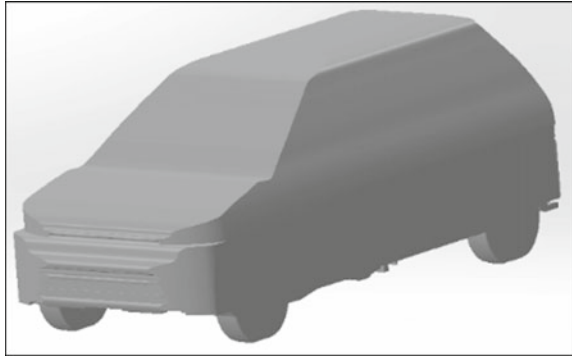
Fig. 4 3D A-Star 2012 model
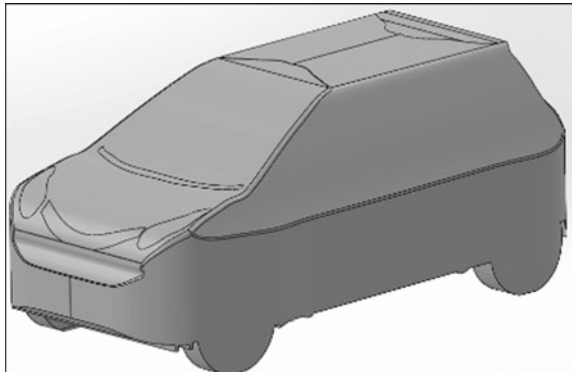
3.2 Import and Preprocessing of Models

3.2.1 2D Model

The model was imported, and the enclosure surface was made around it such that the boundaries of the enclosure were very far from that of the model. This has been done to prevent distortion in actual flow by the enclosure boundaries. However, if the walls were near or touching the wheel boundary of the model, it would either create a nozzle flow or stop the air particles, causing a rise in local pressure near the tires boundary. Practically, the flow of air near this region is never stopped, even though there is no gap between the ground and tires. The air particles move past the tires in a lateral (horizontal) plane or in a direction perpendicular to the vehicle's speed. Thus, this 3D motion was simplified by this assumption [5]. The appropriate Boolean operation was performed to obtain a flat model whose internal cavity was the initial model's boundary. Meshing was done with 100% relevance scale and correction at curvatures and proximities.

3.2.2 3D Model

The model was edited in the Design Modeler to obtain an appropriate 3D enclosure to the model. The approach was to keep the lower boundary of the enclosure in contact with the tires to simulate the road environment. It must be taken into account that a huge enclosure would mean longer processing time, a more significant number of elements created, and subsequently, higher chances of error propagations. Also, a small enclosure would restrict and interfere with the actual flow pattern and may show the presence of localized regions of high intensity and pressures which are non-existent practically. By conducting various trials, appropriate enclosure dimensions were decided. Boolean operations created the desired geometry with an internal cavity having a shape that of the initial 3D model. Meshing was done with 100% relevance and proximity and curvature corrections. Due to highly complex geometry, the meshing pattern consists mainly of tetrahedral elements [6].

3.3 ANSYS Fluent Setup

Parallel processing and multiple GPU rendering settings were applied.

Solver
The pressure-based solver does the 2D and 3D analyses for the investigation which involves the velocity of magnitude very less as compared to the speed of sound (0.057 M). Further, the solver is configured for steady-state conditions [7]. The turbulent kinetic energy and the turbulent dispensing rate are calculated according to the second-order exclusion equations for faster convergence and less time. Hybrid initialization is done. For 3D analysis, the reference area value is assumed to be the front projected area of the vehicle models.

Turbulence model
The standard k-ε model has been selected for the analysis as it provides fast and reliable results when the velocity magnitude is low. Thus, as the flow is confined to a definite volume, with relatively small pressure gradients, this model has provided satisfactory results with a relatively lower number of iterations, as verified practically by Ansari and Rana [8]. Enhanced wall treatment settings have been applied to obtain better results at sharp and uneven edges of the processed model. The transport equations are as follows

$$\frac{\partial}{\partial t}(\rho k) + \frac{\partial}{\partial x_i}(\rho k u_i) = \frac{\partial}{\partial x_j}\left[\left(\mu + \frac{\mu_i}{\sigma_k}\right)\frac{\partial k}{\partial x_j}\right] + G_k + G_b - \rho\varepsilon - Y_M + S_k$$

and

$$\frac{\partial}{\partial t}(\rho\varepsilon) + \frac{\partial}{\partial x_i}(\rho\varepsilon u_i) = \frac{\partial}{\partial x_j}\left[\left(\mu + \frac{\mu_t}{\sigma_\varepsilon}\right)\frac{\partial\varepsilon}{\partial x_j}\right] + C_{1\varepsilon}\frac{\varepsilon}{k}(G_k + C_{3\varepsilon}G_b) - C_{2\varepsilon}\rho\frac{\varepsilon^2}{k} + S_\varepsilon$$

$$(1)$$

Table 1 Font sizes of headings. Table captions should always be positioned *above* the tables

k-ε model	Standard
Cmu	0.09
C1ε	1.44
C2ε	1.92
TKE Prandtl number	1
TDR Prandtl number	1.3

where

G_k	Generation of turbulence kinetic energy due to mean velocity gradients.
G_b	Generation of turbulence kinetic energy due to buoyancy.
Y_M	Fluctuating dilation incompressible turbulence to the overall dissipation rate.
$C_{1\varepsilon}, C_{2\varepsilon}, C_{3\varepsilon}$	Constants.
$\sigma_k, \sigma_\varepsilon$	Turbulent Prandtl numbers.
S_k, S_ε	User-defined source terms.

Solver Constraints
See Table 1.

3.3.1   Input Velocity Parameters

For the sake of understanding the actual velocity that the vehicle would be subjected to, the analysis is limited to the simulation of the cruise condition velocity, that is, 50 km/h. The concept of relative velocity comes into view, where the wind direction is assumed opposite to that of the moving vehicle. These two velocities being unidirectional in nature must be added to get the actual input velocity. The wind velocity is calculated as per two factors, namely location and time. Both the vehicles are subjected to wind conditions as in India, and thus, wind variation ranges from the coastal winds to the winds in the mountains and plains. Also, these winds show marked variation throughout the year, and so, a need for the average annual wind velocity arises. This has been taken 5 m/s after observation from the Annual Wind Resource of India.

3.4   2D Analysis Comparison

See Figs. 5, 6, 7, and 8.
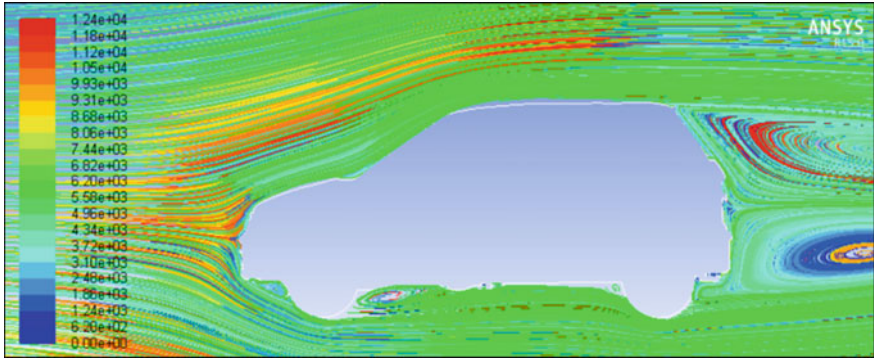
Fig. 5 Air path lines for Alto 2005 model
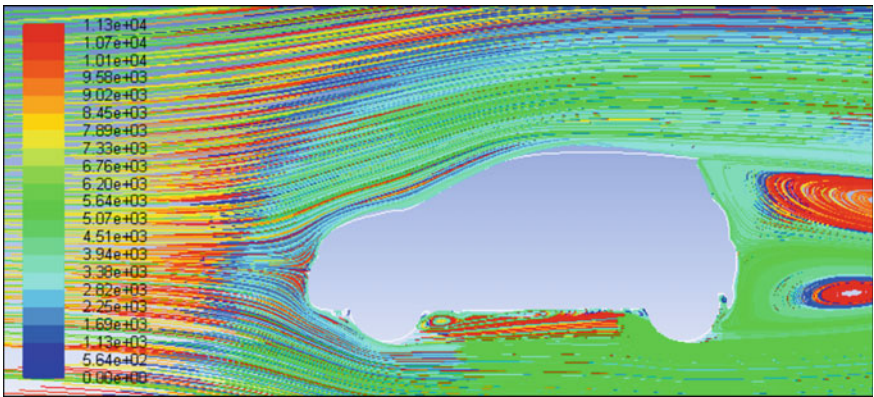
Fig. 6 Air path lines for A-Star 2012 model

Fig. 7 Turbulent kinetic energy contour (I)

Contours of Turbulent Kinetic Energy (k) (m2/s2)

Nov 27, 2018
ANSYS Fluent 15.0 (2d, pbns, ske)
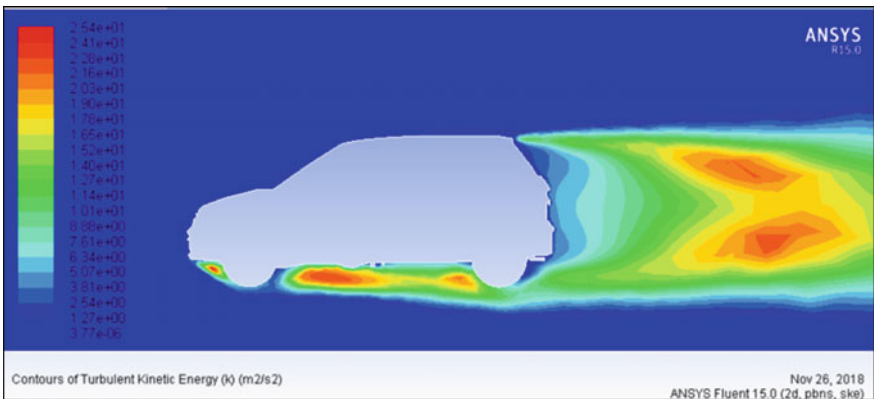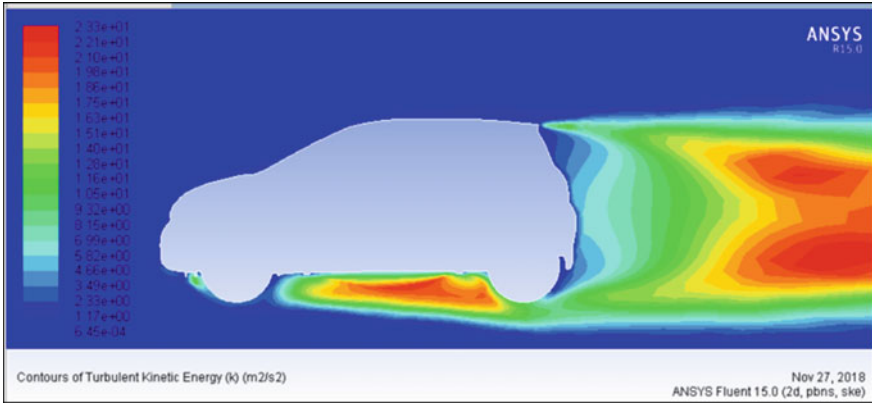
Fig. 8 Turbulent kinetic energy contour (II)
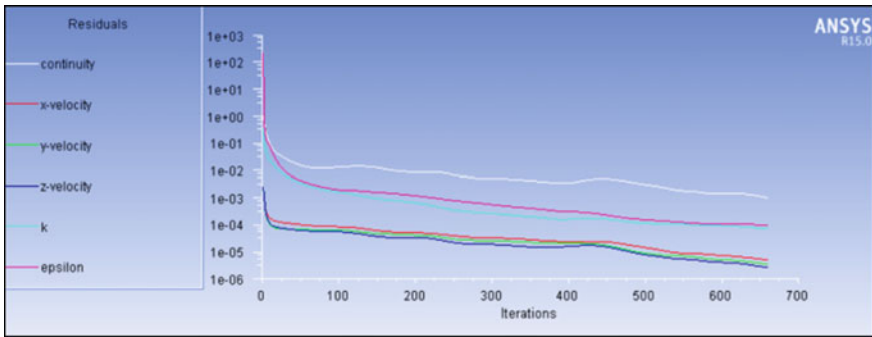
Fig. 9 Constraints variation with iterations (I)

3.5 *3D Analysis Comparison*

See Figs. 9, 10, 11, 12, 13, and 14.

4 Results and Discussions

4.1 *Drag Force (F_d)*

The drag force is resistive force acting on the body by its relative motion in a fluid. This force acts along the direction of motion of the vehicle and is calculated as below:

$$\mathbf{F_d} = \mathbf{C_d} * \mathbf{0.5} * \varrho * \mathbf{A} * \mathbf{V^2}$$
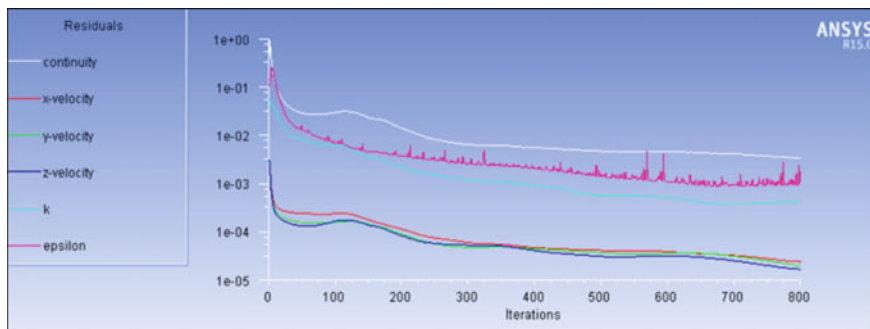
Fig. 10 Constraints variation with iterations (II)
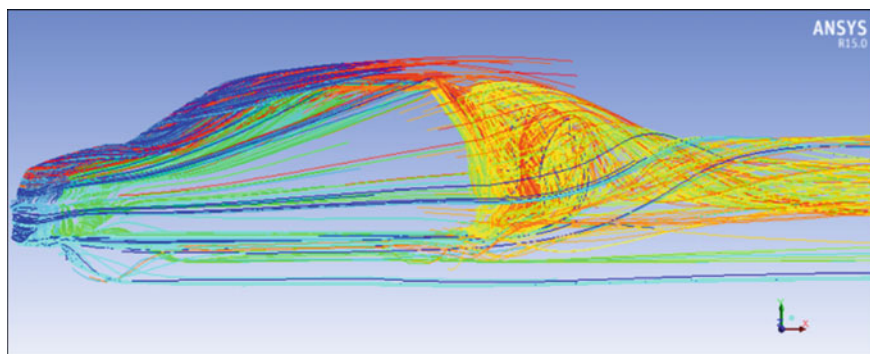
Fig. 11 3D path lines for Alto 2005 model
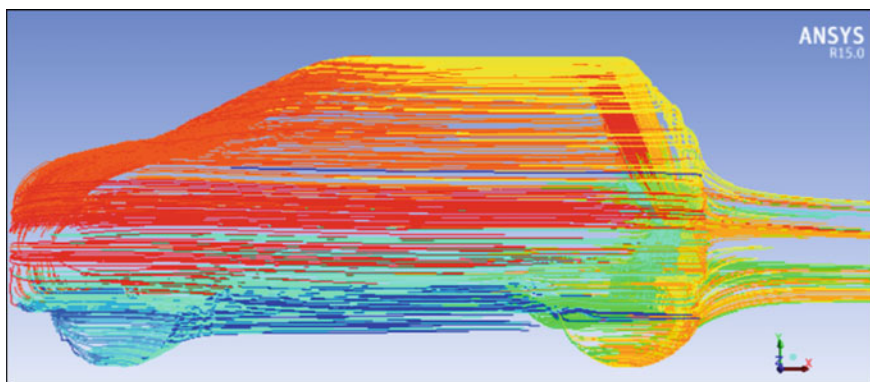
Fig. 12 Path lines for A-Star 2012 model
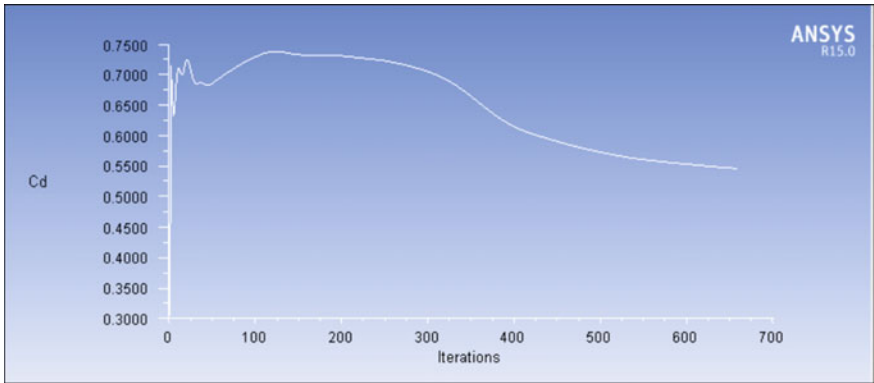
Fig. 13 C_d variation curve for the 2005 model
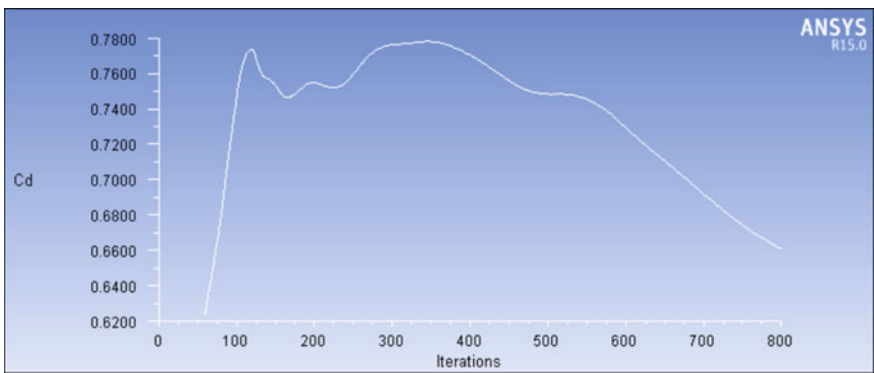
Fig. 14 C_d variation curve for A-Star 2012 model

where

C_d Coefficient of drag
ϱ Density of fluid (Air) $= 1.225$ kg/m^3
A   Projected area of the vehicle on the front plane
V   Relative velocity of the vehicle ($14 + 5 = 19$ ms^{-1}) (Table 2).

Table 2 Comparison of the models

Constraints	Alto 2005 model	A-Star 2012 model
C_d	0.54561	0.66085
A	1.874593	1.998028
F_d	226.153 N	291.956 N

4.2 Wind Flow Pattern

The wind flow pattern is studied by the movement of mass-less particles over the car's surface. The 2D and 3D results must have equal weight while determining the actual fluid flow pattern. **Alto 2005 Model**: From Fig. 5, it can be seen that the lower ride height and gradual sloping along the bonnet provide smooth air flow. However, some flow separation along this surface as well as in the region between the windshield (lower region) and the bonnet is observed. The separation can be reduced if these regions are given a slightly concave (outward) bulge. Figure 11 highlights the sudden change in the direction of flow pattern from the bottom of the front bumper to the lower region of the car. The disturbances in the flow are developed on the trailing edges of the vehicle which do not affect it but may have a substantial effect on another vehicle just behind it. **A-Star 2012 Model**: The greater vehicle height causes an increase in the path of the flow in the upper region of the vehicle. Bonnet and upper areas are given appropriate geometry bulges, which tend to reduce the flow separation and sudden directional changes (Fig. 6). Compared to the 2005 model, the problem of sudden directional change in the lower region of the bonnet reduces. The smooth body styling causes uniform air flow almost along with all directions. The trailing disturbance in the flow is limited to a small region and hence offers a lesser influence on any vehicle/body behind the car. Practically, this model has a trailing roof tail which marks a sudden termination of the roof line. The designers have done this to maintain the compact size of a hatchback vehicle.

4.3 Static Pressure Contour

Pressure contours are highly useful tools in determining the stability of the vehicles at high speeds and loss of traction. The lift forces produced during the motion cause dynamic instability, and the driver may experience loss of comfort if the magnitude is high. Figure 15 depicts more localized pressure regions and rapid transitions from one pressure region to another. This difference in pressure is higher in a span of a small region, which accounts for the generation of undesired forces. Thus, more instability is expected at higher speeds. Also, the generated lift forces are likely to hinder the comfort of the driver and the vehicle's performance. This is because of two factors: High pressure from the grill region will trigger an uplift towards the low-pressure region of the bonnet. High pressure from the grill region will begin the generation of down force because of the low pressure in the lower surface of the vehicle. The A-Star model, by its more round and concave geometry, is less likely to have concentrated pressure regions (Fig. 16) and provides a smooth transition from one pressure region to another. The two probable factors which tend to counterbalance the instability at higher speeds are its more massive engine (998 cc) and lower magnitude of lift forces generated, as compared to that of down force.
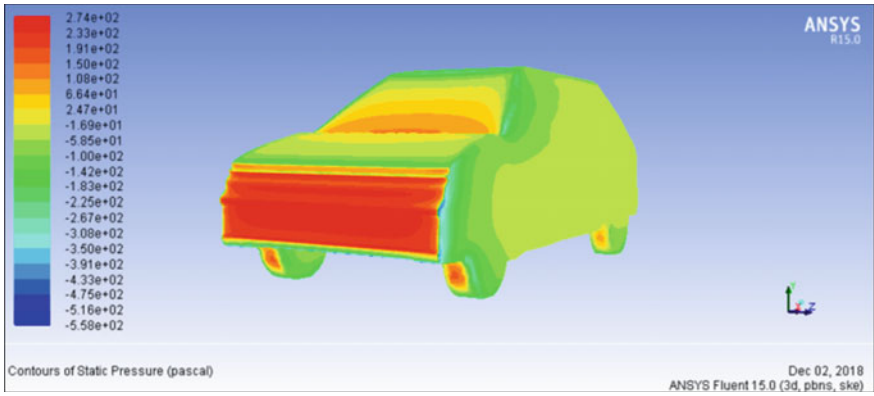
Fig. 15 Pressure contour (I)
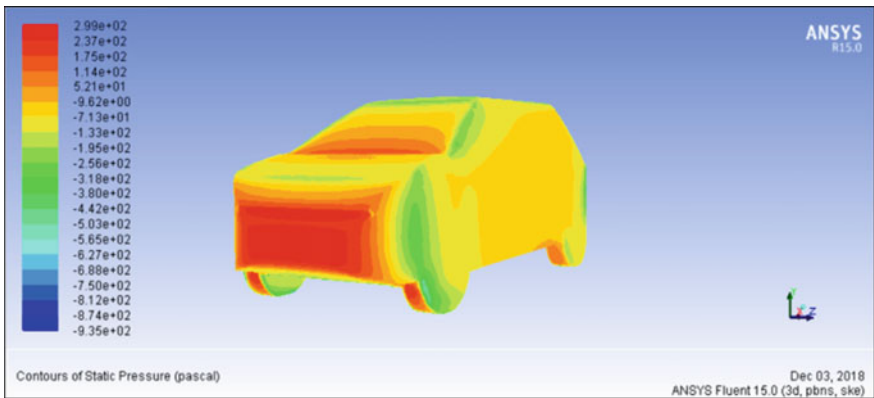
Fig. 16 Pressure contour (II)

4.4 Turbulent Kinetic Energy

To have an accurate contour plot of the turbulent kinetic energy, combined rendering of 2 GPUs (Nvidia and Intel HD Graphics) was used. While Fig. 17 had more turbulent kinetic energy, Fig. 18 had lesser turbulent kinetic energy over the entire region. However, neither of the models showed more significant variation in the magnitude over the whole region of the vehicle.
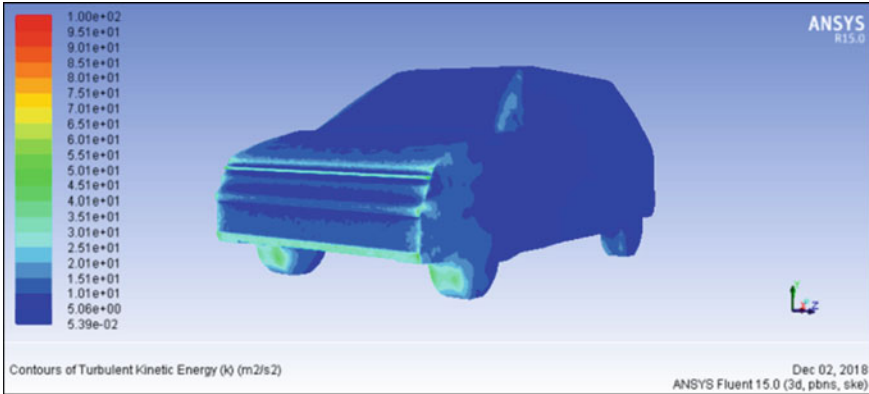
Fig. 17 Turbulent kinetic energy (I)
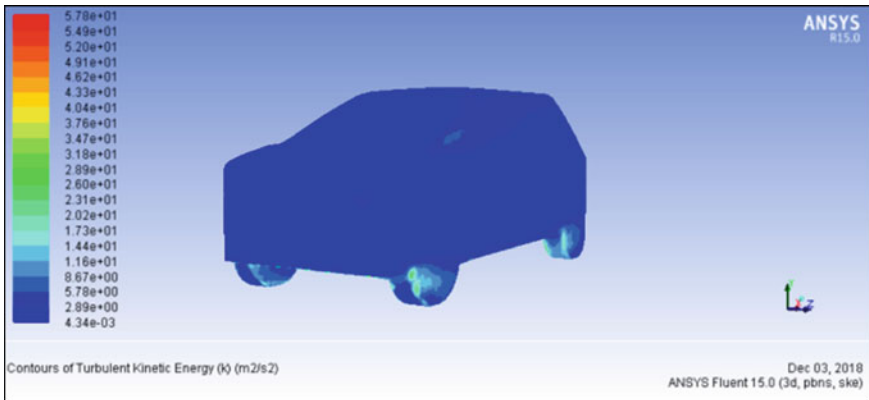
Fig. 18 Turbulent kinetic energy (II)

4.5 Turbulent Viscosity

The same GPUs and settings do rendering. Similar to the above observation, the turbulent dissipation rate was higher in 2005 model than in the A-Star model. In Fig. 20, the total volume of the vehicle shows a uniform turbulent dissipation rate. This lower variation in regions required a higher number of iterations in the processing to reach the desired results as compared to Figs. 19, 20, 21 and 22.
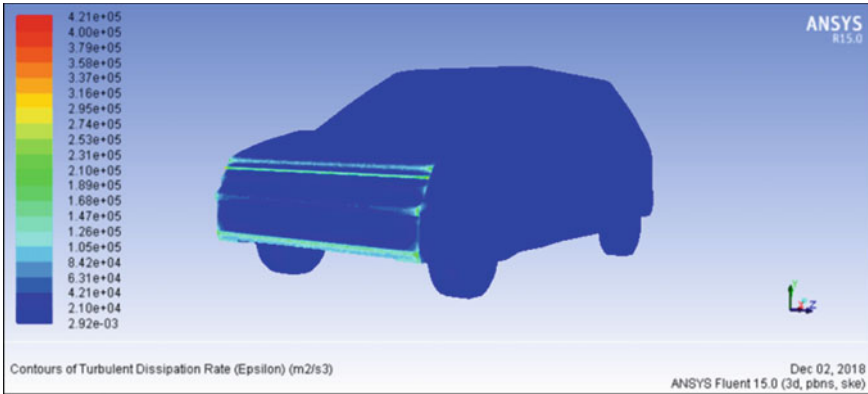
Fig. 19 Turbulent dissipation rate (I)
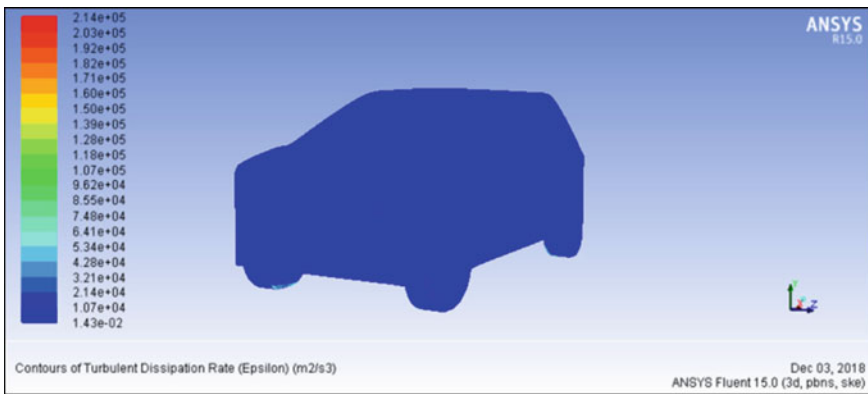
Fig. 20 Turbulent dissipation rate (II)

5 Conclusion

Both models have their own perks. While the 2005 model has lesser weight and a smaller engine, it is an economic model that offers almost the same fuel economy like that of the 2012 model. Due to the small size, the aerodynamic body design seems to counterbalance the drag effect quite well. The A-Star 2012 model had a bigger engine and body. With increased fuel consumption, it was required to make the vehicle more aerodynamic, which has been studied above. The drag coefficient of the 2012 model is approximately 21.12% more than the 2005 model. Reasons are pretty obvious. Owing to its large size and front area (6.58% more), the drag force is higher in magnitude (29.1%). Ideally, if the 2005 model were scaled to the 2012 model and then analyzed, the drag coefficient would be expected to be much higher than the 2012 model (0.82877). The rounded nose and the improved fluid flow across
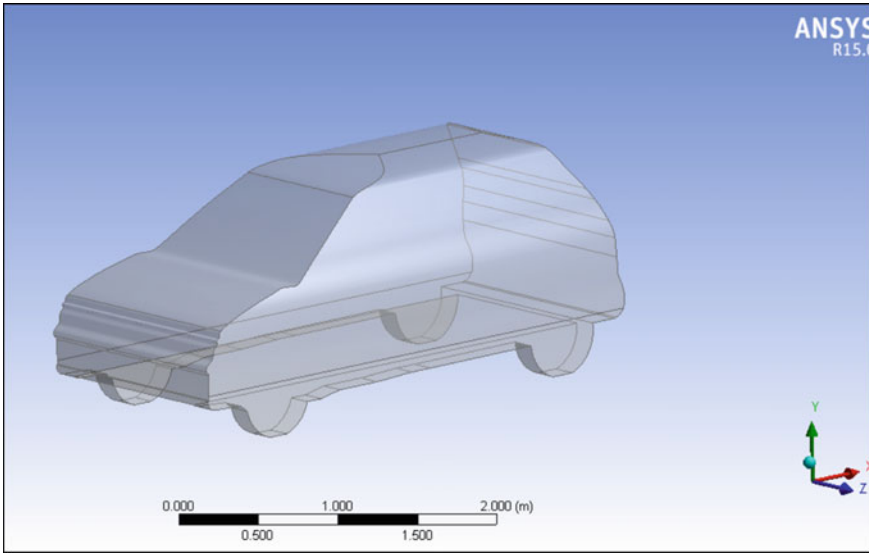
Fig. 21 2005 model scaled to 2012 model
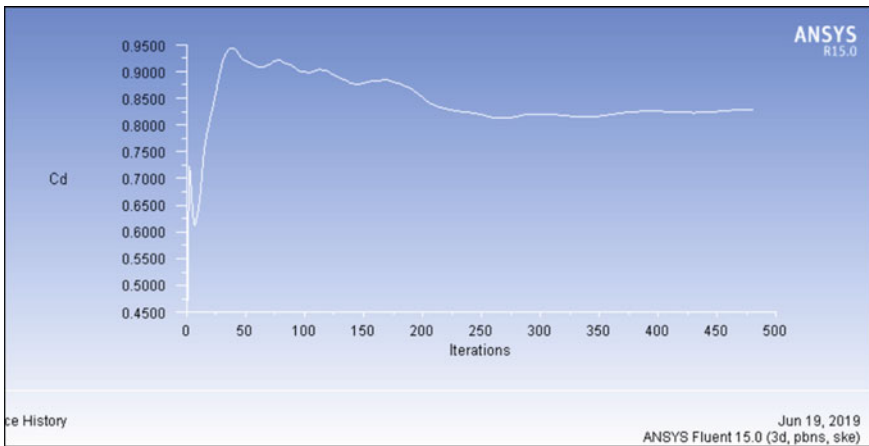
Fig. 22 Coefficient of drag variation of hypothetical 2005 model

the body seem to offer some compensation for the box-like structure of a hatchback vehicle. As far as the economy is concerned, the powerful 1000 cc engine handles the increased drag force effectively and efficiently than the 800 cc engine of 2005 model, if it would have been inside the 2012 model. It can be concluded that over the time, the aerodynamics of the Alto car has been improved (~25.4%), along with the practical reason that both these vehicles are tested to offer similar fuel economy rates.

References

1. Fu C, Uddin M., Robinson AC (2018) Turbulence modeling effects on the CFD predictions of flow over a NASCAR Gen 6 race car. J Wind Eng Ind Aerodyn 176:98–111. https://doi.org/10.1016/j.jweia.2018.03.016
2. Hetawal S et al (2014) Aerodynamic study of formula SAE car. Procedia Eng 97:1198–1207. https://doi.org/10.1016/j.proeng.2014.12.398
3. Sharma RB, Bansal R (2013) CFD simulation for flow over passenger car using tail plates for aerodynamic drag reduction. IOSR J Mech Civil Eng (IOSR-JMCE) 7.5:28–35
4. Singh SP, Singh A (2016) Design and simulate an aerodynamic car body for the Maruti Suzuki 800 with less coefficient of drag. Int Res J Eng Technol (IRJET)
5. Soares RF, Garry KF, Holt J (2017) Comparison of the far-field aerodynamic wake development for three driver model configurations using a cost-effective RANS simulation
6. Tian J et al (2019) Numerical analysis of underbody diffusers with different angles and channels. No. 2019-01-0668. SAE Technical Paper. https://doi.org/10.4271/2019-01-0668
7. Kulkarni S, Gandole G, Gaikwad P (2018) A review of aerodynamic study for reduction of drag force in cars in order to enhance the performance. IJETT 5.1
8. Ansari AR, Rana PK (2017) CFD analysis of aerodynamic design of maruti alto car. Int J Mech Eng Technol 8(3).

Effect of Hydrostatic Stress and Piezoelasticity in a Thermopiezoelectric Layer Resting on Gravitating Half Space with Slip Interface

R. Selvamani and R. Panneer Selvam

Abstract In this paper, an analytical model is developed to study the influence of initial hydrostatic stress and piezoelasticity on elastic waves in a thermopiezoelectric layer embedded on a gravitating half space with slip interface. The thermopiezoelectric layer considered for this study is hexagonal (6 mm) material. The problem is described using equations of linear elasticity with initial hydrostatic stress and piezothermoelastic inclusions. Displacement functions in terms of velocity potential are introduced to separate the motion's equations, heat and electric conduction equations. The frequency equations are obtained by stress-free, insulated thermal and electrically shorted boundary conditions at the gravitating half space. The numerical computation is carried out for the PZT-4A material. The obtained results are presented graphically to show the effect of piezoelastic coupling and hydrostatic stress on the elastic waves.

Keywords Elastic waves · Thermopiezoelectric layers · Hydrostatic stress · Slip interface · Temperature sensors

1 Introduction

The composite medium consisting of piezothermoelastic layer and gravitating half space is the important topic in seismology and construction field due to its self monitoring and controlling ability. The study of elastic waves in smart material like piezoelectric and thermopiezoelectric are utilized in pattern recognition field, sensing and activation process with electrothermomechanical energy transition and high frequencies-small wavelengths characteristics. The elastic waves of compression type in a circular cylinder made of hexagonal symmetry and anisotropy property

R. Selvamani (✉)
Department of Mathematics, Karunya University, Coimbatore, Tamil Nadu 641114, India
e-mail: selvam1729@gmail.com

R. Panneer Selvam
Department of Civil Engineering, University of Arkansas, Fayetteville, AR 72701, USA

were initially developed under linear theory of elasticity [1]. Bhimaraddi [2] developed a higher order theory for the free vibration analysis of circular cylindrical shell.

Thermopiezoelastic components generated by piezothermoelastic field contribute a mechanism to sense the chaotic nature of thermomechanical signal coming from perturbed electric potential, to alter the response of the structure by the force given by electric fields. The thermopiezoelectric theory and its formulation were initially given by Mindlin [3], and then, he developed a analytical modeling for the thermopiezoelectric plate. The laws for the physical behavior of the pyroelectric materials and its characteristics have been formulated detail by Nowacki [4, 5]. In order to achieve the finite thermal signal speed, Chandrasekhariah [6, 7] analyzed the generalized theory of thermopiezoelasticity considering the thermal relaxation times in the analytical formulation [8]. Tang and Xu [9] developed a dynamical equation in general form for the plate composed of anisotropic material which have mechanical, thermal, and electrical influence, and they examined the forces acting on a thermopiezoelastic laminated plate. The frequency shift of a vibration of linear piezoelectric material with heat conduction by using perturbation methods was interpreted by Yang and Batra [10]. An analytical solution is achieved by Peyman Yazdanpanah Moghadam et al. [11] for a piezo-laminated rectangular plate with arbitrary clamped and simply supported boundary conditions under thermoelectromechanical loadings. Sabzikar Boroujerdy and Eslami [12] studied the axisymmetric snap-through nature of Piezo-FGM shallow clamped spherical shells under thermoelectromechanical loading. They found that the coupling effect of thermopiezoelasticity enhances the elastic behavior of the FGM shell.

Further, the wave propagation in a generalized thermoelastic panel was analyzed by Selvamani and Ponnusamy [13]. They found the influence of thermal and magnetic field on the wave characteristics of panel. Selvamani [14] has studied the stress wave pattern in a generalized thermoelastic polygonal plate with inner and outer cross sections using Fourier collocation method. Selvamani and Mahinde [15] have studied the influence of rotation on a thin film coated rod, and also they analyzed the trends of elastic waves due to piezoelectric effect. The presence of initial hydrostatic stress in a vibrating medium will produce changes in the elastic properties, and material will exhibit anisotropy characteristics. De and Sengupta [16] investigated magnetoelastic waves in initially stressed isotropic media. The propagation of elastic waves in an initially stressed magnetoelastic and thermoelastic medium was investigated thoroughly by Acharya and Sengupta [17, 18]. The propagation of waves under the influence of gravitating half space is a significant problem in seismology and geophysics, which has gained the attention of many researchers [19]. The dispersion of Love wave in a fiber-reinforced medium via an isotropic layer and gravitating half space is reads from Kundu et al. [20]. Vinh and Anh [21] studied the Rayleigh waves in an orthotropic half space coated by a thin orthotropic layer with sliding contact.

In present contribution, vibration in a anisotropic and hydrostatic stressed thermopiezoelectric layer resting on gravitating half space is analyzed under linear theory elastic equations. Three displacement equations are considered with its potential derivatives. The frequency equations are obtained for longitudinal and flexural modes at the gravitating half space with thermally insulated and electrically shorted boundary conditions. The numerical results are analyzed for PZT-4 material, and the computed stress, strain, frequency, and phase velocity are presented in the form of dispersion curves.

2 Analytical Model

A rectangular Cartesian coordinates are used to study the deformation of thermopiezoelectric infinite layer of thickness 2 h. The motion which takes place in XZ plane with the origin is considered to be the mid plane of the layer, and the Z axis is at right angle to the to the mid plane. The complete governing equations that explain the behavior of thermopiezoelectric layer have been considered from [3].

$$\Pi_{xx} = c_{11}\frac{\partial u}{\partial x} + (c_{13} - H_s)\frac{\partial w}{\partial z} + e_{31}\frac{\partial \phi}{\partial z} - \beta_1 T,$$

$$\Pi_{yy} = c_{12}\frac{\partial u}{\partial x} + (c_{13} - H_s)\frac{\partial w}{\partial z} + e_{31}\frac{\partial \phi}{\partial z} - \beta_1 T,$$

$$\Pi_{zz} = c_{13}\frac{\partial u}{\partial x} + (c_{33} - H_s)\frac{\partial w}{\partial z} + e_{33}\frac{\partial \phi}{\partial z} - \beta_3 T,$$

$$\Pi_{xz} = c_{44}\left(\frac{\partial w}{\partial x} + \frac{\partial u}{\partial z}\right) + e_{15}\frac{\partial \phi}{\partial x}, \ \Pi_{xy} = 0, \ \Pi_{yz} = 0,$$

$$D_x = e_{15}\left(\frac{\partial w}{\partial x} + \frac{\partial u}{\partial z}\right) - \in_{11}\frac{\partial \phi}{\partial x}, \ D_y = 0,$$

$$D_z = e_{31}\frac{\partial u}{\partial x} + e_{33}\frac{\partial w}{\partial z} - \in_{33}\frac{\partial \phi}{\partial z} + p_3 T$$

$$\tau = \beta_1\frac{\partial u}{\partial x} + \beta_3\frac{\partial w}{\partial z} - p_3\frac{\partial \phi}{\partial z} + \mathrm{d}T \tag{1}$$

where $\Pi_{xx}, \Pi_{yy}, \Pi_{zz}, \Pi_{xy}, \Pi_{yz}, \Pi_{xz}$ are the stress components, u, w are the displacement components, $c_{11}, c_{12}, c_{13}, c_{33}$ are the elastic moduli, e_{31}, e_{33} are the constant of piezoelectricity, $\in_{11}, \in_{33}$ represent constants of dielectric, T is the variation of temperature in the steady state T_0, p_3 is the pyroelectric constant, H_s is the initial hydrostatic stress (when $H_s < 0$ is hydrostatic tension and $H_s > 0$ represents hydrostatic compression), β_1, β_3 gives the coefficients of thermal growth, ϕ is the electric potential, and ρ_1 is the mass density. The equations of motion for hexagonal (6 mm) class are derived as follows

$$c_{11}\frac{\partial^2 u}{\partial x^2} + (c_{13} + c_{44} - H_s)\frac{\partial^2 w}{\partial x \partial z} + c_{44}\frac{\partial^2 u}{\partial z^2}$$

$$+ (e_{31} + e_{15})\frac{\partial^2 \phi}{\partial x \partial z} + (e_{31} + e_{15})\frac{\partial^2 u}{\partial x \partial z} = \rho_1\frac{\partial^2 u}{\partial t^2}$$

$$c_{44}\frac{\partial^2 w}{\partial x^2} + (c_{33} - H_s)\frac{\partial^2 w}{\partial z^2} + (c_{13} + c_{44})\frac{\partial^2 u}{\partial x \partial z}$$

$$+ e_{15}\frac{\partial^2 \phi}{\partial x^2} + e_{33}\frac{\partial^2 \phi}{\partial z^2} = \rho_1\frac{\partial^2 w}{\partial t^2}$$

$$e_{15}\frac{\partial^2 w}{\partial x^2} + (e_{15} + e_{31})\frac{\partial^2 u}{\partial x \partial z} - \in_{11}\frac{\partial^2 \phi}{\partial x^2} + e_{33}\frac{\partial^2 w}{\partial z^2} - \in_{33}\frac{\partial^2 \phi}{\partial z^2} = 0 \qquad (2)$$

$$K_{11}T_{xx} + K_{33}T_{zz} = T_0(\beta_1 u_{xt} + \beta_3 w_{xt} - P_3\varphi_{zt} + dT_t).$$

3   Solution Procedure

The solutions of the displacement vectors in terms of potentials are reads from Paul [22] in order to achieve harmonic elastic wave solution. Thus, the solution of Eq. (2) is used in the following form

$$u = U(z)\sin kx e^{i\omega t}, \ w = W(z)\cos kx e^{i\omega t},$$

$$\varphi = (c_{44}/e_{33})\varphi(z)\cos kx e^{i\omega t}$$

$$T = (c_{44}//\beta_3)kT(z)\cos kx e^{i\omega t} \qquad (3)$$

where $i = \sqrt{-1}$, k, and ω are the wave number and angular frequency, $U(z)$, $W(z)$, $\phi(z)$, and $T(z)$ are the displacement potentials. By introducing the following parameters in nondimensional form $x = rh$, $\eta = kh$, $\bar{c}_{ij} = \frac{c_{ij}}{c_{44}}$; $\bar{\varepsilon}_{ij} = \frac{\varepsilon_{11}}{e_{33}}$; $\bar{p} = \frac{p_1 c_{44}}{\beta_3 e_{33}}$, $k_\beta^{-2} = \frac{\varepsilon_{ij} c_{44}}{\varepsilon_{33}^2}$, $k_j = \left(\frac{1}{h^2}\frac{c_{44}}{\beta_3^2 p T_0}k_{ij}\right)$, $\overline{L_1} = \frac{H_s}{c_{44}}$ and using Eq. (3) in Eq. (2), the following differential equation will be obtained

$$\frac{d^2 U}{dr^2} - \eta^2 c_{11} U - (1 + \bar{c}_{13} + \overline{L_1})\eta\frac{dW}{dr} - (\bar{e}_{31} + \bar{e}_{15})\eta\frac{d\varphi}{dr} = -(ch)^2 U$$

$$(1 + \bar{c}_{13})\eta\frac{dU}{dr} + (\bar{c}_{33} - \overline{L_1})\frac{d^2 W}{dr^2} - \eta^2(W + \varphi) + \frac{d^2\varphi}{dr^2} - \eta\frac{dT}{dr} = -(ch)^2 W$$

$$(\bar{e}_{31} + \bar{e}_{15})\eta\frac{dU}{dr} - \eta^2\bar{e}_{31} W + \frac{d^2 W}{dr^2} - k_{33}^{-2}\frac{d^2\varphi}{dr^2} + k_{13}^{-2}\eta^2\varphi = 0$$

$$\beta\varepsilon u + \frac{dw}{dr} - \bar{p}\frac{d\phi}{dr} + \varepsilon\left[d + (k_3\frac{d^2}{dr^2} - k_1\varepsilon^2)i\right]T = 0, \qquad (4)$$

Equation (4) can be written in the vanishing determinant form as

$$\begin{vmatrix} \frac{d^2}{dr^2} + [(ch)^2 - \varepsilon^2 c_{11}] & -(1+\bar{c}_{13})\varepsilon\frac{d}{dr} & (\bar{e}_{31}+\bar{e}_{15})\varepsilon\frac{du}{dr} & \beta\varepsilon^2 \\ (1+\bar{c}_{13})\varepsilon\frac{d}{dr} & \bar{c}_{33}\frac{d^2}{dr^2}[(ch)^2-\varepsilon^2] & \frac{d^2}{dr^2}-\bar{e}_{15}\varepsilon^2 & \varepsilon\frac{d}{dr} \\ [\bar{e}_{31}+\bar{e}_{15}]\varepsilon\frac{d}{dr} & \frac{d^2}{dr^2}-\bar{e}_{15}\varepsilon^2 & k_{33}^{-2}\left(\bar{e}_{11}\varepsilon^2-\frac{d^2}{dr^2}\right) & \varepsilon\bar{p}\frac{d}{dr} \\ \beta\varepsilon & \frac{d}{dr} & \bar{p}\frac{d}{dr} & \varepsilon\left[d+i\left(k_3\frac{d^2}{dr^2}-k_1\varepsilon^2\right)\right] \end{vmatrix} (U, W, \varphi, T)' = 0$$

(5)

The above relation is specified as

$$\left(\frac{d^{28}}{dr^8} + M\frac{d^6}{dr^6} + N\frac{d^4}{dr^4} + O\frac{d^2}{dr^2} + P\right)(U, W, \varphi, T) = 0 \qquad (6)$$

where the constant coefficients M, N, O, and P are obtained as follows

$$\begin{aligned} M =\ & g_9\big(g_7\bar{c}_{33} + 2g_6 - g_1 g_{10}\bar{c}_{33} - g_1 - g_2^2 g_{10} - 2g_2 g_3 - g_3^2\bar{c}_{33} - g_9 g_5 g_{10}\big) \\ & + g_8(-g_{10}\bar{c}_{33}-1)^2 + \bar{p}\bar{c}_{33} - g_7 g_5 g_{10} + 2\bar{p} - g_{10}]/[-g_9(g_{10}\bar{c}_{33}+1)] \\ N =\ & \big[g_8\big(g_7\bar{c}_{33} + 2g_6 - g_1 g_{10}\bar{c}_{33} - g_1 - g_2^2 g_{10} - 2g_2 g_3 - g_3^2\bar{c}_{33}\big) \\ & + g_9\big(g_5 g_7 - g_6^2 + g_1 g_7\bar{c}_{33} - g_1 g_{10} g_5 + 2g_1 g_6 + g_2^2 g_7 + 2g_2 g_6 g_3 + g_3^2 g_5\big) \\ & + \bar{p}\big(g_5\bar{p} + g_1\bar{p}\bar{c}_{33} + 2g_1 - 2g_6 + g_2^2\bar{p} + 2g_2 g_4 + 2g_2 g_3 - 2g_3 g_4\bar{c}_{33}\big)g_7 \\ & -g_1 g_{10} - 2g_2 g_4 g_{10} + g_3^2 - 2g_3 g_4 + g_4^2 g_{10}\bar{c}_{33} + g_4^2\big]/[-g_9(g_{10}\bar{c}_{33}+1)] \\ O =\ & g_8\big(g_5 g_7 - g_6^2 + g_1 g_7\bar{c}_{33} - g_1 g_5 g_{10} + 2g_1 g_6 + g_2^2 g_7 + 2g_2 g_3 g_6 + g_3^2 g_5\big) \\ & + g_9\big(g_1 g_5 g_7 - g_1 g_6^2 + g_1(g_5^{-2}p + g_7 - 2\bar{p}g_6\big) \\ & + g_3(-g_4 g_5\bar{p} + 2g_4 g_6 - \bar{p}g_4 g_5) \\ & + g_4(-g_2 g_6\bar{p} + 2g_1 g_6 + 2g_2 g_7 - \bar{p}g_2 g_6 - g_4 g_5 g_{10} \\ & -2g_4 g_6)/[-g_9(g_{10}\bar{c}_{33}+1)], \\ P =\ & \big(g_1 g_8 - g_4^2\big)\big(g_5 g_7 - g_6^2\big)/[-g_9(g_{10}\bar{c}_{33}+1)] \end{aligned}$$

(7)

with

$$\begin{aligned} & g_1 = (ch)^2 - \varepsilon^2\bar{c}_{11},\ g_2 = (1+\bar{c}_{13})\varepsilon,\ g_3 = (\bar{e}_{31}+\bar{e}_{15})\varepsilon, \\ & g_4 = \beta\varepsilon^2,\ g_5 = (ch)^2 - \varepsilon^2,\ g_6 = \varepsilon^2\bar{e}_{11},\ g_7 = \varepsilon^2\bar{e}_{11}\big/k_{33}^2, \\ & g_8 = \left(\rho c_u c_{44,}\big/_{\beta_3^2 T_0 - ik_1\varepsilon^2}\right),\ g_9 = ik_3,\ g_{10} = 1\big/k_{33}^2. \end{aligned}$$

(8)

Upon solving, Eq. (6) for the mode in symmetric form is as follows

$$U = \sum_{i=1}^{4} A_i \cosh(\alpha_i r), \quad W = \sum_{i=1}^{4} A_i a_i \sinh(\alpha_i r),$$

$$\varphi = \sum_{i=1}^{4} A_i b_i \cosh(\alpha_i r), \quad T = \sum_{i=1}^{4} A_i c_i \sinh(\alpha_i r), \tag{9}$$

and the solutions for a anti-symmetric mode are obtained as by changing the $\cosh(\alpha_i r)$ into $\sinh(\alpha_i r)$ and vice versa. Here, A_i is the arbitrary constant which is to be determined, and $\alpha_i^2 > 0$, $(i = 1, 2, 3, 4)$ are the roots of the following algebraic equation

$$\alpha^8 + M\alpha^6 + N\alpha^4 + O\alpha^2 + P = 0 \tag{10}$$

The value of the constants a_i, b_i and c_i represented in Eq. (9) is derived from the following relations

$$(1 + \bar{c}_{13})\varepsilon\alpha_i a_i - (\bar{e}_{31} + \bar{e}_{15})\varepsilon\alpha_i b_i + \beta\varepsilon^2 c_i + \{\alpha_i^2[(\mathrm{ch})^2 - \varepsilon^2 \bar{c}_{11})]\} = 0$$

$$\bar{c}_{33}\alpha_i^2 + [(\mathrm{ch})^2 - \varepsilon^2]\}a_i + (\alpha_i^2 - \bar{e}_{15}\varepsilon^2)b_i - \varepsilon\alpha_i c_i(1 + \bar{c}_{13})\varepsilon\alpha_i = 0$$

$$(\alpha_i^2 - \bar{e}_{11}\varepsilon^2)a_i + [\varepsilon^2 \bar{e}_{11} - \alpha_i^2)/k_{33}^2]b_i + \varepsilon\bar{p}\alpha_i c_i + (\bar{e}_{31} + \bar{e}_{15})\varepsilon\alpha_i = 0. \tag{11}$$

4 Formulation of the Gravitating Half Space

The dynamic equation of the gravitating half space is reads from [20].

$$\underset{xx,x}{\bigsqcup} + \underset{xz,z}{\bigsqcup} - \rho_2 g w_z = \rho_2 u_{tt}, \quad \underset{xz,z}{\bigsqcup} + \underset{zz,z}{\bigsqcup} - \rho_2 g u_z = \rho_2 w_{tt} \tag{12}$$

where g is the acceleration due to gravity, $\bigsqcup_{xz}$, $\bigsqcup_{xx}$, and $\bigsqcup_{zz}$ are the stress components of the half space, and the relation between stress and strain for isotropic material is explained as

$$\underset{xx}{\bigsqcup} = (\lambda + 2\mu)e_{xx} + \lambda e_{zz}, \quad \underset{xz}{\bigsqcup} = 2\mu e_{xz}$$

$$\underset{zz}{\bigsqcup} = (\lambda + 2\mu)e_{zz} + \lambda e_{xx} \tag{13}$$

where λ and μ are the Lame's and $e_{xx} = \frac{\partial u}{\partial x}, e_{zz} = \frac{\partial w}{\partial z}$, and $e_{xz} = \frac{1}{2}\left(\frac{\partial u}{\partial z} + \frac{\partial w}{\partial x}\right)$. Using Eq. (13) in (1), we obtain the following relations with displacement components

$$\mu\left(\frac{\partial^2 u_1}{\partial z^2} + \frac{\partial^2 w_1}{\partial x \partial z} + 2\frac{\partial^2 u_1}{\partial x^2}\right) + \lambda\left(\frac{\partial^2 w_1}{\partial x \partial z} + \frac{\partial^2 u_1}{\partial x^2}\right)$$

$$- \rho_2 g \frac{\partial w_1}{\partial x} = \rho_2 \frac{\partial^2 u_1}{\partial t^2}$$

$$\mu\left(2\frac{\partial^2 w_1}{\partial z^2} + \frac{\partial^2 u_1}{\partial x \partial z} + 2\frac{\partial^2 w_1}{\partial x^2}\right) + \lambda\left(\frac{\partial^2 w_1}{\partial z^2} + \frac{\partial^2 u_1}{\partial x \partial z}\right)$$

$$+ \rho_2 g \frac{\partial u_1}{\partial x} = \rho_2 \frac{\partial^2 w_1}{\partial t^2} \tag{14}$$

We can consider the solution of Eq. (14) as follows:

$$u_1 = U_1(z) \sin k_1 x e^{ip_1 t}, \ w_1 = W_1(z) \cos k_1 x e^{ip_1 t}, \tag{15}$$

where k_1 is the wave number and p_1 is the circular frequency of the half space. Introducing nondimensional quantity $y = rh$, $\eta_1 = k_1 h$ and substituting the solution in Eq. (15) in (14), we get

$$\mu\left[\frac{d^2 U_1}{dr^2} - \eta_1\frac{dW_1}{dr} - 2\eta_1^2 U_1\right] - \lambda\left[\eta_1\frac{dW_1}{dr} + \eta_1^2 U_1\right]$$

$$+ \rho_2 g \eta_1 h W_1 = -\rho_2 (p_1 h)^2 U_1$$

$$\mu\left[2\frac{d^2 W_1}{dr^2} + \eta_1\frac{dU_1}{dr} - 2\eta_1^2 W_1\right] + \lambda\left[\frac{d^2 W_1}{dr^2} + \eta_1\frac{dU_1}{dr}\right]$$

$$+ \rho_2 g \eta_1 h U_1 = -\rho_2 (p_1 h)^2 W_1 \tag{16}$$

The nontrivial solution of the above differential Eq. (16) is obtained as follows

$$\begin{vmatrix} \mu\frac{d^2}{dr^2} - 2\mu\eta_1^2 - \lambda\eta_1^2 + \rho_2(p_1 h)^2 & -(\mu+\lambda)\eta_1\frac{d}{dr} + \rho_2 g \eta_1 h \\ (\mu+\lambda)\eta_1\frac{d}{dr} + \rho_2 g \eta_1 h & (2\mu+\lambda)\frac{d^2}{dr^2} - 2\mu\eta_1^2 + \rho_2(p_1 h)^2 \end{vmatrix}(U_1, W_1) = 0 \tag{17}$$

Taking $e_1 = \mu$, $e_2 = -\mu\eta_1^2$, $e_3 = \lambda\eta_1^2$, $e_4 = \rho_2(p_1 h)^2$, $e_5 = (\mu+\lambda)\eta_1$, $e_6 = \rho_2 g \eta_1 h$, $e_7 = (2\mu+\lambda)$ and expanding the above determinant, we get

$$\left(\frac{d^4}{dr^4} + R\frac{d^2}{dr^2} + S\right)(U_1, W_1) = 0 \tag{18}$$

where $R = (e_1 e_2 + e_1 e_4 + e_2 e_7 + e_3 e_7 + e_4 e_7 + e_5^2)/e_1 e_7$, $S = (e_2^2 + 2e_2 e_4 + e_2 e_3 + e_3 e_4 + e_4 e_7 + e_5^2)/e_1 e_7$. The solutions of the above Eq. (18) in symmetric and anti-symmetric mode are obtained as follows

$$U_1 = \sum_{i=1}^{2} B_i \cosh(\beta_i r), \; W_1 = \sum_{i=1}^{2} B_i q_i \sinh(\beta_i r),$$

$$U_1 = \sum_{i=1}^{2} B_i \sinh(\beta_i r), \; W_1 = \sum_{i=1}^{2} B_i q_i \cosh(\beta_i r) \tag{19}$$

Here, B_i is the arbitrary constant which is to be determined, β_i is reached from

$$\beta^4 + R\beta^2 + S = 0 \tag{20}$$

and the constant q_i is given by the following relation for the isotropic half space

$$- (\mu + \lambda)\eta\beta_i q_i + \rho_2 g\eta h q_i + \mu\beta_i^2 + (\rho_2(ph)^2 - 2\eta^2\mu - \lambda\eta^2) = 0$$
$$(2\mu + \lambda)\beta_i^2 q_i + (\rho_2(ph)^2 - 2\eta^2)q_i + (\mu + \lambda)\eta\beta_i + \rho_2 g\eta h = 0 \tag{21}$$

5 Boundary Conditions and Frequency Equations

Boundary conditions are constructed for the anisotropic layer and gravitating half space at the interface. Since the layer and the gravitating half space are in sliding contact, the stress and displacement will become

$$\coprod_{xz} = \prod_{xz} = 0, \coprod_{zz} = \prod_{zz} = 0, U = W_1 = 0 \tag{22}$$

The thermally insulated and electrically shorted boundary conditions are as follows

$$\phi = 0, T = 0, \tag{23}$$

Upon using Eqs. (9) and (17) in the above conditions will lead to a system of algebraic equation for the unknowns A_1, A_2, A_3, A_4 and B_1, B_2, and these system of algebraic equations can be written in the following vector matrix form

$$[P](Z) = (0) \tag{24}$$

where

$$|P| = [\chi_{ij}], \quad i, j = 1, 2, 3, 4, 5, 6, 8. \tag{25}$$

$$\chi_{1j} = (c_{13} - c_{14})k + \left(c_{33}a_j - H_s a_j + c_{44}b_j\right)\frac{\alpha_j}{h},$$

$$\chi_{2j} = (c_{13} - c_{14})k + \left(c_{33}a_j - H_s a_j + c_{44}b_j\right)\frac{\alpha_j}{h},$$

$$\chi_{3j} = c_{44}\frac{\alpha_j}{h} - \left[a_j + e_{15}\left(\frac{c_{44}}{e_{33}}\right)b_j\right]k,$$

$$\chi_{4j} = c_{44}\frac{\alpha_j}{h} - \left[a_j + e_{15}\left(\frac{c_{44}}{e_{33}}\right)b_j\right]k$$

$$j = 1, 2, 3, 4, 5, 6$$

$$\chi_{47} = 0, \ \chi_{48} = 0,$$

$$\chi_{5j} = \mu\left[\frac{a_j}{h} - a_j k\right], \ \chi_{58} = 0,$$

$$\chi_{6j} = \left[(\lambda + 2\mu)a_j\frac{\alpha_j}{h} + \lambda k\right], \ \chi_{67} = 0,$$

$$\chi_{68} = 0, \ \chi_{7j} = \left(s_j - \varepsilon^2 q_j \overline{e_{15}} e_j\right),$$

$$\chi_{78} = 0, \ \chi_{8j} = \left(e_j\right)g(s_j),$$

$$\chi_{88} = \left(r_j\right)f(s_j), \ \chi_{37} = 0, \ \chi_{38} = 0,$$

$$\chi_{18} = 0, \ \chi_{27} = 0, \ \chi_{28} = 0, \ \chi_{17} = 0$$

6 Numerical Results and Discussion

In order to study the effect of hydrostatic stress and applied forces on frequency, we have computed stress, strain, and displacements numerically. For this purpose, we got the values of the relevant material parameters [22]

$c_{11} = 13.9 \times 10^{10}$ N/m², $c_{12} = 7.78 \times 10^{10}$ N/m², $c_{13} = 7.43 \times 10^{10}$ N/m², $c_{33} = 11.5 \times 10^{10}$ N/m², $\beta_1 = 1.52 \times 10^6$ N/Km², $\beta_3 = 1.53 \times 10^6$ N/Km², $T_0 = 298$ K, $c_v = 420$ J/kgK, $p_3 = -452 \times 10^{-6}$ C/Km², $e_{31} = -5.2$ C/m², $e_{33} = 15.1$ C/m², $e_{15} = 12.7$ C/m², $\in_{11} = 6.46 \times 10^{-9}$ C²/Nm², $\in_{33} = 5.62 \times 10^{-9}$ C²/Nm², $\rho_1 = 7500$ Kgm⁻², and for the gravitating half space [20] $\lambda = 67.7$ GPa, $\mu = 74.3$ GPa, and $\rho_2 = 3.323$ g/cm³.

The dispersion curves are drawn in Figs. 1 and 2 for variation of normal stress Π_{xx} versus the wave number of the thermopiezoelectric layer with respect to different piezoelectricconstants. Figure 1 shows the magnitude variation of normal stress modes when wave number is increasing for the different values of hydrostatic stress. Figure 2 reveals oscillating trend in the wave propagation due to the increase in dielectric constant values. It can be noted that the effect of hydrostatic pressure and piezoelectric constants shows increasing effect on the stress magnitude. A comparative illustration is made in Figs. 3 and 4 between the normal strain and the wave number s of the layer for the piezoelectric constant values. It is evident that the lower
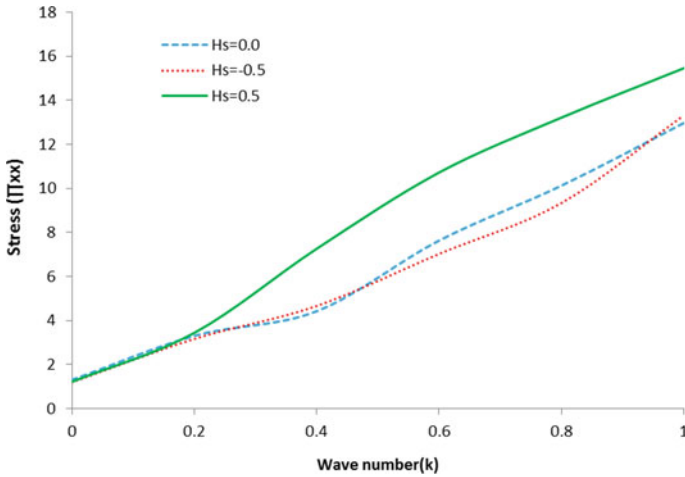
Fig. 1 Variation of radial stress versus wave number of a thermoelastic layer with $e_{31} = -2.5$, $e_{33} = 5.2$, $e_{15} = 6.5$
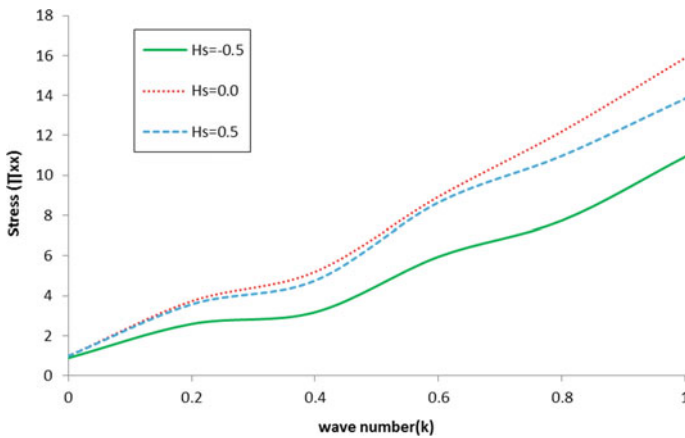
Fig. 2 Variation of radial stress versus wave number of a thermoelastic layer with $e_{31} = -2.5$, $e_{33} = 10.2$, $e_{15} = 11.5$

range of wave number and the normal strain attain minimum value in both cases of piezoelectric constants, and after that, it increases with the increase of hydrostatic stress.

The 3D curve in Figs. 5 and 6 clarifies the relation between the phase velocity cp and frequency ω against the constant values of dielectric and hydrostatic stress. These curves explain the dependence of dielectric and hydrostatic stress values on the frequency and phase velocity.
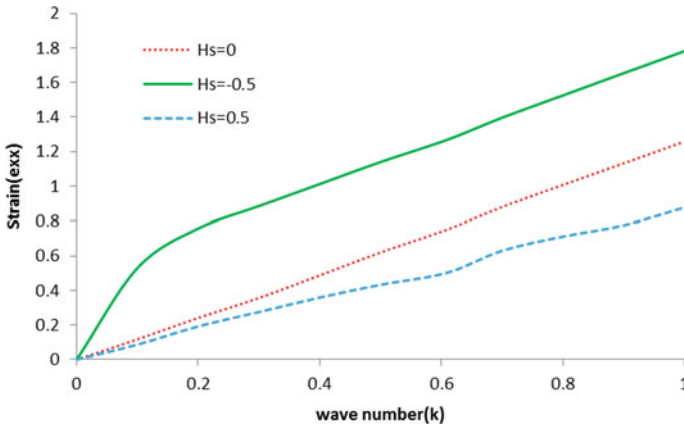
Fig. 3 Variation of radial strain versus wave number of a thermoelastic layer with $e_{31} = -2.5$, $e_{33} = 5.2$, $e_{15} = 6.5$
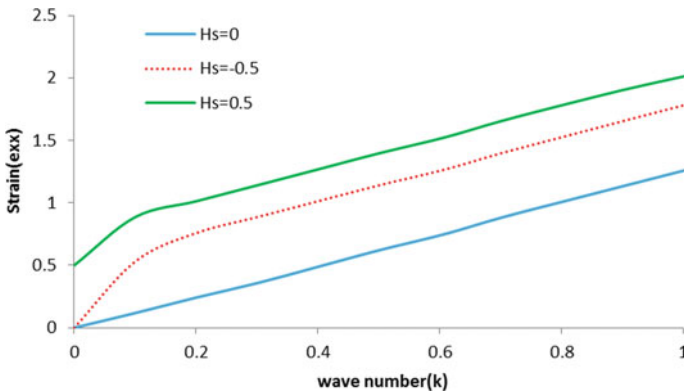
Fig. 4 Variation of radial strain versus wave number of a thermoelastic layer with $e_{31} = -2.5$, $e_{33} = 10.2$, $e_{15} = 11.5$

7 Conclusion

This study demonstrates the effect of hydrostatic stress and piezoelectric effect on elastic waves of a thermoelastic layer embedded on a gravitating half space. The equation of motion is derived using two-dimensional elastic equation coupled with piezoelectric and thermoelastic equations. The frequency equations are obtained for free stress, insulated thermal and electrical boundary conditions at the gravitating half space. The numerical results are analyzed for PZT-4 material and the computed stress, strain, frequency, and phase velocity are presented in the form of dispersion curves. From the results indicated, we can conclude that
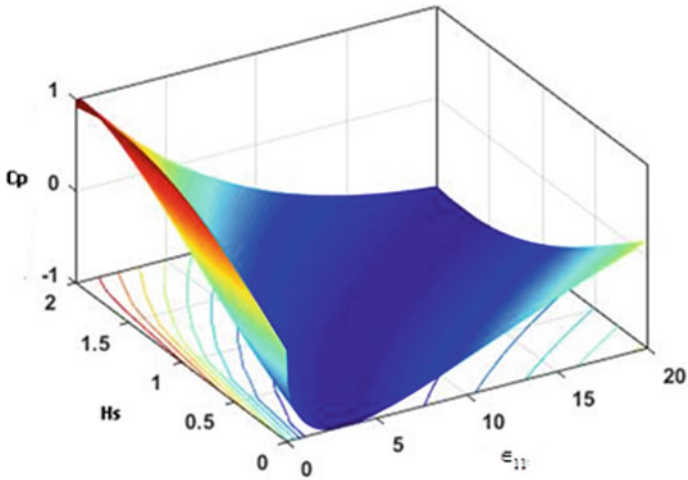
Fig. 5 3D distribution phase velocity Cp with dielectric constant $\in_{11}$ and hydrostatic stress H_s
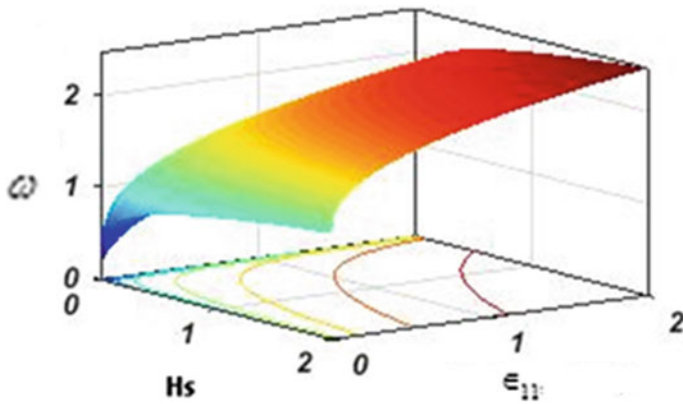
Fig. 6 3D distribution of frequency ω with dielectric constant $\in_{11}$ and hydrostatic stress H_s

(a) The stress and strain increase as the wave number increases with increasing the values of e_{31}, e_{33}, e_{15} and H_s.

(b) Phase velocity decreases with increasing dielectric constant $\in_{11}$ and hydrostatic stress H_s.

(c) The frequency increases with increasing dielectric constant $\in_{11}$ and hydrostatic stress H_s.

References

1. Morse RW (1954) Compressional waves along an anisotropic circular cylinder having hexagonal symmetry. J Acoust Soc America 26:1018–1021. https://doi.org/10.1121/1.1907460
2. Bhimraddi AA (1984) A higher order theory for free vibration analysis of circular cylindrical shell. Int J Solid Struct 20:623–630. https://doi.org/10.1177/0731684407081385
3. Mindlin RD (1979) Equation of high frequency vibrations of thermo-piezoelectric crystal plates. In: Interactions in elastics solids. Springer, Wien
4. Nowacki W (1978) Some general theorems of thermo-piezoelectricity. J Therm Stresses 1:171–182. https://doi.org/10.1080/01495737808926940
5. Nowacki W (1979) Foundations of linear piezoelectricity. In: Parkus H (ed) Electromagnetic interactions in elastic solids. Springer, Wien. (Chapter 1)
6. Chandrasekhariah DS (1984) A temperature rate dependent theory of piezoelectricity. J Therm Stresses **7**:293–306. https://doi.org/10.1080/01495738408942213
7. Chandrasekhariah DS (1988) A generalized linear thermoelasticity theory of piezoelectric media. Acta Mech 71:39–49. https://doi.org/10.1007/BF01173936
8. Chandrasekharaiah DS (1986) Thermoelasticity with second sound—a review. Appl Mech Rev 39:355–376. https://doi.org/10.1115/1.3143705
9. Tang YX, Xu K (1995) Dynamic analysis of a piezothermoelastic laminated plate. J Therm Stresses 18:87–104. https://doi.org/10.1080/01495739508946292
10. Yang JS, Batra RC (1995) Free vibrations of a linear thermo-piezoelectric body. J Therm Stresses 18:247–262. https://doi.org/10.1080/01495739508946301
11. Moghadam PY, Tahani M, Naserian-Nik AM (2003) Analytical solution of piezolaminated rectangular plates with arbitrary clamped/simply-supported boundary conditions under thermo-electro-mechanical loadings. Appl Math Modell 37(5):3228–3241. https://doi.org/10.1016/j.apm.2012.07.034
12. Sabzikar Boroujerdy M, Eslami MR (2014) Axisymmetric snap-through behavior of Piezo-FGM shallow clamped spherical shells under thermo-electro-mechanical loading. Int J Press Vessels Pip 120:19–26. https://doi.org/10.1016/j.ijpvp.2014.03.008
13. Ponnusamy P, Selvamani R (2013) Wave propagation in magneto thermo elastic cylindrical panel. European J Mech A Solids 39:76–85. https://doi.org/10.1016/j.euromechsol.2012.11.004
14. Selvamani R (2017) Stress waves in a generalized thermos elastic polygonal plate of inner and outer cross sections. J Solid Mech 9(2):263–275
15. Selvamani R, Mahinde OD (2018) Influence of rotation on transversely isotropic piezo electric rod coated with thin film. Eng Trans 66(3):211–220
16. De SN, Sengupta PR (1972) Magneto-elastic waves and disturbances in initially stressed conducting media. Pure Appl Geophys 93:41–54. https://doi.org/10.1007/bf00875220
17. Acharya DP, Sengupta PR (1978) Magneto-thermo-elastic waves in an initially stressed conducting layer. Gerlands Beitr Geophys 87:229–239. https://doi.org/10.1007/BF02745739
18. Acharya DP, Sengupta PR (1978) Magneto-thermo-elastic surface waves in initially stressed conducting media. Acta Geophys Polonica 26:299–311
19. Gubbins D (1990) Seismology and plate tectonics. Cambridge University Press, Cambridge
20. Kundu S, Pandit DK, Gupta S, Manna S (2016) Love wave propagation in a fiber-reinforced medium sandwiched between an isotropic layer and gravitating half-space. J Eng Math 100(1):109–119. https://doi.org/10.1002/nag.2254
21. Vinh PC, Anh VTN (2014) Rayleigh waves in an orthotropic half-space coated by a thin orthotropic layer with sliding contact. Int J Eng Sci 75:154–164(2014)
22. Paul HS, Renganathan K (1985) Free vibration of a pyroelectric layer of hexagonal (6 mm) class. J Acoust Soc America 78(2):395–397. https://doi.org/10.1007/BF01177170

Effect of Viscous Dissipation of Laminar Flow over a Flat Plate with Variable Properties

A. K. Singh, G. Iyyappan, and B. Jaganathan

Abstract The current study focused on forced convection water boundary layer flow on permeable diverging channel for variable physical properties of fluid. The formation of coupled nonlinear partial differential equations is expressed in terms of non-dimensional quantity using similarity transformation. The solution of non-dimensional differential equation obtained by numerical finite difference scheme with combination of quasi-linearization technique. It is found that the Eckert number is significant in the boundary layer region in laminar flow, and also, the effects of physical parameters are investigated numerically and shown graphically.

Nomenclature

f	dimensionless streamfunction
T	temperature
N	viscosity ratio
g	acceleration due to gravity

A. K. Singh (✉) · B. Jaganathan
Mathematics Division, School of Advanced Science, VIT University,
Chennai Campus, Chennai 600127, India
e-mail: abhishekkumar.singh@vit.ac.in

B. Jaganathan
e-mail: jaganathan.b@vit.ac.in

G. Iyyappan (✉)
Department of Mathematics, Hindustan Institute of Technology and Science,
Padur, Chennai 603103, India
e-mail: giyyappan88@gmail.com

u_e	flow velocity at the edge
Nu	Nusselt number
C_p	-specific heat at constant pressure
v	-kinematic viscosity
ρ	density
x, y	Cartesian coordinates
ψ	Streamfunction
A	Mass transfer parameter
Ec	Viscous dissipation parameter
μ	dynamic viscosity
Pr	-Prandtl number
Re	Reynolds number
C_f	Skin friction coefficient
U_∞	freestream velocity
U	reference velocity
u	-velocity in x-direction
v	-velocity in y-direction

1 Introduction

The water boundary layer flow induced by forced convection patterns involves many engineering applications including paper production, metal spinning, wire drawing and glass fiber [1–3]. The viscosity and thermal conductivity properties of water are important role play in the field of engineering. These parameters are very challenging, while control and maintain a constant temperature between the fluid and the wall. Ishak et al. [4–6] have been discussed characteristics in parallel stream with constant surface heat flux for a moving flat plate and transpiration of heat transfer over a moving permeable surface. Umavathi et al. [6] investigated free convection laminar flow of thermal conductivity with variable viscosity over a vertical Channel. The double slot suction (injection) properties of rotating and moving fluids over the sphere have been discussed by Roy [7]. Later, Patil et al. [8, 9] are given solution methods and similar solution of transformed coupled partial differential equations using quasi-linearization technique.

In the current study, the special attention is paid to forced convection laminar boundary layer flow of diverging channels with variable viscosity and temperature dependent on flat plate surface. The effects of viscous dissipation (Eckert Number) are more significant in the fluid region laminar to transition.

2 Formation of Governing Equations

We assume fluid with very small viscosity on flat plate horizontally, the freestream velocity U_∞ and the pattern of streamlines and flow are uniform. However, detailed discussion is presented by Schlichting [10]. Viscosity (μ) and Pr values are taken [9], and the thermal conductivity (k) with temperature is quite significant (Table 1) [11].

The mathematical simplification we achieved, the boundary layer equations are

$$\frac{\partial u}{\partial x} + \frac{\partial v}{\partial y} = 0 \tag{1}$$

$$u\frac{\partial u}{\partial x} + v\frac{\partial u}{\partial y} = u_e\left(\frac{du_e}{dx}\right) + \frac{1}{\rho}\frac{\partial}{\partial y}\left(\mu\frac{\partial u}{\partial y}\right) \tag{2}$$

$$u\frac{\partial T}{\partial x} + v\frac{\partial T}{\partial y} = \frac{1}{\rho}\frac{\partial}{\partial y}\left(\frac{\mu}{Pr}\frac{\partial T}{\partial y}\right) + \frac{\mu}{\rho C_p}\left(\frac{\partial u}{\partial y}\right)^2 \tag{3}$$

The physical boundary conditions are given by

$$u(x, y) = v(x, y) = 0, \quad T(x, y) = T_w \text{ at } y = 0 \tag{4}$$

$$u(x, y) \to u_e, \quad v(x, y) \to 0, \quad T \to T_\infty \text{ as } y \to \infty.$$

Table 1 Thermo-physical values of water at different level of temperatures Lide [11]

Temperature T (°C)	Density ρ (g/m³)	Specific heat C_p (J 10^7/kg K)	Thermal conductivity K (erg 10^5/cm s K)	Viscosity μ (g 10^{-2}/cm s)	Prandtl number (Pr)
0	1.00228	4.2176	0.5610	1.7930	13.48
10	0.99970	4.1921	0.5800	1.3070	9.45
20	0.99821	4.1818	0.5984	1.0060	7.03
30	0.99565	4.1784	0.6154	0.7077	5.12
40	0.99222	4.1785	0.6305	0.6532	4.32
50	0.98803	4.1806	0.6435	0.5470	3.55

Using the non-dimensional quantities and streamfunction in Eqs. (1)–(3),

$$x = \xi L; \quad \eta^2 = \left(\frac{u_e}{\nu x}\right) y; \quad \psi = (u_e x \nu)^{\frac{1}{2}} f; \quad u = \psi_y; \quad v = -\psi_x;$$

$$u = u_e f_\eta; \quad f_\eta = F; \quad T - T_\infty = (T_w - T_\infty)G;$$

$$v = -\frac{1}{2}\left(\frac{u_e \nu}{x}\right)^{\frac{1}{2}} \left\{2\xi f_\xi + \eta \left(\frac{x}{u_e}\frac{du_e}{dx} - 1\right) f_\eta + \left(\frac{x}{u_e}\frac{du_e}{dx} + 1\right) f\right\} \quad (5)$$

where continuity Eq. (1) is vanished and the boundary layer Eqs. (2)–(4) are reduced to

$$(NF_\eta)_\eta + \left(\frac{m+1}{2}\right) f F_\eta + (1 - F^2) m = \xi \left[F F_\xi - F_\eta f_\xi\right] \quad (6)$$

$$(N Pr^{-1} G_\eta)_\eta + \left(\frac{m+1}{2}\right) f G_\eta + N Ec F_\eta^2 = \xi \left[F G_\xi - G_\eta f_\xi\right] \quad (7)$$

where m is defined by $m = \dfrac{\xi}{u_e}\dfrac{du_e}{d\xi}$. Here, u_e is the external flow velocity and is defined as $\dfrac{u_e}{(1 - \epsilon e^\xi)} = u_\infty$. Also, Eqs. (4) are transformed to

$$\text{when} \quad \eta = 0; \quad f_\eta = F = 0, \quad G = 1$$

$$\text{when} \quad \eta \to \eta_\infty; \quad f_\eta = F = 1, \quad G = 0 \quad (8)$$

Further, $f = \int_0^\eta F d\eta + f_w$; where $f_w = 0$. The temperature between fluid and wall coefficient $\left(Re^{\frac{-1}{2}} C_f\right)$ and friction between fluid and surface coefficient $\left(Re^{\frac{1}{2}} C_f\right)$ are the physical quantities of practical interest which represent the heat transfer rate and the wall shear stress (skin friction), respectively. Also, the coefficients are defined by

$$C_f = \mu \frac{2\left(\frac{\partial u}{\partial y}\right)_{y=0}}{\rho u_e^2} = 2 Re^{\frac{-1}{2}} \xi^{\frac{-1}{2}} (1 - \epsilon e^\xi)^{\frac{-1}{2}} f_{\eta\eta}(\xi, 0) \quad (9)$$

$$\text{i.e.,} \quad Re^{\frac{1}{2}} C_f = 2\xi^{\frac{-1}{2}} (1 - \epsilon e^\xi)^{\frac{-1}{2}} f_{\eta\eta}(\xi, 0)$$

$$Nu = -x \frac{\left(\frac{\partial T}{\partial y}\right)_{y=0}}{(T_w - T_\infty)} = -Re^{\frac{1}{2}} \xi^{\frac{1}{2}} (1 - \epsilon e^\xi)^{\frac{-1}{2}} G_\eta(\xi, 0) \quad (10)$$

$$\text{i.e.,} \quad Re^{\frac{-1}{2}} Nu = -\xi^{\frac{1}{2}} (1 - \epsilon e^\xi)^{\frac{-1}{2}} G_\eta(\xi, 0)$$

3 Numerical Computations

The physical conditions (8) used in Eqs. (6) and (7) and apply finite difference scheme, we get the following coupled PDE:

$$X_1^n F_{\eta\eta}^{n+1} + X_2^n F_{\eta}^{n+1} + X_3^n F^{n+1} + X_4^n F_{\xi}^{n+1} + X_5^n G_{\eta}^{n+1} + X_6^n G^{n+1} = X_7^n \quad (11)$$

$$Y_1^n G_{\eta\eta}^{n+1} + Y_2^n G_{\eta}^{n+1} + Y_3^n G^{n+1} + Y_4^n G_{\xi}^{n+1} + Y_5^n F_{\eta}^{n+1} + Y_6^n F^{n+1} = Y_7^n \quad (12)$$

Also,

$$\text{when } \eta = 0 \; ; \; F^{n+1} = 0, \; G^{n+1} = 1 \quad (13)$$

$$\text{when } \eta \to \eta_{\infty} \; ; \; F^{n+1} = 1, \; G^{n+1} = 0$$

The coefficients of Eqs. (11) and (12) are given by

$$X_1^n = N$$
$$X_2^n = -a_1 N^2 G_{\eta} + \left(\frac{m+1}{2}\right) f + \xi f_{\xi}$$
$$X_3^n = -\xi F_{\xi} - 2mF \; ;$$
$$X_4^n = -\xi F$$
$$X_5^n = -a_1 N^2 F_{\eta} \; ; \quad X_6^n = -a_1 N^2 F_{\eta\eta} + 2a_1^2 N^3 F_{\eta} G_{\eta}$$
$$X_7^n = -a_1 N^2 F_{\eta} G_{\eta} - a_1 N^2 F_{\eta\eta} G + 2a_1^2 N^3 F_{\eta} G_{\eta} G - \xi F F_{\xi} - m \left(1 + F^2\right)$$

$$Y_1^n = N Pr^{-1}$$
$$Y_2^n = -2a_1 N^2 Pr^{-1} G_{\eta} + 2a_3 G_{\eta} N + \left(\frac{m+1}{2}\right) f + \xi f_{\xi}$$
$$Y_3^n = a_3 N G_{\eta\eta} - a_1 N^2 Pr^{-1} G_{\eta\eta} - 2a_1 a_3 N^2 G_{\eta}^2 + 2a_1^2 N^3 Pr^{-1} G_{\eta}^2 - a_1 N^2 Ec F_{\eta}^2$$
$$Y_4^n = -\xi F$$
$$Y_5^n = 2N Ec F_{\eta} \; ;$$
$$Y_6^n = -\xi G_{\xi}$$
$$Y_7^n = a_3 G_{\eta}^2 N - a_1 G_{\eta}^2 Pr^{-1} N^2 + a_3 G_{\eta\eta} G N - a_1 G_{\eta\eta} G Pr^{-1} N^2 - 2a_1 a_3 G_{\eta}^2 G N^2$$
$$\quad + 2Pr^{-1} a_1^2 G_{\eta}^2 G N^3 - \xi F G_{\xi} + N Ec F_{\eta}^2 - a_1 N^2 Ec F_{\eta}^2 G$$

Applying finite difference scheme in Eqs. (11) and (12), we get system of equation and converted to matrix form. The structure of matrices like tri-diagonal matrices is given by Varga's algorithm [12]. A convergence criterion is if the difference is equal to 10^{-4}, then the computation process is terminated.

$$i.e., Max \left\{ |(F_{\eta})_w^{n+1} - (F_{\eta})_w^n|, \quad |(G_{\eta})_w^{n+1} - (G_{\eta})_w^n| \right\} \leq 10^{-4} \quad (14)$$

4 Discussion and Results

The following investigation has been carried out for different values of parameter, and the boundary of the fluid flow η_{∞} has been taken as 6.0.

The effects of velocity and temperature profiles are shown in Fig. 1. The solid line indicates the effects of temperature profile, and dotted line represents the effects of
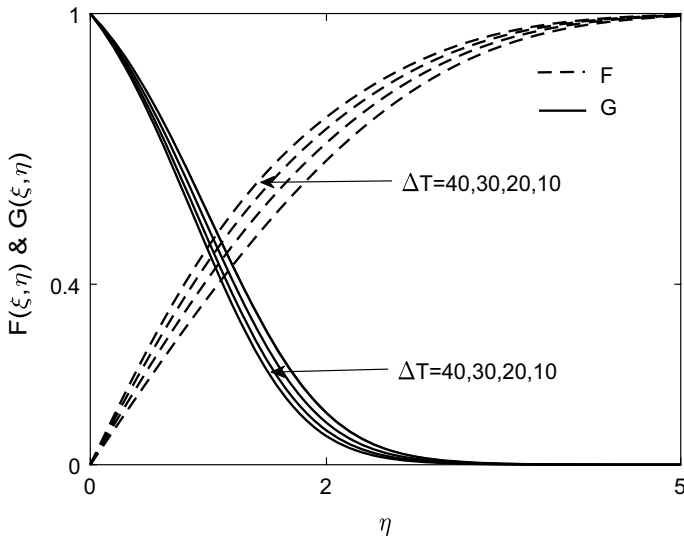
Fig. 1 Effects of ΔT on F and G for $\epsilon = 0.01$ $\xi = 0.5$, $Ec = 0.5$ and $T_\infty = 18.7\,°C$

velocity profile. The effects of ΔT on temperature profiles at $\xi = 0.5$ and $\epsilon = 0.01$ is presented in Fig. 1 for $\xi = 0.5$ and $\epsilon = 0.01$. It should be noted that ΔT increases from $\Delta T = 20$ to $\Delta T = 30$, the velocity profile is increased by 5%, and temperature profile is approximately decreased within 5% of boundary layer. It can be noted the effects of velocity and temperature profiles are very less in case of increasing or decreasing the reference temperature.

Figure 2 displays the effect of Ec on temperature profiles G at $\epsilon = 0.01$ and $\xi = 0.5$. When Ec increases from $Ec = 1.0$ to $Ec = 1.5$, the temperature profiles overshoot the boundary layer, viscous dissipation EC decreases from $E = -1.5$ to $E = -2.0$, and the temperature profiles undershoot the boundary layer. The resulting temperature profiles will consist of two boundary layer profiles on walls in the center of region of laminar to turbulent.

Figure 3 shows the effects of Eckert number (Ec) on $[Nu_x(Re_L\xi \exp(\xi))^{-1/2}]$. Due to the variation of $Ec = 0.5$ to $Ec = 1.0$ for $\epsilon = 0.01$, the heat transfer rate decreases gradually 48% at $\xi = 1.5$. The viscous dissipation decreases from $Ec = -0.5$ to $Ec = -1.0$ for $\epsilon = 0.01$, and the heat transfer rate increased to 90% at $\xi = 1.5$. It is noteworthy that the density of the fluid must be the same for each part of the plate and free stream velocity is lesser than that velocity at the wall. If decreases the Eckert number, the density of the fluid varies inside the wall.
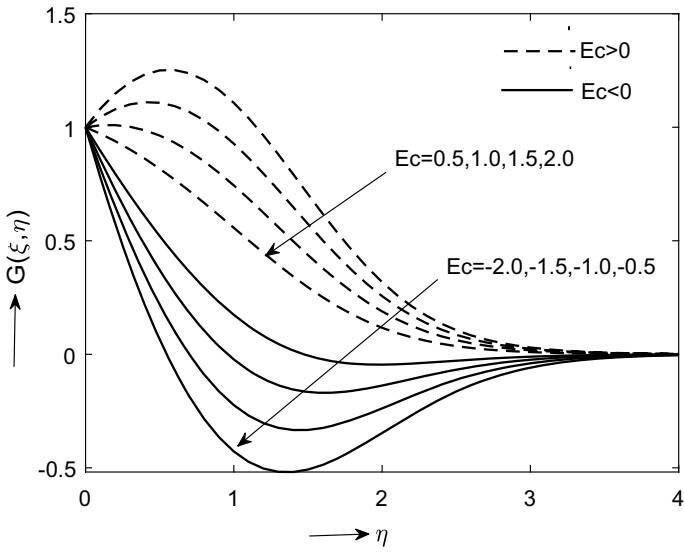
Fig. 2 Effects of Ec on G $\epsilon = 0.01$ $\Delta T_w = 10\,^\circ\text{C}$ and $T_\infty = 18.7\,^\circ\text{C}$
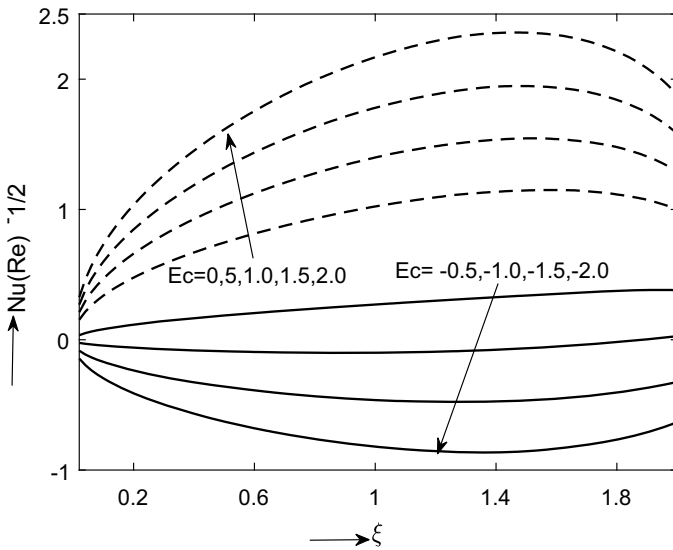
Fig. 3 Effects of Ec on Nu for $\epsilon = 0.01$ $\Delta T_w = 10\,^\circ\text{C}$ and $T_\infty = 18.7\,^\circ\text{C}$

5   Conclusions

A comprehensive study has been performed on force convection laminar boundary layer with variable viscosity and Prandtl number. Also, the effects of viscous dissipation parameter is analyzed over a flat plate with variable properties fluids. The heat transfer coefficient is more significant on laminar flow, but skin friction coefficient is less affected and not presented in the graph. It is found that constant fluid properties differ from those variable fluid properties.

References

 1. Tadmor Z, Klein I (1970) Engineering principles of plasticating extrusion. Polymer science and engineering series. Van Nostrand Reinhold, New York
 2. Altan T, Oh S, Gegel H (1979) Metal forming fundamentals and applications. American Society of Metals, Metals Park
 3. Fisher EG (1976) Extrusion of plastics. Wiley, New York
 4. Ishak A, Nazar R, Pop I (2009) Flow and heat transfer characteristics in a moving flat plate in parallel stream with constant surface heat flux. Heat Mass Transf 45:563–567
 5. Ishak A, Nazar R, Pop I (2009) The effects of transpiration on the flow and heat transfer over a moving permeable surface in a parallel stream. Chem Eng J 148:63–67
 6. Umavathi JC, Chamkha AJ, Mohiuddin S (2016) Combined effect of variable viscosity and thermal conductivity on free convection flow of a viscous fluid in a vertical channel. Int J Numer Methods Heat Fluid Flow 26:18–39
 7. Roy S, Saikrishnan P, Pandey BD (2009) Influence of double slot suction (injection) into water boundary layer flows over sphere. Int Commun Heat Mass Transf 36:646–650
 8. Patil PM, Roy S, Chamkha AJ (2010) Mixed convection flow over a vertical power law stretching sheet. Int J Numer Method Heat Fluid Flow 4:445–458
 9. Saikrishnan P, Roy S, Takhar HS, Ravindran R (2010) Role of thermally stratified medium on a free convection flow from a rotating sphere. Int J Numer Methods Heat Fluid Flow 20:96–110
10. Schlichting H (2000) Boundary layer theory. McGraw Hill, New York
11. Lide DR (ed) (1990) CRC handbook of chemistry and physics, 71st edn. CRC Press, Boca Raton
12. Varga RS (2000) Matrix iterative analysis. Prentice-Hall, Englewood Cliffs

Darcy–Bénard Convection with Internal Heating and a Thermal Nonequilibrium—A Numerical Study

C. Hemanthkumar, I. S. Shivakumara, and B. Rushikumar

Abstract The impact of local thermal nonequilibrium (LTNE) in the presence of a uniform internal heating in both the fluid and solid phases of the porous medium on the onset of Darcy–Bénard convection is investigated. Emphasis is laid on LTNE effect on the steady-state heat conduction in analyzing the onset criterion. The Galerkin method is used to carry out the parametric study on the instability characteristics of the system by numerically computing the critical stability parameters. The presence of LTNE effect on the steady-state heat conduction is found to advance the onset in comparison with its absence and also to increase the dimension of convection cells. The exiting results are obtained as a particular case from the present study.

Keywords Convection · Porous medium · Local thermal nonequilibrium · Internal heat source

Nomenclature

a	Wavenumber in the x-direction
c	Specific heat
d	Width of the layer
$D = \mathrm{d}/\mathrm{d}z$	Differential operator
$\vec{g}$	Acceleration due to gravity
h	Interphase heat transfer coefficient
H	Dimensionless interphase heat transfer coefficient
k	Thermal conductivity
K	Permeability

C. Hemanthkumar · I. S. Shivakumara (✉)
Department of Mathematics, Bangalore University, Jnana Bharathi Campus, Bangalore 560056, India
e-mail: shivakumarais@gmail.com

B. Rushikumar
Department of Mathematics, VIT University, Vellore 632014, India
e-mail: rushibkumar@gmail.com

l & m	Horizontal wave number
p	Pressure
$\vec{q}$	Velocity vector (u, v, w)
q'''	Uniform heat source per unit volume
Q	Dimensionless heat source strength
R_D	Darcy-Rayleigh number
Pr_D	Darcy-Prandtl number
t	Time
T	Temperature
W	Amplitude of perturbed vertical velocity
(x, y, z)	Cartesian coordinates

Greek Symbol

α	Ratio of thermal diffusivity
γ	Porosity modified conductivity ratio
β	Coefficient of thermal expansion of the fluid
ε	Porosity
μ_f	Dynamic viscosity of the fluid
∇^2	Laplacian operator
ρ_f	Fluid density
ρ_0	Fluid density at $T = T_0$
ϕ	Solid temperature
Φ	Amplitude of solid temperature
θ	Fluid temperature
Θ	Amplitude of fluid temperature
ω	Growth factor $(= \omega_r + i\omega_i)$

Subscripts and Superscripts

b	Basic state
f	fluid
s	solid
$'$	Perturbed variable
$*$	Dimensionless variable

1 Introduction

Thermal convective instability in fluid-saturated porous media is one of the classical topics and has attracted researchers for the last seventy years. The reasons for such developments were obvious due to its natural occurrence and applications in engineering practice such as building insulation and infiltration, food processing, crystal growth, underground spread of pollutants, nuclear waste processing, and so on. The studies are largely in light of the presumption that both phases of the porous media are in local thermal equilibrium (LTE). In any case, in numerous common-sense applications including fast streams or extensive temperature contrasts between the two phases the supposition of LTE is deficient in such conditions; it is applicable to evaluate the local thermal nonequilibrium (LTNE) impacts by considering a two-field model for the energy equation, each speaking to the two phases independently [1–3].

The study of thermal convection in porous media using a LTNE model is of recent origin. A systematic study was started with Banu and Rees [4] by considering the thermal nonequilibrium theory given by Nield and Bejan [5]. Subsequently, the study was extended to consider various additional factors such as non-Darcy effect [6, 7], anisotropy of the porous medium [8, 9], nonlinear and Cattaneo effects [10–12], modified boundary conditions [13, 14], throughflow [15, 16], viscous dissipation [17, 18], internal heating [19–25], and so on. The developments are well reported in the literature [26–28].

In the investigation of buoyancy-driven convection in porous media with internal heating and LTNE model, it is pragmatic to allow the heat transfer between the two phases in the basic state as well. As a result, the fluid and solid temperature distributions in the basic state may vary significantly and influence the instability of the system. Although this concern was considered by Nouri-Borujerdi et al. [23], the study was limited to the instability caused by only internal heating either in the solid phase or the fluid phase.

The objective of the present study is to investigate the onset of Darcy–Bénard convection under LTNE conditions in the presence of a uniform internal heating in both the two phases of the porous medium by recognizing the relevance of LTNE on the steady-state heat conduction as well. The Galerkin method is used to numerically study the onset criterion and the effect of physical parameters on the instability of the system is delineated.

2 Mathematical Formulation

The physical configuration is as shown in Fig. 1. An infinite horizontal layer of fluid-saturated internally heated porous medium with the assumption of LTNE is considered. The governing stability equation in dimensionless from is [24]:
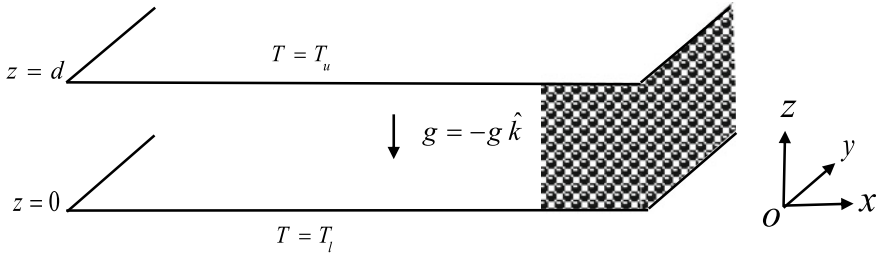
Fig. 1 Physical configuration

$$\left(\frac{1}{\mathrm{Pr}_D}\frac{\partial}{\partial t} + 1\right)\nabla^2 w = R_D \nabla_1^2 \theta, \tag{1}$$

$$\frac{\partial \theta}{\partial t} + (\vec{q}.\nabla)\theta = \nabla^2\theta + H(\phi - \theta) + Q_f, \tag{2}$$

$$\alpha\frac{\partial \phi}{\partial t} = \nabla^2\phi + \gamma H(\theta - \phi) + Q_s, \tag{3}$$

where $\vec{q} = (u, v, w)$ is the velocity vector, p pressure, $R_D = \rho_0 g \beta \Delta T K d (\rho c)_f / \varepsilon\mu_f k_f$ is Darcy–Rayleigh number, $\mathrm{Pr}_D = \mu_f \varepsilon d^2 (\rho c)_f / \rho_0 k_f K$ is the Darcy–Prandtl number, $H = hd^2/\varepsilon k_f$ is the interphase heat transfer coefficient, $Q_f = d^2 q_f'''/k_f(T_l - T_u)$ is the heat source strength of the fluid phase, $Q_s = d^2 q_s'''/k_s(T_l - T_u)$ is the heat source strength of the solid phase, $\gamma = \varepsilon k_f/(1 - \varepsilon)k_s$ is the porosity modified conductivity ratio, $\alpha = \kappa_f/\kappa_s = (\rho c)_s k_f/(\rho c)_f k_s$ is the ratio of diffusivity, $\nabla_1^2 = \frac{\partial^2}{\partial x^2} + \frac{\partial^2}{\partial y^2}$ and $\nabla^2 = \nabla_1^2 + \frac{\partial^2}{\partial z^2}$ are Laplacian operators.

The following quantities are non-dimensionalized as:

$$(x, y, z) = d(x^*, y^*, z^*), \ \vec{q} = \frac{k_f \varepsilon}{d(\rho c)_f}\vec{q}^*, \ t = \frac{d^2(\rho c)_f}{k_f}t^*,$$

$$p = \frac{k_f \varepsilon\mu}{(\rho c)_f}p^*, \nabla = \frac{\nabla^*}{d}, T_f = T_u + (T_l - T_u)\theta, \ T_s = T_u + (T_l - T_u)\phi. \tag{4}$$

The boundaries are impermeable and fixed at constant but different temperatures. Thus, the relevant boundary conditions are

$$w = 0 \text{ at } z = 0, \ 1 \text{ and } \theta = \phi = 1 \text{ at } z = 0, \ \theta = \phi = 0 \text{ at } z = 1. \tag{5}$$

2.1 Basic State—a Thermal Nonequilibrium State of Pure Conduction

The quiescent basic state is

$$w = 0, \ \theta = \theta_b(z), \ \phi = \phi_b(z), \tag{6}$$

The basic state solution is found to be

$$\theta_b(z) = \frac{HN}{\lambda^2} \left[\frac{(z^2 - z)}{2} - \frac{\cos h(\lambda z)}{\lambda^2} + \frac{\sin h(\lambda z)\tan h(\lambda/2)}{\lambda^2} + \frac{1}{\lambda^2} \right]$$
$$- \frac{Q_f}{2}(z^2 - z) + 1 - z, \tag{7}$$

$$\phi_b(z) = \frac{HN}{\lambda^2} \left[\frac{(z^2 - z)}{2} - \frac{\cos h(\lambda z)}{\lambda^2} + \frac{\sin h(\lambda z)\tan h(\lambda/2)}{\lambda^2} + \frac{1}{\lambda^2} \right]$$
$$- \frac{Q_s}{2}(z^2 - z) + 1 - z. \tag{8}$$

where $N = (Q_f - Q_s)$, $\lambda = \sqrt{H(1 + \gamma)}$. We observe that the distributions of temperature of the two phases significantly change due to the consideration of LTNE effect on the basic state.

$$\left. \begin{array}{l} \theta_b(z) = \frac{N}{(1+\gamma)} \left[\frac{\lambda^3(-z+2z^3-z^4)}{12} - \frac{\lambda^5 z^3}{12} + \cdots \right] - \frac{Q_f}{2}(z^2 - z) + 1 - z \\ \phi_b(z) = \frac{N}{(1+\gamma)} \left[\frac{\lambda^3(-z+2z^3-z^4)}{12} - \frac{\lambda^5 z^3}{12} + \cdots \right] - \frac{Q_f}{2}(z^2 - z) + 1 - z \end{array} \right\} \text{ as } \lambda \to 0. \tag{9}$$

If $\lambda = 0$, then Eq. (9) reduces to

$$\theta_b(z) = -\frac{Q_f}{2}(z^2 - z) + 1 - z$$
$$\phi_b(z) = -\frac{Q_s}{2}(z^2 - z) + 1 - z. \tag{10}$$

In the absence of internal heating, it is seen that Eq. (10) turns out be same and coincides with Banu and Rees [4].

Perturbations are superimposed on the basic state to carry out the linear stability analysis as

$$w = w', \ \theta = \theta_b + \theta', \ \phi = \phi_b + \phi', \tag{11}$$

Substituting Eq. (11) into Eqs. (1–3), linearizing the equations (neglecting the primes for simplicity) and the normal mode solution is assumed as:

$$(w, \theta, \phi) = [W(z), \Theta(z), \Phi(z)] \exp\{i(lx + my) + \omega t\}. \tag{12}$$

where $W(z)$, $\Theta(z)$, and $\Phi(z)$ are the amplitude functions of the normal modes. Substituting Eq. (14) into the linearized governing equations we get

$$\left(\frac{\omega}{\Pr_D} + 1\right)(D^2 - a^2)W = -a^2 R_D \Theta, \tag{13}$$

$$[\omega - (D^2 - a^2) + H]\Theta - H\Phi = -D\theta_b W, \tag{14}$$

$$[\alpha\omega - (D^2 - a^2) + H\gamma]\Phi - H\gamma\Theta = 0. \tag{15}$$

The boundary conditions now become

$$W = \Theta = \Phi = 0 \text{ at } z = 0, 1. \tag{16}$$

Equations (13–15) together with boundary condition (16) constitute an eigenvalue problem which is solved numerically by employing the Galerkin method. Accordingly, W, Θ and Φ are expanded in the form

$$W = \sum_{i=1}^{N} A_i \left(z^i - z^{i+1}\right), \ \Theta = \sum_{i=1}^{N} B_i \left(z^i - z^{i+1}\right), \ \Phi = \sum_{i=1}^{N} C_i \left(z^i - z^{i+1}\right) \tag{17}$$

where A_i, B_i, and C_i are unknown coefficients. The usual procedure leads to the generalized eigenvalue problem in the form

$$AX = \omega BX. \tag{18}$$

where A and B are real matrices of order $3N \times 3N$ and X is the eigenvector and ω is the eigenvalue. Following the method explained in Shivakumara et al. [29], Makinde [30, 31] and Makinde and Motsa [32]. The critical Darcy–Rayleigh number as a function of wavenumber is computed. The numerical computations performed for various physical parameters revealed that the instability appears only through stationary mode ($\omega = 0$).

3   Results and Discussion

The critical Darcy–Rayleigh number computed with respect to the wavenumber for various physical parameters found to converge by taking six terms (i.e., $N = 6$) in the Galerkin expansion. To validate the numerical method employed, results are computed under the limiting case of no internal heating ($Q_f = 0 = Q_s$) and compared with the closed-form solutions of Banu and Rees [4] in Table 1. It is observed that the outcomes are in good consistency. The process of convergence of the Galerkin method for selected parametric values is shown in Table 2, and the results get converged for $N = 6$.

Table 1 Comparison of the critical Darcy–Rayleigh number and the critical wavenumber with those of Banu and Rees [4] for different values of H when $\gamma = 1.0$, and $Q_f = Q_s = 0$

	Banu and Rees [4]		Present study	
$Log_{10}H$	a_c	R_{Dc}	a_c	R_{Dc}
-2.0	3.142388	39.498405	3.1423875	39.49840508
-1.5	3.144098	39.541537	3.1440980	39.54153702
-1.0	3.149441	39.677163	3.1494408	39.67716226
-0.5	3.165691	40.098560	3.1656911	40.09856012
0	3.211317	41.362100	3.2113170	41.36210014
0.5	3.313460	44.804663	3.3134594	44.80466358
1	3.436346	52.359639	3.4363457	52.35963914

Table 2 Process of convergence of the Galerkin method for different parametric values

	$\gamma = 1, H = 1, Q_s = 5, Q_f = 5$		$\gamma = 1, H = 1, Q_s = 5, Q_f = 10$	
N	R_{Dc}	a_c	R_{Dc}	a_c
1	41.8851	3.23166	41.8851	3.23166
2	36.4496	3.52978	28.9928	3.88357
3	36.4275	3.49082	28.2351	3.87378
4	35.9930	3.50670	28.5929	3.87131
5	35.9892	3.50815	28.5631	3.88038
6	35.9883	3.50810	28.5617	3.88019

Both fluid and solid temperature distributions of the basic sate are shown in Figs. 2a, b, and 3a, b. The highlight of the present study is that the LTNE effect ($H \neq 0$) on the steady-state basic heat conduction is considered. The figures shown
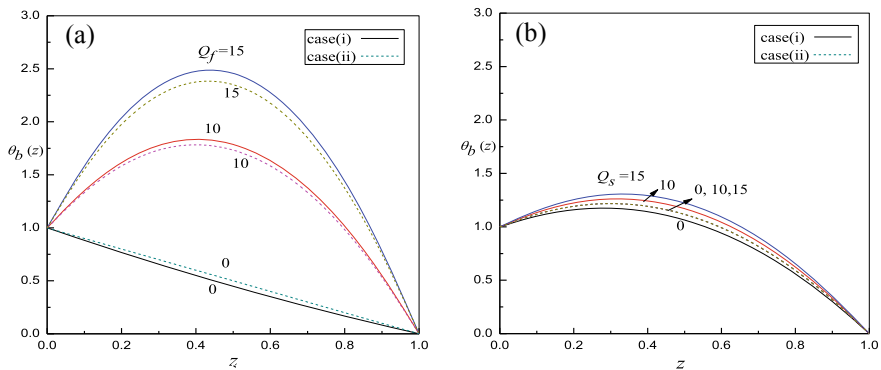
Fig. 2 Basic fluid temperature distributions with z for different values **a** Q_f with $Q_s = 5$ and **b** Q_s with $Q_f = 5$ when $\gamma = 1$
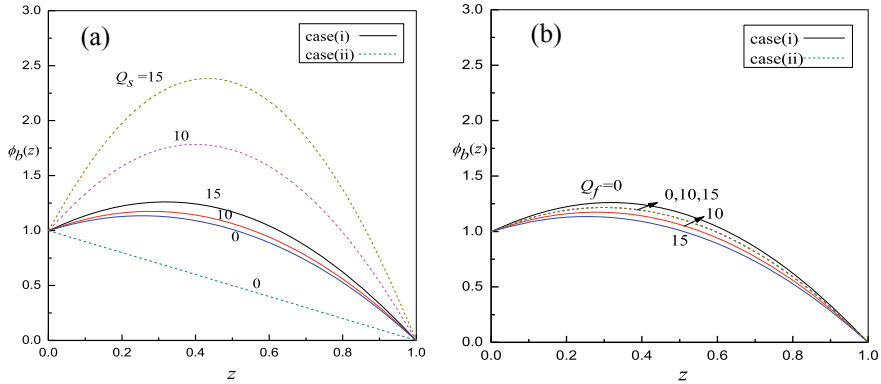
Fig. 3 Basic solid temperature distributions with z for different values **a** Q_f with $Q_s = 5$ and **b** Q_s with $Q_f = 5$ when $\gamma = 1$

correspond to the results obtained for this case which are denoted by case (i). For the sake of comparison, the results are also obtained by considering $H = 0$ (LTE case) in the steady-state basic heat conduction. The dotted curves represent the results for this case in the figures, and they are denoted by case (ii). It is to be noted that the curves are by and large parabolic in nature in the absence of internal heat generation. The curves are linear while an increase in the value of Q_f and Q_s enhance the deviation of basic temperature distributions. The deviation in $\theta_b(z)$ with Q_f is found to be more pronounced than with increasing Q_s.

Figure 4a, b, and c displays the variations of R_{Dc}, a_c and $\gamma R_{Dc}/(1 + \gamma)$ as a function of H for different values of γ when $Q_f = 10$ and $Q_s = 5$. It is evident that for a fixed nonzero value of γ, R_{Dc} increments relentlessly with H, achieves a most extreme and stays unaltered from thereon with further increment in H. Nevertheless, for lower values of $\gamma = 0.01$ and 0.001, R_{Dc} increases abruptly as H increases for case (i) and case (ii). These figures also demonstrate that R_{Dc} and $\gamma R_{Dc}/(1 + \gamma)$ are independent of γ in both small and large H limits. This is due to the fact that for very small values of H and large values of γ, there is no prominent transfer of heat between the two phases in both the cases, and hence, the properties of the solid phase influence the condition for the onset. It is also observed that with an increase in the values of γ the critical Darcy–Rayleigh number decreases for moderate and large values of H. Increase in the value of γ results in significant transfer of heat through both the phases which reduces the stabilizing effect of H and advances the onset of convection. The curves of R_{Dc} for case (i) lie above those of case (ii) indicating the effect of LTNE on steady-state heat conduction (case (i)) retards the onset of convection in comparison with case (ii).

The variation of a_c as a function of H shown in Fig. 4b indicates that, a_c is not affected in the large and small—H limits, while at intermediate values of H it attains a maximum value. It is also apparent that the LTE limit is restored at large values of
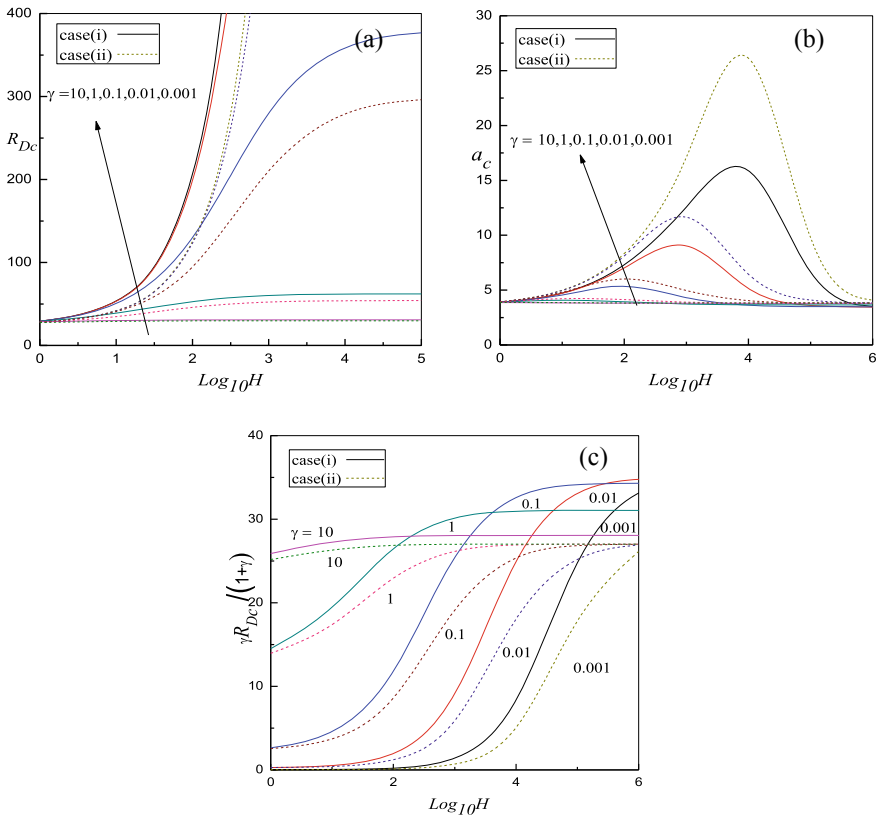
Fig. 4 Variation of **a** R_{Dc}, **b** a_c and **c** $\gamma R_{Dc}/(1 + \gamma)$ with $Log_{10}H$ for specific values of γ when $Q_s = 5$ and $Q_f = 10$

γ with H fixed. It is seen that an increase in the value of γ is to decrease a_c indicating its effect is to increase the size of convection cells at intermediate values of H. The curves of critical wavenumber for case (ii) lie above those of case (i). That is, the cells get contracted more in case (ii) when compared to case (i). When $\gamma = 0.01$, a_c rises sharply and go to an asymptote in both the cases. Figure 4c demonstrates that $\gamma R_{Dc}/(1+\gamma)$ has a normal limit of $4\pi^2$ as $H \to \infty$. In this case, $\gamma R_{Dc}/(1+\gamma)$ varies monotonically as H increases with γ fixed. The results for both the cases considered are seen to be quite similar.

Figure 5a, b displays the variation of R_{Dc} and a_c as a function of H for different values of Q_f when $\gamma = 0.1$ and $Q_s = 5$, respectively. It is obvious that R_{Dc} increases consistently with H, achieves an extreme, and stays unaltered from thereon with further increment in H (Fig. 5a). The figure also indicates that R_{Dc} decreases with increasing value of Q_f and again note that the curves of R_{Dc} for case (i) lie above case (ii). The variation of a_c shown in Fig. 5b indicates that it remains unaffected in the small and large H limits, while in-between for all values of H, a maximum
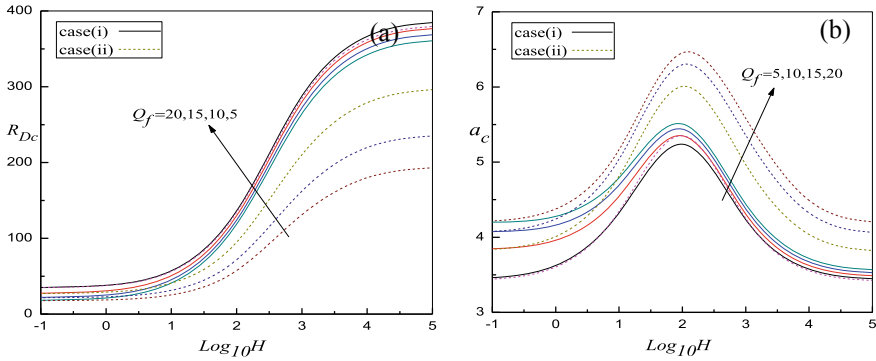
Fig. 5 Variation of **a** R_{Dc} and **b** a_c with $Log_{10}H$ for specific values of Q_f when $Q_s = 5$ and $\gamma = 0.1$

value of a_c is obtained for different values of Q_f. We observe an increase in the size of convection cells for increasing Q_f at intermediate values of H. The critical wavenumber curves for case (ii) lie above those of case (i). That is, the cells get contracted more in case (ii) when compared to case (i). Figure 6a, b displays the variation of R_{Dc} and a_c as a function of H for different values of Q_s when $\gamma = 0.1$ and $Q_f = 10$, respectively. Similar behavior for different values of Q_s is seen, and it is evident from Figs. 5a, b.

Figure 7a, b displays the variations of R_{Dc} and a_c as a function of H for different values of Q_f and Q_s when $\gamma = 0.1$ for the consideration of case (i). The presence of internal heating in both phases (IHBP) is to destabilize the system more when compared to the cases of either internal heating in the fluid phase (IHFP) or internal heating in the solid phase (IHSP) alone (Fig. 7a). Among IHFP and IHSP cases, the system is found to be more stable in the case of IHFP because the thermal conductivity is more in solid phase when compared to the fluid phase. Figure 7b represents that
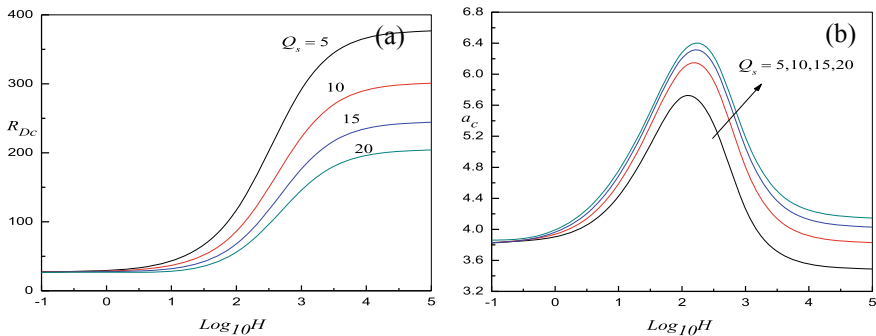
Fig. 6 Variation of **a** R_{Dc} and **b** a_c with $Log_{10}H$ for specific values of Q_s when $Q_f = 10$ and $\gamma = 0.1$
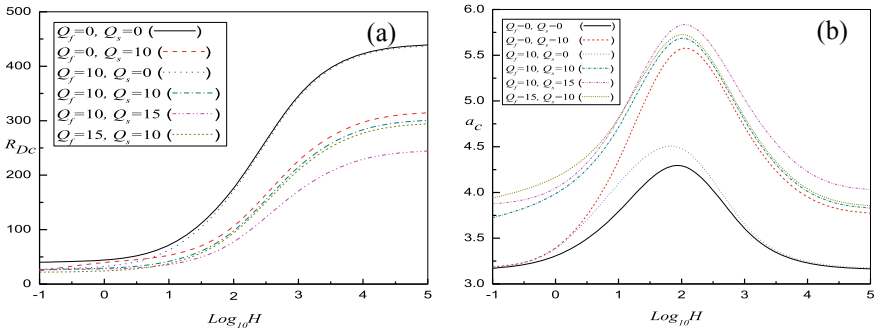
Fig. 7 Variation of **a** R_{Dc} and **b** a_c with $Log_{10}H$ for specific values of Q_f and Q_s when $\gamma = 0.1$

the critical wavenumbers are higher in the case of IHBP related to the cases of IHFP and IHSP.

4 Conclusions

The onset of convection under the condition of LTNE in a heat generating layer of fluid-saturated Darcy porous medium is investigated by focusing LTNE effect on the steady-state heat conduction.

The foregoing results are summarized as under

(i) The presence of LTNE effect on the steady-state heat conduction in the presence of internal heat source in both the phases of the porous medium alters the basic temperature distributions significantly which eventually influences the instability of the system.

(ii) The consideration of LTNE effect in the steady basic state is to delay the onset of convection compared to LTE case. Moreover,

$$(R_{Dc})_{\text{IHFP}} > (R_{Dc})_{\text{IHSP}} > (R_{Dc})_{\text{IHBP}}.$$

(iii) Increasing the value of H delays the onset of convection. The effect of γ is insignificant on the onset of convection for small values of H, whereas for the other values of H, the onset of convection is advanced with an increase in the value of γ. The LTE limit is recovered when either H or γ is sufficiently large.

(iv) The values of critical wavenumber are higher in the case of $H = 0$ than in the case of $H \neq 0$ in the steady basic state. In particular,

$$(a_c)_{\text{IHBP}} > (a_c)_{\text{IHSP}} > (a_c)_{\text{IHFP}}.$$

References

1. Amiri A, Vafai K (1994) Analysis of dispersion effects and non-thermal equilibrium, non-Darcian, variable porosity incompressible flow through porous media. Int J Heat Mass Transf 37(6):939–954
2. Nield DA (1998) Modelling the effects of surface tension on the onset of natural convection in a saturated porous medium. Trans Porous Med 31:365–368
3. Kiwan SM, Al-Nimr MA (2002) Analytical solutions for conjugated heat transfer in pipes and ducts. Int J Heat Mass Transf 38:513–516
4. Banu N, Rees DAS (2002) Onset of Darcy-Benard convection using a thermal non-equilibrium model. Int J Heat Mass Transf 45:2221–2228
5. Nield DA, Bejan A (1999) Convection in porous media2. Springer, New York
6. Malashetty MS, Shivakumara IS, Kulkarni S (2005) The onset of Lapwood-Brinkman convection using a thermal non-equilibrium model. Int J Heat Mass Transf 48:1155–1163
7. Shivakumara IS, Mamatha AL, Ravisha M (2010) Boundary and thermal non-equilibrium effects on the onset of Darcy-Brinkman convection in porous layer. Int J Eng Math 67:317–328
8. Malashetty MS, Shivakumara IS, Kulkarni S (2005) The onset of convection in an anisotropic porous layer using a thermal non-equilibrium model. Trans Porous Med 60:199–215
9. Shivakumara IS, Dhananjaya M, Ng CO (2015) Thermal convective instability in an Oldroyd-B nanofluid saturated porous layer. Int J Heat Mass Transf 84:167–177
10. Straughan B (2006) Global nonlinear stability in porous convection with a thermal non-equilibrium model. Proc R Soc Lond A 462:409–418
11. Straughan B (2013) Porous convection with local thermal non-equilibrium temperatures and with Cattaneo effects in the solid. Proc R Soc A 469:20130187
12. Shivakumara IS, Mamatha AL, Ravisha M (2015) Local thermal non-equilibrium model effects on thermal convection in a rotating anisotropic porous layer. J Appl Math Comp 259:838–857
13. Barletta A, Celli M, Lagziri H (2015) Instability of horizontal porous layer with local thermal non-equilibrium: effects of free surface and convective boundary conditions. Int J Heat Mass Transf 89:75–89
14. Celli M, Barletta A, Storesletten L (2013) Local thermal non-equilibrium effects in the Darcy-Bénard instability of a porous layer heated from below by a uniform flux. Int J Heat Mass Transf 67:902–912
15. Kuznetsov AV, Nield DA (2015) Local thermal non-equilibrium effects on the onset of convection in an internally heated layered porous medium with vertical throughflow. Int J Therm Sci 92:97–105
16. Nield DA, Kuznetsov AV (2015) The effect of vertical throughflow on thermal instability in a porous medium layer saturated by a nanofluid: a revised model. Int J Heat Mass Transf 137(5):14–1521
17. Barletta A, Celli M (2011) Local thermal non-equilibrium flow with viscous dissipation in a plane horizontal porous layer. Int J Therm Sci 50:53–60
18. Makinde OD (2009) On Chebyshev collocation approach to stability of fluid flows in a porous medium. Int J Numer Meth Fluids 59:791–799
19. Harfash AJ (2016) Resonant penetrative convection in a porous media with an internal heat source/sink effect. App Math Comp 281:323–342
20. Nield DA, Kuznetsov AV (2016) The onset of convective in a horizontal porous layer with spatially non-uniform internal heating. Transp Porous Med 111:541–553

21. Nouri-Borujerdi A, Noghrehabadi AR, Rees DAS (2008) Influence of Darcy number on the onset of convection in a porous layer with a uniform heat source. Int J Therm Sci 47:1020–1025
22. Nouri-Borujerdi A, Noghrehabadi AR, Rees DAS (2007) Onset of convection in a horizontal porous channel with uniform heat generation using a thermal non-equilibrium-model. Trans Porous Med 69:343–357
23. Nouri-Borujerdi A, Noghrehabadi AR, Rees DAS (2007) The effect of local thermal non-equilibrium on impulsive conduction in porous media. Int J Heat Mass Transf 50:3244–3249
24. Saravanan S (2009) Thermal non-equilibrium porous convection with heat generation and maximum density. Trans Porous Med 76:35–43
25. Storesletten L, Rees DAS (2019) Onset of convection in n inclined anisotropic porous layer with internal heat generation. Fluids 4:75
26. Nield DA, Bejan A (2017) Convection in porous media, 4th edn. Springer Science and Business Media, New York
27. Nield DA, Simmons CT (2018) A brief introduction to convection in porous media. Trans Porous Med
28. Straughan B (2011) Stability, and wave motion in porous media. In: Applied mathematical sciences, vol. 177. Springer, New York
29. Shivakumara IS, Ravisha M, Ng CO, Varun VL (2015) A thermal non-equilibrium model with cattaneo effect for convection in a Brinkman porous layer. Int J Non-Linear Mech 71:39–47
30. Makinde OD (2003) Magneto-hydromagnetic Stability of plane-Poiseuille flow using multi-deck asymptotic technique. Math Comput Model 37(3–4):251–259
31. Makinde OD (2009) Thermal stability of a reactive viscous flow through a porous-saturated channel with convective boundary conditions. App Therm Eng 29:1773–1777
32. Makinde OD, Motsa SS (2002) Hydromagnetic stability of generalized plane Couette flow. Far East J Appl Math 6(1):77–88

Stability of Natural Convection in a Vertical Anisotropic Porous Channel with Oblique Principal Axes Under Thermal Nonequilibrium Conditions

S. B. Naveen, B. M. Shankar, and I. S. Shivakumara

Abstract The impact of anisotropies in the permeability with slanted principal axes and thermal conductivity of fluid as well as solid phases on the stability properties of convection in a vertical porous layer is deliberated under the contemplation of thermal nonequilibrium. The classical energy analysis is observed to be insufficient in dealing with the stability analysis because of the tilting of the main principal axes of permeability with the gravity vector. Accordingly, the stability eigenvalue problem is solved numerically. It is found that the system is always stable for all infinitesimal disturbances irrespective of the values of physical parameters considered.

Keywords Porous medium · Vertical channel · Local thermal nonequilibrium · Anisotropy

Nomenclature

a	Vertical wave number
$\vec{g}$	Acceleration due to gravity
h	Inter-phase heat transfer coefficient
H	Scaled inter-phase heat transfer coefficient
$\mathrm{Im}(as)$	Growth Rate
$\hat{i}$	Unit vector in the x-direction
$\hat{j}$	Unit vector in the y-direction
$\hat{k}$	Unit vector in the z- direction
$\tilde{k}_f$	Thermal conductivity tensors of the fluid phase
$\tilde{k}_s$	Thermal conductivity tensors of the solid phase
K_h, K_v	Flow permeability along the principal axes

S. B. Naveen · I. S. Shivakumara (✉)
Department of Mathematics, Bangalore University, Bengaluru 560056, India
e-mail: shivakumarais@gmail.com

B. M. Shankar
Department of Mathematics, PES University, Bengaluru 560085, India
e-mail: bmshankar@pes.edu

$\tilde{K}$	Flow permeability tensor
$K^* = K_v / K_h$	Permeability ratio
L	Width of porous layer
P	Fluid pressure
$\vec{q} = (u, v, w)$	Velocity vector
$R_D = g\beta L K_v (T_h - T_c) / \varepsilon \upsilon \kappa_{fv}$	Darcy–Rayleigh number
s	Wave speed
s_i	Growth rate
s_r	Phase velocity
t	Time
T_c	Temperature at cold plate
T_f	Temperature of fluid
T_h	Temperature at hot plate
T_s	Temperature of solid
(x, y, z)	Cartesian coordinates

Greek symbols

$\alpha = (\rho c)_s k_f / (\rho c)_f k_s$	Ratio of thermal diffusivity
β	Coefficient of thermal expansion
$\gamma = \varepsilon k_{fv} / (1 - \varepsilon) k_{sv}$	Porosity modified conductivity ratio
ε	Porosity of porous medium
$\eta_f = k_{fh} / k_{fv}$	Thermal anisotropy for fluid
$\eta_s = k_{sh} / k_{sv}$	Thermal anisotropy for solid
θ	Fluid temperature
Θ	Perturbed fluid temperature
κ	Thermal diffusivity
μ	Dynamic viscosity of the fluid
υ	Kinematic viscosity
ρ_0	Fluid density at $T = T_r$
φ	Inclination of principal axes with the permeability tensor
ϕ	Solid temperature
Φ	Perturbed solid temperature
ψ	Stream function
Ψ	Perturbed stream function

1   Introduction

Buoyancy-driven porous convection has been studied by adopting a two-phase temperature model. In the two-phase model, the local thermal nonequilibrium (LTNE) is used and two temperature equations, one for the fluid phase and another for the solid phase, are considered. The concept of LTNE model is of recent origin compared to the classical local thermal equilibrium (LTE) model and found to be important in many heat transfer-related problems [1]. The stability perspectives in a vertical porous layer employing the standard LTE model have been analyzed comprehensively by several researchers because of its occurrence naturally and in scientific applications [2–14]. A detailed and an up-to-date literature pertaining to this field is covered by Straughan [15, 16] and Nield and Bejan [17].

Nonetheless, the stability of natural convection due to gravitation and buoyancy impact in a vertical fluid-saturated porous layer with LTNE model is still in a rudimentary stage. Rees [18] was the first to extend the Gill [2] problem by invoking the LTNE model and showed that the system is always stable, while Scott and Straughan [19] extended the study to account for nonlinear effects and noted that the system is stable. Shankar and Shivakumara [20] considered the viscoelastic effects on the problem considered by Rees [18] and observed that the system exhibits unstable behavior due to the elasticity of the fluid.

Anisotropy is generally a consequence of preferential orientation geometry of porous matrix or fibers and in fact encountered in numerous systems in industry and nature [21–24]. The Bénard convection in an anisotropic porous media was considered by Zhang et al. [25] and observed that the Nusselt number firmly depends upon the anisotropic parameters. By considering the anisotropy, both thermally and hydro-dynamically, the natural convection in a rectangular porous cavity was examined by Degan et al. [26]. Later, Degan and Vasseur [27] examined the problem in a vertical porous layer with slanted primary axes. Recently, Shankar et al. [13] studied numerically the effect of inertia on the stability of a vertical anisotropic porous layer.

The objective of the present study is to consider the stability properties of convection in a vertical layer of the anisotropic porous medium under LTNE conditions by assuming anisotropy in the permeability with the principal axes orienting obliquely to the gravity vector while the principal directions of thermal conductivity of solid and fluid phases are coinciding with the coordinate axes. In general, the stability eigenvalue problem is solved numerically using the Galerkin method in establishing the stability of the system as the energy analysis fails in deciding the stability characteristics of the system.

2   Mathematical Formulation

The schematic diagram is shown in Fig. (1). We assume horizontal isotropy and consider $\tilde{k}_f$, $\tilde{k}_s$ and $\tilde{K}$ in the form
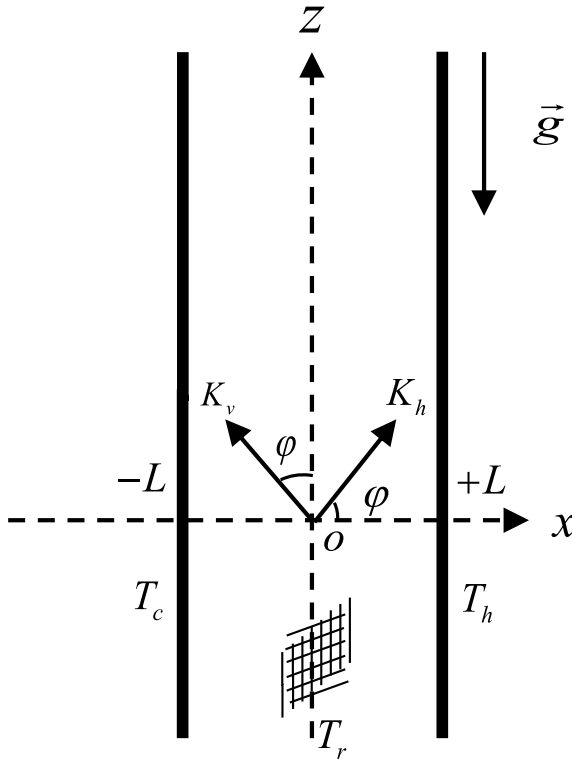
Fig. 1 Schematic diagram

$$\tilde{k}_f = k_{fv}\hat{k}\hat{k} + k_{fh}(\hat{i}\hat{i} + \hat{j}\hat{j}), \ \tilde{k}_s = k_{sv}\hat{k}\hat{k} + k_{sh}(\hat{i}\hat{i} + \hat{j}\hat{j})$$
$$\tilde{K} = M_{11}\hat{i}\hat{i} + M_{22}\hat{k}\hat{k} + M_{12}(\hat{i}\hat{k} + \hat{k}\hat{i}) + M_{33}\hat{j}\hat{j} \tag{1}$$

where

$$M_{11} = K_h \cos^2\varphi + K_v \sin^2\varphi$$
$$M_{22} = K_v \cos^2\varphi + K_h \sin^2\varphi$$
$$M_{12} = (K_h - K_v) \cos\varphi \sin\varphi$$
$$M_{33} = K_h$$

By scaling, length by L, velocity by $L/\varepsilon\kappa_{fv}$, pressure by $K_v/\varepsilon\kappa_{fv}\mu$, time by κ_{fv}/L^2, temperature by $(T_h - T_c)$ with the reference temperature $T_r = (T_c + T_h)/2$. The non-dimensional governing equations are

$$\nabla \cdot \vec{q} = 0 \tag{2}$$

$$K_v \, \tilde{K}^{-1} \cdot \vec{q} = -\nabla P + R_D \theta \hat{k} \tag{3}$$

$$\frac{\partial \theta}{\partial t} + (\vec{q} \cdot \nabla)\theta = \eta_f \frac{\partial^2 \theta}{\partial x^2} + \frac{\partial^2 \theta}{\partial z^2} + H(\phi - \theta) \tag{4}$$

$$\alpha \frac{\partial \phi}{\partial t} = \eta_s \frac{\partial^2 \phi}{\partial x^2} + \frac{\partial^2 \phi}{\partial z^2} - H\gamma(\phi - \theta) \tag{5}$$

We restrict the analysis to two-dimensional motions with the introduction of $\psi(x, z, t)$, a stream function, in the form

$$w = \partial \psi / \partial x, \quad u = -\partial \psi / \partial z, \tag{6}$$

Using Eq. (6), the governing stability equations become

$$\xi_1 \frac{\partial^2 \psi}{\partial z^2} + \xi_2 \frac{\partial^2 \psi}{\partial x^2} + 2\xi_3 \frac{\partial^2 \psi}{\partial x \partial z} = R_D \frac{\partial \theta}{\partial x} \tag{7}$$

$$\frac{\partial \theta}{\partial t} - \frac{\partial \psi}{\partial z} \frac{\partial \theta}{\partial x} + \frac{\partial \psi}{\partial x} \frac{\partial \theta}{\partial z} = H(\phi - \theta) + \eta_f \frac{\partial^2 \theta}{\partial x^2} + \frac{\partial^2 \theta}{\partial z^2} \tag{8}$$

$$\alpha \frac{\partial \phi}{\partial t} = -H\gamma(\phi - \theta) + \eta_s \frac{\partial^2 \phi}{\partial x^2} + \frac{\partial^2 \phi}{\partial z^2} \tag{9}$$

Where

$$\xi_1 = K^* \cos^2 \varphi + \sin^2 \varphi, \, \xi_2 = K^* \sin^2 \varphi + \cos^2 \varphi,$$
$$\xi_3 = (K^* - 1) \cos \varphi \sin \varphi \text{ and } K^* = K_v / K_h$$

The appropriate boundary conditions are

$$\psi = 0 \text{ at } x = \pm 1, \theta = \phi = \pm 1/2 \text{ at } x = \pm 1 \tag{10}$$

2.1 Base Flow

In the base flow, $\psi = \psi_b(x), \theta = \theta_b(x), \phi = \phi_b(x)$ and Eqs. (12–14) then reduce to

$$0 = \xi_2 \frac{d^2 \psi_b(x)}{dx^2} - R_D \frac{d\theta_b(x)}{dx}, 0 = \frac{d^2 \theta_b(x)}{dx^2}, \quad 0 = \frac{d^2 \phi_b(x)}{dx^2} \tag{11}$$

The boundary conditions are

$$\psi_b(x) = 0 \text{ at } x = \pm 1, \ \theta_b(x) = \phi_b(x) = \pm 1/2 \text{ at } x = \pm 1.$$

The basic solution is

$$\psi_b(x) = \frac{R_D}{4\xi_2}(x^2 - 1), \quad \theta_b(x) = \phi_b(x) = \frac{x}{2} \tag{12}$$

2.2 Perturbed Equations

The infinitesimal perturbations are superimposed on the basic state as

$$
\begin{aligned}
\psi &= \psi_b(x) + \hat{\psi}(x, z, t), \\
\theta &= \theta_b(x) + \hat{\theta}(x, z, t), \\
\phi &= \phi_b(x) + \hat{\phi}(x, z, t)
\end{aligned}
\tag{13}
$$

Using Eq. (13) in Eqs. (7–9) and assuming a normal mode solution in the form

$$(\psi, \theta, \phi) = [\Psi(x), \Theta(x), \Phi(x)]e^{ia(z-st)} \tag{14}$$

we get

$$(\xi_2 D^2 - \xi_1 a^2)\Psi + 2i\xi_3 a D\Psi = R_D D\Theta \tag{15}$$

$$(ia/2)\{(R_D x/\xi_2)\Theta - \Psi\} - ias\Theta = (\eta_f D^2 - a^2)\Theta + H(\Phi - \Theta) \tag{16}$$

$$-ias\alpha\Phi = (\eta_s D^2 - a^2)\Phi - H\gamma(\Phi - \Theta) \tag{17}$$

and the corresponding boundary conditions are

$$\Psi = \Phi = \Theta = 0 \quad \text{at } x = \pm 1. \tag{18}$$

3 Energy Analysis

The energy analysis of Gill [2] is used to affirm the stability of the system. Operating $(\xi_2 D^2 - \xi_1 a^2 + 2\xi_3 aiD)$ on both sides of Eqs. (16) and (17) and using Eq. (15), we obtain

$$
\begin{aligned}
&- \mathrm{i}as(\xi_2\Theta'' - \xi_1 a^2\Theta + 2\xi_3 a\mathrm{i}\,\Theta') + \left(\mathrm{i}aR_D\big/2\xi_2\right) \\
&\quad \times \left\{x(\xi_2\Theta'' - \xi_1 a^2\Theta + 2\xi_3 a\mathrm{i}\,\Theta') + 2\xi_2\Theta' + 2a\xi_3\mathrm{i}\Theta\right\} - \left(\mathrm{i}aR_D\big/2\right)\Theta' \\
&= \left(\eta_f\left(-\xi_1 a^2\Theta'' + \xi_2\Theta'''' + 2\xi_3 a\mathrm{i}\Theta'''\right) - a^2\left(-\xi_1 a^2\Theta + \xi_2\Theta'' + 2\xi_3 a\mathrm{i}\Theta'\right)\right) \\
&\quad + H\left(-\xi_1 a^2\Phi + \xi_2\Phi'' + 2\xi_3 a\mathrm{i}\Phi'\right) \\
&\quad - H\left(-\xi_1 a^2\Theta + \xi_2\Theta'' + 2\xi_3 a\mathrm{i}\Theta'\right)
\end{aligned} \tag{19}
$$

$$
\begin{aligned}
&- \mathrm{i}as\alpha(\xi_2\Phi'' + 2\xi_3 a\mathrm{i}\Phi' - \xi_1 a^2\Phi) \\
&= \left((\eta_s\,\xi_2\Phi'' + 2\xi_3\eta_s\,a\mathrm{i}\Phi''' - \xi_1\eta_s\,a^2\Phi'') - a^2\left(-\xi_1 a^2\Phi + \xi_2\Phi'' + 2\xi_3 a\mathrm{i}\Phi'\right)\right) \\
&\quad - H\gamma(-\xi_1 a^2\Phi + \xi_2\Phi'' + 2\xi_3 a\mathrm{i}\Phi') \\
&\quad + H\gamma(-\xi_1 a^2\Theta + \xi_2\Theta'' + 2\xi_3 a\mathrm{i}\Theta')
\end{aligned} \tag{20}
$$

Multiplying Eq. (20) by $\gamma\,\Theta^*$, Eq. (21) by Φ^*, integrating with respect to x between the limits -1 and 1, and adding the resulting equations, we get

$$
\mathrm{i}as\int_{-1}^{1}\left(\xi_2\left(\gamma|\Theta'|^2 + \alpha|\Phi'|^2\right) + \xi_1 a^2\left(\gamma|\Phi|^2 + \alpha|\Phi|^2\right)\right)\mathrm{d}x
$$

$$
+ 2a^2 s\gamma\xi_3\int_{-1}^{1}(\Theta'\Theta^* + \Phi'\Phi^*)\mathrm{d}x = \gamma a^2\int_{-1}^{1}\left(\xi_2|\Theta'|^2 + \xi_1 a^2|\Theta|^2\right)\mathrm{d}x
$$

$$
+ a^2\int_{-1}^{1}\left(\xi_2|\Phi'|^2 + \xi_1 a^2|\Phi|^2\right)\mathrm{d}x + \eta_f\gamma\int_{-1}^{1}\left(\xi_2|\Theta''|^2 + \xi_1 a^2|\Theta'|^2\right)\mathrm{d}x
$$

$$
+ \eta_s\int_{-1}^{1}\left(\xi_2|\Phi''|^2 + \xi_1 a^2|\Phi'|^2\right)\mathrm{d}x + H\gamma\int_{-1}^{1}\left(\xi_2|\Theta' - \Phi'|^2 + a^2\xi_1|\Theta - \Phi|^2\right)\mathrm{d}x
$$

$$
+ \Delta 1 + \Delta 2 + \Delta 3 \tag{21}
$$

where

$$
\Delta 1 = \xi_3(a\gamma R_D/\xi_2)\int_{-1}^{1}(x\Theta)'\Theta^*\mathrm{d}x + (\mathrm{i}a\gamma R_D/\xi_2)\int_{-1}^{1}x\left(\xi_2|\Theta'|^2 + \xi_1 a^2|\Theta|^2\right)\mathrm{d}x
$$

$$
\Delta 2 = 2\xi_3 H a\gamma\mathrm{i}\int_{-1}^{1}(\Theta'\Theta^* + \Phi'\Phi^* - \Phi'\Theta^* - \Theta'\Phi^*)\mathrm{d}x
$$

$$
\Delta 3 = 2\xi_3 a\mathrm{i}\int_{-1}^{1}\left(\gamma\eta_f\Theta'\Theta^* + \eta_s\Phi'\Phi^*\right)\mathrm{d}x - 2\xi_3 a^3\mathrm{i}\int_{-1}^{1}\left(\gamma\Theta'\Theta^* + \Phi'\Phi^*\right)\mathrm{d}x
$$

If the principal axes of the permeability tensor coincides with the coordinate axes ($\varphi = 0$), then Eq. (22) reduces to

$$
ias \int\limits_{-1}^{1} \left(\xi_2\left(\gamma|\Theta'|^2 + \alpha|\Phi'|^2 \right) + \xi_1 a^2\left(\gamma|\Phi|^2 + \alpha|\Phi|^2 \right) \right) dx
$$

$$
= \eta_f \gamma \int\limits_{-1}^{1} \left(\xi_2|\Theta''|^2 + \xi_1 a^2|\Theta'|^2 \right) dx + \eta_s \int\limits_{-1}^{1} \left(\xi_2|\Phi''|^2 + \xi_1 a^2|\Phi'|^2 \right) dx
$$

$$
+ \gamma a^2 \int\limits_{-1}^{1} \left(\xi_2|\Theta'|^2 + \xi_1 a^2|\Theta|^2 \right) dx + a^2 \int\limits_{-1}^{1} \left(\xi_2|\Phi'|^2 + \xi_1 a^2|\Phi|^2 \right) dx
$$

$$
+ H\gamma \int\limits_{-1}^{1} \left(\xi_2|\Theta' - \Phi'|^2 + a^2\xi_1|\Theta - \Phi|^2 \right) dx
$$

$$
+ (ia\gamma R_D/\xi_2) \int\limits_{-1}^{1} x\left(\xi_2|\Theta'|^2 + \xi_1 a^2|\Theta|^2 \right) dx. \tag{22}
$$

In the above equation, the real part turns out to be definitely negative.

4 Discussions and Conclusions

In the present paper, we have utilized the energy analysis of Gill [2] and Rees [18] to testify the stability of the system. A careful glance at Eq. (21) reveals that no definite conclusion about the stability of the system could be arrived because of the irresolute integral terms arising due to the anisotropy effect of permeability with oblique principal axes. Hence, energy analysis becomes ineffective in the present case. Nonetheless, if $\varphi = 0$, then the system is stable for all infinitesimal perturbations; a result noted in the isotropic case [18].

Since the energy analysis fails to decide the stability of fluid flow for $\varphi \neq 0$, one has to resort to the numerical method of solution. Galerkin method is used to solve Eqs. (15–17) together with boundary conditions (18) (generalized eigenvalue problem). Accordingly, Ψ, Θ and Φ are expanded in the form

$$
\Psi(x) = \sum_{n=0}^{N} \xi_{1n}\left(1 - x^2\right) P_n(x),
$$

$$
\Theta(x) = \sum_{n=0}^{N} \xi_{2n}\left(1 - x^2\right) P_n(x),
$$

Table 1 Process of convergence of results with an increase in the number of terms in the Galerkin method for various estimations of physical parameters

N	$\alpha = \gamma = 1, H = 100, K^* = 2$ $\varphi = \pi/4, R_D = 100, a = 2,$ $\eta_s = 2, \eta_f = 2,$	$\alpha = \gamma = 1, H = 100, K^* = 2,$ $\varphi = \pi/3, R_D = 100, a = 2,$ $\eta_s = 2, \eta_f = 2$
	$s_r + is_i$	$s_r + is_i$
4	0–08.8211i	0–8.14915i
5	0–11.2174i	0–9.60460i
6	0–10.4509i	0–9.25281i
7	0–10.5253i	0–9.28335i
8	0–10.5177i	0–9.28047i
9	0–10.5194i	0–9.28119i
10	0–10.5194i	0–9.28112i
11	0–10.5192i	0–9.28111i
12	0–10.5192i	0–9.28111i

$$\Phi(x) = \sum_{n=0}^{N} \xi_{3n}\left(1 - x^2\right) P_n(x) \tag{23}$$

where $P_n(x)$ is the Legendre polynomial of degree n and ξ_{1n}, ξ_{2n} and ξ_{3n} are constants. The method and algorithm of [28–30], Shankar and Shivakumara [14], Shankar et al. [31] is followed to solve the generalized eigenvalue problem. The results so acquired for various estimations of parameters are shown in Table 1. From the table, it is confirmed that the results converge for $N = 8$, in general.

To look at the stability characteristics of the system, the growth rate $\text{Im}(as)$ is found numerically as a function of wave number for various values of physical parameters $H, K^*, R_D, \alpha, \gamma, \eta_f, \eta_s$ and φ (Figs. 2, 3 and 4). From the figures, it is seen that the growth rate has only one negative maximum, which occurs at $a = 0$. Further increase in the value of a, the growth rate is a non-monotonic decreasing function with respect to a. The pattern of each curve is the same for all the anisotropic porous parameters. Increment in the estimation of K^*, φ, η_f and η_s is to diminish the growth rate. Interestingly, the growth rate does not finish up positive in these cases therefore there is no transition takes place from stability to instability. Thus, it can be concluded that the system remains unconditionally stable for all infinitesimal disturbances irrespective of values of physical parameters involved therein.
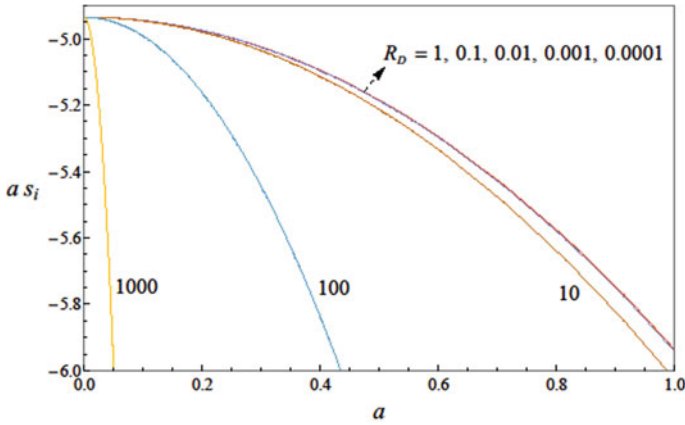
Fig. 2 Variation of growth rate Im(as) versus a for various values of R_D with $\varphi = 45°$, $K^* = 1$, $\alpha = 1$, $\eta_f = 2$ and $\eta_s = 2$
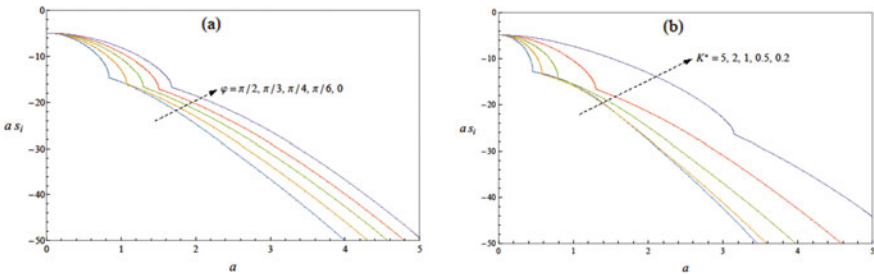
Fig. 3 Variation of growth rate Im(as) versus a for various values of **a** φ with $K^* = 1$ **b** K^* with $\varphi = 45°$ by considering $\alpha = 1$, $R_D = 100$, $\eta_f = 2$ and $\eta_s = 2$
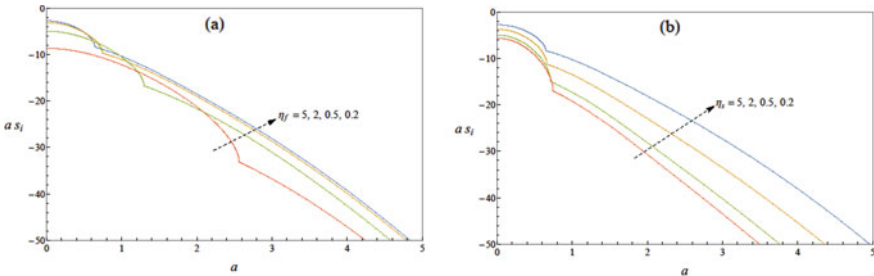
Fig. 4 Variation of growth rate Im(as) versus a for various values of **a** η_f with $\eta_s = 2$, **b** η_s with $\eta_f = 2$ by considering $\alpha = 1$, $H = 1000$, $R_D = 100$, $\gamma = 1$, $\varphi = \pi/4$ and $K^* = 2$

References

1. Virto L, Carbonell M, Castilla R, Gamez-Montero PJ (2009) Heating of saturated porous media in practice: several causes of local thermal non-equilibrium. Int J Heat Mass Transfer 52:5412–5422. https://doi.org/10.1016/j.ijheatmasstransfer.2009.07.003
2. Gill AE (1969) A proof that convection in a porous vertical slab is stable. J Fluid Mech 35:545–547. https://doi.org/10.1017/S0022112069001273
3. Rees DAS (1988) The stability of Prandtl-Darcy convection in a vertical porous slot. Int J Heat Mass Transfer 31:1529–1534. https://doi.org/10.1016/0017-9310(88),90260-8
4. Straughan B (1988) A nonlinear analysis of convection in a porous vertical slab. Geophys Astrophys Fluid Dyn 42:269–275. https://doi.org/10.1080/03091928808213611
5. Makinde OD (2009) On Chebyshev collocation approach to stability of fluid flows in a porous medium. Int J Numerical Methods Fluids 59:791–799. https://doi.org/10.1002/fld.1847
6. Makinde OD (2009) Thermal stability of a reactive viscous flow through a porous-saturated channel with convective boundary conditions. Appl Thermal Eng 29:1773–1777
7. Barletta A, Celli M (2017) Instability of parallel buoyant flow in a vertical porous layer with an internal heat source. Int J Heat Mass Transfer 111:1063–1070. https://doi.org/10.1016/j.ijheatmasstransfer.2017.04.063
8. Barletta A, de Alves LSB (2014) On Gill's stability problem for non-Newtonian Darcy's flow. Int J Heat Mass Transfer 79:759–768. https://doi.org/10.1016/j.ijheatmasstransfer.2014.08.051
9. Barletta A (2015) A proof that convection in a porous vertical slab may be unstable. J Fluid Mech 770:273–288. https://doi.org/10.1017/jfm.2015.154
10. Barletta A (2016) Instability of stationary two-dimensional mixed convection across a vertical porous layer. Phys Fluids 28:014101-1-14. https://doi.org/10.1063/1.4939287
11. Shankar BM, Kumar J, Shivakumara IS (2017a) Stability of natural convection in a vertical layer of Brinkman porous medium. Acta Mech 228:1–19. https://doi.org/10.1007/s00707-016-1690-6
12. Shankar BM, Shivakumara IS (2017) On the stability of natural convection in a porous vertical slab saturated with an Oldroyd-B fluid. Theor Comput Fluid Dyn 31:221–231. https://doi.org/10.1007/s00162-016-0415-8
13. Shankar BM, Kumar J, Shivakumara IS (2017b) Boundary and inertia effects on the stability of natural convection in a vertical layer of an anisotropic Lapwood–Brinkman porous medium. Acta Mech 228:2269–2282. https://doi.org/10.1007/s00707-017-1831-6
14. Shankar BM, Shivakumara IS (2018) Stability of penetrative natural convection in a non-Newtonian fluid-saturated vertical porous layer. Transp Porous Media 124:395–411. https://doi.org/10.1007/s11242-018-1074-6
15. Straughan B (2011) Heat waves. In: Applied mathematical sciences, vol 177. Springer, New York
16. Straughan B (2008) Stability, and wave motion in porous media. In: Applied mathematical sciences, vol 165. Springer, New York
17. Nield DA, Bejan A (2017) In: Convection in porous media, 5th edn. Springer, New York
18. Rees DAS (2011) The effect of local thermal nonequilibrium on the stability of convection in a vertical porous channel. Transp Porous Med 87:459–464. https://doi.org/10.1007/s11242-010-9694-5
19. Scott NL, Straughan B (2013) A nonlinear stability analysis of convection in a porous vertical channel including local thermal nonequilibrium. J Math Fluid Mech 15:171–178. https://doi.org/10.1007/s00021-012-0109-y

20. Shankar BM, Shivakumara IS (2017c) Effect of local thermal nonequilibrium on the stability of natural convection in an Oldroyd-B fluid saturated vertical porous layer. ASME-J Heat Transfer 139:041001-1-9. https://doi.org/10.1115/1.4035199

21. McKibbin R (1986) Thermal convection in a porous layer: effects of anisotropy and surface boundary conditions. Transp Porous Media 1:271–292. https://doi.org/10.1007/BF00238183

22. Shivakumara IS, Lee J, Chavaraddi KB (2011) Onset of surface tension driven convection in a fluid layer overlying a layer of an anisotropic porous medium. Int J Heat Mass Transfer 54:994–1001. https://doi.org/10.1016/j.ijheatmasstransfer.2010.10.023

23. Storesletten L (1993) Natural convection in a horizontal porous layer with anisotropic thermal diffusivity. Transp Porous Media 12:19–29. https://doi.org/10.1007/BF00616359

24. Tyvand PA, Storesletten L (1991) Onset of convection in an anisotropic porous medium with oblique principal axes. J Fluid Mech 226:371–382. https://doi.org/10.1017/S0022112091002422

25. Zhang X, Nguyen TH, Kahawita R (1993) Convection flow and heat transfer in an anisotropic porous layer with principal axles non-coincident with the gravity vector. In: ASME winter annual meeting, Fundamentals of natural convection, vol 264. New Orleans, Louisiana, pp 79–86

26. Degan G, Vasseur P, Bilgen E (1995) Convective heat transfer in a vertical anisotropic porous layer. Int J Heat Mass Transfer 38:1975–1987. https://doi.org/10.1016/0017-9310(94)00330-X

27. Degan G, Vasseur P (1996) Natural convection in a vertical slot filled with an anisotropic Porous medium with oblique principal axes. Numer Heat Transfer, Part A 30:397–412. https://doi.org/10.1080/10407789608913847

28. Makinde OD, Motsa SS (2002) Hydromagnetic stability of generalized plane Couette flow. Far East Jour Appl Math 6(1):77–88

29. Makinde OD (2009) On thermal stability of a reactive third-grade fluid in a channel with convective cooling at the walls. Appl Math Comput 213:170–276. https://doi.org/10.1016/j.amc.2009.03.003

30. Makinde OD (2003) Magnetohydromagnetic stability of plane-Poiseuille flow using multi-Deck asymptotic technique. Math Comput Modell 37(3–4):251–259

31. Shankar BM, Kumar J, Shivakumara IS (2019) Magnetohydrodynamic instability of mixed convection in a differentially heated vertical channel. Eur Phys J Plus:53-1-12

Application of Grey Theory and Fuzzy Logic to Optimize Machining Parameters of Zircon Sand Reinforced Aluminum Composites

M. Vignesh [ORCID]**, R. Ramanujam, G. Rajyalakshmi, and Sayantan Bhattacharya**

Abstract The increasing demand for lightweight materials in various engineering and structural applications led to the introduction of aluminum matrix composites (AMC). In this work, a novel zircon sand ($ZrSiO_4$)-reinforced aluminum (grade-LM25) matrix composites were produced using stir casting method, and experimental investigation on machinability based on 18 orthogonal array of mixed level design is carried out formulated by Taguchi. Machining conditions (Dry/MQL), cutting speed (CS), depth of cut (DoC), feed rate (FR) and zircon sand reinforcement are varied in the experiments, and output responses like resultant cutting force (Fr), surface roughness (Ra) and tool wear (TW) were measured. Fuzzy logic (FL), a soft computing technique coupled with one of a multi-objective optimization technique, grey relational analysis (GRA) is implemented to find the optimal cutting parameters. The significant factors are analyzed using ANOVA. The optimum machining levels obtained are MQL cutting environment with a cutting speed of 200 m/min, feed rate of 0.06 mm/rev, depth of cut of 1 mm and 10% zircon sand particle reinforcement.

Keywords Composites · Zircon sand · Fuzzy logic · Machinability

1 Introduction

Utilization of aluminum alloys and its composites are getting increased day by day in various applications in marine, aircraft, aerospace and automotive industries for replacing the conventional components wherever required [1]. The strength and performance perspective should not be compromised on any aspect, while the material gets replaced. Hence, the addition of reinforcements to the base aluminum metal

M. Vignesh · R. Ramanujam (✉) · G. Rajyalakshmi
School of Mechanical Engineering, Vellore Institute of Technology, Vellore, Tamil Nadu 632014, India
e-mail: ramanujam.r@vit.ac.in

S. Bhattacharya
School of Mechanical Engineering, Lovely Professional University, Phagwara, Punjab 144411, India

matrix plays a major role, and utmost care has to be taken in the selection of reinforcements for the improvement in hardness, strength, strength to weight ratio, wear resistance, etc. [2]. In addition to this, the machinability of composites has also become a challenging one. Hence, a detailed study on the machinability of these composites attracts many researchers to get the optimal machining conditions. The commonly used reinforcement materials are SiO_2, Al_2O_3, SiC, B_4C, etc. Among these various reinforcements, a very limited number of research is carried out on the zircon sand-reinforced aluminum composites. Zircon sand usage is mainly because of its high modulus of elasticity, high thermal stability and increased hardness [3]. It also possesses very good resistance toward work material wear rate due to its increased hardness [4].

Noorul Haq et al. [5] carried out drilling experiments on the LM 25 aluminum grade reinforced with SiC particles and adopted a multi-objective technique called grey relational analysis (GRA) to find out the best level of cutting parameters to get a desired output. For the optimal level, the confirmatory experiments are carried out and found that the GRA is one such effective method for multi-response optimization [6]. Using GRA method, Uday A. Dabade carried out the surface integrity analysis on the silicon carbide-reinforced aluminum composites. The optimal level for the good surface finish is at 40 m/min, 0.05 mm/rev, 0.2 mm, 0.8 mm of machining speed, feed rate, depth of cut and nose radius respectively [7]. In addition to grey relational analysis, Ramanathan et al. [8] used soft computing approach called fuzzy logic for predicting the results of the hot compression tests that are carried out on the SiC-reinforced aluminum composites. Rajasekaran et al. [9] used triangular membership function for the input and output responses for predicting the surface roughness of the CFRP polymer composites during drilling operation on a Mamdani fuzzy system. Based on the optimal level, the confirmation experiments are carried out, and the results are found satisfactory [10]. Few researchers combined grey and fuzzy logic approach for more efficient result prediction. Suresh et al. [11] used this technique for predicting the optimal level for Al–SiC–Gr hybrid composites. Rajmohan et al. [12] generated grey relational coefficient (GRC), and this result is given to the fuzzy logic approach as an input to get the grey fuzzy relational grade (GFRG). In this work, Gaussian membership function and the triangular membership function are used as an input and output parameters [13]. This grey-fuzzy approach could be used for any kind of processes for predicting and optimizing its results [14].

Thus, the present review of literature gives a very limited works on zircon sand-reinforced composites. That too due to its increased hardness, wear studies on the fabricated composites are performed. Very less works are available in machinability studies of zircon sand-reinforced aluminum matrix composites. Multi-objective optimization of machining parameters used in zircon sand-reinforced composites machining has gained higher importance for the effective machining of the components. Hence, the objective of the present study is to fabricate the zircon sand-reinforced aluminum composites, and its machining performance is studied. As part of the optimization study, a multi-response optimization technique called grey relational analysis (GRA) coupled with fuzzy logic controller is utilized to optimize the parameters. Finally, the predicted and experimental results are compared.

Table 1 Machining parametric levels

Factors	Levels		
	1	2	3
Cutting conditions	Dry	MQL	–
Cutting speed (m/min)	100	150	200
Feed rate (mm/rev)	0.06	0.18	0.30
Depth of cut (mm)	0.50	0.75	1
% reinforcement	0	5	10

2 Experimental Details

The workpiece material used was the aluminum alloy LM-25, and the reinforcement material was zircon sand particles ($ZrSiO_4$) of 120 µm of average particle size. Aluminum matrix composites were fabricated using bottom pouring stir casting route by varying reinforcement at three different weight percentages of 0, 5, 10 wt%. The base material was melted in the electrical steel crucible at a temperature of 800 °C, and the zircon particles are added to the melt by preheating it to 450 °C. Magnesium is added as an external agent to base metal and reinforcement to increase its wettability. The mixture is stirred well at 500 rpm, for uniform particle distribution. The molten composite mixture was poured into cylindrical die with a dimension of 300 and 50 mm in length and diameter, preheated up to 300 °C. The experiments are carried out according to Taguchi's L18 mixed level of orthogonal array design. The experiments are conducted on heavy duty lathe by varying the parameters given in Table 1 using uncoated tungsten carbide inserts. During machining, the generated forces are monitored and measured using three-component Kistler force dynamometer (Model: 9257B). Mahr surf surface profilometer is used for the roughness (Ra) measurement. The wear patterns obtained on the tool are captured and measured using the optical microscope (Make: Carl Zeiss).

3 Experimental Results and Discussion

The results (Fr, Ra and TW) obtained in the experimentation process are fed as an input to a multi-response optimization technique called GRA approach. The experimentally obtained data are normalized, and the optimization process is followed. The steps in grey-fuzzy method are depicted as flowchart in Fig. 1.
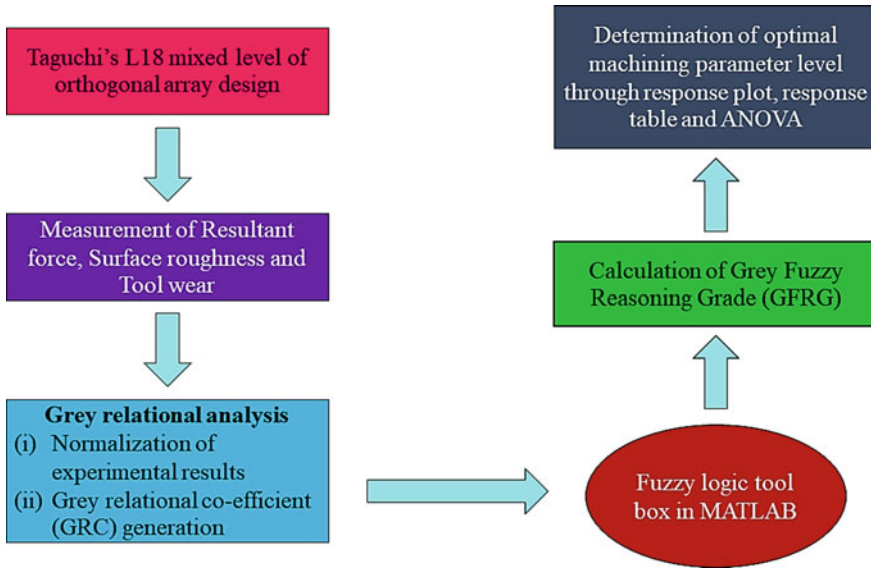
Fig. 1 Steps in Grey-fuzzy method

3.1 Stages Involved in GRA

1. Normalization of the results between 0 and 1 is performed as the first stage in GRA. The normalization is performed for the obtained data to remove the fluctuations between the values, and the larger difference between the obtained data could be reduced between 0 and 1. Since all the output response of the present experimentation being a minimization one, the normalization is done for minimization criterion. The normalization formula [15] for minimization criterion is as follows:

$$x_i * (k) = \frac{\max x_i(k) - x_i(k)}{\max x_i(k) - \min x_i(k)} \tag{1}$$

where $x_i^*(k)$ and $x_i(k)$ are the normalized and the actual data during experimentation for the ith experiment by using kth response.

2. The second step in GRA is generation of grey relational coefficient (GRC). The GRC ($\xi_i(k)$) is calculated based on Eq. (2),

$$\xi_i(k) = \frac{\Delta_{\min} - \zeta \Delta_{\max}}{\Delta_i(k) - \zeta \Delta_{\max}} \tag{2}$$

Table 2 Obtained values of GRC and GFRG

Normalized			GRC			GFRG	Rank
Fr	Ra	TW	Fr	Ra	TW		
0.986	0.000	0.868	0.973	0.333	0.791	0.712	6
0.802	0.013	0.773	0.716	0.336	0.688	0.583	8
0.000	0.202	0.178	0.333	0.385	0.378	0.346	18
1.000	0.649	0.535	1.000	0.587	0.518	0.727	4
0.811	0.640	0.336	0.725	0.582	0.430	0.513	12
0.153	0.474	0.000	0.371	0.488	0.333	0.371	17
0.993	1.000	0.748	0.987	1.000	0.665	0.882	1
0.408	0.785	0.495	0.458	0.699	0.467	0.485	14
0.635	0.647	0.082	0.578	0.586	0.353	0.497	13
0.876	0.668	1.000	0.802	0.601	1.000	0.753	3
0.801	0.002	0.844	0.715	0.334	0.762	0.582	9
0.495	0.021	0.343	0.498	0.338	0.432	0.480	15
0.943	0.846	0.945	0.898	0.765	0.901	0.802	2
0.422	0.225	0.780	0.464	0.392	0.695	0.514	11
0.698	0.036	0.501	0.623	0.342	0.501	0.527	10
0.875	0.706	0.818	0.800	0.629	0.733	0.713	5
0.737	0.664	0.775	0.656	0.598	0.689	0.684	7
0.318	0.742	0.098	0.423	0.660	0.357	0.419	16

where $\Delta_i(k) = \left| x_i^*(k) - x_i^0(k) \right|$. Global maximum and global minimum values are given as $\Delta_{\max}$ and $\Delta_{\min}$ for different output series. The distinguishing coefficient (ζ) is taken as 0.5 [16]. These generated GRCs of the Fr, Ra and TW are given as an input to the fuzzy logic controller to generate the grey fuzzy reasoning grade (GFRG). The results of GRC and GFRG from the fuzzy analysis are given in Table 2.

3.2 Fuzzy Logic Approach

The fuzzy inference system used is the Mamdani system. Fuzzy system includes fuzzifier, membership functions, fuzzy rule, inference engine and defuzzifier (Tzeng and Chen [17]). Membership function is used to fuzzify the GRC obtained to remove the uncertainty in the data. In this study, input parameters GRC of Fr, Ra and TW are modeled using Gaussian membership function and output variable, and GFRG using triangular membership function is shown in Fig. 2. The inference engine with fuzzy rules performs fuzzy reasoning to obtain the fuzzified values. A set of 18 'IF-THEN' rules are framed between the input and output variables are as follows and given in Fig. 3. The input and output variables are assigned to five fuzzy subsets as very low,
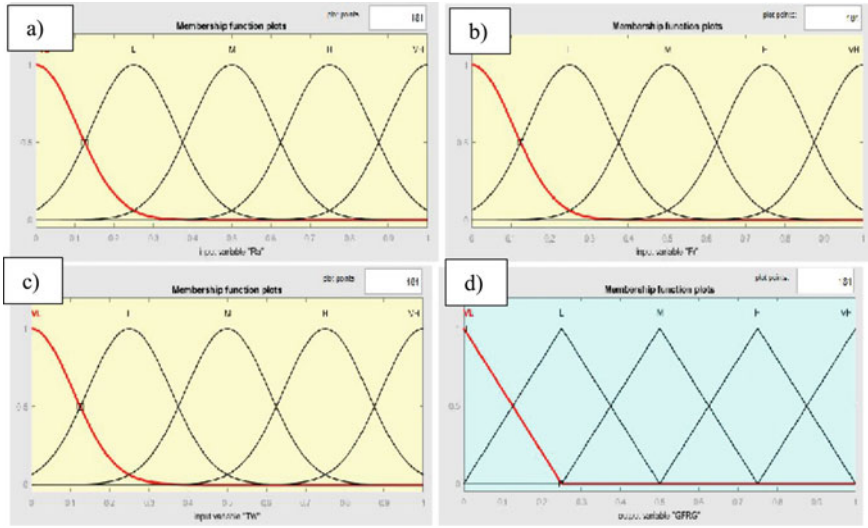
Fig. 2 **a** Input membership function Fr, **b** Ra, **c** TW, **d** Output membership function GFRG
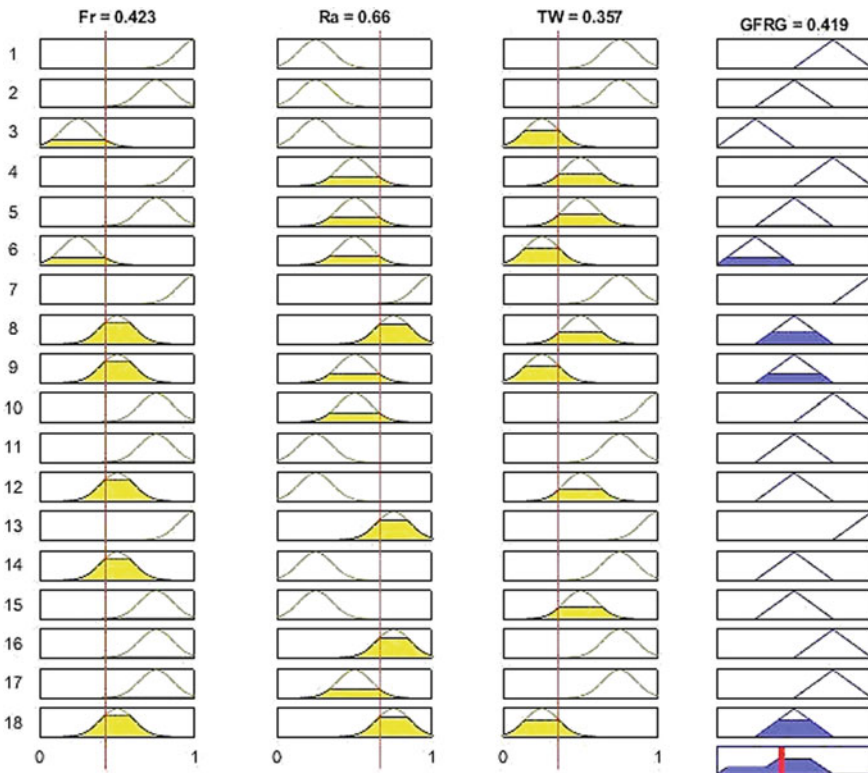
Fig. 3 Fuzzy logic rules

Table 3 Response table for GFRG means

Level	Cutting condition	Cutting speed	Feed rate	Depth of cut	% reinforcement
1	0.5684	0.5760	0.7648	0.6215	0.5800
2	0.6082	0.5757	0.5602	0.6132	0.5858
3	–	0.6133	0.4400	0.5303	0.5992
Delta	0.0398	0.0377	0.3248	0.0912	0.0192
Rank	3	4	1	2	5

low, medium, high and very high, for the corresponding fuzzy membership functions as $Y1$, $Y2$, $Y3$ for input variables ($Y1$, $Y2$, $Y3$ = grey relational coefficient of Fr, Ra, TW) and Z for the output variable GFRG.

Rule 1: If $Y1$ is Very High, $Y2$ is Low, $Y3$ is High, then Z is High; else

Rule 2: If $Y1$ is High, $Y2$ is Low, $Y3$ is High, then Z is Medium; else

………

Rule n: If $Y1$ is Medium, $Y2$ is High, $Y3$ is Low, then Z is Medium.

The defuzzifier converts the predicted fuzzy value to a single performance GFRG. Defuzzification method used is center of area. This method is the widely used and accepted for accurate results. The results that are obtained in this defuzzification are completely based on the rules that are given to each and every variables. From the generated GFRG, the highest value gives the best performance characteristics.

3.3 Main Effects Analysis of GFRG

The main effects plot, response table and ANOVA for GFRG are performed to obtain parametric significance on response. The GFRG means values are tabulated in Table 3.

From Table 3 and Fig. 4, optimal level of parameters is at MQL cutting condition, 200 m/min of cutting speed, 0.06 mm/rev of feed rate, 0.5 mm of depth of cut and 10% of zircon sand reinforcement to achieve lower Fr, SR and TW.

4 Analysis of Variance (ANOVA)

The ANOVA is performed to find out the contributing factor for desired experimental output. The ANOVA for GFRG is performed at 95% confidence limit, and the results are summarized in Table 4. For desired outputs, the feed rate plays a major role with a higher contribution of 81.20%, followed by depth of cut (7.65%). Cutting condition, cutting speed and % reinforcement are found insignificant.

The experiments are carried out to confirm the results at its optimal parametric levels. The experimental GFRG result is compared with the predicted result. The

Main Effects Plot for Means
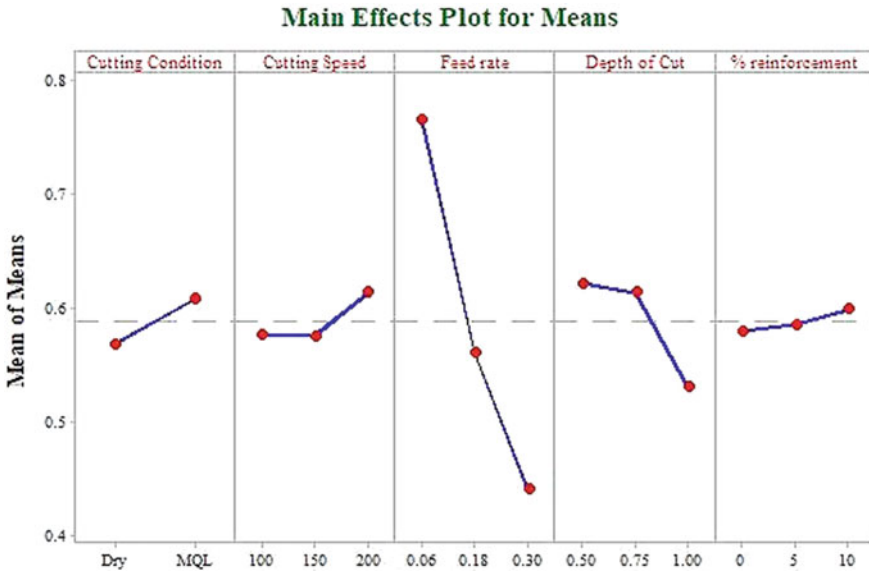
Fig. 4 Main effects of GFRG means

Table 4 ANOVA for the GFRG

Source	DoF	SS	MS	F-value	P-value	% contribution
Cutting condition	1	0.007150	0.007120	1.86	0.209	1.79
Cutting speed	2	0.005625	0.002813	0.74	0.509	1.41
Feed rate	2	0.323690	0.161845	42.35	0.000	81.20
Depth of cut	2	0.030484	0.015252	3.99	0.063	7.65
% reinforcement	2	0.001158	0.000579	0.15	0.862	0.29
Error	8	0.030565	0.003821			7.67
Total	17					100.00

predicted GFRG (Y) is calculated using the formula given in Eq. (3),

$$Y = Y_m + \sum_{i=1}^{q}(Y_i - Y_m) \tag{3}$$

where Y_m, Y_i are the mean GFRG, average GFRG at the optimum level of ith parameter and q is the number of experimental input parameters. The predicted and experimental results are given in Table 5. The experimental results are in good agreement with the predicted values with less than ten percentage deviation.

Table 5 Comparison between predicted and experimental results

Levels	Optimal level analyzed through GFRG		Optimum level obtained through experimentation
	MQL, 200 m/min, 0.06 mm/rev, 0.5 mm, 10% reinforcement		Dry, 200 m/min, 0.06 mm/rev, 0.75 mm, 0% reinforcement
	Predicted	Experimental	
Fr	110.515	101.276	121.468
Ra	3.14	2.912	3.448
TW	104.11	101.8	120
GFRG	0.763	0.688	0.882

5   Conclusions

This paper addresses the use of grey-fuzzy logic approach in optimizing the machining parameters for zircon sand-reinforced aluminum matrix composites. Taguchi's L18 mixed level of experiments are conducted, and the following conclusions are drawn:

1. Input parameters like cutting conditions varied at two levels, cutting speed, feed rate, depth of cut and % reinforcement are varied at three levels for machining zircon sand-reinforced aluminum metal matrix composite.
2. The obtained experimental results are normalized using GRA analysis, and GRC values are given as an input to fuzzy logic approach to generate GFRG.
3. For the obtained GFRG data, the statistical analysis is carried out. The optimal levels obtained are MQL as cutting condition with cutting speed at 200 m/min, feed rate at 0.06 mm/rev, depth of cut at 0.5 mm and 10% of zircon sand reinforcement.
4. The experiments are carried out for the optimal levels obtained through statistical analysis, and the results obtained are with less than 10% error with predicted results.

References

1. Sahoo AK, Pradhan S (2013) Modeling and optimization of Al/SiCp MMC machining using Taguchi approach. Meas 46:3064–3072
2. Karabulut S (2015) Optimization of surface roughness and cutting force during AA7039/Al$_2$O$_3$ metal matrix composites milling using neural networks and Taguchi method. Meas 66:139–149
3. Das S, Udhayabanu V, Das S, Das K (2006) Synthesis and characterization of zircon sand/Al-4.5 wt% Cu composite produced by stir casting route. J Mater Sci 41:4668–4677
4. Das S, Das S, Das K (2007) Abrasive wear of zircon sand and alumina reinforced Al–4.5 wt% Cu alloy matrix composites—a comparative study. Compos Sci Tech 67:746–751

5. Noorul Haq A, Marimuthu P, Jeyapaul R (2008) Multi response optimization of machining parameters of drilling Al/SiC metal matrix composite using grey relational analysis in the Taguchi method. Int J Adv Manuf Technol 37:250–255

6. Taskesen A, Kutukde K (2013) Experimental investigation and multi-objective analysis on drilling of boron carbide reinforced metal matrix composites using grey relational analysis. Meas 47:321–330

7. Dabade UA (2013) Multi-objective process optimization to improve surface integrity on turned surface of Al/SiCp metal matrix composites using grey relational analysis. Proc CIRP 7:299–304

8. Ramanathan S, Karthikeyan R, Gupta M (2007) Development of processing maps for Al/SiCp composite using fuzzy logic. J Mater Process Technol 183:104–110

9. Rajasekaran T, Palanikumar K, Vinayagam BK (2011) Application of fuzzy logic for modeling surface roughness in turning CFRP composites using CBN tool. Prod Eng Res Devel 5:191–199

10. Palanikumar K, Karunamoorthy L, Karthikeyan R, Latha B (2006) Optimization of machining parameters in turning GFRP composites using a carbide (K10) tool based on the Taguchi method with fuzzy logics. Met Mater Inter 12(6):483–491

11. Suresh P, Marimuthu K, Ranganathan S, Rajmohan T (2014) Optimization of machining parameters in turning of Al-SiC-Gr hybrid metal matrix composites using grey-fuzzy algorithm. Trans Nonferrous Met Soc China 24:2805–2814

12. Rajmohan T, Palanikumar K, Prakash S (2013) Grey-fuzzy algorithm to optimise machining parameters in drilling of hybrid metal matrix composites. Composites: Part B 50:297–308

13. Barzani MM, Zalnezhad E, Sarhan AAD, Farahany S, Ramesh S (2015) Fuzzy logic based model for predicting surface roughness of machined Al-Si-Cu-Fe die casting alloy using different additives-turning. Meas 61:150–161

14. Dewangan S, Gangopadhyay S, Biswas CK (2015) Multi-response optimization of surface integrity characteristics of EDM process using grey-fuzzy logic-based hybrid approach. Eng Sci Tech Inter J 18:361–368

15. Vignesh M, Ramanujam R (2018) Response optimization in wire electrical discharge machining of AISI H11 tool steel using Taguchi—GRA approach. Int J Mach Mach Mater 20(5):474–495

16. Sampath Kumar T, Ramanujam R, Vignesh M, Tamiloli N, Sharma N, Srivastava S, Patel A (2018) Comparative evaluation of performances of TiAlN, AlCrN, TiAlN/AlCrN coated carbide cutting tools and uncoated carbide cutting tools on turning Inconel 825 alloy using grey relational analysis. Sens Actuat A-Phys 279:331–342

17. Tzeng Y, Chen F (2007) Multi-objective optimization of high-speed electrical discharge machining process using a Taguchi fuzzy-based approach. Mater Des 28:1159–1168

Performance and Emission Characteristics of Compressed Ignition Engine by Using Non-edible Coconut Biodiesel

Kanikicharla Jaya Sudheer Kumar and **Arekanti Naga Raju**

Abstract Biodiesel is an alternative to diesel made from animal fats or vegetable oils. In this study, fatty acid methyl ester extracted from coconut oil was used as a substitute to diesel for evaluation of properties, performance and exhaust emissions of a one-cylinder high-speed diesel engine. The operating performance and the emission characteristics were compared. The engine did not exhibit any starting difficulties although coconut oil utilization has slightly undesirable effects on engine performance of brake power output and specific fuel consumption; it can be utilized as fall back fuel in diesel engines, by this way CO and NOx emissions can be reduced.

Keywords Biodisel · Coconut oil · Emissions · CI engine

1 Introduction

Biodiesels are derived from renewable biological resources and are environment-friendly but similar to diesel for combustion characteristics. Biodiesels are promoted due to agriculture economy, escalating environmental ramifications and gradually reducing petroleum reserves [1].

In India for the reduction of air pollution and dependence on fossil fuel, biodiesel is derived from the animal fats and vegetable oils. These are used as a substitute to fossil fuel. Since India import fruit and vegetable oils but edible oils are not used for the production of biodiesel, heating and blending of vegetable oils reduce the viscosity and increase volatility with unaltered molecular structure [2]. And also in India, there is no excess production of edible oil. Therefore, the oil that can be used as biodiesel has to be non-edible oil. Even though coconut oil extracted from coconuts harvested from the coconut trees is edible, some oil is unfit to eat due to high saturated fat content [3–5].

K. Jaya Sudheer Kumar (✉) · A. Naga Raju
Jawaharlal Nehru Technological University, Anantapur, India
e-mail: k_sudheer@aol.com

1.1 Materials and Methodology

Transesterification of triglycerides from oils or fats to fatty acid methyl ester is done with the addition of methanol. Triacylglycerols are primary ingredients of coconut oil and they are chemically esters of fatty acids with glycerol [6–8].

6 g of sodium hydroxide (NaOH) pellets are added to 300 ml methyl alcohol to form a solution with the base catalyst as a methoxide mixture. One litre of coconut oil at 600 °C is added to methoxide and filtered from glycerine layer. This is acid washed with 5 ml of concentrated sulphuric acid. This results in a neutralization reaction with salt and water. The salt has to be separated and biodiesel is washed with warm water at 400 °C and brought back to room temperature. Then, it is heated up to 100 °C to remove water by evaporation to obtain biodiesel [9, 10].

Blends B10, B20, B30, B40 and B50 with 10, 20, 30, 40 and 50% of coconut oil concentration were made with mixing them with diesel (Table 1).

The computerized combustion ignition engine set-up with the eddy current dynamometer, high-speed data acquisition system, piezoelectric transducer and engine soft software supplied by M/S Apex Innovations Pvt. Ltd., Sangli, was used on a constant speed (1500 rpm) 661 cc, and single-cylinder, 4-stroke, Kirloskar-made diesel engine was used for this investigation. An electro-optical sensor has been utilized to give a voltage pulse when the top dead centre has been reached. It has a good coordinated pair of photo-transistor and an infrared diode. The infrared rays from the diode hit photo-transistor when it is non-interrupted. And then an analogue-to-digital converter is used to read voltage signals from the optical sensor. An eddy current dynamometer is paired with the engine which is mounted on the shaft running on the bearings.

Table 1 Properties of various coconut oil and diesel blends

Property	Standard method	Diesel	B10	B20	B30	B40	B50
Kinematic viscosity at 40 °C (Cs)	ASTM D445	4	5.6	7.3	10.2	13.1	14.8
Calorific value (MJ/Kg)	ASTM D240	45.23	44.28	43.92	42.69	41.80	39.84
Density at 25 °C (Kg/m^3)	ASTM D127	860.2	873.2	879.3	883.3	896.5	902.8
Flash point(°C)	ASTM D93	40	57	63	69	74	79
Fire point(°C)	ASTM D1310	192	234	278	308	337	365
Cetane number	ASTM D6890	45	45	48	49	51	52

1.2 Results and Discussion

1.2.1 Fuel Properties

Kinematic Viscosity

The kinematic viscosity effects fuel injection equipment operations. And also, high kinematic viscosity will result in accumulation of soot and other engine deposits as a result of improper atomization due to insufficient fuel. The kinematic viscosity of blends increased with the increase in the concentration of oil in the blends.

Calorific Value

The decrease in the calorific value with the increase in the concentration of the oil in the biodiesel blends is due to differences in the chemical compositions of the diesel and the coconut oil. Pure diesel is 14.5% more efficient than the blend B50.

Density

The higher values of densities indicate the delay of the injection time to the combustion time of the fuel in a compressed ignition engine. The kinematic density of blends increased with the increase in the concentration of oil in the blends.

Flash Point Temperature

Flash point temperature is the temperature of fuel at which fuel catches fire to an open spark. Generally, flash point temperature varies inversely to the fuel volatility. It is the lowest temperature at which fuel emits enough vapour to ignite when exposed to a spark. The flash point temperatures of the blends are higher than that of diesel thus reducing the overall hazard of the fuel making our coconut oil biodiesel much safer option.

Fire Point Temperature

Fire point temperature is the temperature of the fuel at which it will auto ignite with the raise in temperature. The fire point temperatures of the blends are higher than that of diesel thus reducing the overall hazard of the fuel making our coconut oil biodiesel much safer option.

Fig. 1 Load versus brake-specific fuel consumption
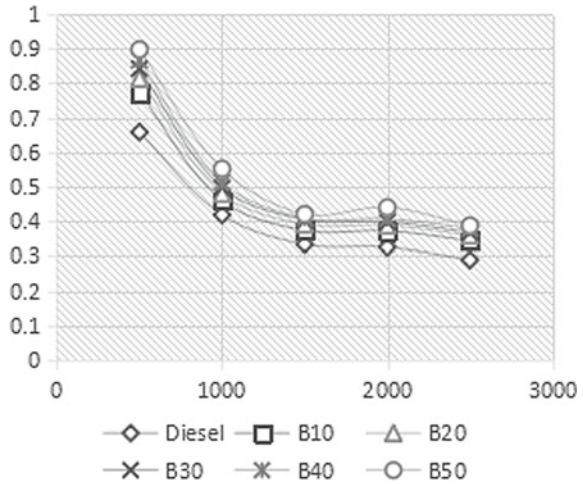
Cetane Number

Cetane number gives us the measure of ignition quality of the fuel during compression ignition. It indicates about the delay time of fuel after its injection into combustion chamber. Higher numeric value of cetane number implies shorter ignition delay. Fuels with lower cetane number are prone to higher exhaust gas emissions and knocking tendencies. With an increase in the concentration of oil in the blends, we had a linear increasing trend which resulted in less emissions.

1.2.2 Performance

Brake-Specific Fuel Consumption

The brake-specific fuel consumption abbreviated as BSFC quantifies the volumetric fuel consumption for a fuel. The varying trend of the brake-specific fuel consumption with increasing power output was plotted in Fig. 1. It is calculated by dividing the total fuel consumption per hour by the power developed from the engine. The change in trend in the blends might be affected by the higher viscosity and the higher densities of the blends.

Mechanical Efficiency

The mechanical efficiency quantifies the effectiveness of the machine in converting the energy and power which is the input of device into an output force resulting in mechanical movement. The mechanical efficiency is the ratio between brake thermal

Fig. 2 Load versus
mechanical efficiency
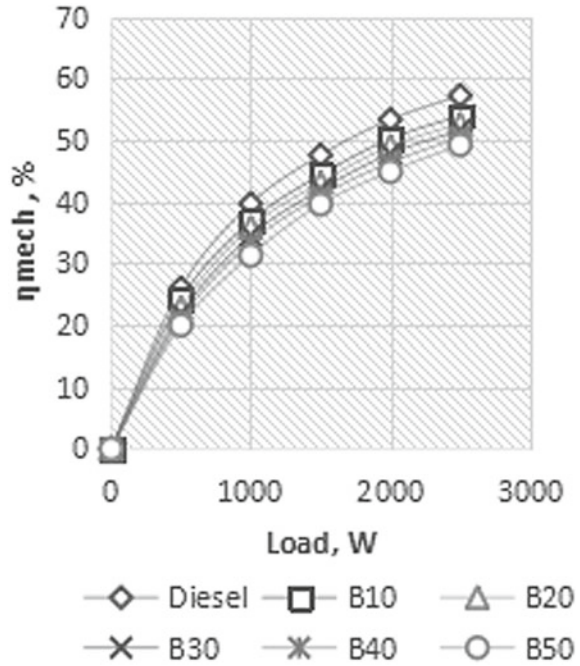
efficiency and the indicated thermal efficiency. Increase in trends of the blends might be due to improvement in the atomization of air–fuel mixtures (Fig. 2).

Brake Thermal Efficiency

The brake thermal efficiency is increased as the engine load increases due to better fuel combustion. At higher loads due to increase in oxygen content in fuel led to better combustion. Blends with higher density and kinematic viscosities with lower calorific value have a tendency to have more brake-specific fuel consumption and lower the brake power as a result of having low atomization (Fig. 3).

1.2.3 Emission

Carbon Monoxide

Carbon monoxide is formed when the fuel is subjected to combustion with insufficient oxygen. Carbon monoxide emission was decreased as the load of the engine increases. At the minimum load conditions, all fuel blends were found to have higher carbon monoxide emissions. As the load increases, carbon monoxide emission was found to

Fig. 3 Load versus brake
thermal efficiency
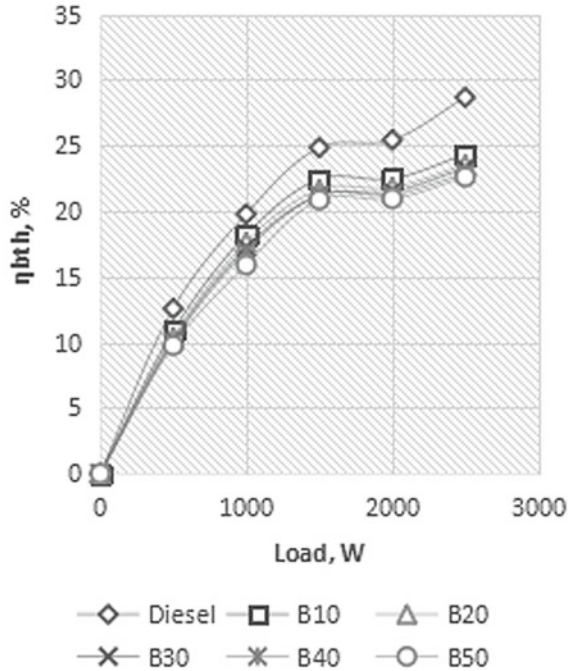
be on the decreasing side for all the blended mixtures because of higher oxygenated
mixture (Fig. 4).

Carbon Dioxide

Carbon dioxide is formed when the fuel is subjected to combustion with excess
oxygen. Carbon dioxide emission was increased as the load of the engine increases.
At the minimum load conditions, all fuel blends were found to have lower carbon
dioxide emissions. As the load increases, carbon dioxide emission was found to be
on the increasing side for all the blended mixtures because of higher oxygenated
mixture (Fig. 5).

Nitrogen Oxides

Nitrogen oxides emission was increasing as the load increases. This is due to the
higher cetane number, calorific value and oxygen content of the fuel. Pure diesel had
the highest nitrogen oxide emission when compared because the blends were more
likely to form complex nitrogen compounds during combustion thus reducing the
amount of nitrogen oxides emission (Fig. 6).

Fig. 4 Load versus carbon monoxide
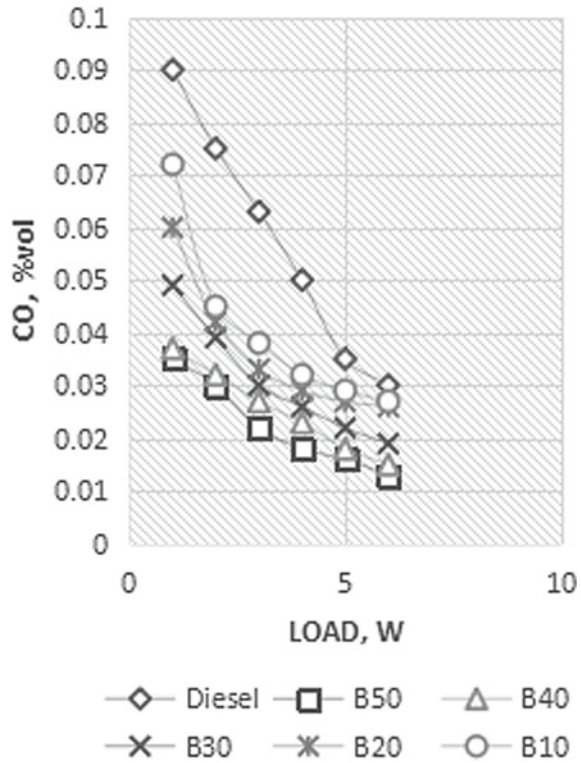
Hydrocarbons

Incomplete combustion diesel results in the hydrocarbon emission. Hydrocarbon emissions increase as the load increases due to an increase in the amount of fuel to attain the power. Pure diesel has higher hydrocarbon emission because it only has diesel in it, whereas in the blends, the hydrocarbons underwent some chemical reactions with oil thus reducing the hydrocarbon emission (Fig. 7).

2 Conclusion

From the current experimental investigation on a computerized one-cylinder, water-cooled and direct ignition four-stroke diesel engine with using coconut oil biodiesel blends, the results concluded that the blends with lower quantities of oil in them have better brake thermal efficiency fuel consumption parameters. From our experimental results, it has been concluded that 10–30% oil to diesel blends can be used as a substitute for diesel without any modifications in the engine. However, 40 and 50% coconut oil diesel have optimum performance.

Fig. 5 Load versus carbon dioxide
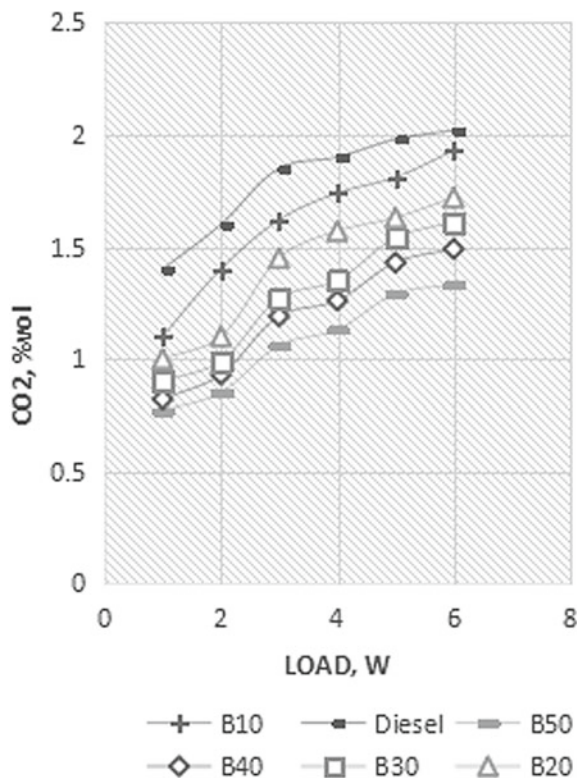
Fig. 6 Load versus nitrogen oxides
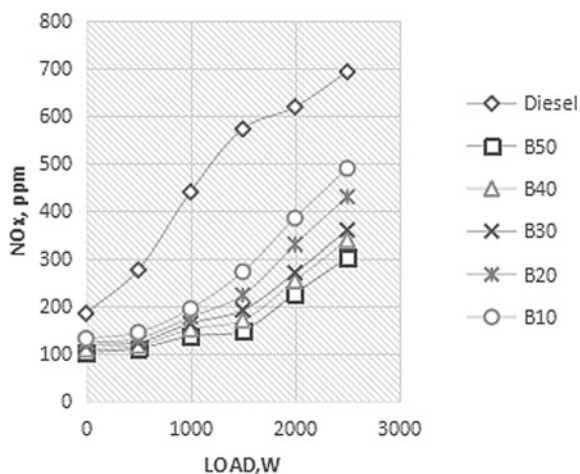
Fig. 7 Load versus hydrocarbons
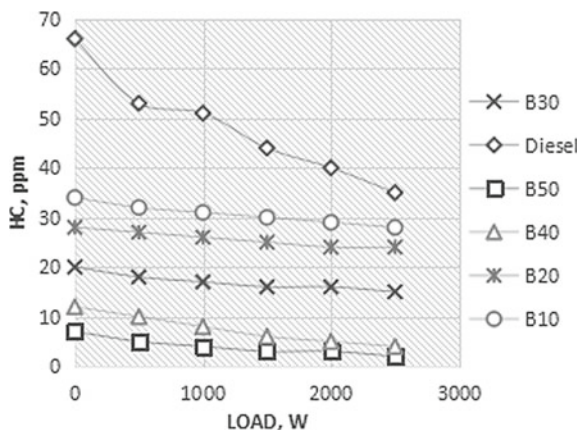
References

1. Sinha S, Mishra NC (1997) Diesel fuel alternative from vegetable oil. Chem Eng World 32(10):77–80
2. Agarwal AK (1998) Vegetable oils verses diesel fuel: development and use of biodiesel in a compression ignition engine. TIDE 8(3):191–204
3. Peterson CL, Cruz RO, Perkings L, Korus R, Auld DL (1990) Transesterification of vegetable oil for use as diesel fuel: a progress report. In: ASAE paper 1990, No. 90–610
4. Rao YVH, Voleti1 RS, Raju AS, Reddy PN (2009) Experimental investigations on jatropha biodiesel and additive in diesel engine. Indian J Sci Technol 2(4). ISSN: 0974-6846
5. Geleta M, Stymne S, Bryngelsson T (2011) Variation and inheritance of oil content and fatty acid composition in niger (Guizotia abyssinica). J Food Comp Anal 24(7):995e1003
6. Knothe G (2005) Dependence of biodiesel fuel properties on the structure of fatty acid alkyl esters. Fuel Process Technol 86:1059–1070
7. Azeez MA, Morakinyo JA (2009) Genetic diversity of lipid and fatty acid profile in nine accessions of sesame (Sesamum and Ceratotheca) seed. In: Proceedings of the 33rd annual conference of genetics society of Nigeria, Ilorin, Nigeria, p 35e45
8. Roschat W, T. Siritanon T. Biodiesel production from palm oil using hydrated lime-derived CaO as a low-cost basic heterogeneous catalyst. Energy Convers Manag 108:459–467
9. Gu H, Jiang Y, Zhou L, Gao J (2011) Reactive extraction and in situ selfcatalyzed methanolysis of germinated oilseed for biodiesel production. Energy Environ Sci 4:1337–1344
10. Kouzu M, Yamanaka S, Hidaka J, Tsunomori M (2009) Heterogeneous catalysis of calcium oxide used for transesterification of soybean oil with refluxing methanol. Appl Catal A: Gen 355:94–99

Bernstein Polynomial Collocation Method for Acceleration Motion of a Vertically Falling Non-spherical Particle

Sudhir Singh and K. Murugesan

Abstract This work deals with the falling of non-spherical particle in incompressible Newtonian media. The Bernstein polynomial collocation method (BPCM) is used to find out velocity and acceleration, and obtained results by BPCM are compared with variational iteration method (VIM), differential transform method (DTM), and the fourth-order Runge–Kutta method (RK-4). It is shown that this method gives a more accurate result when compared to the differential transform method, and the solution converges fast in comparison with VIM. Moreover, the use of BPCM is found to be simple, flexible, efficient, and computationally elegant.

Keywords Solid non-spherical particle · Sedimentation · Bernstein polynomial collocation method · Acceleration motion

1   Introduction

The falling of spherical and non-spherical particles in liquid happens in numerous normal just as mechanical procedures. A portion of the handy circumstances incorporates concoction and powder preparing, diffusive and gravity accumulation and partition, raindrop maximum speed estimation, viscosity estimation, and discharge in pipelines. In cases, for example, raindrop maximum speed estimation and viscosity estimation in the Newtonian liquid, to settle on a definitive choice of the round or non-round spherical particle settling speed by strategy for falling ball, it is required for a given fluid mixture to know the separation and time expected to achieve maximum speed. Be that as it may, by and by, the particles are non-circular, and the molecule movement is influenced by the molecule shape and introduction. With helpful applications, a lot of consideration is given to examine the increasing speed movement of round and non-circular particles in various liquids. Clift et al. have done the hypothetical investigation of the circular molecule [1]. A few assess-

---

S. Singh · K. Murugesan (✉)
Department of Mathematics, National Institute of Technology,
Tiruchirappalli, Tamil Nadu, India
e-mail: murugu@nitt.edu

ments of the accessible information against the prescient relationship are accounted for falling particles in Newtonian media in [2–4].

As of late, investigative strategies [5–11] are used to portray the transient development of the falling round and non-round circular particles in Newtonian fluids. Already, analytical strategies like differential transform method (DTM), homotopy perturbation method (HPM), Padè estimate, variational iteration method (VIM), VIM-Padè, and DTM-Padè have been utilized to unravel speeding up the movement of vertically falling circular and non-round molecule [12–16].

Some theoretical and accurate connections for the drag coefficient on circular particles are given in [1, 2, 17]. For non-round spherical particles, numerous connections for the drag coefficient as far as Reynolds number are available in writing [18–21]. One of the outstanding diagnostic connections between Reynolds number and drag coefficient is given by Chein [20]:

$$C_D = \frac{30}{Re} + 67.289e^{(-5.03\phi)} \tag{1}$$

Equation (1) is expressed to be substantial in the scopes of $0.2 < \varphi < 1$ and $0.001 < Re < 1000$ for various states of the particles [20].

Nonlinear phenomena are widely celebrated in applied science. Many engineering, astrophysics, mathematical physics, and biological modeling are performed by nonlinear dynamical systems. It is difficult to solve the nonlinear problems through analytical methods since much computation is required. The Bernstein basis is used in the computer-aided geometric design [22, 23]. Bernstein polynomial collocation method is applied to solve a much different class of linear, nonlinear, singular initial and boundary value problems, integral equations, integrodifferential equations, and partial differential equations [22, 25–29]. In recent years, a variety of fluid problems have been handled using BPCM [29, 30]. To approximate the solution of the problem defined in [15], the Bernstein polynomial basis is chosen. Using the proposed numerical method, nonlinear ordinary differential equation is converted into nonlinear algebraic system of equations.

This paper is organized as follows. In Sects. 2 and 3, the problem statement and Bernstein polynomials are given. Bernstein polynomials are utilized for solution of the problem in Sect. 4 and results and discussions and presented in Sect. 5, and in last, conclusion is provided.

Nomenclature	
u	$Velocity$, m/s
t	$Time$, s
Re	$Reynolds\ number$
m	$Particle\ mass$, kg
g	$Acceleration\ due\ to\ gravity$, m/s^2
D	$Particle\ equivalent\ volume\ diameter$, m
C_D	$Drag\ coefficient$
Acc	$Acceleration$, m/s^2
$\alpha, \beta, \gamma, \delta$	$Constants$

	Greek symbols
ϕ	Sphericity
μ	Dynamic viscosity, kg/ms
ρ	Fluid density, kg/m^3
ρ_s	Spherical particle density, kg/m^3

2 Statement of the Problem

Let us think about a little, unbending, non-round molecule of mass m, the distance across D and thickness ρ falling endlessly in an incompressible Newtonian liquid of viscosity μ. Let u and g stand to the speed of the molecule and gravity individually. The unsteady movement of the liquid particles can be delineated by Basset–Boussinesq–Oseen condition. Principally the powers following up on the falling body are Basset history constraint, inertia, gravity, buoyancy, virtual mass, and drag compel. The Basset history drive wound up irrelevant by expecting $\rho < \rho_s$, for falling off a thick molecule in light liquid. Henceforth, the condition of the movement of the molecule is given as [15]

$$m\frac{du}{dt} = mg\left(1 - \frac{\rho}{\rho_s}\right) - \frac{1}{8}\pi\rho D^2 C_D u^2 - \frac{1}{12}\pi D^3 \rho\frac{du}{dt}, \qquad (2)$$

Here C_D representing drag coefficient, $mg\left(1 - \frac{\rho}{\rho_s}\right)$ speak to the buoyancy impact, $\frac{1}{8}\pi\rho D^2 C_D u^2$ speak to the drag safe and last term of Eq. (2) related with the additional mass impact because of the acceleration of liquid around the molecule.

Due to the nonlinearity nature of the drag coefficient C_D, the nonlinear terms emerge in Eq. (2), which ends up being the primary trouble in solving Eq. (2). By substituting Eq. (1) in Eq. (2), the accompanying articulation is picked up

$$\alpha\frac{du}{dt} + \beta u + \gamma u^2 - \delta = 0, \ \ u(0) = 0, \qquad (3)$$

where

$$\alpha = \left(m + \frac{1}{12}\pi D^3 \rho\right) \qquad (4)$$

$$\beta = 3.75\pi D\mu \qquad (5)$$

$$\gamma = \frac{67.289 e^{(-5.03\phi)}}{8}\pi D^2 \rho \qquad (6)$$

$$\delta = mg\left(1 - \frac{\rho}{\rho_s}\right) \qquad (7)$$

3 Bernstein Polynomials

The Bernstein polynomials of degree n over $[a, b]$ are defined in [28] as follows

$$B_{i,n}(t) = \binom{n}{i} \frac{(t-a)^i (b-t)^{n-i}}{(b-a)^n}, i = 0, 1, \ldots, n, \tag{8}$$

where $\binom{n}{i} = \frac{n!}{i!(n-i)!}$.

It is not difficult to see that Bernstein polynomials are having degree n satisfy following relations:

1. $B_{i,n}(t) = 0$, if $i < 0$ or $i > n$
2. $B_{i,n}(a) = B_{i,n}(b) = 0$, for $1 \leq i \leq n - 1$
3. $\sum_{i=0}^{n} B_{i,n}(t) = 1$.
4. $B_{i,n}(t) = \frac{1}{b-a} \left[(b-t)B_{i,n-1}(t) + (t-a)B_{i-1,n-1}(t) \right]$

4 Function Approximation

Let $S = L^2[a, b]$ where $a, b \in \mathbb{R}$ and $\{B_{0,n}, B_{1,n}, \ldots, B_{n,n}\} \subset S$ be the set of Bernstein polynomials of nth degree. Let $Y = \text{Span}\{B_{0,n}, B_{1,n}, \ldots, B_{n,n}\}$ and f be any arbitrary element in S. Since Y is finite dimensional vector space, f has unique best approximation from Y, say $y_0 \in Y$. That is $\exists y_0 \in Y; \ \forall y \in Y, \ \|f - y_0\|_2 \leq \|f - y\|_2$ where $\|f\|_2 = \sqrt{\langle f, f \rangle}$. Since $y_0 \in Y$, there exist unique coefficients $\alpha_0, \alpha_1, \alpha_2, \alpha_3, \ldots\ldots, \alpha_n$ such that

$$f \simeq y_0 = \sum_{i=0}^{n} \alpha_i B_i, n = c^T \phi, \tag{9}$$

where $\phi^T = \left[B_{0,n}, B_{1,n}, \ldots, B_{n,n} \right]$, $c^T = [\alpha_0, \alpha_1, \ldots, \alpha_n]$ and c^T can be obtained from $c^T \langle \phi, \phi \rangle = \langle f, \phi \rangle$.

Theorem 1 *Suppose that $f \in C^n[a, b]$, $n + 1$ times continuously differentiable, and $Y = Span\{B_{0,n}, B_{1,n}, \ldots, B_{n,n}\}$. If $c^T \phi$ is the best approximation of f from Y then*

$$\left\| f - c^T \phi \right\| \leq \frac{M(b-a)^{\frac{2n+3}{2}}}{(n+1)!\sqrt{2n+3}} \tag{10}$$

where $M = \max\limits_{x \in [a,b]]} \left| f^{(n+1)}(x) \right|$.
For the proof see [29, 31].

4.1 Solution of the Problem

The Bernstein polynomials over $[a, b]$ defined in Sect. 3 form a basis [28]. By Bernstein polynomial basis function of degree n, a function $u(t)$ defined over $[a, b]$ can be approximated as

$$u(t) \approx \sum_{i=0}^{n} \alpha_i B_{i,n}(t) = C^T B(t) \tag{11}$$

where C and $B(t)$ are $(n+1) \times 1$ vectors defined as

$C = [\alpha_0, \alpha_1, \ldots, \alpha_n]^T$

$B(t) = \left[B_{0,n}(t), B_{1,n}(t), \ldots, B_{n,n}(t) \right]^T$.

For solving Eq. (3), firstly we approximate the unknown functions $u(t)$ as

$$u(t) = C^T B(t) \tag{12}$$

and Eq. (3) can be reduced as

$$\alpha C^T B'(t) + \beta C^T B(t) + \gamma (C^T B(t))^2 - \delta = 0 \tag{13}$$

Now, substituting the collocation points $t_1 = t_0 + rh$, where $t_0 = a$, $h = \frac{b-a}{n}$ and $r = 0, 1, \ldots, n-1$, in Eqs. (3), we have

$$\alpha C^T B'(t_l) + \beta C^T B(t_l) + \gamma (C^T B(t_l))^2 - \delta = 0 \tag{14}$$

Again from initial condition, we get

$$C^T B(0) = 0 \tag{15}$$

In this manner from Eqs. (14) and (15), we acquire $(n+1)$ number of nonlinear equations. Explaining these conditions, we get the vector C, and thus the estimated arrangements of the differential equation (3) can be gotten by utilizing Eq. (11).

By applying this technique, we acquired the solution by the Bernstein Polynomials for $n = 2, 3, 4$ over $[0, 1.4]$ and $n = 3$ over $[0, 2]$ as pursues:

For $n = 2$,

By selecting the collocating point 0 and 0.7, we get the following equations

$-1 - 0.428571\alpha_0 + \alpha_0^2 + 1.42857\alpha_1 = 0$,

$-1 - 0.464286\alpha_0 + 0.5\alpha_1 + (0.25\alpha_0 + 0.5\alpha_1 + 0.25\alpha_2)^2 + 0.964286\alpha_2 = 0$

using the initial condition, we gain

$\alpha_0 = 0.$

The above system provides,

$\alpha_i = 0, 0.7, 0.451811$ for $i = 0, 1, 2$, respectively.

Hence by Eq. (11), we get

$u(t) = (1 - 0.48377t)t.$

For $n = 3$,
By selecting the collocating point 0, 0.46666, and 0.93333, we get the following equations

$-1 - 1.14286\alpha_0 + (\alpha_0)^2 + 2.14286\alpha_2 = 0,$

$-1 - 0.656092\alpha_0 + 0.444465\alpha_1 + 0.936503\alpha_2 + (0.296303\alpha_0 + 0.444444\alpha_1 + 0.222217\alpha_2 + 0.0370354\alpha_3)^2 + 0.275124\alpha_3 = 0,$

$-1 - 0.201061\alpha_0 - 0.492061\alpha_1 + 0.444455\alpha_2 + (0.0370378\alpha_0 + 0.222225\alpha_1 + 0.444444\alpha_2 + 0.296293\alpha_2)^2 + 1.24867\alpha_3 = 0.$

Using the initial condition, we gain

$\alpha_0 = 0.$

The above system provides,

$\alpha_i = 0, 0.466667, 0.546169, 0.576157$ for $i = 0, 1, 2, 3$ respectively.

Hence by Eq. (11), we get

$u(t) = t(1 - 0.592599t + 0.123051t^2).$

For $n = 4$,
By selecting the collocating point 0, 0.35, 0.70, and 1.05, and using initial condition, we get a system of five nonlinear algebraic equation. After solving these equations, we get

$\alpha_i = 0, 0.35, 0.519686, 0.53305, 0.592608$ for $i = 0, 1, 2, 3$, respectively.

Hence by Eq. (11), we get

$u(t) = 1.t - 0.551981t^2 + 0.0349733t^3 + 0.0464714t^4.$

Now for $n = 3$ over [0, 2],

By selecting the collocating point 0, 0.33333, and 1.33333, and using initial condition, we get a system of four nonlinear algebraic equation. After solving these equations, we get

$\alpha_i = 0, 0.228667, 0.191715, 0.213453$ for $i = 0, 1, 2, 3$, respectively.

Hence by Eq. (11), we get

$u(t) = t(1 - 0.580799t + 0.118189t^2).$

5 Results and Discussions

A numerical solution for evaluation of velocity during the acceleration motion of non-spherical particle by BPCM is obtained. The obtained results are compared with DTM, RK-4, and VIM. It is observed that the solution obtained by BPCM is more accurate than VIM [8, 15] and DTM [12] for smaller values of n. BPCM (n=4) gives the better result in comparison with BPCM (n=2) and BPCM (n=3). The values of BPCM for n=2, 3, 4 and 2nd iteration VIM and fourth-order Runge–Kutta method is given in Table 1. Table 2 shows the error between BPCM (n=3) and DTM of order 20, and Fig. 2 shows error plot for DTM and BPCM and claiming BPCM is providing better results than DTM. Figure 1 shows the variation in velocity concerning time for the three methods. BPCM (n=4) gives the better result for the velocity, and hence, it provides a more accurate estimate of acceleration of the particle during falling, and it is affirmed by Fig. 3. This method is simple and easy to implement and requires less computation. Also, coupled ODEs and PDEs also can be solved. All of the calculations are carried out using MATHEMATICA 11.3.

Table 1 Result of BPCM, RK-4, and VIM for $\alpha = \beta = \gamma = \delta = 1$

t	$u(t)_{BPCM(n=2)}$	$u(t)_{BPCM(n=3)}$	$u(t)_{BPCM(n=4)}$	$VIM_{2nditeration}$	$u(t)RK$
0	0	0	0	0	0
0.2	0.1806492016	0.1772804459	0.1782748877	0.1791283812	0.1791133658
0.4	0.3225968066	0.3130594114	0.3151109451	0.3168895074	0.3160071475
0.6	0.4258428149	0.4132433381	0.4148636394	0.4237734755	0.4150283772
0.8	0.4903872266	0.4837386678	0.4836729380	0.5207298702	0.4838375561
1.0	0.5162300416	0.5304518420	0.5294633092	0.5839418925	0.5303298735
1.2	0.5033712599	0.5592893024	0.5619437216	0.2084774709	0.5611508973
1.4	0.4518108815	0.5761574907	0.5926076447	−2.9087036746	0.5813258243

Table 2 Results of DTM and BPCM (n=3) and RK-4 at $\alpha = \beta = \gamma = \delta = 1$

t	$u\,(t)_{BPCM(n=3)}$	$u\,(t)_{DTM\ order\ 20}$	$u\,(t)\,RK-4$	$Error_{BPCM(n=3)}$	$Error_{DTM\ order\ 20}$
0	0	0	0	0	0
0.4	0.3146362341	0.316007092	0.316007131	0.0013708969	0.0000000394
0.8	0.4888012009	0.483835084	0.48387560	0.0049256009	0.0000024755
1.2	0.5678792967	0.552128895	0.561150879	0.0067284177	0.0090219842
1.6	0.5972549178	-2.319449392	0.594422825	0.0028320928	2.9138722166
2.0	0.6223124606	-246.4477393	0.608320171	0.0139922896	247.0560594709

Fig. 1 BPCM ($n = 2, 3, 4$), VIM ($2nd\ iteration$) RK-4 of (3)
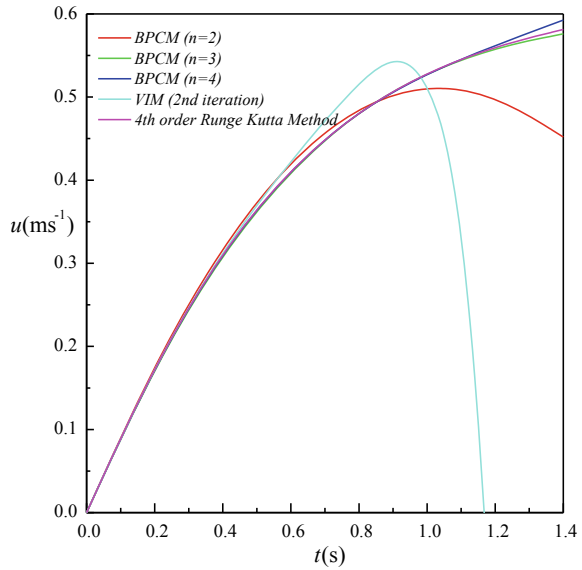
6 Conclusion

The present study deals with the evaluation of velocity and acceleration of non-spherical particle motion in incompressible Newtonian media. The present method is very simple and straightforward. This method is employing the basis of the Bernstein polynomials to approximate the unknown in the differential equation. By choosing the collocation points, the nonlinear differential equation is converted into the algebraic system of equations. Additionally, the proposed method has been compared with the VIM and DTM. The error bound of the method is presented also.

As future work, it will be interesting to apply the present technique to solve different types of physical problems such as (i) settling of non-spherical particle sedimentation in different fluids [12, 14] which play a crucial role in sediment transportation and deposition in pipelines, (ii) spherical particle motion in plane Couette

Fig. 2 Error of DTM (order 20) and BPCM (n = 3) in comparison with the RK-4 method solution for $u(t)$
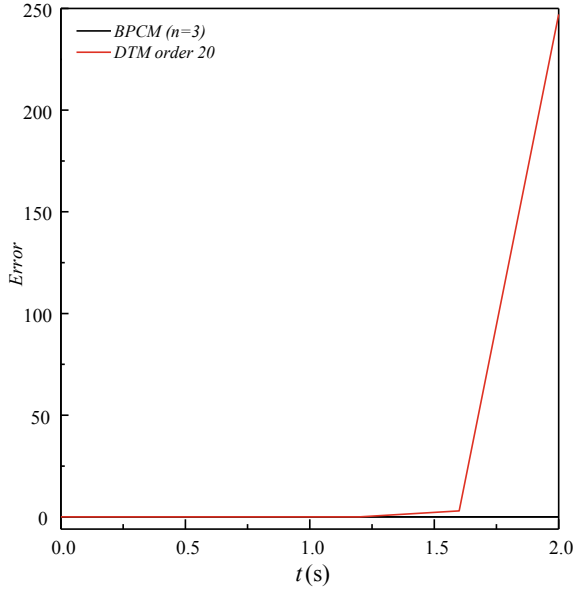
Fig. 3 Variation in acceleration through BPCM
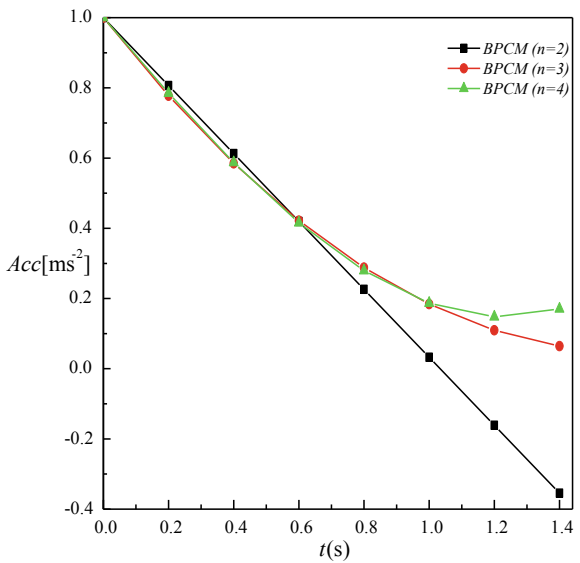
fluid flow [7], (iii) nonlinear equations in heat transfer and transient flows of gas [32, 34], and (iv) nonlinear MHD Jeffery–Hamel problem [33].

References

1. Clift R, Grace J, Weber ME (1978) Bubbles, drops and particles. Academic, New York
2. Chhabra RP (1993) Bubbles, drops and particles in non-Newtonian fluids. CRC Press, Boca Raton
3. Tang P, Chan HK, Rapper JA (2004) Prediction of aerodynamic diameter of particles with rough surfaces. Powder Technol 147:64–78
4. Yow HN, Pitt MJ, Salman AD (2005) Drag correlation for particles of regular shape. Adv Powder Technol 363–372
5. Hatami M, Ganji DD (2014) Motion of a spherical particle on a rotating parabola using Lagrangian and high accuracy multi-step differential transformation method. Powder Technol 258:94–98
6. Hatami M, Domairry G (2014) Transient vertically motion of a soluble particle in a Newtonian fluid media. Powder Technol 253:96–105
7. Jalaal M et al (2011) Homotopy perturbation method for motion of a spherical solid particle in plane Couette fluid flow. Comput Math Appl 61:2267–2270
8. Jalaal M, Ganji DD, Ahmadi G (2012) An analytical study of settling of non-spherical particles. Asia Pac J Chem Eng 7:63–72
9. Jalaal M, Bararnia H, Domairry G (2011) A series exact solution for one-dimensional non-linear particle equation of motion. Powder Technol 207:461–464
10. Ferreira JM, Duarte Naia M, Chhabra RP (1998) An analytical study of the transient motion of a dense rigid sphere in an incompressible Newtonian fluid. Chem Eng Commun 1:168
11. Ferreira JM, Chhabra RP (1998) Acceleration motion of a vertically falling sphere in incompressible Newtonian media: an analytical solution. J Powder Technol 97:6–15
12. Dogonchi AS, Hatami M Hosseinzadeh Kh, Domairry G (2015) Non-spherical particles sedimentation in an incompressible Newtonian medium by Pade' approximation. Powder Technol 278:248–256
13. Torabi M, Yaghoobi H (2013) Accurate solution for acceleration motion of a vertically falling spherical particle in incompressible Newtonian media. Powder Technol 91:376–381
14. Malvandi A, Moshizi SA, Ganji DD (2014) An analytical study of unsteady motion of vertically falling spherical particles in quiescent power-law shear-thinning fluids. J Mol Liq 193:166–173
15. Yaghoobi H, Torabi M (2012) Novel solution for acceleration motion of a vertically falling non-spherical particle by VIM-Pade' approximant. Powder Technol 215–216:206–209
16. Torabi M, Yaghoobi H (2011) Novel solution for acceleration motion of a vertically falling spherical particle by HPM-Pade' approximant. Adv Powder Technol 22:674–677
17. Khan AR, Richardson JF (1987) The resistance to motion of a solid sphere in a fluid. Chem Eng Commun 62:135–150
18. Bagheri G, Bonadonna C (2016) On the drag of freely falling non-spherical particles. Powder Technol 301:526–544
19. Krueger B, Wirtz S, Scherer V (2015) Measurement of drag coefficients of non-spherical particles with a camera-based method. Powder Technol 278:157–170
20. Chein SF (1994) Settling velocity of irregularly shaped particles. SPE Drill Complet 9:281–289
21. Song X, Xu Z, Li G (2017) A new model for predicting drag coefficient and settling velocity of spherical and non-spherical particles in Newtonian fluid. Powder Technol 321:242–250
22. Hoshek J, Lasser D (1993) The fundamental of computer added geometric design. A. K. Peters, Wellesley
23. Farouki RT (2012) The Bernstein polynomial basis: a centennial retrospective. Comput Aided Geom Des 29:379–419
24. Basirat B, Shahdadi MA (2013) Numerical solution of nonlinear integro-differential equations with initial conditions by Bernstein operational matrix of derivatives. Int J Mod Nonlinear Theory Appl 2:141–149
25. Ordokhani Y, Far SD (2013) Application of the Bernstein polynomials for solving the nonlinear Fredholm integro-differential equations. J Appl Math Bionform 1(2):13–31

26. Tabrizidooz HR, Shabanpanah K (2018) Bernstein polynomial basis for numerical solution of boundary value problems. Numer Algorithms 77:211–228
27. Mittal RC, Rohila R (2017) A study of one-dimensional nonlinear diffusion equation by Bernstein polynomial based differential quadrature method. J Math Chem 55:673–695
28. Sahu PK, Saha Ray S (2016) Legendre spectral collocation method for the solution of the model describing biological species living together. J Comput Appl Math 296:47–55
29. Hosseini E, Loghmani GB, Heydari M, Rashidi MM (2017) Investigation of magneto-hemodynamic flow in a semi-porous channel using orthonormal Bernstein polynomials. Eur Phys J Plus 132:326
30. Khataybeh SN, Hasim I, Alshbool M (2018) Solving directly third-order ODEs using operational matrices of Bernstein polynomials methods with application to fluid flow equations. J King Saud Univ-Sci
31. Yousefi SA, Barikbin Z, Dehghan M (2012) Ritz-Galerkin method with Bernstein polynomial basis for finding the product solution form of heat equation with non-classic boundary conditions. Int J Numer Methods Heat Fluid Flow 22:39–48
32. Yaghoobi H, Torabi M (2011) An application of differential transformation method to nonlinear equations arising in heat transfer. Int Commun Heat Mass Transf 38:815–820
33. Moghimi SM, Ganji DD, Bararnia H, Hosseini M, Jalaal M (2011) Homotopy perturbation method for nonlinear MHD Jeffery-Hamel problem. Comput Math Appl 61:2213–2216
34. Noor MA, Mohyud-Din ST (2009) Variational iteration method for unsteady flow of gas through a porous medium using He's polynomials and Pade approximants. Comput Math Appl 58:2182–2189

Overlapping Multi-domain Bivariate Spectral Method for Systems of Nonlinear PDEs with Fluid Mechanics Applications

Musawenkhosi Mkhatshwa, Sandile Motsa, and Precious Sibanda

Abstract An efficient overlapping multi-domain bivariate spectral quasilinearization method (OMD-BSQLM) is introduced for non-similar boundary layer equations arising in fluid mechanics. Previously, the multi-domain approach has been applied to either space or time interval but not both. The new method applies the multi-domain technique in both space and time interval. The time interval is decomposed into non-overlapping sub-intervals, and the space interval is split into overlapping sub-domains. Numerical experiments are carried out to highlight the accuracy and efficiency of the method. An analysis of the convergence and accuracy of the OMD-BSQLM is given using error norms and residual errors. The series solutions are used to validate the accuracy of the OMD-BSQLM results. The new method converges rapidly and gives accurate results after a few iterations and using a few grid points. Moreover, the accuracy does not worsen when a large time domain is considered.

Keywords Multi-domain overlapping technique · Bivariate interpolation · Spectral quasilinearisation method

1 Introduction

Most heat and mass transfer problems arising in fluid dynamics are modelled by non-similar boundary layer partial differential equations (PDEs). These differential equations are often difficult to solve analytically or their exact solutions may not exist. In such instances, we have to solve the differential equations using numerical methods. Analytical solutions can give an insight into the influence of various parameters that have a bearing on the solution, which is not generally the case with numerical

M. Mkhatshwa (✉) · S. Motsa · P. Sibanda
School of Mathematics, Statistics and Computer Science, University of Kwazulu Natal,
Private Bag X01, Scottsville, Pietermarittzburg 3209, South Africa
e-mail: patsonmkhatshwa@gmail.com

S. Motsa
Department of Mathematics, University of Eswatini, Kwaluseni, Kingdom of Eswatini

methods. However, numerical methods are efficient tools that can be used in solving highly nonlinear differential equations that are complex and even impossible to solve analytically. The challenge of finding more accurate, robust and computationally efficient numerical methods for solving strongly nonlinear problems still exists. The development of numerical methods that converge quickly and most accurate is currently attracting the attention of a growing number of researchers. Traditional methods such as the finite difference method require a large number of grid points to produce accurate results. Their accuracy also deteriorates fast as the time domain increases for parabolic nonlinear PDEs.

Spectral collocation-based methods have been used to solve many non-similar boundary layer differential equations. They have shown to be reliable and efficient in solving nonlinear systems of ordinary differential equations (ODEs) and PDEs. Spectral methods have many advantages over traditional methods such as high accuracy and efficiency [1]. When applied to problems with smooth solutions, they use few grid points and require minimal computational time to generate accurate solutions, thus better than traditional methods. Motsa et. al [2] applied the spectral method in space and finite differences in time when solving non-similar boundary layer differential equations. To improve the accuracy and computational speed of spectral methods several researchers [3–5] applied spectral collocation method independently in both space and time. The method gives accurate results for smaller time domains. The accuracy of the method decreases with an increase in the time domain. One of the effective techniques to overcome this problem is using a multi-domain grid. Motsa et al. [6] introduced a non-overlapping multi-domain bivariate spectral quasilinearization method (MD-BSQLM) to increase the accuracy of spectral collocation-based methods for large time variable. The non-overlapping MD-BSQLM applies the multi-domain technique only in the time interval. Following the discretization process, the multi-domain technique can help to make the matrices to be less dense. This means that most of the elements will be zeros. The sparsity of matrices can help to minimize storage for large matrices and make it easy to perform matrix-vector multiplications. This is because there will be a lot of multiplication by zero which reduces the computational time and enable the matrices to be stored efficiently. Yang [7] introduced an overlapping multi-domain technique and used it to solve PDEs exhibiting discontinuous solutions. The technique was found to give accurate results compared to existing numerical methods. The concept of overlapping sub-domains has been discussed by several researchers [8–10].

The need to continually improve on existing spectral collocation-based methods for solving nonlinear differential equations that cannot be solved analytically cannot be overstated. Most studies in the literature used the multi-domain technique in either space or time but not both. However, applying the multi-domain technique in both space and time interval and further utilizing the strategy of overlapping sub-domains can increase the accuracy of spectral collocation-based methods for small and large time variable. The objective of the study is to introduce a method that uses the multi-domain technique, spectral collocation method, bivariate Lagrange interpolation polynomials based on Chebyshev–Gauss Lobatto grid points [11, 12] and quasilinearization method (QLM) [13] in finding solutions of coupled non-similar

boundary layer PDEs over a large time interval. The multi-domain technique employs the strategy of non-overlapping and overlapping sub-domains. Thus, the time interval is partitioned into non-overlapping sub-domains, and the space interval is decomposed into overlapping sub-intervals. The applicability, accuracy and reliability of the proposed method have been tested by solving systems of n coupled non-similar boundary layer partial differential equations arising in fluid mechanics.

2 The Overlapping Multi-domain Bivariate Spectral Quasilinearization Method (OMD-BSQLM)

In this section, we introduce the OMD-BSQLM for a system of n nonlinear PDEs expressed in the form

$$\Gamma_1[F_1, F_2, \ldots, F_n] = 0, \tag{1}$$

$$\Gamma_2[F_1, F_2, \ldots, F_n] = 0, \tag{2}$$

$$\vdots$$

$$\Gamma_n[F_1, F_2, \ldots, F_n] = 0, \tag{3}$$

where the operators $F_i (i = 1, 2, 3, \ldots, n)$ are given by

$$F_1 = \left\{ g_1, \frac{\partial g_1}{\partial \eta}, \frac{\partial^2 g_1}{\partial \eta^2}, \ldots, \frac{\partial^s g_1}{\partial \eta^s}, \frac{\partial g_1}{\partial \xi}, \frac{\partial}{\partial \xi} \left(\frac{\partial g_1}{\partial \eta} \right) \right\}$$

$$\vdots$$

$$F_n = \left\{ g_n, \frac{\partial g_n}{\partial \eta}, \frac{\partial^2 g_n}{\partial \eta^2}, \ldots, \frac{\partial^s g_n}{\partial \eta^s}, \frac{\partial g_n}{\partial \xi}, \frac{\partial}{\partial \xi} \left(\frac{\partial g_n}{\partial \eta} \right) \right\}. \tag{4}$$

We denote the order of differentiation by s, *and* the required solution by $g_k(\eta, \xi)$ and Γ_k denotes the nonlinear operators containing all the spatial and time derivatives of $g_k(\eta, \xi)$. The Chebyshev–Gauss–Lobatto grid points and their corresponding differentiation are defined in the interval $[-1, 1]$. In order to apply the OMD-BSQLM, the time interval $\xi \in [0, T]$ is decomposed into q non-overlapping sub-intervals defined as

$$J_\upsilon = (\xi_{\upsilon-1}, \xi_\upsilon), \quad \upsilon = 1, 2, 3, \ldots, q. \tag{5}$$

The space interval $[a, b]$ is decomposed into p overlapping sub-intervals of length L, denoted by

$$I_\mu = [\eta_0^\mu, \eta_{N_\eta}^\mu], \quad \mu = 1, 2, 3, \ldots, p, \tag{6}$$
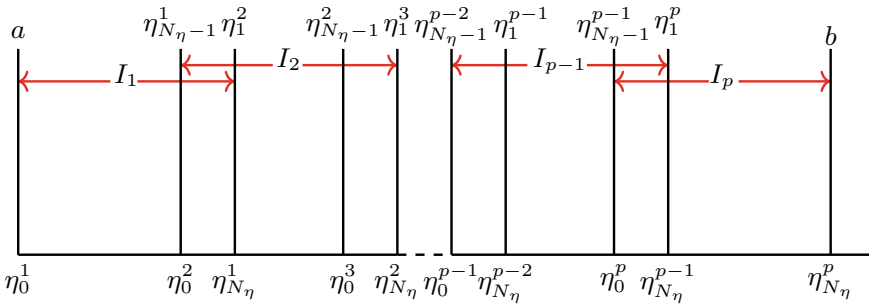
Fig. 1 Overlapping grid

where each I_μ interval is further discretized into $N_\eta + 1$ collocation points. For the overlap to be possible, the sub-intervals must be of equal length given by

$$L = \frac{b - a}{p + \frac{1}{2}(1 - p)(1 - \cos \frac{\pi}{N_\eta})}. \tag{7}$$

In the overlapping multi-domain grid, the first two points of the interval $I_{\mu+1}$ coincide with the last two points of the interval I_μ as shown in Fig. 1. To derive the result in Eq. (7), we note that the total length of the domain is

$$b - a = 2L - \varepsilon + (2L - 2\varepsilon)\left(\frac{p}{2} - 1\right)$$
$$= 2L - \varepsilon + (L - \varepsilon)(p - 2) = \varepsilon(1 - p) + pL, \tag{8}$$

where ε is the overlapping distance between two intervals. We remark that $\varepsilon = \eta_0 - \eta_1$. Considering the first interval I_1 in which $\eta \in [a, \eta_{N_\eta}^1]$, we can define the length $L = \eta_{N_\eta}^1 - a$. The linear transformation $\eta = \frac{L}{2}z + \frac{a + \eta_{N_\eta}^1}{2}$ can be used to transform the interval $[a, \eta_{N_\eta}^1]$ to $[-1, 1]$. Thus, using the Gauss–Lobatto collocation points $z_i = \cos\left(\frac{\pi i}{N_\eta}\right)$, where $i = 0, 1, 2, 3, \ldots, N_\eta$, we obtain $\eta_0 - \eta_1 = \frac{L}{2}(z_0 - z_1) = \frac{L}{2}\left(1 - \cos \frac{\pi}{N_\eta}\right)$. Therefore, Eq. (8) becomes

$$b - a = \frac{L}{2}\left(1 - \cos \frac{\pi}{N_\eta}\right)(1 - p) + pL, \tag{9}$$

and making L the subject in Eq. (9) yields Eq. (7).

Generally, before the spectral collocation method is applied at each sub-interval, the time interval $\xi \in J_\upsilon$ and space interval $\eta \in I_\mu$ are transformed into $\tau \in [-1, 1]$ and $z \in [-1, 1]$ using the linear transformations

$$\xi_j = \frac{1}{2}(\xi_\upsilon - \xi_{\upsilon-1})\tau_j + \frac{1}{2}(\xi_\upsilon + \xi_{\upsilon-1}), \quad \tau_j = \cos\left(\frac{\pi j}{N_\xi}\right), \tag{10}$$

$$\eta_i^\mu = \frac{L}{2}(z_i + 1), \quad z_i = \cos\left(\frac{\pi i}{N_\eta}\right). \tag{11}$$

In terms of the original variable η, the collocation points are arranged as

$$\{\eta_r\}_{r=0}^M = \left\{\eta_0^1, \ldots, \eta_{N_\eta-1}^1 = \eta_0^2, \eta_{N_\eta}^1 = \eta_1^2, \ldots, \eta_k^\mu, \ldots, \eta_{N_\eta-1}^\mu = \eta_0^{\mu+1}, \eta_{N_\eta}^\mu = \eta_1^{\mu+1}, \ldots, \eta_{N_\eta}^p\right\},$$

$$= \left\{\eta_0^1, \ldots, \eta_{N_\eta-1}^1, \eta_1^2, \ldots, \eta_k^\mu, \ldots, \eta_{N_\eta-1}^\mu, \eta_1^{\mu+1}, \ldots, \eta_{N_\eta}^p\right\}, \tag{12}$$

where $M = N_\eta + (N_\eta - 1)(p - 1)$ is the total number of collocation points over the entire space interval. It can be shown that the grid points can be obtained as follows

$$\eta_i^1 = a + \frac{L}{2}(z_i + 1), \ i = 1, 2, 3, \ldots, N_\eta,$$

$$\eta_i^{p-\mu} = \frac{L}{2}(z_i - 1) + b - \frac{L\mu}{2}\left[1 + \cos\left(\frac{\pi}{N_\eta}\right)\right], \ i = 1, 2, \ldots, N_\eta - 1, \mu = 2, 3, \ldots, p - 1,$$

$$\eta_i^p = a + \frac{L}{2}(1 + z_i), \ i = 0, 1, 2, \ldots, N_\eta - 1. \tag{13}$$

In terms of the transformed variables z and τ, the collocation points are arranged as

$$\{z_r\}_{r=0}^M = \left\{z_{N_\eta}^1, \ldots, z_1^1 = z_{N_\eta}^2, z_0^1 = z_{N_\eta-1}^2, \ldots, z_k^\mu, \ldots, z_1^\mu = z_{N_\eta}^{\mu+1}, z_0^\mu = \eta_{N_\eta-1}^{\mu+1}, \ldots, \eta_0^p\right\},$$

$$= \left\{z_{N_\eta}^1, \ldots, z_1^1, z_{N_\eta-1}^2, \ldots, z_k^\mu, \ldots, z_1^\mu, z_{N_\eta-1}^{\mu+1}, \ldots, z_0^p\right\},$$

$$\{\tau_r\}_{r=0}^{N_\xi} = \left\{\tau_{N_\xi}^1, \ldots, \tau_1^1, \tau_{N_\xi}^2, \ldots, \tau_k^\upsilon, \ldots, \tau_1^\upsilon, \tau_{N_\xi}^{\upsilon+1}, \ldots, \tau_0^q\right\}. \tag{14}$$

We assume that at each sub-interval, the solution can be approximated by a bivariate Lagrange interpolation polynomial of the form

$$g_k^{(\mu,\upsilon)}(\eta, \xi) \approx \sum_{i=0}^{N_\eta} \sum_{j=0}^{N_\xi} g_k^{(\mu,\upsilon)}(\eta_i, \xi_j)\mathcal{L}_i(\eta)\mathcal{L}_j(\xi), \tag{15}$$

where the bivariate interpolation polynomial interpolates $g_k^{(\mu,\upsilon)}(\eta, \xi)$ at selected points (η_i, ξ_j) in both η and ξ directions. Applying the QLM on Γ_k gives

$$\Gamma_k[F_1, F_2, \ldots, F_n] \approx (F_{1,r+1} - F_{1,r}, F_{2,r+1} - F_{2,r}, \ldots, F_{n,r+1} - F_{n,r}).\nabla\Gamma_k[F_{1,r}, F_{2,r}, \ldots, F_{n,r}]$$

$$+\Gamma_k[F_{1,r}, F_{2,r}, \ldots, F_{n,r}], \tag{16}$$

where r and $r + 1$ denote previous and current iteration, respectively. The vector of the partial derivatives denoted by ∇ is defined as

$$\nabla = \left\{\nabla_{g_1}, \nabla_{g_2}, \ldots, \nabla_{g_n}\right\}, \tag{17}$$

and

$$\nabla_{g_1} = \left\{ \frac{\partial}{\partial g_1}, \frac{\partial}{\partial g_1'}, \frac{\partial}{\partial g_1''}, \ldots, \frac{\partial}{\partial g_1^{(s)}}, \frac{\partial}{\partial \left(\frac{\partial g_1}{\partial \xi} \right)}, \frac{\partial}{\partial \left(\frac{\partial g_1'}{\partial \xi} \right)} \right\}, \tag{18}$$

$$\vdots$$

$$\nabla_{g_n} = \left\{ \frac{\partial}{\partial g_n}, \frac{\partial}{\partial g_n'}, \frac{\partial}{\partial g_n''}, \ldots, \frac{\partial}{\partial g_n^{(s)}}, \frac{\partial}{\partial \left(\frac{\partial g_n}{\partial \xi} \right)}, \frac{\partial}{\partial \left(\frac{\partial g_n'}{\partial \xi} \right)} \right\}, \tag{19}$$

where the prime denotes differentiation with respect to η. The linearized Eq. (16) can be expressed in a compact form as

$$\sum_{l=1}^{n} F_{l,r+1} \cdot \nabla_{f_l} \Gamma_k \left[F_{1,r}, F_{2,r}, \ldots, F_{n,r} \right] = \sum_{l=1}^{n} F_{l,r} \cdot \nabla_{f_l} \Gamma_k \left[F_{1,r}, F_{2,r}, \ldots, F_{n,r} \right]$$
$$- \Gamma_k \left[F_{1,r}, F_{2,r}, \ldots, F_{n,r} \right], \tag{20}$$

for $k = 1, 2, \ldots, n$. Equation (20) forms a system of n coupled linear PDEs which are solved iteratively for $g_{1,r+1}^{(\mu,\upsilon)}(\eta, \xi), g_{2,r+1}^{(\mu,\upsilon)}(\eta, \xi), \ldots, g_{n,r+1}^{(\mu,\upsilon)}(\eta, \xi)$. Equation (20) can further be expressed as

$$\sum_{\upsilon=1}^{n} \left[\sum_{l=0}^{s} \alpha_{\upsilon,l,r}^{(1,\mu,\upsilon)} g_{\upsilon,r+1}^{(l,\mu,\upsilon)} + \beta_{\upsilon,r}^{(1,\mu,\upsilon)} \frac{\partial g_{\upsilon,r+1}^{(\mu,\upsilon)}}{\partial \xi} + \gamma_{\upsilon,r}^{(1,\mu,\upsilon)} \frac{\partial}{\partial \xi} \left(\frac{\partial g_{\upsilon,r+1}^{(\mu,\upsilon)}}{\partial \eta} \right) \right] = R_1^{(\mu,\upsilon)}$$

$$\sum_{\upsilon=1}^{n} \left[\sum_{l=0}^{s} \alpha_{\upsilon,l,r}^{(2,\mu,\upsilon)} g_{\upsilon,r+1}^{(l,\mu,\upsilon)} + \beta_{\upsilon,r}^{(2,\mu,\upsilon)} \frac{\partial g_{\upsilon,r+1}^{(\mu,\upsilon)}}{\partial \xi} + \gamma_{\upsilon,r}^{(2,\mu,\upsilon)} \frac{\partial}{\partial \xi} \left(\frac{\partial g_{\upsilon,r+1}^{(\mu,\upsilon)}}{\partial \eta} \right) \right] = R_2^{(\mu,\upsilon)} \tag{21}$$

$$\vdots$$

$$\sum_{\upsilon=1}^{n} \left[\sum_{l=0}^{s} \alpha_{\upsilon,l,r}^{(n,\mu,\upsilon)} g_{\upsilon,r+1}^{(l,\mu,\upsilon)} + \beta_{\upsilon,r}^{(n,\mu,\upsilon)} \frac{\partial g_{\upsilon,r+1}^{(\mu,\upsilon)}}{\partial \xi} + \gamma_{\upsilon,r}^{(n,\mu,\upsilon)} \frac{\partial}{\partial \xi} \left(\frac{\partial g_{\upsilon,r+1}^{(\mu,\upsilon)}}{\partial \eta} \right) \right] = R_n^{(\mu,\upsilon)},$$

where $\alpha_{n,s,r}^{(k,\mu,\upsilon)}(\eta, \xi)$, $\beta_{\upsilon,r}^{(k,\mu,\upsilon)}(\eta, \xi)$ and $\gamma_{\upsilon,r}^{(k,\mu,\upsilon)}(\eta, \xi)$ are variable coefficients of $g_{n,r+1}^{(s,\mu,\upsilon)}$, $\frac{\partial g_{\upsilon,r+1}^{(\mu,\upsilon)}}{\partial \xi}$ and $\frac{\partial}{\partial \xi} \left(\frac{\partial g_{\upsilon,r+1}}{\partial \xi} \right)$, respectively. These variable coefficients correspond to the kth equation, for $k = 1, 2, \ldots, n$. The variable coefficients are obtained as

$$\alpha_{n,s,r}^{(k,\mu,\upsilon)} = \frac{\partial \Gamma_k}{\partial g_{n,r}^{(s,\mu,\upsilon)}}, \quad \beta_{\upsilon,r}^{(k,\mu,\upsilon)} = \frac{\partial \Gamma_k}{\partial \left(\frac{\partial g_{\upsilon,r}^{(\mu,\upsilon)}}{\partial \xi} \right)}, \quad \gamma_{\upsilon,r}^{(k,\mu,\upsilon)} = \frac{\partial \Gamma_k}{\partial \left(\frac{\partial}{\partial \xi} \left(\frac{\partial g_{\upsilon,r}^{(\mu,\upsilon)}}{\partial \eta} \right) \right)}.$$

Equation (21) is evaluated at the Chebyshev–Gauss–Lobatto grid points $\xi_j (j = 0, 1, 2, \ldots, N_\xi)$ and $\eta_i (i = 0, 1, 2, \ldots, N_\eta)$. The time derivatives at the Chebyshev–Gauss–Lobatto points (η_i, ξ_j) is computed as

$$\left. \frac{\partial g_n^{(\mu,\upsilon)}}{\partial \xi} \right|_{(\eta_i,\xi_j)} = \left(\frac{2}{\xi_\upsilon - \xi_{\upsilon-1}} \right) \sum_{\tau=0}^{N_\xi} d_{j,\tau} g_n^{(\mu,\upsilon)}(\eta_i, \xi_\tau), \tag{22}$$

The sth order space derivative is computed as

$$\left. \frac{\partial^s g_n^{(\mu,\upsilon)}}{\partial \eta^s} \right|_{(\eta_i,\xi_j)} = \left(\frac{2}{\eta_{N_\eta}^\mu - \eta_0^\mu} \right)^s \sum_{\nu=0}^{N_\eta} \left[D_{i,\nu}^{(\mu)} \right]^s g_n^{(\mu,\upsilon)}(\eta_\nu, \xi_j) = \left[\mathbf{D}^{(\mu)} \right]^s \mathbf{G}_{n,j}^{(\mu,\upsilon)}, \tag{23}$$

where the vector $\mathbf{G}_{n,j}^{(\mu,\upsilon)}$ is defined as

$$\mathbf{G}_{n,j}^{(\mu,\upsilon)} = \left[g_n^{(\mu,\upsilon)}(\eta_0^{(\mu)}, \xi_j^{(\upsilon)}), g_n^{(\mu,\upsilon)}(\eta_1^{(\mu)}, \xi_j^{(\upsilon)}), \ldots, g_n^{(\mu,\upsilon)}(\eta_{N_\eta}^{(\mu)}, \xi_j^{(\upsilon)}) \right]^T \tag{24}$$

and T denotes matrix transpose. Substituting Eqs. (22) and (23) into Eq. (21) yields

$$\sum_{\nu=1}^{n} \left[A_{1,\nu}^{(i,\mu,\upsilon)} \mathbf{G}_{\nu,i}^{(\mu,\upsilon)} + \boldsymbol{\beta}_{\nu,r}^{(1,\mu,\upsilon)} \sum_{j=0}^{N_\xi} d_{i,j} \mathbf{G}_{\nu,j}^{(\mu,\upsilon)} + \boldsymbol{\gamma}_{\nu,r}^{(1,\mu,\upsilon)} \sum_{j=0}^{N_\xi} d_{i,j} \mathbf{D}^{(\mu)} \mathbf{G}_{\nu,j}^{(\mu,\upsilon)} \right] = \mathbf{R}_{1,i}^{(\mu,\upsilon)},$$

$$\sum_{\nu=1}^{n} \left[A_{2,\nu}^{(i,\mu,\upsilon)} \mathbf{G}_{\nu,i}^{(\mu,\upsilon)} + \boldsymbol{\beta}_{\nu,r}^{(2,\mu,\upsilon)} \sum_{j=0}^{N_\xi} d_{i,j} \mathbf{G}_{\nu,j}^{(\mu,\upsilon)} + \boldsymbol{\gamma}_{\nu,r}^{(2,\mu,\upsilon)} \sum_{j=0}^{N_\xi} d_{i,j} \mathbf{D}^{(\mu)} \mathbf{G}_{\nu,j}^{(\mu,\upsilon)} \right] = \mathbf{R}_{2,i}^{(\mu,\upsilon)},$$

$$\vdots$$

$$\sum_{\nu=1}^{n} \left[A_{n,\nu}^{(i,\mu,\upsilon)} \mathbf{G}_{\nu,i}^{(\mu,\upsilon)} + \boldsymbol{\beta}_{\nu,r}^{(n,\mu,\upsilon)} \sum_{j=0}^{N_\xi} d_{i,j} \mathbf{G}_{\nu,j}^{(\mu,\upsilon)} + \boldsymbol{\gamma}_{\nu,r}^{(n,\mu,\upsilon)} \sum_{j=0}^{N_\xi} d_{i,j} \mathbf{D}^{(\mu)} \mathbf{G}_{\nu,j}^{(\mu,\upsilon)} \right] = \mathbf{R}_{n,i}^{(\mu,\upsilon)}, \tag{25}$$

where $A_{k,\nu}^{(i,\mu,\upsilon)} = \sum_{l=0}^{s} \boldsymbol{\alpha}_{\nu,l,r}^{(k,\mu,\upsilon)} \left[\mathbf{D}^{(\mu)} \right]^l$.

3 Numerical Experiments

We first consider the problem of steady two-dimensional laminar free convection flow past a non-isothermal vertical porous cone with variable temperature [14].

$$f''' + \frac{n+7}{4} ff'' - \frac{n+1}{2} f'^2 + \theta + \xi f'' = \frac{1-n}{4} \xi \left(f' \frac{\partial f'}{\partial \xi} - f'' \frac{\partial f}{\partial \xi} \right) \tag{26}$$

$$\frac{1}{Pr} \theta'' + \frac{n+7}{4} f\theta' - nf'\theta + \xi\theta' = \frac{1-n}{4} \xi \left(f' \frac{\partial \theta}{\partial \xi} - \theta' \frac{\partial f}{\partial \xi}, \right) \tag{27}$$

$$f(0, \xi) = 0, \quad f'(0, \xi) = 0, \quad \theta(0, \xi) = 1, \quad f'(\infty, \xi) = 0, \quad \theta(\infty, \xi) = 0. \tag{28}$$

In this example, the highest order of differentiation is $s = 3$, and the number of equations is $n = 2$. Applying OMD-BSQLM to Eqs. (26) and (27) yields

$$\sum_{v=1}^{2}\left[A_{1,v}^{(i,\mu,v)}\mathbf{G}_{v,i}^{(\mu,v)}+\boldsymbol{\beta}_{v,r}^{(1,\mu,v)}\sum_{j=0}^{N_\xi}d_{i,j}\mathbf{G}_{v,j}^{(\mu,v)}+\boldsymbol{\gamma}_{v,r}^{(1,\mu,v)}\sum_{j=0}^{N_\xi}d_{i,j}\mathbf{D}^{(\mu)}\mathbf{G}_{v,j}^{(\mu,v)}\right]=\mathbf{R}_{1,i}^{(\mu,v)},\quad(29)$$

$$\sum_{v=1}^{2}\left[A_{2,v}^{(i,\mu,v)}\mathbf{G}_{v,i}^{(\mu,v)}+\boldsymbol{\beta}_{v,r}^{(2,\mu,v)}\sum_{j=0}^{N_\xi}d_{i,j}\mathbf{G}_{v,j}^{(\mu,v)}+\boldsymbol{\gamma}_{v,r}^{(2,\mu,v)}\sum_{j=0}^{N_\xi}d_{i,j}\mathbf{D}^{(\mu)}\mathbf{G}_{v,j}^{(\mu,v)}\right]=\mathbf{R}_{2,i}^{(\mu,v)},\quad(30)$$

In order to apply the OMD-BSQLM, we let $f(\eta,\xi)=g_1(\eta,\xi)$ and $\theta(\eta,\xi)=g_2(\eta,\xi)$. Imposing the boundary conditions for $j=0,1,2,\ldots,N_\xi-1$, Eqs. (29) and (30) can be expressed as the following $N_\xi(M+1)\times N_\xi(M+1)$ matrix system

$$(31)$$

where

$$A_{i,i}^{(1,1,p,v)}=\boldsymbol{\alpha}_{1,3,r}^{(1,\mu,v)}\left[\mathbf{D}^{(\mu)}\right]^3+\boldsymbol{\alpha}_{1,2,r}^{(1,\mu,v)}\left[\mathbf{D}^{(\mu)}\right]^2+\boldsymbol{\alpha}_{1,1,r}^{(1,\mu,v)}\left[\mathbf{D}^{(\mu)}\right]^1+\boldsymbol{\alpha}_{1,0,r}^{(1,\mu,v)}$$
$$\qquad+\boldsymbol{\beta}_{1,r}^{(1,\mu,v)}d_{i,i}\mathbf{I}+\boldsymbol{\gamma}_{1,r}^{(1,\mu,v)}d_{i,i}\mathbf{D}^{(\mu)},i=j$$

$$A_{i,i}^{(1,2,p,v)}=\boldsymbol{\alpha}_{2,0,r}^{(1,\mu,v)}\mathbf{I},\,A_{i,i}^{(2,1,p,v)}=\boldsymbol{\alpha}_{1,1,r}^{(2,\mu,v)}\left[\mathbf{D}^{(\mu)}\right]^1+\boldsymbol{\alpha}_{1,0,r}^{(2,\mu,v)}+\boldsymbol{\beta}_{1,r}^{(2,\mu,v)}d_{i,i}\mathbf{I},\,i=j$$

$$A_{i,i}^{(2,2,p,v)}=\boldsymbol{\alpha}_{2,2,r}^{(2,\mu,v)}\left[\mathbf{D}^{(\mu)}\right]^2+\boldsymbol{\alpha}_{2,1,r}^{(2,\mu,v)}\left[\mathbf{D}^{(\mu)}\right]^1+\boldsymbol{\alpha}_{2,0,r}^{(2,\mu,v)}+\boldsymbol{\beta}_{2,r}^{(2,\mu,v)}d_{i,i}\mathbf{I},\quad i=j$$

$$A_{i,j}^{(1,1,p,v)}=\boldsymbol{\beta}_{1,r}^{(1,\mu,v)}d_{i,j}\mathbf{I}+\boldsymbol{\gamma}_{1,r}^{(1,\mu,v)}d_{i,j}\mathbf{D}^{(\mu)},\quad A_{i,j}^{(1,2,p,v)}=\mathbf{0},i\neq j$$

$$A_{i,j}^{(2,1,p,v)}=\boldsymbol{\beta}_{1,r}^{(2,\mu,v)}d_{i,j}\mathbf{I},\quad A_{i,j}^{(2,2,p,v)}=\boldsymbol{\beta}_{2,r}^{(2,\mu,v)}d_{i,j}\mathbf{I},\quad i\neq j,$$

$$\mathbf{K}_{1,i}^{(\mu,\upsilon)} = \mathbf{R}_{1,i}^{(\mu,\upsilon)} - \boldsymbol{\beta}_{1,r}^{(1,\mu,\upsilon)} d_{i,N_\xi} \mathbf{G}_{1,N_\xi}^{(\mu,\upsilon)} - \boldsymbol{\gamma}_{1,r}^{(1,\mu,\upsilon)} d_{i,N_\xi} \mathbf{D}^{(\mu)} \mathbf{G}_{1,N_\xi}^{(\mu,\upsilon)}$$

$$\mathbf{K}_{2,i}^{(\mu,\upsilon)} = \mathbf{R}_{2,i}^{(\mu,\upsilon)} - \boldsymbol{\beta}_{1,r}^{(2,\mu,\upsilon)} d_{i,N_\xi} \mathbf{G}_{1,N_\xi}^{(\mu,\upsilon)} - \boldsymbol{\beta}_{2,r}^{(2,\mu,\upsilon)} d_{i,N_\xi} \mathbf{G}_{2,N_\xi}^{(\mu,\upsilon)},$$

and $\mathbf{I}$ is an $(M+1) \times (M+1)$ identity matrix. The matrix system (31) can be solved iteratively for $\mathbf{G}_{k,\delta}^{(\mu,\upsilon)}$ for $k = 1, 2$ and $\delta = 0, 1, 2, \ldots N_\xi - 1$.

We also consider a two-dimensional steady free convective flow of a viscous incompressible fluid over a vertical plate in the presence of soluble species [15].

$$f''' + \frac{n+3}{4} ff'' - \frac{n+1}{2} f'^2 + \xi f'' + (1-w)g + wh$$

$$= \frac{1-n}{4}\xi \left(f' \frac{\partial f'}{\partial \xi} - f'' \frac{\partial f}{\partial \xi} \right) \tag{32}$$

$$\frac{1}{Pr}g'' + \frac{n+3}{4} fg' + \xi g' = \frac{1-n}{4}\xi \left(f' \frac{\partial g}{\partial \xi} - g' \frac{\partial f}{\partial \xi} \right) \tag{33}$$

$$\frac{1}{Sc}h'' + \frac{n+3}{4} fh' + \xi h' = \frac{1-n}{4}\xi \left(f' \frac{\partial h}{\partial \xi} - h' \frac{\partial f}{\partial \xi} \right), \tag{34}$$

$$f(0,\xi) = f'(0,\xi) = 0, \, g(0,\xi) = h(0,\xi) = 1, \, f'(\infty,\xi) = g(\infty,\xi) = h(\infty,\xi) = 0,$$

For the sake of brevity, details on the application of OMD-BSQLM are omitted for this problem.

4 Results and Discussion

In this section, we present and analyse the numerical results of the system of non-similar boundary layer equations obtained using the OMD-BSQLM. In the entire calculations, we have taken the edge of the boundary to be $\eta_\infty = 4$. Grid independence tests revealed that $N_\xi = 5$ collocation points in time were sufficient to give accurate and consistent results. The time interval was decomposed into $q = 40$ non-overlapping sub-intervals. The series solutions obtained using Mathematica NDSolve were used to validate the accuracy of the OMD-BSQLM results. The convergence and stability of the proposed method were determined by considering the norm of the difference in the values of the approximate solution of the unknown function between two subsequent iterations. For brevity, we define the solution errors for the two equation system as

$$E_f = \max_{0 \le k \le N_\xi} ||\mathbf{F}_{r+1,k}^{(\mu,\upsilon)} - \mathbf{F}_{r,k}^{(\mu,\upsilon)}||_\infty, \quad E_\theta = \max_{0 \le k \le N_\xi} ||\boldsymbol{\Theta}_{r+1,k}^{(\mu,\upsilon)} - \boldsymbol{\Theta}_{r,k}^{(\mu,\upsilon)}||_\infty, \tag{35}$$

The decrease in the solution errors as the number of iteration increases shows that the OMD-BSQLM converges. It can be seen from Fig. 2 that full convergence is reached after approximately three iterations with a solution error near 10^{-12}. The node [100,1] represents 100 collocation points and one interval in space, while the other node [20,5] stands for 20 collocation points and five overlapping sub-intervals in space. There-
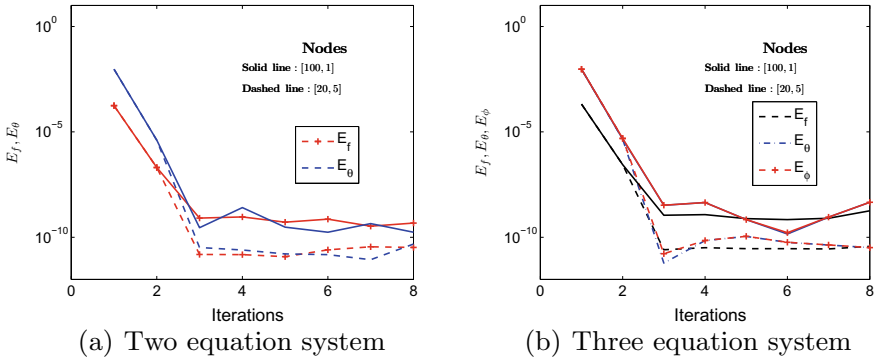
Fig. 2 Solution errors against iterations at different nodes

fore, [100,1] correspond to non-overlapping MD-BSQLM [6], and [20,5] correspond to the OMD-BSQLM. We remark that the total number of collocation points used over the entire space domain was $N_\eta = 100$ and $M = 20 + (20 - 1)(5 - 1) = 96$ in the MD-BSQLM and OMD-BSQLM, respectively. Figure 2 shows that the errors resulting from the OMD-BSQLM were smaller compared to those from the MD-BSQLM. Hence, the OMD-BSQLM provides high accuracy and uses fewer grid points compared to the MD-BSQLM.

The accuracy of the OMD-BSQLM can also be evaluated by considering the residual errors which measure the extent to which the numerical solutions approximate the true solution of the flow PDEs. For the two equation system, we define the residual error functions

$$Res(f) = ||\Gamma_f[\mathbf{F}_i^{(\mu,\upsilon)}, \boldsymbol{\Theta}_i^{(\mu,\upsilon)}]||_\infty, \quad Res(\theta) = ||\Delta_\theta[\mathbf{F}_i^{(\mu,\upsilon)}, \boldsymbol{\Theta}_i^{(\mu,\upsilon)}]||_\infty, (36)$$

where, Γ_f and Γ_θ represent the nonlinear PDEs (26) and (27), respectively, and $\mathbf{F}_i^{(\mu,\upsilon)}$ and $\boldsymbol{\Theta}_i^{(\mu,\upsilon)}$ are the OMD-BSQLM approximate solutions at the time collocation points ξ_i. To calculate the residual errors, we have considered the maximum infinity over all the collocation points. The decrease in the residual errors across the time scale ξ depicts the convergence of the method as observed in Fig. 3. It can also be noted from the figure that the residual error is nearly uniform across ξ. This implies that the accuracy of the OMD-BSQLM does not deteriorate when ξ becomes large. The residual error graphs were plotted using $N_\eta = 120([20, 1])$, $M = 117([30, 40])$ and $M = 115([20, 6])$ collocation points over the whole space domain. Figure 3 exhibits the effect of varying the number of sub-intervals and the number of points. It is seen from the figure that increasing the number of overlapping sub-intervals minimizes the total number of grid points required. However, the accuracy is improved since increasing the number of sub-intervals produces smaller residual errors as observed in Fig. 3. Since the solution and residual errors are always smaller for the OMD-BSQLM, the method can provide accurate, rapidly convergent results with relatively
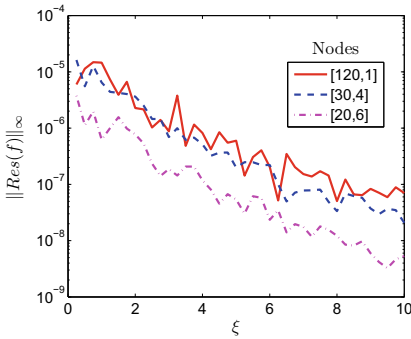
(a) Two equation system
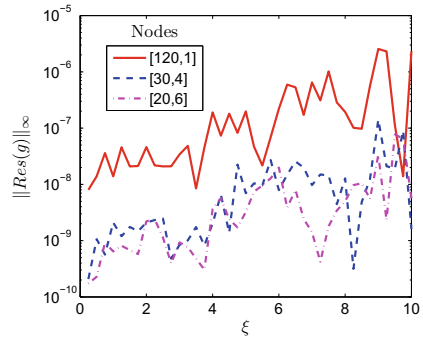
(b) Two equation system
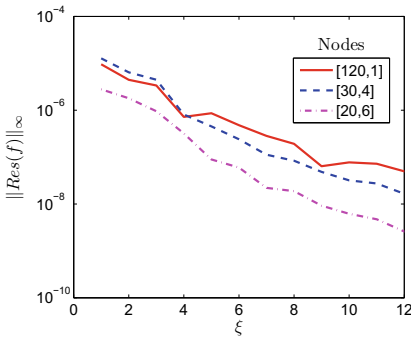
(c) Three equation system
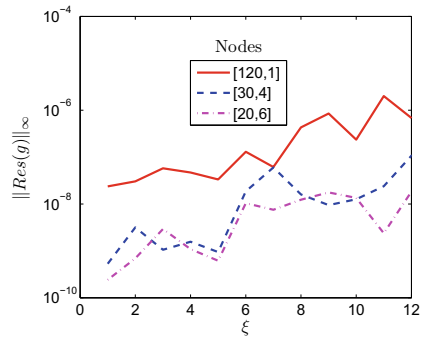
(d) Three equation system
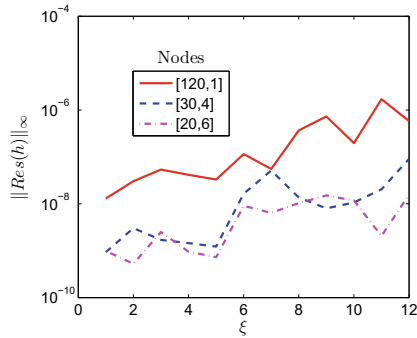
(e) Three equation system

Fig. 3 Residual errors against ξ at different nodes

few grid points compared to existing numerical methods including the MD-BSQLM.
The above analysis of the convergence and accuracy of the method shows that we
can trust the numerical solutions obtained using the OMD-BSQLM.

Table 1 Skin friction and Nusselt Number for two equation system

ξ	MD-BSQLM [120,1]		OMD-BSQLM [40,3]				Series solution [20,6]		k
	$f''(0,\xi)$	$\theta'(0,\xi)$	$f''(0,\xi)$	$\theta'(0,\xi)$	$f''(0,\xi)$	$\theta'(0,\xi)$	$f''(0,\xi)$	$\theta'(0,\xi)$	
5	0.2842685	−3.5066704	0.2842685	−3.5066704	0.2842719	−3.5066677	0.2842719	−3.5066677	3
10	0.1428115	−7.0008400	0.1428115	−7.0008399	0.1428115	−7.0008399	0.1428115	−7.0008399	2
15	0.0952321	−10.5002489	0.0952321	−10.5002490	0.0952321	−10.5002490	0.0952321	−10.5002490	1
20	0.0714271	−14.0001051	0.0714271	−14.0001050	0.0714171	−14.0001050	0.0714171	−14.0001050	1
25	0.0571424	−17.5000538	0.0571424	−17.5000538	0.0571424	−17.5000538	0.0571424	−17.5000538	1
30	0.0476188	−21.0000311	0.0476189	−21.0000311	0.0476189	−21.0000311	0.0476189	−21.0000311	1
35	0.0408162	−24.5000196	0.0408162	−24.5000196	0.0408162	−24.5000196	0.0408162	−24.5000196	1
40	0.0357142	−28.0000132	0.0357142	−28.0000131	0.0357142	−28.0000131	0.0357142	−28.0000131	1
Iter.	3		3		3				

Table 2 Skin friction, Nusselt and Sherwood Number for three equation system

	MD-BSQLM [120,1]			OMD-BSQLM [20,6]			Series solution		
ξ	$f''(\eta,\xi)$	$\theta'(0,\xi)$	$\phi'(0,\xi)$	$f''(0,\xi)$	$\theta'(0,\xi)$	$\phi'(0,\xi)$	$f''(0,\xi)$	$\theta'(0,\xi)$	$\phi'(0,\xi)$
5	0.3088066	−3.5018993	−3.0018843	0.3088214	−3.5018961	−3.0018658	0.3088214	−3.5018961	−3.0018658
10	0.1547399	−7.0002370	−6.0002332	0.1547399	−7.0002370	−6.0002332	0.1547399	−7.0002370	−6.0002332
15	0.1031717	−10.5000705	−9.0000693	0.1031717	−10.5000702	−9.0000691	0.1031717	−10.5000702	−9.0000691
20	0.0773803	−14.0000293	−12.0000289	0.0773803	−14.0000296	−12.0000292	0.0773803	−14.0000296	−12.0000292
25	0.0619045	−17.5000154	−15.0000151	0.0619045	−17.5000152	−15.0000149	0.0619045	−17.5000152	−15.0000149
30	0.0515872	−21.0000087	−18.0000086	0.0515872	−21.0000088	−18.0000086	0.0515872	−21.0000088	−18.0000086
35	0.0442176	−24.5000055	−21.0000054	0.0442176	−24.5000055	−21.0000054	0.0442176	−24.5000055	−21.0000054
40	0.0386905	−28.0000037	−24.0000036	0.0386905	−28.0000037	−24.0000036	0.0386905	−28.0000037	−24.0000036

To validate the OMD-BSQLM results, values of the skin friction, Nusselt and Sherwood Number were compared with those obtained using the series solution method in Tables 1 and 2. Three iterations were enough for the OMD-BSQLM to give comparable results. It can be seen from the tables that the OMD-BSQLM gives accurate results which are in excellent agreement with those obtained using the series solution method, thus validating the accuracy of the proposed method. Moreover, few grid points were needed to generate comparable results in the OMD-BSQLM than in the non-overlapping MD-BSQLM. We remark that the OMD-BSQLM has a great potential to produce highly accurate numerical solutions for bigger time variables ξ with the minimal number of grid points and few iterations compared to existing numerical methods.

5 Conclusion

In this work, we introduced the OMD-BSQLM and applied it in solving non-similar boundary equations to assess its accuracy, robustness and effectiveness. The method applies the QLM technique to linearize the nonlinear PDEs. The space domain is split into overlapping sub-domains, and the time interval is partitioned into non-overlapping sub-intervals. The discretization process is then implemented on both space and time using the spectral collocation method. The approximate solution is obtained by solving the resultant linear matrix system. We have shown the convergence behaviour and accuracy of the OMD-BSQLM scheme. The method was found to be convergent and uses minimal grid points and iterations to produce accurate results. Moreover, the accuracy did not worsen when a large time domain was considered. The results obtained were validated against series solutions and were found to be in excellent concurrence, thus confirming the accuracy of the method over smaller and larger domains. The overlapping grid can improve the accuracy of spectral collocation-based methods by making the coefficient matrix in the matrix equation resulting from the collocation process to be less dense. This work has added to literature an efficient technique for solving the nonlinear system of PDEs defined in smaller and larger domains.

References

1. Boyd JP (1989) Chebyshev and fourier spectral methods. Springer, Berlin, New York
2. Motsa SS, Dlamini PG, Khumalo M (2014) Spectral relaxation method and spectral quasi-linearisation method for solving unsteady boundary layer flow problems. Adv Math Phys 2014:1–12. https://doi.org/10.1155/2014/341964
3. Motsa SS, Magagula VM, Sibanda P (2014) A bivariate Chebyshev spectral collocation quasi-linearization method for nonlinear evolution parabolic equations. Sci World J 2014:1–13. https://doi.org/10.1155/2014/581987

4. Motsa SS, Ansari MS (2015) Unsteady boundary layer flow and heat transfer of Oldroyd- B nanofluid towards a stretching sheet with variable thermal conductivity. Therm Sci 19:239–248
5. Motsa SS, Animasaum IL (2018) Bivariate spectral quasi-linearisation exploration of heat transfer in the boundary layer flow of micropolar fluid with strongly concentrated particles over a surface at absolute zero due to impulsive. Int J Comput Math 9:455–473
6. Magagula VM, Motsa SS, Sibanda P (2017) A multi-domain bivariate pseudospectral method for evolution equations. Int J Comput Meth 14:17500414 https://doi.org/10.1142/s0219876217500414
7. Yang HH (1993) A one-grid-overlapped spectral multi-domain method for the PDEs. Comput Math Appl 26:27–33. https://doi.org/10.1016/0898-1221(93)90023-o
8. Yang HH, Shizgal B (1994) Chebyshev pseudospectral multi-domain technique for viscous calculation. Comput Meth Appl Mech Eng 118:47–61. https://doi.org/10.1016/0045-7825(94)90106-6
9. Olmos D, Shizgal BD (2006) A spectral method for solution of Fisher's equation. J Comput Appl Math 193:219–242
10. Taleei A, Dehgham M (2014) A pseudo-spectral method that uses overlapping multi-domain technique for the numerical solution of sine-Gordon equation in one and two spatial dimensions. Math Meth Appl Sci 37:1909–1923
11. Canuto C, Hussaini MY, Quarteroni A, Zang TA (1988) Spectral methods in fluid dynamics. Springer, Berlin
12. Trefethen, LN (2000) Spectral methods in matlab. SIAM, Philadelphia
13. Bellman RE, Kalaba RE (1965) Quasilinearization and nonlinear boundary-value problems
14. Hossain MA, Paul SC (2001) Free convection from a vertical permeable circular cone with non-uniform surface temperature. Acta Mech 151:103–114. https://doi.org/10.1007/bf01272528
15. Hussain S, Hossain MA, Wilson M (2000) Natural convection flow from a vertical permeable at plate with variable surface temperature and species concentration. Eng Comput 17:789–812. https://doi.org/10.1108/02644400010352261

Electromagnetohydrodynamic Flow of Blood on Unsteady Convective Diffusion of Solute in a Capillary Bounded by Porous Beds

Nirmala P. Ratchagar and R. VijayaKumar

Abstract The mathematical model, presented here, is developed to study the influence of electromagnetohydrodynamic (EMHD) flow of blood on generalized dispersion of an unsteady convective diffusion in a channel bounded by porous beds. Impact of electric and magnetic field, arising as a body couple in the governing equations, is shown to increase the axis dispersion coefficient. The effect of various physical parameters such as Hartmann number, electric number, porous parameter and couple stress parameter on the velocity, dispersion coefficient and mean concentration is discussed in detail with the help of graphs.

Keywords Electromagnetohydrodynamic · Couple stress fluid and generalized dispersion model

1 Introduction

Recent developments concerning different characteristics of dispersion in blood flow have increased interest in fluid dynamics studies. The dispersion of soluble matter in fluid flow has been intensively researched, since the classic papers on the subject by Taylor [16, 17]. Aris [1] extended Taylor's theory to include longitudinal diffusion and developed an approach method of moments to analyze the convection process in steady flow using the first few integral moments. He showed that the mean of the distribution and the second moment about the mean are particularly useful. Theory for large time by the Laplace transform technique was studied by Chatwin [4]. Lighthill [9] obtained the exact solution of the unsteady convection diffusion equation, which is asymptotically valid for small time. On the other hand, Barton [2] has resolved certain

N. P. Ratchagar
Department of Mathematics, Annamalai University, Chidambaram, Tamil Nadu, India
e-mail: nirmalapasala@gmail.co.in

R. VijayaKumar (✉)
Mathematics Section, FEAT, Annamalai University, Chidambaram, Tamil Nadu, India

Department of Mathematics, Periyar Arts College, Cuddalore, Tamil Nadu, India
e-mail: rathirath_viji@yahoo.co.in

technical difficulties in the Aris [1] method of moments and obtained the solutions of the second and third moments equations of the distribution of the solute, which are valid for all time. However, Gill and Sankarasubramanian [15] have developed a generalized dispersion model to analyze the dispersion of solute in a channel.

Korchevskii and Marochnik [8] discussed the idea of electromagnetohydrodynamic to decrease the blood flow in human arterial system, and it is helpful in the treatment of cardiovascular disorders such as brain hemorrhage and hypertension.

Rudraiah et al. [13] utilized the generalized dispersion model to study the dispersion in a Stokes couple stress fluid flow. Later, Rudraiah et al. [14] studied the dispersion of erythrocytes in a channel and observed the hemolysis augmentation due to the impact of electric field. Chiu-On Ng et al. [5, 6] have investigated the dispersion increase and decrease of the concentration of RBCs with the impact of influence of electric field. Nirmala P. Ratchagar and Vijaya Kumar [11] studied the effect of couple stress and magnetic field on the unsteady connective diffusion of erythrocytes in the plasma flow. Meenapriya [10] has investigated the dispersion on air contaminants with chemical reaction under the influence of electric field by utilizing generalized dispersion model. Ashis Kumar Roy et el. [12] analyzed the dispersion of solute in flow of blood for various physiological processes that are involved in by considering Carreau–Yasuda fluid models.

The aim of present paper is to establish the unsteady convective diffusion in blood flow for an incompressible couple stress fluid bounded by the porous layers under the influence of electric and magnetic field by using the generalized dispersion model.

2   Mathematical Formulation

The physical configuration of the problem is shown in Fig. 1. It consists of a poorly conducting couple stress fluid to be steady, fully developed, unidirectional and incompressible. Region 1 denotes the fluid region bounded by porous layers (Region 2). The continuity and momentum equations which govern the steady incompressible blood flow subjected to external applied electric and magnetic fields are given by

Region 1: **Fluid Film Region**

The conservation of mass for an incompressible flow

$$\nabla \cdot \overrightarrow{V} = 0 \tag{1}$$

The conservation of momentum

$$\rho \left(\frac{\partial \mathbf{V}}{\partial t} + (\overrightarrow{V} . \nabla) \overrightarrow{V} \right) = -\nabla p + \mu \nabla^2 \overrightarrow{V} - \lambda \nabla^4 \overrightarrow{V} + \rho_e E_i + J_i \times B \tag{2}$$

The conservation of species
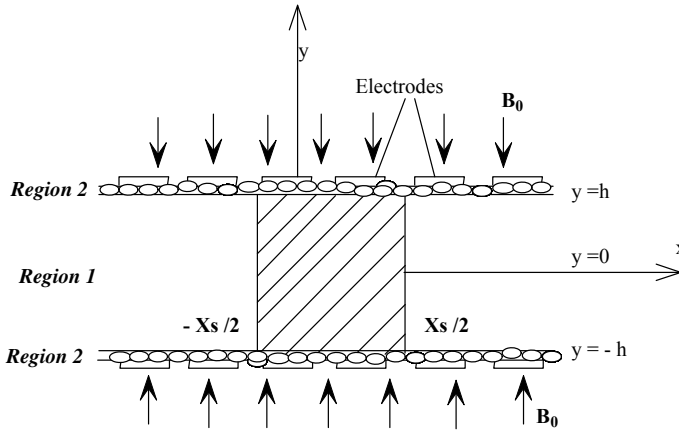
Fig. 1 Physical Configuration

$$\frac{\partial \overrightarrow{C}}{\partial t} + (\overrightarrow{V}.\nabla)\overrightarrow{C} = D\nabla^2\overrightarrow{C} \tag{3}$$

Region 2: **Porous Tissue Region**

The conservation of mass for an incompressible flow

$$\nabla \cdot \overrightarrow{V_p} = 0 \tag{4}$$

The conservation of momentum

$$\rho\left(\frac{\partial \overrightarrow{V_p}}{\partial t} + (\overrightarrow{V}.\nabla)\overrightarrow{V_p}\right) = -\nabla p + \mu\nabla^2\overrightarrow{V_p} - \frac{\mu}{k}(1+\beta)\overrightarrow{V_p} + \rho_e E \tag{5}$$

where $\overrightarrow{V}$ and $\overrightarrow{V_p}$ are the velocity vector in fluid film and porous tissue region, p is the pressure, λ is the couple stress parameter, $\mathbf{B} = (0, B_0, 0)$ the magnetic field, k is the permeability parameter of porous medium, μ is the dynamic viscosity of the blood, $\overrightarrow{C}$ is the concentration, and D is the coefficient of mass diffusivity.

The conservation of charges

$$\frac{\partial \rho_e}{\partial t} + \left(\overrightarrow{V}.\nabla\right)\rho_e + \nabla.J_i = 0 \tag{6}$$

The interaction between the fluid motion and the electromagnetic fields is expressed by Maxwell's equations. Using the electromagnetohydrodynamics (EMHD) approximation, these equations are written as follows:

$$\nabla \cdot \mathbf{B} = 0, \nabla \times \mathbf{B} = \mu_0 J_i$$

$$\nabla \times E_i = -\frac{\partial B_0}{\partial t} \tag{7}$$

where μ_0 magnetic permeability. For small magnetic Reynolds number, the linearized magnetohydrodynamic force becomes $J_i \times \mathbf{B} = -B_0^2 \sigma_0 u^*$.

To compute the electric force $\rho_e E_x$.

Conservation of charges:

$$\frac{\partial \rho_e}{\partial t} + \frac{\partial J_i}{\partial x_j} = 0 \tag{8}$$

$$J_i = \rho_e q_i + \sigma_c E_i \tag{9}$$

Gauss's law

$$\frac{\partial E_i}{\partial x_i} = \frac{\rho_e}{\epsilon_0} \tag{10}$$

where

J_i—current density,

ρ_e— distribution of charge density,

$\rho_e q_i$—convective current,

ϵ_0—dielectric constant for free space,

$\sigma_c E_i$—conduction current,

σ_c—electrical conductivity,

E_i—electric field.

In a poorly conducting fluid, Faraday's law becomes

$$\frac{\partial E_i}{\partial x_j} - \frac{\partial E_j}{\partial x_i} = 0 \tag{11}$$

Conservation of electric field,

$$E_i = -\frac{\partial \phi}{\partial x_i} \tag{12}$$

where ϕ—electric potential. From $\rho_e q_i \ll \sigma_c E_i$, and (9), Eq. (8) can be written

$$\left(\frac{\partial}{\partial t} + q_j \frac{\partial}{\partial x_i}\right)\rho_e + \frac{\partial(\sigma_c E_i)}{\partial x_i} = 0 \tag{13}$$

In Cartesian form, using the above assumptions equations (1)–(5) become

Region 1: **Fluid Film Region**

$$\frac{\partial u^*}{\partial x} = 0 \tag{14}$$

$$0 = -\frac{\partial p^*}{\partial x} + \mu \frac{\partial^2 u^*}{\partial y^2} - \lambda \frac{\partial^4 u^*}{\partial y^4} + \rho_e E_x - B_0^2 \sigma_0 u^* \tag{15}$$

$$0 = -\frac{\partial p^*}{\partial y} + \rho_e E_y \tag{16}$$

The concentration C satisfies convective diffusion equation

$$\frac{\partial C}{\partial t} + u^* \frac{\partial C}{\partial x} = D\left(\frac{\partial^2 C}{\partial x^2} + \frac{\partial^2 C}{\partial y^2}\right) \tag{17}$$

Region 2: **Porous Tissue Region**

$$\frac{\partial u_p^*}{\partial x} = 0 \tag{18}$$

$$0 = -\frac{\partial p^*}{\partial x} - \frac{\mu(1+\beta_1)}{k} u_p^* + \rho_e E_x, \tag{19}$$

$$0 = -\frac{\partial p^*}{\partial y} + \rho_e E_y \tag{20}$$

The velocity boundary conditions are

$$\frac{\partial u^*}{\partial y} = \frac{-\alpha}{\sqrt{k}} (u^* - u_p^*) \quad at \quad y = h, \tag{21}$$

$$\frac{\partial u^*}{\partial y} = \frac{\alpha}{\sqrt{k}} (u^* - u_p^*) \quad at \quad y = -h, \tag{22}$$

The couple stress conditions

$$\frac{\partial^2 u^*}{\partial y^2} = 0 \quad at \quad y = \pm h. \tag{23}$$

The initial and boundary conditions on concentration are

$$C(0, x, y) = \begin{cases} C_0, |x| \leq \frac{x_s}{2} \\ 0, |x| > \frac{x_s}{2} \end{cases} \tag{24}$$

$$\frac{\partial C}{\partial y}(t, x, -h) = \frac{\partial C}{\partial y}(t, x, h) = 0 \tag{25}$$

$$C(t, \infty, y) = \frac{\partial C}{\partial x}(t, \infty, y) = 0 \tag{26}$$

where u^* the axial velocity, u_p^* is the Darcy velocity. It may be noted that (19) is the modified Darcy equation, modified in the sense of incompressible couple stress parameter, α is the slip parameter. Equations (21) and (22) are Beavers and Joseph [3] slip condition. C_0 is the initial concentration of the initial slug input of length x_s

Introducing the non-dimensional variables

$$u = \frac{u^*}{\bar{u}}, u_p = \frac{u_p^*}{\bar{u}}, \eta = \frac{y}{h}, \xi' = \frac{x}{hPe}, \xi_s = \frac{x_s}{hPe}, \rho_e^* = \frac{\rho_e}{\left(\frac{\epsilon_0 V}{h^2}\right)}, Pe = \frac{\bar{u}h}{D},$$

$$\tau = \frac{tD}{h^2}, p = \frac{p^*}{\rho\bar{u}}, E_x^* = \frac{E_x}{\left(\frac{V}{h}\right)}, E_y^* = \frac{E_y}{\left(\frac{v}{h}\right)}, \phi = \frac{\phi^*}{v}$$

where h,v and ϕ are the characteristic length, applied constant, and electric potential.

Equations (14) and (17) in non-dimensional form are
Region 1: **Fluid Film Region**

$$\frac{\partial^4 u}{\partial \eta^4} - a^2 \frac{\partial^2 u}{\partial \eta^2} + a^2 M^2 u = -Ka^2 P + l_1(1 - \alpha_c \eta) \tag{27}$$

and

$$\frac{\partial \theta}{\partial \tau} + u \frac{\partial \theta}{\partial \xi'} = \frac{1}{Pe^2} \left(\frac{\partial^2 \theta}{\partial \xi'^2} + \frac{\partial^2 \theta}{\partial \eta^2} \right) \tag{28}$$

We define the axial coordinate moving with the average velocity of flow as $x_1 = x - t\bar{u}$ which is in dimensionless form $\xi = \xi' - \tau$, where $\xi = \frac{x_1}{hPe}$. Then Eq. (28) becomes

$$\frac{\partial \theta}{\partial \tau} + U^* \frac{\partial \theta}{\partial \xi} = \frac{1}{Pe^2} \left(\frac{\partial^2 \theta}{\partial \xi^2} + \frac{\partial^2 \theta}{\partial \eta^2} \right) \tag{29}$$

with $U^* = \frac{u}{\bar{u}}$(dimensionless in a moving coordinate system)
Region 2: **Porous Tissue Region**

$$u_p = \frac{Re}{\sigma^2(1 + \beta_1)} \left(-\frac{P}{Pe} + \frac{WeX_0\alpha_c(1 - \alpha_c \eta)Pe}{2} \right) \tag{30}$$

The non-dimensional initial and boundary conditions of Eqs. 21–26.

$$\frac{\partial u}{\partial \eta} = -\alpha\sigma(u - u_p) \quad at \quad \eta = 1 \tag{31}$$

$$\frac{\partial u}{\partial \eta} = \alpha\sigma(u - u_p) \quad at \quad \eta = -1 \tag{32}$$

$$\frac{\partial^2 u}{\partial \eta^2} = 0 \qquad at \qquad \eta = \pm 1 \tag{33}$$

where $P = \frac{\partial p}{\partial \xi}$, $K = \frac{D}{\gamma}$, $\alpha_c = \alpha_h \left(\frac{\Delta T}{2}\right)$ is the conductivity variation parameter, $\sigma = \frac{h}{\sqrt{k}}$ is the porous parameter.

$$\theta(0, \xi, \eta) = \begin{cases} 1, |\xi| \leq \frac{\xi_s}{2} \\ 0, |\xi| > \frac{\xi_s}{2} \end{cases} \tag{34}$$

$$\frac{\partial \theta}{\partial \eta}(\tau, \xi, -1) = \frac{\partial \theta}{\partial \eta}(\tau, \xi, 1) = 0 \tag{35}$$

$$\theta(\tau, \infty, \eta) = \frac{\partial \theta}{\partial \xi}(\tau, \infty, \eta) = 0 \tag{36}$$

When perturbation introduced in poorly conducting fluid ($\sigma_c << 1$), it grows with temperature condition, T_b such that

$$\sigma_c = \sigma_0 \left[1 + \sigma_h (T_b - T_0)\right] \tag{37}$$

Here $\sigma_c = \sigma_0$ is that of at $T_b = T_0$, σ_h is the volumetric expansion coefficient of σ_c.

The expression for conduction temperature (T_b) is obtained by solving non-dimensional equation

$$\frac{d^2 T_b}{d\eta^2} = 0 \tag{38}$$

where T_b is non-dimensional equation using $\frac{T_b}{\Delta T}$ with boundary condition in non-dimensional form

$$T_b = T_0 \qquad at \qquad \eta = -1 \tag{39}$$

$$T_b = T_1 \qquad at \qquad \eta = 1 \tag{40}$$

In the solution to Eq. (38) using (39) and (40), we get

$$T_b = \frac{\Delta T}{2}\eta + \frac{\Delta T}{2} + T_0 \tag{41}$$

where $\Delta T = T_1 - T_0$.

Equation (41) using (37) becomes

$$\sigma_c = \sigma_0 \left[1 + \alpha_c (\eta + 1)\right] \approx \sigma_0 e^{\alpha_c(\eta+1)} \quad (\alpha_c << 1) \tag{42}$$

The electrical conductivity

$$\frac{\partial^2 \phi^*}{\partial y^2} + \frac{1}{\sigma_c} \frac{\partial \phi^*}{\partial y} \frac{\partial \sigma_c}{\partial y} = 0 \tag{43}$$

The boundary conditions are

$$\phi^* = \frac{xv}{h} \quad at \quad y = -h \tag{44}$$

$$\phi^* = \frac{(x - x_0)v}{h} \quad at \quad y = h \tag{45}$$

Using the non-dimensional quantities and Eqs. (43)–(45) reduce to

$$\frac{\partial^2 \phi}{\partial \eta^2} + \frac{1}{\sigma_c} \frac{\partial \phi}{\partial \eta} \frac{\partial \sigma_c}{\partial \eta} = 0 \tag{46}$$

with boundary conditions

$$\phi = XPe \quad at \quad \eta = -1 \tag{47}$$

$$\phi = \frac{Pe(X - X_0)}{h} \quad at \quad \eta = 1 \tag{48}$$

Solve the Eq. (46) using the boundary conditions, we get

$$\phi = Pe \left[X - \frac{X_0(1 - e^{-\alpha_c y})}{e^{\alpha_c} - e^{-\alpha_c}} \right] \tag{49}$$

The expression for ρ_e

$$\rho_e = -\frac{Pe X_0 \alpha_c^2 e^{-\alpha_c y}}{e^{\alpha_c} - e^{-\alpha_c}} \tag{50}$$

$$E_x = -1, E_y = \frac{Pe X_0 \alpha_c e^{-\alpha_c y}}{e^{\alpha_c} - e^{-\alpha_c}} \tag{51}$$

Hence

$$\rho_e E_x = \frac{Pe X_0 \alpha_c^2 e^{-\alpha_c \eta}}{e^{\alpha_c} - e^{-\alpha_c}} \approx \frac{Pe X_0 \alpha_c (1 - \alpha_c \eta)}{2} \quad (\alpha_c << 1) \tag{52}$$

3   Method of Solution

3.1   Velocity Distribution

In the solution of equations (27) using the boundary conditions (31)–(33), we obtain the velocity and temperature of blood as
Region 1: **Fluid Film Region**

$$u = C_1 e^{m_1\eta} + C_2 e^{-m_1\eta} + C_3 e^{m_3\eta} + C_4 e^{-m_3\eta} - \frac{KP}{M^2} + \frac{l_1(1 - \alpha_c\eta)}{a^2 M^2} \qquad (53)$$

The normalized axial components of velocity obtained from (53) are

$$U^* = \frac{u}{\bar{u}}$$

where the average velocity is

$$\bar{u} = \frac{1}{2} \int\limits_{-1}^{1} u(\eta)d\eta = \frac{(C_1 + C_2)Sinhm_1}{m_1} + \frac{(C_3 + C_4)Sinhm_3}{m_3} - \frac{2KP}{M^2} + \frac{2l_1}{a^2 M^2}$$

3.2   Generalized Dispersion Model

To obtaining the mean concentration valid for all time τ, we introduce the generalized dispersion model of Gill and Sankarasubramanian [7], formulated as a series expansion in the form

$$\theta(\tau, \xi, \eta) = \theta_m(\tau, \xi) + \sum_{k=1}^{\infty} f_k(\tau, \eta) \frac{\partial^k \theta_m}{\partial \xi^k} \qquad (54)$$

where θ_m is average concentration

$$\theta_m(\tau, \xi) = \frac{1}{2} \int\limits_{-1}^{1} \theta(\tau, \xi, \eta)d\eta \qquad (55)$$

Equation is obtained by integrating equation (29), and we get

$$\frac{\partial \theta_m}{\partial \tau} = \frac{1}{Pe^2} \frac{\partial^2 \theta_m}{\partial \xi^2} + \frac{1}{2} \int\limits_{-1}^{1} \frac{\partial^2 \theta}{\partial \eta^2} \, d\eta - \frac{1}{2} \frac{\partial}{\partial \xi} \int\limits_{-1}^{1} U^* \theta \, d\eta \qquad (56)$$

Substituting value of θ from Eq. (54) in (56), we obtain

$$\frac{\partial \theta_m}{\partial \tau} = \frac{1}{P_e^2} \frac{\partial^2 \theta_m}{\partial \xi^2} - \frac{1}{2} \frac{\partial}{\partial \xi} \int_{-1}^{1} U^* \left(\theta_m(\tau, \xi) + f_1(\tau, \eta) \frac{\partial \theta_m}{\partial \xi}(\tau, \xi) + \ldots \right) d\eta \quad (57)$$

In this model, we write

$$\frac{\partial \theta_m}{\partial \tau} = \sum_{k=1}^{\infty} K_k(\tau) \frac{\partial^k \theta_m}{\partial^k \xi} \quad (58)$$

where the dispersion coefficient—$K_k(\tau)$. Substituting the Eq. (68) in (57), we obtain

$$K_1 \frac{\partial \theta_m}{\partial \xi} + K_2 \frac{\partial^2 \theta_m}{\partial \xi^2} + K_3 \frac{\partial^3 \theta_m}{\partial \xi^3} + \ldots = \frac{1}{P_e^2} \frac{\partial^2 \theta_m}{\partial \xi^2} - \frac{1}{2} \frac{\partial}{\partial \xi} \int_{-1}^{1} U^*(\theta_m(\tau, \xi)$$

$$+ f_1(\tau, \eta) \frac{\partial \theta_m}{\partial \xi} + f_2(\tau, \eta) \frac{\partial^2 \theta_m}{\partial \xi^2}(\tau, \xi) + \ldots) d\eta \quad (59)$$

Comparing the coefficient $\frac{\partial \theta_m}{\partial \xi}, \frac{\partial^2 \theta_m}{\partial \xi^2} \ldots$, we get

$$K_i(\tau) = \frac{\delta_{ij}}{P_e^2} - \frac{1}{2} \int_{-1}^{1} U f_{i-1}(\tau, \eta) d\eta, \quad (i = 1, 2, 3, \ldots \text{ and } j = 2) \quad (60)$$

where Kroneckar delta $\delta_{ij} = \begin{cases} 1, & \text{if } i = j \\ 0, & \text{if } i \neq j \end{cases}$

Substituting Eq. (54) in (29), we get

$$\frac{\partial}{\partial \tau} \left(\theta_m(\tau, \xi) + f_1(\tau, \eta) \frac{\partial \theta_m}{\partial \xi}(\tau, \xi) + f_2(\tau, \eta) \frac{\partial^2 \theta_m}{\partial \xi^2}(\tau, \xi) + \ldots \right)$$

$$+ U^* \frac{\partial}{\partial \xi} \left(\theta_m(\tau, \xi) + f_1(\tau, \eta) \frac{\partial \theta_m}{\partial \xi}(\tau, \xi) + f_2(\tau, \eta) \frac{\partial^2 \theta_m}{\partial \xi^2}(\tau, \xi) + \ldots \right)$$

$$= \frac{1}{P_e^2} \frac{\partial^2}{\partial \xi^2} \left(\theta_m(\tau, \xi) + f_1(\tau, \eta) \frac{\partial \theta_m}{\partial \xi}(\tau, \xi) + f_2(\tau, \eta) + \ldots \right)$$

$$+ \frac{\partial^2}{\partial \eta^2} \left(\theta_m(\tau, \xi) + f_1(\tau, \eta) \frac{\partial \theta_m}{\partial \xi} + \ldots \right) \quad (61)$$

Substituting Eq. (58) in (61), rearranging the terms and using

$$\frac{\partial^{k+1}\theta_m}{\partial\tau\partial\xi^k} = \sum_{i=1}^{\infty} K_i(\tau)\frac{\partial^{k+i}\theta_m}{\partial\xi^{k+i}}$$

we obtain

$$\left[\frac{\partial f_1}{\partial\tau} - \frac{\partial^2 f_1}{\partial\eta^2} + U^* + K_1(\tau)\right]\frac{\partial\theta_m}{\partial\xi} + \left[\frac{\partial f_2}{\partial\tau} - \frac{\partial^2 f_2}{\partial\eta^2} + f_1 U^* + K_1(\tau)f_1 + K_2(\tau) - \frac{1}{P_e^2}\right]\frac{\partial^2\theta_m}{\partial\xi^2}$$

$$+ \sum_{k=1}^{\infty}\left[\frac{\partial f_{k+2}}{\partial\tau} - \frac{\partial^2 f_{k+2}}{\partial\eta^2} + f_{k+1}\,U^* + f_{k+1}\,K_1(\tau) + \left(K_2(\tau) - \frac{1}{P_e^2}\right)f_k \right.$$

$$\left. + \sum_{i=3}^{k+2} K_i f_{k+2-i}\right]\frac{\partial^{k+2}\theta_m}{\partial\xi^{k+2}} = 0$$

$$(62)$$

with $f_0 = 1$. Comparing the coefficients of $\frac{\partial^k\theta_m}{\partial\xi^k}$ $(k = 1, 2, 3, \ldots)$ in (62) and equating to zero, we get

$$\frac{\partial f_1}{\partial\tau} = \frac{\partial^2 f_1}{\partial\eta^2} - U^* - K_1(\tau) \tag{63}$$

$$\frac{\partial f_2}{\partial\tau} = \frac{\partial^2 f_2}{\partial\eta^2} - f_1\,U^* - K_1(\tau)f_1 - K_2(\tau) + \frac{1}{P_e^2} \tag{64}$$

$$\frac{\partial f_{k+2}}{\partial\tau} = \frac{\partial^2 f_{k+2}}{\partial\eta^2} - f_{k+1}\,U^* - K_1(\tau)f_{K+1} - \left(K_2(\tau) - \frac{1}{P_e^2}\right)f_k - \sum_{i=3}^{k+2} K_i f_{k+(65)} \tag{65}$$

To find K_is, we know the f_ks and its corresponding initial and boundary conditions are

$$f_k(0, \eta) = 0 \tag{66}$$

$$\frac{\partial f_k}{\partial\eta}(\tau, -1) = 0 \tag{67}$$

$$\frac{\partial f_k}{\partial\eta}(\tau, 1) = 0 \tag{68}$$

$$\int_{-1}^{1} f_k(\tau, \eta)d\eta = 0, \tag{69}$$

for $k = 1, 2, 3, \ldots$

From Eq. (60) for $i = 1$, we get

$$K_1(\tau) = 0 \tag{70}$$

From Eq. (60) for $i = 2$, we get K_2 as,

$$K_2(\tau) = \frac{1}{P_e^2} - \frac{1}{2} \int_{-1}^{1} U^* f_1 d\eta \tag{71}$$

To evaluate $K_2(\tau)$, let

$$f_1 = f_{10}(\eta) + f_{11}(\tau, \eta) \tag{72}$$

where $f_{10}(\eta)$ is independent of τ and f_{11} is $\tau-$ dependent satisfying

$$\frac{df_{10}}{d\eta} = 0 \ \ at \ \ \eta = \pm 1 \tag{73}$$

$$\int_{-1}^{1} f_{10} d\eta = 0 \tag{74}$$

Using the (72) in (63) gives

$$\frac{d^2 f_{10}}{d\eta^2} = U^* \tag{75}$$

$$\frac{\partial f_{11}}{\partial \tau} = \frac{\partial^2 f_{11}}{\partial \eta^2} \tag{76}$$

Solving the Eq. (75) with conditions (73) and (74) is

$$f_{10} = \frac{1}{\bar{u}} \left(\frac{C_1 e^{m_1 \eta} + C_2 e^{-m_1 \eta}}{m_1^2} + \frac{C_3 e^{m_3 \eta} + C_4 e^{-m_3 \eta}}{m_3^2} + \left(\frac{l_1}{a^2 M^2} - \frac{KP}{M^2} \right) \frac{\eta^2}{2} \right)$$
$$- \frac{\alpha l_1 \eta^3}{6a^2 M^2 \bar{u}} - C_5 \eta - C_6 \tag{77}$$

Equation (76) is heat conduction type and its solution satisfying condition $f_{11}(\tau, \eta) = -f_{10}(\eta)$ of the form

$$f_{11} = \sum_{n=1}^{\infty} B_n e^{-\lambda_n^2 \tau} \cos(\lambda_n \eta) \tag{78}$$

$$where, \quad B_n = -2 \int_{0}^{1} f_{10}(\eta) \cos(\lambda_n \eta) d\eta$$

Substituting (77) and (78) in Eq. (72), we get

$$f_1 = \frac{1}{\bar{u}} \left(\frac{C_1 e^{m_1 \eta} + C_2 e^{-m_1 \eta}}{m_1^2} + \frac{C_3 e^{m_3 \eta} + C_4 e^{-m_3 \eta}}{m_3^2} + \left(\frac{l_1}{a^2 M^2} - \frac{KP}{M^2} \right) \frac{\eta^2}{2} \right)$$

$$- \frac{\alpha l_1 \eta^3}{6 a^2 M^2 \bar{u}} - C_5 \eta - C_6 + e^{-\pi^2 \tau} \cos(\pi \eta) \left(\frac{2 l_1}{\pi^2 a^2 M^2} + \frac{(C_1 + C_2) e^{-m_1} \left(e^{2m_1} - 1 \right)}{m_1 \left(m_1^2 + \pi^2 \right)} \right.$$

$$+ \frac{(C_3 + C_4) e^{-m_3} \left(e^{2m_3} - 1 \right)}{m_3 \left(m_3^2 + \pi^2 \right)} - \frac{2KP}{\pi^2 M^2} \right) + e^{-4\pi^2 \tau} \cos(2\pi \eta) \left(\left(- \frac{2 l_1}{\pi^2 a^2 M^2} \right. \right.$$

$$\left. - \frac{(C_1 + C_2) e^{-m_1} \left(e^{2m_1} - 1 \right)}{m_1 \left(m_1^2 + 4\pi^2 \right)} - \frac{(C_3 + C_4) e^{-m_3} \left(e^{2m_3} - 1 \right)}{m_3 \left(m_3^2 + 4\pi^2 \right)} + \frac{2KP}{\pi^2 M^2} \right)$$

$$+ e^{-9\pi^2 \tau} \cos(3\pi \eta) \left(\frac{2 l_1}{9\pi^2 a^2 M^2} + \frac{(C_1 + C_2) e^{-m_1} \left(e^{2m_1} - 1 \right)}{m_1 \left(m_1^2 + 9\pi^2 \right)} \right.$$

$$+ \frac{(C_3 + C_4) e^{-m_3} \left(e^{2m_3} - 1 \right)}{m_3 \left(m_3^2 + 9\pi^2 \right)} - \frac{2KP}{9\pi^2 M^2} \right)$$

Substituting f_1 into Eq. (71) and performing the integration, we get solution of dispersion coefficient with help of MATHEMATICA 8.0, where C_1, C_2, C_3, C_4, C_5, and C_6 are constant and are given in the appendix.

Similarly, $K_3(\tau)$, $K_4(\tau)$ and so on are negligibly small compared to dispersion coefficient $K_2(\tau)$.

Dispersion model Eq. (58) brings to

$$\frac{\partial \theta_m}{\partial \tau} = K_2 \frac{\partial^2 \theta_m}{\partial \xi^2} \tag{79}$$

The exact solution of (79) satisfying the conditions (34)–(36) can be obtained using Fourier transform [Sankar Rao [15]] as

$$\theta_m(\xi, \tau) = \frac{1}{2} \left[erf \left(\frac{\frac{\xi_s}{2} + \xi}{2\sqrt{T}} \right) + erf \left(\frac{\frac{\xi_s}{2} - \xi}{2\sqrt{T}} \right) \right]$$

where $T = \int\limits_{0}^{\tau} K_2(\eta) d\eta$ and $erf(x) = \frac{2}{\sqrt{\pi}} \int\limits_{0}^{x} e^{-z^2} dz$

4 Results and Discussions

The aim of the present study is to investigate the dispersion of a solute in a couple stress fluid (blood) flow through a rectangular channel bounded by porous beds with effects of magnetic and electric field. The generalized dispersion model is used for the analysis.

Final results are discussed by using graphs. It illustrates the influence of the Hartmann number ($M = 1.1, 1.2, 1.3, 1.4$), electric number ($We = 30, 40, 50$), couple stress parameter ($a = 1, 5, 10$), dimensionless time $\tau = 0.06, 0.3, 0.6$ and porous parameter $\sigma = (60, 120, 180)$ on the velocity, dispersion coefficient and the concentration profiles, while the values of some of the physical parameters are taken as constant such as $Pe = 100, \alpha = 0.1$ and $\beta_1 = 0.1$ in all the figures. We have extracted interesting insights regarding the influence of all the parameters that govern this problem. The influence of the parameters M, We, a, τ and σ on horizontal velocity, dispersion coefficient and concentration profiles can be analyzed from Figs. 2, 3, 4, 5, 6, 7, 8, 9, 10, 11, 12, 13 and 14.
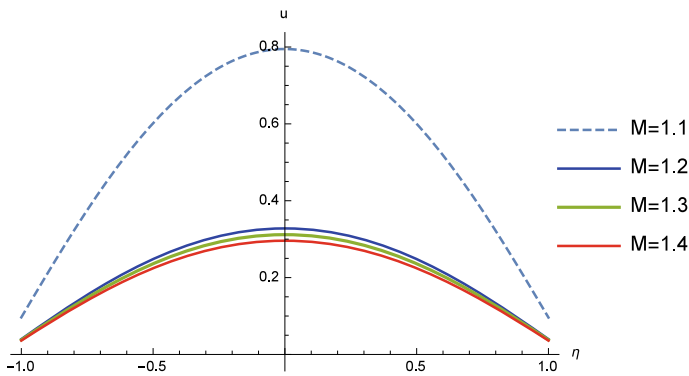
Fig. 2 Velocity u versus η for different (M)
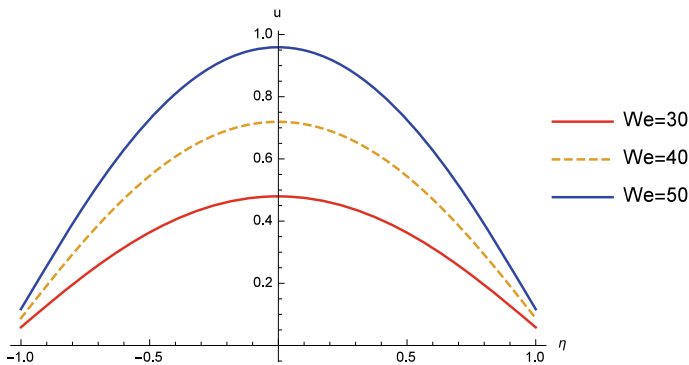
Fig. 3 Velocity u versus η for different (We)
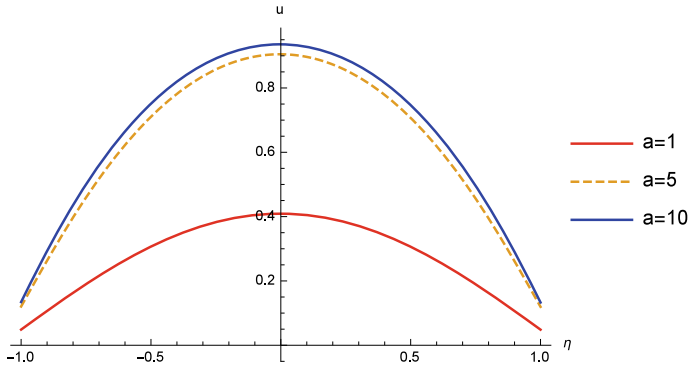
Fig. 4 Velocity u versus η for different (a)
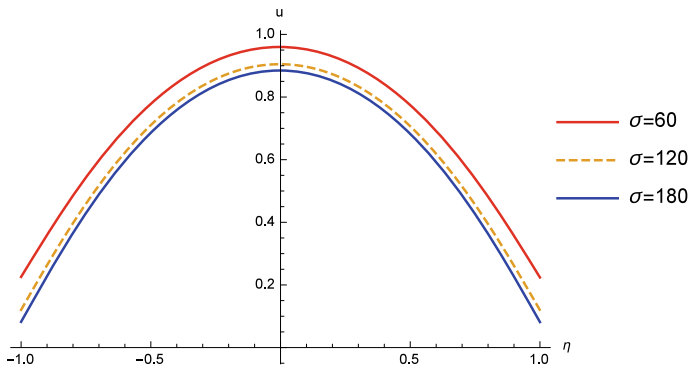
Fig. 5 Velocity u versus η for different (σ)
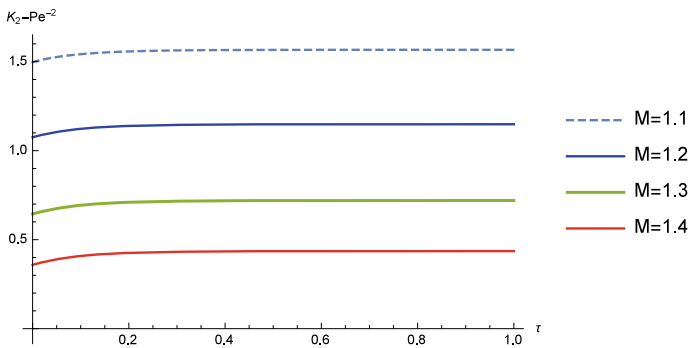
Fig. 6 Velocity $K_2(\tau) - Pe^{-2}$ with dimensionless time τ for different (M)
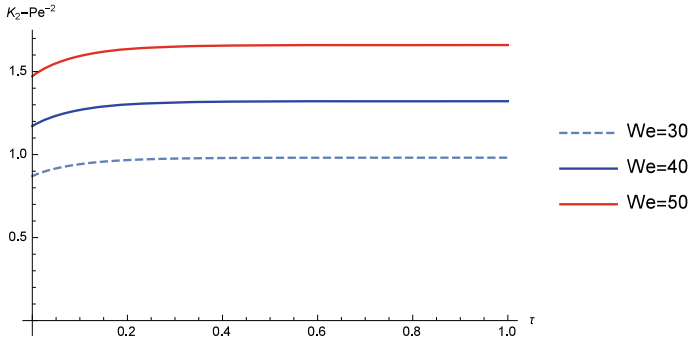
Fig. 7 Dispersion coefficient $K_2(\tau) - Pe^{-2}$ with dimensionless time τ for different (We)
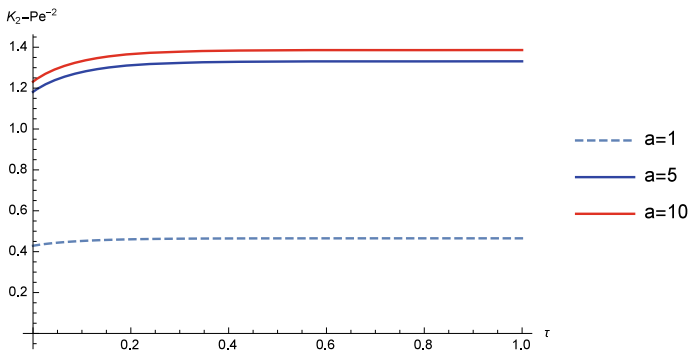
Fig. 8 Dispersion coefficient $K_2(\tau) - Pe^{-2}$ with dimensionless time τ for different (a)
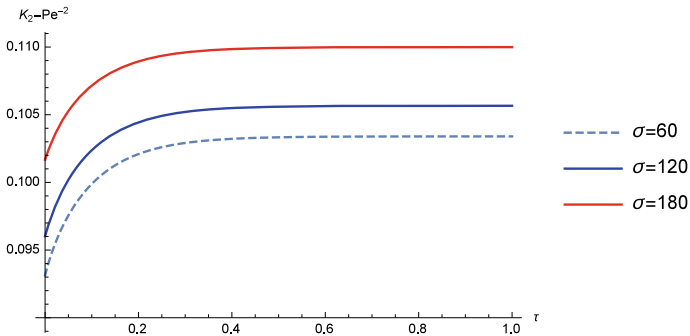
Fig. 9 Dispersion coefficient $K_2(\tau) - Pe^{-2}$ with dimensionless time τ for different (σ)
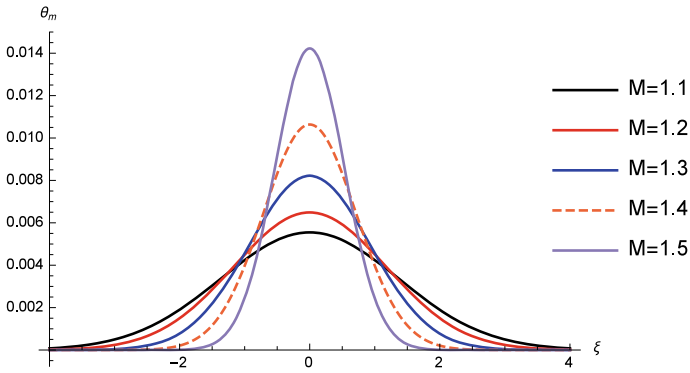
Fig. 10 Mean concentration θ_m varying along dimensionless axial distance ξ for different (M)
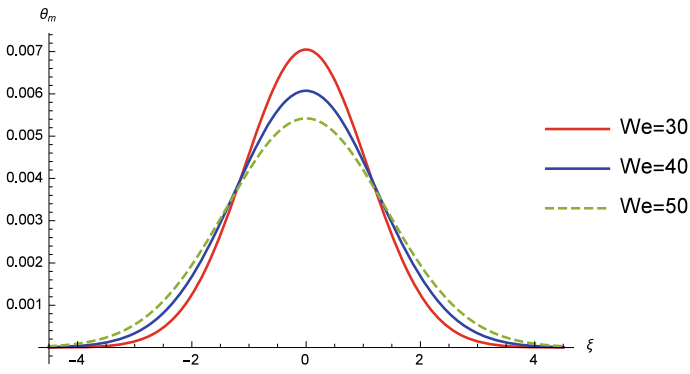
Fig. 11 Mean concentration θ_m varying along dimensionless axial distance ξ for different (We)
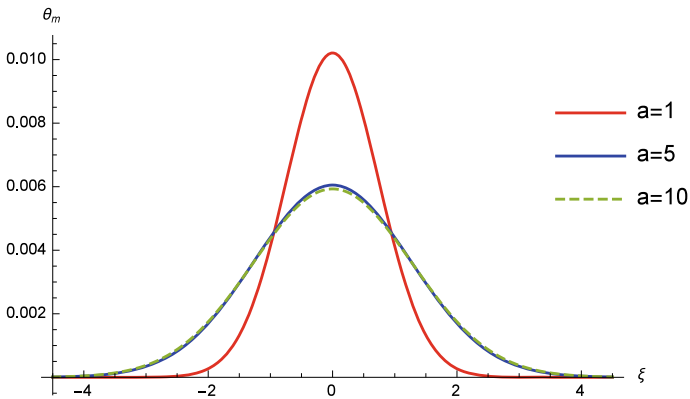
Fig. 12 Mean concentration θ_m varying along dimensionless axial distance ξ for different (a)
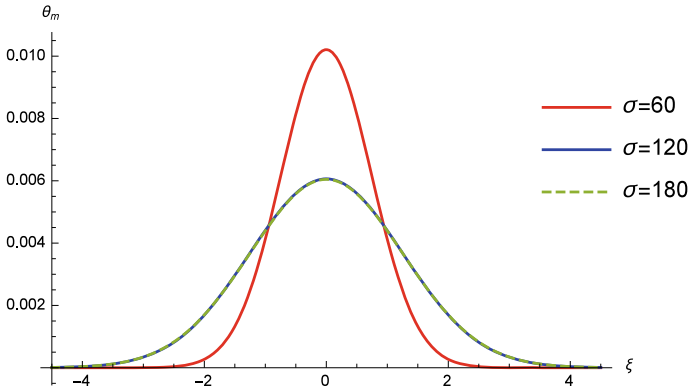
Fig. 13 Mean concentration θ_m varying along dimensionless axial distance ξ for different (σ)
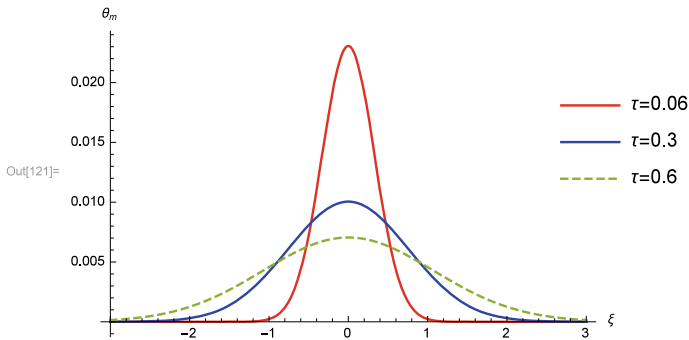
Fig. 14 Mean concentration θ_m varying along dimensionless axial distance ξ for different (τ)

The effects of the velocity profiles for different values of the electric number(We) and couple stress parameter(a) are shown in Figs. 3 and 4. It is seen that the effect of increasing electric number and couple stress parameter increases the velocity profile of the blood flow, found to be parabolic in nature. Figures 2 and 5 are plots of the velocity u versus η for different values of M and σ. These figures depict that the velocity profile decreases with the increase of the Hartmann number (M) and porous parameter (σ). The effect of the magnetic field parameter M on the velocity profile is displayed. The presence of magnetic field is normal to the flow in an electrical conducting fluid and introduces a Lorentz force which acts against the flow. This resistive force tends to slow down the blood flow, and hence, the boundary layer decreases with the increase of the magnetic field.

Dispersion coefficient is evaluated for various values of M, We, a and σ. The results obtained are plotted in Figs. 6, 7, 8 and 9. From these figures, the axial dispersion coefficient increases $K_2(\tau) - Pe^{-2}$ with the increase of electric number, couple stress and porous parameter. From Fig. 6, it is evident that $K_2(\tau) - Pe^{-2}$ decreases with an increase in the value of the Hartmann number (M). This result is useful in

understanding one of the causes for hemolysis, which in turn is useful in the design of an artificial organs free from impurities and in the effective removable of liquid particles in industrial problems.

Figures 10, 11, 12, 13 and 14 are plot of θ_m mean concentration versus axial distance ξ for different values of M, We, a, σ and τ. From Fig. 10, it is depicted that θ_m mean concentration increases with an increase in the value of the Hartmann number (M). Figures 11, 12, 13 and 14 illustrate that there is marked variation of concentration with axial distance ξ. It is apparent from these figures that the effect of increasing We, a, σ and τ is to decrease the peak value of the mean concentration. This implies that the concentration is more distributed in ξ-direction for larger and larger values of We. The curves are bell shaped and symmetrical about the origin. From these results, it is very helpful to analyze the transport of solute at various times.

5 Conclusions

The dispersion of a solute in blood flow under the influence of electric field and magnetic field is discussed. The influence of electric field is to increase the dispersion coefficient and reduce the mean concentration. Also, it is found that the dispersion coefficient decrease along the mean concentration increases with increasing the value of Hartmann number. The time-dependent coefficients are evaluated using a generalized dispersion model which is valid for all time. It is shown that the effect of couple stress is predominant only for small values of 'a' and when $a \to \infty$ the flow characteristics tend to their equivalents in Newtonian theory. The results of Taylor's dispersion model are recovered as a particular case in the limit $\tau \to \infty$. For large values of σ, the results of particular case of the present study matches with Rudraiah et al. [13].

Appendices

$m_1 = \frac{\sqrt{a^2 + \sqrt{a^4 - 4a^2 M^2}}}{\sqrt{2}};\ m_3 = \frac{\sqrt{a^2 - \sqrt{a^4 - 4a^2 M^2}}}{\sqrt{2}};\ a_1 = e^{m_1}(\alpha\sigma + m_1);$

$a_2 = e^{-m_1}(m_1 - \alpha\sigma);\ a_3 = e^{m_3}(\alpha\sigma + m_3);\ a_4 = e^{-m_3}(m_3 - \alpha\sigma);\ a_5 = m_1^2 e^{m_1};$

$a_6 = m_1^2 e^{-m_1};\ a_7 = m_3^2 e^{m_3};\ a_8 = m_3^2 e^{-m_3};\ l_1 = Ka^2 We Pe^2 \alpha_c x_0;$

$u_{p_0} = \frac{Re}{\sigma^2(1+\beta_1)}\left(\frac{-P}{Pe} + \frac{We Pex_0 \alpha_c (1-\alpha_c)}{2}\right);\ u_{p_1} = \frac{Re}{\sigma^2(1+\beta_1)}\left(\frac{-P}{Pe} + \frac{We Pex_0 \alpha_c (1+\alpha_c)}{2}\right);$

$l_2 = -\alpha\sigma\left(\frac{-KP}{M^2} + \frac{l_1(1-\alpha_c)}{a^2 M^2} - u_{p_0}\right) + \frac{l_1 \alpha_c}{a^2 M^2};$

$l_3 = \alpha\sigma\left(\frac{-KP}{M^2} + \frac{l_1(1+\alpha_c)}{a^2 M^2} - u_{p_1}\right) + \frac{l_1 \alpha_c}{a^2 M^2};$

$l_4 = a_1^2 a_7^2 - a_1^2 a_8^2 - 2a_1 a_3 a_5 a_7 + 2a_1 a_3 a_6 a_8 - 2a_1 a_4 a_5 a_8 + 2a_1 a_4 a_6 a_7 - a_2^2 a_7^2 + a_2^2 a_8^2 + 2a_2 a_3 a_5 a_8 - 2a_2 a_3 a_6 a_7 + 2a_2 a_4 a_5 a_7 - 2a_2 a_4 a_6 a_8 + a_3^2 a_5^2 - a_3^2 a_6^2 - a_4^2 a_5^2 +$

$a_4^2 a_6^2$

$C_1 = \frac{-1}{l_4}(a_3 a_5 a_7 l_2 - a_4 a_6 a_7 l_2 + a_4 a_5 a_8 l_2 - a_3 a_6 a_8 l_2 + a_1 a_8^2 l_2 - a_4 a_5 a_7 l_3 +$
$a_3 a_6 a_7 l_3 + a_2 a_7^2 l_3 - a_3 a_5 a_8 l_3 + a_4 a_6 a_8 l_3 - a_2 a_8^2 l_3);$

$C_2 = \frac{1}{l_4}(a_4 a_5 a_7 l_2 - a_3 a_6 a_7 l_2 - a_2 a_7^2 l_2 + a_3 a_5 a_8 l_2 - a_4 a_6 a_8 l_2 + a_2 a_8^2 l_2 - a_3 a_5 a_7 l_3$
$+ a_4 a_6 a_7 l_3 + a_1 a_7^2 l_3 - a_4 a_5 a_8 l_3 + a_3 a_6 a_8 l_3 - a_1 a_8^2 l_3);$

$C_3 = \frac{-1}{l_4}(-a_3 a_5^2 l_2 + a_3 a_6^2 l_2 + a_1 a_5 a_7 l_2 + a_2 a_6 a_7 l_2 - a_2 a_5 a_8 l_2 - a_1 a_6 a_8 l_2 + a_4 a_5^2 l_3$
$- a_4 a_6^2 l_3 - a_2 a_5 a_7 l_3 - a_1 a_6 a_7 l_3 + a_1 a_5 a_8 l_3 + a_2 a_6 a_8 l_3);$

$C_4 = \frac{-1}{l_4}(-a_4 a_5^2 l_2 + a_4 a_6^2 l_2 + a_2 a_5 a_7 l_2 + a_1 a_6 a_7 l_2 - a_1 a_5 a_8 l_2 - a_2 a_6 a_8 l_2 + a_3 a_5^2 l_3$
$- a_3 a_6^2 l_3 - a_1 a_5 a_7 l_3 - a_2 a_6 a_7 l_3 + a_2 a_5 a_8 l_3 + a_1 a_6 a_8 l_3);$

$C_5 = \frac{1}{\bar{u}}\left(-\frac{\alpha l 1}{2a^2 M^2} + \frac{(C_1 - C_2)\cosh(m_1)}{m_1} + \frac{(C_3 - C_4)\cosh(m_3)}{m_3}\right);$

$C_6 = \frac{1}{\bar{u}}\left(\frac{1}{3}\left(\frac{l_1}{a^2 M^2} - \frac{KP}{M^2}\right) + \frac{(C_1 + C_2)\sinh(m_1)}{m_1^3} + \frac{(C_3 + C_4)\sinh(m_3)}{m_3^3}\right);$

References

1. Aris R (1956) On the dispersion of a solute in a fluid flowing through a tube. Proc R Soc Lond A 235:67–77
2. Barton NG (1986) Solute dispersion and weak second-order recombination at large times in parallelflow. J Fluid Mech 164:289
3. Beavers GS, Joseph DD (1967) Boundary conditions at a naturally permeable wall. J Fluid 30:197–207
4. Chatwin PC (1971) On the interpretation of some longitudinal dispersion experiments. J Fluid Mech 48:689–702
5. Chiu-On Ng, Rudraiah N, Nagaraj C (2005) Dispersion mechanism in biomechanics of artificial synovial joints in the presence of electric field. In: Proceedings of the international conference on advances in applied mathematics (ICAAM-05), pp 1–10
6. Chiu-On Ng, Rudraiah N, Nagarajc C, Nagaraj HN (2006) Electrohydrodynamic dispersion of macromolecular components in biological bearing. J Energy, Heat Mass Trans 28:261–280
7. Gill WN, Sankarasubramanian R (1970) Exact analysis of unsteady convective diffusion. Proc R Soc Lond A 316:341–350
8. Korchevskii M, Marochnik LS (1965) Magnetohydrodynamic version of movement of blood. Biophysics 10:411–413
9. Lighthill MJ (1966) Initial development of diffusion in Poiseuille flow. J Inst Math Appl 2:97–108
10. Meenapriya P (2019) Analysis of transport phenomena in air contaminants with chemical reaction in the presence of electric field. Int J Sci Res Math Stat Sci 6(1):69–75
11. Ratchagar NP, Vijaya Kumar R (2014) Effect of couple stress and magnetic field on the unsteady convective diffusion in blood flow. World J Eng 11(4):403–412
12. Roy AK, Saha AK, Debnath S (2018) Unsteady convective diffusion with interphase mass transfer in Casson liquid. Period Polytech Chem Eng 6(2):215–223
13. Rudraiah N, Pal D, Siddheshwar PG (1986) Effect of couple stresses on the unsteady convective diffusion in fluid flow through a channel. Biorheology 23(4):349–58
14. Rudraiah N, Siddeshwar PG, Veena BH (1989) Effect of couple stress and electric field on haemolysis. In: A review, biomechanics. Wiley, New Jersey, pp 95–102
15. Sankar R (1995) Introduction to partial differential equations, Prentice-Hall, India
16. Taylor GI (1953) Dispersion of soluble matter in solvent flowing slowly through a tube. Proc R Soc Lond A 219:186–203

17. Taylor GI (1954) Conditions under which dispersion of a solute in a stream of solvent can be used to measure molecular diffusion. Proc R Soc A 225:473–477

Chemical Reaction and Thermophoresis Effects on MHD Mixed Convection Flow Over an Inclined Porous Plate with Variable Suction

D. Harish Babu, S. Samantha Kumari, and P. V. Satya Narayana

Abstract The current work describes the chemical reaction and thermophoresis impacts on MHD flow past an inclined plate at an angle α within the presence of variable suction and uniform porous medium. Perturbation technique is used to determine the solution of non-dimensional equations, and the obtained results are discussed with the help of graphs on physical quantities for the consequences of the pertinent parameters.

Keywords Chemical reaction · Inclined plate · MHD · Thermophoresis

Nomenclature

B_0	Magnetic induction
C^*	Species concentration
Cf_x	Local skin-friction coefficient
c_p	Specific heat due to constant pressure
C_w^*	Species concentration at wall
C_∞^*	Species concentration of the ambient fluid
D	Chemical molecular diffusivity
f	Dimensionless stream function
f_w	Dimensionless wall suction
g	Acceleration due to gravity
Gr_x	Local Grashof number
Gm_x	Local modified Grashof number

D. Harish Babu
Department of Mathematics, Sree Vidyanikethan Engineering College, Tirupati, Andhra Pradesh, India

S. Samantha Kumari
Department of Mathematics, JNTUA, Anantapuramu, Andhra Pradesh, India

P. V. Satya Narayana (✉)
Department of Mathematics, SAS, VIT, Vellore 632014, Tamil Nadu, India
e-mail: pvsatya8@yahoo.co.in

J_s	Rate of transfer of species concentration
k	Thermophoretic coefficient
k_1	Mean absorption coefficient
K_l	Chemical reaction constant
Kn	Knudsen number
Kr	Chemical reaction parameter
M	Magnetic field parameter
N	Radiation parameter
Nu_x	Local Nusselt number
Pr	Prandtl number
q_r	Radiative heat flux
q_w	Rate of heat transfer
Re_x	Local Reynolds number
S	Heat source parameter
T^*	Temperature of the fluid
Sc	Schmidt number
T_∞^*	Temperature of the ambient fluid
T_w^*	Temperature at the surface
U_∞	Free stream velocity
U^*, V^*	The x-, y-component of the velocity field
V_w^*	Transpiration velocity

Greek Symbols

α	Angle of inclination to vertical
β	Volumetric coefficient of thermal
δ	Local modified buoyancy parameter
γ	Local buoyancy parameter
ρ	Fluid density
σ	Electrical conductivity
σ_1	Stefan–Boltzmann constant
ψ	Stream function
η	Similarity variable
υ	Kinematic viscosity
μ	Fluid viscosity
τ_w	Wall shear stress
θ	Dimensionless temperature
$\varnothing$	Dimensionless concentration
λ_g	Thermal conductivity of fluid
λ_p	Thermal conductivity of diffused particles
τ	Thermophoretic parameter

Subscripts

w	Sheet surface
∞	Infinity

Superscript

$'$	Differentiation with respect to η

1 Introduction

The impact of reaction in mass transfer is massively vital in chemical and hydromet-allurgical industries, like injury of crops because of freezing, design of chemical processing instrumentality, distribution of temperature and wet over agricultural fields. For instance, impact of chemical reaction with heat and mass transfer flow on a semi-infinite plate is investigated by Anjalidevi et al. [1]. Moreover, chemical reaction effects on heat and mass transfer of Newtonian and non-Newtonian fluids are mentioned by Rashidi et al. [2], Satyanarayana and Harish Babu [3]. Another vital impact is thermophoresis; notably, this is a mass transfer mechanism of micro-particle transport because of a gradient within the fields. MHD free convection and mass transfer flow have been investigated by Alam and Sattar [4]. The impact of thermophoresis on mixed convection flow owing a past flat plate is studied by Selim et al. [5]. Recently, there are many papers on thermal radiation effects on MHD heat and mass transfer flows over varied geometrical aspects see as an example Refs. [6–9].

The novelty of the current study is to look at the MHD flow behavior over an inclined porous plate in the presence of reaction and thermophoresis effects. Analytical solutions are derived (velocity field, temperature field and concentration filed) by perturbation technique. The expressions for the first-order, the second-order and third-order solutions are obtained, and physical quantities of interest are bestowed graphically.

2 Mathematical Formulation of the Problem

Two-dimensional steady viscous fluid over an inclined semi-infinite flat plate with an oblique angle α from the vertical in presence of thermophoresis is perused (see Fig. 1).

Fig. 1 Schematic of the problem
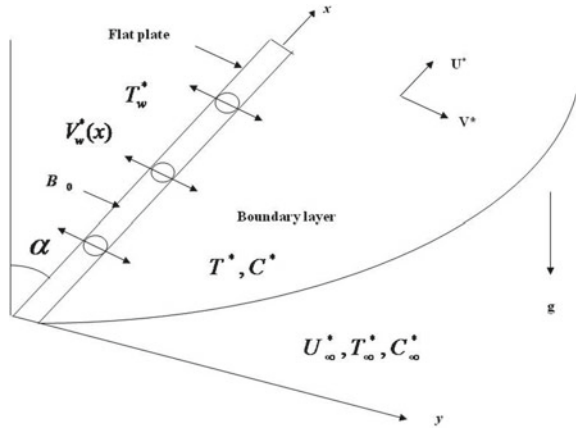
Based on the Boussinesq approximation, the governing equations for the current model can be depicted as [10]:

$$\frac{\partial V^*}{\partial y} + \frac{\partial U^*}{\partial x} = 0 \tag{1}$$

$$V^* \frac{\partial U^*}{\partial y} + U^* \frac{\partial U^*}{\partial x} = \upsilon \frac{\partial^2 U^*}{\partial y^2} + \left(g.\beta_f.(T - T_\infty) + g.\beta_c.(C - C_\infty)\right) \cos \alpha$$
$$- \frac{\upsilon}{K^*} U^* - \frac{\sigma B_0^2}{\rho} U^* \tag{2}$$

$$V^* \frac{\partial T^*}{\partial y} + U^* \frac{\partial T^*}{\partial x} = \frac{\lambda_g}{\rho c_p}.\frac{\partial^2 T^*}{\partial y^2} - \frac{Q}{\rho c_p}.(T^* - T_\infty^*) - \frac{1}{\rho c_p}.\frac{\partial q_r}{\partial y} \tag{3}$$

$$V^* \frac{\partial C^*}{\partial y} + U^* \frac{\partial C^*}{\partial x} = D_T.\frac{\partial^2 C^*}{\partial y^2} - \frac{\partial (V_T C^*)}{\partial y} - K_l.(C^* - C_\infty^*) \tag{4}$$

The appropriate conditions (Singh et al. [11]) are as follows:

$$V^* = V_w^*(x), U^* = U_0, T^* = T_w^*, C^* = C_w^* \text{ as } y \to 0$$
$$U^* \to 0, T^* \to T_\infty^*, C^* \to C_\infty^* \text{ as } \qquad y \to \infty \tag{5}$$

The radiative heat flux q_r beneath Rosseland approximation has the forms [12]

$$q_r = -\frac{4\sigma_1}{3k_1}.\frac{\partial T^{*4}}{\partial y} \tag{6}$$

where

$$T^{*4} \cong 4.T_\infty^{*3} - 3.T_\infty^{*4} \tag{7}$$

Utilizing Eqs. (6) and (7) in Eq. (3), we have

$$V^* \frac{\partial T^*}{\partial y} + U^* \frac{\partial T^*}{\partial x} = \frac{\lambda_g}{\rho c_p} \cdot \frac{\partial^2 T^*}{\partial y^2} + \frac{16\sigma_1 T_\infty^{'*3}}{3\rho C_p k_1} \cdot \frac{\partial^2 T^*}{\partial y^2} - \frac{Q}{\rho c_p} \cdot \left(T^* - T_\infty^*\right) \quad (8)$$

The thermophoretic velocity V_T defined as (Talbot et al. [13]):

$$V_T = -k.\upsilon.\frac{\nabla T'}{T_r'} = -\frac{k\upsilon}{T_r'}.\frac{\partial T'}{\partial y}$$

where T_r' refers to temperature and k_1 is outlined (see Talbot et al. [13]) as follows:

$$k_1 = \frac{2.C_s.\left[(\lambda_g/\lambda_p) + C_t.K_1.n\right].\left[1 + K_1.n.(C_1 + C_2.e^{-C_3/K_1 n})\right]}{(1 + 3.C_m.K_1.n).\left[1 + (\lambda_g/\lambda_p) + 2.C_t.K_1.n\right]}$$

Introducing the subsequent similarity variables:

$$\eta = y.\sqrt{\frac{U_0}{2.\upsilon.x}}, \ \psi = \sqrt{2.\upsilon.x.U_0}.f(\eta), \ \left(T_w^* - T_\infty^*\right).\theta(\eta) = T^* - T_\infty^*,$$
$$\left(C_w^* - C_\infty^*\right).\phi(\eta) = C^* - C_\infty^* \quad (9)$$

where

$$V^* = -\sqrt{\frac{\upsilon.U_0}{2.x}}.\left[f(\eta) - \eta.f'(\eta)\right] \text{ and } U^* = U_0 f'(\eta) \quad (10)$$

Utilize Eq. (9) gives:

$$\frac{d^3 f(\eta)}{d\eta^3} + f(\eta).\frac{d^2 f(\eta)}{d\eta^2} + \gamma \, \theta f(\eta) \cos\alpha + \delta \, \phi f(\eta) \cos\alpha$$
$$- \left(M + \frac{1}{K}\right).\frac{df(\eta)}{d\eta} = 0 \quad (11)$$

$$(3R + 4).\frac{d^2\theta(\eta)}{d\eta^2} + 3R \Pr f(\eta).\frac{d\theta(\eta)}{d\eta} - 3R \Pr S.\theta(\eta) = 0 \quad (12)$$

$$\frac{d^2\phi(\eta)}{d\eta^2} + \mathrm{Sc}\left(f(\eta) - \tau_p \frac{d\theta(\eta)}{d\eta}\right).\frac{d\phi(\eta)}{d\eta} - \mathrm{Sc}\left(\tau_p \frac{d^2\theta(\eta)}{d\eta^2} + K_r\right).\phi(\eta)$$
$$- A Sc \tau_p.\frac{d^2\theta(\eta)}{d\eta^2} = 0 \quad (13)$$

with subject to the conditions

$$\frac{df(\eta)}{d\eta} = 1,\ f(\eta) = f_w,\ \theta(\eta) = 1,\ \phi(\eta) = 1 \quad \text{at } \eta = 0$$

$$\frac{df(\eta)}{d\eta} \to 0,\ \theta(\eta) \to 0,\ \phi(\eta) \to 0 \quad \text{as } \eta \to \infty \tag{14}$$

where $f_w = -V_w^*(x).\sqrt{\frac{2.x}{\upsilon.U_0}}$. Here, $f_w > 0$ signifies the suction,

$$R = \frac{\lambda_g k_1}{4T_\infty^{*3}\sigma_1},\ \text{Pr} = \frac{\upsilon\rho c_p}{\lambda_g},\ \text{Re}_x = \frac{U_0 2x}{\upsilon},\ \text{Gr}_x = \frac{g\beta(T_w^* - T_\infty^*).(2x)^3}{\upsilon^2},\ \text{Sc} = \frac{\upsilon}{D_T},$$

$$\text{Gm}_x = \frac{g\beta^*.(C_w^* - C_\infty^*).(2x)^3}{\upsilon^2},\ M = \frac{2x\sigma B_0^2}{\rho U_0},\ \tau_p = -\frac{k.(T_w^* - T_\infty^*).f_w^2}{T_r}$$

$$S = \frac{Q}{\rho C_p U_0},\ \gamma = \frac{\text{Gr}_x}{\text{Re}_x^2},\ \delta = \frac{\text{Gm}_x}{\text{Re}_x^2},\ N = \frac{3R}{3R+4},\ K^* = \frac{2x\upsilon K}{U_0},\ K_r = \frac{2xK_l}{U_0}$$

3   Solution

To attain the velocity, temperature and concentration field, we assume:

$$\xi = \eta.f_w, f(\eta) = f_w.\Theta(\xi), \theta(\eta) = f_w^2.\Phi(\xi), \phi(\eta) = f_w^2.\Psi(\xi), \tau_{mp} = f_w^2.\tau_p$$

Substituting above functions into Eqs. (11)–(13), we obtain:

$$\frac{d^3\Theta(\xi)}{d\xi^3} + \Theta(\xi)\frac{d^2\Theta(\xi)}{d\xi^2} = \varepsilon\left[\left(M + \frac{1}{K}\right)\frac{d\Theta(\xi)}{d\xi}\right.$$
$$\left. -\gamma\,\Phi(\xi)\cos\alpha - \delta\,\Psi(\xi)\cos\alpha\right] \tag{15}$$

$$\frac{d^2\Phi(\xi)}{d\xi^2} + N\,\text{Pr}\,\Theta(\xi)\frac{d\Phi(\xi)}{d\xi} - N\,\text{Pr}\,S\varepsilon\,\Phi(\xi) = 0 \tag{16}$$

$$\text{Sc}\tau_p.\left(\frac{d^2\Phi(\xi)}{d\xi^2}.\Psi(\xi) + \frac{d\Phi(\xi)}{d\xi}.\frac{d\Psi(\xi)}{d\xi}\right)$$
$$= \varepsilon.\begin{pmatrix} \dfrac{d^2\Psi(\xi)}{d\xi^2} + \text{Sc}\Theta(\xi).\dfrac{d\Psi(\xi)}{d\xi} \\ -\varepsilon\text{KrSc}.\Psi(\xi) - \text{Sc}\tau_p A.\dfrac{d^2\Phi(\xi)}{d\xi^2} \end{pmatrix} \tag{17}$$

The boundary conditions are

$$\Theta(\xi) = 1, \frac{d\Theta(\xi)}{d\xi} = \varepsilon, \Phi(\xi) = \varepsilon, \Psi(\xi) = \varepsilon \text{ at } \xi = 0$$

$$\frac{d\Theta(\xi)}{d\xi} \to 0, \Phi(\xi) \to 0, \Psi(\xi) \to 0 \text{ at } \xi \to \infty \tag{18}$$

where $\varepsilon = 1/f_w^2$ is very small and $f_w > 1$.

Hence, $\Theta(\xi)$, $\Phi(\xi)$, $\Psi(\xi)$ can be represented in terms of ε as follows:

$$\Theta(\xi) = 1 + \varepsilon\Theta_1(\xi) + \varepsilon^2\Theta_2(\xi) + \varepsilon^3\Theta_3(\xi) + \cdots \tag{19}$$

$$\Phi(\xi) = \varepsilon\Phi_1(\xi) + \varepsilon^2\Phi(\xi) + \varepsilon^3\Phi(\xi) + \cdots \tag{20}$$

$$\Psi(\xi) = \varepsilon\Psi_1(\xi) + \varepsilon^2\Psi_2(\xi) + \varepsilon^3\Psi_3(\xi) + \cdots \tag{21}$$

Based on (19)–(21) and corresponding up to $O(\varepsilon^3)$, Eqs. (15)–(17) are altered as:
First-order O(ε):

$$\frac{d^2\Theta_1(\xi)}{d\xi^2} + \frac{d^3\Theta_1(\xi)}{d\xi^3} = 0 \tag{22}$$

$$N.\Pr.\frac{d\Theta_1(\xi)}{d\xi} + \frac{d^2\Phi_1(\xi)}{d\xi^2} = 0 \tag{23}$$

$$\mathrm{Sc}.\frac{d\Psi_1(\xi)}{d\xi} + \frac{d^2\Psi_1(\xi)}{d\xi^2} = A.\mathrm{Sc}.\tau_p.\frac{d^2\Phi_1(\xi)}{d\xi^2} \tag{24}$$

The boundary conditions are

$$\Theta_1(\xi) = 0, \frac{d\Theta_1(\xi)}{d\xi} = 1, \Phi_1(\xi) = 1, \Psi_1(\xi) = 1 \text{ at } \xi = 0$$

$$\frac{d\Theta_1(\xi)}{d\xi} \to 0, \Phi_1(\xi) \to 0, \Psi_1(\xi) \to 0 \text{ at } \xi \to \infty \tag{25}$$

Second-order O(ε^2):

$$\frac{d^3\Theta_2(\xi)}{d\xi^3} + \frac{d^2\Theta_2(\xi)}{d\xi^2} + \Theta_1(\xi)\frac{d^2\Theta_1(\xi)}{d\xi^2} = \left(M + \frac{1}{K}\right)\frac{d\Theta_1(\xi)}{d\xi}$$

$$- \gamma\,\Phi_1(\xi)\cos\alpha - \delta\,\Psi_1(\xi)\cos\alpha \tag{26}$$

$$\frac{d^2\Phi_2(\xi)}{d\xi^2} + N\Pr\frac{d\Phi_2(\xi)}{d\xi} = -N\Pr\Theta_1(\xi)\frac{d\Phi_1(\xi)}{d\xi} + N\Pr S\Phi_1(\xi) \tag{27}$$

$$\frac{d^2\Psi_2(\xi)}{d\xi^2} + \mathrm{Sc}\frac{d\Psi_2(\xi)}{d\xi} = -\mathrm{Sc}\Theta_1(\xi)\frac{d\Psi_1(\xi)}{d\xi} + \mathrm{Sc}\,\tau_p\frac{d^2\Phi_1(\xi)}{d\xi^2}\Psi_1(\xi)$$

$$+ \,\text{Sc}\,\tau_p \frac{d\Phi_1(\xi)}{d\xi}\frac{d\Psi_1(\xi)}{d\xi} + \text{KrSc}\Psi_1(\xi) + A\text{Sc}\,\tau_p\frac{d^2\Phi_1(\xi)}{d\xi^2} \tag{28}$$

The boundary conditions are

$$\Theta_2(\xi) = 0, \ \frac{d\Theta_2(\xi)}{d\xi} = 0, \ \Phi_2(\xi) = 0, \ \Psi_2(\xi) = 0 \quad \text{at } \xi = 0$$

$$\frac{d\Theta_2(\xi)}{d\xi} \to 0, \ \Phi_2(\xi) \to 0, \ \Psi_2(\xi) \to 0 \quad \text{at } \xi \to \infty \tag{29}$$

Third-order $O(\varepsilon^3)$:

$$\frac{d^3\Theta_3(\xi)}{d\xi^3} + N\,\text{Pr}\,\frac{d^2\Theta_3(\xi)}{d\xi^2} = \left(M + \frac{1}{K}\right)\frac{d\Theta_2(\xi)}{d\xi}$$

$$- \left[\gamma\,\Phi_2(\xi) - \delta\,\Psi_2(\xi)\right]\cos\alpha - \Phi_1(\xi)\frac{d^2\Theta_2(\xi)}{d\xi^2} - \frac{d^2\Theta_1(\xi)}{d\xi^2}\Phi_2(\xi) \tag{30}$$

$$\frac{d^2\Phi_3(\xi)}{d\xi^2} + N\,\text{Pr}\,\frac{d\Phi_3(\xi)}{d\xi} = -N\,\text{Pr}\,\Theta_1(\xi)\frac{d\Phi_2(\xi)}{d\xi}$$

$$- N\,\text{Pr}\,\frac{d\Phi_1(\xi)}{d\xi}\Theta_1(\xi) + N\,\text{Pr}\,S\Phi_2(\xi) \tag{31}$$

$$\frac{d^2\Psi_3(\xi)}{d\xi^2} + \text{Sc}\frac{d\Psi_3(\xi)}{d\xi} = \text{Sc}\tau_p\left[\begin{array}{c}\dfrac{d^2\Phi_1(\xi)}{d\xi^2}\Psi_2(\xi) + \dfrac{d^2\Phi_2(\xi)}{d\xi^2}\Psi_1(\xi)\\[2mm] + \dfrac{d\Phi_1(\xi)}{d\xi}\dfrac{d\Psi_2(\xi)}{d\xi} + \dfrac{d\Phi_2(\xi)}{d\xi}\dfrac{d\Psi_1(\xi)}{d\xi}\end{array}\right]$$

$$- \text{Sc}\left[\Theta_1(\xi)\frac{d\Psi_2(\xi)}{d\xi} + \Theta_2(\xi)\frac{d\Psi_1(\xi)}{d\xi}\right] + K_r\text{Sc}\Psi_2(\xi) + A\tau_p\text{Sc}\frac{d^2\Phi_3(\xi)}{d\xi^2} \tag{32}$$

The boundary conditions are

$$\Theta_3(\xi) = 0, \ \frac{d\Theta_3(\xi)}{d\xi} = 0, \ \Phi_3(\xi) = 0, \ \Psi_3(\xi) = 0 \quad \text{at } \xi = 0$$

$$\frac{d\Theta_3(\xi)}{d\xi} \to 0, \ \Phi_3(\xi) \to 0, \ \Psi_3(\xi) \to 0 \quad \text{at } \xi \to \infty \tag{33}$$

The solutions of these coupled equations satisfying the corresponding boundary conditions are:

$$\Theta_1(\xi) = 1 - e^{-\xi} \tag{34}$$

$$\Phi_1(\xi) = e^{-N\,\text{Pr}\,\xi} \tag{35}$$

$$\Psi_1(\xi) = (1 - k_1)e^{-Sc\xi} + k_1 e^{-N\Pr\xi} \tag{36}$$

$$\Theta_2(\xi) = k_4 + k_5 e^{-\xi} + k_2 e^{-N\Pr\xi} + k_3 e^{-Sc\xi} + (N_1 + 1)\xi e^{-\xi} + \frac{1}{4}e^{-2\xi} \tag{37}$$

$$\Phi_2(\xi) = k_6 e^{-N.\Pr\xi} - (N.\Pr + S)\xi e^{-N.\Pr\xi} - k_6 e^{-(1+N.\Pr)\xi} \tag{38}$$

$$\Psi_2(\xi) = k_{14} e^{-Sc\xi} + k_{17}\xi + k_8 e^{-(1+Sc)\xi} e^{-Sc\xi} + k_9 e^{-(1+N\Pr)\xi} + k_{10} e^{-(N\Pr + Sc)\xi}$$
$$+ k_{11} e^{-2N\Pr\xi} + k_{12}\xi e^{-N\Pr\xi} + k_{13} e^{-N\Pr\xi} \tag{39}$$

$$\Theta_3(\xi) = k_{30} + k_{29} e^{-\xi} + k_{15}\xi e^{-\xi} + k_{16}\left(\frac{\xi^2}{2} + 2\xi\right)e^{-\xi}$$
$$+ k_{17} e^{-N\Pr\xi} + k_{18} e^{-Sc\xi} + k_{19} e^{-2\xi}$$
$$+ k_{20} e^{-(1+N\Pr)\xi} + k_{21} e^{-(1+Sc)\xi}$$
$$+ k_{22} e^{-(N\Pr + Sc)\xi} + k_{23} e^{-2N\Pr\xi} - \frac{5}{72}e^{-3\xi}$$
$$+ k_{24}(\xi + k_{25})e^{-N\Pr\xi} + k_{26}(\xi + k_{27})e^{-Sc\xi}$$
$$+ k_{28}\left(\xi + \frac{5}{2}\right)e^{-2\xi} \tag{40}$$

$$\Phi_3(\xi) = k_{38} e^{-N\Pr\xi} + k_{31}\xi e^{-N\Pr\xi} + k_{32} e^{-(1+N\Pr)\xi}$$
$$+ k_{33} e^{-(2+N\Pr)\xi} + k_{34} e^{-(N\Pr + Sc)\xi}$$
$$+ k_{35} e^{-2N\Pr\xi} + k_{36}\left(\frac{\xi^2}{2} + \frac{\xi}{N.\Pr}\right)e^{-N\Pr\xi}$$
$$+ k_{37}\left(\xi + \frac{2 + N.\Pr}{1 + N.\Pr}\right)e^{-(1+N\Pr)\xi} \tag{41}$$

$$\Psi_3(\xi) = k_{68} e^{-Sc\xi} + k_{38}\xi e^{-Sc\xi} + k_{40}\left(\frac{\xi^2}{2} + 2\xi\right)e^{-Sc\xi} + k_{41} e^{-(1+Sc)\xi}$$
$$+ k_{42}\left(\xi + \frac{2 + N.\Pr}{1 + N.\Pr}\right)e^{-(1+Sc)\xi} + k_{43} e^{-2Sc\xi} + k_{44} e^{-(1+N\Pr)\xi}$$
$$+ k_{45}(\xi + k_{46})e^{-(1+N\Pr)\xi} + k_{47} e^{-(1+N\Pr + Sc)\xi}$$
$$+ k_{48} e^{-2N\Pr\xi} + (k_{49} - k_{67})e^{-N\Pr\xi} + k_{50}(\xi + k_{51})e^{-N\Pr\xi}$$
$$+ k_{52} e^{-(2+Sc)\xi} + k_{53} e^{-(2+N\Pr)\xi} + k_{54} e^{-(1+2N\Pr)\xi} + k_{55} e^{-(N\Pr + Sc)\xi}$$
$$+ k_{56}(\xi + k_{57})e^{-(N\Pr + Sc)\xi} + k_{58} e^{-(2N\Pr + Sc)\xi} + k_{59} e^{-3N\Pr\xi}$$
$$+ k_{60}(\xi + k_{61})e^{-N\Pr\xi} + k_{62}\left(\frac{\xi^2}{2} + \frac{\xi}{N.\Pr}\right)e^{-N\Pr\xi}$$
$$- k_{66}(1 - (2N.\Pr - Sc)\xi)e^{-N\Pr\xi}$$

$$+ K_{64}(\xi + K_{65})e^{-(1+N\,Pr)\xi} \tag{42}$$

The skin-friction coefficient (τ), local Nusselt number (Nu*)* and the local Sherwood numbers (Sh) are defined as:

$$\tau = \mu\left(\frac{\partial u}{\partial y}\right)_{y=0}, \text{Nu} = -\left(\frac{\partial T}{\partial y}\right)_{y=0}, \text{ and Sh} = -\left(\frac{\partial C}{\partial y}\right)_{y=0} \tag{43}$$

Equation (43) becomes:

$$\tau \propto [f''(\eta)]_{\eta=0} = -1 + \varepsilon[k_5 - N^2 Pr^2 k_2 - k_3 Sc^2 + 2(N_1 + 1) + 1]$$
$$+ \varepsilon^2[A_{32} + A_{33}] \tag{44}$$

$$Nu \propto [\theta'(\eta)]_{\eta=0} = N\,Pr + \varepsilon[N\,Pr + S - k_6] + \varepsilon^2[A_{34} + A_{35}] \tag{45}$$

$$Sh \propto [\phi'(\eta)]_{\eta=0} = Sc(1 - k_1) + k_1 N Pr + \varepsilon A_{36}$$
$$+ \varepsilon^2[A_{37} + A_{38} + A_{39} + A_{40}] \tag{46}$$

4 Results and Discussion

The velocity profiles are premeditated in Fig. 2a for various values of *M*. It is detected that the rise in magnetic field parameter *M* decreases the fluid velocity distribution. Figure 2b shows concentration profiles against span-wise coordinates for various values of reaction parameter *Kr*. It is determined that increasing *Kr* decreases the concentration distribution.

Figure 3a, b depicts the result of a thermophoretic parameter on the velocity and temperature profiles, respectively. It is disclosed that velocity decreases with an increase in the values of τ_p and reverse trend seen with the temperature profiles.
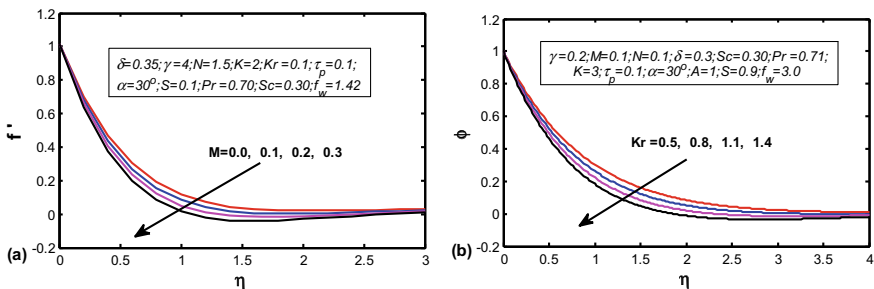
Fig. 2 a Effect of *M* on velocity profiles. **b** Effect of *Kr* on concentration profiles
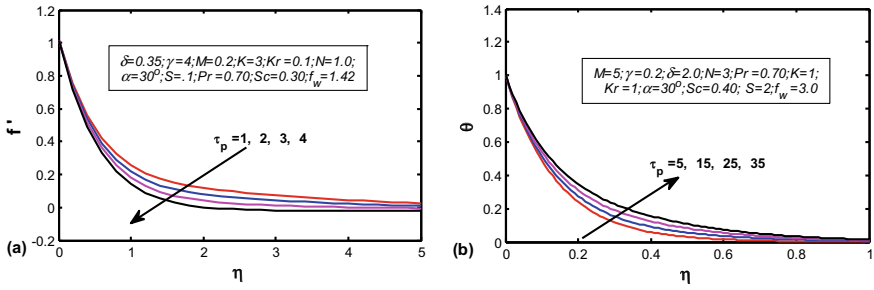
Fig. 3 **a** Effect of τ_p on velocity profiles. **b** Effect of τ_p on temperature profiles

Figure 4a–c show the velocity, temperature and concentration profiles against span-wise coordinates for different values of angle of inclination (α). In Fig. 4a, it is found that with rising values of α, the velocity decreases. Similar behavior has been seen by Alam et al. [4]. From Figs. 4b and c, we observe that the thermal and concentration physical phenomenon thickness enhances for larger values of α.

The effects of magnetic field (M) and thermophoretic parameter (τ_p) on τ, Nu and Sh are shown in Fig. 5a–c, respectively. From these figures, it is seen that both τ as well as Sh enhance, whereas Nu declines with rising values of τ_p for all values of M.
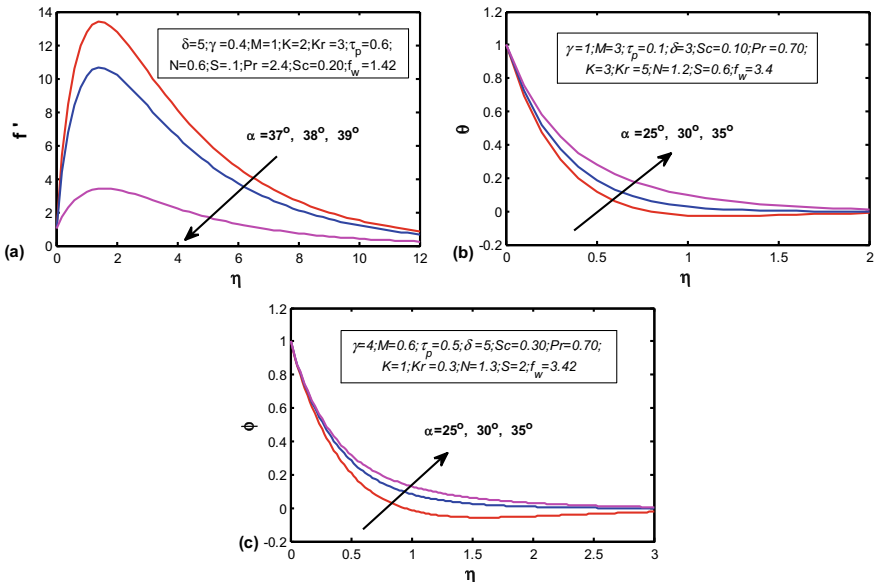
Fig. 4 **a** Effect of α on velocity profiles. **b** Effect of α on temperature profiles. **c** Effect of α on concentration profiles
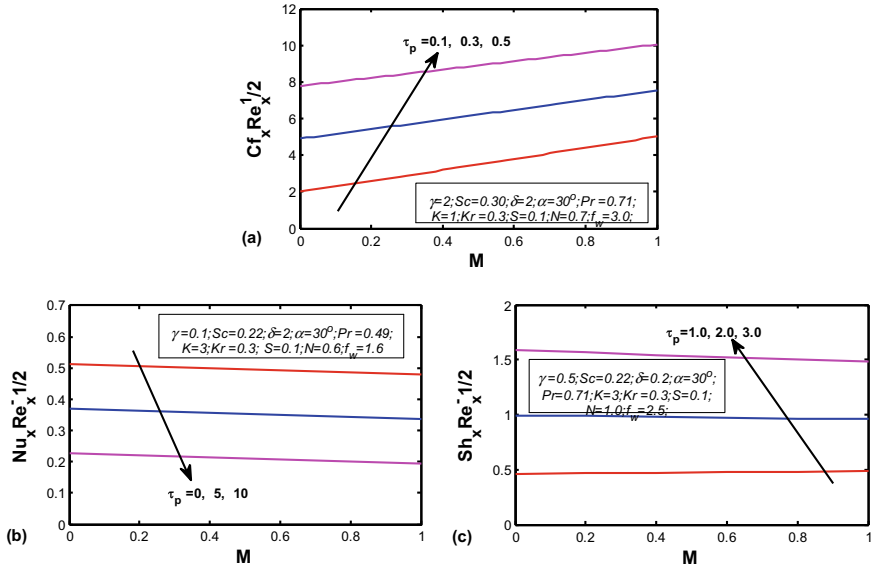
Fig. 5 **a** Variation of skin-friction coefficient for different values of τ_p. **b** Nusselt number for different values of τ_p. **c** Sherwood number for different values of τ_p

5 Conclusions

The conclusions drawn from this can be listed as follows:

1. As *M, Kr* values enhance, there is retardation in fluid velocity and concentration in physical phenomenon.
2. Increasing τ_p diminishes the velocity as well as concentration while augments in thermal boundary layer.
3. The thermal and concentration boundary layer rises by increasing values of α, while the velocity boundary layer reduces.
4. The local skin-friction coefficient in addition to Sherwood number increases with growing values of τ_p, whereas Nusselt number declines.

References

1. Anjalidevi SP, Kandasamy R (1999) Effects of chemical reaction, heat and mass transfer on laminar flow along a semi infinite horizontal plate. Heat Mass Transfer 35:465–467
2. Rashidi MM, Rahimzadeh N, Ferdows M, Uddin MJ, Bég OA (2012) Group theory and differential transform analysis of mixed convective heat and mass transfer from a horizontal surface with chemical reaction effects. Chem Eng Commun 199:1012–1043

3. Satyanarayana PV, Harish Babu D (2016) Numerical study of MHD heat and mass transfer of a Jeffrey fluid over a stretching sheet with chemical reaction and thermal radiation. J. Taiwan Ins Chem Eng 59:18–25
4. Alam MM, Sattar MA (1999) Local solutions of an MHD free convection and mass transfer flow with thermal diffusion. Ind J Theor Phys 47:19–34
5. Selim A, Hossain MA, Das R (2003) The effect of surface mass transfer on mixed convection flow past a heated vertical flat permeable plate with thermophoresis. Int J Thermal Sci 42:973–982
6. Hayat T, Alsaedi A (2011) On thermal radiation and joule heating effects in MHD flow of an Oldroyd-B fluid with thermophoresis. Arab J Sci Eng 36:1113–1124
7. Satyanarayana PV (2015) Effects of variable permeability and radiation absorption on (MHD) mixed convective flow in a vertical wavy channel with traveling thermal waves. Propul Power Res 4(3):150
8. Mondal H, Dulal P, Chatterjee S, Sibanda P (2018) Thermophoresis and Soret-Dufour on MHD mixed convection mass transfer over an inclined plate with non-uniform heat source/sink and chemical reaction. Ain Shams Eng J 9:2111–2121
9. Harish Babu D, Satyanarayana PV (2016) Joule heating effects on MHD mixed convection of a Jeffrey fluid over a stretching sheet with power law heat flux: a numerical study. J Magn Mag Mater 412:185–193
10. Kundu PK, Kalidas D, Subroto J (2014) Impact of chemical reaction on MHD mixed convection heat and mass transfer flow with thermophoresis. Walailak J Sci Tech 11(2):149–170
11. Singh NP, Singh AK, Singh AK, Agnihotri P (2011) Effects of thermophoresis on hydromagnetic mixed convection and mass transfer flow past a vertical permeable plate with variable suction and thermal radiation. Commun Nonlinear Sci Numer Simulat 16:2519–2534
12. Rosseland S (1936) Theoretical astrophysics. Oxford University Press, London
13. Talbot L, Chang RK, Schefer AW, Wills DR (1980) Thermophoresis of particles in a heated boundary layer. J Fluid Mech 101:737–758

The Characteristics of Heat and Mass Transfer on MHD Fluid Flow over a Moving Melting Surface

S. Harinath Reddy, D. Harish Babu, K. Kumaraswamy Naidu, M. C. Raju, and P. V. Satya Narayana

Abstract The magneto-hydrodynamics (MHD) fluid flow above a moving melting surface in the existence of sticky intemperance under heat in addition mass transfer characteristics are examined theoretically and to be furnished in this article. The flow equivalent equations are solved by means of R-K method of 4th order. The impact of notable parameters on velocity, concentration, and temperature is deliberated through graphs. A comparison is made with the previous literature to validate the method and found good agreement. Concentration of the fluid decreases up to $\eta = 2$ and it increases for $\eta > 2$ with increasing values of Sc and Sherwood number increases for raising Sc values.

Keywords Moving melting surface · MHD · Viscous dissipation · Heat as well as mass transfer

Nomenclature

B_0	Constant
C_f	Skin friction coefficient
C_s	Heat capacity of the solid surface
Ec	Eckert number
H	Dimensionless melting parameter
M	Magnetic field parameter

S. Harinath Reddy
Department of Mathematics, AITS, New Boyanapalli, Rajampet, AP, India

D. Harish Babu · K. Kumaraswamy Naidu
Department of Mathematics, Sree Vidyanikethan Engineering College, Tirupati, AP, India

M. C. Raju
Department of Mathematics, JNTUACEP, Pulivendula, AP, India

P. V. Satya Narayana (✉)
Department of Mathematics, SAS, VIT University, Vellore 632014, Tamil Nadu, India
e-mail: pvsatya8@yahoo.co.in

k^* Mean absorption coefficient
k Thermal conductivity
Nu   Nusselt number
Pr   Prandtl number
Q Heat source parameter
q_r Radiative heat flux
R Thermal radiation parameter
Re_x Reynolds number
T Temperature of the fluid
$\mathbf{C}$ Concentration of the fluid
T_m Solid surface temperature
$(x. y)$ Cartesian co-ordinates
υ Kinematic viscosity
σ Electrical conductivity
σ^* Stefan–Boltzmann constant
η Similarity variable
λ_1 Latent heat of the fluid
λ Moving parameter
μ Coefficient of viscosity
τ_w Wall shear stress
ψ Stream function
$\theta(\eta)$ Dimensionless temperature
$\phi(\eta)$ Dimensionless concentration
T_∞ Temperature away from the plate

Subscripts

ω Condition at the wall
∞ Condition at free stream

1 Introduction

Heat as well as mass transfer characteristics on MHD flow over a moving surface place a significant role in polymer industries, lamination process, water refining, and melting spinning process. For intended, Chandra Reddy et al. [1] explored heat as well as mass transfer properties of free convective fluid flow of nanofluid in conducting fluid considering three cases of moving plate. Zheng et al. [2] discussed effect of instable flow of MHD oscillatory stretching surface with existence of Soret and Dufour properties. Mishra et al. [3] studied heat as well as mass transfer on viscoelastic fluid with MHD over a stretching sheet. Oscillatory flow of MHD polar fluid under

simultaneous heat as well as mass transfer with interior heat source was investigated by Veena et al. [4]. Sandeep and Reddy [5] analyzed MHD Cu–water nanofluid flow geometrically in dual cases on heat transfer. Pal [6] examined theoretically on MHD effects on heat transfer over thermal radiation and hall current. Cortell [7] gave a detailed note on heat transfer over a broadening sheet with viscoelastic fluid flow. Reddy et al. [8] studied the nature of MHD flow over a stretching sheet with the existence of heat source and viscous dissipation. Syed et al. [9] offered the study of MHD as well as thermal properties of shrinking surface over stagnation point flow with viscous dissipation. Jafar et al. [10] have analyzed several effects of stretching/shrinking sheets on MHD flow. Aktar and Alim [11] examined the characteristics of MHD flow along a vertical horizontal plate. Kalteh et al. [12] considered and analyzed viscous dissipation effects on fluid flow over a stretching cylinder. Hakiem [13] investigated MHD natural convective micropolar fluid flow over a non isothermal surface over viscous dissipation effects. Ishak et al. [14] considered steady laminar flow over a moving surface under melting heat transfer.

In view of the above studies, theoretical investigation has been performed on MHD fluid flow over a moving melting surface in the existence of viscous dissipation under heat as well as mass transfer. The novelty of this presentation is the consideration of mass transfer. We have protracted the work of Venkateswarlu et al. [15] by introducing mass transfer result which is not considered in his analysis.

2   Formulation of the Problem

The characteristics of heat as well as mass transfer on magnetohydrodynamic fluid flow over a moving melting surface have been deliberated in two-dimensional form. The model of the flow and geometry of the problem is existing in Fig. 1. The fluid flow

Fig. 1 Physical model and coordinate system
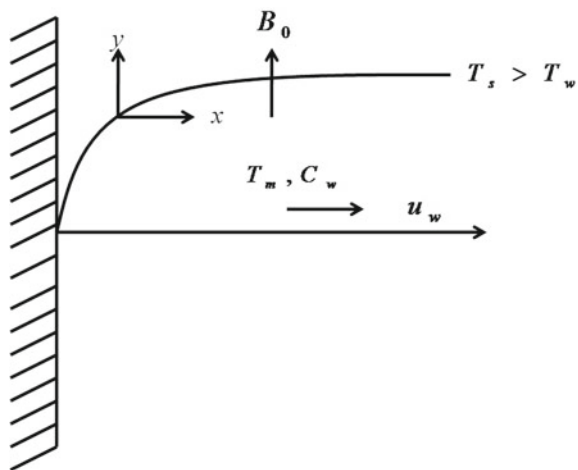
along the moving surface is occupied in the x-direction and y-axis is perpendicular to it. The succeeding conventions are prepared in the current study.

- The movement of the surface is at constant velocity U_w and the temperature and concentration of the melting surface are taken as T_m and C_w, respectively.
- A uniform and induced magnetic field is taken in the positive way perpendicular to the surface.

The governing equations pertinent to the flow are listed as follows:

$$\frac{\partial U'}{\partial x} + \frac{\partial V'}{\partial y} = 0 \tag{1}$$

$$U'\frac{\partial U'}{\partial x} + V'\frac{\partial U'}{\partial y} = \upsilon\frac{\partial^2 U'}{\partial y^2} - \frac{\sigma B^2(x)}{\rho}(U' - U_\infty) \tag{2}$$

$$U'\frac{\partial T'}{\partial x} + V'\frac{\partial T'}{\partial y} = \alpha\frac{\partial^2 T'}{\partial y^2} - \frac{Q_H}{\rho C_p}(T' - T_\infty) - \frac{1}{\rho C_p}\frac{\partial q_r}{\partial y} + \frac{\upsilon}{\rho C_p}\left(\frac{\partial U'}{\partial y}\right)^2 \tag{3}$$

$$U'\frac{\partial C'}{\partial x} + V'\frac{\partial C'}{\partial y} = D\frac{\partial^2 C'}{\partial y^2} \tag{4}$$

The suitable boundary conditions of the present problem are given as

$$\begin{aligned} U' = U_w(x); \quad T' = T_m; \quad C' = C_w \quad \text{at} \quad y = 0 \\ U' \rightarrow U_\infty; \quad T' \rightarrow T_\infty; \quad C' \rightarrow C_\infty \quad \text{at} \quad y \rightarrow \infty \end{aligned} \tag{5}$$

$$k\left(\frac{\partial T'}{\partial y}\right)_{y=0} = \rho\{\lambda_1 + c_s(T_m - T_s)\}\upsilon(x, 0) \tag{6}$$

The radiative heat flux term q_r according to Rosseland estimate is as follows

$$q_r = -\frac{4\sigma^*}{3k^*}\frac{\partial T'^4}{\partial y} \tag{7}$$

Where

$$T'^4 = 4T' T_\infty^3 - 3T_\infty^4$$

Hence, we take

$$\frac{\partial q_r}{\partial y} = -\frac{16\sigma^* T_\infty^3}{3k^*}\frac{\partial^2 T'}{\partial y^2} \tag{8}$$

The succeeding similarity conversions are considered to transform the governing equations.

$$\eta = \sqrt{\frac{U_\infty}{\upsilon\, x}}\, y, \; \psi(x, y) = \sqrt{\upsilon x U_\infty}\, f(\eta), \; \theta(\eta) = \frac{T' - T_m}{T_\infty - T_m}, \; \phi(\eta) = \frac{C' - C_w}{C_\infty - C_w},$$

$$(9)$$

The stream function ψ is determined as follows.

$$u = \frac{\partial \psi}{\partial y} \text{ and } \upsilon = -\frac{\partial \psi}{\partial x} \tag{10}$$

By means of Eq. (9), Eqs. (2)–(4) can be inscribed as follows

$$f''' + \frac{1}{2} f\, f'' - M(f' - 1) = 0 \tag{11}$$

$$frac1P_r \theta'' + \frac{1}{P_r} R\theta'' + \frac{1}{2} f\, \theta' - Q\,\theta + \text{Ec}\, f''^2 = 0 \tag{12}$$

$$\phi'' - \left\{ \frac{1}{2} \text{Sc}\, f'\phi' - \text{Sc}\, f\phi' \right\} = 0 \tag{13}$$

The related edge conditions are

$$f' = \lambda; \; \theta = 0; \; \text{Pr}\; f + H\theta' = 0; \; \phi(\eta) = 0; \; \text{ for } \eta = 0 \tag{14}$$

$$f' \to 1; \; \theta \to 1; \quad \phi(\eta) = 1 \text{ as } \eta \to \infty \tag{15}$$

where $\lambda = \frac{U_w}{U_\infty}$ is the moving parameter. $\lambda = 0$ relates to the flow over a fixed surface whereas $0 < \lambda < 1$ means that the plate and fluid are passing in the similar path.

$$H = \frac{c_f(T_\infty - T_m)}{\lambda_1 + c_s(T_m - T_s)}, \; M = \frac{\sigma x}{\rho U_\infty} B^2(x),$$

$$Ec = \frac{U_\infty^2}{\rho C_p(T_\infty - T_m)}, \; Q = \frac{Q^*}{\rho C_p U_\infty}, \; R = \frac{16\sigma^* T_\infty^3}{3kk^*}, \; \text{Pr} = \frac{\mu}{\alpha}.$$

The skin friction, Nusselt number, and Sherwood number are as follows.

$$C_f = \frac{\tau_w}{\rho u_e^2} = \text{Re}_x^{-1/2} f''(0) \tag{16}$$

$$\text{Nu} = -\text{Re}_x^{1/2}(1 + R)\theta'(0) \tag{17}$$

$$\text{Sh} = -\text{Re}_x^{\frac{1}{2}}\phi(0) \tag{18}$$

where $\tau_w = \mu \left\{ \frac{\partial u}{\partial y} \right\}_{y=0}$ is the wall shear stress and $\text{Re}_x = \frac{U_\infty x}{v}$ is the local Reynolds number.

3   Results and Discussion

The heat as well as mass transfer characteristics of MHD flow of a viscous dissipative fluid over a moving melting surface are analyzed, Figure 2a, b gives the deviations in velocity profiles for dissimilar H values when $\lambda = 2.0$ and $\lambda = -2.0$, respectively. The fluid velocity enhances for growing H values in case of $\lambda > 0$, but opposite trend is observed when $\lambda < 0$ case.

Figure 3 exhibits that the fluid temperature grows under the existence of Ec. This occurs due to the energy dissipation on the fluid particles created by enhanced values of Ec.

The temperature as well as profiles of concentration growing H values is displayed in Fig. 4. The temperature boundary layer improves with increased values of H, but concentration falls down with same values of H. Similar trend is seen under the influence of Pr which is examined from Fig. 5. Fluid temperature decreases and fluid concentration rises for growing values of R as shown in Fig. 6. This happens due to impact of thermal radiation on fluid particles which results in reducing the heat and improving the concentration.

From Fig. 7, it is detected that temperature of the fluid falls down through the existence of Q. It is because the heat generation on fluid particles results in enhancing the temperature boundary layer. Figure 8 exhibits the concentration profiles for increasing values of Sc. Concentration of the fluid decreases up to the point $\eta = 2$ and if $\eta > 2$, it increases for dissimilar values of Sc. Figures 9, 10, display the changes in skin friction coefficient for dissimilar M values against λ and Pr against M. From
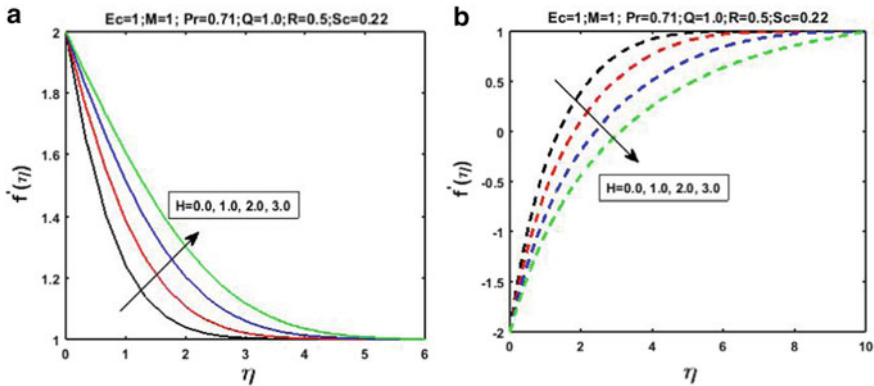
Fig. 2 **a** Velocity profiles for different values of H (for $\lambda = 2.00$). **b** Velocity profiles for different values of H (for $\lambda = -2.0$)

Fig. 3 Temperature profiles
for different values of Ec
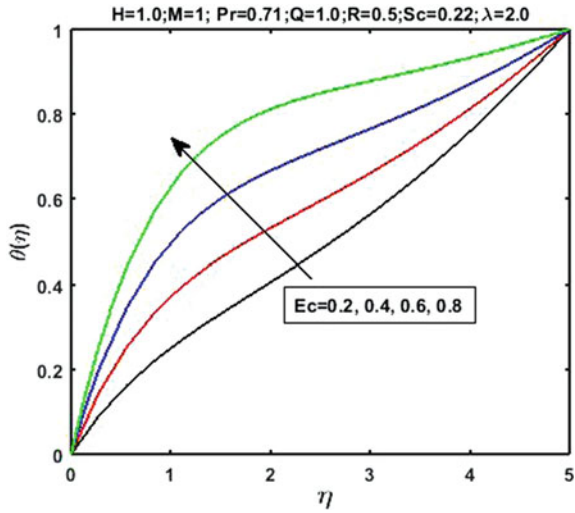
Fig. 4 Temperature and
concentration profiles for
different values of *H*
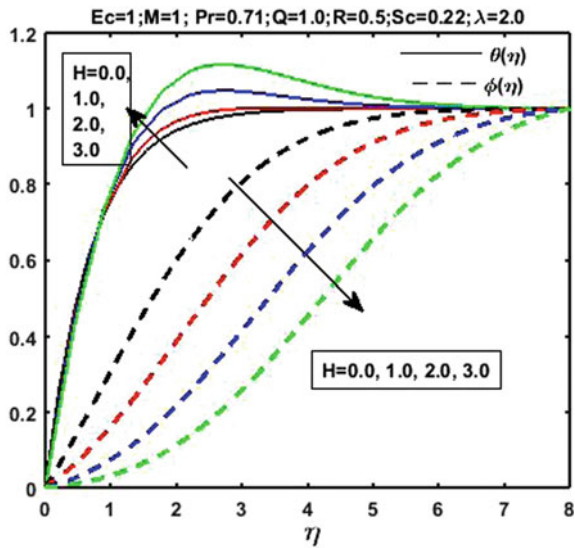
Fig. 9 it is clear that the skin friction coefficient rises under enhanced values of M and it comes down when λ increases. Figure 10 exhibits that the skin friction coefficient falls down under the impact of both Pr and *M*. Figure 11 reveals that the Nusselt number drops when Ec increases and it increases when *R* values are increased. Sherwood number grows under the enhanced values of Sc and λ, which is evident from Fig. 12.

Fig. 5 Temperature and concentration profiles for different values of Pr
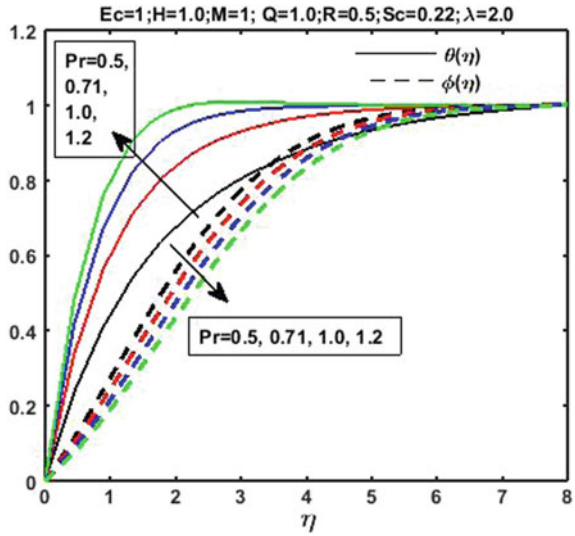
Fig. 6 Temperature and concentration profiles for different values of R
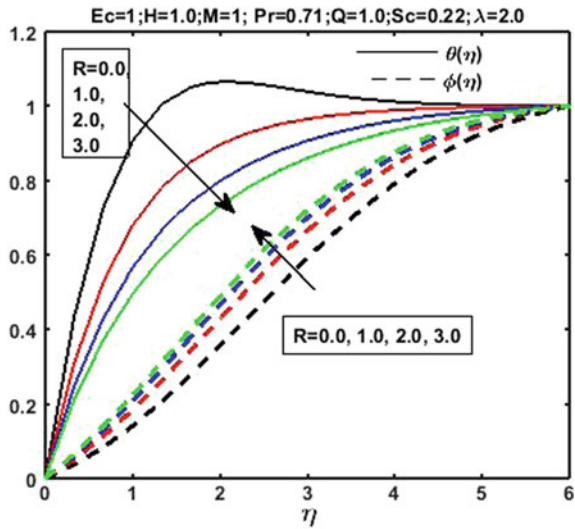
4   Conclusions

The significant characteristic of MHD fluid flow over a moving melting surface under viscous dissipation is evaluated with the use of graphical presentations and tables. Some of the outstanding points from this study are specified below (Table 1).

(i)   The fluid velocity profiles grow under the impact of H and it falls down when $\lambda < 0$.

Fig. 7 Temperature profiles for different values of Q

Ec=1;H=1.0;M=1; Pr=0.71;R=0.5;Sc=0.22;λ=2.0

Q=1.0, 1.5, 2.0, 2.5

Fig. 8 Concentration profiles for different values of Sc

Ec=1;H=1.0;M=1; Pr=0.71;Q=1.0;R=0.5;λ=2.0

Sc=0.30, 0.60, 1.0, 2.26
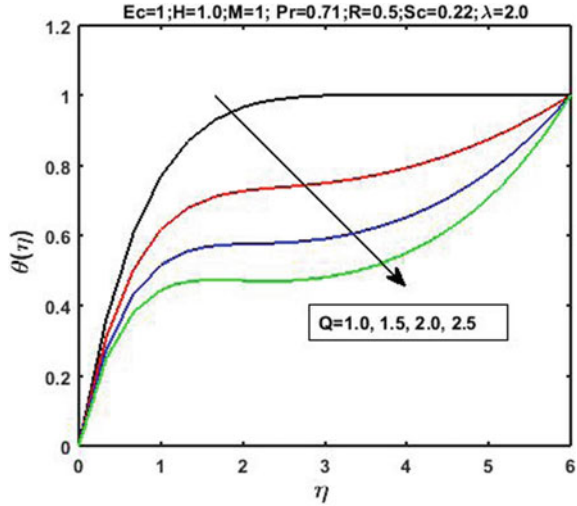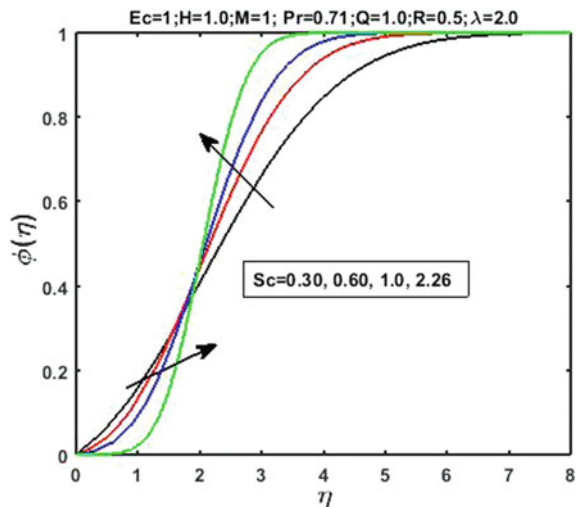
(ii) An enhancement in the temperature of the fluid is noticed for increasing values of Ec, H, and Pr, but it displays opposite effect in the case of Q and R.

(iii) The concentration profiles of the fluid increase for increasing values of R, Sc up to $\eta = 2$ and it drop for accumulative values of Pr, H, and Sc when $\eta > 2$.

(iv) Skin friction enhances as M values increases, but it drops for raising values of Pr.

(v) Nusselt number decreases when Ec increases and it increases when R values are increased.

(vi) Sherwood number grows under the enhanced values of Sc and λ.

Fig. 9 Skin friction coeff.
for different values of M
against λ
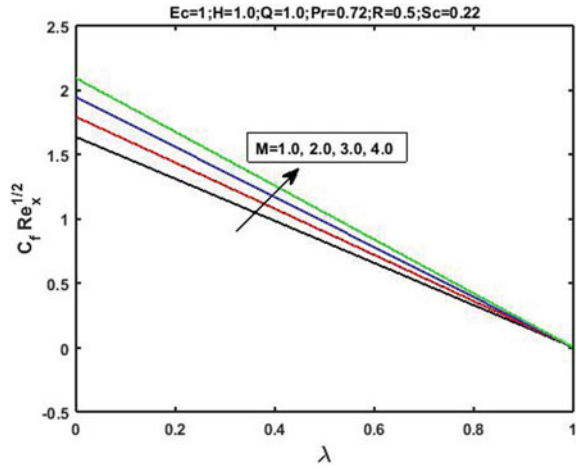
Fig. 10 Skin friction coeff.
for different values of Pr
against M
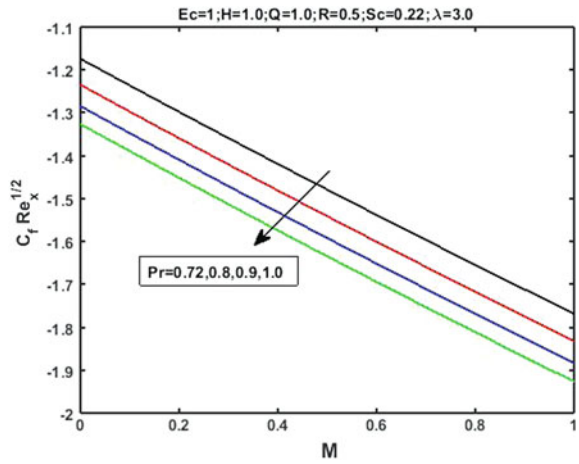
Fig. 11 Nusselt number for different values of Ec against *R*
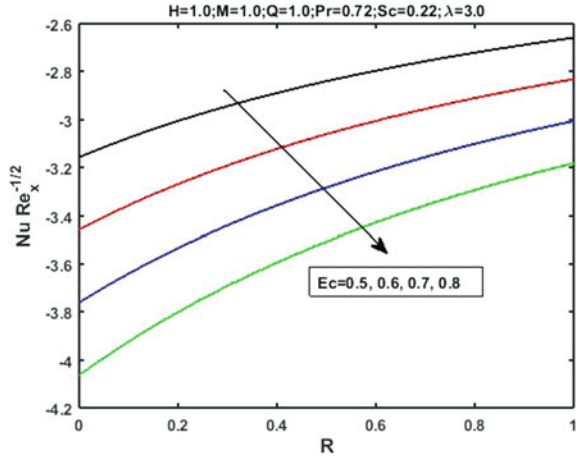
Fig. 12 Sherwood number for different values of Sc against λ
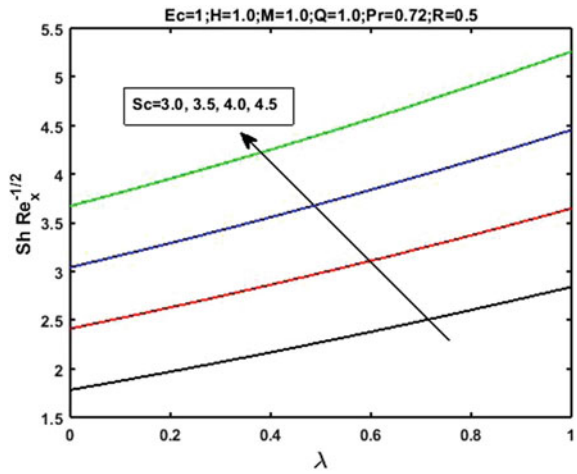
Table 1 Comparison of Nusselt number of the present case with those of Das [16] and Venkateswarulu et al. [15] for different values of $\varepsilon = 0.5$, Ec = 1.0, $H = 1.0$, $K = 1.0$, $M = 1.0$, and $Q = 1.0$

Pr	Das [16] Ec $= Q = 0$	Venkateswarulu et al. [15] (Sc $= 0$)	Present results
0.1	2.0833	2.0833	2.0833
0.2	1.4586	1.4536	1.4554
0.3	1.2521	1.2586	1.2594
0.4	1.1461	1.1463	1.1459

References

1. Chandra Reddy P, Raju MC, Raju GSS (2016) Free convective heat and mass transfer flow of heat generating Nanofluid past a vertical moving porous plate in conducting field. Spec Topics Rev Porous Media 7(2):161–180
2. Zheng LC, Jin X, Zhang XX, Zhang JH (2013) Unsteady heat and mass transfer in MHD flow over an oscillatory stretching surface with Soret and Dufour efects. Acta Mech Sin 5:667–675
3. Mishra SR, Pattnaik PK, Bhatti MM, Abbas T (2017) Analysis of heat and mass transfer with MHD and chemical reaction effects on viscoelastic fluid over a stretching sheet. Indian J Phys 91(10):1219–1227
4. Veena PH, Raveendra N, Pravin VK (2016) Oscillatory flow of MHD polar fluid with heat and mass transfer past a vertical moving porous plate with internal heat generation. Int J Mech Eng Technol 7(2):212–231
5. Sandeep N, Reddy MG (2017) Heat transfer of nonlinear radiative magnetohydrodynamic Cu-water nanofluid flow over two different geometries. J Mol Liq 225:87–94
6. Pal D (2013) Hall current and MHD effects on heat transfer over an unsteady stretching permeable surface with thermal radiation. Comput Math Appl 66(7):1161–1180
7. Cortell R (2006) A note on flow and heat transfer of a viscoelastic fluid over a stretching sheet. Int J Non Linear Mech 41(1):78–85
8. Gnaneswara Reddy M, Padma P, Shankar B (2015) Effects of viscous dissipation and heat source on unsteady MHD flow over a stretching sheet. Ain Shams Eng J 6(4):1195–1201
9. Syed KS, Ahmad S, Ashraf M (2012) Study of magnetohydrodynamic and thermal characteristics of axisymmetric stagnation point flow with viscous dissipation over a shrinking surface. World Appl Sci J 18(1):43–54
10. Jafar K, Nazar R, Ishak A, Pop I (2012) MHD flow and heat transfer over stretching/shrinking sheets with external magnetic field, viscous dissipation and Joule effects. Can J Chem Eng 90(5):1336–1346
11. Aktar S, Alim MA (2014) Effects of conduction and convection on magneto hydrodynamic flow along a vertical flat plate with viscous dissipation and heat generation. Procedia Eng 90:411–417
12. Kalteh M, Ghorbani S, Kademinejad T (2016) Viscous dissipation and thermal radiation effects on the magnetohydrodynamic (MHD) flow and heat transfer over a stretching slender cylinder. J Appl Mech Tech Phys 57(3)
13. Hazarika GC, Konch J (2014) Effects of variable viscosity and thermal conductivity on MHD free convective flow along a vertical porous plate with viscous dissipation. Int J Math. Trends Technol 15(1)
14. Ishak A, Nazar R, Bachok N, Pop I (2010) Melting heat transfer in steady laminar flow over a moving surface. Heat Mass Transfer 46:463–468
15. Venkatewsarlu B, Satya Narayana PV, Tarakaramu N (2018) Melting and viscous dissipation effects on MHD flow over a moving surface with constant heat source. Trans A. Razmadze Math Inst. https://doi.org/10.1016/j.trmi.2018.03.007
16. Das K (2014) Radiation and melting effects on MHD boundary layer flow over a moving surface. Ain Shams Eng J 5(4):1207–1214

Casson Nanoliquid Flow Due to a Nonlinear Stretched Sheet with Convective Conditions

S. Samantha Kumari and G. Sankara Sekhar Raju

Abstract This work is explored to test the influence of convective boundary conditions on magnetohydrodynamic three-dimensional Casson nanoliquid motion generated by a nonlinear stretched sheet. Using suitable functions, the flow governing PDEs are changed into a set of ODEs. The resulting set of coupled nonlinear equations is solved computationally with the help of BVP-4 MATLAB software. The characteristics of different flow parameters such as Biot number, thermophoresis parameter, magnetic field parameter, non-Newtonian parameters on the flow, energy, and species concentration are discussed and displayed pictorially. The results reviled that the both energy and species concentration distributions rise with increasing Biot number.

Keywords Casson nanoliquid · Nonlinear stretched sheet · 3D flow · MHD

1 Introduction

Recently, the study of rheology fluid flows over different geometries has been addressed by many researchers. Casson fluid (e.g., soup, honey and human blood) is treated as one of the simple non-Newtonian liquids because of their rheological characteristics. Sulochana et al. [1] studied the effect of convective conditions on 3D rheological fluid past a sheet stretching. This study reviles that the energy and concentration transfer rates of the fluid are enhanced with the increase of stretching ratio parameter and non-Newtonian fluid heat transfer is comparatively more than that of Newtonian fluid. Ibukun et al. [2] presented the effects of slip conditions on a Casson nanoliquid motion caused by a stretched sheet. Ganesh Kumar et al. [3] analyzed the effects of thermal heat on 3D motion of a non-Newtonian nanoliquid. Ahmad et al. [4] investigated the different flow characteristics on micro polar fluid flow generated

S. Samantha Kumari (✉)
Research Scholar, Department of Mathematics, JNTUA, Anantapuramu, AP, India
e-mail: hkesavulu6@gmail.com

G. Sankara Sekhar Raju
Department of Mathematics, JNTUA College of Engineering, Pulivendula,
Y.S.R. District 516390, India

by a sheet stretching. The influence of different heat characteristics over different mathematical geometries in the presence of nanofluids has been studied by [5–15].

The target of this study is to characterize the Casson nanofluid motion generated due to a nonlinear stretched sheet. The self-similar functions are used to transform flow PDEs into ODEs. The set of nonlinear ODEs is solved by using MATLAB software. The effects of physical constraints on flow variables are presented and conferred in detail by displaying graphically.

2 Mathematical Analysis

The incompressible viscous electrically conducting Casson nanofluid flow past by a nonlinear stretched sheet is measured in this work. A non-similar magnetic force is assumed perpendicular to the xy-plane. The induced magnetic field effects are neglected due to the low magnetic Reynolds number. The velocities of the fluid along x- and y-directions are defined as: $U_W(x, y) = a(x + y)^n$ and $V_w(x, y) = b(x + y)^n$, respectively, with $a; b; n > 0$ as the constants (Fig. 1).

The steady Casson fluid flow is taken by

$$
\tau_{ij} = \begin{cases} \pi > \pi_c, \ 2\left(\mu_0 + p_y(2\pi)^{\frac{-1}{2}}\right)e_{ij}, \\ \pi < \pi_c, \ 2\left(\mu_0 + p(2\pi)^{\frac{-1}{2}}\right)e_{ij}, \end{cases}.
\tag{1}
$$

where $p_y = \mu_0\sqrt{2\pi}/\beta$, $\pi = e_{ij}e_{ij}$.

The flow equations are defined as follows:

$$
u_x + v_y + w_z = 0
\tag{2}
$$
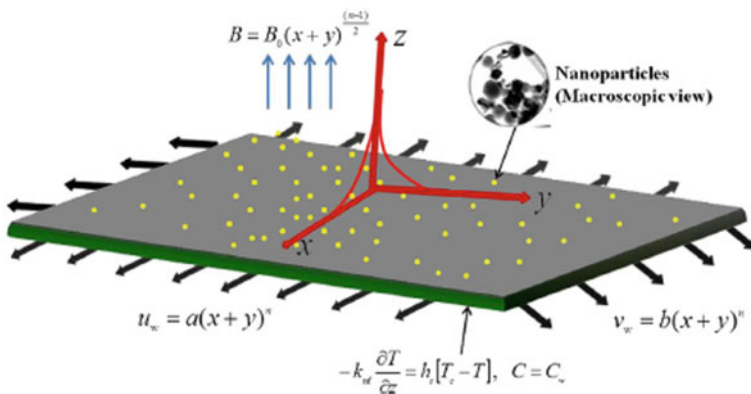
Fig. 1 Physical geometry

$$uu_x + vu_y + wu_z = \upsilon\left(1 + \frac{1}{\beta}\right)u_{zz} - \frac{\sigma B^2(x, y)}{\rho_f}u \tag{3}$$

$$uv_x + vv_y + wv_z = \upsilon\left(1 + \frac{1}{\beta}\right)v_{zz} - \frac{\sigma B^2(x, y)}{\rho_f}v \tag{4}$$

$$uT_x + vT_y + wT_z = \alpha_m T_{zz} + \frac{(\rho c)_p}{(\rho c)_f}(D_B(T_z C_z) + \frac{D_T}{T_\infty}(T_z)^2) \tag{5}$$

$$uC_x + vC_y + wC_z = D_B(C_{zz}) + \frac{D_T}{T_\infty}(T_{zz}) \tag{6}$$

The boundary conditions are

$$\text{at } Z = 0, \quad u = a(x + y)^n, \quad v = b(x + y)^n \; W = 0,$$

$$- kT_z = h_f(T_f - T), \; D_B C_z + \frac{D_T}{T_\infty} T_z = 0 \tag{7}$$

$$\text{as } Z \to \infty, \quad u \to 0, \quad v \to 0, \quad T \to T_\infty, \; C \to C_\infty \tag{8}$$

The similarity functions are

$$\left.\begin{array}{c} \eta = \left(\frac{a(n + 1)}{2\upsilon}\right)^{\frac{1}{2}}(x + y)^{\frac{n-1}{2}} z, \quad v = a(x + y)^n g'(\eta), \\[2mm] u = a(x + y)^n f'(\eta), \quad \theta(\eta) = \frac{T - T_\infty}{T_f - T_\infty}, \; \phi(\eta) = \frac{C - C_\infty}{C_\infty} \\[2mm] w = -\left(\frac{a\upsilon(n + 1)}{2}\right)^{\frac{1}{2}}(x + y)^{\frac{n-1}{2}}\left\{(f + g) + \frac{n - 1}{n + 1}\eta(f' + g')\right\} \end{array}\right\} \tag{9}$$

In view of Eq. (6), the Eqs. (2)–(5) are transformed to

$$\left(\frac{\beta}{1 + \beta}\right)(f + g)f'' + f''' - \left(\frac{\beta}{1 + \beta}\right)M^2 f' - \left(\frac{\beta}{1 + \beta}\right)\frac{2n}{n + 1}(f' + g')f' = 0, \tag{10}$$

$$\left(\frac{\beta}{1 + \beta}\right)(f + g)g'' + g''' - \left(\frac{\beta}{1 + \beta}\right)M^2 g' - \left(\frac{\beta}{1 + \beta}\right)\frac{2n}{n + 1}(f' + g')g' = 0, \tag{11}$$

$$\theta'' + \Pr(Nt\theta'^2 + (f + g)\theta' + Nb\theta'\phi') = 0, \tag{12}$$

$$\phi'' + \frac{Nt}{Nb}\theta'' + Le\Pr(f + g)\phi' = 0, \tag{13}$$

Corresponding boundary conditions are as below

$$\left.\begin{array}{r}g^{'}(0) = \alpha, \, f(0) = 0, \, g(0) = 0, \, f^{'}(0) = 1, \\ \theta^{'}(0) = -\gamma(1 - \theta(0)), \\ \text{Nt}\theta^{'}(0) + \text{Nb}\phi^{'}(0) = 0, \\ g^{'}(\infty) \to 0, \, f^{'}(\infty) \to 0, \, \phi(\infty) \to 0, \, \theta(\infty) \to 0, \end{array}\right\} \quad (14)$$

Moreover, the skin-friction coefficient and Nusselt number are defined as follows

$$\left.\begin{array}{r}(\text{Re}_x)^{1/2} C_{fx} = -\left(\dfrac{n+1}{2}\right)^{\frac{1}{2}} \left(1 + \dfrac{1}{\beta}\right) f''(0), \\[3mm] \left(\text{Re}_y\right)^{1/2} C_{fx} = -\alpha^{-\frac{3}{2}} \left(\dfrac{n+1}{2}\right)^{\frac{1}{2}} \left(1 + \dfrac{1}{\beta}\right) g''(0) \\[3mm] \text{Re}_x^{-\frac{1}{2}} \text{Nu}_x = -\left(\dfrac{n+1}{2}\right)^{\frac{1}{2}} \theta^{'}(0) \end{array}\right\} \quad (15)$$

3 Result Analysis

The coupled system of Eqs. (7)–(9) with associated BC's (10) has been solved computationally. The pictorial results are represented in Figs. 2, 3, 4, 5, 6, 7, 8, and 9 for different parameters on the flow variables.

The impact of Casson parameter on axial, transverse velocities, and temperature is displayed, respectively, in Fig. 2a, b. The velocity of the fluid in both directions
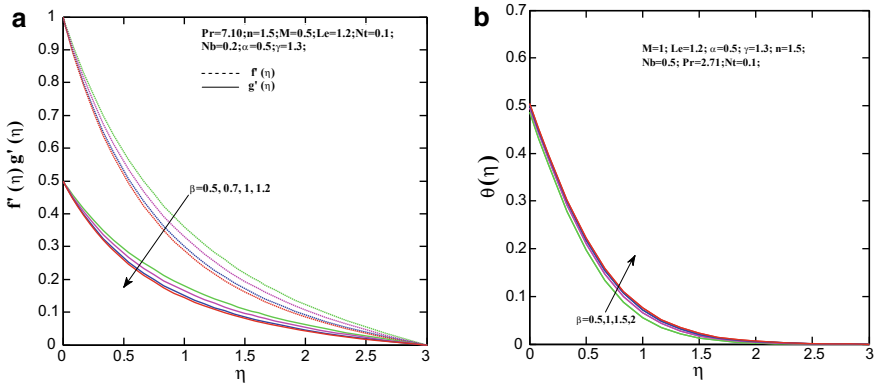
Fig. 2 **a** β on the velocity profiles. **b** β on temperature profiles
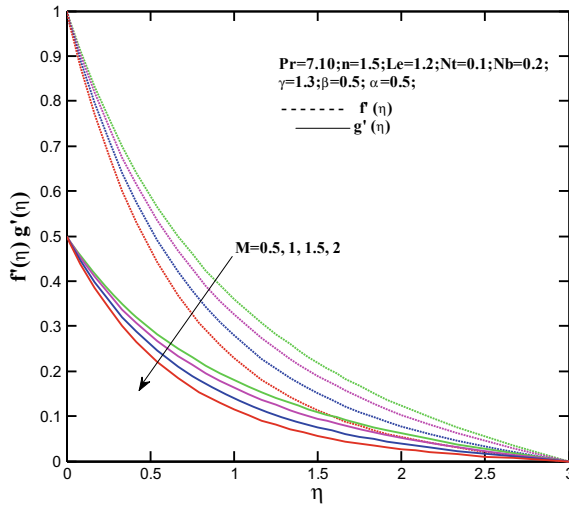
Fig. 3 M on the velocity profiles
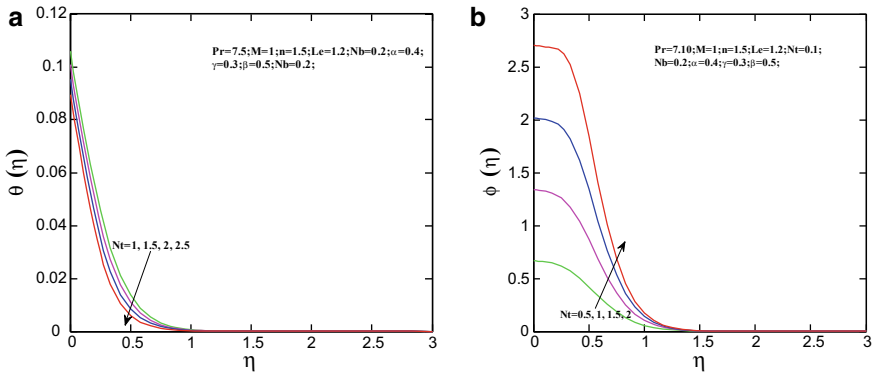
Fig. 4 a Nt on temperature. **b** Nt on concentration

decreases with increasing non-Newtonian Casson parameter. Physically, increasing β will increases the fluid viscosity and hence reduces the fluid velocity. Also, noticed that the axial velocity is more than that of normal velocity of the fluid. On the other hand, the temperature of Casson fluid shows opposite effect.

Figure 3 is the plot of both velocities against magnetic field parameter (M). In the lack of M, both the velocities from its prescribed higher value on the boundary steadily decrease and reach zero value meeting the far upstream condition. Presence of Lorentz force primes to a rapid suppression of the velocity in the vicinity of the boundary due to the action of magnetic field which opposes the liquid motion. Also, the axial velocity of the fluid is more than that of normal velocity.

Fig. 5 Nb on concentration
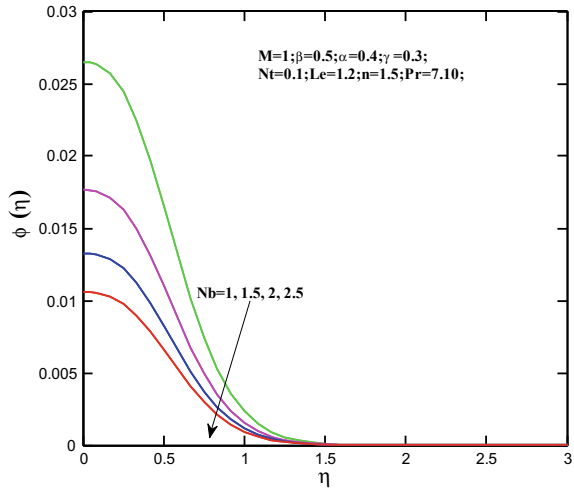
Fig. 6 Le on concentration
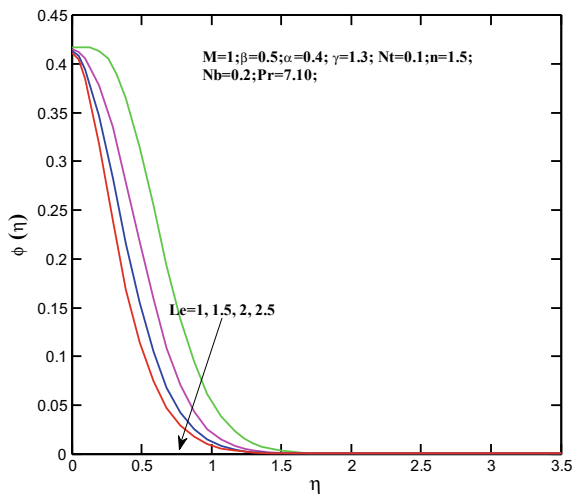
The impact of Nt on $\theta(\eta)$ and $\phi(\eta)$ is, respectively, elucidated in Fig. 4a, b. The growing values of Nt cause a robust temperature and species concentration distributions and more thickness of the thermal and solutal layers. Physically, larger values of Nt cause more thermophoretic force. This is accountable for a maximum moment of nanofluid particles in the ambient fluid.

Figure 5 displays the influence of Nb on concentration profiles. The nanoparticle concentration of the fluid increases with rising values of Nb.

Figure 6 demonstrates the effect of Le on the variations in $\phi(\eta)$. It is noticed that $\phi(\eta)$ is a reducing function of Le. Physically, Lewis number and Brownian
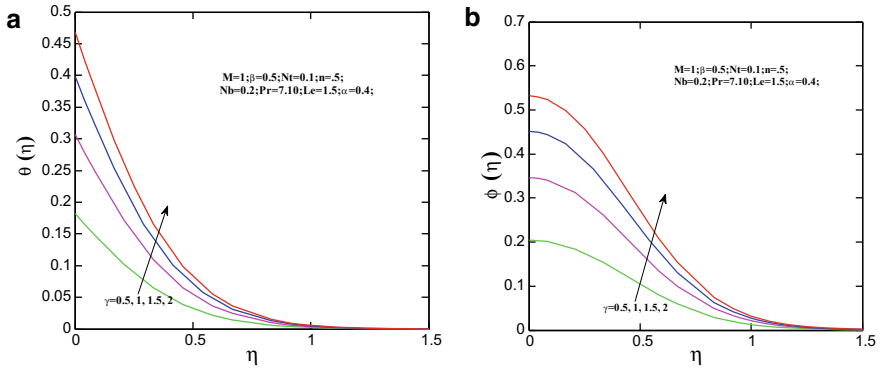
Fig. 7 **a** γ on temperature. **b** γ on concentration
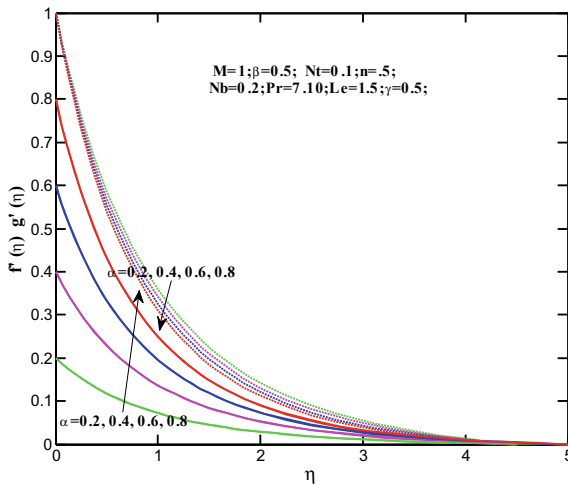
Fig. 8 α on the velocity profiles
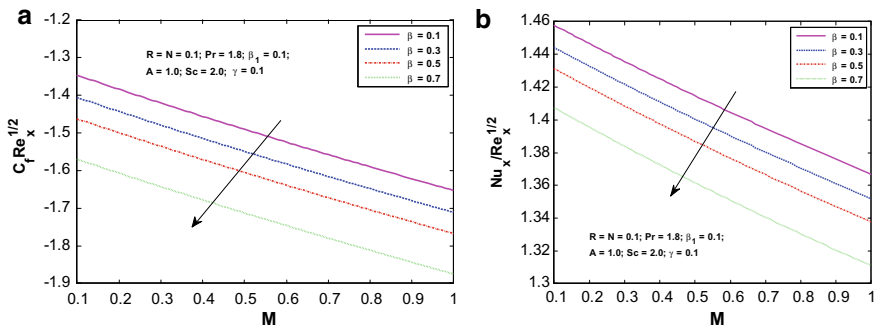
Fig. 9 **a** β on skin friction. **b** β on Nusselt number

diffusivity are related inversely. Hence, by growing Le, the thickness of nanoparticles concentration layer reduces due to decrease in Brownian diffusivity.

The characteristics of γ on the energy and $\phi(\eta)$ are displayed, respectively, in Fig. 7a, b. It is noticed that the both $\theta(\eta)$ and $\phi(\eta)$ variation and hence the thickness of both boundary layers increases with increasing Biot number γ. Physically, increasing γ corresponds to stronger convection.

Figure 8 elucidates to analyze the influence of ratio parameter α on the velocity profiles. The axial velocity decreases and transient velocity of the liquid increases with increasing values of α. Also, the fluid velocity along y-axis is less than that of x-axis.

The skin-friction coefficient and Nusselt number against M for altered values of β are plotted, respectively, in Fig. 9a, b. It is noticed that the all physical quantities are declined for an escalation in M and β.

4 Conclusion

The impact of non-Newtonian nanofluid characteristics on MHD 3D flow over a nonlinear stretched sheet is investigated and main points are listed below.

- $\phi(\eta)$ and $\theta(\eta)$ surge with rising of M.
- $\theta(\eta)$ of the Casson fluid is more than that of viscous fluid.
- Both $\theta(\eta)$ and $\phi(\eta)$ are amplified by rising γ.
- $\theta(\eta)$ and $\phi(\eta)$ are more with rising Nt.
- Larger Nb shows a weaker $\phi(\eta)$ distribution.

References

1. Sulochana C, Ashwinkumar GP, Sandeep N (2016) Similarity solution of 3D Casson nanofluid flow over a stretching sheet with convective boundary conditions. J Nigerian Math Soc 35:128–141
2. Oyelakin IS, Mondal S, Sibanda P (2016) Unsteady Casson nanofluid flow over a stretching sheet with thermal radiation, convective and slip boundary conditions. Alexandria Eng J 55(2):1025–1035
3. Ganesh Kumar K, Ramesh GK, Gireesha BJ, Gorla RSR (2017) Characteristics of Joule heating and viscous dissipation on three-dimensional flow of Oldroyd B nanofluid with thermal radiation. Alexandria Eng J (article in press)
4. Ahmad K, Nazar R, Ishak A, Pop I (2012) Unsteady three-dimensional boundary flow due to a stretching surface in a micropolar fluid. Int J Numer Methods Fuids 68:1561–1573
5. Mahanthesh B, Gireesha BJ, RamaSubbaReddy G (2016) Numerical solutions for magneto hydrodynamic flow of nanofluid over a bidirectional non-linear stretching surface with prescribed surface heat flux boundary. J Magnetism Magnetic Mater 417:189–196
6. Sarojamma G, Lakshmi RV, Satyanarayana PV, Makinde OD (2018) Non linear radiative flow of a micropolar nanofluid through a vertical channel with porous collapsible walls. Defect Diffus Forum 387:498–509

7. Ahmad K, Abdul Halim S, Hanouf Z (2018) Variable viscosity of Casson Fluid flow over a stretching sheet in porous media with newtonian heating. J Inf Math Sci 10:1–2

8. Venkateswarlu B, Satyanarayana PV (2016) Influence of variable thermal conductivity on MHD Casson fluid flow over a stretching sheet with viscous dissipation, Soret and Dufour effects. Frontiers Heat Mass Transf 7(16):1–9

9. Narayana PV, Tarakaramu N, Makinde OD, Venkateswarlu B, Sarojamma G (2018) MHD stagnation point flow of viscoelastic nanofluid past a convectively heated stretching surface. Defect Diffus Forum 387:106–120

10. Satyanarayana PV, Venkateswarlu B (2016) Heat and mass transfer on MHD nanofluid flow past a vertical porous plate in a rotating system. Front Heat Mass Transf (FHMT) 7(1)

11. Narayana PVS, Babu DH (2016) Numerical study of MHD heat and mass transfer of a Jeffrey fluid over a stretching sheet with chemical reaction and thermal radiation. J Taiwan Inst Chem Eng 59:18–25

12. Raju MC, Chamkha AJ, Philip J, Varma SVK (2017) Soret effect due to mixed convection on unsteady magneto hydrodynamic flow past a semi infinite vertical permeable moving plate in presence of thermal radiation, heat absorption. Int J Appl Comput Math 3(2):947–961

13. Kamran S, Hussain A, Sagheer M, Akmal N (2017) A numerical study of magneto hydrodynamics flow in Casson nanofluid combined with Joule heating and slip boundary conditions. Results Phys 7:3037–3048

14. Durgaprasad P, Varma SVK, Hoque MM, Raju CSK (2018) Combined effects of Brownian motion and thermophoresis parameters on three-dimensional (3D) Casson nanofluid flow across the porous layers slendering sheet in a suspension of graphene nanoparticles. Neural Comput Appl, 1–12

15. Haritha A, Sarojamma G (2014) Radiation effect on heat and mass transfer in MHD flow of a Casson fluid over a stretching surface. Int J Sci Inno Math Res 2(6):546–553

Effects of Aligned Magnetic Field and Slip on Peristaltic Flow of a Williamson Fluid in a Flexible Conduit with Porous Medium

G. Sucharitha, G. Yasodhara, S. Sreenadh, and P. Lakshminarayana

Abstract In this paper, we have studied the joint effects of slip and aligned magnetic field on the peristaltic transport of a Williamson fluid in an elastic conduit with porous medium. The basic equations of Williamson fluid model in Cartesian coordinate system are built and simplified by using small Reynolds number and long wave length approximations. The simplified nonlinear equations are solved by adapting the perturbation method. The stream function and the axial velocity expressions are obtained. The impacts of important physical parameters on the flow are shown in graphs and discussed in detail.

Keywords Williamson fluid · Aligned magnetic field · Slip · Peristaltic flow · Flexible conduit · Porous medium

1 Introduction

Peristaltic pumping is very useful technique which happens due to the contractions and relaxations of the wave that propagates along the wall of the channel or tube. This principle involves many biological applications such as food movement through the esophagus, small and large intestine, the bile transport from gallbladder to duodenum, urine transport through ureters and movement of chyme. It has many advantages in industry such as purity of the fluid, accuracy and fluid flow without contaminating the machinery. Many industries are using the peristaltic pumps to transport different types of chemicals, pharmaceutical materials and food products, etc. In view of these uses, several investigators have been studied the peristaltic pumping of different fluids

G. Sucharitha
Department of Mathematics, SITAMS, Chittoor, Andhra Pradesh, India

G. Yasodhara · S. Sreenadh
Department of Mathematics, Sri Venkateswara University, Tirupati, Andhra Pradesh, India

P. Lakshminarayana (✉)
Department of Mathematics, VIT, Vellore, Tamil Nadu, India
e-mail: laxminarayana.pallava@gmail.com

759

under various situations [1–5]. The influence of peristalsis on Williamson fluid flow by considering various conditions is investigated by different authors. [6–10].

Magnetohydrodynamics plays a significant role in medicine and biology. The electromagnetic devices (thermal or non-thermal) are designed which are used in reducing pain, inflammation, muscle heeling potential, diagnostic process, bone healing and ultrasound, etc. The studies with MHD effects are useful to the engineers to design several electromagnetic devices. Very recently, Sucharitha et al. [10, 11] examined the impact of magnetohydrodynamics on peristaltic transport of nanofluids. Krishna murthy et al. [12] studied the MHD effect on three-dimensional flow of a Casson nanofluid. Further, the consequences of wall properties on peristalsis are presented by Srinivas and Kothandapani [13], Radhakrishnamacharya and Srinivasulu [14] and Sucharitha et al. [15].

By keeping the aforesaid observations in mind, we have investigated the influence of slip and the aligned magnetic field on the peristaltic flow of a Williamson fluid in a flexible channel with porous medium. The elementary equations of Williamson model are simplified by using the small Reynolds number and long wave length approximations. Hence, solved the nonlinear governing equations with the help of perturbation technique. The obtained results are explained through graphs.

2 Formulation of the Problem

In this study, we consider the flow of a Williamson fluid through a non-uniform flexible channel with porous medium. The flow is formed by a peristaltic wave which is propagating on the elastic channel walls. The aligned magnetic field is applied. The velocity slip effect is also considered. The expression of the wavy wall is given by (see Fig. 1)

$$H\left(x', t'\right) = d(x) + a\,Sin\frac{2\pi}{\lambda}\left(x' - ct'\right), d(x) = d + m'\,x, \ m' << 1 \qquad (1)$$

Fig. 1 Flow alignment
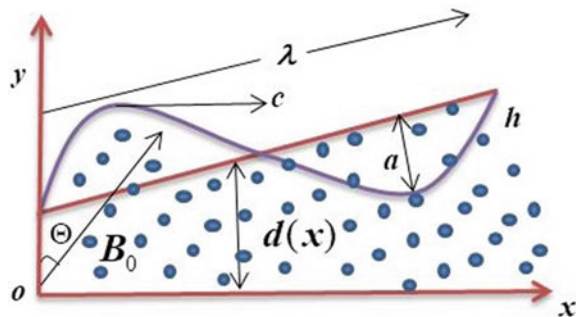
where d, a, λ, c, m' represent the mean width of the channel, amplitude, wavelength, wave speed and dimensional non-uniform parameter, respectively.

The governing equations for the present study are presented as follows (see [6, 7]):

$$\frac{\partial u'}{\partial x'} + \frac{\partial v'}{\partial y'} = 0,$$ (2)

$$\rho \left[\frac{\partial u'}{\partial t'} + u' \frac{\partial u'}{\partial x'} + v' \frac{\partial u'}{\partial y'} \right] = -\frac{\partial p'}{\partial x'} + \frac{\partial \tau'_{x'x'}}{\partial x'} + \frac{\partial \tau'_{x'y'}}{\partial x'} - \sigma B_0{}^2 \cos \Theta (u' \cos \Theta - v' \sin \Theta) - \frac{\mu}{k} u',$$ (3)

$$\rho \left[\frac{\partial v'}{\partial t'} + u' \frac{\partial v'}{\partial x'} + v' \frac{\partial v'}{\partial y'} \right] = -\frac{\partial p'}{\partial y'} + \frac{\partial \tau'_{x'y'}}{\partial x'} + \frac{\partial \tau'_{y'y'}}{\partial x'} + \sigma B_0{}^2 \sin \Theta (u' \cos \Theta - v' \sin \Theta) - \frac{\mu}{k} v',$$ (4)

where $\tau'_{x'x'}, \tau'_{x'y'}, \tau'_{y'y'}$ are the stress components [6], $u', v', \rho, \mu, p, \sigma_0, B_0, k, \Theta$ are the velocities in x- and y-directions, density, viscosity, pressure, electrical conductivity, magnetic field, permeability and inclination angle of the magnetic field, respectively.

We define the stream function (ψ) and non-dimensional quantities as follows:

$$\left. \begin{array}{l} u = \frac{\partial \psi}{\partial y}, v = -\delta \frac{\partial \psi}{\partial x}, x = \frac{x'}{\lambda}, \ y = \frac{y'}{d}, \ \psi = \frac{\psi'}{cd}, \ p = \frac{d^2 p'}{\mu c \lambda}, \ t = \frac{ct'}{\lambda}, \\[2mm] m = \frac{\lambda m'}{d}, \delta = \frac{d}{\lambda}, \varepsilon = \frac{a}{d}, M = \sqrt{\frac{\sigma_0}{\mu}} B_0, \sigma = \frac{d}{\sqrt{k}}, We = \frac{\Gamma c}{d}, \\[2mm] h = \frac{H}{d} = 1 + mx + \varepsilon \sin 2\pi (x - t), E_1 = \frac{-\tau d^3}{\lambda^3 \mu c}, E_2 = \frac{m_1 cd^3}{\lambda^3 \mu}, \\[2mm] \text{Re} = \frac{\rho cd}{\mu}, E_3 = \frac{cd^3}{\lambda^2 \mu}, \tau_{xx} = \frac{\lambda}{\mu c} \tau'_{x'x'}, \tau_{xy} = \frac{d}{\mu c} \tau'_{x'y'}, \tau_{yy} = \frac{\lambda}{\mu c} \tau'_{y'y'} \end{array} \right\}$$ (5)

where $We, M, \text{Re}, E_1, E_2, E_3, m, \sigma, \delta, \varepsilon$ are the Weissenberg number, magnetic parameter, Reynolds number, elasticity parameters, dimension less non-uniform parameter, permeability parameter, wave number and amplitude ratio, respectively.

Using the above dimension less quantities and the approximations of small Reynolds number and long wavelength, the governing equations for this study are obtained as follows:

$$\frac{\partial p}{\partial x} = \frac{\partial}{\partial y} \left[\left(1 + We \frac{\partial^2 \psi}{\partial y^2} \right) \frac{\partial^2 \psi}{\partial y^2} \right] - N^2 \frac{\partial \psi}{\partial y},$$ (6)

where $N^2 = M^2 \cos^2 \Theta + \sigma^2$

$$\frac{\partial p}{\partial y} = 0,$$ (7)

The non-dimensional boundary conditions ([15]) are given by

$$\psi = \frac{\partial^2 \psi}{\partial y^2} = 0 \ \ at \ \ y = 0, \tag{8}$$

$$\frac{\partial \psi}{\partial y} = -\beta \frac{\partial^2 \psi}{\partial y^2} \ \ at \ \ y = h, \tag{9}$$

$$\frac{\partial}{\partial y}\left[\left(1 + We\frac{\partial^2 \psi}{\partial y^2}\right)\frac{\partial^2 \psi}{\partial y^2}\right] - N^2\frac{\partial \psi}{\partial y} = \left(E_3\frac{\partial^2 h}{\partial x \partial t} + E_1\frac{\partial^3 h}{\partial x^3} + E_2\frac{\partial^3 h}{\partial x \partial t^2}\right) \ \ at \ \ y = h, \tag{10}$$

After eliminating pressure term from Eq. (6), we obtain:

$$\frac{\partial^2}{\partial y^2}\left[\left(1 + We\frac{\partial^2 \psi}{\partial y^2}\right)\frac{\partial^2 \psi}{\partial y^2}\right] - N^2\frac{\partial^2 \psi}{\partial y^2} = 0, \tag{11}$$

3 Perturbation Solution

Since the Eq. (11) is nonlinear and its exact solution is very difficult, therefore we are using the perturbation technique with the small Weissenberg number as below:

$$\psi = \psi_0 + We\,\psi_1 + We^2\,\psi_2 + \cdots, \tag{12}$$

3.1 System of Order Zero (We^0) and Solution

$$\frac{\partial^4 \psi_0}{\partial y^4} - N^2\frac{\partial^2 \psi_0}{\partial y^2} = 0, \tag{13}$$

$$\psi_0 = \frac{\partial^2 \psi_0}{\partial y^2} = 0 \ \ at \ \ y = 0, \tag{14}$$

$$\frac{\partial \psi_0}{\partial y} = -\beta\frac{\partial^2 \psi_0}{\partial y^2} \ \ at \ \ y = h, \tag{15}$$

$$\frac{\partial^3 \psi_0}{\partial y^3} - N^2\frac{\partial \psi_0}{\partial y} = \left(E_3\frac{\partial^2 h}{\partial x \partial t} + E_1\frac{\partial^3 h}{\partial x^3} + E_2\frac{\partial^3 h}{\partial x \partial t^2}\right) \ \ at \ \ y = h, \tag{16}$$

By solving the zeroth order system from Eqs. (13)–(16), we obtain the zeroth order stream function and velocity as follows:

$$\psi_0 = C_4 \sinh(Ny) - \frac{C_1 y}{M_0{}^2} \tag{17}$$

$$u_0 = C_4 N \cosh(Ny) - \frac{C_1}{M_0{}^2} \tag{18}$$

3.2 System of Order One (We^1) and Solution

$$\frac{\partial^4 \psi_1}{\partial y^4} - N^2 \frac{\partial^2 \psi_1}{\partial y^2} + \frac{\partial^2}{\partial y^2}\left(\frac{\partial^2 \psi_0}{\partial y^2}\right)^2 = 0, \tag{19}$$

$$\psi_1 = \frac{\partial^2 \psi_1}{\partial y^2} = 0 \ \ at \ y = 0, \tag{20}$$

$$\frac{\partial \psi_1}{\partial y} = -\beta \frac{\partial^2 \psi_1}{\partial y^2} \ \ at \ y = h, \tag{21}$$

$$\frac{\partial^3 \psi_1}{\partial y^3} - N^2 \frac{\partial \psi_1}{\partial y} + \frac{\partial}{\partial y}\left(\frac{\partial^2 \psi_0}{\partial y^2}\right)^2 = \left(E_3 \frac{\partial^2 h}{\partial x \partial t} + E_1 \frac{\partial^3 h}{\partial x^3} + E_2 \frac{\partial^3 h}{\partial x \partial t^2}\right) \ \ at \ y = h, \tag{22}$$

By solving the first-order system from Eqs. (19)–(22), we obtain the first-order stream function and velocity as follows:

$$\psi_1 = 2C_4{}^2 \cosh(Ny) + C_8 \sinh(Ny) - \frac{C_4{}^2}{M_0{}^2} - \frac{C_4{}^2}{2}(1 + \cosh(2Ny)) \tag{23}$$

$$u_1 = 2C_4{}^2 N \sinh(Ny) + C_8 N \cosh(Ny) - C_4{}^2 N \sinh(2Ny) \tag{24}$$

4 Results of the Problem

The impacts of significant parameters of the present study for both Newtonian fluid and Williamson fluid cases are explained with the help of graphs for the fixed values: $t = 0.25$, $\sigma = 1$, $\beta = 0.2$, $m = 0.1$, $We = 0.02$, $x = 0.2$, $\varepsilon = 0.3$, $M = 2$, $\Theta = \frac{\pi}{3}$, $E_3 = 0.1$, $E_2 = 0.2$, $E_1 = 0.3$.

In this study, we have investigated both Newtonian and Williamson fluids. Further, the flow in an uniform non-porous channel also covered by taking $m = \sigma = 0$. It is observed that the velocity of the Williamson fluid is more than Newtonian fluid

and the same behavior is observed in the study of Hayat et al. [2]. Also noticed that velocity profiles are parabolic. Figure 2 depicts that the increase in amplitude ratio increases the velocity in the midway of the channel, and the velocity profiles coincide at the channel walls. Figure 3 shows that the rise in m (non-uniform parameter) enhances the velocity throughout the channel. From Fig. 4, we found that the growth in M (magnetic parameter) reduces the velocity. Physically, the magnetic force generates a force which works against the fluid velocity. Figure 5 describes that the increment in Θ (inclination angle of magnetic field) enhances the velocity, and this result is agreed with the existing works (Ramesh [3] and Jagadeesh et al. [4]). Figure 6 shows that the large values of permeability parameter decline the velocity.

Figure 7 depicts that the large values of slip parameter (β) improve the velocity (generally slip diminishes the friction between the channel wall and the fluid). From Figs. 8, 9 and 10, we noticed that the velocity is a decreasing function of wall parameters (wall tension parameter (E_1), the mass characterization parameter (E_2) and the damping force parameter (E_3)). We have validated our results with the previous study Hayat et al. [2] in Fig. 11. It shows that the results of the present study in a uniform non-porous channel without slip are in good agreement with the study of

Fig. 2 Velocity profiles for different values of ε
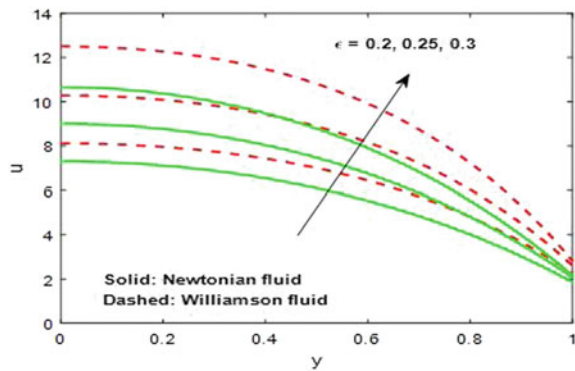
Fig. 3 Velocity profiles for different values of m
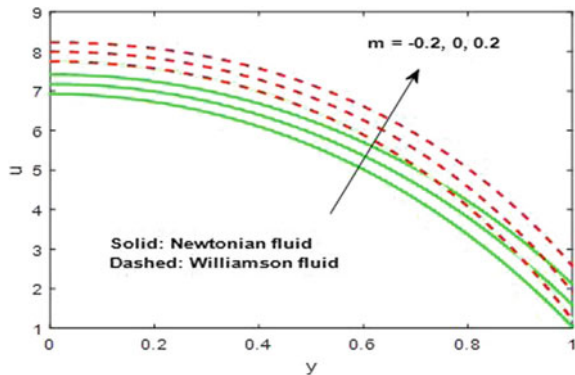
Fig. 4 Velocity profiles for different values of M
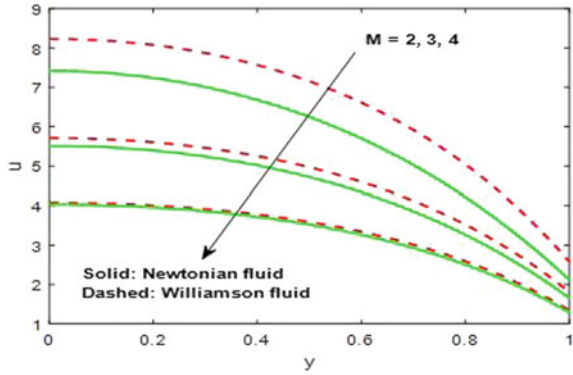
Fig. 5 Velocity profiles for different values of Θ
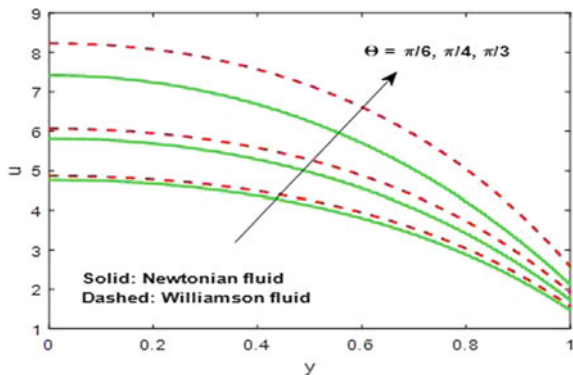
Fig. 6 Velocity profiles for different values of σ
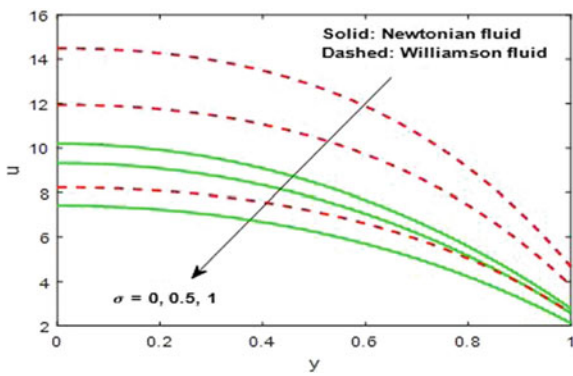
Fig. 7 Velocity profiles for different values of β
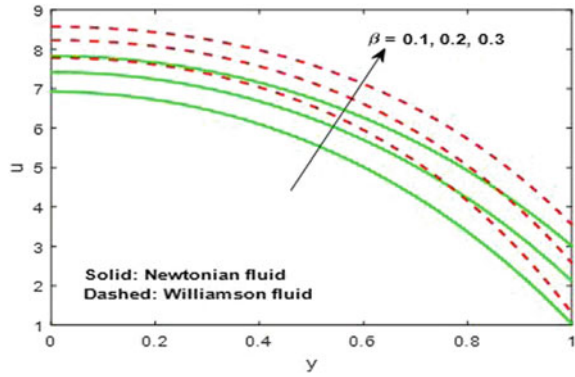
Fig. 8 Velocity profiles for different values of E_1
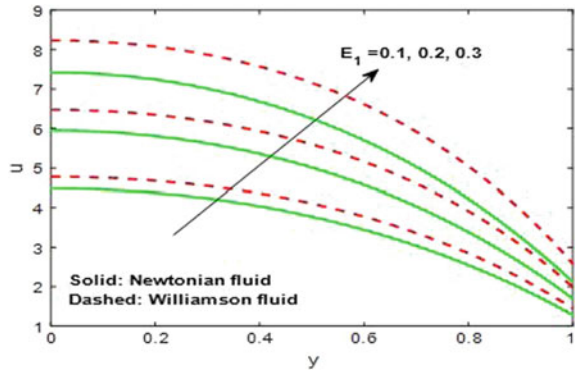
Fig. 9 Velocity profiles for different values of E_2
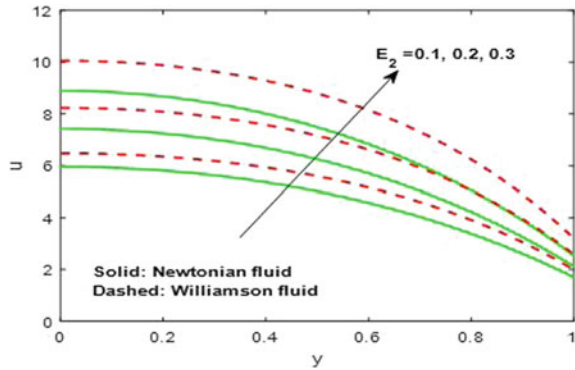
Fig. 10 Velocity profiles for different values of E_3
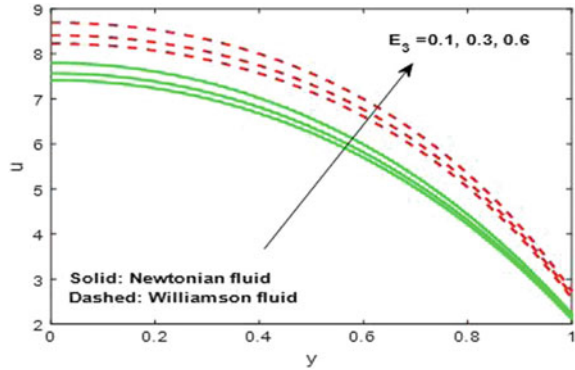
Fig. 11 Validation with previous results
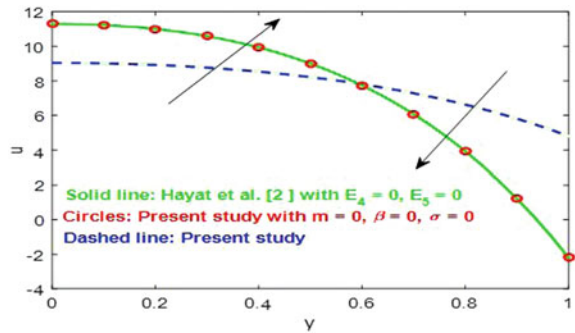
Hayat et al. [2]. Further, in the present study, we have noticed that the velocity is reduced in the middle of the channel due to the porous medium and it is increased with the increase in velocity slip.

5 Trapping Phenomenon

The important trapping phenomenon is discussed for different values of the pertinent parameters, and it is shown in figures from Figs. 12, 13, 14, 15 and 16. The size of the trapped bolus is decreased for the large values of M, σ and We. The increase in Θ and β reduces the size of trapped bolus.
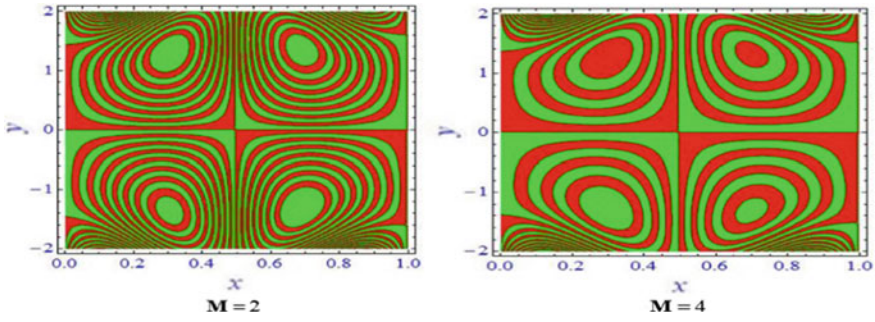
Fig. 12 Magnetic parameter effect on trapping
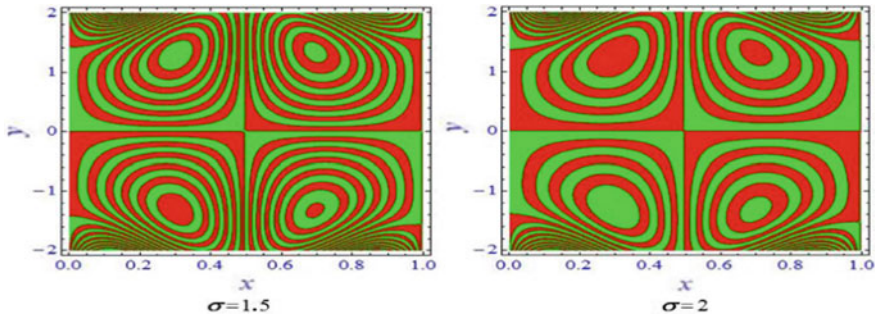
Fig. 13 Permeability parameter effect on trapping
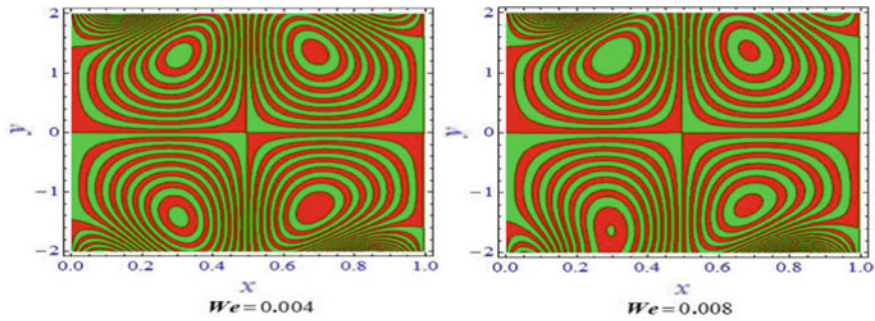
Fig. 14 Williamson fluid parameter effect on trapping
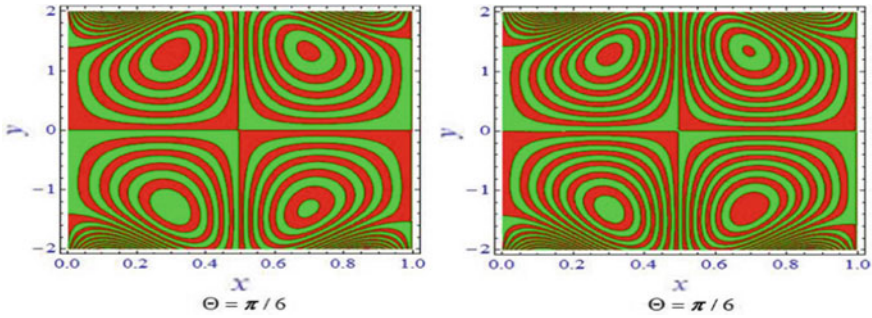
Fig. 15 Inclination angle of magnetic field effect on trapping
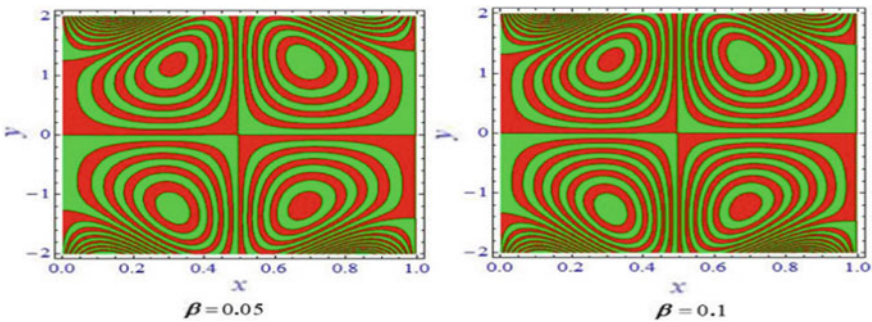
Fig. 16 Slip parameter effect on trapping

References

1. Vajravelu K, Sreenadh S, Dhananjaya S, Lakshminarayana P (2016) Peristaltic flow and heat transfer of a conducting phan-thien-tanner fluid in an asymmetric channel - application to chyme movement in small intestine: Int. J Appl Mech Eng 21(3):713–736
2. Sucharitha G, Sreenadh S, Lakshminarayana P (2012) Non-linear peristaltic transport of a conducting prandtl fluid in a porous asymmetric channel. Int J Eng Res Technol 1(10):1–10
3. Ramesh K (2016) Influence of heat and mass transfer on peristaltic flow of a couple stress fluid through porous medium in the presence of inclined magnetic field in an inclined asymmetric channel. J Molec Liquids 219:256–271
4. Lakshminarayana P, Sreenadh S, Sucharitha G (2012) Peristaltic pumping of a conducting fluid in a channel with a porous peripheral layer. Adv Appl Sci Res 3:2890–2899
5. Ellahi R, Bhatti MM, Riaz A, Sheikholeslami M (2014) Effects of magnetohydrodynamics on the peristaltic flow of Jeffrey fluid in a rectangular duct through a porous medium. J Porous Med 17:143–157
6. Vajravelu K, Sreenadh S, Rajanikanth K (2012) Changhoon Lee: Peristaltic transport of a Williamson fluid in asymmetric channels with permeable walls. Nonlinear Anal: Real World Appl 13:2804–2822
7. Hayat T, Bibi S, Rafiq M, Alsaedi A, Abbasi FM (2016) Effect of an inclined magnetic field on peristaltic flow of Williamson fluid in an inclined channel with convective conditions. J Mag Mag Mater 401:733–745 (2016)

8. Nadeem S, Akram S (2010) Peristaltic flow of a Williamson fluid in an asymmetric channel. Commun Nonlinear Sci Numer Simulat 15:1705–1716
9. Akram S, Nadeem S, Hanif M (2013) Numerical and analytical treatment on peristaltic flow of Williamson fluid in the occurrence of induced magnetic field. J Mag Mag Mater 346:142–151
10. Sucharitha G, Lakshminarayana P, Sandeep N (2019) MHD and cross diffusion effects on peristaltic flow of a Casson nanofluid in a duct. Appl Math Sci Comput 191–201
11. Sucharitha G, Vajravelu K, Lakshminarayana P (2019) Magnetohydrodynamic nanofluid flow in a non-uniform aligned channel with joule heating. J Nanofluids 8(7):1373–1384
12. Krishna Murthy M, Sreenadh S, Lakshminarayana P, Sucharitha G, Rushikumar B (2019) Thermophoresis and Brownian motion effects on three dimensional MHD slip flow of a Casson nanofluid over an exponentially stretching surface. J Nanofluids 8(6):1267–1272
13. Srinivas S, Kothandapani M (2009) The influence of heat and mass transfer on MHD peristaltic flow through a porous space with compliant walls. Appl Math Comput 213:197–208
14. Radhakrishnamacharya,G., Srinivasulu, Ch.: Influence of wall properties on peristaltic transport with heat transfer. C.R.Mec. **335**, 369-373 (2007)
15. Sucharitha G, Rashidi MM, Sreenadh S, Lakshminarayana P (2018) Effects of magnetic field and slip on convective peristaltic flow of a non-Newtonian fluid in an inclined nonuniform porous channel with flexible walls. J Porous Media 21(10):895–910

Influence of Electromagnetic Force on the Blood Flow in an Asymmetric Channel with Heat Dissipation

R. Latha and B. Rushi Kumar

Abstract The present article examines the magnetohydrodynamic blood flow in an asymmetric channel with heat dissipation. The exact solutions for the velocity, pressure gradient and temperature are provided for both the cases such as the presence and absence of electromagnetic force under the long wavelength and low Reynolds number assumptions. The pressure rise expression has been computed using numerical integration. The graphical results have been presented to analyze the physical behavior of various physical parameters of interest. The present study reveals that the higher values of pressure gradient and axial velocity appears in the presence of electromagnetic force as compared with an absence of electromagnetic force. This result highlights that electromagnetic force is useful for strengthening the pressure gradient and velocity of fluid. The physiologists use the concept of electromagnetic or magnetic forces to maintain the pressure gradient levels in patients. The role of the heat exchange coefficient may control body temperature.

Keywords Peristaltic propulsion · Couple stress fluid · Electromagnetic force · Slip boundary condition

1 Introduction

Rheological fluid can move from one place to another place with extraordinary mechanism known as peristalsis. Over the past few decades, the peristaltic system has picked up the unique consideration of specialists because of its various applications in complex rheological fluids. The peristaltic mechanism can be seen in many natural organs, for example, transport of food bolus in esophagus, pee spill out of kidney to bladder over ureter, the ovum transport in female fallopian tube, bile flow from bladder to the duodenum, spermatozoa development in the conduit efferent of the male conceptive tract and bloodstream in little veins. In addition, this has abuse in

R. Latha · B. Rushi Kumar (✉)
Department of Mathematics, School of Advanced Sciences, VIT, Vellore 632 014,
Tamil Nadu, India
e-mail: rushikumar@vit.ac.in

modern fluid mechanical and biomechanical instruments, for example, finger pump, hose pump, a heart–lung machine, blood pump machine and dialysis machine. Couple stress fluids have increased much consideration because of its wide applications in different physical issues. The couple stress fluid model can anticipate the qualities of blood flows and oils. Stokes has given a detailed theory of couple stress fluid in 1966 to depict the polar impacts.

Initially, Latham [1] and Shapiro et al. [2] have examined the peristaltic transport of viscous fluid. Later on these studies, many investigators focused their work in the field of peristaltic mechanisms. Ali et al. [3] have explored the peristaltic transport of a Maxwell fluid in an asymmetric channel. Hayat et al. [4, 5] have focused their study on the Jeffrey model with the peristaltic transport of viscoelastic fluid and the peristaltic transport of viscoelastic fluid with the impact of relaxation and retardation time. In addition, Hayat et al. [6] have studied the flow of a viscoelastic fluid by utilizing Burgers model. Tripathi et al. [7] have researched the fractional Maxwell model with the peristaltic transport of viscoelastic fluids over an alternate channel. They used Adomian decay strategy and the homotopy technique to find the solution of the problem. Tripathi [8] conducted a numerical review on the crawling transport of Burgers' fluids under the impact of MHD over a peristaltic tube. Li et al. [9] have proposed a reversed-phase elite fluid chromatography method for the synchronous quantitation of the lactone and carboxylate types of the novel normal item anticancer operator 10-hydroxycamptothecin in biological fluids and tissues. He et al. [10] have studied the impact of immediate blood pressure lessening on death and real disability in patients with intensive ischemic stroke using the CATIS randomized clinical trial. Yang et al. [11] have examined the efficient induction of pluripotent stem cells from menstrual blood. Liang et al. [12] have explored the coupling mechanism of dew point corrosion and viscous ash deposits at different temperature ranges with applications to engineering. Ramesh [13] inspected the slip and convective conditions on the peristaltic flow of couple stress fluid in an asymmetric channel over a permeable medium. Bergmann et al. [14] have explored the frictional heating of total hip implants and measurements in patients. Philippe et al. [15] have examined how the intrinsic viscoelasticity increases the body temperature in knee cartilage under physiological loading. Some of the relevant approaches in peristaltic mechanism can be referred from [16–42] and the references therein.

In the present study, we found that the couple stress fluid and its viscosity play an important role in human active joints. The role of the heat exchange coefficient in total hip replacement, where it may be controlled at body temperature (approx. 37 degrees Celsius), may not mimic the rising and falling temperature that pertained to such varying levels in alive joint activity. It is important to examine the existing mathematical examination in order to highlight the essential nature of the peristaltic movement of a couple stress fluids with the impact of magnetohydrodynamic in an asymmetric channel, which follows peristaltic waves of different amplitudes and phases. The present study is important in realizing blood flow by considering the molecule size effect. The precise result is inferred on the premise that the diameter of wavelength is large and the relevant Reynolds number is small enough for inertia; these conditions be reasonably well met in the human ureter and, to a lesser extent,

in the gastrointestinal tract and in mechanical roller pumps using viscous fluids. Graphical results for the fluid velocity and the temperature of fluid have been examined. The dimensionless expressions of the heat exchange coefficient are additionally examined in detail.

2 Mathematical Formulation

2.1 Case I: In the Absence of Electromagnetic Force

This study considers the peristaltic movement of electrically conducting couple stress fluid in a channel of width. The walls of the channel are adaptable, which are taken as an extended membrane with viscous damping forces. The x-axis and y-axis are along and opposite the channel walls, separately. A uniform applied magnetic field of strength acts in the y-direction (see Fig. 1). The waveform along the walls is characterized as

$$H_1(X', t') = d_1 + a_1 \cos \frac{2\pi}{\lambda}(X' - ct') \tag{1}$$

$$H_2(X', t') = -d_2 - a_2 \cos \left[\frac{2\pi}{\lambda}(X' - ct') + \theta \right] \tag{2}$$

whereas a_1, a_2, λ, c and θ are the wave amplitudes, the wavelength, the wave speed and the phase difference, respectively. θ is the phase difference varying in the range $(0 \leq \theta \leq \pi)$. It must be noticed that $\theta = 0$ corresponds to the symmetric channel on waves out of phase and for $\theta = \pi$ the waves in phase.

Using the following transformations
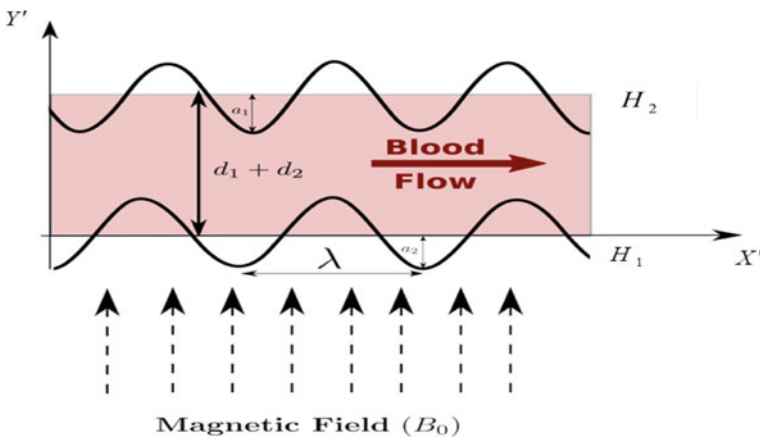
Fig. 1 Schematic diagram of the problem

$$x' = X' - ct', \quad y' = Y', \quad u_1' = U' - c, \quad v_1' = V', \quad p'(x) = \bar{P}(X, t) \quad (3)$$

where p and P' are pressures in wave and fixed frame, respectively, and (u_1', v_1') are the velocity components in the wave frame (x', y'). The governing equations of fluid motion in the wave frame become

$$\frac{\partial u_1'}{\partial x'} + \frac{\partial v_1'}{\partial y'} = 0 \quad (4)$$

$$\rho \left\{ u_1' \frac{\partial u_1'}{\partial x'} + v_1' \frac{\partial u_1'}{\partial y'} \right\} = -\frac{\partial p_1'}{\partial x'} + \mu \nabla^2 u_1' - \eta \nabla^4 u_1' - \sigma' B_0^2 u_1' \quad (5)$$

$$\rho \left\{ u_1' \frac{\partial v_1'}{\partial x'} + v_1' \frac{\partial v_1'}{\partial y'} \right\} = -\frac{\partial p'}{\partial y'} + \mu \nabla^2 v_1' - \eta \nabla^4 v_1' \quad (6)$$

$$\rho \xi \left[u_1' \frac{\partial T'}{\partial x'} + v_1' \frac{\partial T'}{\partial y'} \right] = k \left(\frac{\partial^2 T'}{\partial x'^2} + \frac{\partial^2 T'}{\partial y'^2} \right)$$
$$+ \mu \left[2 \left\{ \left(\frac{\partial u_1'}{\partial x'} \right)^2 + \left(\frac{\partial v_1'}{\partial y'} \right)^2 \right\} + \left(\frac{\partial u_1'}{\partial y'} + \frac{\partial v_1'}{\partial x'} \right)^2 \right] \quad (7)$$
$$+ \eta \left[\left(\frac{\partial^2 v_1'}{\partial x'^2} + \frac{\partial^2 v_1'}{\partial y'^2} \right)^2 + \left(\frac{\partial^2 u_1'}{\partial x'^2} + \frac{\partial^2 u_1'}{\partial y'^2} \right)^2 \right]$$

ξ is the specific heat at the constant temperature, η is the couple stress fluid parameter, μ is the fluid viscosity, σ is electrical conductivity of the fluid, u_1' and v_1' are the velocity of the fluid particle, B_0 is the applied magnetic field, ρ is the density of the fluid. The corresponding boundary conditions are

$$u_1' + \beta \left(\frac{\partial u_1'}{\partial y'} - \frac{1}{\gamma^2} \frac{\partial^3 u_1'}{\partial y'^3} \right) = -1, \quad v_1' = \frac{dh_1'}{dx'},$$
$$- \left(\delta^4 \frac{\partial^2 v_1'}{\partial x'^2} - \delta^2 \frac{\partial^2 u_1'}{\partial x' \partial y'} \right) \frac{dh_1'}{dx'} + \delta^2 \frac{\partial^2 v_1'}{\partial x' \partial y'} - \frac{\partial^2 u_1'}{\partial y'^2} = 0 \quad at \ y' = h_1' \quad (8)$$

$$u_1' + \beta \left(\frac{\partial u_1'}{\partial y'} - \frac{1}{\gamma^2} \frac{\partial^3 u_1'}{\partial y'^3} \right) = -1, \quad v_1' = \frac{dh_2'}{dx'},$$
$$- \left(\delta^4 \frac{\partial^2 v_1'}{\partial x'^2} - \delta^2 \frac{\partial^2 u_1'}{\partial x' \partial y'} \right) \frac{dh_2'}{dx'} + \delta^2 \frac{\partial^2 v_1'}{\partial x' \partial y'} - \frac{\partial^2 u_1'}{\partial y'^2} = 0 \quad at \ y' = h_2' \quad (9)$$

Consider the following non-dimensional variables,

$$x = \frac{x'}{\lambda}, \quad y = \frac{y'}{d_1}, \quad u_1 = \frac{u_1'}{c}, \quad v_1 = \frac{\lambda v_1'}{d_1 c}, \quad p = \frac{d_1^2}{\lambda \mu c} \bar{p}, \quad t = \frac{ct'}{\lambda},$$
$$Re = \frac{\rho c d_1}{\mu}, \quad M_1 = \sqrt{\frac{\sigma}{\mu}} B_0 d_1, \quad \delta = \frac{d_1}{\lambda}, \quad h_1 = 1 + a \cos 2\pi x,$$
$$h_2 = -d - b \cos(2\pi x + \varphi) \, a = \frac{a_1}{d_1}, \quad b = \frac{a_2}{d_1}, \quad d = \frac{d_1}{d_2}, \quad Re = \frac{c d_1}{v}, \quad (10)$$
$$\theta = \frac{T - T_s}{T_1 - T_s}, \quad Ec = \frac{c^2}{\xi(T_1 - T_s)}, \quad \gamma = \sqrt{\frac{\mu}{\eta}} d_1, \quad Pr = \frac{\mu \xi}{k}$$

where T_s is the temperature of fluid (static condition), β is the partial slip parameter, Re is the Reynolds number, δ is the dimensionless wave number, Pr is the Prandtl

number, Ec is the Eckert number and $\gamma(\gamma > 0)$ is the couple stress fluid parameter showing the proportion of the channel width to material characteristic length. The non-dimensional equations of governing equations of the continuity, momentum and energy equations for unsteady two-dimensional case are

$$\frac{\partial u_1}{\partial x} + \frac{\partial v_1}{\partial y} = 0 \tag{11}$$

$$Re\delta \left\{ u_1 \frac{\partial u_1}{\partial x} + v_1 \frac{\partial v_1}{\partial y} \right\} = -\frac{\partial p_1}{\partial x} + \nabla^2 u_1 - \frac{1}{\gamma^2} \nabla^4 u_1 - M_1^2 u_1 \tag{12}$$

$$Re\delta^3 \left\{ u_1 \frac{\partial v_1}{\partial x} + v_1 \frac{\partial v_1}{\partial y} \right\} = -\frac{\partial p_1}{\partial y} + \delta^2 \nabla^2 u_1 - \frac{\delta^2}{\gamma^2} \nabla^4 u_1 \tag{13}$$

$$Pr\,\delta Re \left[u_1 \frac{\partial \theta_1}{\partial x} + v_1 \frac{\partial \theta_1}{\partial y} \right] = \delta^2 \frac{\partial^2 \theta_1}{\partial x^2} + \frac{\partial^2 \theta_1}{\partial y^2}$$
$$+ Pr\,Ec \left\{ \begin{array}{l} 2\delta^2 \left\{ \left(\frac{\partial u_1}{\partial x}\right)^2 + \left(\frac{\partial v_1}{\partial y}\right)^2 \right\} + \left(\frac{\partial u_1}{\partial y} + \delta^2 \frac{\partial v_1}{\partial x}\right)^2 \\ + \frac{1}{\gamma^2} \left[\delta^2 \left(\frac{\partial^2 v_1}{\partial x^2} + \frac{\partial^2 v_1}{\partial y^2}\right)^2 + \left(\frac{\partial^2 u_1}{\partial y^2} + \delta^2 \frac{\partial^2 u_1}{\partial x^2}\right)^2 \right] \end{array} \right\} \tag{14}$$

Under lubrication approach (inertia free small Reynolds number $Re \to 0$ and width of wavelength is large $\delta \ll 1$)
The Eqs. (11)–(14) reduce to

$$\frac{\partial p_1}{\partial x} = \frac{\partial^2 u_1}{\partial y^2} - \frac{1}{\gamma^2} \frac{\partial^4 u_1}{\partial y^4} - M_1^2 u_1 \tag{15}$$

$$\frac{\partial p_1}{\partial y} = 0 \tag{16}$$

$$\frac{\partial^2 \theta_1}{\partial y^2} + Pr\,Ec \left\{ \left(\frac{\partial u_1}{\partial y}\right)^2 + \frac{1}{\gamma^2} \left(\frac{\partial^2 u_1}{\partial y^2}\right)^2 \right\} = 0 \tag{17}$$

with the boundary conditions

$$u_1 + \beta \left(\frac{\partial u_1}{\partial y} - \frac{1}{\gamma^2} \frac{\partial^3 u_1}{\partial y^3} \right) = -1 \,, \quad v_1 = \frac{\partial h_1}{\partial x}, \quad \frac{\partial^2 u_1}{\partial y^2} = 0, \quad at \quad y = h_1 = 1 + a \cos 2\pi x \tag{18}$$

$$u_1 - \beta \left(\frac{\partial u_1}{\partial y} - \frac{1}{\gamma^2} \frac{\partial^3 u_1}{\partial y^3} \right) = -1,$$

$$v_1 = \frac{\partial h_2}{\partial x}, \quad \frac{\partial^2 u_1}{\partial y^2} = 0, \quad at \ \ y = h_2 = -d - b\cos(2\pi x + \varphi) \qquad (19)$$

$$\theta_1 = 1 \ \ at \ \ y = h_1, \qquad \theta_1 = 0 \ \ at \ \ y = h_2 \qquad (20)$$

The solution of Eq. (14) valid in $h_2 \leq y \leq h_1$ satisfying the corresponding boundary conditions (17) is given by

$$u_1 = A\cosh m_1 y + B\sinh m_1 y + C\cosh m_2 y + D\sinh m_2 y - G \qquad (21)$$

The corresponding stream function is obtained as

$$\psi_1 = \frac{A}{m_1}\sinh m_1 y + \frac{B}{m_1}\cosh m_1 y + \frac{C}{m_2}\sinh m_2 y + \frac{D}{m_2}\cosh m_2 y - Gy \qquad (22)$$

To determine the temperature, substitute Eq. (18) in Eq. (16), and using the corresponding boundary conditions, we get

$$\theta_1 = -\Pr Ec \left\{ \frac{m_1^2 E^2}{2} \left[\frac{y^2}{2}\left(1 + \frac{m_1^2}{\gamma^2}\right) + \frac{\cosh 2\left(\frac{(h_1+h_2)m_1}{2} - m_1 y\right)}{4m_1^2}\left(-1 + \frac{m_1^2}{\gamma^2}\right) \right] \right.$$
$$+ \frac{m_2^2 F^2}{2}\left[\frac{y^2}{2}\left(1 + \frac{m_2^2}{\gamma^2}\right) + \frac{\cosh 2\left(\frac{(h_1+h_2)m_2}{2} - m_2 y\right)}{4m_2^2}\left(-1 + \frac{m_2^2}{\gamma^2}\right) \right]$$
$$\left. - m_1 m_2 EF \left[\begin{array}{l} \frac{\cosh\frac{(h_1+h_2-2y)(m_1+m_2)}{2}}{(m_1+m_2)^2}\left(1 + \frac{m_1 m_2}{\gamma^2}\right) + \\ \frac{\cosh\frac{(h_1+h_2-2y)(m_1-m_2)}{2}}{(m_1-m_2)^2}\left(-1 + \frac{m_1 m_2}{\gamma^2}\right) \end{array} \right] \right\} + Hy + I \qquad (23)$$

The dimensionless mean flow Q is defined by [16]

$$Q = f + 1 + d \qquad (24)$$

where

$$f = \int_{h_1}^{h_2} u \, dy \qquad (25)$$

From Eqs. (18) and (22), the expression for pressure gradient is determined as

$$\frac{dp}{dx} = \frac{M^2 (a_1 + a_2)}{a_3 + a_4} \qquad (26)$$

The non-dimensional expression for the pressure rise per wavelength ΔP is defined as

$$\Delta P = \int_0^1 \left(\frac{dp}{dx}\right) dx. \tag{27}$$

2.2   Case II: In the Presence of Electromagnetic Force

Consider the peristaltic flow of an incompressible electrically conducting couple stress fluid in a two-dimensional channel. A uniform transverse magnetic field of strength H_0' offer increment to an induced magnetic field $H'(h'_{x'}(x', y', t'), h'_{y'}(x', y', t'), 0)$, and the total of the magnetic field will be $H'^+(h'_{x'}(x', y', t'), H_0' + h'_{y'}(x', y', t'), 0)$. Let b, λ, c and t' are the wave amplitude, the wavelength, wave speed, and the time, respectively. The non-dimensional equations are directly written as [10]

$$\frac{\partial u}{\partial x} + \frac{\partial v}{\partial y} = 0 \tag{28}$$

$$\frac{\partial p}{\partial x} = \frac{\partial^2 u}{\partial y^2} - \frac{1}{\gamma^2}\frac{\partial^4 u}{\partial y^4} + ReS^2\frac{\partial(h_x)}{\partial y}, \tag{29}$$

$$\frac{\partial^2 \theta}{\partial y^2} + Pr\,Ec\left\{\left(\frac{\partial u}{\partial y}\right)^2 + \frac{1}{\gamma^2}\left(\frac{\partial^2 u}{\partial y^2}\right)^2\right\} = 0 \tag{30}$$

$$\frac{\partial p}{\partial y} = 0 \tag{31}$$

$$u + \frac{1}{Rm}\frac{\partial hx}{\partial y} = E, \tag{32}$$

in which E is electromagnetic force. Dimensionless boundary conditions are

$$u = -1, \quad \frac{\partial^2 u}{\partial y^2} = 0, \quad at \quad y = h_1 = 1 + a\cos 2\pi x \tag{33}$$

$$u = -1, \quad \frac{\partial^2 u}{\partial y^2} = 0, \quad at \quad y = h_2 = -d - b\cos(2\pi x + \varphi) \tag{34}$$

$$\theta = 1 \;\; at \;\; y = h_1, \qquad \theta = m \;\; at \;\; y = h_2 \tag{35}$$

From Eqs. (26) and (29), we get

$$\frac{\partial p}{\partial x} = \frac{\partial^2 u}{\partial y^2} - \frac{1}{\gamma^2}\frac{\partial^4 u}{\partial y^4} + \mathrm{Re}S^2(E - u)Rm \tag{36}$$

$$\frac{\partial^2 \theta}{\partial y^2} + \mathrm{Pr}\, Ec\left\{\left(\frac{\partial u}{\partial y}\right)^2 + \frac{1}{\gamma^2}\left(\frac{\partial^2 u}{\partial y^2}\right)^2\right\} = 0 \tag{37}$$

The exact solution of equation (31) can be written as

$$u = A_1\cosh(m_1 y) + B_1\sinh(m_1 y) + C_1\cosh(m_2 y) + D_1\sinh(m_2 y) + G_1 \tag{38}$$

In the above equations, magnetic Reynolds number $(Rm = \sigma\mu_e ac)$, Reynolds number $\left(\mathrm{Re} = \frac{cd_1\rho}{\mu}\right)$, couple stress parameter $\left(\gamma = \sqrt{\frac{\mu}{\eta}}d_1\right)$, Strommer's number (magnetic force number)

$$\left(S = \frac{H_0}{c}\sqrt{\frac{\mu_e}{\rho}}\right),$$

H_0 is constant magnetic field and μ_e is magnetic permeability. The corresponding stream function, pressure gradient and temperature solutions are

$$\psi = \frac{A_1}{m_1}\sinh(m_1 y) + \frac{B_1}{m_1}\cosh(m_1 y) + \frac{C_1}{m_2}\sinh(m_2 y) + \frac{D_1}{m_2}\cosh(m_2 y) + G_1 y \tag{39}$$

$$\frac{dp}{dx} = \frac{m_1 m_2 M^2(m_1^2 - m_2^3)}{a_{61}}[F - E(h_1 - h_2) + a_{71} + a_{81} + a_{91} + a_{101}] \tag{40}$$

$$\theta = -\mathrm{Pr}\, Ec\left\{\frac{m_1^2 F_1^2}{2}\left[\frac{y^2}{2}\left(-1 + \frac{m_1^2}{\gamma^2}\right) + \frac{\cosh 2\left(\frac{(h_1+h_2)m_1}{2} - m_1 y\right)}{4m_1^2}\left(1 + \frac{m_1^2}{\gamma^2}\right)\right]\right.$$
$$+ \frac{m_2^2 H_1^2}{2}\left[\frac{y^2}{2}\left(-1 + \frac{m_2^2}{\gamma^2}\right) + \frac{\cosh 2\left(\frac{(h_1+h_2)m_2}{2} - m_2 y\right)}{4m_2^2}\left(1 + \frac{m_2^2}{\gamma^2}\right)\right]$$
$$\left.-m_1 m_2 F_1 H_1\left[\begin{array}{l}\frac{\cosh\frac{(h_1+h_2-2y)(m_1+m_2)}{2}}{(m_1+m_2)^2}\left(1 + \frac{m_1 m_2}{\gamma^2}\right)\\ +\frac{\cosh\frac{(h_1+h_2-2y)(m_1-m_2)}{2}}{(m_1-m_2)^2}\left(-1 + \frac{m_1 m_2}{\gamma^2}\right)\end{array}\right]\right\} + I_1 y + J_1 \tag{41}$$

From Eq. (29), we get the magnetic force characteristic inside the shape

$$\frac{\partial^2 \phi}{\partial y^2} = (E - u)Rm \tag{42}$$

The corresponding boundary situations

$$\phi = 0 \ \ at \ \ y = 0 \, and \, y = h \tag{43}$$

Equation (37) satisfying the boundary condition (38) can be written as

$$\phi = Rm \left[\frac{1}{M^2} \frac{\partial P}{\partial x} \frac{y^2}{2} - \left(\frac{A_1 \cosh m_1 y}{m_1^2} + \frac{B_1 \sinh m_1 y}{m_1^2} + \frac{C_1 \cosh m_2 y}{m_2^2} + \frac{D_1 \sinh m_2 y}{m_2^2} \right) \right] + c_1 y + c_2$$

(44)

The formulation of axial induced magnetic field is given by

$$hx(x, y) = \left[\frac{1}{M^2} \frac{dp}{dx} y - \left(\frac{A_1 \sinh m_1 y}{m_1} + \frac{B_1 \cosh m_1 y}{m_1} + \frac{C_1 \sinh m_2 y}{m_2} + \frac{D_1 \cosh m_2 y}{m_2} \right) \right] Rm + c_1$$

(45)

The current density distribution takes the subsequent shape

$$Jz(x, y) = \left[\frac{1}{M^2} \frac{dp}{dx} - (A_1 \cosh m_1 y + B_1 \sinh m_1 y + C_1 \cosh m_2 y + D_1 \sinh m_2 y) \right] Rm$$

(46)

The pressure rise Δp in the channel of length L, in their non-dimensional forms, is given by

$$\Delta p = \int_0^{L/\lambda} \left(\frac{dp}{dx} \right) dx$$

(47)

The coefficient of heat exchange at the lower wall is given by

$$Zh_1 = \left(\frac{\partial \theta}{\partial y} \frac{\partial h_1}{\partial x} \right)_{y=h_1}$$

(48)

3 Results and Discussions

The standard differential equations that agree to boundary conditions have been solved analytically. The detailed results with the help of physical features on axial velocity and temperature profile, respectively, have been presented in this section. Here, we considered the non-dimensionless parameter values $M = 1$, $\gamma = 3$, $E = 2$, $a = 0.7$, $b = 1.2$, $d = 2$, $Q_1 = 0.5$, $Rm = 2$, $Q = -0.5$, $\varphi = \pi/2$, $\theta = 0$, $x = 0$, $dp/dx = 0.5$. These values kept throughout the whole review, apart from the changed values as shown in the figures and tables.

3.1 Velocity Characteristics

The axial velocity u against y for various values of couple stress parameter γ and magnetic field parameter M is plotted in Figs. 2 and 3, respectively. Figure 2 reveals that the axial velocity straightforwardly agrees to the couple stress fluid (γ). In light of this finding, we find that axial velocity of fluid improves when the couple stress fluid parameter increases, and when the velocity of fluid increases, the fluid changes from couple stress to Newtonian. Figure 3 depicts that fluid velocity can expand by

Fig. 2 Velocity along y for different γ
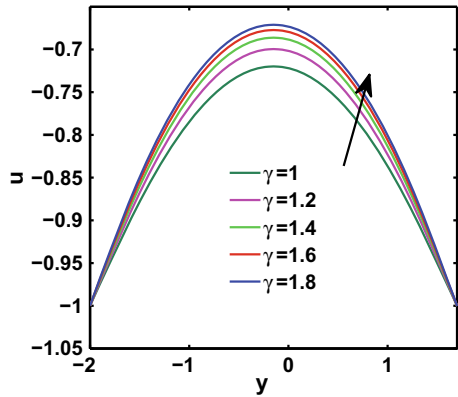
Fig. 3 Velocity along y for different M
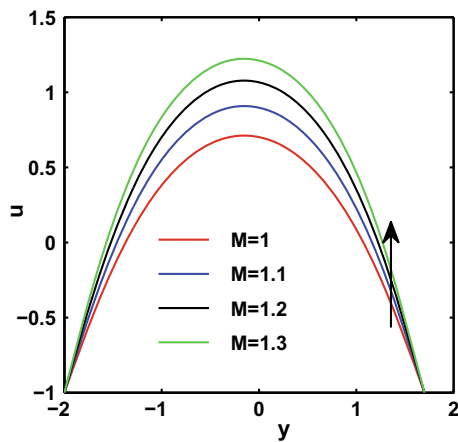
applying the magnetic field. By increasing the magnetic field, the viscosity of the fluid lessens, or in other words, the velocity of fluid enlarges. Thus, this result is during strokes and heart attacks, because thickening of blood damages the blood vessels. The velocity profiles are high in the $E = 1$ case compared with the case of $E = 0$ as shown in Fig. 18.

3.2 Pumping Characteristics

The pressure gradient dp/dx against x for various values of φ and M is plotted in Figs. 4 and 5, respectively. Figure 4 illustrates the variation of pressure gradient as more than one wavelength $x \in [0, \ 1]$ for various phase differences φ. It is noticed the pressure gradient does not straightforwardly correspond to the phase difference, i.e., the phase difference increases as the pressure gradient reduces in the restricted some portion of the channel, with increments in the more extensive portion of the

Fig. 4 Pressure gradient for various values of φ
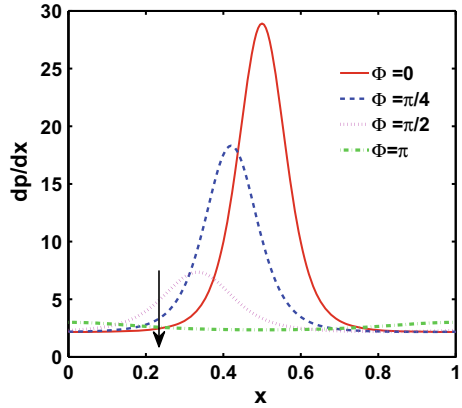
Fig. 5 Pressure gradient for various values of M
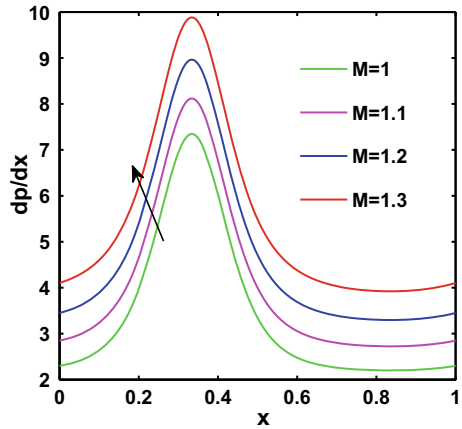
channel. Additionally, some parts are moved to one side with an expansion in phase difference, and a lower measure of the pressure gradient is needed to pass the flow in the more extensive portion of an asymmetric channel contrasted with the symmetric channel. Regardless, it is reversed in more extensive portion of the channel. Figure 5 shows that the pressure gradient is straightforwardly similar to the magnetic field. The pressure gradient is high in the $E = 1$ case, compared with the $E = 0$ case, as shown in Fig. 18.

3.3 Heat Characteristics

The temperature θ against y for various values of a magnetic field parameter M, Eckert number Ec, Prandtl number Pr and couple stress parameter γ is plotted in Figs. 6, 7, 8 and 9, respectively, as well as its fixed values, $y = 0$ and $Q = 0.5$.

Fig. 6 Temperature for
various values of *M*
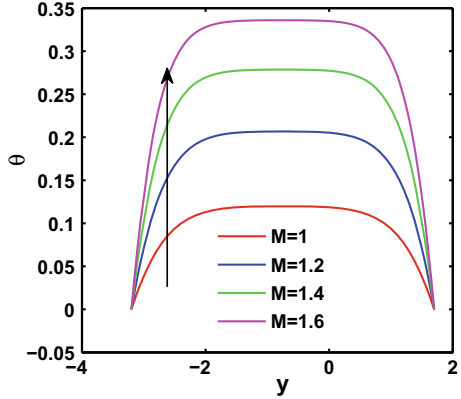
Fig. 7 Temperature for
various values of *Ec*
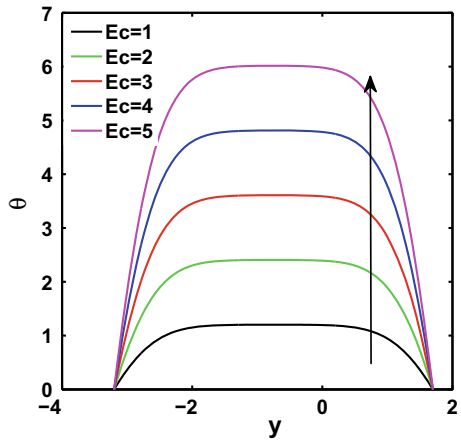
Figure 6 reveals that the temperature increments as the magnetic field increases. As an importance, the fluid changes from couple stress to Newtonian. Figure 7 depicts that the temperature increases as the Eckert number increments. The increasing values of Eckert number, we have seen the increment in the temperature profiles. because of this reason, we have seen increment in temperature. Figure 8 reveals that the temperature increments as the Prandtl number increments. Figure 9 reveals that the temperature lessens as the couple stress parameter increments. According to result, the viscosity of the fluid strengthens in human active joints, where the body temperature reduces from $36.7°c$ to $33°c$ (Philippe Abdel-Sayed et al.)

Fig. 8 Temperature for various values of Pr
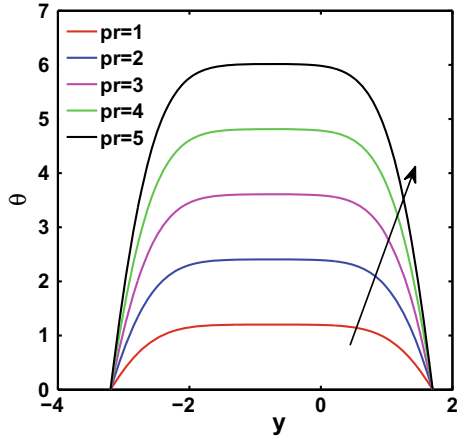
Fig. 9 Temperature for various values of γ
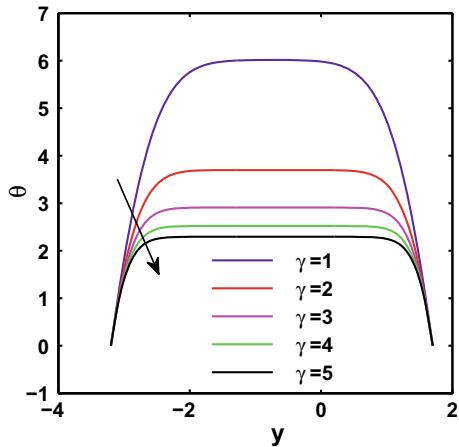
3.4 Magnetic Force Function

The magnetic force function φ against y for various values of electromagnetic force E and magnetic Reynolds number Rm is plotted in Figs. 10 and 11, respectively, and its fixed values are $\varphi = 0$ and $Q = 0.5$. Magnetic force is perpendicular to electric force in the channel at the same time expanding the electromagnetic force increments near to the boundary walls as shown in Figure 10. The channel at the same time expanding the electromagnetic force; because of this reason, the magnetic force role is controlled in the inside part of the channel, while it increments close to the boundary walls as shown in Fig. 10. The increment of magnetic Reynolds number in magnetic force role where the expanding magnetic Reynolds number would allow to control the magnetic diffusivity on the center part of the channel is shown in Fig. 11. The current density distribution Jz against y for various values of magnetic

Fig. 10 Magnetic force
function ϕ for various values
of E
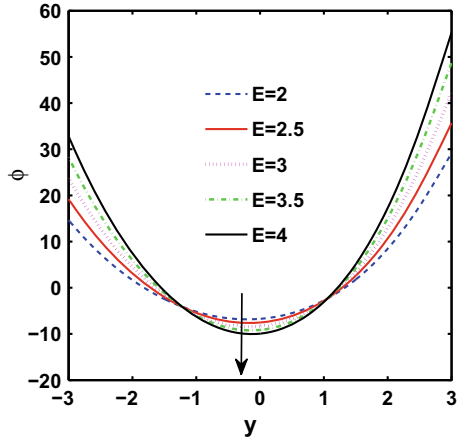
Fig. 11 Magnetic force
function ϕ for various values
of Rm
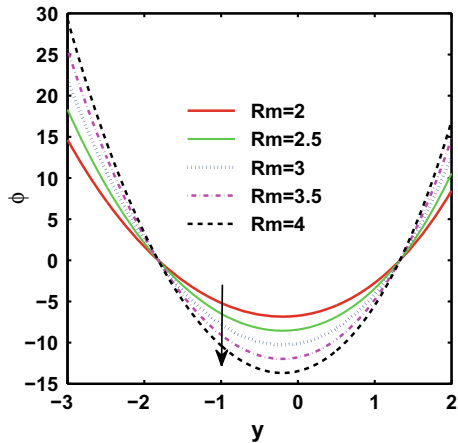
field parameter M is plotted in Fig. 12 and its fixed values are $\varphi = 0$ and $Q = 0.5$.
Figure 11 reveals that the current density is controlled in the centre part of the channel,
while it increments close to the boundary walls by the increment of Lorentz force.
Friction force ΔF against flow rate for various values of γ is plotted in Fig. 12
and its fixed values are $\varphi = 0$, $x = 0.5$, $y = 0$ and $Q = 0.5$. Figure 13 depicts that
friction force increments in the lower half of the region x [0, 0.36] and reduces in the
upper half of the region x [0.37, 1] with an increases of couple stress parameter. The
pressure rise ΔP against flow rate Q for various values of couple stress parameter
γ is plotted in Fig. 14 and its fixed values are $\varphi = 0$, $x = 0.5$, $y = 0$ and $Q = 0.5$.
Figure 14 depicts that pressure rise decreases in the upper half of the region x [0, 0.2]
and increases in the lower half of the region x [0.2, 1] with an increase of couple
stress parameter, i.e., pressure rise is opposite to the behavior of friction force.

Fig. 12 Current density distribution Jz for various values of M
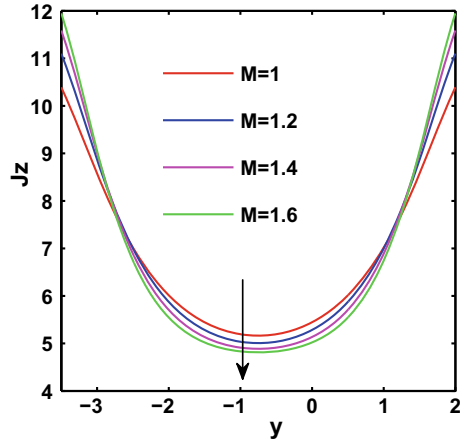
Fig. 13 Friction force for various values of γ
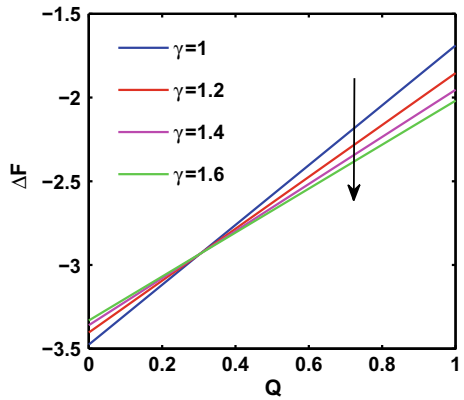
Fig. 14 Pressure rise for various values of γ
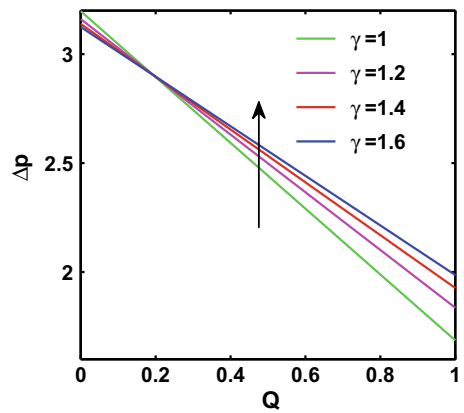
3.5 *Heat Exchange Coefficient*

The heat exchange coefficient Zh_1 against x for various values of Eckert number Ec, Prandtl number Pr and magnetic field parameter M is plotted in Figs. 15, 16 and 17, respectively, and its fixed values are $\varphi = 0$, $x = 0.5$, $y = 0$ and $Q = 0.5$. Figures. 15, 16 and 17 are outlined to concentrate the behavior of various parameters on heat exchange coefficient. Heat transfer coefficient is a quantitative measure of heat transfer between a fluid and the wall. Thermal flux (i.e., thermal rate by unit area) to the thermodynamic primary driving force for moving heat, i.e., difference of temperature $(T_1 - T_0)$. The oscillatory behavior of coefficient of heat exchange over the peristaltic wall is seen because of the closeness of sinusoidal wave. The heat exchange coefficient for different values of Pr and Ec are shown in Figure 15 and Figure 16. because of low viscosity, such conditions which have been apply in human active joints will damaged reveals in Fig. 15. Figure 16 shows same behavior.

Fig. 15 Heat exchange coefficient for various values of Pr
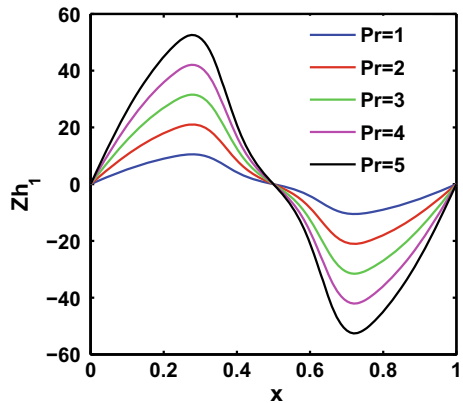
Fig. 16 Heat exchange coefficient for various values of Ec
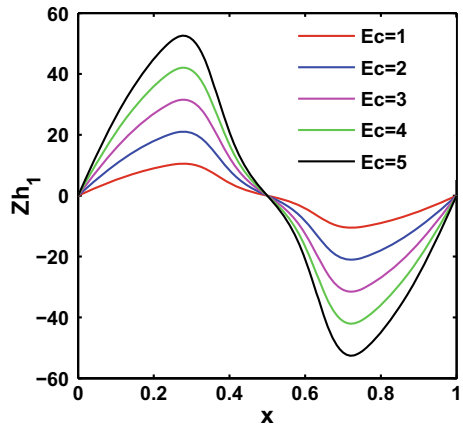
Fig. 17 Heat exchange coefficient for various values of M
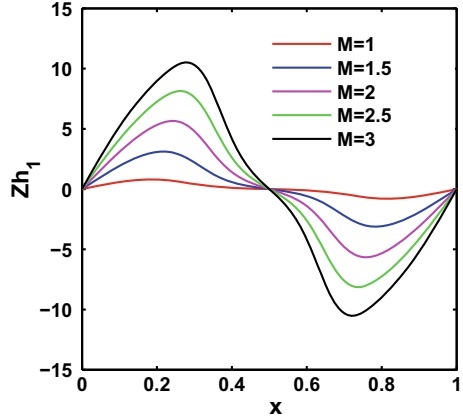
Fig. 18 Pressure gradient for various values of electromagnetic force
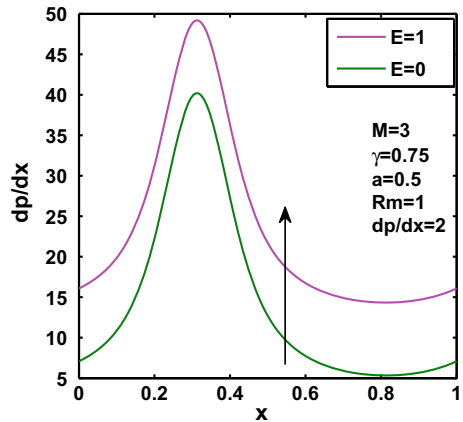
Figure 17 shows the variations of the heat transfer coefficient for different values of magnetic flux parameter. where the magnetic field would allow for better viscosity and the heat dissipation greater to the prandtl number and the Eckert number such conditions have express mimic measurements of rising and falling way. For example, in healthy hip replacement, the viscosity to raise the temperature from 33°C to 36.7°C after one hour of walking. Again, the temperature reduced to 33°C at rest (Philippe Abdel-Sayed et al.).

3.6 Trapping Phenomena

Figure 22a, b and c elucidate the measure of trapped bolus and for rotations increments with an increment in couple stress parameter γ. Figure 22d, e and f depict

Fig. 19 Velocity for various values of electromagnetic force
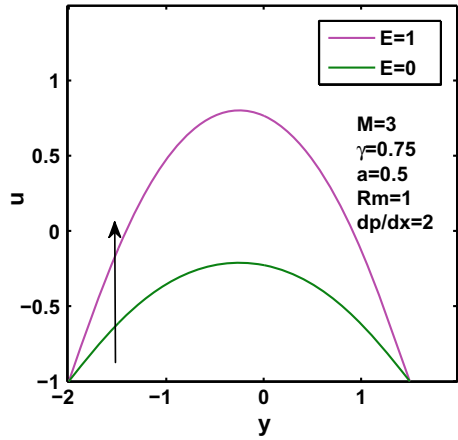
the influence of different values of phase difference on the stream function. on the stream function ψ and if gradually increasing the phase difference φ than the lower part of the trapped bolus slowly comes to the left side. However, the measure of trapped bolus and the rotations decreases with an extension in phase difference φ. Figure 23a, b and c are plotted to see the behavior of phase difference on magnetic force function. It is noticed that the numbers of magnetic lines are decreased, and it comes toward left when the phase differences gradually increase.

3.7 Pressure Gradient

Fig. 20 shows the variation of dp2/dx verses x for different values of the slip parameter. It is seen that the pressure gradient lessened with an expansion in slip parameter

Fig. 20 Pressure gradient for various values of β
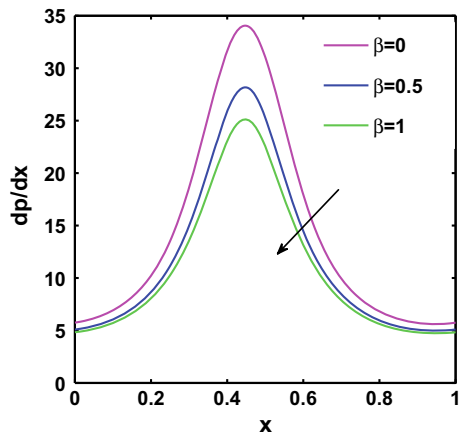
because of the higher values of β stands for the movement which was approaching toward Newtonian; however, the small values of β noticed that the movement had control of molecular size effects. Similarly, in the more extensive portion of the channel, the pressure gradient is moderately lesser, that is, the movement can easily go without imposition of the great pressure gradient. In restricted some portion of the channel, an extensive pressure gradient needs to keep up a similar flux to pass. Figure 21 shows the effect of couple stress parameter on pressure gradient. Here we
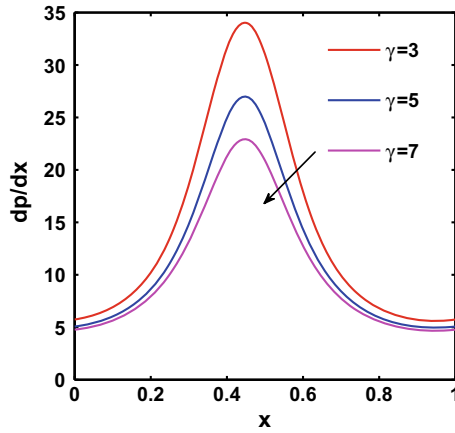
Fig. 21 Pressure gradient for various values of γ
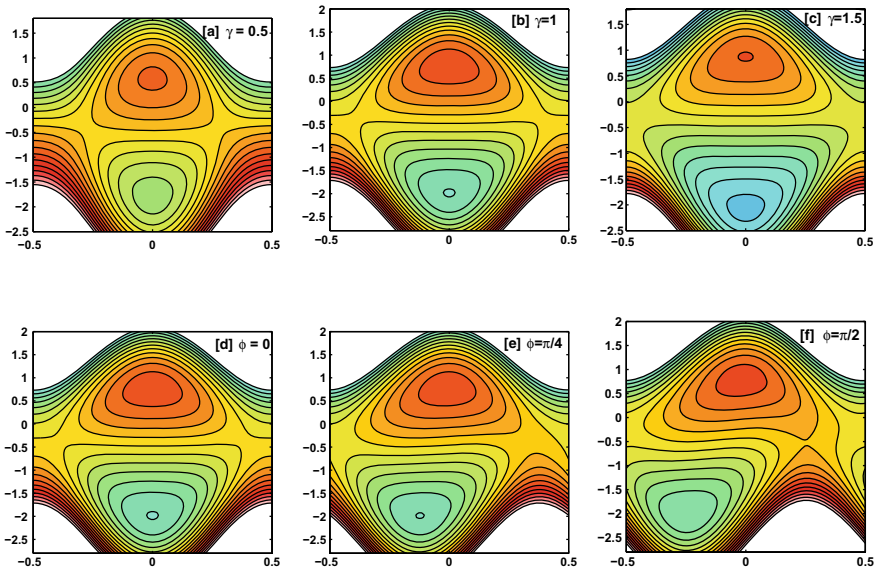
Fig. 22 Streamline for various values of couple stress parameter γ and phase difference φ
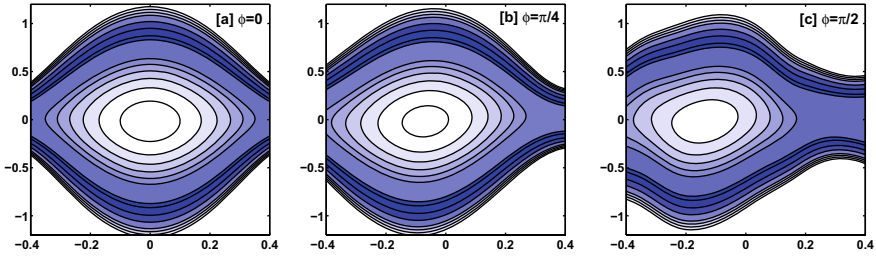
Fig. 23 Magnetic field for various values of phase difference φ

notice that the greater amplitude of pressure gradient reduces for the increasing values of couple stress parameter. reduced as γ expanded the more extensive part of the channel showed the same. The narrow part of channel gap reduces between the crest of the wall.

According to Figs. 18 and 19, we have to realize that in the presence of electromagnetic force, the pressure gradient and axial velocity increase when compared with the absence of electromagnetic force. Figures 18 and 19 are drawn by using case I and case II. The remaining figures are drawn based on case II only (Figs. 20, 21 and 22).

4   Conclusions

In this paper, we analyzed the consequence of heat transfer on the MHD peristaltic flow of couple stress fluid. The main conclusions of this study are as follows: The temperature, axial velocity and pressure gradient increase with increase of magnetic field parameter. The behavior of pressure rise is opposite to the behavior of frictional force. Increase of pressure gradient and axial velocity is observed with electromagnetic force as compared to without electromagnetic force. The size of trapped bolus increases with increase of couple stress parameter.

References

1. Latham TW (1966) Fluid motion in a peristaltic pump. MIT, Cambridge MA
2. Shapiro AH, Jaffrin MY, Weinberg SL (1969) Peristaltic pumping with long wavelengths at low Reynolds number. J Fluid Mech 37:799–825
3. Ali N, Hayat T, Asghar S (2009) Peristaltic flow of a Maxwell fluid in a channel with compliant walls, chaos. Solitons Fractals 39:407–416
4. Hayat T, Ali N, Asghar S, Siddiqui AM (2006) Exact peristaltic flow in tubes with an endoscope. Appl Math Comput 182:359–368
5. Hayat T, Ali N (2008) Peristaltic motion of a Jeffrey fluid under the effect of a Magnetic field in a tube. Commun Nonlinear Sci Numer Simul 13:1343–1352

6. Hayat T, Ali N, Asghar S (2007) Peristaltic motion of a Burger's fluid in a planar channel. Appl Math Comput 186:309–329

7. Tripathi D, Pandey SK, Das S (2010) Peristaltic flow of viscoelastic fluid with fractional Maxwell model through a channel. Appl Math Comput 215:3645–3654

8. Dharmendra Tripathi, Numerical study on creeping flow of Burger's fluids through a peristaltic tube, Journal of Fluids Engineering, 133 (2011) 121104 (1-9)

9. Li YF, Zhang R (1996) Reversed-phase high-performance liquid chromatography method for the simultaneous quantitation of the lactone and carboxylate forms of the novel natural product anticancer agent 10-hydroxycamptothecin in biological fluids and tissues. J Chromatogr B Biomed Sci Appl 686:257–265. https://doi.org/10.1016/S0378-4347(96)00222-8

10. He J, Zhang Y, Xu T, Zhao Q, Wang D, Chen CS, Tong W, Liu C, Xu T, Ju Z, Peng Y, Peng H, Li Q, Geng D, Zhang J, Li D, Zhang F, Guo L, Sun Y, Wang X, Cui Y, Li Y, Ma D, Yang G, Gao Y, Yuan X, Bazzano LA, Chen J (2014) CATIS Investigators, Effects of immediate blood pressure reduction on death and major disability in patients with acute ischemic stroke: the CATIS randomized clinical trial. JAMA 311:479–89. https://doi.org/10.1001/jama.2013.282543

11. Li Yang, Li Xiaoni, Zhao Hongxi (2013) RuopengFeng. Xiaoyan Zhang, Dapeng Tai, Guangyu An, Jinhua Wen, and Jichun Tan, Efficient Induction of Pluripotent Stem Cells from Menstrual Blood, Stem Cells and Development. 22:1147–1158. https://doi.org/10.1089/scd.2012.0428

12. Liang ZY, Zhao QX, Wang YG, Li YX, Zhang ZC (2014) Coupling mechanism of dew point corrosion and viscous ash deposits. Mater Corros 65:797–802

13. K. Ramesh, Effects of slip and convective conditions on the peristaltic flow of couple stress fluid in an asymmetric channel through porous medium, computer methods and programs in biomedicine, 135 (2016) 1-14

14. G. Bergmann, F. Graichen, A. Rohlmann, N. Verdonschot, G.H. van Lenthe, Frictional heating of total hip implants.Part 1. measurements in patients, Journal of Biomechanics, 34 (2001) 421-428

15. Abdel-Sayed Philippe (2014) MohamadrezaNassajianMoghadam, RaresSalomir, DavidTchernin, DominiqueP. Pioletti, Intrinsic viscoelasticity increases temperature in knee cartilage under physiological loading, journal of the mechanical behavior of biomedical materials 30:123–130

16. Tripathi D, Pandey SK, Das S (2010) Peristaltic flow of viscoelastic fluid with fractional Maxwell model through a channel. Appl Math Comput 215:3645–3654

17. Tripathi D, Pandey SK, Das S (2011) Peristaltic transport of a generalized Burgers' Fluid: Application to the movement of chyme in small intestine. Acta Astronaut 69:30–39

18. Y. Abd Elmaboudand Kh. S. Mekheimer, Non-linear peristaltic transport of a second-order fluid through a porous medium,Appl. Math. Modell.,35,(2011) 2695-2710

19. Hayat T, Mehmood OU (2011) Slip effects on MHD flow of third order fluid in a planar channel. Commun Nonlinear Sci Numer Simul 16:1363–1377

20. T. Hayat, S. Noreen,N. Ali and S. Abbas bandy, Peristaltic motion of Phan-thien-tanner fluid in a planar channel,Numer. Methods Partial Differ. Equ. 28(2010) 737-748

21. Vajravelu K, Sreendah S, Lakshrinarayana P (2011) The influence of heat transfer on peristaltic transport of Jeffrey fluid in a vertical porous stratum. Commun. Non-linear Sci. Numer. Simul. 16:3107–3125

22. Y. Abd elmaboud , Kh. S. Mekheimer and A. I. Abdellateef, Thermal properties of Couple-Stress fluid flow in an Asymmetric channel with peristalsis, Journal of Heat Transfer, 1350 (2013) (044502-1 - 044502-8)

23. Mekheimer KhS (2004) Peristaltic flow of blood under effect of a magnetic field in a non-uniform channels. Appl Math Comput 153:763–777

24. Ravikumar S (2014) peristaltic flow of blood through coaxial vertical channel with effect of magnetic field: blood flow study. International Journal of Recent advances in Mechanical Engineering (IJMECH) 3:85–96

25. Noreen S, Alsaedi A, Hayat T (2012) Peristaltic flow of Pseudoplastic fluid in an Asymmetric channel. J Appl Mech 79:054501-1–6

26. Kh. S. Mekheimer,S. Z. A. Husseny, and Y. Abd Elmaboud, Effects of heat transfer and space porosity on peristaltic flow in a vertical Asymmetric channel,Numer. Methods Partial Differ. Equ., 26 (2010) 747-770
27. Hayat T, Noreen S, Asghar S, Hendi AH (2011) Influence of induced magnetic field on the peristaltic transport in an Asymmetric channel. Chem Eng Commun 198:609–628
28. Hayat T, Afsar A, Ali N (2008) Peristaltic transport of a Johnson-Segalman fluid in an Asymmetric channel. Math Comput Modell 47:380–400
29. Nadeem S, Akbar NS (2011) Peristaltic flow of a couple stress fluid under the effect of induced magnetic field in an asymmetric channel. Arch Appl Mech 81:97–109
30. Mekheimer KhS, Abdel-Wahab AN (2009) Effect of wall compliance on compressible fluid transport induced by a surface Acoustic wave in a Microchannel. Numer. Methods Partial Differ. Equ. 27:621–636
31. Mekheimer KhS (2011) Effect of lateral walls on peristaltic flow through an Asymmetric rectangular duct. AppliedBionics and Biomechanics 8:1–14
32. Vajravelu K, Radhakrishnamacharya G, Radhakrishnamurthy V (2007) Peristaltic flow and heat transfer in a vertical porous annulus, with long wave approximation. Int J Non-Linear Mech 42:754–759
33. Kh. S. Mekheimer and Y. Abd elmaboud, The Influence of heat transfer and magnetic field on peristaltic transport of a newtonian fluid in a vertical annulus: Application of an Endoscope,Phys. Lett. A, 372 (2008) 1657-1665
34. Noreen S, Alsaedi A, Hayat T (2012) Peristaltic flow of Pseudoplasticfluid in an Asymmetric channel. ASME J Appl Mech 79:054501
35. Mekheimer KhS, El Shehawey EF, Elaw AM (1998) Peristaltic motion of a particle-fluid suspension in a planar channel. Int J Theor Phys 37:2895–2920
36. Mekheimer KhS (2003) Non-linear peristaltic transport through a porous medium in an inclined planar channel. J. Porous Medium 6:189–201
37. Mekheimer KhS (2003) Non-linear peristaltic transport of magneto-hydrodynamic flow in an inclined planar channel. Arabian J. Sci. Eng. 28:183–201
38. Mekheimer KhS, Al-Arabi TH (2003) Nonlinear peristaltic transport of MHD Flow through a porous medium. Int. J. Math. Math. Sci. 1663–1682:
39. Tripathi D (2011) Peristaltic transport of a Viscoelastic fluid in a channel. Acta Astron. 68:1379–1385
40. Tripathi D (2010) Numerical and analytical simulation of peristaltic flows of generalized Oldroyd-B Fluids. Int. J. Numer. https://doi.org/10.1002/fld.2466
41. Tripathi D (2011) Peristaltic transport of fractional Maxwell fluids in uniform tubes: Application of an Endoscope. Comput. Math. App. 62:1116–1126
42. Tripathi D (2011) A Mathematical model for the peristaltic flow of chyme movement in small iintestine. Math Biosci 233:90–97

Numerical Investigation of Non-Fourier Flux Theory with Chemical Action on Maxwell Radiating Nanoliquid: A Biomedical Application

Suneetha Sangapatnam, Subbarayudu Ketineni, Ali J. Chamkha, and Bala Anki Reddy Polu

Abstract In the modern critique, we deliberated a theoretical model of blood with carbon nanotubes (CNT's)—ejected in a Maxwell fluid with dissipative nanoparticles through binary chemical reaction lying on a stretching sheet by means of aligned field of magnetism. A customized Arrhenius function is imposed for energy activation. A non-linear radiation and a heat source/sink which is not uniform are incorporated in the energy equation which named as Cattaneo–Christov model of heat diffusion. Convective slip and suction are also added. Single and multiple walled nanotubes of carbon are employed with human blood as working liquid. A non-linear system is obtained for the considered problem, and an attempt is made by using Runge–Kutta fourth order through shooting (RK4S) method—bvp4c codes in MATLAB. The results are discussed and plotted in graphs for embedded parameters of concern. Higher activation energy improves the concentration, and a rise in chemical reaction rate constant raises Sherwood number. This study is thoughtful for medical surgeons during surgery in regulating the blood flow.

Keywords Cattaneo–Christov heat flux · SWCNT and MWCNT's · Activation energy · Binary chemical reaction · Human blood · Non-uniform heat source/sink

Nomenclature

g'	Acceleration due to gravity
T_∞	Ambient fluid temperature
T_f	Hot fluid temperature

S. Sangapatnam (✉) · S. Ketineni
Department of Applied Mathematics, Yogi Vemana University, Kadapa 516005, India
e-mail: suneethayvu@gmail.com

A. J. Chamkha
Mechanical Engineering Department, Prince Mohammad Endowment for Nanoscience and Technology, Prince Mohammad Bin Fahd University, Al-Khobar 31952, Saudi Arabia

B. A. R. Polu
Department of Mathematics, School of Advanced Sciences, VIT, Vellore 632014, India

h_f	Convective heat transfer coefficient
Ec	Eckert number
M	Magnetic parameter
E	Non-dimensional activation energy
Pr	Prandtl number
$\lambda*$	Thermal buoyancy parameter
Nr	Solutal buoyancy parameter
q_r	Radiative heat flux
Sc	Schmidt number
S	Suction/injection parameter
T	Temperature
$\bar{k}_{CNT}$	Thermal conductivities of CNT's
$\bar{k}_f$	Thermal conductivity of the host fluid
$\bar{k}_{nf}$	Thermal conductivity of the nanofluid
Rd	Radiation parameter
B_0	Uniform magnetic field strength
U_w	Velocity at wall
u	Velocity component along the x-axis
v	Velocity component along y-axis
A	Velocity slip factor
v_w	Wall mass flux
T_w	Wall temperature
C_w	Wall concentrate
Σ	Non-dimensional chemical reaction rate constant
θ_w	Temperature ratio parameter
μ_f	Fluid viscosity
μ_{nf}	Nanofluid viscosity
χ	Nanoparticles fraction
ρ_f	Fluid density
ρ_{CNT}	Thermal conductivities of CNT's
$(\rho C_p)_f$	Fluid heat capacitance
$(\rho C_p)_{nf}$	Nanofluid heat capacitance
$(\rho C_p)_{CNT}$	CNT's heat capacity
ρ_{nf}	Density of the nanofluid
$\sigma**$	Electric conductivity
α_{nf}	Thermal diffusivity of nanofluids
ξ	Aligned magnetic field parameter

1 Introduction

With the enormous awareness of current engineering technology, a new material known as nanomaterial that had got extensive enactment in fields like industry, biomedicine, electronics and transportation [1]. Nanofluid is a fluid having nano-sized metallic or non-metallic particles. Carbon atoms are arranged in empty cylindrical forms which are known as Carbon nanotubes, and the walls are in hexagonal shape of graphite. Furthermore, depending upon the number of graphene sheets rolled concentrically, single-wall and multi-wall carbon nanotubes are prepared. Fluid mechanics is the branch of physics concerned with the mechanics of fluids which are in movement. Here, blood is treated as a liquid that helps the bioengineers to model an upgraded synthetic organ and discovering remedies related to the human body diseases. Fourier did the introductory work for describing the flow temperature in parabolic equations and got a negative feature which discloses a small interruption throughout the medium. So, several investigators make an effort to alter the classical Fourier's law. Among them, Cattaneo [2] was one who productively modified the law by attaching the heat relaxation time which let the movement of heat by the employment of transmission of heat waves with unchanging speed. Christov [3] renovated the Maxwell–Cattaneo law with time derivative to get material invariance. Bala Anki Reddy and Suneetha [4] disclosed the fluid temperature and the heat relaxation time which are encountered in nature. Kolin [5] was the first person who has given the concept of electromagnetic fields in medical research. A force branded as Lorentz force has been generated by both magnetic and electric fields which has empathy to oppose the motion of the liquid (blood). By applying external magnetic field, the diseases like cardiovascular, haemorrhages and hypertension can be treated and have many real applications such as MRI, cancer therapy. Some authors [6, 7] suggested that when a human system is rendered to a magnetic flux externally, it starts to slow down the blood flow. The impact of radiation on blood flow has many uses in medical treatment methods. With the help of electromagnetic radiation, oncologist treats the cancerous tissues (Szasz [8]) by overheating them. Many investigators [9–11] explored the characteristics of non-Newtonian fluids where the heat radiation is not linear. Non-linear radiation is apt for peak and small temperature variations of surface and the fluid far from the surface. MHD flow over a stretching surface with Maxwell nanofluid was numerically explained by Reddy et al. [12]. Blood flow through a vessel with slip velocity near the wall was developed by Misra and Kar [13]. Gebhart [14] was first who revealed the significance of dissipation in convection. The process in which a part of kinetic energy converts into thermal energy by the viscosity of the fluid in motion is an irreversible process known as viscous dissipation. Reddy et al. [15] conducted a numerical experiment on the magneto-hydrodynamic flow of blood over a porous inclined plate with dissipation. By generating heat in the fluid mass, the temperature circulation can be changed which affects the rate of particle deposition. At present, we consider source/sink of heat which is not uniform. Some related studies on this were carried out by several investigators [16–20]. Svante Arrhenius was the first person who proposed the term activation energy in 1889. He narrated

it as the least energy required to start the reaction. In 1990, Bestman [21] disclosed binary chemical reaction in a fluid flow. An equation which describes the association with the activation energy and the reaction rate is referred as the Arrhenius equation. The Arrhenius equation is $K = B_1(T - T_\infty)^m \, e^{\left(\frac{-E_a}{k(T-T_\infty)}\right)}$ where K—reaction rate, B_1—exponential factor, E_a—the activation energy, T—temperature of the fluid and $k = 8.61 \times 10^{-5}$ eV/K is the Boltzmann constant. Actually, when temperature rises regularly, the rate of reaction rises. A reaction that occurs in two steps which is familiar in both (liquid and vapour) deposition processes is known as a binary chemical reaction, and some of its applications are varnishing of metallic objects and manufacturing of electronic tools investigated by Shafique et al. [22]. Few existing reviews aforementioned topic is revealed in Refs. [23, 24]. The literature survey shows that there are many investigations done on nanofluids with C-CHF model on stretching plane. Still there is no work has been explored to discuss the aligned magneto-radiating fluid on blood. To fill the gap in this regard, current attempt is done to analyze the effect on aligned magneto-hydrodynamic 2D Maxwell nanofluid with CNT's on blood flow past a stretching sheet with non-linear heat radiation of non-Fourier flux theory. The specific attention of the present effort is to inspect the comparable solutions of the non-linear partial differential equations for some values of the parameters by using the shooting method.

2   Description of the Problem

Let us consider the Maxwell nanofluid past a stretchable plane with blood flow. In this autopsy, SWCNT's and MWCNT's are used. The physical characteristics of the host fluid and CNT's are drafted in Table 1. In this autopsy, Cattaneo—Christov heat flux model (C-CHFM) is considered. The primary fluid is taken as blood which is viscous in nature. The problem is characterized under the action of viscous dissipation, activation energy, binary chemical reaction, thermal radiation which is not linear, non-uniform heat source/sink and aligned magnetic field. Sheet stretches in the route of x-axis and erects to the y-axis. The magnetic flux B is employed vertically to the sheet. The stimulated magnetic field is tiny as a result a very minute Reynolds number exist. $U_w(x) = cx \ (c > 0)$ be the velocity along the stretching direction. Temperature is synchronized by convection and depicted in

Table 1 Thermo-physical characteristics of base fluids and CNTs [25]	Physical properties	Host fluid (human blood)	Nanoparticles	
			SWCNT	MWCNT
	C_p	3594	425	796
	ρ	1053	2600	1600
	κ	0.492	6600	3000
	$\beta \times 10^{-5}$	0.18	2.6	2.8

Fig. 1 Flow framework
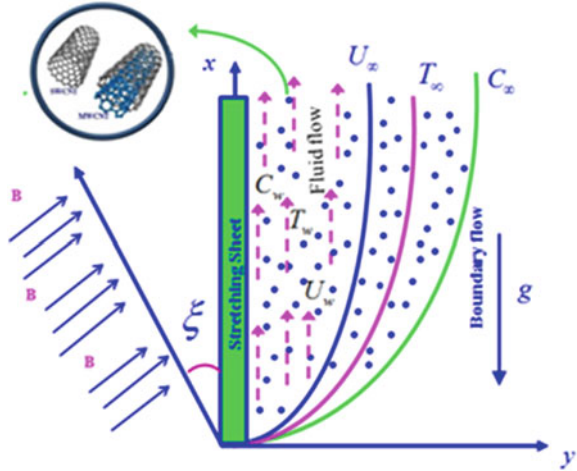
Fig. 1. The flow under these attentions can be put into the ensuing form:

$$\partial_x u + \partial_y v = 0 \tag{1}$$

$$u\,(\partial_x u) + \lambda_1\big(u^2(\partial_{xx} u) + v^2(\partial_{yy} u) + 2uv(\partial_{xy} u)\big) + v(\partial_y u)$$
$$= \frac{1}{\rho_{\text{nf}}}\big(\mu_{\text{nf}}(\partial_{yy} u) + (\rho\beta)_f g'(T - T_\infty) - (\rho\beta^*)_f g'(C - C_\infty) - \sin^2\xi\sigma B_0^2(x)u\big) \tag{2}$$

$$\big(\rho C_p\big)_{\text{nf}}\big(u\,(\partial_x T) + v\,(\partial_y T)\big) = -\nabla \cdot q_0 - \frac{1}{\upsilon}\big(\partial_y q_r\big) + \frac{\upsilon}{c_p}\big(\partial_y u\big)^2 + q''' \tag{3}$$

$$u(\partial_x C) + v\big(\partial_y C\big) = D\big(\partial_{yy} C\big) - k_r^2\left(\frac{T}{T_\infty}\right)^m (C - C_\infty)e^{-\frac{E_a}{kT}} \tag{4}$$

The expression $k_r^2\left(\frac{T}{T_\infty}\right)^m e^{-\frac{E_a}{kT}}$ in Eq. (4) designates the modified Arrhenius equation, reaction rate—k_r^2, the fixed rate constants—m, $-1 < m < 1$.

The C-CHF is expressed as

$$q_0 + \lambda^*\big(\partial_t q_0 + V' \cdot \nabla q_0 - q_0 \cdot \nabla V' + (\nabla \cdot V')q_0\big) = -\bar{k}_f(\nabla \cdot T) \tag{5}$$

where λ^*—flux relaxation time and V'—velocity vector. Equation (5) is transformed into Fourier's law for $\lambda^* = 0$, $\nabla \cdot V' = 0$, and for incompressible fluid, Eq. (5) receipts the outline

$$q_0 + \lambda^*\big(\partial_t q_0 + V' \cdot \nabla q_0 - q_0 \cdot \nabla V'\big) = -\bar{k}_f\,(\nabla \cdot T) \tag{6}$$

The energy equation after eliminating q_0 from Eqs. (3) and (6) is

$$
\begin{aligned}
&u(\partial_x T) + \lambda^* \Big(\big(u(\partial_x T) + v(\partial_y T) \big)^2 + u \big((\partial_x u)(\partial_x T) + (\partial_x v)(\partial_y T) \big) \\
&+ v \big((\partial_y v)(\partial_y T) + (\partial_y u)(\partial_x T) \big) \Big) \\
&+ v(\partial_y T) = \alpha_{\mathrm{nf}}(\partial_{yy} T) - \frac{1}{v}(\partial_y q_r) + \frac{\upsilon}{c_p}(\partial_y u)^2 + q'''
\end{aligned}
\tag{7}
$$

The non-uniform source/sink of heat q''' is modelled as

$$
q''' = \frac{kU_w}{x v} \Big[A * (T_w - T_\infty) f' + B * (T - T_\infty) \Big]
$$

where A^* and B^* denote the space- and temperature-dependent coefficients. For $A^* > 0$ and $B^* > 0$, internally heat is generated, and for $A^* < 0$, $B^* < 0$, heat is absorbed internally.

The heat flux q_r is given by means of the Rosseland approximation

$$
q_r = -\left(\frac{4}{3 K^*} \right) \mathrm{grad}(\sigma^* T^4)
\tag{8}
$$

where K^*—the absorption coefficient, e_b—the emission from a blackbody and $\sigma^* = 5.6697 \times 10^{-8}\ \mathrm{Wm^{-2} K^{-4}}$ be the Stefan–Boltzmann constant.

The term T^4 is a function of temperature and can be extended as Taylor series in terms of T_∞ and estimated by ignoring terms with higher order.

$$
T^4 = T_\infty^4 \{1 + (\theta_w - 1)\theta\}^4
\tag{9}
$$

where $\theta_w = \frac{T_w}{T_\infty}$, $\theta_w > 1$ be the wall temperature ratio parameter.

Xue launched a model which depends on Maxwell theory and reimburses the effect of the space distribution on CNT's. In this paper, Xue model is used as follows:

$$
\frac{\bar{k}_{\mathrm{nf}}}{\bar{k}_f} = \frac{1 - \chi + 2\chi \left(\frac{\bar{k}_{\mathrm{CNT}}}{\bar{k}_{\mathrm{CNT}} - \bar{k}_f} \right)\ \log \frac{\bar{k}_{\mathrm{CNT}} + \bar{k}_f}{2\bar{k}_f}}{1 - \chi + 2\chi \left(\frac{\bar{k}_f}{\bar{k}_{\mathrm{CNT}} - \bar{k}_f} \right)\ \log \frac{\bar{k}_{\mathrm{CNT}} + \bar{k}_f}{2\bar{k}_f}}
\tag{10}
$$

which is interpreted as:

$$
\left.
\begin{aligned}
&\frac{\rho_{\mathrm{nf}}}{\rho_f} = (1 - \chi) + \frac{\chi \rho_{\mathrm{CNT}}}{\rho_f}\ ,\quad \frac{(\rho C_p)_{\mathrm{nf}}}{(\rho C_p)_f} = (1 - \chi) + \frac{\chi (\rho C_p)_{\mathrm{CNT}}}{(\rho C_p)_f} \\
&\mu_{\mathrm{nf}} = (\upsilon \rho)_{\mathrm{nf}},\ \ \mu_{\mathrm{nf}} = \mu_f (1 - \chi)^{-2.5}\ ,\ \ \bar{k}_{\mathrm{nf}} = \big(\alpha (\rho C_p) \big)_{\mathrm{nf}}
\end{aligned}
\right\}
\tag{11}
$$

and undergoes the boundary conditions:

$$y = 0: u = U_w(x) + A\left(\partial_y u\right),\ v = -v_w,\ -k\left(\partial_y T\right) = h_f(T_f - T),\ C = C_w$$

$$y \to \infty:\ u \to 0\ ,\ T \to T_\infty,\ C \to C_\infty \tag{12}$$

Using the similarity transformations,

$$\eta = \sqrt{\frac{c}{v}}\,y,\ \psi(x, y) = \sqrt{cv}\,xf(\eta),\quad \theta(\eta) = \frac{T - T_\infty}{T_w - T_\infty},\quad \phi(\eta) = \frac{C - C_\infty}{C_w - C_\infty}$$

$$u = cxf'(\eta),\ v = -\sqrt{cv}\,f(\eta) \tag{13}$$

Adopting Eqs. (10, 11, 13) in Eqs. (1, 2, 7, 4), we have

$$d_{\eta\eta\eta}f + (1-\chi)^{2.5}\left\{\left(1-\chi+\chi\frac{(\rho\beta)_{\text{CNT}}}{(\rho\beta)_f}\right)(\lambda\theta - Nr\phi) - \sin^2\xi\,M^2\left(d_\eta f\right)\right\}$$

$$-(1-\chi)^{2.5}\left(1-\chi+\chi\frac{\rho_{\text{CNT}}}{\rho_f}\right)\left\{\left(d_\eta f\right)^2 - f\left(d_{\eta\eta}f\right)\right.$$

$$+\alpha\left(f^2\left(d_{\eta\eta\eta}f\right) - 2f\left(d_\eta f\right)\left(d_{\eta\eta}f\right)\right)\right\} = 0 \tag{14}$$

$$\frac{1}{\text{Pr}}\left\{\left(d_{\eta\eta}\theta\right)\left\{\frac{k_{\text{nf}}}{k_f} + \frac{4}{3}\text{Rd}[(\theta_w - 1)\theta + 1]^3\right\} + 4\text{Rd}[(\theta_w - 1)\theta + 1]^2(\theta_w - 1)\left(d_\eta\theta\right)^2\right\}$$

$$+\left\{1 - \chi + \chi\frac{(\rho c_p)_{\text{CNT}}}{(\rho c_p)_f}\right\}\left\{f\left(d_\eta\theta\right) - \gamma\left(f\left(d_\eta f\right)\left(d_\eta\theta\right) + f^2\left(d_{\eta\eta}\theta\right)\right)\right\}$$

$$+\text{Ec}\left(d_{\eta\eta}f\right) + A*\left(d_\eta f\right) + B*\theta = 0 \tag{15}$$

$$d_{\eta\eta}\phi + \text{Sc}\,f\left(d_\eta\phi\right) - \text{Sc}\,\sigma\,\phi\,[\theta(\theta_w - 1) + 1]^m e^{-\frac{E}{\theta(\theta_w - 1) + 1}} = 0 \tag{16}$$

Together with the boundary conditions

$$f(\eta) = S,\ d_\eta f(\eta) = 1 + \delta\,d_{\eta\eta}f(0),\ d_\eta\theta(\eta) = -Bi\left(1 - \theta(\eta)\right), \phi(\eta) = 1 \text{ at } \eta = 0,$$

$$d_\eta f(\eta) = 0,\quad \theta(\eta) = 0,\quad \phi(\eta) = 0\quad \text{at } \eta = 0 \text{ at } \eta \to \infty \tag{17}$$

where

$$\text{Sc} = \frac{\upsilon}{D}, \quad \sigma = \frac{k_r^2}{c}, \quad E = \frac{E_a}{kT_\infty}, \quad \lambda = \frac{\text{Gr}_x}{\text{Re}_x^2}, \quad \text{Gr}_x = \frac{(\rho\beta)_f g'(T_w - T_\infty)x^3}{\upsilon^2\rho_f},$$

$$Nr = \frac{\text{Gc}_x}{\text{Re}_x^2}, \text{Gc}_x = \frac{(\rho\beta^*)_f g'(C_w - C_\infty)x^3}{\upsilon^2\rho_f}, \quad \text{Re}_x^2 = \frac{U_w^2 x^2}{\upsilon^2}, \quad M = B_0\sqrt{\frac{\sigma}{a\rho_f}}\,x,$$

$$\alpha = \lambda_1 c, \quad \gamma = \lambda^* c, \text{Rd} = \frac{4\sigma^* T_\infty^{*3}}{kk_1}, \quad \text{Ec} = \frac{U_w^2}{C_p(T_w - T_\infty)}, \quad \text{Pr} = \frac{(\mu C_p)_f}{k},$$

$$S = \frac{v_w}{a\upsilon_f}, \quad \delta = A\sqrt{\frac{c}{\upsilon}}, \quad Bi = \left(\frac{h_f}{\overline{k}_f}\right)\sqrt{\upsilon_f/c}$$

3   Quantities of Interest

The quantities of interest for considering flow are surface drag force, local Nusselt number and Sherwood number, which are as follows:

$$C_{f_x} = \frac{\tau_w}{\rho_f U_w^2}, \quad Nu_x = \frac{xq_w}{\overline{k}_f(T_w - T_\infty)} \text{ and } \text{Sh}_x = \frac{xq_m}{D(C_w - C_\infty)} \qquad (18)$$

where τ_w(skin friction of the wall), q_w(heat flux of the wall) and q_m(mass flux of the wall) which are specified as

$$\tau_w = \mu_{\text{nf}}\big(\partial_y u\big)_{y=0}, \; q_w = -x\overline{k}_{\text{nf}}\big(\partial_y T\big)_{y=0} + (q_r)_{y=0} \text{ and } q_m = -D\big(\partial_y C\big)_{y=0} \qquad (19)$$

In view of Eqs. (18) and (19), the dimensionless surface drag force, local Nusselt number and local Sherwood number are given by

$$C_f \text{Re}_x^{1/2} = \frac{1}{(1-\chi)^{2.5}}\left(d_{\eta\eta} f(0)\right),$$

$$Nu_x \text{Re}_x^{-1/2} = -\left\{\frac{\overline{k}_{\text{nf}}}{\overline{k}_f} + \frac{4}{3}\text{Rd}[(\theta_w - 1)\theta(0) + 1]^3\right\}\left(d_\eta \theta(0)\right)$$

$$\text{and } \text{Sh}_x \text{Re}_x^{-1/2} = -d_\eta \phi(0), \qquad (20)$$

wherever $\text{Re}_x = \frac{U_w x}{\upsilon}$ signifies Reynolds number.

4 Results and Discussion

Blood flow (host fluid) of MHD-based CNT's on C-CHFM with non-linear radiant heat along with binary chemical changes on Maxwell nanofluid covering the stretching sheet. In this segment, we inspect the physical outcomes of sundry parameters with respect to the velocity $f'(\eta)$, temperature $\theta(\eta)$ and species distribution $\phi(\eta)$. This segment contains the effects of dimensionless parameters like M, θ_w, Pr, Sc, Ec, σ, Rd, E which are demonstrated in Figs. 2, 3, 4, 5, 6, 7, 8 and 9. The outcomes are obtained for two diverse cases of CNT's, predominantly, SWCNT's and MWCNT's (blue coloured solid line denotes SWCNT's and green coloured dashed lines denotes MWCNT's) for blood flow. In Table 1, the numerical standards of CNT's and host fluid are revealed. The Prandtl number of blood is engaged as 21,and it behaves as non-Newtonian due to the existence of red blood cells. The variation of other parameters are constant, i.e., $M = 0.5$, $\lambda = 0.5$, $Nr = 0.5$, $\gamma = 0.1$, $Sc = 0.5$,

Fig. 2 M versus $f'(\eta)$
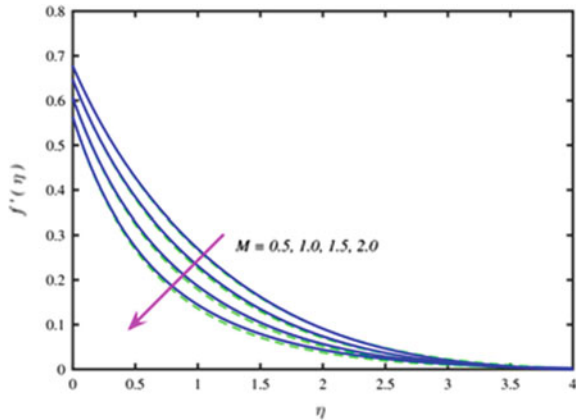
Fig. 3 Pr versus $\theta(\eta)$
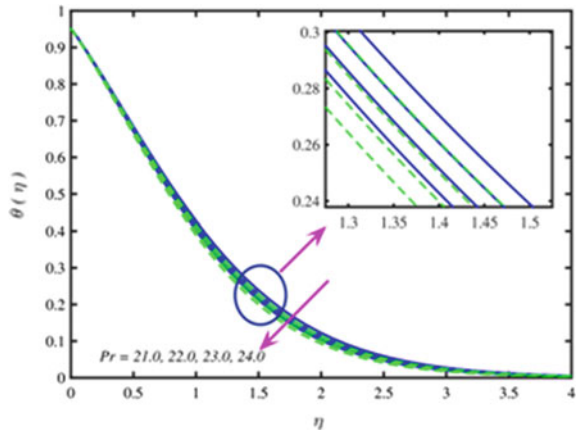
Fig. 4 *Sc* versus $\phi\ (\eta)$
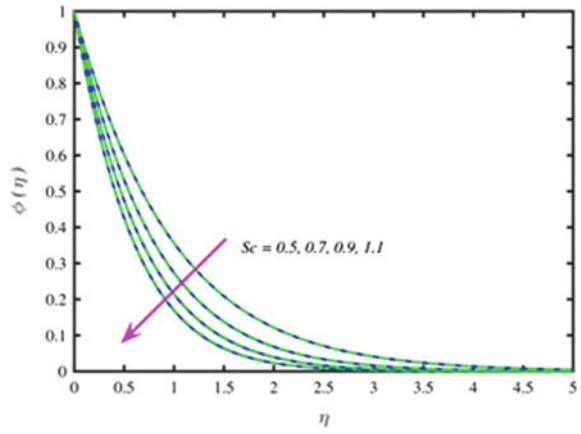
Fig. 5 $\theta\ _w$ versus $\theta\ (\eta)$
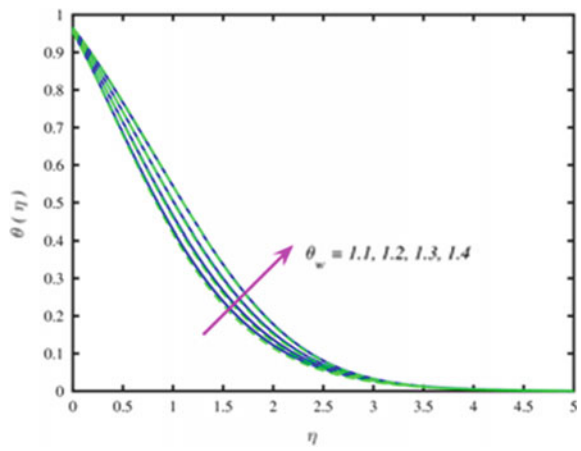
Fig. 6 Rd versus $\theta(\eta)$
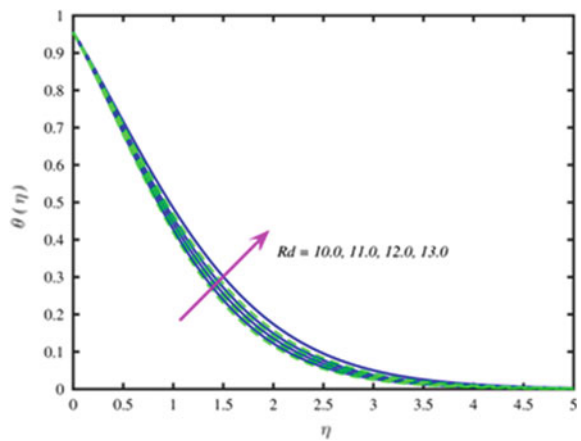
Fig. 7 E versus $\phi(\eta)$
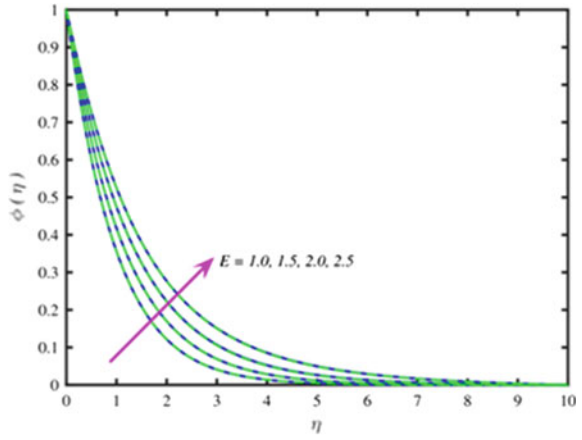
Fig. 8 Ec versus $\theta\ (\eta)$

Fig. 9 σ versus $\phi(\eta)$
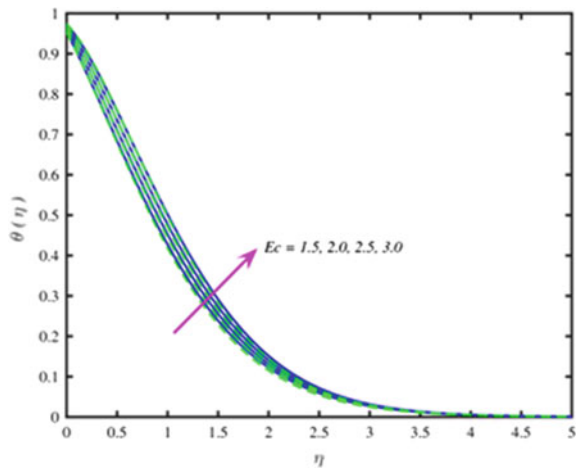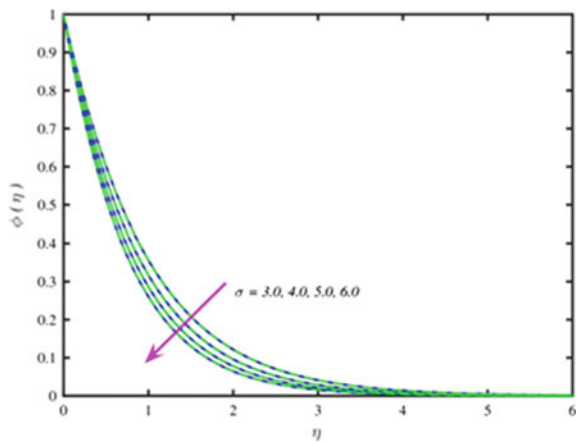
Ec = 1.5, θ_w = 1.1, Bi = 10, E = 1.0, δ = 0.5, S = 0.5, A^* = 0.05, B^* = 0.05, Rd = 10.0, σ = 3.0, χ = 0.06, $\xi = \frac{\pi}{4}$, unless otherwise specified. Table 2 describes the deviations of skin friction for different parameters. The skin friction decreases with growing of M and ξ, and a reverse trend for Ec and χ. Table 3 displays the variations in rate of heat transfer for different values of M, Pr, Ec and χ. Heat transfer rate accelerates with Pr and decelerates with M, Ec and χ. Table 4 provides the sample values of mass transfer for several values of embedding parameters. Mass transfer declines for M, whereas it inclines with Sc, θ_w and χ. The upshot of M on velocity is perceived in Fig. 2. As M is grown, the velocity of the fluid diminishes (for both types of CNT's), and a decrease in the width of the velocity boundary layer is seen. Physically, a force called as Lorentz force opposes the movement and boosts up the molecules to collide. This force slows down the flow and is accountable in velocity decrement. Analysis of Pr on temperature is drafted in Fig. 3. Physically, the temperature and the width of the temperature boundary layer are counter in nature with

Table 2 Deviations in skin friction coefficient and various dimensionless parameters

M	Ec	χ	ξ	$f''(0)$	
				SWCNT	MWCNT
0.2	0.02	0.06	$\frac{\pi}{4}$	−0.6096	−0.6310
0.3	0.02	0.06	$\frac{\pi}{4}$	−0.6162	−0.6378
0.4	0.02	0.06	$\frac{\pi}{4}$	−0.6253	−0.6472
0.2	0.03	0.06	$\frac{\pi}{4}$	−0.6092	−0.6307
0.2	0.04	0.06	$\frac{\pi}{4}$	−0.6089	−0.6305
0.2	0.02	0.07	$\frac{\pi}{4}$	−0.5926	−0.6215
0.2	0.02	0.08	$\frac{\pi}{4}$	−0.5658	−0.6076
0.2	0.02	0.06	$\frac{\pi}{3}$	−0.6122	−0.6337
0.2	0.02	0.06	$\frac{\pi}{2}$	−0.6149	−0.6365

Table 3 Deviations in the rate of heat transfer and various dimensionless parameters

M	Pr	Ec	χ	$-\theta'(0)$	
				SWCNT	MWCNT
0.2	21.0	0.02	0.06	7.3704	8.0949
0.3	21.0	0.02	0.06	7.3513	8.0748
0.4	21.0	0.02	0.06	7.3253	8.0471
0.2	22.0	0.02	0.06	7.7201	8.4573
0.2	23.0	0.02	0.06	8.0652	8.8149
0.2	21.0	0.03	0.06	7.3468	8.0708
0.2	21.0	0.04	0.06	7.3232	8.0467
0.2	21.0	0.02	0.07	5.3761	6.6444
0.2	21.0	0.02	0.08	1.9658	4.4405

Table 4 Deviations in the rate of mass transfer and various dimensionless parameters

M	Sc	θ_w	χ	$-\phi'(0)$	
				SWCNT	MWCNT
0.2	0.6	1.1	0.06	1.1088	1.1067
0.3	0.6	1.1	0.06	1.1081	1.1059
0.4	0.6	1.1	0.06	1.1070	1.1048
0.2	0.7	1.1	0.06	1.2179	1.2155
0.2	0.8	1.1	0.06	1.3218	1.3192
0.2	0.6	1.2	0.06	1.1366	1.1340
0.2	0.6	1.3	0.06	1.1671	1.1641
0.2	0.6	1.1	0.07	1.1139	1.1107
0.2	0.6	1.1	0.08	1.1209	1.1156

Pr. The reduction in temperature profile for high Pr involves low heat conductivity which results in low fluid temperature for both SWCNT's and MWCNT's. As Sc is inversely associated with the mass diffusion coefficient D, as a result, larger values of Sc denote smaller D and for that leads to thinner concentration at the boundary layer. Thus, the nanoparticle concentration depreciates for both types of CNT's by the elevated values of Sc which is portrayed in Fig. 4. As values of θ_w mounts, a climb in temperature is seen in Fig. 5, and for that reason, growing θ_w results in elevation of wall temperature that successively yields a wider penetration depth for temperature when compared to ambient temperature, consequently fluid temperature enriches. Figure 6 depicts the impression of Rd on temperature and examined that the temperature inflates by raising the values of Rd. The reason behind is the mean absorption coefficient downwards for an upwards in Rd. In point of physics, at radiation, more heat absorbed by the working fluid consequently shows a rise in temperature. Further, the thickness of the thermal boundary layer was built up strongly by raising the values of non-linear radiation parameter. Activation energy E is plotted in Fig. 7 which is evident that as E enlarges the concentration would be larger. To initiate a larger chemical reaction, a huge amount of energy is needed. With the increasing values of E, the Arrhenius function decreases, and as a consequence, the chemical action raises the concentration. With more activation energy and less temperature, it results to a minor reaction rate that decelerates the chemical action. Therefore, the concentration of species increases. To explore the behaviour of Ec on the temperature profiles is plotted in Fig. 8. As Ec rises, the heat of the fluid also rises which leads to solidify the thermal boundary layer which is constant with heat generation due to the frictional property of the fluid. The heat generated by viscous dissipation owed to haul among the fluid particles, and this additional heat results an enhancement in temperature of the initial fluid for both single- and multi-walled CNT's. Figure 9 depicts the impact of reaction rate constant σ on concentration. When we gradually increase σ, the concentration becomes thin out. A favourable destructive reaction rises which consecutively results in a fall in concentration. Due to this concentration,
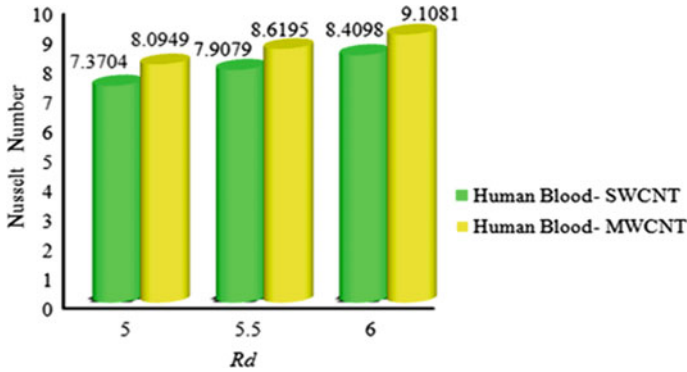
Fig. 10 *Rd* versus Nusselt number

profile decreases, and same consequence is seen for both CNT's. Figure 10 illustrates the variation in local Nusselt number for different values of non-linear thermal radiation. It is clear that escalating values of Rd improves the heat transformation rate for both cases. The enhancement for MWCNT's is slightly more when compared with SWCNT's. The effect of θ_w on local Nusselt number is demonstrated in Fig. 11 and is detected that rising values of θ_w raises the local Nusselt number for both circumstances. The effect of A^* and B^* on local Nusselt number is demonstrated in Figs. 12 and 13. It is noted that rising values of A^* and B^* fall the local Nusselt number for both SWCNT's and MWCNT's. The increment for MWCNT's is more than with SWCNT's. Figure 14 exemplifies the effect of Sherwood number on chemical reaction rate constant. The outcomes show a rise in σ which raises Sherwood number for both SWCNT's and MWCNT's. Figure 15 exemplifies the effect of Sherwood number on Activation Energy. The figure shows a rise in E which has a fall in the Sherwood number for both conditions.
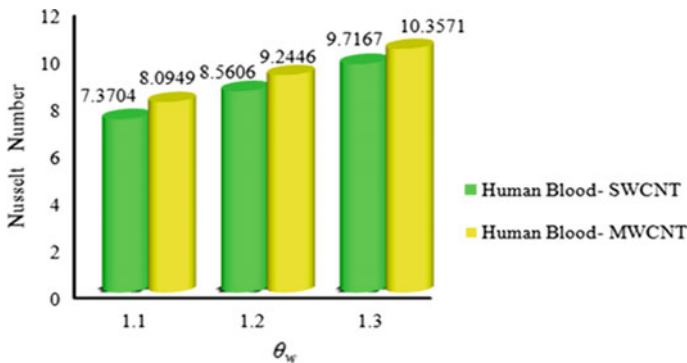
Fig. 11 θ_w versus Nusselt number
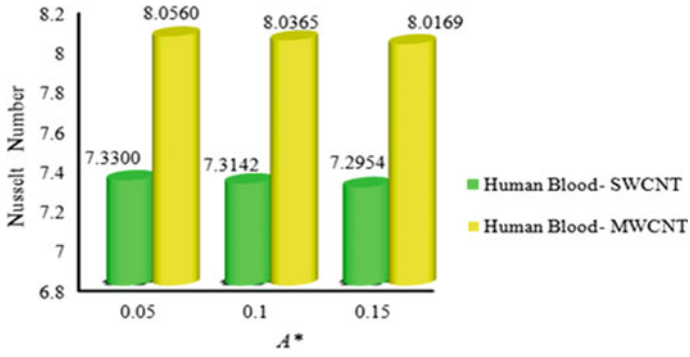
Fig. 12 *A** versus Nusselt number
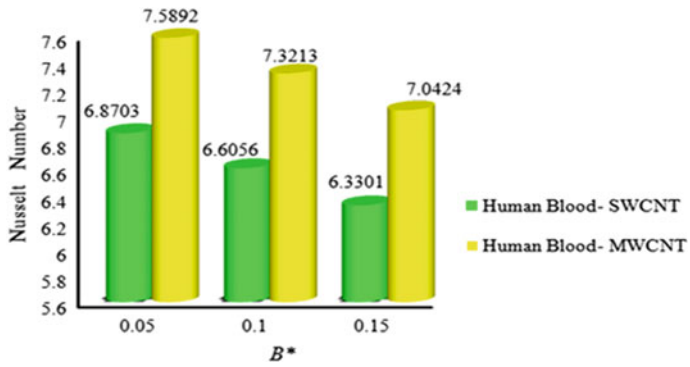
Fig. 13 *B** versus Nusselt number
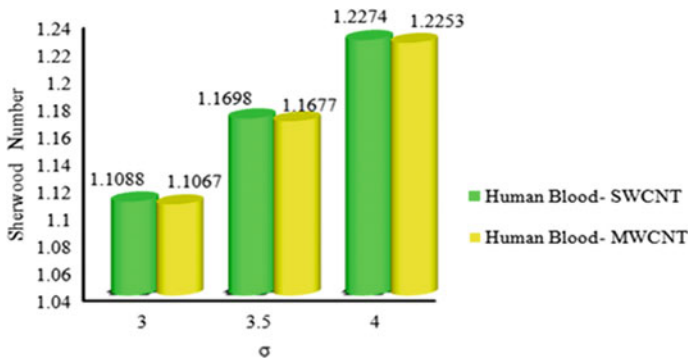
Fig. 14 *σ* versus Sherwood number
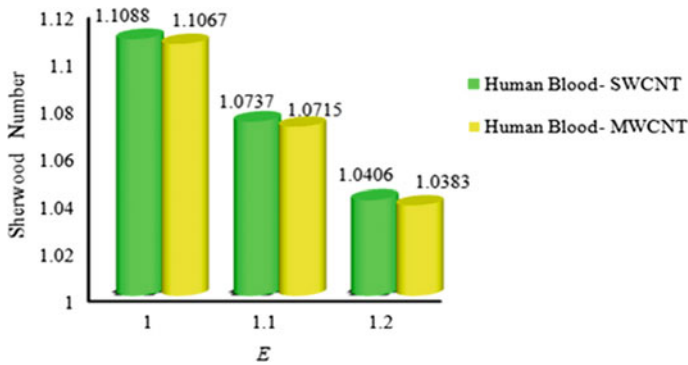
Fig. 15 *E* versus Sherwood number

5 Final Conclusions

The current communication scrutinizes a theoretical model of blood with carbon nanotubes (CNT's)—ejected in a Maxwell fluid with nanoparticles through binary chemical reaction lying on a stretching sheet by means of aligned magnetic field. The strategic upshots of this framework are outlined below

- Increasing values of Rd, θ_w, Ec and χ, lead to stronger temperature distribution.
- The higher value of Sc, reaction rate parameter and concentration decreases.
- The fluid concentration rises with E.
- A rise in σ raises Sherwood number.
- A rise in E has a fall in the Sherwood number.

References

1. Baughman RH, Zakhidov AA, De Heer WA (2002) Carbon nanotubes-the route toward applications. Science 297(5582):787–792. https://doi.org/10.1126/science.1060928
2. Cattaneo C (1948) Sulla conduzionedelcalore, AttiSemin. Mat Fis Univ Modena Reggio Emilia 3:83–101
3. Christov CI (2009) On frame indifferent formulation of the Maxwell-Cattaneo model of finite speed heat conduction. Mech Res Commun 36:481–486. https://doi.org/10.1016/j.mechrescom.2008.11.003
4. Bala Anki Reddy P, Suneetha S (2018) Impact of Cattaneo-Christov heat flux in the Casson fluid flow over a stretching surface with aligned magnetic field and homogeneous heterogeneous chemical reaction. Front Heat Mass Transfer 10(7). https://doi.org/10.5098/hmt.10.7
5. Kolin (1936) Electromagnetic flow meter: principle of method and its applications to blood flow measurement. In: Proceedings of the society for experimental biology and medicine, vol. 35, pp. 53–56

6. Sinha A, Misra JC, Shit GC (2016) Effect of heat transfer on unsteady MHD flow of blood in a permeable vessel in the presence of non-uniform heat source. Alexandria Eng J 55(3):2023–2033. https://doi.org/10.1016/j.aej.2016.07.010

7. Sud VK, Sekhon GS (1989) Blood flow through the human arterial system in the presence of a steady magnetic field. Physiol Med Biol 34(7):795–805

8. Szasz A (2007) Hyperthermia, a modality in the wings. J Cancer Res Ther 3(1):56–66

9. Shehzad SA, Hayat T, Alsaedi A, Obid MA (2014) Nonlinear thermal radiation in three-dimensional flow of Jeffrey nanofluid: a model for solar energy. Appl Math Comput 248:273–286. https://doi.org/10.1016/j.amc.2014.09.091

10. Hayat T, Imtiaz M, Alsaedi A, Kutbi MA (2015) MHD three-dimensional flow of nanofluid with velocity slip and nonlinear thermal radiation. J Magn Magn Mater 396:31–37. https://doi.org/10.1016/j.jmmm.2015.07.091

11. Hayat T, Muhammad T, Alsaedi A, Alhuthali M (2015) Magnetohydrodynamic three-dimensional flow of viscoelastic nanofluid in the presence of nonlinear thermal radiation. J Magn Magn Mater 385:222–229. https://doi.org/10.1016/j.jmmm.2015.02.046

12. Bala Anki Reddy P, Suneetha S, Bhaskar Reddy N (2017) Numerical study of MHD Boundary Layer Slip Flow of a Maxwell Nanofluid over an exponentially stretching surface with convective boundary condition. Propulsion Power Res **6**(4):259–268 (2017). https://doi.org/10.1016/j.jppr.2017.11.002

13. Misra JC, Kar BM (1989) Momentum integral method for studying flow characteristics of blood through a stenosed vessel. Biorheology **26**(1):23–25 (1989). https://doi.org/10.3233/BIR-1989-26102

14. Gebhart B (1962) Effects of viscous dissipation in natural convection. J Fluid Mech 14(2):225–232. https://doi.org/10.1017/S0022112062001196

15. Reddy SRR, Bala Anki Reddy P, Suneetha S (2018) Magneto hydro dynamic flow of blood in a permeable inclined stretching viscous dissipation, non-uniform heat source/sink and chemical reaction. Front Heat Mass Transfer 10(22). https://doi.org/10.5098/hmt.10.22

16. Gireesha BJ, Mahanthesh B, Rashidi MM (2015) MHD boundary layer heat and mass transfer of a chemically reacting Casson fluid over a permeable stretching surface with non-uniform heat source/sink. Int J Indus Math 7(3):247–260

17. Mabood F, Ibrahim SM, Rashidi MM, Shadloo MS, Lorenzini G (2016) Non-uniform heat source/sink and Soret effects on MHD non-Darcian convective flow past a stretching sheet in a micropolar fluid with radiation. Int J Heat Mass Transf 93:674–682. https://doi.org/10.1016/j.ijheatmasstransfer.2015.10.014

18. Ali N, Ullah Khan S, Sajid M, Abbas Z (2016) MHD flow and heat transfer of couple stress fluid over an oscillatory stretching sheet with heat source/sink in porous medium. Alexandria Eng J 55(2):915–924. https://doi.org/10.1016/j.aej.2016.02.018

19. Srinivas S, Reddy PBA, Prasad BSRV (2014) Effects of chemical reaction and thermal radiation on MHD flow over an inclined permeable stretching surface with non-uniform heat source/sink: an application to the dynamics of blood flow. J Mech Med Biol 14(5):1450067. https://doi.org/10.1142/S0219519414500675

20. Mohammadein SA, Raslan K, Abdel-Wahed MS, Abedel-Aal Elsayed M (2018) KKL-model of MHD CuO-nanofluid flow over a stagnation point stretching sheet with nonlinear thermal radiation and suction/injection. Results Phys 10:194–199. https://doi.org/10.1016/j.rinp.2018.05.032

21. Bestman AR (1990) Natural convection boundary layer with suction and mass transfer in a porous medium. Int J Eng Res 14:389–96

22. Shafique Z, Mustafa M, Mushtaq A (2016) Boundary layer flow of Maxwell fluid in rotating frame with binary chemical reaction and activation energy. Results Phys 6:627–633. https://doi.org/10.1016/j.rinp.2016.09.006

23. Lu D, Ramzan M, Ahmad S, Dong Chung J, Farooq U (2017) Upshot of binary chemical reaction and activation energy on carbon nanotubes with Cattaneo-Christov heat flux and buoyancy effects. Phys Fluids 29:123103 (2017)

24. Dhlamini M, Kameswaran PK, Sibanda P, Motsa S, Mondal H (2018) Activation energy and binary chemical reaction effects in mixed convective nanofluid flow with convective boundary conditions. J Comput Design Eng 6:149–158. https://doi.org/10.1016/j.jcde.2018.07.002
25. Khalid A, Khana I, Khan A, Shafied S, Tlilie I (2018) Case study of MHD blood flow in a porous medium with CNTS and thermal analysis. Case Stud Thermal Eng 12:374–380. https://doi.org/10.1016/j.csite.2018.04.004

Mechanics of Multifunctional Composites and Their Applications: A Review of Challenges and Emerging Trends

V. Sowjanya, B. Rammohan, and P. R. Budarapu

Abstract Multifunctional structural materials are designed to perform more than one function, apart from their inherent load bearing capabilities. Therefore, multifunctional materials are composite in nature and are in great demand in various applications. Several researchers have been working on enhancing designs of multifunctional composite structures. Fabrication of multifunctional composite materials is a confronting task due to the involved critical structures. The new generation of multifunctional composite materials will consist of not only interacting components and micro-structural morphologies but also materials that respond differently under combined external influence. Therefore, the material selection and hence the structural design of multifunctional systems that can efficiently handle multiple fields such as mechanical, thermal, electromagnetic fields, to name a few, is a challenging task. An attempt has been made here to present a review of the latest technologies in the field of multifunctional structures. The main aim of the present review is on the study of modified constitutive laws for various scenarios and the relevant applications in fields like aerospace, automotive, construction, energy, clean water generation, to name few.

Keywords Multifunctional composites · Load bearing · Applications · Material selection

1 Introduction

By coalescing the various functionalities like piezoelectric, photovoltaic, and thermoelectric equipment into the arrangement of composite laminates, outmoded constituents can be eliminated from a system, devised to the weight saving and volume of the structure. The hypothesis of multifunctionality in material structures targets to mingle numerous vital tasks hooked on solitary constituent to increase the complete

V. Sowjanya · B. Rammohan (✉)
PES University, Bangalore, India
e-mail: rammohanb@pes.edu

P. R. Budarapu
IITB, Odisha, India
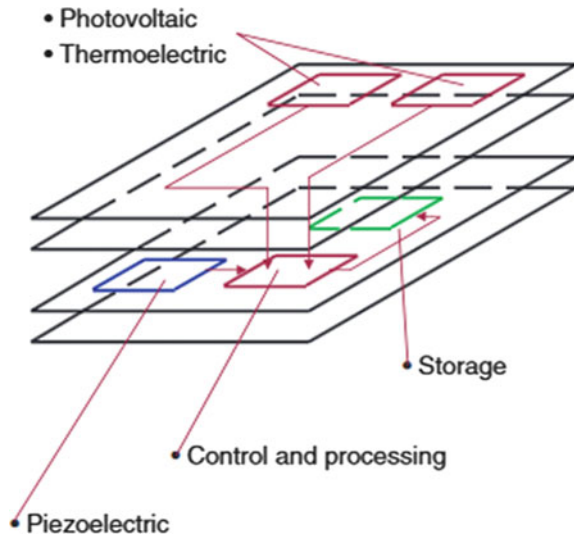
functioning of a structure [1]. The mechanical properties of the structural components
can be modified to approximate the stresses confronted in the active circumstances.
Examples include personal digital assistant, active radio-frequency identification,
micro-aerial vehicles, unmanned aerial vehicles, etc. (Fig. 1).

The nonlinear nature of the complicated geometries that are experienced in bukliphilia makes the derivation of closed analytical results a challenging work, which
can be handled by establishing cutting-edge algorithms in distinction to computeraided design that accomplishes the capability of various differential mathematics for
numerically adequate computational approaches for engineering mechanics [2]. The
outlook of this work is to equip an analysis of emerging technologies that have been
prominent toward the awareness of multifunctional composite materials and structural components, which on one hand can exhibit exceptional structural performance
with significance in their damage tolerance, and on the other hand, can possess builtin sensing potential. Multifunctional composite materials conventionally symbolize
a leading structural material solution with high specific strength and stiffness as well
as contributing remarkable toughness. However, they have an appealing outlook for
the future of additional functionality by connecting disparate materials that can afford
specific traits that perhaps respond together interdependently.

2 Material Modeling

Chen et al. [3] presented a consolidated inverse homogenization proceeding incorporating the antecedent physical properties and their consolidations with the elasticity
tensor to design multifunctional composites for engineering practices.

Yin et al. [4] demonstrated a tensile constitutive association and a finite element representation of electrospun nanofibrous mats. The organization for micromechanics constitutive model is as shown in Fig. 2.

The modeling of damage advancement on multiple length scales in structural composites is imperative in designing both sensing and actuation accomplishments. Furthermore, temperature changes modify the assessment of operating components over changes in thermomechanical fields and modifications in coupled functions, as an illustration in pyroelectric materials. These complexities appeal to an innovative modeling access to the problem proposed by Yehia Bahei and Amany Micheal [5]. The researcher also described the laminate geometry, load, and material (see Fig. 3) presenting constitutive equations for effective, homogenous material in addition to fibrous composites applying micro-mechanics. Constitutive equations of the phases can be written as (Fig. 4):

$$\sigma_r = L_r * \varepsilon_r + \lambda_r \text{ [5]} \tag{1}$$

Fig. 2 Organization of the micro-mechanics constitutive model [4]

Constitutive model (microscopic structure parameters

Experimental and Theoritical verification

Plastic behavior (material yield criterion)

Elastic behavior(equations of elastic theory)
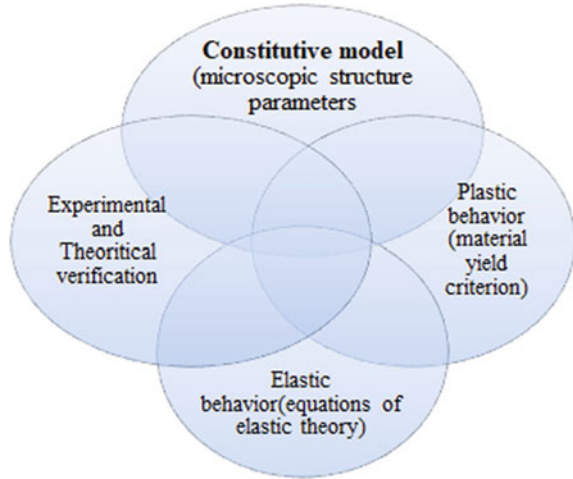
Fig. 3 Load and geometry of a fibrous laminate. "Reproduced with permission from [5]"
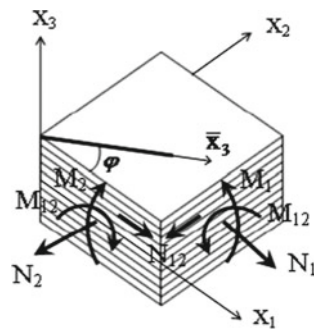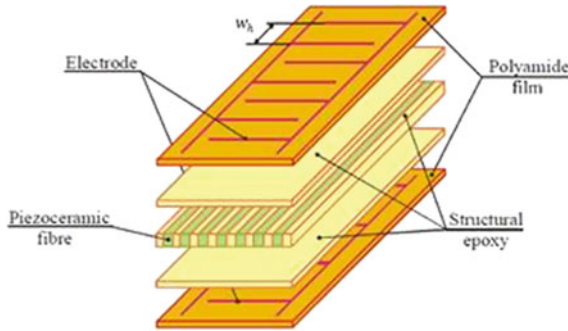
Fig. 4 MFC actuator construction. "Reproduced with permission from [6]"

$$\varepsilon_r = M_r * \sigma_r + \mu_r \ [5] \tag{2}$$

Narayana et al. [7] reported that the multifunctional composites consist of rectangular piezo-ceramic rods interceding between layers of adhesive electrodes and a polyimide film. The electrodes adhere to the film in an interlocking package which carries the applied voltage accurately to and from the ribbon-shaped rods. This congregation aids in-plane poling, actuation, and sensing in a closed and stable package. The multifunctional composite can also be imposed as a thin, surface-conformable sheet to different groups of structures. If the voltage is applied, it will distort materials, or generate vibrations. If no voltage is applied, it can behave as a responsive strain gauge, anticipating fluctuations, noise, and deformation. Compton et al. [8] reported a continuous epoxy-built ink which aids three-dimensional printing of cellular composites with the composed arrangement of multiscale, extreme aspect ratio fiber reinforcement to design stratified structures activated by balsa wood. Using this exclusive mixture of hierarchical inks and 3D printing, they created lightweight cellular composites which display Young's modulus values that are an order of magnitude larger than those acquired by thermoplastics and photo-curable resins refined for commercial additive manufacturing mechanisms while reserving durability (see Fig. 5).

Lin and Sodano [9] examined the advancement of a multifunctional material manufactured from a conductive structural fiber enclosed in a piezoelectric shell, which would then be entrenched into a polymer matrix to model an active fiber composite that promotes for energy harvesting. In order to assess the future of this material system, researchers fabricated a prototype ASF by coating a silicon carbide fiber with $BaTiO_3$ (see Fig. 6).

Design and analysis of functionally graded materials have been inspected by Birman and Byrd [10], the field of structural health supervision is well admissible here, and several research articles have come in recent past. Rawal [11] introduced thermal control design elucidation aimed at rising thermal loads for electronic constituents, multifunctional structures panel comprising a structural board with central thermal
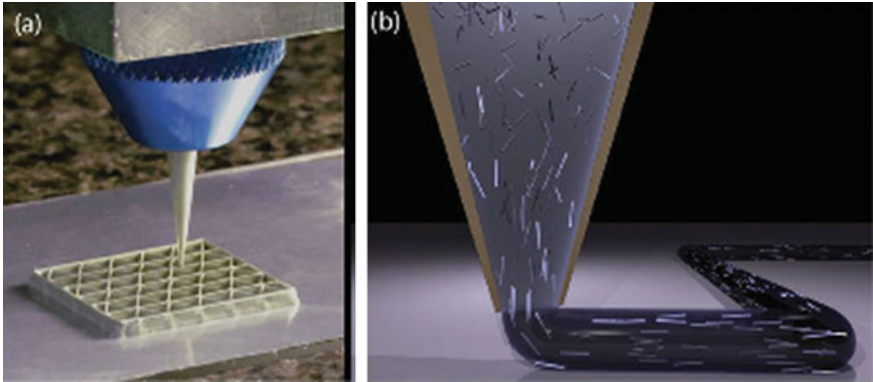
Fig. 5 **a** Visual image of additive manufacturing of a three-cornered honeycomb composite structure. "Reproduced with permission from [8]". **b** Illustration of the continuous arrangement of large aspect ratio fillers inside the nozzle at the time of composite ink discharge [8]

Fig. 6 Schematic showing electrophoretic deposition. "Reproduced with permission from [9]"
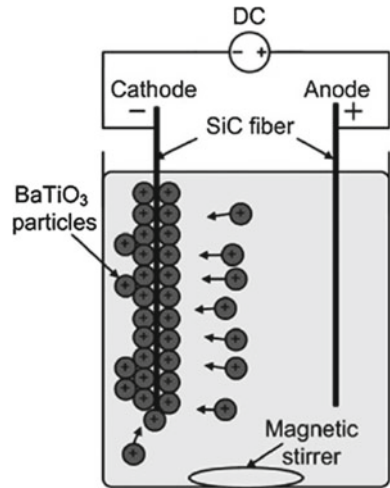
control, polyimide flex circuitry, multichip module plugs, and composed case which afford to electromagnetic guarding and preservation.

3 Multifunctional Mechanics

Jang et al. [12] described the manufacturing of hexagonal honeycomb texture (see Fig. 7b) by the chilled expansion of the laminate of fine metal foils evaluating the consequence of the expansion on the compressive reaction of the honeycomb. A finite element model of characteristic cell is developed utilizing shell elements and implementing to it the applicable periodicity requirements. Theocaris et al. [13] determined an suitable mathematical procedure for utilization of homogenization method based on finite element modeling for the absolute cell of the structure and optimality benchmark. Teik et al. [14] presented one set of equations to evaluate constitutive properties of honeycomb micro-structural material whether it possess positive or negative Poisson's ratio. The constitutive law developed would be useful for engineering applications involving micro-structural design. Li et al. [15] presented the different forms of smoothed finite element method (SFEM) to promote a new asymptotic homogenization approaches (see Fig. 7a) for evaluating miscellaneous adequate physical features of periodic micro-structural composite materials. Idealizing multifunctional composites behaving similar to a 2D orthotropic structure, the following equations are given in [16].

$$\varepsilon_1 = \frac{1}{E1}\left(\sigma_1 - \upsilon'_{12} * \sigma_2\right) \, [16] \tag{3}$$

$$\varepsilon_2 = \frac{1}{E2}\left(\sigma_2 - \upsilon'_{21} * \sigma_1\right) \, [16] \tag{4}$$

Nelson [17] conceptualized a constitutive law for a high-temperature elastic memory composite material adopting fixed strain micro-mechanics. As resin and fibers do not exhibit material nonlinearity, the model will only be considered for nonlinearity correlated with mathematical consequences. Jeong-Beom et al. [18] introduced a built-in technique using piezoelectric sensor/actuator network for detection and monitoring of hidden fatigue crack growth, validated using riveted joints, and fixed with a
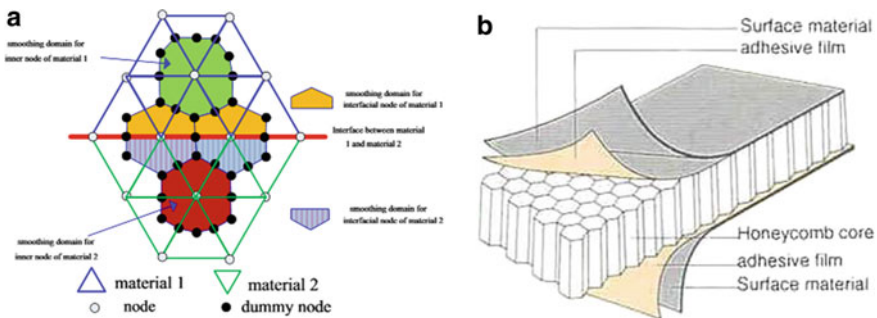
Fig. 7 a Smoothing domain for multi-material. "Reproduced with permission from [15]". **b** Structure of honeycomb sandwich. "Reproduced with permission from [16]"

bonded composite strip. Ray and Mallik [19] employed static considerations of laminated composite covers consolidated with a piezoelectric fiber-reinforced composite sheet interim as dispensed actuators have been approved by a generalized-energy-based finite element method. A first-order shear distortion concept is used aimed at originating the theory. Eight-node isoparametric serendipity elements are used for discretizing the domain. The effect of piezoelectric fiber alignment on the control authority of the piezoelectric fiber-reinforced composite film. White et al. [20] explained an absolutely independent multifunctional structure able to perform healing itself when busted, as a biological structure do, and current study has manifested the expediency of self-healing polymer composites established on the application of a micro-encapsulated restorative agent and a stimulant for polymerizing. As shown in Fig. 8a, the impairment causes fracture in the polymer, the cracks open the micro-capsules, inducing the healing agent to flow into the crack by capillary force. The healing agent then reacts with the catalyst, causing polymerization that bonds the crack faces as a group. Figure 8b shows a hexagonal honeycomb, where in-plane stiffness's and strengths (those in X_1-X_2 plane) are smallest since stresses in this plane make the cell walls to deform. The out-of-plane stiffness in addition to strength (those in X_3 path) is much better, as a result, they require axial extension or compression of the cell walls proposed by Zhang et al. [21].
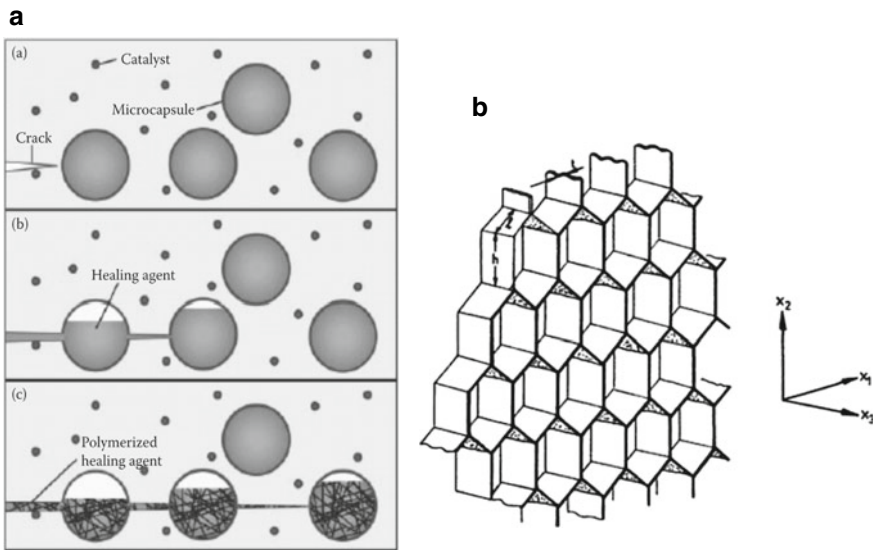
Fig. 8   a Demonstration of self-restorative cracks in polymers. **a** Cracks arrangement in the matrix; **b** Crack splits the micro-capsules, clearing the healing. Promoter into the crack during capillary force. **c** Curing promoter associates the stimulant, provoking polymerization that binds the crack faces sealed. "Reproduced with permission from [20]". **b** A honeycomb with hexagonal cells. "Reproduced with permission from. [21]"

4 Characteristics

See Table 1.

5 Structural Applications of Multifunctional Composites

Composite structural components are utilized in different elements for aerospace, automotive, architectural, and marine structures. Most of the present composites technology emerged from aerospace applications. Carbon fiber composite structural elements like horizontal and vertical stabilizers, flaps, wing skins, and various control surfaces have been used in fighter aircraft for many years. More recently, carbon fiber composite fuselage and wing structures have been integrated into fighter aircraft such as the F-35 Lightning II Joint Strike Fighter (Fig. 9a) and in the complete structure of the B2 stealth bomber (Fig. 9b).

Qing [32] developed a concurrent functional smart patch structure for observing the reliability of fused restoration on an aircraft structure. These repairs provide an efficient method for restoring the ultimate load capability of the structure (Figs. 10 and 11).

The NASA technology transfer program [35] released a report on the invention of macro-fiber composite which is an ingenious, economical piezoelectric device created for controlling vibration, noise, and deviations in composite structural beams. It was proposed for mitigating tail buffeting in aircraft, regulating unstable aviation and buzz on helicopter rotor blades, and actively compressing fluctuations in large portable spacecraft structures.

The applications in the medical field are explained by modeling of chemo-mechanical transduction in sub-cellular components such as motor proteins and modeling cell behavior of dynamic reorganization of the cytoskeleton that is caused by biochemical mechanism which was detailed in a Report by USNC on theoretical and applied mechanics [36].

Lou et al. [37] projected the application of reduced graphene oxide (rGO) sheets within multifunctional composites for generation of clean water from contaminated water by adsorption, photo-degradation, and interfacial heat-assisted distillation mechanism (Fig. 12).

A genetic algorithm-based multidisciplinary escalation technique was used to blend the subsystem to a micro-air vehicle for maximal endurance forecasted by Grasmeyer et al. [38]. Lithium-ion batteries were used for power repository in the micro-air vehicle due to its immense energy density, accuracy, and low price (Fig. 13).

Barnett et al. [39] introduced multifunctional structure technology elements which facilitate an advanced class of inflatable spacecraft that is dependent on miniature, packed volumes and calculable arrangement that is free from cabling and entanglements.

Table 1 Recent research and advancements in multifunctional composites: a gist on structural characteristics from various research investigations

Researcher names	Material	Function	Characteristics
Amit Patel et al. [22]	Urea-formaldehyde micro-capsules incorporating dicyclopentadiene liquid heating agent and paraffin wax micro-spheres comprising 10% weight Grubbs catalyst assimilated in the reinforced epoxy composite	Automatic self-healing/repairing of impact damage, selective permeation	Residual compressive strength, average stress at the maximum tangent stiffness
Saafi et al. [23]	Potassium–geopolymeric(KGP) cementitious composites	Reserve and distribute energy, self-monitoring/diagnostics	Sensors for structural health monitoring, intelligent concrete structures with innate capacitors. (electrical energy storage)
Huang et al. [24]	Carbon fiber-reinforced thermoset composite	Tolerance to damage	Damage detection, damage repair
Khocha et al. [25]	Renewable energy sources, such as photovoltaic generators	Energy management system for a smart house based on hybrid PV-battery and V2G	Vehicle to grid operation, motile energy storage device
Shirshova et al. [26]	Carbon fibers unified with a porous bicontinuous monolithic carbon aerogel Over the matrix	Immense strength and electrochemical surface area	Ionic conductivity, energy storage super capacitors
Ladpli et al. [27]	Li-ion battery materials embed to structural carbon fiber composites	Structural health monitoring and prognostics	Damage detection, battery charge, and health state.
Zhang et al. [28]	Graphene and hardened cement paste	High and ionically-accessible surface area and good conductivity, as well as thermal and chemical stability	Compressive strength and specific capacitance

Table 1 (continued)

Researcher names	Material	Function	Characteristics
Williams et al. [29]	Vascular networks carrying two liquid components of the epoxy resin	Vascular self-healing, damage tolerance	Escalating the reclamation of core elastic support by augmenting the degree of cure in the catastrophe zone, restoration of compressive strength after impact
Till Julian Adam et al. [30]	Glass-fiber-reinforced composite based on ceramic electrolyte [LATP]	Structural energy storage	Load carrying ability, electrical resistivity, high energy density, enhanced structural properties
Yanyu Chen et al. [31]	Architected metamaterials	Tunable photonic properties, heat mitigation capability	Load carrying capacity, improved thermal resistance, specific stiffness

a   **b**
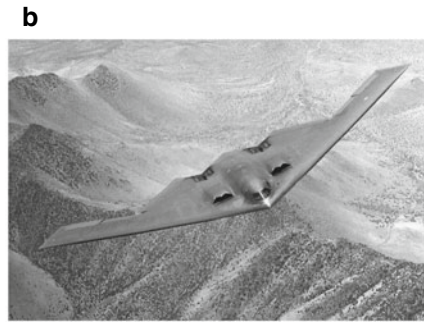
Fig. 9   **a** Fighter aircraft. "Reproduced with permission from [16]". **b** Stealth bomber [16]
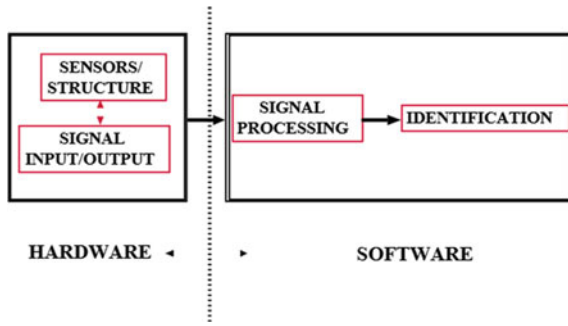
Fig. 10 Components of the proposed structural strength control system. "Reproduced with from [33]"
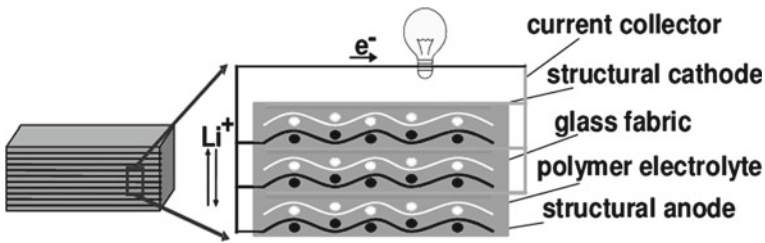
Fig. 11 A concept of a structural battery. "Reproduced with permission from [34]
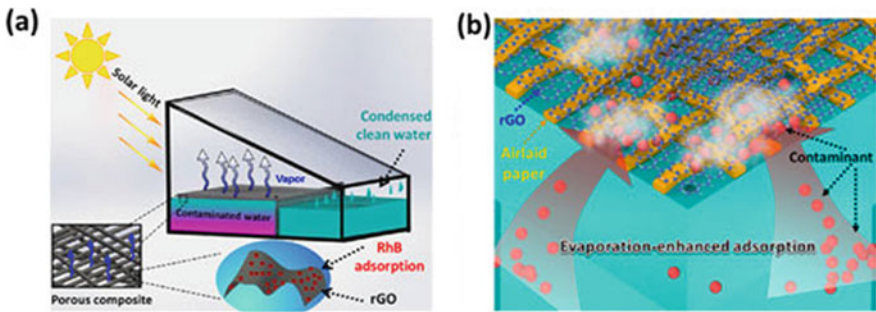
Fig. 12 **a** Schematic for clean water generation by floating under solar irradiation [37]. **b** Schematic of adsorption removal RhB air-laid paper-based rGO composite

Sercel et al. [40] introduced progressive materials and structures that conveyed low mass, low cost, and low launch volume and allowed micro-spacecraft to setup large-diameter apertures with acceptable surface precision fixing power collection, thermal management, communications, and science instruments thereby diminishing the expenditure and mass of new millennium spacecraft.
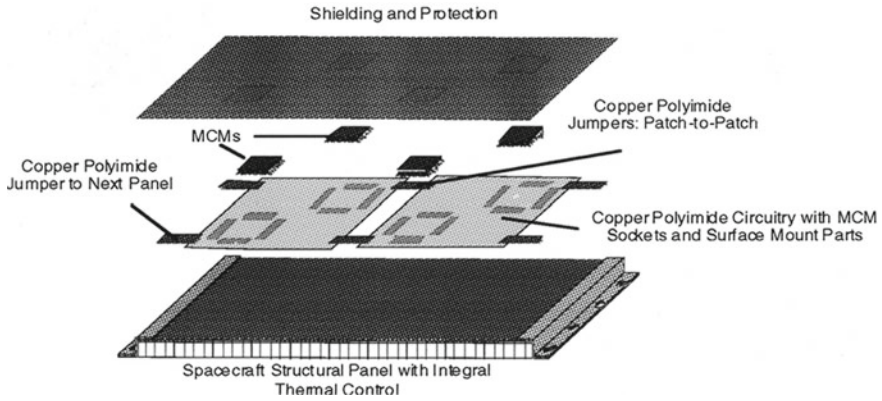
Fig. 13 MFS panel comprising a structural board with thermal control, polyimide flex circuitry, MCM sockets formed cover, providing electromagnetic guarding and protection. "Reproduced with permission from [40]"

Volvo collectively with Imperial college of London, nine organizations, and nine other European enterprises have been rising body panels for cars that accumulate power (Fig. 14) [41]. The charging of a simple sheet of a carbon fiber multifunctional composite being charged and subsequently being consumed to irradiate a light was demonstrated in an interview. Moderate approximations on weight savings approach
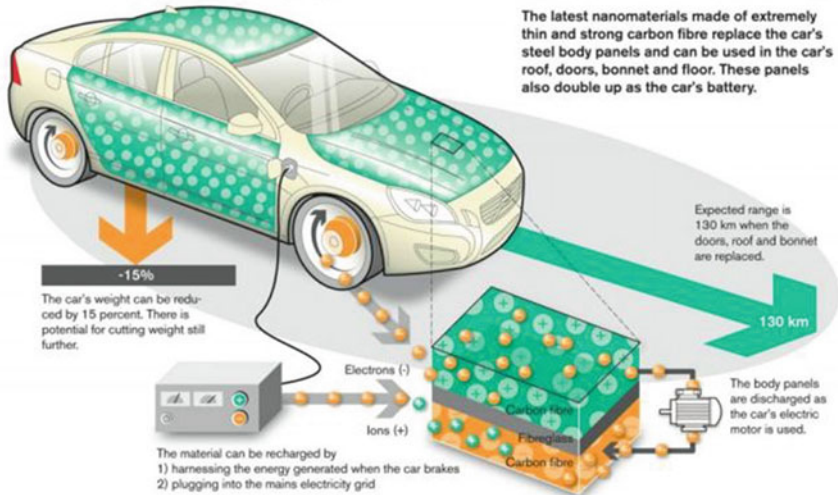
Fig. 14 Schematic of car body panels that serve as a battery. "Reproduced with permission from [41]"

15% carbon fibers, nano-structured capacitors, and super capacitors which serve as materials.

6 Conclusion

This paper reviewed the challenges in mechanics of multifunctional composites' characteristics which allow us to analyze the output results of the system, and their applications in aerospace examples refer to: improvement of process ability; self-diagnostic capability; improvement of the allowances acting on reduction of the knock down factor required to take in account the environmental aging effects. The reinforcement of fibers could have two distinctive alignments which when imbedded in a conducting polymer matrix would produce a galvanic current. Such materials are source for modern generation of sustained-service, less-weight electric vehicles. Civil infrastructure industry uses multifunctional composites for following applications like bridge construction with bridge deck systems, bridge construction with composites for following applications, hybrid materials, bridge strengthening and repair, seismic column retrofit, bridge construction with FRP deck systems. A general strategy was proposed with multifunctional composite materials which remove microbial, organic, and radioactive impurities without requirement of multiple filters for producing pure water. The analysis of in-plane properties of a honeycomb structure focuses the procedure by which cellular solids distort and fail, whereas the out-of-plane investigation gives the bonus stiffness needed for the design of honeycomb cores in sandwich panels. Resolving multifunctional composites dynamic response and accomplishing modification in the constitutive law, using variational asymptotic method (VAM) for evaluation is the further scope of this work.

References

1. Pereira T, Guo Z, Nieh S, Arias J, Hahn HT (2009) Energy storage structural composites: a review. J Compos Mater 43(5):549–560
2. Reis PM (2015) A perspective on the revival of structural (in) stability with novel opportunities for function: from Buckliphobia to Buckliphilia. J Appl Mech 82(11):111001
3. Chen Y, Zho S, Li Q (2009) Computational design for multifunctional microstructural composites. Int J Modern Phys B 23(06n07):1345–1351
4. Yin Y, Pan Z, Xiong J (2018) A tensile constitutive relationship and a finite element model of electrospun nanofibrous mats. Nanomaterials 8(1):29
5. Bahei-El-Din Y, Micheal A (2012) Micromechanical modeling of multifunctional composites. In: Design, materials and manufacturing, Parts A, B, and C, vol 3
6. Kovalovs A, Barkanov E, Gluhihs S (2007) Active control of structures using macro-fiber composite (MFC). J Phys: Conf Series 93
7. Narayana KJ, Gupta Burela R (2018) A review of recent research on multifunctional composite materials and structures with their applications. Mater Today: Proc 5(2):5580–5590
8. Compton BG, Lewis JA (2014) 3D-printing of lightweight cellular composites. Adv Mater 26(34):5930–5935

9. Lin Y, Sodano HA (2009) Fabrication and electromechanical characterization of a piezoelectric structural fiber for multifunctional composites. Adv Func Mater 19(4):592–598

10. Birman V, Byrd LW (2007) Modeling and analysis of functionally graded materials and structures. Appl Mech Rev 60(5):195

11. Rawal SP, Barnett DM, Martin DE (1999) Thermal management for multifunctional structures. IEEE Trans Adv Packag 22(3):379–383

12. Jang W-Y, Kyriakides S (2015) On the buckling and crushing of expanded honeycomb. Int J Mech Sci 91:81–90

13. Theocaris PS, Stavroulakis GE (1998) The homogenization method for the study of variation of Poisson's ratio in fiber composites. Arch Appl Mech (Ingenieur Archiv) 68(3–4):281–295

14. Lim T-C (2003) Constitutive relationship of a material with unconventional Poisson's ratio. J Mater Sci Lett 22(24):1783–1786

15. Li E, Zhang Z, Chang CC, Zhou S, Liu GR, Li Q (2016) A new homogenization formulation for multifunctional composites. Int J Comput Methods 13(02):1640002

16. Lorna J, Gibson, Ashby MF (1999) Cellular solids—structures and properties. Cambridge solid state science series, Cambridge University Press

17. Nelson E, Hansen A, Key C, Francis W (2007) Multicontinuum analysis of fiber microbuckling in elastic memory composite structures. In: 48th AIAA/ASME/ASCE/AHS/ASC structures, structural dynamics, and materials conference

18. Ihn J-B, Chang F-K (2004) Detection and monitoring of hidden fatigue crack growth using a built-in piezoelectric sensor/actuator network: II. Validation using riveted joints and repair patches. Smart Mater Struct 13(3):621–630

19. Ray MC, Mallik N (2004) Finite element analysis of smart structures containing piezoelectric fiber-reinforced composite actuator. AIAA J 42(7):1398–1405

20. White SR, Sottos NR, Geubelle PH, Moore JS, Kessler MR, Sriram SR, Brown EN, Viswanathan S Autonomic healing of polymer composites. Nature Journal Publication

21. Zhang J, Ashby MF (1992) The out-of-plane properties of honeycombs. Int J Mech Sci 34(6):475–489

22. Patel AJ, Sottos NR, Wetzel ED, White SR (2010) Autonomic healing of low-velocity impact damage in fiber-reinforced composites. Compos A Appl Sci Manuf 41(3):360–368

23. Saafi M, Gullane A, Huang B, Sadeghi H, Ye J, Sadeghi F (2018) An inherently multifunctional geopolymeric cementitious composite as electrical energy storage and self-sensing structural material. Compos Struct 201:766–778

24. Huang X, Zhao S (2017) Damage tolerance characterization of carbon fiber composites at a component level: a thermoset carbon fiber composite. J Compos Mater 52(1):37–46

25. Khoucha F, Benbouzid M, Amirat Y, Kheloui A (2015) Integrated energy management of a plug. In: Electric vehicle in residential distribution systems with renewables, IEEE proceedings 2015, ISIE, June 2015, Buzios-Rio de Janeiro, Brazil, IEEE, pp 775–780

26. Shirshova N, Qian H, Houllé M, Steinke JHG, Kucernak ARJ, Fontana QPV, Shaffer MSP (2014) Multifunctional structural energy storage composite supercapacitors

27. Ladpli P, Nardari R, Kopsaftopoulos F, Wang Y, Chang F-K (2016) Design of multifunctional structural batteries with health monitoring capabilities. In: 8th European Workshop On Structural Health Monitoring (EWSHM 2016), 5–8 July 2016, Spain, Bilbao

28. Zhang J, Xu J, Zhang D (2015) A structural supercapacitor based on graphene and hardened cement paste. J Electrochem Soc 163(3):E83–E87

29. Williams HR, Trask RS, Bond IP (2008) Self-healing sandwich panels: restoration of compressive strength after impact. Compos Sci Technol 68(15–16):3171–3177

30. Adam T, Liao G, Petersen J, Geier S, Finke B, Wierach P, Wiedemann M (2018) Multifunctional composites for future energy storage in aerospace structures. Energies 11(2):335

31. Chen Y, Jia Z, Wang L (2016) Hierarchical honeycomb lattice metamaterials with improved thermal resistance and mechanical properties. Compos Struct 152:395–402

32. Qing XP, Beard SJ, Kumar A, Hannum R (2006) A real-time active smart patch system for monitoring the integrity of bonded repair on an aircraft structure. Smart Mater Struct 15(3):N66–N73

33. Lin M, Chang F-K (1999) Composite structures with built-in diagnostics. Mater Today 2(2):18–22
34. Snyder JF, Baechle DM, Wetzel ED (2006) Multifunctional structural composite Batteries for U.S Army Applications. U. S. Army Research Laboratory, A reprint from the proceedings of the 2006 Army Science Conference, Orlando, Florida, 27–30 November 2006
35. A report of NASA Technology transfer program. NASA invention of the year, controls Noise and Vibration, 2018
36. A report Research directions in computational and composite mechanics of the United States National Committee on Theoretical and Applied Mechanics (USNC/TAM), June 2007
37. Lou J, Liu Y, Wang Z, Zhao D, Song C, Wu J, Deng T (2016) Bioinspired multifunctional paper-based rGO composites for solar-driven clean water generation. ACS Appl Mater Interf 8(23):14628–14636
38. Grasmeyer M, Keennon MT, Development of the Black Widow Micro Air Vehicle (2001) Fixed and flapping wing aerodynamics for micro air vehicle applications, 519–535
39. Barnett DM, Rawal S, Rummel K (2001) Multifunctional structures for advanced spacecraft. J Spacecraft Rockets 38(2):226–230
40. Sercel J, Hanks B, Boynton W, Cassapakis C, Crawley E, Curcio M et al (1996) Modular and multifunctional systems in the New Millennium Program. 34th Aerospace Sciences Meeting and Exhibit
41. Volvo cars, Tomorrow's Volvo car: body panels serve as the car battery, 2015

Oscillatory Darcy-Bénard-Poiseuille Mixed Convection in An Oldroyd-B Fluid-Saturated Porous Layer

G. Pallavi, C. Hemanthkumar, I. S. Shivakumara, and B. Rushikumar

Abstract The combined effect of horizontal pressure gradient and the thermal buoyancy caused by gravity forces on the onset of convective instability in a layer of an Oldroyd-B fluid-saturated porous medium is investigated. The stability equations are found to be with complex coefficients, and the ensued generalized eigenvalue problem is solved numerically by utilizing the Galerkin method with the aid of *QZ* algorithm as well as analytically using a single-term Galerkin approach. The instability is instilled as oscillatory under certain conditions. The effect of constant horizontal pressure gradient is to advance the onset of oscillatory convection and also to increase the range of values of the strain retardation parameter within which the oscillatory convection is preferred. Besides, the critical frequency of oscillations is suppressed.

Keywords Oscillatory convection · Local thermal equilibrium · Pressure gradient · Oldroyd-B fluid · Porous layer

Nomenclature

a	Wave number in the x-direction
d	Depth of the porous layer
$D = d/dz$	Differential operator
$\vec{g}$	Acceleration due to gravity
κ	Effective thermal diffusivity
K	Permeability of the porous medium

G. Pallavi · C. Hemanthkumar · I. S. Shivakumara (✉)
Department of Mathematics, Bangalore University, Bengaluru 560 056, India
e-mail: shivakumarais@gmail.com

G. Pallavi
Department of Mathematics, NMIT, Bengaluru 560 064, India

B. Rushikumar
Department of Mathematics, VIT University, Vellore 632 014, India
e-mail: rushibkumar@gmail.com

827

p	Pressure
$\vec{q}$	Velocity vector
R_D	Darcy-Rayleigh number
t	Time
T	Temperature
T_1	Temperature at upper boundary
T_0	Temperature at lower boundary
W	Amplitude of perturbed vertical component of velocity
(x, y, z)	Cartesian coordinates

Greek Symbol

α	Heat capacity ratio
β	Thermal expansion coefficient
ε	Porosity
λ_1	Relaxation time
λ_2	Retardation time
Λ_1	Stress relaxation parameter
Λ_2	Strain retardation parameter
μ_f	Viscosity of the fluid
ω	Growth factor ($= \omega_r + i\omega_i$)
ρ	Fluid density
ρ_0	Fluid density at $T = T_0$
Π	Dimensionless pressure gradient
ψ	Stream function
Ψ	Amplitude of the perturbed stream function
θ	Perturbed temperature
Θ	Amplitude of perturbed temperature

Subscripts and Superscripts

b	Basic state
$*$	Dimensionless variable
$'$	Perturbed variable

1 Introduction

Fluids which exhibit both viscous and elastic behaviors under some conditions are termed as viscoelastic fluids, and they form a general type of non-Newtonian fluids. There exist different types of viscoelastic fluid models proposed by Oldroyd, Maxwell, Rivlin-Ericksen, Walters, and so on. The fluid flows encountered in geophysics such as in improved oil recovery processes, polymer dispensation, filtration of solids from fluids, and lubrication are often modeled as viscoelastic fluid flows through porous media [2, 19, 21].

The problem of onset of Darcy-Bénard convection for viscoelastic fluids has been studied extensively by utilizing a modified Darcy-Oldroyd model introduced for the first time by Alishaev and Mirzadjanzade [1]. Subsequently, many authors continued their research on this topic for different type of extension covering linear and nonlinear analyses [5, 11, 13, 15, 18, 20, 22, 23]. A general result that was established is that the instability sets in as oscillatory motions rather than stationary under certain conditions. A detailed literature survey is found in the books by Straughan [16, 17] and Nield and Bejan [9].

The study on convection in porous media is largely devoted to thermal buoyancy-induced flows due to constant pressure gradient. The contact between these two modes of convection, termed as Darcy-Bénard-Poiseuille mixed convection, has not received due consideration in the literature in spite of its relevance to geothermal reservoir applications and in the disposal of nuclear waste. Postelnicu [9] studied the onset of thermal convection in a layer of Newtonian fluid-saturated Darcy porous medium in presence of a horizontal pressure gradient. Hirata et al. [3] studied the Rayleigh-Bénard-Poiseuille mixed convection for Maxwell and Oldroyd-B type of viscoelastic fluids.

The main aim of the existing study is to examine the impact of a constant horizontal pressure gradient on the onset of convection in an Oldroyd-B fluid-saturated porous medium. A modified Darcy-Oldroyd formulation is adopted to explain the flow, and the porous medium is assumed to be in LTE. A linear stability analysis is carried out, and the resulting complex eigenvalue problem is solved numerically utilizing the Galerkin method and analytically by using a single-term Galerkin technique. The outcomes are graphically shown for different values of physical parameters.

2 Mathematical Formulation

An incompressible Oldroyd-B fluid-saturated horizontal layer of Darcy porous medium of thickness d is considered as shown in Fig. 1. The lower and upper impermeable boundaries are held at fixed yet various temperatures T_0 and $T_1 (< T_0)$, respectively. Besides, a constant pressure gradient is acting along the horizontal direction in the presence of gravity. The governing stability equation in dimensionless form is [1, 4, 12]:
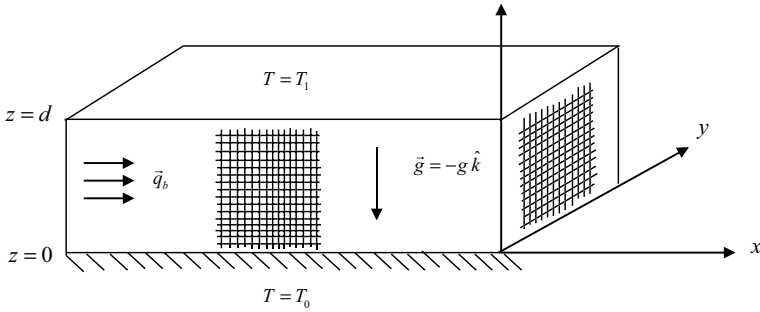
Fig. 1 Schematic of the physical configuration

$$\nabla \cdot \vec{q} = 0, \tag{1}$$

$$\left(1 + \Lambda_1 \frac{\partial}{\partial t}\right)\left(\nabla p - R_D \theta \hat{k}\right) = -\left(1 + \Lambda_2 \frac{\partial}{\partial t}\right)\vec{q}, \tag{2}$$

$$\alpha \frac{\partial \theta}{\partial t} + (\vec{q} \cdot \nabla)\theta = \nabla^2 \theta, \tag{3}$$

where $\vec{q} = (u, v, w)$ is the velocity vector, p is pressure, $R_D = \rho_0 g \beta \, \Delta T \, K d / \varepsilon \mu_f \kappa$ is the Darcy-Rayleigh number, $\Lambda_1 = \lambda_1 \kappa / d^2$ is the stress relaxation parameter, $\Lambda_2 = \lambda_2 \kappa / d^2$ is the strain retardation parameter, α is the ratio of heat capacities, and $\nabla^2 = \partial^2 / \partial x^2 + \partial^2 / \partial z^2$ is the Laplacian operator.

The following quantities are non-dimensionalized as:

$$(x, z) = d(x^*, z^*), \quad \vec{q} = \frac{\kappa \, \varepsilon}{d} \vec{q}^*, t = \frac{d^2}{\kappa_f} t^*, \quad p = \frac{\mu \kappa \varepsilon}{K} p^*, \quad T = (T_0 - T_1)\theta + T_1. \tag{4}$$

The boundary conditions are

$$\vec{q} = 0 \text{ at } z = 0, \, 1 \, ,$$
$$\theta = 1 \text{ at } z = 0, \quad \theta = 0 \text{ at } z = 1. \tag{5}$$

3 Linear Instability Analysis

Let the dimensionless horizontal constant pressure gradient be Π. Then, the basic state is characterized by

$$\vec{q}_b = u_b \, \hat{i} = \Pi \, \hat{i}; \, \theta_b = 1 - z \tag{6}$$

where $\hat{i}$ is the unit vector in the horizontal x-direction. The basic state given by Eq. (6) is perturbed by setting:

$$\vec{q} = \Pi\,\hat{i} + \vec{q}', \quad \theta = 1 - z + \theta'. \tag{7}$$

Equation (7) is substituted back in Eqs. (1)–(3), and then, the equations are linearized. Curl is operated to remove pressure term from the momentum equation and the stream function $\psi'(x, z, t)$ for the perturbed flow which is introduced through

$$\left(u', 0, w'\right) = \left(-\frac{\partial \psi'}{\partial z}, 0, \frac{\partial \psi'}{\partial x}\right). \tag{8}$$

to obtain finally the linear stability equations in the form (after neglecting the primes)

$$\left(1 + \Lambda_2 \frac{\partial}{\partial t}\right)\nabla^2 \psi = R_D\left(1 + \Lambda_1 \frac{\partial}{\partial t}\right)\frac{\partial \theta}{\partial x}, \tag{9}$$

$$\alpha \frac{\partial \theta}{\partial t} + \Pi \frac{\partial \theta}{\partial x} - \frac{\partial \psi}{\partial x} = \nabla^2 \theta. \tag{10}$$

The boundary conditions are

$$\psi = \theta = 0 \quad \text{at} \ z = 0, 1. \tag{11}$$

The normal mode solution is assumed in the form

$$(\psi, \theta) = [\Psi(z), \Theta(z)]\exp\{i(ax) + \omega t\}. \tag{12}$$

Equation (12) is substituted back in Eqs. (9)–(11), to obtain

$$(1 + \Lambda_2\omega)\left(D^2 - a^2\right)\Psi = iaR_D(1 + \Lambda_1\omega)\Theta, \tag{13}$$

$$ia\Psi + \left[(D^2 - a^2) - \alpha\omega - ia\Pi\right]\Theta = 0. \tag{14}$$

$$\Psi = \Theta = 0 \quad \text{at} \ z = 0, 1. \tag{15}$$

Equations (13)–(15) form a complex eigenvalue problem and are numerically solved to extract the critical stability parameters with respect to a as a function of Π, Λ_1, Λ_2 and α. Since $\omega = \omega_r + i\omega_i$, the system is stable if $\omega_r < 0$ and unstable if $\omega_r > 0$. The Galerkin method is observed to be progressively reasonable to take care of the followed eigenvalue problem, and accordingly $\Psi(z)$ and $\Theta(z)$ are expanded in the form:

$$\Psi = \sum_{i=1}^{N} A_i\left(z^i - z^{i+1}\right), \ \Theta = \sum_{i=1}^{N} B_i\left(z^i - z^{i+1}\right). \tag{16}$$

where A_i and B_i are unknown coefficients. The standard technique leads to the generalized eigenvalue problem in the form

$$MX = \omega N X. \tag{17}$$

where M and N are real matrices of order $3N \times 3N$, X is the characteristic vector, and ω is the eigenvalue, following the procedure explained in the work of Shivakumara et al. [14].

4 Discussion of Results

The combined effect of constant pressure gradient and the buoyancy force on the onset of convection in a viscoelastic Oldroyd-B fluid-saturated porous layer is numerically studied using the Galerkin method. The elasticity of the fluid is to instill the instability through oscillatory motions rather than stationary under certain conditions. R_{Dc}, a_c, and ω_{ic} are computed numerically and converged to the desirable degree of accuracy by considering six terms (i.e., N = 6) in the Galerkin expansion, and the process of convergence is shown in Table 1 for various values of known physical parameters. At this juncture, it is intuitive to look at the solution for a single-term Galerkin method as the method supposed to give satisfactory results for thermal instability problems [8]. Taking N = 1 with $\sin\pi z$ as the trial function, an analytical expression from Eq. (16) is obtained for the Darcy-Rayleigh number, and noting that R_D is a real quantity, in the form

$$R_D = \frac{\delta^2\left[\delta^2 + a(\Lambda_1 - \Lambda_2)\Pi\omega_i + (\alpha(\Lambda_1 - \Lambda_2) + \delta^2\Lambda_1\Lambda_2)\omega_i^2\right]}{a^2(1 + \Lambda_1^2\omega_i^2)} \tag{18}$$

Table 1 Process of convergence of Galerkin method when $\alpha = 1$

N	$\Lambda_1 = 0.5, \Lambda_2 = 0.2, \Pi = 0.1$			$\Lambda_1 = 0.5, \Lambda_2 = 0.2, \Pi = 100$		
	a_c	R_{Dc}	ω_{ic}	a_c	R_{Dc}	ω_{ic}
1	3.16,213	19.8259	-7.2615	3.16275	16.0024	-316.465
2	3.16156	19.8178	-7.2524	3.16212	15.9826	-316.182
3	3.15874	19.6945	-7.2458	3.15945	15.8438	-315.254
4	3.14115	19.6589	-7.2286	3.14258	15.8542	-314.458
5	3.14142	19.6178	-7.2145	3.14212	15.7940	-314.398
6	3.14144	19.6172	-7.2052	3.14207	15.7938	-314.395
Single term	3.14144	19.6172	-7.2052	3.14207	15.7938	-314.395

where ω_i is the positive root of the equation

$$\alpha \Lambda_1 \Lambda_2 \omega_i^3 + \Lambda_1 \Lambda_2 a \Pi \omega_i^2 + \left[\alpha - \delta^2(\Lambda_1 - \Lambda_2)\right]\omega_i + a\Pi = 0 \qquad (19)$$

When $\Pi = 0$, Eqs. (18) and (19) yield the critical values

$$R_{Dc} = \frac{(a_c^2 + \pi^2)\left[\alpha + (a_c^2 + \pi^2)\Lambda_2\right]}{a_c^2 \Lambda_1}; \quad a_c^2 = \pi\sqrt{\pi^2 + \frac{\alpha}{\Lambda_2}}$$

$$\omega_{ic}^2 = \frac{(a_c^2 + \pi^2)(\Lambda_1 - \Lambda_2) - \alpha}{\Lambda_1 \Lambda_2 \alpha} \qquad (20)$$

which coincide with those of Kim et al. [5] and Raghunatha et al. [10]. Equation (19) demonstrates that the oscillatory convection is not possible if $\Lambda_1 < \Lambda_2$.

The computed values of critical stability parameters $(R_{Dc}, a_c, \omega_{ic})$ are presented in Figs. 2, 3, and 4a, b, c as a function of Λ_2 for various values of Λ_1 (with $\Pi = 100$, $\alpha = 1$), Π (with $\Lambda_1 = 1$, $\alpha = 1$), and α (with $\Lambda_1 = 1$, $\Pi = 100$), respectively. The result for $\Lambda_2 = 0$ in these figures corresponds to Maxwell fluid, and note that increasing Λ_2 delays the onset of oscillatory convection. Thus, the system is more destabilizing for Maxwell fluid when compared to Oldroyd-B fluid. To the contrary,
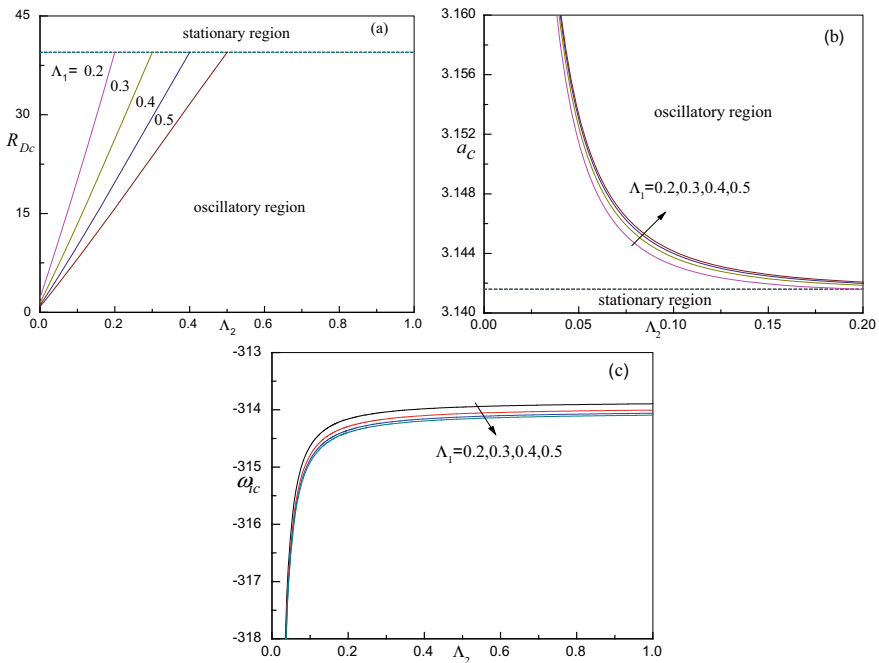
Fig. 2 Critical value of **a** R_{Dc}, **b** a_c, and **c** ω_{ic} with Λ_2 for various values of Λ_1 when $\alpha = 1$ and $\Pi = 100$
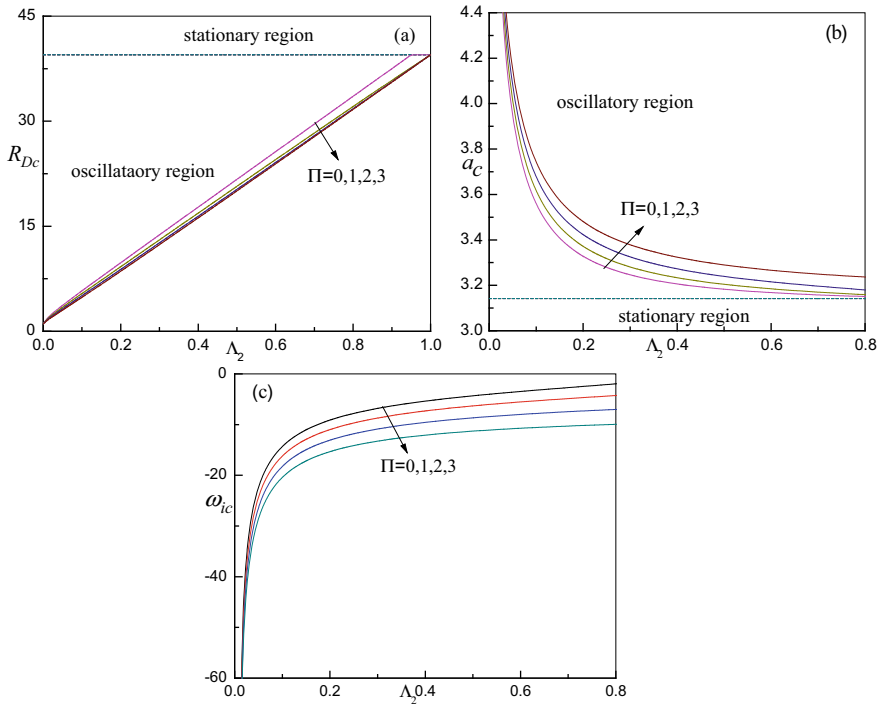
Fig. 3 Critical value of **a** R_{Dc}, **b** a_c, and **c** ω_{ic} with Λ_2 for various values of Π when $\alpha = 1$ and $\Lambda_1 = 1$

increasing Λ_1 hastens the onset of oscillatory convection, and also up to certain range, Λ_2 is preferred (Fig. 2a). This is because; the stickiness of the fluid gets relaxed if the relaxation is enlarged, and hence, lower values of R_{Dc} are enough to trigger the onset. On the other hand, friction will be higher with an increasing retardation parameter, and hence, larger values of R_{Dc} are required to initiate instability.

Increasing Π (Fig. 2a) hastens the onset of convection, and their impact is to build the range of Λ_2 inside which the oscillatory convection is possible. Increase in the horizontal pressure gradient may lead to less stable conduction process in the porous medium, and hence, more heating is not essential to instill instability with increasing Π. An opposite effect is seen with increasing α (Fig. 4a).

The values of a_c decreases monotonically with increasing Λ_2, in general. There is no significant change in a_c with increasing Λ_1 (Fig. 2b), while the curves of ω_{ic} tend to a constant value as Λ_2 increases. It is also observed that increasing Λ_1 increases the critical frequency, because of an increase in the fluid elasticity (Fig. 2c). Increase in the value of Π, however, the critical wave number a_c is same evident from Fig. 3b, while ω_{ic} decreases with increasing Π (Fig. 3c). Increasing α diminishes the size of convection cells (Fig. 4b) and increases ω_{ic} (Fig. 4c).
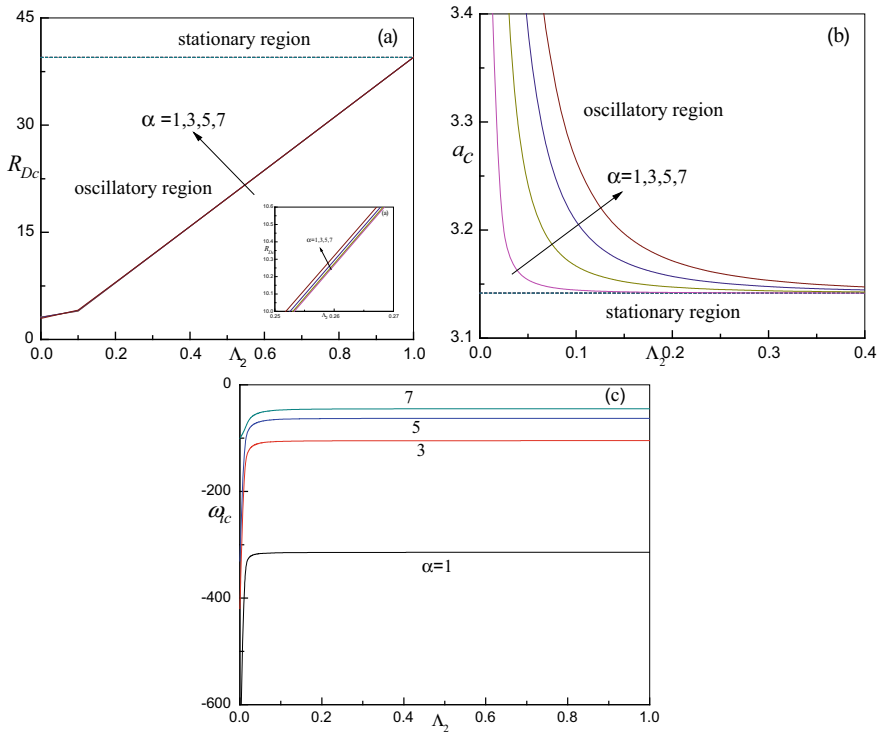
Fig. 4 Critical value of **a** R_{Dc}, **b** a_c, and **c** ω_{ic} with Λ_2 for specific values of α when $\Lambda_1 = 1$ and $\Pi = 100$

Figure 5a–c distinctly illustrates the critical value of R_{Dc}, a_c, and ω_{ic} as a function of Π for different values of Λ_1 and Λ_2 when $\alpha = 1$. From Fig. 5a, it is clear that for small values of Π, R_{Dc} maintains a constant value. For intermediate values of Π, R_{Dc} decreases and remains invariant thereafter with further increase in the value of Π. The trend is the same for all values of Λ_1 and Λ_2 considered. Figure 5b shows that a_c decreases rapidly, and finally, all the curves coalesce at higher values of Π. Increasing Π decreases ω_{ic} rapidly for various values of Λ_1 and Λ_2 (Fig. 5c).

5 Conclusions

The onset of Darcy-Bénard convection in an Oldroyd-B fluid-saturated porous layer in the occurrence of constant horizontal pressure gradient is investigated. The Galerkin technique is used to solve the generalized eigenvalue problem numerically. Even a single-term Galerkin method is shown to give equally convincing results with minimum mathematical computations. The onset of convection is influenced by four different parameters. namely Π, α, Λ_1, and Λ_2.
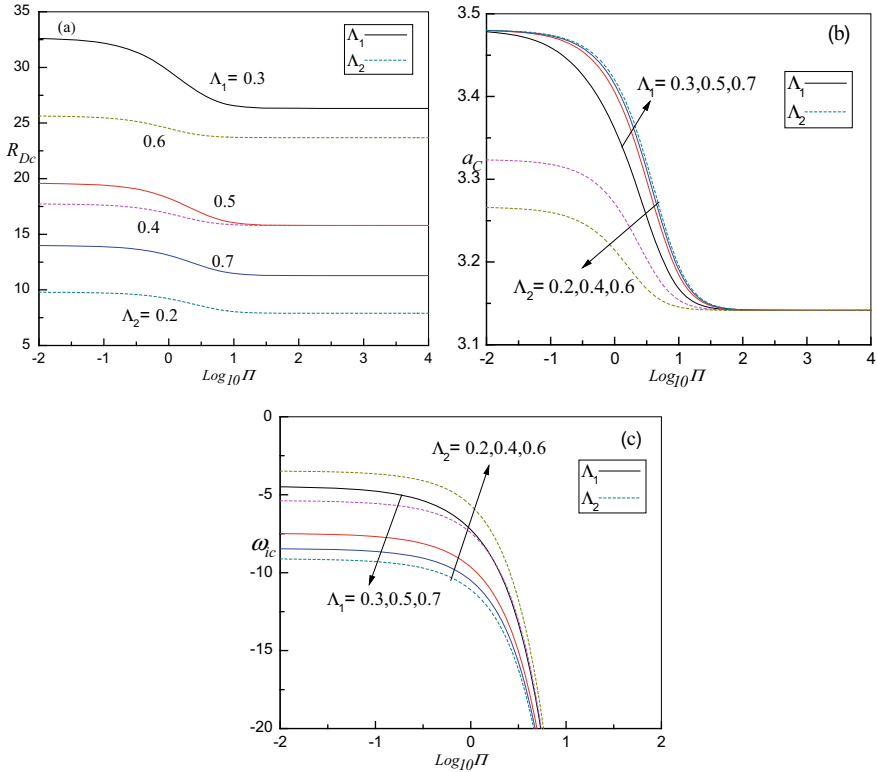
Fig. 5 Critical value of **a** R_{Dc}, **b** a_c, and **c** ω_{ic} with Π for various values of Λ_1 and Λ_2 when $\alpha = 1$

The important observations are pointed out below:

(i)   The oscillatory convection is preferred only if Λ_2 is less than Λ_1, and also it is below some threshold value which is dependent on the values of other parameters appearing in the study.

(ii) The effect of increasing Λ_1 and Π is to advance, while increasing Λ_2 and α are to delay the onset of oscillatory convection.

(iii) The value of Λ_2 within which the instability sets in as oscillatory convection increases with decreasing α and increasing Λ_1 and Π.

(iv) For small and large values of Π, the a_c becomes constant, while a_c decreases for the intermediate values of Π.

(v)   The ω_{ic} increases with increasing Λ_2 and α, whereas opposite effect is seen with increase in Λ_1 and Π.

References

1. Alishaev MG, Mirzadjanzade AK (1975) For the calculation of delay phenomenon in filtration theory. Izvestiya Vuzov Neft i Gaz 6:71–77
2. Chhabra RP, Comiti J, Machač I (2001) Flow of non-Newtonian fluids in fixed and fluidised beds. C. E. S. 56(1):1–27
3. Hirata SC, Alves LDB, Delenda N, Ouarzazi MN (2015) Convective and absolute instabilities in Rayleigh–Bénard–Poiseuille mixed convection for viscoelastic fluids. J Fluid Mech 765:167–210
4. Khuzhayorov B, Auriault JL, Royer P (2000) Derivation of macroscopic filtration law for transient linear viscoelastic fluid flow in porous media. Int J Eng Sci 38(5):487–504
5. Kim MC, Lee SB, Kim S, Chung BJ (2003) Thermal instability of viscoelastic fluids in porous media. Int J Heat Mass Transf 46:5065–5072
6. Li Z, Khayat RE (2005) Finite amplitude Rayleigh-Benard convection and pattern selection for viscoelastic fluids. J Fluid Mech 529:221–225
7. Neild DA, Bejan A (2017) Convection in porous media, 4th edn. Springer Science and Business Media, New York
8. Nield DA, Kuznetsov AV (2015) Local thermal non-equilibrium effects on the onset of convection in an internally heated layered porous medium with vertical throughflow. Int J Therm Sci 92:97–105
9. Postelnicu A (2010) The effect of a horizontal pressure gradient on the onset of Darcy-Benard convection in thermal non-equilibrium conditions. Int J Heat Mass Transf 53:68–75
10. Raghunatha KR, Shivakumara IS, Sowbhagya (2018) Stability of buoyancy driven convection in a Oldroyd-B fluid saturated anisotropic porous layer. Appl Math Mech—Engl Ed 39(5):653–666 (2018)
11. Rudraiah N, Kaloni PN, Radhadevi PV (1989) Oscillatory convection in a viscoelastic fluid through a porous layer heated from below. Rheol Acta 28:48–53
12. Shankar BM, Shivakumara IS (2017) On the stability of natural convection in a porous vertical slab saturated with an Oldroyd-B fluid. Theor Comput Fluid Dyn 31(3):221–231
13. Sheu LJ, Tam LM, Chen JH, Chen HK, Lin KT, Kang Y (2008) Chaotic convection of viscoelastic fluids in porous media. Chao Solitons Fract 37:113–124
14. Shivakumara IS, Dhananjaya M, Chiu-On Ng (2015) Thermal convective instability in an Oldroyd-B nanofluid saturated porous layer. Int J Heat Mass Transf 84:167–177
15. Shivakumara IS, Malashetty MS, Chavaraddi KB (2006) onset of convection in a viscoelastic fluid-saturated sparsely packed porous layer using a thermal non-equilibrium model. Can J Phys 84:973–990
16. Straughan B (2011) Stability, and wave motion in porous media. Appl Math Sci 177. Springer, New York
17. Straughan B (2013) The energy method, stability, and nonlinear convection, vol 91. Springer Science & Business Media
18. Tan W, Masuoka T (2005) Stokes' first problem for an Oldroyd-B fluid in a porous half space. Phys Fluids 17:023101
19. Taylor KC, Nasar-El-Din HA (1998) Water- soluble hydrophobic ally associating polymer for improved oil recovery: a literature review. J Petrol Sci Eng 19:265–280
20. Wang S, Tan W (2011) Stability analysis of soret-driven double-diffusive convection of Maxwell fluid in a porous medium. Int J Heat Fluid Flow 32:88–94
21. Wissler Wissler EH (1971) Viscoelastic effects in the flow of non-Newtonian fluids through a porous medium. Ind Eng Chem Fund 10:411–417
22. Yoon DY, Kim MC, Choi CK (2004) The onset of oscillatory convection in a horizontal porous layer saturated with viscoelastic liquid. Trans Porous Med 55:275–284
23. Zhang Z, Fu C, Tan W (2008) Linear and nonlinear stability analyses of thermal convection for Oldroyd-B fluids in porous media heated from below. Phys Fluids 20(8):084103

Inertia Effects in the Planar Squeeze Flow of a Bingham Fluid: A Matched Asymptotics Analysis

Pavan Kumar Singeetham and Vishwanath Kadaba Puttanna

Abstract The effects of inertia on the squeeze flow of a Bingham fluid between two approaching parallel plates with a constant squeeze velocity is investigated using matched asymptotic expansions. This analysis is an extension to the prior study of Muravleva (2015), who has investigated the planar squeeze flow of a Bingham fluid in the absence of inertia. In the present study, the expressions for the shear stress field, velocity, pressure field and squeeze force are derived. The combined effects of the fluid inertia and yield stress on the pressure field and squeeze force are investigated. We found that the pressure and eventually squeeze force increases with increase in Reynolds number. The squeeze force decreases with an increase in the value of the gap aspect ratio.

Keywords Squeeze flow · Bingham material · Yield surface · Squeeze flow paradox · Reynolds number

1 Introduction

Squeeze flow phenomenon occurs when a material is squeezed between two parallel plates/disks and thus crushed out horizontally/radially. Some of the researchers [1–3] have investigated the Newtonian fluids in various squeeze flow geometries under the assumptions of lubrication theory. The squeeze flow of viscoplastic fluids is peculiar since these fluids flow only when the stress in the gap surpasses a definite yield threshold, which divides the flow domain into shear/yielded and plastic/unyielded regions [4]. We consider the same for a viscoplastic Bingham fluid in a planar geometry.

Many of the industrial processes involve viscoplastic fluids, most commonly approximated by the Bingham constitutive equation (toothpaste, foams, slurries, pulp suspensions, etc.) [4]. As per the lubrication assumptions, there exists an unyielded region at the center of the flow domain in which material flows with a constant

P. K. Singeetham (✉) · V. K. Puttanna
Mathematical and Computational Sciences, National Institute of Technology Karnataka,
Mangalore, India
e-mail: singeetham.pavan@gmail.com

velocity (or behaves like a rigid plug). This prediction causes to the known "squeeze flow paradox" as basic kinematic arguments demonstrate that in the unyielded region there exists a finite gradient in velocity. Subsequently, the true-unyielded region cannot exist. Most of the earlier works that deal with the problem of squeeze flow of viscoplastic fluids debate on the presence or non-presence of true unyielded plug regions [5–7].

In the literature, few reports have described the flow behaviour of non-Newtonian fluids in planar squeeze film geometries [8–12]. For the Bingham materials, Lipscomb and Denn [6] first showed that in complex confined geometries true unyielded regions cannot exist concerning the squeeze flow. However one can resolve the paradox using a technique of asymptotic expansions, wherein one suggests separate expansions within the shear and plastic zones; in this regard, we follow the same method employed in [5, 7, 13, 14]. Recently, using a method of asymptotic expansions, Singeetham and Puttanna [15] have investigated the squeeze flow behaviour of Herschel-Bulkley and Casson materials in the planar geometry.

The effects of fluid inertia are essential to analyze when the non-Newtonian lubricants are used in high speed operating machines. Previously, some of the researchers investigated the effects of fluid inertia on various geometries of squeeze flow [16–22]. Using the method of averaged inertia, Hashimoto and Wada [18] studied the effects of fluid inertia on the axisymmetric squeeze flow of a pseudo-plastic fluid. Batra and Kandasamy [19] have analytically described the inertia effects on the bearing performances in an axisymmetric squeeze flow of a Bingham lubricant. Vishwanath and Kandasamy [20] have investigated the effects of inertia on the axisymmetric squeeze flow of a Herschel-Bulkley material. Using a Bingham lubricant, Raymand and Amalraj [22] investigated the effects of fluid inertia in an externally pressurized thrust bearing in an axisymmetric geometry.

In the present study, we extend the work of Muravleva [5] to investigate the effects of fluid inertia in a planar squeeze flow geometry. The combined effects of the yield stress and fluid inertia on the pressure field and squeeze force are investigated. The current work is organized in the following manner. The construction to the problem (Sect. 2) and its solution using the method of asymptotic expansions are analyzed separately in both shear and plastic regions. Further, the velocity, pressure field and the squeeze force up to $\mathcal{O}(\epsilon)$ are obtained by incorporating the effects of fluid inertia. The obtained results are analyzed in Sect. 3. Finally, Sect. 4 concludes the present work.

2   Mathematical Formulation

The main target of the present study is to investigate the effects of fluid inertia for a steady flow of an incompressible Bingham fluid in a 2D planar geometry and hence obtain consistent solutions. The schematic design of the configuration considered is shown in Fig. 1. A Bingham fluid of viscosity μ^* and density ρ^* is squeezed between two rectangular plates of length $2L^*$, which are at a distance $2H^*$. The velocity

Fig. 1 Graphical interpretation of the Bingham material in the squeeze flow geometry
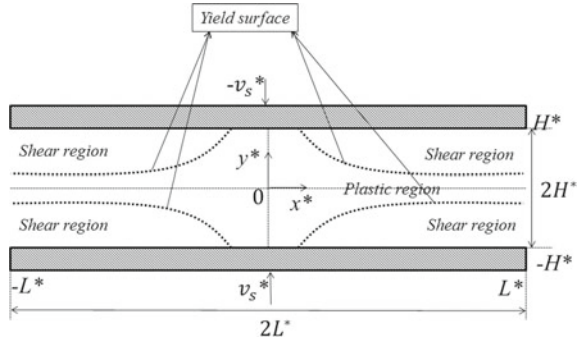
field is given by (u^*, v^*), wherein (u^*, v^*) are the velocity components in (x^*, y^*) directions, respectively. The plates are impending each other with a constant speed v_s^*, such that its value is positive and negative at the walls, $y^* = -H^*$ and H^*, respectively.

The flow is governed by the following dimensionless systems of equations:

$$Re\left(\frac{\partial u^2}{\partial x} + \frac{\partial (uv)}{\partial y}\right) = -\frac{\partial p}{\partial x} + \epsilon^2 \frac{\partial \tau_{xx}}{\partial x} + \frac{\partial \tau_{xy}}{\partial y}, \tag{1}$$

$$\epsilon^2 Re\left(\frac{\partial (uv)}{\partial x} + \frac{\partial v^2}{\partial y}\right) = -\frac{\partial p}{\partial y} + \epsilon^2 \left(\frac{\partial \tau_{yx}}{\partial x} + \frac{\partial \tau_{yy}}{\partial y}\right), \tag{2}$$

$$\frac{\partial u}{\partial x} + \frac{\partial v}{\partial y} = 0, \tag{3}$$

where (u, v) are the velocity components, p denotes pressure and τ_{xx}, τ_{xy}, τ_{yx} and τ_{yy} are the components of stress tensor. A classical lubrication approximation [13] is used as $H^* \ll L^*$, such that the aspect ratio, $\epsilon = H^*/L^* \ll 1$. To non-dimensionalize the problem, we followed same as that of Muravleva [5] except for the inclusion of Reynolds number, Re, which is defined as $Re = \rho^* v_s^* H^*/\mu^*$. The effects of fluid inertia are important for conditions where the Reynolds number depends on squeeze velocity as well as the separation between the surfaces. Here, the inertia terms will be of the same order of magnitude as the viscous forces, in other words, $Re \simeq \mathcal{O}(1)$.

The dimensionless form of constitutive equation for a Bingham fluid is given by:

$$\dot{\gamma}_{ij} = \begin{cases} \tau_{ij}/\left(1 + \frac{B_n}{\dot{\gamma}}\right) & \text{for} \quad \tau > B_n, \\ 0 & \text{for} \quad \tau \le B_n. \end{cases} \tag{4}$$

where the dimensionless measure of the yield stress (τ_0^*) is the Bingham number, defined by

$$B_n = \frac{\tau_0^*(H^*)^2}{\mu^* v_s^* L^*}. \tag{5}$$

Here, $\tau = \sqrt{\tau_{xy}^2 + \epsilon^2 \tau_{xx}^2}$ and $\dot{\gamma} = \sqrt{\dot{\gamma}_{xy}^2 + \epsilon^2 \dot{\gamma}_{xx}^2}$ are the second invariants of $\bar{\bar{\tau}}$ and $\bar{\bar{\dot{\gamma}}}$, respectively. The components of strain rate tensor $\dot{\gamma}_{ij}$ are $\dot{\gamma}_{xx} = 2\frac{\partial u}{\partial x}$, $\dot{\gamma}_{yy} = 2\frac{\partial v}{\partial y}$ and $\dot{\gamma}_{xy} = \dot{\gamma}_{yx} = \frac{\partial u}{\partial y} + \epsilon^2 \frac{\partial v}{\partial x}$.

As the flow is symmetrical about $x = 0$ and $y = 0$, the domain $0 \le x \le 1$ and $0 \le y \le 1$ is considered in the present study. The governing equations are solved using the following boundary conditions:

$$u = 0, \ v = \mp 1 \text{ at } y = \pm 1, \tag{6}$$

$$\tau_{xy} = 0, \ v = 0 \text{ along } y = 0, \tag{7}$$

$$u = 0, \ \tau_{xy} = 0 \text{ along } x = 0, \tag{8}$$

$$\sigma_{xx} = -p + \epsilon^2 \tau_{xx} = 0, \ \tau_{xy} = 0 \text{ at } x = 1. \tag{9}$$

In Sect. 2.1, Eqs. (1)–(3) are solved using the boundary conditions given in Eqs. (6)–(9).

2.1 Solution to the Problem Using Asymptotic Expansions

The squeeze flow paradox (discussed in [5, 7, 13–15]) can be resolved using a technique of matched asymptotic expansions, wherein one suggests separate expansions within the shear and plastic regions. In the present configuration (Fig. 1), the shear/yielded region is present near the plates, where $\tau > B_n$. The inner region is the plastic region, where $\tau < B_n$. This is also termed as "pseudo-plug" region. These regions are divided by an interface called a smooth pseudo-yield surface $y = y_0(x)$ (shown by the dotted lines in Fig. 1). The yielded region conforms to the lubrication paradigm with the developed shear stress being much greater than all other stress components, and in the pseudo-plug region the shear and normal stresses are proportional with the total magnitude of stress being asymptotically close to but just above the yield stress. Hence, Eqs. (1)–(3) along with (6)–(9) are solved in $0 \le x \le 1$ and $0 \le y \le 1$ by the following asymptotic expansions.

$$u(x, y) = u^0 + \epsilon u^1 + \epsilon^2 u^2 + \cdots, \quad v(x, y) = v^0 + \epsilon v^1 + \epsilon^2 v^2 + \cdots, \tag{10}$$

$$p(x, y) = p^0 + \epsilon p^1 + \epsilon^2 p^2 + \cdots, \quad \tau_{ij}(x, y) = \tau_{ij}^0 + \epsilon \tau_{ij}^1 + \epsilon^2 \tau_{ij}^2 + \cdots. \tag{11}$$

Now, following the analysis as in [5, 14, 15], we obtain the separate expressions for velocity in both these regions up to $\mathcal{O}(\epsilon)$. Substituting Eqs. (10)–(11) in Eqs. (1)–(3) and separating the leading order terms (i.e., $\mathcal{O}(1)$ terms), we obtained the following $\mathcal{O}(1)$ equations:

$$Re\left(\frac{\partial(u^0)^2}{\partial x} + \frac{\partial(u^0 v^0)}{\partial y}\right) = -\frac{\partial p^0}{\partial x} + \frac{\partial \tau_{xy}^0}{\partial y}, \quad 0 = -\frac{\partial p^0}{\partial y}, \quad \frac{\partial u^0}{\partial x} + \frac{\partial v^0}{\partial y} = 0. \quad (12)$$

Assuming the effect of fluid inertia to be a constant over the film thickness, averaging the inertia terms [16–20, 22] in Eq. (12), one obtains:

$$f^0(x) = \frac{\partial \tau_{xy}^0}{\partial y}, \quad 0 = -\frac{\partial p^0}{\partial y}, \quad \frac{\partial u^0}{\partial x} + \frac{\partial v^0}{\partial y} = 0, \quad (13)$$

where

$$f^0(x) = \frac{\partial p^0}{\partial x} + Re\frac{\partial}{\partial x}\left(\int_0^1 (u^0)^2 dy\right). \quad (14)$$

Here the superscripts '0' represent variables at $\mathcal{O}(1)$. Also, the shear stress τ_{xy}^0 has a negative sign in $0 \leq x \leq 1$ and $0 \leq y \leq 1$ and when the material is squeezed, velocity becomes positive (i.e $u > 0$) implying $\frac{\partial u^0}{\partial y} < 0$. Solving Eqs. (13), using (6) and (7), one can obtain both shear stress and velocities at $\mathcal{O}(1)$ in these regions as follows:

$$\tau_{xy}^{s,0} = \tau_{xy}^{p,0} = yf^0(x), \quad (15)$$

$$u^{s,0}(x, y) = \frac{B_n}{2y_0}\left((1 - y_0)^2 - (y - y_0)^2\right), \quad u^{p,0}(x, y) = \frac{B_n}{2y_0}(1 - y_0)^2, \quad (16)$$

where $B_n = -y_0(x)f^0(x)$. The pseudo-yield surface, $y_0(x)$, can be obtained by using the integral form of continuity (Eq. (13)), as:

$$y_0^3 - 3y_0\left(1 + \frac{2x}{B_n}\right) + 2 = 0. \quad (17)$$

Further, one can write the equations at $\mathcal{O}(\epsilon)$ by comparing the powers of ϵ in Eqs. (1)–(3) as follows:

$$f^1(x) = \frac{\partial \tau_{xy}^1}{\partial y}, \quad 0 = -\frac{\partial p^1}{\partial y}, \quad \frac{\partial u^1}{\partial x} + \frac{\partial v^1}{\partial y} = 0, \quad (18)$$

where

$$f^1(x) = \frac{\partial p^1}{\partial x} + 2Re\frac{\partial}{\partial x}\left(\int_0^1 u^0 u^1 dy\right). \quad (19)$$

Solving Eq. (18) with $\tau_{xy}^{s,1} = \frac{\partial u^1}{\partial y}$ (from Eq. (4)), using (6) and (7), we get the shear stress and velocity in the shear region at $\mathcal{O}(\epsilon)$ as:

$$\tau_{xy}^{s,1}(x, y) = yf^1(x) + g_p(x), \tag{20}$$

$$u^{s,1}(x, y) = \frac{y^2 - 1}{2} f^1(x) + g_p(x)(y - 1), \tag{21}$$

where $g_p(x)$ is an unknown integral constant. Following the analysis as in [5, 7, 15], we incorporate the higher order terms of an asymptotic expansion in the pseudo-plastic region. Let us consider the center plane domain $(0 \leq y \leq y_0)$. Below the 'pseudo-yield' surface, $y = y_0(x)$, the asymptotic expansion for u (Eq. (10)) is not valid since the absence of normal stress components [7, 13, 14]. To obtain the applicable solution in this region, which incorporates changes in the x directional velocity component, we modify the velocity $u(x, y)$ as follows:

$$u(x, y) = \underbrace{u^0(x)}_{\text{Modified term}} + \epsilon u^1(x, y) + \epsilon^2 u^2(x, y) + \cdots. \tag{22}$$

Using this expansion (22) along with the expansions of v, p and τ_{ij} (from (10)–(11)), one can get the modified $\mathcal{O}(\epsilon)$ equations in the plastic region as follows:

$$2Re \frac{\partial}{\partial x} \left(\int_0^1 u^0 u^1 dy \right) = -\frac{\partial p^1}{\partial x} + \frac{\partial \tau_{xy}^1}{\partial y} + \frac{\partial \tau_{xx}^{-1}}{\partial x}, \tag{23}$$

$$0 = -\frac{\partial}{\partial y}(p^1 + \tau_{xx}^{-1}), \tag{24}$$

$$\frac{\partial u^1}{\partial x} + \frac{\partial v^1}{\partial y} = 0. \tag{25}$$

Following the analysis of [5, 7, 15], one obtains $\tau_{xx}^{-1} = B_n \sqrt{1 - \frac{y^2}{y_0^2}}$. Again, the superscripts '−1' and '1' represent the terms of order $1/\epsilon$ and ϵ, respectively. Solving (23) and (24) along with τ_{xx}^{-1}, using (7), we get the shear stress and velocity at $\mathcal{O}(\epsilon)$ as:

$$\tau_{xy}^{p,1}(x, y) = yf^1(x) + \frac{3}{(y_0^3 - 1)} \left(y_0^2(x) \sin^{-1} \left(\frac{y}{y_0(x)} \right) - y\sqrt{y_0^2(x) - y^2} \right) \tag{26}$$

$$u^{p,1}(x, y) = 2(u^0(x))' \sqrt{y_0^2 - y^2} + u_p^*(x), \tag{27}$$

where $u_p^*(x)$ is an unknown integral constant. One can be determined the unknown integral constants by utilizing the traditional matching approach [5, 15].

$$g_p(x) = \frac{3\pi y_0^2}{2(y_0^3 - 1)}, \quad u_p^*(x) = \frac{(y_0^2 - 1)}{2} f^1(x) + \frac{3\pi y_0^2}{2(y_0^2 + y_0 + 1)}, \tag{28}$$

and

$$f^1(x) = \frac{-9\pi}{2} \frac{y_0^2(y_0 + 1)}{(y_0^3 - 1)(y_0^2 + y_0 + 1)}. \tag{29}$$

Therefore, the asymptotic expressions (16), (21), (27) along with (28) and (29) are velocities and (15), (20) and (26) are shear stresses up to $\mathcal{O}(\epsilon)$. Although, the expressions for modified pressure gradients $f^0(x) = \dfrac{-B_n}{y_0}$ and $f^1(x) =$ $\dfrac{-9\pi}{2} \dfrac{y_0^2(y_0 + 1)}{(y_0^3 - 1)(y_0^2 + y_0 + 1)}$ are same as the pressure gradients $\dfrac{\partial p^0}{\partial x}$ and $\dfrac{\partial p^1}{\partial x}$ in [5], the modified pressure gradients at $\mathcal{O}(1)$ and $\mathcal{O}(\epsilon)$ are $f^0(x) = \dfrac{\partial p^0}{\partial x} +$ $Re\dfrac{\partial}{\partial x}\left(\displaystyle\int_0^1 (u^0)^2 dy\right)$ and $f^1(x) = \dfrac{\partial p^1}{\partial x} + 2Re\dfrac{\partial}{\partial x}\left(\displaystyle\int_0^1 u^0 u^1 dy\right)$ respectively, incorporate the effects of fluid inertia. Hence, we use the expressions $f^0(x)$ and $f^1(x)$ to determine the squeeze flow characteristics, such as pressure distribution and squeeze force.

Pressure distribution The pressure gradient, $\frac{\partial p^s}{\partial x}$, in shear region up to $\mathcal{O}(\epsilon)$ is given by

$$\frac{\partial p^s}{\partial x} = \frac{\partial p^{s,0}}{\partial x} + \epsilon \frac{\partial p^{s,1}}{\partial x}, \tag{30}$$

where $\frac{\partial p^{s,0}}{\partial x}$ and $\frac{\partial p^{s,1}}{\partial x}$ are the pressure gradients at $\mathcal{O}(1)$ and $\mathcal{O}(\epsilon)$, respectively. From the modified pressure gradient Eq. (14), along with the leading order velocities (Eq. (16)) and $f^0(x) = -B_n/y_0$, we have $\frac{\partial p^{s,0}}{\partial x}$ as:

$$\frac{\partial p^{s,0}}{\partial x} = \frac{-B_n}{y_0} - Re\frac{B_n(1 - y_0)^2(16 + 23y_0 + 21y_0^2)}{20y_0(1 + y_0 + y_0^2)}. \tag{31}$$

Again, from Eq. (19) along with velocities at both orders ((16), (21), (27)) and (29), one obtains $\frac{\partial p^{s,1}}{\partial x}$ as:

$$\begin{aligned}
\frac{\partial p^{s,1}}{\partial x} = &\frac{-9\pi}{2} \frac{y_0^2(y_0 + 1)}{(y_0^3 - 1)(y_0^2 + y_0 + 1)} \\
&- Re\frac{3\pi y_0^2(y_0 - 1)(7 - 15y_0 - 91y_0^2 - 40y_0^3 + 4y_0^5)}{40(1 + y_0 + y_0^2)^4}.
\end{aligned} \tag{32}$$

Integrating (30), by substituting Eqs. (31) and (32), along with $x = \frac{B_n(y_0^3 - 3y_0 + 2)}{6y_0}$ and $dx = -\frac{B_n(1 - y_0^3)}{3y_0^2}dy_0$ (from (17)), gives the pressure field in the shear region up to $\mathcal{O}(\epsilon)$, with an integral constant C, as follows:

$$
\begin{aligned}
p^s(x) = C &- \frac{B_n^2}{60 y_0^2} \left(10 + 20 y_0^3 + Re \left(8 - 25 y_0 + 10 y_0^3 - 20 y_0^4 + 7 y_0^5 \right) \right) \\
&- \frac{\epsilon B_n \pi}{40} \left(20\sqrt{3} \tan^{-1} \left(\frac{1 + 2 y_0}{\sqrt{3}} \right) + 30 \log(1 + y_0 + y_0^2) \right. \\
&+ \left. Re \left(y_0^2 - 20 y_0 + 18 + \frac{9(2 + 7 y_0)}{(1 + y_0 + y_0^2)^2} - \frac{81(1 + y_0)}{(1 + y_0 + y_0^2)} \right) \right).
\end{aligned}
\tag{33}
$$

In plastic region, the pressure field up to $\mathcal{O}(\epsilon)$ can be obtained by solving Eq. (24) along with τ_{xx}^{-1}, as:

$$
\begin{aligned}
p^p(x, y) = C &- \frac{B_n^2}{60 y_0^2} \left(10 + 20 y_0^3 + Re \left(8 - 25 y_0 + 10 y_0^3 - 20 y_0^4 + 7 y_0^5 \right) \right) \\
&- \epsilon B_n \sqrt{1 - \frac{y_0^2}{y^2}} - \frac{\epsilon B_n \pi}{40} \left(20\sqrt{3} \tan^{-1} \left(\frac{1 + 2 y_0}{\sqrt{3}} \right) + 30 \log(1 + y_0 + y_0^2) \right. \\
&+ \left. Re \left(y_0^2 - 20 y_0 + 18 + \frac{9(2 + 7 y_0)}{(1 + y_0 + y_0^2)^2} - \frac{81(1 + y_0)}{(1 + y_0 + y_0^2)} \right) \right).
\end{aligned}
\tag{34}
$$

According to (9), $x = 1$ is a stress free boundary, so one can choose $p^s|_{x=1} = 0$ [5, 15]. The constant C can be calculated using $p^s = 0$ at $x = 1$, we have

$$
\begin{aligned}
C = \frac{B_n^2}{60 y_0^2(1)} &\left(10 + 20 y_0^3(1) + Re \left(8 - 25 y_0(1) + 10 y_0^3(1) - 20 y_0^4(1) + 7 y_0^5(1) \right) \right) \\
+ \frac{\epsilon B n \pi}{40} &\left(20\sqrt{3} \tan^{-1} \left(\frac{1 + 2 y_0(1)}{\sqrt{3}} \right) + 30 \log(1 + y_0(1) + y_0^2(1)) \right. \\
+ Re &\left. \left(y_0^2(1) - 20 y_0(1) + 18 + \frac{9(2 + 7 y_0(1))}{(1 + y_0(1) + y_0^2(1))^2} - \frac{81(1 + y_0(1))}{(1 + y_0(1) + y_0^2(1))} \right) \right).
\end{aligned}
\tag{35}
$$

Thus, Eq. (33) along with (35) gives the pressure field in the shear region. Again, the pressure field expression (33) matches with the expression (92) of [5] when the Reynolds number approaches zero. Finally, using the expression for pressure field one can compute the squeeze force as described below.

Squeeze Force The squeeze force in dimensionless form is given by $F = 2 \int_0^1 p \, dx = (2xp)|_0^1 - \int_0^1 2x \frac{\partial p}{\partial x} dx$, where $F^* = \frac{\mu^* v_s^* (L^*)^3}{(H^*)^3} F$. Substituting Eqs. (31)–(32) in F, along with (9), one obtains the squeeze force in y_0-terms:

$$F = -\frac{B_n^3}{9}\left(-\log(y_0(1)) - \frac{2}{3y_0^3(1)} + \frac{3}{2y_0^2(1)} + 3y_0(1) - \frac{y_0^3(1)}{3}\right.$$

$$+ Re\left(\frac{-\log(y_0(1))}{5} - \frac{8}{15y_0^3(1)} + \frac{49}{20y_0^2(1)} - \frac{15}{4y_0(1)} + \frac{17y_0(1)}{4} - \frac{81y_0^2(1)}{20}\right.$$

$$\left.+ \frac{53y_0^3(1)}{60} + \frac{y_0^4(1)}{2} - \frac{21y_0^5(1)}{100}\right) - \left(\frac{7}{2} - \frac{23Re}{50}\right)\right) - \frac{B_n^2\pi\epsilon}{9}\left(-\frac{9y_0^2(1)}{4}\right.$$

$$-9\log(y_0(1)) + \frac{27}{2}\log(y_0^2(1) + y_0(1) + 1) + Re\left(-\frac{447y_0(1)}{40} + \frac{9y_0^2(1)}{20}\right.$$

$$+ \frac{y_0^3(1)}{2} - \frac{3y_0^4(1)}{40} - \frac{\left(729 + 1296y_0(1) + 2025y_0^2(1) + 1539y_0^3(1)\right)}{40\left(y_0^4(1) + 2y_0^3(1) + 3y_0^2(1) + 2y_0(1) + 1\right)}$$

$$- \frac{21\log(y_0(1))}{20} + \frac{189\sqrt{3}}{20}\tan^{-1}\left(\frac{1 + 2y_0(1)}{\sqrt{3}}\right) + \frac{81}{40}\log(y_0^2(1) + y_0(1) + 1)\right)$$

$$\left.-\left(\frac{-9}{4} + \frac{27\log(3)}{2} + Re\left(\frac{-1033}{40} + \frac{63\sqrt{3}\pi}{20} + \frac{81\log(3)}{40}\right)\right)\right),$$

$$(36)$$

where $y_0(0) = 1$ and $y_0(1)$ can be calculated using Eq. (17) at $x = 1$.

3   Results and Discussion

The effect of fluid inertia plays a vital role with an increase in both squeeze velocity and the gap between the surfaces (aspect ratio). To analyze the squeeze force, we need to examine the pressure field along the principal flow direction. Figure 2a shows the effect of inertia on pressure field (Eq. (33) along with (35)) at $\epsilon = 0.05$ and Bingham number $B_n = 10$. From this figure, we notice that, with an increase in fluid inertia, pressure increases significantly and these results are analogous to the results of [19, 20] for the axisymmetric case of a Bingham fluid. The pressure field along x direction for different aspect ratios (ϵ) and at a particular Bingham number $B_n = 10$ and Reynolds number Re are as shown in Fig. 2b. We notice that the significant decrease in pressure with increasing ϵ.

The squeeze force (see Eq. (36)) for different aspect ratios (ϵ), Reynolds numbers (Re) and Bingham numbers (B_n) are calculated, and results are shown in Fig. 3. It must be noted that, in Fig. 3a we scaled Bingham number B_n by ϵ and squeeze force F by ϵ^2. We notice that the considerable increase in the squeeze force with increasing B_n and Re. Also, the moderate decrease in squeeze force with increasing ϵ. From Fig. 3b, we see that the rate of increment in the squeeze force diminishes with an expansion in Reynolds number, where the dimensionless squeeze force of a Newtonian fluid is $F_N = 2\left(1 + \frac{4Re}{5}\right)$. Further, when the Reynolds number (Re) is zero, these asymptotic solutions coincide with the results of [5] (see Fig. 3a).
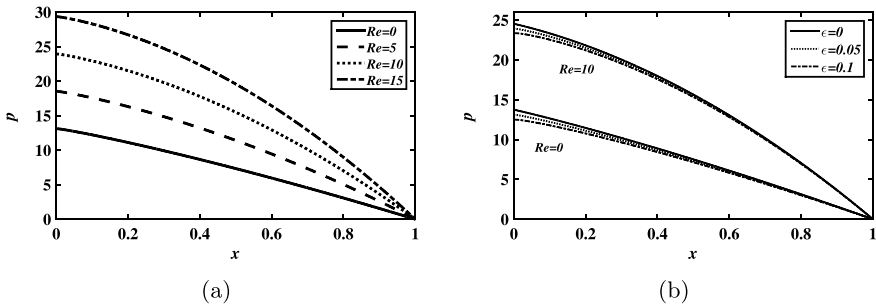
Fig. 2 Effect of **a** the fluid inertia (Re) for $\epsilon = 0.05$ **b** the aspect ratio ϵ for $Re = 0, 10$ on the pressure field $p(x)$ (33), at $B_n = 10$
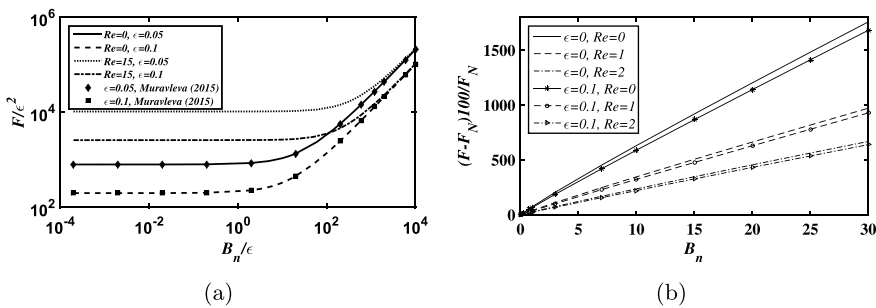
Fig. 3 The variations of $F(B_n)$ (Eq. (36)) versus B_n for different ϵ

4 Conclusions

The squeeze flow characteristics such as pressure field and the squeeze force between two parallel plates lubricated by a Bingham fluid under constant squeeze motion is theoretically described using the technique of matched asymptotic expansions. We separately derive the expressions for the pressure field and squeeze force which incorporate the effects of fluid inertia. We found that with an increase aspect ratio pressure decreases marginally. The effect of fluid inertia is significant in the squeeze flow of a Bingham material in a planar geometry. The pressure and eventually squeeze force increases with increase in Reynolds number. Further, the squeeze force decreases with an increase in the value of the aspect ratio.

References

1. Turns SR (1983) Annular squeeze films with inertial effects. J Lubr Technol 105:361–363. https://doi.org/10.1115/1.3254611
2. Denn MM, Marrucci G (1999) Squeeze flow between finite plates. J Non-Newtonian Fluid Mech 87:175–178. https://doi.org/10.1016/S0377-0257(99)00062-2

3. Singh P, Radhakrishnan V, Narayan KA (1990) Squeezing flow between parallel plates. Ingenieur-Archiv 60:274–281. https://doi.org/10.1007/BF00577864
4. Bird RB, Dai GC, Yarusso BJ (1983) The rheology and flow of viscoplastic materials. Rev Chem Eng 1:1–70. https://doi.org/10.1515/revce-1983-0102
5. Muravleva L (2015) Squeeze plane flow of viscoplastic Bingham material. J Non-Newtonian Fluid Mech 220:148–161. https://doi.org/10.1016/j.jnnfm.2015.01.012
6. Lipscomb GG, Denn MM (1984) Flow of Bingham fluids in complex geometries. J Non-Newtonian Fluid Mech 14:337–346. https://doi.org/10.1016/0377-0257(84)80052-X
7. Balmforth NJ, Craster RV (1999) A consistent thin-layer theory for Bingham plastics. J Non-Newtonian Fluid Mech 84:65–81. https://doi.org/10.1016/s0377-0257(98)00133-5
8. Sherwood JD, Durban D (1996) Squeeze flow of a power-law viscoplastic solid. J Non-Newtonian Fluid Mech 62:35–54. https://doi.org/10.1016/0377-0257(95)01395-4
9. Adams MJ, Aydin I, Briscoe BJ, Sinha SK (1997) A finite element analysis of the squeeze flow of an elasto-viscoplastic paste material. J Non-Newtonian Fluid Mech 71:41–57. https://doi.org/10.1016/S0377-0257(96)01546-7
10. Sherwood JD, Durban D (1998) Squeeze-flow of a Herschel-Bulkley fluid. J Non-Newtonian Fluid Mech 77:115–121. https://doi.org/10.1016/S0377-0257(97)00099-2
11. Smyrnaios DN, Tsamopoulos JA (2001) Squeeze flow of Bingham plastics. J Non-Newtonian Fluid Mech 100:165–189. https://doi.org/10.1016/s0377-0257(01)00141-0
12. Matsoukas A, Mitsoulis E (2003) Geometry effects in squeeze flow of Bingham plastics. J Non-Newtonian Fluid Mech 109:231–240. https://doi.org/10.1016/s0377-0257(02)00170-2
13. Frigaard IA, Ryan DP (2004) Flow of a visco-plastic fluid in a channel of slowly varying width. J Non-Newtonian Fluid Mech 123:67–83. https://doi.org/10.1016/j.jnnfm.2004.06.011
14. Putz A, Frigaard IA, Martinez DM (2009) On the lubrication paradox and the use of regularisation methods for lubrication flows. J Non-Newtonian Fluid Mech 163:62–77. https://doi.org/10.1016/j.jnnfm.2009.06.006
15. Singeetham PK, Puttanna VK (2019) Viscoplastic fluids in 2D plane squeeze flow: a matched asymptotics analysis. J Non-Newtonian Fluid Mech 263:154–175. https://doi.org/10.1016/j.jnnfm.2018.12.003
16. Pinkus O, Sternlicht B (1961) Theory of hydrodynamic lubrication. McGraw-Hill, New York
17. Usha R, Vimala P (2002) Curved squeeze film with inertial effects- energy integral approach. Fluid Dyn Res 30:139–153. https://doi.org/10.1016/S0169-5983(01)00043-0
18. Hashimoto H, Wada S (1986) The effects of fluid inertia forces in parallel circular squeeze film bearings lubricated with pseudo-plastic fluids. J Tribol 108:282–287. https://doi.org/10.1115/1.3261177
19. Batra RL, Kandasamy A (1989) Inertia effects in rheodynamic lubrication of a squeeze film bearing. Wear 132:273–282. https://doi.org/10.1016/0043-1648(89)90169-5
20. Vishwanath KP, Kandasamy A (2010) Inertia effects in circular squeeze film bearing using Herschel-Bulkley lubricants. Appl Math Model 34:219–227. https://doi.org/10.1016/j.apm.2009.04.001
21. Jafargholinejad S, Najafi M (2018) Inertia flows of Bingham fluids through a planar channel: hydroelastic instability analysis. Proc Inst Mech Eng Part C: J Mech Eng Sci 232:2394–2403. https://doi.org/10.1177/0954406217711470
22. Raymand GA, Amalraj IJ (2019) Inertia Effects in rheodynamic lubrication of an externally pressurized converging thrust bearing using Bingham fluids. J Appl Fluid Mech 12:587–594. https://doi.org/10.29252/jafm.12.02.28914

The Stationary Investigation on Multi-server Fluid Queueing Model with Unreliable Server

M. Seenivasan, K. Pattabiraman, and M. Indumathi

Abstract We consider multi-server fluid queueing system including working vacation and with server breakdown. A steady-state distribution of the fluid buffer queueing distance is calculated using matrix geometric solution approach. We calculate differential equations which are satisfied by steady-state joint distribution of the function of the fluid flow.

1 Introduction

This type of fluid queueing model has become dazzling research field in the current years—fluid queue spread application of manufacturing system Mitra [12], communication and computer system Bekker et al. [3] and Latouche et al. [9]. In this Markov fluid, flowing system is IO system. That type of fluid queueing is a useful tool for mathematical modeling, for example, video systems and packet voice without or with background data, computer networks with call admission control, modeling of TCP, traffic production, and inventory control. In this type of model, it is either replete or vacant or both at rates fixed by the ongoing element of the traditional Markov process. The particular class of fluid model is an Markov fine-tune fluid queues that play momentous act in ATM network (Elvalid and Mitra [5], Anick et al. [2], Simonian and Virtomo [18]) and useful in many concrete anomaly and they biddable analysis in Kulkarni [8]. Certain fascinating absolute world function of Markov model fluid

M. Seenivasan (✉) · K. Pattabiraman · M. Indumathi
Department of Mathematics, Annamalai University, Annamalainagar,
Chidambaram 608002, India
e-mail: emseeni@rediffmail.com

K. Pattabiraman
e-mail: pramank@gmail.com

queue conceivable is obtained in Tzenova [19] and Yan et al. [23]. In the recent years, the static circulation of the liquefied queue with definite bulwark as tapering combo of matrix geometric methods was studied by Silver Soares et al. [17]. The fluid models consumed by a multi-server queueing system with WV and conferred a matrix geometric explanation method for the static cushion distribution was prepared by Xu et al. [22]. Mao et al. [10, 11] expressed fluid systems queued by an $M/M/1/N$ queueing system with multiple and single aggressive vacations. The retrial queueing system with unreliable server in K behavior was introduced by Seenivasan et al. [15].

In communication, networks are achieved by a birthplace mode which are expressed in their target by repulsing them through a multiplexer, an information processor, a sequence of intermediate nodes, a switch. The reliable-state investigation of the cushion content is useful in learning congestion in huge speed network Izmailov [6]. Fluid queues have been widely used in the performance evaluation of high-speed communication network that was studied by Blaabjerg et al. [4]. Elementary scrutiny of fluid queue guided by $M/M/1$ queue was studied by Adan and Resing [1]. Van Doorn and Scheinhardt [20] studied in birth and death fluid queues. Fluid queue consumed by $M/M/1$ queue was studied by Virtamo and Norros [21]. batch arrival queueing system with unreliable server was studied by Seenivasan et al. [16]. Anick et al. [2] studied problematic approach of a data handling model with multiple birthplaces, and Mitra [12] expressed the problematic approach of fluid model of manufacturer and buyer paired by a buffer. Kulkarni [8] analyzed the fluid models for single cushion models. Damp models for a type of clue cushion obstacle were studied by Kosten [7]. Ramaswami [14] studied Matrix inquiry methods for vague fluid stream. Let N_t define the number of units in the system and Z_t fulfilled of the credit pool at time t. The communication between the processes $\{N_t, t \geq 0\}$ and $\{Z_t, t \geq 0\}$ is compile graphically in Fig. 1. Two-dimensional process $\{(N_t, Z_t), t \geq 0\}$ composes Markov processes which, under convenient balance status, retain unique static distribution.

Fig. 1 Communication between the Processes $\{Nt, t \geq 0\}$ and $\{Zt, t \geq 0\}$

2 Analysis for the Queueing Model

We describe the WV approach into a multi-server queue with customer appears to bestow to a Poisson process with parameter λ and normal supply limitation μ_b for all c servers, when the queue becomes empty, if the server starts a WV of irregular length at instant, and vacation period pursues an exponential distribution with limitation θ. During a working vacation (WV), an arrival is served at a low service with parameter $\mu_\nu < \mu_b$. If units(arrival) are in the system, the servers shift service parameter from μ_ν to μ_b and continue to serve broken customer; in similar period of time, normal busy period (BP) begins, when vacation ends. Otherwise, take the another working vacation. Server is unstable and may fail during dollop fluid; the failure server is sent for repair immediately, and after reconstruction, it shifts as good as before the failure. The failure time of the server follows exponential distribution with limitation is denoted by β. The repair time of the server ensures an exponential distribution with criterion is γ.

We take that interarrival, service, and WV times are mutually independent. The service regulation is first-in, first-out (FIFO).

Let $L(t)$ be the number of customer in the system at time t, and

$$M(t) = \begin{cases} 0, & \text{the server is in the state of working vacation period at time } t. \\ 1, & \text{the server is in the state of busy period at time } t. \\ 2, & \text{the server is in the state of breakdown at time } t. \end{cases}$$

Then stochastic processes $\{(L(t), M(t), t \le 0)\}$ are a QBD process and category space set arranged in lexicographical order is $\Omega = \{(0, 0)\} \bigcup \{(g, m), g \ge 1, m = 0, 1, 2\}$, here element $(g, 0)$ means that $g(g \ge 0)$ number of customers in system and server is in state of WV state; state $(g, 1)$ means that g$(g \ge 1)$ number of unit in the system and server is state of busy period; state $(g, 2)$ means that $g(g \ge 1)$number of client in model and server is element of breakdown. Infinitesimal generator matrix

Q is $Q = \begin{bmatrix} A_{00} & C_{01} & & & & & \\ B_{10} & A_1 & C & & & & \\ & B_2 & A_2 & C & & & \\ & & \ddots & \ddots & \ddots & & \\ & & & B_{c-1} & A_{c-1} & C & \\ & & & & B & A & C \\ & & & & & \ddots & \ddots & \ddots \end{bmatrix}$.

where $A_{00} = -\lambda$, $C_{01} = (\lambda, 0, 0)$ $B_{10} = (\mu_\nu, \mu_b, 0)^T$,

$$A_g = \begin{bmatrix} -(\lambda + g\mu_\nu + \theta) & \theta & 0 \\ 0 & -(\lambda + g\mu_b + \beta) & \beta \\ 0 & \gamma & -(\lambda + \gamma) \end{bmatrix}; B_g = \begin{bmatrix} g\mu_\nu & 0 & 0 \\ 0 & g\mu_b & 0 \\ 0 & 0 & 0 \end{bmatrix}$$

$$B = \begin{bmatrix} c\mu_\nu & 0 & 0 \\ 0 & c\mu_b & 0 \\ 0 & 0 & 0 \end{bmatrix}; A = \begin{bmatrix} -(\lambda + c\mu_\nu + \theta) & \theta & 0 \\ 0 & -(\lambda + c\mu_b + \beta) & \beta \\ 0 & \gamma & -(\lambda + \gamma) \end{bmatrix}; c = \begin{bmatrix} \lambda & 0 & 0 \\ 0 & \lambda & 0 \\ 0 & 0 & \lambda \end{bmatrix}$$

Lemma 1 *If $\rho < 1$, the following quadratic matrix mathematical statement $R^2 B + RA + C = 0$, the minimal nonnegative solution in R.*

$$R = \begin{bmatrix} r & \frac{\theta r}{pc\mu_b} & \frac{\theta r\beta}{\lambda pc\mu_b} \\ 0 & s_1 & \frac{\beta s_1}{\lambda} \\ 0 & 0 & r_3 \end{bmatrix} \tag{1}$$

$$c\mu_\nu z^2 - (\lambda + c\mu_\nu + \theta)z + \lambda = 0 \tag{2}$$

and $0 < r < 1$, $\quad r = \frac{1}{2c\mu_\nu}\left(\lambda + c\mu_\nu + \theta - \sqrt{(\lambda + c\mu_\nu + \theta)^2 - 4c\lambda\mu_\nu}\right)$
$\lambda + \theta + c\mu_\nu(1 - r) = \frac{\theta}{1-r} + c\mu_\nu = \frac{\lambda}{r}$

It is the quasi-birth and death processes $\{(L(t), M(t)), t \geq 0\}$ is stability iff the spectral radius $SP(R)$ of the (rate matrix) R satisfies $SP(R) < 1$, $xB[R] = 0$.

$$B[R] = \begin{bmatrix} A_{00} & C_{01} & & & & \\ B_{10} & A_1 & C & & & \\ & B_2 & A_2 & C & & \\ & & \ddots & \ddots & \ddots & \\ & & & B_{c-1} & A_{c-1} & C \\ & & & & B & RB + A \end{bmatrix}$$

The process $\{(L(t), M(t)), t \geq 0\}$ is stable if and only if the system workload $\rho < 1$. If $\rho < 1$, let (L, M) define the static irregular vector $\{(L(t), M(t)), t \geq 0\}$, motionless distribution is

$$\pi_{gm} = P(L = g, M = m) = \lim_{t \to \infty} P\{L(t) = g, M(t) = m\}, (g, m) \in \Omega$$

From equation one and two

$$RB + A = \begin{bmatrix} rc\mu_\nu - (\lambda + c\mu_\nu + \theta) & \frac{\theta r}{p} + \theta & 0 \\ 0 & s_1 c\mu_b - (\lambda + c\mu_b + \beta) & \beta \\ 0 & \gamma & -(\lambda + \gamma) \end{bmatrix}$$

Derive the steady-state distribution (L, M)

$$
\begin{cases}
\phi_0 = 1 \\
\phi_g = \dfrac{\theta r}{r(1-r)} + \dfrac{(c-g)\mu_\nu}{\lambda}\phi_{g-1} + \dfrac{\theta}{\lambda}\displaystyle\sum_{\nu=0}^{g-1}\phi_\nu, \quad 1 \le g \le c-1
\end{cases}
\tag{3}
$$

$$\Pi_g = (\pi_{g0}, \pi_{g1}, \pi_{g2}), \quad g \ge 1, \quad x = (\pi_{00}, \Pi_1, \Pi_2, ... \Pi_c)$$

Theorem 2 *If $\rho < 1$, the static distribution of (L, M) perhaps explicit*

$$
\pi_{g0} =
\begin{cases}
g\phi_{c-1-g}, & 0 \le g \le c-1, \\
gr, & g = c
\end{cases}
\tag{4}
$$

$$
\pi_{g1} =
\begin{cases}
g\left(\dfrac{\lambda}{\mu_b}\phi_{c-1} - \dfrac{\mu_\nu}{\mu_b}\phi_{c-2}\right), & g = 1 \\[2mm]
g\dfrac{1}{g!}\left[\dfrac{\lambda+\mu_b+\beta}{\gamma}\left[\dfrac{\lambda}{\mu_b}\phi_{c-1} - \dfrac{\mu_\nu}{\mu_b}\phi_{c-2}\right]\displaystyle\sum_{m=1}^{g-1}\left(\dfrac{\gamma}{\mu_b}\right)^m (g-m)! \right. \\[2mm]
\quad -\left(\dfrac{\gamma}{\mu_b}\right)^{g-1}\left[\dfrac{\beta}{\lambda+\gamma}\left[\dfrac{\lambda}{\mu_b}\phi_{c-1} - \dfrac{\mu_\nu}{\mu_b}\phi_{c-2}\right]\right] \\[2mm]
\quad \left. +\dfrac{\theta}{\gamma}[1 - \displaystyle\sum_{\nu=g+1-m}^{c-1}\phi_{c-1-\nu}]\sum_{m=1}^{g-1}\left(\dfrac{\gamma}{\mu_b}\right)^j (g-m)!\right], & 2 \le g \le c
\end{cases}
\tag{5}
$$

$$
\pi_{g2} =
\begin{cases}
\left[g\dfrac{\beta}{\lambda+\gamma}\left[\dfrac{\lambda}{\mu_b}\phi_{c-1} - \dfrac{\mu_\nu}{\mu_b}\phi_{c-2}\right]\right], & g = 1 \\[2mm]
\dfrac{g\beta}{\lambda+\gamma}\left\{\dfrac{\lambda}{\lambda+\gamma}\left[\dfrac{\lambda}{\mu_b}\phi_{c-1} - \dfrac{\mu_\nu}{\mu_b}\phi_{c-2}\right] + \dfrac{1}{g!}\left[\dfrac{\lambda+\mu_b+\beta}{\gamma}\left[\dfrac{\lambda}{\mu_b}\phi_{c-1} - \dfrac{\mu_\nu}{\mu_b}\phi_{c-2}\right]\right.\right. \\[2mm]
\displaystyle\sum_{m=1}^{g-1}\left(\dfrac{\gamma}{\mu_b}\right)^m (g-m)! - \left(\dfrac{\gamma}{\mu_b}\right)^{g-1}\left[\dfrac{\beta}{\lambda+\gamma}\left[\dfrac{\lambda}{\mu_b}\phi_{c-1} - \dfrac{\mu_\nu}{\mu_b}\phi_{c-2}\right]\right] \\[2mm]
\quad \left.\left. +\dfrac{\theta}{\gamma}[1 - \displaystyle\sum_{\nu=g+1-m}^{c-1}\phi_{c-1-\nu}]\sum_{m=1}^{g-1}\left(\dfrac{\gamma}{\mu_b}\right)^m (g-m)!\right]\right\}, & 2 \le g \le c \quad and
\end{cases}
$$

$$
\begin{cases}
\pi_{g0} = \pi_{c0}r^{g-c}, & g > c \\[2mm]
\pi_{g1} = \pi_{c1}s_1^{g-c} + \pi_{c0}\dfrac{\theta r}{pc\mu_b}\displaystyle\sum_{\nu=0}^{g-c-1} r^\nu s_1^{g-c-1-\nu}, & g > c \\[2mm]
\pi_{g2} = \pi_{c2}r_3^{g-c} + \pi_{c1}\dfrac{\beta s_1}{\lambda}\displaystyle\sum_{\nu=0}^{g-c-1} r_3^\nu s_1^{g-c-1-\nu} \\[2mm]
\quad + \pi_{c0}\dfrac{\theta r\beta}{\lambda pc\mu_b}\left[\displaystyle\sum_{\nu=0}^{g-c-1} r^\nu s_1^{g-c-1-\nu} + r_3(r + s_1 + r_3)\right], & g > c
\end{cases}
$$

where g is a constant, which can be solved by the normalizing condition

$$\sum_{g=0}^{\infty}\pi_{g0}^m + \sum_{g=1}^{\infty}\pi_{g1}^m + \sum_{g=1}^{\infty}\pi_{g2}^m = 1$$

Proof Equation $x B[R] = 0$ can be modified

$$
\begin{cases}
-\lambda\pi_{00} + \mu_\nu\pi_{10} + \mu_b\pi_{11} = 0, \\
\lambda\pi_{g-1,0} - (\lambda + g\mu_\nu + \theta)\pi_{g0} + (g+1)\mu_\nu\pi_{g+1,0} = 0, \quad 1 \le g \le c-1 \\
\theta\pi_{g-1,0} - (\lambda + (g-1)\mu_b + \beta)\pi_{g-1,1} + \gamma\pi_{g-1,2} + g\mu_b\pi_{g1} = 0, \quad 2 \le g \le c-1 \\
\beta\pi_{11} - (\lambda + \gamma)\pi_{12} = 0, \\
\lambda\pi_{g-1,2} + \beta\pi_{g1} - (\lambda + \gamma)\pi_{g2} = 0, \quad 2 \le g \le c-1 \\
\lambda\pi_{c-1,0} + [rc\mu_\nu - (\lambda + c\mu_\nu + \theta)]\pi_{c,0} = 0,
\end{cases}
\tag{A}
$$

The equations in (A) respectively are denoted by (A)1–(A)6

$$
\text{From (A)6, we have, } \pi_{c,0} = r\pi_{c-1,0}
\tag{6}
$$

Substituting Eq. (6) into A(2), we recursively gain
$\pi_{g,0} = \pi_{c-1,0}\phi_{c-1-g} \quad 0 \le g \le c-1$, $\pi_{c-1,0} = g$ and $\pi_{g,0} = g\phi_{c-1-g}$.
Based on Eq. (A)1 and Eq. (4),we have

$$
\pi_{11} = g\left[\frac{\lambda}{\mu_b}\phi_{c-1} - \frac{\mu_\nu}{\mu_b}\phi_{c-2}\right]
\tag{7}
$$

Substituting Eq. (7) into A(4)

$$
\pi_{12} = \frac{g\beta}{\lambda+\gamma}\left[\frac{\lambda}{\mu_b}\phi_{c-1} - \frac{\mu_\nu}{\mu_b}\phi_{c-2}\right]
\tag{8}
$$

From Eq. (A)3

$$
\pi_{g1} = \frac{1}{g!}\left\{\frac{\lambda+\mu_b+\beta}{\gamma}\pi_{11}\sum_{m=1}^{g-1}\left(\frac{\gamma}{\mu_b}\right)(g-m)! - \frac{\theta}{\gamma}\left[\sum_{\nu=g}^{c-1}\pi_{\nu,0} - \pi_{c-1,0}\right]\sum_{m=1}^{g-1}\left(\frac{\gamma}{\mu_b}\right)(g-m)!\right.
$$
$$
\left. - \left(\frac{\gamma}{\mu_b}\right)^{g-1}\pi_{12}\right\}, \quad 2 \le g \le c-1
\tag{9}
$$

Substituting Eqs. (7), (8), and (4) into Eq. (9), we get

$$
\pi_{g1} = g\frac{1}{g!}\left\{\frac{\lambda+\mu_b+\beta}{\gamma}\left[\frac{\lambda}{\mu_b}\phi_{c-1} - \frac{\mu_\nu}{\mu_b}\phi_{c-2}\right]\sum_{m=1}^{g-1}\left(\frac{\gamma}{\mu_b}\right)^m(g-m)!\right.
$$
$$
- \left(\frac{\gamma}{\mu_b}\right)^{g-1}\left[\frac{\beta}{\lambda+\gamma}\left[\frac{\lambda}{\mu_b}\phi_{c-1} - \frac{\mu_\nu}{\mu_b}\phi_{c-2}\right]\right]
$$
$$
\left. + \frac{\theta}{\gamma}\left[1 - \sum_{\nu=g+1-m}^{c-1}\phi_{c-1-\nu}\right]\sum_{m=1}^{g-1}\left(\frac{\gamma}{\mu_b}\right)^m(g-m)!\right\} \quad 2 \le g \le c
\tag{10}
$$

From Eq. (A)5, we have

$$(\lambda + \gamma)\pi_{g2} = \lambda\pi_{g-1,2} + \beta\pi_{g,1}, \quad 2 \le g \le c - 1 \tag{11}$$

Substituting Eqs. (8) and (10) into Eq. (11)

$$\pi_{g2} = \frac{g\beta}{\lambda+\gamma}\left\{\frac{\lambda}{\lambda+\gamma}\left[\frac{\lambda}{\mu_b}\phi_{c-1} - \frac{\mu_\nu}{\mu_b}\phi_{c-2}\right] + \frac{1}{g!}\left\{\frac{\lambda+\mu_b+\beta}{\gamma}\left[\frac{\lambda}{\mu_b}\phi_{c-1} - \frac{\mu_\nu}{\mu_b}\phi_{c-2}\right]\right.\right.$$

$$\sum_{m=1}^{g-1}\left(\frac{\gamma}{\mu_b}\right)^m (g-m)! - \left(\frac{\gamma}{\mu_b}\right)^{g-1}\left[\frac{\beta}{\lambda+\gamma}\left[\frac{\lambda}{\mu_b}\phi_{c-1} - \frac{\mu_\nu}{\mu_b}\phi_{c-2}\right]\right]$$

$$\left. + \frac{\theta}{\gamma}\left[1 - \sum_{\nu=g+1-m}^{c-1}\phi_{c-1-\nu}\right]\sum_{m=1}^{g-1}\left(\frac{\gamma}{\mu_b}\right)^m (g-m)!\right\}\right\} \quad 2 \le g \le c$$

On the other way, using matrix geometric method (see Neuts [13])

$$\Pi_g = \Pi_c R^{g-c} = (\pi_{c,0}, \pi_{c,1}, \pi_{c,2})R^{g-c}, \qquad g > c.$$

From Eq. (1), we have

$$R^g = \begin{bmatrix} r^g & \frac{\theta r}{pc\mu_b}\sum_{\nu=0}^{g-1}r^\nu s_1^{g-1-\nu} & \frac{\theta r\beta}{\lambda pc\mu_b}\{\sum_{\nu=0}^{g-1}r^\nu s_1^{g-1-\nu} + r_3[r + s_1 + r_3]\} \\ 0 & s_1^g & \frac{\beta s_1}{\lambda}\sum_{\nu=0}^{g-1}r_3^\nu s_1^{g-1-\nu} \\ 0 & 0 & r_3^g \end{bmatrix}, g \ge 1$$

Theorem 2 is proved, g perhaps determined by the normalizing condition

$$\sum_{g=0}^{\infty}\pi_{g0} + \sum_{g=1}^{\infty}\pi_{g1} + \sum_{g=1}^{\infty}\pi_{g2} = 1$$

3 Analysis of the Fluid Buffer Queueing Model

Introduce the fluid buffer queueing model flowed by a unreliable fluid queueing model with working vacation. Let N(t) be the function of the fluid buffer at time t, which is a nonnegative random variable. The net input rate of fluid queue to the fluid buffer is the content of the process $\{(N(t), L(t), M(t)), t \ge 0\}$.

Let $L(t)$ be the number of customer in the system at time t, and

$$M(t) = \begin{cases} 0, & \text{the system stay in a working vacation period at time } t. \\ 1, & \text{the system stay in a busy period at time } t. \\ 2, & \text{the system stay in a breakdown at time } t. \end{cases}$$

$$\sigma[N(t), L(t), M(t)] = \frac{dN(t)}{dt} = \begin{cases} \eta_1, & (L(t), M(t)) = (g, 0), g \geq 1, \\ \eta_2, & (L(t), M(t)) = (g, 1), \quad g \geq 1, \\ \eta_3, & (L(t), M(t)) = (g, 2), \quad g \geq 1, \\ \eta, & (L(t), M(t)) = (0, 0), N(t) > 0, \\ 0, & (L(t), M(t)) = (0, 0), N(t) = 0, \end{cases}$$

$\eta > 0, \eta_2 > \eta_1 > \eta_3 > 0$.

The fluid is increasing with parameter η_3 when customers in the system and the flowing system stay in breakdown; The fluid is increasing with parameter η_1 when units in system and the flowing system stay in WV period; the fluid increased with parameter η_2 when there are customer in flowing system in busy period; otherwise, the fluid is decreasing at the parameter of $(-\eta)$ when the flowing queue is empty. Fluid flow cannot decrease until the fluid is empty. Fluid queueing model flowed by a unreliable fluid queueing model with WV is three-dimensional Markov processes $\{(N(t), L(t), M(t)), t \geq 0\}$ and net inflow parameter $\sigma[N(t), L(t), M(t)]$.

The average drift of the fluid buffer queueing system is

$$d = \eta\pi_{00} + \eta_1 \sum_{g=1}^{+\infty} \pi_{g0} + \eta_2 \sum_{g=1}^{+\infty} \pi_{g1} + \eta_3 \sum_{g=1}^{+\infty} \pi_{g2},$$

where π_{gj}, $(g, j) \in \Omega$ in Theorem 2. Proved the fluid buffer queue is stable if $\rho < 1$ and $d < 0$ (see Kulkarni [8]).

If $\rho < 1$ and $d < 0$, its stable irregular vector is defined (N, L, M), here N is the static fluid buffer content. Define the static distribution

$$H_{gj}(y) = \lim_{t \to \infty} P\{N(t) \leq y, L(t) = g, M(t) = m\}$$
$$= P\{N \leq y, L = g, M = m\}, y \geq 0, (g, m \in \Omega),$$

the static distribution for the fluid buffer part N is

$$H(y) = P\{N \leq y\} = H_{00}(y) + \sum_{g=1}^{\infty} \sum_{m=0}^{1} H_{gm}(y).$$

It is not difficult to obtain differential equations satisfied by the steady-state joint distribution $H_{gm}(y)$

$$
\begin{cases}
\eta \frac{d\widehat{H}_{00}(y)}{dy} = -\lambda\widehat{H}_{00}(y) + \mu_\nu\widehat{H}_{10}(y) + \mu_b\widehat{H}_{11}(y), \\
\eta_1 \frac{d\widehat{H}_{g,0}(y)}{dy} = -(\lambda + g\mu_\nu + \theta)\widehat{H}_{g,0}(y) + \lambda\widehat{H}_{g-1,0}(y) \\
\qquad\qquad\qquad + (g+1)\mu_\nu\widehat{H}_{g+1,0}(y), \ \ 1 \le g \le c-1, \\
\eta_2 \frac{d\widehat{H}_{11}(y)}{dy} = -(\lambda + \mu_b + \beta)\widehat{H}_{11}(y) + \theta\widehat{H}_{10}(y) + \gamma\widehat{H}_{12}(y) + 2\mu_b\widehat{H}_{21}(y),
\end{cases}
$$

$$
\begin{cases}
\eta_2 \frac{d\widehat{H}_{g,1}(y)}{dy} = -(\lambda + g\mu_b + \beta)\widehat{H}_{g,1}(y) + \lambda\widehat{H}_{g-1,1}(y) + \theta\widehat{H}_{g,0}(y) + \gamma\widehat{H}_{g,2}(y) \\
\qquad\qquad\qquad + (g+1)\mu_b\widehat{H}_{g+1,1}(y), \ \ 2 \le g \le c-1 \\
\eta_3 \frac{d\widehat{H}_{12}(y)}{dy} = -(\lambda + \gamma)\widehat{H}_{12}(y) + \beta\widehat{H}_{11}(y) \\
\eta_3 \frac{d\widehat{H}_{g,2}(y)}{dy} = -(\lambda + \gamma)\widehat{H}_{g,2}(y) + \beta\widehat{H}_{g,1}(y) + \lambda\widehat{H}_{g-1,2}(y) \ \ \ 2 \le g \le c-1 \\
\eta_1 \frac{d\widehat{H}_{g,0}(y)}{dy} = -(\lambda + c\mu_\nu + \theta)\widehat{H}_{g,0}(y) + \lambda\widehat{H}_{k-1,0}(y) + c\mu_\nu\widehat{H}_{g+1,0}(y), \ \ g \ge c, \\
\eta_2 \frac{d\widehat{H}_{g,1}(y)}{dy} = -(\lambda + c\mu_b + \beta)\widehat{H}_{g,1}(y) + \lambda\widehat{H}_{g-1,1}(y) + \theta\widehat{H}_{g,0}(y) + \gamma\widehat{H}_{g,2}(y) \\
\qquad\qquad\qquad + c\mu_b\widehat{H}_{g+1,1}(y) \ \ g \ge c, \\
\eta_3 \frac{d\widehat{H}_{g,2}(y)}{dy} = -(\lambda + \gamma)\widehat{H}_{g,2}(y) + \beta\widehat{H}_{g,1}(y) + \lambda\widehat{H}_{g-1,2}(y) \ \ g \ge c
\end{cases}
$$

with the boundary conditions

$$
H_{00}(0) = a, \ \ H_{gm}(0) = 0, \ g \ge 1, m = 0, 1, 2, \ \ H_{gm}(\infty) = \pi_{gm}, \ \ (g, m) \in \Omega.
$$

The probability $H_{00}(0) = P\{N = 0, L = 0, M = 0\}$

$$
H_g(y) = (H_{g0}(y), H_{g1}(y), H_{g2}(y)), g \ge 1; \quad \mathcal{H}(y) = (H_{00}(y), H_1(y), H_2(y), \cdots).
$$

Equations can be modified as matrix format

$$
\frac{d}{dy}\mathcal{H}(y)\Lambda = \mathcal{H}(y)Q \tag{12}
$$

where $\Lambda = diag(\eta, (\eta_1, \eta_2, \eta_3), (\eta_1, \eta_2, \eta_3), \cdots)$, the infinitesimal generator of the QBD process $\{(L(t), M(t)), t \ge 0\}$ is Q. We use the LT of the pdf $H_{gm}(y)$ and $H(y)$ as

$$
\widehat{H}_{gm}(s) = \int_0^{+\infty} e^{-sy} H_{gm}(y)dy, \ s > 0, \ (g, m) \in \Omega
$$

$\widehat{H}(s) = \int_0^{+\infty} e^{-sy} H(y)dy, \ s > 0$ denoted by

$$\widehat{H}_g(s) = (\widehat{H}_{g0}(s), \widehat{H}_{g1}(s), \widehat{H}_{g2}(s)), g \geq 1, \widehat{\mathcal{H}}(s) = (\widehat{H}_{00}, \widehat{H}_1(s), \widehat{H}_2(s), \cdots).$$

Putting LT on both sides of Eq. (12) and using the boundary conditions, we get

$$\widehat{\mathcal{H}}(s)(Q - s\Lambda) = -\mathcal{H}(0)\Lambda = (-a\eta, 0, 0, \cdots). \tag{13}$$

4 The Stationary Distribution and the Mean of the Fluid Buffer Content

LT $\{\widehat{H}_g(s), g \geq c\}$ are of matrix structure. Here, we introduce two crucial quadratic equations, whose roots play an important role in the following fluid queue analysis. For any $s \geq 0$, it is easy to show that the quadratic equation

$$c\mu_\nu z^2 - (\lambda + c\mu_\nu + \theta + s\eta_1)z + \lambda = 0 \tag{14}$$

$z_1(s)$ and $z_2(s)$ are real roots

$$roots = \frac{(\lambda + c\mu_\nu + \theta + s\eta_1) \pm \sqrt{(\lambda + c\mu_\nu + \theta + s\eta_1)^2 - 4c\lambda\mu_\nu}}{2c\mu_\nu}$$

It is easy to verify $0 < z_1(s) < 1$, $z_1(0) = r$, $z_2(s) > 1$.

$$c\mu_b z^2 - (\lambda + c\mu_b + \beta(1 - \frac{\gamma}{\lambda}) + s\eta_2)z + \lambda = 0. \text{ for any } s \geq 0 \tag{15}$$

$G_1(s)$ and $G_2(s)$ are real roots

$$roots = \frac{(\lambda + c\mu_b + \beta(1 - \frac{\gamma}{\lambda}) + s\eta_2) \pm \sqrt{(\lambda + c\mu_b + \beta(1 - \frac{\gamma}{\lambda}) + s\eta_2)^2 - 4c\lambda\mu_b}}{2c\mu_b}$$

where $0 < G_1(s) < 1$, $G_2(s) > 1$, $G_1(0) = s_1$ and $\gamma = 0, s \geq 0$

$$A(s) = \begin{bmatrix} -(\lambda + c\mu_\nu + \theta + s\eta_1) & \theta & 0 \\ 0 & -(\lambda + c\mu_b + \beta + s\eta_2) & \beta \\ 0 & \gamma & -(\lambda + \gamma + s\eta_3) \end{bmatrix}$$

Theorem 3 *For $s > 0$, the quadratic matrix mathematical structure*

$$R^2 B + RA(s) + C = 0 \tag{16}$$

has the minimal nonnegative solution

$$R(s) = \begin{bmatrix} R_{11}(s) & R_{12}(s) & R_{13}(s) \\ 0 & R_{22}(s) & R_{23}(s) \\ 0 & 0 & R_{33}(s) \end{bmatrix}, s \geq 0. \tag{17}$$

where $z_1(s)$, $G_1(s)$ decided by Eqs. (14) and (15).

And $R_{12}(s) = \dfrac{\theta z_1(s)}{\{1 + \frac{\lambda+\beta+s\eta_2}{c\mu_b} - [z_1(s) + G_1(s)]\}c\mu_b}, R_{33}(s) = 1$

$R_{13}(s) = \dfrac{\beta\theta z_1(s)}{(\lambda + s\eta_3)\{1 + \frac{\lambda+\beta+s\eta_2}{c\mu_b} - [z_1(s) + G_1(s)]\}c\mu_b}, R_{23}(s) = \dfrac{\beta G_1(s)}{\lambda + s\eta_3}.$

Proof Upper triangular matrices are B, A(s), and C. Put $R(s)$ in Eq. (16),

$$\begin{cases} c\mu_v R_{11}^2(s) - (\lambda + c\mu_v + \theta + s\eta_1)R_{11}(s) + \lambda = 0 \\ R_{12}(s)[R_{11}(s)c\mu_b + R_{22}(s)c\mu_b - (\lambda + c\mu_b + \beta + s\eta_2)] + \theta R_{11}(s) + \gamma R_{13}(s) = 0 \\ \beta R_{12}(s) - (\lambda + \gamma + s\eta_3)R_{13}(s) = 0 \\ c\mu_b R_{22}^2(s) + (\lambda + c\mu_b + \beta + s\eta_2)R_{22}(s) + \gamma R_{23}(s) + \lambda = 0 \\ \beta R_{22}(s) - (\lambda + \gamma + s\eta_3)R_{23}(s) = 0 \\ \gamma R_{33}(s) = 0 \\ \lambda - (\lambda + \gamma + s\eta_3)R_{33}(s) = 0 \end{cases} \tag{18}$$

$R_{11}(s) = z_1(s)$, $R_{22}(s) = G_1(s)$ in the first and fourth equations of Eq. (18).

$$\text{From Eq. (18)(6), we have } \gamma = 0. \tag{19}$$

Substituting Eq. (19) into (18)7, where $R_{33}(0) = r_3$

$$R_{33}(s) = 1 \tag{20}$$

Substituting $z_1(s)$, $G_1(s)$ and Eq. (19) in (18)2

where $p = [1 + \frac{\lambda+\beta}{c\mu_b}] - [r + s_1]$

$$R_{12}(s) = \frac{\theta z_1(s)}{\{1 + \frac{\lambda+\beta+s\eta_2}{c\mu_b} - [z_1(s) + G_1(s)]\}c\mu_b} \tag{21}$$

Substituting Eqs. (19) and (21) in (18)3

$$R_{13}(s) = \frac{\beta\theta z_1(s)}{(\lambda + s\eta_3)\{1 + \frac{\lambda+\beta+s\eta_2}{c\mu_b} - [z_1(s) + G_1(s)]\}c\mu_b}$$

Substituting $G_1(s)$ and Eq. (19) in (18)5

$R_{23}(s) = \dfrac{\beta G_1(s)}{\lambda + s\eta_3}$. Therefore, we obtain Theorem 3.

5 Numerical Study

In this section, we investigate how stochastic fluid flow in the above section behaves as in multi-server queueing model with working vacation and with unreliable server. We only consider steady-state distribution, which we calculated by matrix geometric approach.

We take the particular values of the parameters $\lambda = 0.45$; $\mu_b = 0.1$; $\mu_\gamma = 0.4$; $\ominus = 0.3$; $c = 2$; $\gamma = 0.2$. From the values, we calculated rate matrix R. From the rate matrix R, we computed probability vectors by MGM. We obtained mean drift of the fluid flow of the model using Theorem 2.

Figure 2. shows that if the fluid Buffer content is linear increasing with parameter (η_1), then flowing system is also increasing which is working vacation period. Figure 3 shows that if the fluid buffer content is linear increasing with parameter (η_2), then flowing system is also increasing which is busy period. Figure 4 shows that if fluid is increasing parameter (η_1), then average drift of the fluid buffer is also increasing. Figure 5 shows that if fluid is increasing parameter (η_2), then average drift of the fluid buffer is also increasing.

6 Conclusion

We prepare unreserved logical utterances for the joint static distribution in the fluid queueing model and content of the buffer under steady state, for the fluid queueing adjusted by multi-server queueing model with working vacation and with unreliable server. Such a matrix form expressions will greatly aid in an extensively analysis of the physical model for the specialist. Also, the mean of the fluid buffer content of the queueing model is computed by matrix geometric approach. If fluid flow is increasing, then the customer in the flowing system is busy period or working vacation is verified by the above figures from Figs. 2, 3, 4, and 5.
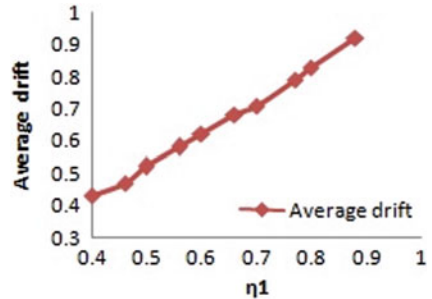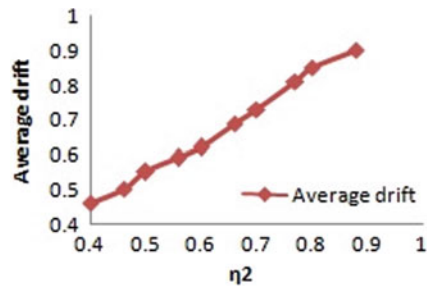

Fig. 2 η_1 versus flowing system
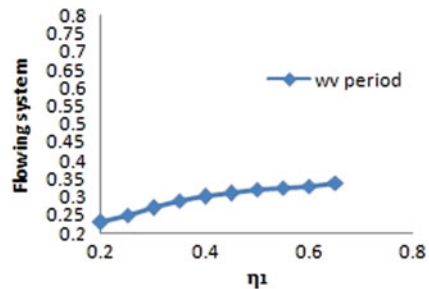
Fig. 3 η_2 versus flowing system
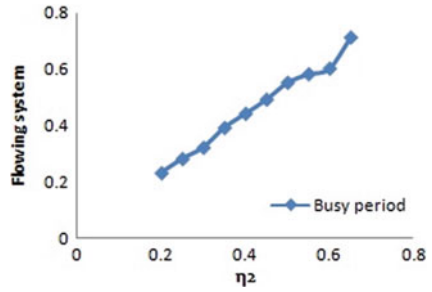
Fig. 4 η_1 versus average drift

Fig. 5 η_2 versus average drift

References

1. Adan IJBF, Resing JAC (1996) Simple analysis of a fluid queue driven by an M/M/1 queue. Queueing Syst 22:171–174
2. Anick D, Mitra D, Sondhi MM (1982) Stochastic theory of a data-handling system with multiple sources. Bell Syst Tech J 61:1871–1894
3. Bekker R, Mandjes M (2009) A fluid model for a relay node in an ad noc network: the case of heavy-tailed input. Math Methods Oper Res 70:357–384
4. Blaabjerg S, Andersson H (1995) Approximating the heterogeneous fluid queue with a birth-death fluid queue. IEEE Trans Commun 43(5):1884–1887
5. Elvalid A, Mitra D (1993) Effective bandwidth of general Markovian sources and admission control of high-speed networks. IEEE/ACM Trans Netw 1:329–343
6. Izmailov R (1996) Deterministic service of identical and independent on-off fluid sources. Stoch Models 12(2):329–342

7. Kosten L (1986) Liquid models for a type of information buffer problem. Delft Prog Rep 11:71–86
8. Kulkarni VG (1997) Fluid models for single buffer systems. In: Dshalalow JH (ed) Frontiers in Queueing. CRC Press, Boca Raton, pp 321–338
9. Latouche G, Taylor PG (2009) A stochastic fluid model for an ad hoc mobile network. Queueing Syst 63:109–129
10. Mao B, Wang F, Tian N (2010a) Fluid model driven by an M/M/1/N queue with single exponential vacation. Int J Inf Manag Sci 21:29–40
11. Mao B, Wang F, Tian N (2010b) Fluid model driven by an M/M/1/N queue with multiple exponential vacations. J Comput Inf Syst 6:1809–1816
12. Mitra D (1988) Stochastic theory of a fluid model of producers and consumers couple by a buffer. Adv Appl Probab 20:646–676
13. Neuts M (1981) Matrix-geometric solutions in stochastic models. Johns Hopkins University Press, Baltimore, pp 62–64
14. Ramaswami V (1999) Matrix analysis methods for stochastic fluid flow. In: Key P, Smith D (eds) ITC-16. Elsevier, NY, pp 1019–1030
15. Seenivasan M, Indumathi M (2018) A retrial queueing model with unreliable server in K policy., vol 1. Trends in mathematics. Springer Nature Switzerland AG, Berlin, pp 361–372
16. Seenivasan M, Subasri KS (2018) Batch arrival queueing model with unreliable server. Int J Eng Technol 7(4.10):269-273
17. Silver Soares A, Latouche G (2006) Matrix analytic methods for fluid queues with finite buffers. Perform Eval 63:295–314
18. Simonian A, Virtoma J (1991) Transient and stationary distributions for fluid queues and input processes with a density. SIAM J Appl Math 51:1732–1739
19. Tzenova E, Adan I, Kulkarni VG (2005) Fluid models with jumps. Stoch Models 21:37–55
20. Van Doorn EA, Scheinhardt WRW (1996) Analysis of birth-death Fluid queues. In: Proceedings of Applied Mathematics Workshop, pp 13–29
21. Virtamo J, Norros I (1994) Fluid queue driven by an M/M/1 queue. Queueing Syst 16:373–386
22. Xu X, Geng J, Liu M, Guo H (2013) Stationary analysis for fluid model driven by the M/M/C working vacation queue. J Math Anal Appl 403:423–433
23. Yan K, Kulkarni VG (2008) Optimal inventory policies under stochastic production and demand rates. Stoch Models 24

Dynamical Properties and Synchronization Between Two Chaotic Blood Flow Models

N. A. A. Fataf, N. A. L. Aladdin, and A. S. Normurniyati

Abstract Human heart is a complex system. It has many interacting subunits to make the whole unit complex. It has also been noticed that the dynamics in blood flow changes from laminar to turbulent flows and that can be the origin of chaos. In this paper, we discuss a coronary artery (CA) model which has a rich chaotic dynamics. We discuss the dynamical properties using bifurcation and Lyapunov exponents. We design a synchronization scheme to synchronize the dynamics of flow in the CA model. The results are effective in terms of biomathematical applications.

Keywords Chaos · Synchronization · Blood flow

1 Introduction

Chaos is a branch of mathematics focusing on the behaviour of dynamical systems that are highly sensitive to initial conditions. Small differences in initial condition yield widely diverging outcomes for such dynamical systems [1]. Sensitivity to initial condition means that each point in a chaotic system is arbitrarily closely approximated by other points with significantly different future paths, or trajectories. Chaotic behaviour exists in many natural systems, such as weather and climate [2]. It also occurs spontaneously in some systems with artificial components, such as road traffic [3]. This behaviour can be studied through analysis of a chaotic mathematical model, or through analytical techniques such as recurrence plots and Poincare maps.

Chaotic system can be very simple, but surprisingly they produce complex signals. One of the characteristics of a chaotic system is that the signals produced do not synchronize with any other system [4]. Therefore, it seems impossible for two chaotic systems to synchronize with each other; but if the two systems exchange information in just the right way, they can synchronize. Chaos synchronization is a phenomenon that may occur when two or more chaotic systems are coupled. The

N. A. A. Fataf (✉) · N. A. L. Aladdin · A. S. Normurniyati
School of Foundation Studies, Universiti Pertahanan Nasional Malaysia,
Kuala Lumpur, Malaysia
e-mail: n.aisyah@upnm.edu.my

idea of synchronization is to use the output of the master system to control the slave system so that the output of the slave system follows the output of the master system asymptotically [5]. The motivation for the study of chaotic synchronization relies on its numerous potential applications since the applications of chaotic synchronization range from living systems applications to the non-living systems applications. Among the examples of applications of chaotic synchronization to living systems include synchronization in neurobiology [6] and chemical reactions among pancreatic cells [7]. Meanwhile, the example of applications of chaotic synchronization to non-living systems includes synchronization of chaotic electrochemical oscillators [8].

Synchronization occurs when oscillatory (or repetitive) systems via some kind of interaction adjust their behaviours relative to one another so as to attain a state where they work in unison. Normally, all the systems of the body including blood circulation, respiration, metabolism, etc., work in different phases and frequencies, exhibiting nonlinearity and independence [9]. A nonlinear chaotic behaviour of the CA system may result in various cardiovascular problems, including myocardial infarction, angina, and even death [10]. Therefore, in this paper, we propose a master–slave synchronization control system to synchronize the dynamics of flow in the CA model.

This paper applies the ordinary differential equation to solve the blood flow model whereby the periodic and chaotic phase space, Lyapunov exponents, bifurcation diagram are investigated. Further, we propose a synchronization between two blood flow models to suppress the nonlinear chaotic behaviour of the CA model. The simulation results show that the derived controller enables to synchronize the dynamics of flow in the CA models.

The rest of the paper is organized as follows. In Sect. 2, the chaotic blood flow model is presented and its attractor is investigated. In Sect. 3, the coupled synchronization of the models is studied. The suitable controller is derived by using nonlinear adaptive controller. The results are summarized in Sect. 4.

2   The Blood Flow Model and Its Dynamics

The governing equations of the CA system were originally derived by [11] in 2002 and were subsequently converted by [12] in the form of:

$$\dot{x} + bx + cy = 0,$$
$$\dot{y} + (\lambda + b\lambda)x + (\lambda + c\lambda)y - \lambda x^3 - E\cos(\omega t) = 0, \tag{1}$$

where x is the variation of the blood vessel diameter, y is the change in the blood pressure, $E\cos(\omega t)$ is the external disturbance factor acting on the blood vessel, and b, c, λ are the system parameters.

In this paper, we present chaotic blood flow model given as:

$$\dot{x} = a - bx - cy,$$
$$\dot{y} = -d(1+b)x - d(1+c)y + dx^3 + E\cos(\omega t). \qquad (2)$$

where a, b, c, and d are the system parameters. We define $\dot{x}$ as the rate of the thickness of the blood vessel and $\dot{y}$ as the rate of the blood flow. A defining feature of chaotic system is sensitivity to initial condition. The system is said to be chaotic if two trajectories which start off close to each other deviate more and more over the time. The dynamic behaviour of the CA system is characterized by means of the phase portraits, Lyapunov exponents, and bifurcation diagram.

We examine the periodic and chaotic phase space of the blood flow model with the system parameters $a = 2, b = 0.15, c = -1.7, d = -0.6$. Figure 1 shows the attractor of system (2) when $E = 2$, $\omega = 1.4$ with the initial condition $x = 2$ and $y = -2$. Observed that the orbit exhibits regular and periodic motion. While Figs. 2 and 3 show the time series plot of the solution to the system (2) with aforesaid values of system parameters.

Now, we make change of the value $E = -1$ and $\omega = 1.875$, with the same initial values and system parameters, the system exhibits chaos as in Fig. 4. Figures 5 and 6 show the time series with respect to x and y, respectively.

The rate at which nearby trajectories deviate from each other with time is characterized by Lyapunov exponents (LE). The sign of the LE determines whether the system is chaotic or not. Note that the system exhibits chaos if there is at least one positive LE. We calculate the values of LE for some values of parameter ω of
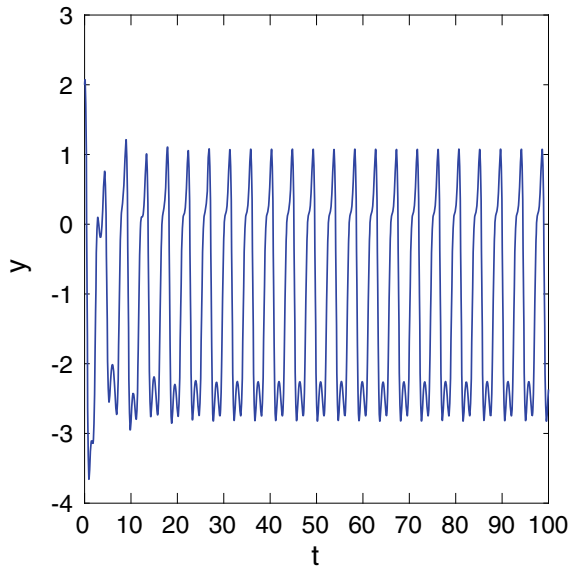
Fig. 1 Periodic orbital of the blood flow model with iteration $n = 1000$
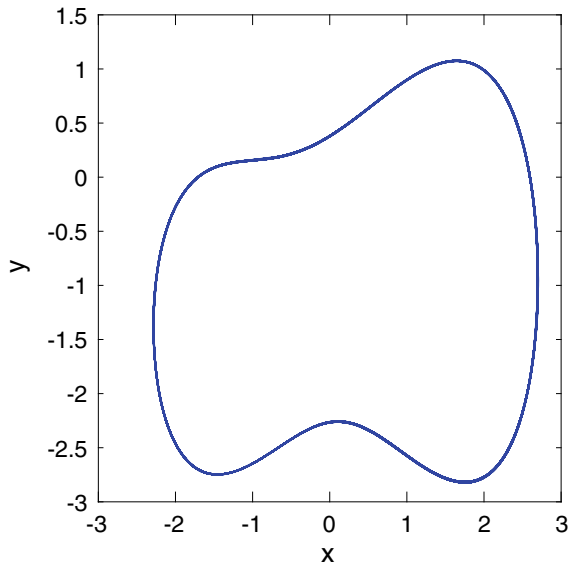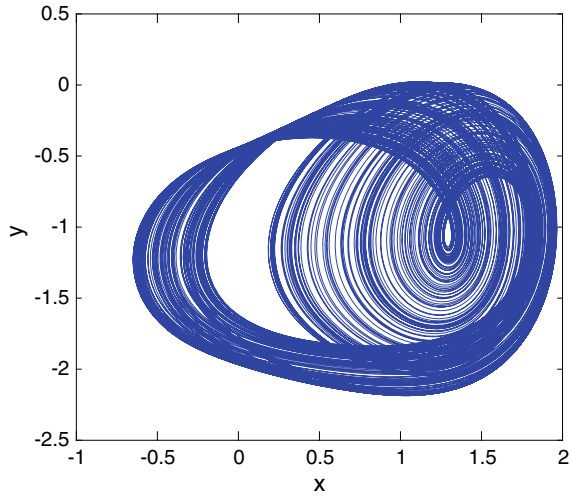
Fig. 2 Time series of the
state variable x for $n = 100$
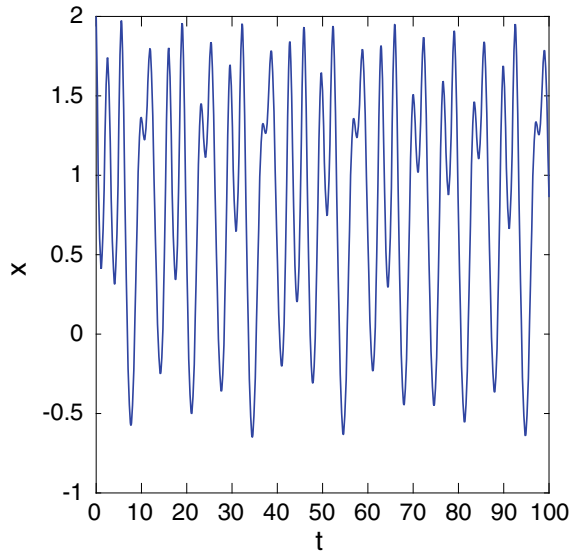of the chaotic blood flow
model
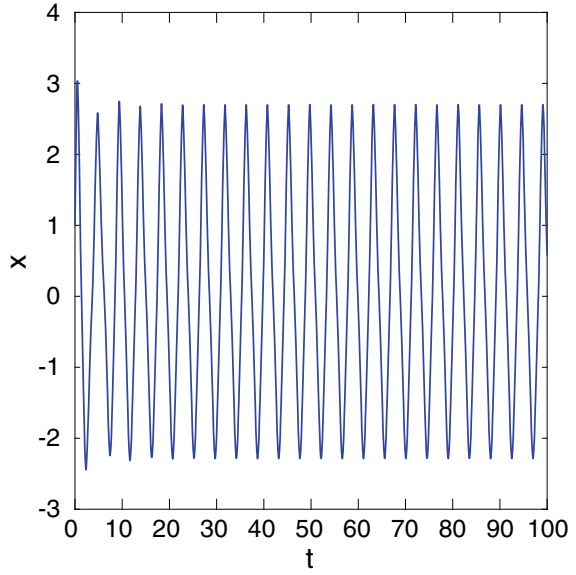
Fig. 3 Time series of the
state variable y for $n = 100$
of the chaotic blood flow
model

Fig. 4 Strange attractor of the blood flow model with iteration $n = 1000$
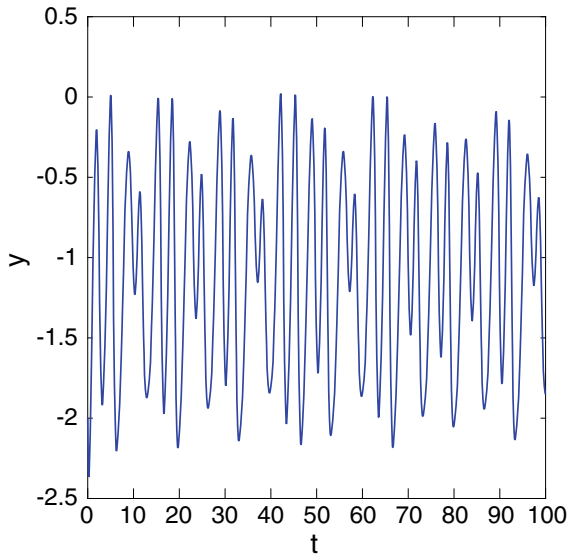

Fig. 5 Time series of the state variable x for $n = 100$ of the chaotic blood flow model


system (2). Figure 7 shows the graph of LE. Observe that there are three LE, one is positive, one negative, and one null LE.

A bifurcation is a qualitative change in dynamics upon a small variation in the parameter of a system. The bifurcation diagram shows the forking of the periods of stable orbits. We explore the chaotic properties through the bifurcation diagram for parameter ω, E and a. Figure 8 shows the bifurcation diagram of the blood flow model with respect to ω. We observe that there are bands for $1.5 < \omega < 2.2$, which means that the model is chaotic. While the single line such $\omega > 2.2$ shows that the model

Fig. 6 Time series of the state variable y for $n = 100$ of the chaotic blood flow model
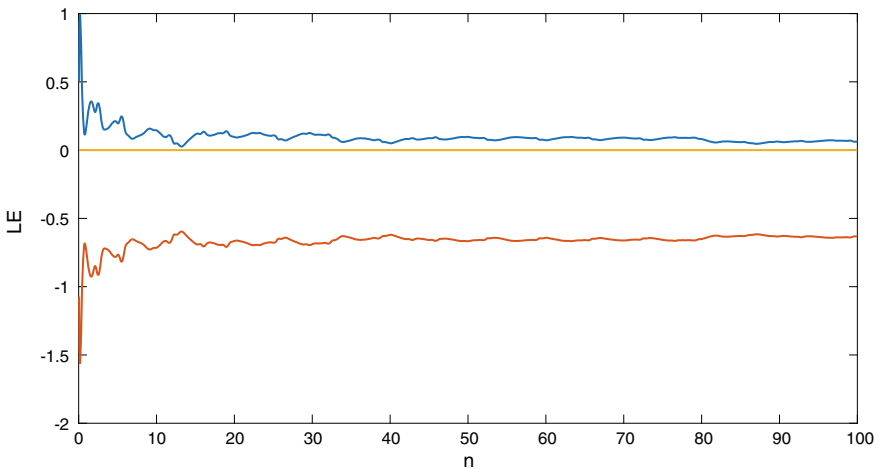
Fig. 7 Lyapunov exponents spectrum of blood flow model for $n = 100$

is periodic. We also investigate the bifurcation diagram of the blood flow model with respect to E as in Fig. 9. Figure 9 reveals that the blood flow model showing chaotic behavior when $1 < E < 1.8$ and the model is periodic when $0 < E < 1$ and $1.8 < E < 3$, while Fig. 10 shows that the model is chaotic for almost values of a.

Fig. 8 Bifurcation diagram of chaotic blood flow model for $\omega \in (0, 3)$

(a)
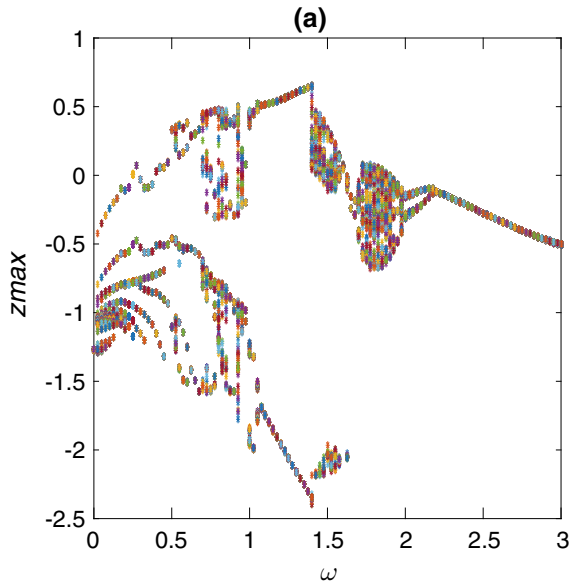
Fig. 9 Bifurcation diagram of chaotic blood flow model for $E \in (0, 3)$

(b)
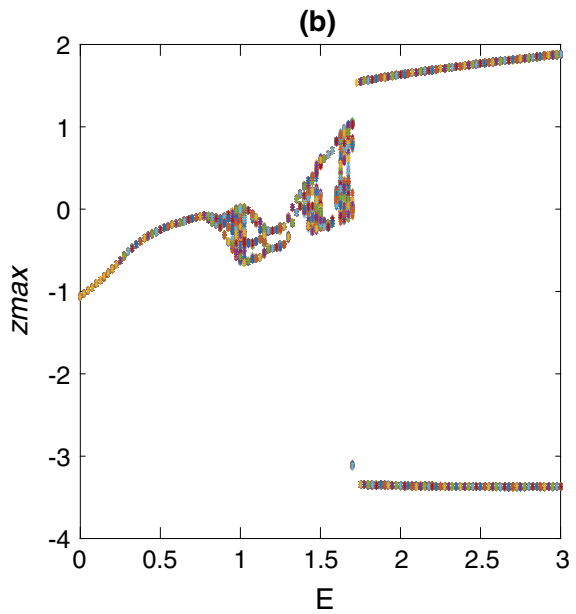
Fig. 10 Bifurcation diagram
of chaotic blood flow model
for $a \in (0, 3)$

3 Synchronization of Two Blood Flow Models

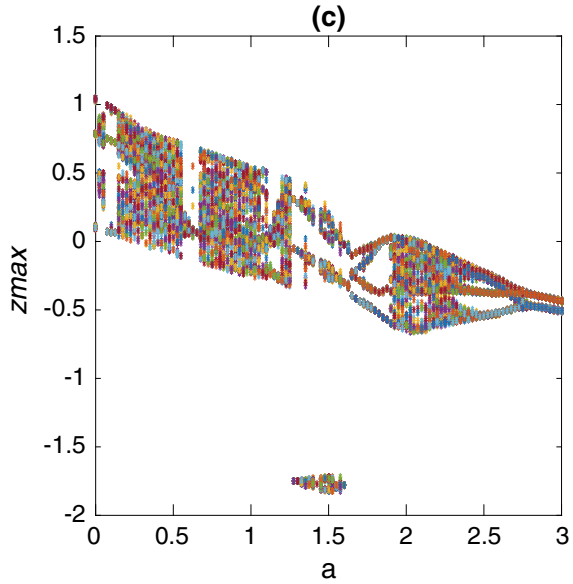From the above analysis, it can be seen that the CA model has very complex behaviour. In this section, we studied the synchronization between two blood flow models, where the controller is designed to synchronize the dynamics of flow in the CA models. For synchronization process, we consider nonautonomous CA models.

Let the driver system as:

$$
\begin{aligned}
\dot{x}_1 &= a - bx_1 - cy_1, \\
\dot{y}_1 &= -d(1 + b)x_1 - d(1 + c)y_1 + dx_1^3 + E\cos(\omega t).
\end{aligned}
\tag{3}
$$

and the response system as:

$$
\begin{aligned}
\dot{x}_2 &= a - bx_2 - cy_2 + u_1, \\
\dot{y}_2 &= -d(1 + b)x_2 - d(1 + c)y_2 + dx_2^3 + E\cos(\omega t) + u_2.
\end{aligned}
\tag{4}
$$

Let the error dynamics between two blood flow models as:

$$
\begin{aligned}
e_1 &= x_2 - x_1, \\
e_2 &= y_2 - y_1.
\end{aligned}
\tag{5}
$$

We introduce the nonlinear controller to forcefully make the driver and the response systems completely synchronized:

$$u_1 = be_1 + ce_2 - ke_1$$
$$u_2 = d(1 + b)e_1 + d(1 + c)e_2 - d(x_2^3 - x_1^3) - ke_2, \tag{6}$$

where k denotes the coupling strength.

Thus, the error dynamics takes the form:

$$\dot{e}_1 = -ke_1$$
$$\dot{e}_2 = -ke_2. \tag{7}$$

We define the Lyapunov function as $V = \frac{1}{2}(e_1^2 + e_2^2)$. Therefore,

$$\dot{V} = e_1(\dot{e}_1) + e_2(\dot{e}_2)$$
$$= -k(e_1^2 + e_2^2) < 0. \tag{8}$$

Since $\dot{V} < 0$, by Lyapunov stability theory [13], the error dynamics given by Eq. (7) is globally exponentially stable. To show the synchronization, we plot x_2 versus x_1 and y_2 versus y_1. Figure 11 shows the result. Observed that for both figures, the line is concentrated in the line $y = x$ and indicates the occurrence of synchronization between the driver and the response systems. The error dynamics between the driver and response system is shown in Fig. 12.
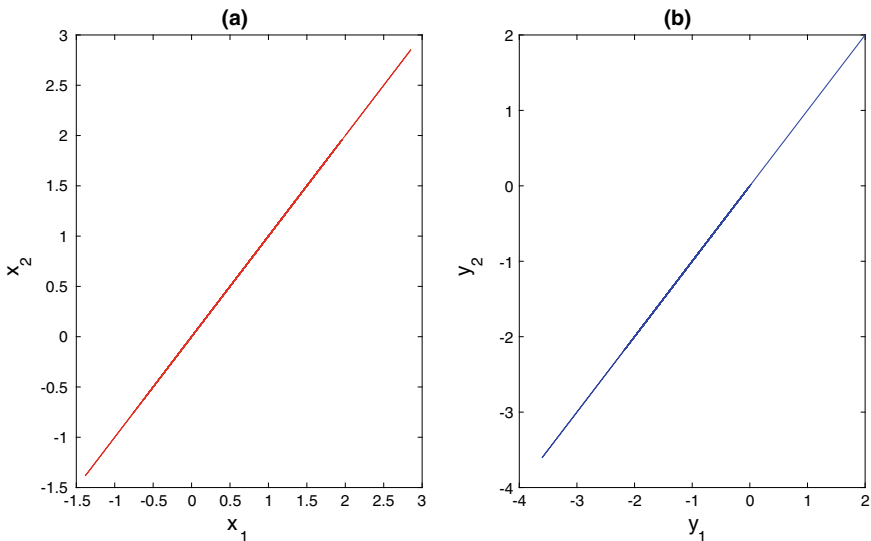
Fig. 11 Plot of **a** $x_2(t)$ versus $x_1(t)$ **b** $y_2(t)$ versus $y_1(t)$ implying occurence of synchronization between two blood flow models
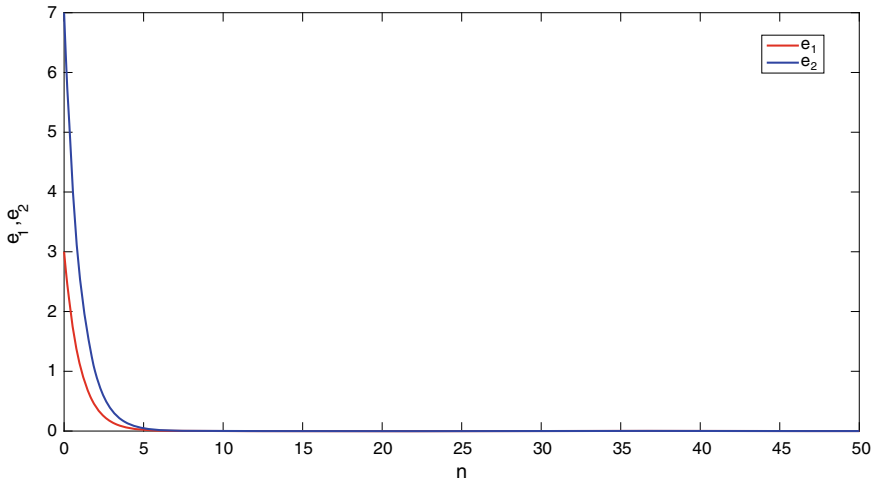
Fig. 12 Values error dynamics between the driver and response system

4 Conclusion

In this paper, we present a blood flow model and applied the ordinary differential equation method to investigate its dynamics behaviour. Phase trajectories, Lyapunov exponents, and bifurcation diagrams have been used to characterize the dynamics of the system. Further, nonlinear controller is derived as a controller to synchronize the dynamics of flow in the CA model. The result is effective for biomathematical applications.

References

1. Solev D, Janjic P, Kocarev L (2011) Introduction to chaos. SCI 354:1–25
2. Lorenz EN (1963) J Atmosp Sci 20(2):130–141
3. Akhavan A, Samsudin A, Akhshani A (2017) Optics Laser Technol 95:94–99
4. Pecora LM, Carroll TL (2015) Chaos: Interdisp J Nonlinear Sci 25(6):097611-1–097611-12
5. Park JH (2006) Chaos, Solitons Fractals 27:549–554
6. Gonzalez-Miranda JM (2004) Synchronization and control of chaos. Imperial College Press, London
7. Mosekilde E, Maistrenko Y, Postnov D (2002) Chaotic Synchronization Applications to Living Systems. World Scientific Publishing Co. Pte. Ltd, Singapore
8. Kiss IZ, Hudson JL (2003) Chaos 13(3):999–1009

9. V. Andrey Dunaev, V. Victor Sidorov, I. Alexander Krupatkin, E. Ilya Rafailov, G. Scott Palmer, G. Sergei Sokolovski, A. Neil Stewart, U. Erik Rafailov, Proc. of SPIE, 893, 89350A-1 - 89350A - 9 (2014)
10. Cheng CW, Her TY (2013) Vol. 2013. Hindawi Publishing Corporation, 11 p. Article ID 209718
11. Guan XP, Fan ZP, Chen CL (2002) National Defence Industry Press. Beijing, China
12. Gong CY, Li YM, Sun XH (2006) J Appl Sci 24:604–607
13. Hahn W (1967) The stability of motion. Springer, Berlin

Blasius and Sakiadis Unsteady Flow of Chemically Reacted MHD Williamson Fluid with Variable Conductivity: A Comparative Study

Narsu Siva Kumar and B. Rushi Kumar

Abstract The present work reports a study two-dimensional (2D) Blasius and Sakiadis an unsteady magnetohydrodynamic (MHD) radiated Williamson flow with variable conductivity of a chemically reacting fluid is considered. An approximate transformation was developed to transform PDEs into nonlinear ODEs. To current numerical calculation shooting technique is implemented. The computational results of the Blasius and Sakiadis flow on concentration, temperature and velocity distributions for some physical quantities are presented graphically and in tabular form.

Keywords Blasius/Sakiadis flows · Williamson fluid · MHD · Shooting approximation · Chemical reaction

1 Introduction

Non-Newtonian fluids are extensively used in various sectors like technical, food processing, biological, and medical, etc. The Navier–Stokes equations are deficient for the examination of non-Newtonian fluids because of its nonlinear connection among stress and rate of strain; hence, various kinds of rheological models are proposed to the description of non-Newtonian fluids. One of the classical rheological models is the Williamson model and it has a pseudo-plastic or shear-thinning behaviour. The following are some of the investigations about non-Newtonian fluids. Williamson [1] proposed flow of a pseudo-plastic material and he exhibited a condition to depict pseudo-plastic fluids with the test results and furthermore he concluded there are some of the fluid flows that do not follow the viscous fluids. This type of flows is said to be pseudo-plastic flows. Chu et al. [2] studied viscosity of pseudo-plastic

N. Siva Kumar
Department of Mathematics, SRMIST, Chennai, Tamil Nadu 603203, India
e-mail: nsivakumar15@gmail.com

B. Rushi Kumar (✉)
Department of Mathematics, School of Advanced Sciences, Vellore Institute of Technology, Vellore, Tamil Nadu 632014, India
e-mail: rushikumar@vit.ac.in

fluids. Pantokratoras [3] discussed the Sakiadis and Blasius flows of power-law non-Newtonian fluid, and he observed that the Sakiadis and Blasius flows have positive, negative skin friction, respectively. Bognar and Hriczo [4] presented the steady flow of non-Newtonian fluid on an impermeable flat-plat, and they considered that the plate is heated at the bottom with convection. They noticed that the increment of power-law index or Prandtl number causes to decreasing of thermal boundary layer. A pseudoplastic flow of Williamson fluid on a stretching sheet was investigated by Nadeem et al. [5] and they have found that Williamson fluid parameter accelerates the thickness of the momentum boundary layer. Bognar and Csati [6] presented the boundary layer flow of non-Newtonian power-law fluid and considered the sheet is impermeable, moving with constant velocity. Khabazi et al. [7] proposed the Sakiadis flow of a non-Newtonian Harris fluid with high Reynolds number. Hayat et al. [8] discussed thickness of the boundary layer of non-Newtonian type of the Carreau fluid model through stretching surface and also they assumed that sheet is permeable and convectively heated. Zahra et al. [9] analyzed the Poiseuille and Couette flow of Williamson's fluid with pressure dependent viscosity and they have shown that increasing Weisenberg number enhances the fluid velocity.

The extensive scope of electrically conducting non-Newtonian fluid flows which are extensively used in many fields, hence many researchers have the curiosity to investigate these type of flows. Few investigations of hydromagnetic non-Newtonian flows are presented here. Pantokratoras and Fang [10] discussed the Sakiadis and Blasius fluid flow of conducting non-Newtonian and they noticed that thickness of the boundary layer is reduced with magnetic field parameter in both 'Blasius' and 'Sakiadis' flows. Mustafa et al. [11] considered a Sakiadis flow of conducting Maxwell fluid with convective condition and they noticed that the heat transfers rate which diminishes with magnetic field parameter. Hayat et al. [12] performed a boundary layer analysis on hydromagnetic flow of Williamson fluid over a stretching surface, and they finalized that with the effect of the magnetic field, the fluid temperature and velocity are increasing and decelerating functions, respectively.

From the above researchers we motivated, the point of the current examination is to explore an unsteady MHD radiative Williamson fluid with chemical reaction and heat source in both 'Blasius and Sakiadis' cases. It is seen that mass and heat transfer rates are high in Blasius flow compared to Sakiadis flow case. The numerical results are computed for Sherwood number, Nusselt number, and skin friction coefficients for some physical parameters.

2 Mathematical Formulation

Now we consider the flow of Williamson fluid over a horizontal permeable plate with u, v, respectively, the velocity components (u, v) in (x, y) directions, where x is taken in the fluid flow direction and y is taken normal to it. The effects of the Williamson fluid, Brownian motion, and thermophoresis are presented. Under these assumptions:

$$\frac{\partial v}{\partial y} + \frac{\partial u}{\partial x} = 0 \tag{1}$$

$$\left(\frac{\partial u}{\partial t} + u \frac{\partial u}{\partial x} + v \frac{\partial u}{\partial y} \right) = v \frac{\partial^2 u}{\partial y^2} + \sqrt{2} v \Gamma \frac{\partial u}{\partial y} \frac{\partial^2 u}{\partial y^2} + g[\beta_T (T - T_\infty)]$$

$$+ g[\beta_C (C - C_\infty)] - \frac{\sigma B_0^2}{\rho} u - u \frac{v}{K_0} \tag{2}$$

$$\rho C_p \left(\frac{\partial T}{\partial t} + u \frac{\partial T}{\partial x} + v \frac{\partial T}{\partial y} \right) = \frac{\partial}{\partial y} \left(K(T) \frac{\partial T}{\partial y} \right) - Q[T - T_\infty]$$

$$+ \tau \left(\frac{D_T}{T_\infty} \left(\frac{\partial T}{\partial y} \right)^2 + D_B \frac{\partial C}{\partial y} \frac{\partial T}{\partial y} \right) - \frac{\partial q_r}{\partial y} \tag{3}$$

$$\frac{\partial C}{\partial t} + u \frac{\partial C}{\partial x} + v \frac{\partial C}{\partial y} = D_B \left(\frac{\partial^2 C}{\partial y^2} \right) + \frac{D_T}{T_\infty} \frac{\partial^2 T}{\partial y^2} - K_c (C - C_\infty) \tag{4}$$

The boundary conditions for free stream case (Blasius problem) and moving plate case (Sakiadis problem) are

$$\left. \begin{array}{l} u = 0, v = 0, C = C_w, T = T_w \text{ at } y = 0 \\ u = U, C = C_\infty, T = T_\infty, \text{ as } y \to \infty \end{array} \right\}$$

$$\left. \begin{array}{l} u = U, v = 0, C = C_w, T = T_w \text{ at } y = 0 \\ u = 0, C = C_\infty, T = T_\infty \text{ as } y \to \infty \end{array} \right\} \tag{5}$$

We present now the accompanying non-dimensional functions $f(\zeta)$, $\theta(\zeta)$, $\phi(\zeta)$ (see the ref. [13]).

$$\zeta = y \left[\frac{a}{v(1 - ct)} \right]^{1/2}, \psi = x f(\zeta) \left(\frac{a v}{(1 - ct)} \right)^{1/2}, \phi(\zeta) = \frac{C - C_\infty}{C_w - C_\infty},$$

$$\theta(\zeta) = \frac{T - T_\infty}{T_w - T_\infty} \tag{6}$$

where ψ is stream function, which is defined as $u = \frac{\partial \psi}{\partial y}$ and $v = -\frac{\partial \psi}{\partial x}$.

These satisfy identically the continuity Eq. (1). Now, substituting Eq. (6) in Eqs. (2–4), we get

$$f''' - f'^2 + f f'' - A \left(f' + \frac{1}{2} \zeta f'' \right) + \Lambda f'' f''' - (M + K) f'$$

$$+ \lambda_C \phi + \lambda_T \theta = 0 \tag{7}$$

$$\frac{1}{Pr}\left(\theta'' + \varepsilon\theta'^2 + \varepsilon\theta\theta''\right) - Q_H\theta + \frac{Nr}{Pr}\theta'' + f\theta' - \theta f' - \frac{1}{2}A\zeta\theta'$$
$$- 2A\theta + N_b\theta'\phi' + N_t\theta'^2 = 0 \tag{8}$$

$$\phi'' + Sc\left(f\phi' - \phi f'\right) - Sc\frac{A}{2}\zeta\phi' - 2ASc\phi - KrASc\phi + Sc\frac{N_t}{N_b}\theta'' = 0 \tag{9}$$

Corresponding boundary conditions are

(i) Blasius problem

$$f'(0) = 0, \ f(0) = 0, \ \phi(0) = 1, \ f'(\infty) = 1, \ \theta(0) = 1,$$
$$\theta(\infty) = 0, \ \phi(\infty) = 0 \tag{10}$$

(ii) Sakiadis problem

$$f'(0) = 1, \ f(0) = 0, \ \phi(0) = 1, \ f'(\infty) = 0, \ \theta(0) = 1,$$
$$\theta(\infty) = 0, \ \phi(\infty) = 0$$

where $A = \frac{c}{a}$, $\Lambda = \Gamma x\left(\frac{a^3}{\sqrt{1-ct}}\right)^{1/2}$, $\lambda_T = g\beta_T b/a^2$, $\lambda_C = g\beta_C b/a^2$, $Pr = \frac{\rho C_p v}{K_\infty}$, $M = \frac{\sigma B_0^2}{\rho c}$, $K = \frac{v}{K_0 c}$, $Q_H = \frac{Q}{\rho C_p a}$, $Nr = \frac{16T_\infty^3 \sigma^*}{3k^* K_\infty}$, $N_t = \frac{\tau D_T(T_w - T_\infty)}{T_\infty v}$, $Sc = \frac{v}{D_B}$, $Kr = \frac{K_c v^2}{D_B U^2}$, $N_b = \frac{\tau D_B(C_w - C_\infty)}{v}$.

From the engineering interest, the flow of Sherwood number, Nusselt number, and skin friction coefficient is

$$Sh_x = \frac{xj_m}{D_B(C_w - C_\infty)}, \ Nu_x = \frac{xq_w}{K_\infty(T_w - T_\infty)}, \ C_f = \frac{\tau_w}{\rho U_w^2/2}$$

where

$$\tau_w = \mu\left[\frac{\partial u}{\partial y} + \frac{\Gamma}{\sqrt{2}}\left[\frac{\partial u}{\partial y}\right]^2\right]_{y=0}, \ q_w = -K_\infty\left[\frac{\partial T}{\partial y} + \frac{16\sigma * T_\infty^3}{3k * K_\infty}\frac{\partial T}{\partial y}\right]_{y=0},$$
$$j_m = -D_B\left[\frac{\partial C}{\partial y}\right]_{y=0}$$

3 Results and Discussion

The set of ODEs (7–9) subjected to the boundary condition (10) are solved using shooting technique. For numerical computations, it is convenient to use the following non-dimensional values
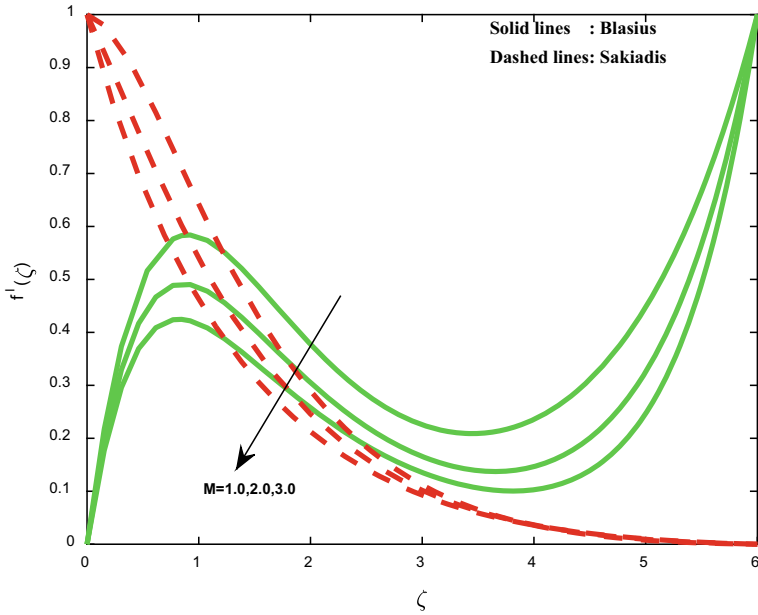
Fig. 1 Sketch of M on f'

$$Q_H = 0.5, Kr = 0.1, \text{Pr} = 0.7, N_b = 1, Nr = 0.2, K = 0.5,$$
$$N_t = 1, A = 0.2, \varepsilon = 0.1, \Lambda = 0.2, \zeta = 0.5, M = 2.0$$

During our analysis, we reserved these values are common except the various values that are displayed in the respective graphs. The effect of Williamson fluid parameter Λ, chemical reaction parameter Kr, Schmidt number Sc on temperature, and concentration and velocity fields is presented graphically.

Figures 1 and 2 elucidate the influence of magnetic field parameter on velocity and temperature distributions in both Sakiadis and Blasius flows. It is observed from Fig. 1 that the fluid velocity diminishes with enhancing values of M. This is because of drag force namely Lorentz force which arises with magnetic-field, these force oppose the flow and hence fluid velocity diminishes. The Lorentz forces create internal friction due to this reason and the fluid temperature raised with magnetic field; it is noted from Fig. 2.

In both Sakiadis and Blasiusflow cases, the fluid flow velocity decreases with increasing values of Williamson fluid parameter which is shown in Fig. 3. Increasing values of Williamson fluid parameter reduces the fluid velocity. Physically speaking higher values of Williamson fluid parameter causes to increasing of relaxation time and it causes to high viscosity hence the fluid velocity diminishes.

The chemical reaction is inversely proportional to the fluid density hence fluid has a low density at the high chemical reaction. Due to this reason the specious
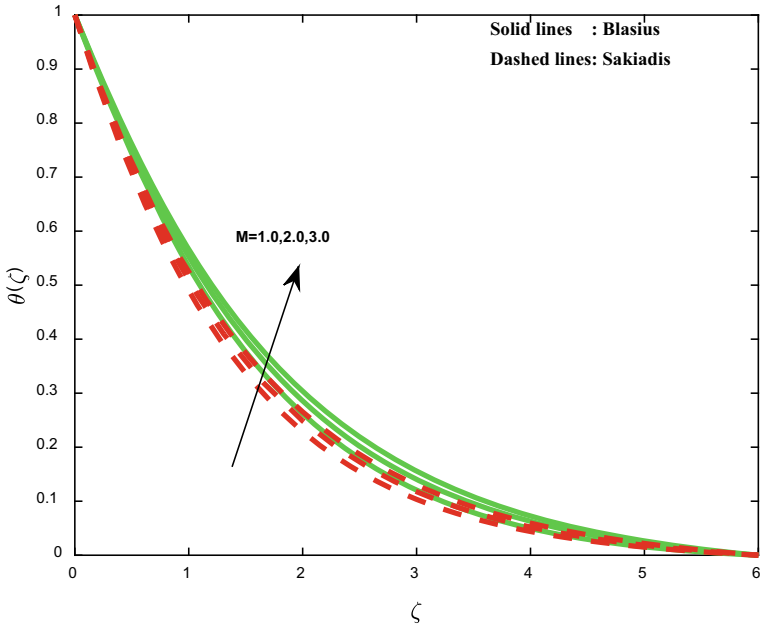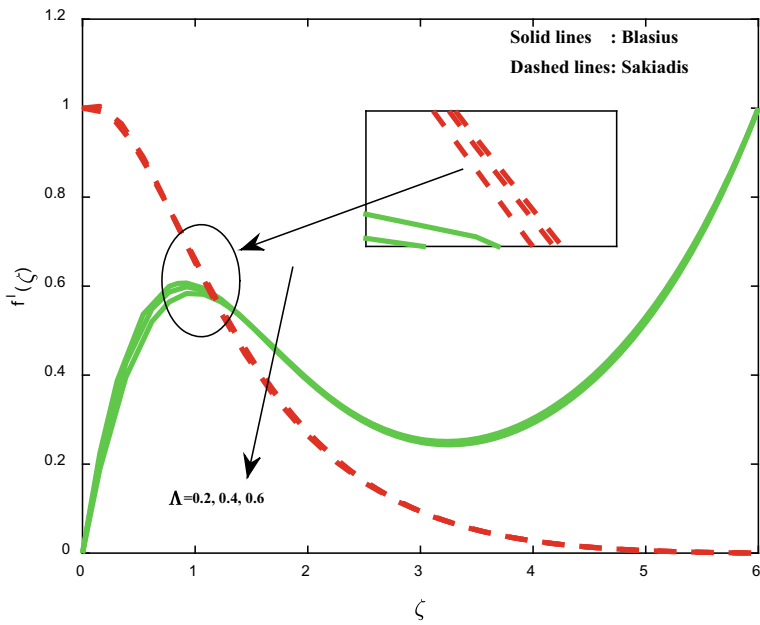
Fig. 2 Sketch of M on θ

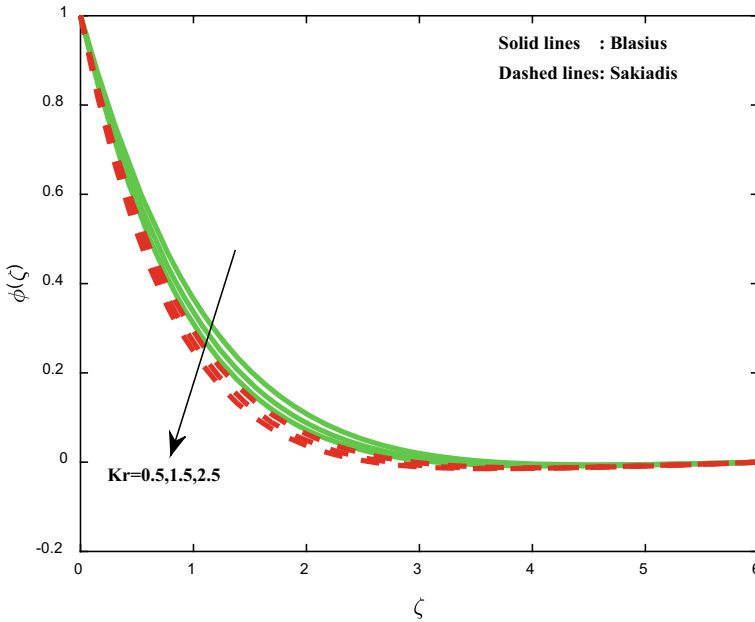**Fig. 3** Sketch of Λ on f'

Fig. 4 Sketch of Kr on ϕ

concentration decreases with increasing values of chemical reaction parameter, this behaviour is noticed in Fig. 4 for both Sakiadis and Blasius flow cases.

The specious concentrations are retarded for increasing values of Sc, and this is shown in Fig. 5. Practically, Sc represents the ratio between the momentum diffusivity and the mass diffusivity. It is observed that as the Sc increases, the species concentration decreases. Physically, the increase of Schmidt number means a decrease of molecular diffusion.

Figure 6 depicts the influence of thermal conductivity parameter $\phi(\zeta)$ on temperature distribution with Sakiadis and Blasius cases. From this figure, we noticed that the temperature distribution increases with increasing values of variable thermal conductivity parameter.

The numerical results of Sherwood, Nusselt numbers, and skin friction coefficient for Blasius/Sakiadis flow cases are represented by Tables 1 and 2, respectively. The magnetic field parameter M minimizes the skin friction, Sherwood number, and Nusselt number in both Sakiadis and Blasius flows, and the similar attitude occurred with porosity parameter K also. Physically, M and K depressed the flow velocity hence local friction reduced, the temperature transferred from plate to the fluid in the presence of magnetic and porosity parameters hence heat transfer reduced at the plate. In both Blasius and Sakiadis flow, the rate of heat transfer reduces with the increasing values of thermal radiation parameter and the opposite tendency is noticed in skin friction and the rate of mass transfer. This is because, in the presence of the working fluid, the heat is absorbed from the plate. The local friction increases as the
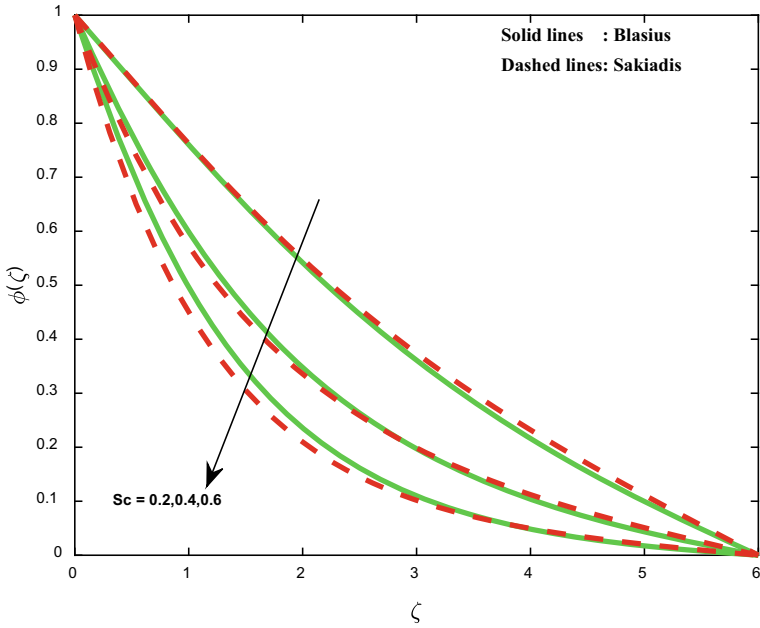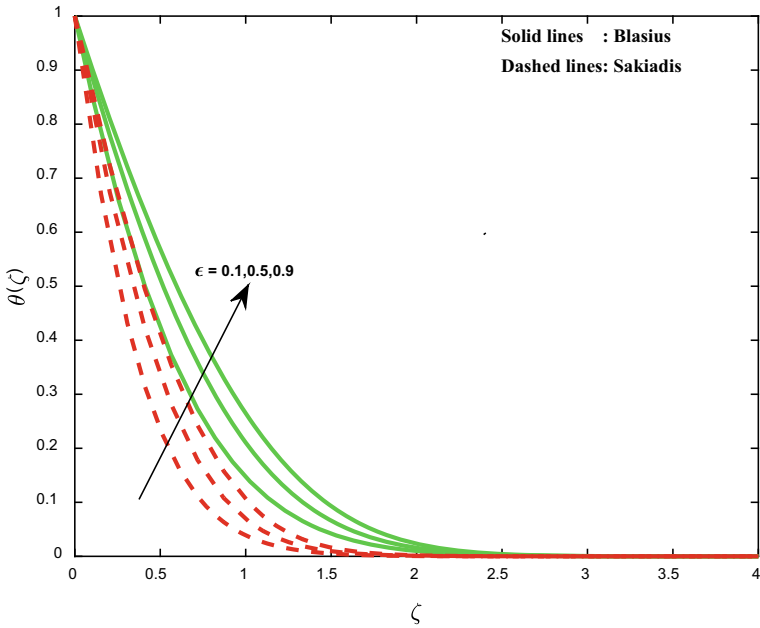
Fig. 5 Sketch of *Sc* on ϕ

Fig. 6 Sketch of ε on ϕ

Table 1 Numerical values of friction factor coefficient, Nusselt and Sherwood numbers in Blasius flow case

M	K	Nr	Pr	Nt	Nb	Kr	Q_H	Λ	Sc	C_f	Nu_x	Sh_x
1.0										−0.048732	1.343869	1.148740
2.0										−0.529496	1.295855	1.103996
3.0										−0.969535	1.256061	1.066035
	0.5									2.061890	1.121597	0.884924
	1.5									1.860648	1.073850	0.884924
	2.5									1.709450	1.038766	0.810188
		1.0								2.100054	0.763676	0.910101
		2.0								2.152275	0.550786	0.940935
		3.0								2.187105	0.462510	0.959133
			0.71							2.011228	1.539469	0.844801
			7.0							1.726667	17.298206	0.521930
				0.1						1.993338	1.551113	0.908040
				0.5						2.061965	1.503628	0.675251
				0.9						2.123008	1.454591	0.494317
					0.1					2.063432	1.626234	0.536791
					0.5					2.020015	1.474665	0.907959
					0.9					2.008727	1.357786	0.953022
						0.5				2.007290	1.536718	0.874565
						1.5				1.995349	1.528546	0.968571
						2.5				1.984884	1.521586	1.055849
							0.1			2.019215	1.475142	0.889361
							0.5			1.974574	1.712001	0.831765
							0.9			1.936788	1.927279	0.777998
								0.2		2.007290	1.536718	0.874565
								0.4		2.158034	1.525609	0.866997
								0.6		2.464787	1.508622	0.855438
									0.2	2.138176	1.643359	0.242374
									0.4	2.085629	1.599193	0.475223
									0.6	2.051636	1.571476	0.638971

thermophoresis parameter N_t increase. This is because of the reason that the fluid velocity increases as increasing values of thermophoresis parameter N_t. The rate of heat and mass transfer decelerated as N_t improved. We observed that the Brownian motion N_b accelerates the Sherwood number whereas suppressed the friction factor coefficient and Nusselt number. The chemical reaction K_r declines the specious concentration; hence, the rate of mass transfer improved at the plate and opposite behavior occurred in local skin friction and heat transfer rate. Increasing values of heat source parameter Q_H increase the heat transfer rate. However, increasing the values of heat source parameter Q_H leads to a decrease in both skin friction coefficient and mass transfer rate. The fluid velocity retarded when raising Williamson parameter Λ

Table 2 Numerical values of friction factor coefficient, Nusselt and Sherwood numbers in Sakiadis flow case

M	K	Nr	Pr	Nt	Nb	Kr	Q_H	Λ	Sc	C_f	Nu_x	Sh_x
1.0										1.953325	1.095678	0.862114
2.0										1.780181	1.055101	0.825347
3.0										1.646657	1.024378	0.796674
	0.5									0.212307	1.371645	1.174139
	1.5									−0.295184	1.318702	1.125426
	2.5									−0.753705	1.275057	1.084260
		1.0								0.197547	1.218680	1.161701
		2.0								0.269806	0.813080	1.207833
		3.0								0.318536	0.653996	1.233844
			0.71							0.145343	1.935490	1.122462
			7.0							−0.237662	25.973221	0.590399
				0.1						0.121597	1.948768	1.222261
				0.5						0.212732	1.894151	0.847202
				0.9						0.294187	1.836953	0.534263
					0.1					0.218200	2.043728	0.658442
					0.5					0.150428	1.852890	1.216343
					0.9					0.139590	1.703872	1.280794
						0.5				0.141987	1.933210	1.148029
						1.5				0.131781	1.926419	1.229320
						2.5				0.122825	1.920601	1.305534
							0.1			0.153470	1.876250	1.159707
							0.5			0.110795	2.095246	1.113870
							0.9			0.075241	2.294371	1.070250
								0.2		0.141987	1.934757	1.149226
								0.4		0.177587	1.933694	1.148400
								0.6		0.258853	1.933210	1.148029
									0.2	0.315478	2.066269	0.233500
									0.4	0.247462	2.012680	0.555306
									0.6	0.202184	1.977897	0.792568

hence local skin friction increased with increasing values of Λ, whereas Nusselt and Sherwood numbers are reduced with Λ. Sherwood number improved with Schmidt number S_c due to the reason that the mass diffusion rate enhanced when the S_c increases and Nusselt number and local frictions are reduced with S_c.

4 Concluding Remarks

The hypothetical examination to discuss the influence of chemically reacting MHD Williamson fluid in Sakiadis and Blasius flow cases with thermophoresis and Brownian motion effects with an internal heat source (or sink). The shooting method is utilized to produce the solutions for the problem. Findings of the present study are as follows:

- The magnetic field parameter has a very significant effect on the velocity and temperature distributions, due to magnetic field that acts as an accelerating force in reducing frictional resistance in Blasius and Sakiadis cases.
- The chemical reaction Kr declines the specious concentration hence mass transfer rate improved at the plate and opposite behavior occurred in local skin friction and heat transfer rate.
- The mass and heat transfer rates are high in Blasius flow compared with Sakiadis fluid flow case.

References

1. Williamson RV (1929) The flow of pseudoplastic materials. Ind Eng Chem Res 21:1108–1111
2. Chu JC, Burridge KC, Brown F (1954) The viscosity of pseudo-plastic fluids. Chem Eng Sci Genie Chimique 3:229–247
3. Pantokratoras A (2011) Blasius and Sakiadis flow with uniform blowing or suction in non-Newtonian power-law fluids. Chem Eng Comm 198:332–343
4. Bognar G, Hriczo K (2011) Similarity Solution to a thermal boundary layer model of a non-Newtonian fluid with a convective surface boundary condition. Acta Polytechnica Hungarica 8:131–140
5. Nadeem S, Hussain ST, Lee C (2013) Flow of a Williamson fluid over a stretching sheet. Brazilian J Chem Eng 30:619–625
6. Bognar G, Csati Z (2014) Numerical solution to boundary layer problems over moving flat plate in non-Newtonian media. J Appl Math Phys 2:8–13
7. Khabazi NP, Aryan M, Jamali J, Sadeghy K (2014) Sakiadis flow of Harris fluids: a series-solution. Nihon ReorojiGakkaishi 42:245–253
8. Hayat T, Asad S, Mustafa M, Alsaedi A (2014) Boundary layer flow of Carreau fluid over a convectively heated stretching sheet. Appl Math Comput 246:12–22
9. Zehra I, Yousaf MM, Nadeem S (2015) Numerical solutions of Williamson fluid with pressure dependent viscosity. Results Phys 5:20–25
10. Pantokratoras A, Fang T (2011) A note on the Blasius and Sakiadis flow of a non-Newtonian power-law fluid in a constant transverse magnetic field. Acta Mech 218:187–194
11. Mustafa M, Khan JA, Hayat T, Alsaedi A (2015) Sakiadis flow of Maxwell fluid considering magnetic field and convective boundary conditions. AIP Adv 5:1–9
12. Hayat T, Shafiq A, Alsaedi A (2016) Hydromagnetic boundary layer flow of Williamson fluid in the presence of thermal radiation and Ohmic dissipation. Alexandria Eng J 55:2229–2240
13. Vajravelu K, Prasad KV (2013) Chiu-On Ng: unsteady convective boundary layer flow of viscous fluid at a vertical surface with variable fluid properties. Nonlinear Anal Real World Appl 14:455–464

Computational Analysis of Conjugate Buoyant Convective Transport in an Annulus

S. Kiran, N. Keerthi Reddy, M. Sankar, and Younghae Do

Abstract In the present work, the convective flow and thermal pattern, associated heat transport rates of buoyant convection in an annular geometry is theoretically analyzed. The inner cylindrical wall has finite thickness and is kept at high temperature, while the outer cylindrical wall is held at low temperature. The vorticity-stream function form of model equations are solved using FDM based on ADI and SLOR techniques. The numerical simulations for various parameters are presented. In particular, this analysis focused on the effects of conjugate heat transport characteristics.

Keywords Conjugate heat transfer · FDM · Annulus

1 Introduction

The study of natural convection in annular enclosures has grown to be the object of diverse research because of its significance in a number of natural phenomena and in industrial engineering applications, such as energy conversion exchanges of heat through multi-shell packaging, cooling of electronic chips, building comfort, storage and transmission systems and other alternative fields.

The first attempt to made a detailed analysis on buoyancy driven convection in an annulus geometry is by Thomas and De Vahl Davis [1]. Further, the effect of various parameters on the buoyant convection are studied in the literature [2–4]. Kumar and Kalam [5] proposed an updated details on the thermal transport processes and discussed the differences in heat transfer correlations of earlier studies. Choukairy

S. Kiran
Department of Mathematics, Nitte Meenakshi Institute of Technology, Bengaluru 560064, Karnataka, India

N. Keerthi Reddy · M. Sankar (✉)
Department of Mathematics, School of Engineering, Presidency University, Bengaluru, India
e-mail: msankar@presidencyuniversity.in

Y. Do
Department of Mathematics, Kyungpook National University, Daegu, Republic of Korea

et al. [6] presented the effects of horizontal partition in the annular enclosure on the average thermal transport rate, for this they considered the inner and the outer boundaries of the annular enclosure to be maintained at different constant temperature with adiabatic top and bottom walls. Venkatachalappa et al. [7] made an attempt to comprehend the buoyant convective flow caused by buoyancy and angular velocity in an annular geometry. Sankar and co-workers [8–13] made a pioneering numerical simulations to understand the influences of single and multiple thermal sources on buoyancy-driven convective transport in an annular region enclosed by two cylindrical tubes with same center. They found that the source location and size produces subtle impacts on convective transport rates.

Prasad and Kulacki [14] and Hickox and Gartling [15] performed numerical simulations to analyze the curvature ratio on buoyant flow in a vertical annulus filled with porous material. Further investigations were carried out by Havstad and Burns [16] for the same geometry to know about the heat transfer rate in the annuli filled with a porous medium. Later, Sankar et al. [17, 18] reported the importance of discretely heated cylindrical wall of a porous annulus on buoyancy-driven convection. For the same geometry, Sankar et al. [19] determined the importance of a single thermal and solute segment on the thermal and solute transfer. The impacts of discrete source and sink locations in a porous geometry is investigated by Sankar et al. [20]. The cases of effect of magnetic field for the above configuration are studied by Venkatachalappa et al. [21]. The influence magnetic field on buoyant-convection in the annulus filled with electrically conducting fluid has been numerically examined by Sankar et al. [22, 23]. In a porous annular geometry, Shivakumara et al. [24] analyzed free convective flow and transport for wide range of parameters.
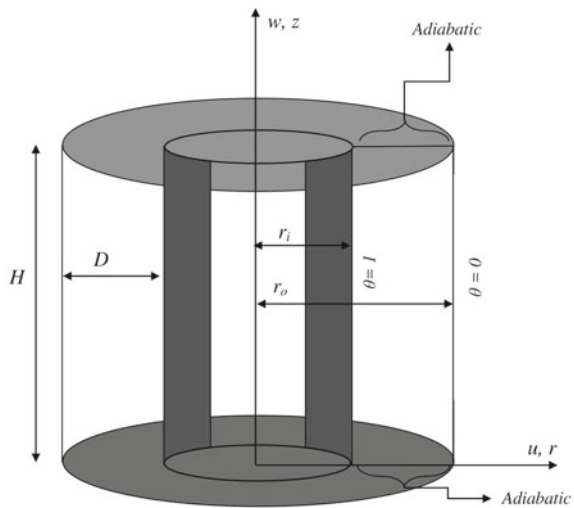
Natural convection heat transport within the cavity without accounting the impact of a conductive wall may not aptly describe some important practical situations. The conductive wall may be located, for instance, in lots of practical situations, particularly with the design of thermal insulation, high performance insulation for homes. Kim and Viskanta [25, 26] were the first to took up the investigation to analyze conjugate convection in square enclosure. They reported both experimental and numerical results for three different combinations of wall heating and found that the wall heat conductivity suppresses the thermal variations. Kaminski and Prakash [27] performed numerical simulations for convective flow in a square shaped geometry with finite thickness on one wall. Yedder and Bilgen [28] presented the results on convection in a tilted geometry with a wall thickness. Subsequently, Nouanegue et al. [29] broadened the study of [30] to incorporate the impact of radiation in the enclosure. Ben and Chamkha [31] focused on conjugate buoyant convection by introducing a thin fin into the square geometry. In a porous geometry, Baytas et al. [32] reported conjugate buoyant convection having conducting horizontal boundaries of finite thickness. Later, Saeid [33] applied finite volume method, and considered Darcy model to study the conjugate natural convection in an enclosure with the vertical walls of equal thickness bounding the porous layer maintained at distinct temperatures.

Through the comprehensive survey of literature performed on thrust area of the paper, authors understood that the effects of combined conduction-buoyant convection is vastly investigated in regular and non-regular shaped enclosures, except in cylindrical annular space. However, buoyancy-driven convection in an annular space having finite thickness on inner wall is not investigated in the current literature. Therefore, due to lack of understanding of this phenomenon in an annular geometry, in this paper the coupled convection-conduction heat transfer in an annular geometry with closed upper and lower boundaries has been numerically investigated.

2 Mathematical Model and Governing Equations

The geometrical enclosure chosen in the present analysis is displayed in Fig. 1. The physical configuration is an annular geometry of length H, annular space D and is enclosed by two cylindrical tubes with same center and inner radius r_i, and exterior radius r_o. The upper and lower portions of the annular space are assumed to be closed and insulated. However, the inner cylindrical wall has finite thickness and is retained at higher temperature, however, the external cylinder is retained at constant lower temperature. By discarding the pressure gradients from the governing equations and introducing the stream function, the governing equations in dimensionless form can be written as

Fig. 1 Physical configuration, coordinate system and boundary conditions

$$\frac{\partial T_w}{\partial t} = \frac{\alpha_w}{\alpha_f} \left[\frac{\partial^2 T_w}{\partial R^2} + \frac{1}{R} \frac{\partial T_w}{\partial R} + \frac{\partial^2 T_w}{\partial Z^2} \right]. \tag{1}$$

$$\frac{\partial T_f}{\partial t} + U \frac{\partial T_f}{\partial R} + W \frac{\partial T_f}{\partial Z} = \left[\frac{\partial^2 T_f}{\partial R^2} + \frac{1}{R} \frac{\partial T_f}{\partial R} + \frac{\partial^2 T_f}{\partial Z^2} \right]. \tag{2}$$

$$\frac{\partial \zeta}{\partial t} + U \frac{\partial \zeta}{\partial R} + W \frac{\partial \zeta}{\partial Z} - \frac{U}{R} \zeta = Pr \left[\nabla^2 \zeta - \frac{\zeta}{R^2} \right] - Ra Pr \frac{\partial T_f}{\partial R}. \tag{3}$$

$$\zeta = \frac{1}{R} \left[\frac{\partial^2 \Psi}{\partial R^2} - \frac{1}{R} \frac{\partial \Psi}{\partial R} + \frac{\partial^2 \Psi}{\partial Z^2} \right]. \tag{4}$$

$$U = \frac{1}{R} \frac{\partial \Psi}{\partial Z}, \qquad W = -\frac{1}{R} \frac{\partial \Psi}{\partial R}. \tag{5}$$

The non-dimensional variables used in the above equations are:

$$(R, Z) = (r, z) \big/ D, \quad (U, W) = (u, w) \bigg/ \left(\frac{\alpha_f}{D} \right), \quad t = t^* \bigg/ \left(\frac{D^2}{\alpha_f} \right),$$

$$T = (\theta - \theta_c) / \Delta\theta, \ P = p \bigg/ \left(\frac{\rho_0 \alpha_f^2}{D^2} \right), \ \zeta = \zeta^* \bigg/ \left(\frac{\alpha_f}{D^2} \right), \ \Psi = \Psi \bigg/ \left(D\alpha_f \right),$$

where $D = r_o - r_i$, $\Delta\theta = \theta_h - \theta_c$

The dimensionless auxiliary conditions are:

$$t = 0 : \Psi(R, Z, 0) = \zeta(R, Z, 0) = T_w(R, Z, 0) = T_f(R, Z, 0) = 0.$$

$$t > 0 : T_w \left(\frac{1}{\lambda - 1}, Z, t \right) = 1, \ T_w \left(\frac{\lambda}{\lambda - 1}, Z, t \right) = 0,$$

$$\frac{\partial T_w}{\partial Z}(R, 0, t) = \frac{\partial T_f}{\partial Z}(R, 0, t) = 0, \tag{6}$$

$$\frac{\partial T_w}{\partial Z}(R, A, t) = \frac{\partial T_f}{\partial Z}(R, A, t) = 0.$$

Along the interface, following condition is utilized.

$$T_w(\epsilon, Z, t) = T_f(\epsilon, Z, t) \text{ and } \frac{\partial T_w}{\partial R}(\epsilon, Z, t) = \frac{\partial T_f}{\partial R}(\epsilon, Z, t) \tag{7}$$

The local Nusselt number is defined by $Nu = \frac{\partial T}{\partial R}$. The overall Nusselt number at the inner boundary $\overline{Nu_w}$ and at interface $\overline{Nu_I}$ are estimated through the following expressions:

$$\overline{Nu_w} = \frac{1}{A} \int_0^A Nu_w dz \text{ and } \overline{Nu_I} = \frac{1}{A} \int_0^A Nu_I dz.$$
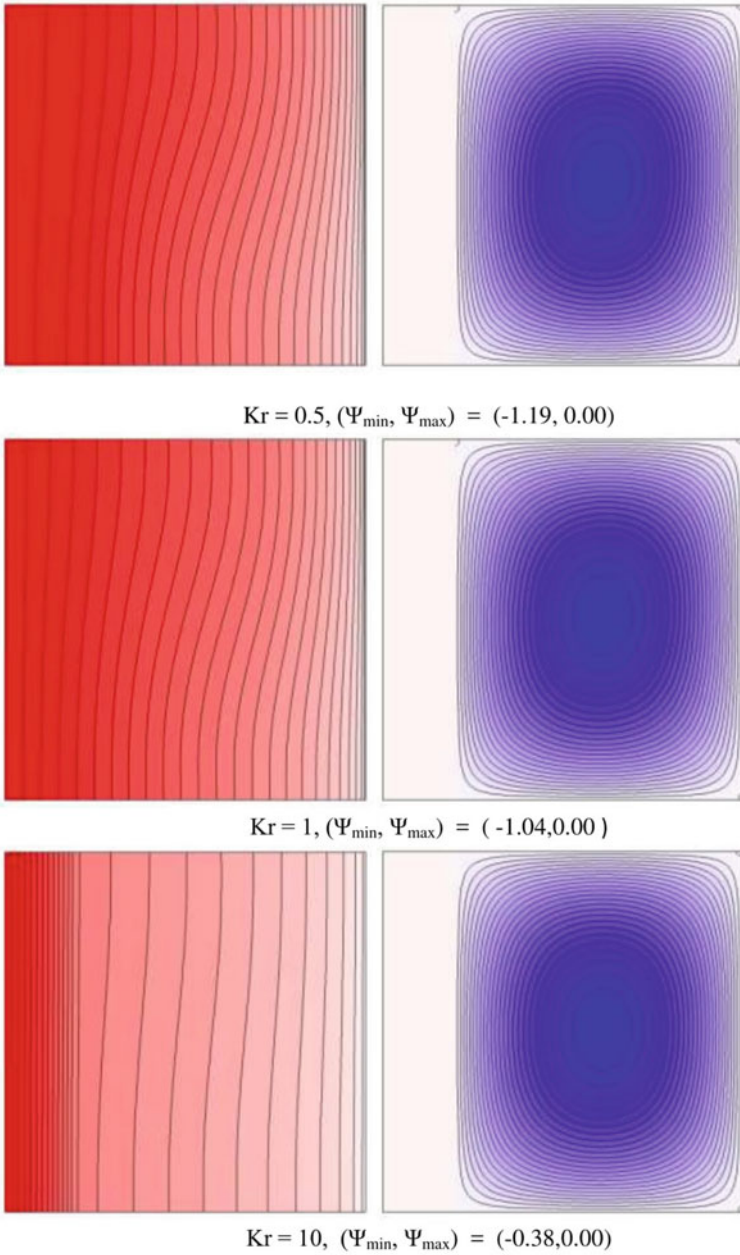
3   Solution Procedure

The dimensionless model equations of this analysis are solved by the ADI and SLOR methods. The procedure to solve these set of coupled, non-linear differential equations are similar to the procedures used in our earlier papers [17–20] and are not repeated here. Due to the finite thickness at inner wall, the energy equation without convection terms is used in solid region, while the regular energy equation is used in the fluid domain. The Fortran code employed in our earlier works has been modified to include the solid-fluid interface effects and several trial runs were made to have optimum grid size before the actual simulations.
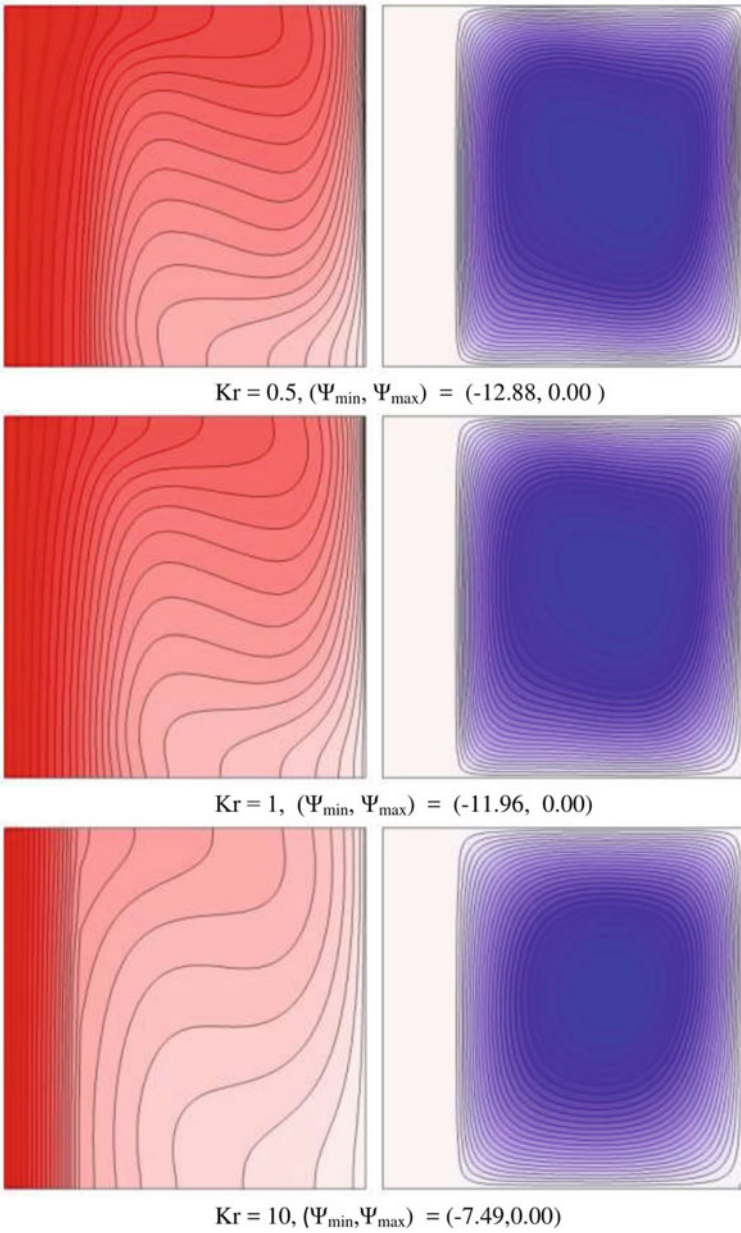
4   Results and Discussion

4.1   Effects of Rayleigh Number on the Conductivity Ratio

The circulation of the fluid and the variation of the temperature in the annular space can be well illustrated with the help of streamlines and the isotherms. Figures 2, 3 and 4 depicts the consequences of Rayleigh number (Ra) and conductivity ration (Kr) on flow and temperature distributions. In Fig. 2, isotherms and streamlines are respectively depicted to the left and right panel, for three values of conductivity ratio $Kr = 0.5, 1, 10$ and by setting $Ra = 10^3$, $\epsilon = 0.2$. A similar parameter variation is set in Figs. 3 and 4, except the change in Ra, $Ra = 10^5$ and $Ra = 10^7$, to study the combined effects of Ra on Kr. $Kr = 0.5$ represent a weak conducting wall, $Kr = 1$ represents equal fluid/wall conductivity and $Kr = 10$ represent high wall conductivity ratio. A large circular cell is observed and is covering the entire annulus as seen in Figs. 2 and 3 for all conductivity ratios. The fluid flow is in clockwise direction, since the fluid near hot boundary is less dense than in the core region, hence, the lesser density fluid moves upward reaches the upper wall and cools, as it gains the density it flows downward along the outer cold wall. This pattern is seen in all the cases of the Rayleigh number $10^3 - 10^5$ (Figs. 3 and 4). As the value of Ra is further amplified to $Ra = 10^7$, the flow circulation becomes stronger and the circular pattern breaks the fluid flows along the walls of annulus. From the dimensionless stream function Ψ, it is noted that the fluid circulation magnitude increases as the values of Kr is increased. It can be observed through the dimensionless streamlines that the strength of fluid circulation increases as the conductivity ratio increased from $Kr = 0.5$ to $Kr = 10$. As a result of temperature difference, a convective mode of heat transfer defines the flow.
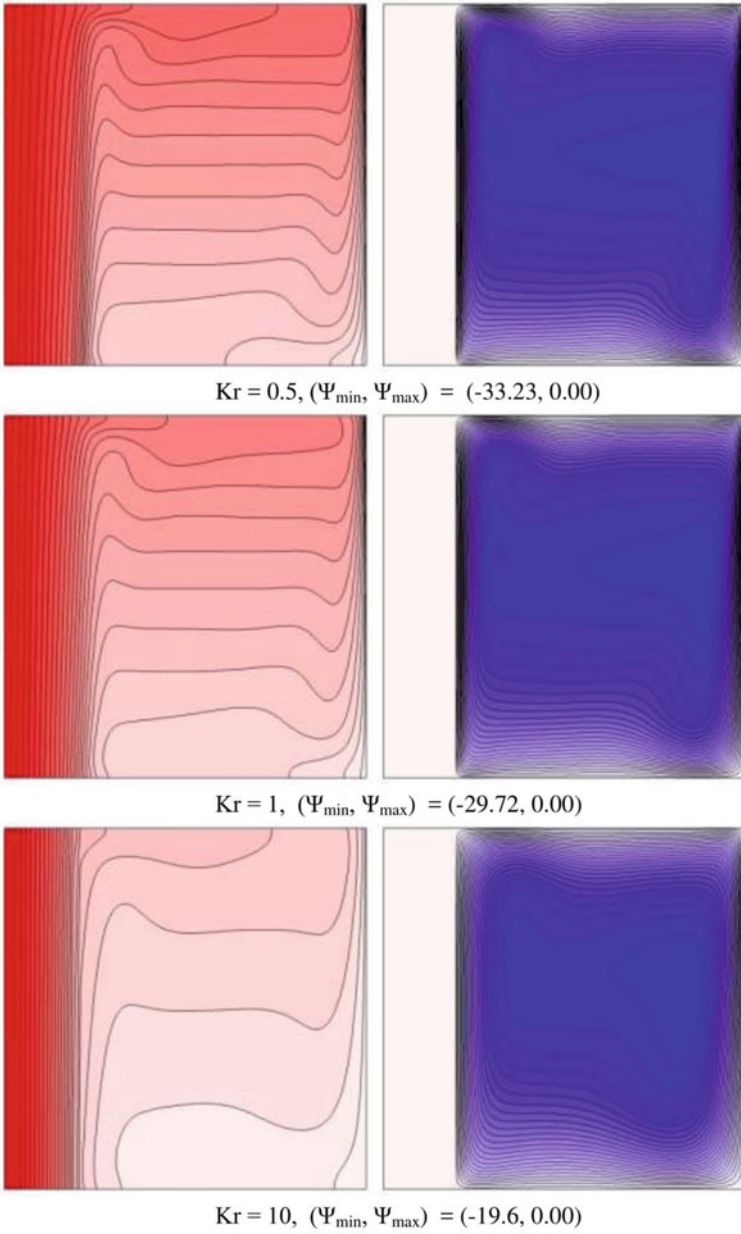
The isothermal plots reveals the poor conductive wall at $Kr = 0.5$ and also the thermal transfer rate is less compared to that of $Kr = 1$ and $Kr = 10$. This is expected because decreasing the wall thermal conductivity causes an upsurge in the thermal resistivity and hence the thermal transport is mainly from heat conduction. As the value of Kr increases, conduction in the solid wall takes place which

Kr = 0.5, $(\Psi_{min}, \Psi_{max}) = (-1.19, 0.00)$

Kr = 1, $(\Psi_{min}, \Psi_{max}) = (-1.04, 0.00)$

Kr = 10, $(\Psi_{min}, \Psi_{max}) = (-0.38, 0.00)$

Fig. 2 Effect of Kr and Ra on isotherms and streamlines for $\epsilon = 0.2$, $Ra = 10^3$ and $Kr = 0.5, 1, 10$

Kr = 0.5, (Ψ_{min}, Ψ_{max}) = (-12.88, 0.00)

Kr = 1, (Ψ_{min}, Ψ_{max}) = (-11.96, 0.00)

Kr = 10, (Ψ_{min}, Ψ_{max}) = (-7.49, 0.00)

Fig. 3 Effect of Kr and Ra on isotherms and streamlines for $\epsilon = 0.2$, $Ra = 10^5$ and $Kr = 0.5, 1, 10$

Kr = 0.5, $(\Psi_{min}, \Psi_{max}) = (-33.23, 0.00)$

Kr = 1, $(\Psi_{min}, \Psi_{max}) = (-29.72, 0.00)$

Kr = 10, $(\Psi_{min}, \Psi_{max}) = (-19.6, 0.00)$

Fig. 4 Effect of Kr and Ra on isotherms and streamlines for $\epsilon = 0.2$, $Ra = 10^7$ and $Kr = 0.5, 1, 10$

in turn sets convection type of heat transfer in the fluid region. As the solid wall conductivity ratio increased to $Kr = 10$, the thermal lines in the solid wall region becomes thicker and stratified in the fluid region Figs. 3 and 4 for $Kr = 0.5$ and $Kr = 1$. This anomaly is due to thermal variations across the inner cylinder expands with an increase in conductivity ratio Kr. Thus, more thermal transport from the inner thick wall to the fluid is received for higher conductivity ratio. This can be more clearly noticed as the Rayleigh number is raised from 10^3 to 10^7 in Figs. 3 and 4. It is also observed that the isothermal line appears to be more parallel to the solid wall which shows that convection in the fluid is more dominant for increasing Ra.
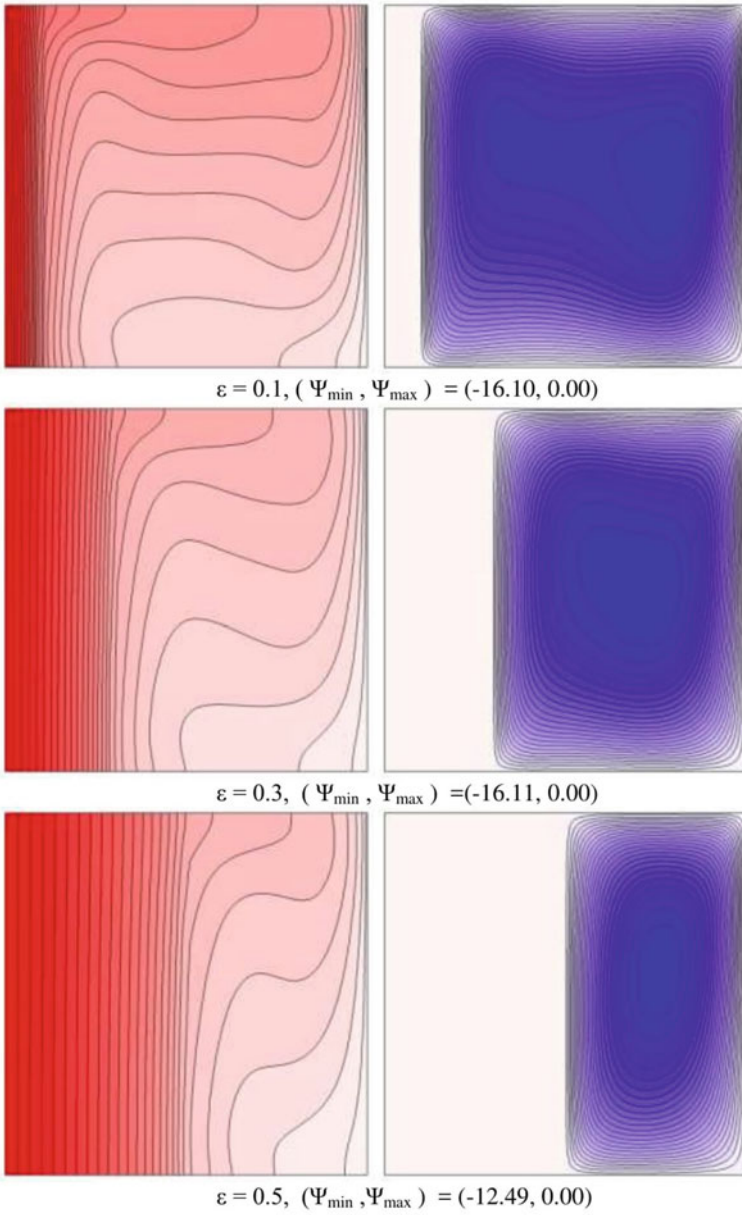
4.2 Effects of Rayleigh Number on the Wall Thickness

In this section, the effect of different values of wall thickness for a fixed solid wall conductivity ratio ($Kr = 5$) and for two different cases $Ra = 10^4$ (Fig. 5) and $Ra = 10^7$ (Fig. 6), is discussed. Figures 5 and 6 illustrates the flow and thermal fields for $Ra = 10^4$ and $Ra = 10^7$ in the annulus in which inner solid wall is hot and outer wall is cooled. A clockwise rotating circular eddy is formed and the circulation strength is almost same throughout the annulus region for $\epsilon = 0.1$ (Fig. 5). An increase in the thickness of inner cylinder from 0.1 to 0.5 causes the deformation of circular cell into an elliptical shape and this is because of less heat transform from solid wall to the fluid region. Hence, the flow strength decreases with an increase in wall thickness and this can be noted from the extreme values of stream function. A weaker convection is observed and also temperature drops at the wall. A similar phenomenon is observed for $Ra = 10^7$, at all three wall thickness (see Fig. 6). From the isothermal plots, it is visible that the thickness of the wall is more important to impart convection thermal transfer. It can be concluded that higher heat transfer can be attained for thinner solid wall and lower heat transport is achieved for thick solid wall and this is due to the rate convection in to the fluid part.

4.3 Effects of Rayleigh Number, Wall Thickness and Conductivity Ratio on Local Nusselt Number

Figures 7 and 8 illustrate the effect of Rayleigh number, conductivity ratio and thickness of wall on the local Nu. Figure 7 display the plot of varying Rayleigh number with fixed wall thickness of $\epsilon = 0.2$ and conductive ratio $Kr = 5$. Here the solid curve represents the Nusselt number at the wall and discontinuous lines represent the local Nu at the solid wall-fluid interface. It can be observed that as the Rayleigh number increases from $Ra = 10^4$ to 10^7, the local heat flux is always more for the wall than at the interface. Therefore, lesser temperature is transported to fluid due to the thickness of inner cylinder, illustrating an increment in thermal transport with

$\varepsilon = 0.1$, $(\Psi_{min}, \Psi_{max}) = (-4.66, 6.89)$

$\varepsilon = 0.3$, $(\Psi_{min}, \Psi_{max}) = (-2.34, 0.00)$

$\varepsilon = 0.5$, $(\Psi_{min}, \Psi_{max}) = (-0.678, 0.00)$
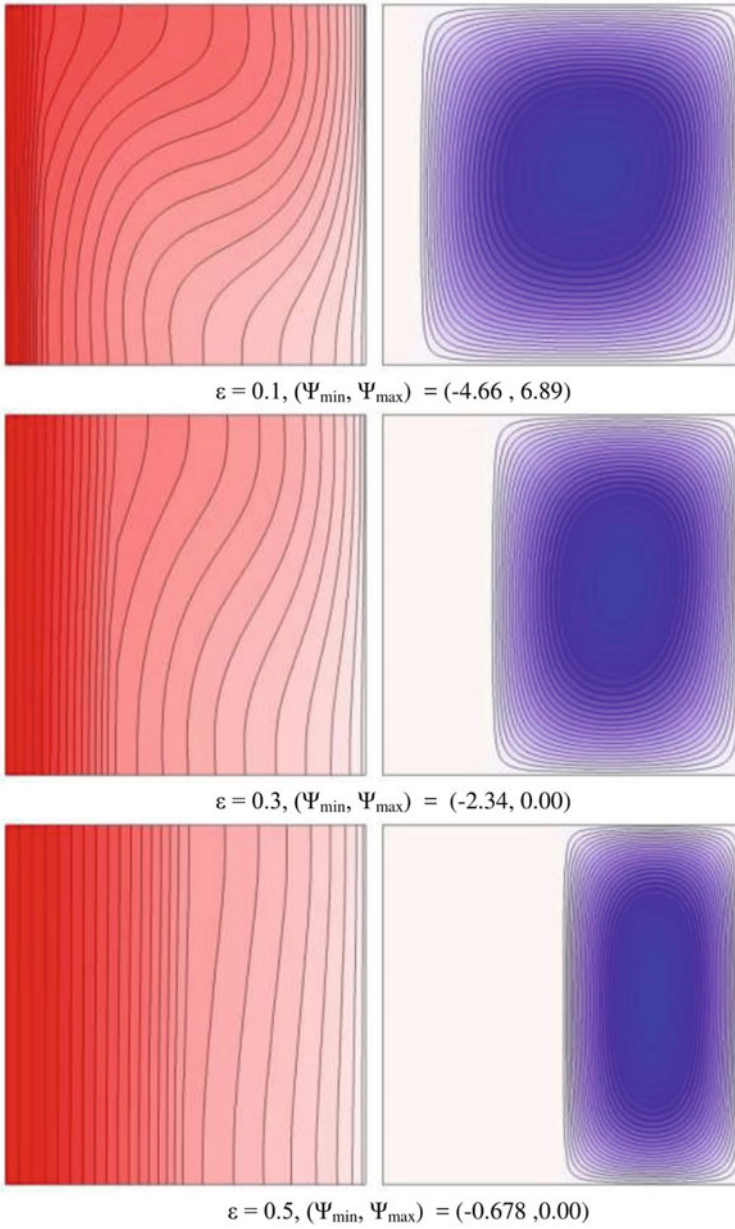
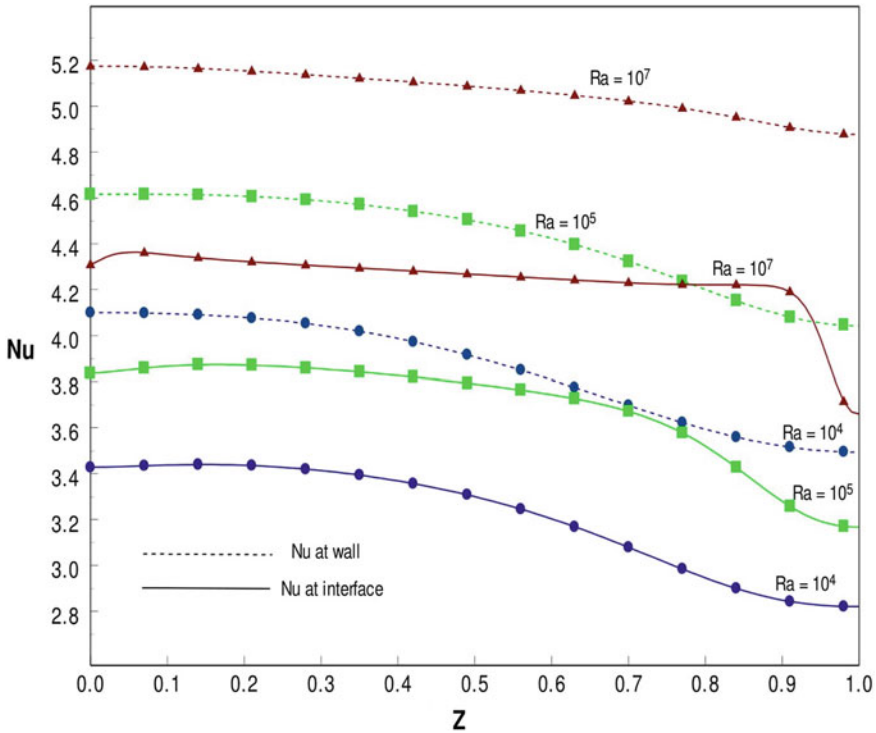**Fig. 5** Effect of ϵ on isotherms and streamlines for $Kr = 5$, $Ra = 10^4$ and $\epsilon = 0.1, 0.3, 0.5$

$\varepsilon = 0.1,\ (\Psi_{min},\Psi_{max}) = (-16.10, 0.00)$

$\varepsilon = 0.3,\ (\Psi_{min},\Psi_{max}) = (-16.11, 0.00)$

$\varepsilon = 0.5,\ (\Psi_{min},\Psi_{max}) = (-12.49, 0.00)$

Fig. 6 Effect of ϵ on isotherms and streamlines for $Kr = 5$, $Ra = 10^6$ and $\epsilon = 0.1, 0.3, 0.5$

Fig. 7 Effect of Rayleigh number on the local Nusselt number for $\epsilon = 0.2$ and $Kr = 5$

an enhancement in the Rayleigh number. Figure 8 shows the effect of local Nusselt number for different wall thicknesses ε, for constant $Ra = 10^6$ and $Kr = 5$. Here it is noticed that the local Nu enhances with decrease in wall thickness (ϵ) and heat transfer is less at the interface, which remain constant throughout the interface and slightly decreases near upper region. The local Nu is higher for thinner solid wall than all other wall thickness.

4.4 Effects of Rayleigh Number, Wall Thickness and Conductivity Ratio on the Average Nusselt Number

Figure 9 represents the change of average Nu for various wall thickness and Rayleigh numbers for a constant conductive ratio Kr. It can be seen that for $Ra \leq 10^4$ and wall thickness $0.2 \leq \epsilon \leq 0.5$, there is negligible change in the average Nusselt number, which remains constant at both the wall and wall/fluid interface. As the Rayleigh number is increased from $Ra = 10^4$ to 10^7, the heat transfer also increases across the wall and interface. For $\epsilon = 0.1$, thinner solid cylinder, the thermal transfer augments
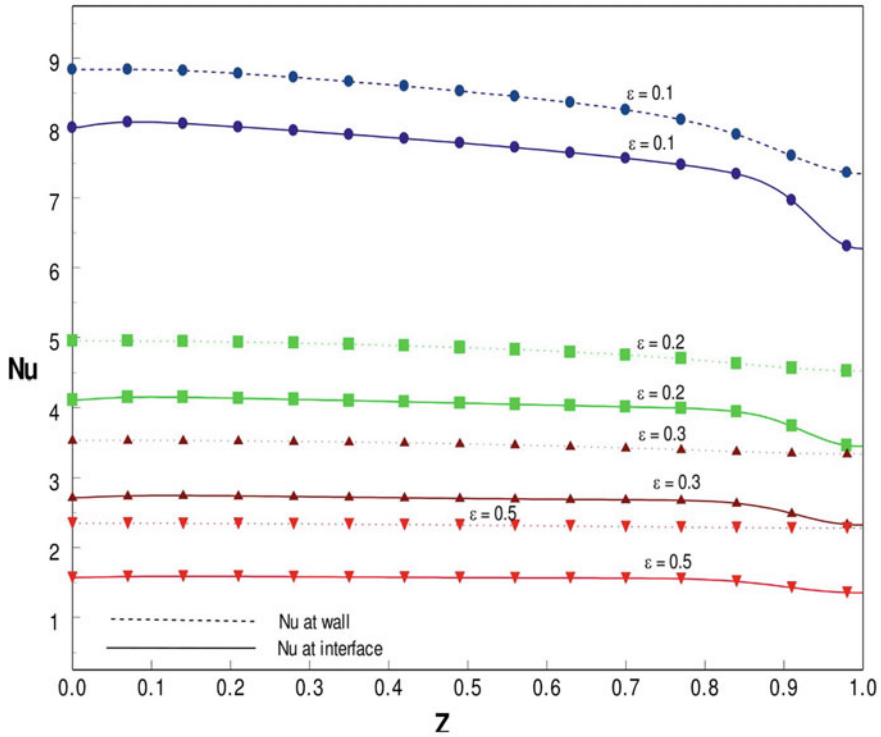
Fig. 8 Effect of different wall thickness on the local Nusselt number for $Kr = 5$ and $Ra = 10^6$

with an increase in Ra which reveals a downturn in thermal transport with an increase in solid wall thickness and this indicates that the thickness of cylinder acts as an effective control mechanism for heat transport. The diversity of average Nu with wall conductive ratio is presented in Fig. 10 for $10^3 \leq Ra \leq 10^6$. It can be observed that there is significance difference in lower and higher solid wall conductive ratio Kr on the overall heat transport rates. For $Kr = 0.5$ the heat transfer is less and the solid wall behaves like an insulator, therefore a negligible heat is dissipated to the solid fluid interface as compared to other values of Kr. In this case most of the heat transfer is by conduction. As solid wall conductivity ratio increases to $Kr = 1$, the heat transfer also increases which leads to heat transfer by natural convection. For higher solid wall conductivity ratio of $Kr = 10$, the average Nusselt number also increases to a maximum $Nu = 4$ and $Nu = 5$ at the wall and solid fluid interface.
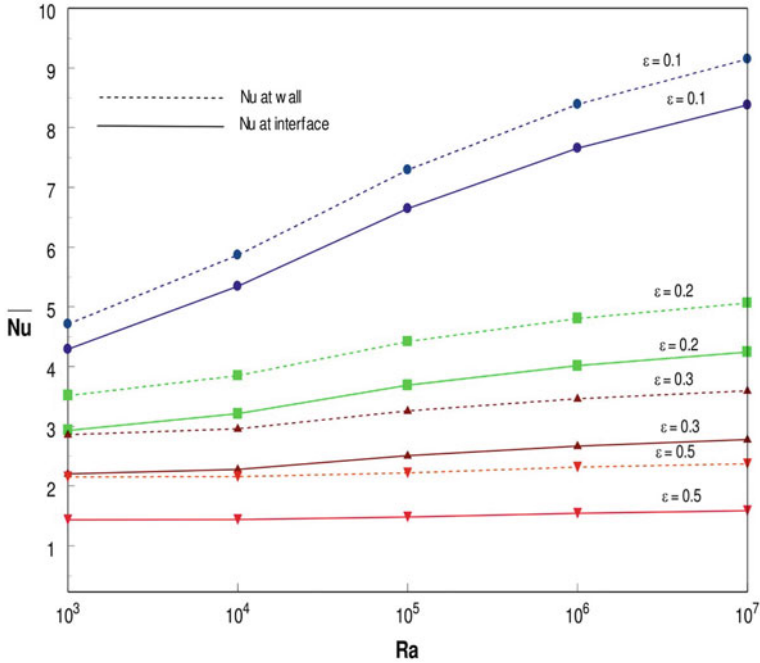
Fig. 9 Effect of Ra on average Nusselt number for different values ϵ at $Kr = 5$

5   Conclusions

In this paper, conjugate buoyant thermal transport in an annular shaped enclosure constructed from two upright, co-axial cylinders of which inner cylinder is having finite thickness and maintained at higher temperature than the outer cylinder. The significant implications of conductivity ratio, thickness of the interior cylinder and Rayleigh number upon the buoyant flow and thermal transport is elaborately analyzed numerically. From the extensive numerical simulations, it has been learnt that increasing the ratio of thermal conductivity and thickness of cylinder reduces the convective flow in annulus. In particular, as the conductivity ratio increases for a fixed wall thickness, isothermal contours confined to solid region rather than fluid region. The thermal transport calculated at the cylindrical wall and at interface reveals that the heat transport from the solid wall is greater rather than the heat transport measured at the solid-fluid interface. Further, the overall heat transport rate can be enhanced by either increasing the conductivity ratio or decreasing the wall thickness.
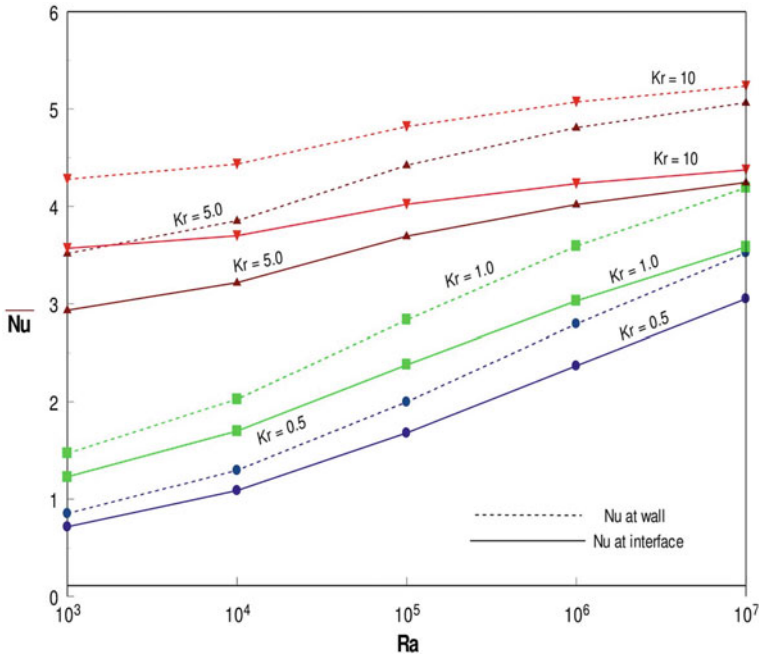
Fig. 10 Effect of Ra on average Nusselt number for different values of Kr at $\epsilon = 0.2$

References

1. Thomas RW, De Vahl Davis G (1970) Natural convection in annular and rectangular cavities a numerical study. In: Proceeding of 4th international heat transfer conference. Elsevier 4 NC 2.4
2. De Vahl Davis G, Thomas RW (1969) Natural convection between concentric vertical cylinders, high-speed computing in fluid dynamics. Phys Fluids Suppl 2:198–207
3. Farouk B, Ball KS, Dixit VC (1990) Aspect and radius ratio effects on natural convection in a vertical annulus. In: Proceeding of 9th international heat transfer conference. Jerusalem, Israel no. 2, pp 585–590 (1990)
4. Schwab HT, Witt JKD (1970) Numerical investigation of free convection between two vertical coaxial cylinders. AIChE J 16(6):1005–1010
5. Kumar R, Kalam A (1991) Laminar thermal convection between vertical coaxial isothermal cylinders. Int J Heat Mass Transf 34(2):513–524
6. Choukairy K, Bennacer R, Mohamad AA (2005) Natural convection in a partitioned vertical annulus. Int J Transp Phenom 7:339–350

7. Venkatachalappa M, Sankar M, Natarajan AA (2001) Natural convection in an annulus between two rotating vertical cylinders. Acta Mech 147(1–4):173–196
8. Sankar M, Park J, Do Y (2011) Natural convection in a vertical annuli with discrete heat sources. Numer Heat Transf, Part A: Appl 59(8):594–615
9. Sankar M, Do Y (2010) Numerical simulation of free convection heat transfer in a vertical annular cavity with discrete heating. Int J Heat Mass Transf 37(6):600–606
10. Sankar M, Jang B, Do Y (2014) Numerical study of non-darcy natural convection from two discrete heat sources in a vertical annulus. J Porous Media 17(5):373–390
11. Sankar M, Hong S, Do Y, Jang B (2012) Numerical simulation of natural convection in a vertical annulus with a localized heat source. Meccanica 47(8):1869–1885
12. Lopez JM, Sankar M, Do Y (2012) Constant-flux discrete heating in a unit aspect ratio annulus. Fluid Dyn Res 44(6):065507 (18pp)
13. Sankar M, Do Y, Ryu S, Jang B (2015) Cooling of heat sources by natural convection heat transfer in a vertical annulus. Numer Heat Transf, Part A: Appl 68(8):847–869
14. Prasad V, Kulacki FA (1984) Natural convection in a vertical porous annulus. Int J Heat Mass Transf 27(2):207–219
15. Hickox CE, Gartling DK (1985) A numerical study of natural convection in a vertical, annular, porous layer. Int J Heat Mass Transf 28(3):720–723
16. Havstad MA, Burns PJ (1982) Convective heat transfer in vertical cylindrical annuli filled with a porous medium. Int J Heat Mass Transf 25(11):1755–1766
17. Sankar M, Kim B, Lopez JM, Do Y (2012) Thermosolutal convection from a discrete heat and solute source in a vertical porous annulus. Int J Heat Mass Transf 55(15–16):4116–4128
18. Sankar M, Park Y, Lopez JM, Do Y (2011) Numerical study of natural convection in a vertical porous annulus with discrete heating. Int J Heat Mass Transf 54(7–8):1493–1505
19. Sankar M, Park J, Kim D, Do Y (2013) Numerical study of natural convection in a vertical porous annulus with an internal heat source: effect of discrete heating. Numer Heat Transf, Part A: Appl 63(9):687–712
20. Sankar M, Bhuvaneswari M, Sivasankaran S, Do Y (2011) Buoyancy induced convection in a porous cavity with partially thermally active sidewalls. Int J Heat Mass Transf 54(25–26):5173–5182
21. Venkatachalappa M, Do Y, Sankar M (2011) Effect of magnetic field on the heat and mass transfer in a vertical annulus. Int J Eng Sci 49(3):262–278
22. Sankar M, Venkatachalappa M, Shivakumara IS (2006) Effect of magnetic field on natural convection in a vertical cylindrical annulus. Int J Eng Sci 44(20):1556–1570
23. Sankar M, Venkatachalappa M, Do Y (2011) Effect of magnetic field on the buoyancy and thermocapillary driven convection of an electrically conducting fluid in an annular enclosure. Int J Heat Fluid Flow 32(2):402–412
24. Shivakumara IS, Prasanna BMR, Rudraiah N, Venkatachalappa M (2002) Numerical study of natural convection in a vertical cylindrical annulus using a non-Darcy equation. J Porous Media 5:87–102
25. Kim DM, Viskanta R (1984) Study of the effects of wall conductance on natural convection in differently oriented square cavities. J Fluid Mech 144:153–176
26. Kim DM, Viskanta R (1985) Effect of wall heat conduction on natural convection heat transfer in a square enclosure. J Heat Transfer 107(4):139–146
27. Kaminski DA, Prakash C (1986) Conjugate natural convection in a square enclosure: effect of conduction in one of the vertical walls. Int J Heat Mass Transf 29(12):1979–1988
28. Yedder RB, Bilgen E (1997) Laminar natural convection in inclined enclosures bounded by a solid wall. Heat Mass Transf 32(6):455–462
29. Nouanegue H, Muftuoglu A, Bilgen E (2009) Heat transfer by natural convection, conduction and radiation in an inclined square enclosure bounded with a solid wall. Int J Therm Sci 48(5):871–880
30. Varol Y, Oztop HF, Koca A (2008) Entropy generation due to conjugate natural convection in enclosures bounded by vertical solid walls with different thicknesses. Int Comm Heat Mass Transf 35(5):648–656

31. Ben-Nakhi A, Chamkha AJ (2007) Conjugate natural convection in a square enclosure with inclined thin fin of arbitrary length. Int J Therm Sci 46(5):467–478
32. Baytas AC, Liaqat A, Grosan T, Pop I (2001) Conjugate natural convection in a square porous cavity. Heat Mass Transf 37:467–473
33. Saeid NH (2007) Conjugate natural convection in a vertical porous layer sandwiched by finite thickness walls. Int Comm Heat Mass Transf 34(2):210–216

Radiation and Heat Generation Effects on Couple Stress Fluid Through Expanding Channel

Odelu Ojjela, N. Naresh Kumar, and D. R. V. S. R. K. Sastry

Abstract The problem of magnetohydrodynamics (MHD) radiating flow of couple stress fluid through a porous channel is studied. Fluid is injected with different injection velocities by which the flow is generated between two parallel porous walls. The equations that govern flow are numerically solved by method of quasilinearization. Flow physical properties corresponding to various physical parameters are addressed through graphs.

Keywords Radiation · Couple stress · Asymmetric flow · Heat source · Chemical reaction · MHD · Quasilinearization

Nomenclature

t	Time
Pr	Prandtl number, $\frac{\mu c}{k}$
$a(t)$	Distance from the origin to the lower/upper wall
Ha	Hartmann number, $B_0 a \sqrt{\frac{\sigma}{\mu}}$
p	Fluid pressure
Q_h	Heat source/sink
c	Specific heat at constant temperature

O. Ojjela
Applied Mathematics Department, Defence Institute of Advanced Technology, Pune 411025, India

N. Naresh Kumar · D. R. V. S. R. K. Sastry (✉)
Mathematics Department, SASTRA Deemed to be University, Thirumalaisamudram, Thanjavur, TamilNadu 613401, India
e-mail: drvsrksastry@gmail.com

k	Thermal conductivity
u_x	Axial velocity
u_y	Radial velocity
C	Concentration
C_0	Concentration at the lower wall
D_1	Mass diffusivity
k_1	Permeability of the porous medium
k_2	Chemical reaction rate
k_3	Radiative heat flux
D^{-1}	Inverse Darcy's parameter, $\frac{a^2}{k_1}$
A	Asymmetric flow parameter, $\frac{V_1}{V_2}$
K_r	Non-dimensional chemical reaction parameter, $\frac{k_2 a^2}{\upsilon}$
Sc	Schmidt number, $\frac{\upsilon}{D_1}$
Hs	Non-dimensional heat source/sink parameter, $\frac{Q_h a^2}{k}$
g	Acceleration due to gravity
q_w	Uniform heat flux
q_m	Uniform mass flux
h_f	Non-dimensional heat flux parameter, $\frac{q_w a}{(\theta_2 - \theta_1)k}$
m_f	Non-dimensional mass flux parameter, $\frac{q_m a}{(C_2 - C_1)D_1}$
Gr	Thermal Grashof number, $\frac{g\beta_\theta(\theta_2 - \theta_1)a^3}{\upsilon^2}$
Gm	Concentration Grashof number, $\frac{g\beta_C(C_1 - C_0)a^3}{\upsilon^2}$
$\hat{i}, \hat{j}, \hat{k}$	Unit vectors

Greek Letters

θ	Temperature
ξ	Dimensionless y coordinate, $\frac{y}{a}$
ζ	Dimensionless axial variable, $\frac{x}{a}$
ρ	Fluid density
μ	Fluid viscosity
μ'	Magnetic permeability
σ	Electric conductivity
α	Couple stress parameter, $\sqrt{\frac{\eta}{\mu a^2}}$
α_1	The injection–suction ratio (mixed injection), $\frac{V_2}{V_1} - 1$
β_θ	Thermal expansion coefficient
β_C	Solutal expansion coefficient

1 Introduction

Viscous fluid flow problems through porous boundaries appear in science and technology fields. Bujurke et al. [1] exposed the behaviour of flow across a channel with variable permeability, and a series solution is obtained for different cases. Natural convection MHD flow of viscous fluid over vertical plates is examined by Barik et al. [2]. The heat generation process can take place in nuclear reactors, which is constructed of several parallel vertical plates. Loganathan et al. [3] applied Laplace transform and solved the problem of transient convective viscous nanofluid flow. Hossain et al. [4] studied free convection flow over a vertical wall. Heat generation on transient free convective viscous fluid flow through a wavy surface is examined by Molla et al. [5]. Hady et al. [6] considered MHD convective flow along the vertical wavy surface with heat generation. The various models are exhibited to understand the properties of non-Newtonian fluids whose stress tensor is not symmetric. The couple stress fluid is first addressed by Stokes [7, 8]. Couple stress fluid problem with chemical and magnetic effects is studied by Khan et al. [9]. Ali et al. [10] addressed the problem of magnetic couple stress fluid over oscillatory stretching. Gaikwad and Kouser [11] studied couple stress model with heat source. Srinivasacharya and Kaladhar [12] discussed diffusion thermo and thermal diffusion effects on free convective couple stress fluid. The same problem with radiation and diffusion effects is analysed by Kaladhar et al. [13].

Heat transfer and mass transfer in viscous fluids over porous boundaries have been attracting because of numerous applications. Some of the areas are found in propellant burning, gaseous diffusion, natural transpiration, ablation cooling, and transpiration cooling, and uniformly distribute irrigation. Srinivas et al. [14] investigated many physical properties of viscous and incompressible fluid flow. Dauenhauer and Majdalani [15] studied the transient incompressible viscous fluid flow over a semi infinite rectangular expanding channel with injection. Micropolar fluid in expanding/contracting porous walls is examined by Si et al. [16, 17] and the closed-form solutions obtained by perturbation and HAM methods. Pravin et al. [18] considered the viscoelastic UCM fluid between squeezing channel and solved the governing equations by shooting method. Srinivasacharya et al. [19] studied unsteady couple stress fluid through parallel walls. Khan et al. [20] got analytical solution for couple stress fluid problem with homotopy analysis. Ojjela and Naresh [21] used quasilinearization method to obtain the solution of couple stress model.

A numerical solution for an initial value problem can easily be obtained using powerful methods such as Runge–Kutta and predictor–corrector methods. The difficulty arises only for the boundary value problems. Quasilinearization method was addressed by Bellman and Kalaba [22]. Huang [23] has applied quasilinearization method for the problem of a viscous fluid. As an application of the quasilinearization technique, the problem of viscoelastic fluid with magnetic effects over a stretching sheet has been considered by Hymavathi and Shanker [24]. The two-dimensional second-grade steady fluid flow over annulus is studied by Bhatnagar et al. [25].

In view of above literature, we study radiation and heat generation effects in couple stress fluid through expanding walls. Governing equations are numerically solved by quasilinearization technique. Physical characteristics of the flow against various parameters are graphically exhibited. Results are compared with the existing problems on Newtonian fluid.

2 Mathematical Model

Consider an unsteady couple stress fluid passing through a rectangular channel. The flow is laminar and incompressible. Further, the walls are expanding at a transverse time-dependent rate which is shown in Fig. 1. Constant heat and mass fluxes are assumed at lower wall. Let θ_2, C_1 be constant temperature and concentration at the upper wall. Further, assume V_1 and V_2 be injected fluid velocities at the walls. A magnetic field is employed on the flow in its normal direction.

The flow field, energy, and species concentration equations for the couple stress fluid in the presence of constant magnetic field and heat source are (Eckert and Drake [26]; Stokes [27]; Sutton and Sherman [28]) given by
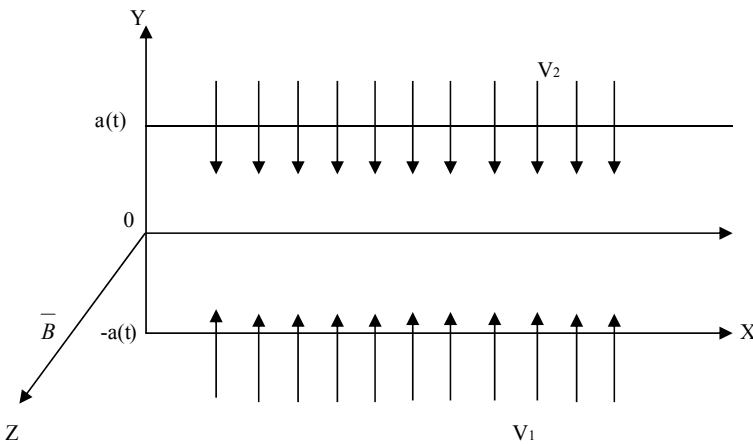
Fig. 1 Flow model

$$\frac{\partial u_x}{\partial x} + \frac{\partial u_y}{\partial y} = 0 \tag{1}$$

$$\rho\left[\frac{\partial u_x}{\partial t} + u_x\frac{\partial u_x}{\partial x} + u_y\frac{\partial u_x}{\partial y}\right] = -\frac{\partial P}{\partial x} + \mu\nabla^2 u_x - \eta\nabla^4 u_x - \sigma B_0^2 u_x - \frac{\mu}{k_1}u_x$$
$$+ \rho g(\beta_\theta(\theta - \theta_1) + \beta_C(C - C_0)) \tag{2}$$

$$\rho\left[\frac{\partial u_y}{\partial t} + u_x\frac{\partial u_y}{\partial x} + u_y\frac{\partial u_y}{\partial y}\right] = -\frac{\partial P}{\partial y} + \mu\nabla^2 u_y - \eta\nabla^4 u_y$$
$$- \sigma B_0^2 u_y - \frac{\mu}{k_1}u_y \tag{3}$$

$$\rho c\left[\frac{\partial\theta}{\partial t} + u_x\frac{\partial\theta}{\partial x} + u_y\frac{\partial\theta}{\partial y}\right] = \eta(\nabla^2 u_x)^2 + \eta(\nabla^2 u_y)^2 + k\nabla^2\theta + \sigma B_0^2(u_x^2 + u_y^2)$$
$$- \nabla\cdot q_r + \mu\left[2\left(\frac{\partial u_x}{\partial x}\right)^2 + 2\left(\frac{\partial u_y}{\partial y}\right)^2\right.$$
$$\left. + \left(\frac{\partial u_x}{\partial y} + \frac{\partial u_y}{\partial x}\right)^2\right] + \frac{\mu}{k_1}(u_x^2 + u_y^2) + Q_h(\theta - \theta_1) \tag{4}$$

$$\left[\frac{\partial C}{\partial t} + u_x\frac{\partial C}{\partial x} + u_y\frac{\partial C}{\partial y}\right] = D_1\nabla^2 C - k_2(C - C_0) \tag{5}$$

where radiative heat flux, $q_r = -\frac{4\sigma_1}{3k_3}\nabla\theta^4$

Following Odelu and Naresh [21], we take temperature, concentration, velocity components, as,

$$\theta = \theta_1 + \frac{\mu V_2}{\rho ac}\left(g_1(\xi) + \frac{x^2}{a^2}g_2(\xi)\right)$$
$$C = C_0 + \frac{\dot{n}_A}{av}\left(G(\xi) + \frac{x^2}{a^2}H(\xi)\right)$$
$$u_x = -\frac{vx}{a^2}U^{*\prime}(\xi, t), \quad u_y = \frac{v}{a}U^*(\xi, t) \tag{6}$$

where $\xi = \frac{y}{a(t)}$.with the boundary conditions

$$u_x = 0,\ u_y = V_1,\ \frac{\partial u_y}{\partial x} - \frac{\partial u_x}{\partial y} = 0,\ k\frac{\partial \theta}{\partial y} = -q_\mathrm{w},\ D_1\frac{\partial C}{\partial y} = -q_\mathrm{m}$$

at $\xi = -1$

$$u_x = 0,\ u_y = V_2,\ \frac{\partial u_y}{\partial x} - \frac{\partial u_x}{\partial y} = 0,\ \theta = \theta_2,\ C = C_1$$

at $\xi = 1$ (7)

Substituting (6) in (2)–(4)

$$U^{VI} = \frac{1}{\alpha^2}\Big(\xi\beta U''' + \mathrm{Re}\big(U'U'' - UU'''\big) + 3\beta U'' + U^{IV}$$
$$- \big(\mathrm{Ha}^2 + D^{-1}\big)U'' - \frac{\mathrm{Ec\,Gr}}{\mathrm{Re}\zeta\alpha^2}\big(g_1' + \zeta^2 g_2'\big)$$
$$- \frac{\mathrm{Sh\,Gm}}{\mathrm{Re}\zeta\alpha^2}\big(G' + \zeta^2 H'\big) \tag{8}$$

$$g_1'' = -2g_2 - \frac{\mathrm{Re\,Pr}}{(1+\mathrm{Rd})}\big(4U'^2 + \big(\mathrm{Ha}^2 + D^{-1}\big)U^2 + \alpha^2 U''^2$$
$$+ \frac{\beta\xi g_1'}{\mathrm{Re}} + \frac{\beta g_1}{\mathrm{Re}} - Ug_1'\big) - \frac{\mathrm{Hs}}{(1+\mathrm{Rd})}g_1 \tag{9}$$

$$g_2'' = -\frac{\mathrm{Re\,Pr}}{(1+\mathrm{Rd})}\bigg(U''^2 + \alpha^2 U'''^2 + \big(\mathrm{Ha}^2 + D^{-1}\big)U'^2 + \frac{\xi\beta g_2'}{\mathrm{Re}} + \frac{3\beta g_2}{\mathrm{Re}}$$
$$+ 2U'g_2 - U'g_2\bigg) - \frac{\mathrm{Hs}}{(1+\mathrm{Rd})}g_2 \tag{10}$$

$$G'' = -2H + \mathrm{Kr\,Sc}\,G + \mathrm{Re\,Sc}\bigg(UG' - \frac{\beta}{\mathrm{Re}}(G + \xi G')\bigg) \tag{11}$$

$$H'' = \mathrm{Kr\,Sc}\,H + \mathrm{Re\,Sc}\bigg(-2U'H + U\,H' - \frac{\beta}{\mathrm{Re}}(3H + \xi H')\bigg) \tag{12}$$

where $U(\xi) = \frac{U^*(\xi,t)}{\mathrm{Re}}$, $\mathrm{Re} = \frac{\rho V_2 a}{\mu}$ is the Reynolds number, $\mathrm{Rd} = \frac{16\sigma_1\theta_1^3}{3k_3 k}$ is the radiation parameter and $\beta = \frac{a\dot{a}}{\upsilon}$ is wall expansion ratio, Eckert number $\mathrm{Ec} = \frac{\mu V_2}{\rho a c(\theta_2 - \theta_1)}$, Sherwood number $\mathrm{Sh} = \frac{\dot{n}_A}{a\upsilon(C_1 - C_0)}$, and non-dimensional axial component, $\zeta = \frac{x}{a}$.

The non-dimensional boundary conditions are

$$U(-1) = A,\ U'(-1) = 0,\ U''(-1) = 0,\ U(1) = 1,\ U'(1) = 0,\ U''(1) = 0,$$
$$g_1'(-1) = -\frac{h_\mathrm{f}}{\mathrm{Ec}},\ g_2'(-1) = 0,\ G'(-1) = -\frac{m_\mathrm{f}}{\mathrm{Sh}},\ H'(-1) = 0$$
$$g_1(1) = 1/\mathrm{Ec},\ g_2(1) = 0,\ G(1) = 1/\mathrm{Sh},\ H(1) = 0 \tag{13}$$

3 Result Analysis

The transformed dimensionless Eqs. (8)–(12) are fully coupled and nonlinear for which closed-form solution is difficult to obtain. Following [21, 24, 25], we have solved these system of equations numerically. And graphs are plotted for various physical parameters.

Figure 2 depicts, as 'Hs' increases, temperature increases and radial velocity decreases whereas axial velocity suppresses in the first half and then increases. Hs > 0 means that the heat transfer from the lower wall to the upper wall is increased when the heat generation is taking place. From Fig. 3, it is found that radiation increases, and velocity and temperature profiles exhibit a reverse trend to the corresponding profiles plotted against Hs. From Fig. 4, one can notice that the effects of h_f and Hs on profiles of temperature and velocity are same. Figure 5 witnesses that, when 'm_f' enhances, first axial velocity decreases up to the centre of the channel and then increases. Further radial velocity is decreasing, and the concentration is increasing on increasing m_f. This is because of decreasing the mass diffusivity and concentration difference, and the mass flux and the concentration are increased. This trend is reversed in the case of increasing Kr that can be noticed in Fig. 6. It also found an increase in axial velocity towards centre of the channel, and from there, we observe a down trend with the increase in D^{-1}. Further, Darcy parameter reduces the radial velocity. However, it is found that there is an increase in temperature distribution from lower to upper wall. It is the fact that when the permeability of the medium decreases, the effective porosity is increased; because of this increment, the porosity reduces the resultant flow. Figure 8 witnesses the impact of Ha on velocity and temperature distributions and noticed the same trend as that of D^{-1} (Fig. 7). This is because the imposed magnetic field reduces the flow and enhances the heat transfer between the expanding walls.

The numerical values of non-dimensional shear stresses are provided in Table 1. From this, it is noticed that the values are showing good concurrence with the existing literature Bujurke et al. [1] for the Newtonian fluid case.

4 Conclusions

Looking into the above illustrations, we can conclude that

- Temperature increases with heat flux and decreases with radiation.
- Concentration increases with mass flux and decreases with chemical reaction rate.
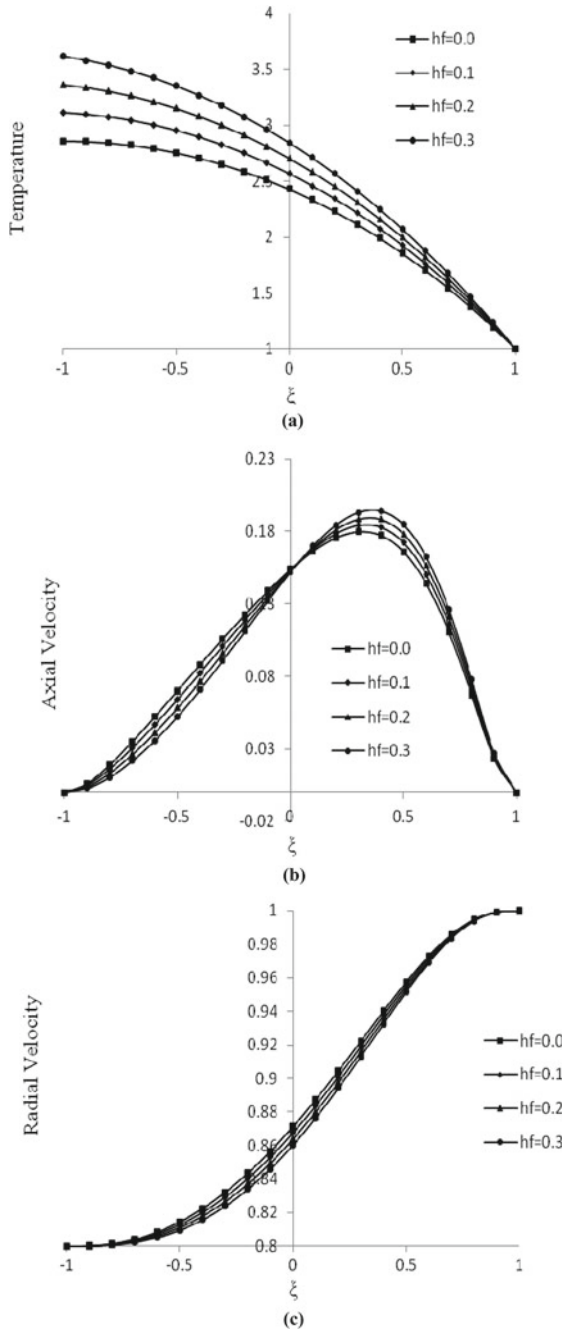- The radiation and heat source/sink parameters have the opposite effect on velocity and temperature distributions.
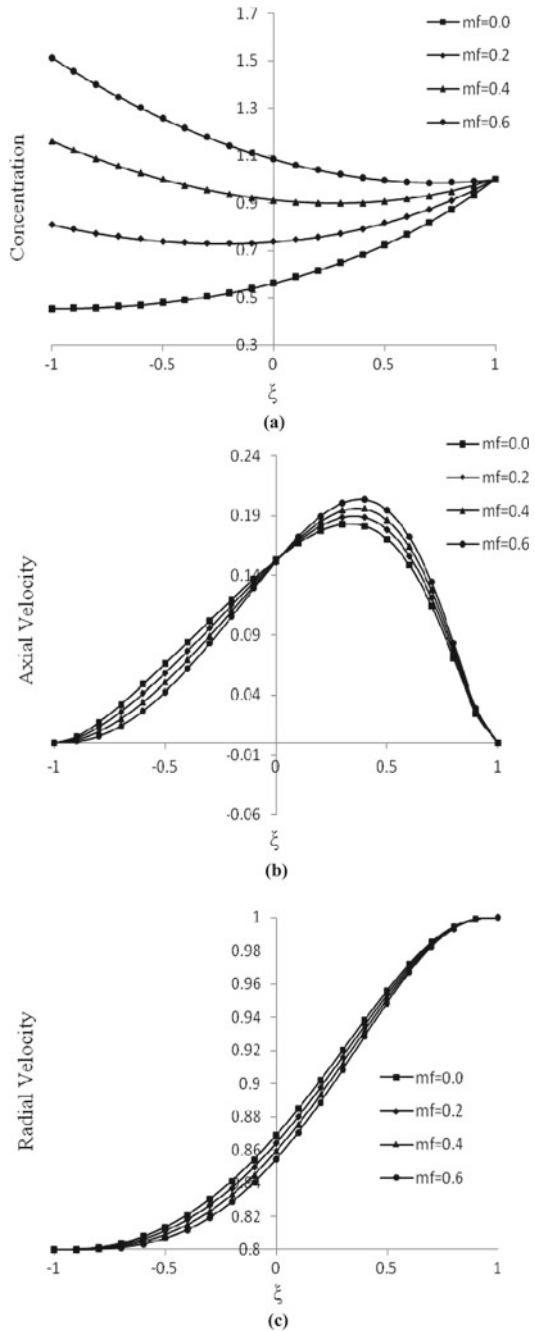
(a)

(b)

(c)
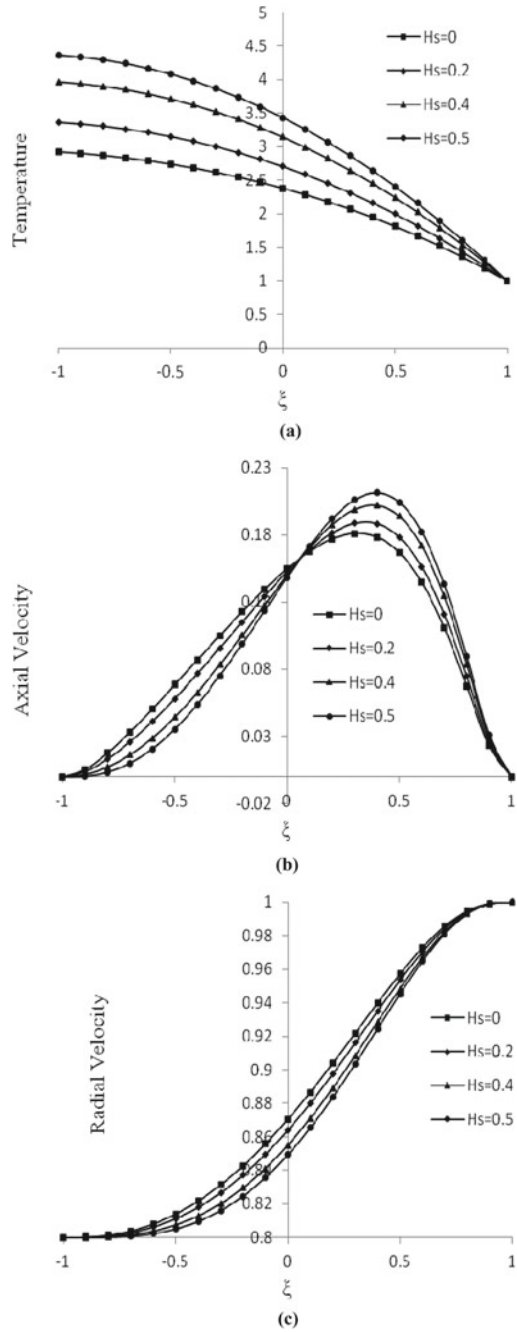
Fig. 3 Influence of Rd on (**a**) θ, (**b**) u_x, (**c**) u_y for Kr = 2, Sc = 0.22, Pr = $\beta = \alpha = h_f = \text{Hs} = m_f = 0.2$, Ha = Re = $D^{-1} = 2$, $A = 0.8$, Gr = Gm = 5
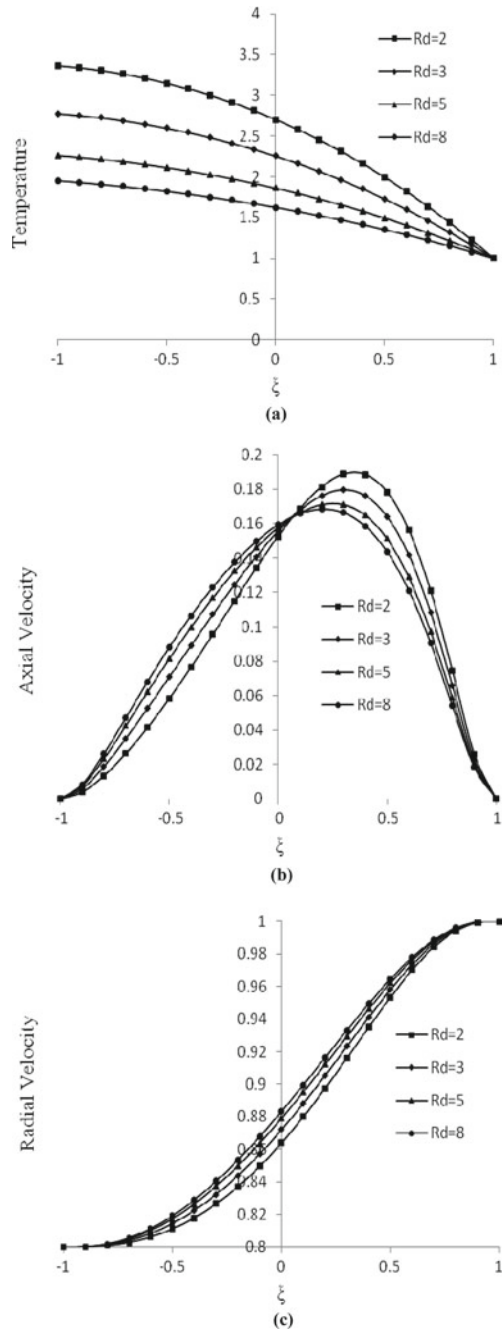
Fig. 4 Influence of 'h_f' on
(**a**) θ, (**b**) u_x, (**c**) u_y for Kr =
2, Sc = 0.22, Re = 2, β =
0.2, Ha = 2, Rd = 2, Hs =
0.2, a = 0.8, Gr = 5, Gm =
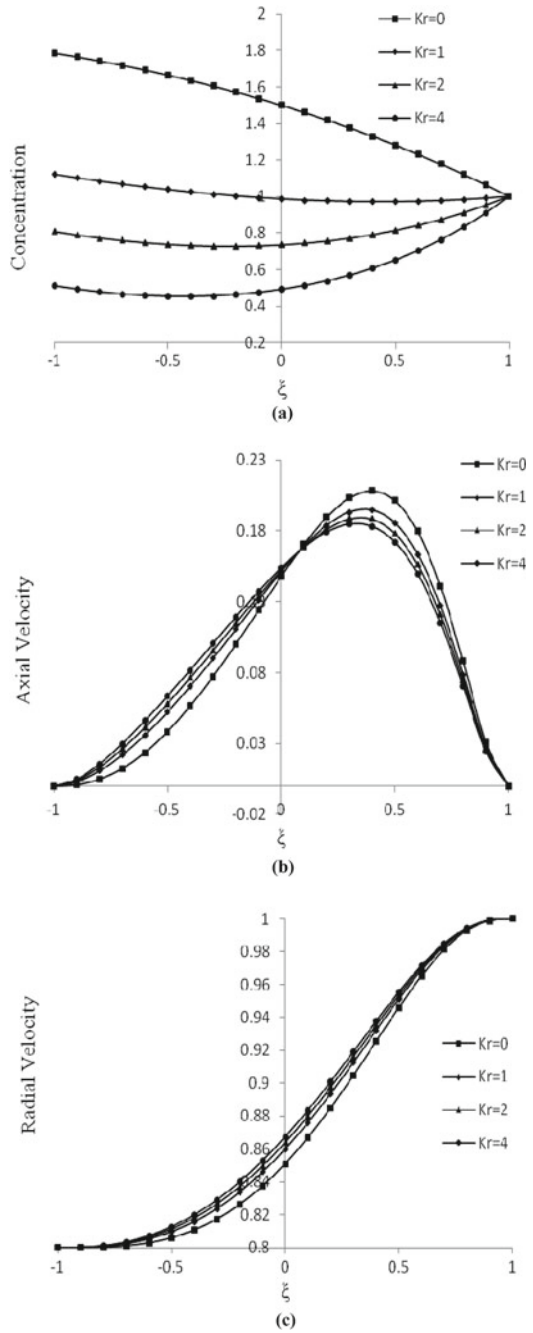5, D^{-1} = 2, m_f = 0.2, α =
0.2, Pr = 0.2

(a)

(b)

(c)

Fig. 5 Influence of 'm_f' on (**a**) C, (**b**) u_x, (**c**) u_y for $Kr = 2$, $Sc = 0.22$, $Re = 2$, $\beta = 0.2$, $Ha = 2$, $Rd = 2$, $Hs = 0.2$, $A = 0.8$, $Gr = 5$, $Gm = 5$, $Pr = 0.2$, $D^{-1} = 2$, $h_f = 0.2$, $\alpha = 0.2$
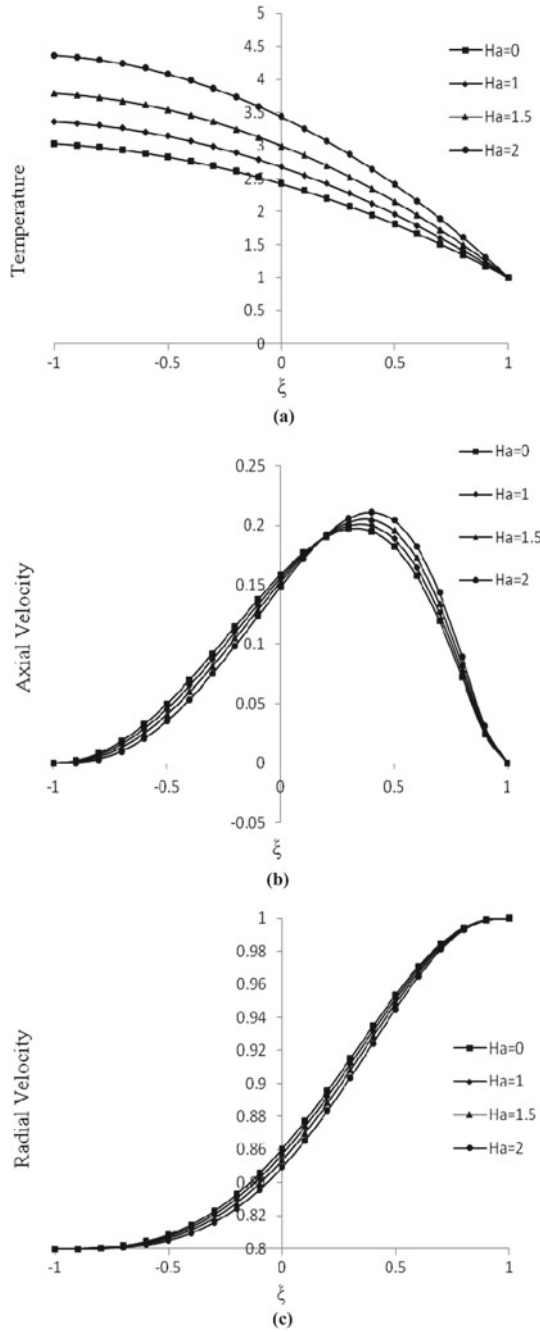
Fig. 6 Influence of 'Kr' on
(**a**) C, (**b**) u_x, (**c**) u_y for $m_f =$
0.2, Sc = 0.22, Pr = 0.2, Re
= 2, β = 0.2, α = 0.2, Ha =
2, Rd = 2, Hs = 0.2, A =
0.8, Gr = 5, Gm = 5, D^{-1} =
2, h_f = 0.2

Fig. 7 Influence of 'D^{-1}'
on (**a**) θ, (**b**) u_x, (**c**) u_y for Kr
= 2, Sc = 0.22, Pr = 0.2, Re
= 2, β = 0.2, α = 0.2, Ha =
2, Rd = 2, Hs = 0.2, A =
0.8, Gr = 5, Gm = 5, h_f =
0.2, m_f = 0.2
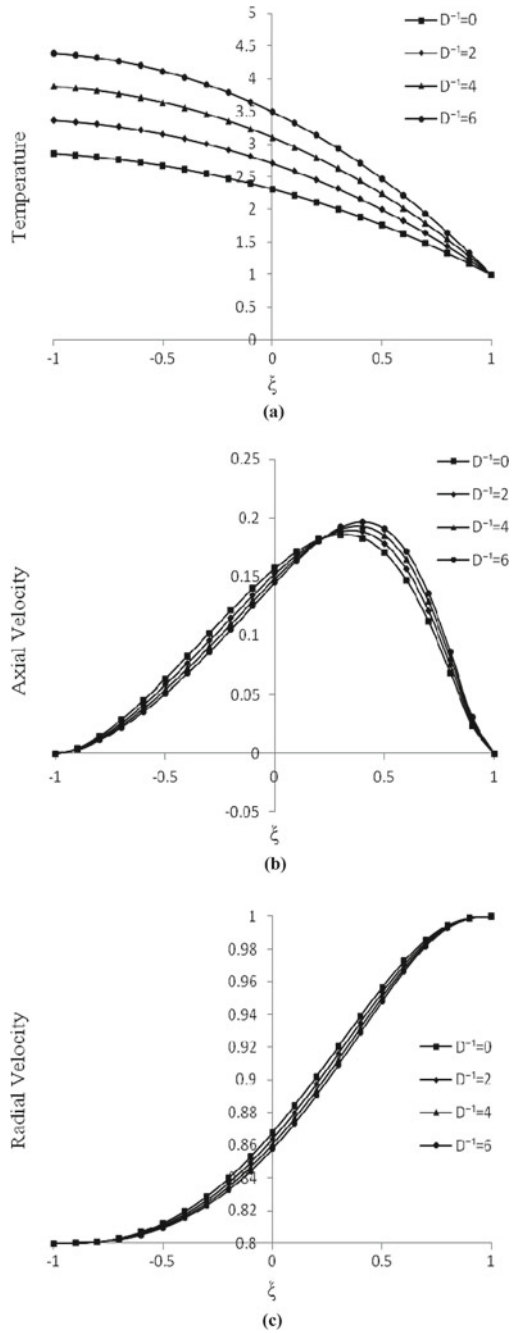
Fig. 8 Influence of 'Ha' on
(**a**) θ, (**b**) u_x, (**c**) u_y for Kr =
2, Sc = 0.22, $\beta = 0.2$, D^{-1}
= 2, Rd = 2, Hs = 0.5, A =
0.8, Gr = 5, Gm = 5, h_f =
0.2, $\alpha = 0.2$, $m_f = 0.2$, Pr =
0.2, Re = 2

(a)

(b)

(c)

Table 1 Comparison of non-dimensional shear stress values with the existing literature for the Newtonian fluid case

Re	$U''(1)$			
	$\alpha_1 = -0.20820$		$\alpha_1 = -0.3341$	
	Present	Bujurke et al. [1]	Present	Bujurke et al. [1]
1	−1.07938	−1.079	−1.7493	−1.749
5	−0.70067	−0.698	−1.17026	−1.166
15	−0.51324	−0.505	−0.86016	−0.839
25	−0.47874	−0.470	−0.7981	−0.777
35	−0.46415	−0.458	−0.77126	−0.753
45	−0.4547	−0.451	−0.75478	−0.754
54.75	−0.42728	−0.448	−0.73876	−0.742

References

1. Bujurke NM, Madalli VS, Mulimani BG (1998) Long series analysis of laminar flow through parallel porous walls of different permeability. Comput Methods Appl Mech Eng 160:39–56
2. Barik RN, Dash GC, Kar M (2013) Free convection heat and mass transfer MHD flow in a vertical porous channel in the presence of chemical reaction. J Fluids 2013:1–14
3. Loganathan P, Nirmal Chand P, Ganesan P (2015) Transient natural convective flow of a nanofluid past a vertical plate in the presence of heat generation. J Appl Mech Tech Phys 56(3):433–442
4. Hossain MA, Alim MA, Rees DAS (1999) The effect of radiation on free convection from a porous vertical plate. Int J Heat Mass Transf 42:181–191
5. Molla MM, Hossain MA, Yao LS (2004) Natural convection flow along a vertical wavy surface with uniform surface temperature in presence of heat generation/absorption. Int J Therm Sci 43(2):157–163
6. Hady FM, Mohamed RA, Mahdy A (2004) MHD free convection flow along a vertical wavy surface with heat generation or absorption effect. Int Commun Heat Mass Transfer 33(10):1253–1263
7. Stokes VK (1966) Couple stresses in fluids. Phys Fluids 9:1709–1715
8. Stokes VK (1968) Effects of couple stress in fluid on hydro magnetic channel flow. Phys Fluids 11(5):1131–1133
9. Khan NA, Riaz F, Sultan F (2014) Effects of chemical reaction and magnetic field on a couple stress fluid over a non-linearly stretching sheet. Eur Phys J Plus 129:1–12
10. Ali N, Khan SU, Sajid M, Abbas Z (2016) MHD flow and heat transfer of couple stress fluid over an oscillatory stretching sheet with heat source/sink in porous medium. Alexandria Eng J
11. Gaikwad SN, Kouser S (2014) Double diffusive convection in a couple stress fluid saturated porous layer with internal heat source. Int J Heat Mass Transf 78:1254–1264
12. Srinivasacharya D, Kaladhar K (2013) Soret and Dufour effects on free convection flow of a couple stress fluid in a vertical channel with chemical reaction. Chem Ind Chem Eng Q 19(1):45–55
13. Kaladhar K, Motsa SS, Srinivasacharya D (2015) Thermal radiation and diffusion effects on natural convection flow of couple stress fluid in a vertical channel. Prog Comput Fluid Dyn 15(6):388–395
14. Srinivas S, Subramanyam Reddy A, Ramamohan TR (2012) A study on thermal-diffusion and diffusion-thermo effects in a two-dimensional viscous flow between slowly expanding or contracting walls with weak permeability. Int J Heat Mass Transf 55:3008–3020

15. Dauenhauer EC, Majdalani J (1999) Unsteady flows in semi-infinite expanding channels with wall injection. AIAA 99–3523:1–8
16. Si X, Zheng L, Lin P, Zhang X, Zhang Y (2013) Flow and heat transfer of a micropolar fluid in a porous channel with expanding or contracting walls. Int J Heat Mass Transf 67:885–895
17. Si X, Zheng L, Zhang X, Chao Y (2011) The flow of a micropolar fluid through a porous channel with expanding or contracting walls. Central Eur J Phys 9(3):825–834
18. Kashyap KP, Ojjela O, Das SK (2019) MHD slip flow of chemically reacting UCM fluid through a dilating channel with heat source/sink. Nonlinear Eng Modell Appl 8(1):523–533
19. Srinivasacharya D, Srinivasacharyulu N, Ojjela O (2009) Flow and heat transfer of couple stress fluid in a porous channel with expanding and contracting walls. Int Commun Heat Mass Transf 36(2):180–185
20. Khan NA, Mahmood A, Ara A (2013) Approximate solution of couple stress fluid with expanding or contracting porous channel. Eng Comput Int J Computer-Aided Eng Softw 30(3):399–408
21. Ojjela O, Kumar NN (2014) Hall and ion slip effects on free convection heat and mass transfer of chemically reacting couple stress fluid in a porous expanding or contracting walls with Soret and Dufour effects. Front Heat Mass Transf 5:1–12
22. Bellman RE, Kalaba RE (1965) Quasilinearization and boundary-value problems. Elsevier publishing Co., Inc., New York
23. Huang CL (1978) Application of quasilinearization technique to the vertical channel flow and heat convection. Int J Non-Linear Mech 13:55–60
24. Hymavathi T, Shanker B (2009) A quasilinearization approach to heat transfer in MHD visco—elastic fluid flow. Appl Math Comput 215:2045–2054
25. Bhatnagar R, Vayo HW, Okunbor D (1994) Application of quasilinearization to viscoelastic flow through a porous annulus. Int J Non-Linear Mech 29(1):13–22
26. Eckert ERG, Drake RM (1972) Analysis of heat and mass transfer. McGraw-Hill, New York
27. Stokes VK (1984) Theories of fluids with microstructure—an introduction. Springer, Verlag
28. Sutton GW, Sherman A (1965) Engineering magneto hydrodynamics. McGrawhill, New York

Heat Source Location Effects on Buoyant Convection of Nanofluids in an Annulus

F. Mebarek-Oudina, N. Keerthi Reddy, and M. Sankar

Abstract In this paper, the impacts of the location of a thermal source on buoyant convection of nanofluids in an annular region are analyzed numerically through the finite volume technique. Five different thermal source positions along the inner cylinder of the annulus have been analyzed. The prime objective is to identify the optimal position of the source to maximize or minimize the thermal transport at different values of Ra and diverse volume fractions of the nanoparticle ranging from 0 to 10%. The location of the thermal source has a profound impact on the flow and temperature patterns as well as thermal transfer from the discrete source to the nanofluid. Further, the volume fraction of nanoparticles also controls the heat transport in the annular geometry.

Keywords Nanofluid · Annulus · Heat source · Finite volume method

1 Introduction

Nanofluids belong to different types of thermal transport fluids that are designed by dissolving nanometer-sized solid particles in traditional fluids like water and ethylene glycol. This field is becoming a fast upcoming multidisciplinary arena for nanoscientists, nanotechnologists, and thermal engineers. Most of the liquid coolants used in the thermal design or cooling of electronic equipment at moderate temperatures portray poor thermal conductivity and heat storage capacity causing lower convective thermal transport characteristics. Though the thermal transport can be enhanced by using turbulent model or by increasing the surface area, the thermal transport performance could not be increased due to limited thermal properties of the conventional fluids. As a result, these traditional cooling methods may not provide the solution to the cooling requirement of electronic industries. It has been demonstrated that

F. Mebarek-Oudina
Departement of Physics, Faculty of Sciences, University of 20 août 1955-Skikda, Skikda, Algeria

N. Keerthi Reddy · M. Sankar (✉)
Department of Mathematics, School of Engineering, Presidency University, Bangalore 560064, India
e-mail: manisankariyer@gmail.com

the thermal conductivity of conventional liquids is much smaller than the metallic particles. Since Choi [1] innovated the novel concept of nanofluids, the research has attracted remarkable interest from many investigators.

An enclosed finite-sized geometry with differently heated sidewalls and insulated horizontal boundaries represents the physical system of many industrial applications. Among the finite shaped enclosures, an annular geometry designed from two vertical coaxial cylinders is an important enclosure in many scientific and industrial applications, and hence investigated by many researchers. In a cylindrical annulus, Sankar et al. [2] numerically examined convection heat transport by applying a constant magnetic field. It is observed that the direction of the magnetic field has a profound influence on the type of enclosures. Kakarantazas et al. [3] performed 3D magnetoconvection in a vertical annular enclosure. The vertical surfaces are heated differently and horizontal surfaces are considered as insulated. The results reported that the turbulent flow is developed for the non-magnetic case, and an increase of magnetic force makes the flow to be laminar. In an annular geometry, Venkatachalappa et al. [4] analyzed thermosolutal convection to understand the magnetic field effects applied in either axial or radial directions. They found that the suppression of double-diffusive convection by the magnetic field greatly depends on the buoyancy ratio. Later, Sankar et al. [5] reported the collective impact of magnetic force and thermocapillary force on buoyat convection.

The oscillatory behavior of magnetoconvection in an annular cavity has been analyzed by Oudina et al. [6–8] for various Prandtl numbers. Recently, Girish et al. [9] studied developing laminar convection in cylindrical annular space having two passages caused by a baffle. They observed the baffle that has profound effect on velocity and thermal patterns, and thermal transport as well. It has been theoretically determined by many researchers that the thermal transport in an enclosure could be enhanced significantly by heating the walls of the enclosure discretely rather than uniformly [10–12]. Also, it was found that the thermal performances in an enclosure could be effectively controlled by attaching a thin conductive baffle to one of the thermally active walls of the cavity [13]. Recently, Sankar et al. [14] found interesting flow and thermal behavior of buoyancy convective flow in an annulus subjected to sinusoidal thermal conditions at the vertical walls.

Buoyancy-driven convection in finite geometries, such as rectangular, trapezoidal, triangular, and annular enclosures filled with nanofluid, has been widely examined because of its occurrence in important applications related to cooling of electronic components. In a two-dimensional enclosure, Khanafer et al. [15] studied the impacts of copper nanoparticles in water-based nanofluids and found the enhancement of heat transport by increasing the volume fraction of nanoparticles. Putra et al. [16] reported experimental findings of Al_2O_3 and Cu water-based nanofluids and reported contrary findings that the heat transfer coefficient for nanofluids is lower than that of the clear fluid. Later, Das et al. [17] made an excellent review of heat transfer of nanofluids in different geometries and using various nanofluids. Oztop and Abu-Nada [18] examined the impacts of partial heating on thermal transport of nanofluids in a rectangular enclosure. For water-based nanofluids, Minsta et al. [19] performed experiments on

to understand the various nanoparticle size and concentration of nanofluids and suggested new correlations for temperature and thermal conductivity. The influence of variable properties of nanofluids on the thermal transport augmentation is numerically studied by Abu-Nada [20]. Sivasankaran and Pan [21] observed that the non-uniform thermal conditions along the active walls significantly modify the buoyant flow and thermal rates in the enclosure. Recently, using two-phase model, Qi et al. [22] reported the convective thermal transport characteristics of Ag-Ga nanofluids in shallow rectangular enclosures by considering different volume fractions and radius of nanoparticles.

The thermal transport enhancement utilizing nanofluids in a horizontal cylindrical annulus has been studied by many researchers. Abu-Nada et al. [23] presented the results on the influence of different nanoparticles on buoyant convection. For a differently heated horizontal annular geometry, Parvin et al. [24] analyzed thermal transport processes of water-based nanofluid using two different thermal conductivity models. Recently, Ali et al. [25] performed a numerical study of water-Cu nanofluid in a horizontal annulus with inner cylinder having sinusoidal shape and rotating outer circular cylinder. It has been established from theoretical as well as experimental observations that the shape of the geometry has a stronger effect on the heat transport rates. As a result, many investigations have been performed in different types of non-rectangular enclosures such as triangular, trapezoidal, and parallelogrammic enclosures utilizing different nanofluids [26–31]. Aminossadati and Ghasemi [26] made a detailed study on thermal transport of nanofluids in an isosceles triangular enclosure. Later, the buoyant thermal transport of nanofluids in a triangular geometry containing a thermal source is reported by Sun and Pop [27]. For a parallelogrammic enclosure, the impact of inclination angle of sidewalls of the enclosure on the heat transfer rate of different nanofluids has been examined by Hussain and Hussein [28] and Ghalambaz et al. [29] for porous and non-porous geometries. Parvin and Chamkha [30] numerically analyzed the convective flow characteristics and entropy generation in reverse *L*-shaped geometry. Rashad et al. [31] employed FVM in a trapezoidal cavity to analyze the influences of geometrical and physical parameters on buoyant flow of nanofluids. Buoyant convection of nanofluids in annular space between two concentric cylinders has been investigated for complete heating [32] and discrete heating [33] of cylindrical walls as this geometry aptly portrays a number of applications involving nanofluids. From the vast literature survey made in this analysis, it has been observed that the influence of an energy source on buoyant transport of nanofluids is not examined for a vertical annulus. To address this gap, a numerical simulation to comprehend the effects of discrete thermal source on buoyant convection of nanofluids is performed in a vertical annular geometry. The proposed configuration has many industrial applications, particularly to the situations where the convection heat transfer of nanofluids is essential.

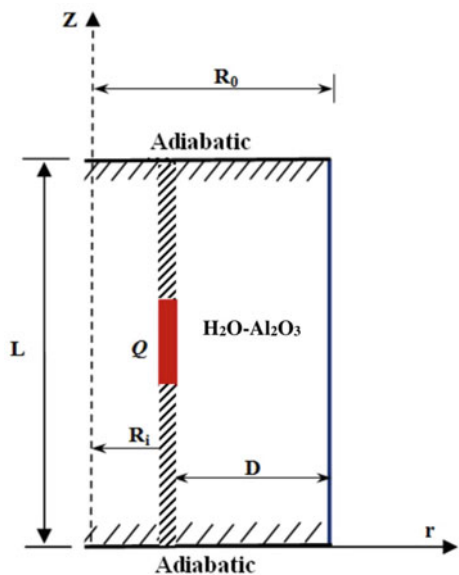## 2 Governing Equations and Mathematical Formulation

The schematic configuration of discretely heated vertical annular geometry of annular space D and height L is shown in Fig. 1. The annulus is formed by two coaxial cylindrical tubes with r_i as radius of inner and r_o as radius of outer tubes. It is assumed that the annular region is occupied with nanofluid consisting water-based Al_2O_3 nanoparticles. Further, the water and nanoparticle are presumed to be in thermal equilibrium and ensures no slip between them. The inner cylindrical tube contains a thermal source and outer tube is kept at a lower temperature, while the upper, lower, and unheated inner tube surfaces are chosen as adiabatic. As suggested by several investigations in the literature, the nanofluid density is approximated using Boussinesq model. By applying these approximations, the dimensional governing equations are:

$$\frac{\partial(ru)}{\partial r} + \frac{\partial(rv)}{\partial z} = 0 \tag{1}$$

$$\rho_{nf}\left(\frac{\partial u}{\partial t} + u\frac{\partial u}{\partial r} + v\frac{\partial u}{\partial z}\right) = -\frac{\partial P}{\partial r} + \mu_{nf}\left(\frac{1}{r}\frac{\partial}{\partial r}\left(r\frac{\partial u}{\partial r}\right) + \frac{\partial^2 u}{\partial z^2} - \frac{u}{r^2}\right) \tag{2}$$

$$\rho_{nf}\left(\frac{\partial v}{\partial t} + u\frac{\partial v}{\partial r} + v\frac{\partial v}{\partial z}\right) = -\frac{\partial P}{\partial z} + \mu_{nf}\left(\frac{1}{r}\frac{\partial}{\partial r}\left(r\frac{\partial v}{\partial r}\right) + \frac{\partial^2 v}{\partial z^2}\right)$$
$$+ (\rho\beta)_{nf}g(\theta - \theta_C)) \tag{3}$$

Fig. 1 Annular cavity filled with Al_2O_3-water nanofluid and discrete heat source

$$\frac{\partial \theta}{\partial t} + u \frac{\partial \theta}{\partial r} + v \frac{\partial \theta}{\partial z} = \alpha_{nf} \left(\frac{1}{r} \frac{\partial}{\partial r} \left(r \frac{\partial \theta}{\partial r} \right) + \left(\frac{\partial^2 \theta}{\partial z^2} \right) \right) \tag{4}$$

The dimensionless transformations chosen in this study are (Fig. 2):

$$R = (r - r_i)/D, \; Z = z/D, \; (U, V) = (u, v)/(\alpha_f/D),$$
$$\tau = t/(D^2/\upsilon_{nf}), \; T = (\theta - \theta_c) \, k_{nf}/QD,$$
$$P = pD^2/\rho_{nf}\alpha_f^2, \; \text{where } D = r_o - r_i.$$

Applying above transformations, the dimensionless form of Eqs. (1)–(4) are
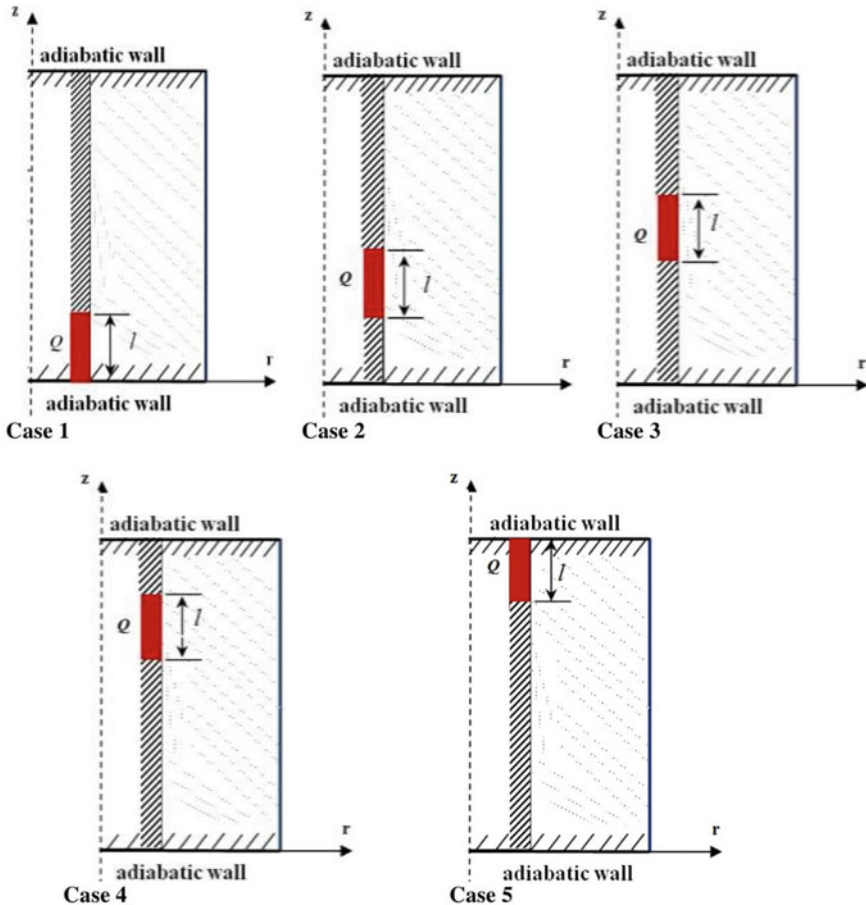
Fig. 2 Geometry of problem with different locations of heat source

$$\frac{1}{R}\frac{\partial(RU)}{\partial R} + \frac{\partial V}{\partial Z} = 0 \tag{5}$$

$$\frac{\partial U}{\partial \tau} + U\frac{\partial U}{\partial R} + V\frac{\partial U}{\partial Z} = -\frac{\rho_f}{\rho_{nf}}\frac{\partial P}{\partial R} + \Pr\frac{\upsilon_{nf}}{\upsilon_f}\nabla^2 U \tag{6}$$

$$\frac{\partial V}{\partial \tau} + U\frac{\partial V}{\partial R} + V\frac{\partial V}{\partial Z} = -\frac{\rho_f}{\rho_{nf}}\frac{\partial P}{\partial Z} + \Pr\frac{\upsilon_{nf}}{\upsilon_f}\nabla^2 V + \operatorname{Ra}\Pr\frac{(\rho\beta)_{nf}}{\rho_{nf}\beta_f}T \tag{7}$$

$$\frac{\partial T}{\partial \tau} + U\frac{\partial T}{\partial R} + V\frac{\partial T}{\partial Z} = \frac{\alpha_{nf}}{\alpha_f}\nabla^2 T \tag{8}$$

where $\nabla^2 = \frac{1}{R}\frac{\partial}{\partial R}\left(R\frac{\partial}{\partial R}\right) + \frac{\partial^2}{\partial Z^2}$.

The stream function for the flow distribution is defined as

$$U = \frac{1}{R}\frac{\partial \psi}{\partial Z}, \quad V = -\frac{1}{R}\frac{\partial \psi}{\partial R}. \tag{9}$$

The thermal conductivity, heat capacity, coefficient of thermal expansion, density, thermal diffusivity, and dynamic viscosity are, respectively, chosen as,

$$k_{nf} = k_f\left[\frac{(k_s - 2k_f) - 2\phi(k_f - k_s)}{(k_s - 2k_f) + \phi(k_f - k_s)}\right] \tag{10}$$

$$(\rho C_p)_{nf} = (1 - \phi)(\rho C_p)_f + \phi(\rho C_p)_s \tag{11}$$

$$(\rho\beta)_{nf} = (1 - \phi)(\rho\beta)_f + \phi(\rho\beta)_s \tag{12}$$

$$\rho_{nf} = (1 - \phi)\rho_f + \phi\rho_s \tag{13}$$

$$\alpha_{nf} = k_{nf}/(\rho C_p)_{nf} \tag{14}$$

$$\mu_{nf} = \frac{\mu_f}{(1 - \phi)^{2.5}} \tag{15}$$

The non-dimensional parameters of the present problem are:
$\operatorname{Ra} = \frac{g\beta_f Q D^4}{k_f \upsilon_f \alpha_f}$, the Rayleigh number, $\Pr = \frac{\upsilon_f}{\alpha_f}$, the Prandtl number, $A = \frac{H}{D}$, the aspect ratio, and $\lambda = \frac{R_o}{R_i}$, the radius ratio.
The dimensionless initial and boundary conditions are:

$$\text{At } \tau = 0: U = V = T = P = 0;$$

$$\text{At } \tau < 0: \text{ on all rigid walls: } U = V = 0;$$

$$\text{on the heat source: } \frac{\partial T}{\partial R} = -\frac{k_f}{k_n f};$$

Table 1 Thermophysical properties of water and nanoparticles

Properties	Fluid (water)	Al$_2$O$_3$
C_p (J/kgK)	4179	765
ρ (kg/m^3)	997.1	3970
k (W/mK)	0.613	25
$\beta \times 10^{-5}$ (1/K)	21	0.85

on the outer wall: $T = 0$;

on the bottom and top walls: $\dfrac{\partial T}{\partial Z} = 0.$

The local and overall thermal transport rates are, respectively, obtained by $\mathrm{Nu} = -\frac{k_{nf}}{k_f} \frac{\partial T}{\partial R}\Big|_{R=1}$ and $\overline{\mathrm{Nu}} = \frac{1}{A} \int\limits_0^A \mathrm{Nu} \, dZ.$

3 Numerical Method

The model Eqs. (5)–(9) are numerically solved using the finite volume method. The well-known procedure of SIMPLER [34] technique is employed to tackle the velocity–pressure combination. The system of equations arising from these finite volume techniques is solved using TDMA algorithm. More information on the methods can be found in our recent papers [6–8, 11, 33, 35], and for brevity, the same is not provided here.

4 Results and Discussion

This section describes the impacts of a discrete thermal source on buoyant-driven convection of H$_2$O–Al$_2$O$_3$ nanofluid motion and thermal transport in a cylindrical annular space. As the study involves several parameters, we have fixed the values of Ar and λ. In this analysis, the aspect ratio is chosen as Ar = 2, while the radius ratio is kept at λ = 2. However, other parameters, such as the location of thermal source, Ra, and nanoparticle volume fraction are varied over different parameter regimes. In this analysis, five different positions of the thermal source are considered. The flow and thermal development for the range of parameters considered in this analysis are described through streamline and isotherm contours, and the thermal transport is estimated from local and global Nusselt numbers.

Figure 3 illustrates the impact of Rayleigh number on flow and thermal variations for a fixed source location and Φ. The relative significance of Ra is vividly seen through the streamlines and isothermal lines. For an increasing value of Ra is
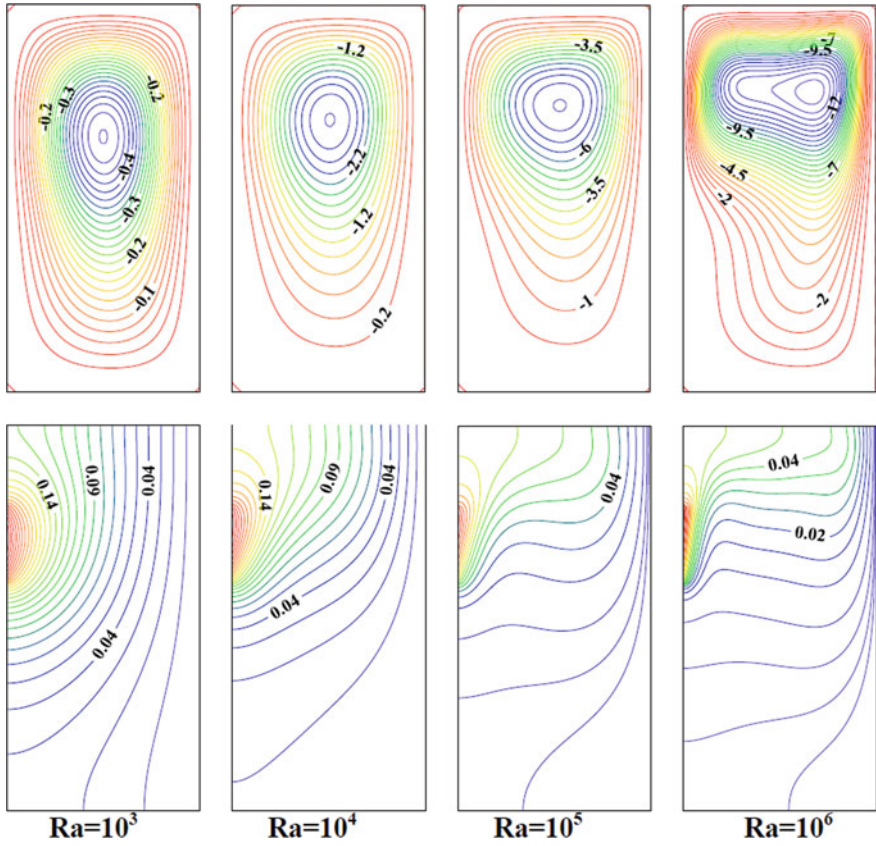
Fig. 3 Streamlines and isotherms for $A = 2$, $Ra = 10^4$, $\Phi = 5\%$, and various Ra at case 4

increased, the moderately varying isotherms for conduction regime have been transformed to thermally stratified zone of isotherms for convection-dominated regime. Also, as the thermal source is located near the upper boundary, the main eddy is located near the upper portion of the annulus, and the size and strength of this eddy enhance with an increment of Rayleigh number. As the volume fraction of nanoparticle is fixed, its effect is uniform for all Rayleigh numbers.

Figure 4 depicts the effects of volume fraction of nanoparticle on flow and thermal patterns for constant values of Ra and source position. The presence of nanoparticle makes a strong impact on the velocity as well as thermal variations. It is witnessed that the flow and temperature contours are well distributed in the annulus as we increase the volume fraction of nanoparticles. For clear fluid ($\Phi = 0\%$), the movement of flow and thermal lines are confined mostly near the upper portion of the geometry. However, as the value of Φ is increased, the entire annulus is filled with streamline and isotherm contours. In addition, as the source is fixed near the top boundary, the location effect of the heater is uniform for all values of Φ. Figure 5 reports the effect
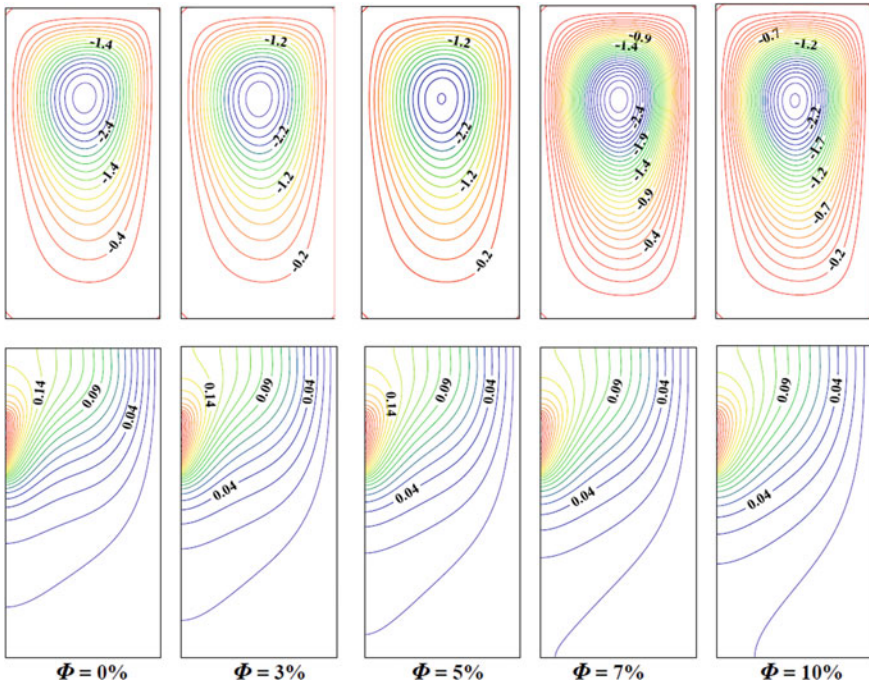
Fig. 4 Streamlines and isotherms for $A = 2$, Ra $= 10^4$, and various Φ at case 4

of five different thermal source locations on the contours of streamline and isotherm. The impact of the source location can be vividly witnessed through streamlines and isotherms. The nanofluid flow and the corresponding thermal circulation have undergone severe changes as the source location changes from lower portion of the inner wall to the upper portion. From Fig. 5, it is detected that the maximum stream function increases as the source location is shifted from lower to the upper boundary of annular space. For the position of source at lower middle of inner cylinder wall, the flow strength is higher and at this location, the annular space is completely occupied by streamline and isotherm contours. Also, the lower portion of the enclosure is sparsely filled by isotherms as the heat source is positioned at the top. From the simulations, it can be witnessed that there exists an optimal location at which the flow rate and thermal variations could be effectively controlled through the source locations.

The knowledge of thermal variations along the wall in which heat source is mounted reveals much important information to thermal designers and is exhibited in Fig. 6. Figure 6 depicts the variation of thermal profiles along the inner cylinder with various Rayleigh numbers for a fixed location of the thermal source. The temperature rises near the source and inclines toward the edge of the source for all values of Ra. However, steep variations are observed for lower Ra compared to higher Rayleigh number. In Fig. 7, temperature variation along the inner cylinder for different ther-
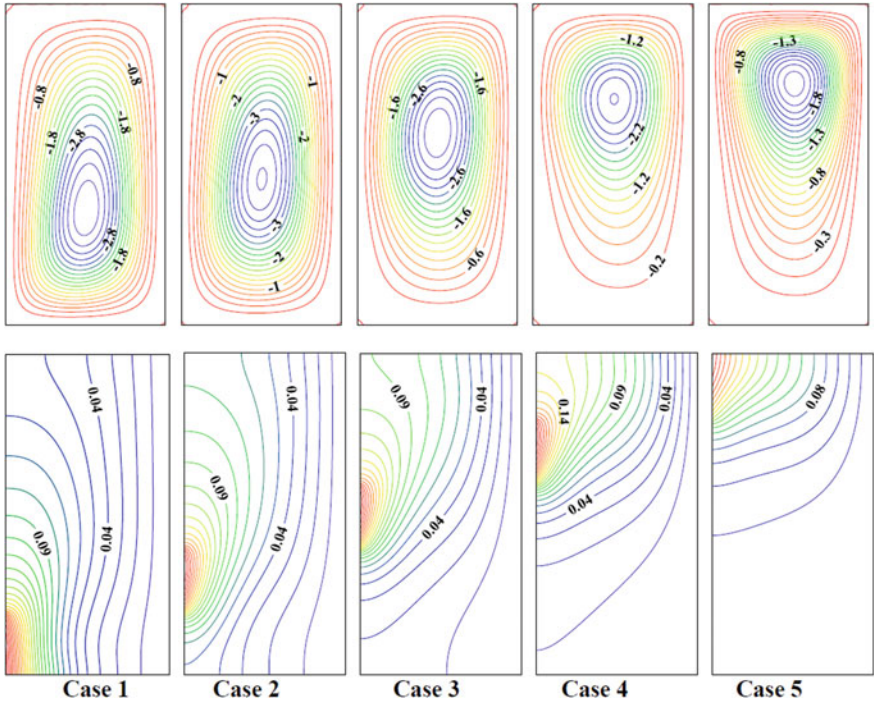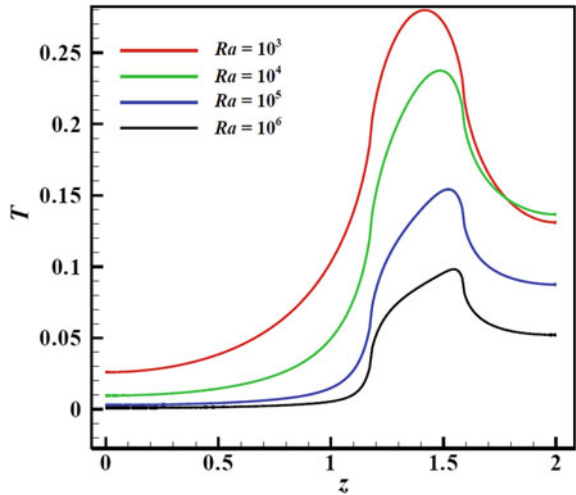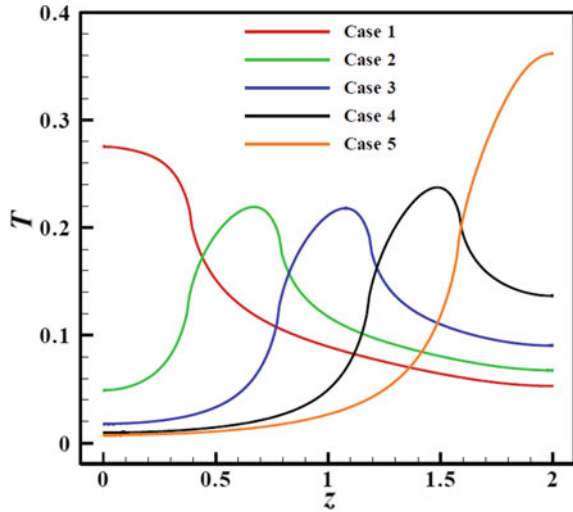
Fig. 5 Streamlines and isotherms for $A = 2$, $Ra = 10^4$, and $\Phi = 5\%$ at different cases

**Fig. 6** Thermal profiles along inner wall for different Rayleigh numbers, $\Phi = 5\%$, and $A = 2$ at case 4

Fig. 7 Heat source location effects on thermal profiles along the heated source for $\Phi = 5\%$, $Ra = 10^4$, and $A = 2$ for various cases

mal source location is displayed for a fixed value of Ra. It is exciting to notice that the thermal variations are akin as the source is placed between the upper and lower boundaries of the annulus. However, as the source is placed at the bottom or top boundary, thermal variations are different.

For a thermal design engineer or heat transfer analyst, the most important quantity of interest is the amount of thermal transport from the source to the fluid as the source is placed at different locations. This information helps to design better quality and efficient equipment so as to maximize the heat transport. Figure 8 reports the variation in local heat transport for different Rayleigh numbers when the source is positioned

Fig. 8 Variation of *Nu* against Rayleigh number along the source for $\Phi = 5\%$ and $A = 2$ for case 4
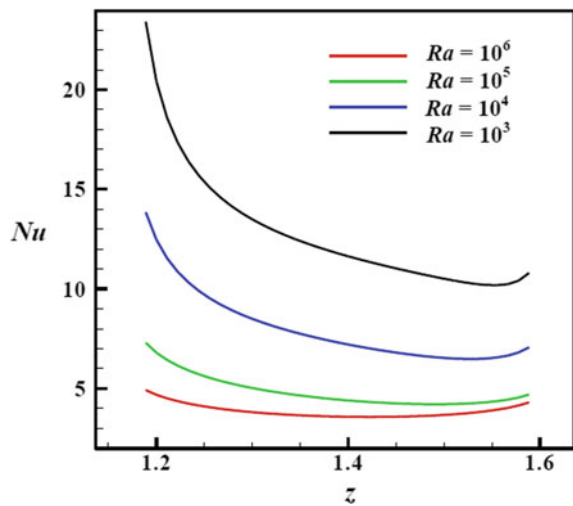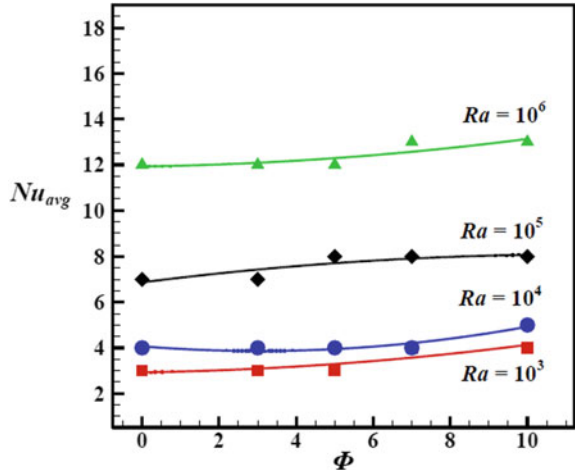
Fig. 9 Effect of heat source
locations on *Nu* for different
cases and $A = 2$, Ra $= 10^4$
and different nanofluid
volume fractions
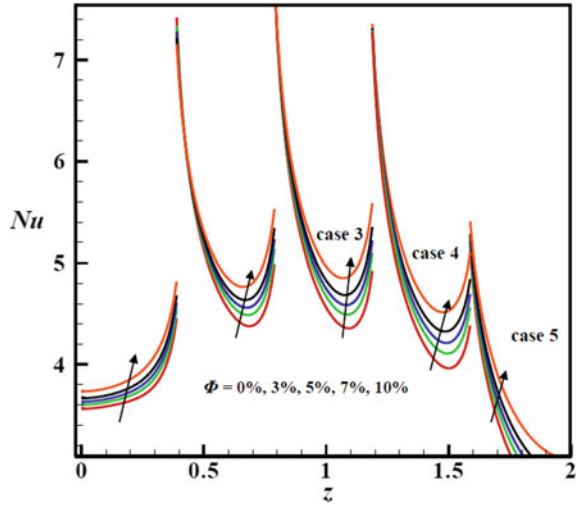

near the top boundary (case 4) and for a fixed value of Φ. It is detected that the thermal
transport rate is maximum at starting part of the source, but declines toward the end
part of the source for all values of Ra. Figure 9 depicts the local heat transport along
the thermal source for all five different locations and various volume fraction levels.
As observed in Fig. 8, the heat transport rates decrease along the source and increase
toward the end of the source. As regards to the volume fraction of nanoparticle,
it can be noticed that higher heat transport occurs for the larger volume fraction of
nanoparticles. Further, the local Nu profiles are similar when the source is positioned
between top and bottom boundaries rather than near the horizontal walls.

The local heat transport rates provide only information at a point of the source.
However, the total transport of heat from the entire source can be estimated from
overall heat transport through the average Nu and this quantity is depicted in Figs. 10
and 11 for various parameters. The influence of nanofluid volume fraction upon the
overall thermal transport is provided in Fig. 10 for various magnitudes of Ra. In
broad-spectrum, the average Nu is increasing with an increase in Ra. Also, the simu-
lations reveal that the transport of heat could be augmented by enhancing the volume
fraction of nanoparticles. Among the different thermal source locations considered
in the present analysis, it is interesting to identify the optimum location to achieve
higher thermal transport from the source. Figure 11 suggests the best location to
increase the thermal transport from the inner wall to the adjacent nanofluid. From
the detailed simulations, it can be concluded that the heat transport can be augmented
by positioning the thermal source near the lower middle portion on the inner cylinder.

Fig. 10 Effect of the nanofluid volume fraction on the average Nusselt number for different Rayleigh number and $A = 2$ at the case 4

Fig. 11 Effect of heat source locations on the average Nusselt number for various cases at $A = 2$, Ra $= 10^4$, and $\Phi = 5\%$
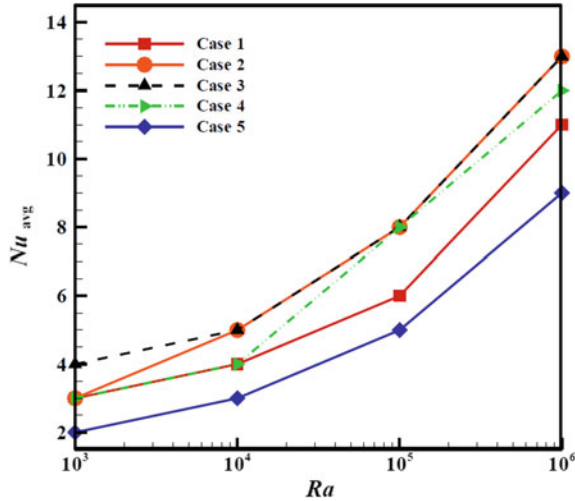
5   Conclusions

The prime intention of this study is to numerically investigate the buoyant thermal transport in an annular space filled with nanofluids and subjected to partial heating. Through the elaborative and systematic numerical results, it has been detected that the position of the thermal source is a key parameter in controlling the heat transport rate. Also, the position of source profoundly modifies the flow circulation rate and thermal pattern. From the numerical simulations, we conclude that it is possible to choose a thermal source location to optimize the rate of buoyant convective transport based on the needs of the application.

References

1. Choi SUS (1995) Enhancing thermal conductivity of fluids with nanoparticles. ASME FED 231:99–105
2. Sankar M, Venkatachalappa M, Shivakumara IS (2006) Effect of magnetic field on natural convection in a vertical cylindrical annulus. Int J Eng Sci 44:1556–1570
3. Kakarantzas C, Sarris IE, Vlachos NS (2011) Natural convection of liquid metal in a vertical annulus with lateral and volumetric heating in the presence of horizontal magnetic field. Int J Heat Mass Transf 54:3347–3356
4. Venkatachalappa M (2011) Y Do, Sankar M. Effect of magnetic field on the heat and mass transfer in a vertical annulus: Int J Eng Sci 49:262–278
5. Sankar M, Venkatachalappa M, Do Y (2011) Effect of magnetic field on the buoyancy and thermocapillary driven convection of an electrically conducting fluid in an annular enclosure. Int J Heat Fluid Flow 32:402–412
6. Mebarek-Oudina F, Bessaïh R (2014) Numerical modelling of MHD stability in a cylindrical configuration. J Franklin Inst 351(2):667–681
7. Mebarek-Oudina F, Bessaïh R (2016) Oscillatory magnetohydrodynamic natural convection of liquid metal between vertical coaxial cylinders. J Appl Fluid Mech 9(4):1655–1665
8. Mebarek-Oudina F, Makinde OD (2018) Numerical simulation of oscillatory MHD natural convection in cylindrical annulus: prandtl number effect. Defect Diffus Forum 387:417–427
9. Girish N, Makinde OD, Sankar M (2018) Numerical investigation of developing natural convection in vertical double-passage porous annuli. Defect Diffus Forum 387:442–460
10. Sankar M, Do Y, Ryu S, Bongsoo J (2015) Cooling of heat sources by natural convection heat transfer in a vertical annulus. Numer Heat Transf Part A Appl 68(8):847–869
11. Mebarek-Oudina F (2017) Numerical modelling of the hydrodynamic stability in vertical annulus with heat source of different lengths. Eng Sci Technol Int J 20:1324–1333
12. Sankar M, Kemparaju S, Prasanna BMR, Eswaramoorthi S (2018) Buoyant convection in porous annulus with discrete sources-sink pairs and internal heat generation. IOP Conf Ser J Phys Conf Ser 1139
13. Sankar M, Pushpa BV, Prasanna BMR, Do Y (2016) Influence of size and location of a thin baffle on natural convection in a vertical annular enclosure. J Appl Fluid Mech 9:2671–2684
14. Sankar M, Kiran S, Do Y Effect of non-uniform heating on natural convection in a vertical porous annulus. In: Narayanan N, Mohanadhas B, Mangottiri V (eds) Flow and transport in subsurface environment, springer transactions in civil and environmental engineering. Springer, Singapore
15. Khanafer K, Vafai K, Lightstone M (2003) Buoyancy-driven heat transfer enhancement in a two-dimensional enclosure utilizing nanofluids. Int J Heat Mass Transf 46(19):3639–3653
16. Putra N, Roetzel W, Das SK (2003) Natural convection of nanofluids. Heat Mass Transf 39:775–784
17. Das SK, Choi SUS, Patel HE (2006) Heat transfer in nanofluids-A review. Heat Transf Eng 27(10):3–19
18. Oztop HF, Abu-Nada E (2008) Numerical study of natural convection in partially heated rectangular enclosure filled with nanofluids. Int J Heat Fluid Flow 29(5):1326–1336
19. Minsta HA, Roy G, Nguyen CT, Doucet D (2009) New temperature and conductivity data for water-based nanofluids. Int J Therm Sci 48(2):363–371
20. Abu-Nada E (2009) Effects of variable viscosity and thermal conductivity of Al_2O_3-water nanofluid on heat transfer enhancement in natural convection. Int J Heat Fluid Flow 30:679–690

21. Sivasankaran S, Pan KL (2014) Natural convection of nanofluids in a cavity with non-uniform temperature distributions on side walls. Numer Heat Transf Part A Appl 65(3):247–268
22. Qi C, Yang L, Wang G (2017) Numerical study on convective heat transfer enhancement in horizontal rectangle enclosures filled with Ag-Ga nanofluids. Nanoscale Res Lett 326(12)
23. Abu-Nada E, Masoud Z, Hijazi A (2008) Natural convection heat transfer enhancement in horizontal concentric annuli using nanofluids. Int Commun Heat Mass Transf 35(5):657–665
24. Parvin S, Nasrin R, Alim MA, Hossain NF, Chamkha AJ (2012) Thermal conductivity variation on natural convection flow of water-alumina nanofluid in an annulus. Int J Heat Mass Transf 55:5268–5274
25. Ali FH, Hamzah HK, Abdulkadhim A (2019) Numerical study of mixed convection nanofluid in an annulus enclosure between outer rotating cylinder and inner corrugation cylinder. Heat Transfer-Asian Res 48:343–360
26. Aminossadati SM, Ghasemi B (2011) Enhanced natural convection in an isosceles triangular enclosure filled with a nanofluids. Comput Math Appl 61:1739–1753
27. Sun Q, Pop I (2011) Free convection in a triangle cavity filled with a porous medium saturated with nanofluids with flush mounted heater on the wall. Int J Therm Sci 50:2141–2153
28. Hussain SH, Hussein AK (2014) Natural convection heat transfer enhancement in a differentially heated parallelogrammic enclosure filled with copper-water nanofluids. J Heat Transf 136:1–8
29. Ghalambaz M, Sheremet MA, Pop I (2015) Free convection in a parallelogrammic porous cavity filled with a nanofluid using Tiwari and Das' nanofluid model. PLoS ONE 10(5): e0126486, 1–17
30. Parvin S, Chamkha AJ (2014) An analysis on free convection flow, heat transfer and entropy generation in an odd-shaped cavity filled with nanofluid. Int Commun Heat Mass Transf 54:8–17
31. Rashad AM, Sivasankaran S, Mansour MA, Bhuvaneswari M (2017) Magneto-convection of nanofluids in a lid-driven trapezoidal cavity with internal heat generation and discrete heating. Numer Heat Transf Part A Appl 71(12):1223–1234
32. Abouali O, Falahatpisheh A (2009) Numerical investigation of natural convection of Al_2O_3 nanofluid in vertical annuli. Heat Mass Transf 46:15–23
33. Mebarek-Oudina F (2019) Convective heat transfer of titania nanofluids of different base fluids in cylindrical annulus with discrete heat source. Heat Transf Asian Res 48:135–147
34. Patankar SV (1980) Numerical heat transfer and fluid flow. Hemisphere, Washinton, DC
35. Raza J, Mebarek-Oudina F, Chamkha AJ (2019) Magnetohydrodynamic flow of molybdenum disulfide nanofluid in a channel with shape effects. Multidiscipline Modell Mater Struct 15(4):737–757

Analytical Approach for Mixed Convective Flow in Presence of Casson Fluid in a Porous Channel

B. V. Shilpa, D. V. Chandrashekhar, P. A. Dinesh, and A. T. Eswara

Abstract An analytical approach have been carried to study the mixed convective flow in presence of Casson fluid in a porous channel with an external constraint of magnetic field applied uniformly to the physical model. Perturbation technique has been implemented to find the characteristics of non-linear coupled partial differential equations of concentration, temperature and velocity. The pictorial representation of the effect of physical parameters such as Reynolds number R, Hartman number M^2, Casson parameter β, buoyancy parameter λ, chemical reaction rate γ, concentration buoyancy parameter N, Prandtl number Pr, Schmidt number Sc on concentration, temperature and velocity has been studied. As the variation of non-dimensional parameters make an important role in studying the changes on concentration, temperature and velocity. The analysis of the solution is also compared with the earlier work, and for a particular case, it has been found to be good agreement.

Keywords Perturbation technique · Casson fluid · Magnetic field · Porous channel

1 Introduction

The study of Casson fluid flow in a channel has many applications in engineering. Casson fluid is one of the non-Newtonian fluids in which shear stresses are non-linearly proportional to the velocity gradient. Casson fluid is one of the most

B. V. Shilpa · D. V. Chandrashekhar
Department of Mathematics, Vivekananda Institute of Technology, Bangalore 560074, India
e-mail: shilpabvsr@gmail.com

D. V. Chandrashekhar
e-mail: dvchandru@gmail.com

P. A. Dinesh (✉)
Department of Mathematics, M. S. Ramaiah Institute of Technology, Bangalore 560054, India
e-mail: dineshdpa@msrit.edu

A. T. Eswara
Department of Mathematics, GSSS Institute of Engineering & Technology for Women,
Mysuru 570016, India
e-mail: ateswara@gmail.com

important non-Newtonian fluids possessing a yield value which has more applications in biomechanics and polymer-processing industries. Many researchers have been attracted towards Casson fluid due to its applications in food processing, metallurgy, drilling and bioengineering operations [1, 2]. Casson fluid can be used in manufacturing of coal in water, paints, china clay, synthetic lubricants and biological fluids such as synovial fluids, tomato sauce, sewage sludge, jelly, soup, honey and blood due to its contents such as fibrinogen, plasma and protein [3] which are the few important applications. Casson-derived Casson constitutive equation [4] in which the stress and rate of strain relationship is not linear. Tao studied problems on combined free and forced convection in channels by introducing a complex function which is directly related to the velocity and temperature fields, where Helmholtz wave equation combines momentum and energy equation in complex domain [5], and an approximate Casson fluid model for tube flow of blood was studied by Walawender et al. [6] in which pressure drop and volumetric flow rate was measured experimentally. Batra and Jena studied the steady, laminar flow of a Casson fluid in a slightly curved tube of circular cross section which has been analysed for large value of Dean numbers, and the governing equations to a system of non-linear ordinary differential equations has been solved numerically by using Runge-Kutta Merson technique followed by an iterative procedure [7].

Eldabe studied the flow of Casson fluid between two rotating cylinders [8] in which magnetic induction, velocity distribution, temperature distribution, stress, shear rates and rate of heat transfer are obtained analytically by using perturbation method. Sayed Ahmed and Attia considered the unsteady MHD flow of an electrically conducting viscous incompressible Casson fluid bounded by two parallel non-conducting parallel plates to transfer heat with Hall effect and solved numerically [9]. Flow and heat transfer of a micro-polar fluid in a porous channel with expanding or contracting walls by introducing suitable similarity transformation have been studied by Si et al. [10] in which homotopy analysis method (HAM) is employed to obtain series solution of velocity, micro-rotation and temperature distribution.

Significance of Soret, Joule heating and Hall effects on free convection in an electrically conducting Casson fluid in a vertical channel in the presence of viscous dissipation has been studied by Reddy et al. [11] in which homotopy analysis method is used to find the solution, and the obtained solution is compared with Adomian decomposition method. Unsteady MHD Casson fluid flow through a parallel plate with Hall current was studied by Afikuzzaman et al. [12] where fluid motion is subjected to uniform suction and injection, and explicit finite difference method is used to solve energy and momentum equation. Das studied the influence of Newtonian heating effect on heat and mass transfer in unsteady hydro-magnetic flow of Casson fluid flow past a flat plate in presence of thermal radiation and chemical reaction by using Laplace transforms technique [13]. The unsteady free convective hydro-magnetic boundary layer Casson fluid flow past an oscillating vertical plate with porous medium in presence of magnetic field, thermal radiation and chemical reaction radiation has been studied by Kataria et al. [14], and the governing equations were solved by using Laplace transform technique.

With all the above-cited investigations and its applications, the aim of the present study is to find an analytical solution for mixed convective flow in presence of Casson fluid in a porous channel under the influence of the magnetic field and amplification using perturbation method. The effect of physical parameters such as Reynolds number R, buoyancy parameter λ, Hartman number M^2, Casson parameter β, chemical reaction rate γ, concentration buoyancy parameter N, Schmidt number Sc, Prandtl number Pr, on concentration, temperature and velocity has been studied graphically.

2 Mathematical Formulation

Here, the physical configuration of the system which is laminar, steady, incompressible Casson fluid flow under the influence of external constrain of the applied constant magnetic field in a channel is considered. For such a model, the two-dimensional system consists of upper wall and lower wall which are situated at $y = \pm H$. The x-axis is along the centreline of the channel, parallel to the channel surfaces, and the y-axis is perpendicular to it. The fluid is injected into the channel and extracted out at a uniform velocity V (>0 suction and <0 injection) from upper wall and lower wall, respectively. B_o is the strength of uniform magnetic field applied perpendicular to the velocity field. The induced magnetic field is negligible as compared with the imposed field.

The governing equations for MHD boundary layer flow of Casson fluid are expressed as the following equations.

$$\frac{\partial u}{\partial x} + \frac{\partial v}{\partial y} = 0, \tag{1}$$

$$u\frac{\partial u}{\partial x} + v\frac{\partial u}{\partial y} = -\frac{1}{\rho}\frac{\partial p}{\partial x} + \upsilon\left(1 + \frac{1}{\beta}\right)\frac{\partial^2 u}{\partial y^2} - \frac{\sigma B_0^2 u}{\rho}$$
$$\pm g(\beta_T (T - T_2) + \beta_c (C - C_2)), \tag{2}$$

$$u\frac{\partial v}{\partial x} + v\frac{\partial v}{\partial y} = -\frac{1}{\rho}\frac{\partial p}{\partial y} + \upsilon\left(1 + \frac{1}{\beta}\right)\frac{\partial^2 v}{\partial x^2}, \tag{3}$$

$$u\frac{\partial T}{\partial x} + v\frac{\partial T}{\partial y} = \frac{k}{\rho C_p}\frac{\partial^2 T}{\partial y^2}, \tag{4}$$

$$u\frac{\partial C}{\partial x} + v\frac{\partial C}{\partial y} = D\frac{\partial^2 C}{\partial y^2} - Ck_1, \tag{5}$$

where υ is kinematic viscosity, β is Casson fluid parameter, ρ is density, σ is electrical conductivity, T is the temperature of the fluid, k is thermal conductivity, μ is dynamic viscosity, C is the concentration field, D is mass diffusion and k_1 is reaction rate.

2.1 Boundary Conditions

$$u = 0, v = \frac{V}{2}, C = C_2, T = T_2, \text{ at } y = H,$$

$$\frac{\partial u}{\partial y} = 0, v = 0, C = C_1, T = T_1, \text{ at } y = 0. \tag{6}$$

Eliminating the pressure P, from (2) to (3), we get

$$
\begin{aligned}
& u\frac{\partial^2 u}{\partial x \partial y} + \frac{\partial u}{\partial x}\frac{\partial u}{\partial y} + v\frac{\partial^2 u}{\partial y^2} + \frac{\partial v}{\partial y}\frac{\partial u}{\partial y} - u\frac{\partial^2 v}{\partial x^2} \\
& \quad - \frac{\partial u}{\partial x}\frac{\partial v}{\partial x} - \frac{\partial v}{\partial x}\frac{\partial v}{\partial y} - v\frac{\partial^2 v}{\partial x \partial y} \\
& = v\left(1 + \frac{1}{\beta}\right)\left(\frac{\partial^3 u}{\partial y^3} - \frac{\partial^3 v}{\partial x^3}\right) - \frac{\sigma B_0^2}{\rho}\frac{\partial u}{\partial y} \\
& \quad \pm \frac{\partial}{\partial y}[g(\beta_T(T - T_2) + \beta_C(C - C_2))]
\end{aligned}
\tag{7}
$$

2.2 Non-dimensionalisation

To obtain the dimensionless equations, the following parameters are introduced:

$$
\begin{aligned}
x^* &= \frac{x}{H}, y^* = \frac{y}{H}, u = -Vx^* f'(y^*), \\
v &= aVf(y^*), \theta(y^*) = \frac{T - T_2}{T_1 - T_2}, \\
\phi(y^*) &= \frac{C - C_2}{C_1 - C_2}.
\end{aligned}
\tag{8}
$$

With these parameters, Eqs. (7), (4) and (5) become,

The non-linear momentum and energy equations which are governing the proposed problem can be written as

$$\left(1 + \frac{1}{\beta}\right)f'''' - M^2 f'' + R\left[(2 - a)f' f'' - aff'''\right] \pm \lambda\left[\theta' + N\phi'\right] = 0, \tag{9}$$

$$\theta'' - a\Pr f\theta' = 0, \tag{10}$$

$$\phi'' - a\mathrm{Sc} f\phi' - \mathrm{Sc}\gamma(\phi + A) = 0, \text{ where } A = \frac{c_2}{c_1 - c_2}. \tag{11}$$

The boundary conditions reduce into

$$f(1) = \frac{1}{2}, \, f'(1) = 0, \, \theta(1) = 0, \, \phi(1) = 0,$$
$$f''(0) = 0, \, f(0) = 0, \, \theta(0) = 1, \, \phi(0) = 1. \tag{12}$$

where $M^2 = \sigma B_0^2 H^2 / \mu$ is Hartman number, $R = VH/\upsilon$ is Reynolds number ($R > 0$ for suction $R < 0$ for injection), $N = \beta_C(C_1 - C_2)/\beta_T(T_1 - T_2)$ is concentration of buoyancy parameter, $\lambda = Gr_x/R^2$ is the thermal buoyancy parameter, $Gr_x = VH^4 g \beta_T(T_1 - T_2)/x\upsilon^3$ is Grashof number, $Pr = \rho C_p H V/k$ is Prandtl number, $\gamma = k_1 H/\upsilon$ is chemical reaction rate and $Sc = HV/D$ is Schmidth number.

2.3   Analytical Solution by Perturbation Technique

We seek the solution of the above non-linear ordinary differential equations for the physical configuration by using classical perturbation technique in the form of assuming the solution of f, θ, ϕ as

$$f = f_{01} + R * f_{02} + a * f_{11} + R * a * f_{12},$$
$$\phi = \phi_0 + a * \phi_1,$$
$$\theta = \theta_0 + a * \theta_1,$$

with the boundary conditions,

$$f_0(1) = \frac{1}{2}, \, f_0'(1) = 0, \, f_1'(1) = 0, \, f_1(1) = 0, \, \theta_0(1) = 0,$$
$$\phi_0(1) = 0, \, \theta_1(1) = 0, \, \phi_1(1) = 0,$$
$$f_0''(0) = 0, \, f_0(0) = 0, \, f_1(0) = 0, \, \theta_0(0) = 1,$$
$$\phi_0(0) = 1, \, f_1''(0) = 0, \, \theta_1(0) = 0, \, \phi_1(0) = 0,$$
$$f_{01}(1) = \frac{1}{2}, \, f_{02}'(1) = 0, \, f_{01}(0) = 0,$$
$$f_{01}''(0) = 0, \, f_{01}'(1) = 0, \, f_{02}(1) = 0, \, f_{02}''(0) = 0, \, f_{02}(0) = 0,$$
$$f_{11}(1) = \frac{1}{2}, \, f_{11}'(1) = 0, \, f_{12}(1) = 0, \, f_{12}''(0) = 0,$$
$$f_{12}'(1) = 0, \, f_{11}''(0) = 0, \, f_{11}(0) = 0, \, f_{12}(0) = 0,$$

on solving these equations, we get

$$\left(1 + \tfrac{1}{\beta}\right) f_0'''' - M^2 f_0'' + 2R f_0' f_0'' \pm \lambda\left[\theta_0' + N\phi_0'\right] = 0,$$
$$\left(1 + \tfrac{1}{\beta}\right) f_{01}'''' - M^2 f_{01}'' \pm \lambda\left[\theta_{01}' + N\phi_{01}'\right] = 0,$$
$$\left(1 + \tfrac{1}{\beta}\right) f_{02}'''' - M^2 f_{02}'' + 2 f_{01}' f_{01}'' \pm \lambda\left[\theta_{02}' + N\phi_{02}'\right] = 0,$$
$$\left(1 + \tfrac{1}{\beta}\right) f_1'''' - M^2 f_1'' + R\left[2 f_1' f_0'' + 2 f_0' f_1'' - f_0' f_0'' - f_0 f_0'''\right] \pm \lambda\left[\theta_1' + N\phi_1'\right] = 0,$$
$$\left(1 + \tfrac{1}{\beta}\right) f_{11}'''' - M^2 f_{11}'' \pm \lambda\left[\theta_{11}' + N\phi_{11}'\right] = 0,$$
$$\left(1 + \tfrac{1}{\beta}\right) f_{12}'''' - M^2 f_{12}'' + 2 f_{11}' f_{01}' + 2 f_{11}'' f_{01}' - f_{!01}' f_{01}'' - f_{01} f_{01}'''' \pm \lambda\left[\theta_{12}' + N\phi_{12}'\right] = 0,$$
$$\theta_0'' = 0,$$
$$\theta_1'' - \Pr f_0 \theta_0' = 0,$$
$$\phi_0'' - \phi_0 - \mathrm{Sc}\gamma A = 0,$$
$$\phi_1'' - \mathrm{Sc} f_0 \phi_0' - \mathrm{Sc}\gamma \phi_1 = 0.$$

Solutions of these equations are given below. The constants involved in the solutions are not given for the want of space.

$$\begin{aligned}
\phi = {} & d_2 e^{d_1 y} + d_3 e^{-d_1 y} - A + a\big(d_{145} + d_{144} y + d_{78} e^{d_1 y} + d_{79} e^{-d_1 y} \\
& + d_{212} y e^{d_1 y} + d_{213} y e^{-d_1 y} + d_{214} y^2 e^{-d_1 y} + d_{215} y^2 e^{d_1 y} \\
& + d_{216} y^3 e^{-d_1 y} + d_{217} y^3 e^{d_1 y} + d_{218} e^{d_{87} y} + d_{219} y e^{d_{87} y} \\
& + d_{220} e^{d_{89} y} + d_{221} e^{2 d_1 y} + d_{222} y e^{d_{116} y} + d_{223} e^{d_{166} y} \\
& + d_{224} y e^{d_{117} y} + d_{225} e^{d_{117} y} + d_{226} y e^{d_{89} y} + d_{227} e^{-2 d_1 y} \\
& + d_{155} e^{d_{92} y} + d_{156} e^{d_{94} y} + d_{161} e^{d_{97} y} + d_{162} e^{d_{99} y} \\
& + d_{163} e^{d_{101} y} + d_{164} e^{d_{103} y} + d_{165} e^{d_{105} y} + d_{166} e^{d_{107} y} \\
& + d_{167} e^{3 d_1 y} + d_{168} y^2 e^{d_{87} y} + d_{171} y^2 e^{d_{89} y} + d_{177} e^{d_{121} y} \\
& + d_{178} e^{d_{123} y} + d_{179} y^4 e^{d_1 y} + d_{183} y e^{2 d_1 y} + d_{194} e^{d_{127} y} \\
& + d_{195} e^{d_{129} y} + d_{196} e^{d_{137} y} + d_{197} e^{d_{131} y} + d_{198} e^{d_{133} y} \\
& + d_{199} e^{d_{135} y} + d_{200} e^{-3 d_1 y} + d_{203} y^2 e^{d_{117} y} + d_{206} y^2 e^{-d_1 y} \\
& + d_{210} y e^{-2 d_1 y} + + d_{201} y^2 e^{d_{116} y}\big)
\end{aligned}$$

$$\begin{aligned}
\phi = {} & d_4 + d_5 y + a\big(d_{228} + d_{229} y + d_{230} y^2 + d_{231} y^3 \\
& + d_{232} y^4 + d_{257} y^5 + d_{262} e^{d_7 y} + d_{263} e^{-d_7 y} + d_{264} e^{d_1 y} \\
& + d_{265} e^{-d_1 y} + d_{266} y e^{d_7 y} + d_{267} y e^{-d_7 y} + d_{237} e^{d_{15} y} \\
& + d_{238} e^{-d_{15} y} + d_{243} e^{d_{24} y} + d_{244} e^{d_{28} y} + d_{245} e^{d_{30} y} \\
& + d_{246} e^{-d_{32} y} + d_{247} e^{2 d_7 y} + d_{248} e^{-2 d_7 y} + d_{249} e^{2 d_1 y} \\
& + d_{250} e^{-2 d_1 y} + d_{258} y e^{d_1 y} + d_{260} y e^{-d_1 y} \\
& + d_{251} y^2 e^{d_1 y} + d_{254} y^2 e^{-d_1 y}\big)
\end{aligned}$$

$$\begin{aligned}
f = {} & d_8 + d_9 y + d_{10} e^{d_7 y} + d_{11} e^{-d_7 y} + d_{12} y^2 \\
& + d_{13} e^{d_1 y} + d_{14} e^{-d_1 y} + R\big(d_{16} + d_{17} y + d_{18} e^{d_{15} y} \\
& + d_{19} e^{-d_{15} y} + d_{42} y^2 + d_{43} y e^{d_7 y} + d_{44} y e^{-d_7 y} \\
& + d_{45} e^{d_{24} y} + d_{46} e^{d_1 y} + d_{47} e^{d_1 y} + d_{48} e^{d_{28} y} \\
& + d_{49} e^{d_{30} y} + d_{50} e^{-d_{32} y} + d_{51} e^{2 d_7 y} + d_{52} e^{-2 d_7 y} \\
& + d_{53} e^{2 d_1 y} + d_{54} e^{-2 d_1 y} + d_{58} y^2 e^{d_7 y} + d_{59} y e^{d_7 y} \\
& + d_{63} y^2 e^{-d_7 y} + d_{64} y e^{-d_7 y} + d_{70} y e^{d_1 y} + d_{65} y^3 + d_{71} e^{d_1 y} \\
& + d_{77} e^{-d_1 y} + d_{76} y e^{-d_1 y}\big) \\
& + a\big(d_{268} + d_{269} y + d_{270} e^{d_7 y} + d_{271} e^{-d_1 y} + d_{447} y^2 \\
& + d_{448} y^3 + d_{449} y^4 + d_{300} y^5 + d_{302} y^6 + d_{450} e^{d_1 y} \\
& + d_{451} e^{-d_1 y} + d_{452} y e^{d_7 y} + d_{453} y e^{-d_7 y} \\
& + d_{154} y^2 e^{d_7 y} + d_{155} y^2 e^{-d_7 y} + d_{441} y^3 e^{d_7 y} \\
& + d_{444} y^3 e^{-d_7 y} + d_{456} y e^{d_1 y} + d_{457} y e^{-d_1 y} + d_{458} y^2 e^{d_1 y} \\
& + d_{459} y^2 e^{-d_1 y} + d_{460} y^3 e^{d_1 y} + d_{461} y^3 e^{-d_1 y} + d_{393} y^4 e^{d_1 y} \\
& + d_{4270} y^4 e^{-d_1 y} + d_{462} e^{d_{87} y} + d_{463} e^{d_{89} y} + d_{464} e^{d_{116} y} \\
& + d_{465} e^{d_{117} y} + d_{466} y e^{d_{87} y} + d_{467} y e^{d_{89} y} + d_{468} e^{-2 d_1 y} \\
& + d_{469} e^{2 d_1 y} + d_{470} y e^{d_{117} y} + d_{471} y e^{d_{117} y} + d_{419} y^2 e^{d_{117} y} \\
& + d_{432} y^2 e^{d_{116} y} + d_{439} y e^{-2 d_1 y} + d_{374} e^{d_{72} y} + d_{375} e^{d_{94} y} \\
& + d_{376} e^{d_{97} y} + d_{377} e^{d_{99} y} + d_{378} e^{d_{101} y} + d_{379} e^{d_{103} y} + d_{380} e^{d_{105} y} \\
& + d_{381} e^{d_{107} y} + d_{382} e^{3 d_1 y} + d_{386} y^2 e^{d_{89} y} + d_{389} e^{d_{121} y} + d_{390} e^{d_{123} y} \\
& + d_{402} y e^{2 d_1 y} + d_{404} e^{d_{127} y} + d_{405} e^{d_{129} y} + d_{406} e^{d_{137} y} + d_{407} e^{d_{131} y} \\
& + d_{408} e^{d_{133} y} + d_{409} e^{d_{135} y} + d_{410} e^{-3 d_1 y} + d_{411} y e^{d_{15} y} + d_{412} e^{d_{24} y} \\
& + d_{413} y e^{-d_1 5 y} + d_{414} e^{d_{28} y} + d_{415} e^{d_{30} y} \\
& + d_{416} e^{2 d_7 y} + d_{417} e^{-d_{32} y}\big)
\end{aligned}$$

.

3 Result and Discussion

The governing equation for physical configuration of channel flow for Casson fluid of heat and mass has derived. The 2D model has been converted from (x, y) coordinates to a single coordinate system using similarity transformation, i.e., (u, v) of velocity component along x and y has been converted to a function of dependent variable f which satisfy continuity equation of the fluid flow model. By the analytical approach using regular perturbation technique, we modified the governing PDEs to a set of
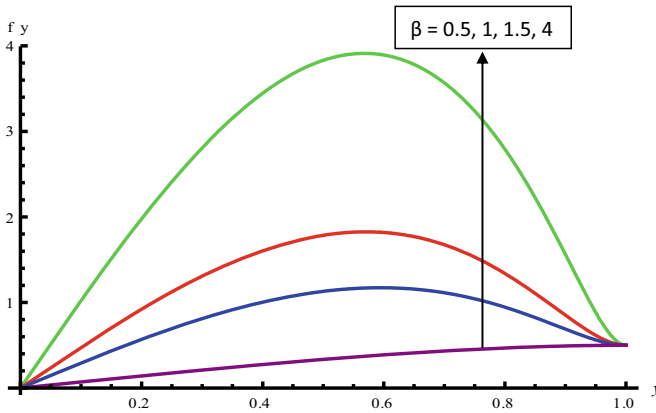
Fig. 1 Effect of Casson parameter (β)

simultaneous ODEs with perturbation parameter 'a'. Similarly, the corresponding boundary conditions of physical model are also converted in terms of the perturbation parameter. In total, we obtained the analytical expressions for six set of ODEs and obtained the complete solution for these ODEs.

The computation work is been carried out to find the characteristics of velocity, temperature and concentration which are the functions of non-dimensional parameters Reynolds number R, Hartman number M^2, Casson parameter β, buoyancy parameter λ, chemical reaction rate γ, concentration buoyancy parameter N, Prandtl number Pr, Schmidt number Sc on concentration, temperature and velocity have been studied. The solution of these parameters are presented graphically and discussed.

The effect of these parameters are more on velocity compared to concentration and temperature because of the above assumptions, in case of Casson parameter, the fluid flow changes from non-Newtonian to Newtonian as β increases, velocity profile decreases with increase in the value of Casson parameter due to non-Newtonian character of the fluid this can be seen in Fig 1. Figure 2 indicates the effect of Buoyancy parameter on velocity, where velocity decreases with increase in Buoyancy parameter. The effect of Hartmann number on velocity is seen in Fig. 3 Hartmann number decreases the flow as it offers resistance to the fluid. Figure 4 shows the effect of perturbation parameter, as the perturbation parameter is increased the velocity also increases. This results in the fact that the flow can be controlled by perturbation parameter. Figure 5 indicates the effect of Reynolds number, velocity increases with increases in Reynolds number this is due to decrease in viscosity. Figure 6 shows the effect of concentration buoyancy parameter (N), where it increases the velocity profile with increase in N. Effect of chemical reaction (γ) increases the concentration profile but there is no much effect of chemical reaction on temperature and velocity is observed in Fig. 7. The increasing effect of Prantdl number decreases the velocity profile and there is no much variation seen in temperature profile related to the Prantdl number (Pr) is seen in Fig. 8. Figure 9 shows the increasing effect of Schmidt number
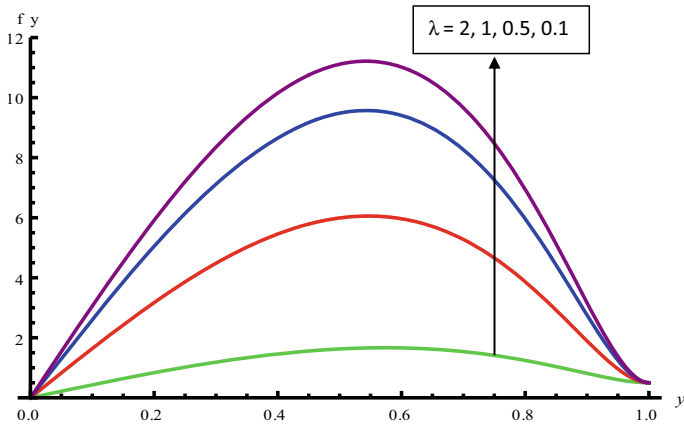
Fig. 2 Effect of Buoyancy parameter (λ)

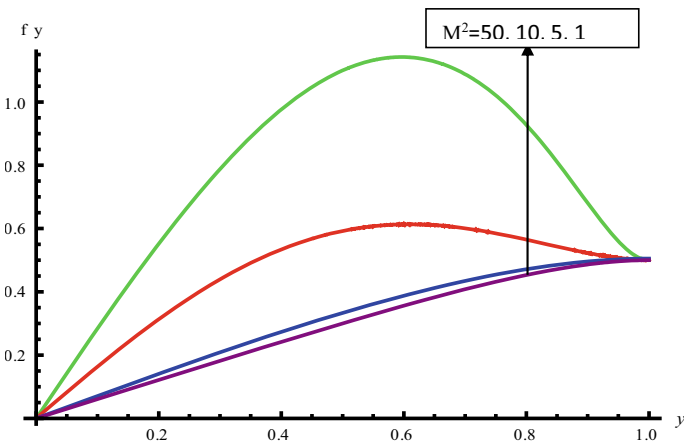**Fig. 3** Effect of Hartmann number (M^2)

(Sc) increases the magnitude of the concentration profile. The results obtained are good agreement with the previous work of multiple solutions of mixed convective MHD Casson fluid flow in a channel by Jawad Raza et al. [15] if we consider the perturbation parameter (a) equals to 1.

4 Conclusion

- The variation of velocity verses the non-dimensional axis of the horizontal channel from 0 to 1. The increasing effect of Casson parameter β will diminish the
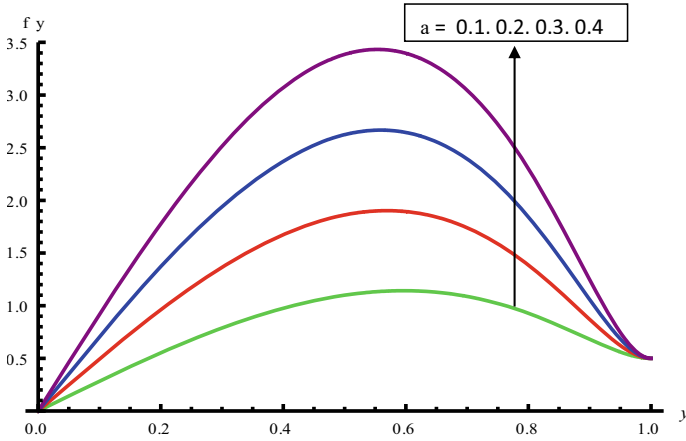
Fig. 4 Effect of perturbation parameter (a)
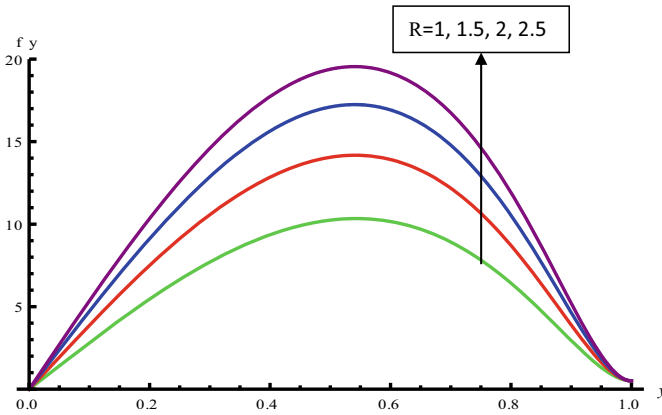
Fig. 5 Effect of Reynolds number (R)

magnitude of the velocity in a higher rate at the lower values of β compared to that of higher values. This behaviour is due to the non-Newtonian fluid of Casson on the flow which indicates the rigidity of the fluid property on the motion. The effect of β is not seen much variation in case of temperature and concentration, since in this work we are neglected the direct effect of velocity on temperature and concentration.

• The increasing effect of Buoyancy parameter (λ) and Reynolds number (R) will increase the magnitude of the velocity in a higher rate at the lower values of λ and R.
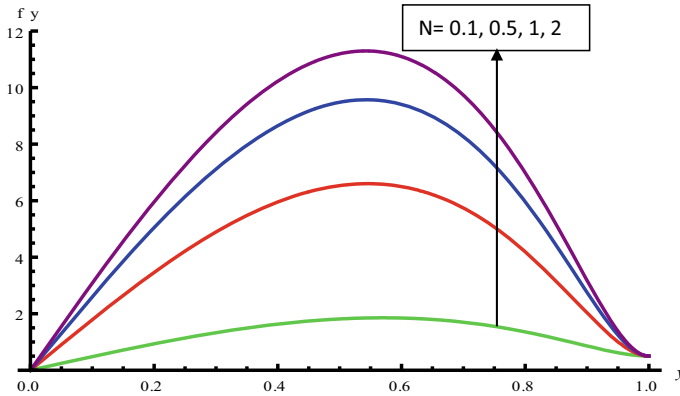
Fig. 6 Effect of concentration buoyancy parameter (N)
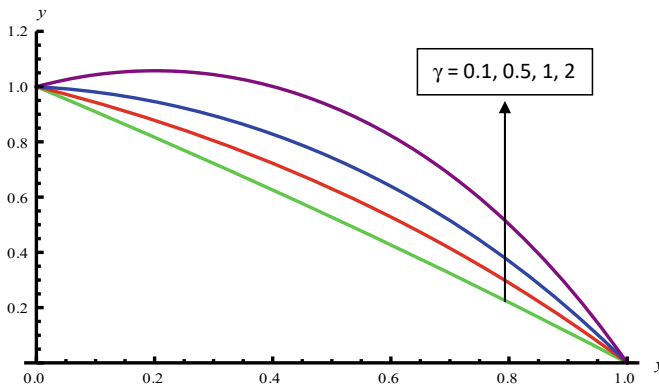
Fig. 7 Effect of chemical reaction (γ)

- The increasing effect of Hartmann number (M^2) will diminish the magnitude of the velocity in a higher rate at the lower values of M^2 compared to that of higher values, and this is due to magnetic field which enhances the viscosity of the fluid.
- The increasing effect of perturbation parameter will increase the magnitude of the velocity in a higher rate at the lower values of perturbation parameter.
- The increasing effect of concentration buoyancy parameter (N) will increase the magnitude of the velocity with increasing value of N.
- The increasing effect of chemical reaction rate (γ) will increase the magnitude of the concentration profile.
- The increasing effect of Prandtl number (Pr) decreases the magnitude of the velocity in a higher rate at the lower values of Pr due to high viscosity.
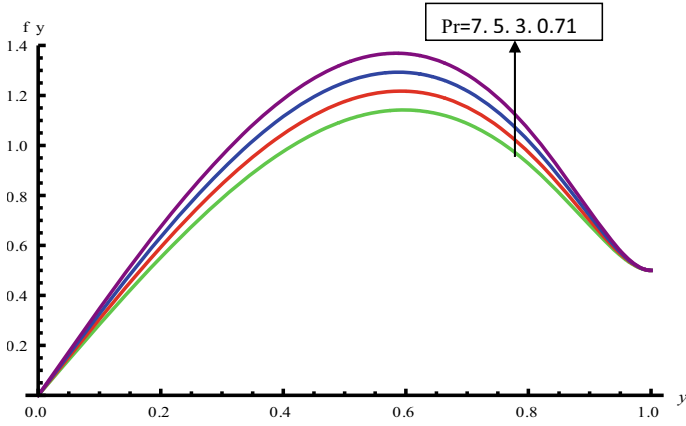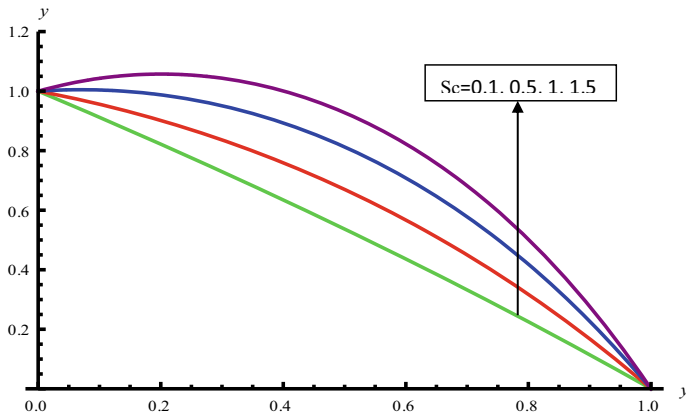
Fig. 8 Effect of Prandtl number (Pr)

Fig. 9 Effect of Schmidt number (Sc)

- The increasing effect of Schmidt number (Sc) will increase the magnitude of the concentration profile.

References

1. Ramesh K, Devakar M (2015) Some analytical solutions for flows of Casson fluid with slip boundary conditions. Ain Shams Eng J 6(3):967–975
2. Mc Donald D (1974) Blood flows in arteries, 2nd ed. Arnold, London, UK
3. Merrill EW, Benis AM, Gilliland ER, Sherwood TK, Salzman EW (1965) Pressure-flow relations of human blood in hollow fibers at low flow rates. J Appl Physiol 20(5):954–967
4. Casson M (1959) A flow equation for pigment-oil suspensions of the printing ink type. In: Mills CC (ed) Rheology of disperse systems. Pergamon, Oxford, USA, pp 84–104
5. Tao LN (1960) On combined free and forced convection in channels. J Heat Transf 82(3):233–238
6. Walawender WP, Chen TY, Cala DF (1975) An approximate casson fluid model for tube flow of blood. Bioheology 12(2):111–119
7. Batra RL, Jena B (1991) Flow of a Casson fluid in a slightly curved tube. Int J Eng Sci 29(10):1245–1258
8. Eldabe NTM, Salwa MGE (1995) Heat transfer of MHD non-Newtonian Casson fluid flow between two rotating cylinders. J Phys Soc Jpn 64:41–64
9. Attia HA, Sayed-Ahmed ME (2010) Transient MHD couette flow of a Casson fluid between parallel plates with heat transfer. Italian J Pure Appl Math 27:19–38
10. Si X, Zheng L, Lin P, Zhang X, Zhang Y (2013) Flow and heat transfer of a micro polar fluid in a porous channel with expanding or contracting walls. Int J Heat Mass Transf 67:885–895
11. Reddy C, Rao CV, Surender O (2015) Soret, joule heating and hall effects on free convection in a Casson fluid saturated porous medium in a vertical channel in the presence of viscous dissipation. Procedia Eng 127:1219–1226
12. Afikuzzaman M, Ferdows M, Alam MM (2015) Unsteady MHD casson fluid flow through a parallel plate with hall current. Procedia Eng 105:287–293
13. Das M, Mahato R, Nandkeolyar R (2015) Newtonian heating effect on unsteady hydro magnetic Casson fluid flow past a flat plate with heat and mass transfer. Alexandria Eng J 54(4):871–879
14. Kataria HR, Patel HR (2016) Radiation and chemical reaction effects on MHD Casson fluid flow past an oscillating vertical plate embedded in porous medium. Alexandria Eng J 55:583–595
15. Raza J, Rohni AAM, Omar Z (2016) Multiple solutions of mixed convective MHD Casson fluid flow in a channel. J Appl Math 7535793

D-Shaped Biosensor with MoS$_2$ as a Sensing Layer Using a Photonic-Crystal Fiber

Melwin Gnanasekaran and Senthilnathan Krishnamoorthy

Abstract We design a D-shaped photonic-crystal fiber (PCF) based on surface plasmon resonance (SPR) for the detection of cancer cells. It is coated with layers of gold (Au) and molybdenum disulfide (MoS$_2$). Au layer is used to accurately determine the spectral sensitivity in the visible region. The analyte is placed over MoS$_2$ layer. The sensitivity of the sensor is enhanced with the help of MoS$_2$. The designed sensor is highly suitable for detecting cancer cells having refractive indices 1.45 and 1.46. The proposed sensor exhibits a maximum sensitivity of 3000 nm/RIU.

Keywords D-shaped photonic-crystal fiber · Surface plasmon resonance · Liquid-filled core

1 Introduction

Cancer is a deadly disease that affects millions of people across the globe which has caused about 14.6% of human deaths every year. It is the abnormal growth of cells which have the probability of invading or spreading to other body parts. The common types of cancers are blood, mouth, lung, prostate, cervical, skin cancers, etc. Detection of cancer in its early stage is not usually performed due to high cost detection techniques and complicated procedures. According to cancer biology, the refractive index (RI) of cancer cells is relatively higher than that of the normal cells [1]. There are several techniques to determine the RI of the cancer cells such as solution matching [2], Fabry–Perot resonant cavity [3], etc. In this paper, we consider the leukemia cells [1] whose RI ranges from 1.45 to 1.48 which depend on the stage of the cancer.

Surface plasmon resonance is an optical technique used in different fields for various applications. For the first time, SPR was observed by Wood in 1902 [4]. This technique is based on the principle of total internal reflection (TIR). When a beam of plane-polarized light is incident on a metal–dielectric interface with medium of high

M. Gnanasekaran · S. Krishnamoorthy (✉)
Department of Physics, School of Advanced Science, Vellore Institute of Technology, Vellore, Tamil Nadu 632014, India
e-mail: senthee@gmail.com

RI, TIR occurs, but some of the energy is absorbed by the metal–dielectric region in the form of evanescent waves which, in turn, excites the plasmons present on the surface of the metal. When both the energy and momentum of the surface plasmon waves and incident light match, resonance occurs. These excited plasmons react with the analyte which results in change in intensity of the reflected beam of light, i.e., a sharp dip in intensity of the reflected beam [5]. This sharp dip in intensity of the reflected beam helps to detect cancer-affected cells of different refractive indices.

PCF is a type of optical fiber with several unique properties that cannot be achieved in normal optical fibers. Photonic crystals are dielectrics constructed with microscopic air holes arranged in a periodic array that runs throughout the fiber [6]. Thus, a PCF is a combination of properties of photonic crystals and optical fibers. The cladding is made up of photonic crystals surrounding the core. It is difficult to find the mode which produces the excitation of surface plasmons. Hence, we choose a single-mode fiber to enhance the excitation of surface plasmons. This can also be achieved by the help of a D-shaped PCF in which some part of the cladding region is removed by polishing any region of the cladding side of the fiber. This helps in reducing the effective distance traveled by the evanescent waves through the interface to excite the surface plasmons present on the metal surface [7].

A layer of gold is deposited on the flat surface of the polished fiber. Au is an active metal which displays a narrow width of SPR curve and helps in efficient detection accuracy. The plasma frequency of Au falls in the visible region of the electromagnetic spectrum. It is chemically stable when compared to other active metals and shows a higher resonance shift. The imaginary part of the dielectric constant of the metal decides the sharpness of the resonance curve.

A layer of MoS_2 is coated over the Au layer. It is an inorganic compound composed of molybdenum and sulfide. MoS_2 is, in general, used to enhance the sensitivity of the sensor. It has larger surface-to-volume ratio and thereby can interact with more number of analyte atoms in the analyte channel.

2 Design and Geometrical Parameters

We design a D-shaped PCF to detect cancer cells. Figure 1 shows the cross-sectional view of the designed structure which describes a D-shaped PCF with numerous air holes of diameter 1.2 μm. A thin layer of gold is coated followed by a layer of MoS_2. The analyte channel is placed above the MoS_2 layer. The thickness of the gold layer, MoS_2 and analyte channel is 40 nm, 1.3 nm and 80 nm, respectively.

The Sellmeier equation [8] can be used to determine the RI of the pure silica cladding, and the same is given by

$$n_1(\lambda) = \sqrt{1 + \frac{a_1\lambda^2}{\lambda^2 - b_1^2} + \frac{a_2\lambda^2}{\lambda^2 - b_2^2} + \frac{a_3\lambda^2}{\lambda^2 - b_3^2}} \qquad (1)$$
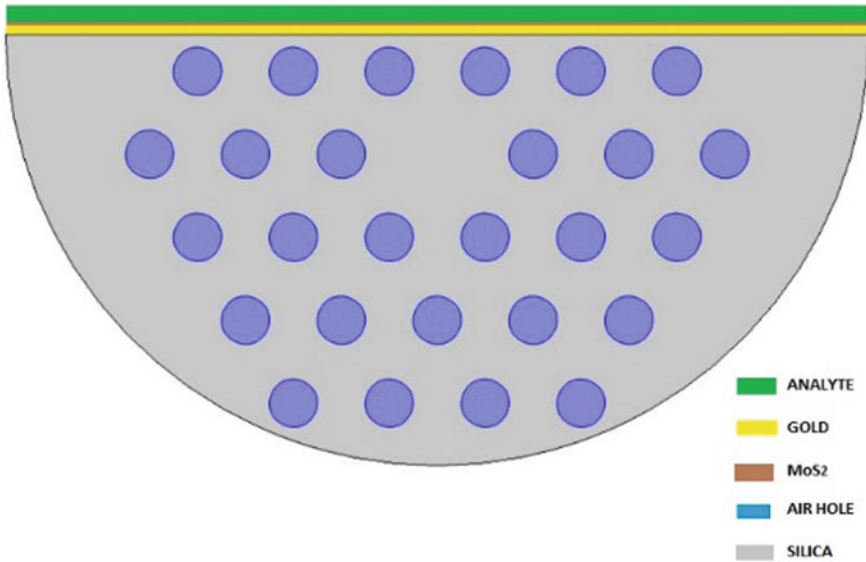
Fig. 1 Cross-sectional design of the sensor

The dispersion model can be used to determine the RI of gold, and the corresponding expression is

$$\varepsilon(\lambda) = \varepsilon_\infty - \frac{\lambda^2 \lambda_c}{\lambda_p^2 (\lambda_c + i\lambda)}$$
(2)

Here, λ_p and λ_c are the dispersion coefficients in micrometers. λ_p is the plasma frequency for the corresponding wavelength, and λ_c is the collision wavelength, and it is related to loss. The MoS₂ layer thickness can be calculated as $N \times 0.65$ nm, ($N =$ number of MoS₂ layers). The dispersion relation of MoS₂ is fitted with the polynomial equations.

The dispersion relation for MoS₂ is given as [9]

$$n_{\text{MoS}_2} = n_{\text{real MoS}_2} + i n_{\text{img MoS}_2}$$
(3)

Here, the real part is expressed as

$$n_{\text{real MoS}_2} = p_0 + p_1 * \lambda + p_2 * \lambda^2 + p_3 * \lambda^3 + p_4 * \lambda^4 + p_5 * \lambda^5$$
(4)

Similarly, imaginary part is given by

$$n_{\text{img MoS}_2} = s_0 + s_1 * \lambda + s_2 * \lambda^2 + s_3 * \lambda^3 + s_4 * \lambda^4 + s_5 * \lambda^5$$
(5)

Here, various coefficients are determined by using curve fitting,

$$p_0 = -2481.6, \quad p_1 = 18.465,$$
$$p_2 = -0.052872, \quad p_3 = 7.2283 \times 10^{-5},$$
$$p_4 = -4.6339 \times 10^{-8} \text{ and } p_5 = 1.07267 \times 10^{-11}$$

Similarly, the other set of coefficients is determined to be,

$$s_0 = -27.239, \quad s_1 = -0.60969,$$
$$s_2 = 0.0056183, \quad s_3 = -1.6447 \times 10^{-5},$$
$$s_4 = 2.0377 \times 10^{-8} \text{ and } s_5 = -9.2194 \times 10^{-12}$$

Here, the wavelength λ is measured in nanometers. The PCF is designed in such a way that it has to enhance detection accuracy. We design the PCF with COMSOL Multiphysics v 5.2.

3 Results and Discussions

Confinement loss is defined as the transfer from the core region to the analyte region. The following expression is used to calculate the confinement loss.

$$\alpha(\text{dB/m}) = \frac{40\pi \, \text{Im}(n_{\text{eff}})}{\ln(10)\lambda} \tag{6}$$

Here,

$\text{Im}(n_{\text{eff}})$　Imaginary part of the effective RI of the fundamental mode.
λ　　　　　Operating wavelength (nm).

The spectral sensitivity is calculated by using the following formula.

$$S = \frac{\Delta\lambda}{\Delta n_{\text{a}}} \text{ nm/RIU} \tag{7}$$

Here,

λ　Operating wavelength (nm)
n_{a}　RI of the analyte used.

Figure 2 represents the mode field distribution of the fundamental mode which is highly required to compute the loss spectra for various analytes. Figure 3 describes the difference in the confinement loss of two different values of the analytes ($n = 1.45$ and 1.46). It is clearly seen that the confinement loss curve is shifted toward the higher wavelength for increase in the refractive index. The less transfer of energy

Fig. 2 Fundamental mode distribution at 720 nm
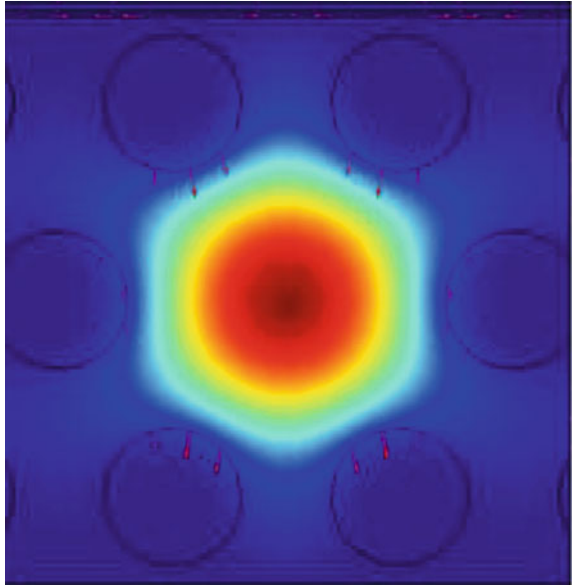
Fig. 3 Variation of loss with different RI of the analyte
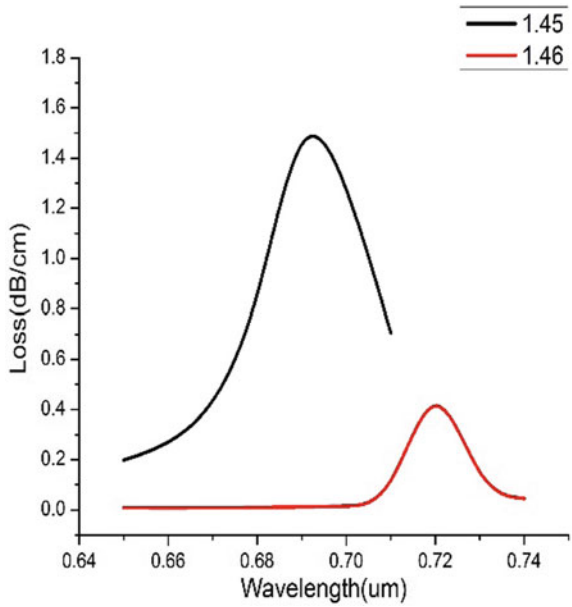
from the core region to the analyte region attributes the low loss. The maximum loss for the analyte of refractive index 1.45 is 1.65742 dB/cm at 690 nm. And the maximum loss for $n_a = 1.46$ is 0.59892 dB/cm at 720 nm.

4 Conclusion

We have designed a D-shaped PCF sensor for the detection of cancer cells, and its loss spectrum is measured. The spectral sensitivity of the sensor has been studied for the leukemia affected blood cells with refractive indices of 1.45 and 1.46. A maximum sensitivity of 3000 nm/RIU has been observed for the designed sensor. Further, this can be developed to optimize the sensor for a wide range of analytes in the visible spectrum which would be a promising tool for sensing applications.

References

1. Choi WJ, Jeon DI, Ahn SG, Yoon JH, Lee BH (2010) Full-field optical coherence microscopy for identifying live cancer cells by quantitative measurement of refractive index distribution. Opt Express 18:23285–23295. https://doi.org/10.1364/oe.18.023285
2. Kanso M, Cuenot S, Louran G (2007) Roughness effect on the SPR measurements for an optical fibre configuration: experimental and numerical approaches. J Opt A Pure Appl Opt 19:586. https://doi.org/10.1088/1464-4258/9/7/008
3. Dash JN, Jha R (2014) SPR biosensor based on polymer PCF coated with conducting metal oxide. IEEE Photon Technol Lett 26(6):595–598. https://doi.org/10.1109/lpt.2014.2301153
4. Wood RW (1902) On a remarkable case of uneven distribution of light in a diffraction grating spectrum. Proc Phys Soc London 18:269. https://doi.org/10.1088/1478-7814/18/1/325
5. Gupta BD, Verma RK (2009) Surface plasmon resonance based fiber optic sensors: principle, probe designs, and some applications. J Sens. https://doi.org/10.1155/2009/979761
6. Russell P (2003) Photonic crystal fibers. Science 299:358–362. https://doi.org/10.1126/science.1079280
7. Choi SH, Young LK, Kyung MB (2011) Graphene-on-silver substrates for sensitive surface plasmon resonance imaging biosensors. Opt Express 19:458–466. https://doi.org/10.1364/oe.19.000458
8. Adams MJ (1981) An introduction to optical waveguides, 14. Wiley, New York
9. Mishra AK, Mishra SK, Verma RK (2016) Graphene and beyond graphene MoS2: a new window in surface-plasmon-resonance-based fiber optic sensing. J Phys Chem C 120(5):2893–2900. https://doi.org/10.1021/acs.jpcc.5b08955

Surface Plasmon Resonance-Based Photonic Crystal Fiber Sensor with Selective Analyte Channels and Graphene-Indium Tin Oxide Deposited Core

Nivedha Sambathu and Senthilnathan Krishnamoorthy

Abstract We design a refractive index (RI) based triple core photonic crystal fiber sensor, which works on the principle of surface plasmon resonance. The analyte to be sensed is placed inside all the three cores. The middle core is surrounded by a layer of graphene, followed by a layer of Indium tin oxide (ITO). ITO is used as the bio-sensing layer for operating in the infrared region. The graphene layer is used to enhance the sensitivity of the proposed sensor. Numerical results corroborate that the proposed sensor exhibits a maximum sensitivity of 2000 nm/RIU when refractive index of the analyte, n_a is increased from 1.44 to 1.48.

Keywords Surface plasmon · Photonic crystal fiber · Sensor · Analyte

1 Introduction

For the first time, R. W. Wood observed the surface plasmon resonance (SPR) phenomena in 1902 [1]. In this technique, when the plane polarized light is incident at the interface between the dielectric and metal region, electrons get excited and they undergo oscillation along the interface [2]. Such waves are called as surface plasmon (SP) waves. When the light is incident at an angle greater than the critical angle, the excitation of SPs results in a reduced reflected light intensity. The angle at which a dip is observed in the reflected intensity of light is known as the resonant angle. It is well known that the propagation of light in a fiber optic medium is based on the principle of total internal reflection and so is the excitation of SPs. A resonance occurs when the frequency of the incident wave matches with the frequency of the SP waves. This process ultimately results in a considerable loss in the reflected light intensity. The resonance condition depends on the thickness and the dielectric constants of

N. Sambathu
School of Electronics Engineering, Vellore Institute of Technology, Vellore 632014, Tamil Nadu, India

S. Krishnamoorthy (✉)
Department of Physics, School of Advanced Science, Vellore Institute of Technology, Vellore 632014, Tamil Nadu, India
e-mail: senthee@gmail.com

both metal and dielectric. A minimal change in the RI of the surrounding medium leads to change in the intensity of the SPR signal, which can be used to detect the biomolecules and to study the interaction of surface molecules in real time.

Photonic crystal fiber (PCF) is one of the special optical fibers which possesses a series of unique properties which are not available in conventional optical fibers [3]. It is well known that PCF combines the properties of optical fibers and photonic crystals. PCF is made up of a low-loss cladding region where in the air holes are periodically arranged. The core region is formed by creating a defect in the periodic arrangement of air holes. In this paper we choose a single mode fiber to enhance the excitation of surface plasmons. The number of air holes is increased in order to get a tight confinement at the core.

Graphene is an allotrope of carbon which is thinnest and strongest man made inorganic compound. It has large carrier mobility, large field enhancement and large surface area which helps in higher absorption of biomolecules. More over fabrication of graphene is relatively cheap and easy. Thus graphene is used to enhance the sensing property of the proposed sensor.

Majority of the available SPR sensors are constructed in the visible region by using gold and silver as the active materials [4]. Gold and silver have their peak absorptions in the visible region. Most of the bio-molecules have their absorption in the infrared (IR) region [5] and Indium tin oxide (ITO) also has its absorption wavelength at IR region. So we use ITO as an active metal layer. With the change in doping concentration of tin oxide and indium oxide, the plasma frequency of ITO can be tuned in the desired operating wavelength range [6].

2 Structure and Theoretical Modeling

In this paper, we design a triple core PCF. The geometry of the triple core sensor is shown in Fig. 1. There are three cores filled with liquid that form a straight line with

Fig. 1 Cross—section of the triple core sensor
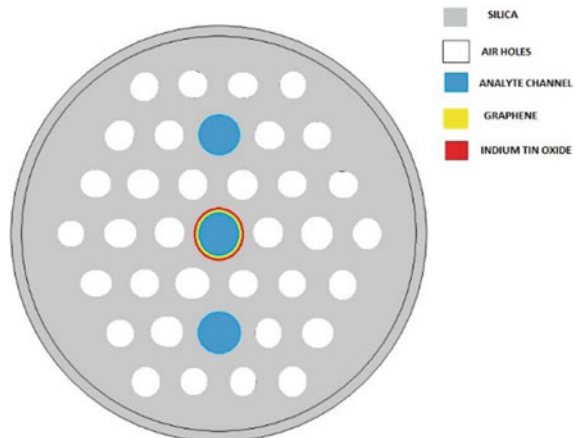
the central core. It has numerous air holes with a diameter of 0.95 µm. The air holes are arranged in a triangular lattice with a pitch value of $\Lambda = 1.90$ µm. The diameter of all the three cores is 1.52 µm. The center core is coated by a 3 nm graphene layer followed by a 30 nm Indium tin oxide layer. The RI of sample is changed from 1.44 to 1.48 [7]. The surface plasmon resonance occurs at the center core. The plasmonic mode occurs at the Indium tin oxide-graphene layer interface and the analyte.

The RI of the silica cladding is calculated using the Sellmeier's equation [8]

$$n(\lambda) = \sqrt{1 + \frac{a_1\lambda^2}{\lambda^2 - b_1^2} + \frac{a_2\lambda^2}{\lambda^2 - b_2^2} + \frac{a_3\lambda^2}{\lambda^2 - b_3^2}}. \tag{1}$$

The Sellmeier constants a_1, a_2, a_3, b_1, b_2 and b_3 for fused silica are 0.69616300, 0.407942600, 0.897479400, 0.00467914826, 0.0135120631 and 97.9340025, respectively. The refractive index of Indium tin oxide was computed by the Drude model [9] as follows

$$\varepsilon(\lambda) = \varepsilon_\infty - \frac{\lambda^2\lambda_c}{\lambda_p^2(\lambda_c + i\lambda)} \tag{2}$$

Here, λ_p and λ_c are the dispersion coefficients in micrometres. λ_p is the plasma frequency for the corresponding wavelength ($\lambda_p = 0.56497$) and λ_c is the collision wavelength ($\lambda_c = 11.21076$) and is loss related. Here the wavelength λ is measured in micrometres.

The graphene RI is obtained using following equation,

$$n_g = 3 + i\frac{C_1}{3}\lambda \tag{3}$$

Here λ denotes wavelength and $C_1 \approx 5.446 \mu m^{-1}$.

The PCF has been designed in such a way to enhance detection accuracy and for maximum confinement. We employ finite element method to study the mode propagation of the proposed sensor, by including a perfectly matched layer boundary conditions to minimise the scattering radiation. We designed the PCF with COMSOL multiphysics v4.4.

Figures 2 and 3 represent the electric field distribution of the fundamental and the surface plasmon mode, respectively. These modes are highly useful to compute the loss spectra for analyte of RI, $n_a = 1.44$ at 1.5 µm wavelength.

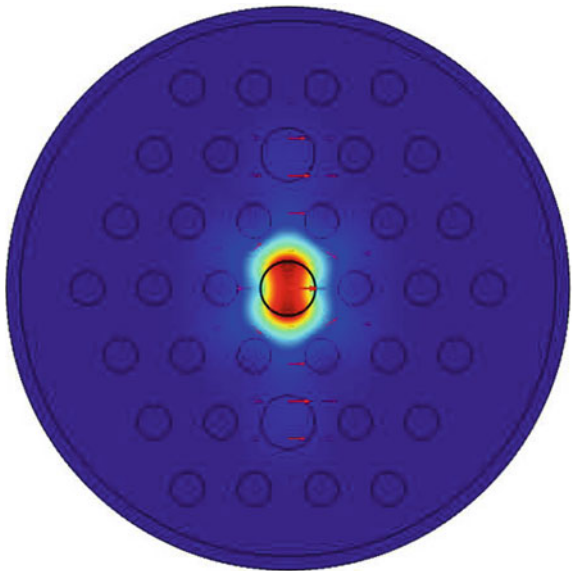## 3 Results and Discussions

Confinement loss is calculated using the following expression.

Fig. 2 Fundamental mode at
1.5 μm
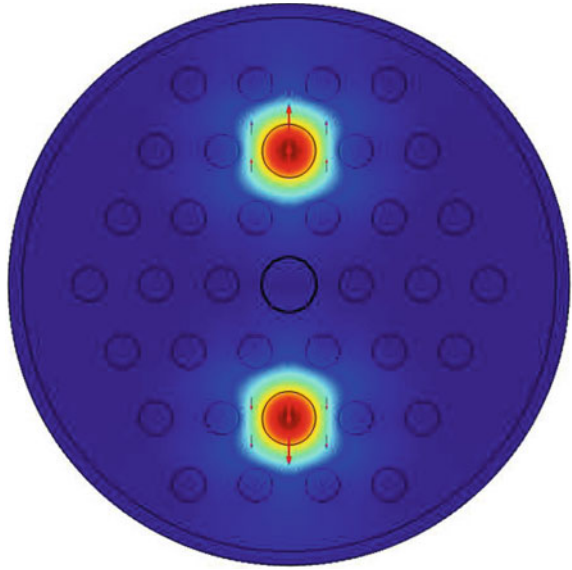
Fig. 3 Surface plasmon
mode at 1.5 μm

$$\alpha(\text{dB/m}) = \frac{40\pi \, \text{Im}(n_{\text{eff}})}{\ln(10)\lambda} \tag{4}$$

Here, $\text{Im}(n_{\text{eff}})$ represents the imaginary part of the effective RI of the fundamental
mode which accounts for the loss and λ is the operating wavelength.

Figure 4 depicts the variation of the confinement loss for different values of the analytes ($n = 1.44, 1.45, 1.46, 1.47, 1.48$). It is clearly seen that the loss peak shifts towards the higher wavelength for the increase in the RI of analyte (Table 1).

The spectral sensitivity is calculated by using the following formula.

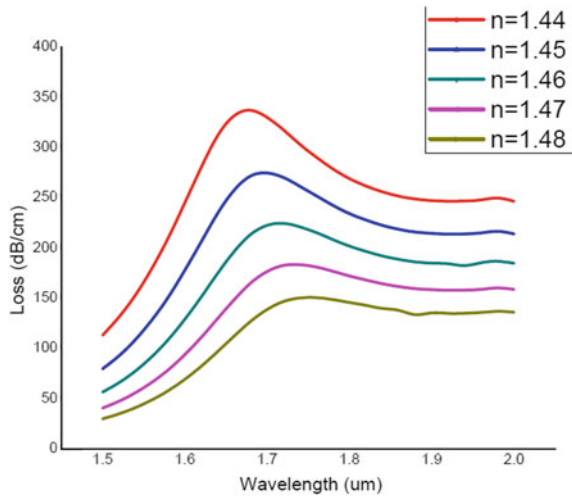$$S = \frac{\Delta\lambda_{peak}}{\Delta n_a} \text{ nm/RIU} \tag{5}$$

Here,

$\Delta\lambda_{peak}$ shift in peak wavelength
Δn_a change in RI of analyte

The proposed sensor exhibits maximum sensitivity of 2000 nm/RIU.

Fig. 4 Loss peak for various analyte refractive index, from 1.44 to 1.48

Table 1 Loss peak for different RIs of analyte

RI of analyte	Wavelength (μm)	Loss peak (dB/cm)
1.44	1.68	337.21
1.45	1.70	271.71
1.46	1.72	224.56
1.47	1.74	183.39
1.48	1.76	150.59

4 Conclusion

We have proposed a triple core PCF based SPR sensor. The sensitivity of the proposed sensor has been studied for five different analytes of 1.44, 1.45, 1.46, 1.47 and 1.48. The maximum sensitivity of 2000 nm/RIU has been observed for the designed sensor. The proposed fiber sensor can be further optimized for a wide range of analytes in the IR region which would be a promising tool for sensing applications.

References

1. Wood RW (1902) On a remarkable case of uneven distribution of light in a diffraction grating spectrum. Proc Phys Soc London 18:26. https://doi.org/10.1088/1478-7814/18/1/325
2. Gupta BD, Verma RK (2009) Surface plasmon resonance based fiber optic sensors: principle, probe designs, and some applications. J Sens. https://doi.org/10.1155/2009/979761
3. Russel PJ (2003) Photonic crystal fibers. Science: 358–362. https://doi.org/10.1126/science.1079280
4. Sharma AK, Jha R, Gupta BD (2007) Fiber-optic sensors based on surface plasmon resonance: a comprehensive review. IEEE Sens J 7(8):1118–1129. https://doi.org/10.1109/jsen.2007.897946
5. Barth A (2007) Infrared spectroscopy of proteins. Biochim Biophys Acta 1767(9):1073–1101. https://doi.org/10.1016/j.bbabio.2007.06.004
6. Rhodes C, Cerruti M, Efremenko A, Losego M, Aspnes DE, Maria JP, Franzen S (2008) Dependence of plasmon polaritons on the thickness of indium tin oxide thin films. J Appl Phys 103(9):0931081–0931086. https://doi.org/10.1063/1.2908862
7. Rifat AA, Mahdiraji GA, Chow DM, Shee YG, Ahmed R, Adikan FRM (2015) Photonic crystal fiber-based surface plasmon resonance sensor with selective analyte channels and graphene-silver deposited core. Sensors 15:11499–11510. https://doi.org/10.3390/s150511499
8. Adams MJ (1981) An introduction to optical waveguides, 14. Wiley, New York
9. Singh S, Gupta BD (2010) Simulation of a surface plasmon resonance-based fiber-optic sensor for gas sensing in visible range using films of nano composites. Meas Sci Technol 21(11):1152021–1152028. https://doi.org/10.1088/0957-0233/21/11/115202

Designing a High Sensitivity Dual Steering-Wheel Micro-structured Gas Sensor in THz Region

Ramachandran Arumugam, Ramesh Babu Padmanaban, and Senthilnathan Krishnamoorthy

Abstract In this paper, we intend to design a novel dual steering-wheel micro-structured optical fiber (DSW-MOF)-based evanescent-field sensor. The proposed dual steering-wheel structure consists of circular core and noncircular cladding region. By employing full-vectorial finite element method (FEM), the relative sensitivities of the gas sensor are found to be 97 and 92% for incident frequencies of 0.5 and 1 THz, respectively. The proposed sensor exhibits a low loss and a high sensitivity, and hence, it would highly be appropriate for identifying different types of chemical and biological gasses.

Keywords Steering wheel · Gas sensor · Terahertz wave band · Evanescent field · Relative sensitivity · Photonic crystal fiber

1 Introduction

Recently, the photonic crystal fiber (PCF) has become unsung hero in the field of fiber-based sensors. Especially, PCF sensor plays a vital role in medical and biological industries because of its unique design features [1, 2]. The main feature of the PCF is that the desired optical properties can be optimized by playing the arrangement of air holes in the cladding region. We note that any liquid or gas can be filled in air holes. This unique feature gives a well-regulated interaction of light and sample. A PCF could also be designed for remote sensing purposes. Even though the evanescent-field sensing is popular in optical sensing techniques, it still faces the difficulties of inadequate mode-field overlap with the measurable analytes in the core region. Hence, the sensitivity of these sensors is limited. Recently, it has been found that the relative sensitivity of the conventional PCF is very low [3]. At this juncture, it

R. Arumugam
School of Electronics Engineering, Vellore Institute of Technology, Vellore, Tamil Nadu 632014, India

R. B. Padmanaban · S. Krishnamoorthy (✉)
Department of Physics, School of Advanced Science, Vellore Institute of Technology, Vellore, Tamil Nadu 632014, India
e-mail: senthee@gmail.com

should be emphasized that evanescent-based sensors produce high sensitivity when compared to other techniques. In the production of medicines, papers, chemical pesticides, cosmetics, etc., various types of gaseous or chemical substances are released in the outlet. Especially, in a chemical production company, the concentration of the outlet gas must be examined and then re-treated. Consequently, accuracy of gas detection turns out to be important in the industries.

It is well known that relative sensitivity is defined as the amount of light interacted with analytes, and it is the primary characteristic of a gas sensor. In order to achieve this, some portion of a cladding region is removed. Here, the core is made of organic material instead of silicon or quartz to avoid transmission loss in the terahertz region. We point out that polymers such as polycarbonate (PC), polyethylene (HDPE), polymethyl-methacrylate (PMMA), cyclic-olefin copolymer (COC), polytetrafluoroethylene (PTFE) and cyclo-olefin polymer (COP) are used as background material for a terahertz PCF sensor. We choose Teflon as the core material of these materials because it exhibits very low material absorption at THz compared to other organic materials [4].

1.1 Evanescent Filed Theory

Evanescent wave absorption can be achieved by removing the some portion of the cladding of the fiber, which will allow an interaction between analyte and evanescent field. Concentration of the analyte will determine the light absorption. The transmitted power absorbed by the analyte is determined by the following expression [5],

$$P = P(0) * \exp(-\gamma C L). \tag{1}$$

Here, P and $P(0)$ represent the power diffused over the fiber in the presence and absence of an absorbing medium over an unclad portion of length L, respectively. C and γ represent the concentration of the analytes and evanescent-field absorption coefficient, respectively. Hence, γ can be computed using the following expression [5],

$$\gamma = r_\mathrm{f} * \alpha_\mathrm{m}. \tag{2}$$

Here, r_f and α_m are the effective total power fraction of guided mode in the sensing region and absorption co-efficient of the analyte, respectively.

Recently, various gas sensors based on the evanescent field have been proposed for the detection of gaseous and chemical molecules. In order to achieve high relative sensitivity and low confinement loss, the core material and the proposed geometrical structure have to be optimized. In this paper, we design a novel DSW-MOF-based evanescent-field sensor, and it also fulfills the above requirements.

2 Proposed Structure

The perfect gas sensor should have high relative sensitivity and low confinement loss. The core background material is polytetrafluroethylene (PTFE or Teflon). When compared to glass, a THz transmission loss is minimum in plastic fiber [6]. We theoretically find that the optimum evanescent-field-based sensing structure can be obtained by tuning the fiber parameters, such as core air hole diameter and thickness of rectangular bar. This DSW-MOF gas sensor consists of eight noncircular air holes in the cladding region.

Another significant parameter is the confinement loss of the proposed sensor. It can be optimized by controlling the air holes count in the core region. Theoretically, when the number of air holes becomes infinite, the loss of leakage can be overlooked. However, in this structure, the air holes are countable. Consequently, the propagating modes are leaky for these types of special fibers. The imaginary part accounts for the modal loss. By analyzing this imaginary part, we can calculate the confinement loss of the designed fiber. In order to avoid this leakage mode, an open edge condition is required, which does not generate reflection at the edge. Based on the boundary layer, we can reduce this kind of loss [7]. In the recent times, perfectly matched layers (PMLs) are included to absorb the scattered rays at the boundary region [8–10].

2.1 Design of DSW-MOF

The proposed design of DSW-MOF PCF has been designed in such a way that it ensures a maximum light intensity interaction within air holes and large amount of light intensity penetrate into the noncircular cladding region. The proposed design is easy to implement because of the size of the air holes which is greater than the conventional PCF design [11]. Figure 1 shows the geometrical structure of the DSW-MOF gas sensor. The design parameters of the DSW-MOF are as follows: pitch (the distance between the two air holes), $\Lambda = 35\,\mu m$, rectangular bar thickness is $20\,\mu m$, $D_{core} = 0.250\,mm$, $R1 = 1.005\,mm$, $R2 = 0.871\,mm$, $R3 = 0.508\,mm$, $W2 = 21\,\mu m$, and the diameter of the core air hole varies ranging from 20–24 μm.

2.2 Mode-Field Distribution

This novel DSW-MOF PCF has been designed using beam propagation method. This model is used to investigate the fundamental mode thereby to calculate the confinement loss and sensitivity. The sensitivity of DSW-MOF sensor entirely depends on the power ratio between input light and evanescent wave [12]. Figure 2 represents the mode-field confinement of the proposed sensor.
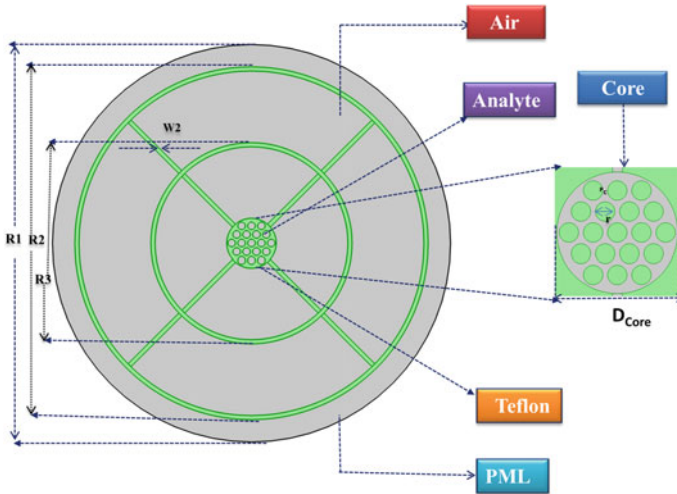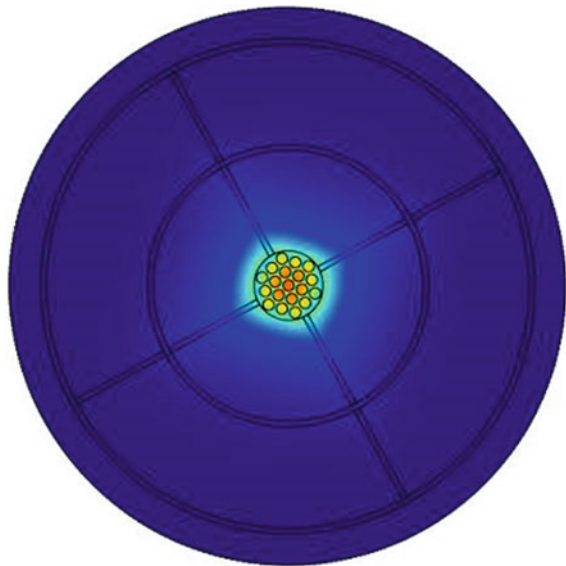
Fig. 1 Geometrical structure of the DSW-MOF fiber

Fig. 2 Mode-field
confinement of DSW-MOF
at 1 THz frequency

3 Design Parameters

Sensitivity of this proposed design is greater than convention model as the guided
mode efficiently overlap with immediate core air holes. The novel DSW-MOF gas
sensor is a modified total internal reflection-based PCF. The power of the fundamental

mode is concentrated at the center of the core region, while only a considerable amount of the energy is penetrated in the large noncircular air holes.

The leaky evanescent wave is absorbed by the air holes in the cladding. The gas concentration can found from the intensity through the Beer–Lambert law [13],

$$I(\lambda) = I_0(\lambda) * \exp[-r\alpha_{\mathrm{m}}(\lambda)lC]. \tag{3}$$

Here, I and I_0 represent the intensity of the output light for the presence and absence of gas, respectively. α_{m} is the absorption coefficient of the analytes. Here, we calculate the mode-field distribution within the air holes of the core region and analyze the evanescent-field distribution in the cladding air holes.

The sensitivity of the proposed DSW-MOF can be determined by the following expression [14],

$$r = \frac{n_{\mathrm{r}}}{n_{\mathrm{e}}} f. \tag{4}$$

Here, n_{r}, n_{e}, and r represent the analyte refractive index, the refractive index of effective guided mode, and the relative sensitivity coefficient, respectively. f is the ratio between the optical power in the samples and the total power. This can be determined by following equation [15],

$$f = \frac{\iint_{\mathrm{sample}} (E_x H_y - E_y H_x)\mathrm{d}x\mathrm{d}y}{\iint_{\mathrm{total}} (E_x H_y - E_y H_x)\mathrm{d}x\mathrm{d}y} \times 100 \tag{5}$$

Here, E_x, E_y, H_x, and H_y indicate the electric and magnetic fields in transverse and longitudinal directions, respectively.

4 Results and Discussion

The power percentage in the cladding air holes, relative sensitivity, and confinement loss are calculated for the proposed gas sensor for various core diameters ranging from 20 to 24 µm. The results are shown in Fig. 3. The refractive indices of cladding and core air holes are 1 and 1.38, respectively.

4.1 Analysis of Power Percentage

Figure 3 shows the decrease in power percentage with the increase in frequency, and it is increased with the increase in diameter of the air holes. When the core air holes radius, d, is 24 µm, the power percentage becomes to 92% at 1 THz frequency. The

**Fig. 3** Variation of power percentage against frequency for various core diameters
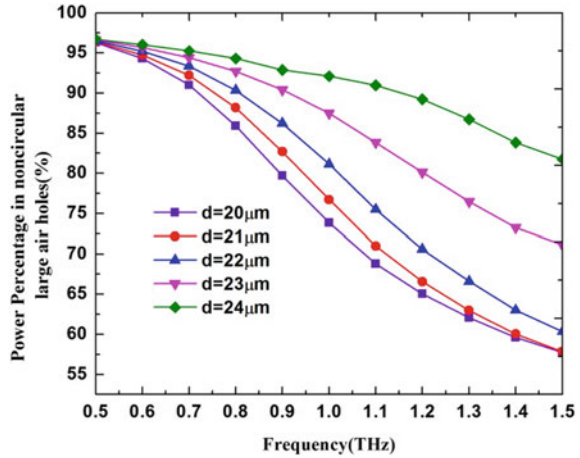
power percentage is larger for lower frequency region, and it is smaller for higher frequency region in the THz band.

4.2 DSW-MOF Sensitivity Analysis

As seen in Fig. 4, sensitivity is higher in lower frequency region as the evanescent wave highly interacts with analytes. Therefore, the highest sensitivity at 1 THz is 92% when the diameter of the air hole is 24 μm.

Fig. 4 Variation of relative sensitivity against frequency for various core air holes diameters
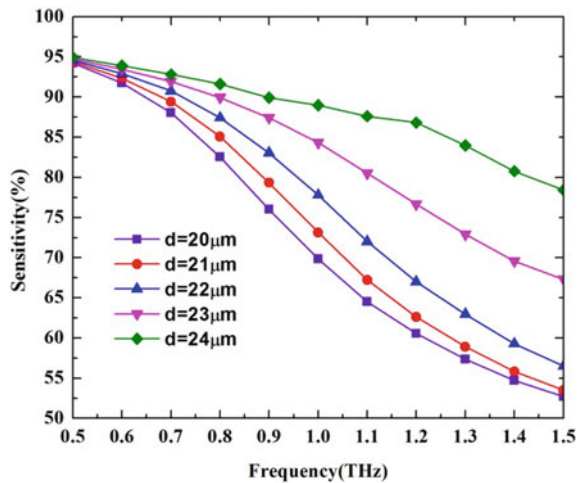
Fig. 5 Variation of confinement loss against frequency for different *d* values
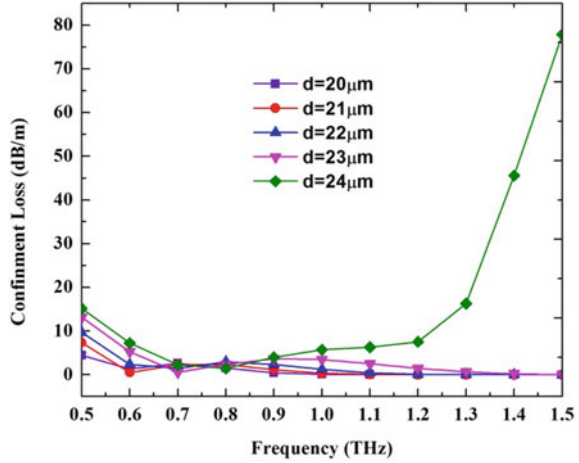
4.3 Confinement Loss Analysis

In this section, we compute the confinement loss, which turns out to be another important parameter in fiber sensor. It can be minimized by an appropriate structural design. The confinement loss can be determined by [16],

$$CL(\text{dB/m}) = 40\pi \times \frac{\text{Im}(n_{\text{eff}})}{\lambda \ln 10}. \tag{6}$$

Here, λ and Img (n_{eff}) represent the wavelength of input light and the imaginary part of effective refractive index, respectively. From this equation, it is clear that imaginary part of the effective refractive index and the input wavelength determines the confinement loss [17].

Figure 5 depicts the variation of confinement loss against THz frequency region for different diameters of core. It clearly shows that loss decreases up to 0.7 THz, and then, it increases in the THz region. The confinement loss is low at 0.7 THz for various core air hole diameters. From this analysis, we find that air hole size influences the confinement loss. It is low when air hole diameter is 24 µm, and it is optimized value for low loss. From Fig. 5, the lowest possible confinement loss is found to be 0.00002 dB/m.

5 Conclusion

We have proposed a dual steering-wheel micro-structured PCF gas sensor. It works on the principle of evanescent-field sensing. Using finite element method, we have achieved a power percentage of 93% in large noncircular holes at 1THz. The evanescent wave distribution turns maximum when core air diameter is 24 µm at 1 THz.

The proposed sensor exhibits a maximum relative sensitivity of 92% at 1 THz. We envisage that proposed fiber sensor will turn out to be an appropriate candidate for detecting the various bio-chemicals.

References

1. Zhang L, Ren GJ, Yao JQ (2013) A new photonic crystal fiber gas sensor based on evanescent wave in terahertz wave band: design and simulation. Opt Lett 9(6):438–440. https://doi.org/10.1007/s11801-013-3157-5
2. Zhu Y, Bise RT, Kanka J, Peterka P, Du H (2008) Fabrication and characterization of solid-core photonic crystal fiber with steering-wheel air-cladding for strong evanescent field overlap. Opt Comm 281(1):55–60. https://doi.org/10.1016/j.optcom.2007.08.071
3. Ritari T, Tuominen J, Ludvigsen H, Petersen JC, Sørensen T, Hansen TP, Simonsen HR (2004) Gas sensing using air-guiding photonic bandgap fibers. Opt Exp 12(17):4080–4087. https://doi.org/10.1364/OPEX.12.004080
4. Monro TM, Richardson DJ, Bennett PJ (1999) Developing holey fibres for evanescent field devices. Electron Lett 35(14):1188–1189. https://doi.org/10.1049/el:19990780
5. Hoo YL, Jin W, Shi C, Ho HL, Wang DN, Ruan SC (2003) Design and modeling of a photonic crystal fiber gas sensor. Appl Opt 42(18):3509–3515. https://doi.org/10.1364/AO.42.003509
6. Nielsen MD, Mortensen NA, Albertsen M, Folkenberg JR, Bjarklev A, Bonacinni D (2004) Predicting macrobending loss for large-mode area photonic crystal fibers. Opt Express 12(8):1775–1779. https://doi.org/10.1364/OPEX.12.001775
7. Bise RT, Trevor D (2005) Solgel-derived microstructured fibers: fabrication and characterization. In: Optical fiber communication conference. Optical Society of America. https://doi.org/10.1364/josab.33.000d12
8. Peterka P, Kaňka J, Honzátko P, Káčik D (2008) Measurement of chromatic dispersion of microstructure optical fibers using interferometric method. Opt Appl 38(2)
9. Zhu Y, Bise RT, Kanka J, Peterka P, Du H (2008) Fabrication and characterization of solid-core photonic crystal fiber with steering-wheel air-cladding for strong evanescent field overlap. Opt Commun 281(1):55–60. https://doi.org/10.1016/j.optcom.2007.08.071
10. Mägi EC, Steinvurzel P, Eggleton BJ (2004) Tapered photonic crystal fibers. Opt Express 12(5):776–784. https://doi.org/10.1364/OPEX.12.000776
11. Youk Y, Young Kim D, Wook Park K (2004) Guiding properties of a tapered photonic crystal fiber compared with those of a tapered single-mode fiber. Fiber Integr Opt 23(6):439–446. https://doi.org/10.1080/01468030490510261
12. Russell P (2003) Photonic crystal fibers. Science 299(5605):358–362
13. Nielsen MD, Jacobsen C, Mortensen NA, Folkenberg JR, Simonsen HR (2004) Low-loss photonic crystal fibers for transmission systems and their dispersion properties. Opt Express 12(7):1372–1376. https://doi.org/10.1364/OPEX.12.001372
14. Temelkuran B, Hart SD, Benoit G, Joannopoulos JD, Fink Y (2002) Wavelength-scalable hollow optical fibres with large photonic bandgaps for CO_2 laser transmission. Nature 420(6916):650. https://doi.org/10.1038/nature01275
15. Bing PB, Li ZY, Yao JQ, Lu Y, Di ZG, Yan X (2012) Theoretical and experimental researches on a PCF-based SPR sensor. Opto electron 8(4):245–248. https://doi.org/10.1007/s11801-012-1182-4
16. Yuan YQ, Guo ZQ, Ding LY (2010) Influence of metal layer on the transmitted spectra of SPR-based optical fiber sensor. Opto electron 6(5):346–349. https://doi.org/10.1007/s11801-010-0048-x
17. Petrovich MN, Van Brakel A, Poletti F, Mukasa K, Austin E, Finazzi V, Monro TM (2005) Microstructured fibers for sensing applications. In: Photonic crystals and photonic crystal fibers for sensing applications 6005 (60050E). Opt Photon. https://doi.org/10.4172/2155-6210.1000251

Experimental and Mathematical Analysis of Performance Characteristics of Neem Blended Biodiesel Run Diesel Engine

S. Rajeesh, S. V. Prakash, and P. A. Dinesh

Abstract The paper focuses on the mathematical validation of experimental performance estimates of Neem-derived biofuels mixed with diesel fuel in a proportion of 10%, as an alternative to conventional fossil fuels as a working substance in a single-cylinder, four-stroke Kirloskar AV I diesel engine with mechanical load. Biodiesel performance is evaluated in terms of braking power and mechanical efficiency at compression ratios 12:1, 15:1, and 17:1. The methodology is to find the best fit curve using nonlinear multivariate analysis that predicts the nature of the change in the corresponding output parameter of the diesel engine. The input parameters dynamic viscosity, load, CR and fuel consumption time of 10 cm^3 were taken into account in the calculation of BP and mechanical efficiency for NB. The output performance parameters, namely BP and mechanical efficiency, have unique mathematical empirical expression and found strong correlation between results of experimental and mathematical modeling with the R^2 values 0.9555, 0.9845, and 0.9829 for BP and 0.9963, 0.9882, and 0.9993 for mechanical efficiency at CR 12:1, 15:1, and 17:1, respectively. It is felt that the prediction of the mathematical model and the experimental and theoretical results available are closely synchronized. Wolfram Mathematica 9 was used as input for model programming.

Keywords Neem-blended biodiesel · Curve fit mathematical model · BP · Mechanical efficiency

S. Rajeesh
Department of Mechanical Engineering, M.S. Ramaiah Institute of Technology, Bengaluru 560054, India
e-mail: rajeesh@msrit.edu

S. V. Prakash
Department of Mechanical Engineering, Sri Krishna Institute of Technology, Bengaluru, India
e-mail: yagprash@hotmail.com

P. A. Dinesh (✉)
Department of Mathematics, M.S. Ramaiah Institute of Technology, Bengaluru 560054, India
e-mail: dineshdpa@msrit.edu

1   Introduction

Energy is one of the fundamental requirements for all industrial activities and modern human life, in general. The energy can be produced by different sources such as petroleum, natural gas, coal, nuclear, hydro, and other sources. The consumption of energy from these sources is shown in Fig. 1.

With the current demand for energy, there is fast depletion of the sources of energy. Fossil fuels are estimated to be available up to year 2040 [1]. With a stumbling economy, climbing gas prices, global climate change, and predicted shortage of fossil fuels have encouraged use of alternative sources of fuel. Supplementing diesel with organic oils resulting in biofuels is one way experts recommend to reduce the problem to a certain extent [1].

1.1   Biodiesel

Biodiesels are liquid fuels derived from biomass resource, meant to be used in blend with diesel in standard diesel engines with no special engine modifications or extra machinery. According to the American Society for Testing and Materials (ASTM Designation D6751) for petroleum-based diesel fuel, biodiesels are designated with an alphabet and two-digit index system, in which the first alphabet B refers blend, and with the last two digits, representing the share (in percentage volume) of biodiesel derived from bio-oil in the blend. Various blends viz a blend of 10% biodiesel & 90% petroleum diesel, blend of 15% biodiesel & 85% petroleum diesel, blend of 20% biodiesel & 80% petroleum diesel and a blend of 25% biodiesel & 75% petroleum diesel are designated as B10, B15, B20 and B25 respectively [2].

Today's world is experiencing two crises: fossil fuel depletion and environmental degradation. Therefore, some researchers are investigating alternative sources other than oil as fuel [3]. Thanks to these strategies, growing populations and growing energy demand in the transport sector, biofuels can be assured of a significant market

Fig. 1   Sources for energy

World energy consumption from different sources

- Natural Gas
- Petroleum
- Coal
- Nuclear
- Hydro electricity
- Other Renewables
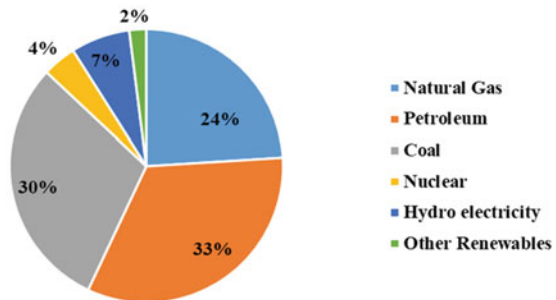
in India. On September 12, 2008, the Government of India announced its "National Biofuel Policy." It aims to meet 20% of India's diesel demand from plant fuel [3].

1.2 Neem

The neem (*Azadirachha indica*) is a tree of the Melaisi Mahogany family, which is grown in different parts of India. Neem grows on almost all types of soil, including soil, salt and alkaline conditions. The neem seeds obtained from this tree are collected, dried in the sun, and crushed to extract the oil, and the pulp is dissolved. The seeds have 45% oil, which has a large production capacity of biodiesel [4]. Neem oil is usually light brown, bitter and has a very strong smell that combines the aromas of peanuts and garlic. It contains mainly large amounts of triglycerides and tritpanoid compounds responsible for the bitter taste. It is hydrophobic in nature, and for the application to be emulsifying in water, it must be prepared with the appropriate surfactant. Neem oil has unique characteristics with a heating value of 39.1 mg/kg, a viscosity of 5.3 (cp) at 40 °C, a density at 15 °C of 0.78 (g/cc) and a Cetanenumber is 46 and that of diesel is 51. The cetane number measures the fuel's ignition delay and hence a low cetane number would result in an increase in the delay of the fuel's ignition. The oil contains surprisingly high stability at room temperature. The combination of a high proportion of neem oil was found to improve the properties of the oil, the viscosity, and the pH, while the stability of the mixture was kept in mind at less than 10% by weight in the form of a combination [5]. The low cost, easy handling and availability and excellent solubility in diesel–neem oil come out to be a good choice as alternative to fossil fuel used in CI engine.

2 Testing Procedure

In the current work initially, various blends of transesterified neem biodiesels were procured from University of Agricultural Science, Gandhi Krishi Vignan Kendra, Bengaluru, India, and their basic properties viz calorific value, kinematic viscosity, flash and fire point, and density were tested at Sneha Test House, Bangalore, India, and a professional testing service provider. The properties of biodiesels are listed in Table 1.

2.1 Experimental Setup

In this work, an experimental setup was carried out to evaluate engine performance characteristics (PC) at different compression ratios (CR) 12:1. 15:1, and 17:1, respectively. Various blends, namely B10, B15, B20, and B25, of neem biodiesel were tested

Table 1 Properties of the different blends of neem biodiesel

Properties	Diesel	Neem			
		NB10	NB15	NB20	NB25
Calorific value (kJ/kg)	44,800	41,533	40,946	40,361	39,775
Density (kg/m^3)	840	841	844	846	850
Kinematic viscosity (mm^2/c)	4	3.78	3.8175	3.855	4.96
Flash point (°C)	61	57	59	62	65
Fire point (°C)	65	67	71	74	78

in a four-stroke single-cylinder variable compression ratio, water-cooled, and 553 cc Kirloskar AV-1 CI engine in Mechtrix Engineers Pvt. Ltd., Bangalore, India. The tests were performed for CR 12:1, 15:1, and 17:1 at different loads [9–10].

2.2 Performance Evaluation Procedure

The performance parameters of four-stroke diesel engine like BP, mass of fuel consumption, BTE, and BSFC are determined [6] as mentioned below:

(a) Fuel Consumption: The mass of the fuel consumed by CI engine in one minute.

$$m_{\mathrm{f}} = \frac{(\text{Fuel consumed 10 ml}) * \text{Density of fuel} * 60}{(1000 * \text{Time taken in s})} \text{ in kg/min} \qquad (1)$$

(b) Total Fuel Consumption: The mass of the fuel consumed by CI engine in 1 h.

$$\mathrm{TFC} = m_{\mathrm{f}} * 60 \text{ in kg/h} \qquad (2)$$

(c) BP: The amount of power available at the crankshaft. The BP is usually measured by attaching a power absorption device to the drive shaft of the engine. The BP of the engine at different operating conditions was determined using the following equation

$$BP = \frac{2\pi NT}{60 * 1000} \text{ in kW} \qquad (3)$$

where

T = Torque = (net effective tension * R) in Nm
N = Speed in rpm
R = Radius of brake drum in m = 0.185 m.

(d) Specific Fuel Consumption: It is used to describe the fuel efficiency of an engine design. It measures the amount of fuel consumed by CI engine for 1 kW of power

in 1 h.

$$SFC = \frac{TFC}{BP} \text{ in kg/kW h} \tag{4}$$

(e) BTE: The ratio of power output to the heat supplied by the combustion of fuel.

$$\eta_{bte} = \frac{BP}{TFC * CV} * 100 \tag{5}$$

where CV = Calorific value of fuel

(f) Mechanical Efficiency: The ratio of BP to IP

$$\eta_{mech} = \frac{BP}{IP} * 100 \tag{6}$$

(g) IP: The total power developed inside the engine cylinder. It is obtained from William's line method.

3 Results and Discussion

3.1 Experimental BP of Neem Biodiesel

Figures 2, 3, and 4 show the variation of BP with load for diesel and different blends of NB for different CRs viz 12:1, 15:1, and 17:1, respectively [7].

The variation of brake power for neem biodiesel blends with different loading conditions as shown in Figs. 2, 3, and 4. It is observed that the brake power will increase with increase in load on the engine for all fuel samples except neem biodiesel blend B25 (increases up to 40% load for CR 12:1 and 15:1, and 60% load for CR 17:1, and decreases for further maximum load conditions). As the CR increases, the
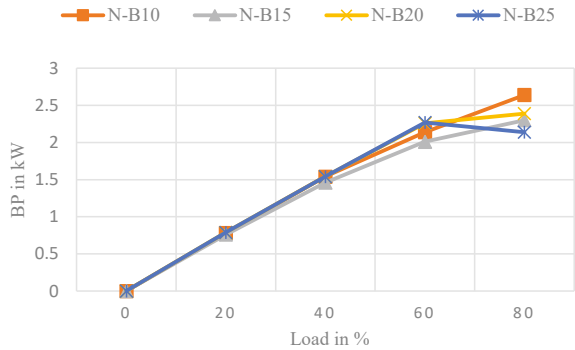

Fig. 2 Variation of BP for NB at CR 12:1
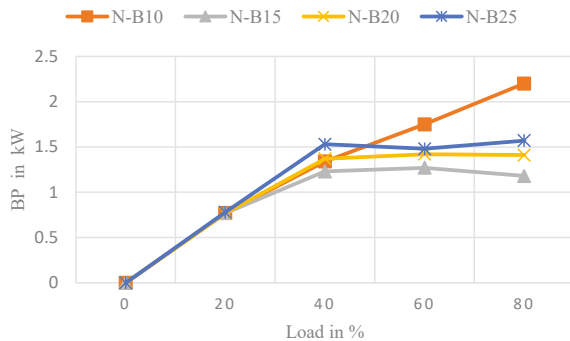
Fig. 3 Variation of BP for
NB at CR 15:1
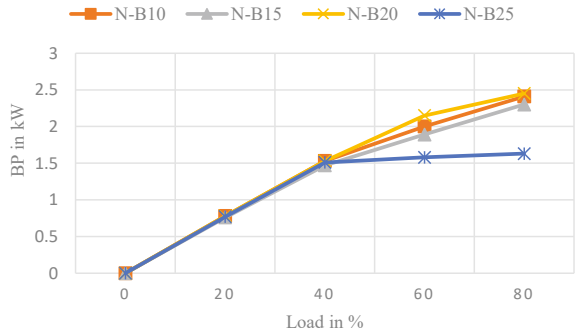
Fig. 4 Variation of BP for
NB at CR 17:1

load at which BP decreases has shoot up due to higher temperature of mixture and
early combustion of fuel (i.e., decrease in ignition delay). It is also observed that the
brake power decreases with an increase in the amount of neem biodiesel in the blend,
as well as under maximum load conditions. This is often due to the higher viscosity
and lower calorific value of the neem biodiesel. The higher viscosity of the neem
biodiesel results in poor atomization, fuel vaporization, and combustion. This may
be a possible cause of reduced brake power. The neem biodiesel blend B25 has the
lowest thermal efficiency at all loads as compared to diesel fuel and neem biodiesel
blends B5, B10, B15, and B20.

BP is the amount of input percent thermal energy associated with the engine's
net output power. The figure shows that BP increases with CR for all fuels tested.
The observed trend is caused by higher brake power at higher CR that leads to the
best combustion of fuel that, in turn, is caused by high temperature of compressed
air. The BP is observed to decrease as the content of the neem biodiesel in the blend
increases at constant CR. The trend is related to the lower calorific value of the neem
biodiesel. Therefore, it can be concluded that combustion is better at CR 17:1 for all
blends of neem biodiesel [6].

However, at a maximum load of 80%, the NB10 shows better performance than all
biodiesel blends. There are no studies reported on combustion analysis at VCRs using

neem biodiesel as fuel, although many studies have been conducted at a constant CR. Hence, NB10 has chosen for mathematical analysis.

3.2 Mathematical Models for BP and Mechanical Efficiency

To our knowledge in the literature, no one has derived a mathematical expression which relates the brake power and mechanical efficiency for biofuels at various compression ratios on CI engines for the model. We made an attempt to develop a mathematical empirical expression for this relation between brake power and mechanical efficiency as discussed below.

The methodology is to find the best fit curve using nonlinear multivariate analysis that predicts the nature of the change in the corresponding output parameter of the diesel engine. The input parameters dynamic viscosity, load, CR, and fuel consumption time of 10 cm^3 were taken into account in the calculation of BP and mechanical efficiency for NB.

The same experimental inputs and outputs were also taken into account in mathematical modeling [8]. The data table for BP is shown in Table 2. An empirical expression derived from the data available in the above experiment is obtained as:

$$BP_{mathematical} = \frac{\omega * (Load^b)}{(Dynamic\ viscocity^a) * (Compression\ Ratio^c) * (Time^d)}$$

Table 2 Experimental and theoretical values of BP in kW for neem blends

Blend ratio	Dynamic viscosity (Ns/m^2) (x)	Load (kg) (y)	CR (z)	Time for 10 cm^3 fuel consumption (s) (w)	Experimental BP (kW) (s)	Mathematical BP (kW) (s')	% error
B10	3.78	5	12.1	55	0.78	0.94	−21.4053
	3.78	5	12.1	55	0.78	0.94	−21.4053
	3.78	10	12.1	45	1.54	1.51	2.30561
	3.78	15	12.1	36	2.14	2.04	4.753214
	3.78	20	12.1	31	2.64	2.51	4.725189
	3.78	5	15.1	47	0.78	0.83	−7.52913
	3.78	10	15.1	39	1.53	1.33	13.18479
	3.78	15	15.1	33	2.00	1.76	11.54196
	3.78	20	15.1	28	2.41	2.19	9.353857
	3.78	5	17.1	46	0.77	0.76	1.192895
	3.78	10	17.1	38	1.34	1.22	8.99198
	3.78	15	17.1	34	1.75	1.60	8.612191
	3.78	20	17.1	29	2.20	1.98	10.15585

where ω, a, b, c, and d are obtained using a novel method which is derived using mathematical and math lab programme, and the values obtained for this particular case are found to be are 7.8982, 0.166, 0.6016, 0.7455, and 0.2526, respectively.

Similarly

$$\text{Mechanical efficiency}_{\text{Mathematical}} = \frac{\omega * \left(\text{Load}^b\right) * \left(\text{Time}^d\right)}{\left(\text{Dynamic viscocity}^a\right) * \left(\text{Compression ratio}^c\right)}$$

where ω, a, b, c, and d obtained for this particular case are found to be 13.56307, 0.5052, 0.3870, and 0.480854, respectively.

3.3   Comparison of Experimental and Mathematical Values of BP

Figures 5, 6, and 7 show the comparison of experimental and mathematical values of BP for NB10 at CR 12:1, 15:1, and 17:1, respectively.

It is indicated that similar curve trend was observed with strong correlation between experimental and mathematical modeling-based results with R^2 values being 0.9555, 0.9845, and 0.9829 for CR 12:1, 15:1, and 17:1, respectively.

Similarly, the results were obtained for mechanical efficiency for NB10, and they are plotted below.
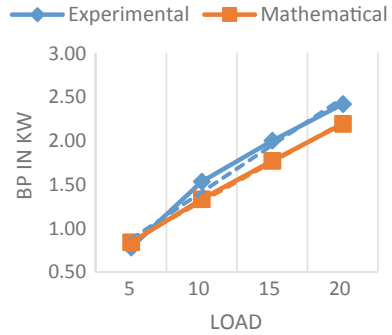
Fig. 5 Comparison of experimental and mathematical BP for NB10 at CR 12:1
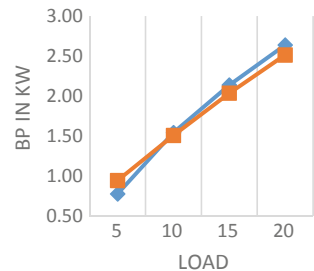
Fig. 6 Comparison of experimental and mathematical BP for NB10 at CR 15.1
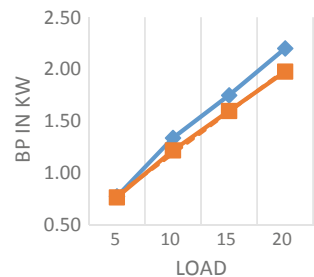
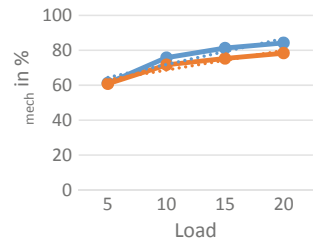Fig. 7 Comparison of experimental and mathematical BP for NB10 at CR 17.1

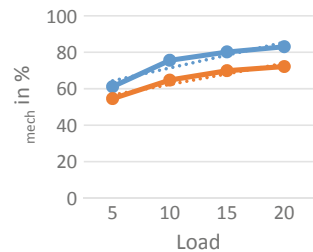## 3.4 Comparison of Experimental and Mathematical Values of Mechanical Efficiency

Figures 8, 9, and 10. show the comparison of experimental and mathematical values of mechanical efficiency for NB10 at CR 12:1, 15:1, and 17:1, respectively.

It is indicated that similar curve trend was observed with strong correlation between experimental and mathematical modeling-based results with R^2 values being 0.9963, 0.9882, and 0.9993 for CR 12:1, 15:1, and 17:1, respectively.
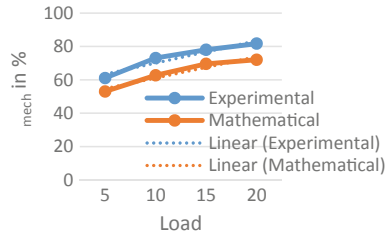

Fig. 8 Comparison of experimental and mathematical mechanical efficiency for NB10 at CR 12:1

Fig. 9 Comparison of experimental and mathematical mechanical efficiency for NB10 at CR 15.1

Fig. 10 Comparison of experimental and mathematical mechanical efficiency for NB10 at CR 17.1

4   Conclusion

The variation of experimental brake power for neem biodiesel 10% blends with different loading conditions shows the following trends

- Reduces with increase in blend ratio
- Increases as the compression ratio increases.
- Exhibits optimum results at higher compression ratio against higher load.

    The present work exposes

- The strong correlation (average $R^2 = 0.9845$) between the results obtained experimentally and mathematically for performance characteristics BP and mechanical efficiency.

    Thus, the mathematical model that is developed is useful for validating the performance characteristics of CI engine. This could be a useful model for the future researchers.

References

1. World energy Outlook 2016: International Energy Agency Report, France
2. Knothe G, Van Gerpen J, Krahl J (2005) The biodiesel handbook. AOCS Press, Champaign
3. Hägerdal BH, Himmel ME, Somerville C, Wyman C (2008) Welcome to biotechnology for biofuels. J Biotechnol Biofuels 1
4. Fazal MA, Haseeb ASMA, Masjuki HH (2011) Biodiesel feasibility study: an evaluation of material compatibility; performance; emission and engine durability. Renew Sustain Energy Rev 15(2):1314–1324
5. Foglia TA, Jones KC, Haas MJ, Scott KM (2000) Technologies supporting the adoption of biodiesel as an alternative fuel
6. Heywood J (1989) Internal combustion engines. McGraw-Hill Education Publication, New York
7. Rajeesh S, Prakash SV, Kulkarni GV (2018) Effect of compression ratio on performance characteristics of diesel engine run by biodiesel derived from neem & pongamia. Int J Innov Res Sci Eng Technol (IJIRSET). 7(Special Issue 7). ISSN-2319-8753
8. Rajeesh S, Rao AB, Bhandary SS, Rajarathnam SR, Dinesh PA (2014) Experimental and mathematical analysis of bio fuel (CNSL blended with diesel) run diesel engine. In: 2nd IEEE conference on power engineering and renewable energy (ICPERE 2014), Bali, Indonesia, 09–11 Dec 2014

9. Sivalakshmi S (2011) Experimental performance and emission analysis of vegetable oil ester operated C.I engine for various injection pressure. SAE Tech Pap 3(9):1–10
10. Sangeetha K, Rajan K, Prabhahar M (2016) Performance and emission characteristics of a diesel engine using preheated cashew nut shell liquid (CNSL). Diesel Blend 9(05):338–345

Characteristic Study of Coriolis Force on Free Convection in a Finite Geometry with Isotropic and Anisotropic Porous Media

Sudhir Patel, P. A. Dinesh, S. P. Suma, and N. L. Ramesh

Abstract Work carried out in this paper deals with classic Rayleigh–Bènard problem for an unsteady, laminar, viscous incompressible fluid of a horizontal layer heated from below which is extended to the three-dimensional convection in a rectangular box with anisotropic and isotropic porous media rotating with constant angular velocity that is investigated. For the given physical system, seven governing PDEs are transformed to system of non-dimensional ODEs using similarity transformation. The investigation demands to apply Fourier series method to study the characteristic of velocity and temperature for the effect of Taylor number, Rayleigh number and Prandtl number for both isotropic and anisotropic cases. The results of the stream function and isotherms on various parameters have been discussed and found to be good agreement for the physical system.

Keywords Isotropic and anisotropic porous media · Free convection · Coriolis force

Nomenclature

a	width of the rectangular channel
β	Thermal expansion co-efficient
c	Specific hear at constant pressure

S. Patel
Department of Mathematics, New Horizon College of Engineering, Bengaluru 560103, India
e-mail: sudhirp@newhorizonindia.edu

P. A. Dinesh (✉) · N. L. Ramesh
Department of Mathematics, M. S. Ramaiah Institute of Technology, Bengaluru 560054, India
e-mail: dineshdpa@msrit.edu

N. L. Ramesh
e-mail: nlramesh1607@yahoo.com

S. P. Suma
Department of Mathematics, Cambridge Institute of Technology, Bengaluru 560036, India
e-mail: drsumasp@gmail.com

985

$\vec{g} = (0, 0, -g)$	acceleration due to gravity
h	Height of the rectangular channel
κ	Thermal diffusivity in isotropic case
$\kappa = (\kappa_x, \kappa_y, \kappa_z)$	Thermal diffusivity along x, y, z axis in anisotropic case
k	Permeability in isotropic case
$k = (k_x, k_y, k_z)$	Permeability along x, y, z axis in anisotropic case
$p = p_1 - \frac{1}{2}|\Omega \times r|$	$p_1 = $ Pressure
$\vec{q} = (u, v, w)$	Velocity of the fluid
R_a	Thermal Rayleigh Number
t	Time
T	Temperature
ΔT	Characteristic temperature difference
T_0	Reference temperature
θ	Deviation from static temperature
ρ	Density
ρ_0	Reference density
$(\rho c_v)_S$, $(\rho c_v)_f$	Heat capacity per unit volume of the solid and fluid
x, y, z	Space coordinate
ν	Thermal viscosity
$\psi = \psi(x, y)$	Streamline function
R_c	Solutal Rayleigh Number
S	Concentration
S_0	Reference Concentration
ΔS	Characteristic Concentration difference
s	Deviation from the static concentration
σ	Growth rate
$T_a = \frac{2\Omega d^2}{\nu}$	Taylors Number
$\xi = \frac{k_x}{k_z}\left(\frac{h}{a}\right)^2$	Anisotropic ratio
$\eta = \frac{\kappa_x}{\kappa_z}\left(\frac{h}{a}\right)^2$	Aspect ratio
$\Omega = (0, 0, \Omega)$	Uniform angular velocity of the system
$\nabla = \left(\frac{\partial}{\partial x}, \frac{\partial}{\partial y}, \frac{\partial}{\partial z}\right)$	Three dimensional gradient operator
$\nabla^2 = \left(\frac{\partial^2}{\partial x^2}, \frac{\partial^2}{\partial y^2}, \frac{\partial^2}{\partial z^2}\right)$	Three dimensional Laplacian operator

1   Introduction

The prerequisite in the study of natural convection in an enclosure is considered as the challenges of convection in a rectangular cavity. A lot of research is done in analytical and empirical study of this problem. Davis [1] in 1967 and Segel [2] in 1969 both have studied the convection of fluid in a rectangular box heated from below. The research on onset convection in anisotropic media is comparatively less to

isotropic media [3]. Davis [1] obtained the upper bound of the critical Rayleigh number by adopting Galerkin's procedure, and in his investigation, Weierstrass theorem was not considered and in the region of observation, he set the governing equations. In his study, he also considered the side walls of the rectangular box to perfectly conducting. Catton [4] included the Weierstrass theorem and formulated the governing function using Galerkin's procedure, with this modified function, the result obtained by him was more relevant for aspect ratio which is small compared to that of Davis [1] results. In 1982, another paper on two-dimensional convection investigation in the rectangular box is carried out by Mcdonough and Catton [5], and used the combination of Galerkin and finite difference method for obtaining the results. In the study, a finite difference method was applied in the perpendicular direction and Galerkin's procedure was applied in the parallel direction. Temperature volatility in a fluid layer is explored by Kihm [6], when the top layer is exposed to the sudden temperature difference. The study also anticipates the amplification theory, relation between wavenumber and Rayleigh number. The flow in a square cavity with a constant flux or isothermal (heating) situation on the depressed surface at the same time one side wall temperature was reduced isothermally and was studied by Anderson and Lauriat [7]. In their result, it is found that for flux, Rayleigh numbers in the range 106–1010 predict a single cell flow with a steady boundary layer adjoining to the heated depressed surface. Experimental study [7] shows for flux Rayleigh numbers as big as 5×10^{13}, and Benard-mentioned volatility was negligible.

Analytical study of convection of air in a right circular cylindrical cavity, having a height of the cylinder equal to the radius, by small hot spots at the centre of the base surface, is done by Torrance and Rockett [8]. A theoretical study of the condition of a square cavity with isothermal reducing temperature on the walls and limited heating on the depressed surface was explored by Ganzarolli and Milanez [9]. The study mainly concentrated on the thermal convection and the flow format in the neighbourhood of flux singularity on the depressed surface where the boundary condition of temperature is volatile. It is established in [9] that while local heat flux in the neighbourhood of the flux singularity is not limited, the unified energy flow is definite. Nilsen and Storesletten [10] studied the two-dimensional natural convection in horizontal rectangular channel filled with porous media.

The main objective of the present work is to understand that the characteristic changes will take with the inclusion of external coriolies force on the study of the free convection in a finite rectangular box filled with isotropic or anisotropic porous media. Such a study has not been given any attention in the above literature sited to our knowledge. But in many practical situations which are mentioned in the application of science and technology demands, the rotational effects on the physical system play an important significant role in the industrial domain. The following sections elaborately obtained the governing equations and the corresponding boundary conditions of the physical configuration. Later, to understand the characteristics of velocity, temperature and concentration, we invoke the solution by using Fourier series analysis. The last section is dedicated to the numerical computation of the solution and interpreting the results of the physical problem on various non-dimensional parameters of the problem.

2 Mathematical Formulation

A 3D free convection in a rectangular porous box, non-uniformly heated from down is considered. The porous media is considered to be saturated and anisotropic by a incompressible homogeneous fluid. The rectangular box is of width a and height h, and we choose vertical direction of the box as z-axis, the horizontal walls of the box are at $z = (0, h)$ and the horizontal direction along the length of the box as x-axis, vertical walls are at $x = \pm a/2$ (Fig. 1). In order to neglect the inertia terms and appeal to the Boussinesq approximation, Prandtl–Darcy number is assumed to be very large. The 3D model of the Darcy–Boussinesq equations takes the form

$$\frac{\partial u}{\partial x} + \frac{\partial u}{\partial z} = 0, \tag{2.1}$$

$$\frac{1}{\rho_0}\frac{\partial p}{\partial x} + \frac{v}{k_x}u - 2\Omega v = 0, \tag{2.2}$$

$$\frac{1}{\rho_0}\frac{\partial p}{\partial y} + \frac{\upsilon}{k_y}v + 2\Omega u = 0, \tag{2.3}$$

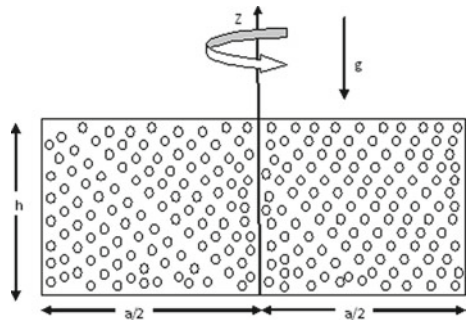$$\frac{1}{\rho_0}\frac{\partial p}{\partial z} - \frac{\sigma}{\rho_0}g + \frac{\upsilon}{k_z}w = 0, \tag{2.4}$$

$$c\frac{\partial T}{\partial t} + v \cdot \nabla T = \kappa_x\frac{\partial^2 T}{\partial x^2} + \kappa_z\frac{\partial^2 T}{\partial z^2}, \tag{2.5}$$

$$\frac{\partial S}{\partial t} + u\frac{\partial S}{\partial x} + w\frac{\partial S}{\partial z} = \sigma_x\frac{\partial^2 S}{\partial x^2} + \sigma_z\frac{\partial^2 S}{\partial z^2}, \tag{2.6}$$

$$\rho = \rho_0[1 - \beta(T - T_0) + \alpha(S - S_0)]. \tag{2.7}$$

The lower and the upper walls of the box are at isothermal temperatures T_0 and $T_0 + \Delta T$, and here, ΔT is the absolute temperature. All the walls of the box are considered to be heat conducting and impermeable. From Eqs. (2.1) to (2.7), we
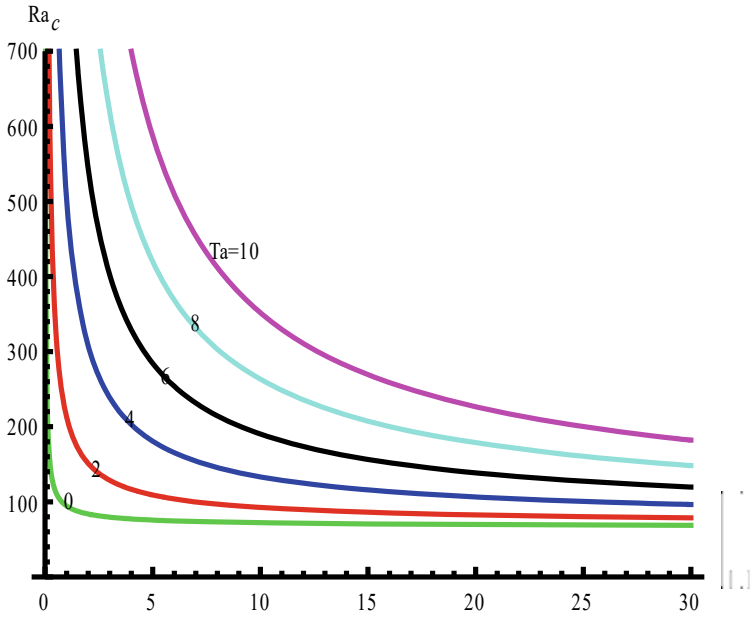
Fig. 1 Physical configuration

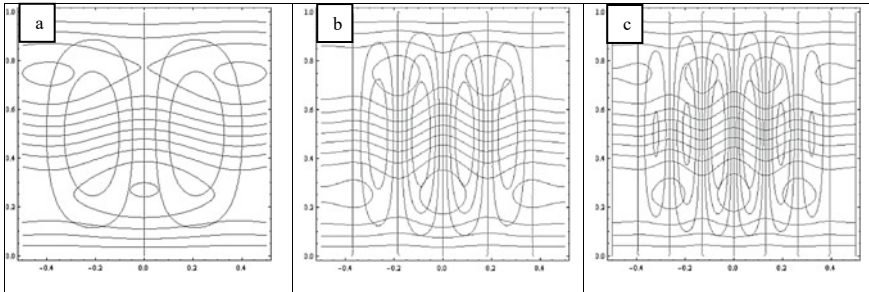**Fig. 2** Plot Ra$_c$ versus ξ/η ($R_s = 50$, $\xi = 0.5$, $\eta = 0.125$)

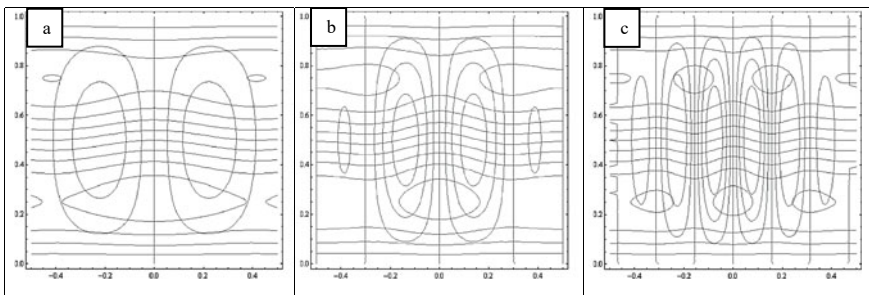**Fig. 3** Flow pattern isothermal lines and stream lines in isotropic case (T_a-varying)

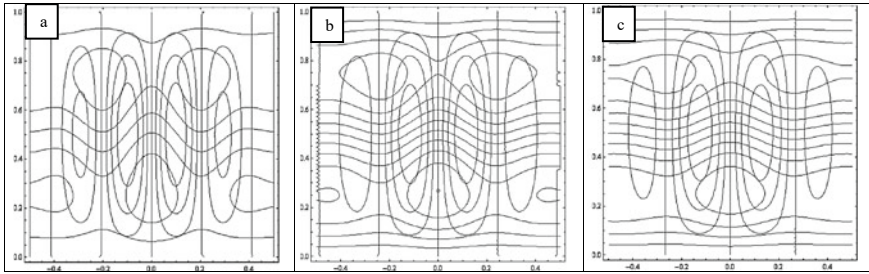**Fig. 4** Flow pattern isothermal lines and stream lines in anisotropic case (T_a-varying)

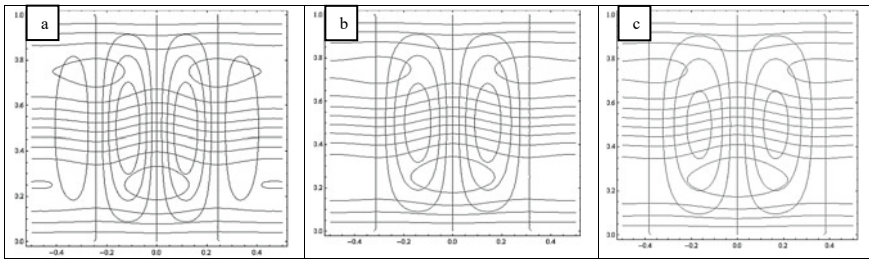**Fig. 5** Flow pattern isothermal lines and stream lines in anisotropic case (η-varying)

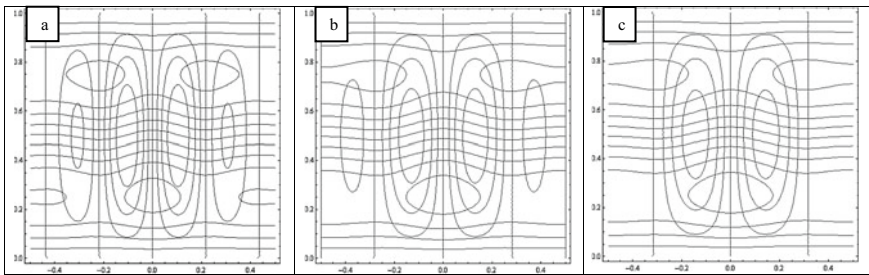**Fig. 6** Flow pattern isothermal lines and stream lines in asotropic case (ξ-varying)

Fig. 7 Flow pattern isothermal lines and stream lines in anisotropic case (χ-varying)

get that a static conduction occurs if the constant temperature circulation depends linearly on z and is sovereign of x.

$$T = \left[T_0 + \Delta T \left(1 - \frac{z}{h} \right) \right] + \theta, \quad S = \left[S_0 + \Delta S \left(1 - \frac{z}{h} \right) \right] + s \qquad (2.8)$$

where θ and s are the deviations from the static temperature and concentration, respectively. Because the flow is axisymmetric, stream function $\psi = \psi(x, y)$ by

$$u = \frac{\partial \psi}{\partial z}, \quad w = -\frac{\partial \psi}{\partial x}. \qquad (2.9)$$

Non-dimensional terms are represented by asterisks

$$u = \frac{\kappa_x a u^*}{h^2}, \; v = \frac{\kappa_y a v^*}{h^2}, \; w = \frac{\kappa_z w^*}{h}, \; t = \frac{ch^2 t^*}{\kappa_z}; \quad x = ax^*, \; y = ay^*, \; z = hz^*,$$

$$\psi = \frac{\kappa_z a \psi^*}{h}, \; \theta = \Delta T \theta^*, \; T_0 = \Delta T T_0^*, \; p = \frac{v k_z \rho_0 p^*}{k_z}, \; S = \Delta S S^* \tag{2.10}$$

On introduction of above expressions into Eqs. (2.1)–(2.7), the governing equation takes the form:

$$\left(\xi \frac{\partial^2}{\partial x^2} + \frac{\partial^2}{\partial z^2} \right) \psi + \xi R_a \frac{\partial \theta}{\partial x} - \xi R_S \frac{\partial s}{\partial x} - T_a \frac{\partial v}{\partial z} = 0, \tag{2.11}$$

$$\chi \frac{\partial v}{\partial z} + T_a \frac{\partial^2 \psi}{\partial z^2} = 0, \tag{2.12}$$

$$P_c \left(\zeta \frac{\partial^2}{\partial x^2} + \frac{\partial^2}{\partial z^2} \right) s - \frac{\partial \psi}{\partial t} = \frac{\partial s}{\partial t}, \tag{2.13}$$

$$\left(\eta \frac{\partial^2}{\partial x^2} + \frac{\partial^2}{\partial z^2} \right) \theta - \frac{\partial \psi}{\partial x} = \frac{\partial \theta}{\partial t} + \frac{\partial \psi}{\partial z} \frac{\partial \theta}{\partial x} - \frac{\partial \psi}{\partial x} \frac{\partial \theta}{\partial z} \tag{2.14}$$

where R_s is the Solutal Rayleigh number (or Darcy–Solutal Rayleigh number) and R_a is the Rayleigh number (or Darcy–Rayleigh number and are given by

$$R_S = \frac{\alpha g \Delta S k_z h}{\kappa_z \upsilon}, \quad R_a = \frac{\beta g \Delta T k_z h}{\kappa_z \upsilon}. \tag{2.15}$$

The anisotropy aspect ratio of permeability and diffusivity of temperature is represented by ξ, η, ζ and χ

$$\xi = \frac{k_x}{k_z} \left(\frac{h}{a} \right)^2, \; \eta = \frac{\kappa_x}{\kappa_z} \left(\frac{h}{a} \right)^2, \; \zeta = \frac{\sigma_x}{\sigma_z} \left(\frac{h}{a} \right)^2, \; \chi = \frac{k_x}{k_z}. \tag{2.16}$$

The boundary condition for absolutely impermeable boundaries and heat conducting walls is given by

$$S = \psi = \theta = \frac{\partial v}{\partial z} = 0 \quad \text{on} \begin{cases} x = -\frac{1}{2}, x = \frac{1}{2} & 0 < z < 1 \\ z = 0, z = 1 & -\frac{1}{2} < x < \frac{1}{2} \end{cases} \tag{2.17}$$

3 Steady Flow Patterns and Linear Stability

Free convection is mentioned by linear versions of Eqs. (2.11)–(2.14). The solution of these equations can be expended in Fourier series as

$$\psi = e^{\sigma t}\left[\frac{C_0}{2} + \sum_{n=1}^{\infty} C_n(x)\,\cos n\pi z + D_n(x)\,\sin n\pi z\right] \tag{3.1}$$

$$\theta = e^{\sigma t}\left[\frac{F_0}{2} + \sum_{n=1}^{\infty} F_n(x)\,\cos n\pi z + G_n(x)\,\sin n\pi z\right] \tag{3.2}$$

$$v = e^{\sigma t}\left[\frac{A_0}{2} + \sum_{n=1}^{\infty} A_n(x)\,\cos n\pi z + B_n(x)\,\sin n\pi z\right], \tag{3.3}$$

$$S = e^{\sigma t}\left[\frac{S_0}{2} + \sum_{n=1}^{\infty} S_n(x)\,\cos n\pi z + H_n(x)\,\sin n\pi z\right] \tag{3.4}$$

where C_n, D_n, F_n, G_n, A_n, B_n, S_n and H_n are in terms of x only and the growth rate is represented σ. To satisfy the boundary conditions (2.17), we need to consider $C_n = F_n = S_n = B_n = 0$ for all x. On substituting Eqs. (3.1)–(3.4) to the linearized governing equations, we get differential equations:

$$\left(\xi\frac{d^2}{dx^2} - n^2\pi^2\right)D_n + \xi R_a\frac{dG_n}{dx} - \xi R_S\frac{dH_n}{dx} + T_a n\pi A_n = 0, \tag{3.5}$$

$$\chi A_n + T_a n\pi D_n = 0, \tag{3.6}$$

$$P_c\left(\zeta\frac{d^2}{dx^2} - n^2\pi^2\right)H_n - \frac{dH_n}{dx} = \sigma H_n, \tag{3.7}$$

$$\left(\eta\frac{d^2}{dx^2} - n^2\pi^2\right)G_n - \frac{dD_n}{dx} = \sigma G_n. \tag{3.8}$$

And the boundary conditions for D_n, G_n, A_n and H_n as below

$$D_n(\pm0.5) = A_n(\pm0.5) = G_n(\pm0.5) = H_n(\pm0.5) = 0' \tag{3.9}$$

We can conclude from Eqs. (2.11)–(2.14) and from boundary condition (2.17) that σ to be real. Thus, to find critical Rayleigh number Ra_c which is a function of (ξ, η, ζ, χ), for the marginal stability we can substitute $\sigma = 0$ in Eqs. (3.7) and (3.8). The set of Eqs. (3.5)–(3.8) together with the bcs (3.9) gives Ra as the eigenvalue, Ra_c is the smallest eigenvalue. The general solution is of the form

$$D_n(x, R_a) = [C_1 \cos px + C_2 \sin px + C_3 \cos qx + C_4 \sin qx], \tag{3.10}$$

$$G_n(x, R_a) = s[rC_1 \sin px - rC_2 \cos px + C_3 \sin qx - C_4 \cos qx], \qquad (3.11)$$

$$H_n(x, R_a) = t[rC_1 \sin px - rC_2 \cos px + C_3 \sin qx - C_4 \cos qx], \qquad (3.12)$$

$$A_n = \frac{-n\pi T_a}{\xi}[C_1 \cos px + C_2 \sin px + C_3 \cos qx + C_4 \sin qx]. \qquad (3.13)$$

where C_1, C_2, C_3 and C_4 are arbitrary constants and

$$p_q = \frac{1}{2\sqrt{\xi}}\left\{\left[\sqrt{\left(R_a - \frac{R_s}{P_c}\right) - n^2\pi^2\left(2 + \frac{T_a^2}{\xi}\right) + 2n^2\pi^2\sqrt{1 + \frac{T_a^2}{\xi}}}\right]\right.$$
$$\left. \pm \left[\sqrt{\left(R_a - \frac{R_s}{P_c}\right) - n^2\pi^2\left(2 + \frac{T_a^2}{\xi}\right) - 2n^2\pi^2\sqrt{1 + \frac{T_a^2}{\xi}}}\right]\right\} \qquad (3.14)$$

$$r = \frac{q\left(\xi p^2 + n^2\pi^2\left(1 + \frac{T_a^2}{\xi}\right)\right)}{p\left(\xi q^2 + n^2\pi^2\left(1 + \frac{T_a^2}{\xi}\right)\right)}, \quad s = \frac{\xi q^2 + n^2\pi^2\left(1 + \frac{T_a^2}{\xi}\right)}{\xi q\left(R_a - \frac{R_s}{P_c}\right)},$$

$$t = \frac{\xi q^2 + n^2\pi^2\left(1 + \frac{T_a^2}{\xi}\right)}{\xi q(R_a P_c - R_s)}. \qquad (3.15)$$

Here, $p \neq q$ is assured by the boundary conditions at $Ra \neq Ra_c$. From (3.9) boundary condition, we get the non-trivial solution of the given problem when

$$\text{I.}(1 - r)\sin\left(\frac{p+q}{2}\right) - (1 + r)\sin\left(\frac{p-q}{2}\right) = 0 \quad \text{and} \quad C_2 = C_4 = 0$$
$$(3.16)$$

$$\text{II. } (1 - r)\sin\left(\frac{p+q}{2}\right) + (1 + r)\sin\left(\frac{p-q}{2}\right) = 0 \quad \text{and} \quad C_2 = C_4 = 0. \quad (3.17)$$

In the case of isotropic medium where $\xi = \eta =, \zeta = \chi$, Ra_c can be calculated by solving the equations analytically. Where else in case of anisotropic medium where $\xi \neq \eta = \zeta \neq \chi$, Ra_c found numerically.

(i) **The isotropic porous media case**: In this case, the condition $\xi = \eta = \zeta = \chi$ is fullfilled if $\frac{k_x}{\kappa_z} = \frac{k_x}{k_z}$, i.e., the proportion of the parallel and perpendicular component of thermal diffusivity and the permeability are equal. The following condition for case I and II are obtained at $r = 1$, we get

$$p - q = 2m\pi, \quad \text{for } m = 1, 2, 3, 4\ldots \qquad (3.18)$$

$$R_a = 4\pi^2 \left(\xi m^2 + \frac{n^2}{2} \left(1 + \frac{T_a^2}{2\xi} + \sqrt{1 + \frac{T_a^2}{\xi}} \right) \right) + \frac{R_s}{P_c} \tag{3.19}$$

where $n = 1, 2, 3, 4 \ldots$ and $m = 1, 2, 3, 4 \ldots$ Critial Rayleigh Equation (3.19) the critical Rayleigh number, which is the smallest possible value of R_a

$$Ra_c = 4\pi^2 \left(\xi + \frac{1}{2} \left(1 + \frac{T_a^2}{2\xi} + \sqrt{1 + \frac{T_a^2}{\xi}} \right) \right) + \frac{R_s}{P_c}. \tag{3.20}$$

For an isotropic medium, the smallest eigenvalue corresponds to $n = 1$ and $m = 1$

$$Ra_c = 4\pi^2 \left(\left(\frac{h}{a} \right)^2 + \frac{1}{2} \left(1 + \left(\frac{a}{h} \right)^2 \frac{T_a^2}{2} + \sqrt{1 + \left(\frac{a}{h} \right)^2 T_a^2} \right) \right) + \frac{R_S}{P_c}. \tag{3.21}$$

As the limit $\left(\frac{h}{a} \right) \to 0$ and $T_a \to 0$, the channel tends to infinitesimal horizontal porous layer. In such case, critical Rayleigh number $Ra_c = 4\pi^2$ and it is in line with a well-known conclusion for the permeable layers [11]. The critical value from Eq. (3.21) is not same as the conclusion found for a channel with absolutely insulating walls done by [12]. In case $h = a$, i.e., we get a square box, Eq. (3.21) gives $Ra_c = 8\pi^2$ whereas the result corresponding to perfectly insulating lateral walls gives $Ra_c = 4\pi^2$. Since, in this case, the heat transfer over the walls. A greater critical value is expected with conducting lateral wall box. The flow at the onset of neutral convection is the flow for moderately super-critical Rayleigh number. Since Eqs. (3.16) and (3.17) coincide when $\xi = \eta = \zeta = \chi$, i.e. when $r = 1$, the boundary value problem gives two linearly independent solutions. It can also seen from (2.11) and (2.14) equations. Let ψ_0, θ_0, S_0 and v_0 are the solutions at $R_a = Ra_c$, then $\psi_1 = -\xi R_a \theta_0, \theta_1 = \psi_0$ and $v_1 = v_0$ are linearly independent solutions. The two set of solutions are given by,

$$\psi^{(1)} = Q \cos Kx \, \sin \pi x \, \sin \pi z; \, \theta^{(1)} = Q s \sin Kx \, \sin \pi x \, \sin \pi z$$
$$v^{(1)} = \frac{-n\pi T_a}{\xi} Q \cos Kx \, \sin \pi x \, \cos \pi z; \, s^{(1)} = -Q \sin Kx \, \sin \pi x \, \sin \pi z \tag{3.22}$$

$$\psi^{(2)} = \frac{S}{s} \cos Kx \, \sin \pi x \, \sin \pi z; \, \theta^{(2)} = S \sin Kx \, \cos \pi x \, \sin \pi z,$$
$$v^{(2)} = -\frac{St}{s} \sin Kx \, \cos \pi x \, \cos \pi z; \, s^{(2)} = -\frac{\pi S T_a}{s\xi} \cos Kx \, \cos \pi x \, \sin \pi z \tag{3.23}$$

where amplitude constants are Q and S. A symmetric flow pattern having $2n$ cells is given by Eq. (3.22), where the number of cells n depends on ξ. A symmetric flow arrangement having of $2n \pm 1$ cells is given by (3.23). The critical Rayleigh number for various values of ξ and η are tabulated in the Table 1.

Table 1 Values for Ra_c for different values of ξ and η

ξ/η	0.125	0.25	0.5	1	2	4	8
0.125	25,756	13,115	6734	3502	1855	1011	574
0.25	50,874	25,761	13,120	6739	3507	1860	1016
0.5	100,870	50,884	25,771	13,130	6749	3516	1870
1	200,523	100,890	50,904	25,791	13,149	6769	3536
2	399,350	200,563	100,929	50,943	25,830	13,189	6808
4	796,326	399,429	200,642	101,008	51,022	25,909	13,268
8	1,589,319	796,484	399,587	200,800	10,1166	51,180	26,067

The principal diagonal coincide with the isotropic case

(ii) **The anisotropic case**: This case deals with the condition $\xi \neq \eta = \zeta \neq \chi$ the non-trivial solutions for D_n, A_n, H_n and G_n when the Eqs. (3.16) and (3.17) are fulfilled. Case I gives the solution in the form of

(i) $D_n(x) = \left[\sin px - \frac{\sin \frac{p}{2}}{\sin \frac{q}{2}} \sin qx\right]$, $G_n(x) = -s\left[r \cos px - \frac{\sin \frac{p}{2}}{\sin \frac{q}{2}} \cos qx\right]$,

$H_n(x) = -t\left[r \cos px - \frac{\sin \frac{p}{2}}{\sin \frac{q}{2}} \cos qx\right]$, $A_n(x) = \frac{-n\pi T_a}{\chi}\left[\sin px - \frac{\sin \frac{p}{2}}{\sin \frac{q}{2}} \sin qx\right]$,

(ii) $D_n(x) = \left[\cos px - \frac{\cos \frac{p}{2}}{\cos \frac{q}{2}} \cos qx\right]$, $G_n(x) = -s\left[r \sin px - \frac{\cos \frac{p}{2}}{\cos \frac{q}{2}} \sin qx\right]$,

$H_n(x) = t\left[r \sin px - \frac{\cos \frac{p}{2}}{\cos \frac{q}{2}} \sin qx\right]$, $A_n = \frac{-n\pi T_a}{\chi}\left[\cos px - \frac{\cos \frac{p}{2}}{\cos \frac{q}{2}} \cos qx\right]$.

Solutions (i) and (ii) are defined for a large numbers of eigenvalues. Let two smallest eigenvalues in each of the above case Ra_1 and Ra_2. These values will exist at $n = 1$. Form Eqs. (3.16) and (3.17), Ra_1 and Ra_2 are calculated for a given value of ξ, η, ζ and χ. Critical Rayleigh number $Ra_c = \{Ra_1 \text{ and } Ra_2\}$. Normally, Ra_1 and Ra_2 are not equal, it means there exist exclusive values for Ra_1 and Ra_2, i.e. at the convection there exists a different laminar flow pattern.

4 Summary

In this study, the effect of uneven temperature gradient on the free convection in a horizontal rectangular box in three dimensions is investigated. The three-dimensional problem is transformed to a two-dimensional double diffusive convection problem, in which diffusing components are temperature and solute in a anisotropic and isotropic rectangular channels. Channel is considered to heat conducting and impermeable. The channel is heated non-uniformly from below and added solutes to build a linear concentration and temperature distributions in the perpendicular directions.

Apart from the Boussinesq approximation, in which state density remains constant throughout the momentum equation except for the body force and also the following assumptions have been considered. Large heating at the walls implies that the
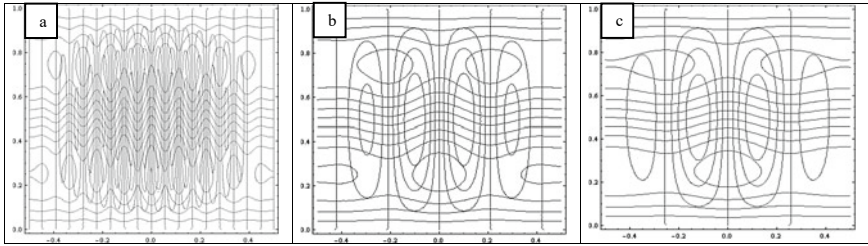
Fig. 8 Flow pattern isothermal lines and stream lines in isotropic case (ξ-varying)

non-dimensional parameters Darcy–Prandtl numbers are large and hence the iner-
tial and viscous terms are neglected in the momentum equation. Flow is symmetric
with respect to *Y*-axis and thereby introduced the stream function which enables to
determine the critical Rayleigh number and solutal Rayleigh number based on the
linear stability theory. The expression for critical Rayleigh number Ra_c is obtained
by solving the resulting eigenvalue problem for the anisotropy case and as well as
for isotropic case. The result is in accordance with the previous result, in the absence
of corialise force, that is, it reduces to Rayleigh number found in the non-rotating
case, and as the limit $h/a \to 0$, it reduces to the standard results $Ra_c = R_S + 4\pi^2$ and
$Ra_c = 4\pi^2$ when $R_s = 0$ in the absence of the second diffusing components which
is in line with the acclaimed result for the porous layers [11]. Two sets of solution
which are linearly independent are derived, which present different nice steady flow
patterns at moderate super-critical Rayleigh number. Figure 2 represents the plotted
graph of critical Rayleigh number versus ratio of permeability to thermal diffusivity.
The observation shows that the critical Rayleigh number Ra_c varies inversely with
ratio ξ/η.

The critical Rayleigh number further increases with increasing Taylor's number,
solutal Rayleigh number and the effects of rotation therefore to destabilize the system
more significantly. It is observed from steady flow patterns that the flow pattern is
of the streamlines and isothermal lines. The number of cells found to be increased
with the increase in the Taylor's number for both isotropic and anisotropic cases
(Figs. 3 and 4). Increase in Taylor's number increases the coriolis force, which in
turn increases the number of rotation. Increase in rotation increases the streamlines
and isothermal lines. The isothermal lines show the increase in the oscillatory flow
behaviour with rotation in anisotropic case (Fig. 5). The number of cells found to be
decreased with increase in aspect ratio and thermal diffusivity in the anisotropic case
(Figs. 6 and 7). The isotherm becomes more and more flattened with the anisotropy
(Fig. 8).

References

1. Davis SH (1967) Convection in a box: linear theory. Int J Fluid Mech 30:465–478. https://doi.org/10.1017/s0022112067001545
2. Segel LA (1969) Distant sidewalls cause slow amplitude modulation of cellular convection. Int J Fluid Mech 38:203–206. https://doi.org/10.1017/s0022112069000127
3. Kvernvold O, Tyvand PA (1979) Nonlinear thermal convection in anisotropic porous media. J Fluid Mech 90:609–624. https://doi.org/10.1017/s0022112079002445
4. Catton I (1970) Convection in a closed rectangular region: the onset of motion. Trans ASME Heat Transfer C- 92:186–188. https://doi.org/10.1115/1.3449626
5. Mcdonouch JM, Catton I (1982) A mixed finite difference—Galerkin procedure for two-dimensional convection in a square box. Int J Heat Mass Transfer 25:1137–1146. https://doi.org/10.1016/0017-9310(82)90208-3
6. Khim KD, Choi CK, Yaoo JY (1982) The onset of instability in a horizontal fluid due to a step change in temperature. Int J Heat Mass Transfer 25:1829–1837. https://doi.org/10.1016/0017-9310(82)90105-3
7. Anderson R, Lauriat G (1986) The horizontal natural convection boundary layer regime in a closed cavity. In: Proceedings of 8th international heat transfer conference, San Francisco, CA, pp 1453–1458. https://doi.org/10.1615/ihtc8.2970
8. Torrance K, Rockett J (1969) Numerical study of natural convection in an enclosure with localized heating from below-creeping flow to the onset of laminar instability. J Fluid Mech 36:33–54. https://doi.org/10.1017/s0022112069001492
9. Ganzarolli MM, Milanez LF (1987) Natural convection in rectangular enclosures heated from below and cooled along one side. Int J Heat Mass Transfer 2433–2440. https://doi.org/10.1016/0017-9310(94)00217-j
10. Nilsen T, Storesletten L (1990) An analytical study on natural convection in isotropic and anisotropic porous channels. J Heat Transfer. https://doi.org/10.1115/1.2910390
11. Bories S (1987) Natural convection in porous media. In: Advances in transport phenomena in porous media. NATO ASI Series book series, vol 128, pp 77–141
12. Sutton FM (1970) Onset of convection in a porous channel with net through flow. Phys Fluids 13(8):1931. https://doi.org/10.1063/1.1693188

Effects of Forchheimer, MHD and Radiation Absorption for Chemically Reacting Unsteady Dusty Viscoelastic Fluid Couette Flow in an Irregular Channel

P. A. Dinesh, A. S. Vasudevamurthy, and M. Uma

Abstract In this work, a study which contributes toward the combined effects of Forchheimer, MHD, and radiation absorption for a laminar two-dimensional chemically reacting unsteady dusty viscoelastic fluid in an irregular channel is considered. The physical model demands nonlinear coupled partial differential equations under the wavy channel conditions. Computational results are obtained to understand the characteristics of velocity, temperature, and concentration for various physical parameters involved in the model using a novel analytical perturbation method with combined Soret and Forchheimer number. Obtained results are well matched with the physical model and found to be a good agreement with the earlier works for a particular case.

Keywords Forchheimer · Radiation absorption · Couette flow · Irregular channel

1 Introduction

The demand for the present study is on the non-Newtonian fluids on heat and mass transfers, which play an important role in the control of the fluid flow and enhancement of heat transfer in fluids. Such a study is seen in many applications in science, technology, and industries, viz., food processing, chemical process industries, power engineering, and petroleum production industries. The flow of a viscoelastic fluid between parallel plates and its heat and mass transfer behaviors are helpful in the study of boundary layer problems. Beard and Walter [1] studied the treatment of the boundary layer for a viscoelastic fluid. Due to the electromagnetic field, the MHD flows have a variety of practical applications in astrophysical and geophysical

P. A. Dinesh (✉) · M. Uma
Department of Mathematics, M.S. Ramaiah Institute of Technology, Bengaluru 560054, India
e-mail: dineshdpa@msrit.edu

M. Uma
e-mail: umashivaram@gmail.com

A. S. Vasudevamurthy
Tata Institute of Fundamental Research Campus, Yelahanka, Bengaluru 560065, India
e-mail: vasu@math.tifrbng.res.in

situations, in cooling of continuous strips and filaments, metallurgy industry (see examples Tao [2], Hayat and Kara [3]). The heat transfer behavior of fluids (Walters liquid Model-B by Prakash et al. [4]) plays an important role in the design of many advanced energy convection systems. The theories of radiation heat transfer play a vital role in nuclear power plants, gas turbines, and in space vehicles (see Rajagopal and Na [4], Chang and Lundgren [5], Syed-Ahmed [6], Attia [7], Mekheimer and Kot [8]). Some of the industrial applications include evaporation, pasteurization, and dehydration of food products (see Pal and Mondal [9]).

In these applications, we come across a Couette flow fashion in an irregular channel under the influence of several external forces which drives the flow, temperature, and species or concentration with varying mass diffusion MHD drag force, and viscous dissipation. In the literature to the best of our knowledge, the mathematical modeling for such a physical system involving additional forces for a plane channel studied by many authors (Patil and Kulkarni [10], Nalinakshi et al. [11] for a wavy channel with the effect of Soret and Dufour) [12, 13]. Sivaraj et al. [14] have studied the effects of unsteady MHD dusty viscoelastic fluid Couette flow in an irregular channel with varying mass diffusion analytically.

Jean et al. [15] have studied the chemical reaction effect on MHD viscoelastic fluid flow over a vertical stretching sheet with a heat source/sink. Venkateswarlu et al. [16] have investigated the effects of chemical reaction and heat source on MHD oscillatory flow of a viscoelastic fluid. The influence of chemical reaction and thermal radiation for a micropolar flow is studied by Mohamed RA et al. [16]. Prasad et al. [17] studied the effects of thermal radiation on MHD for a variable porosity regime. For the irregular channel, Shivaraj et al. [18] studied the effects of a chemical reaction and radiation absorption for a dusty viscoelastic fluid. Uma et al. [19] obtained an analytical solution in the absence of Dufour and radiation absorption for unsteady MHD dusty viscoelastic fluid Couette flow in vertical wavy channel with varying mass diffusion.

But, in these models to our knowledge, the drag force in terms of contraction or expansion called Forchheimer effect experienced by the velocity and radiation effect has not been considered in the earlier studies. The main idea of this study is to find an analytical solution for the effects of Forchheimer, MHD, and chemically reacting unsteady dusty viscoelastic fluid Couette flow in an irregular channel because of its applications stated earlier. In this model, we examine the influence of MHD, heat absorption, radiation absorption, viscous dissipation, Joule effect, chemical reaction, and thermal diffusion on Couette flow of a viscoelastic fluid in a vertical irregular porous channel with convective varying mass diffusion. In this analysis, the resulting partial coupled nonlinear differential equations are solved using the perturbation method in the subsequent sections of the paper.

2 Mathematical Formulation

The two-dimensional flow of an unsteady, incompressible, chemically reacting, electrically conducting, dusty viscoelastic fluid Couette flow in a vertical irregular porous channel with convective cooling and varying mass diffusion is as shown in Fig. 1. Here, X-axis is along the channel and which is in motion. The Y-axis is perpendicular to it. A uniform magnetic field of strength B_o is applied transverse to the fluid flow and the external constraints like buoyancy effects, thermal radiation, heat absorption, radiation absorption and chemically reactive species are applied for the physical configuration. Hall effect and induced magnetic field are neglected because of very small magnetic Reynolds number is the assumption carried in this work. In Fig. 1 above, T_{W1} and C_{W1} are temperature and concentration of the wavy wall, and T_{W2} and C_{W2} are temperature and concentration of the flat wall, where it will be higher than the wavy wall. The convective boundary conditions are given by $-k\frac{\partial T}{\partial Y} = h_f(T_1 - T + (T_2 - T_1)At^*)$ and $C_{W_1} = C_1 + (C_2 - C_1)At^*$ for a wavy wall and $-k\frac{\partial T}{\partial Y} = h_f(T_2 - T + (T_2 - T_1)At^*)$ and $C_{W2} = C_2 + (C_2 - C_1)At^*$ for a flat wall. Here, thermal conductivity, viscosity, diffusivity, density, and pressure with negligible body forces are taken as constants. Considering all the above assumptions, the physical problem can be expressed in Cartesian system as

$$\frac{\partial U}{\partial t^*} = \nu\left(1 - K_0\frac{\partial}{\partial t^*}\right)\frac{\partial^2 U}{\partial Y^2} + \frac{K_1 N_0}{\rho}(V - U) - \frac{\nu}{K^*}U - \frac{\sigma_e B_0^2}{\rho}U$$
$$+ g\beta_T(T - T_1) + g\beta_c(C - C_1) - \frac{C_b U^2}{\sqrt{K^*}} \tag{1}$$

$$m\frac{\partial V}{\partial t^*} = K_1(V - U) \tag{2}$$

$$\frac{\partial T}{\partial t^*} = \frac{k}{\rho C_P}\frac{\partial^2 T}{\partial Y^2} - \frac{Q_T}{\rho C_P}(T - T_1) - \frac{1}{\rho C_P}\frac{\partial q_r}{\partial Y} + \frac{\nu}{C_P}\left(\frac{\partial U}{\partial Y}\right)^2$$

Fig. 1 Physical configuration of the problem
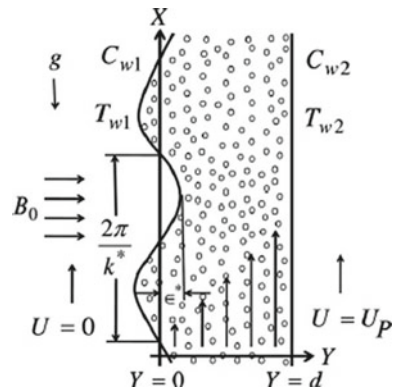
$$+ \frac{\sigma_e B_0^2}{\rho C_P} U^2 + \frac{Q_c}{\rho C_P}(C - C_1) \tag{3}$$

$$\frac{\partial C}{\partial t^*} = D \frac{\partial^2 C}{\partial Y^2} - K_R(C - C_1) + \frac{D K_T}{\bar{T}} \frac{\partial^2 T}{\partial Y^2}. \tag{4}$$

The suitable boundary conditions of the physical problem are:
For a wavy wall

$$Y \in \left(\varepsilon^* \cos(K_2 X), d\right) t^* = 0: U = 0 = V, T = T_1, C = C_1$$

$$t^* > 0: U = 0 = V, -k \frac{\partial T}{\partial Y} = h_f\left(T_1 - T + (T_2 - T_1)At^*\right) \tag{5}$$

$$C = C_1 + (C_2 - C_1)At^* \quad \text{at } Y = \varepsilon^* \cos(K_2 X), \tag{6}$$

For a flat wall

$$Y = d; U = U_p = V, -k \frac{\partial T}{\partial Y} = h_f\left(T_2 - T + (T_2 - T_1)At^*\right);$$

$$C = C_2 + (C_2 - C_1)At^*. \tag{7}$$

On introducing the non-dimensional parameters like

$$x = \frac{X}{d}, y = \frac{Y}{d}, v = \frac{V}{U_0}, \theta = \frac{T - T_1}{T_2 - T_1}, S_c = \frac{v}{d}, A = \frac{U_0^2}{v}, P_r = \frac{\mu C_p}{k},$$

$$\phi = \frac{C - C_1}{C_2 - C_1}, \alpha_T = \frac{Q_T d^2}{\mu C_p}, t = \frac{vt^*}{d^2}, S_r = \frac{D K_T d^2 (T_2 - T_1)}{v \bar{T}(C_2 - C_1)},$$

$$M^2 = \frac{\sigma_e B_0^2 d^2}{\mu}, \frac{1}{K} = \frac{d^2}{K^*}, E = \frac{K_0 v}{d^2}, \delta = \frac{m N_0}{\rho}, F = \frac{4 I' d^2}{\mu C_p},$$

$$\alpha_c = \frac{Q_c d^2}{\mu C_p}, W = \frac{mv}{K_1 d^2}, G_c = \frac{g \beta_c (C_2 - C_1) d^2}{v U_0}, B_i = \frac{h_f d}{k},$$

$$K_r = \frac{K_R d^2}{v}, G_r = \frac{g \beta_T (T_2 - T_1) d^2}{v U_0}, u_p = \frac{U_p}{U_0}, \varepsilon = \frac{\varepsilon^*}{d} \lambda = K_2 d,$$

$$h = \varepsilon \cos(\lambda x), E_c = \frac{U_0^2}{C_p((T_2 - T_1))}, \Gamma = \frac{C_b u_0 d}{\sqrt{kv}} \tag{8}$$

All the other physical quantities involved in the governing equations have their usual meaning. The radiative heat flux is given by

$$\frac{\partial q_r}{\partial Y} = 4(T - T_1)I' \quad \text{where } I' = \int_0^\infty K_{\lambda_1 W} \frac{\partial e_{b\lambda_1}}{\partial T} d\lambda_1.$$

Using the non-dimensional quantities, Eqs. (1)–(4) can be expressed as

$$\frac{\partial u}{\partial t} = \left(1 - E\frac{\partial}{\partial t}\right)\frac{\partial^2 u}{\partial y^2} + \frac{\delta}{w}(v - u) - \left(M^2 + \frac{1}{k}\right)u + G_r\theta + G_c\phi - \Gamma u^2, \quad (9)$$

$$w\frac{\partial v}{\partial t} = v - u, \quad (10)$$

$$\frac{\partial\theta}{\partial t} = \frac{1}{p_r}\frac{\partial^2\theta}{\partial y^2} - (\alpha_T + F)\theta + E_c\left[M^2 u^2 + \left(\frac{\partial u}{\partial y}\right)^2\right] + \frac{\alpha_c}{\mu\,c_p}, \quad (11)$$

$$\frac{\partial\phi}{\partial t} = \frac{1}{S_c}\frac{\partial^2\phi}{\partial y^2} - K_r\phi + S_r\frac{\partial^2\theta}{\partial y^2}, \quad (12)$$

The dimensionless boundary conditions (5)–(7) become

$$t = 0: u = 0 = v, \theta = 0, \phi = 0, y \in (h, 1), \quad (13)$$

$$t > 0: u = 0 = v, \frac{\partial\theta}{\partial y} = B_i(\theta - t), \phi = t, y = h, \quad (14)$$

$$u = u_p = v, \frac{\partial\theta}{\partial y} = B_i(\theta - 1 - t), \phi = 1 + t \quad \text{at } y = 1. \quad (15)$$

3 Method of Solution

Equations (9)–(15) are solved using perturbation method by taking

$$u(y, t) = u_0(y) + S_r\Gamma\,e^{-nt}u_1(y) + o(\Gamma^2), \quad (16)$$

$$v(y, t) = v_0(y) + S_r\Gamma\,e^{-nt}v_1(y) + o(\Gamma^2), \quad (17)$$

$$\theta(y, t) = \theta_0(y) + S_r\Gamma\,e^{-nt}\theta_1(y) + o(\Gamma^2), \quad (18)$$

$$\phi(y, t) = \phi_0(y) + S_r\Gamma\,e^{-nt}\phi_1(y) + o(\Gamma^2), \quad (19)$$

Equations (16)–(19) are substituted into Eqs. (9)–(15), and we get

$$u_0'' - Nu_0 = -(G_r\theta_0 + G_c\phi_0), \quad (20)$$

$$(1 + nE)u_1'' - \left(N - n + \frac{\delta n}{n+1}\right)u_1 = -(G_r\theta_1 + G_c\phi_1) + u_0^2 e^{nt}, \quad (21)$$

$$\theta_0'' - P_r(\alpha_T + F)\theta_0 = \frac{\alpha_c}{k}, \tag{22}$$

$$\theta_1'' - P_r(\alpha_T + F - n)\theta_1 = -P_r\left((u_0')^2 + M^2 u_0^2\right), \tag{23}$$

$$\phi_0'' - K_r S_c \phi_0 = -S_r S_c \theta_0'', \tag{24}$$

$$\phi_1'' - (K_r - n)_r S_c \phi_1 = -S_r S_c \theta_1''. \tag{25}$$

And the corresponding boundary conditions reduce to

$$\begin{aligned}
&u_0 = 0 = v_0, \theta_0' = B_i\theta_0, \phi_0 = t, \\
&u_1 = 0 = v_1, \theta_1' = B_i(\theta_1 - 1), \phi_1 = 1 \quad \text{at } y = h,
\end{aligned} \tag{26}$$

$$\begin{aligned}
&u_0 = u_p = v_0, \theta_0' = B_i(\theta_0 - 1), \phi_0 = 1 + t, \\
&u_1 = 0 = v_1, \theta_1' = B_i(\theta_1 - 1), \phi_1 = 0 \quad \text{at } y = 1.
\end{aligned} \tag{27}$$

Equations (20)–(27) are solved analytically using suitable boundary conditions, and the expression of dusty fluid velocity, temperature, and concentration is obtained as follows

$$u(y, t) = a_7 e^{b31\,y} + a_8 e^{b41\,y} + a_9 e^{b1y} + a_{10}e^{b2y} + a_{11}e^{b3y} + a_{12}e^{b4y} + S_r \Gamma e^{-nt}(u_1),$$

$$v(y, t) = a_7 e^{b31\,y} + a_8 e^{b41\,y} + a_9 e^{b1y} + a_{10}e^{b2y} + a_{11}e^{b3y} + a_{12}e^{b4y} + S_r \Gamma e^{-nt}(v_1),$$

$$\theta(y, t) = a_1 e^{b1y} + a_2 e^{b2y} - \frac{\alpha_c}{b_1^2} + S_r \Gamma e^{-nt}(\theta_1),$$

$$\varphi(y, t) = a_3 e^{b3y} + a_4 e^{b4y} + a_5 e^{b1y} + a_6 e^{b2y} + S_r \Gamma e^{-nt}(\phi_1).$$

4 Results and Discussion

The expressions of velocity, temperature, and concentration for Forchheimer, Soret effects on Couette flow in an irregular channel for a dusty viscoelastic fluid with radiation absorption have been derived analytically using the perturbation method. The non-dimensional parameters which are involved in the physical model are S_r, B_i, G_r, G_c, M, P_r, k_r. To study the effect of these non-dimensional parameters on velocity, temperature, and concentration of the dusty fluid and particle, a numerical work has been carried out. For the computation, some of the parameters are fixed as $\lambda = 2\pi$, $x = 1$, $G_r = 10$, $G_c = 10$, $P_r = 5$, $k_r = 1$, $W = 3$. The representation of the velocity profile for the dusty fluid and particle, temperature, and concentration of various parameters is shown graphically in Figs. 2, 3, 4, 5, 6, 7, 8, 9, 10, 11, 12, 13, 14, 15, 16, 17, 18, 19, 20, 21, 22, 23, and 24]. Figures 2, 3, 4, 5, 6, 7, 8, 9, 10, 11, and 12 show the variation of velocity of the fluid and dust particles, respectively. In
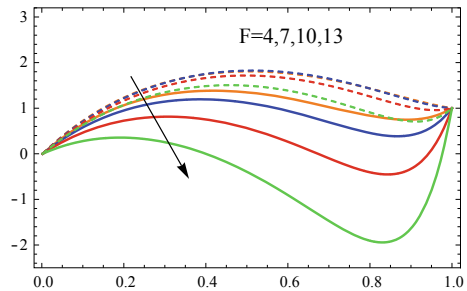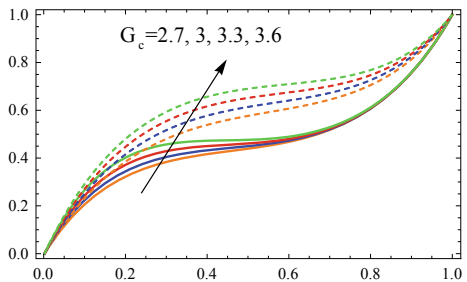
Fig. 2 Velocity profiles of Biot number

$B_i = 0, 0.5, 1, 1.5$
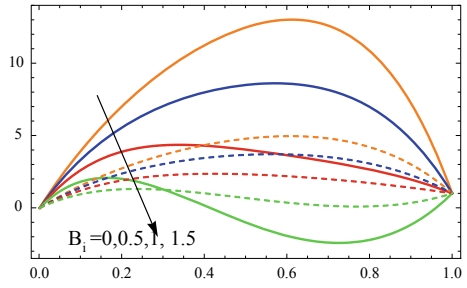
Fig. 3 Velocity profiles of viscoelastic parameter

$E = 1, 2, 3, 4$

Fig. 4 Velocity profiles of thermal radiation parameter

$F = 4, 7, 10, 13$
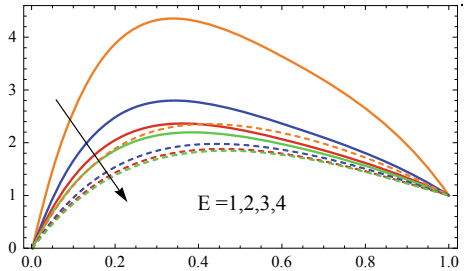
Fig. 5 Velocity profiles of solutal Grashof number

$G_c = 2.7, 3, 3.3, 3.6$

Fig. 6 Velocity profiles of thermal Grashof number

G_r =2.7, 3, 3.3, 3.6
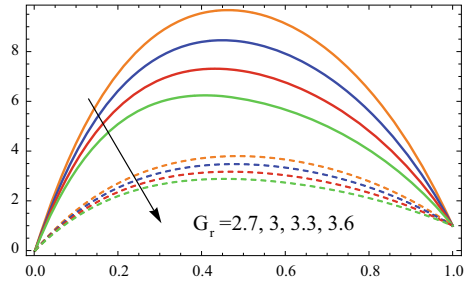
Fig. 7 Velocity profiles of porous permeability

K=0.5,0.8,1.1,1.4
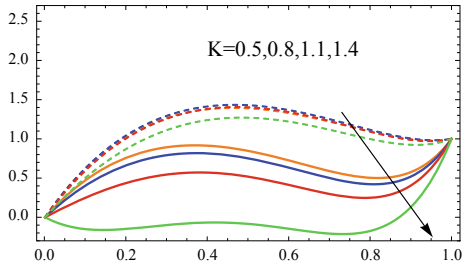
Fig. 8 Velocity profiles of chemical reaction parameter

K_r =1.6, 1.9, 2.3, 2.6
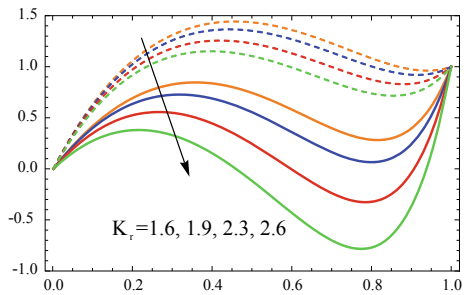
Fig. 9 Velocity profiles of magnetic field

M=2.5,2.8,3.1,3.4
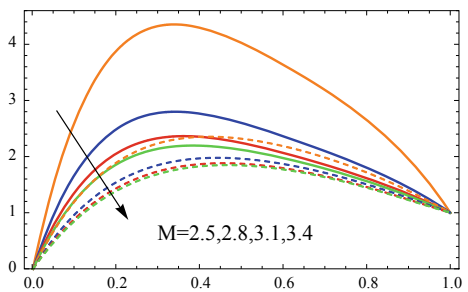
Fig. 10 Velocity profiles of Prandtl number

P_r =2.5, 2.8, 3.1, 3.4
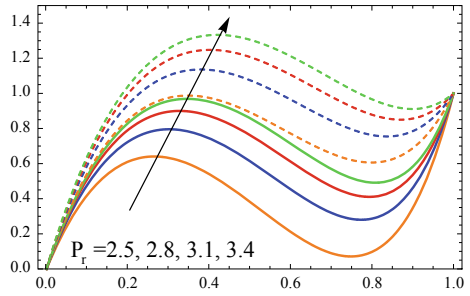
Fig. 11 Velocity profiles of Soret number

S_r=4.4.3, 4.6, 4.9
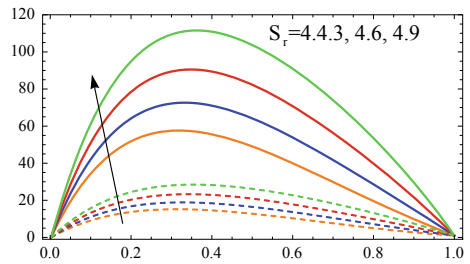
Fig. 12 Velocity profiles of Forchheimer

Γ =.01,.02,.03,.04
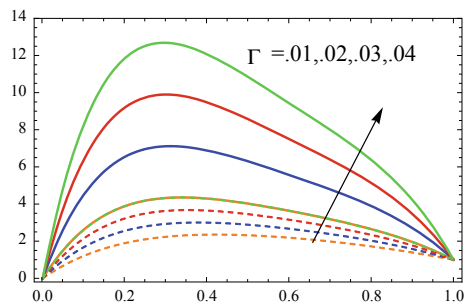
Fig. 13 Temperature profiles of Biot number

B_i=0,0.5,1, 1.5
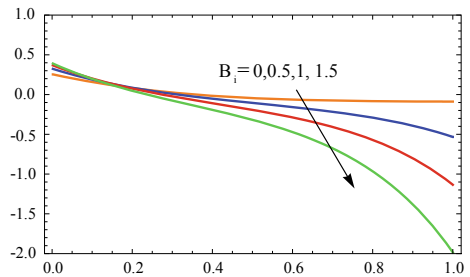
Fig. 14 Temperature profiles of radiation absorption parameter

$\alpha_c = 0, 2, 4, 6$
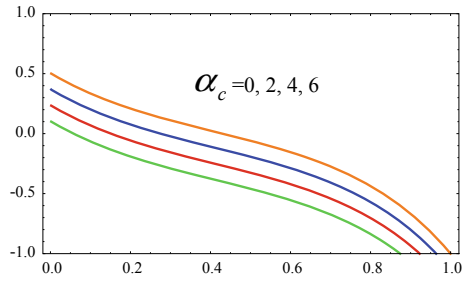
Fig. 15 Temperature profiles of heat absorption parameter

$\alpha_T = 0, 1, 2, 3$
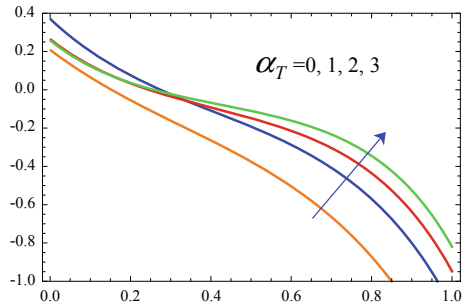
Fig. 16 Temperature profiles of Prandtl number

$P_r = 2.5, 2.8, 3.1, 3.4$
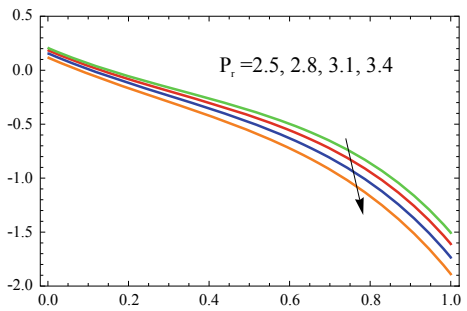
Fig. 17 Temperature profiles of Forchheimer

$\Gamma = 0.01, 0.02, 0.03, 0.04$
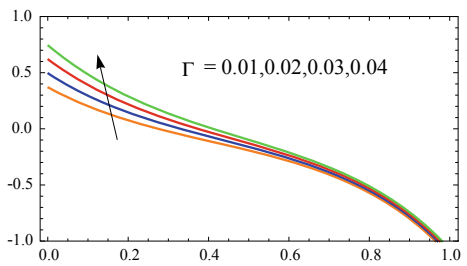
Fig. 18 Temperature profiles of Soret number

$S_r = 4, 4.3, 4.6, 4.9$
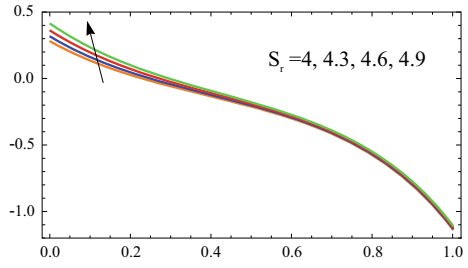
Fig. 19 Temperature profiles of thermal radiation parameter

$F = 4, 7, 10, 13$
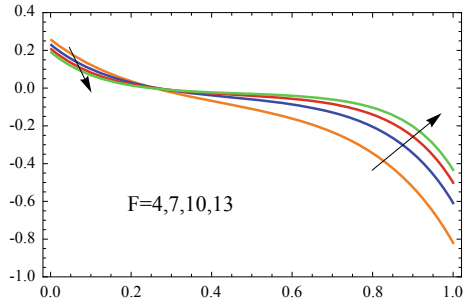
Fig. 20 Concentration profiles of Soret number

$S_r = 4.4.3, 4.6, 4.9$
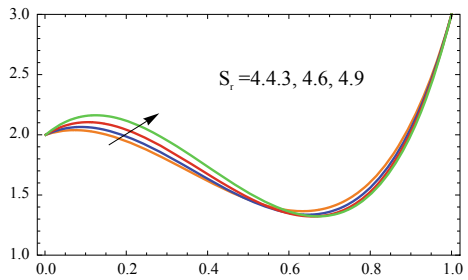
Fig. 21 Concentration profiles of Forchheimer

$\Gamma = 0.01, 0.02, 0.03, 0.04$
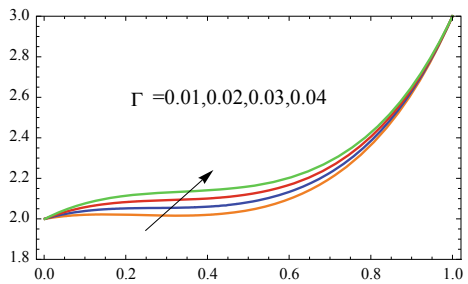
Fig. 22 Concentration profiles of chemical reaction parameter

$K_r = 1.6, 1.9, 2.3, 2.6$
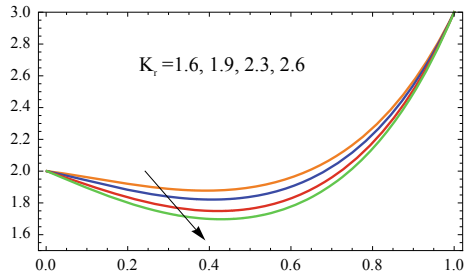
Fig. 23 Concentration profiles of Biot number

$B_i = 0, 0.5, 1, 1.5$
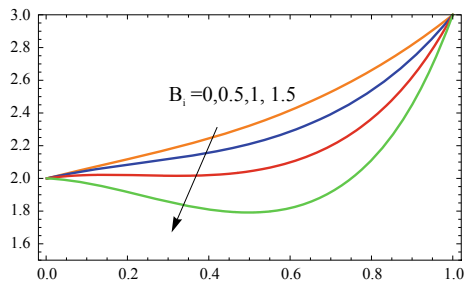
Fig. 24 Concentration profiles of thermal radiation parameter

$F = 4, 7, 10, 13$
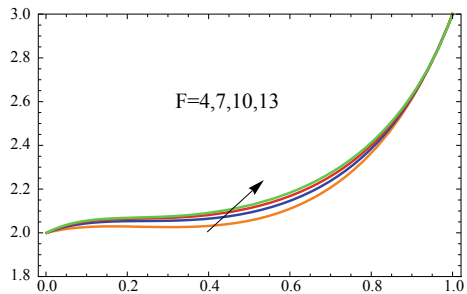
Figs. 2 and 3, it is observed that as Biot number and viscoelastic parameter increase, there is a decrease in velocity of the fluid and the particle due to the increased thermal conductivity and kinematic viscosity. It is clear from Fig. 4 that the velocity of the fluid and particle decrements as the radiation parameter is enhanced because as the thermal radiation increases, there will be a decrease in the momentum boundary layer thickness. In Fig. 5, the velocity profile of solutal Grashof number is presented, and we can observe that as solutal Grashof number increases, the velocity of the fluid and the particle increases. In Fig. 6, it is observed that as thermal Grashof number increases, the velocity of the fluid and the particle decreases. As the porous permeability and chemical reaction parameters are enhanced, the velocity of the fluid and the particle decreases due to porosity and enhancement of its viscosity and is shown in Figs. 7 and 8. It is evident from Fig. 9 that as the magnetic parameter is increased, the velocity

of the fluid and the particle decreases due to a resistive force known as Lorentz force. Figures 10, 11, and 12 illustrate that the velocity of the fluid and particle increases as Prandtl number, Soret, and Forchheimer due to viscous diffusion rate and increase of porosity or decrease of permeability of the porous medium. Figures 13, 14, 15, 16, 17, 18, and 19 show the variation of temperature for different parameters. In Figs. 13, 14, and 16, it is observed that the temperature of the fluid decreases as the Biot number, radiation absorption parameter, and Prandtl number are increased due to channel resistance and increase of convective heat transfer and thermal diffusivity.

Figures 15, 17, and 18 show that the temperature of the fluid increases as the heat absorption parameter, Forchheimer, and Soret numbers are enhanced. In Fig. 19, it is observed that as the thermal radiation parameter increases, it lowers the heat transfer in the boundary layer; hence, the absorption coefficient increases at the wall. Figures 20, 21, 22, 23, and 24 show the concentration variations of different parameters. In Figs. 20, 21, and 24, it is observed that the concentration of the fluid increases as Soret, Forchheimer, and thermal radiation parameter enhance due to the temperature differences and dynamic viscosity. In Figs. 22 and 23, the concentration of the fluid reduces as the chemical reaction parameter and Biot number are increasing due to the change in diffusion rates, which changes the chemical reaction.

5 Conclusion

In this work, we investigated the combined effects of Soret, radiation absorption, and Forchheimer in a two-dimensional magnetohydrodynamic Couette flow through an irregular channel for a dusty viscoelastic fluid. Here, we apply regular perturbation method to solve the equations analytically, and the results are evaluated numerically and displayed graphically. Some of the observations made in this work are with the higher values of Soret number, the velocity, temperature, and concentration profiles increase; with the enhancement of radiation absorption parameter, the temperature of the fluid decreases, but the opposite behavior is seen in heat absorption parameter. The velocity, temperature, and concentration of the fluid and particle increase as the Forchheimer parameter is raised. The velocity of the fluid and the particle decreases as the magnetic field increases. An increase in chemical reaction parameter reduces the concentration and the velocity of the fluid and particle. The profiles of velocity reduce near the wavy wall.

References

1. Beard DW, Walters K (1964) Elastico-viscous boundary layer flows I.Two dimensional flow near a stagnation point. Math Proc Camb Philos Soc 60(3):667–674
2. Tao LN (1960) Magnetohydrodyanamic effects on the formation of Couette flow. J Aerospace Sci 27(5):334–340

3. Hayat T, Kara AH (2006) Couette flow of a third-grade fluid with variable magnetic field. Math Comp Model 43(1–2):132–137
4. Prakash O, Kumar D, Dwivedi YK (2010) Effects of thermal diffusion and chemical reaction on MHD flow of dusty viscoelastic (Walters liquid Model-B) fluid. J Electromagn Anal Appl 2(10):581–587
5. Chang CC, Lundgren TS (1961) Duct flow in magnetohydro dynamics. Zeitschrift fur AngevandteMathematik and Physic 12(2):100–114
6. Sayed-Ahmed ME, Attia HA (2000) MHD flow and heat transfer in a rectangular duct with temperature dependent viscosity and Hall Effect. Int Commun Heat Mass 27(8):1177–1187
7. Attia HA (2006) Hall Effect on Couette flow with heat transfer of a dusty conducting fluid between parallel porous plates under exponential decaying pressure gradient. JMST 20(4):569–579
8. Mekheimer KhS, El Kot MA (2008) Influence of magnetic field and Hall current on blood flow through a stenotic artery. Appl Math Mech 29(8):1093–1104
9. Pal D, Mondal H (2011) MHD non-Darcian mixed convection heat and mass transfer reaction. Int Commun Heat Mass Transfer 38(4):463–467
10. Patil PM, Kulkarni PS (2008) The effect of chemical reaction on free convective flow of a polar fluid through porous medium in the presence of internal heat generation. Int J Therm Sci 47(8):1040–1054
11. Dinesh PA, Nalinakshi N, Sandeep N (2015) Double diffusive mixed convection in a couple stress fluids with variable fluid properties. Adv Phys Theor Appl 41:30–42
12. Mahdy A (2009) MHD non Darcian free convection from a vertical wavy surface embedded in porous media in the presence of Soret and Dufoureffect. Int Commun Heat Mass Transfer 36(10):1067–1074
13. Vajravelu K, Sastri KS (1978) Free convection heat transfer in a viscous incompressible fluid confined between a long vertical wavy wall and a parallel flat wall. J Fluid Mech 86(2):365–383
14. Sivaraj R, Rushikumar B (2012) Unsteady MHD dusty viscoelastic fluid Couette flow in an irregular channel with varying mass diffusion. Int J Heat Mass Trans 55(11–12):3076–3089
15. Jean S, Dash GC, Mishra SR (2016) Chemical reaction effect on MHD Viscoelastic fluid flow over a vertical stretching sheet with heat source/sink. Ain Shams Eng J 9(4):1205–1213
16. Venkateswarlu B, Satya Narayana PV, Devika B (2017) Effects of chemical reaction and heat source on MHD oscillatory flow of a viscoelastic fluid in a vertical porous channel. Int J App Compl Math 3(1):937–952
17. Prasad VR, Vasu B, Beg OA, Prashad RD (2012) Thermal radiation effects on magnetohydro-dynamic free convection heat and mass transfer from a sphere in a variable porosity regime. Commun Nonlin Sci Numer Simulat 17(2):654–671
18. Sivaraj R, Rushikumar B (2013) Chemically reacting dusty viscoelastic fluid flow in an irregular channel with convective boundary. Ain Shams Eng J 4(1):93–101
19. Uma M, Dinesh PA, Sreevallabha Reddy A, Neeraja G (2017) An analytical approach for unsteady MHD dusty viscoelastic fluid couette flow in a vertical wavy channel with varying mass diffusion. Int J Innov Res Sci Eng Technol 6(13):105–110

Radiation Absorption on MHD Convective Flow of Nanofluids over a Moving Vertical Porous Plate

M. Veera Krishna, B. V. Swarnalathamma, and J. Prakash

Abstract We discussed the unsteady MHD free convective flow over an infinite moving vertical porous plate in nanofluids taking radiation absorption into account. The exact solutions for governing equations are obtained using Laplace transform technique. The nanofluid concentration, temperature, velocity, the Sherwood number, Nusselt number, and the shear stresses at the plate are found analytically and discussed graphically for the pertinent parameters.

Keywords Porous media · MHD flows · Nanofluid · Radiation absorption · Vertical plate

1 Introduction

The magnetohydrodynamic (MHD) flows through porous media have several engineering and industrial problems like the development of cooling of filaments and strips, plasma studies, MHD pumps, blood flow capacities, and metallurgical courses. Sarpakaya [1] discussed the flow of non-Newtonian fluids. Elbashbeshy et al. [2] investigated the time-dependent mixed convection flow over an exponentially stretching sheet. Animasaun [3] reported heat and mass transfer on the flow of Casson fluid with some important physical variables. Nayak et al. [4] investigated three-dimensional micro-convection flow of nanofluids past a stretching sheet. Abel et al. [5] investigated the MHD flow and heat transfer with effects of buoyancy, viscous and Joule dissipation over a nonlinear vertical stretching porous sheet with partial

M. Veera Krishna
Department of Mathematics, Rayalaseema University, Kurnool, Andhra Pradesh 518007, India
e-mail: veerakrishna_maths@yahoo.com

B. V. Swarnalathamma (✉)
Department of Science and Humanities, JB institute of Engineering & Technology, Moinabad, Hyderabad, Telangana 500075, India
e-mail: bareddy_swarna@yahoo.co.in

J. Prakash
Department of Mathematics, University of Botswana, Privatebag, 0022 Gaborone, Botswana
e-mail: prakashj@mopipi.ub.bw

slip. Kishan and Deepa [6] investigated the effects of heat transfer with viscous dissipation on the stagnation point flow. Alim et al. [7] investigated the Joule heating and viscous dissipation on Newtonian fluid over vertical plate. Ferdows et al. [8] have discussed the viscous dissipation and Hall current on the boundary layer flow over a stretching surface. Recently, Veera Krishna et al. [9] discussed heat and mass transfer on unsteady MHD oscillatory flow of blood through porous arteriole. Veera Krishna et al. [10] discussed the effects of radiation and Hall current on MHD free convective flow past vertical porous channel. Hall effects on unsteady MHD flow of second-grade fluid through porous medium with ramped wall temperature and ramped surface concentration have been studied by Veera Krishna and Chamkha [11]. Reddy et al. [12] investigated MHD flow of viscous incompressible nanofluid through a saturating porous medium. Veera Krishna and Chamkha [13] discussed the MHD squeezing flow of a water-based nanofluid through a saturated porous medium between two parallel disks, taking the Hall current into account. Sravanthi and Gorla [14] discussed the effects of heat source/sink and chemical reaction on MHD Maxwell nanofluid flow over a convectively hated exponentially stretching sheet using homotopy analysis method.

In this paper, the unsteady MHD convective flow past a moving vertical porous plate in nanofluids with radiation absorption has been carried out.

2 Formulation and Solution of the Problem

The radiation absorption on unsteady free convective flow of nanofluid (Al_2O_3 and TiO_2) past an infinite vertical flat porous plate affecting with an impulsive motion has been considered. A uniform transverse magnetic field of strength B_0 is applied parallel to the y-axis. It is assumed that a radiative heat flux q_r is applied in the normal direction to the plate. The thermal equilibrium is considered for both fluid and nanoparticles. Some properties of the nanofluids are furnished in Table 1. The plate is infinitely extended, and the velocity, temperature, and concentration fields are functions of y and t only (Fig. 1).

Neglecting pressure gradient, induced magnetic field and effect of polarization of fluid, we consider an electrical field $\vec{E} \equiv (0, 0, 0)$ and magnetic field $\vec{B} = (0, 0, B_0)$. Under the above assumptions, the governing equations expressed as

Table 1 Thermophysical properties of water, Al_2O_3, and TiO_2

	Base fluid (water)	Al_2O_3 (alumina)	TiO_2 (titanium dioxide)
c_p (J/kg K)	4179	765	686.2
ρ (kg/m^3)	997.1	3970	4250
k (W/m K)	0.613	40	8.9538
$\beta \times 10^5$ (1/K)	21	0.85	0.9
σ (S/m)	5.5×10^{-6}	35×10^6	2.6×10^6

Fig. 1 Physical configuration of the problem
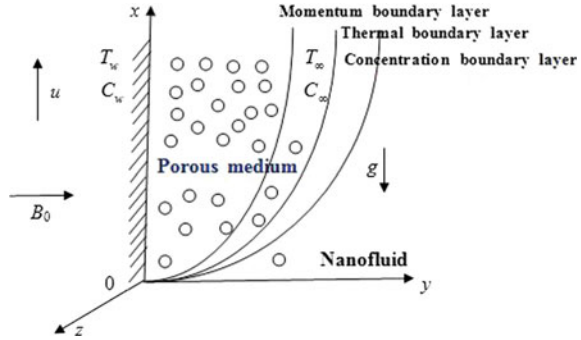
$$\rho_{nf}\frac{\partial u}{\partial t} = \mu_{nf}\frac{\partial^2 u}{\partial y^2} - \sigma_{nf}B_0^2 u - \frac{\mu_f}{k\rho_{nf}}u + g(\rho\beta)_{nf}(T - T_\infty) \tag{1}$$

$$(\rho c_p)_{nf}\frac{\partial T}{\partial t} = k_{nf}\frac{\partial^2 T}{\partial y^2} - \frac{\partial q_r}{\partial y} - Q_1(C - C_\infty) \tag{2}$$

$$\frac{\partial C}{\partial t} = D\frac{\partial^2 C}{\partial y^2} \tag{3}$$

The thermophysical properties of nanofluid are,

$$\mu_{nf} = \frac{\mu_f}{(1-\varphi)^{2.5}}, \rho_{nf} = (1-\varphi)\rho_f + \varphi\rho_s, \left(\rho c_p\right)_{nf} = (1-\varphi)\left(\rho c_p\right)_f + \varphi\left(\rho c_p\right)_s,$$

$$(\rho\beta)_{nf} = (1-\varphi)(\rho\beta)_f + \varphi(\rho\beta)_s, \sigma_{nf} = \sigma_f\left(1 + \frac{3(\sigma-1)\varphi}{(\sigma+2) - (\sigma-1)\varphi}\right), \sigma = \frac{\sigma_s}{\sigma_f}, \tag{4}$$

All physical quantities are their usual meaning. The effective thermal conductivity of the nanofluid given by Hamilton and Crosser model followed by Kakac and Pramuanjaroenkij [15] and Oztop and Abu-Nada [16] is given by

$$k_{nf} = k_f\left(\frac{k_s + 2k_f - 2\varphi(k_f - k_s)}{k_s + 2k_f + \varphi(k_f - k_s)}\right), \tag{5}$$

The initial and boundary conditions are

$$u = 0, T = T_\infty, C = C_\infty, \quad \text{at } t = 0 \text{ for all } y \geq 0,$$
$$u = \lambda u_0, \ T = T_w \ C = C_w \ \text{ at } t > 0, y = 0,$$
$$u \to 0, T \to T_\infty, C \to C_\infty, \quad t > 0 \text{ as } y \to \infty, \tag{6}$$

According to the Rosseland approximation [17], the radiation heat flux q_r is

$$q_r = -\frac{4\sigma*}{3k*}\frac{\partial T^4}{\partial y},\tag{7}$$

Using Taylor's series, T^4 on a free stream temperature T_∞ as follows

$$T^4 = T_\infty^4 + 3T_\infty^3(T - T_\infty) + 6T_\infty^2(T - T_\infty)^2 + \cdots\tag{8}$$

Neglecting higher-order terms in Eq. (8) beyond the first order in $(T - T_\infty)$, we get

$$T^4 \approx 4T_\infty^3 T - 3T_\infty^4\tag{9}$$

On the use of Eqs. (7) and (8), Eq. (2) becomes

$$\frac{\partial T}{\partial t} = \frac{1}{(\rho c_p)_{nf}}\left(k_{nf} + \frac{16\sigma*T_\infty^3}{3k*}\right)\frac{\partial^2 T}{\partial y^2} + Q_1(C - C_\infty)\tag{10}$$

Introducing non-dimensional variables

$$\eta = \frac{u_0 y}{v_f},\ t* = \frac{u_0^2 t}{v_f},\ u* = \frac{u}{u_0},\ \theta = \frac{T - T_\infty}{T_w - T_\infty},\ \phi = \frac{C - C_\infty}{C_w - C_\infty},$$

$$M^2 = \frac{\sigma_f B_0^2 v_f}{\rho_f u_0^2},\ \mathrm{Nr} = \frac{16\sigma*T_\infty^3}{3k_f k*}$$

$$\mathrm{Pr} = \frac{\mu_f c_p}{k_f},\ \mathrm{Gr} = \frac{g\beta_f v_f(T_w - T_\infty)}{u_0^3},\ \mathrm{Sc} = \frac{v}{D},\ K = \frac{ku_0^2}{v_f^2},\ Q = \frac{v_f Q_1(C_w - C_\infty)}{u_0^2(T_w - T_\infty)}$$

The governing Eqs. (2), (3), and (10) reduce to,

$$\frac{\partial u}{\partial t} = a_1 \frac{\partial^2 u}{\partial \eta^2} - \left(M^2 + \frac{1}{K}\right)a_3 u + \mathrm{Gr}\, a_2 \theta\tag{11}$$

$$\frac{\partial \theta}{\partial t} = a_4 \frac{\partial^2 \theta}{\partial \eta^2} + Q\phi\tag{12}$$

$$\frac{\partial \phi}{\partial t} = \frac{1}{\mathrm{Sc}}\frac{\partial^2 \phi}{\partial \eta^2}\tag{13}$$

where

$$x_1 = (1 - \varphi) + \varphi\left(\frac{\rho_s}{\rho_f}\right),\ x_2 = (1 - \varphi) + \varphi\frac{(\rho\beta)_s}{(\rho\beta)_f},\ x_3 = (1 - \varphi) + \varphi\frac{(\rho c_p)_s}{(\rho c_p)_f},$$

$$x_4 = \frac{k_s + 2k_f - 2\varphi(k_f - k_s)}{k_s + 2k_f + \varphi(k_f - k_s)}, \; x_5 = 1 + \frac{3(\sigma - 1)\varphi}{(\sigma + 2) - (\sigma - 1)\varphi}, \; x_6 = \frac{x_4}{x_3},$$

$$a_1 = \frac{1}{(1 - \varphi)^{2.5} x_1}, \; a_2 = \frac{x_2}{x_1}, \; a_3 = \frac{x_5}{x_1}, \; a_4 = \frac{1}{x_3 \Pr}(x_4 + \mathrm{Nr})$$

The corresponding initial and boundary conditions are

$$u = 0, \;\; \theta = 0, t = 0 \;\; \text{for all } \eta \ge 0, u = \lambda, \theta = 1, t > 0 \text{ at } \eta = 0,$$
$$u \to 0, \;\; \theta \to 0, \;\;\; t > 0 \text{ as } \eta \to \infty \tag{14}$$

Taking Laplace transforms on Eqs. (11)–(13) become

$$a_1 \frac{\partial^2 \bar{u}}{\partial \eta^2} - (s + M^2 a_3)\, \bar{u} + \mathrm{Gr}\, a_2 \bar{\theta} = 0, \tag{15}$$

$$a_4 \frac{\partial^2 \bar{\theta}}{\partial \eta^2} - s\bar{\theta} + Q\bar{\phi} = 0, \tag{16}$$

$$\frac{\partial^2 \overline{\phi}}{\partial \eta^2} - s\mathrm{Sc}\, \overline{\phi} = 0, \tag{17}$$

The corresponding boundary conditions for $\bar{u}$ and $\bar{\theta}$ are

$$\bar{u} = \frac{\lambda}{s}, \bar{\theta} = \frac{1}{s}, \bar{\phi} = \frac{1}{s} \;\; \text{at } \eta = 0; \;\; \bar{u} \to 0, \bar{\theta} \to 0, \bar{\phi} \to 0 \;\; \text{as } \eta \to \infty. \tag{18}$$

Transformed solutions of Eqs. (15)–(17) subject to the boundary conditions (18) are easily obtained and are given by

$$\overline{\phi}(\eta, s) = \frac{1}{s^2} \mathrm{e}^{-\eta\sqrt{s\mathrm{Sc}}} \tag{19}$$

$$\bar{\theta}(\eta, \; s) = \frac{1}{s} \mathrm{e}^{-\sqrt{\alpha s}\,\eta} + \frac{Q}{s^3(\mathrm{Sc} - \alpha)} \mathrm{e}^{-\eta\sqrt{s\mathrm{Sc}}} \tag{20}$$

$$\bar{u}(\eta, s) = \frac{\lambda}{s} \mathrm{e}^{-\sqrt{s+\gamma}\,\eta} + \frac{\mathrm{Gr}\, a_5}{b}\left(\frac{1}{s - b} - \frac{1}{s}\right)\left[\mathrm{e}^{-\sqrt{s+\gamma}\,\eta} - \mathrm{e}^{-\sqrt{\alpha s}\,\eta}\right], \tag{21}$$

where $\alpha = \frac{1}{a_4}, \gamma = a_3 M^2, a_5 = \frac{a_2 a_4}{a_1 - a_4}, b = \frac{a_3 a_4 M^2}{a_1 - a_4}$.

Taking inverse Laplace transforms of Eqs. (19)–(21), then, we obtained the solutions for the concentration, temperature, and velocity fields as

$$\phi(\eta, t) = \mathrm{erf}\left(\frac{\eta}{2}\sqrt{\frac{\mathrm{Sc}}{t}}\right), \tag{22}$$

$$\theta(\eta, t) = f_1(\eta\sqrt{\alpha}, Sc, t) \tag{23}$$

$$
\begin{aligned}
u(\eta, t) &= \lambda f_2(\eta, \gamma, t) \\
&+ \frac{Gr\, a_5}{b}\left(f_4(\eta, \gamma, b, t) - f_3(\eta\sqrt{\alpha}, b, t) - f_2(\eta, \gamma, t) + f_1(\eta\sqrt{\alpha}, t)\right)
\end{aligned}
\tag{24}
$$

The shear stress, Nusselt number, and Sherwood number at the plate $\eta = 0$ are evaluated as,

$$\tau_x = \left(\frac{\partial u}{\partial \eta}\right)_{\eta=0}, \; Nu = \left(\frac{\partial \theta}{\partial \eta}\right)_{\eta=0}, \; Sh = \left(\frac{\partial \theta}{\partial \eta}\right)_{\eta=0} \tag{25}$$

Some terms are not mentioned because of paucity of the space.

3   Results and Discussion

Figure 2 discloses that the velocity reduces with increasing M. The momentum boundary layer thickness decreases with increasing M for the cases of the stationary plate ($\lambda = 0$) and moving plate($\lambda = 1$). Due to the magnetic lines of Lorentz forces, the fluid slows down by the viscous force. Figure 3 depicts that the velocity increases with increasing permeability parameter K on either cases. From Fig. 4, the velocity enhances with Nr for both cases. The velocity profiles augment brusquely by the facade of the plate, and after attaining maximum, the curves quite down to the asymptotic worth. Hence, the momentum boundary layer thickness enlarges with an increase in Nr inside a boundary layer region. Figure 5 depicts that the velocity boosts with increasing for either cases and increase the momentum boundary layer thickness. Figure 6 shows that the velocity increases with an increase in Grashof number Gr for both the cases. Figure 7 tells us that the velocity increases with increase in radiation absorption parameter Q on both cases. The velocity increases with increasing time
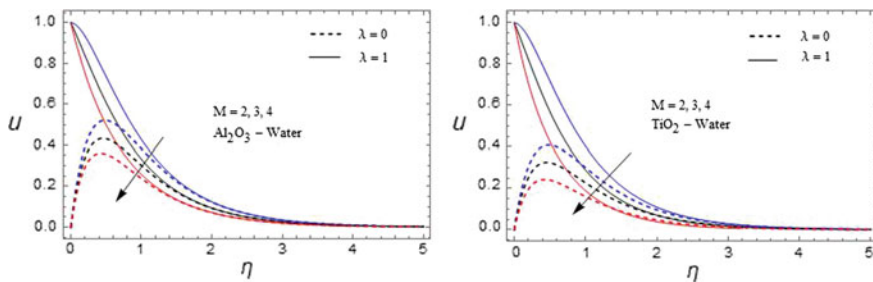
Fig. 2 Velocity profile with M. $K = 0.5$, Nr $= 0.5$, $\varphi = 0.05$, Gr $= 3$, $Q = 0.5, t = 0.1$
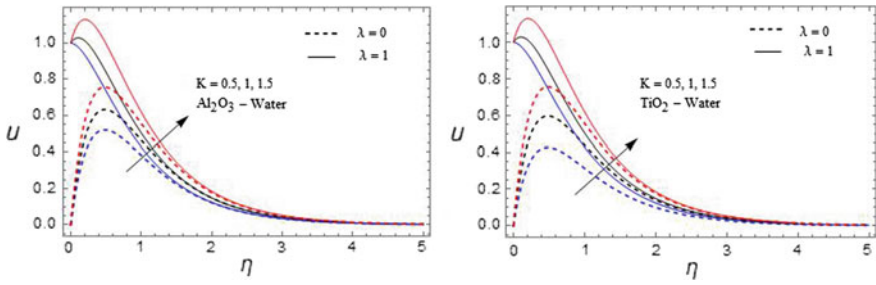
Fig. 3 Velocity profile with K. $M = 2$, Nr $= 0.5$, $\varphi = 0.05$, Gr $= 3$, $Q = 0.5$, $t = 0.1$

Fig. 4 Velocity profile with Nr. $M = 2$, $K = 0.5$, $\varphi = 0.05$, Gr $= 3$, $Q = 0.5$, $t = 0.1$

Fig. 5 Velocity profile with φ. $M = 2$, $K = 0.5$, Nr $= 0.5$, Gr $= 3$, $Q = 0.5$, $t = 0.1$
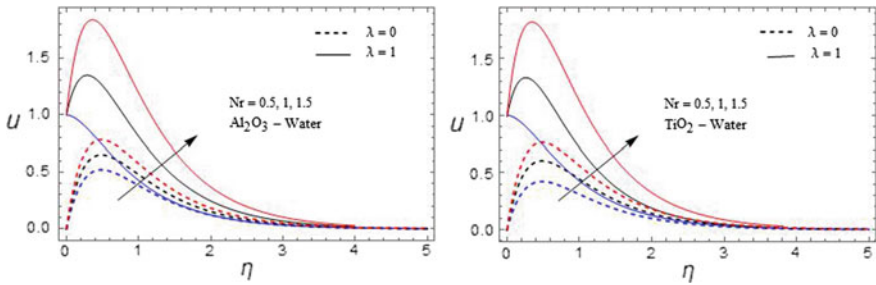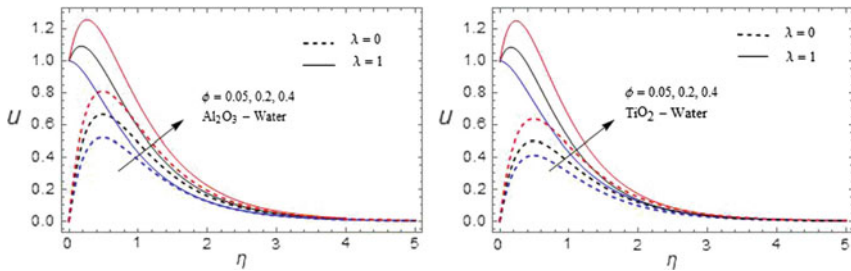

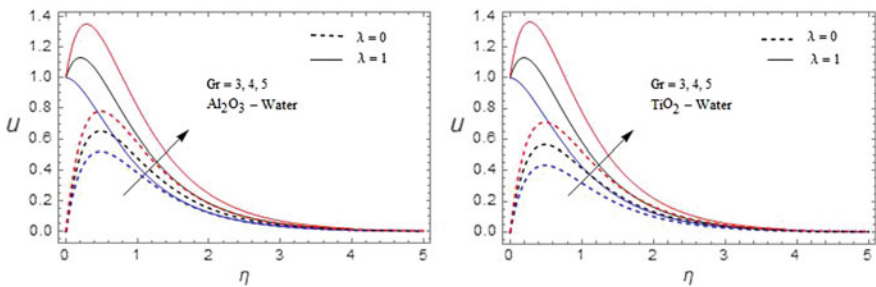**Fig. 6** Velocity profile with Gr. $M = 2$, $K = 0.5$, Nr $= 0.5$, $\varphi = 0.05$, $Q = 0.5$, $t = 0.1$
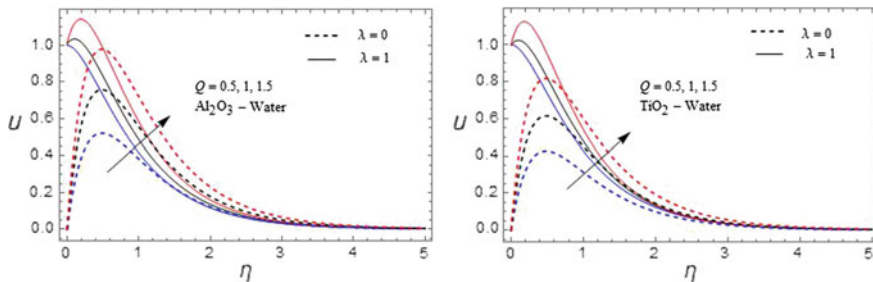
Fig. 7 Velocity profile with Q. $M = 2$, $K = 0.5$, Nr $= 0.5$, $\varphi = 0.05$, Gr $= 3$, $t = 0.1$
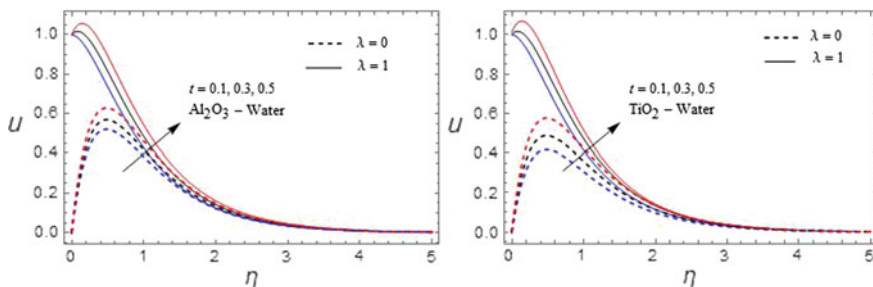
Fig. 8 Velocity profile with t. $M = 2$, $K = 0.5$, Nr $= 0.5$, $\varphi = 0.05$, Gr $= 3$, $Q = 0.5$

for both cases (Fig. 8). Figure 9 represents the variation of nanofluid temperature for Prandtl number Pr, φ, Nr, Q, and t. The temperature reduces as Pr enhances. This is due to the fact that a higher Prandtl number fluid has relatively low thermal conductivity, which reduces heat conduction and there by the thermal boundary layer thickness; and as a result, temperature decreases. Also an increase in radiation parameter Nr means the release of heat energy from the flow region and so the fluid temperature increases. This means that, the thermal boundary layer increases and more uniform temperature distribution across the boundary layer. The fluid temperature increases as volume fraction parameter φ enlarges or Q or t. Figure 10 represents the concentration profiles with Schmidt number Sc and time t. The concentration reduces with increasing Sc and enhances with time. Also, we noticed that the concentration will be zero as it moves away from the plate. Table 2 depicts the stress component, and it reduces with increasing K, Nr, φ, and Sc enhances with increasing M, Gr, Q, and time t. From Table 3, the Nusselt number reduces with Pr, Sc and accelerates with increasing Nr, φ, and time t. From Table 4, the Sherwood number reduces with increasing Sc and enlarges with increasing time. The results are excellent harmony with consequences of Das and Jana [18] (Table 5).
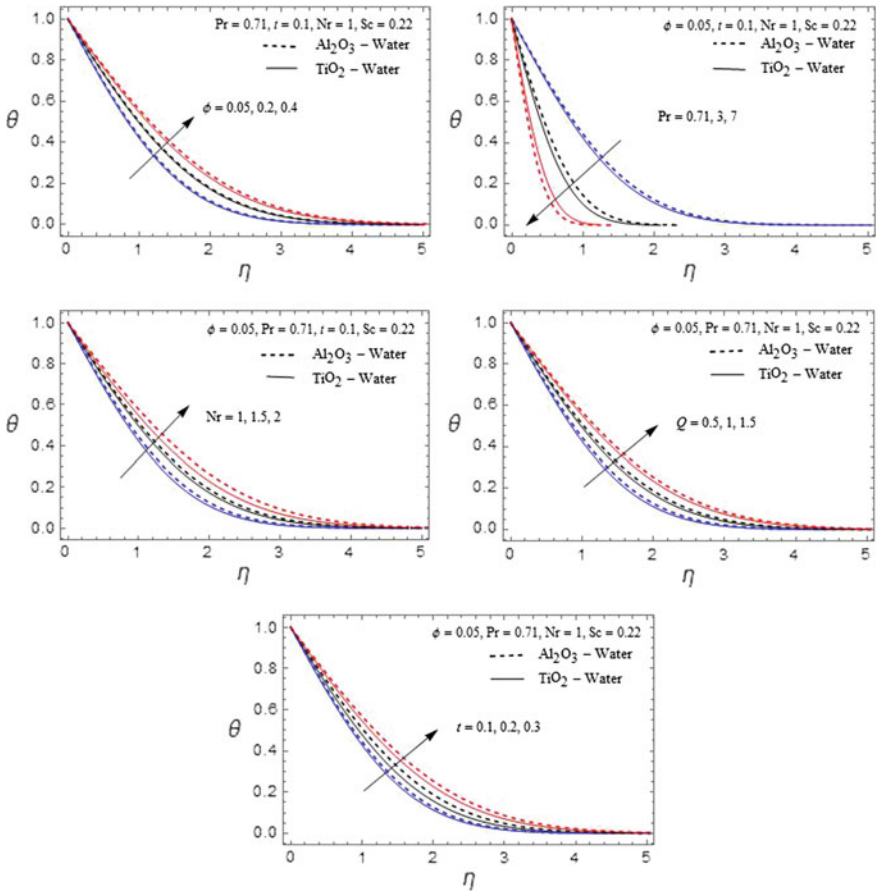
Fig. 9 Temperature profiles with φ, Pr, Nr, Q and t
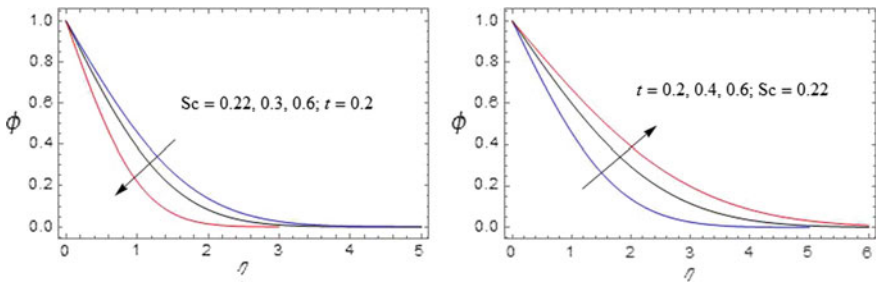
Fig. 10 Concentration profiles with Sc and t

Table 2 Shear stress

M	K	Nr	φ	Sc	Gr	Q	t	τ_x (Al$_2$O$_3$–water)	τ_x (TiO$_2$–water)
2	0.5	1	0.05	0.22	3	0.5	0.2	0.510052	0.455872
3								2.983180	2.565585
4								4.218522	3.988542
	1							0.407968	0.377858
	1.5							0.333386	0.285975
		1.5						0.409731	0.374882
		2						0.373085	0.320142
			0.2					0.501324	0.487528
			0.4					0.483255	0.442517
				0.3				0.485220	0.439858
				0.6				0.395887	0.332569
					4			1.655895	1.202545
					5			2.114558	1.524468
						1		0.985545	0.932565
						1.5		1.522458	1.220358
							0.3	0.652554	0.621454
							0.4	0.854478	0.820112

Table 3 Nusselt number (Sc = 0.22)

Pr	Nr	φ	Q	t	Nu (Al$_2$O$_3$–water)	Nu (TiO$_2$–water)
0.71	1	0.05	0.5	0.1	−1.01909	−0.96658
3					−2.09480	−1.96652
7					−3.19985	−2.88574
	1.5				−0.91821	−0.84574
	2				−0.84237	−0.78554
		0.2			−0.89126	−0.78445
		0.4			−0.72632	−0.68559
			1		−0.85665	−0.62015
			1.5		−0.68855	−0.65145
				0.2	−0.72060	−0.69025
				0.3	−0.58837	−0.55214

Table 4 Sherwood number

Sc	t	Sh
0.22	0.1	−0.626504
0.3		−0.731599
0.6		−1.034640
0.78		−1.179670
	0.2	−0.526825
	0.3	−0.476040
	0.4	−0.443005

Table 5 Comparison of the results for velocity ($\eta = 0.2$, $\lambda = 0$)

M	K	Nr	φ	Previous work (Das and Jana [18])	Present results $K \rightarrow \infty$, $Q = 0$
2	0.5	1	0.05	0.522142	0.522145
3				0.458448	0.458496
4				0.355487	0.355447
	1			0.565894	0.565852
	1.5			0.605221	0.605241
		1.5		0.587447	0.587463
		2		0.622465	0.622447
			0.2	0.597995	0.597996
			0.4	0.650632	0.650621

4 Conclusions

Radiation absorption parameter leads to an increase in the fluid velocity and temperature in the boundary layer region. The velocity enhances with increasing permeability parameter and thermal Grashof number. Nu is found to be higher for Al_2O_3–water than TiO_2–water nanofluid. The stress increases with increasing M.

References

1. Sarpakaya T (1961) Flow of non-Newtonian fluids in a magnetic field. Am Inst Chem Eng 7(2):324–328
2. Elbashbeshy EMA, Emam TG, Abdelgaber KM (2012) Effects of thermal radiation and magnetic field on unsteady mixed convection flow and heat transfer over an exponentially stretching surface with suction in the presence of internal heat generation/absorption. J Egypt Math Soc 20:215–222
3. Animasaun L (2013) Effects of thermophoresis, variable viscosity and thermal conductivity on free convective heat and mass transfer of non-Darcian MHD dissipative Casson fluid flow with suction and nth order of chemical reaction. J Niger Math Soc 30:187–195
4. Nayak MK, Akbar NS, Pandey VS, Khan ZH, Tripathi D (2017) 3D free convective MHD flow of nanofluid over permeable linear stretching sheet with thermal radiation. Powder Technol 315:205–215
5. Abel MS, Kumar K, Ravi Kumara R (2011) MHD flow and heat transfer with effects of buoyancy, viscous and Joule dissipation over a nonlinear vertical stretching porous sheet with partial slip. Engineering 3:285–291
6. Kishan N, Deepa G (2012) Viscous dissipation effects on stagnation point flow and heat transfer of a micropolar fluid with uniform suction or blowing. Adv Appl Sci Res 3:430–439
7. Alim MA, Alam MM, Mamun AA, Hossain B (2008) Combined effect of viscous dissipation and Joule heating on the coupling of conduction and free convection along a vertical flat plate. Int Commun Heat Mass Transfer 35:338–346
8. Ferdows M, Afify AA, Tzirtzilakis EE (2017) Hall current and viscous dissipation effects on boundary layer flow of heat transfer past a stretching sheet. Int J Appl Comput Math 3(4):3471–3487
9. Veera Krishna, M, Swarnalathamma BV, Prakash J (2018) Heat and mass transfer on unsteady MHD Oscillatory flow of blood through porous arteriole. Appl Fluid Dyn XXII:207–224 (Lecture Notes in Mechanical Engineering). https://doi.org/10.1007/978-981-10-5329-0_14
10. Veera Krishna M, Subba Reddy G, Chamkha AJ (2018) Hall effects on unsteady MHD oscillatory free convective flow of second grade fluid through porous medium between two vertical plates. Phys Fluids 30:023106. https://doi.org/10.1063/1.5010863
11. Veera Krishna M, Chamkha AJ (2018) Hall effects on unsteady MHD flow of second grade fluid through porous medium with ramped wall temperature and ramped surface concentration. Phys Fluids 30:053101. https://doi.org/10.1063/1.5025542
12. Reddy BSK, Veera Krishna M, Rao KVSN, Bhuvana Vijaya R (2018) HAM Solutions on MHD flow of nano-fluid through saturated porous medium with Hall effects. Mater Today Proc 5:120–131. https://doi.org/10.1016/j.matpr.2017.11.062
13. Veera Krishna M, Chamkha Ali J (2019) Hall effects on MHD Squeezing flow of a water based nano fluid between two parallel disks. J Porous Media 22(2):209–223. https://doi.org/10.1615/jpormedia.2018028721
14. Sravanthi CS, Gorla RSR (2018) Effects of heat source/sink and chemical reaction on MHD Maxwell Nanofluid flow over a convectively hated exponentially stretching sheet using Homotopy analysis method. Int J Appl Mech Eng 23(1):137–159

15. Kakac S, Pramuanjaroenkij A (2009) Review of convective heat transfer enhancement with nanofluids. Int J Heat Mass Transfer 52:3187–3196
16. Oztop HF, Abu-Nada E (2008) Numerical study of natural convection in partially heated rectangular enclosures filled with nanofluids. Int J Heat Fluid Flow 29:1326–1336
17. Rosseland S (1931) Astrophysik und atom-theoretische Grundlagen. Springer, Berlin
18. Das S, Jana RN (2015) Natural convective magneto-nanofluid flow and radiative heat transfer past a moving vertical plate. Alexandria Eng J 54:55–64

Hall Effects on MHD Free Convective Flow Through Porous Medium in Vertical Channel

B. V. Swarnalathamma, M. Veera Krishna, and J. Prakash

Abstract We have considered the steady fully developed MHD free convection flow through porous medium between two infinite vertical parallel plates due to asymmetric heating of plates taking Hall current into account. Effects of velocity slip and temperature jump have been considered on the micro-channel surfaces and analytical solutions have been obtained for momentum and energy equations under relevant boundary conditions. The influence of governing parameters on flow formation is discussed with the aid of graphs. The significant result from the study is that, increase in the value of rarefaction parameter leads to enhancement in volume flow rate. Furthermore, it is evident that volume flow rate is found to be increasing function of Hall current parameter. The impact of the fluid wall interaction parameter is found to enhance the primary and secondary velocity profile.

Keywords Convection · Hall effects · MHD flows · Microchannels · Porous medium · Rare faction parameter

1 Introduction

Micro-electro-mechanical system has developed a large number of micro-fluidic devices and their applications, such as micro-pump, micro-valves, micro-mixers, micro-heat exchangers, micro-channel heat sinks, and micro-fuel cells. A fundamental understanding of physical aspect of micro-fluidics, which may deviate from those at the macroscale, is required for the technological demands. Seth et al. [1]

B. V. Swarnalathamma
Department of Science and Humanities, JB institute of Engineering & Technology, Moinabad, Hyderabad, Telangana 500075, India
e-mail: bareddy_swarna@yahoo.co.in

M. Veera Krishna (✉)
Department of Mathematics, Rayalaseema University, Kurnool, Andhra Pradesh 518007, India
e-mail: veerakrishna_maths@yahoo.com

J. Prakash
Department of Mathematics, University of Botswana, Privatebag 0022, Gaborone, Botswana
e-mail: prakashj@mopipi.ub.bw

investigated the combined free and forced convection Couette–Hartmann flow of a viscous, incompressible and electrically conducting fluid in rotating channel with arbitrary conducting walls in the presence of Hall current. Seth and Ansari [2] conducted a study on MHD convective flow in a rotating channel with Hall effects. Seth et al. [3] investigated the effects of Hall current and rotation on unsteady hydromagnetic natural convection flows. Hall effects applications include, using magnetic flux leakage, in order to properly inspect items such as pipes or tubes; Hall Effect probes work with something called magnetic flux leakage. This is a way of testing such items, and being able to spot potential corrosion, erosion, or pitting. This is specifically used in steel items, and can give important information about lifespan or safety. Sensors to detect rotation speed, a Hall Effect probe can be used to in bicycle wheels, speedometers in the automotive world, electronic types of ignition systems, and gear teeth. To include studies of magneto-micropolar fluid with Hall current currents with heat transfer due to vast possible engineering applications in areas like power generators, MHD accelerators, refrigeration coils, electric transformers, and heating elements.

Unsteady hydromagnetic Couette flow of a viscous, incompressible, and electrically conducting fluid between two parallel porous plates taking Hall current into account in a rotating system was carried out by Seth et al. [4]. Seth et al. [5] investigated the unsteady hydromagnetic Couette flow of a viscous incompressible electrically conducting fluid in a rotating system in the presence of an inclined magnetic field and Hall current. Veera Krishna et al. [6–20] discussed flow through porous medium in different physical configurations. Veera Krishna et al. [21] discussed Hall effects on unsteady hydromagnetic natural convective rotating flow of second grade fluid past an impulsively moving vertical plate entrenched in a fluid inundated porous medium, while temperature of the plate has a temporarily ramped profile. Veera Krishna and Chamkha [22] discussed the MHD squeezing flow of a water-based nanofluid through a saturated porous medium between two parallel disks, taking the Hall current into account. Veera Krishna et al. [23] discussed Hall effects on MHD peristaltic flow of Jeffrey fluid through porous medium in a vertical stratum.

Motivated by the above studies, in this paper, it was considered the free convection flow of an electrically conducting, viscous incompressible fluid through porous medium between two electrically non-conducting infinite vertical parallel plates taking hall current into account.

2 Formulation and Solution of the Problem

We have considered the free convection flow of an electrically conducting, viscous incompressible fluid through porous medium between two electrically non-conducting infinite vertical parallel plates taking hall current into account. The flow is assumed to be steady and fully developed, i.e., the transverse velocity is zero. The x-axis is taken vertically upward along the plates and the y-axis normal to it as presented in Fig. 1. The distance between the plates is b.

Fig. 1 Physical
configuration of the problem
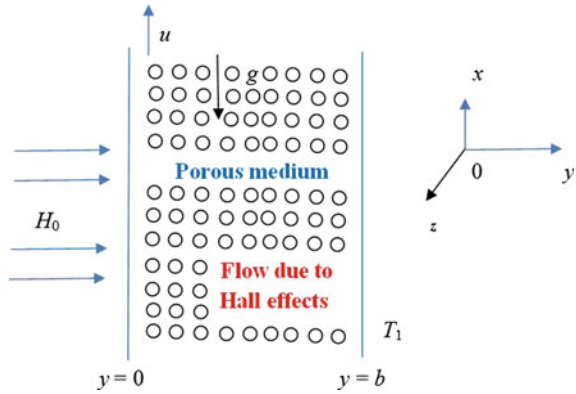
The plates are heated asymmetrically with one plate maintained at a temperature $T1$ while the other plate at a temperature $T2$ where $T1 > T2$. Due to temperature gradient between the plates, natural convection flow occurs in the microchannel. A magnetic field of uniform strength $H0$ is assumed to be applied in the direction perpendicular to the direction of flow. Both plates $y = 0$ and $y = b$ are taken to be non-conducting. As stated earlier, our emphasis in this study is to investigate the effect of induced magnetic field on the flow formation inside the vertical microchannel. It is shown that fluid flow and heat transfer at microscale differ greatly from those at macroscale. At microscale, classical conservation equations successfully coupled with the corresponding wall boundary conditions are valid only if the fluid flow adjacent to the surface is in thermal equilibrium. However, they are not valid for fluid flow at microscale. For this case, the fluid no longer reaches the velocity or the temperature of the surface and therefore a slip condition for the velocity and a jump condition for the temperature should be adopted.

In this present study, the usual continuum approach is applied by the continuum equations with the two main characteristics of the micro-scale phenomena, the velocity slip, and the temperature jump. Velocity slip is defined as

$$u_{\mathrm{s}} = \frac{2 - \sigma_{\mathrm{v}}}{\sigma_{\mathrm{v}}} \lambda \frac{\partial u}{\partial y}\Big|_{y=b} \tag{1}$$

The temperature jump is defined as

$$T_{\mathrm{s}} - T_{\mathrm{w}} = \frac{2 - \sigma_{\mathrm{t}}}{\sigma_{\mathrm{t}}} \frac{2\gamma}{\gamma + 1} \frac{\lambda}{\mathrm{Pr}} \frac{\partial T}{\partial y}\Big|_{y=b} \tag{2}$$

where T_{s}, T_{w}, and σ_{t} which depend on the gas and surface materials. However, for air, it assumes typical values near unity. For the rest of the analysis, σ_{v} and σ_{t} will be assumed to be 1.

By taking into account the conducting fluid, transverse magnetic field and induced magnetic field, the governing equations of the system are given in dimensional from:

$$v\frac{d^2u}{dy^2} - \frac{\mu_e J_z H_0}{\rho} - \frac{v}{k}u + g(T - T_0) = 0 \tag{3}$$

$$v\frac{d^2w}{dy^2} + \frac{\mu_e J_x H_0}{\rho} - \frac{v}{k}w = 0 \tag{4}$$

$$k_1\frac{d^2T}{dy^2} = 0 \tag{5}$$

When the strength of the magnetic fell is very large, the generalized ohm's law is modified to include the Hall current, so that

$$J + \frac{\omega_e \tau_e}{H_0}(J \times H) = \sigma(E + \mu_e q \times H) \tag{6}$$

The components of Eq. (6) are

$$J_x - m J_z = -\sigma \mu_e H_0 w \tag{7}$$

$$J_z + m J_x = -\sigma \mu_e H_0 u \tag{8}$$

where $m = \omega_e \tau_e$ is the hall parameter, solving Eqs. (7) and (8),

$$J_x = \frac{\sigma \mu_e H_0}{1 + m^2}(um - w) \tag{9}$$

$$J_z = \frac{\sigma \mu_e H_0}{1 + m^2}(u + wm) \tag{10}$$

Substitute Eqs. (7) and (8) in Eqs. (4) and (3), respectively, we get

$$v\frac{\partial^2 u}{\partial y^2} - \frac{\sigma \mu_e^2 H_0^2}{\rho}(u + wm) - \frac{v}{k}u + g(T - T_0) = 0 \tag{11}$$

$$v\frac{\partial^2 w}{\partial y^2} + \frac{\sigma \mu_e^2 H_0^2}{\rho}(um - w) - \frac{v}{k}w = 0 \tag{12}$$

With the boundary conditions for the velocity, induced magnetic field and temperature field are as follows:

$$u = \frac{2 - \sigma_v}{\sigma_v}\lambda\frac{\partial u}{\partial y}, \, w = 0, \, T = T_2 + \frac{2 - \sigma_t}{\sigma_t}\frac{2\gamma}{\gamma + 1}\frac{\lambda}{\Pr}\frac{\partial T}{\partial y}, \quad \text{at } y = 0 \tag{13}$$

$$u = -\frac{2-\sigma_v}{\sigma_v}\lambda\frac{\partial u}{\partial y}, w = 0, T = T_1 - \frac{2-\sigma_t}{\sigma_t}\frac{2\gamma}{\gamma+1}\frac{\lambda}{\Pr}\frac{\partial T}{\partial y} \quad \text{at } y = b \quad (14)$$

Making use of the following non-dimensional quantities

$$y^* = \frac{y}{b}, \theta = \frac{T-T_0}{T_1-T_0}, (u^*, w^*) = \frac{(u,w)\nu}{g\beta\Delta Tb^2}, \Delta T = T_1 - T_0$$

$$\Pr = \frac{\nu}{\alpha}, M^2 = \frac{\sigma\mu_e^2 H_0^2 b^2}{\rho\nu}, K = \frac{b^2}{k}, m = \omega_e\tau_e \quad (15)$$

The non-dimensional governing equations are (Dropping asterisks)

$$\frac{d^2u}{dy^2} - \frac{M^2}{1+m^2}(u+mu) + \frac{\nu}{K}u + \theta = 0 \quad (16)$$

$$\frac{d^2w}{dy^2} + \frac{M^2}{1+m^2}(mu-w) + \frac{\nu}{K}w = 0 \quad (17)$$

$$\frac{d^2\theta}{dy^2} = 0 \quad (18)$$

Subject to the following non-dimensional boundary conditions are

$$u = \beta_v Kn\frac{du}{dy}, w = \beta_v Kn\frac{dw}{dy}, \theta = \xi + \beta_v Kn \ln\frac{d\theta}{dy} \quad \text{at } y = 0 \quad (19)$$

$$u = -\beta_v Kn\frac{du}{dy}, w = -\beta_v Kn\frac{dw}{dy}, \theta = 1 - \beta_v Kn \ln\frac{d\theta}{dy}, \quad \text{at } y = 1 \quad (20)$$

By defining the complex velocity $Q = u + iw$, Eqs. (16) and (17) now become

$$\frac{d^2Q}{dy^2} - \left(\frac{M^2}{1+im} + \frac{1}{K}\right)Q = -\theta \quad (21)$$

With the boundary conditions in non-dimensional form are as follows:

$$\theta(y) = \xi + \beta_v Kn \ln\frac{d\theta}{dy}; \ Q(y) = \beta_v Kn\frac{dQ}{dy} \quad \text{at } y = 0 \quad (22)$$

$$\theta(y) = 1 - \beta_v Kn \ln\frac{d\theta}{dy}; \ Q(y) = -\beta_v Kn\frac{dQ}{dy} \quad \text{at } y = 1 \quad (23)$$

Referring the values of σ_v and σ_t given in Eckert and Drake [24] and Goniak and Duff [25], the values of β_v is near unity, and the values of β_t ranges from near

to more than 100 for actual wall surface conditions and is near 1.667 for many engineering applications, corresponding to $\alpha_v = 1$, $\alpha_t = 1$, $\gamma_s = 1.4$ and $Pr = 0.71$ ($\beta_v = 1$, $\beta_t = 1.667$). The physical quantities used in the above equations are defined in the nomenclature.

The solution to Eqs. (18) and (21) with the boundary conditions (22) and (23) is as follows:

$$\theta(y) = A_0 + A_1 y \tag{24}$$

$$Q(y) = C_1 \cosh(M_1 y) + C_2 \sinh(M_1 y) + \frac{1}{M_1^2}(A_0 + A_1 y) \tag{25}$$

Two important performances for buoyancy-induced micro-flow are the volume flow rate (δ) and skin-friction (τ). The complex volume flow rate is as follows:

$$\delta = Q_x + i Q_z = \int\limits_0^1 Q(y)\mathrm{d}y \tag{26}$$

where,

$$Q_x = \Re e(\delta) \quad \text{and} \quad Q_z = \mathrm{Im}(\delta) \tag{27}$$

$$\delta = \frac{C_1}{M_1}\sinh(M_1) + \frac{C_2}{M_1}(\cosh(M_1) - 1)\frac{1}{M_1^2}\left(A_0 + \frac{A_1}{2}\right) \tag{28}$$

Using expression (25), the dimensionless skin-friction at the micro-channel surface due to primary and secondary flows is as follows:

$$\tau_{x_0} + i \tau_{z_o} = \left.\frac{\mathrm{d}Q}{\mathrm{d}y}\right|_{y=0} = M_1 C_2 + \frac{A_1}{M_1^2} \tag{29}$$

$$\tau_{x_1} + i \tau_{z_1} = \left.\frac{\mathrm{d}Q}{\mathrm{d}y}\right|_{y=1} = \frac{A_1}{M_1^2} - M_1(C_1 \sinh(M_1) + C_2 \cosh(M_1)) \tag{30}$$

The Nussle number at both the plates is obtained by the following formula.

$$\mathrm{Nu} = \left(\frac{\mathrm{d}\theta}{\mathrm{d}y}\right) = A_1 \tag{31}$$

3 Results and Discussion

For computational purpose, we are fixing wall-ambient temperature difference ratio $\xi = 1$. Figure 2 displays the effect of the Hartmann number M on the primary and secondary velocity profiles. It is seen in the primary and secondary velocities that, increasing the values of Hartmann number has a tendency to slow down of the fluid in the microchannel. Figures 3 and 4 show the effects of the permeability parameter K and Hall current parameter m on the primary and secondary velocities. It is evident from the Fig. 3 that, both the primary and secondary velocities are increasing with increase in the value of permeability parameter. Also, the primary velocity reduces and secondary velocity enhances with increasing Hall parameter and leads to enhancement in the resultant fluid velocity. Lower the permeability lesser the fluid speed is observed in the entire fluid region. Furthermore, an increase in the Hall parameter decreases the reducing effect of the magnetic field on the complex velocity Q thereby increasing the velocity in both primary velocity and secondary velocity. Figures 5 and 6 illustrate the effects of the rarefaction parameter $\beta_v K n$, as well as wall-Knudsen number Kn on the primary and secondary velocities. It is observed for both primary velocity and secondary velocity that, increasing the Knudsen number as well as rarefaction parameter leads to enhancement in the fluid velocity and velocity slip. These effects are more pronounced in the case of secondary velocity. This result yields an observable increase in the fluid velocity. This physical phenomenon can
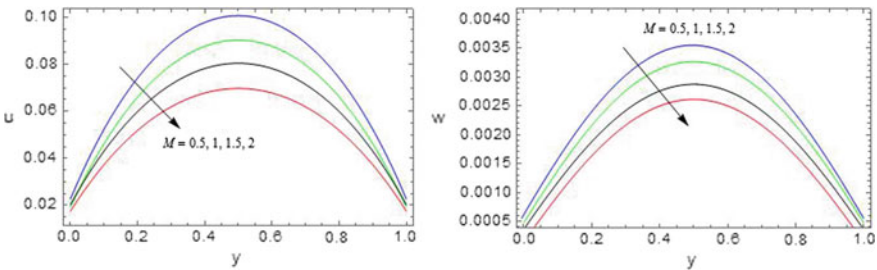

Fig. 2 Velocity profiles for u and w against M. $K = 0.5$, $m = 1$, $\ln = 5$, $\beta_v = 0.05$, $Kn = 1$

Fig. 3 Velocity profiles for u and w against K. $M = 0.5$, $m = 1$, $\ln = 5$, $\beta_v = 0.05$, $Kn = 1$

Fig. 4 Velocity profiles for u and w against m. $M = 0.5$, $K = 0.5$, $\ln = 5$, $\beta_v = 0.05$, $Kn = 1$

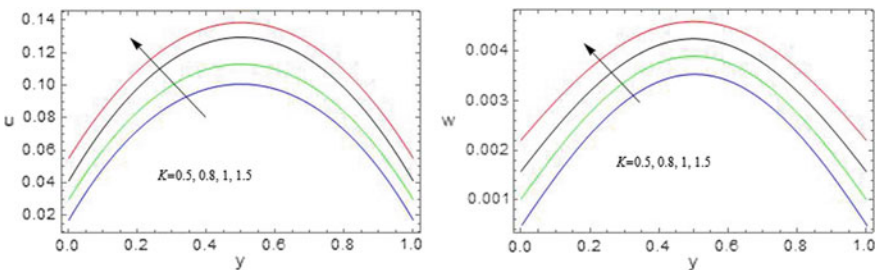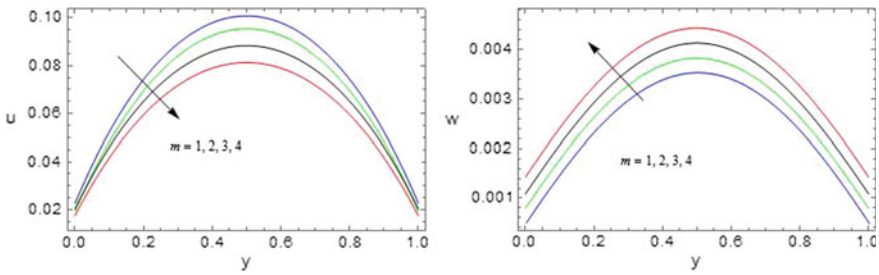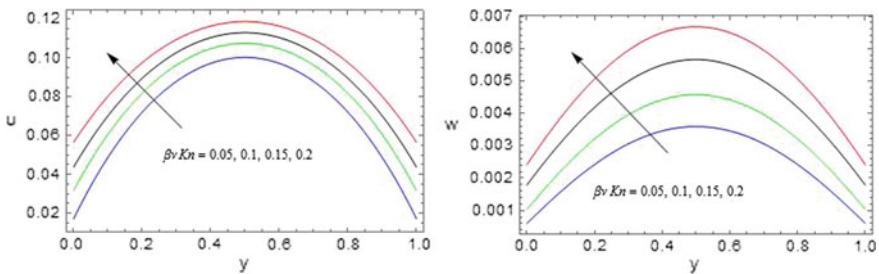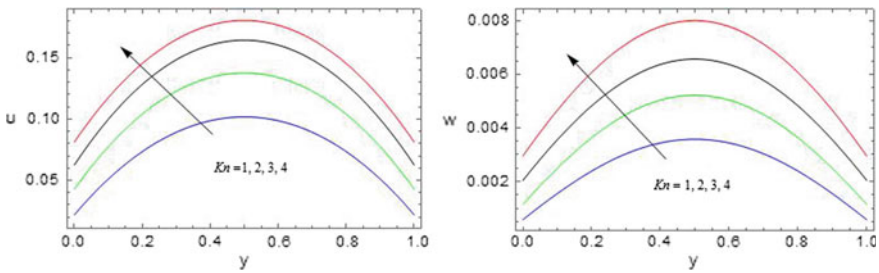**Fig. 5** Velocity profiles for u and w against $\beta_v Kn$. $M = 0.5$, $K = 0.5$, $m = 1$, $\ln = 5$, $Kn = 1$

Fig. 6 Velocity profiles for u and w against Kn. $M = 0.5$, $K = 0.5$, $m = 1$, $\ln = 5$, $\beta_v = 0.05$

be explained from the fact that, as rarefaction parameter increases, the temperature jump increases and this reduces the amount of heat transfer from the micro-channel surfaces to the fluid. The reduction in fluid velocity due to the reduction in heat transfer is offset by the increase in the fluid velocity due to the reduction in the frictional retarding forces near the micro-channel surfaces. Figure 7 displays the effect of fluid wall interaction parameter ln on the primary and secondary velocities. It is clearly seen for both cases that, the role of the fluid wall interaction parameter is found to enhance the primary and secondary velocities profile. Furthermore, the influences of fluid wall interaction parameter on the micro-channel slip velocity
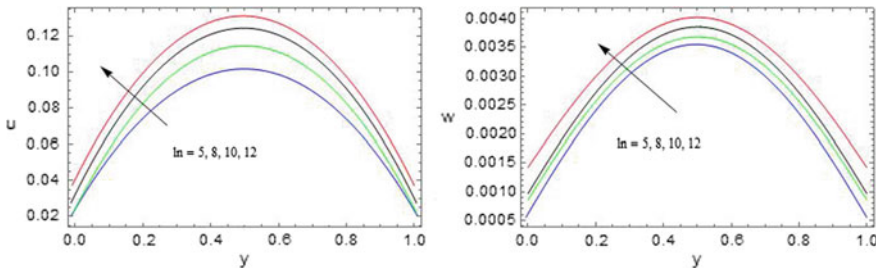
Fig. 7 Velocity profiles for u and w against ln. $M = 0.5$, $K = 0.5$, $m = 1$, $\beta_v = 0.05$, $Kn = 1$

become significant with the decrease in the wall-ambient temperature difference ratio which is more pronounced in the case of primary velocity. Further, it was noticed that from Fig. 8 of the temperature on ln, ξ, $\beta_v Kn$ and Kn, the magnitude of the temperature retards with increasing fluid wall interaction parameter ln and increases with increasing wall-ambient temperature difference ratio ξ. Likewise, temperature initially improves up in $y \leq 3$ and then gradually reduces with increasing rarefaction parameter $\beta_v Kn$, and Knudsen number Kn throughout the fluid region. Here, we are fixing the values of $\beta_v Kn = 0.05$, $Kn = 1$, $\xi = 0.1$, $ln = 1.667$. This study exactly agrees with the finding of Chen and Weng [26] in the absence of Hartmann number, Jha et al. [27] in the absence of Hall current, and Jha et al. [28] in the absence of permeability of porous medium (Table 1). Table 2 illustrates the volumetric flow rate with the variations of the governing parameters. The volumetric flow rate increases
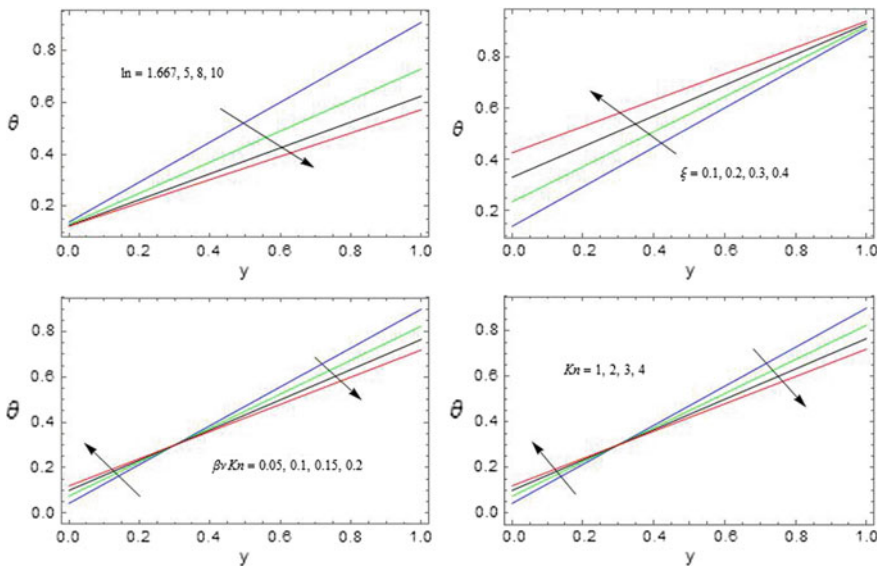
Fig. 8 Temperature profiles against ln, ξ, β_v and Kn

Table 1 Numerical comparison of the values of primary velocity (u) obtained in the present work ($\beta_v Kn = 0.05$, $Kn = 1$, $\xi = 1$, $ln = 1.667$)

y	Chen and Weng [26]	Present work $M = 0, K \to \infty$	Jha et al. [27]	Present work $m = 0, K \to \infty$	Jha et al. [27]	Present work $K \to \infty$
0.2	0.105045	0.105045	0.071522	0.071522	0.0254	0.025452
0.4	0.145012	0.145012	0.069418	0.069418	0.0455	0.04552
0.6	0.145022	0.145022	0.096400	0.096401	0.0526	0.05267
0.8	0.105044	0.105044	0.071521	0.071523	0.0456	0.04557
1.0	0.025000	0.025000	0.017225	0.017628	0.0288	0.02881

Table 2 Volume flow rate (mass flux)

M	m	K	$\beta_v Kn$	Kn	ln	ξ	δ
0.5	1	0.5	0.05	1	1.667	0.1	0.566943
1							0.347740
1.5							0.162930
	2						0.625473
	3						0.646992
		1					1.705020
		1.5					2.706420
			0.1				0.525029
			0.15				0.487768
				2			0.525029
				3			0.487768
					5		0.512124
					8		0.532691
						0.2	0.177853
						0.3	0.040327

with increasing Hall parameter m, permeability parameter K, ln and reduces with M, β_v, Kn and ξ. We noticed from Table 3 that the magnitude of the stresses τ_{x0} reduces and τ_{z0} enhances with increasing Hartmenn number M; the opposite behaviour is observed with increasing Hall parameter m. Both τ_{x0} and τ_{z0} stresses retard with increasing $\beta_v Kn$, Kn, ln and ξ increases with increasing K. The similar behaviour is observed for τ_{x1} and τ_{z1}. Nusselt number reduces with $\beta_v Kn$, Kn and ln and reversal behaviour is observed with increasing ξ (Table 4).

Table 3 Shear Stress (Frictional force)

M	m	$\beta_v Kn$	Kn	$1n$	K	ξ	τ_{x_0}	τ_{z_0}	τ_{x_1}	τ_{z_1}
0.5	1	0.05	1	1.667	0.5	0.1	4.83603	0.360294	1.21929	0.20054
1							3.75345	0.920258	0.62962	0.39551
1.5							2.58246	1.124730	0.19200	0.26275
	2						5.07050	0.316121	1.35419	0.18294
	3						5.15910	0.245006	1.40766	0.14366
		0.1					4.60291	0.356291	1.06489	0.18394
		0.15					4.43936	0.354721	0.94814	0.17054
			2				4.60291	0.342214	1.06489	0.18394
			3				4.43936	0.330221	0.94744	0.16922
				5			4.78136	0.352434	1.17537	0.19926
				8			4.74946	0.347849	1.14974	0.19852
					0.8		8.61869	1.142830	3.77128	0.86082
					1.0		11.5416	2.012350	6.03851	1.60494
						0.2	2.57447	0.203369	0.78654	0.10792
						0.3	1.82940	0.152648	0.67211	0.07903

Table 4 Nusselt number

β_v	Kn	ln	ξ	Nu
0.05	1	1.667	0.1	0.87140
0.1				0.77496
0.15				0.69996
	2			0.77496
	3			0.69985
		5		0.70000
		8		0.60000
			0.2	0.88569
			0.3	0.89998

4   Conclusions

1. The impact of the fluid wall interaction parameter is found to enhance the primary and secondary velocity profiles.
2. Increasing the wall-ambient temperature difference ratio and rarefaction parameter leads to enhancement in the fluid velocity and velocity slip for both primary velocity and secondary velocity.
3. An increase in the value of Hall current parameter leads to enhancement in the skin frictions due to primary as well as secondary flow.
4. The frictional force on the micro-channel surfaces can be controlled by applying suitable value of Hartmann number, Hall current parameter, Knudsen number and fluid wall interaction parameter.

References

1. Seth GS, Sarkar S, Makinde OD (2016) Combined free and forced convection Couette-Harmann flow in rotating channel with arbitrary conducting walls and Hall effects. J Mech 32(5):613–629
2. Seth GS, Ansari MdS (2009) Magnetohydrodynamic convective flow in a rotating channel with Hall effects. Int J Theor Appl Mech 4(2):205–222
3. Seth GS, Sarkar S, Hussain SM (2014) Effects of Hall current, radiation and rotation on natural convection heat and mass transfer flow past a moving vertical plate. Ain Shams Eng. J. 5(2):489–503
4. Seth GS, Singh JK, Mahato GK (2012) Effects of Hall current and rotation on unsteady hydromagnetic couette flow within a porous channel. Int J Appl Mech 4(2)
5. Seth GS, Nandkeolyar R, Ansari MdS (2015) Effects of Hall current and rotation on unsteady MHD Couette flow in the presence of an inclined magnetic field. J Appl Fluid Mech 8(1):7–20
6. Veera Krishna M, Gangadhar Reddy M (2018) MHD free convective boundary layer flow through porous medium past a moving vertical plate with heat source and chemical reaction. Mater Today Proc 5:91–98. https://doi.org/10.1016/j.matpr.2017.11.058

7. Veera Krishna M, Subba Reddy G (2018) MHD forced convective flow of Non-Newtonian fluid through stumpy permeable porous medium. Mater Today Proc 5:175–183. https://doi.org/10.1016/j.matpr.2017.11.069

8. Veera Krishna M, Jyothi K (2018) Hall effects on MHD rotating flow of a visco-elastic fluid through a porous medium over an infinite oscillating porous plate with heat source and chemical reaction. Mater Today Proce 5:367–380. https://doi.org/10.1016/j.matpr.2017.11.094

9. Reddy BSK, Veera Krishna M, Rao KVSN, Bhuvana Vijaya R (2018) HAM Solutions on MHD flow of nano-fluid through saturated porous medium with Hall effects. Mater Today Proc 5:120–131. https://doi.org/10.1016/j.matpr.2017.11.062

10. VeeraKrishna M, Swarnalathamma BV (2016) Convective heat and mass transfer on MHD peristaltic flow of Williamson fluid with the effect of inclined magnetic field. AIP Conf Proc 1728:020461. https://doi.org/10.1063/1.4946512

11. Swarnalathamma BV, Veera Krishna M (2016) Peristaltic hemodynamic flow of couple stress fluid through a porous medium under the influence of magnetic field with slip effect. AIP Conf Proc 1728:020603. https://doi.org/10.1063/1.4946654

12. VeeraKrishna M, Gangadhar Reddy M (2016) MHD free convective rotating flow of Visco-elastic fluid past an infinite vertical oscillating porous plate with chemical reaction. IOP Conf Ser Mater Sci Eng 149:012217. https://doi.org/10.1088/1757-899x/149/1/012217

13. VeeraKrishna M, Subba Reddy G (2016) Unsteady MHD convective flow of second grade fluid through a porous medium in a rotating parallel plate channel with temperature dependent source. IOP Conf Ser Mater Sci Eng 149:012216. https://doi.org/10.1088/1757-899x/149/1/012216

14. Veera Krishna M, Swarnalathamma BV, Prakash J (2018) Heat and mass transfer on unsteady MHD oscillatory flow of blood through porous arteriole. I?: Applications of fluid dynamics, lecture notes in mechanical engineering, vol XXII, pp 207–224. https://doi.org/10.1007/978-981-10-5329-0_14

15. Veera Krishna M, Subba Reddy G, Chamkha AJ (2018) Hall effects on unsteady MHD oscillatory free convective flow of second grade fluid through porous medium between two vertical plates. Phys Fluids 30:023106. https://doi.org/10.1063/1.5010863

16. Veera Krishna M, Chamkha AJ (2018) Hall effects on unsteady MHD flow of second grade fluid through porous medium with ramped wall temperature and ramped surface concentration. Phys Fluids 30:053101. https://doi.org/10.1063/1.5025542

17. Veera Krishna M, Jyothi K, Chamkha AJ (2018) Heat and mass transfer on unsteady, magneto-hydrodynamic, oscillatory flow of second-grade fluid through a porous medium between two vertical plates, under the influence of fluctuating heat source/sink, and chemical reaction. Int J Fluid Mech Res 45(5):459–477. https://doi.org/10.1615/InterJFluidMechRes.2018024591

18. Veera Krishna M, Gangadhara Reddy M, Chamkha AJ (2019) Heat and mass transfer on MHD free convective flow over an infinite non-conducting vertical flat porous plate. Int J Fluid Mech Res 46(1):1–25. https://doi.org/10.1615/InterJFluidMechRes.2018025004

19. Veera Krishna M, Jyothi K (2019) Heat and mass transfer on MHD rotating flow of a visco-elastic fluid through porous medium with time dependent oscillatory permeability. J Anal 27:643–662. https://doi.org/10.1007/s41478-018-0099-0

20. Veera Krishna M, Subba Reddy G (2019) Unsteady MHD reactive flow of second grade fluid through porous medium in a rotating parallel plate channel. J Anal 27:103–120. https://doi.org/10.1007/s41478-018-0108-3

21. Veera Krishna M, Gangadhara Reddy M, Chamkha AJ (2019) Heat and mass transfer on MHD rotating flow of second grade fluid past an infinite vertical plate embedded in uniform porous medium with hall effects. Appl Math Sci Comput Trends Math 1:417–427. https://doi.org/10.1007/978-3-030-01123-9_41

22. Veera Krishna M, Chamkha AJ (2019) Hall effects on MHD Squeezing flow of a water based nano fluid between two parallel disks. J Porous Media 22(2):209–223. https://doi.org/10.1615/jpormedia.2018028721

23. Veera Krishna M, Bharathi K, Chamkha AJ (2019) Hall effects on MHD peristaltic flow of Jeffrey fluid through porous medium in a vertical stratum. Interf Phenom Heat Transfer 6(3):253–268. https://doi.org/10.1615/interfacphenomheattransfer.2019030215

24. Eckert ERG, Drake Jr RM (1972) Analysis of heat and mass transfer. Mcgraw-Hill, New York
25. Goniak R, Duffa G (1995) Corrective term in wall slip equations for knudsen layer. J Thermophys Heat Transfer 9:383–384
26. Chen CK, Weng HC (2005) Natural convection in a vertical microchannel. J Heat Transfer 127:1053–1056
27. Jha BK, Aina B, Ajiya AT (2015) MHD Natural convection in a vertical parallel plate microchannel. J Ain Shams Eng 6:289–295
28. Jha BK, Malgwi PB, Aina B (2018) Hall effects on MHD natural convection in a vertical micro-channel. Alexandria Eng J 57(2):983–993. https://doi.org/10.1016/j.aej.2017.01.038